EVOLUTIONARY INTENSITY MEASURES FOR MORE ACCURATE AND INFORMATIVE EVALUATION OF LIQUEFACTION TRIGGERING

Samuel S. Sideras

A dissertation

submitted in partial fulfillment of the

requirements for the degree of

Doctor of Philosophy

University of Washington

2019

Reading Committee:

Steven L. Kramer, Chair

Pedro Arduino

Jeffrey Berman

Brett Maurer

Program Authorized to Offer Degree:

Civil & Environmental Engineering

© Copyright 2019

Samuel S. Sideras

University of Washington

Abstract

EVOLUTIONARY INTENSITY MEASURES FOR MORE ACCURATE AND INFORMATIVE EVALUATION OF LIQUEFACTION TRIGGERING

Samuel S. Sideras

Chair of the Supervisory Committee:
Professor Steven L. Kramer
Civil & Environmental Engineering

Soil liquefaction is a seismic hazard that can have a devastating effect on the stability of buildings, bridges, dams, and other critical infrastructure elements. Accurate evaluation of liquefaction hazards requires accurate evaluation of the potential for triggering of liquefaction, and its effects. A recently developed framework for evaluation of liquefaction hazards considers the timing of the liquefaction process, and requires consideration of the response of liquefiable soils to transient loading histories – an aspect of behavior of liquefiable soils that has not previously been quantified. The development of this framework served as the motivation for the current study.

Specifically, the goal of this study was to evaluate evolutionary intensity measures, or measures of the earthquake loading that build up with time over the duration of the ground motion, for prediction of the initiation of liquefaction. This represents the critical first step in the timing-based framework. This study used both cyclic simple shear and centrifuge testing to systematically investigate the response of liquefiable soils to fully transient earthquake loading

histories. The results of these tests were used to evaluate the efficiency of evolutionary intensity measures that are typically associated with the initiation of liquefaction.

In addition, observations from these tests identified key aspects of an earthquake loading history that are closely related to the generation of excess pore pressure and the initiation of liquefaction. These observations were used to develop a new evolutionary intensity measure that was able to predict the pore pressure response from the laboratory test programs more efficiently than existing intensity measures. The insights that were generated by this study offer the potential to dramatically reduce the uncertainty in the prediction of the initiation of liquefaction as compared to the conventional procedures used in current design practice.

TABLE OF CONTENTS

List of Figures vii

List of Tables xx

Chapter 1. Introduction 1

1.1 Project Goals 2

1.2 Document Organization 2

Chapter 2. Liquefiable Soil Behavior 5

2.1 General Mechanics of Liquefiable Soils 6

2.2 Liquefaction Susceptibility 7

2.2.1 Historical Criteria 8

2.2.2 Geologic Criteria 8

2.2.3 Compositional Criteria 9

2.2.4 State Criteria 10

2.3 Initiation of Liquefaction 15

2.3.1 Flow Liquefaction 15

2.3.2 Cyclic Mobility 18

2.3.3 Evaluation of Initiation of Liquefaction 20

2.4 Effects of Liquefaction 39

2.4.1 Alteration of Ground Motion 39

2.4.2 Sand Boils 45

2.4.3 Settlement 46

2.4.4 Instability 47
2.4.5 Lateral Spreading 49
2.5 Discussion 51
Chapter 3. Performance-based Earthquake Engineering (PBEE) 53
3.1 Overview of PBEE Framework 53
3.1.1 Probabilistic Seismic Hazard Analysis 54
3.1.2 PBEE Equation 55
3.1.3 Graphical Representation of PBEE Framework 57
3.1.4 Introduction to Uncertainty in PBEE Framework 58
3.2 Effects of Predictability, Efficiency and Sufficiency 59
3.3 Discussion 62
Chapter 4. Timing-based Framework for Liquefaction Hazard Evaluation using Evolutionary Intensity Measures 63
4.1 Evolutionary Intensity Measures 64
4.2 Framework Development 70
4.2.1 Liquefaction Resistance Curve 70
4.2.2 Loading-response Curves 72
4.2.3 The Complete Framework 73
4.3 Verification of Timing-based Framework 75
4.4 Application of Timing-Based Framework 76
4.5 Probabilistic Implementation of Timing-based Framework 79
4.5.1 Uncertainty in the Time of Liquefaction 80

4.5.2 Uncertainty in Pre- and Post-triggering Intensity Measures....80
4.5.3 Uncertainty in the Engineering Demand Parameter....86
4.5.4 Performance-based Implementation of the Timing-based Framework....86
4.6 Discussion....88
Chapter 5. Prior Work on Identification of Evolutionary IMs for Evaluation of Liquefaction Triggering....91
5.1 Kramer and Mitchell (2006)....91
5.2 Abegg (2010)....94
5.3 Dashti and Karimi (2017)....100
5.4 Discussion....106
Chapter 6. Cyclic Simple Shear experimental testing program....109
6.1 Introduction....110
6.2 CSS Testing Overview....111
6.2.1 Soil Description....111
6.2.2 CSS Apparatus and Specimen Preparation....112
6.2.3 CSS Test Data Processing....115
6.3 CSS Tests with Harmonic Loading....115
6.3.1 Constant Amplitude Harmonic Loading....116
6.3.2 Irregular Harmonic Loading....122
6.3.3 Modulated Harmonic Loading....127
6.3.4 Discussion....140
6.4 CSS Tests with Transient Loading....141

6.4.1 Development of Transient Loading Histories....142
6.4.2 Example Results....153
6.4.3 CSS Dataset Used to Analyze IM Efficiency....156
6.4.4 Computing Accelerations from CSS Shear Stress Histories....160
6.5 Relationship Between Pore Pressure and Standard Intensity Measures....166
6.5.1 Surface Fitting Methodology....167
6.5.2 Results of Surface Fitting Using Standard Intensity Measures....179
6.5.3 Efficiency of Standard Intensity Measures for Prediction of Initiation of Liquefaction....190
6.5.4 Discussion....198
6.6 Liquefaction-specific Intensity Measure....203
6.6.1 Development of a Liquefaction-specific Intensity Measure....203
6.6.2 Implementation of the Liquefaction-specific Intensity Measure....213
6.6.3 Results of Liquefaction-specific Intensity Measure Optimization....214
6.7 Numerical Modeling of Transient CSS Tests....222
6.7.1 Constitutive Models and Model Calibration....222
6.7.2 Relative Density Calibration....224
6.7.3 Results....225
6.7.4 Discussion....231
6.8 Discussion....231
Chapter 7. Centrifuge Testing Program....235
7.1 Introduction....235
7.2 Other Centrifuge Studies for Models Subjected to Multiple Shaking Events....238

7.2.1 El-Sekelly et al. (2016) 238
7.2.2 Darby et al. (2017), Darby et al. (2018), and Darby et al. (2019) 243
7.2.3 Discussion 249
7.3 Centrifuge Loading Histories 250
7.4 Centrifuge Experimental Testing Program 255
7.4.1 Centrifuge Model Construction 257
7.4.2 Centrifuge Model Sensors 260
7.5 Processing of Centrifuge Data 266
7.5.1 Processing of acceleration, pore pressure, and settlement data 266
7.5.2 Development of Acceleration and Pore Pressure Time History Data for Analyses 267
7.5.3 Estimation of Relative Density 287
7.5.4 Experiment 1 Data Processing 297
7.5.5 Experiment 2 Data Processing 304
7.5.6 Experiment 3 Data Processing 314
7.5.7 Experiment 4 Data Processing 317
7.5.8 Experiment 5 Data Processing 321
7.5.9 Experiment 6 Data Processing 327
7.5.10 Uncertainties in centrifuge modeling 330
7.6 Observations from Centrifuge Testing Program 331
7.6.1 Relationship Between the Loading History and Excess Pore Pressure 332
7.6.2 Discussion 343
7.7 Evaluation of IM Efficiency Using the Centrifuge Test Data 344
7.7.1 Methodology to Evaluate IM Efficiency using Centrifuge Test Data 344

7.7.2 Efficiency of Evolutionary Intensity Measures to Predict the Pore Pressure Response from Centrifuge Data 347
7.8 Discussion 365
Chapter 8. Summary, Conclusions, and Recommendations for Future Research 369
8.1 Summary 370
8.2 Conclusions 372
8.3 Recommendations for Future Research 374
Bibliography 377
Appendix A: Transient Cyclic Direct Simple Shear Test Summaries 387
Appendix B: Numerical Analyses of Transient Cyclic Direct Simple Shear Tests 409
Appendix C: Centrifuge Test Summaries 431
Appendix D: Centrifuge Test regression analysis Summaries 649

LIST OF FIGURES

Figure 1.1: Flow-chart illustrating the various topics presented in this dissertation. 4
Figure 2.2. Example of generation of excess pore pressure 7
Figure 2.3: Stress-strain (a) and stress-void ratio (b) curves for a dense and a loose sample tested at the same effective confining pressure. 11
Figure 2.4: Behavior of loose and dense samples under drained and undrained loading conditions 12
Figure 2.5: Castro results for liquefaction, limited liquefaction and dilation 13
Figure 2.6: Steady state line in e-p'-q space with projections onto the q-p', e-q and e-p' planes 14
Figure 2.7: Flow liquefaction surface 16
Figure 2.8: Initiation of flow liquefaction during monotonic and cyclic loading 17
Figure 2.9: Zone of susceptibility for flow liquefaction 17
Figure 2.10: Zone of susceptibility for cyclic mobility 18
Figure 2.11: Example of stress path behavior during cyclic mobility 19
Figure 2.12: Behavior of Sacramento River Sand to undrained cyclic triaxial test performed by Boulanger and Truman (1996) 20
Figure 2.13: Cyclic simple shear tests on reconstituted clean sand by Boulanger and Seed (1995) 22
Figure 2.14: Comparison of MSF relationships from Boulanger and Idriss (2014), Liu et al. (2001), and Cetin et al. (2018). 27
Figure 2.15: Comparison of overburden correction factors from Youd et al. (2001), Boulanger and Idriss (2014), and Cetin et al. (2018). 29
Figure 2.16: CRR-SPT relationships derived from case history data, from Idriss and Boulanger (2010) 30
Figure 2.17: I_H-SPT scatter plots including liquefaction resistance curves from Kayen and Mitchell (1997). 33
Figure 2.18: NED case histories and liquefaction resistance curve from Green (2001) ...37

Figure 2.19: Yerba Buena Island acceleration time history, East-West component, highlighting the three temporal sections described by Zhang (2009) 41
Figure 2.20: East-West components of the acceleration histories from (a) Yerba Beuna Island and (b) Treasure Island recording stations.....42
Figure 2.21: Fourier amplitude spectrum for Yerba Buena Island and Treasure Island ...43
Figure 2.22: Surface recording of liquefied soil profile from centrifuge testing at the surface and at the base of the model illustrating dilatancy spikes, and amplification. 44
Figure 2.23: Stacked plot showing the recorded base and surface acceleration time histories and a colormap of the variation in r_u in the underlying soil profile. 45
Figure 2.24: Photo of sand boils taken after the 2011 Christchurch earthquake 46
Figure 2.25: Normalized residual shear strength ratio as a function of corrected SPT blow count for liquefied sands.....49
Figure 2.26: Contours of maximum shear strain as a function of CSR and corrected SPT blow count based on procedure proposed by Idriss and Boulanger (2008).....50
Figure 2.27: Illustration of the relationship between the timing of liquefaction and lateral spreading displacement from a centrifuge test 51
Figure 3.1: Schematic of PBEE analysis process. 55
Figure 3.2: Examples of (a) IM hazard curve and (b) IM-EDP fragility curves. 57
Figure 3.3: Graphical schematic of PBEE process. 58
Figure 3.4: Effect of uncertainty in PBEE framework using closed form solutions 59
Figure 3.5: Illustration of the effects of uncertainties for a hypothetical site.....61
Figure 4.1: Comparison of two motions Motion A (a) and Motion B (b) that have identical PGA/MSF 63
Figure 4.2: Comparison of the cycle weighting factors (a) and magnitude scaling factors (b) used to compute PGA_m using the procedures of Liu et al. (2001) and Boulanger and Idriss (2014).....67
Figure 4.3: Evolutionary IM behavior for two acceleration time histories using IMs defined in Table 4.1. 68
Figure 4.4: Results of a centrifuge experiment where lateral spreading was observed.....69

Figure 4.5: Generic liquefaction resistance curve based on corrected SPT resistance and the IM used to evaluate liquefaction triggering, IM^{trig} 71
Figure 4.6: Combining liquefaction resistance curves and evolutionary IM time histories to determine the timing of liquefaction.....71
Figure 4.7: Determining the post-liquefaction loading based on the time of liquefaction determined from the liquefaction resistance relationship. 72
Figure 4.8: Loading-response curves showing contours of multiple levels of displacement, δ, as a function of post-triggering loading and the corrected SPT blow count of the liquefiable soil layer. 73
Figure 4.9: Proposed framework for liquefaction hazard evaluation. 73
Figure 4.10: Illustration of application of the proposed framework for soils of different densities. 74
Figure 4.11: Soil profile used in the analyses from Kramer et al. (2016) and Greenfield (2017) 75
Figure 4.12: Spectrum compatible motions (a) and relationship between IM^{trig} and IM^{eff}_P (b) using IM^{trig} defined using PGA_m and IM^{eff}_P defined using I_A from study by Kramer et al. (2016).....77
Figure 4.13: Timing-based framework for prediction of the lateral spreading displacement, δ from Kramer et al. (2016) 78
Figure 4.14: Timing-based framework for prediction of the lateral spreading displacement, δ from Kramer et al. (2016) including uncertainty in the SPT resistance and the liquefaction triggering relationship.....79
Figure 4.15: Example of evolution of parameters α_1 and α_2 using Motion B from Figure 4.3. 82
Figure 6.16: Relationship between α_1 and α_2 from Greenfield (2017).....83
Figure 6.17: Mean and variance in α_1 and α_2 from Greenfield (2017) 83
Figure 4.18: Calculated and fitted beta distribution parameters for the analyses performed by Greenfield (2017).....85
Figure 5.1: Generic soil profile used by Kramer and Mitchell (2006). 92

Figure 5.2: Average pore pressure ratio efficiency plots for (a) peak acceleration and (b) I_A, from Kramer and Mitchell (2006). 93
Figure 5.3: Peak acceleration sufficiency plots for (a) *M* and (c) log*R* and I_A sufficiency plots for (b) *M* and (d) log*R,* from Kramer and Mitchell (2006). 93
Figure 5.4: Characteristics of CAV_5 for liquefaction evaluation: (a) efficiency of pore pressure generation, (b) magnitude sufficiency, and (c) distance sufficiency, from Kramer and Mitchell (2006). 94
Figure 5.5: Generic profile used in numerical study by Abegg (2010) 95
Figure 5.6: General methodology for motion selection, from Abegg, 2010. 96
Figure 5.7: Time histories of the four motions identified in Figure 5.6, from Abegg, 2010.97
Figure 5.8: IM-D_r plots for EDP levels of $r_{u,crit}$ = 1.0, corresponding to the initiation of liquefaction. Upper plot shows the standard deviations of each IM across each of the eight soil profiles from Abegg (2010). 98
Figure 5.9: Standard deviations of the IM-EDP relationship across range of $r_{u,crit}$ levels and relative density levels from Abegg (2010). 99
Figure 5.10: Sufficiencies of each candidate IM with respect to both magnitude, *M*, and the log of source to site distance, *R*, in terms of both r_u-averaged and D_r-averaged sufficiencies from Abegg (2010). 100
Figure 5.11: Schematic of the soil profile and structure that was evaluated in the parametric study of Dashti and Karimi (2017).....101
Figure 5.12: Peak excess pore pressure ratio in the far-field as a function of the PGA of the base input motion for two models from Dashti and Karimi (2017).....103
Figure 5.13: Residuals of the IM-EDP relationship as a function of the moment magnitude and source-to-site distance from Dashti and Karimi (2017).....104
Figure 5.14: Mean and standard deviation of σ, c^m, and c^r for the ten most efficient IMs at predicting the peak r_u value in the far field from Dashti and Karimi (2017).....105
Figure 6.1: Schematic of NGI-type cyclic simple shear apparatus. 111
Figure 6.2: Grain size distribution of Nevada sand 112
Figure 6.3: UT-Austin CSS testing apparatus schematic 113

Figure 6.4: The new mold fabricated for the SGI-type stacked ring and membrane assembly (from Kwan, 2015). 114
Figure 6.5: Liquefaction resistance curves for constant amplitude harmonic CSS tests. 117
Figure 6.6: r_u as a function of the cycle ratio for the constant amplitude harmonic load tests. 118
Figure 6.7: The change in excess pore pressure ratio, Δr_u, as a function of the cycle ratio119
Figure 6.8: Constant amplitude harmonic loading test summary plot for a sample at a relative density of 51% with an applied CSR of 0.14 where liquefaction was observed after 21 cycles. 121
Figure 6.9: Irregular harmonic loading test summary 123
Figure 6.10: Final r_u value (a) and r_u value following the first cycle (b) as a function of relative density from the irregular harmonic loading tests. 124
Figure 6.11: Summary of irregular harmonic tests corrected for relative density. 125
Figure 6.12: Development of a taper-up modulated harmonic loading. 128
Figure 6.13: Development of a taper-down modulated harmonic loading. 129
Figure 6.14: Enveloping functions and normalized loading input time histories for the taper-up and taper-down modulated harmonic loading histories. 130
Figure 6.15: Summary of test results for the taper-up modulated harmonic loading performed on loose sand samples. 132
Figure 6.16: Taper-up modulated harmonic test result for Test 2013-0619. 134
Figure 6.17: Summary of test results for the taper-down modulated harmonic loading performed on loose sand samples. 136
Figure 6.18: Summary of test results for the taper-up modulated harmonic loading performed on dense sand samples. 138
Figure 6.19: Comparison of taper-up and taper-down Tests 2013-0621 and 2013-0719 on loose sand samples. 140
Figure 6.20: Motions selected for use in CSS testing program based on IM behavior. ..143
Figure 6.21: Motions selected for use in CSS testing program based on IM behavior. ..144
Figure 6.22: Scatterplot matrix showing the relationships of the IMs for the motions selected based on the IM behavior.....145

Figure 6.23: Summary plots for motions selected based on the rate of energy buildup..146
Figure 6.24: Motions selected for use in CSS testing based on their rate of energy buildup. 147
Figure 6.25: Husid parameter for the six motions selected based on their rate of energy buildup. 148
Figure 6.26: Soil profile used in ProSHAKE to generate shear stress loading histories used as input for CSS testing. 150
Figure 6.27: Normalized shear stress loading histories from ProSHAKE analyses that produced the largest difference between the acceleration and shear stress time histories at the critical layer. 152
Figure 6.28: Example results from a transient CSS test. 154
Figure 6.29: Example results from a transient CSS testing where liquefaction was not reached during the transient loading portion of the history. 155
Figure 6.30: Results from CSS Test 130115. 157
Figure 6.31: Results from CSS Test 130115 over the interval of 60-120 seconds. 158
Figure 6.32: Schematic of layered soil deposit for equivalent-linear calculations 161
Figure 6.33: Acceleration time histories comparing ProSHAKE to the shear stress-based equivalent linear code written for this project (a) the entire time history and (b) zoomed in on the first 10 seconds of the time history. 164
Figure 6.34: Transfer function between shear stress and acceleration for both ProSHAKE and the shear stress-based equivalent linear code. 165
Figure 6.35: (a) Acceleration response at 5.5 m depth derived using shear stress-based equivalent-linear analysis using the soil profile shown in Figure 6.26 and (b) shear stress input time history. 166
Figure 6.36: Example of hypothetical test results showing (a) Pore pressure ratio, (b) acceleration and (c) evolutionary IM time histories generated by CSS or centrifuge test. 168
Figure 6.37: Example of a hypothetical pore pressure ratio-IM plot. 168
Figure 6.38: Schematic of hypothetical experimental data analysis to illustrate the proposed method. 170
Figure 6.39: IM-D_r fit at the time of liquefaction (r_u = 0.99) for the Standard IMs 172

Figure 6.40: Investigation of the shape of the r_u function based on the evolutionary IM normalized by an initial estimate of the IM at the time of liquefaction (Equation 6.22) for the standard IMs.....173
Figure 6.41: Results from a transient CSS test 130925. 175
Figure 6.42: Results from Test ID 130925 (Test 18) showing the acc, r_u, and standard IM time histories, a plot of the normalized standard IM vs r_u, and the stress path.....177
Figure 6.43: Investigation to the shape of the r_u function based on IM normalized by an initial estimate of the IM at the time of liquefaction (Equation 6.22) with a fit provided in Equation 6.23 shown for (a) PGA_{mL}, (b) PGA_{mB}, (c) I_a, (d) CAV, and (e) CAV_5.....178
Figure 6.44: Summary of the surface fit results of PGA_{mL} 180
Figure 6.45: Summary of the surface fit results of PGA_{mB} 181
Figure 6.46: Summary of the surface fit results of I_A 182
Figure 6.47: Summary of the surface fit results of CAV.....183
Figure 6.48: Summary of the surface fit results of CAV_5 184
Figure 6.49: Summary response of Test 130711-02 (Ref. No. 8) 186
Figure 6.50: Summary of the acceleration and IM behavior for Test 130711-02 188
Figure 6.51: Rate of change of r_u, PGA_{mB}, and CAV for Test 130711-02.....189
Figure 6.52: Measured and fitted values of (a) PGA_{mL}, (b) PGA_{mB}, (c) I_A, (d) CAV, and (e) CAV_5 at the initiation of liquefaction ($r_u = 0.99$) as a function of relative density. 191
Figure 6.53: Relationship between r_u and PGA_{mB} and CAV with the time of initiation of phase transformation indicated as red scatterpoints.....193
Figure 6.54: Correlation between the IM value at the onset of phase transformation and the IM value at the initiation of liquefaction 194
Figure 6.55: Residuals of the $IM_{liq}|IM_{PT}$ fit as a function of relative density and the difference in the Husid parameter between the onset of phase transformation and the initiation of liquefaction. 195
Figure 6.56: Correleation between relative density and the amount of loading betwee the onset of phase transformation and the initiation of liquefaction as evaluated using the Husid parameter. 196

Figure 6.57: Measured and fitted values of (a) PGA_{mL}, (b) PGA_{mB}, (c) I_A, (d) CAV, and (e) CAV_5 at the onset of phase transformation behavior as a function of relative density.197
Figure 6.58: Development of cycle counting- and integral-based IMs for irregular harmonic loading showing time histories 201
Figure 6.59: Comparison of normalized r_u and normalized PGA_{mB} and CAV for irregular harmonic Tests A (top) and E (bottom). 202
Figure 6.60: General behavior of the cycle ratio factor for different values of the exponent θ_3 206
Figure 6.61: Behavior of normalized LIM with a constant amplitude harmonic loading for various values of θ_1. 208
Figure 6.62: Behavior of LIM_0 with constant amplitude harmonic loading. 209
Figure 6.63: Behavior of LIM_0 with a linearly increasing harmonic loading. 210
Figure 6.64: Behavior of LIM_0 with a linearly decreasing harmonic loading. 212
Figure 6.65: Summary of the surface fit results of LIM 215
Figure 6.66: Plots of the acceleration, r_u, and LIM time histories for Test 130215-02. ..217
Figure 6.67: Measured and fitted values of LIM at the onset of phase transformation behavior as a function of relative density. 218
Figure 6.68: Comparison of the evolutionary response of PGA_{mB} and LIM for Test 130215-02 219
Figure 6.69: Comparison of the evolutionary response of PGA_{mB} and LIM for Test 130711-02 221
Figure 6.70: Calibration results for PDMY02 and PM4Sand compared to the Boulanger and Idriss (2014) liquefaction triggering curve. 224
Figure 6.71: Comparison of CSS test data and numerical simulations using PDMY02 and PM4Sand for Test 130118 226
Figure 6.72: Comparison of CSS test data and numerical simulations using PDMY02 and PM4Sand for Test 130711-02 228
Figure 6.73: Comparison of CSS test data and numerical simulations using PDMY02 and PM4Sand for Test 130119 230
Figure 7.1: Side view of RPI centrifuge. 237

Figure 7.2: Centrifuge model and sensor layout from the study of El-Sekelly et al. (2016)239
Figure 7.3: Excess pore pressure response from El-Sekelly et al. (2016) for a centrifuge model subjected to multiple shaking events. 240
Figure 7.4: Change in V_{s1} and relative density from El Sekelly et al. (2016) for a centrifuge model subjected to multiple shaking events. 241
Figure 7.5: The peak r_u value as a function of relative density and V_{s1} (after El-Sekelly et al., 2016) 242
Figure 7.6: Relationship between maximum r_u and permanent vertical strain from El-Sekelly et al. (2016). 243
Figure 7.7: Centrifuge model and sensor layout from the study of Darby et al. (2019)..244
Figure 7.8: Test summary of Model 2 (D_r 25%) from Darby et al. (2019) 245
Figure 7.9: Example of model densification based on CPT tip resistances from Darby et al. (2017) for Model 2 (D_r = 25%).....246
Figure 7.10: Example of model densification based on CPT tip resistances from Darby et al. (2017) for Model 3 (D_r = 85%).....247
Figure 7.11: Comparison of relative density evaluated using mini-CPT data conducted during testing and the relative density estimated based on surface settlements for the 3 centrifuge models provided by Darby et al. (2019). 248
Figure 7.12: Motions selected for use in centrifuge testing based on IM behavior.....252
Figure 7.13: Motions selected for use in centrifuge testing based on 253
Figure 7.14: Motions selected for use in centrifuge testing based on IM behavior.....254
Figure 7.15: Scatterplot matrix showing the relationships of the IMs for the motions selected based on the IM behavior for use in centrifuge testing.....255
Figure 7.16: One-dimensional laminar box used in centrifuge tests. 258
Figure 7.17: Pluviation device used to construct centrifuge models, (a) side view of device, (b) view of the holes drilled in bottom of device. 259
Figure 7.18: Interior centrifuge sensors, plan view and Section AA.....261
Figure 7.19: Interior centrifuge sensors Section BB. 261
Figure 7.20: Settlement monuments used in the centrifuge study. 262
Figure 7.21: Typical placement of PPT in centrifuge model.....262

Figure 7.22: Typical placement of accelerometers and settlement monument in centrifuge model. 263
Figure 7.23: Sensors placed on exterior laminar rings of centrifuge model. 264
Figure 7.24: Sensors placed on baseplate of centrifuge model 264
Figure 7.25: Typical placement of sensors on laminar ring and front of baseplate and actuator for centrifuge tests. 265
Figure 7.26: Accelerometers placed on baseplate to measure vertical and transverse response of the base input motion. 265
Figure 7.27: Example of the recorded acceleration, and computed velocity, and displacement response from interior ACCs during Experiment 3 Test 3. 268
Figure 7.28: Example of the recorded pore pressure response for Experiment 3 Test 3.270
Figure 7.29: Example of r_u time histories from Experiment 3 Test 3.....271
Figure 7.30: Isochrones of excess pore pressure as a function of depth for Experiment 3 Test 3. 273
Figure 7.31: Plots of the base and surface acceleration time histories, and a colormap of the r_u as a function of depth and time for Experiment 3 Test 3. 274
Figure 7.32: Acceleration and r_u time histories and colormap of hydraulic gradient as a function of time and depth for Experiment 3 Test 3. 276
Figure 7.33: Centrifuge test summary plot for Experiment 3 Test 3. 278
Figure 7.34: Determination of c_v for each individual layer based on the dissipation portion of the pore pressure time history (Step 1) for Experiment 3 Test 3. 282
Figure 7.35: Adjustment of excess pore pressures based on theoretical dissipation time histories for Experiment 3 Test 3. 284
Figure 7.36: Comparison of the recorded acceleration, r_u, and drainage-corrected r_u time histories for Layer 3 in Experiment 3 Test 3. 286
Figure 7.37: Total settlement (a) and total vertical strain (b) as a function of test number for Experiment 3. 290
Figure 7.38: Box plots of the peak pore pressure developed in each layer during Experiment 3. 291

Figure 7.39: Relationship between vertical strain and the average r_u and peak shear strain for Layers 1 and 4 from Experiment 3. 292
Figure 7.40: Change in layer height (a), relative density (b), and input base motion amplitude with respect to PGA_{mb} (c) as a function of test number for Experiment 3. 293
Figure 7.41: Relative density profiles for Experiment 3 using all of the recorded settlement data. 294
Figure 7.42: Relative density profiles for Experiment 3 excluding the recorded settlement from Layer 4. 295
Figure 7.43: Comparison of relative density computed for each individual layer and the average relative density of the entire profile using the surface settlement for Experiment 3.296
Figure 7.44: Acceleration and r_u response for each of the six liquefiable soil layers for Experiment 1 Test 2. 300
Figure 7.45: Comparison of the absolute value of the recorded acceleration time history, the pore water pressure from the raw data file, and the recorded surface settlement for Experiment 1 Test 2.....301
Figure 7.46: Comparison of the absolute value of the recorded acceleration time history, the pore water pressure from the raw data file, and the recorded surface settlement for Experiment 3 Test 3.....302
Figure 7.47: Evolution of relative density as a function of test number for Experiment 1304
Figure 7.48: Acceleration and r_u response for each of the six liquefiable soil layers for Experiment 2 Test 4. 308
Figure 7.49: Comparison of the absolute value of the recorded acceleration time history, the pore water pressure from the raw data file, and the recorded surface settlement for Experiment 2 Test 4.....309
Figure 7.50: Average vertical strain as a function of average peak r_u and average peak shear strain for Experiment 2. 311
Figure 7.51: Volumetric strain as a function peak shear strain and relative density from Ishihara and Yoshimine (1992) 312
Figure 7.52: Average vertical strain as a function of average peak r_u including the estimated vertical strain for Experiment 2 Test 6. 312

Figure 7.53: Evolution of relative density as a function of test number for Experiment 2313
Figure 7.54: Evolution of relative density as a function of test number for Experiment 4320
Figure 7.55: Average vertical strain as a function of the average peak r_u for Layers 1 and 2 in Experiment 5. 325
Figure 7.56: Acceleration and r_u response in Layers 1 and 2 for Experiment 5 Test 7 ...326
Figure 7.57: Evolution of relative density as a function of test number for Experiment 5327
Figure 7.58: Evolution of relative density as a function of test number for Experiment 6330
Figure 7.59: Comparison of the acceleration time history, excess pore pressure, and evolutionary IM response for Experiment 6 Test 2 Layer 2. 333
Figure 7.60: Comparison of the acceleration time history, excess pore pressure, and evolutionary IM response for Experiment 4 Test 26 Layer 2. 335
Figure 7.61: Comparison of the acceleration time history, excess pore pressure, and evolutionary IM response for Experiment 5 Test 7 Layer 3. 338
Figure 7.62: Comparison of the acceleration time history, excess pore pressure, and evolutionary IM response for Experiment 5 Test 7 Layer 3 from 20 to 40 seconds. 339
Figure 7.63: Comparison of the acceleration time history, excess pore pressure, and evolutionary IM response for Experiment 5 Test 7 Layer 3 from 55 to 90 seconds. 340
Figure 7.64: Comparison of the acceleration time history, excess pore pressure, and evolutionary IM response for Experiment 2 Test 9 Layer 3. 342
Figure 7.65: Histogram of maximum r_u generated within the liquefiable layer for all of the centrifuge tests 347
Figure 7.66: Results of regression analyses using Equation 7.5 and the entire centrifuge dataset for PGA_{mB}. 348
Figure 7.67: Results of regression analyses using Equation 7.6 and the entire centrifuge dataset for PGA_{mB}. 352
Figure 7.68: Comparison of K_σ from the simplified liquefaction triggering procedures and k_σ computed directly from the coefficient β_3 evaluated from the regression analyses for each IM. 354
Figure 7.69: Comparison of K_σ from the simplified liquefaction triggering procedures and k_σ evaluated using a manually adjusted β_3 coefficient 356

Figure 7.70: Regression results for stress-dependent density profile using the supplementary data from Darby et al. (2019). 358
Figure 7.71: Assumed stress-dependent relative density profile, shown for average relative densities of 40 and 70%. 359
Figure 7.72: Comparison of K_σ from the simplified liquefaction triggering procedures and k_σ evaluated the coefficient β_3 evaluated from regression assuming a stress-dependent relative density profile. 360
Figure 7.73: Summary of σ_{ln} from regression on each individual centrifuge experiment362
Figure 7.74: Log residuals from the regression analyses plotted as a function of the peak r_u within the given layer from the prior test 364

LIST OF TABLES

Table 2.1: Equivalent number of cycles from Seed et al. (1975) 25
Table 2.2: Number of equivalent cycles and magnitude scaling factor from Seed et al. (1983) 25
Table 4.1: Evolutionary formulation of scalar IMs used in liquefaction hazard evaluation procedures detailed in Section 2.3.3.1. 66
Table 4.1: Uncertainty in predicted lateral displacements for PGA_m, I_A, and CAV computed using the total and post-triggering IM values from Kramer et al. (2016). 76
Table 5.2: Average standard deviation of each IM over all D_r and r_u from Abegg (2010).99
Table 5.3: Averaged sufficiency plot slope of each IM over all D_r and $r_{u,crit}$ levels. 99
Table 6.1: Soil index properties of Nevada sand 112
Table 6.2: Metadata for applied motions during CSS testing program. 149
Table 6.3: Summary of the 28 selected CSS tests from Kwan (2015). 159
Table 6.4: Standard deviation of the log residuals, σ_ε, for each of the five standard IMs computed using the fit for r_u values ranging from 0.05 to 0.99. 185
Table 6.5: Standard deviation of the log residuals, σ_{ln}, for the IM-D_r fit at the initiation of liquefaction (r_u = 0.99) for each of the five standard IMs. 191
Table 6.6: Standard deviation of the log residuals, σ_{ln}, for the IM-D_r fit at the onset of phase transformation behavior for each of the five standard IMs. 198
Table 6.7: LIM coefficients determined using constrained optimization to the transient CSS test data. 214
Table 7.1: Centrifuge parameter scaling factors 236
Table 7.2: Characteristics of input motions selected based on their IM behavior. 251
Table 7.3: Summary of centrifuge experiments. 256
Table 7.4: Nevada sand relative density properties provided by RPI. 259
Table 7.5: Experiment 1 Interior Sensor Data 298
Table 7.6: Experiment 1 Exterior Sensor Data 299
Table 7.7: Experiment 2 Interior Sensor Data 306

Table 7.8: Experiment 2 Exterior Sensors 307
Table 7.9: Experiment 3 Interior Sensor Data 315
Table 7.10: Experiment 3 Exterior Sensor Data 316
Table 7.11: Experiment 4 Interior Sensor Data 318
Table 7.12: Experiment 4 Exterior Sensor Data 319
Table 7.13: Experiment 5 Interior Sensor Data 322
Table 7.14: Experiment 5 Exterior Sensor Data 323
Table 7.15: Experiment 6 Interior Sensor Data 328
Table 7.16: Experiment 6 Exterior Sensor Data 329
Table 7.17: Summary of regression analyses using entire centrifuge dataset 353
Table 7.18: Summary of regression analyses using entire centrifuge dataset and an assumed stress-dependent relative density profile 360
Table 7.19: Summary of σ_{ln} from regression on each individual centrifuge experiment 362

ACKNOWLEDGEMENTS

I would like to thank Profs. Steven Kramer and Pedro Arduino for their support and guidance throughout my graduate studies at the University of Washington. I want to acknowledge the contributions of Prof. Chadi El Mohtar and Wing Shun Kwan (now Prof. Wing Shun Kwan) who performed the cyclic shear testing at the University of Texas, Austin. In addition, I am indebted to the staff of the geotechnical centrifuge facility at Rensselaer Polytechnic Institute who helped me during the centrifuge testing performed as part of this study. In particular I would like to highlight the contributions of Dr. Anthony Tessari and John Lawler who sacrificed their personal time to assist me with my experiments. I also greatly appreciate the thoughtful review and comments provided by Profs. Jeffrey Berman, Brett Maurer, and Paul Bodin. Most importantly I am extremely thankful for the opportunity to work with my advisor, Professor Steven Kramer, who I consider both a mentor and a friend.

DEDICATION

To my wife, Selena.

[This page intentionally left blank]

Chapter 1. INTRODUCTION

Liquefaction is a phenomenon that can occur when loose, saturated sands are subjected to loading under undrained conditions. It is most commonly associated with earthquake loading and can result in a dramatic loss of strength and stiffness in affected soil layers. Recent events in Chile, New Zealand, and Japan have demonstrated the devastating effect liquefaction can have on the stability of buildings, bridges and other critical infrastructure elements, and highlighted the need to account for liquefaction in design.

Current procedures for assessing the liquefaction hazard of a given soil deposit are based on comparing measures of the seismic loading and a soil's capacity to resist that loading. While numerous enhancements and modifications have been implemented over the years, the basic procedures used for liquefaction evaluation in current practice are nearly identical to those that were developed over 40 years ago, particularly with respect to how the earthquake loading is defined. In essence, the liquefaction potential of a soil deposit is based on a peak ground surface acceleration value. As a result, a rich, complex, transient ground motion time history is reduced to a single point, its maximum value, which is then scaled using a proxy to account for the duration of the motion. Liquefaction, however, is a phenomenon that occurs as excess pore pressure builds up over the course of the dynamic excitation. Given the numerous advances in the field of geotechnical earthquake engineering, it seems inadequate to design for a complex, transient, evolutionary process, such as liquefaction, using a static parameter calculated at a single point in a time history.

In the context of this document, evolutionary measures of ground motion intensity are parameters that build up with time over the duration of the ground motion. These measures explicitly account for both the amplitude and duration of a ground motion and would allow the missing aspect of time to be directly accounted for in liquefaction hazard evaluation. In addition, by having an intensity measure (IM), defined in the form of a time history, one could in theory track the generation of excess pore pressure, and thus could indicate not only if liquefaction would occur, but also when it would occur.

Having knowledge of the timing of the initiation of liquefaction offers the ability to divide the earthquake loading into pre- and post-initiation components. This ability to partition

the earthquake loading history has the potential to be extremely beneficial for liquefaction hazard analysis. Given that the characteristics of a soil deposit change drastically upon the initiation of liquefaction, it is reasonable to expect the triggering of liquefaction would be correlated to the loading that occurs prior to the onset of liquefaction, while the effects of liquefaction would be better correlated to the loading that occurs after liquefaction has been triggered. As opposed to merely relating the initiation of liquefaction to the total amount of loading imposed on a soil deposit, the use of evolutionary IMs offers an avenue for improving the current design methods both for determining if liquefaction will occur and predicting what the consequences will be.

1.1 PROJECT GOALS

Inspired by the ideas outlined above, Kramer et al. (2016) introduced a timing-based liquefaction hazard evaluation framework that explicitly accounts for the transient behavior of a liquefiable soil and can account for the dramatic change in the characteristics of a soil that occur after liquefaction has been triggered. The purpose of this research was to identify optimal evolutionary intensity measures for the prediction of the initiation of liquefaction. Specifically, the project goals can be detailed as follows:

- Use advances in laboratory methods and techniques to systematically investigate what aspects of an earthquake loading history are related to the generation of excess pore pressure and the initiation of liquefaction under transient loading conditions.
- Based on the results and observations made in the controlled laboratory setting, identify evolutionary ground motion intensity measures that can best predict the occurrence and timing of liquefaction.

1.2 DOCUMENT ORGANIZATION

This dissertation contains eight chapters. Following this introduction, Chapter 2 provides background information on soil liquefaction, including the general mechanics of liquefaction and the generation of excess pore pressure. Chapter 2 describes in detail the three main facets of liquefaction hazard assessment—susceptibility, initiation and effects.

Chapter 3 provides an overview on the performance-based earthquake engineering framework, which serves as the foundation for an alternative, timing-based framework for

liquefaction hazard analysis based on evolutionary intensity measures. Chapter 4 goes on to explain the timing-based liquefaction hazard framework in detail. Chapter 5 provides a review of prior studies that were performed to develop the liquefaction hazard framework with respect to the initiation of liquefaction. Chapter 6 details the CSS testing program conducted as part of this research. The CSS testing program included both simple harmonic and fully transient loading histories to methodically identify which aspects of a cyclic loading history had the strongest effect on the generation of excess pore pressures and the initiation of liquefaction for an element of soil. To extend the findings of the CSS test program, centrifuge testing was performed on model soil profiles, the results of which are summarized in Chapter 7. The centrifuge testing program simulated the response of a liquefiable soil profile subjected to earthquake loading applied at the base and provides a more realistic representation of liquefiable soil behavior as observed in the field. The final chapter, Chapter 8, reviews the work performed in this study, describes the significant conclusions that can be drawn from it, and outlines ideas for future research.

As described above, this dissertation includes several interrelated topics that explain the motivation behind, and the results of, this research study. These topics include liquefiable soil behavior, performance-based earthquake engineering, the timing-based liquefaction hazard analysis framework, and the current experimental study using CSS and centrifuge data to evaluate evolutionary intensity measures for the prediction of liquefaction triggering. Figure 1.1 provides a guide for the reader and illustrates the relationship between each of the topics that are presented in this dissertation.

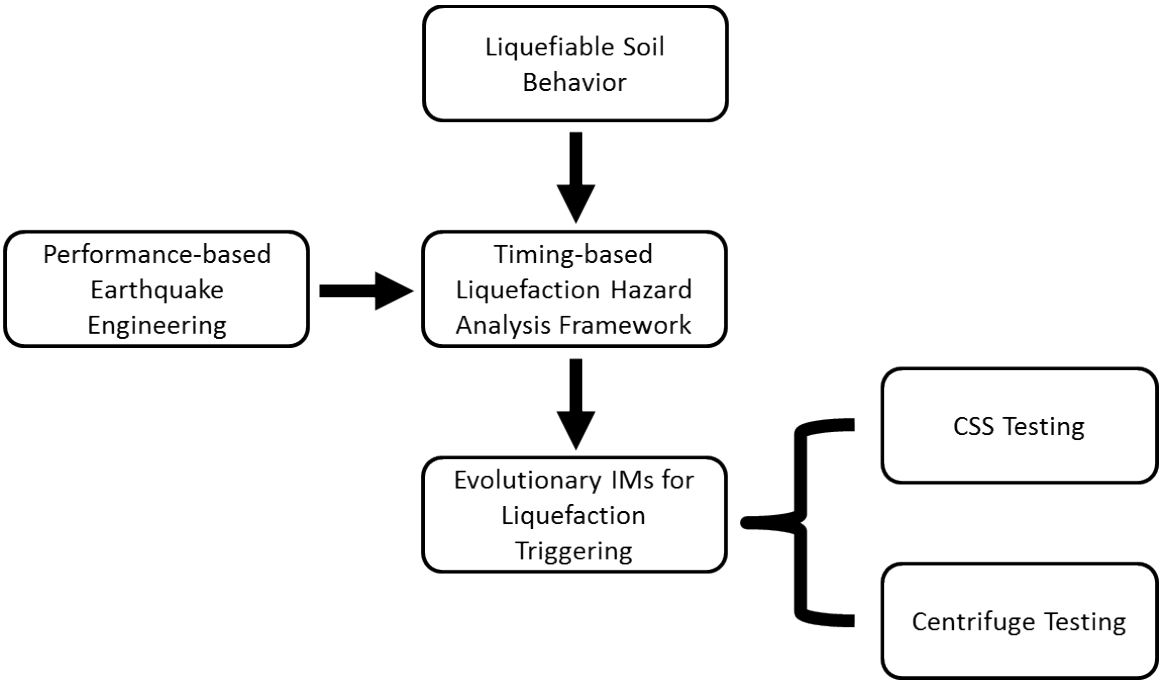


Figure 1.1: Flow-chart illustrating the various topics presented in this dissertation.

Chapter 2. LIQUEFIABLE SOIL BEHAVIOR

Liquefaction is a soil phenomenon that can drastically affect the response and stability of structures and built environments located at the ground surface. The term liquefaction has been applied to several similar phenomena, but it is broadly characterized by the dramatic loss of stiffness and shear strength of cohesionless soils due to the generation of excess pore pressure. This loss of strength and stiffness can lead to the instability of overlying, embedded and surrounding structures and have catastrophic effects on built environments.

Liquefaction results from the generation of excess pore pressure, and corresponding reduction in effective stress, within saturated cohesionless soils. During an earthquake soil undergoes rapid cyclic loading. Loose, dry sand has a tendency to densify under cyclic loading. However, if the same sand is saturated during rapid cyclic loading, undrained conditions can exist. In this case, the penchant for the sand to densify leads to an increase in pore pressure that can ultimately result in a dramatic loss of strength within the liquefiable soil deposit (Kramer 1996).

The need to account for soil liquefaction in design was formally identified from field reconnaissance following earthquakes that occurred in 1964 in Alaska and Niigata, Japan. In both events widespread liquefaction was observed and caused severe damage to nearly all forms of civil engineering structures, including buildings, foundations, roads, utilities and slopes. Following these earthquakes soil liquefaction has been extensively researched and various procedures for prediction and analysis have been proposed. A single prevailing approach, however, has yet to emerge (Abegg, 2010).

This chapter serves as the foundation for the results and discussions presented later in this document. The subsequent sections include a summary of the basic mechanics of soil liquefaction followed by an overview of liquefaction through the lens of liquefaction hazard evaluation. Generally, the framework of liquefaction hazard evaluation can be condensed to three critical aspects (Kramer, 1996):

1. Susceptibility: Is the given soil deposit vulnerable to liquefaction?
2. Initiation: If the soil is susceptible to liquefaction, will liquefaction be triggered?
3. Effects: If liquefaction is triggered, what are the outcomes?

2.1 General Mechanics of Liquefiable Soils

The term "liquefaction" has been used to describe several different events that are characterized by large shear deformations in saturated cohesionless soil caused by monotonic, transient, or repeated disturbance of the soil during undrained conditions. These large deformations are a result of softening/weakening of the soil due to the generation of pore pressure. Pore pressure is the pressure of the ground water within a soil (or rock) in gaps, or pores, between the soil particles. Excess pore pressure, u_e, refers to the amount of pore pressure in excess of hydrostatic pressure, expressed symbolically as

$$u_e = u - u_h \tag{2.1}$$

where u is the total pore water pressure and u_h is the hydrostatic pore water pressure.

If a cyclic load is applied to saturated soil under undrained conditions, the sand's tendency to densify results in the generation of excess pore pressure in order to maintain a constant volume. This increase in excess pore water pressure causes a proportional reduction of effective stress in the soil. It is this loss of effective stress that makes the saturated, cohesionless soil deposit susceptible to the large deformations observed in liquefaction case histories and laboratory tests (Kramer 1996).

A useful definition that is commonly used when discussing liquefaction is the pore pressure ratio, r_u, which is defined as

$$r_u = \frac{u_e}{\sigma'_{v0}} = \frac{u - u_h}{\sigma'_{v0}} = 1 - \frac{\sigma'_v}{\sigma'_{v0}} \tag{2.2}$$

where σ'_{v0} is the initial overburden effective stress and σ'_v is the vertical effective stress at any point in time during or after loading. The pore pressure ratio takes on values from 0 to 1 as the effective stress drops from its initial value to zero. At $r_u = 1.0$, or when the effective stress becomes 0, there are no longer any effective contact forces between the soil particles and initial liquefaction occurs. The pore pressure ratio is a convenient parameter because by normalizing the excess pore water pressure by the initial overburden stress condition, it allows for direct comparison of how close a given soil is to initial liquefaction, regardless of its depth within a soil profile (Abegg, 2010). An example of excess pore pressure generation in a centrifuge model due to earthquake loading is shown in Figure 2.2. For the given example the pore pressure ratio time history indicated initial liquefaction was triggered around 11 seconds into the record.

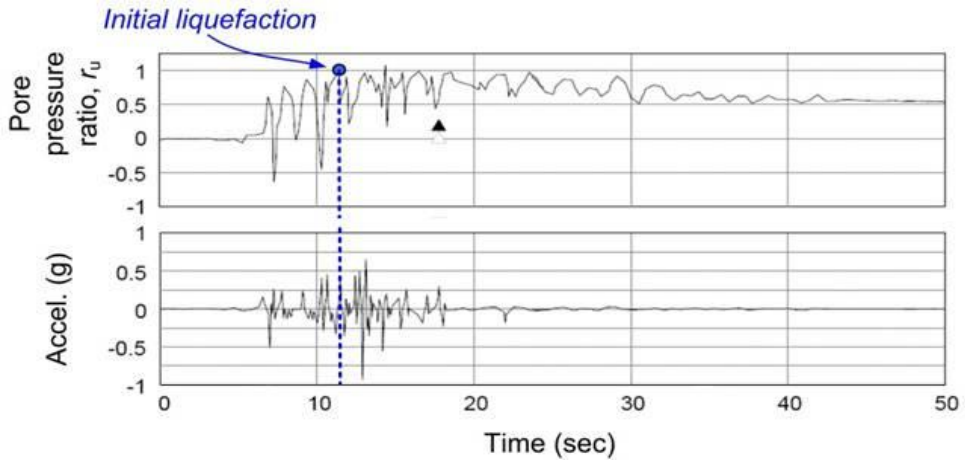


Figure 2.2. Example of generation of excess pore pressure, presented in the form of pore pressure ratio resulting from earthquake loading applied during a centrifuge test (after Brandenburg et. al, 2005).

As stated previously "liquefaction" is a term that has been used to describe several different events. While these events can have similar effects, the different mechanisms that drive the failure suggest that liquefaction can be divided into two main categories—flow liquefaction and cyclic mobility.

Flow liquefaction occurs when the shear stress required for static equilibrium is greater than the shear strength of the soil in its liquefied state and results in deformations that are driven by the static shear stress conditions. Conversely, cyclic mobility occurs when the static shear stress required for equilibrium is less than the shear strength of the liquefied soil, and deformation occurs incrementally during earthquake shaking. Throughout this document the two liquefaction failure mechanisms will be treated separately as needed, however if no distinction is explicitly made the term "liquefaction" can be assumed to apply to both cyclic mobility and flow liquefaction. The focus of the work described in this dissertation, however, will be on the cyclic mobility failure mechanism.

2.2 LIQUEFACTION SUSCEPTIBILITY

The first step in a liquefaction hazard evaluation is evaluating whether the given soils are susceptible to liquefaction. Liquefaction is most commonly associated with saturated cohesionless soils, which tend to build up excess pore pressure upon cyclic shear loading and mobilize a strength that is proportional to the effective stress. However, merely being saturated

and cohesionless does not automatically make a soil susceptible to liquefaction. This section describes several additional factors that can be used to judge the liquefaction susceptibility of a soil deposit. These factors have been grouped into four general categories, historical, geologic, compositional and state criteria (Kramer, 1996).

2.2.1 *Historical Criteria*

A large amount of information on liquefaction and liquefiable behavior has been generated by post-earthquake site investigations. Case history data and earthquake reconnaissance reports are useful in identifying specific locations and areas that have been observed to be susceptible to liquefaction from past events. They can similarly be used to outline general site conditions which have shown to be susceptible to liquefaction based on observational studies. Historical evidence can also be used to create maps of liquefaction susceptibility and can be useful for estimation of regional liquefaction hazard scenarios (Youd, 1991).

2.2.2 *Geologic Criteria*

Youd (1991) noted that liquefiable soil deposits are formed by a relatively narrow range of geologic environments. High liquefaction susceptibility is associated with loose soils that have uniform grain size distributions. Loose, uniformly graded soils are commonly associated with saturated fluvial, colluvial, and aeolian deposits. Additionally, liquefaction has been observed in alluvial-fan, alluvial-plain, beach, terrace, playa, and estuarine deposits. Loose, human-made fills are also very susceptible to liquefaction. In addition, age has been observed to affect the liquefaction susceptibility, as newer deposits tend to be more susceptible than older soil deposits (Kramer, 1996).

Another vital geologic aspect is the groundwater depth, since liquefaction can only occur in saturated soils. Liquefaction susceptibility decreases as the depth of the groundwater table increases, and is most commonly associated with sites where the groundwater is within a few meters of the ground surface. At sites where the groundwater depth fluctuates seasonally, the liquefaction hazard can fluctuate seasonally as well (Kramer, 1996).

2.2.3 *Compositional Criteria*

Liquefaction is a product of excess pore pressure. A soil's affinity to develop pore pressure is closely related the soil's potential for volume change; therefore, compositional traits that are associated with high volume change potential tend to be associated with high liquefaction susceptibility. Compositional characteristics that influence volume change include particle size and plasticity, particle shape and gradation.

2.2.3.1 Particle Size and Plasticity

In general sands are considered to be the most liquefiable soils because of their tendency to change volume upon shear loading. Typically, fine-grained soils are cohesive and not as susceptible to volume change during shearing, while coarser-grained soils such as gravels are often too permeable to sustain high excess pore pressures. Originally, it was believed that only sands were susceptible to liquefaction, however liquefaction has been observed in nonplastic silts (e.g. Ishihara, 1985) as well as in gravels (e.g. Evans and Seed, 1987). These findings suggest that particle size alone is not a good indicator of liquefaction susceptibility, and additional soil characteristics, most notably plasticity, play a vital role as well.

More recent research has been conducted on the liquefaction susceptibility of fine-grained soils. Studies based on cyclic laboratory testing (Boulanger and Idriss, 2006) and laboratory testing and field observations (Bray et al. 2004) have suggested liquefaction susceptibility criteria that are a function of plasticity, which for particle sizes below 0.075 mm is more closely related to minerology than to solely particle size (Beroya et al., 2009). Boulanger and Idriss (2006) recommended that soils with a plasticity index (PI) less than or equal to seven can generally be considered "sand-like" and therefore susceptible to liquefaction. Bray et al. (2004) concluded that a soil is susceptible to liquefaction if the PI was less than or equal to 12 and the ratio of the soil's natural water content (w_c) to its liquid limit (LL) is greater than or equal to 0.85. For practical purposes a soil with a PI below seven is generally considered liquefiable and a soil with a PI above 12 is generally considered non-liquefiable. Soils with PIs between 7 and 12 warrant additional laboratory testing to determine their liquefaction susceptibility.

2.2.3.2 Particle Shape

Rounded soil particles tend to densify more easily than soils whose particles are more angular. As a result, soils composed of rounded particles are more susceptible to liquefaction than soils composed of angular particles. Fluvial and alluvial deposition are often associated with rounded soil particles. In addition, these types of deposits are commonly loose and saturated, and as a result are regarded as having high liquefaction susceptibility.

2.2.3.3 Gradation

Gradation also affects liquefaction susceptibility. In well-graded soils, smaller particles fill the voids between the larger particles. This reduces the capacity for volume change and increases the density of the soil making it less susceptible to liquefaction. In addition, empirical evidence suggests that most liquefaction failures have occurred in uniformly graded soils (Kramer, 1996).

2.2.4 *State Criteria*

In addition to the historical, geologic and compositional criteria outlined previously, liquefaction susceptibility depends strongly on the initial density, or void ratio, and stress conditions of the soil. These parameters define the soil's initial "state". Laboratory studies have shown that the initial state conditions heavily influence a soil's tendency to generate excess pore pressures. Currently there are two graphical methods for evaluating the state criteria of a given soil deposit, namely the critical void ratio (CVR) and steady state line (SSL). Each is described in the following sections.

2.2.4.1 Critical Void Ratio (CVR)

Our modern conception of the behavior of cohesionless soil is based upon the work of Casagrande (1936), who performed a series of strain-controlled, drained triaxial tests on sand specimens of varying degrees of initial densities. Ultimately the tests showed that samples of variable initial densities tested at the same effective confining pressure reached approximately the same final density when sheared to very large strains. However, the behavior of individual sand samples before reaching large strains were significantly different, as illustrated in Figure 2.3. Loose samples contracted, shown by a decreasing void ratio in Figure 2.3(b), while dense samples displayed dilative behavior indicated by an increase in void ratio. However, once large

strains had been developed, both specimens reached essentially the same ultimate void ratio and mobilized the same constant shearing resistance (Kramer 1996).

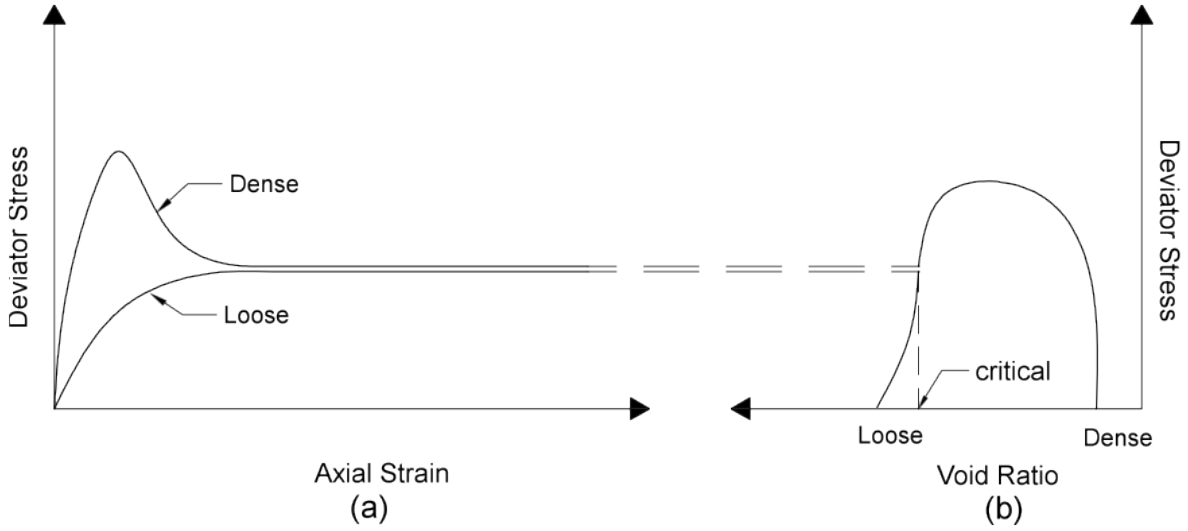


Figure 2.3: Stress-strain (a) and stress-void ratio (b) curves for a dense and a loose sample tested at the same effective confining pressure.Small strain behavior is unique for each specimen but at large strains both samples achieve the same void ratio, known as the critical void ratio, and mobilize the same amount of shearing resistance (after Kramer 1996).

Casagrande (1936) called this ultimate void ratio, at which continuous shearing deformation occurred without any change in principal stress difference, the critical void ratio. After performing similar tests across a wide range of initial densities and confining pressures Casagrande (1936) further determined that this critical void ratio was related exclusively to the effective confining pressure (Holtz and Kovacs, 1981). A plot of the critical void ratio or CVR as a function of effective confining pressure is shown in Figure 2.4. The position of a soil sample's initial void ratio and stress conditions i.e. the "state" of the soil, relative to the position of the CVR line indicates the expected behavior of the sample during shearing. Specimens that plot below the CVR display dilative behavior when sheared monotonically, while samples that plot above the CVR line contract.

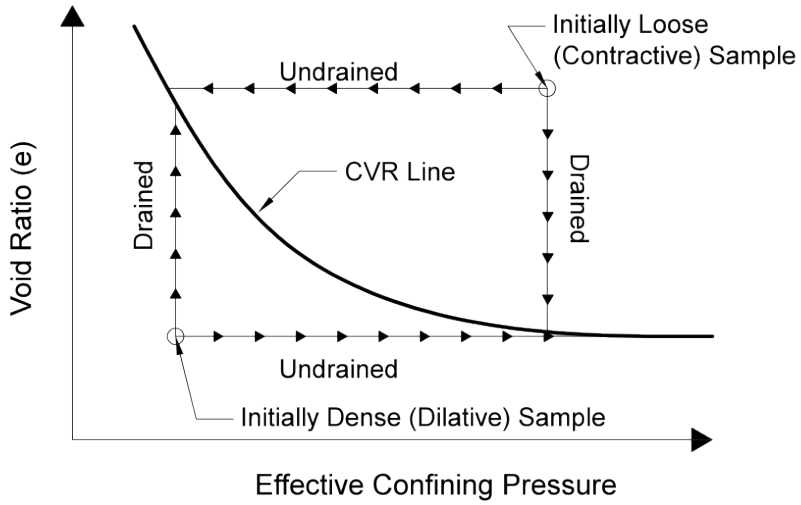


Figure 2.4: Behavior of loose and dense samples under drained and undrained loading conditions(after Kramer 1996)

During drained tests the volume (i.e., void ratio) of the sample changed until it reached the value on the CVR line, as indicated by vertical paths in Figure 2.4. While methods for measuring pore water pressure were not available at the time, Casagrande hypothesized that a loose sample would generate positive pore pressure under undrained conditions (and thus decrease the effective stress) due to its affinity to contract, while a dense sample would generate negative pore pressure as a result of its tendency to dilate (as indicated by the horizontal paths in Figure 2.4). This hypothesis was proven true by subsequent experiments (Castro, 1969). Because the strength and stiffness in cohesionless deposits is proportional to the effective stress, contractive soils that plot above the CVR line are much more susceptible to liquefaction than similar soils that plot below the CVR line.

It was initially believed that the CVR line was the ultimate threshold between sands that could liquefy (initial state above the CVR line) and those that could not liquefy (initial state below the CVR line). However, case history data, particularly the failure of the Fort Peck Dam during construction in 1938 (Middlebrooks, 1942), discredited this theory. Investigations of the Fort Peck Dam site demonstrated that some of the soils that liquefied would have plotted slightly below the CVR line. This inconsistency was attributed to the inability of strain-controlled drained tests to simulate all of the factors that influence a stress-controlled undrained loading condition that led to the liquefaction failure (Kramer, 1996).

2.2.4.2 Steady State Line (SSL)

Castro (1969) performed a number of undrained, stress-controlled static and cyclic triaxial tests on saturated sand samples. Castro (1969) identified three general types of stress-strain behavior, illustrated by Samples A, B, and C in Figure 2.5. Sample A represents a very loose sample. This sample reached its peak strength at very small strains, while at slightly larger strains the sample showed a dramatic reduction in strength, eventually shearing with a constant strength that was well below the peak shear strength. Castro (1969) termed this behavior liquefaction. Specimen B represents a very dense sample; these samples contracted slightly at very small strains, but then dilated until a high, constant, ultimate strength was reached. Sample C represents specimens of intermediate densities. These samples displayed characteristics of both loose and dense specimens. An initial peak strength was achieved at very low strains, followed by a strength reduction. However, at an intermediate strain level the soil began to dilate, and increasing strains led to further dilation and higher strengths. This intermediate behavior was referred to as limited liquefaction (Castro 1969).

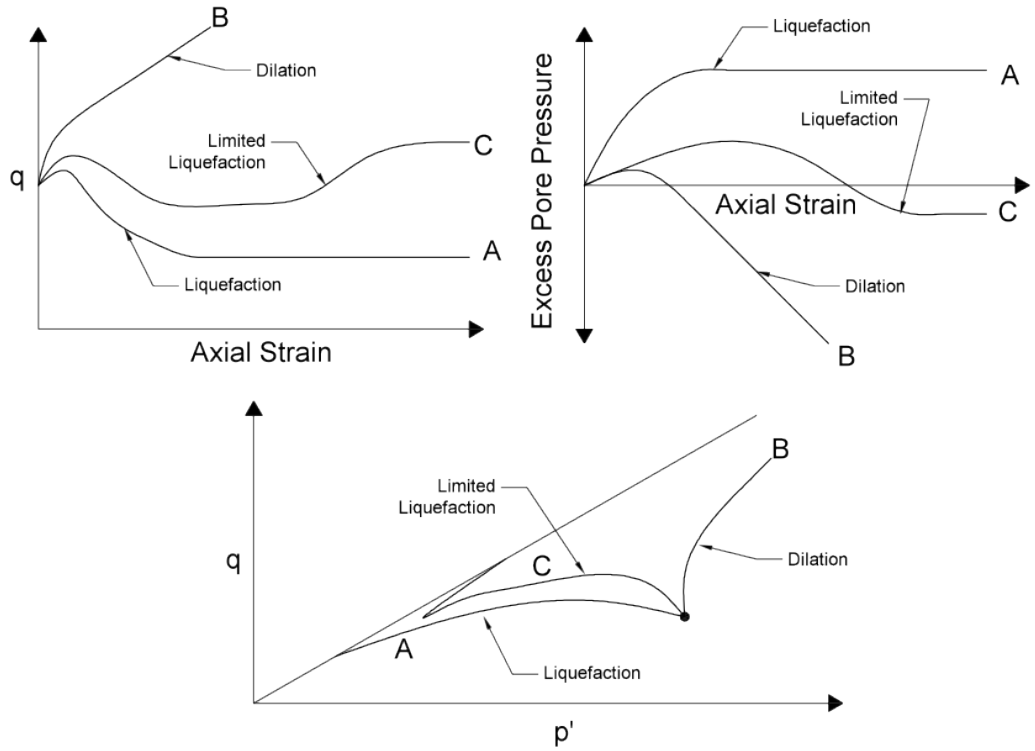


Figure 2.5: Castro results for liquefaction, limited liquefaction and dilation(after Kramer 1996)

Castro (1969) repeated a large number of these tests and, like Casagrande (1936), eventually determined a relationship between void ratio and effective confining pressure at large deformations. The graphical relationship that Castro found could be expressed as a curve that was very similar to the CVR line. The two lines were essentially parallel in log-p space, the relationship from Castro (1969) line plotted slightly lower than CVR line from Casagrande (1936). Castro (1969) theorized that soil forms a 'flow-structure', a condition that occurs in sands when the individual grains rotate to orient themselves in a manner that minimizes frictional resistance under stress-controlled conditions. Castro and Poulos (1977) and Poulos (1981) defined the steady state of deformation as the state in which soil flows continuously at constant velocity with constant volume, under constant shear stress and constant confining pressure. The steady state line (SSL) describes the void ratio and stress conditions that result in a steady state of deformation for a given soil sample. In the most general sense, the SSL can be thought of as a three-dimensional curve in e-p'-q space (or e-σ-τ space). The position of the SSL and its projections onto two dimensional planes are shown as Figure 2.6 (Kramer, 1996).

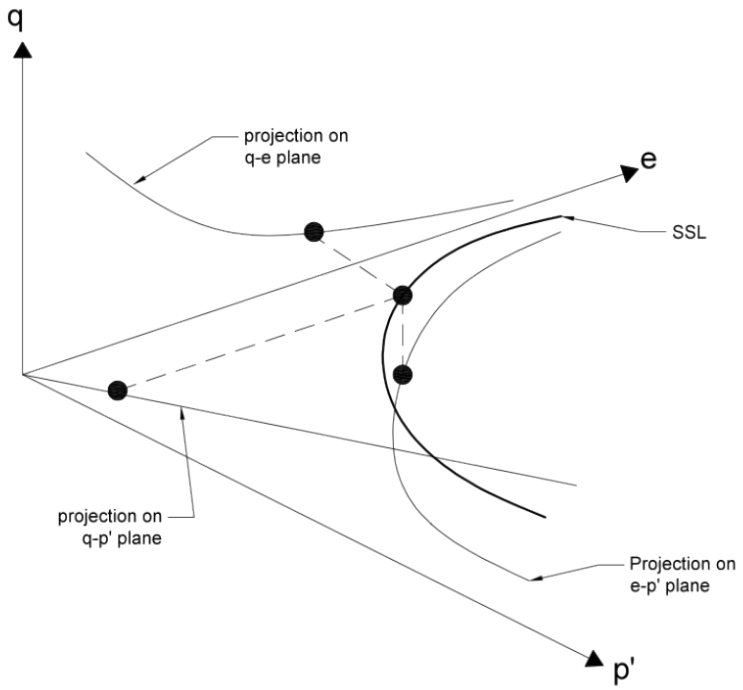


Figure 2.6: Steady state line in e-p'-q space with projections onto the q-p', e-q and e-p' planes(after Kramer 1996)

The SSL is useful for determining if a given soil is susceptible to flow liquefaction. Soils that plot below the SSL with respect to the e-p' 2D projection are not susceptible to flow liquefaction. Soils that plot above the SSL (in terms of the e-p' projection) are susceptible to flow liquefaction if the static shear strength exceeds the residual strength of the liquefied soil. However, cyclic mobility can occur in soils that plot above or below the SSL.

2.3 INITIATION OF LIQUEFACTION

Just because a soil is deemed to be susceptible to liquefaction does not mean liquefaction will occur in any given earthquake. Liquefaction of a given soil deposit requires a disturbance or excitation that is strong enough to initiate or "trigger" the onset of liquefaction. Evaluating the magnitude of the disturbance that is required to liquefy a given soil is one of the most vital parts of any liquefaction hazard evaluation and is the primary goal of this study. Due to the differences in the triggering mechanisms between flow liquefaction and cyclic mobility, the following sections discusses each of them separately.

2.3.1 *Flow Liquefaction*

While cyclic mobility is primarily associated with earthquake loading, flow liquefaction can be initiated in a number of ways. In addition to earthquake shaking, flow liquefaction-induced failures have been attributed to monotonic loading and non-seismic vibrations, such as those that arise from pile driving or train traffic.

Hanzawa et al. (1979) were the first to explicitly describe the conditions required for flow liquefaction. Using stress paths, Hanzawa et al. (1979) illustrated the strain-softening behavior that is a staple of flow liquefaction. Figure 2.7 shows the behavior of five soil samples, all with the same void ratio but confined at different initial effective pressures subjected to monotonic loading during undrained conditions. All of the tests converged to the same point on the failure surface, since they have the same initial void ratio, but they reached that point by unique paths. The convergence point corresponds to the stress conditions described by the SSL.

Samples A and B, which were at low initial effective confining stresses, displayed dilative behavior when subjected to shear loading and their peak strength was the same as the steady-state strength. Specimens C, D and E, which were at higher initial effective stresses, all displayed contractive behavior. These specimens reached peak strength at low strains; however,

upon further shearing the strain increased rapidly until the steady state point was reached. Connecting a line through the points of shear stress reversal (marked by an 'X' in Figure 2.7) forms the flow liquefaction surface (FLS). This surface is the boundary between stable and unstable undrained shear conditions. If a soil element reaches the stress conditions described by the FLS, flow liquefaction will be provoked and the shear strength of the soil will be diminished to the steady-state strength (Kramer, 1996).

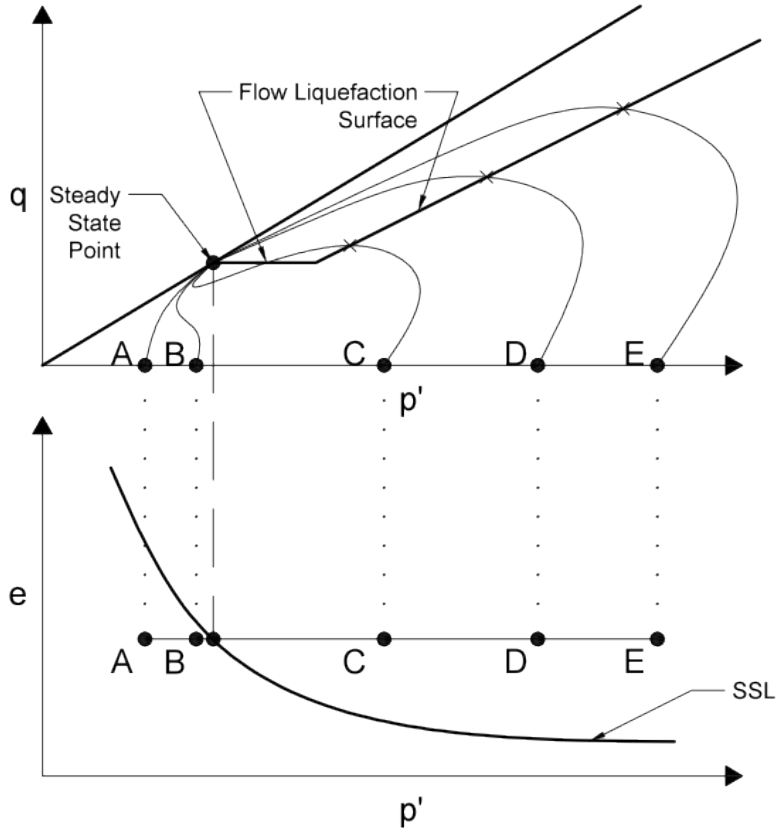


Figure 2.7: Flow liquefaction surface(from Kramer 1996)

Vaid and Chern (1983) were the first to show that the FLS was applicable to both monotonic and cyclic loading conditions. Repeated shear cycles generated pore pressure and reduce the effective stress conditions. If these stress conditions happen to cross the FLS, then the result is the same as in the case of monotonic loading. Figure 2.8 demonstrates the behavior of two specimens with identical initial conditions. One specimen is monotonically loaded, while the other is cyclically loaded. While the stress paths and initial behavior are distinctly different, the consequences of crossing the flow liquefaction surface are essentially the same.

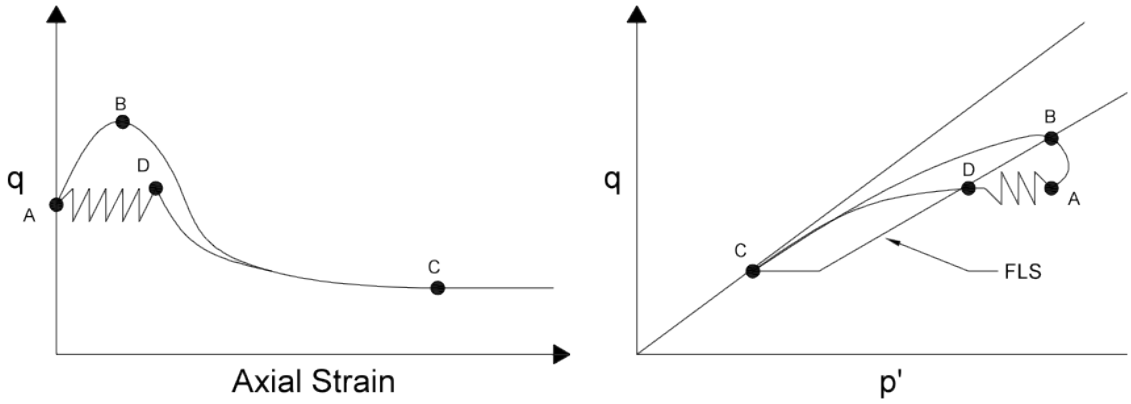


Figure 2.8: Initiation of flow liquefaction during monotonic and cyclic loading

Flow liquefaction is initiated during cyclic loading when the steady-state strength is less than the static shear stress required for equilibrium. For most geotechnical problems the static shear stress required for equilibrium is driven by gravity and can be regarded as relatively constant assuming large deformations (in excess of 1 %) do not develop. As a result, soils whose initial stress state plots within the shaded region, shown in Figure 2.9, are susceptible to flow liquefaction due to cyclic loading. For soils whose initial stress conditions plot close to the FLS, only a small increase in excess pore pressures would be required to trigger flow liquefaction. Conversely, a soils resistance to flow liquefaction will be much greater if the initial stress conditions plot farther away from the FLS (Kramer, 1996).

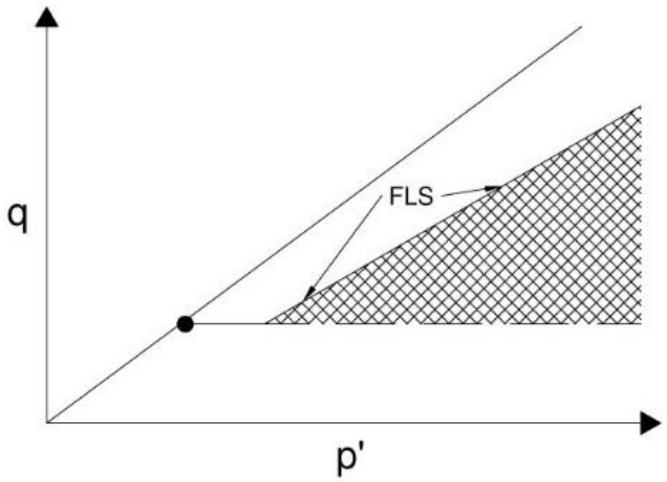


Figure 2.9: Zone of susceptibility for flow liquefaction

2.3.2 *Cyclic Mobility*

Cyclic mobility is a phenomenon that can occur when the static shear stress is less than the steady-state strength of the soil. The zone of susceptibility for cyclic mobility is shown in Figure 2.10. It should be noted that cyclic mobility can occur in both loose and dense soils, as the shaded region in Figure 2.10 corresponds to high and low confining pressures and can correspond to states both above and below the SSL (Kramer, 1996).

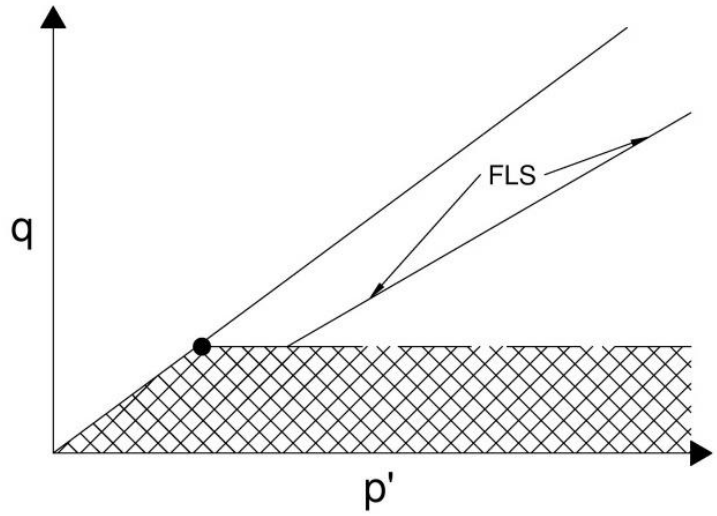


Figure 2.10: Zone of susceptibility for cyclic mobility

Figure 2.11 shows an example of the stress path behavior during cyclic mobility. The cyclic loading generates excess pore pressure causing the effective stress path to move to the left until it reaches the failure envelope. The stress path cannot exceed the failure envelope; therefore, any additional loading cycles cause the stress path to move up and down along the envelope. Moving along the failure envelope causes the soil to dilate which results in a temporary increase in the effective stress. When a stress reversal occurs, the soil contracts which leads to a decrease in the effective stress. This transition from contractive to dilative behavior during cyclic loading is known as phase transformation behavior, and it is an important concept in terms of predicting displacements and ground motions in a liquefied soil. The following section discusses phase transformation in more detail. Each time the effective stress path passes through the origin, the sample is in a state of zero effective stress (r_u=1.0). The first time the soil reaches a state of zero effective stress is referred to as initial liquefaction. However, even though the soil is momentarily at a state of zero effective stress (thus it essentially has no stiffness),

large, flow-style deformations do not occur because the tendency of the soil to dilate when stress and strains become large.

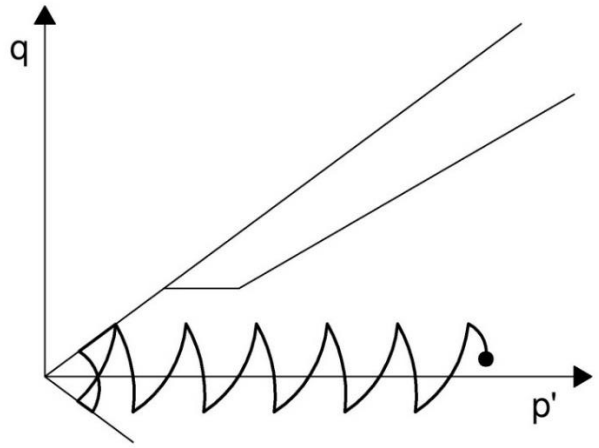


Figure 2.11: Example of stress path behavior during cyclic mobility

2.3.2.1 Phase Transformation Behavior

Figure 2.12 shows the results of a cyclic triaxial test on an anisotropically consolidated sample of Sacramento River sand (Boulanger and Truman, 1996). Prior to any loading or disturbance, i.e., under hydrostatic conditions, the pore pressure ratio was zero. As loading cycles were applied excess pore pressure was generated, the pore pressure ratio increased, and the effective stress decreased. Based on laboratory investigations, the shear modulus of the soil is related to the square root of the effective confining stress. This behavior was observed during the test, as the shear strain amplitude increased at a slower rate than the pore pressure ratio with respect to the number of loading cycles. As the pore pressure ratio approached 1.0 the shear strain amplitude increased very rapidly. At a value of $r_u = 1.0$ the effective stress path was at the origin (Point A in Figure 2.12) and all of the effective stress had been transferred to the pore water; at this instant the soil has lost all capacity to resist shearing.

As soon as the shear stress increased, however, the soil began to dilate. When this occured the pore pressure ratio temporarily decreased, and the sample was able to resist shearing up to the steady state shear strength. Once the shear loading was reversed (just after Point B) the sample exhibited contractive behavior, which resulted in an increase in pore pressure ratio and a decrease in shearing resistance. This alternation between contractive and dilative response is referred to as phase transformation. After the point of initial liquefaction (i.e. the first time the

sample reached r_u of 1.0, which occurred after 27 cycles for test shown in Figure 2.12) the stress-strain behavior of the sample displayed an inverted s-shape as the sample alternated between dilative behavior (decrease in r_u, increase in effective stress and hence stiffness) during shear loading, and contractive behavior (increase in r_u, decrease in shearing resistance) during unloading (Idriss and Boulanger, 2008).

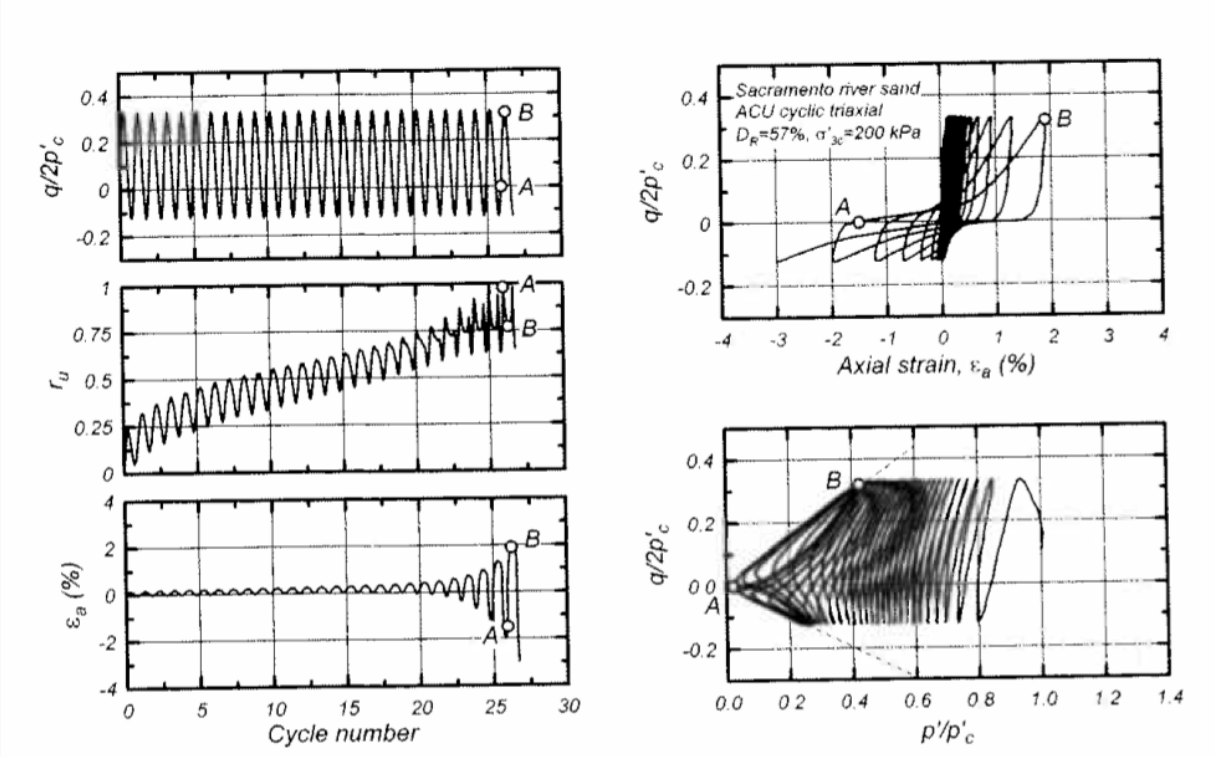


Figure 2.12: Behavior of Sacramento River Sand to undrained cyclic triaxial test performed by Boulanger and Truman (1996)(from Idriss and Boulanger, 2008)

Unlike flow liquefaction, there is no well-defined point at which cyclic mobility is initiated. Permanent strains and deformations develop incrementally, and the magnitude of the deformations depends on the static stress conditions as well as the amplitude and duration of the ground motion.

2.3.3 *Evaluation of Initiation of Liquefaction*

Even if a soil is susceptible to liquefaction, it still requires some level of external loading in order to generate excess pore pressure and initiate liquefaction. A number of different procedures for evaluating the loading required to initiate liquefaction for a given soil have been proposed. One method involves laboratory testing of undisturbed soil samples, much like the study shown

previously for Sacramento River Sand from Idriss and Boulanger (2008). Obtaining undisturbed samples of cohesionless soil is both difficult and expensive, and reconstituted samples do not fully capture the insitu soil fabric and stress state that affect liquefaction resistance. As a result, empirical procedures for evaluating the liquefaction potential of a site are the predominant method used in engineering practice.

Empirical relationships employ field and laboratory test data in conjunction with earthquake loading parameters to calculate a factor of safety against, or probability of, liquefaction for a given event. The factor of safety is a comparison of the capacity, which is a measure of the liquefaction resistance the soil, to the demand, or a measure of loading imposed on a soil deposit. This section will describe four of the predominant empirical approaches for evaluating liquefaction potential: a cyclic stress ratio (CSR) method, an Arias intensity (I_A)-based approach, a cumulative absolute velocity calculated using a 5 cm/s^2 threshold (CAV_5)-based method, and a normalized energy demand (NED)-based method.

2.3.3.1 Cyclic Stress-based Approach

The most widely used frameworks for evaluating the liquefaction potential of a site are founded on a cyclic stress-based approach (Seed and Idriss, 1982; Youd et al. 2001; Boulanger and Idriss, 2014; Cetin et al. 2018). This type of approach compares the seismically induced cyclic stresses with the cyclic resistance of the soil to determine a factor of safety against liquefaction (Seed and Idriss, 1971). The cyclic stress-based approach relies on multiple key assumptions, namely that excess pore pressure generation is primarily related to the applied cyclic shear stresses, and that the complex, transient earthquake-induced shear stress time history can be adequately represented by an equivalent series of uniform stress cycles.

The theoretical basis for the cyclic stress-based approach was experimental studies that simulated the cyclic shear stresses induced by earthquake loading using a constant amplitude sinusoid (e.g. De Alba et al., 1976; Boulanger and Seed, 1995; and Okamura et al., 2003). In these experiments, the amplitude of the sinusoidal loading history was expressed in terms of a cyclic stress ratio, CSR, defined as the ratio of the applied cyclic shear stress, τ_{cyc}, to the initial overburden effective stress of the soil sample, σ'_{v0}, as shown in Equation 2.3.

$$CSR = \frac{\tau_{cyc}}{\sigma'_{v0}} \tag{2.3}$$

Numerous experimental studies, such as those listed above, have found that, for a given soil sample at a given relative density and initial effective stress, there is a unique relationship between the applied CSR and the number of uniform stress cycles to cause failure due to liquefaction (N_{liq}). The definition of failure can vary from one experimental study to another. Common definitions for failure include an excess pore pressure ratio of 1.0, a peak shear strain of three percent, and a double amplitude (i.e. peak-to-peak) shear strain of five percent. The results of these laboratory studies were commonly summarized using liquefaction resistance curves, where the CSR is plotted as a function of N_{liq}. An example based on cyclic simple shear testing on reconstituted sand samples is provided in Figure 2.13. Note that for this example failure was defined as the number of cycles to cause peak shear strain of three percent.

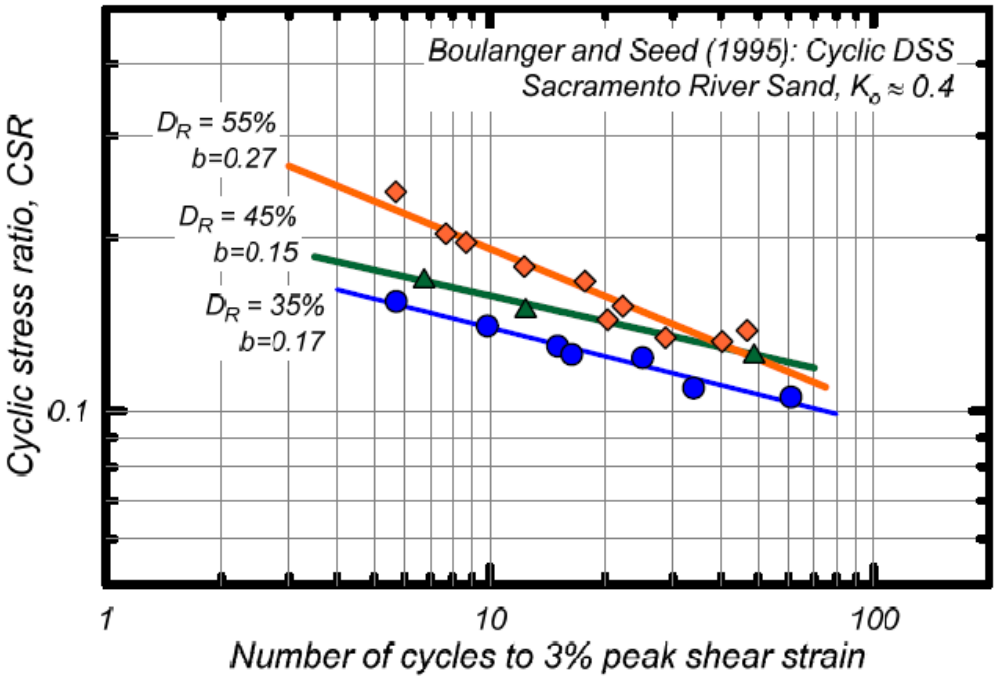


Figure 2.13: Cyclic simple shear tests on reconstituted clean sand by Boulanger and Seed (1995) (after Boulanger and Idriss, 2014).

In the cyclic stress-based approach, a soil's resistance to liquefaction is quantified as a cyclic resistance ratio (CRR), defined as the CSR required to cause failure of the soil sample, which depends on the number of applied cycles. As noted by Boulanger and Idriss (2014), the laboratory-based CRR-N_{liq} relationship can be reasonably approximated using a power function as,

$$CRR = aN_{liq}{}^{-b} \tag{2.4}$$

In order to apply the observations made in the laboratory to observations made in the field, Seed and Idriss (1971) proposed a simplified method for estimating the CSR from a given earthquake according to Equation 2.5.

$$CSR = 0.65\frac{a_{max}\sigma_{v0}}{g\ \ \sigma_{v0}'}r_d \tag{2.5}$$

where a_{max} is the peak horizontal acceleration of a given earthquake time history at the ground surface, g is the gravitational constant, σ_{v0} is the initial total vertical stress, and r_d is a depth reduction factor. The depth reduction factor accounts for the decrease in peak shear stress with depth and takes on a value of 1.0 at the ground surface. The value of 0.65 represents a reference stress level of 65% of the peak cyclic stress. The choice of 65% as a reference stress level is arbitrary (so long as it is consistently applied) and has been employed since the beginning of the development of the stress-based liquefaction procedures (Seed and Idriss, 1971), and has been retained in each of the subsequent CSR-based procedures as well (Idriss and Boulanger, 2008).

The CSR as defined by Equations 2.3 and 2.5 only captures the amplitude of the ground motion. The original CSR relationships were based on data from events with magnitudes ranging from 7.3 to 7.8. As such they were considered appropriate for events around magnitude 7.5. As shown in Figure 2.12 pore pressure builds up incrementally and increases with the number of cycles, or duration of the loading history. In order to apply the CSR-based approach to events with different magnitudes (and consequently, different durations) a magnitude scaling factor was developed to account for the effect of duration, quantified by the number of equivalent cycles at the reference stress level, N. Based on this definition the MSF is described in Equation 2.6 as

$$MSF = \frac{CSR_{M=m}}{CSR_{M=7.5}} \tag{2.6}$$

where $CSR_{M=7.5}$ is the CSR corresponding to a magnitude 7.5 event, and $CSR_{M=m}$ is the CSR corresponding to a magnitude m event. Seed et al. (1983), Liu et al. (2001), Idriss and Boulanger (2008), and Boulanger and Idriss (2014) evaluated MSF using a method developed from laboratory-based CRR-N_{liq} relationships provided in Equation 2.4. This method involves converting an irregular earthquake loading history to an equivalent N and evaluating MSF by comparing the number of cycles for the given event with the number of cycles corresponding to an event with a magnitude of 7.5.

As described by Boulanger and Idriss (2014), an irregular cyclic loading history can be converted to an equivalent N using a weighting scheme derived from Equation 2.4. Consider two stress cycles with amplitudes CSR_A and CSR_B. If a damage parameter, D, is defined as $D = r_u$, where occurs when $D = r_u = 1.0$, and assuming a linear relationship between D and N/N_{liq}, the equivalent damage caused by one cycle at CSR_A compared to N cycles at CSR_B (N_B) can be evaluated using the CRR-N_{liq} relationship as,

$$D_A = \frac{1}{N_{liq,A}} = \frac{N_B}{N_{liq,B}} \rightarrow N_B = \frac{N_{liq,B}}{N_{liq,A}} = \frac{\left(CSR_B / a\right)^{-1/b}}{\left(CSR_A / a\right)^{-1/b}} = \left(\frac{CSR_A}{CSR_B}\right)^{1/b} \quad (2.7)$$

Equation 2.7 can then be used to convert an irregular time series from a recorded earthquake into an equivalent number of uniform stress cycles, N_{ref}, at a reference stress level, CSR_{ref} (defined above as N_B and CSR_B, respectively) using the following procedure:

1. Determine the peaks in the time history, evaluated as the peak amplitude between two successive zero crossings;
2. Determine N_{ref} for each peak based on the ratio of the peak amplitude to the reference amplitude and a scaling function such as Equation 2.7; and
3. Sum the N_{ref} for each individual peak to determine a total number of equivalent cycles.

Using this procedure, the total number of equivalent uniform stress cycles at a reference stress level can then be evaluated for actual recorded earthquake ground motions to determine representative values of N for a given earthquake magnitude, N_M. Based on the definition of CSR provided in Equation 2.5, the MSF can be computed as,

$$MSF = \frac{CSR_{M=m}}{CSR_{M=7.5}} = \frac{aN_{M=m}{}^{-b}}{aN_{M=7.5}{}^{-b}} = \left(\frac{N_{M=7.5}}{N_{M=m}}\right)^b \quad (2.8)$$

The original cycle weighting scheme developed by Seed et al. (1975), and incorporated in the MSF relationship proposed by Seed and Idriss (1982), used a modified weighting function that was similar to the weighting function presented in Equation 2.7 with a b value of 0.34, but included adjustments based on engineering judgement. Their weighting scheme is summarized in Table 2.1. Seed et al. (1975) also assumed that cycles with peak amplitudes less than 30% of the maximum amplitude were too low to contribute to excess pore pressure generation.

Table 2.1: Equivalent number of cycles from Seed et al. (1975) (after Greenfield, 2017)

Cycle Amplitude a / a_{max}	Number of Equivalent Cycles	Cycle Amplitude a / a_{max}	Number of Equivalent Cycles
1	3	0.6	0.7
0.95	2.7	0.55	0.4
0.9	2.4	0.5	0.2
0.85	2.05	0.45	0.1
0.8	1.7	0.4	0.04
0.75	1.4	0.35	0.02
0.7	1.2	<0.3	0
0.65	1		

Using the cycle weighting scheme provided in Table 2.1, and the available ground motion records at the time, Seed et al. (1983) developed N_M values and MSF recommendations for earthquakes ranging from magnitude 5.25 to 8.5, as summarized in Table 2.2.

Table 2.2: Number of equivalent cycles and magnitude scaling factor from Seed et al. (1983)

Magnitude, M	Number of Equivalent Cycles, N_M	Magnitude Scaling Factor, MSF
8.5	26	0.89
7.5	15	1
6.75	10	1.13
6	5	1.32
5.25	2	1.5

Boulanger and Idriss (2014) noted that the b value is dependent on numerous factors, most notably the relative density of the soil, with b ranging from 0.14 for loose soils and up to 0.4 for dense soils. As such the cycle weighting scheme (Equation 2.7) and MSF relationship (Equation 2.8) should also be a function of relative density. Based on these observations, Boulanger and Idriss (2014) developed an MSF relationship that was a function of both earthquake magnitude and relative density (evaluated using the clean sand corrected SPT blow count, $(N_1)_{60cs}$) shown in Equation 2.9 as

$$MSF = 1 + \left(MSF_{max} - 1\right)\left(8.64\, e^{-M/4} - 1.325\right) \tag{2.9a}$$

$$MSF_{max} = 1.09 + \left(\frac{(N_1)_{60cs}}{31.5}\right)^2 \leq 2.2 \tag{2.9b}$$

where MSF_{max} is the MSF corresponding to a small magnitude event that is dominated by a single large stress cycle.

Liu et al. (2001) developed an MSF relationship by performing regression analyses to evaluate N_M based on the weighting scheme provided in Table 2.1 using over 1,600 recorded ground motion records. Liu et al. (2001) found that N was primarily a function of the earthquake magnitude, source to site distance, and site conditions (evaluated as either soil or rock sites) as shown below

$$\ln N_M = \ln\left\{\frac{\left(\frac{\exp\left[b_1 + b_2\left(M - m^*\right)\right]}{10^{1.5M + 16.05}}\right)^{-1/3}}{4.9 \cdot 10^6 \beta} + S \cdot c_1 + R \cdot c_2\right\} \tag{2.10}$$

where β is the shear wave velocity of the source (generally equal to 3.2 km/s in the western United States), R is the source-to-site distance, and S is a dummy variable that is equal to 0 for rock sites and 1 for soil sites. Variables b_1, b_2, m^*, c_1, and c_2 are coefficients that were determined by Liu et al. (2001) through their regression analyses. Liu et al. (2001) recommended values corresponding to 1.53, 1.51, 5.8, 0.095 and 0.75, for b_1, b_2, m^*, c_1, and c_2, respectively. The corresponding MSF from Liu et al. (2001) was expressed as

$$\ln MSF = a_1 + a_2 \ln N \tag{2.11}$$

where a_1 and a_2 are coefficients related to the reference number of cycles and the exponent b. Lui et al. (2001) recommended values of 1.3 and -0.41, for a_1 and a_2, respectively. Note that these recommended values correspond to a $N_{M=7.5}$ of approximately 24 and a b value of 0.41.

Cetin et al. (2018) developed a relationship for MSF based on regression analyses from case history data and evaluated MSF solely as a function of earthquake magnitude using a power function expressed as,

$$MSF = \left(\frac{M}{7.5}\right)^{-2.324} \tag{2.12}$$

Figure 2.14 compares the MSF relationships described above for Boulanger and Idriss (2014), Liu et al. (2001), and Cetin et al. (2018). The density-dependent relationship from Boulanger and Idriss (2014) is provided at $(N_1)_{60cs}$ values of 10, 20, and 30 to illustrate the range of MSF response, and show that the MSF relationship becomes flatter as the density of the soil (and correspondingly the exponent b) decreases. The relationship from Liu et al. (2001) is provided for a soil site at source-to-site distances of 20 and 40 km which is representative of the source-to-site distance for the majority of the available liquefaction case history data (Liu et al., 2001). The general trends for each relationship shown in Figure 2.14 are similar. The value of MSF for each relationship is greater than one for magnitudes less than 7.5, is equal to a value of 1.0 for magnitude 7.5 events, and is less than one for events greater than magnitude 7.5. Note that the relationship from Liu et al. (2001) may not equal a value of exactly 1.0 at magnitude 7.5 because their MSF relationship considers the effect of source-to-site distance on N.

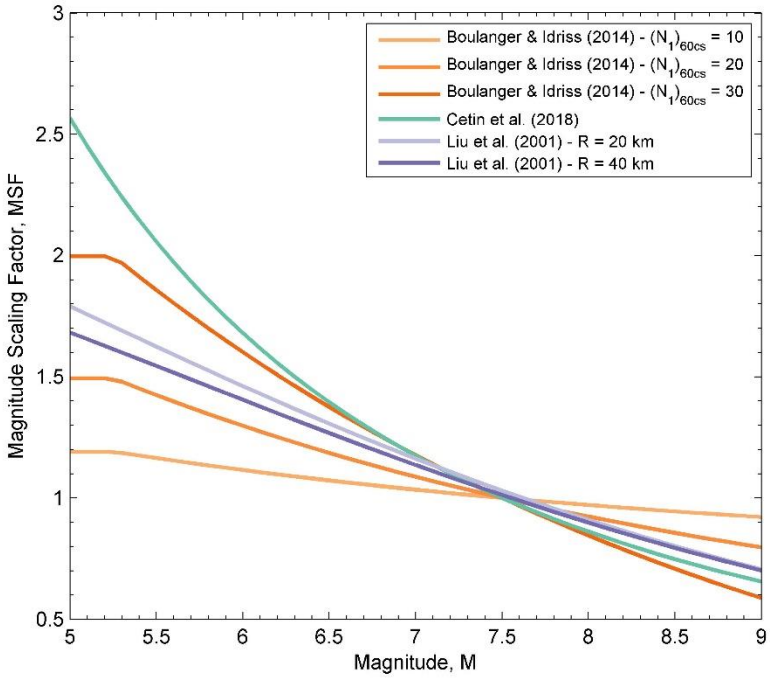


Figure 2.14: Comparison of MSF relationships from Boulanger and Idriss (2014), Liu et al. (2001), and Cetin et al. (2018).

Combining the definition of MSF with Equation 2.5, the CSR-based approach quantifies the demand imposed on the soil by an earthquake as

$$CSR_{M=7.5} = 0.65 \frac{a_{max}\sigma_v}{g\ \sigma_v'} r_d \frac{1}{MSF} \tag{2.13}$$

Equation 2.13 shows that the demand is a function of the initial stress conditions and the peak acceleration value that is scaled by a factors that account for the effects of depth and the duration of the loading.

The capacity of the soil to resist liquefaction, CRR, is simply the value of CSR required to initiate liquefaction for the soil of interest. The CRR is inherently related to the state of the soil, as described in Section 2.2.4, expressed as the distance to the critical state line. The state is a function of both the void ratio, or density of the soil, and the initial effective overburden pressure. In the stress-based procedures, the CRR is empirically determined using regression analyses with case history data. The density of the soil is typically correlated to an insitu test parameter. Historically, the most common CRR relationships have been expressed in terms of standard penetration resistance (SPT) (Seed and Idriss, 1971; Youd et al. 2001; Boulanger and Idriss 2014; Cetin et al. 2018), although CRR expressions developed for cone penetration test resistance (Robertson and Wride, 1988; Moss et al. 2006; Boulanger and Idriss 2014) are superseding those based on SPT resistance procedures. Procedures based on shear wave velocity (Andrus and Stokoe, 1997; Kayen et al. 2013) have also been proposed.

Laboratory tests have shown that the CRR tends to decrease as the confining stress increases for a soil with a constant relative density. To account for the effect, an overburden correction factor, K_σ, first introduced by Seed (1983), was applied to CRR to normalize the case history data to a common overburden stress of one atmosphere. Youd et al. (2001) presented an overburden correction factor based on the work of Hynes and Olsen (1999) of the form,

$$K_\sigma = \left(\frac{\sigma'_v}{P_a}\right)^{f-1} \tag{2.14}$$

where σ'_v is vertical effective stress, P_a is atmospheric pressure, and f is a constant based on the relative density of the soil. Youd et al. (2001) recommended f values ranging from 0.6 to 0.8 for soils with relative densities from 40 to 80%, respectively. Based on regression analyses, Cetin et al. (2018) recommended an f value of approximately 0.66. Boulanger and Idriss (2014) provide an overburden correction factor that accounts for the relative density of the soil, evaluated based on using $(N_1)_{60cs}$, as follows,

$$K_\sigma = 1 - C_\sigma \ln\left(\frac{\sigma'_v}{P_a}\right) \leq 1.1 \tag{2.15a}$$

$$C_\sigma = \frac{1}{18.9 - 2.55\sqrt{(N_1)_{60cs}}} \leq 0.3 \tag{2.15b}$$

Figure 2.15 compares the overburden correction factors from Youd et al. (2001), Boulanger and Idriss (2014), and Cetin et al. (2018). By definition, all the relationships have a value of 1.0 at an effective stress of one atmosphere and decrease with increasing effective stress overburden stresses. The differences in the recommended relationships are largely due to differences in the case history databases, the laboratory tests used for guidance, and engineering judgement.

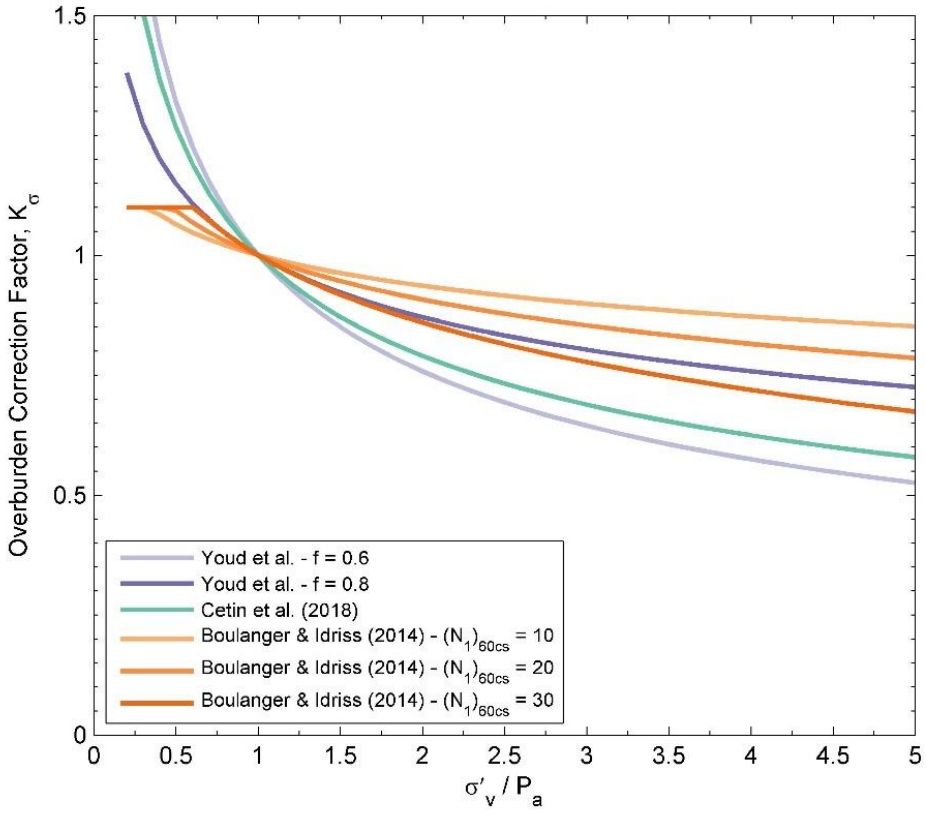


Figure 2.15: Comparison of overburden correction factors from Youd et al. (2001), Boulanger and Idriss (2014), and Cetin et al. (2018).

The overburden correction factor is commonly applied to the estimate of the applied loading, CSR, to normalize the demand to an effective confining stress of one atmosphere. Combining Equation 2.13 with the overburden correction factor, the CSR value that is normalized to a common earthquake magnitude of 7.5 and an overburden stress of one atmosphere ($CSR_{M=7.5,\ \sigma=1atm}$) can be expressed as,

$$CSR_{M=7.5,\sigma=1atm} = 0.65 \frac{a_{max}\sigma_v}{g \quad \sigma_v'} r_d \frac{1 \quad 1}{MSF K_\sigma} \tag{2.16}$$

The soil's resistance to liquefaction, CRR, is evaluated empirically using case history databases. These databases are created based on post-earthquake reconnaissance at sites that contain potentially liquefiable soil layers. Field tests are performed to characterize the density of the liquefiable soil deposit. The loading is evaluated using estimates of the peak acceleration at the site that can be obtained from near-site seismometer recordings, shake maps, or ground motion predictive equations (GMPEs). Then the estimated CSR is converted to the normalized value, $CSR_{M=7.5,\sigma=1atm}$ per Equation 2.16, and plotted as a function of the insitu test parameter. The CRR that separates the cases where liquefaction was and was not observed is then evaluated using logistic regression. An example of this process from Idriss and Boulanger (2014) is shown in Figure 2.16. In this figure, the closed circles represent case histories where liquefaction was observed and open circles represent cases where liquefaction was not observed.

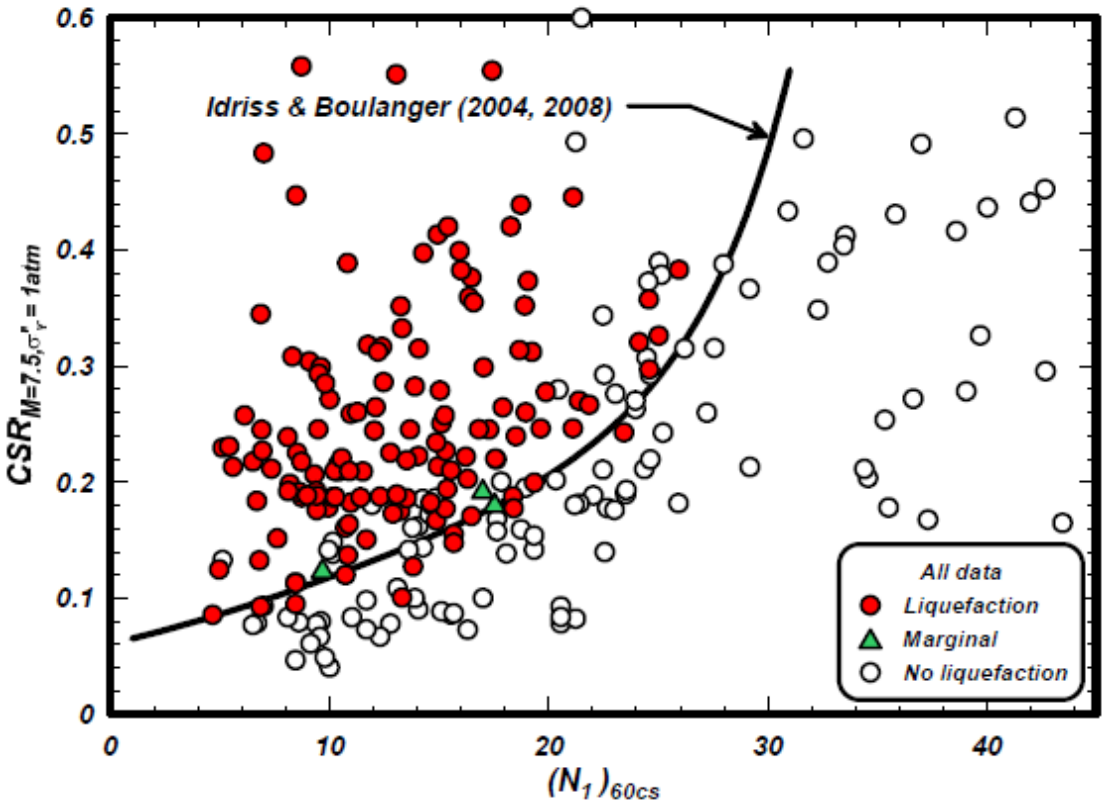


Figure 2.16: CRR-SPT relationships derived from case history data, from Idriss and Boulanger (2010)

The CRR equation developed by Idriss and Boulanger (2014) is expressed as,

$$CRR_{M=7.5,\sigma=1atm} = \exp\left[\frac{(N_1)_{60,cs}}{14.1} + \left(\frac{(N_1)_{60,cs}}{126}\right)^2 - \left(\frac{(N_1)_{60,cs}}{23.6}\right)^3 + \left(\frac{(N_1)_{60,cs}}{25.4}\right)^4 - 2.8\right] \quad (2.17)$$

where, $CRR_{M=7.5,\sigma=1atm}$ is the CRR of the soil for a magnitude 7.5 event at an overburden stress of one atmosphere, and $(N_1)_{60cs}$ is the measured SPT resistance of the liquefiable soil layer, corrected for overburden stress, energy, and fines content (Boulanger and Idriss, 2014).

The CSR-based approach evaluates the liquefaction potential of a given site as a factor of safety against liquefaction, expressed as,

$$FS_{liq.} = \frac{CRR_{M=7.5,\ \sigma=1atm}}{CSR_{M=7.5,\ \sigma=1atm}} \quad (2.18)$$

Using Equation 2.18, liquefaction is predicted when $FS_{liq.} \leq 1.0$.

As an alternative to a factor of safety, Boulanger and Idriss (2014) and Cetin et al. (2018) also evaluated estimates of CRR that correspond to a given probability of liquefaction. For the case where only the model uncertainty is considered (as opposed to also considering the uncertainty in the input parameters, such as $(N_1)_{60}$), Idriss and Boulanger (2014) presented the following equation,

$$CRR_{M=7.5} = \exp\left[\frac{(N_1)_{60,cs}}{14.1} + \left(\frac{(N_1)_{60,cs}}{126}\right)^2 - \left(\frac{(N_1)_{60,cs}}{23.6}\right)^3 + \left(\frac{(N_1)_{60,cs}}{25.4}\right)^4 - 2.67 + \sigma_{\ln(R)}\Phi^{-1}(P_l)\right] \quad (2.19)$$

where $\sigma_{\ln(R)}$ is the standard deviation of the log residuals of the model fit, Φ^{-1} is the standard normal inverse function, and P_l is the probability of liquefaction. For routine practice, Idriss and Boulanger recommended a $\sigma_{\ln(R)}$ of 0.13. Based on these values, the CRR relationship provided in Equation 2.17 represents a probability of liquefaction of approximately 16 percent. The topics of uncertainty and probability in liquefaction hazard analyses will be revisited in detail in the later chapters.

2.3.3.2 Arias Intensity (I_A)-based Approach

Kayen and Mitchell (1997) proposed an alternative to the stress-based approach using Arias Intensity (Arias, 1970), I_A, to quantify the earthquake loading and the soil's resistance to liquefaction. Arias (1970) defined Arias intensity, I_A, as "the sum of the two-component energy per unit weight stored in a population of undamped linear oscillators evenly distributed in

frequency, at the end of earthquake shaking." The single component version of Arias intensity is computed as

$$I_A = \frac{\pi}{2g}\int_0^{\infty} a(t)^2 dt \tag{2.20}$$

where g is the acceleration of gravity. Kayen and Mitchell (1997) defined the two-component Arias intensity, I_H, as the sum of the two perpendicular horizontal components of a recorded ground motion, shown in Equation 2.21.

$$I_H = I_x + I_y = \frac{\pi}{2g}\int_0^{\infty} a_x(t)^2 dt + \frac{\pi}{2g}\int_0^{\infty} a_y(t)^2 dt \tag{2.21}$$

where I_x and a_x are the Arias intensity and acceleration time history in the x-direction, and similarly, I_y and a_y are the Arias intensity and acceleration time history in the y-direction, respectively. Note that the unit for Arias Intensity is velocity. Since I_A is defined as an integral ground motion intensity measure, it naturally is influenced by the amplitude, frequency content and duration of a ground motion. This is advantageous because by explicitly accounting for ground motion duration, additional scaling factors, such as MSF, are not needed to compare motions from different magnitude events.

In the I_A-based approach, the demand imposed on the soil is expressed in terms of I_H, and is evaluated based on a GMPE for I_H, such as those proposed by Kayen and Mitchell (1997) and Travasarou et al. (2003). The surface motion is then multiplied by an Arias intensity depth reduction factor to account for the change in Arias intensity with depth. As with the CSR-based approach, the capacity of soil in terms of I_H and symbolically represented as I_{HB}, is analyzed using a resistance curve based on a liquefaction case history database and is presented as a function of the corrected SPT blow count of the liquefiable soil layer. An equation for the curve developed by Kayen and Mitchell (1997) was not provided, however, the resistance of the liquefiable soil can be determined graphically using their provided plot, shown in Figure 2.17.

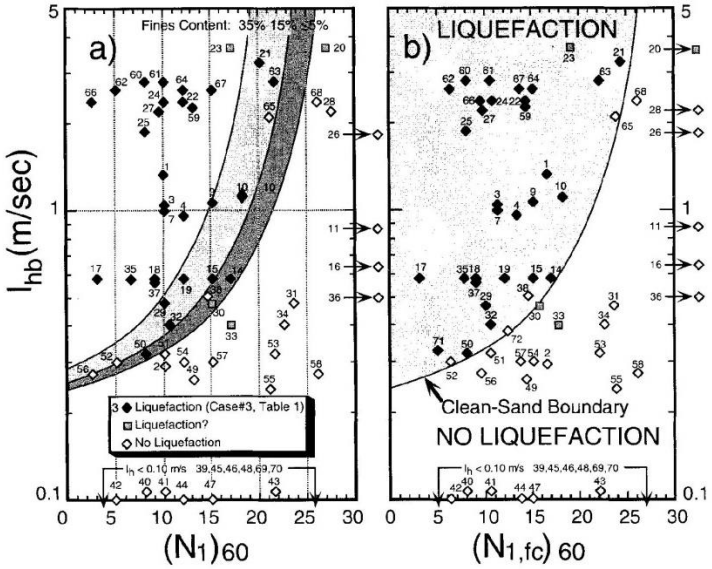


Figure 2.17: I_H-SPT scatter plots including liquefaction resistance curves from Kayen and Mitchell (1997).(a) does not include the fines correction factor and instead provides capacity curve contours corresponding to different percentages of fines content, (b) includes the fines content correction factor in the SPT correction.

The factor of safety against liquefaction, FS_{liq}, is computed as the ratio of the seismic soil's resistance to the loading demand as follows,

$$FS_{liq} = \frac{I_{HB}}{I_H} \tag{2.22}$$

While the I_A-based approach has conceptual advantages over the CSR-based approach because the intensity measure used to define the earthquake loading and the soil's resistance to liquefaction naturally accounts for the duration of shaking, the CSR-based approach is more prevalent in engineering practice. The CSR-based approach is generally preferred because (a) the case history database for the CSR-based approach is much more developed than the database used for the I_A-based approach and (b) Arias intensity GMPEs are notable for their high standard errors, which indicate a high degree of uncertainty in the prediction of Arias intensity. The effect of uncertainty in liquefaction hazard analysis is explained further in later chapters.

2.3.3.3 CAV_5-based Method

Kramer and Mitchell (2006) identified an alternative intensity measure based on a modified formulation of cumulative absolute velocity (CAV), called CAV_5, that was found to be a very effective predictor of pore water pressure based on extensive numerical analyses. In its standard form CAV is computed as,

$$CAV = \int_0^{\infty} |a(t)| \tag{2.23}$$

Kramer and Mitchell (2006) defined the parameter CAV_5, as the cumulative absolute velocity above a threshold acceleration of 5 cm/s^2, which has units of velocity. CAV_5 is computed as follows,

$$CAV_5 = \int_0^{\infty} \langle \chi \rangle |a(t)| \tag{2.24}$$

where $\langle \chi \rangle$ is defined as,

$$\langle \chi \rangle = \begin{Bmatrix} 0 \; for \; |a(t)| \leq 5 \, {}^{cm}/_{s^2} \\ 1 \; for \; |a(t)| \geq 5 \, {}^{cm}/_{s^2} \end{Bmatrix} \tag{2.25}$$

Based on these findings Mayfield (2007) developed a CAV_5-based liquefaction evaluation framework in a similar manner as described previously for I_A. The demand for CAV_5 is evaluated using a GMPE, such as the one developed by Kramer and Mitchell (2006), multiplied by a depth reduction factor. The capacity for the CAV_5-based relationship is developed using liquefaction case histories based on corrected SPT resistance. A liquefaction resistance curve was developed by Mayfield (2007) as the boundary between liquefaction and nonliquefaction cases (Figure 2.14). Mayfield (2007) expressed the median capacity curve (P_L=50%) as

$$\ln\left(CAV_5\right) = \frac{\left(N_1\right)_{60,cs} - 4.20 \ln\left(\frac{\sigma'_{v0}}{p_a}\right) - 9.45}{6.47} \tag{2.26}$$

where p_a is atmospheric pressure.

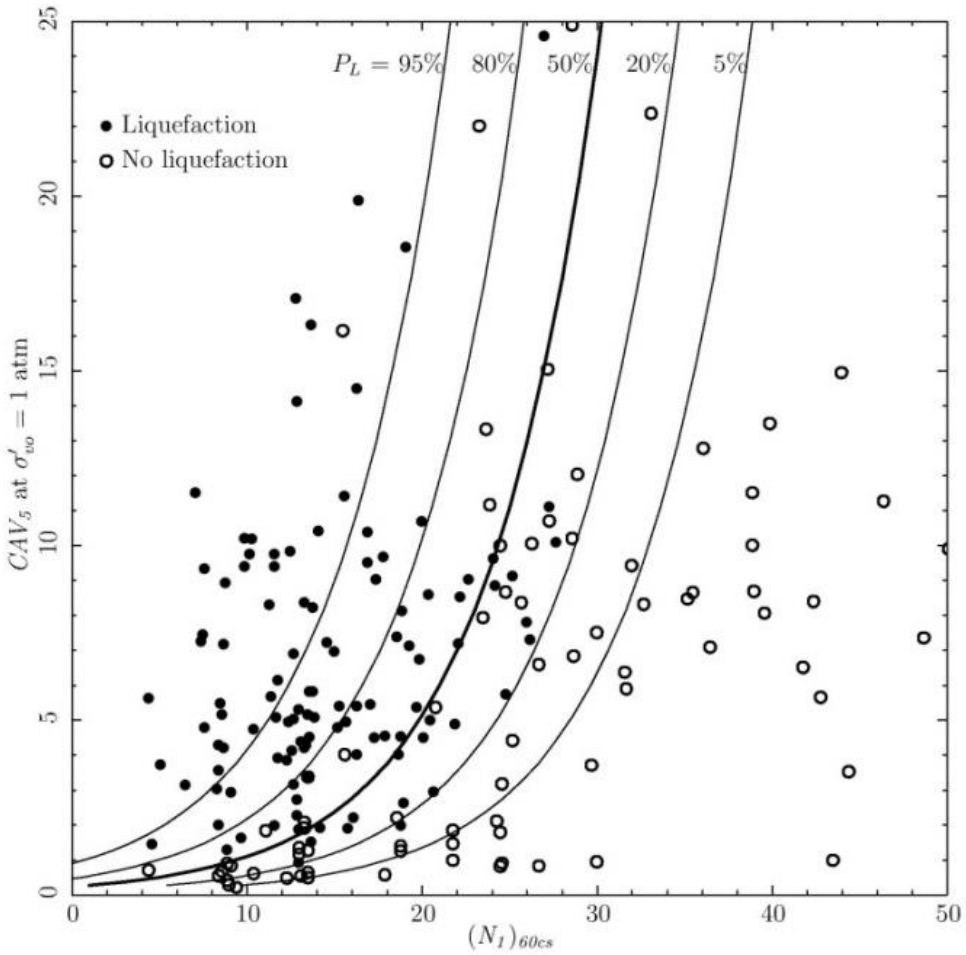


Figure 2.14: CAV_5 liquefaction resistance curves from Mayfield (2007).Contours represent different probabilities of liquefaction

The factor of safety against liquefaction, taken as the ratio of capacity to demand is expressed as,

$$FS_{liq} = \frac{CAV_{5_{liq}}}{CAV_{5_{motion}}} \tag{2.27}$$

where $CAV_{5_{liq}}$ is the CAV_5 determined from the capacity curve and $CAV_{5_{motion}}$ is the CAV_5 determined from the GMPE multiplied by a depth reduction factor. However, for the same reasons as noted for the I_A-based procedure, namely the high standard error in the CAV_5 GMPE obtained by Campbell and Bozorgnia (2010), the CSR-based liquefaction evaluation method is the preferred design procedure currently used in engineering practice.

2.3.3.4 Normalized Energy Demand (NED)-based Approach

The normalized energy demand (NED)-based approach, developed by Green (2001), is an energy-based approach founded on the theory that the energy dissipated during earthquake loading by frictional mechanisms of the sand is proportional to the sand's ability to resist liquefaction (Abegg, 2010). NED is calculated based on a linearized hysteretic model as the cumulative energy dissipated per unit volume of the material, ΔW, normalized by the initial mean effective stress, σ'_{m0}, to produce a dimensionless quantity. NED is symbolically represented by,

$$NED = \frac{\Delta W}{\sigma'_{m0}} \tag{2.28}$$

ΔW is calculated using trapezoidal integration on the product of the stress and strain time history outputs from a total stress equivalent linear site response analysis as shown below.

$$\Delta W = \frac{1}{2}\sum_{i=1}^{n-1}(\tau_{i+1} - \tau_i)(\gamma_{i+1} - \gamma_i) \tag{2.29}$$

where τ_i is the ith value of shear stress, γ_i is the ith value of shear strain and n is the total number of time steps in the motion. It is important to note that NED, as defined here, is not a inherently a ground motion intensity measure because it requires an approximation of the stress-strain response of the soil profile from numerical analyses.

The capacity of the soil to resist liquefaction in terms of NED, dubbed the normalized energy capacity, or NEC, was developed much like the previous approaches. A case history database was developed by Green (2001) for NED as a function of corrected SPT resistance, and a bounding curve between liquefied and nonliquefied points was determined and as shown in Figure 2.18. The median value of NEC is given by

$$NEC = 1.195 \cdot 10^{-4} \exp\left(0.185(N_1)_{60,cs}\right) \tag{2.30}$$

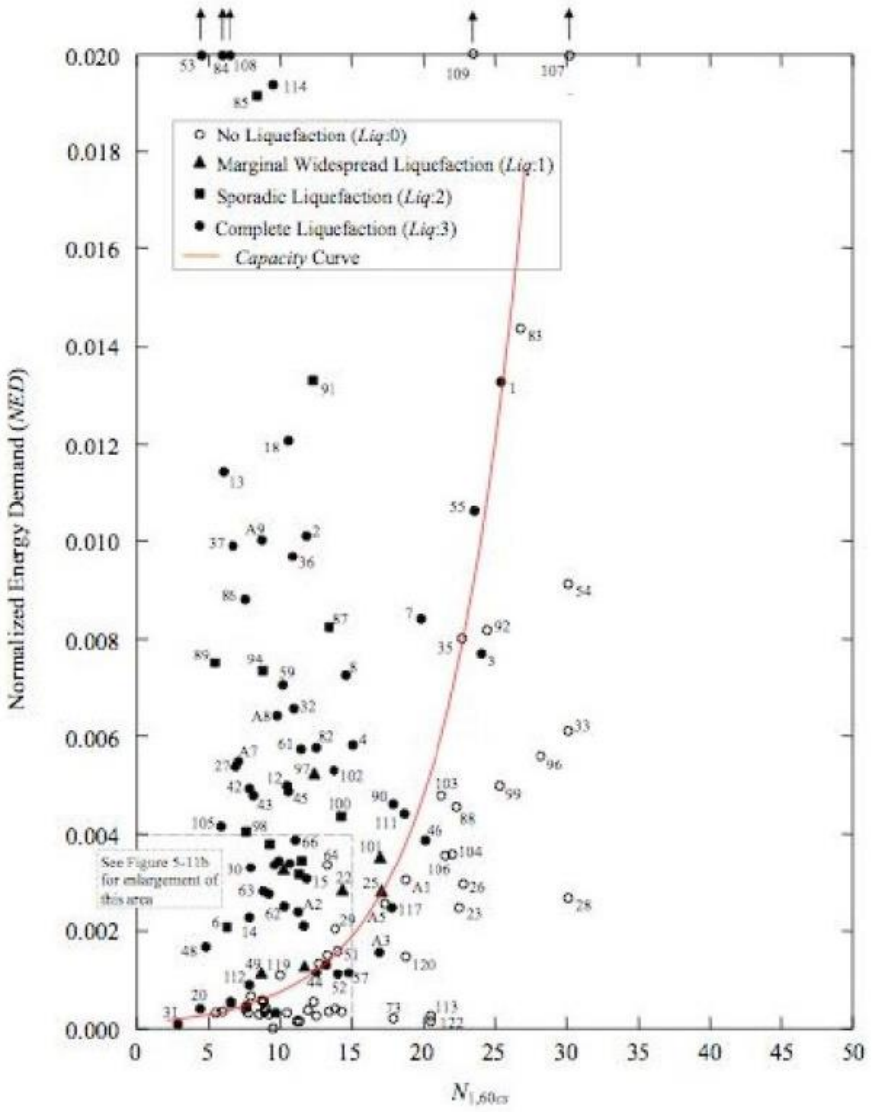


Figure 2.18: NED case histories and liquefaction resistance curve from Green (2001)

The factor of safety is defined as the ratio of NEC to NED and is shown in Equation 2.31.

$$FS_{liq} = \frac{NEC}{NED} \tag{2.31}$$

In the NED-based procedure the seismic demand is evaluated based on the results of site response analyses as opposed to an estimate provided by a GMPE. Site response analyses require input ground motion time histories and estimates of the dynamic behavior of the entire soil profile, which add a significant amount of complexity to the problem as compared to the other approaches. Therefore, the NED-based approach is not routinely employed in engineering practice.

2.3.3.5 Summary of Liquefaction Initiation Procedures

The previous subsections described four alternative ways of evaluating the liquefaction potential of a soil deposit. Each procedure is based on comparing the demand imposed by a design event to the capacity of a given soil deposit. With the exception of NED, which requires a site response analysis, each approach uses a ground motion intensity measure in conjunction with scaling factors for depth, overburden stress, and in the case of CSR, duration, to assess the demand. Each of the triggering procedures uses case history data to derive a capacity curve that divides points where liquefaction was observed from points where liquefaction was not observed.

The CSR-based approach is the most extensively researched and commonly used procedure in geotechnical practice. However, since it requires estimation of two parameters, peak acceleration and magnitude, additional uncertainty is incorporated in the results. In addition, the use of peak acceleration defines the entire time history based on a single point. While the purpose of the MSF is to correct for the duration aspects of a ground motion, it can only do so in an average sense (Abegg, 2010).

I_A and CAV_5, avoid this issue because the effects of duration are explicitly accounted for through integration of the time history. As discussed further in Chapter 5, the work of Kramer and Mitchell (2006) indicated that CAV_5 was better correlated with liquefaction in comparison to I_A and peak acceleration based on numerical analysis. This finding is supported by past research and theory. Experimental analysis by Dobry et al. (1982) showed that pore pressure generation was closely related to strain amplitude. Basic wave propagation theory indicates that shear strains are directly proportional to particle velocity ($\gamma = \dot{u}/v_s$, where $\dot{u}$ is the particle velocity, γ is the strain and v_s is the shear wave velocity of the medium the wave is travelling in). Thus, since pore pressures are highly correlated with strain amplitudes, which are related to particle velocity, it is rational to assume pore pressures should closely related to particle velocity (Abegg, 2010).

NED differs from each of the other approaches because it is not a ground motion parameter, but rather is a parameter computed based on the total stress equivalent linear response of a soil element to earthquake loading. Incorporating site response analysis adds a good deal of complexity (and uncertainty) to the problem due to the numerous assumptions and input parameters required to perform the analyses. However, since NED directly uses strains in its formulation it could provide a better correlation with pore pressure generation than alternative methods.

The preceding sections provided background information as well as outlined current techniques for evaluating both whether a soil is susceptible to liquefaction and, if it is deemed susceptible, assessing whether or not liquefaction will be triggered for a given earthquake loading. The final step in a liquefaction hazard evaluation, provided that the soil is susceptible and liquefaction is triggered for the design event, is estimating the effects of liquefaction. A discussion of the effects of liquefaction is presented in the following section.

2.4 EFFECTS OF LIQUEFACTION

Provided that liquefaction is initiated, the last step in a liquefaction hazard evaluation is to assess the effects of liquefaction. Liquefaction can have catastrophic effects on practically every kind of civil structure. The effects of liquefaction can range from massive flow slides and foundation failures to excessive settlements and ground oscillations. All of these effects can have drastic implications both in terms life-safety as well as monetary loss, which makes effectively evaluating liquefaction so vital. However, evaluating the effects of liquefaction is probably the least understood aspect of liquefaction hazard evaluation. This section describes some of the more common effects of liquefaction and, when available, provides a brief description of existing methods to evaluate them.

2.4.1 *Alteration of Ground Motion*

The stiffness of a liquefiable soil decreases as excess pore pressures develop during earthquake shaking. This softening of the soil can significantly affect the dynamic behavior of the entire soil deposit, particularly at the ground surface. The soil softening works to reduce the magnitude of high frequency seismic energy, while amplifying the transmitted low frequency energy. Since the generation of excess pore pressures and subsequent softening of the liquefiable soil is transient and occurs during the seismic event, the dynamic characteristics of the liquefiable layer change with time and are unique for each specific soil deposit and earthquake ground motion.

A typical recorded earthquake time history (i.e. a recording at a site where liquefaction does not occur) can often be divided into three general sections that are based on the inherent mechanisms of fault rupture and the properties of propagating seismic waves. Zhang (2009) identified these three sections of an earthquake time history as follows:

1. The pressure wave, or P-wave, dominated portion of the time history characterized by high frequency excitations
2. The shear wave, or S-wave, dominated portion of the time history characterized by excitations at intermediate frequencies
3. Surface and coda wave dominated portion of the time history characterized by low frequency excitation.

Figure 2.19 showns an example earthquake time history recorded at the Yerba Buena Island seismic station during the Loma Prieta earthquake. The recording station was located on a rock outcropping and was not influenced by the nonlinear dynamic behavior associated with liquefaction. The three sections described previously are delineated in the figure. The p-wave dominated portion of the record was observed from 0 to about 7 seconds, and features low amplitude, high frequency, acceleration response. From about 7 to 17 seconds the higher amplitude s-waves arrive and produce an acceleration response at frequencies that were slightly lower than the response observed during the initial portion of the time history. The portion of the record after 17 seconds shows the low-amplitude low-frequency surface wave portion of the motion. The transitions between each of the temporal regions are relatively smooth, which indicates that the change in frequency content is a function of the seismic waves and not the result of a sudden change in dynamic site properties.

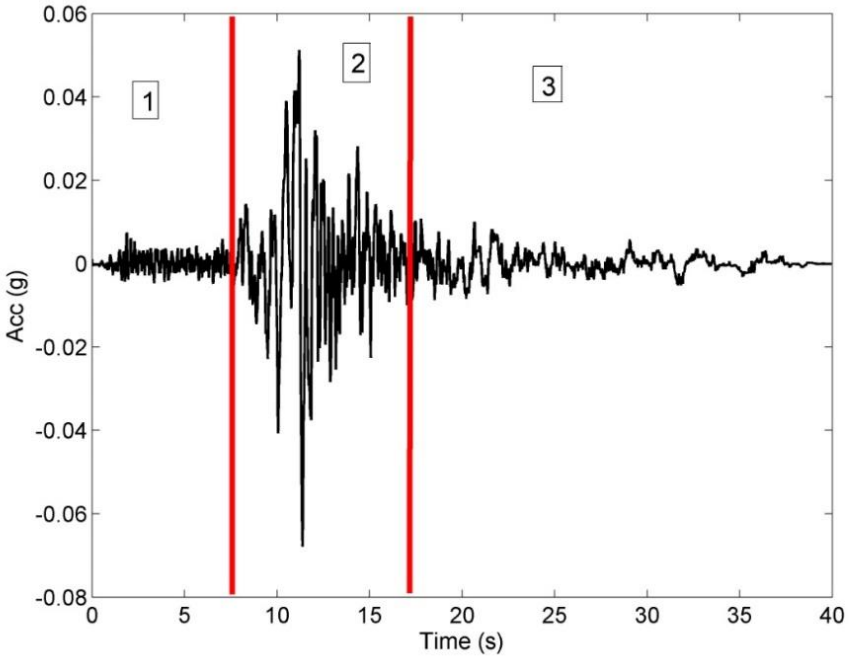


Figure 2.19: Yerba Buena Island acceleration time history, East-West component, highlighting the three temporal sections described by Zhang (2009)

The Loma Prieta event was also recorded by a station located on Treasure Island. The Treasure Island station is on a man-made island approximately 2.5 km away from the Yerba Buena Island recording station. Unlike the rock site of the Yerba Buena recording station, the Treasure Island station is located on top of approximately 11 meters of hydraulic fill constructed on a natural sand deposit underlain by a deep layer of soft silt and clay sediments known as San Francisco Bay Mud (Darragh and Shakal 1991). Bennett (1998) documented the presence of sand boils and differential settlement, which suggested that a portion of the subsurface liquefied during the earthquake. Figure 2.20 shows the response of both the Treasure Island and Yerba Buena Island records at the same time and amplitude scales for comparison.

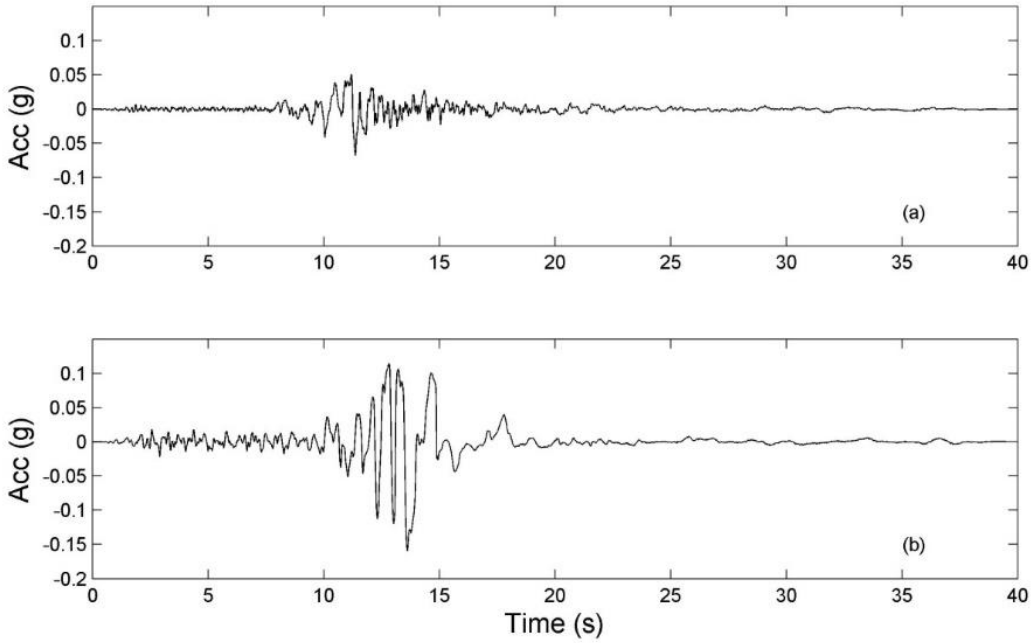


Figure 2.20: East-West components of the acceleration histories from (a) Yerba Beuna Island and (b) Treasure Island recording stations

The initial portion of the Treasure Island acceleration time history, from 0 to approximately 9 seconds, featured high frequency, relatively low amplitude acceleration response as was observed in the initial portion of the Yerba Island record. However, after the arrival of the s-waves at approximately 9 seconds into the time history, the acceleration record exhibited a high amplitude, lower frequency response. After about 15 seconds into the record, only very low frequency motion was observed in the record. It is observed from the two records that the amplitudes of the s-wave dominated portion of the record is significantly larger at the Treasure Island site. In addition, the sharp transition to low frequency response at about 15 seconds into the record as observed in the Treasure Island record was not observed in the Yerba Buena Island time history.

Another way to compare the time histories is to examine the acceleration response in the frequency domain using a fast Fourier transform (FFT). Figure 2.21 shows a plot of both Yerba Buena and Treasure Island Fourier amplitude spectra. Due to the loss of stiffness associated with liquefaction, a liquefied soil deamplifies high frequency signals and amplifies low frequency signals. The spectral response of the Treasure Island site showed a large degree of amplification at low frequencies (approximately 0.3-0.8 Hz), especially when compared to the Yerba Buena

site. The amplitudes of the high frequency components of the Treasure Island motion were much smaller than the low frequency components.

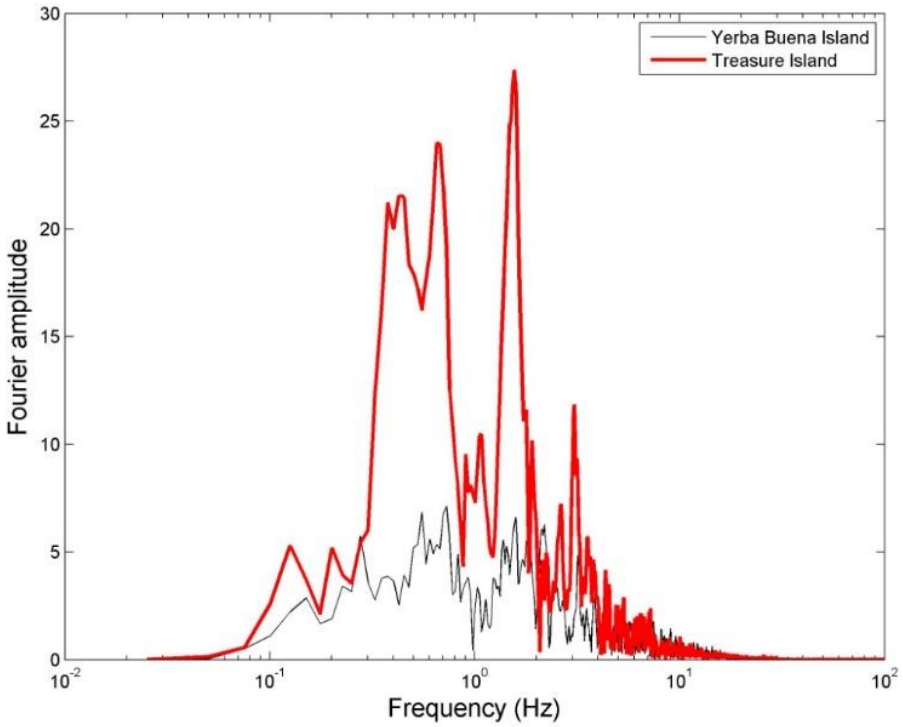


Figure 2.21: Fourier amplitude spectrum for Yerba Buena Island and Treasure Island

While liquefiable soils generally soften as excess pore pressure is generated, various studies, such as Ishihara (1985), have shown that at large strains a liquefied soil deposit can regain a significant amount of strength and stiffness due to an increase in effective stress caused by dilation of the soil during phase transformation behavior. When sand stiffens in its dilatant state, it is able to transmit higher frequency components of the motion to the surface. However, when the strain direction is reversed the liquefied soil deposit loses its stiffness and is no longer able to transmit high frequency waveforms. As a result, the acceleration record can include sporadic high frequency acceleration spikes due to dilation. These spikes are intermittent between the low frequency dominated motion that is characteristic of a liquefied soil deposit.

An example of an acceleration record at the ground surface and at the base of a liquefiable soil profile from a centrifuge experiment is shown in Figure 2.22, and clearly shows the effect of phase transformation behavior on a time history recorded at the ground surface, as illustrated by the high frequency high amplitude spikes seen in the surface record but were not observed in the base motion after about 13 seconds into the record. The testing was conducted at

the NEES centrifuge facilities at Rensselaer Polytechnic Institute in Troy, New York as part of this research study and is described in detail in Chapter 7. This experiment simulated a 7-meter tall soil profile posed of one meter of cemented sand at the base overlain by 6 meters of saturated sand and subjected to one-dimensional cyclic loading applied at the base of the model. The layers above the cemented sand were saturated Nevada sand initially placed at 50% relative density.

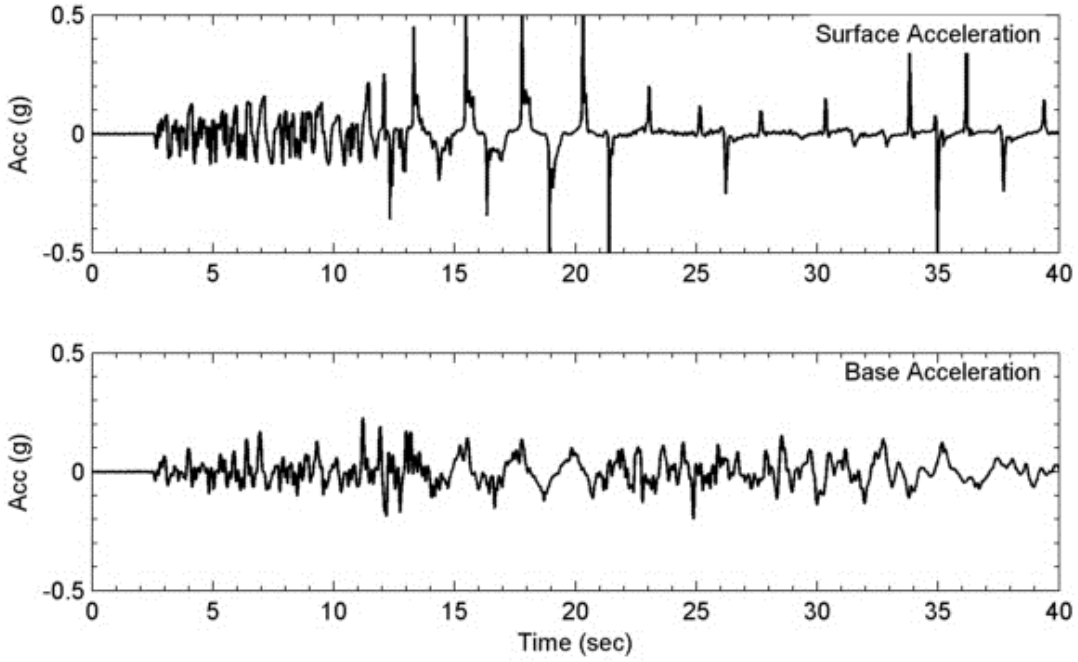


Figure 2.22: Surface recording of liquefied soil profile from centrifuge testing at the surface and at the base of the model illustrating dilatancy spikes, and amplification.

Based on pore pressure measurements, the soil liquefied at about 13 seconds, after which the motion was generally dominated by long period motion. However, this long period behavior was temporarily interrupted by high amplitude, high frequency acceleration pulses. Figure 2.23 shows a stacked plot of the base and surface acceleration records and includes a color map of the pore pressure ratios within the soil profile. The colormap shows that high pore pressure ratios began to develop in the upper 2 meters of the profile after approximately 8 seconds into the record. Pore pressure ratios in excess of 0.9 were observed at about 13 seconds, which was when the long period motion began to dominate the response of the surface acceleration. Note that during the dilation spikes, the pore pressure ratio was temporarily reduced, indicating the soil was temporarily in a dilative state. This phenomenon can be seen as the blue streaks in the pore

pressure plot at approximately the same time as the dilatancy spikes appear in the acceleration record. This reduction in pore pressure lead to temporary increase in effective stress, which in turn resulted in a temporary increase of the sands capacity to resist shear stresses and transmit high frequency motion to the ground surface. At about 22 seconds into the record the upper 4 m of the profile had reached r_u levels above 0.95 and the surface response does not include any of the high frequency motion observed in the base motion with the exception of a few intermittent dilatancy spikes.

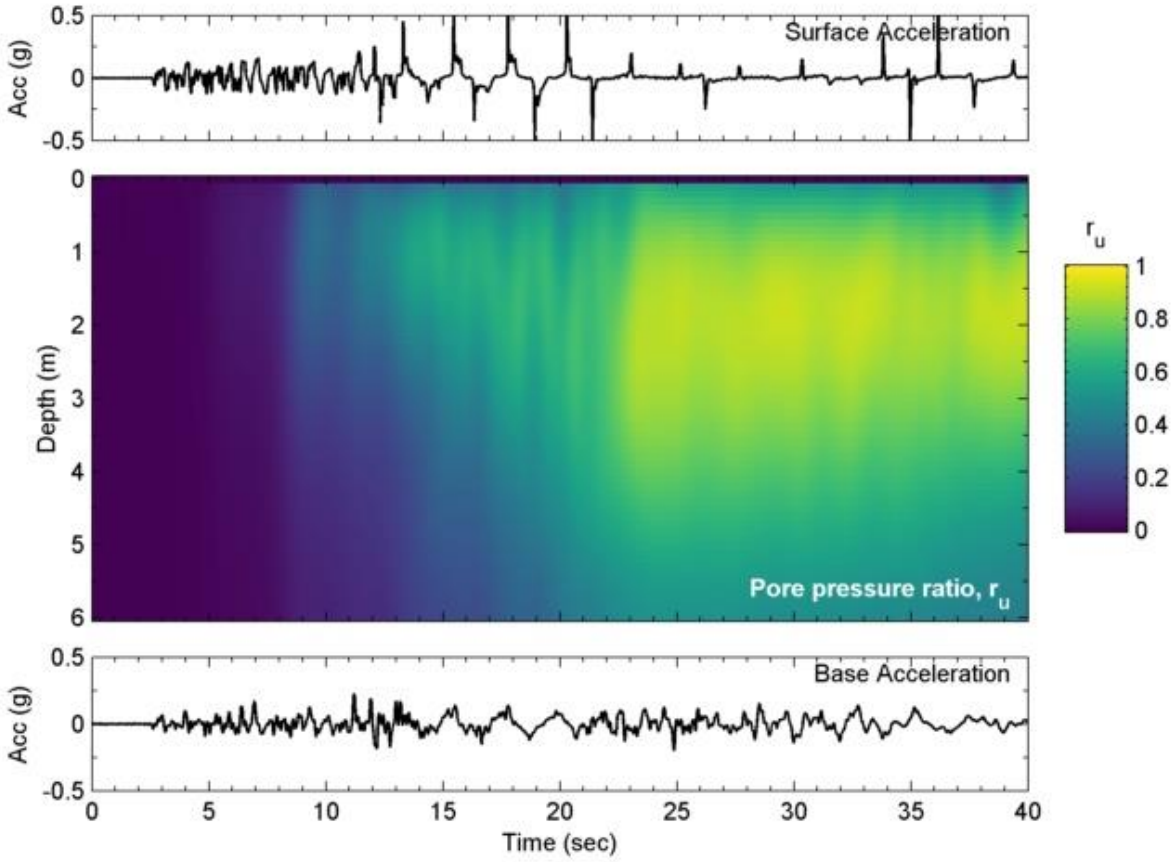


Figure 2.23: Stacked plot showing the recorded base and surface acceleration time histories and a colormap of the variation in r_u in the underlying soil profile.The colormap legend is provided to the right of the colormap.

2.4.2 *Sand Boils*

Sand boils are formed as a result of the dissipation of the excess pore pressures that are developed during earthquake shaking. The dissipation of the pore pressure can occur both during and/or after an earthquake and cause the pore water to flow upwards towards the ground surface.

If the flow is fast enough it can carry sand particles up to the surface which are deposited as sand boils (Abegg, 2010). The migration of soil particles can contribute to settlement of the underlying soils. A further discussion of liquefaction-induced settlement is provided in the next section. Examples of sand boils can be seen in Figure 2.24 which shows a photo taken after the 2011 Christchurch earthquake. Sand boils are are a very useful indicator that liquefaction has occurred and are often cited in earthquake reconnaissance as evidence of liquefaction.



Figure 2.24: Photo of sand boils taken after the 2011 Christchurch earthquake

2.4.3 *Settlement*

In addition to sand boils, another result of post-earthquake excess pore pressure dissipation is consolidation settlement. As water flows out of the voids the soil particles realign and densification occurs, resulting in ground settlement. This settlement can cause damage to structures supported on shallow foundations and utilities and can also result in flooding of low-lying land (Abegg, 2010). The magnitude and rate of settlement that occurs in saturated sands is influenced by a number of factors including the initial density of the sand, the maximum shear strain induced by the event, the amount of excess pore pressure generated, the permeability of the sand, and the characteristics of the overlying soil layers and drainage path (Kramer, 1996).

Settlements are notoriously difficult to predict even in static loading scenarios and are particularly challenging to estimate when dealing with saturated sands subject to earthquake

loading. However, a number of researchers have developed design charts to estimate free-field earthquake-induced settlements in sands. Tokimatsu and Seed (1987) developed a chart where corrected SPT blowcount and CSR are used to estimate the amount of volumetric strain that would develop in saturated sands due to the earthquake loading defined by CSR. In addition, Ishihara and Yoshimine (1992) and Ishihara et al. (2016) created charts where the factor of safety against liquefaction, the initial relative density of the sand, and the maximum shear strain are used to predict the resulting volumetric strain of the liquefiable sand layer. For all of the existing liquefaction settlement procedures the settlement is computed as the product of the estimated volumetric strain and the height of the liquefiable layer.

Due the vast number of complexities predicting free-field liquefaction settlement, it is likely that more in-depth, site-specific analysis such as finite-element modeling would be required to accurately predict liquefaction induced settlements. However, the design charts and simplified methods provide insight into the general behavior and mechanisms of seismically-induced settlements of saturated sands and provide a rough estimate of the anticipated free-field settlement.

2.4.4 *Instability*

Liquefaction-induced instabilities are some of the most destructive of all earthquake hazards and encompass a wide range of effects including flow slides and foundation and retaining wall failures. When the shear strength of the soil is reduced to the point that it approaches or becomes less than the shear strength required for equilibrium, failure potentially producing large displacements can develop. Evaluating the shear strength of the liquefied soil (termed the residual strength of the soil) is paramount in evaluating the effects of liquefaction induced stability. If the residual strength of the liquefied soil is only slightly below that required for equilibrium, it is logical to estimate the permanent displacements would be small. Large differences, however, could lead to excessive permanent displacements (Kramer, 1996).

Evaluating the residual shear strength of a liquefied soil is one of the more difficult problems in geotechnical earthquake engineering practice, as the residual strength is known to be extremely sensitive to a host of different factors including soil fabric, the initial state of the soil, partial drainage, mixing of soil layers, hydroplaning, and the stress path. One method used to estimate the residual strength involves laboratory testing of undisturbed samples. Theoretically,

if a perfectly sampled specimen were obtained, the residual or steady-state strength could be determined from a single triaxial test using methods similar to Castro (1969). Regrettably, a perfect sample is essentially impossible to obtain from a cohesionless soil due to issues involved with the acts of sampling, handling, transporting, and consolidating the test specimen (Kramer, 1996). Sampling methods that can produce high quality soil samples are available, such as frozen sampling techniques, however the associated cost is often prohibitive for use in most design and research applications.

The most common approach used to estimate the residual shear strength of liquefiable soils is based on empirical data from back analysis of flow slide case history data. This process involves performing post-earthquake static slope stability analysis of an earthen structure (typically dams) where flow liquefaction failure was observed (e.g. Seed, 1987; Seed and Harder, 1990; Olson and Stark, 2002, Kramer and Wang, 2015). Non-liquefied soil strata are assigned shear strength values based on laboratory data, when available, or using the researcher's best estimate. The liquefied soil is given an unknown shear strength value. An upper bound estimate of the residual shear strength of the liquefied soil is the shear strength value that produces a factor of safety against failure of 1.0. If the final deformed geometry of the structure is known an additional estimate of the residual shear strength can be made by iterating until the final deformed geometry is reasonably approximated by the analysis (Idriss and Boulanger, 2008). The results of these types of analysis are typically presented by curves that represent the residual shear strength ratio, S_r/σ'_v, as a function of corrected SPT blow count. An example of this type of design chart, created by Idriss and Boulanger (2008), is provided in Figure 2.25.

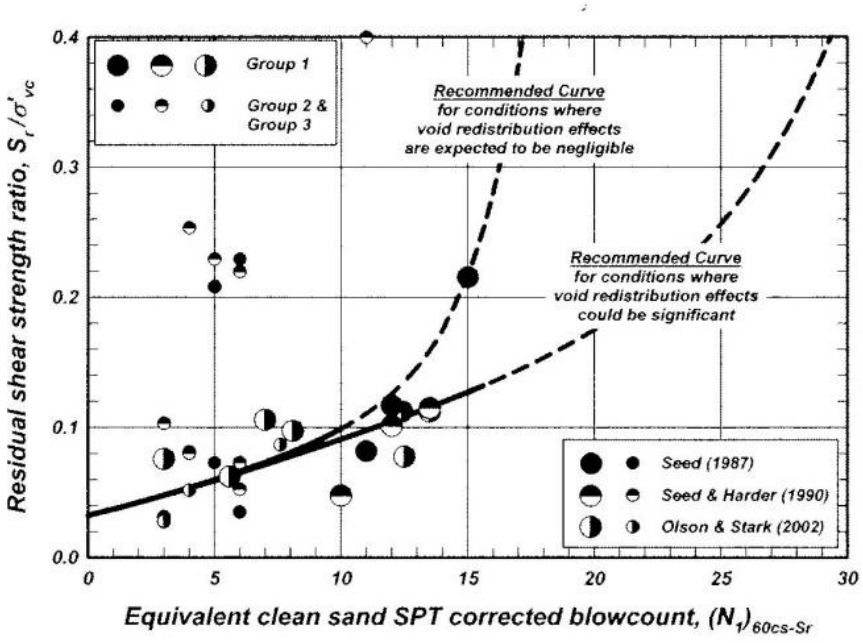


Figure 2.25: Normalized residual shear strength ratio as a function of corrected SPT blow count for liquefied sands.The upper curve represents condition where void-redistribution affects can be considered negligible, while the lower curve represents conditions where the effects of void-redistribution would be considered significant.

2.4.5 *Lateral Spreading*

Lateral spreading is a form of instability that occurs on sloping ground and is commonly associated with areas adjacent to rivers and lakes. Unlike flow liquefaction, where the deformations tend to occur suddenly, the deformations induced by lateral spreading tend to develop incrementally during earthquake loading and are driven by both static and cyclic shear stresses. Permanent deformations can be substantial, and when structures are present, lateral spreading can induce a significant amount of damage.

One method for estimating the response due to lateral spreading is a semi-empirical approach suggested by Idriss and Boulanger (2008). Their approach combines laboratory work done by a number of different researchers (e.g. Seed et al., 1984; Nagase and Ishihara, 1988) to create a method that allows for the calculation of the maximum induced shear strain as a function of the CSR and corrected SPT blow count, $(N_1)_{60,cs}$. Contours created based on this method are shown in Figure 2.26. The resulting shear strain can be multiplied by the thickness of the liquefaible soil layer to estimate the deformation due to lateral spreading.

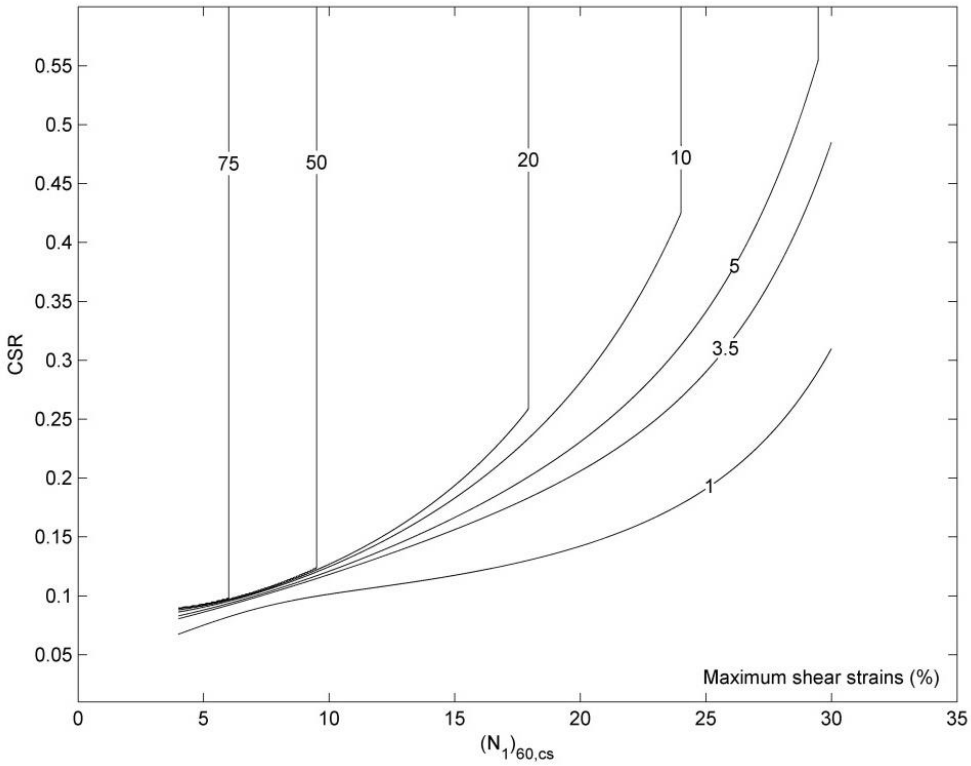


Figure 2.26: Contours of maximum shear strain as a function of CSR and corrected SPT blow count based on procedure proposed by Idriss and Boulanger (2008).

Other methods for evaluating the effects of lateral spreading include purely empirical methods such as those proposed by Rauch and Martin (2000), Youd et al. (2002), and Bardet et al. (2002). However, the main drawback of all the aforementioned procedures is the significant amount of variability in the results. Lateral spreading is an area where knowledge of the timing of liquefaction could prove to be extremely valuable in terms of evaluating the effects of liquefaction. The results from a centrifuge experiment by Brandenburg et al. (2005) highlight the relationship between the timing of liquefaction and the permanent displacement driven by lateral spreading and are shown in Figure 2.27.

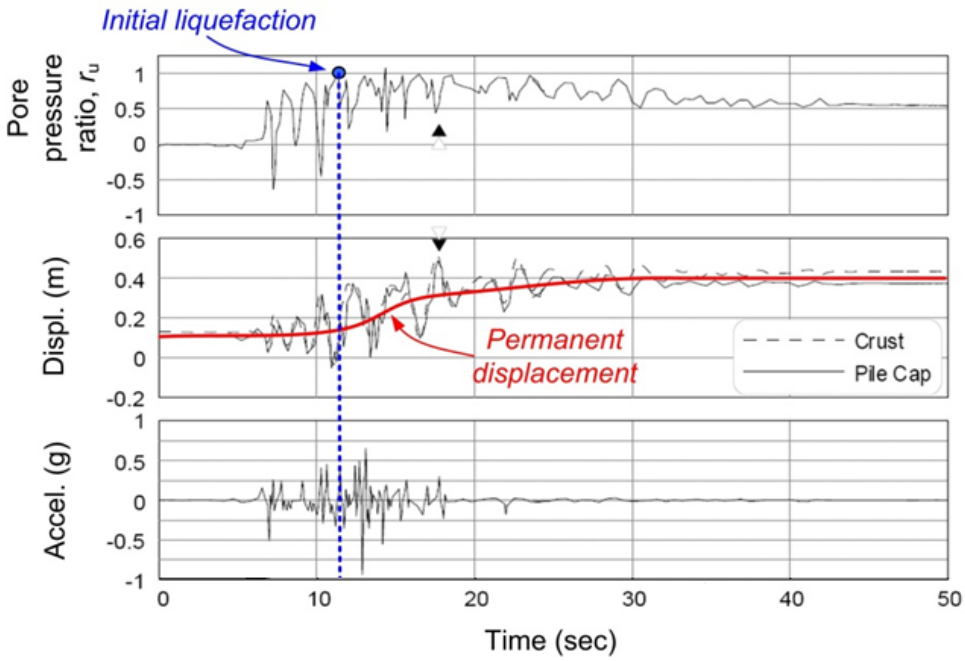


Figure 2.27: Illustration of the relationship between the timing of liquefaction and lateral spreading displacement from a centrifuge test(after Brandenburg et al., 2005).

The results shown in Figure 2.27 indicated that prior to the triggering of liquefaction (r_u = 1.0, indicated by the blue line) the permanent displacement was very small. Once liquefaction was triggered, however, the displacements rapidly increased until the shaking subsided. Laboratory results suggest that lateral spreading deformations largely develop after liquefaction has been triggered. Therefore, knowing the timing of liquefaction and amount of loading that occurs after liquefaction has been initiated may provide insight that could greatly improve the accuracy of lateral spreading evaluation. Observations such as these led to the development of the timing-based liquefaction hazard evaluation framework, presented in Chapter 4.

2.5 DISCUSSION

Liquefaction is a complex phenomenon that has proven to have devastating consequences on all facets of civil structures and must be accounted for in design in seismically active regions. This chapter described the mechanics of liquefaction and outlined current methods for evaluating liquefaction potential and the effects of liquefaction of a soil deposit. However, in its current state, liquefaction hazard analysis offers ample room for improvement. The goal of the research presented in this document is to investigate the use of evolutionary intensity measures to evaluate the initiation of liquefaction for use in an improved, timing-based, liquefaction evaluation

framework. The timing-based framework explicitly uses the timing of liquefaction to make improved estimates of the effects of liquefaction. The following section presents a generalized framework, known as performance-based earthquake engineering (PBEE), which is becoming more prevalent in engineering practice and whose concepts and terminology serve as the basis for the timing-based liquefaction hazard framework presented later in this document.

Chapter 3. PERFORMANCE-BASED EARTHQUAKE ENGINEERING (PBEE)

Limitations in the current methods for performing liquefaction hazard analyses served as the motivation for the development of a timing-based liquefaction hazard evaluation framework. This chapter details the performance-based earthquake engineering (PBEE) framework developed by the Pacific Earthquake Engineering Research Center (PEER). This framework, and the concepts and terminology associated with it, serve as the foundation for the liquefaction-specific framework presented in the following chapter.

3.1 Overview of PBEE Framework

The ultimate goal of the PBEE framework is to quantify the seismic risk in terms of mean annual rate, or frequency, of exceedance of one or more measures of loss, referred to as Decision Variables (DVs). Decision variables are typically expressed in terms of repair cost, the time required to restore the facility to operable conditions, potential casualties, or some combination of all three. Yet, directly predicting *DV*s from earthquake source parameters is not practical considering the many important factors, such as soil conditions, structural design, repair rates, etc., which are known to affect the losses for a given facility. The PBEE framework separates the DV prediction into a series of discrete components, where prediction of hazard and risk can be made with more certainty, and then sums the individual hazard contributions to assess the total seismic risk presented at a site (PBEE) (Mayfield, 2007).

In general, the PBEE framework is composed of four main stages: hazard analysis, response analysis, damage analysis and loss analysis. Hazard analysis refers to the characterization of ground motion hazards for a given site. Ground motions are often quantified in terms of an intensity measure (IM), such as peak-ground acceleration. The return period of the IM is obtained by means of a probabilistic seismic hazard analysis (PSHA). Response analysis involves assessing the response of a site/structure at the level(s) of earthquake loading specified from the hazard analysis; the response itself is quantified in terms of one or more engineering demand parameters (EDPs). Common examples of EDPs include permanent ground displacement, settlement and inter-story drift. The next stage, damage analysis, involves

determining the degree of physical damage resulting from the predicted response. That damage is characterized by one or more damage measures (DMs), that would be expected to occur based on a given EDP. The purpose of the DMs is to quantify the necessary repairs and to assess any functional or life safety complications resulting from the seismic damage. The final step in the process is loss analysis, whose purpose is to inform the stakeholder (developers, municipalities, etc.) for use in making decisions concerning future performance of the site/structure in question and is expressed in terms of DVs (Moehle and Deierlein, 2004).

3.1.1 *Probabilistic Seismic Hazard Analysis*

Probabilistic seismic hazard analysis (PSHA) is the first step of the PBEE process and is an approach for estimating the ground motion hazard at a site expressed in terms of a mean annual rate of exceedance of a particular ground motion intensity measure. The graphical representation of this relationship is called a hazard curve. Cornell (1968) presented a process for developing an IM hazard curve that is a function of the frequency and probability of occurrence of all possible earthquake magnitudes at all possible source-to-site distances, based on the total probability theorem. The mean annual rate an IM exceeds a particular value, *im*, can be expressed as,

$$\lambda_{IM}(im) = \sum_{i=1}^{N_S} v_i \int\int P[IM > im|m,r] \cdot f_{M_i}(m) \cdot f_{R_i}(r)\, dm\, dr \tag{3.1}$$

where N_S is the number of seismic sources that can affect the given site, v_i is the annual rate of exceedance of the minimum magnitude of interest for the ith seismic zone, P[IM > *im*|*m,r*] is the probability that IM is greater than *im* conditional upon the particular magnitude, *m*, and source-to-site distance, *r*, and $f_{M_i}(m)$ and $f_{R_i}(r)$ are the probability density functions for magnitude and source-to-site distance for the ith seismic source zone, respectively (Kramer, 1996).

Equation 3.1 can be reduced by noting that, according to the total probability theorem,

$$P[IM > im]_i = \int\int P[IM > im|m,r] \cdot f_{M_i}(m) \cdot f_{R_i}(r)\, dm\, dr \tag{3.2}$$

So that,

$$\lambda_{IM}(im) = \sum_{i=1}^{N_S} v_i \cdot P[IM > im]_i \tag{3.3}$$

Thus, the mean annual rate of exceedance can be expressed as the sum, across all seismic sources, of the product of a complimentary cumulative probability distribution, P[IM > *im*] implicitly conditional upon the occurrence of a significant earthquake, and the mean annual rate of occurrence of significant earthquakes, i.e. those that exceed the minimum threshold magnitude (Mayfield, 2007).

3.1.2 *PBEE Equation*

The PBEE framework provides a method to extend a ground motion hazard curve, λ_{IM}, from a PSHA, to a DV hazard curve, λ_{DV}, based on the following rationale (from Mayfield, 2007)

1. The ground motion at a particular site can be described by an IM, such as PGA, and the hazard can be quantified, most often based on a PSHA.
2. The IM causes some level of response at the site, which can be defined using an EDP, such as settlement or level of excess pore pressure generation.
3. The EDP causes some level of physical damage to the structure, which can be described by a DM, such as crack width or downslope displacement.
4. The DM leads to some loss, as described by a DV, such as casualties, downtime or cost.

Figure 3.1 shows a simple schematic of the PBEE process. The ground motion hazard is quantified using a PSHA. Then a response model is used along with the ground motion hazard to determine the system response. Next, a damage model is incorporated to assess the physical damage to the structure. Lastly, a loss model is used to generate the DV hazard curve.

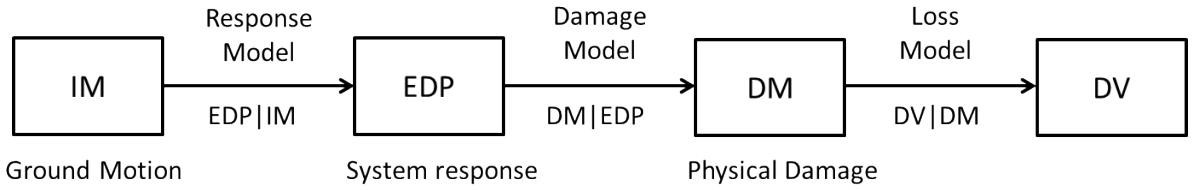


Figure 3.1: Schematic of PBEE analysis process.

As indicated in Figure 3.1, once the seismic hazard in the first step is quantified, the hazard at each additional stage in the process is estimated based on the hazard determined in the previous stage and the conditional probability distribution between the two stages. For example, in the second stage the EDP hazard, λ_{EDP}, is determined based on IM hazard, λ_{IM}, and the

conditional probability distribution, P[EDP > *edp*|*im*], which is obtained from a response model. From the total probability theorem,

$$P[EDP > edp] = \int P[EDP > edp \,|\, im] \cdot f_{IM}(im)\, dim \tag{3.4}$$

where $f_{IM}(im)$ is the probability density function for IM. As shown previously, complementary cumulative distributions can be converted into mean annual rates of exceedance by multiplying them by the mean annual rate of threshold magnitude exceedance for a given source, v, so that,

$$\lambda_{IM}(im) = vP[IM > im]$$

$$\lambda_{EDP}(edp) = vP[EDP > edp] = \int P[EDP > edp|im]\left|\frac{d\lambda_{IM}(im)}{dim}\right| dim \tag{3.5}$$

A similar process can be applied to the third step in the process to get the DM hazard from the EDP hazard:

$$\lambda_{DM}(dm) = \int P[DM > dm|edp]\left|\frac{d\lambda_{EDP}(edp)}{dedp}\right| dedp \tag{3.6}$$

Using Equation 3.5,

$$\frac{d\lambda_{EDP}(edp)}{dedp} = \int \frac{P[EDP > edp|im]}{dedp}\left|\frac{d\lambda_{IM}(im)}{dim}\right| dim \tag{3.7}$$

Noting that the derivative of $\lambda_{EDP}(edp)$ in terms of edp, does not affect the λ_{IM} term because λ_{IM} is independent of *EDP*. Combining Equations 3.6 and 3.7 gives,

$$\lambda_{DM}(dm) = \int\int P[DM > dm|edp]\frac{P[EDP > edp|im]}{dedp}\left|\frac{d\lambda_{IM}(im)}{dim}\right| dim\, depd \tag{3.8}$$

This process is then extended to the full PBEE framing equation to express the *DV* hazard, λ_{DV}, as,

$$\lambda_{DV}(dv) = \int\int\int P[DV > dv \,|\, dm]\frac{P[DM > dm \,|\, edp]}{ddm} \frac{P[EDP > edp|im]}{dedp}\left|\frac{d\lambda_{IM}(im)}{dim}\right| dim\, dedp\, ddm \tag{3.9}$$

where $P[DV > dv \,|\, dm]$ is obtained from a probabilistic loss model. The preceding equations show how the hazard terms for each step in the PBEE process (λ_{IM}, λ_{EDP} and λ_{DM}) all contribute, in series, to λ_{DV}. Yet, as shown in Equation 3.9, only λ_{IM}, in conjunction with a set of conditional probability distributions, is needed to evaluate λ_{DV} (Mayfield, 2007).

3.1.3 *Graphical Representation of PBEE Framework*

The hazard functions and conditional probability distributions required in the PBEE framing equation are represented graphically using hazard and fragility curves, respectively. Figure 3.2a shows an IM hazard curve, or the mean annual rate of exceedance as a function of IM. Fragility curves represent the conditional probability distributions that describe the relationship between two levels in the PBEE framework. An example set of IM-EDP fragility curves are shown in Figure 3.2b. In the formulation shown in Equation 3.5, each fragility curve is integrated with respect to the derivative of the hazard curve to produce a single point on the subsequent EDP hazard curve, λ_{EDP}. This process is repeated with additional fragility curves until the EDP hazard curve can be adequately defined.

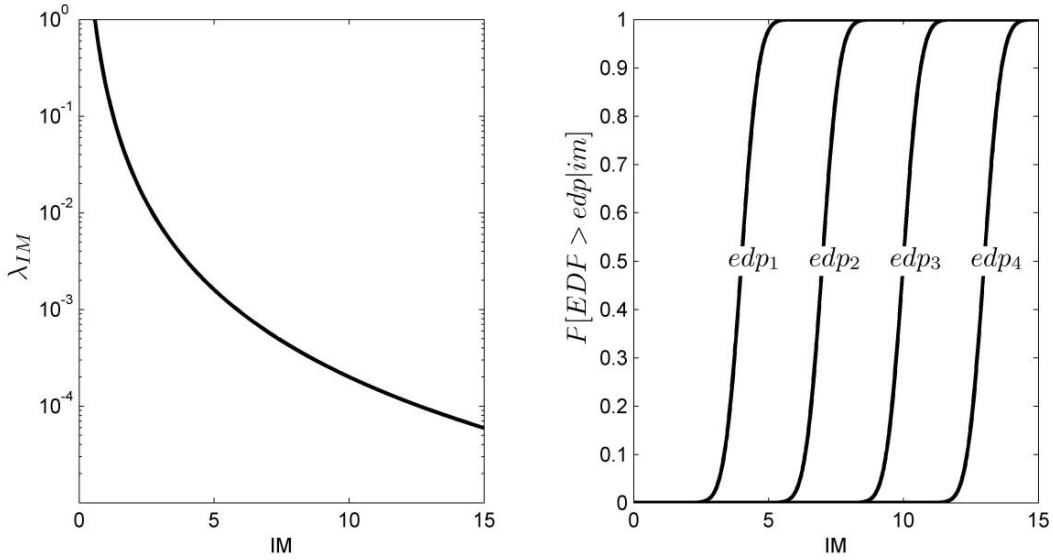


Figure 3.2: Examples of (a) IM hazard curve and (b) IM-EDP fragility curves.

As expressed in Equation 3.9, the integration process involving hazard and fragility curves is repeated at each level of the PBEE framework to develop the hazard curve for the following level. This process is shown schematically in Figure 3.3. In practice, due to the lack of well-defined, closed form solutions for the hazard and fragility curves, the integration process in the PBEE framing equation is generally carried out numerically.

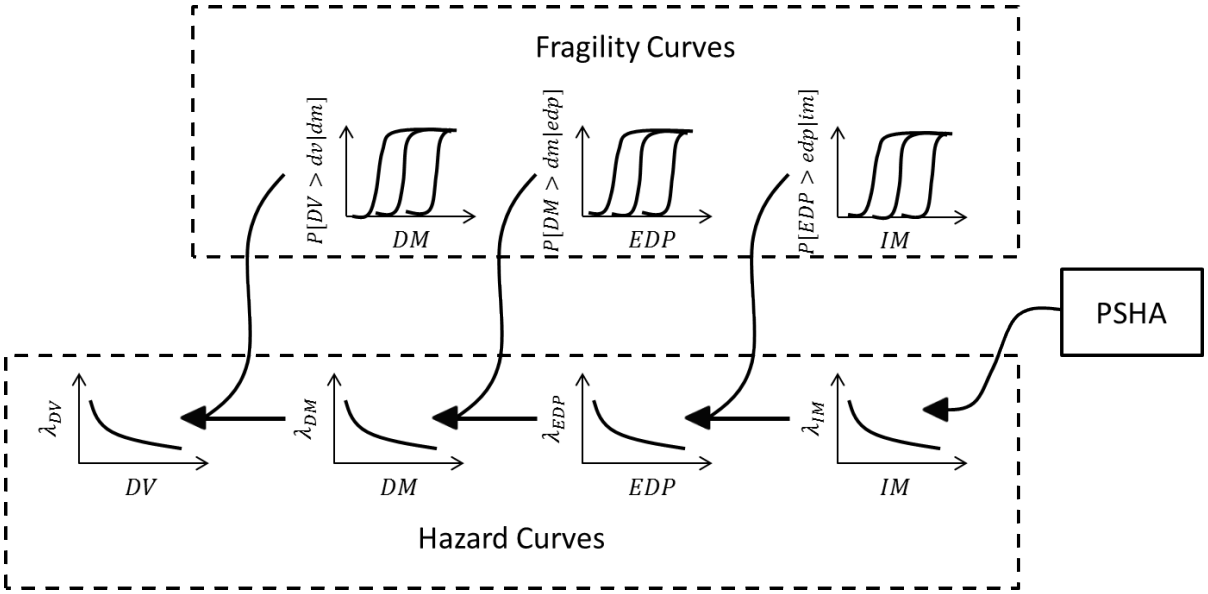


Figure 3.3: Graphical schematic of PBEE process.

3.1.4 *Introduction to Uncertainty in PBEE Framework*

In the aforementioned formulations, it is important to note that the accuracy and degree of conservatism in the results are not solely a function of the mean value of the various relationships, but also are highly dependent on the degree of uncertainty present in each of the relationships (Kramer and Mitchell, 2006). To highlight this notion a brief exercise was conducted using a closed form solution to develop λ_{EDP}, assuming the IM hazard curve is defined as $\lambda_{IM} = k_0(im)^k$, and the EDP is related to the IM so that $edp = a(im)^b$ where k_o, k, a and b are constants, and the uncertainty in the EDP-IM relationship is lognormally distributed with standard deviation, $\sigma_{\ln epd|im}$.

Based on these assumptions, Jalayer and Cornell (2003) showed that the EDP hazard curve can be defined as,

$$\lambda_{EDP} = k_0\left(\frac{edp}{a}\right)^{-k/b}\exp\left[\frac{k^2}{2b^2}\sigma^2_{\ln edp|im}\right] \tag{3.10}$$

Equation 3.10 indicates there are two terms in the closed form derivation of λ_{EDP}. The first term is based upon the median of the EDP-IM relationship, while the second, exponential term, essentially amplifies the first term based on the uncertainty in the EDP-IM relationship. Figure 3.4 shows plots illustrating the process described above. Figure 3.4 (a) and (b) show plots of the

IM hazard curve and EDP-IM relationship. Figure 3.4 (c) displays the resulting EDP hazard curves for different levels of uncertainty and shows the dramatic affect uncertainty can have on the resulting hazard curves.

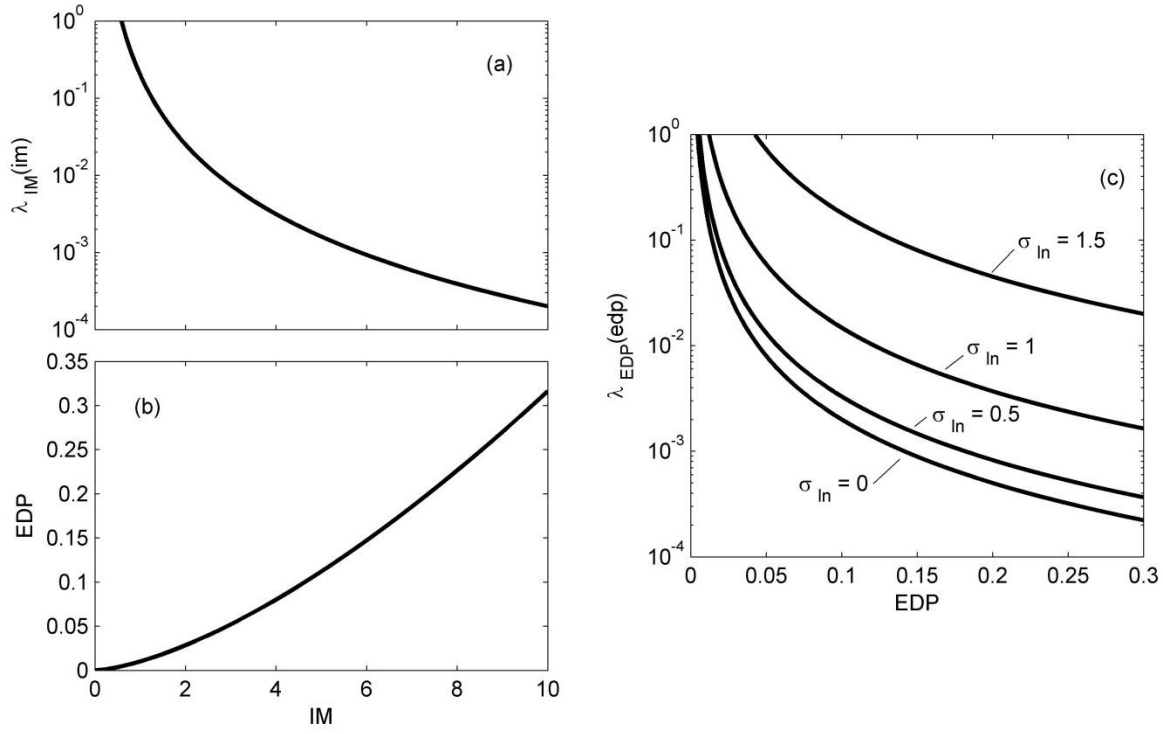


Figure 3.4: Effect of uncertainty in PBEE framework using closed form solutionsfor the IM hazard curve (a), the EDP-IM relationship (b), and the resulting EDP hazard curve (c). The resulting EDP hazard curves are provided for different levels of uncertainty. Note that σ_{ln} in the figures above represents $\sigma_{ln\ EDP|IM}$

3.2 Effects of Predictability, Efficiency and Sufficiency

The research described in this dissertation is focused on the second process in PBEE framework, prediction of the EDP hazard for the problem of soil liquefaction. The value of the EDP at a particular hazard level (or return period) will be influenced by the predictability of the IM and the efficiency with which the IM predicts the EDP. Predictability refers to the accuracy with which an IM can be predicted given magnitude, distance, site condition, etc.; it is expressed by the standard error term in the GMPE used to determine the mean annual rate of exceedance of the IM, λ_{IM}. Efficiency, on the other hand, is a measure of the uncertainty involved in the

relationship used to estimate the EDP conditional upon a given IM (EDP|IM) (Cornell, 1968; Kramer and Mitchell, 2006).

Sufficiency is a somewhat different concept than predictability or efficiency. A sufficient IM is defined by Luco and Cornell (2007) as an IM whose prediction of EDP is conditionally independent of earthquake magnitude and source-to-site distance. For example, a peak ground motion parameter might be a sufficient predictor of the response of a steel building, but an insufficient predictor of response for degrading systems such as concrete buildings or liquefiable soil deposits, where response is also influenced by the number of loading cycles, which is, in turn a function of the duration and magnitude of the ground motion. Sufficiency is an important issue for liquefaction, where the insufficiency of peak ground acceleration, a_{max} has led to the development of a magnitude scaling factor to better predict EDPs such as factor of safety against liquefaction or lateral spreading displacements. Because both a_{max} and magnitude (M_w) are used, the uncertainty in both must be accounted for in a performance-based evaluation of liquefaction potential. This can be accomplished by integrating over their joint hazard surface to compute the EDP hazard curve. In this case, the standard relationship of Equation 3.5 must be modified as follows to account for the fact that the IM is a vector,

$$\lambda_{EDP}(edp) = \int_{a_{max}} \int_{M_w} P[EDP > edp | a_{max}, M_w] d\lambda_{a_{max}, M_w}(a_{max}, M_w) \tag{3.11}$$

where λ_{a_{max}, M_w} is the joint hazard surface for a_{max} and M_w.

This adds significant complexity to the analysis since the joint hazard of a_{max} and magnitude must be evaluated. Mayfield (2007) used deaggregation data to develop a suite of curves, each corresponding to a different magnitude, and summed the contribution to the EDP hazard from all magnitudes at each acceleration level.

The effects of predictability and efficiency can be pronounced. Kramer and Mitchell (2006) illustrated the effects of these uncertainties within the PBEE framework. They performed a simple PSHA for a hypothetical site (Figure 3.5a) using a GMPE by Boore et al. (1997) and a generic EDP fragility curves (Figure 3.5b). EDP hazard curves (Figure 3.5c) were calculated from Equation 3.5 and the results were used to compute EDP probability distributions (Figure 3.5d) for an EDP hazard recurrence frequency of $\lambda_{EDP} = 0.02$. Initially the calculations were conducted with the original uncertainty values, which produced the results labeled “Base” in

Figure 3.5. Then the calculations were repeated, allowing the uncertainty in the GMPE (predictability), and the fragility curves (efficiency) to vary by +/-20%. For example, the curve labeled $^{\sigma}/_{\sigma_{\ln IM}} = 0.8; ^{\sigma}/_{\sigma_{EDP|IM}} = 1.2$ represents a function that was calculated using a 20% increase in the predictability (reduced variability in the IM prediction), and a 20% decrease in the efficiency (increased variability in the EDP|IM predictive equation).

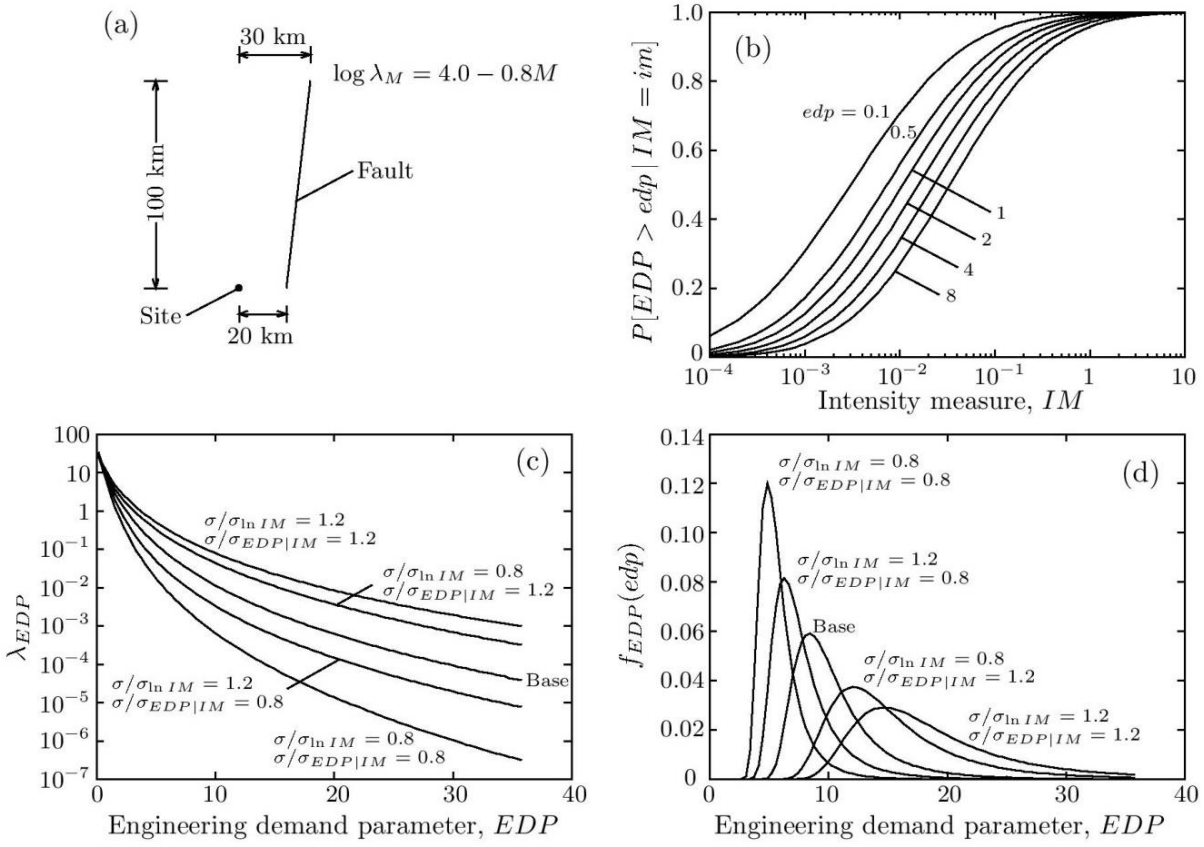


Figure 3.5: Illustration of the effects of uncertainties for a hypothetical site(a), (b) fragility curves for EDP|IM, (c) effects of uncertainties in terms of an EDP hazard curve and (d) probability distributions for λ_{EDP} = 0.02 values, from Mayfield (2007).

While the results shown in Figure 3.5 are from an overly simplified example, they do indicate the pronounced effects of both predictability and efficiency on the results. For example, when $\lambda_{EDP} = 0.01$ the base case indicates an *EDP* of about 10. When the predictability and efficiency are each improved by 20% (reduction in uncertainty in both by 20%), the curve labeled $^{\sigma}/_{\sigma_{\ln IM}} = 0.8; ^{\sigma}/_{\sigma_{EDP|IM}} = 0.8$) the *EDP* level drops to about 5. When the uncertainty in both

the IM (predictability) and the *EDP*|*IM* relationship (efficiency) is increased by 20% (the curve labeled $^{\sigma}/_{\sigma_{\ln IM}} = 1.2; ^{\sigma}/_{\sigma_{EDP|IM}} = 1.2$), the *EDP* level rises to about 19.

This example illustrated how higher uncertainty leads to increased values of EDP at a given hazard level (Figure 3.5c). In addition, there can also be a dramatic effect on the shapes of the probability distribution functions (Figure 3.5d), which tended to broaden as the uncertainty increased. In the PEER framework, this effect of increased EDP hazard estimates resulting from large uncertainties in IM predication and in the EDP|IM relationships are propagated through to the DM and DV stages and can result in overly conservative and very costly design decisions.

3.3 DISCUSSION

The PBEE framework provides a rational, modular approach for the design, construction, maintenance, and rehabilitation of facilities that focuses on meeting the needs of the facility stake-holders (owners, users, government) rather than satisfying minimum requirements outlined by building codes (Mayfield, 2010). As opposed to designing for binary conditions such as failure or non-failure, PBEE works to relate earthquake loading levels to damage and, in turn, to variables that are informative to people outside of the engineering and construction communities, such as cost, downtime and life-safety. The probabilistic framework is a natural environment for designing for random occurrences such as earthquakes. The increased availability of high-quality recorded, experimental, and simulated data now makes such analyses feasible.

However, current liquefaction procedures lack a unified methodology to go from a prediction of the imposed loading to a prediction of response, in a predictable, efficient, and sufficient manner. As illustrated previously, improving the accuracy in EDP|IM relationships can have a pronounced and beneficial effect on EDP hazard levels. This effect is propagated all the way through to the decision variables which ultimately result in more efficiently designed structures. Identifying IMs and EDP|IM relationships that have the highest possible predictability, efficiency and sufficiency with respect to liquefaction is the primary goal of the timing-based liquefaction hazard evaluation framework presented in the following chapter.

Chapter 4. TIMING-BASED FRAMEWORK FOR LIQUEFACTION HAZARD EVALUATION USING EVOLUTIONARY INTENSITY MEASURES

Existing procedures for evaluating the potential for liquefaction involve comparing consistent measures of loading and resistance. With respect to the most popular, stress-based liquefaction evaluation procedure, many important refinements have been made over the years. The basic procedure, however, has remained essentially unchanged for nearly 40 years, and is not especially well-suited for use in emerging performance-based design methods due to how the loading is characterized. In the stress-based procedures a complex acceleration time history is represented by a single point, its peak value, and a crude proxy for duration. Figure 4.1 shows plots of two motions, Motion A (Figure 4.1a) and Motion B (Figure 4.1b), that have the same value of PGA/MSF as computed using the method described in Section 2.3.3.1 using the cycle weighting function methods and magnitude scaling function from Liu et al. (2001). For these two motions, the stress-based triggering and effects evaluation procedures would compute the same response.

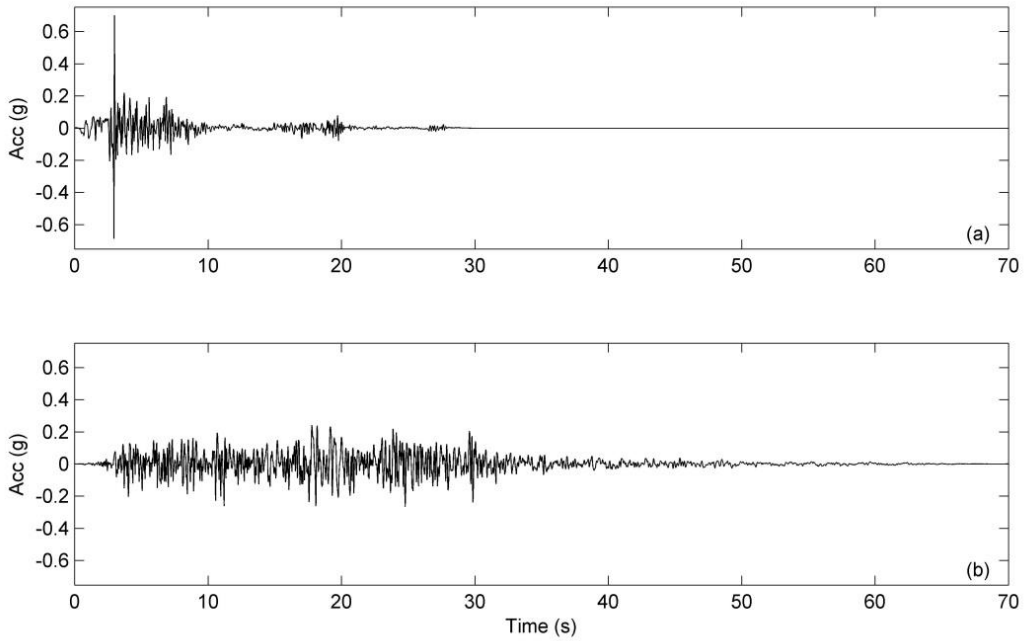


Figure 4.1: Comparison of two motions Motion A (a) and Motion B (b) that have identical PGA/MSFcomputed using the method of Liu et al. (2001).

However, it is reasonable to believe that identical soil profiles subjected to these two motions would not produce the same level of excess pore pressure. Motion A is dominated by a single pulse at very high frequency and features less than 10 seconds of strong ground motion, whereas Motion B features fairly constant amplitude motion with about 30 seconds of strong ground motion that induce many more reversals of stress in the soil than Motion A. These two motions highlight how knowledge of the timing of liquefaction could prove to be beneficial when evaluating the effects of liquefaction. Figure 2.27 showed that, with respect to lateral spreading, the effects of liquefaction were primarily a function of the post-liquefaction loading. If Motion A induced liquefaction at around 10 seconds, after which the remaining ground motion is very weak, it is logical to assume that the effects would be drastically different than if liquefaction was induced in Motion B after 10 seconds, where the post-liquefaction loading features over 20 seconds of significant ground shaking.

In addition, Figure 2.27 illustrated that the peak acceleration of the ground motion can in some instances occur after liquefaction had been triggered, and therefore is not an accurate representation of the loading that induced liquefaction. Observations such as these are what motivated this investigation to improve the current liquefaction hazard evaluation techniques using evolutionary intensity measures. The following section provide background on evolutionary intensity measures and show how they can be incorporated in a new framework for liquefaction hazard evaluation.

4.1 Evolutionary Intensity Measures

Evolutionary intensity measures (IMs) are intensity measures that build up with time over the duration of an earthquake ground motion. Some intensity measures are based on integration of ground motion characteristics, and therefore are inherently evolutionary. However, non-integral IMs can often be reformulated and expressed in an evolutionary form. For example, an evolutionary form of peak ground acceleration, PGA(t), can be expressed in evolutionary form as

$$PGA(t) = \max\left[|a(0{:}t)|\right] \tag{4.1}$$

where a is the acceleration time history and 0:t represents all the points from the start of the record up to the current time, t.

Historically, researchers have focused on using the final ($t = \infty$) values of a given intensity measure for use in liquefaction hazard evaluation. Each of the most commonly used

scalar IMs used in the liquefaction triggering procedures can be expressed as evolutionary intensity measures, as shown in Table 4.1. The IM from the stress-based procedure, PGA/MSF or PGA_m, can be formulated as an evolutionary intensity measure by evaluating the PGA per Equation 4.1 and dividing it by an evolutionary implementation of MSF computed based on a number of equivalent cycles that evolves with time using the methodology described in Section 2.3.3.1. Table 4.1 provides definitions for two different formulations for PGA_m, PGA_{mL} and PGA_{mB}, which use slightly different MSF formulations and cycle weighting functions as descibed by Liu et al. (2001) and Boulanger and Idriss (2014), respectively. To create a time history of PGA_m, the increase in PGA_m from an individual pulse, or half-cycle, of loading was distributed evenly across the zero-crossing interval of the pulse.

Note that, per Boulanger and Idriss (2014), both the MSF and cycle scaling method are functions of the exponent b which is in turn a function of the relative density of the soil. This would correspond to an intensity measure that is also dependent on the relative density of the soil. In the PBEE framework descrived in Chapter 3, a density-dependent IM would require significantly more rigourous analyses, including but not limited to, having to evaluate GMPEs that cover a range of densities and evaluating the joint distribution of both the IM and density. To develop a density-indpendent representation of the Boulanger and Idriss (2014) MSF, Greenfield (2017) redifined the MSF as the product of two independent terms, MSF_L and K_m, where MSF_L is a magnitude scaling term that is independent of relative density, and K_m is a factor that scales MSF_L based on the relative density of the soil. MSF_L is defined as the MSF computed using Equations 2.7 and 2.8 with N_{ref} equal to 15 and a b value of 0.236. The b value of 0.236 corresponds to a corrected SPT blow count of 15 blosws per foot. In this study, PGA_{mB} was defined as,

$$PGA_{mB}(t) = \frac{PGA(t)}{MSF_L(t)} \tag{4.2}$$

Table 4.1: Evolutionary formulation of scalar IMs used in liquefaction hazard evaluation procedures detailed in Section 2.3.3.1.

IM	Evolutionary IM formulation
PGA_{mL}	$$PGA_m(t) = PGA(t)/MSF(t)$$ where PGA(t) is the absolute peak acceleration of the acceleration time history up to time t, and $MSF(t)$ is an evolutionary magnitude scaling factor, as defined by Liu et al. (2001) per Equation 2.11 and the number of cycles is evaluated using the scaling factors listed in Table 2.1.
PGA_{mB}	$$PGA_m(t) = PGA(t)/MSF_L(t)$$ where $MSF_L(t)$ is computed using Equation 2.8 with N_{ref} = 15 and the number of equivalent cycles is evaluated using Equation 2.7 with b = 0.236.
IA	$$I_A(t) = \int_0^t a(t)^2 dt$$
CAV	$$CAV(t) = \int_0^t \lvert a(t)\rvert dt$$
CAV5	$$CAV_5(t) = \int_0^t \langle\chi\rangle \lvert a(t)\rvert$$ where $$\langle\chi\rangle = \begin{cases} 0 \; for \; \lvert a(t)\rvert \leq 5 \, {}^{cm}/_{s^2} \\ 1 \; for \; \lvert a(t)\rvert \geq 5 \, {}^{cm}/_{s^2} \end{cases}$$

A comparison of the differences in the cycle weighting factors and MSF functions used to compute PGA_{mL} and PGA_{mB} are provided in Figure 4.2. The cycle weighting functions determined using Table 2.1 for the Liu et al. (2001) method and Equation 2.7 using a b value of 0.236 for the Boulanger and Idriss (2014) method are shown in Figure 4.2a as a function of the amplitude ratio, defined as the amplitude of a given cycle, a_i, divided by the PGA. By definition, both relationships equal 1.0 when a_i is equal to 65% of PGA. However, the cycle weighting relationship from Boulanger and Idriss (2014) using a b value of 0.236 was almost uniformly

higher than the Liu et al. (2001) relationship, especially at amplitude ratios above 0.65. Therefore, for a given earthquake time history, the Boulanger and Idriss (2014) method will compute a higher number of equivalent cycles than the Liu et al. (2001) method. Figure 4.2b shows the MSF relationships for the two methods. The MSF relationship from Boulanger and Idriss (2014) is lower than the MSF relationship from Liu et al. (2001) for N values less than about 45. Based on observations from Figure 4.2, for most loading time histories, PGA_{mB} is anticipated to be greater than PGA_{mL}.

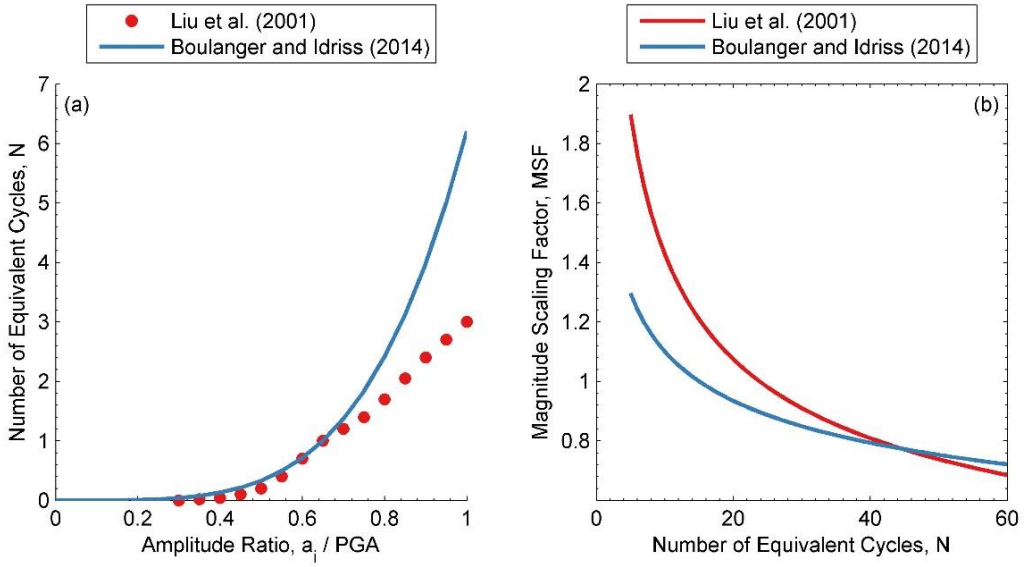


Figure 4.2: Comparison of the cycle weighting factors (a) and magnitude scaling factors (b) used to compute PGA_m using the procedures of Liu et al. (2001) and Boulanger and Idriss (2014).

Figure 4.3 compares the behavior of each of the evolutionary intensity measures with respect to the two ground motions presented previously in Figure 4.1. Motion A reached its peak value early in the record and was dominated by a single large amplitude cycle. This behavior was reflected in the time histories of the various evolutionary IMs, all of which increased rapidly around the time of the large amplitude cycle. The behavior of both PGA_m formulations were entirely dominated by the peak value. I_A, CAV, and CAV_5, on the other hand, were influenced by motion that occurs both before and after the occurrence of the large amplitude peak cycle, with I_A more influenced by the peak value than CAV and CAV_5. Motion B reached its peak value at about 12 seconds into the record, but also included numerous other cycles with amplitudes similar to the peak. This behavior was captured by the evolutionary IMs, which all increase relatively steadily over the duration of the strong ground motion. The integral parameters, I_A,

CAV, and CAV_5 each reached larger values for Motion B than Motion A. PGA_{mB}, reached a higher final value for Motion A than for Motion B. Due to the differences in the cycle scaling methods and MSF formulations, PGA_{mL} and PGA_{mB} can differ significantly from one another. Consistent with the observations made previously, PGA_{mB} reached a larger peak value than PGA_{mL} for both Motion A and Motion B.

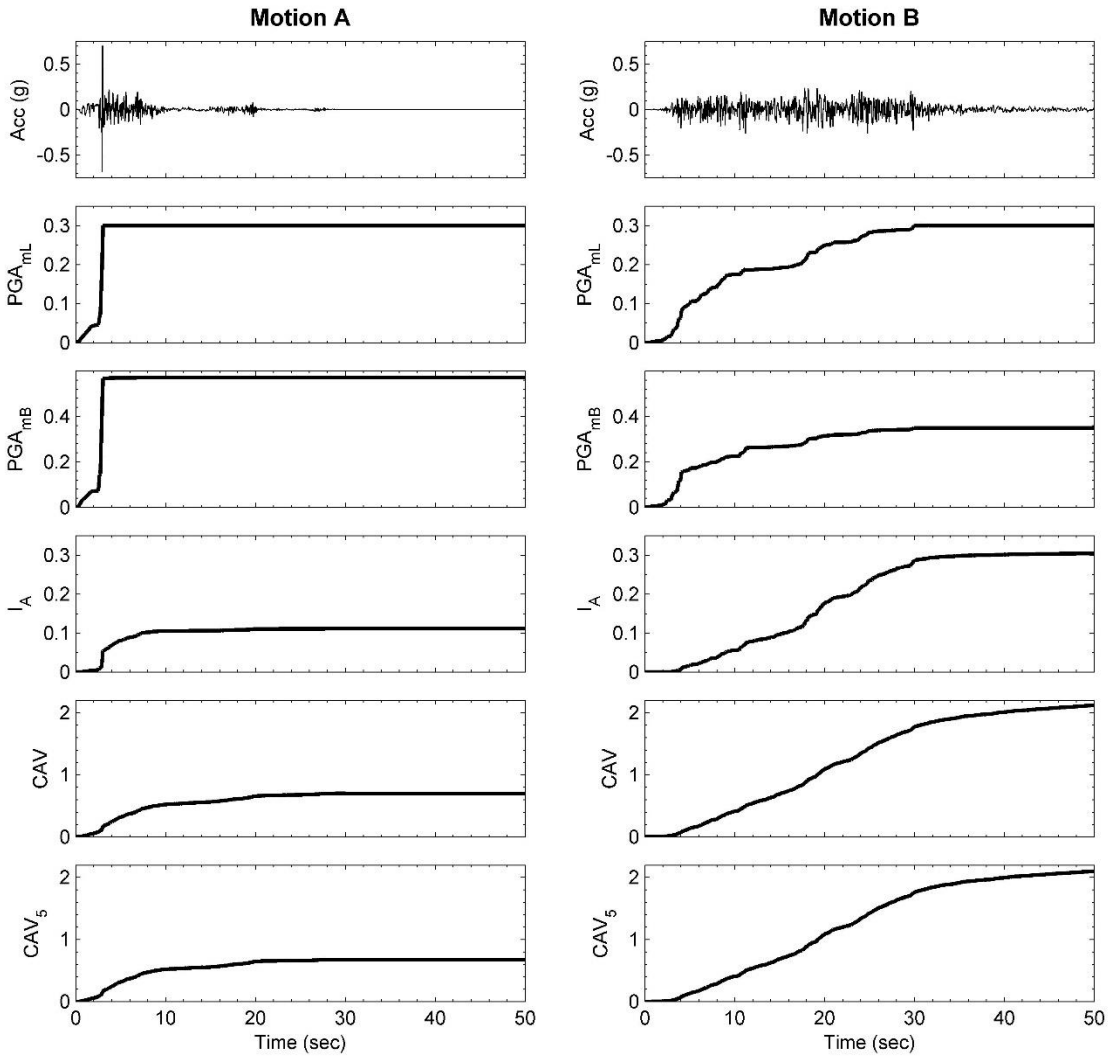


Figure 4.3: Evolutionary IM behavior for two acceleration time histories using IMs defined in Table 4.1.

Evolutionary IMs can be formulated to capture various aspects of an acceleration time history. In general, PGA_m type cycle counting formulations will reach their peak value sooner (and level out faster) than the integral-based IMs. and are not as affected by low acceleration values as compared to I_A, CAV, and CAV_5. Of the integral parameters, I_A is most strongly

influenced by large acceleration pulses in the record, however, it evolves more smoothly than the PGA_m formulations and can be influenced by low amplitude portions of a time history. CAV and CAV_5 generally evolve similarly to I_A but do not increase as rapidly during the strongest part of the motion and are more strongly influenced by the lower amplitude portions of a time history.

Defining an intensity measure that develops with time potentially offers many advantages in terms of liquefaction hazard evaluation because it allows for decomposition of the earthquake time history into pre- and post-liquefaction components. Figure 4.4 provides an example of the response of a sloping-ground liquefiable soil deposit subjected to strong ground motion during a centrifuge study from Brandenburg et al. (2005). Prior to liquefaction, observed at about 11 seconds into the record, the displacements were essentially negligible despite acceleration amplitudes of approximately 0.5 g. After liquefaction was initiated, the displacements increased rapidly.

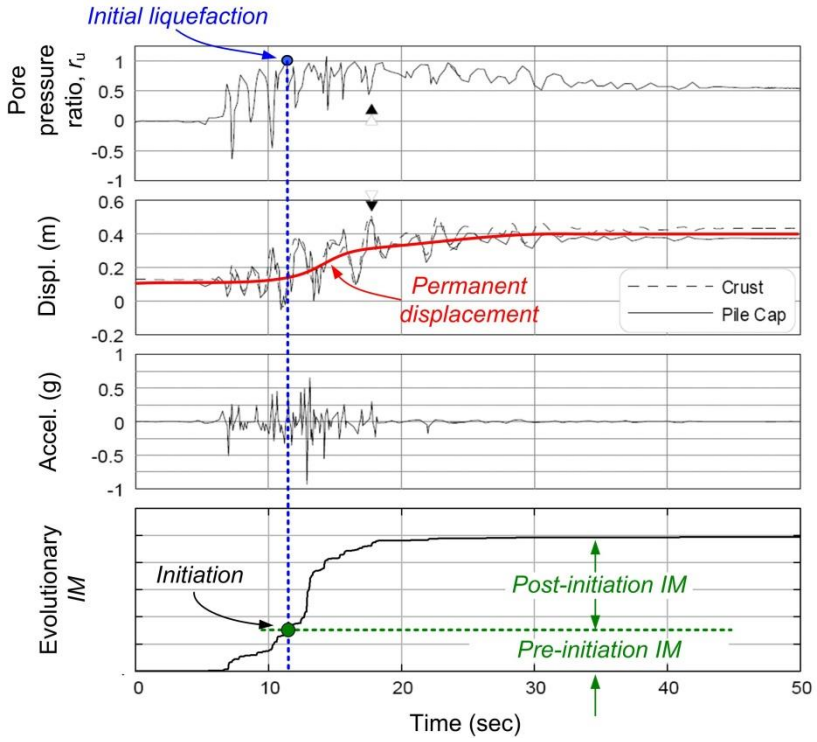


Figure 4.4: Results of a centrifuge experiment where lateral spreading was observed (after Brandenburg et al. 2005)

In current analysis procedures, the IM computed from the entire time history is used to estimate the effects of liquefaction, even though the portion of the record prior to triggering contributed very little to the deformation response. Based on these observations Kramer et al.

(2016) proposed an alternative, timing-based liquefaction hazard evaluation framework, as presented in the next section.

4.2 FRAMEWORK DEVELOPMENT

The timing-based framework for liquefaction hazard evaluation was presented by Kramer et al. (2016) and provides a simple and flexible method to estimate the effects of liquefaction. The framework allows for different evolutionary IMs to be used for evaluating the triggering and effects of liquefaction. This is important because, as discussed in Section 2.4, the characteristics of a soil profile can change dramatically following the initiation of liquefaction, and there is no reason to assume that an evolutionary IM that efficiently predicts the generation of excess pore pressure and liquefaction triggering while the soil is still relatively stiff should also efficiently predict the effects of liquefaction when the soil is much softer. The timing-based framework uses evolutionary IMs to relate the liquefaction resistance relationship, which evaluates the initiation of liquefaction, and the loading-response relationship, to provide a more efficient evaluation of the effects of liquefaction.

4.2.1 *Liquefaction Resistance Curve*

Liquefaction resistance curves describe relationships that are used to determine whether liquefaction will be triggered at a site. They present a characteristic loading that a soil would be able to resist, defined in terms of an IM, as a function of a measure of the state of the liquefiable soil deposit, typically represented by an insitu test parameter such as an CPT tip resistance, SPT blow count, or relative density. Examples of these relationships in terms of CSR, I_A, CAV_5 and NED were described in Sections 2.3.3.1-2.3.3.4 respectively. Figure 4.5 gives an example of a generic liquefaction resistance curve as a function of corrected SPT blow count and a generic IM. The IM used to define the liquefaction triggering relationship is denoted as IM^{trig}. Points on the liquefaction resistance curves represent the IM^{trig} value at which the liquefaction would be initiated for a soil of a particular blow count.

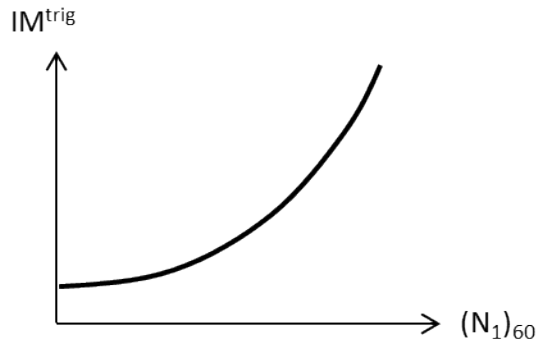


Figure 4.5: Generic liquefaction resistance curve based on corrected SPT resistance and the IM used to evaluate liquefaction triggering, IM^{trig}

The liquefaction resistance relationship is used to decompose a time history into pre- and post-triggering components. Figure 4.6 illustrates how the timing of liquefaction can be evaluated for a single ground motion time history. For a soil with an SPT resistance evaluated at (Point A), the IM^{trig} value at liquefaction, IM^{trig}_L can be computed using the liquefaction resistance curve (Point B). With IM^{trig}_L, the time history of IM^{trig} can be used to evalute the time of liquefaction, t_L, as the time that IM^{trig} reaches IM^{trig}_L (Point C).

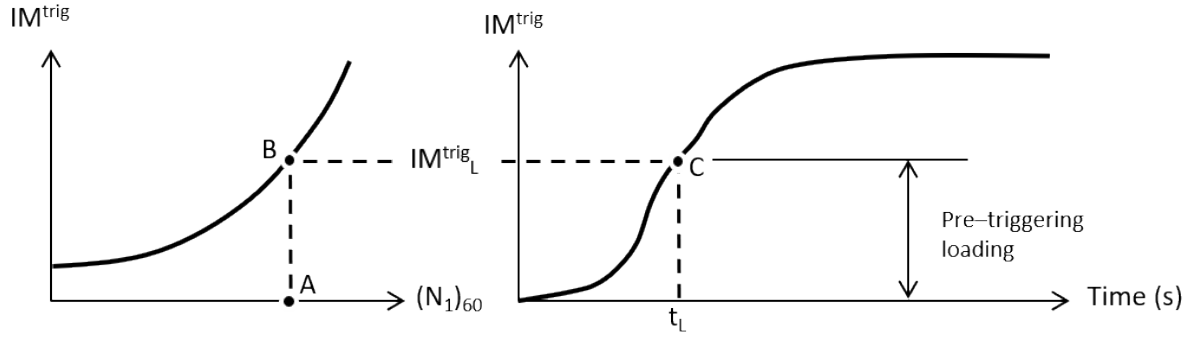


Figure 4.6: Combining liquefaction resistance curves and evolutionary IM time histories to determine the timing of liquefaction

Defining IM^{eff} as an evolutionary intensity measure used to predict the effects of liquefaction, the post-triggering value of IM^{eff}, IM^{eff}_{PL} can be evaluated using t_L. If the soil liquefied at the beginning of the loading, the entire motion would act on the liquefied soil. As t_L increases the amount of remaining loading that is available to drive the effects of liquefaction decreases. The value of IM^{eff} remaining in the time history at any time, t, is defined as IM^{eff}_P and is computed as

$$IM^{eff}{}_P(t) = IM^{eff}{}_{tot} - IM^{eff}(t) \tag{4.3}$$

where IM^{eff}_{tot} is the value of IM^{eff} computed using the entire ground motion time history and IM^{eff}_{PL} is the value of IM^{eff}_{P} at $t = t_L$. This process is illustrated graphically in 4.7 as Point D. The time history of IM^{eff}_{P} is equivalent to IM^{eff} flipped vertically.

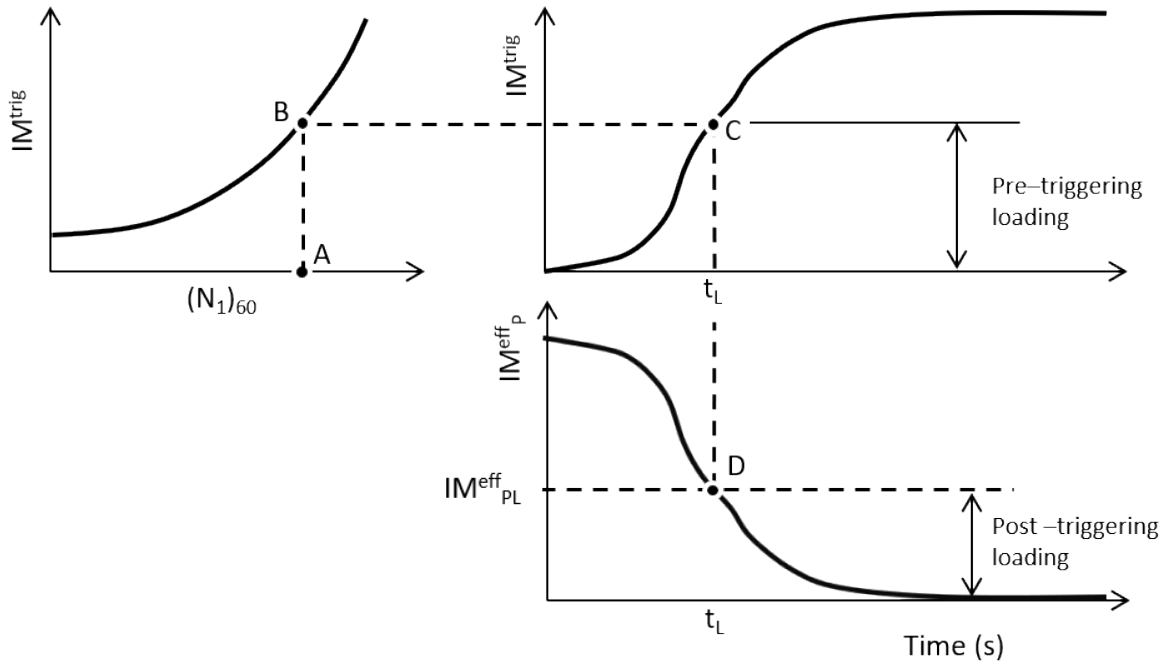


Figure 4.7: Determining the post-liquefaction loading based on the time of liquefaction determined from the liquefaction resistance relationship.

4.2.2 *Loading-response Curves*

After the post-triggering loading has been determined, the last step in the framework involves quantifying the effects of liquefaction, such as displacement due to lateral spreading or settlement, based on the post-triggering loading and characteristics of the soil deposit. An example was provided in Figure 2.26 which showed contours of maximum shear strain as a function of CSR and corrected SPT blow count. These curves generally plot a measure of response as a function of the earthquake loading and a measure of soil density. The loading-response curves required for the proposed framework are nearly identical to conventional loading-response curves, except that the loading is specified as the IM^{eff}_{P}, as opposed to the IM computed using the entire time history. Figure 4.8, for example, shows contours of displacement as a function of the post-liquefaction loading and SPT resistance.

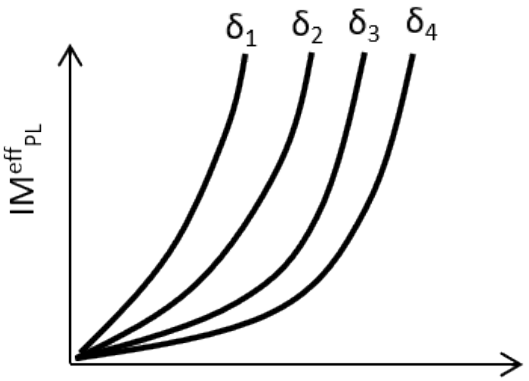


Figure 4.8: Loading-response curves showing contours of multiple levels of displacement, δ, as a function of post-triggering loading and the corrected SPT blow count of the liquefiable soil layer.

4.2.3 *The Complete Framework*

Using the each of the components described previously, the timing-based framework can be assembled in its entirety. The proposed method combines resistance and loading-response curves by way of evolutionary intensity measures to create a unified framework for evaluating the entire liquefaction hazard, both in terms of initiation and effects. A graphical illustration of the complete timing-based framework is shown in Figure 4.9.

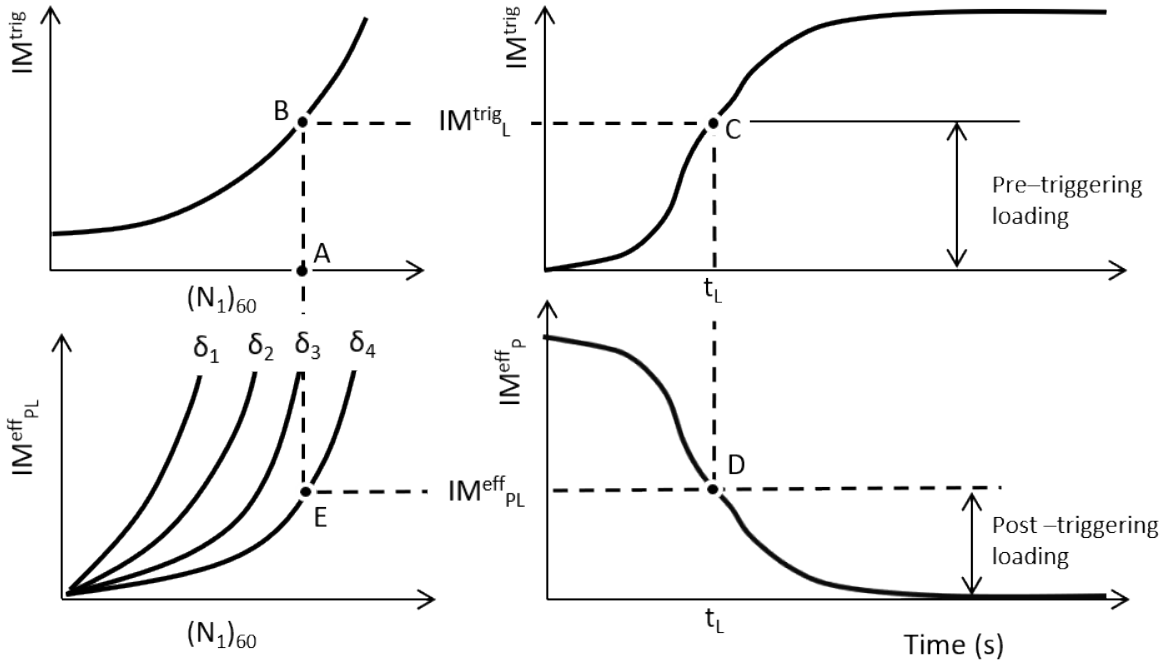


Figure 4.9: Proposed framework for liquefaction hazard evaluation.

Points A through C describe the process used to determine t_L using the liquefaction triggering relationship. Using t_L, the amount of the post-triggering loading, IM^{eff}_{PL}, can be evaluated (Point D). Then based on IM^{eff}_{PL} and the penetration resistance of the soil, a loading-response curve is used to determine the anticipated effects of liquefaction such as final displacements or total settlements.

Figure 4.10 illustrates the effect of density in the proposed framework. Liquefiable soils that have higher densities require more severe loading to initiate liquefaction. For a given motion, liquefaction of a denser soil would occur later in the loading history, and thus the remaining post-triggering loading, IM^{eff}_{P}, would be lower than for a looser soil that would liquefy earlier in the motion. As expected, the resulting displacements would be larger in looser soils, not only because of the loading-response relationships, which for the same IM^{eff}_{P} level would predict higher displacements in looser soils, but also because the post-liquefaction loading would be expected to be greater as well. This type of framework could be useful in determining the degree of ground improvement that would be necessary at a given site in order to reduce the effect of liquefaction to a satisfactory level.

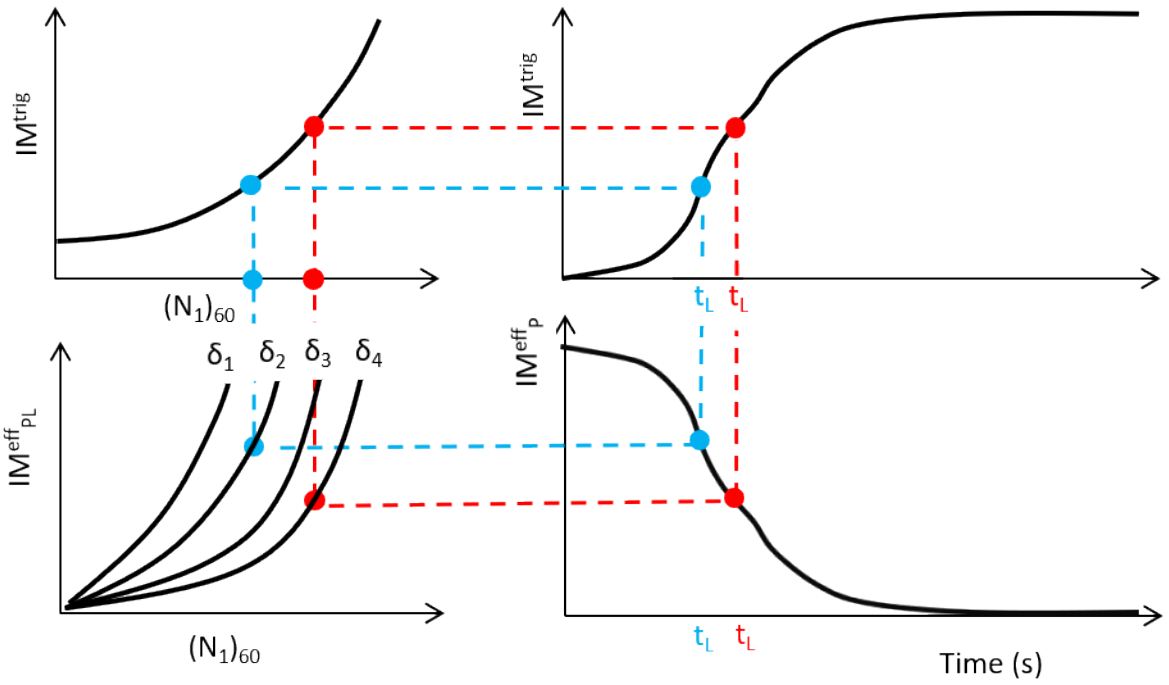


Figure 4.10: Illustration of application of the proposed framework for soils of different densities.

4.3 VERIFICATION OF TIMING-BASED FRAMEWORK

The purpose of the timing-based framework is to reduce the uncertainty in predicting the effects of liquefaction (the EDP in the PBEE framework) by partitioning the ground motion into pre- and post-triggering components. IMs computed using these individual components should be better correlated to the initiation and effects of liquefaction, respectively, than IMs computed using the entire time history. As demonstrated in Section 3.2, reducing the uncertainty in EDP|IM can significantly reduce the demand at a given hazard level, even if the mean estimate of the EDP remains constant.

To investigate whether the timing-based framework can provide benefits in a probabilistic hazard analysis, Kramer et al. (2016) and Greenfield (2017) used the results of a simple numerical study to see if using IM^{eff}_{P} provided a better estimate of the lateral spreading displacements than estimates computed using IM^{eff}_{tot}. Their analyses modeled a 1-dimensional infinite slope of 2%. The profile consisted of a 2.7-m-thick layer of sand with a 0.6-m-deep water table (Figure 4.11) using the multi-spring constitutive model FLIP (https://www.flip.or.jp/). The sand was assumed to have corrected SPT resistances of 4, 8, 12, 16, and 20 blows per foot and the model was subjected to 80 input motions evenly distributed across four magnitude and four site-to-source distance bins scaled by factors of 1.0 and 2.0 (Kramer et al. 2016).

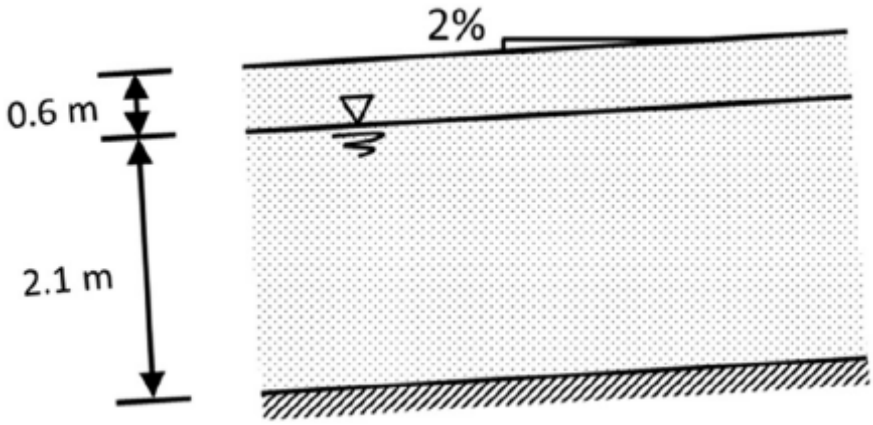


Figure 4.11: Soil profile used in the analyses from Kramer et al. (2016) and Greenfield (2017)

These analyses produced 160 computed displacements for each SPT resistance for a total of 800 analyses. The relationship between the displacement, blow count, and ground motion intensity was evaluated using a function of the form,

$$\ln \delta = a + b \cdot \left(N_1\right)_{60}{}^{c} + d \cdot IM^{e} \tag{4.4}$$

Regression was performed to identify the constants a, b, c, and d using an IM computed from the total (IM^{eff}_{tot}) and post-triggering (IM^{eff}_{PL}) portions of the acceleration time history. The IMs included in this study were PGA_m, I_A, and CAV. The efficiency was evaluated based on the standard deviations of the natural log residuals, $\sigma_{ln\delta}$, computed as the log of the displacement determined from the numerical analyses minus the log of the fitted displacement. The $\sigma_{ln\delta}$ values from regression using IM^{eff}_{tot} and IM^{eff}_{PL} are summarized in Table 4.1. The $\sigma_{ln\delta}$ for each IM was consistently lower when the IM was defined as IM^{eff}_{PL} as opposed to IM^{eff}_{tot} indicating that IM^{eff}_{PL} was a more efficient predictor of lateral spreading displacements than IM^{eff}_{tot}. The results showed that based on numerical analyses using a simple soil profile, the timing-based framework that incorporates the post-triggering IM as opposed to the total IM can significantly reduce the uncertainty in the predicted response. However, additional studies are needed to confirm this finding.

Table 4.1: Uncertainty in predicted lateral displacements for PGA_m, I_A, and CAV computed using the total and post-triggering IM values from Kramer et al. (2016).

IM	$\sigma_{ln\delta}$	
	Total Motion Values, IM^{eff}_{tot}	Post-triggering values, IM^{eff}_{P}
PGA_m	0.981	0.818
I_A	0.829	0.602
CAV	1.04	0.705

4.4 APPLICATION OF TIMING-BASED FRAMEWORK

Kramer et al. (2016) provided an example application of the full the timing-based framework for prediction of liquefaction-induced lateral spreading displacements using numerical analyses. The soil profile described in Section 4.3 with an SPT blow count of 10 blows per foot was subjected to 30 spectrum compatible ground motions (Figure 4.12a). Kramer et al. (2016) defined IM^{trig} as PGA_m and IM^{eff}_{P} as I_A. The relationship between IM^{trig} and IM^{eff}_{P} for all 30 motions are shown in 4.12b. Note that if the same IM was used for both IM^{trig} and IM^{eff}_{P}, the results in Figure 4.12b

would plot as a straight line sloping downwards at a 45 degree angle. Deviations from a straight line represent differences in the manner the two IMs characterize the ground motion intensity over the duration of a ground motion.

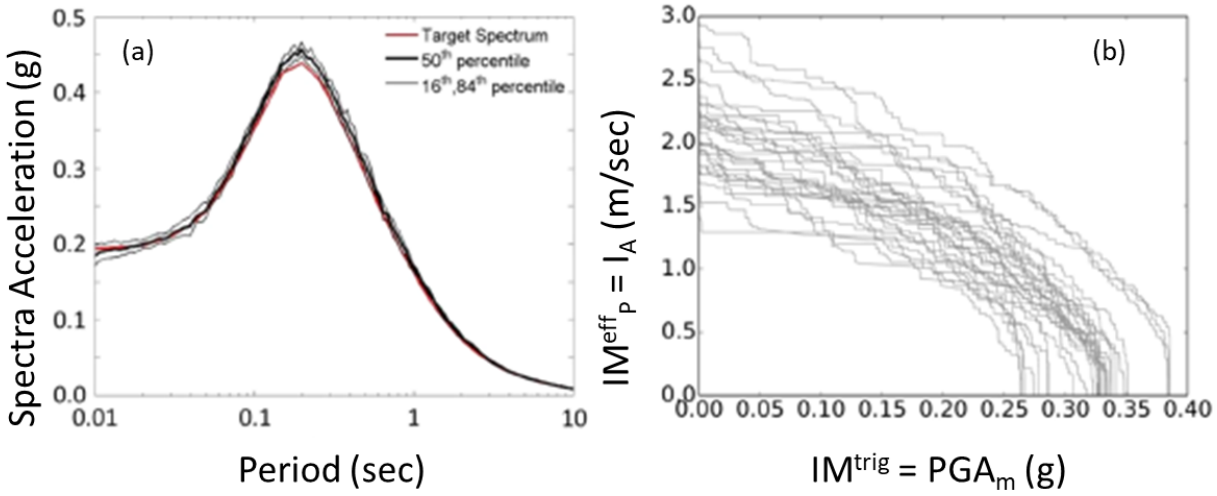


Figure 4.12: Spectrum compatible motions (a) and relationship between IM^{trig} and IM^{eff}_P (b) using IM^{trig} defined using PGA_m and IM^{eff}_P defined using I_A from study by Kramer et al. (2016).

The implementation of the timing-based framework is shown in Figure 4.13. The value of IM^{trig} at the initiation of liquefaction, IM^{trig}_L was computed based on the liquefaction triggering curve from Boulanger and Idriss (2014) (Figure 4.13a). Ignoring the uncertainty in the triggering relationship, the value of IM^{trig}_L at the center of the uniform 10 bpf saturated sand layer was 0.15 g. The time of liquefaction was evaluated for each of the 30 motions in Figure 4.13b. Note that even though the response spectrum for each of the motions was nearly identical, the transient aspects of the motions differed such that PGA_m evolved at different rates and the time of liquefaction varied significantly across each of the motions. The resulting $IM^{eff}_P = I_A(t_L)$ values are provided in Figure 4.13c. The differences in the evolution of the two IMs lead to different IM^{eff}_P values for each of the time histories. The resulting lateral spreading displacements estimated using IM^{eff}_P from Figure 4.13c and the SPT resistance (10 bpf) are shown in Figure 4.13d. The predicted displacements ranged from about 0.3 m to 0.9 m with a dispersion, $\sigma_{ln\delta}$ of 0.23 m.

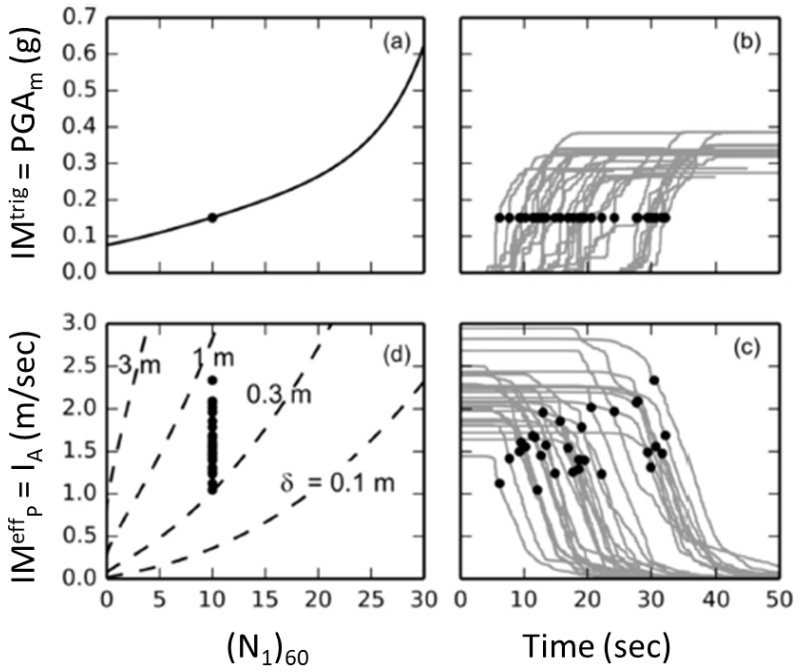


Figure 4.13: Timing-based framework for prediction of the lateral spreading displacement, δ from Kramer et al. (2016): (a) liquefaction resistance curve, (b) evolution of triggering IM, (c) remaining effects IM with time, and (d) lateral spreading loading-response relationship. The results do not include uncertainty in SPT resistance or the triggering relationship.

The example provided in Figure 4.13 assumed that both the SPT resistance and liquefaction resistance relationship were known with certainty. Kramer et al. (2016) repeated the analysis provided above including uncertainty in the corrected SPT blowcount and the liquefaction resistance relationship. Per Boulanger and Idriss (2012) the SPT resistance and CRR were assumed to be lognormally distributed with standard deviations of 0.3 and 0.24, respectively. Kramer et al. (2016) repeated the analyses provided in Figure 4.13, but included variability in the corrected SPT blowcount and liquefaction resistance relationship by randomizing the parameters using the distributions noted above. As expected, including variability in the blowcount and triggering relationship increased the variability in the predicted displacements, which ranged from approximately 0.2 m to just above 1.0 m with a dispersion of 0.49, which was over twice as large as the dispersion for the case that did not account for the uncertainty in the blowcount and triggering relationship.

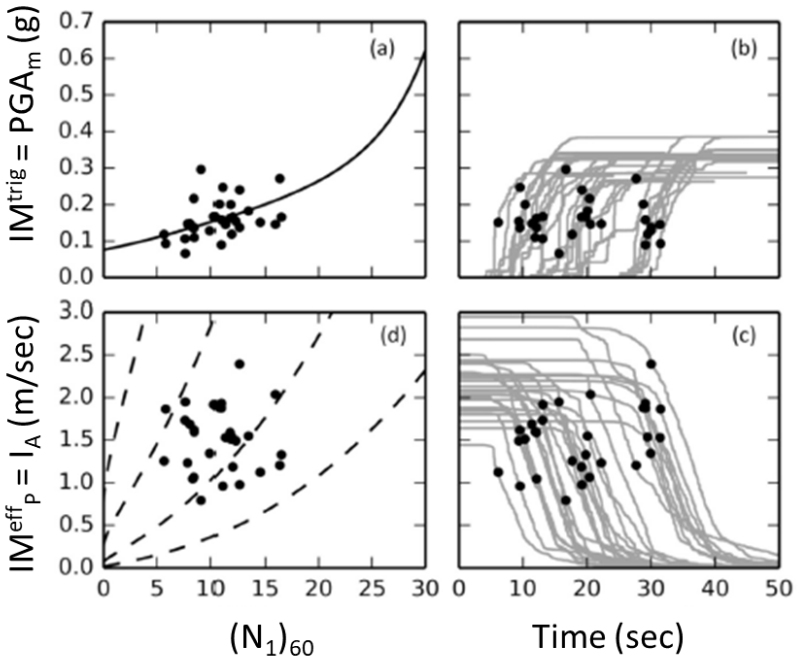


Figure 4.14: Timing-based framework for prediction of the lateral spreading displacement, δ from Kramer et al. (2016) including uncertainty in the SPT resistance and the liquefaction triggering relationship: (a) liquefaction resistance curve, (b) evolution of triggering IM, (c) remaining effects IM with time, and (d) lateral spreading loading-response relationship.

4.5 PROBABILISTIC IMPLEMENTATION OF TIMING-BASED FRAMEWORK

The example provided in Figure 4.14 was a simple example of how the timing-based framework can account for uncertainty. To implement the timing-based framework into the PBEE framework presented in Chapter 3, each step of the process needs to be accounted for probabilistically to compute a probability of exceedance of a given engineering demand parameter which is then integrated over an IM hazard curve to produce a compute the EDP hazard curve.

As noted by Greenfield (2017), the sources of uncertainty in the timing-based framework include,

1. The density of the soil, typically quantified using a corrected SPT blow count, $(N_1)_{60}$ (Point A in Figure 4.9),
2. The relationship between IM^{trig}_L and $(N_1)_{60}$ (Point B in Figure 4.9),
3. The relationship between IM^{eff}_{PL} and IM^{trig}_L (Points C and D in Figure 4.9), and
4. The relationship between the EDP given IM^{eff}_{PL} and $(N_1)_{60}$ (Point D in Figure 4.9).

Each of these sources of uncertainty are discussed in the following sections.

4.5.1 *Uncertainty in the Time of Liquefaction*

The first step in the framework involves determining the value of IM^{trig} that is required to trigger liquefaction, IM^{trig}_L, for a soil of a given density defined using $(N_1)_{60}$ and the liquefaction resistance relationships. This procedure was illustrated in Section 4.2.1 and existing procedures are described in Section 2.3.3. Some available resistance relationships have been defined probabilistically (e.g. Boulanger and Idriss, 2014; Cetin et al. 2018) and account for uncertainties in $(N_1)_{60}$ and the conditional uncertainty of the resistance to liquefaction, IM^{trig}_L given $(N_1)_{60}$. Therefore, both $(N_1)_{60}$ and IM^{trig}_L are considered random variables, N and IM^{trig}_L (random variables denoted in *italics*).

As an example, based on their case history database Boulanger and Idriss (2012) assumed N was a normally distributed random variable,

$$N = \mathrm{E}[N] + \sigma_N \cdot \varepsilon \tag{4.5}$$

where E[N] is the expected value of N, σ_N is the standard deviation of N, and ε is a standard normally distributed random variable. Boulanger and Idriss (2012) assumed that while σ_N varied with N, the coefficient of variation of N (COV_N) was constant with a value of 0.15 such that $\sigma_N = COV_N \cdot N$. Since IM^{trig}_L is evaluated based on a function of N, the calculations of IM^{trig}_L are therefore conditional upon N. Typically IM^{trig}_L is assumed to be a lognormally distributed random variable such that

$$\ln IM^{trig}{}_L = \mathrm{E}\left[\ln IM^{trig}{}_L\right] + \sigma_{\ln IM^{trig}{}_L|N} \cdot \varepsilon \tag{4.6}$$

where E[lnIM^{trig}_L] is the expected value of lnIM^{trig}_L, computed using the liquefaction resistance relationship as a function of N, $\sigma_{\ln IM^{trig}{}_L|N}$ is the conditional standard deviation of lnIM^{trig}_L given N, and ε is a standard normally distributed random variable. Greenfield (2017) evaluated Equation 4.6 for PGA_m based on the stress-based procedure of Boulanger and Idriss (2012) and computed the $\sigma_{\ln IM^{trig}{}_L|N}$ value to be 0.25.

4.5.2 *Uncertainty in Pre- and Post-triggering Intensity Measures*

The next part of the framework involves using the value of $IM^{trig}{}_L$ to estimate the amount of post-triggering IM, $IM^{eff}{}_P$, that is remaining in the motion after liquefaction has been triggered, $IM^{eff}{}_{PL}$. Based on discussions presented previously, IM^{trig} and IM^{eff} were assumed to be different IMs. As noted in Sections 4.1 and 4.4, while the values of different IMs are generally correlated (since all IMs to some degree capture the amplitude, frequency content, and duration of an earthquake), due to their different formulations they evolve differently with time as illustrated in the example provided in Figure 4.12. Greenfield (2017) developed a procedure to estimate $IM^{eff}{}_{PL}$ given $IM^{trig}{}_L$, the total IM^{trig}, $IM^{trig}{}_{tot}$ and the total IM^{eff}, $IM^{eff}{}_{tot}$. Greenfield (2017) defined two normalized parameters, α_1 and α_2 to track the relative evolution of IM^{trig} and $IM^{eff}{}_P$, respectively as follows,

$$\alpha_1 = \frac{IM^{trig}}{IM^{trig}{}_{tot}} \tag{4.7}$$

$$\alpha_2 = 1.0 - \frac{IM^{eff}{}_P}{IM^{eff}{}_{tot}} \tag{4.8}$$

Figure 4.15 illustrates the evolution of α_1 and α_2 using Motion B from Figure 4.3. α_1 was calculated using IM^{trig} defined as PGA_{mL} and α_2 was calculated using $IM^{eff}{}_P$ defined using PGA_{mL}, CAV, and I_A to illustrate how the relationship between α_1 and α_2 can vary based on the choice IM^{trig} and $IM^{eff}{}_P$. When the same IM is used for both IM^{trig} and $IM^{eff}{}_P$ the plot of α_1 and α_2 is represented by a 45-degree straight line. When different IMs are used for IM^{trig} and $IM^{eff}{}_P$ the relationship between α_1 and α_2 can be highly nonlinear. For the example shown, when $IM^{eff}{}_P$ was defined as I_A or CAV, which both evolved more slowly than PGA_{mL}, the relationship between α_1 and α_2 was concave down.

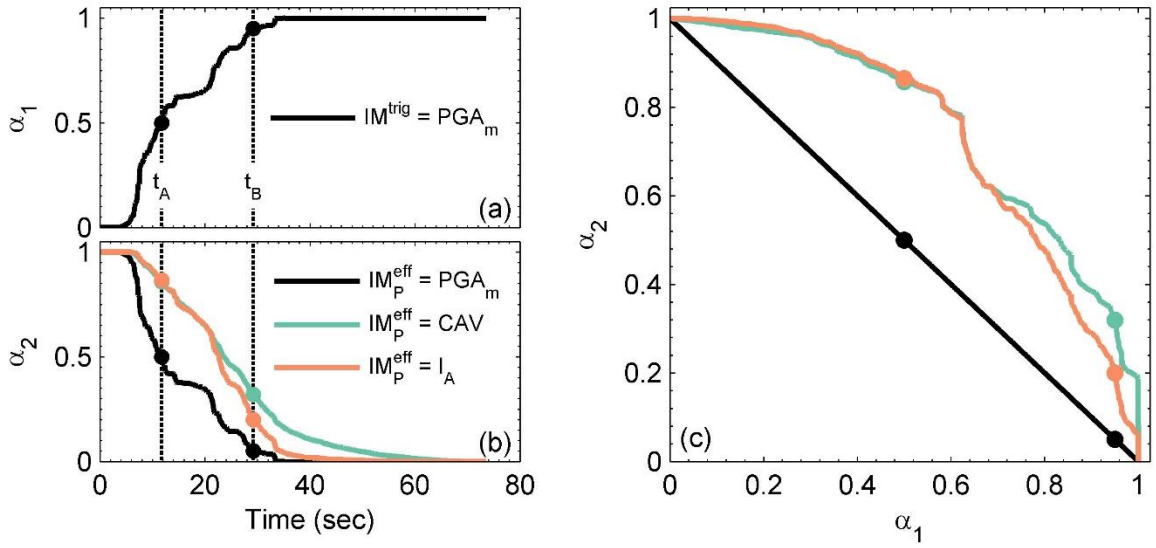


Figure 4.15: Example of evolution of parameters α_1 and α_2 using Motion B from Figure 4.3. (a) α_1 time history computed using PGA_m for IM^{trig}, (b) α_2 time history computed using IM^{eff}_P of PGA_m, CAV, and I_A, and (c) relationship between α_1 and α_2 (adopted from Greenfield, 2017).

In conventional liquefaction analyses IM^{trig}_{tot} is either a known quantity in deterministic analyses or is evaluated probabilistically via a PSHA. Assuming the probabilistic representation, IM^{trig}_{tot} is considered a random variable IM^{trig}_{tot}. IM^{trig}_{L} can be evaluated based on the SPT blow count as discussed in Section 4.5.1. Given IM^{trig}_{L} and IM^{trig}_{tot}, α_1 can be calculated using Equation 4.7. Then α_2 can be computed assuming a relationship between of α_1 and α_2. Lastly, if IM^{eff}_{tot} can be estimated, IM^{eff}_{PL} can be calculated by rearranging Equation 4.8

$$IM^{eff}{}_{p} = \alpha_2 IM^{eff}{}_{tot} \tag{4.9}$$

and noting that IM^{eff}_P is equal to IM^{eff}_{PL} when α_2 is calculated as described above with IM^{trig} equal to IM^{trig}_L.

The relationship between α_1 and α_2 are dependent on the IMs selected for IM^{trig} and IM^{eff} and can be evaluated by performing regression analyses from recorded ground motions. An example of this process was provided in Greenfield (2017) with IM^{trig} defined as PGA_m and IM^{eff} defined as I_A, using a ground motion suite consisting of over 350 motions. The motions were from recorded events with magnitudes between 5.25 and 9 and PGAs greater than 0.05 that were recorded at sites with a time-averaged shear wave velocity in the upper 30 meters greater than 600 m/s (Greenfield, 2017). The values of α_1 and α_2 were computed for each ground motion and are shown in Figure 6.16. The mean relationship from the analyses of Greenfield (2017) showed the familiar concave down shape that was observed in the example provided in Figure 4.15.

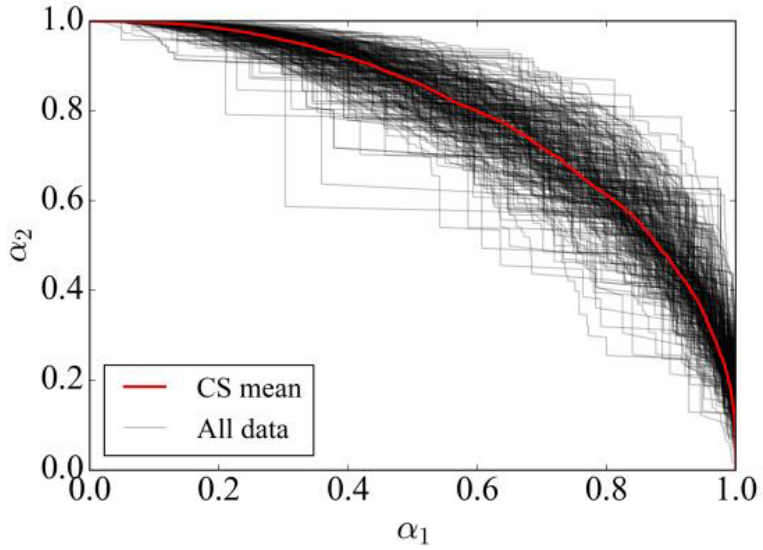


Figure 6.16: Relationship between α_1 and α_2 from Greenfield (2017)

In addition to the mean, Greenfield (2017) also estimated the variance of the α_2 as a function of α_1, shown in Figure 6.17 which provides the 50th, 16th, and 84th percentile values from the given analyses. Since both α_1 and α_2 are bounded by 0 and 1, the conditional variance of α_2 given α_1 approached zero at the extremes of the plot. However, at intermediate values of α_1 the conditional variance of α_1 given α_2 was relatively large, with the maximum variance observed at approximately α_1 equal to 0.75 for the example shown.

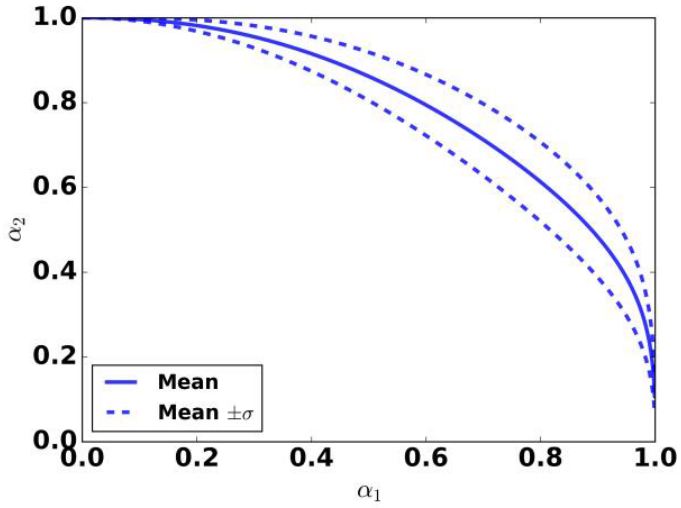


Figure 6.17: Mean and variance in α_1 and α_2 from Greenfield (2017)

Greenfield (2017) found that probability distribution of α_2 given α_1 could be approximated using a beta distribution. The beta distribution was selected because it is highly flexible, bounded by values of 0 and 1.0, and capable of fitting both the narrow distribution of α_2 as α_1 approaches 0 and 1.0, and the broader distribution of α_2 when α_1 is at intermediate values. The probability density function (p) for the beta distribution of a random variable x is defined by

$$p(a,b) = \frac{\Gamma(a) \cdot \Gamma(b)}{\Gamma(a+b)} x^{a-1}(1-x)^{b-1} \tag{4.10}$$

where a and b are beta distribution coefficients and Γ is the gamma function. The coefficients a and b can be calculated based on the expected value and variance of x , E[x] and V[x], respectively

$$a = \left(\frac{1 - \mathrm{E}[x]}{\mathrm{V}[x]} - \frac{1}{\mathrm{E}[x]}\right) \cdot \mathrm{E}[x]^2 \tag{4.11}$$

$$b = a\left(\frac{1}{\mathrm{E}[x]} - 1\right) \tag{4.12}$$

The conditional distribution of α_2 given α_1 can be evaluated from the data presented previously to evaluate E[$\alpha_2|\alpha_1$] and V[$\alpha_2|\alpha_1$], which can then be used to compute the beta coefficients a and b from Equations 4.11 and 4.12. For the present example, Greenfield (2017) developed a function to express the coefficients a and b as a function of α_1 as

$$\ln w = c_0 + c_1 \ln \alpha_1 + c_2 \ln (1 - \alpha_1) \tag{4.13}$$

where w is a general parameter that is either a or b and c_0, c_1, and c_2 are coefficients determined through regression. The regression coefficients depend on which parameter is used for w and are specific to the IMs used to define IM^{trig} and IM^{eff} and the ground motion data set. The results of this analysis for the provided example are shown in Figure 4.18, which shows both the fitted values and the actual values for a and b. For the example provided, the fitted values provided a good estimate of the actual data, particularly at α_1 values greater than 0.15.

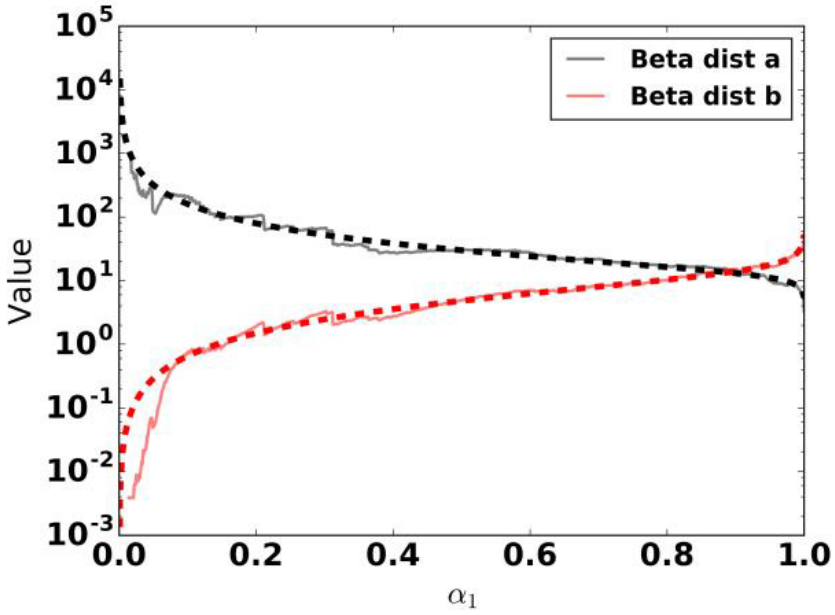


Figure 4.18: Calculated and fitted beta distribution parameters for the analyses performed by Greenfield (2017).The solid lines represent the values calculated from the ground motion data and the dashed lines represent the values estimated using the equation presented above.

The methodology provided above allows both the mean and the distribution of α_2 to be estimated given α_1. The last step required to estimate the IM^{eff}_{PL} is to determine an estimate of IM^{eff}_{tot}. An initial estimate of the expected value and distribution of IM^{eff}_{tot} can be made using ground motion prediction equations (GMPEs). However, as noted previously, most IMs are correlated to each other. As noted by Greenfield (2017), the correlation between two IMs can be used to reduce the uncertainty in one IM provided the value of another IM is known. For two normally distributed random variables *x* and *y*, the correlation coefficient, $\rho_{x,y}$, quantifies the amount of variance in *y* that is explained by the variance in *x*. The conditional mean, $\mu_{y|x}$, and variance $\sigma^2_{y|x}$ can be expressed as

$$\mu_{y|x} = \mu_y + \rho_{x,y}\frac{\sigma_y}{\sigma_x}(x - \mu_x) \tag{4.14}$$

$$\sigma^2{}_{y|x} = \sigma^2{}_y(1 - \rho_{x,y}) \tag{4.15}$$

Note that if *x* and *y* are independent, $\rho_{x,y}$ equals zero and the conditional mean and variance are equal to the mean and variance of *y*. The relationships provided above can be used to estimate IM^{eff}_{tot} given IM^{trig}_{tot} when the correlation coefficient between the two is known.

4.5.3 *Uncertainty in the Engineering Demand Parameter*

The last part of the timing-based framework involves estimating an engineering demand parameter (EDP) given IM^{eff}_{PL}. Currently, there are no existing empirical relationships to estimate an EDP based on the post-triggering intensity of shaking, largely because the existing case history database does not contain enough information to evaluate the pre- and post-triggering ground motion intensity. Therefore, at this time numerical analyses must be used to develop the load-response relationship. An example of this type of analyses was provided by Kramer et al. (2016) as described in Section 4.3. In a probabilistic framework, both the expected value and the distribution of the EDP are required. Using the example from Kramer et al. (2016) discussed in Section 4.3 with the EDP defined as the lateral spreading displacement, δ, the distribution of the EDP can be expressed as

$$\ln \delta = d_0 + d_1 \cdot \ln (N_1)_{60} + d_2 \cdot \ln IM^{eff}{}_{PL} + \sigma_{\ln \delta|N} \cdot \varepsilon \qquad (4.16)$$

where d_o, d_1, and d_2 are regression constants, $\sigma_{\ln\delta|N}$ is the standard deviation of the log displacement conditional on the value of $(N_1)_{60}$, and ε is a standard normally distributed random variable.

4.5.4 *Performance-based Implementation of the Timing-based Framework.*

The timing-based framework is compatible with the PBEE framework shown in Chapter 3 and can be used to compute a probability of exceedance of a given engineering demand parameter which is then integrated over an IM hazard curve to produce an EDP hazard curve. Early numerical work performed by Kramer et al. (2016) and Greenfield (2017) has shown that timing-based framework can improve the efficiency of the EDP estimate. As discussed in Section 3.2, improving the efficiency has notable benefits in a probabilistic design framework. The probability of exceedance of a given EDP was provided as a closed-form solution in Equation 3.4. However, in practice the probability of exceedance often cannot be solved as a closed-form solution because it requires integration across multiple variables with different probability distributions, and is typically solved numerically (Mayfield, 2007). Expressing Equation 3.4 as a summation results in

$$P[EDP > edp] = \sum_{IM} P[EDP > edp|IM] \cdot P[IM] \qquad (4.17)$$

where P[*IM*] is the discrete form of the probability density function for *IM*. For liquefiable soils, the response is also a function of SPT blow count, *N*. In the timing-based framework *IM* in Equation 4.17 is the post-triggering effects IM, IM^{eff}_{PL}. Equation 4.17 then becomes

$$P[EDP > edp] = \sum_{IM^{eff}_{PL},N} P\left[EDP > edp | IM^{eff}_{PL},N\right] \cdot P\left[IM^{eff}_{PL},N\right] \tag{4.18}$$

where P[IM^{eff}_{PL}, *N*] is the joint probability distribution of IM^{eff}_{PL} and *N*. In the timing-based framework *N* and IM^{eff}_{PL} are not independent, however P[IM^{eff}_{PL}, *N*] can be expanded using the total probability theorem (Greenfield, 2017). From Equation 4.9, IM^{eff}_{PL} can be computed as the product of α_2 and IM^{eff}_{tot}. Using the product distribution, the probability of the product of two random variables can be computed as

$$P[xy] = \sum_i P\left[y = \frac{xy}{x_i} | x_i\right] \cdot P[x_i] \tag{4.19}$$

Substituting in α_2 and IM^{eff}_{tot}

$$P\left[IM^{eff}_{PL}\right] = P\left[\alpha_2 \cdot IM^{eff}_{tot}\right] = \sum_{IM^{eff}_{tot}} P\left[\alpha_2 | IM^{eff}_{tot}\right] \cdot P\left[IM^{eff}_{tot}\right] \tag{4.20}$$

Referring to Section 4.5.2, the calculation of α_2 also depends on α_1 which is computed using IM^{trig}_{tot} and IM^{trig}_{L}. In addition, due to the correlation between of IM^{trig}_{tot} and IM^{eff}_{tot} the conditional mean and variance can be used to reduce the uncertainty in IM^{eff}_{tot}. Using the total probability theorem Equation 4.20 becomes

$$\begin{aligned} P\left[IM^{eff}_{PL}\right] = & \sum_{IM^{eff}_{tot}} \sum_{IM^{trig}_{tot}} \sum_{IM^{trig}_{L}} P\left[\alpha_2 | IM^{eff}_{tot}, IM^{trig}_{tot}, IM^{trig}_{L}\right] \\ & \cdot P\left[IM^{eff}_{tot} | IM^{trig}_{tot}\right] \cdot P\left[IM^{trig}_{tot}\right] \cdot P\left[IM^{trig}_{L}\right] \end{aligned} \tag{4.21}$$

IM^{trig}_{L} depends on *N*, therefore P[IM^{trig}_{L}] can be expanded with the total probability theorem as

$$P\left[IM^{trig}_{L}\right] = \sum_N P\left[IM^{trig}_{L} | N\right] \cdot P[N] \tag{4.22}$$

Substituting Equation 4.22 into Equation 4.21 results in

$$\begin{aligned} P\left[IM^{eff}_{PL}\right] = & \sum_{IM^{eff}_{tot}} \sum_{IM^{trig}_{tot}} \sum_{IM^{trig}_{L}} \sum_N P\left[\alpha_2 | IM^{eff}_{tot}, IM^{trig}_{tot}, IM^{trig}_{L}\right] \\ & \cdot P\left[IM^{eff}_{tot} | IM^{trig}_{tot}\right] \cdot P\left[IM^{trig}_{tot}\right] \cdot P\left[IM^{trig}_{L} | N\right] \cdot P[N] \end{aligned} \tag{4.23}$$

Substituting Equation 4.23 into Equation 4.18 results in the complete equation for computing the probability of exceedance of a given EDP using the timing-based framework.

$$P[EDP > edp] = \sum_{IM^{eff}_{PL}} \sum_{IM^{eff}_{tot}} \sum_{IM^{trig}_{tot}} \sum_{IM^{trig}_{L}} \sum_{N} P\left[EDP > edp | IM^{eff}_{PL}, N\right] \cdot P\left[\alpha_2 | IM^{eff}_{tot}, IM^{trig}_{tot}, IM^{trig}_{L}\right] \cdot P\left[IM^{eff}_{tot} | IM^{trig}_{tot}\right] \cdot P\left[IM^{trig}_{tot}\right] \cdot P\left[IM^{trig}_{L} | N\right] \cdot P[N] \quad (4.24)$$

Examples of how to calculate each of the distributions required to calculate the individual terms in Equation 4.24 were discussed in Sections 4.5.1 through 4.5.3. The full implementation is described in further detail in Greenfield (2017), which includes a step-by-step illustration of the probabilistic implementation of the timing-based framework using an example analysis.

4.6 DISCUSSION

The timing-based liquefaction hazard evaluation framework described in this chapter offers many conceptual advantages over the total IM-based approaches that are prevalent in current practice. A timing-based framework that incorporates evolutionary intensity measures allows for the earthquake time history to be divided into pre- and post-triggering components. Preliminary analyses have shown that the timing-based framework can improve the efficiency of the prediction of the effects of liquefaction.

One of the most important aspects of the proposed framework is its simplicity. It is founded on conventional procedures that are already familiar to practicing engineers. The framework begins with a liquefaction resistance curve to predict liquefaction initiation, uses the knowledge of timing to determine the post-liquefaction loading, and uses loading-response relationships to ultimately characterize the effects of liquefaction. In addition, the timing-based framework can be implemented probabilistically, and is compatible with the performance-based engineering framework described in Chapter 3.

The purpose of this research is to identify the most efficient evolutionary intensity measure for predicting the initiation of liquefaction, shown as Step A in Figure 4.9. As illustrated in Section 4.4, reducing the uncertainty in the triggering relationship can significantly reduce the uncertainty in the predicted effects of liquefaction. From the probabilistic implementation of the timing-based framework shown in Section 4.5, the uncertainty in the liquefaction triggering relationship is expressed as the uncertainty in IM^{trig} given the density of the soil (expressed as the

corrected SPT blow count) at the initiation of liquefaction. This definition of uncertainty will be used in the IM evaluations presented later in this document. The next chapter summarizes provides a literature review on the use of evolutionary IMs to predict the initiation of liquefaction.

[This page intentionally left blank]

Chapter 5. PRIOR WORK ON IDENTIFICATION OF EVOLUTIONARY IMS FOR EVALUATION OF LIQUEFACTION TRIGGERING

The framework outlined in the previous chapter is founded on the concept that evolutionary intensity measures can be used to determine not only if liquefaction will occur, but when it will occur for a given loading history, and uses the post-triggering portion of the loading to estimate the corresponding effects of liquefaction. This research project is focused on the first step of the framework, to investigate evolutionary intensity measures (IMs) that can efficiently predict the generation of excess pore pressure and the initiation of liquefaction. The following sections describe previous studies that have been conducted on the topic.

5.1 KRAMER AND MITCHELL (2006)

Kramer and Mitchell (2006), performed an extensive numerical study that investigated different types of evolutionary intensity measures that correlated well with the generation of excess pore-water pressure, and hence, the initiation of liquefaction. Kramer and Mitchell (2006) simulated the response of liquefiable soil deposits with variable densities and thicknesses subjected to a suite of input motions. They compared the pore pressure response of the model to numerous candidate intensity measures computed using the entire input acceleration time history.

The generic soil profile used in the study by Kramer and Mitchell (2006) is shown in Figure 5.1. Analyses were performed on all possible combinations of liquefiable layer thicknesses of 4, 9 and 14 m, and uniform corrected SPT blow counts of 5, 15 and 25 blows per foot. The soil profiles were modeled using the site response analysis program WAVE, which incorperates the *UWsand* constitutive model (Kramer and Arduino, 1999) to represent the response of the liquefiable layer. The *UWSand* model was able to capture the nonlinear, inelastic response of liquefiable sands, and could simulate the response of liquefiable soils that were consistent with field observations (Kramer and Mitchell, 2006). Further details of the development and validation of the *UWSand* model can be found in Baska (2002).

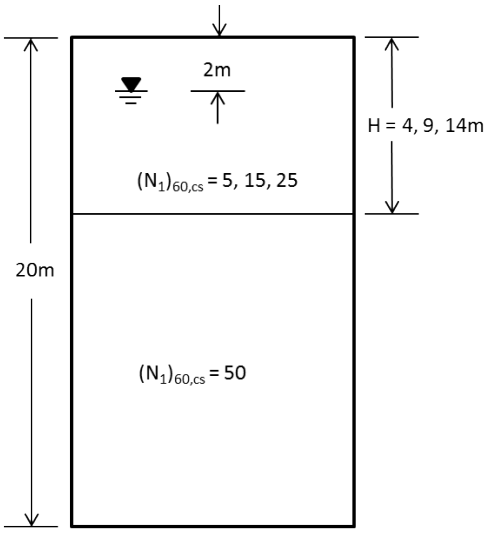


Figure 5.1: Generic soil profile used by Kramer and Mitchell (2006).

Each of the soil profiles was subjected to a suite of input motions applied at the base of the dense soil layer. The suite consisted of 450 recorded ground motions from 22 earthquakes of magnitudes range from 5.2 to 7.4 and source-to-site distances ranging from 1 to 200 km. The resulting analyses produced over 4000 data sets.

The pore pressure response from each of the analyses was then compared to over 300 candidate IMs to identify efficient and sufficient IMs. The candidate IMs included common parameters such as PGA_m and I_A in addition to numerous other parameters that reflected various aspects of the amplitude, frequency content, and duration of the various earthquake ground motions. Additional details regarding the various candidate IMs used in the study can be found in Kramer and Mitchell (2006).

Kramer and Mitchell (2006) quantified the pore pressure response of the soil profile in terms of average peak pore pressure ratio of the liquefiable layer, $\overline{r_u}$, which was calculated as the unweighted average of r_u within the saturated portion of the liquefiable layer. In the context of the performance-based framework presented earlier, $\overline{r_u}$ represents the EDP. The efficiency of each of the IMs was quantified in terms of a standard deviation of the residuals about the EDP|IM relationships. Based on visual interpretation of the data, a sigmoidal function based on the CDF of the beta distribution was fit to the $\overline{r_u}$ response for each of the candidate IMs. An example of this type of analysis using the results of a single soil profile is shown in Figure 5.2 for candidate IMs defined as peak acceleration and I_A. In the given example, the standard

deviation of the residuals for I_A was lower than that for PGA, which indicated that I_A is a more efficient predictor of pore pressure than PGA for this soil profile.

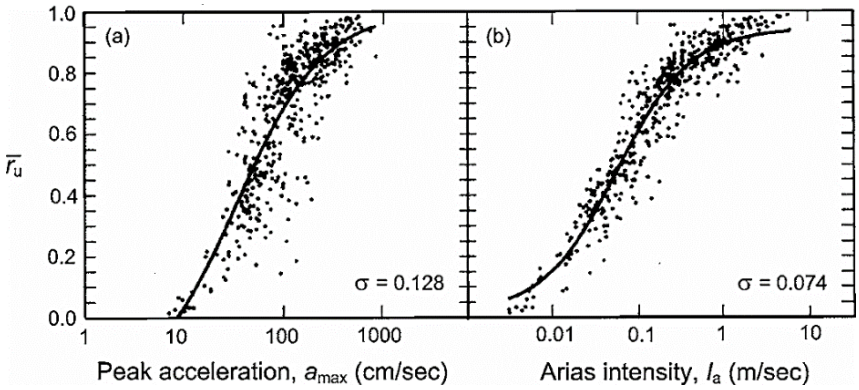


Figure 5.2: Average pore pressure ratio efficiency plots for (a) peak acceleration and (b) I_A, from Kramer and Mitchell (2006).

The sufficiency of each of the candidate IMs was assessed by evaluating the dependence of the residuals from the EDP|IM relationship with the magnitude, M, and source-to-site distance, R, of the input ground motions. The residuals were plotted as functions of M and R and a standard linear regression was performed. The slope of the regression line was used to judge the sufficiency of each IM, with large slopes indicating an insufficient IM, and a slope of 0 indicating a perfectly sufficient IM. Figure 5.3 shows I_A was a more sufficient IM than peak acceleration.

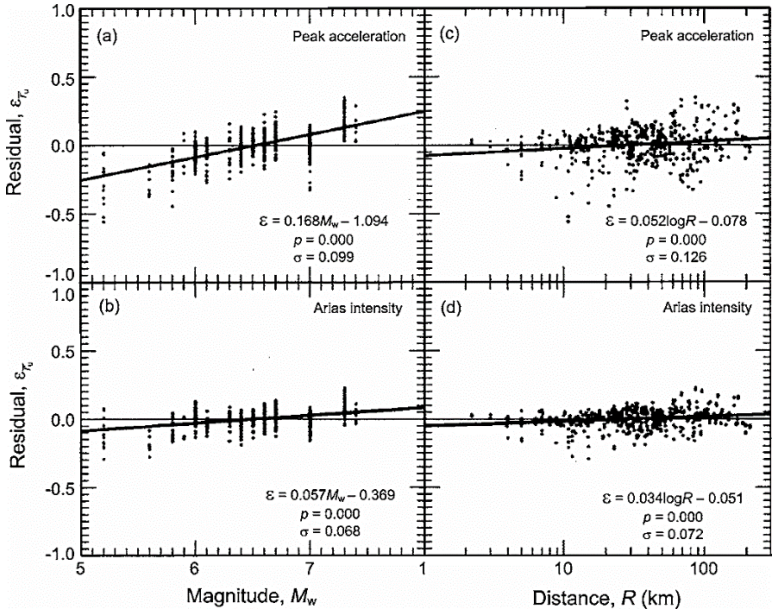


Figure 5.3: Peak acceleration sufficiency plots for (a) *M* and (c) log*R* and I_A sufficiency plots for (b) *M* and (d) log*R*, from Kramer and Mitchell (2006).

Kramer and Mitchell (2006) determined that the IM with the best combination of efficiency and sufficiency was a form of cumulative absolute velocity (CAV), which they called CAV_5. CAV_5 was defined in Equation 2.25, and was used by Mayfield (2007) to develop a liquefaction triggering relationship. Figure 5.4 shows the efficiency and sufficiency results for CAV_5. The small standard deviation of the residuals of the pore pressure prediction in Figure 5.4a indicated that CAV_5 was an efficient predictor of the average pore pressure ratio and the flat linear regression lines in Figures 5.4b and c illustrated that CAV_5 was sufficient with respect to M and R for the analyses performed as part of this study.

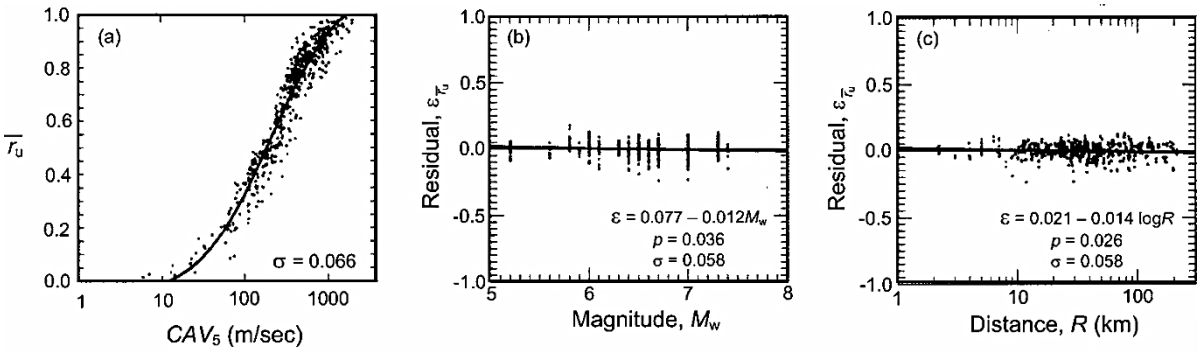


Figure 5.4: Characteristics of CAV_5 for liquefaction evaluation: (a) efficiency of pore pressure generation, (b) magnitude sufficiency, and (c) distance sufficiency, from Kramer and Mitchell (2006).

Campbell and Bozorgnia (2010) evaluated a GMPE for CAV and found that CAV was a highly predictable IM. The average standard deviation of the log residuals, σ, of the CAV GMPE was 0.420 which was significantly lower than the σ values for other IMs associated with the initiation of liquefaction. For comparison, similar studies by Campbell and Bozorgnia (2012; 2014) found that GMPEs for PGA and I_A featured σ values of 0.588 and 0.831, respectively. Given the formulation of CAV_5, it is reasonable to expect that CAV_5 would be a predictable intensity measure as well.

5.2 ABEGG (2010)

To extend the findings of Kramer and Mitchell (2006), Abegg (2010) conducted additional numerical analyses to investigate optimal evolutionary intensity measures for prediction of the initiation of liquefaction. While Kramer and Mitchell (2006) investigated a very large pool of candidate IMs, the study from Abegg (2010) involved a more rigorous evaluation of efficiency

focused on four candidate evolutionary IMs, PGA_{mL}, I_A, CAV_5 and NED. These IMs were selected because of their prevalence in proposed liquefaction initiation analysis relationships, as presented in Section 2.3.3.1. The analysis of Abegg (2010) differed from previous research in that as opposed to using the final or peak value of the IM, Abegg formulated each IM as evolutionary, as outlined in Chapter 4, and evaluated the value of the evolutionary IM at the time of liquefaction, t_L.

Abegg (2010) used the analysis program PSNL—developed by Professor Steven L. Kramer at the University of Washington—to model a generic soil profile containing liquefiable soils of varying relative densities, subjected to a suite of input motions. PSNL is a one-dimensional nonlinear site response analysis program capable of performing both total and effective stress analyses. The liquefiable soil constitutive model incorporated in PSNL was essentially a more refined, further calibrated, alternative to the *UWsand* model used by Kramer and Mitchell (2006). Additional information on PSNL can be found in Abegg (2010). Nonlinear total- and effective-stress site response analyses were performed for each profile and input motion combination. The ground surface acceleration response, quantified in terms of the various evolutionary IMs, was determined by total stress analysis, and was compared to the pore pressure response and t_L as determined by the effective stress analyses.

Eight soil profiles were used in the study. In anticipation of centrifuge tests to be performed subsequently, each profile had the geometry shown in Figure 5.5, and featured a 6 m thick liquefiable sand layer of uniform relative density above a 2 m thick, dense, cemented sand layer. The eight profiles were constructed at liquefiable sand layer relative densities of 30, 40, 50, 60, 70, 80, 90 and 100%. The properties of the dense cemented sand layer were the same for each profile.

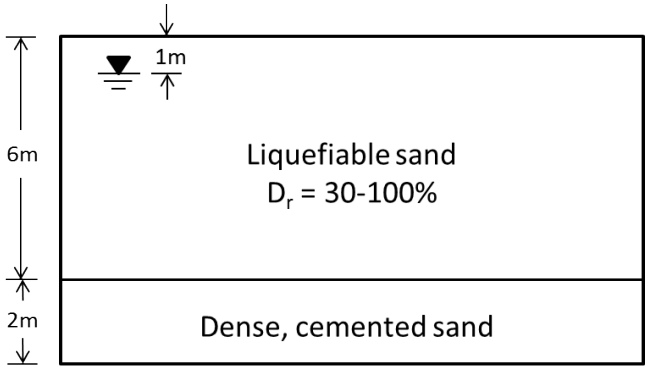


Figure 5.5: Generic profile used in numerical study by Abegg (2010)

A suite of 120 motions were selected from the PEER NGA strong motion database for use in the numerical study. The motions were carefully selected to have different spectral and temporal characteristics, while also spanning a range of magnitudes, source-to-site distances, and faulting mechanisms. The motions were specifically chosen in order to distinguish between each of the candidate IMs. This process involved identifying motions that produced significantly different values for each of the four IMs. An illustration of this process is shown in Figure 5.6, which shows scatter plots of CAV_5 versus PGA_{mL} for motions from the PEER database. In general, each IM generally increased as the other IM increased, but there is a large amount of scatter in the data. Four specific motions from the database are shown in Figure 5.6—two have the same PGA_{mL} values (labeled "High PGA/MSF" and "Low PGA/MSF"), but very different CAV_5 values. Using the CSR-based approach, both motions would have the same liquefaction potential. The other two motions have nearly identical CAV_5 values (labeled "High CAV_5" and "Low CAV_5"), but very different PGA_m values. Figure 5.7 shows the time histories for all four motions.

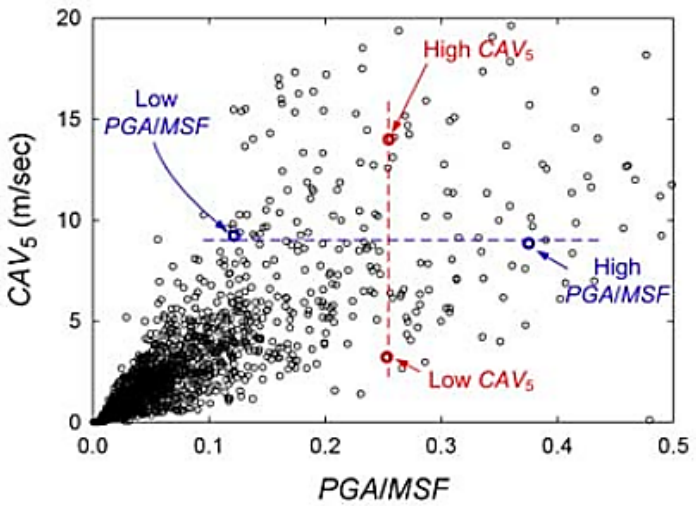


Figure 5.6: General methodology for motion selection, from Abegg, 2010.

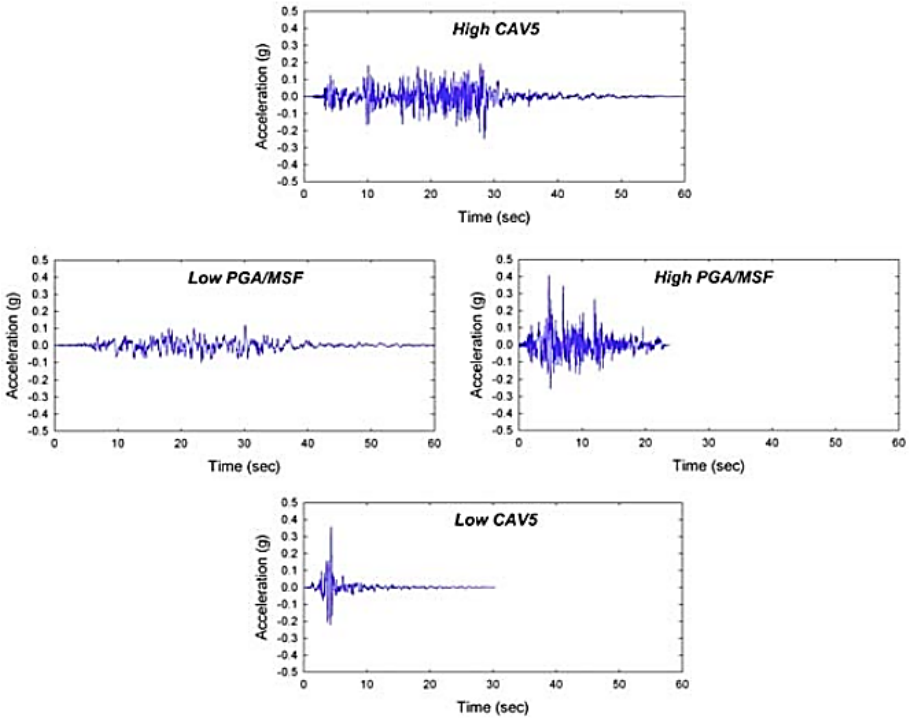


Figure 5.7: Time histories of the four motions identified in Figure 5.6, from Abegg, 2010.

Additional motions were selected in this fashion in an attempt to clearly differentiate which of the four candidate IMs was the most efficient. For example, if CAV_5 were the ideal evolutionary IM for the prediction of pore water pressure, the two motions identified in Figures 5.6 and 5.7 as "Low PGA/MSF" and "High PGA/MSF", and have essentially the same CAV_5 value, would produce the same amount of pore pressure when used as input motions in the analysis. Motions that are high with respect to one IM while average or low with respect to another IM could be more effective at distinguishing which IM is the most efficient predictor of liquefaction, as compared to using motions that are high or low with respect to each of the IMs. The 120 selected motions correspond to five motions from each of the 12 combinations of Average IM_i—High IM_j pairs and the 12 combinations of Average IM_i—Low IM_j pairs. In creating the motion suite, Abegg (2010) used great care to ensure each motion was reasonable with respect to liquefaction analysis (i.e. very weak motions that produce negligible pore pressures are not of interest) and the suite included recorded motions from wide ranges of different earthquake magnitudes, site distances and faulting mechanisms. Further details can be found in Abegg (2010).

The goal of the analysis by Abegg (2010) was to quantify the IM-EDP relationship up to the point of liquefaction. The IMs were computed from the total-stress surface motions, and the EDP was the pore pressure ratio in the critical portion of the generic soil profile, at a depth of 5.5 m, just above the dense-cemented sand layer, $r_{u,crit}$. This layer was considered the critical layer because it was observed to generate the most excess pore pressure and, in the cases where multiple layers liquefied, this layer was observed to have liquefied earlier in the time history than the other layers.

As opposed to Kramer and Mitchell (2006), who used the final IM value and the average pore pressure ratio, Abegg (2010) focused on the loading up to liquefaction within the critical layer, which represented the pre-liquefaction loading identified in the timing-based framework outlined in Chapter 4. For every profile-input motion pair, the IM value at the time $r_{u,crit}$ reached levels of 0.1, 0.3, 0.5, 0.7, 0.9 and 1.0 was calculated. The efficiency was evaluated over a range of six EDP levels and over all eight soil profiles based on the standard deviation of the IM values in each EDP level-soil profile bin. Example results from Abegg (2010) are shown in Figures 5.8 and 5.9.

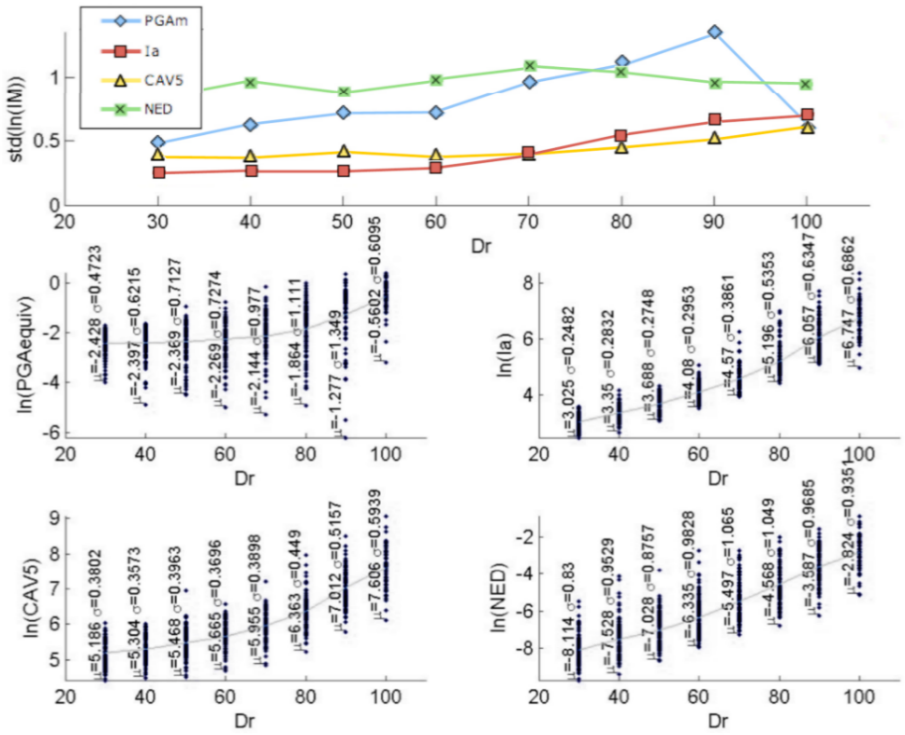


Figure 5.8: IM-D_r plots for EDP levels of $r_{u,crit}$ = 1.0, corresponding to the initiation of liquefaction. Upper plot shows the standard deviations of each IM across each of the eight soil profiles from Abegg (2010).

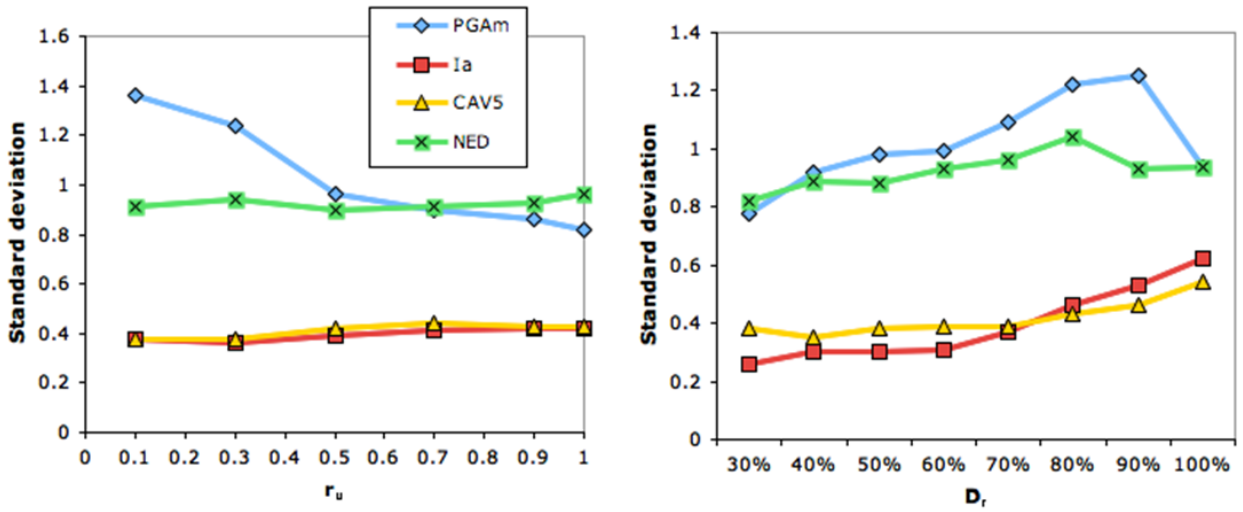


Figure 5.9: Standard deviations of the IM-EDP relationship across range of $r_{u,crit}$ levels and relative density levels from Abegg (2010).

The standard deviations of a particular IM for each of the 64 EDP level-soil profile bins were computed and the most efficient IM was taken as the IM that had the lowest average of standard deviations across the 64 bins. The results of this analyses are shown in Table 5.2, and indicated that I_A was the most efficient predictor of the initiation of liquefaction followed closely by CAV_5. Both were found to be significantly more efficient than PGA_m and NED.

Table 5.2: Average standard deviation of each IM over all D_r and r_u from Abegg (2010).

PGA_m	I_A	CAV_5	NED
1.02	0.39	0.41	0.92

Abegg (2010) also evaluated the sufficiency of each of the four candidate IMs. This process was identical to the method used by Kramer and Mitchell (2006). Linear regression was performed on the residuals of a fitted IM|EDP curve, and the slope of the regression was taken as a measure of sufficiency. This was repeated across all EDP and D_r levels. The results from Abegg (2010) are summarized in Table 5.3 and Figure 5.10. The results indicated I_A, followed by CAV_5, was also the most sufficient IM for prediction of liquefaction initiation.

Table 5.3: Averaged sufficiency plot slope of each IM over all D_r and $r_{u,crit}$ levels.

	PGA_m	I_A	CAV_5	NED
M	-0.52	-0.1	0.25	-0.35
log*R*	-0.4	-0.12	0.21	-0.31

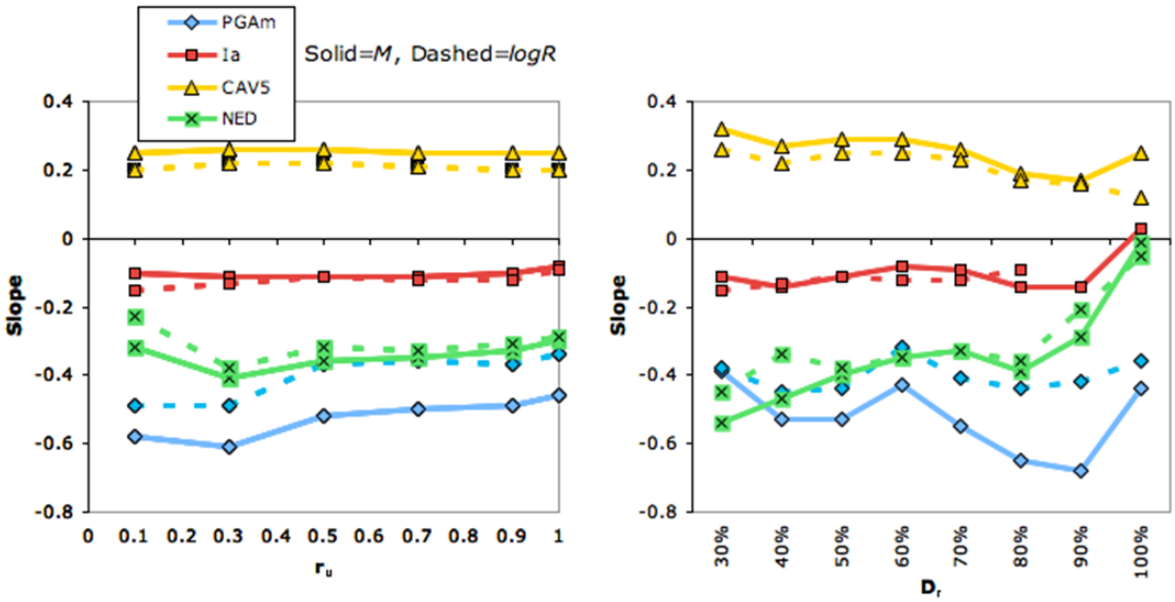


Figure 5.10: Sufficiencies of each candidate IM with respect to both magnitude, *M*, and the log of source to site distance, *R*, in terms of both r_u-averaged and D_r-averaged sufficiencies from Abegg (2010).

5.3 DASHTI AND KARIMI (2017)

Dashti and Karimi (2017) performed a parametric study using fully coupled solid-fluid three-dimensional dynamic finite element analyses of a layered liquefiable soil deposit. The model included an elastic single degree of freedom (SDOF) structure founded on a mat foundation near the ground surface. The finite element analyses were based on, and calibrated to, centrifuge experiments performed by Dashti et al. (2010a and 2010b). The study included numerical simulations of the layered liquefiable soil profile subjected to a diverse suite of input ground motions. Dashti and Karimi (2017) compared the peak excess pore pressure for soils in the far-field (outside the foundation footprint) and beneath the foundation to IMs computed from the acceleration time histories at the base of the model, at the far-field soil surface, and at the base of the foundation. The goal of the study was to evaluate the optimal IM for predicting the peak r_u in the liquefiable layer.

The soil model that was used in the analyses and centrifuge testing is shown in Figure 5.11. The profile included a non-liquefiable Monterrey sand layer at the top of the model with a thickness of D_L and a relative density of 85%. Below the non-liquefiable surface layer was a liquefiable Nevada sand layer with thickness H_L and relative density of $D_{r,liq}$. Between the liquefiable layer and the rigid base at the bottom of the model was a dense Nevada sand layer

that had a relative density of 85% and thickness H_D. The groundwater table was located 1 m below the ground surface. All of the soil layers were modeled using the pressure-dependent, multi-yield surface constitutive model PDMY02 (Elgamal et al., 2002; Yang et al., 2003) implemented in OpenSees (Yang et al., 2008). The PDMY02 model was calibrated to simulate the response of both the liquefiable and the non-liquefiable soil layers as described in Dashti and Karimi (2017) and Karimi and Dashti (2017). The layer thickness and density of the liquefiable layers were varied in the parametric analyses. D_L was varied between 2 and 4 m, H_L was varied between 2 and 24 m, and $D_{r,liq}$ was varied between 30 and 85%. The thickness, H_D, was adjusted so that the total height of the model was constant at 26 m.

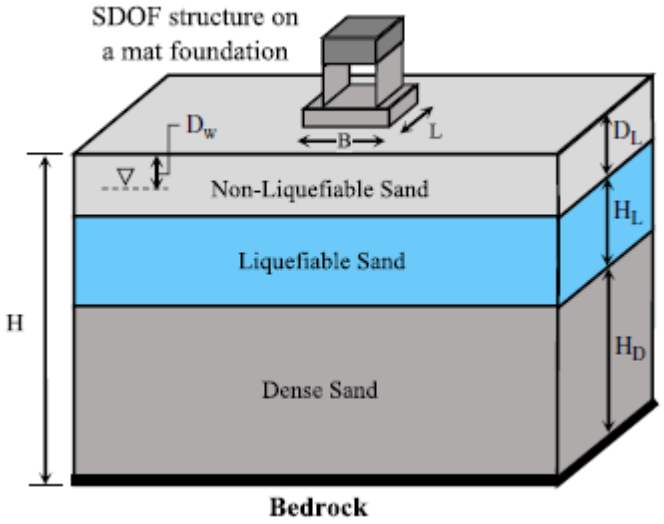


Figure 5.11: Schematic of the soil profile and structure that was evaluated in the parametric study of Dashti and Karimi (2017)

The structure and mat foundation located at the ground surface was modeled as linear elastic. The foundation dimensions, contact pressure, mass and height of the structure, and the fundamental structural period were varied in the parametric study of Dashti and Karimi (2017). The foundation width was varied between 6 and 9 m, and the footing length was varied between 9 and 13.5 m. The contact pressure was varied between 76 and 130 kPa, the height of the structure was varied between 3.4 and 6.8 m, the mass of the structure was varied between 412 and 917 metric tons. The fundamental structural period was varied between 0.24 and 0.78 seconds. A total of 21 models were investigated that covered the range of soil profile and structural characteristics described above.

Each of the 21 models were subjected to a suite of 78 earthquake ground motions selected from the PEER Strong Motion Database (Ancheta et al., 2013). The motion suite included motions recorded on sites that were classified as either rock or very dense soil/soft rock from earthquakes with magnitudes ranging from 4.5 to 7.5, at source-to-site distances that generally ranged from 16 to 50 km. The suite also included 26 near-sources ground motions that had source-to-site distances less than 16 km. The motions were selected to capture a broad range of excess pore pressure and IM response.

For each analysis, Dashti and Karimi (2017) evaluated the EDP as the peak r_u value in the far-field and below the foundation and computed IMs using the entire acceleration time history from the base motion and the computed acceleration response at the surface in the far-field and at the base of the foundation. Dashti and Karimi (2017) investigated 28 different candidate intensity measure that included both conventional IMs such as PGA, I_A, and CAV, as well as IMs that capture the frequency content (e.g. spectral acceleration values at specific periods) and duration (e.g. significant and bracketed duration). A full description of each of the 28 candidate IMs are provided in Dashti and Karimi (2017).

The IMs were then evaluated in terms of their efficiency, sufficiency, and predictability in a manner that was similar to the methods used in Kramer and Mitchell (2006). The IM-EDP relationship was defined as an integrated beta distribution. The efficiency of a given IM to predict the EDP was evaluated using the standard deviation of the residuals computed using the natural logarithm of the predicted EDP and the EDP computed in the numerical analyses. An example of this process from Dashti and Karimi (2017) is provided in Figure 5.12 for two of the 28 models, where the EDP was defined as the peak r_u in the far-field and the IM was the PGA of the base motion. The example includes both the fitted response and the peak r_u value computed during the analysis.

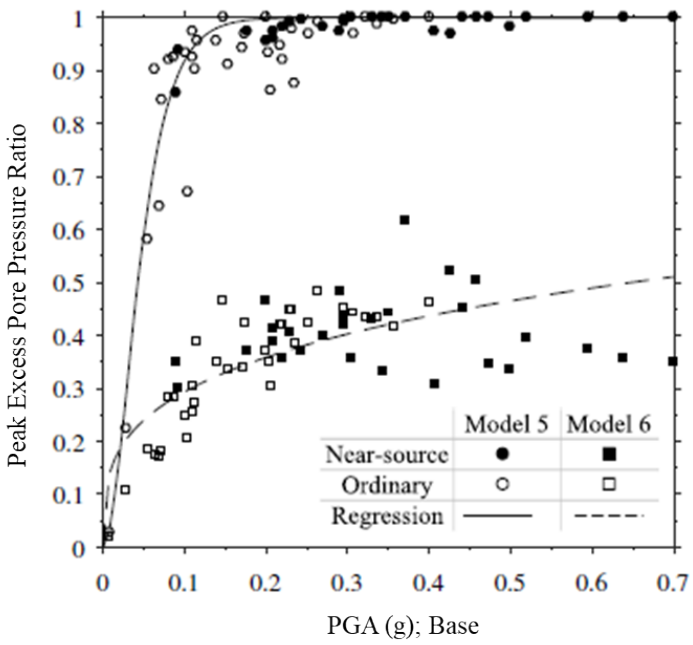


Figure 5.12: Peak excess pore pressure ratio in the far-field as a function of the PGA of the base input motion for two models from Dashti and Karimi (2017).

The sufficiency was evaluated in the same manner as Kramer and Mitchell (2006) using the slope (c) of a standard linear regression fit to the residuals of the r_u-IM relationship as a function of moment magnitude (M_w) and source-to-site distance (R). The larger the value of c, the less sufficient the IM is with respect to M_w and R. An example of this analysis is provided in Figure 5.13 for the IM defined as the PGA of the base motion and the EDP defined as the peak r_u in the far field. For the given example, the IM-EDP relationship shows a slight dependence on the magnitude of the motion (as expected based on the stress-based liquefaction procedures) and is relatively independent of the source-to-site distance.

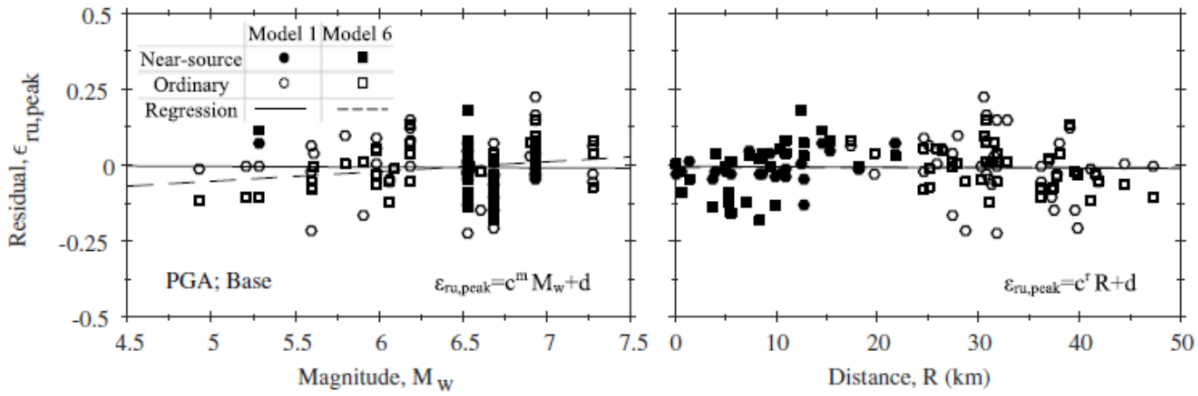


Figure 5.13: Residuals of the IM-EDP relationship as a function of the moment magnitude and source-to-site distance from Dashti and Karimi (2017). In this example the EDP was defined peak excess pore pressure in the far-field and the IM corresponded to the PGA of the base input motion.

A summary of the standard deviation of the log residuals, σ, and the c values from the sufficiency evaluation for magnitude, c^m, and source-to-site distance, c^r, for the ten IMs that were most efficient at predicting the peak r_u in the far-field is presented in Figure 5.14. Dashti and Karimi (2017) identified the ten most efficient IMs as the pseudo spectral acceleration at the natural site period, PSA[T_{s0}], the characteristic intensity (Park et al., 1985), CI (defined as the root-mean-square acceleration raised to the power of 1.5 multiplied by the square root of the total duration of the ground motion), sustained maximum acceleration (Nuttli, 1979), SMA (evaluated as the third highest absolute value of acceleration), root-mean-square of acceleration (McCaan and Shah, 1979), a_{rms}, I_A, A_{95} (Sarma and Yang, 1987), and effective design acceleration (Benjamin and Associates, 1988), EDA (peak acceleration after a lowpass filter with a cut-off frequency of 9 Hz is applied to the acceleration time history), computed using the base motion, and the shaking intensity rate (Dashti et al., 2010b), SIR (defined as the difference between I_A at 5 and 75% of the total I_A divided by the corresponding duration between the two points), SMA, and PGA computed using the far-field surface time history. The standard deviation of the log residuals for these IMs ranged from 0.07 for PSA[T_{s0}] computed using the base input motion to 0.09 for PGA computed using the far-field surface time history. Dashti and Karimi (2017) identified PSA[T_{s0}] computed using the base input motion and SIR computed using the far-field surface motion as the most efficient and sufficient IMs for predicting the peak r_u response in the far-field.

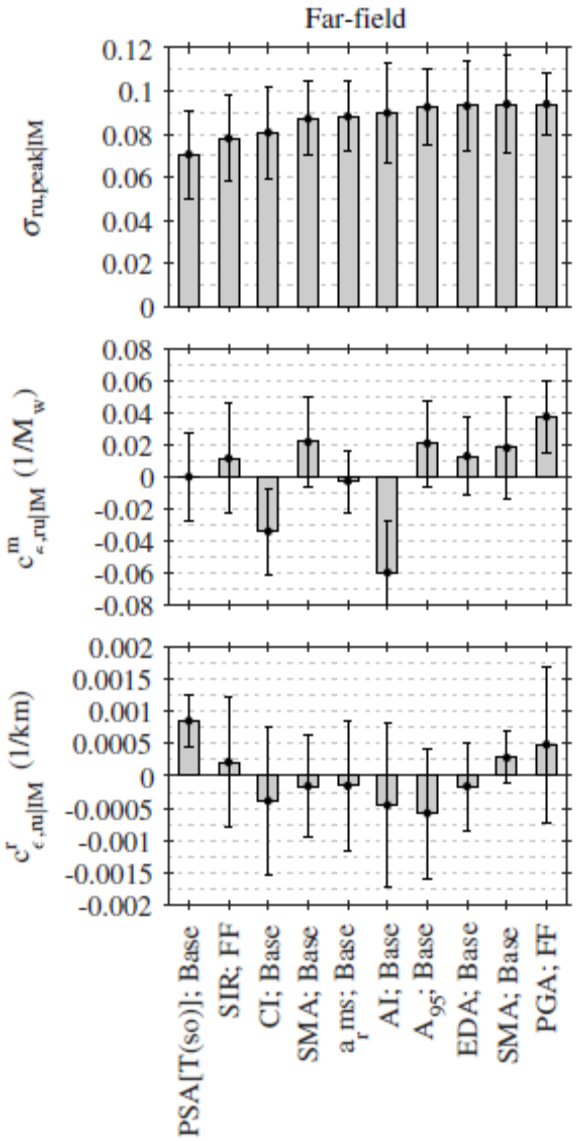


Figure 5.14: Mean and standard deviation of σ, c^m, and c^r for the ten most efficient IMs at predicting the peak r_u value in the far field from Dashti and Karimi (2017).

Dashti and Karimi (2017) repeated the analyses presented above using EDPs defined as the peak r_u below the center and the edge of the foundation. They identified EDA and PGA computed using the base motion were the most efficient and sufficient IMs for predicting the peak r_u beneath the center of the foundation. When the EDP was defined as the peak r_u beneath the edge of the footing, Dashti and Karimi (2017) identified CI computed using the far-field surface time history and I_A computed using the base motion as the most efficient and sufficient IMs.

Dashti and Karimi (2017) note that the mechanisms that control the r_u response, such as confining stresses and drainage paths, differ between the far-field and at different locations beneath the foundation. As a result, the IM that is the most efficient and sufficient at predicting the peak r_u in the far-field may not be the most efficient and sufficient IM at predicting the peak r_u beneath the foundation. This was reflected in the results from Dashti and Karimi (2017), who found that the most efficient and sufficient IM differed based on the location that the peak r_u value was evaluated at. An interesting observation from the results presented by Dashti and Karimi (2017) was that PGA was consistently among the top ten most efficient IMs for predicting the peak r_u level, regardless of whether the r_u was evaluated in the far-field or beneath the foundation. In addition, CAV and CAV_5 were not among the ten most efficient IMs for predicting the peak r_u response for any of the analyses performed by Dashti and Karimi (2017).

5.4 DISCUSSION

The numerical investigations of Kramer and Mitchell (2006), Abegg (2010), and Dashti and Karimi (2017) identified evolutionary IMs that are efficient and sufficient predictors of both the initiation of liquefaction. The models used and the findings obtained from each study differed. Kramer and Mitchell (2006) and Abegg (2010) found that that I_A and CAV_5 were the most efficient predictors of the initiation of liquefaction based on 1-D effective stress site response analyses. Both of these numerical studies showed that the magnitude-corrected PGA, the IM most commonly used in current liquefaction evaluation practice, was a significantly less efficient indicator of liquefaction initiation than alternative IMs that were identified in the studies.

Using three-dimensional finite element analyses, Dashti and Karimi (2017) identified the pseudo spectral acceleration at the fundamental site period, $PSA[T_{s0}]$ and the shaking intensity rate, SIR, were the most efficient at predicting the peak r_u that was computed in the far-field, and that I_A, PGA, the effective design acceleration, EDA, and the characteristic intensity, CI, were the most efficient IMs for predicting the peak r_u levels beneath a shallow foundation. Interestingly, the results from Dashti and Karimi (2017) suggested that PGA, uncorrected for magnitude, was among the best predictors of the peak r_u value regardless of whether the r_u was taken from the far-field or beneath the foundation. In addition, CAV_5 was not among the most efficient predictors of r_u, which contradicts the findings of Kramer and Mitchell (2006) and

Abegg (2010). The differences could be due to differences in the numerical modeling methods, the constitutive models for the liquefiable soil, and the model geometry.

Unfortunately, not all of the IMs that Dashti and Karimi (2017) identified as being the most efficient and sufficient predictors of peak r_u can be formulated in an evolutionary sense, and therefore cannot be used in the timing-based framework. The pseudo spectral acceleration value at the natural site period is the peak response of a single-degree-of-freedom oscillator. SIR is defined as the difference between I_A at 5 and 75% of the total I_A divided by the corresponding duration between the two points (Dashti et al., 2010b). CI is defined as the root-mean-square acceleration raised to the power of 1.5 multiplied by the square root of the total duration of the ground motion (Park et al., 1985). Each of these parameters are inherently static values and are not applicable for the timing-based liquefaction hazard evaluation framework.

The next step, and the focus of this dissertation, is to further investigate and validate the findings of the numerical studies of Kramer and Mitchell (2006), Abegg (2010) and Dashti and Karimi (2017) using experimental data to systematically investigate the response of liquefiable soils subjected to transient loading histories. The goal of the study is to evaluate optimal evolutionary IMs to incorporate in the timing-based liquefaction hazard evaluation framework proposed in Chapter 4 with respect to the triggering of liquefaction. The experimental program was designed to methodically investigate the response of liquefiable soils to transient ground motions and included both centrifuge and cyclic simple shear (CSS) testing. The next chapter presents the methodology and results from the CSS experimental testing program.

[This page intentionally left blank]

Chapter 6. CYCLIC SIMPLE SHEAR EXPERIMENTAL TESTING PROGRAM

The initial chapters of this document introduced the phenomenon of soil liquefaction, described the mechanics of liquefaction, detailed the effects of liquefaction, and discussed current procedures for evaluating liquefaction hazards. It was established that the current procedures offer significant room for improvement, and the current vector form of the most popular, stress-based relationships are difficult to implement into the probabilistic PBEE framework. The difficulties arise from the lack of a coherent methodology to go from an estimate of the imposed loading to an estimate of response in a predictable, efficient, and sufficient manner.

These observations led to the development of the timing-based framework for liquefaction hazard evaluation based on evolutionary IMs, which was discussed in Chapter 4. The incorporation of evolutionary IMs in the timing-based framework allows the timing of liquefaction to be explicitly accounted for, something that has been lacking in previous liquefaction evaluation procedures. The timing-based framework provides a methodology for a designer to seamlessly step from a prediction of the imposed loading, to a prediction of not only if, but when, liquefaction will occur. If liquefaction does occur, the timing-based framework can incorporate knowledge of the post-triggering loading to make an improved prediction of the response. Additionally, the timing-based liquefaction hazard evaluation framework is organized such that it can be quantified in a probabilistic sense in order to maximize its effectiveness in the PBEE framework.

The purpose of this research is to identify efficient evolutionary IMs to calculate the triggering of liquefaction (IM^{trig}), which represents the first step of the timing-based framework. The previous chapter provided a literature review of the subject. Previous studies that used numerical methods have been performed; however, the results of these studies are at this time inconclusive, and the stress-based method continues to be the predominant method used in practice. This research is based on an extensive and systematic experimental testing program that was performed to investigate the behavior of liquefiable soil deposits to transient loading histories. The results of these tests were intended to allow identification of optimum IMs for evaluating the triggering of liquefaction. The optimum evolutionary IM is the one that has the

best balance of being predictable, in a seismic hazard analysis sense, as well as the most efficient and sufficient in terms of predicting the initiation of liquefaction.

The experimental data for this study fell into two categories, cyclic simple shear (CSS) test data and centrifuge test data. This chapter presents the CSS testing and results; the centrifuge experiments and results are discussed in the following chapter.

6.1 INTRODUCTION

In general, three predominant, small scale laboratory tests capable of simulating the response of an element of soil to the type of cyclic loading that would occur during an earthquake are currently available to engineers. These are the cyclic triaxial, torsional ring shear, and CSS tests. The CSS test was chosen for this study because it more accurately represents the stress conditions that occur in the field than the cyclic triaxial test and it is utilized more often by practicing engineers than the ring shear device.

A schematic illustration of a typical CSS device is shown in Figure 6.1. In CSS tests, a thin, cylindrical soil sample is placed within either rigid platens (Cambridge-type device), wire reinforced membranes (NGI-type), or a series of stacked rings (SGI-type) to restrain the sample against lateral expansion (Kramer, 1996). An overburden pressure is imposed at the top of the sample, and the upper platen is held in place to maintain constant volume conditions throughout the test. During testing, a lateral cyclic shear stress is applied to either the top or bottom platens, and the specimen deforms in a manner that is consistent with the type of deformation that would be expected in an element of soil subjected to vertically propagating shear waves (as is assumed in site response analysis, Figure 6.1). As the loads are applied LVDTs are used to measure the horizontal and vertical deformations that occur due to the cyclic stress loading. In addition, pore pressure transducers located at the bottom of the specimen record the excess pore pressure that occurs during undrained testing.

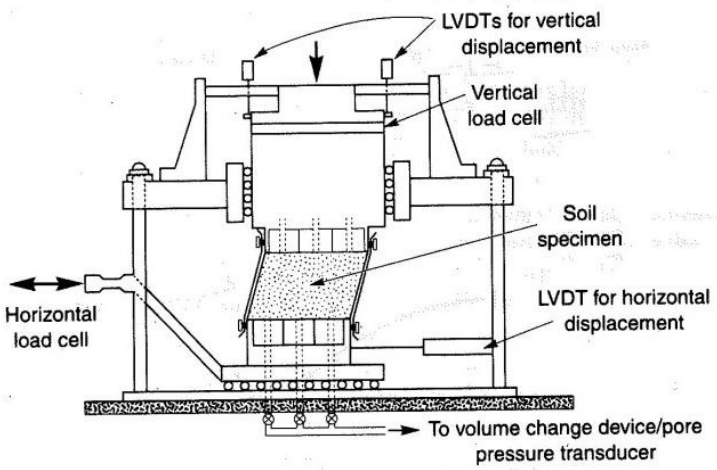


Figure 6.1: Schematic of NGI-type cyclic simple shear apparatus. NGI-type devices house the soil specimen in a wire reinforced latex membrane (After Airey and Wood, 1987).

For this study CSS testing was conducted at the University of Texas-Austin and is thoroughly documented in Kwan (2015). The CSS testing included two distinct testing programs, a harmonic test program that utilized simple loading histories, and a transient test program involving loading histories derived from actual recorded ground motions. The following section provides an overview of the aspects common to both testing programs.

6.2 CSS TESTING OVERVIEW

This section describes the soil sample, testing apparatus, and basic data reduction methods used in both the harmonic and transient CSS testing programs. Each of these aspects are discussed individually in the following subsections.

6.2.1 *Soil Description*

Nevada 120, or simply Nevada sand, was used in both the CSS and centrifuge testing programs. According to the USCS, Nevada sand is classified as poorly graded sand (SP), with the soil index properties shown in Table 6.1 and the grain size distribution shown in Figure 6.2. Nevada sand is a very common testing sand and has been used extensively in past projects, especially those concerning liquefaction (i.e. VELACS, etc.). Prior work has indicated that the friction angle of Nevada sand generally varies between 33 and 37° depending on the testing method used and the relative density of the sample (Arumoli et al., 1992). Hydraulic conductivity values of Nevada

sand are generally on the order of 0.002 to 0.006 cm/s depending on the relative density of the sample (Arumoli et al. 1992).

Table 6.1: Soil index properties of Nevada sand(from Kwan, 2015)

Sand Type	e_{min}	e_{max}	S.G.	C_u	C_c	D_{50}
Nevada	0.56	0.76	2.67	2	1.13	0.17 mm

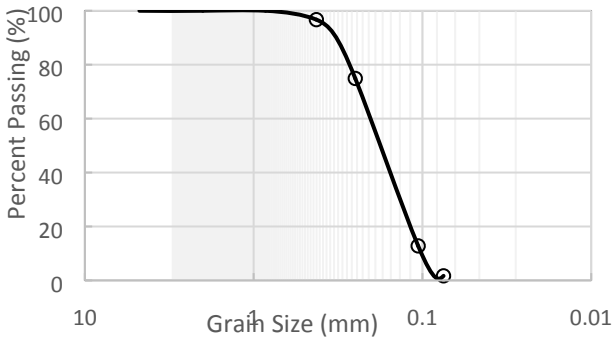


Figure 6.2: Grain size distribution of Nevada sand(from Kwan, 2015).

6.2.2 *CSS Apparatus and Specimen Preparation*

The CSS testing apparatus used at UT-Austin in this study is shown in Figure 6.3. The soil sample was pluviated in a latex membrane and confined within a series of stacked rings (SGI-type apparatus). Originally an NGI-type wire reinforced membrane was to be used, however availability of the NGI-type membranes was limited, so an SGI-type device was utilized in order to have consistency between each of the tests in the testing program. The soil samples were constructed to be approximately 1 inch tall and 4 inches in diameter. In order to pluviate the sample, a vacuum was applied to pull the membrane into contact with the stacked rings. Then the sand was placed using a wet deposition method similar to Kammerer et al. (2002) with some modifications as described in Kwan (2015). To prepare samples with high relative density (70% and above) the sample was prepared in two lifts, with each lift densified with vibration applied at the top of the lift.

After preparation, the samples were sealed and back pressure saturated. The vertical load was applied via a pneumatic actuator. Two LVDTs were used to measure the horizontal and vertical displacement of the sample during testing. In addition, changes in specimen height

during consolidation were monitored and used to compute final sample relative densities. A pore pressure transducer, located on the bottom platen, was used to record the pore pressure response. More detailed descriptions of the testing apparatus and testing methodology can be found in Kwan (2015).

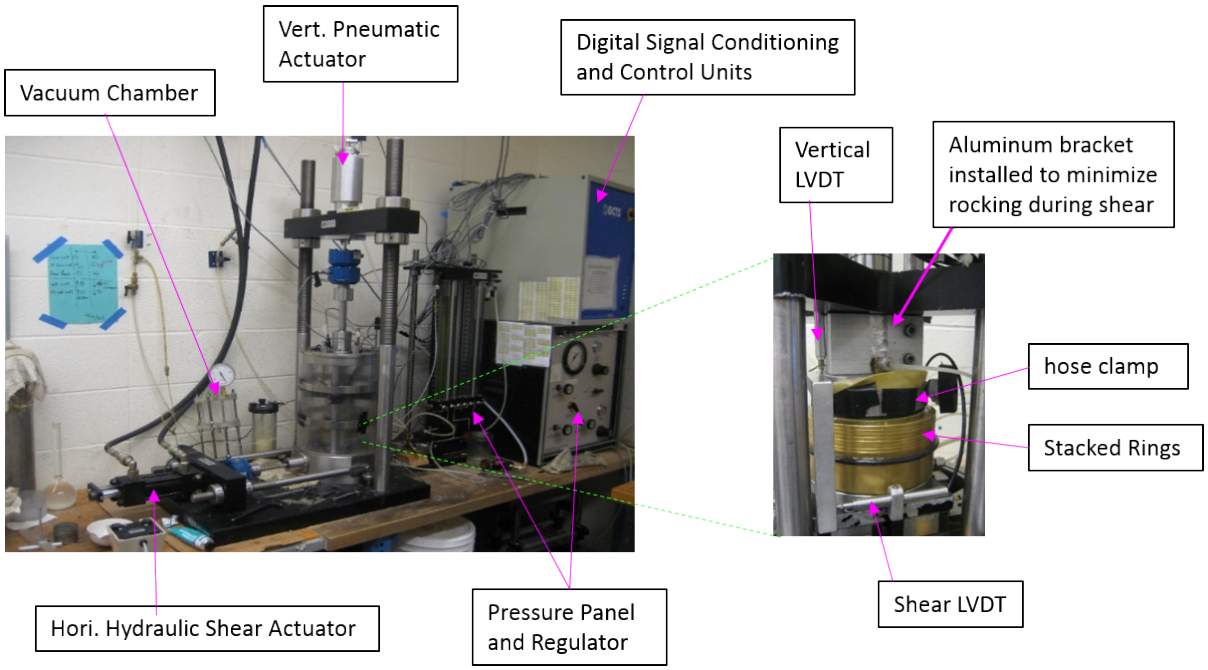


Figure 6.3: UT-Austin CSS testing apparatus schematicfrom Kwan (2015).

Several complications arose during the CSS experimental testing program; however, these complications caused numerous improvements to be made to the UT-Austin CSS device. As stated previously, the limited availability of the NGI-type, wire reinforced membranes led to the decision to use an SGI-type stacked ring setup to ensure consistency between all of the tests. In order to facilitate the model preparation process, a mold was fabricated at UT Austin to house the stacked ring setup in order to apply a vacuum to the sample. The new mold, stacked ring, and membrane setup is shown in Figure 6.4.

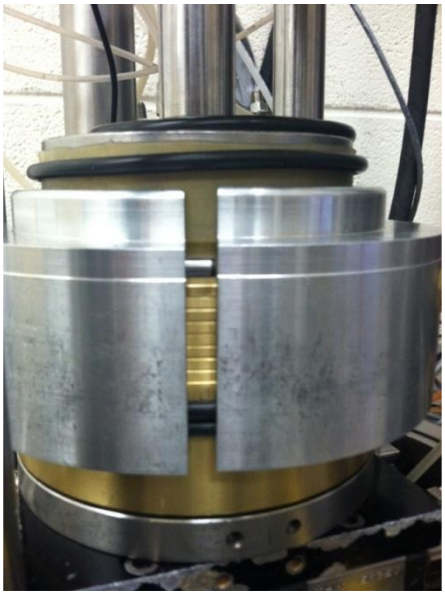


Figure 6.4: The new mold fabricated for the SGI-type stacked ring and membrane assembly (from Kwan, 2015).

Other issues arose due to the fact that this was the first, large-scale, high-amplitude testing program conducted using transient loading histories with the UT Austin apparatus. Recalibration and modifications were made to the shear-actuator and shear roller assemblies in order to ensure that the intended load and the actual applied load were in good agreement. The vertical loading system was replaced because the vertical actuator was not able to maintain a constant load when the sample was subjected to high amplitude, high frequency shear loading. Furthermore, it was observed that the large amplitude, transient loading produced rocking of the top platen in some instances. In order to minimize the rocking, Kwan (2015) designed an aluminum bracket to stiffen the connection between the top platen and the piston that applied vertical load to the specimen. The bracket not only reduced the rocking behavior significantly, but also reduced the changes in vertical stress and displacements that were observed on tests performed prior to installation of the aluminum bracket. Another improvement was the introduction of hose clamps to the system in order to prevent leakage between the membranes and the platens when the excess pore pressures became large. Toward the latter stages of the project the improved UT Austin CSS apparatus was able to produce high quality transient test data at a relatively fast rate (Kwan, 2015).

6.2.3 *CSS Test Data Processing*

For each of the CSS tests, initial processing of the raw data was done by UT-Austin and is described in Kwan (2015). Prior to testing, precise measurements of the specimen weight, height and diameter were taken. The reported relative density value for each test represents the average relative density of the sample after consolidation and prior to undrained cyclic loading. Each sample was tested at an overburden pressure of 100 kPa. Prior to testing a B-Value was calculated to assess the degree of saturation of each sample.

During testing, values of the axial and shear loads, vertical and transverse displacements, cell pressure, pore pressure and internal vertical and transverse displacements were recorded. Based on these measurements, Kwan (2015) calculated the pore pressure, vertical and shear strain, vertical total and effective stresses, and shear stress imposed on the sample during the testing process. Further details of this process can be found in Kwan (2015).

6.3 CSS TESTS WITH HARMONIC LOADING

Prior to conducting CSS tests using fully transient loading histories developed from actual earthquake recordings, a series of CSS tests were performed using simple harmonic type loading histories. As discussed in Section 2.3.3.1, the response of a liquefiable soil sample to uniform harmonic loading has been studied extensively in the past. The stress-based procedure presented in Chapter 2 uses a rational methodology to extend the results of the uniform harmonic laboratory test data to transient earthquake loading which has been substantiated through case history data. However, a systematic study on the response of liquefiable soils to transient earthquake loading histories has yet to be conducted. In order to methodically investigate the response liquefiable soils subjected to transient loading, the first part of the CSS testing program included simple harmonic tests. The purpose of these tests was to (a) validate the UT CSS testing apparatus and sample preparation methods and (b) use relatively simple test loading histories to attempt to identify which aspects of a transient loading history are best correlated with the generation of excess pore pressure.

The harmonic testing program consisted of three types of loading histories, each of which were based on a sinusoid. The three types of harmonic loading histories are described as follows:

1. Constant amplitude harmonic loading: sinusoidal loading at a constant stress amplitude,

2. Irregular harmonic loading: a single large amplitude loading cycle was superimposed on a uniform sinusoidal loading history, and
3. Modulated harmonic loading: a uniform sinusoidal load was scaled using enveloping functions to modify the sequencing of the loading amplitudes.

An overview of each of three harmonic test programs are presented individually in the following sections.

6.3.1 *Constant Amplitude Harmonic Loading*

To validate the performance of the UT CSS testing apparatus and sample preparation methods, a series of conventional, constant amplitude harmonic CSS tests were performed by Kwan (2015). A total of 13 tests were conducted on samples consolidated to 100 kPa with initial relative densities ranging from 35 to 85 percent. The samples were subjected to uniform harmonic loads with peak CSRs that ranged from approximately 0.1 to 0.35. The uniform harmonic loads were applied until the sample reached an r_u value of 1.0. The constant amplitude harmonic tests were conducted using a loading frequency 0.2 hertz (Hz). Previous research by Riemer et al. (1994) has shown that the liquefaction resistance is relatively independent of the frequency of the applied load (National Academies of Sciences, Engineering, and Medicine; 2016). Therefore, a relatively slow loading rate was used to allow for better pore pressure measurement due to the location of pore pressure transducer at the bottom of the specimen (Kwan, 2015).

As noted in Chapter 2, the resistance to liquefaction of a given soil at a certain relative density under uniform harmonic loading conditions can be defined using liquefaction resistance curves that relate the CSR versus number of cycles to liquefaction (N_{liq}). The liquefaction resistance curves are commonly evaluated using the power function provided in Equation 2.4. To define the liquefaction resistance curves for this study, the samples were grouped into loose and dense tests based on the sample preparation method. The relative densities ranged from 34 to 55% for the loose tests and 74 to 85% for the dense tests. The liquefaction resistance curves for the uniform harmonic tests are summarized in Figure 6.5. Equation 2.4 was fit to the results of the uniform harmonic load test data for the loose and dense tests individually, and the results are presented in Figure 6.5. The resulting b values for the loose and dense tests were determined to be 0.19 and 0.29, respectively. Boulanger and Idriss (2014) performed a literature review of uniform harmonic test results that incorporated a wide range of testing procedures and soil

specimens. The work of Boulanger and Idriss (2014) showed that for clean sand samples the value of b from Equation 2.4 generally range from 0.14 to 0.54, with the b value typically increasing as the density of the sample increases. The b values determined from the present study were consistent with these observations.

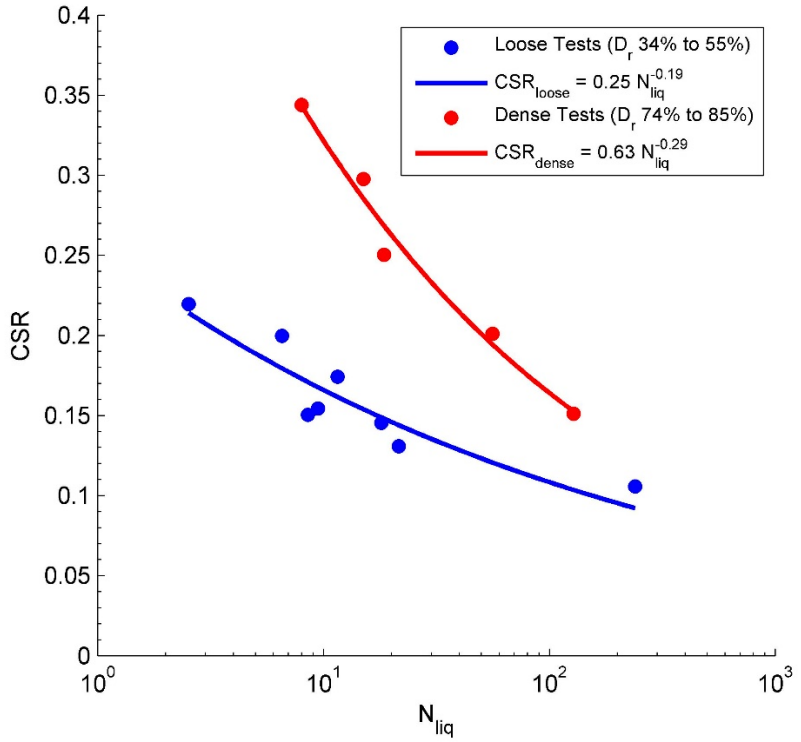


Figure 6.5: Liquefaction resistance curves for constant amplitude harmonic CSS tests.

Another way the harmonic tests were evaluated included plotting the r_u response as a function of the cycle ratio, computed as the number of cycles, N, divided by N_{liq}. The r_u versus cycle ratio curves from the uniform harmonic CSS tests are presented in Figure 6.6. To investigate the potential influence of the amplitude of the uniform harmonic load, the lines for the CSS data were colored with respect to the loading amplitude. The figure also contains plots showing the upper and lower bounds from a similar study performed by De Alba et al. (1975), as well as the fitted relationship to the results of the present study. The r_u response from the current study tended to be slightly larger than the range provided by De Alba et al. (1975) for cycle ratios less than about 0.2, while the r_u response at cycle ratios greater than 0.2 generally fell within the range of values presented by De Alba et al. (1975). In addition, the relationship between r_u and the cycle ratio was found to be independent of the CSR amplitude.

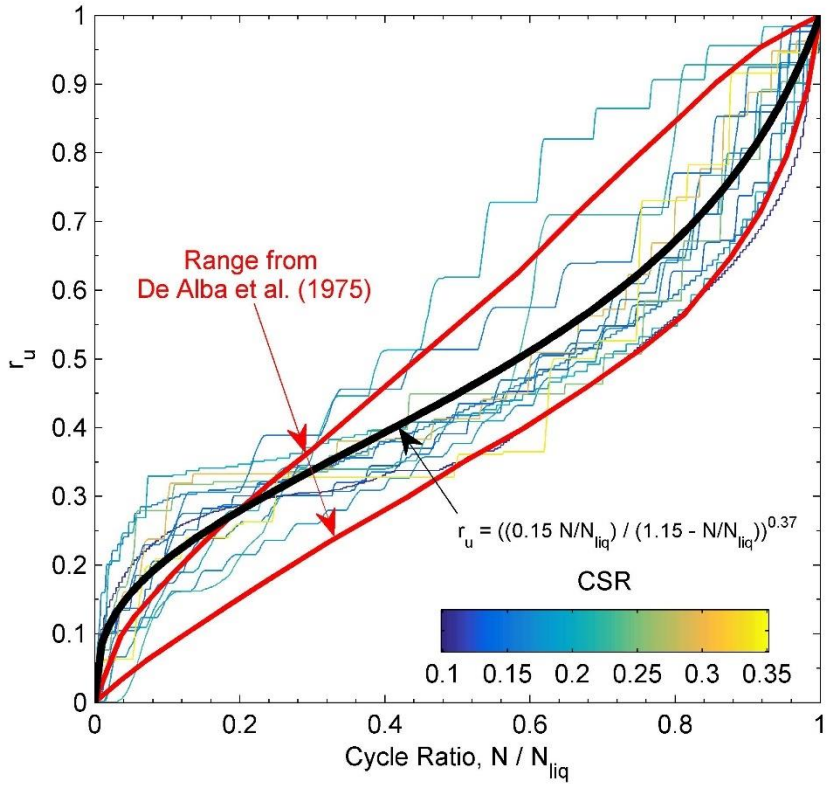


Figure 6.6: r_u as a function of the cycle ratio for the constant amplitude harmonic load tests.The line color for the test data is presented as a function of the CSR amplitude of the test. Included on the plot are the range of responses from the study of De Alba et al. (1975) in red and the fitted relationship to the response from the present study in black.

While constant amplitude harmonic tests represent the most basic type of cyclic load, the results provide important insights into the relationship between the generation of excess pore pressure and the applied load. Note that the general shape of the r_u versus cycle ratio curves, both from this study and from other researchers, is non-linear. This suggests that the amount of excess pore pressure generated by each cycle was non-uniform, even though the amplitude of the applied load was constant. Therefore, the excess pore pressure response of the soil depended on the loading history. The load-dependent relationship between r_u and uniform cyclic stress loading has been observed in numerous previous studies including Seed et al. (1975), Ishibashi et al. (1977), and Konstandinou and Georginnou (2014).

Konstandinou and Georginnou (2014) identified three zones in the r_u versus cycle ratio plot referred to as Zones 1 to 3 as follows:

- Zone 1: where the excess pore pressure increases rapidly during the initial loading,

- Zone 2: where the rate of excess pore pressure generation stabilizes at a relatively low value, and
- Zone 3: where the rate of excess pore pressure increases rapidly due to phase transformation, which for uniform harmonic loading typically occurs once the r_u value reaches a value of approximately 0.6.

A plot of the change in excess pore pressure ratio, Δr_u, versus cycle ratio for the fitted relationship from the present study shown in Figure 6.6 is provided in Figure 6.7. This figure demonstrates that the average response of the constant amplitude harmonic tests performed for this study were consistent with the observations of Konstandinou and Georginou (2014). The three zones mentioned above were delineated in Figure 6.7 using dashed lines. At low cyclic ratios (less than about 0.25), the rate of excess pore pressure generation per applied cycle was large, and gradually decreased as the cycle ratio increased. At a cycle ratio of about 0.25 the rate of excess pore pressure generation stabilized at a relatively low value (Δr_u of about 0.015 for the loading levels used in this study). Above cycle ratios of about 0.65, the excess pore pressure response began to increase at a faster rate until liquefaction was initiated at an r_u value of 1.0.

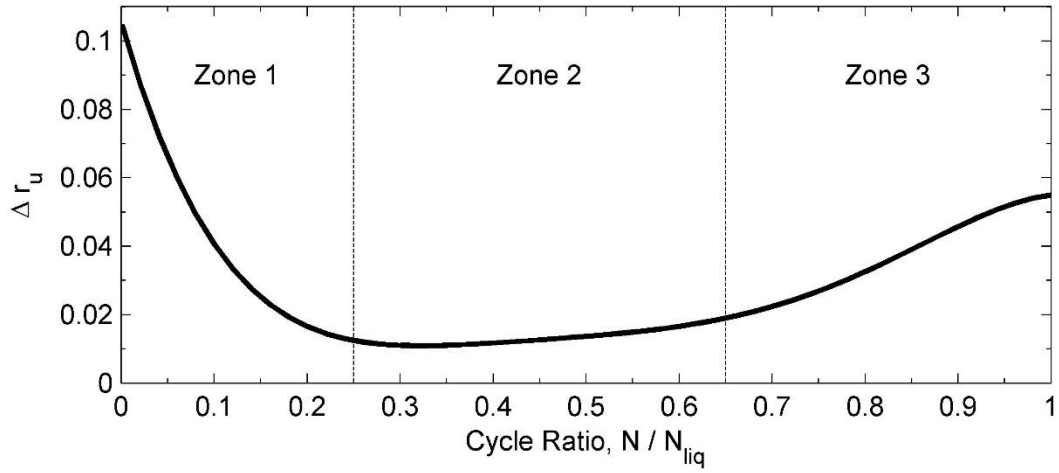


Figure 6.7: The change in excess pore pressure ratio, Δr_u, as a function of the cycle ratiocomputed using the fitted relationship to the constant amplitude harmonic test data.

This phenomenon was further investigated by examining the response of individual test results, an example of which is provided in Figure 6.8 for test on a soil sample with a relative density of 51% subjected to a 0.14 CSR harmonic load. For this test liquefaction was observed after approximately 21 cycles. The results shown in Figure 6.8 include plots of the shear strain,

shear stress, and r_u time histories, as well as plots of the stress path and stress-strain response. The line in each plot was colored with respect to the number of cycles to allow for comparison between the time histories and the stress path and stress-strain response. The three zones discussed previously were delineated on the plot of the r_u time history.

Prior to applying the loading, the individual soil particles of the test sample were oriented in a given structure or fabric that depends on the soil gradation and pluviation method. As the initial cycles were applied, the particles realigned themselves in response to the shear loading. Under constant volume conditions, this realignment resulted in relatively rapid generation of excess pore pressure – up to an r_u of approximately 0.25 – in the first three cycles of the loading history (Zone 1), indicated in dark blue.

As more cycles were applied, the initial fabric was further degraded and eventually the soil particles became aligned in a structure that was comparatively more resistant to volume change in response to the constant amplitude shear loads. After the initial fabric had been destroyed, the rate of excess pore pressure generation under constant amplitude loading stabilized. This behavior was observed between the third and 16th cycles (Zone 2), shown as light blue to yellow. The increment of excess pore pressure generated by each cycle in this zone was relatively constant and much lower than the increments generated during the initial loading in Zone 1.

However, as more cycles of shear stress were applied the effective stress gradually decreased. Eventually, as the stress path moved toward the origin, the stress path crossed the phase transformation line. As described in Chapter 2.3.2.1, the phase transformation line represents the boundary between contractive and dilative behavior. Once the phase transformation line is crossed, the soil began to dilate as the magnitude of the shear stress increased, and the excess pore pressure ratio temporarily decreased. Following a stress reversal, the soil contracted. The transitions between dilative and contractive behavior led to rapid increases in the excess pore pressure over a given cycle of loading. This behavior was observed following the 16th cycle (Zone 3), as the line color transitioned from orange to red. The stress path plots show that phase transformation behavior was initiated during the Zone 3 loading cycles, with the transition between dilative and contractive behavior manifesting as closed loops in the stress path plot. In this zone the rate of pore pressure increased rapidly until liquefaction was observed.

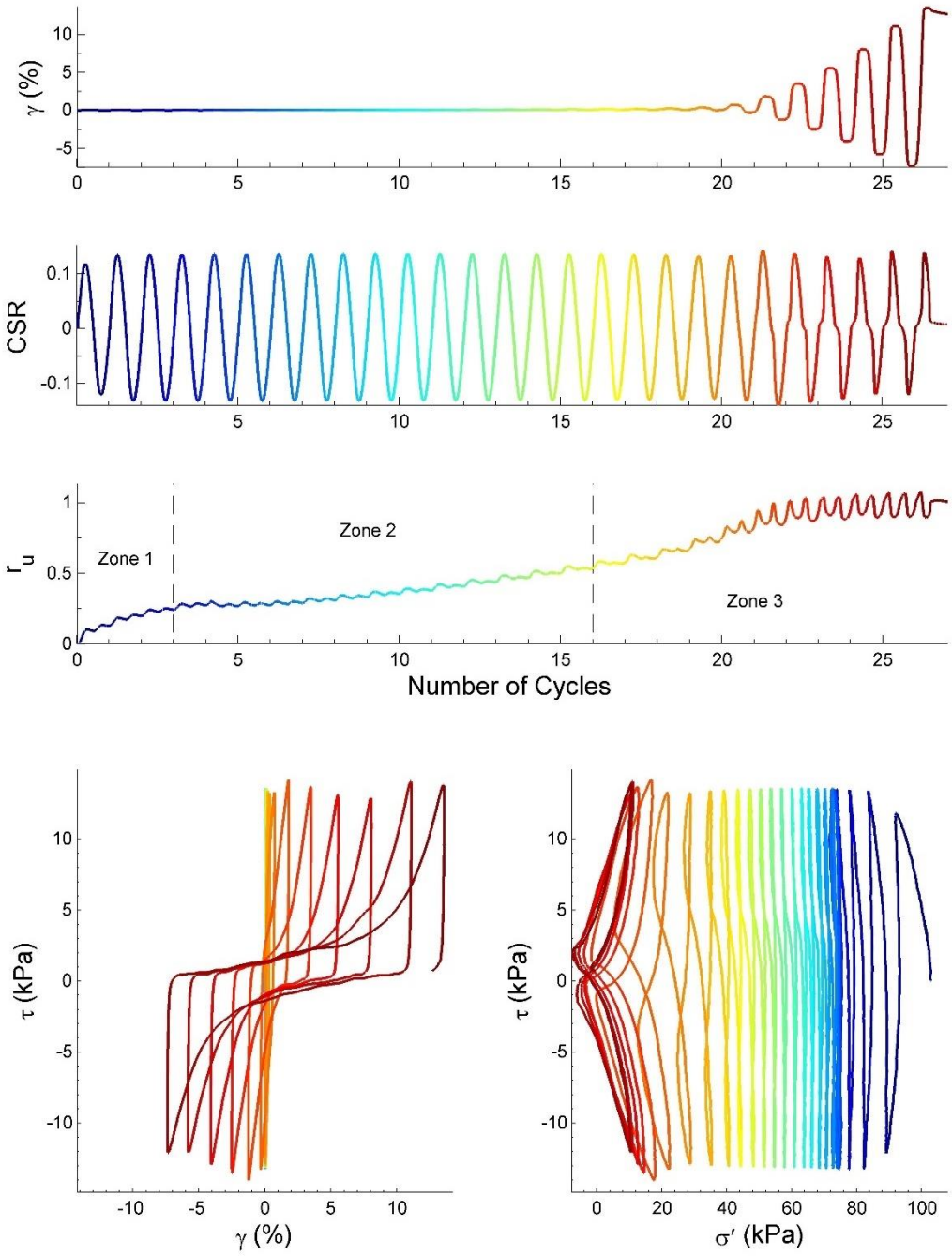


Figure 6.8: Constant amplitude harmonic loading test summary plot for a sample at a relative density of 51% with an applied CSR of 0.14 where liquefaction was observed after 21 cycles.Plots are provided for the shear strain, shear stress, and r_u time histories, and plots of the stress path and stress-strain response. The lines are colored with respect to time to allow for comparison between the time histories and the stress path and stress-strain plots.

In summary, while uniform harmonic tests are overly simplified representations of actual cyclic earthquake loads, the uniform harmonic tests performed as part of this study and reviewed in literature provided valuable insights into what aspects of a loading history do and don't contribute to the generation of excess pore pressure and the initiation of liquefaction. Observations based on constant amplitude harmonic testing include:

- Excess pore pressure generation is related to the amplitude and duration of the applied load,
- The generation of excess pore pressure is insensitive to the frequency of the applied load,
- The generation of excess pore pressure is dependent on the stress history. Generally, cycles applied earlier in a test generate more pore pressure than later arriving cycles; however, as the excess pore pressure increases phase transformation behavior can lead to a rapid increase in excess pore during later arriving cycles.

6.3.2 *Irregular Harmonic Loading*

The irregular harmonic loading tests involved applying a constant amplitude harmonic load with a single large amplitude stress cycle superimposed at various locations in the constant amplitude harmonic loading history. Soil samples with relative densities between 50 and 70 percent were consolidated to an effective stress of 100 kPa and subjected to a constant amplitude harmonic load with a CSR of 0.075 for 10 cycles at 1 Hz. A single, 0.15 CSR cycle, was applied to the sample during the 2^{nd}, 4^{th}, 6^{th}, 8^{th}, and 10^{th} loading cycles for Tests A through E, respectively. The test results are provided in Figure 6.9, and show the time histories of CSR, shear strain, and excess pore pressure ratio, r_u, for each test. Note that these tests were performed very early in the CSS testing program, before all of the modifications to the CSS apparatus had been made and the sample preparation procedures had been finalized (Section 6.2.2), which complicated the interpretation of the results, particularly with respect to relative density. However, these tests still provided valuable insights on the response of a liquefiable soil to a simple transient loading history.

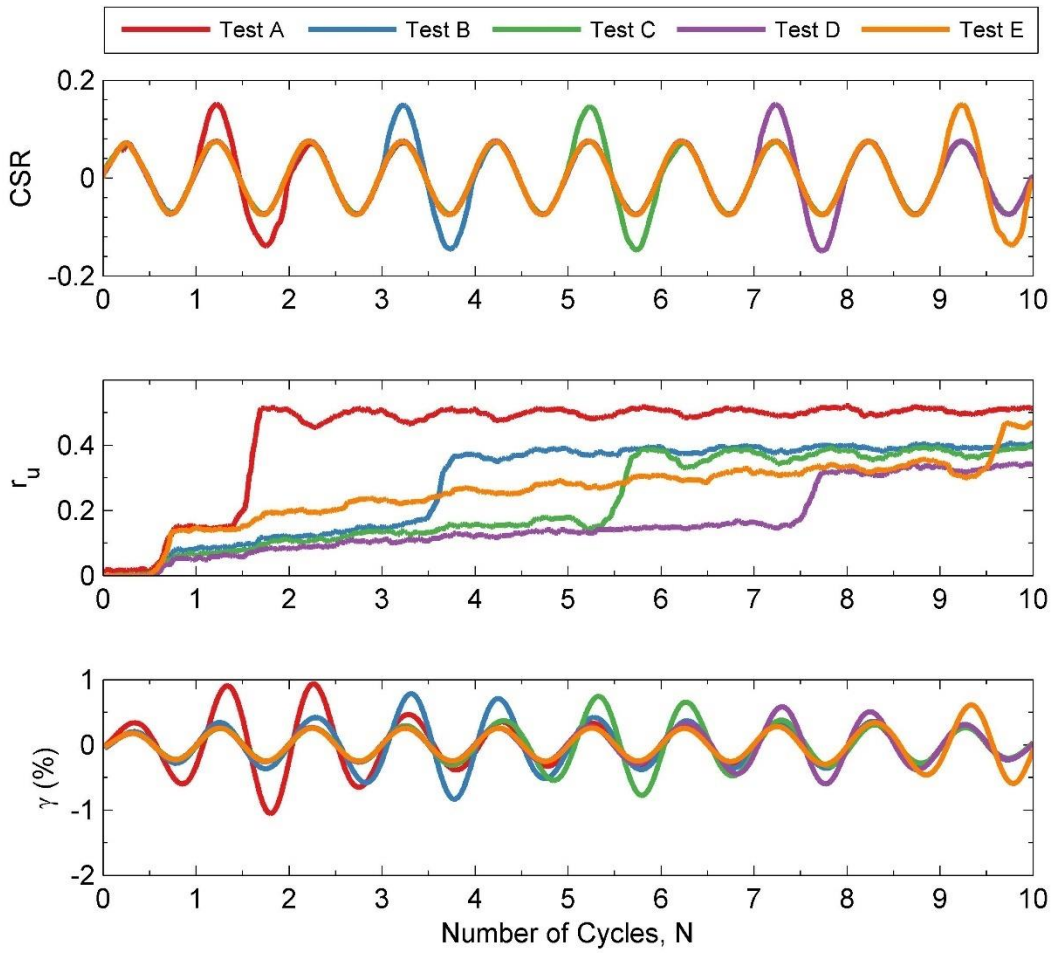


Figure 6.9: Irregular harmonic loading test summaryshowing the applied CSR, r_u, and shear strain time histories.

Note that if all the samples were at the same relative density and had the same initial soil fabric, the first loading cycle, which was the same for all of the tests, should have produced an identical pore pressure response. In addition, within the stress-based liquefaction framework all the irregular harmonic tests shown in Figure 6.9 were subjected to the same total loading intensity since the number of stress cycles at a particular amplitude were identical for each test (nine cycles at a CSR of 0.075 and one cycle at a CSR of 0.15). Therefore, the stress-based procedure would indicate that the final r_u value for each test should be the same; however, as shown in Figure 6.9 this was not the case. The relative density of the test samples shown in Figure 6.9 were between 50 to 70%. To investigate the effect of relative density, both the final r_u value, and the r_u value following the first loading cycle (which were identical for each test) was plotted as a function of relative density, shown in Figure 6.10. Both the final r_u value and the r_u

value after the first loading cycle, r_{u1}, showed a strong relationship with relative density and both measures of r_u decreased as the relative density increased. This finding was consistent with the anticipated response. Therefore, the difference in the r_u response was judged to be primarily due to differences in the density and the initial fabric of the soil, as opposed to differences in the loading history. A power function was determined to provide the best fit to the observed response, and the fitted relationship for both r_u metrics are provided in Figure 6.10.

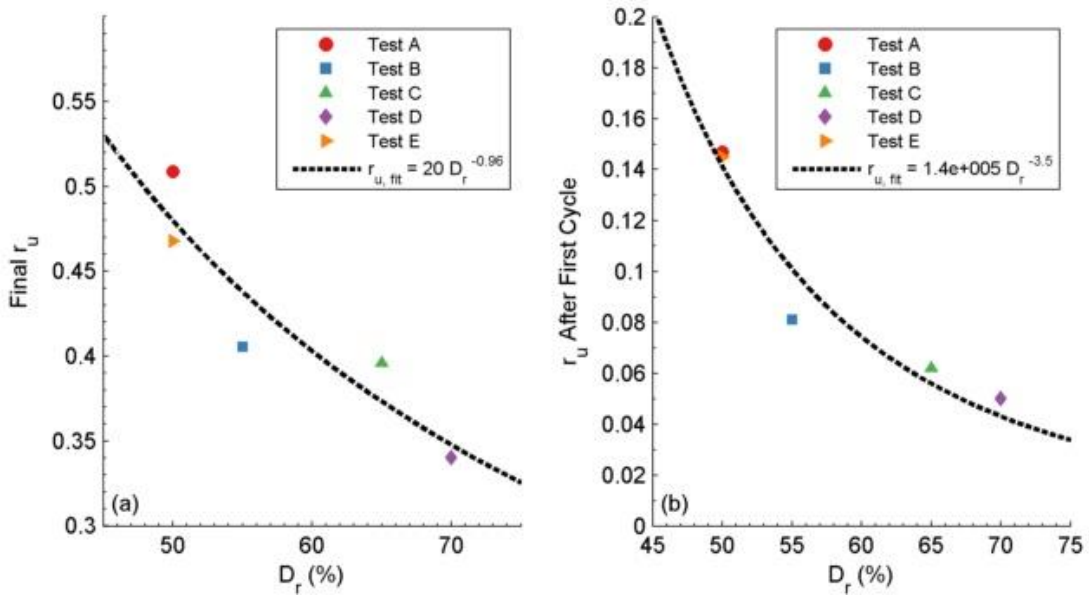


Figure 6.10: Final r_u value (a) and r_u value following the first cycle (b) as a function of relative density from the irregular harmonic loading tests.

While the relationships of the final r_u and r_{u1} both decreased as the relative density increased, the relationship with r_{u1} was very steep with respect to relative density as indicated by the exponent on the power function. As stated previously, these tests were performed early in the testing program when the sample preparations were still being finalized. The response to the first cycle of load is highly sensitive to the initial fabric and uniformity of the sample. The final r_u value includes the response after the initial fabric has been degraded and is likely more representative of the average relative density of the sample. While the differences in the r_u response was likely due to relative density, objectively correcting for this effect was not possible. However, the general behavior of these tests still provided valuable insight and the r_u response of the tests show some interesting trends. As expected, large increases in r_u are associated with the large amplitude pulse. However, cycles that followed the large amplitude pulse did not

contribute to the excess pore pressure response at all. Figure 6.11, shows a summary of the irregular sine data, and includes plots of the applied CSR loading history, the r_u response, and the Δr_u as a function of the number of applied stress cycles. Note that the scatter plot of Δr_u includes a slight offset in the N values for each test to avoid over-plotting the data.

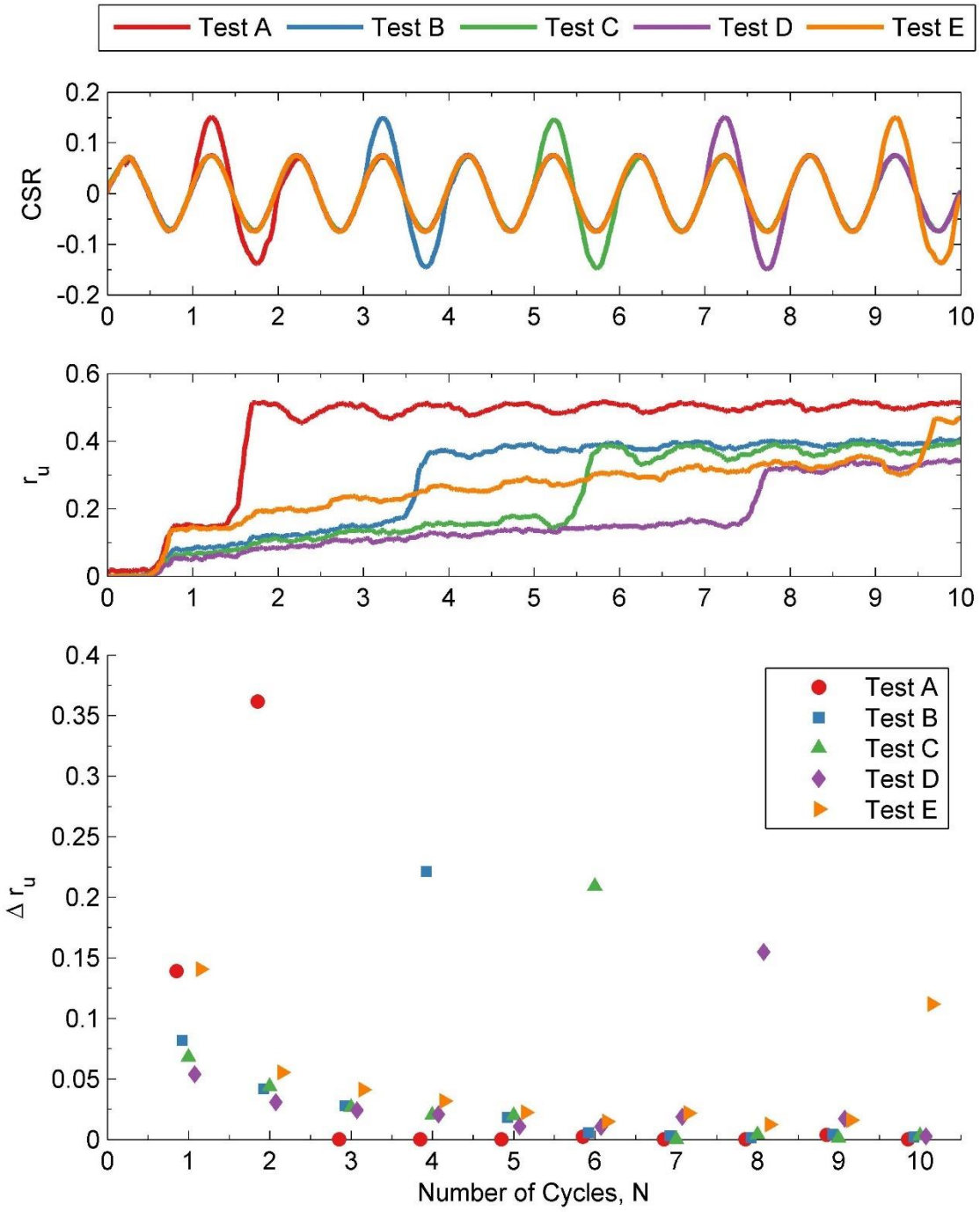


Figure 6.11: Summary of irregular harmonic tests corrected for relative density.The figure includes plots of CSR, r_u, and the change in r_u as a function of the number of applied loading cycles.

For Tests B, C, D, and E, where the arrival of the large amplitude cycle occurred during the 4th cycle or later, the general response of the samples to the initial three uniform loading cycles were identical to the observations presented in Section 6.3.2. The initial uniform cycle generated a high excess pore pressure increment. The incremental increase in excess pore pressure for subsequent cycles decreased as the number of applied stress cycles increased. Note that since the final r_u values in these tests were low, generally below 0.5, the test results were not influenced by phase transformation behavior. Another observation from the results shown in Figure 6.11 is that the amount of excess pore pressure generated by single large amplitude stress cycle tended to decrease as the number of preceding low amplitude loading cycles increased. This is consistent with the observations from the constant amplitude tests and provides further evidence that the cumulative loading history and soil fabric are important factors for determining the increment of excess pore pressure that is generated by a given loading cycle.

In addition to the cumulative loading history, the irregular harmonic test results suggested that the amplitude of a given cycle relative to the maximum amplitude of the preceding cycles was an important factor that influenced the excess pore pressure response for a given cycle of loading. For example, in Test A where the 0.15 amplitude CSR loading was applied during the second cycle, the single large amplitude cycle generated a significant amount of excess pore pressure. In addition, all the lower amplitude cycles that followed the large amplitude cycle did not contribute at all to the excess pore pressure response of the sample. The observation that a preceding large amplitude cycle decreased the excess pore pressure contribution of the following smaller amplitude cycles was consistent for Tests B, C, and D as well.

The observations from the irregular harmonic load tests agreed with the general observations made for the uniform harmonic tests. From the irregular harmonic tests, an additional observation was made with respect to the relationship between the loading history and the generation of excess pore pressure:

- The generation of excess pore pressure is related to the peak shear stress the soil has been subjected to. If the soil has experienced a large amplitude stress cycle, subsequent stress cycles of lower amplitude generate less excess pore pressures than would be expected had that larger stress cycle not been applied.

The hypothesis that the generation of excess pore pressure is sensitive to the prior peak stress (and will be shown later, acceleration) amplitude is explored extensively in this document. For the purpose of future discussions, the peak loading amplitude that the soil has been subjected to is referred to as the prior peak amplitude, or PPA. This hypothesis is conceptually similar to the consolidation settlement framework for fine-grained soils, where PPA is analogous to preconsolidation pressure. Additional shear loading that is less than the PPA was observed to generate relatively little excess pore pressure, while shear loading greater than the PPA was observed to generate relatively large amounts of excess pore pressure.

6.3.3 *Modulated Harmonic Loading*

To further investigate the observations made in Sections 6.3.1 and 6.3.2, tests using modulated harmonic loading histories were performed. The loading histories in the modulated harmonic loading test program were generated using a baseline uniform harmonic time history consisting of 20 cycles applied at 0.2 Hz. The amplitude of the baseline time history was then modified by an enveloping function to create loading histories that gradually increased or decreased in amplitude as a function of time. Two types of enveloping functions were used to generate motions with amplitudes that either tapered up or tapered down as the number of loading cycles increased. The enveloping function for the taper up motions was of the form,

$$f(t) = \left(\frac{t}{N \cdot T}\right)^n \leq 1.0 \qquad (6.1)$$

where f(t) is the enveloping function, t is time, N is the number of cycles to modify, T is the period of the harmonic motion, and n is a scaling factor that was varied from 0.1 to 10 to produce motions that tapered up at different rates. This process is illustrated in Figure 6.12 for a taper-up motion with an enveloping function applied to the first 10 cycles. Figure 6.12a, b, and c show the baseline uniform harmonic motion, the enveloping function with n = 0.4, N = 10 cycles, and T = 5 seconds, and the resulting modulated harmonic loading history computed as the product of (a) and (b), respectively.

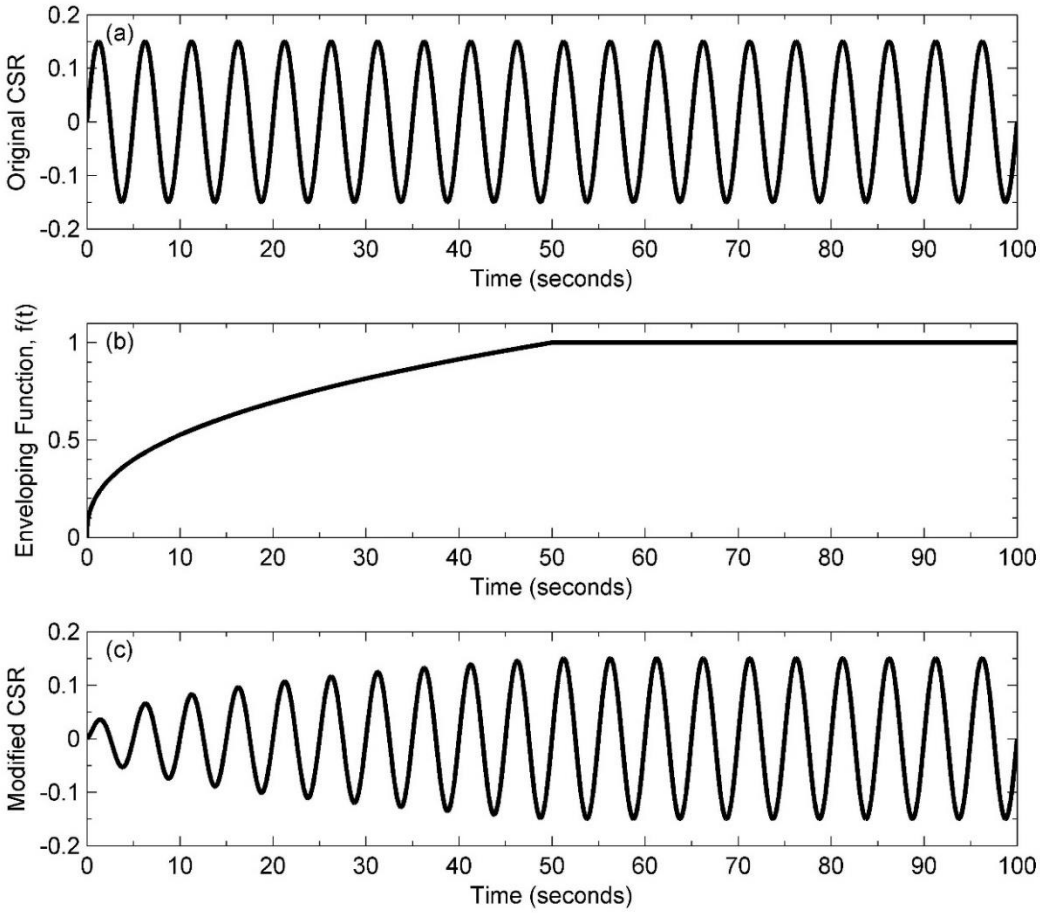


Figure 6.12: Development of a taper-up modulated harmonic loading.(a) the baseline harmonic loading history, (b) the enveloping function computed using n=0.4, N=10 cycles, and T=5 seconds, and (c) the resulting modulated harmonic CSR loading history computed as the product of (a) and (b).

To create the taper-down motions, Equation 6.1 was modified as follows

$$f(t) = \left(\frac{N_{max} \cdot T - t}{N \cdot T}\right)^n \leq 1.0 \tag{6.2}$$

where N_{max} is the total number of cycles in the baseline time history, which was equal to 20 cycles for all the modulated time histories used in this study. An example of the development of the taper-down input time histories is shown in Figure 6.13, using the same input properties as shown in Figure 6.12 to allow for comparison between the taper-up and taper-down motions. As shown in Figure 6.13, the taper-down motions were identical to the taper-up motions but with the order of the cycle amplitudes reversed in time.

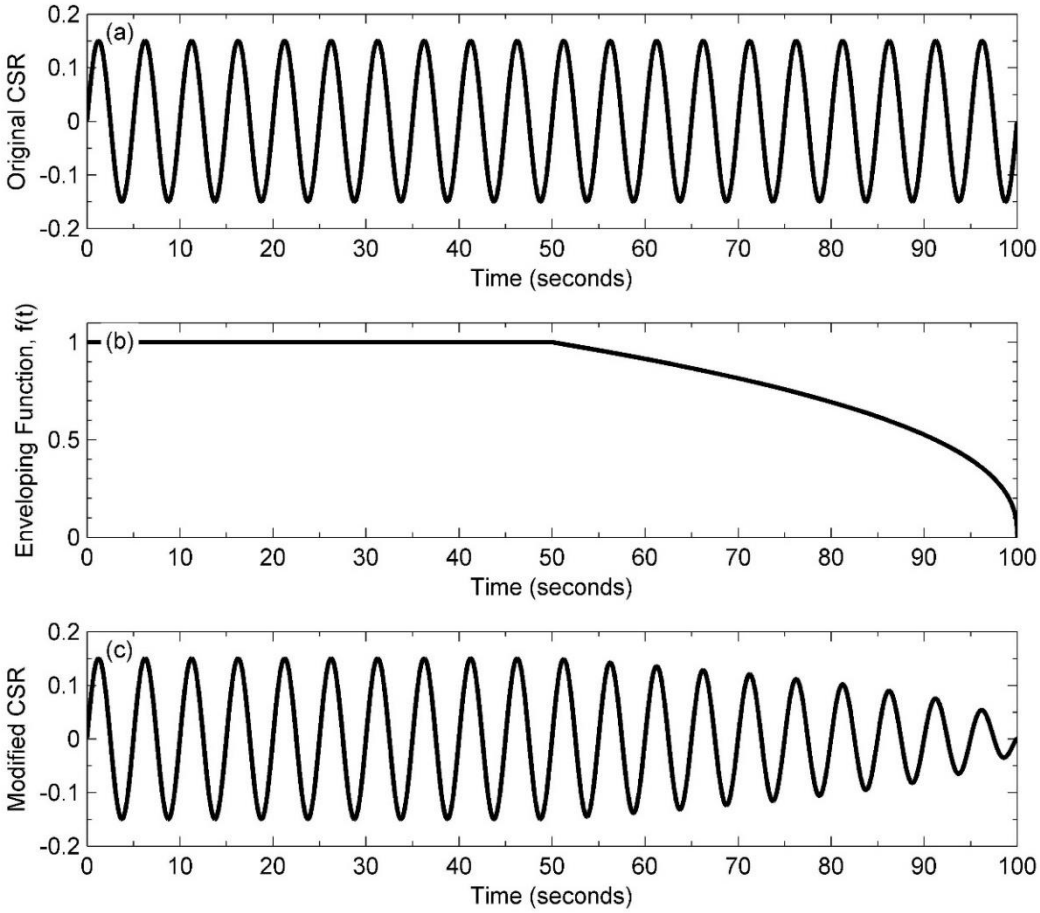


Figure 6.13: Development of a taper-down modulated harmonic loading.(a) the baseline harmonic loading history; (b) the enveloping function computed using n=0.4, N=10 cycles, T=5 seconds, and N_{max}=20 cycles; and (c) the resulting modulated harmonic CSR loading history computed as the product of (a) and (b).

In the present study 9 taper-up and 9 taper-down motions were constructed using n values of 0.1, 0.2, 0.4, 0.67, 1, 1.5, 2.5, 5, and 10. The enveloping functions modified the first and last 10 cycles of the baseline harmonic motion for the taper-up and taper-down motions, respectively. Figure 6.14 provides a summary of the enveloping functions and resulting modulated harmonic loading histories for both the taper-up and taper-down functions. As shown in the enveloping functions provided in Figure 6.14a and b, for the taper-up and taper-down motions, respectively, as the exponent n in the enveloping function was increased, the slope of the enveloping function increased, and the amplitude of the loading history changed at a faster rate.

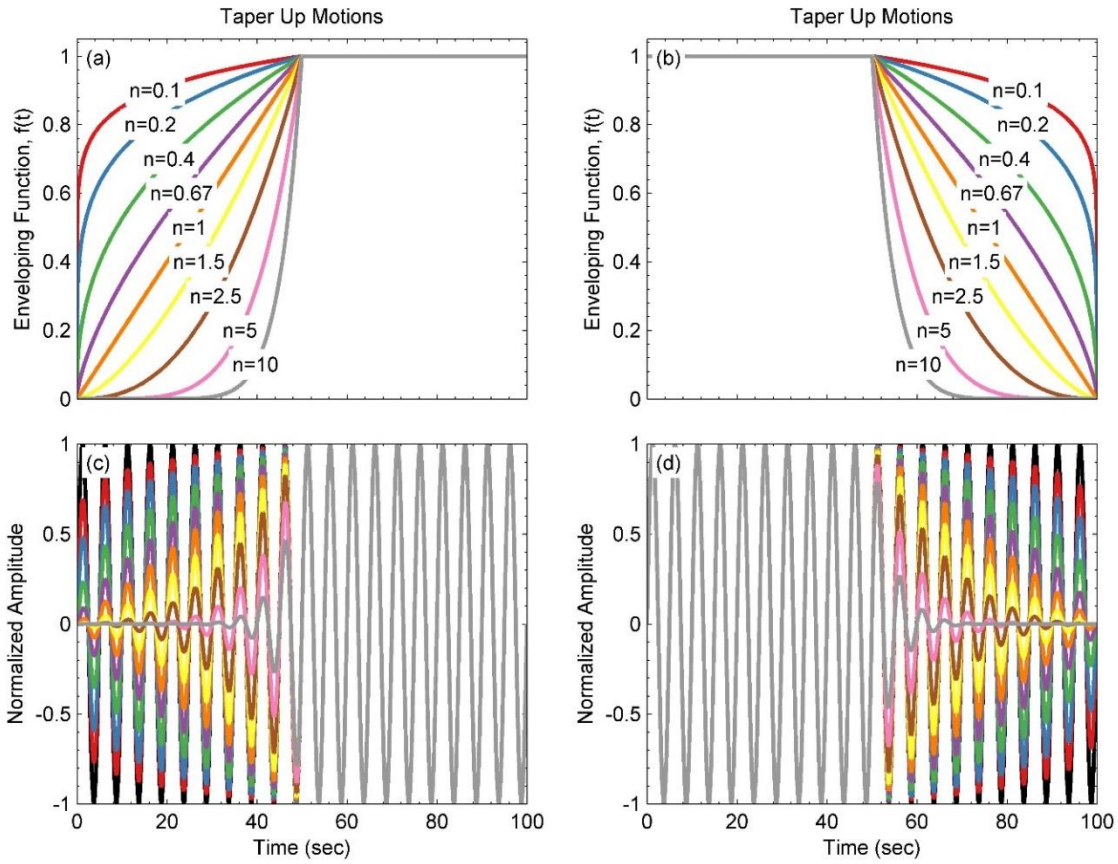


Figure 6.14: Enveloping functions and normalized loading input time histories for the taper-up and taper-down modulated harmonic loading histories.The enveloping functions and normalized harmonic loading histories are provided in (a) and (c) for the taper-up modulated sine functions, and (b) and (d) for the taper-down modulated sine functions, respectively. The exponent, n, in the taper function is provided in plots (a) and (b).

A total of 27 tests were performed using the modulated harmonic motions described above on samples consolidated to a common vertical effective stress of 100 kPa. The 27 tests were divided into three general groups as follows:

- Taper-up motions on loose sand samples (9 tests),
- Taper-down motions on loose sand samples (9 tests), and
- Taper-up motions on dense sand samples (9 tests).

Each of these three test groups are discussed individually in the following sections.

6.3.3.1 Taper-up Motions on Loose Sand Samples

The taper-up motions were applied to loose sand samples with relative densities that ranged from 39 to 50%. The loading histories were developed from a baseline uniform harmonic motion with

an amplitude of 0.15 CSR. The results of each test are summarized in Figure 6.15, which show the CSR, r_u, and shear strain versus the number of cycles for each test. The response of the tests with respect to the final r_u value were somewhat inconsistent, as observed when comparing the response of Test 2013-0527 (red) and Test 2013-0531 (blue). The relative densities and loading histories between the two tests were very similar, however the pore pressure response was dramatically different. Test 2013-0527 had a relative density of 54%, a modulation exponent, n, of 0.1, and reached a peak r_u value of 1.0. Test 2013-0531 had a relative density of 56% and n value of 0.2, but only reached a peak r_u value of approximately 0.55. The reason for this discrepancy is unknown. Kwan (2015) hypothesized that there could be a critical rate of ascent that maximizes the pore pressure response of a sample. Alternatively, the differences could be due to nonhomogeneous sample preparation or sensor malfunction.

Some interesting trends in the load excess pore pressure were observed in Figure 6.15. Except for Test 2013-0531 the rate of pore pressure generation generally matched the rate of which the load amplitude increased. As the load tapered-up, the PPA was exceeded in each cycle, and excess pore pressures were generated at a rate that corresponded to the exceedance of the PPA. This was especially apparent for Tests 2013-0528, 2013-0603, 2013-0618, 2013-0619-02, and 2013-0621, which had relative densities between 47 and 52%. Each of these tests reached peak r_u value between 0.4 and 0.6. In the first 10 cycles, during the taper-up portion of the loading history, the rate of increase in both excess pore pressure and loading were relatively consistent. After 10 cycles, when the load was constant, and the loading cycles were approximately equal to the PPA, the rate of excess pore pressure generation tended to decrease even though the cycle amplitudes were higher than the cycles applied during the taper-up portion of the loading history.

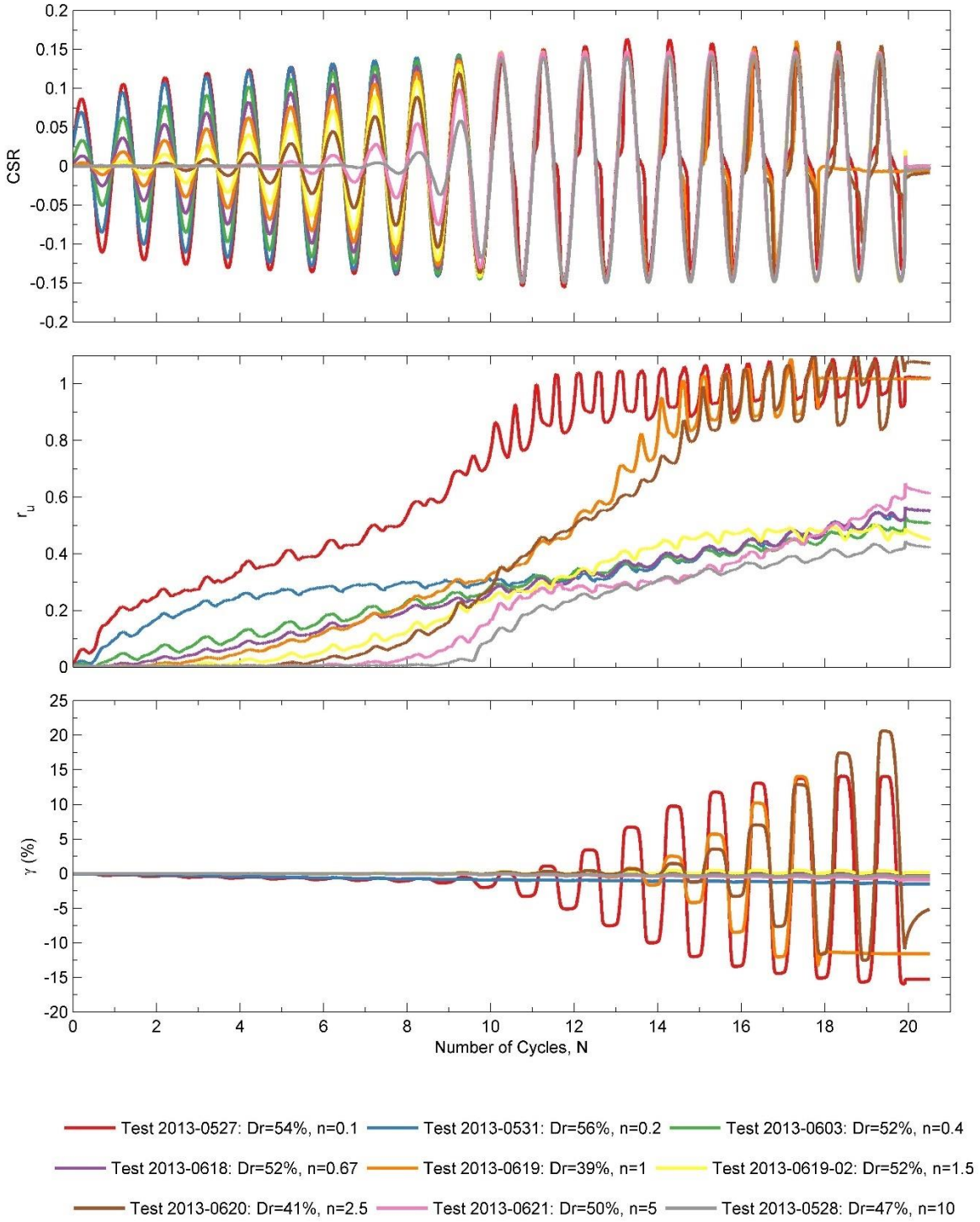


Figure 6.15: Summary of test results for the taper-up modulated harmonic loading performed on loose sand samples.The results for all 9 tests are presented with respect to the CSR, r_u, and shear strain time histories.

The two tests with the lowest relative densities, Tests 2013-0619 (D_r = 39%) and 2013-0620 (D_r = 42%) both liquefied. The results for Test 2013-0619 are examined further in Figure 6.16. The sample was prepared at a relative density of 39% and subjected to a taper-up modulated harmonic load using an n value of 1.0, which produced a linear taper-up response. The initial 2.5 cycles of loading induced negligible amounts of excess pore pressure, shown as the blue portion of the lines provided in Figure 6.16. The amplitudes of these cycles had a CSR less than 0.05 and induced shear strains of approximately 0.005%, which were below the threshold shear strain to induce pore pressure generation identified by Dobry and Abdoun (2015) as 0.01%. As the loading exceeded a CSR of 0.05, and the cyclic strains increased, the pore pressure began to increase. The rate of increase was close to linear through the taper-up portion of the loading (through cycle 10), as well as the first two cycles of harmonic loading (cycles 11 and 12). After cycle 12 (as the line color in Figure 6.16 begins to transition from yellow to orange) phase transformation behavior was observed in the stress path plot and the pore pressures increased rapidly.

Referring back to the constant amplitude harmonic tests and Figure 6.7, this test did not exhibit the behavior described by Zone 2, where the rate of excess pore pressure generation momentarily decreased under constant amplitude loading. During the taper-up portion of the record, the amplitude of each loading cycle was the maximum amplitude the sample had been subjected to (i.e. the PPA was successively exceeded with each stress cycle), therefore the soil fabric continued to degrade, and excess pore pressures were generated at an approximately linear rate. After the loading reached the constant amplitude phase, the excess pore pressure was large enough that the stress path crossed the phase transformation line and the pore pressure rapidly increased. Conceptually it is logical that the relationship between the generation of excess pore pressure and the PPA would break down during phase transformation behavior when the changes in soil fabric and the generation of pore pressure are related to both the applied loading history and the stress state of the soil as opposed to the loading history alone. This observation will be investigated further in subsequent discussions.

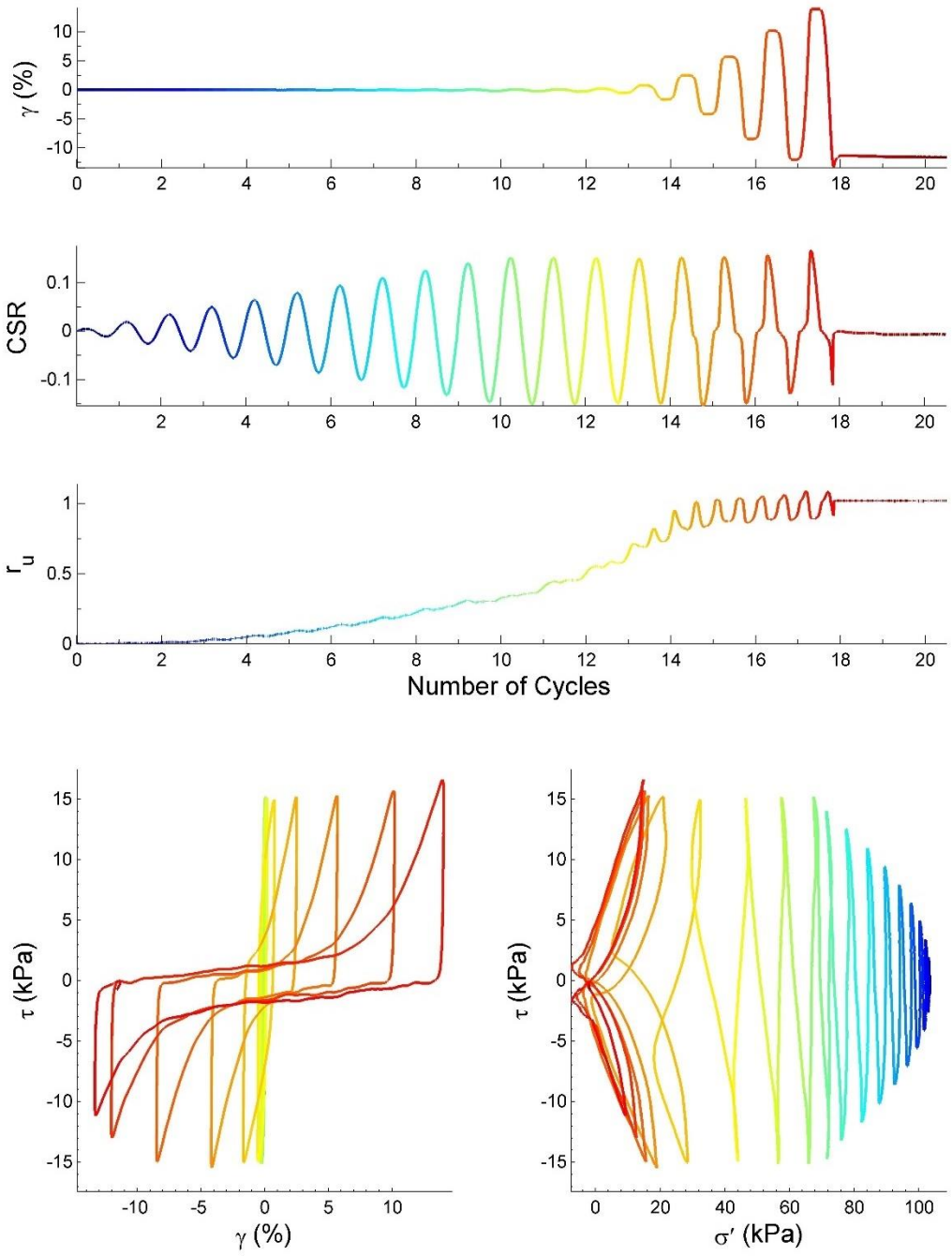


Figure 6.16: Taper-up modulated harmonic test result for Test 2013-0619.The sample had an initial relative density of 39% and the exponent of the modulation function, n, was equal to 1.0. Plots are provided for the shear strain, shear stress, and r_u time histories, and plots of the stress path and stress-strain response. The lines are colored with respect to time to allow for comparison between the time histories and the stress path and stress-strain plots.

6.3.3.2 Taper-down Motions on Loose Samples

The taper-down motions were applied to loose sand samples ranging in relative density from 33 to 53% using a loading history based on a harmonic load with a peak CSR of 0.15. The results of each test are summarized in Figure 6.17. In general, the tests with relative densities below 40% reached a peak r_u of 1.0 within the first 10 cycles, where the loading history was constant amplitude, while tests with relative densities above 40% did not. The one exception being Test 2013-0717 which had a relative density of 43% and was observed to reach an r_u of 1.0 at about 8 cycles of loading. The CSR-N_{liq} relationship provided in Figure 6.5 shows that the fitted relationship for the loose samples the CSR required to induce liquefaction after 10 cycles of loading would be approximately 0.17. However, given the scatter in the fitted values these results were considered to be consistent with the results from the uniform harmonic tests.

The tests that did not liquefy during the uniform amplitude portion of the loading history included Tests 2013-0718-02, 2013-0719, and 2013-0724. For these tests the taper-down portion of the record generally did not contribute at all to the excess pore pressure generated during the test. This observation was consistent with the irregular harmonic test results, where cycles with amplitudes less than the PPA produced very little to no excess pore pressure.

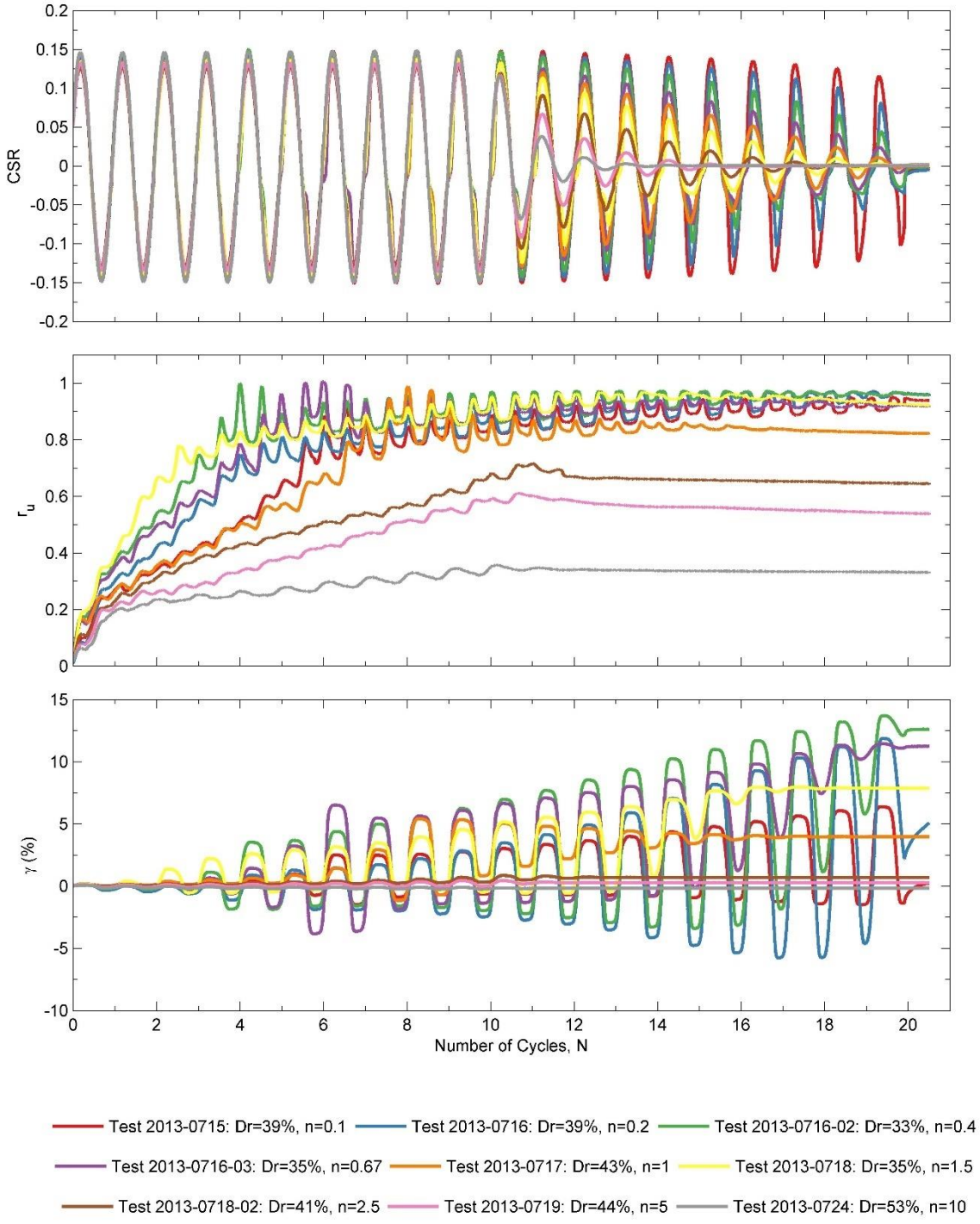


Figure 6.17: Summary of test results for the taper-down modulated harmonic loading performed on loose sand samples.The results for all 9 tests are presented with respect to the CSR, r_u, and shear strain time histories.

6.3.3.3 Taper-up Motions on Dense Samples

The taper-up motions with the same shapes as those applied to the loose sand samples were also applied to dense sand samples. The relative densities of the dense sand samples ranged from 72 to 94% and the amplitude of the baseline harmonic load corresponded to a CSR of 0.25. The results of all nine taper-up motions on dense sand samples are summarized in Figure 6.18. As with the taper-up motions on the loose sand samples, as the load amplitude increased during the first 10 cycles, and the PPA was exceeded with each subsequent cycle, the excess pore pressures increased at a similar rate that as the load amplitude. Tests with modulation exponent, n, below 1.0 (concave down enveloping function) generated large pore pressures during the initial loading cycles, but the rate of excess pore pressure generation tended to decrease with each subsequent cycle as the ratio between the load amplitude and the PPA decreased. Tests with n values greater than 1.0 (concave up enveloping function) generated less pore pressure during the initial cycles, but the rate of excess pore pressure increased rapidly as the ratio between the load amplitude and the PPA became increased.

Interestingly, the test with an n value of 0.1, Test 2013-0731, generated excess pore pressures at a significantly faster rate than was observed for the Tests 2013-0802 and 2013-0802-02 which had n values of 0.2 and 0.4, respectively. This observation was consistent with the behavior from the modulated harmonic tests performed on the loose sand samples. However, for the dense set of experiments Test 2013-0731 (n=0.1) had a relative density of 76% which was significantly lower than the relative densities for Tests 2013-0802 (D_r = 94%) and 2013-0802-02 (D_r = 89%). Therefore, the difference in response was likely more influenced by the differences in the relative densities as opposed to the slight differences in the loading histories.

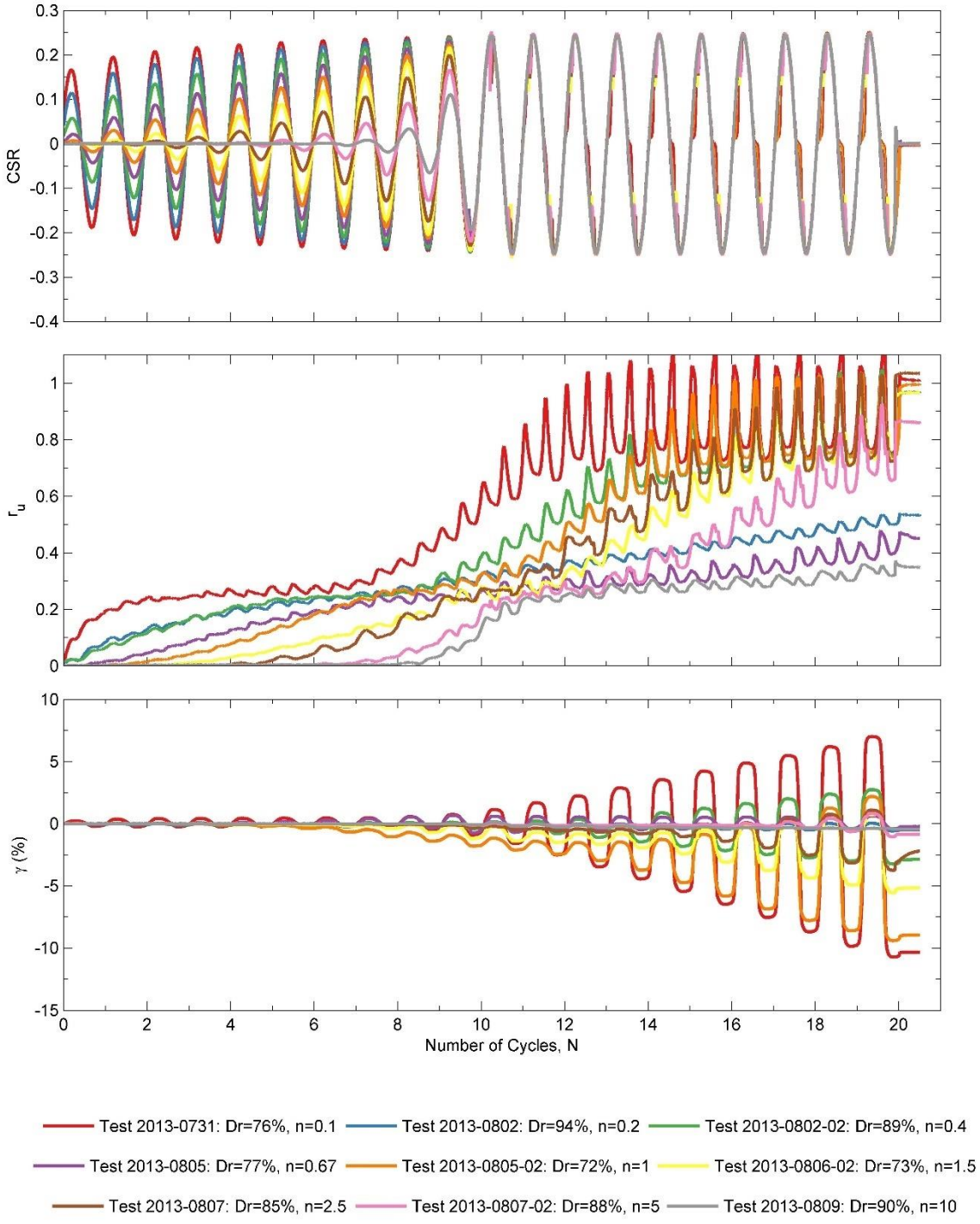


Figure 6.18: Summary of test results for the taper-up modulated harmonic loading performed on dense sand samples.The results for all 9 tests are presented with respect to the CSR, r_u, and shear strain time histories.

6.3.3.4 Discussion of Modulated Harmonic Results

Modulated harmonic tests that included both taper-up and taper-down loading histories were applied to loose and dense sand samples to investigate how the phasing of the loading history and the relative amplitudes of the applied stress cycles affected the generation of excess pore pressure. These tests confirmed the observation from the irregular harmonic loading that prior to phase transformation, the generation of excess pore pressure is very sensitive to the phasing and relative amplitude of a stress cycle. Large increments of excess pore pressure were generated when the loading cycle was significantly greater than the PPA and cycles with amplitudes less than the PPA were observed to generate relatively little excess pore pressure.

To illustrate this, the results of a taper-up (Test 2013-0621, D_r = 50%) and a taper-down test (Test 2013-0719, D_r = 44%) performed on loose sand samples that use the same modulation parameter, n = 5.0, are shown in Figure 6.19. The relative densities of both tests were relatively similar, as was the final r_u value generated by each test. Figure 6.19 shows plots of the CSR, r_u, and change in r_u, Δr_u, histories versus the number of cycles. The Δr_u was computed as the change in r_u between zero crossings and correspond to a half cycle of applied load. For the taper-down test, the first 10 cycles of load were of uniform amplitude and the soil responded similarly to the constant amplitude tests discussed in Section 6.3.1. The first cycle of load generated a large amount of excess pore pressure and the Δr_u for the following load cycles was relatively constant. After the 10th cycle, as the loading amplitude decreased, the Δr_u generated by each cycle descreased significantly. After cycle 12, which had a CSR amplitude of about 0.05, or 33% of the peak amplitude, Δr_u was essentially zero.

For the taper-up test the first two loading cycles which were of very low amplitude and produced essentially zero excess pore pressure. The peak strain during this portion of the test was 0.008%, which was less than the threshold shear strain identified by Dobry and Abdoun (2015). As the loading increased the sample began to generate excess pore pressure. During the taper-up portion of the test, i.e. the first six cycles of loading, the rate of excess pore pressure generation roughly matched the rate at which the cycle stress amplitudes increased. During the constant amplitude portion of the test the rate of pore pressure generation initially decreased between cycles six and 11. Due to phase transformation behavior, however, the rate of pore pressure generation began to increase following cycle 11. Note that at cycle 4, which had a CSR amplitude of about 0.05, Δr_u was greater than zero. Cycle-12 in the taper down test had an

equivalent amplitude, but generated no excess pore pressure. The difference between the two cycles was that the relative amplitude for Cycle 4 for the taper-up test exceeded the PPA, where as the relative amplitude of Cycle 12 in the taper-down test was significantly lower than the PPA. This shielding effect, where a larger amplitude stress cycle dimishes the amount of excess pore pressure generated by subsequent lower amplitude peaks, was consistent with the observations from the irregular harmonic tests.

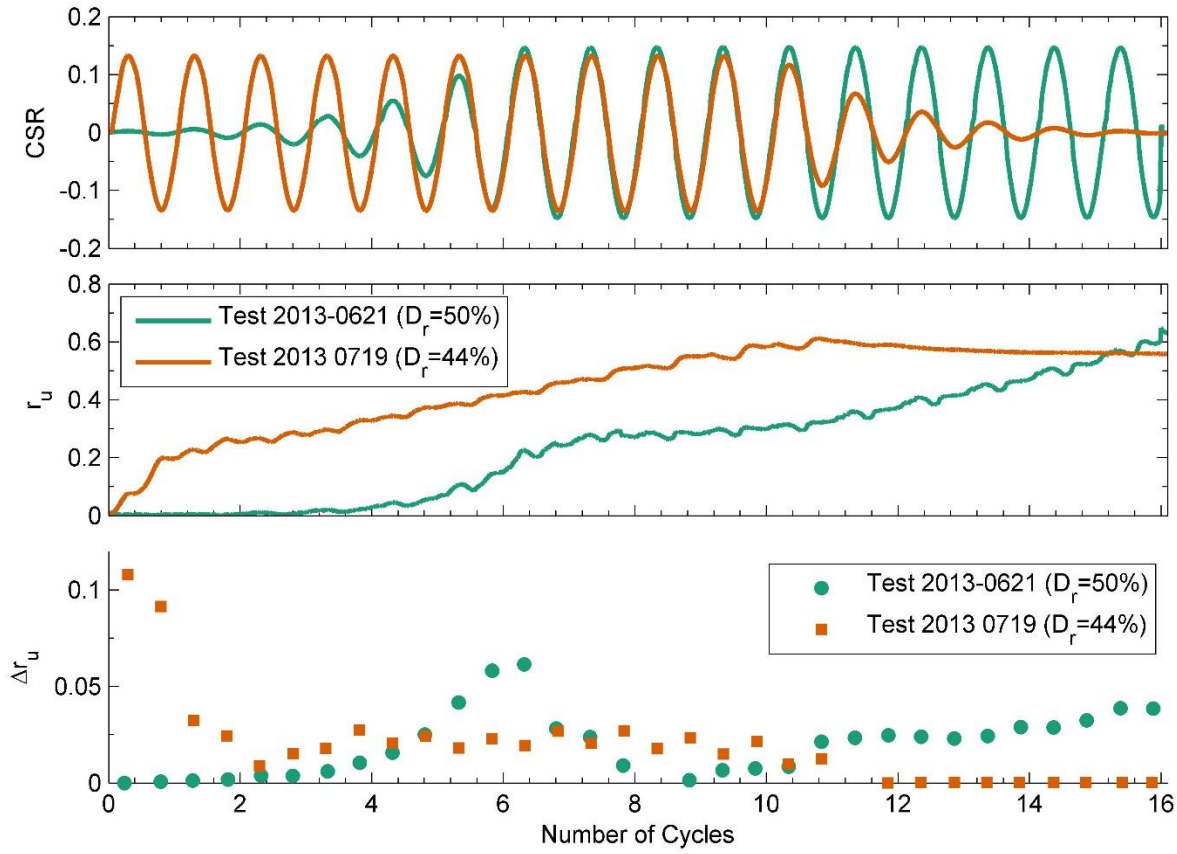


Figure 6.19: Comparison of taper-up and taper-down Tests 2013-0621 and 2013-0719 on loose sand samples.The modulation functions both used an n value of 5.0.

6.3.4 *Discussion*

The harmonic CSS test program was performed to validate the sample preparation and testing apparatus and to use simple test results to attempt to identify what aspects of a transient loading history are best correlated with the generation of excess pore pressure. The results of the constant amplitude harmonic tests were summarized by liquefaction resistance curves and r_u versus cycle

ratio plots, both of which produced results that were consistent with prior studies on the response of clean sand to cyclic uniform harmonic loading.

While the loading histories were relatively simple, the tests performed using constant amplitude harmonic, irregular harmonic, and modulated harmonic loading histories provided valuable insight on the relationship between excess pore pressure and the applied loading history. Observations made during the harmonic loading test program suggested that the generation of excess pore pressure is related to

- The amplitude of the applied load.
- The duration, or number of cycles, of loading.
- The stress history, early cycles generate more excess pore pressure than later cycles of the same amplitude due to the initial degradation of the soil fabric.
- The relative amplitude or phasing of the loading. Prior to phase transformation behavior, the generation of excess pore pressure appeared to be highly dependent on the peak prior amplitude or PPA. Two critical aspects of this relationship include:
    a) Large increments of pore pressure generation are associated with shear stress pulses of amplitude that exceeds the PPA, and
    b) Shear stress pulses of amplitude lower than the PPA are shielded and generate significantly less pore pressure than if they had not been preceded by the PPA.
- The initiation of phase transformation behavior.

These themes will be revisited in subsequent discussions. The following section presents the CSS testing performed using transient loading histories.

6.4 CSS TESTS WITH TRANSIENT LOADING

The goal of the CSS testing was to identify evolutionary intensity measures that can efficiently predict the onset of liquefaction for use in the timing-based liquefaction hazard analysis framework. The previous section discussed tests that used constant amplitude, irregular, and modulated harmonic loading histories which provided important observations on the relationship between the generation of excess pore pressure and the loading history; however, actual earthquake loading is far from harmonic. To evaluate the response of liquefiable soils to transient loading, a CSS test program was performed using time histories derived from actual recorded earthquake ground motions. This section describes the input ground motions used in the transient

test program, presents the transient CSS test database, and provides details on the data processing. The analyses that were performed using the transient CSS test data are provided in Sections 6.5 and 6.6.

6.4.1 *Development of Transient Loading Histories*

Since only a finite number of tests could be conducted due to equipment issues and time and budget constraints, it was important to carefully select motions that could distinguish between the predictive capabilities of various IMs as efficiently as possible. This section describes the transient motions used in the CSS testing program.

6.4.1.1 Motion Selection

The database of Abegg (2010), described in Section 5.2, served as the primary source for the motions used in the CSS test program. This database was composed of motions selected from the PEER NGA database (Chiou et al. 2008) and were chosen based on their ability to distinguish between standard IMs, PGA_m, I_A, CAV and CAV_5 – in the same fashion as the motions that comprise the database of Abegg (2010), as illustrated in Figure 5.6. The formulations for each of these IMs were presented in Section 4.1. A detailed description of the development of the baseline ground motion database is provided in Abegg (2010). The rationale behind the selection of these five IMs was that there are defined predictive equations for each of them and all, except for CAV, have been included in prior liquefaction hazard evaluation investigations. CAV was included because the predictive equation for CAV (Campbell and Bozorgnia, 2010) indicated that the IM was relatively predictable (total uncertainty for the logarithm of the IM was 0.420, as compared to 0.526 for PGA, noting that the uncertainty for PGA does not include the additional uncertainty involved in MSF). A predictable IM has notable benefits in a probabilistic framework as discussed in Chapter 3.

Motions from the Abegg (2010) database were selected based on their IM characteristics. The selected motions behaved relatively regularly (i.e. near the average value of the dataset) with respect to one IM, but deviated from the average value with respect to a different IM, this process was illustrated previously in Figure 5.6 from Abegg (2010). Special care was taken to achieve a good balance of this average-outlier behavior for each IM combination. Figure 6.20 and Figure 6.21 show the time histories for each of the motions selected from the Abegg (2010)

database and subsequently used for CSS testing. The NGA file description is given in the upper right-hand corner for each time history. Figure 6.22 shows a scatterplot matrix between the IMs for each motion shown in Figure 6.20 and Figure 6.21. This plot shows that the selected motions featured a wide range of IM behavior.

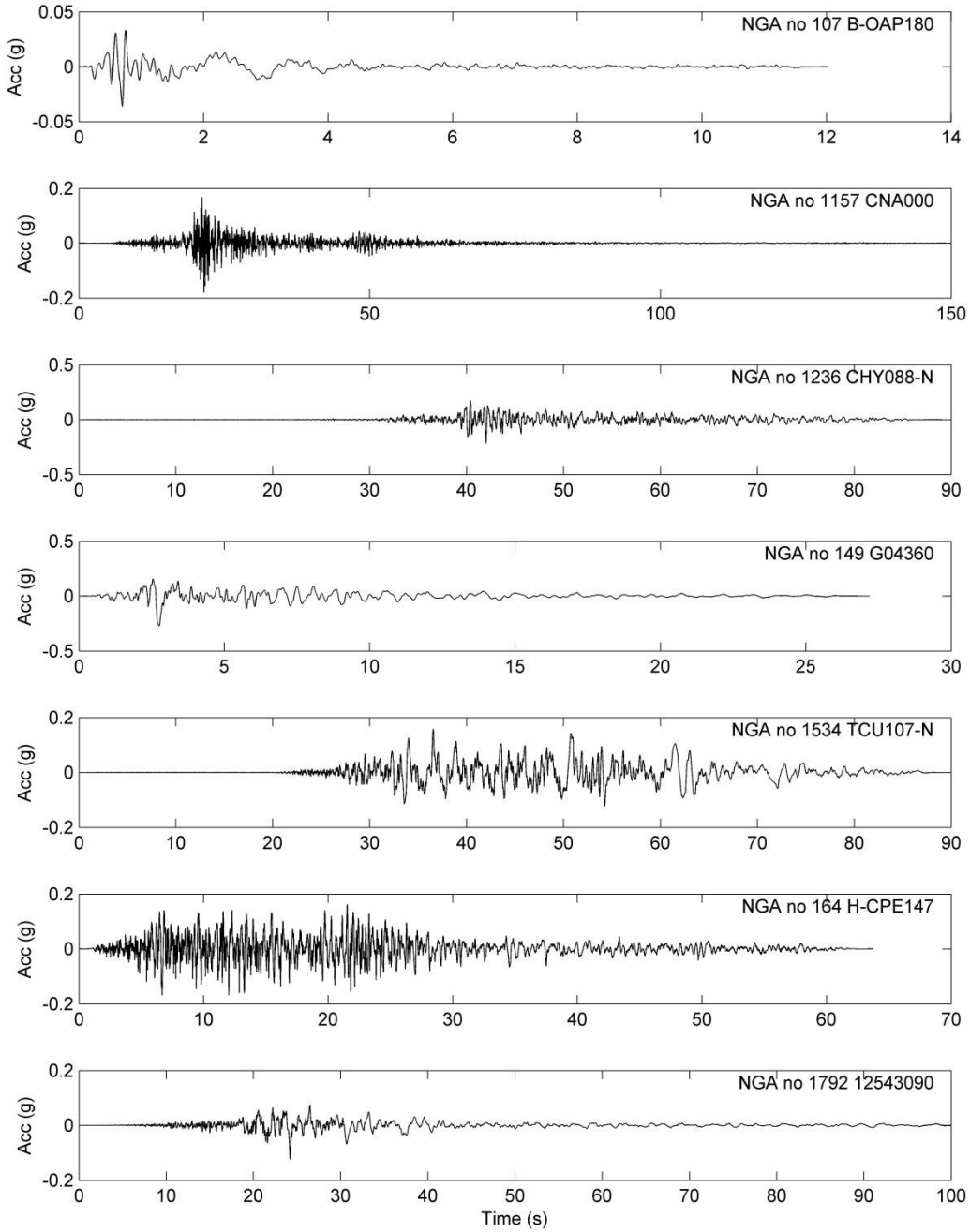


Figure 6.20: Motions selected for use in CSS testing program based on IM behavior.

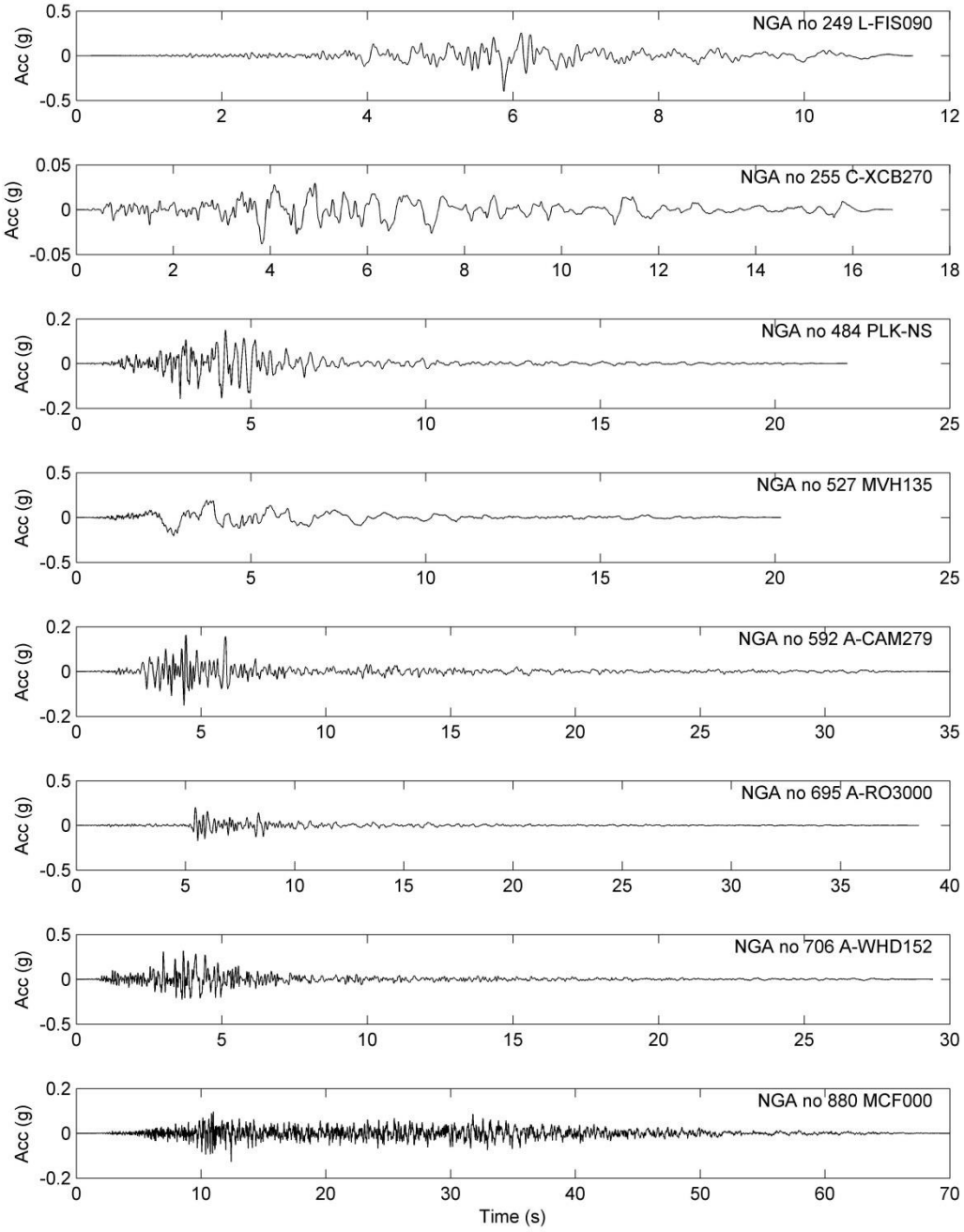


Figure 6.21: Motions selected for use in CSS testing program based on IM behavior.

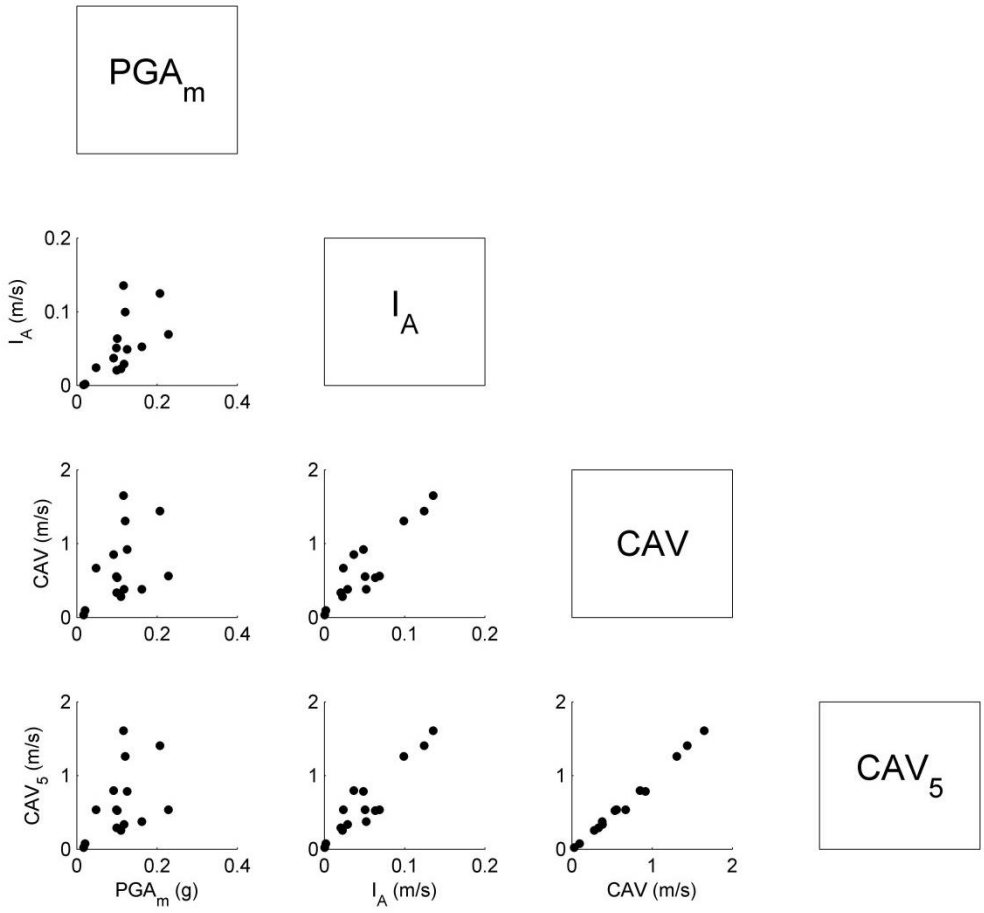


Figure 6.22: Scatterplot matrix showing the relationships of the IMs for the motions selected based on the IM behavior.

Based on observations from harmonic testing program, a number of supplementary motions were added to the testing program. As noted in Section 6.3, it was observed that not only the amplitude but the order the loading cycles were applied in appeared to impact the pore pressure generation response of the sample. Motions that featured high intial loading cycles induced a different pore pressure response than motions that featured large cycles that occured later in the record. To investigate this behavior further, motions that built up energy very rapidly and motions that built up energy very slowly were selected and included in the testing program.

To find motions that had different rates of energy buildup, the PEER NGA database was utilized. The rate of energy buildup was assessed using the Husid parameter (Husid, 1969), H, defined as,

$$H(t) = \frac{I_A(t)}{I_A(t_f)} \tag{6.3}$$

where t_f is the time at the end of the record.

To select the candidate motions, each motion in the dabase was truncated at the point at which the PGA was reached. Then plots of the Husid parameter were made using the truncated time histories for each of the motions in the database as shown in Figure 6.23a. In Figure 6.23 the time scale was normalized by the time at which the PGA of the motion was reached. Motions that featured large cycles prior to the PGA exhibited more of an increasing concave-down shape (upper curves in Figure 6.23), while motions that only featured relatively small cycles up to the PGA displayed a concave-up shape (lower curves in Figure 6.23 a and b). Figure 6.23b shows the Husid plots for motions that featured a PGA above 0.1 g. This cutoff was used to remove motions that were from very small events or were recorded from very large source to site distances and are considered to be of relatively low engineering significance. In addition, for clarity, motions where the fit between the Husid plot and a 1:1 line had a coefficient of determination greater than 0.5 were removed to produce the plot shown in Figure 6.23b.

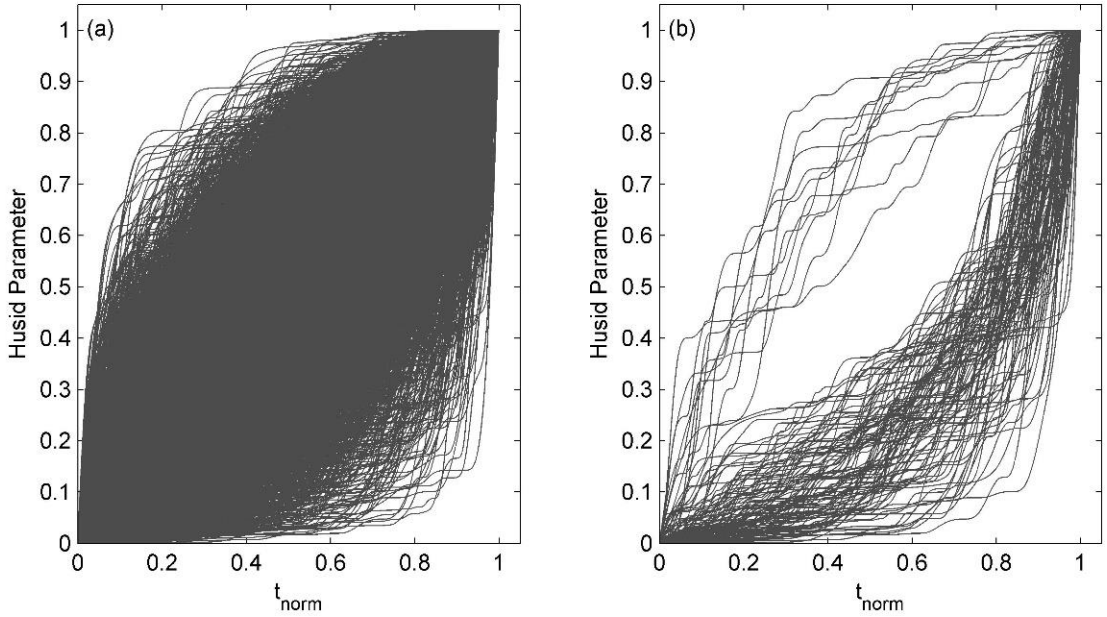


Figure 6.23: Summary plots for motions selected based on the rate of energy buildup. (a) Husid parameter for all motions in the PEER NGA database and (b) Husid parameter for all motions where the PGA was greater than 0.1 g and motions that had a coefficient of determination greater than 0.5 for a fit to a 1:1 line where removed for clarity. In both plots the Husid parameter was calculated using time histories truncated up to the PGA. The time scale has been normalized by the time at which the PGA occurs.

The time histories of the motions selected based on the rate of energy buildup are shown in Figure 6.24. These motions were selected by visually identifying the motions that featured the most concave up or concave down behavior. Following the visual identification, the time history metadata was reviewed to ensure that any individual event or recording station was not overrepresented in the motion suite. Following this process, a total of six motions were selected for use in the transient CSS test program. Husid plots for each of the selected motions are shown in Figure 6.25.

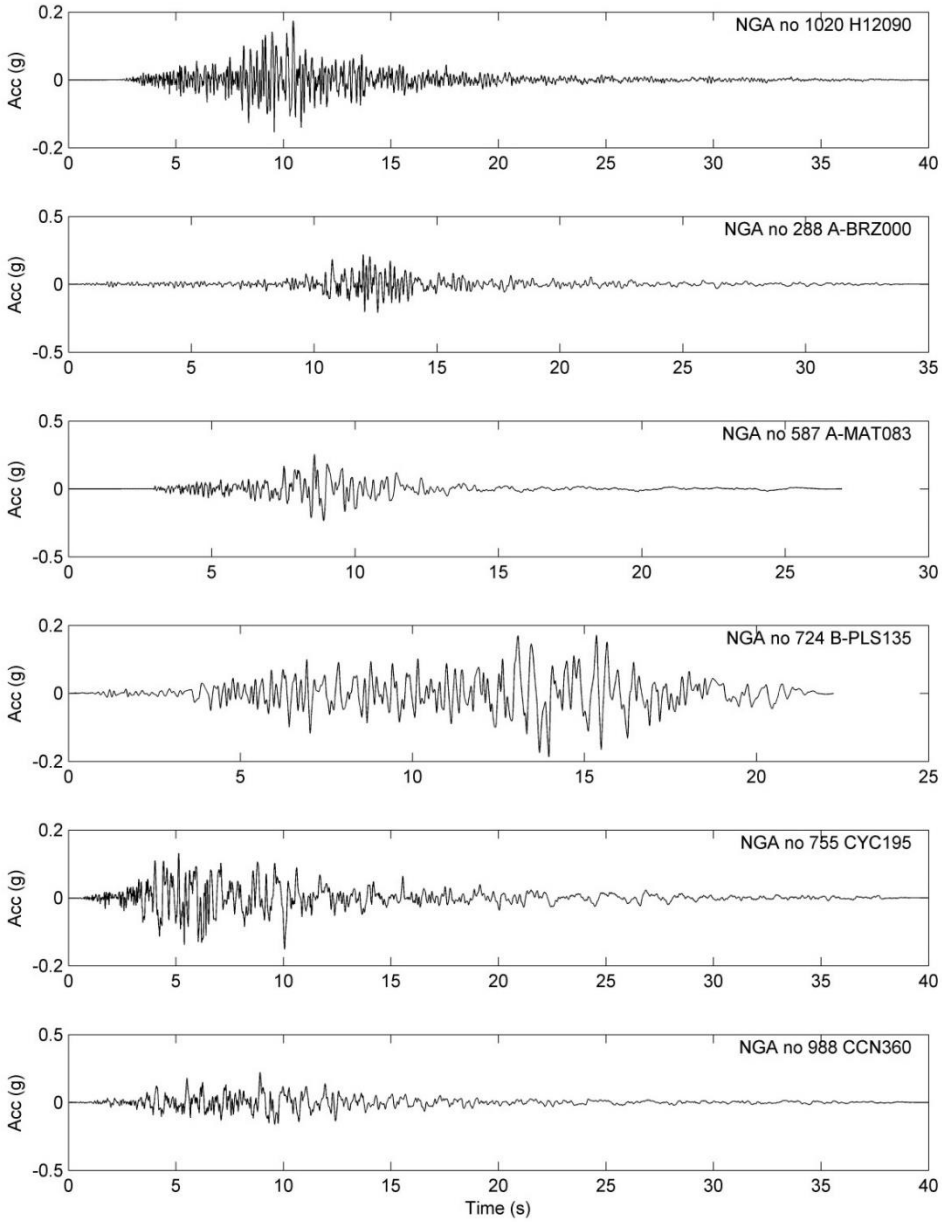


Figure 6.24: Motions selected for use in CSS testing based on their rate of energy buildup.

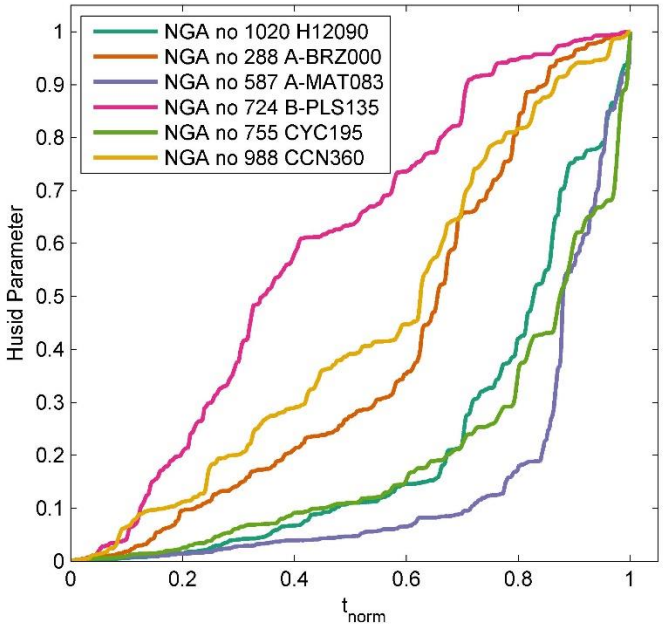


Figure 6.25: Husid parameter for the six motions selected based on their rate of energy buildup.

Metadata for each of the motions described previously are shown in Table 6.2. The table includes source magnitude and site distance information, as well as metadata such as significant and bracketed duration, peak amplitude and duration data PGA, PGV, PGD, $T_{5\text{-}95}$, as well as the final IM values for PGA_m, I_A, CAV and CAV_5.

Table 6.2: Metadata for applied motions during CSS testing program.

NGA filename	M_w	R_{JB} (km)	PGA (g)	PGV (m/s)	PGD (cm)	T_{5-95} (s)	PGA_m (g)	I_A (m/s)	CAV (m/s)	CAV_5 (m/s)
NGA_no_107_B-OAP180	4.79	13.5	0.04	0.02	0.82	3.4	0.02	0.01	0.30	0.19
NGA_no_149_G04360	5.74	4.8	0.27	0.26	4.78	11.4	0.10	0.50	5.41	5.24
NGA_no_164_H-CPE147	6.53	15.2	0.17	0.12	4.24	29.7	0.21	1.22	14.1	13.78
NGA_no_249_L-FIS090	5.94	6.8	0.40	0.15	1.39	5.0	0.16	0.51	3.73	3.68
NGA_no_255_C-XCB270	4.73	8.3	0.04	0.03	0.36	8.8	0.02	0.02	0.93	0.72
NGA_no_288_A-BRZ000	6.90	22.5	0.22	0.14	3.29	10.3	0.17	0.51	5.79	5.53
NGA_no_484_PLK-NS	3.54	155.8	0.16	0.08	0.54	4.3	0.11	0.22	2.74	2.52
NGA_no_527_MVH135	6.06	3.7	0.20	0.41	15.02	6.3	0.10	0.62	5.26	5.13
NGA_no_587_A-MAT083	6.60	16.1	0.26	0.22	6.39	6.2	0.15	0.65	5.46	5.29
NGA_no_592_A-CAM279	5.99	4.5	0.16	0.07	0.72	10.5	0.10	0.20	3.27	2.86
NGA_no_695_A-RO3000	5.99	30.3	0.20	0.08	0.86	8.3	0.12	0.29	3.74	3.29
NGA_no_706_A-WHD152	5.99	2.6	0.32	0.12	1.36	7.4	0.23	0.68	5.49	5.25
NGA_no_724_B-PLS135	6.54	22.2	0.19	0.21	5.39	11.3	0.14	0.63	6.45	6.36
NGA_no_755_CYC195	6.93	20.0	0.15	0.16	7.33	15.7	0.12	0.43	5.97	5.62
NGA_no_825_CPM000	7.01	0.0	1.50	1.25	39.7	6.2	0.49	5.96	14.2	14.00
NGA_no_880_MCF000	7.28	27.0	0.13	0.07	2.32	34.6	0.09	0.36	8.35	7.80
NGA_no_988_CCN360	6.69	15.5	0.22	0.25	5.77	13.6	0.14	0.75	8.20	7.93
NGA_no_1020_H12090	6.69	20.8	0.17	0.12	4.63	9.8	0.12	0.33	4.65	4.27
NGA_no_1157_CNA000	7.51	65.0	0.18	0.18	18.3	30.8	0.13	0.48	9.01	7.69
NGA_no_1236_CHY088-N	7.62	37.5	0.22	0.20	14.2	32.4	0.12	0.97	12.8	12.36
NGA_no_1534_TCU107-N	7.62	16.0	0.16	0.47	32.8	35.2	0.12	1.33	16.2	15.76
NGA_no_1792_12543090	7.13	74.0	0.12	0.19	15.0	28.1	0.05	0.23	6.56	5.26

6.4.1.2 Conversion to Shear Stress Time Histories

The UT CSS testing apparatus requires a shear stress loading history as input. The previous sections described the selection of a diverse motion suite. However, these time histories were in terms of acceleration. For these loading histories to be used during testing they had to be converted to equivalent shear stress time histories.

The conversion process was done using the equivalent linear analysis program ProSHAKE. In order to relate the experimental studies presented in this research with the numerical studies performed by Abegg (2010), which was developed with consideration of the model geometry used in the centrifuge study presented in Chapter 7, the general soil profile shown in Figure 6.26, was used to develop the shear stress loading histories. The profile

consisted of 1 m of dry sand underlain by 6 m of saturated sand. The base of the profile was modeled as perfectly rigid. The dynamic properties of all the sand layers were modeled using the Seed upper bound curves for the modulus reduction and the Seed lower bound curves for the damping ratio. Additional properties were determined by assuming a relative density of the sand layers taken as 55%, which corresponded to the median value of the relative density range that was tested in the laboratory. Shear wave velocity was computed by converting the relative density to an equivalent blow count using the correlation from Idriss and Boulanger (2008). Then the overburden effective stress and blow count was used to estimate a shear wave velocity using the empirical relationship of Ohta and Goto (1976). The base of the model was assumed to be rigid with a 2% damping ratio.

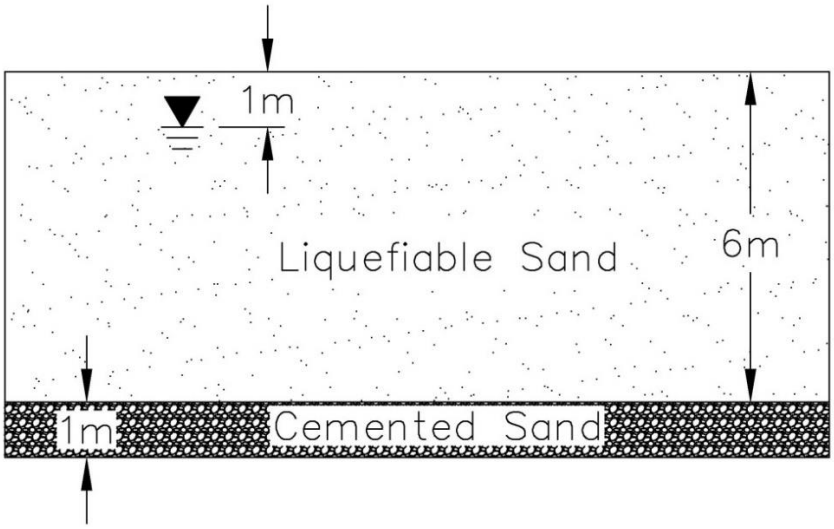


Figure 6.26: Soil profile used in ProSHAKE to generate shear stress loading histories used as input for CSS testing.The liquefiable sand layer was assigned a relative density value of 55%.

To determine the shear stress time history, each motion was applied at the base of the model and the computed shear stress history was extracted from the critical layer, identified by Abegg (2010) as the layer located 5.5 meters below the ground surface. This shear stress time history was then converted to a format that allowed it to be read by the actuator control system and provided to UT-Austin in terms of a cyclic stress ratio (CSR) to be used as input loading histories.

6.4.1.3 Additional CSS Loading Histories

During the process of converting the base motion acceleration time histories to shear stress time histories it was observed that often the shear stress time histories were highly correlated to the acceleration time histories at the same depth. This was likely because the representative soil profile used to extract the shear stress time history was shallow and relatively stiff. As a result, the natural site frequency was high and the resulting transfer functions between acceleration and shear stress only influenced the higher frequency components of the motion, which were generally relatively weak. The transfer function was often flat at lower frequencies and, as a result, did not have a large impact on the higher amplitude (lower frequency) components of the motion.

In order to investigate the impact of the shear stress conversion process on the results, the 22 motions provided in Table 6.2 were used as input loading histories and batch-processed through ProSHAKE using a variety of different input profiles with uniform relative densities. The six shear stress time histories extracted at the critical depth and motions that produced the biggest difference, i.e. were the least correlated, between the acceleration and shear stress time histories at the same depth, were extracted and used as CSS loading histories. The CSS loading histories, expressed as normalized shear stress values ($\hat{\tau} = {\tau(t)}/{\tau_{max}}$), are provided in Figure 6.27.

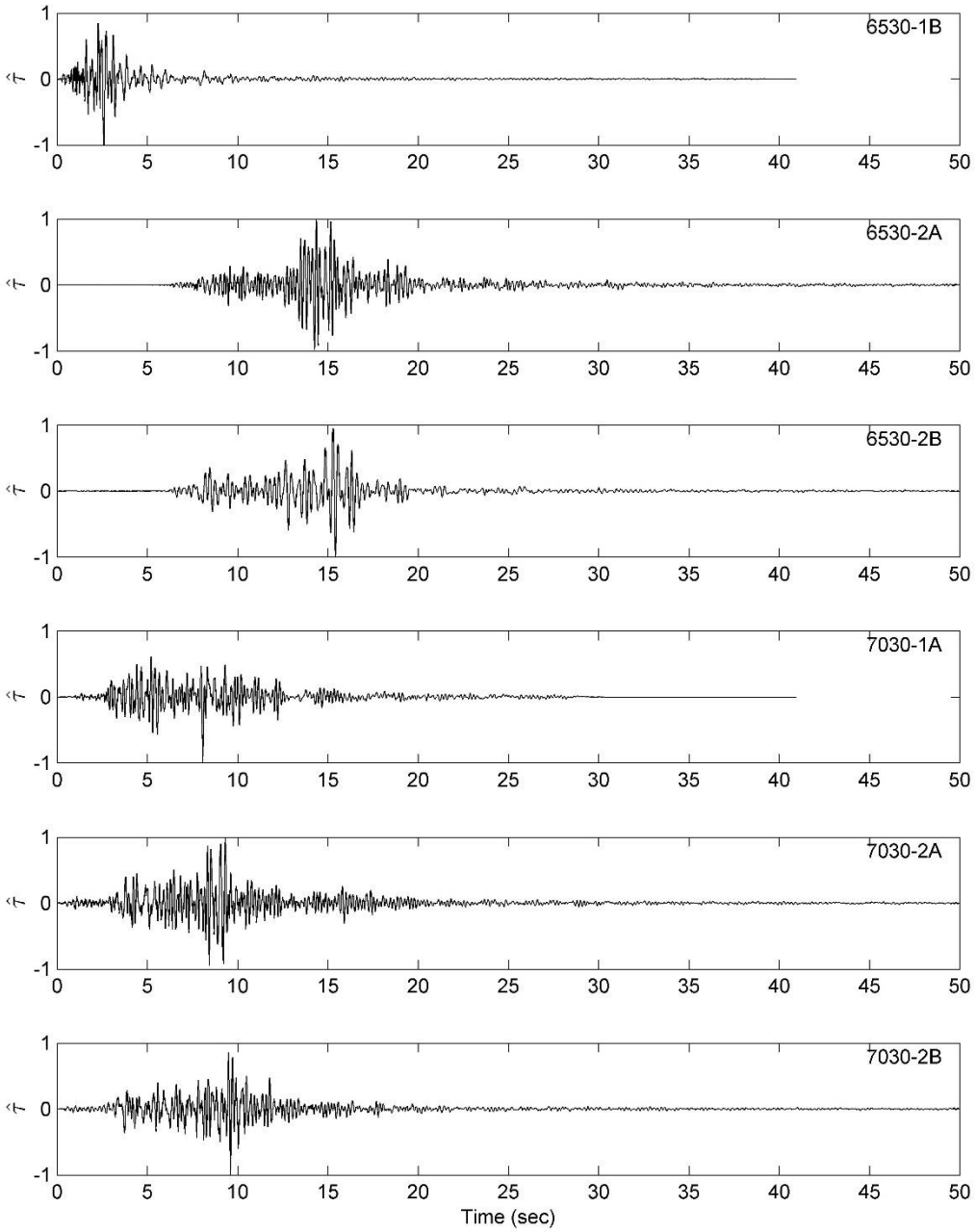


Figure 6.27: Normalized shear stress loading histories from ProSHAKE analyses that produced the largest difference between the acceleration and shear stress time histories at the critical layer.

6.4.1.4 Loading Protocols

The shear stress loading histories described previously were scaled to various amplitudes and applied to a series of samples at a variety of initial relative densities. During testing it was observed that, likely due to the location of the pore pressure transducer at the bottom of the specimen (as opposed to the center), the pore pressure response lagged behind the loading time

history. In order to mitigate this lag, the loading rate of each time history was reduced by a factor of 5.0.

Ideally, the motions would have been scaled so that liquefaction would occur during the transient loading history. However, in order to distinguish between which aspects of the time history are important in identifying the onset of liquefaction, it was important that the motions not be scaled to be so large that liquefaction was induced after only a few initial cycles of loading. In instances where liquefaction did not occur during the transient portion of the record, all drainage valves were kept closed and the sample was returned to a state of zero applied shear stress. Then a ramped sine load of linearly increasing amplitude was applied to the sample until liquefaction occurred. While the ramped sine load portion of the record was not used directly in subsequent analyses presented in this dissertation it does provide valuable insight into the behavior of liquefiable soils, particularly for the validation and calibration of constitutive models, and is unique, available data that the reader should be aware of.

6.4.2 *Example Results*

An example of a transient loading test results is shown in Figure 6.28. The figure shows plots of the shear strain, shear stress and excess pore pressure time histories, as well as stress-strain and stress path behavior. Each of the plot traces are colored with respect to time. The applied shear stress history included a series of stress pulses whose amplitudes, both positive and negative, varied with time. Some pulses were stronger than the immediately preceding pulse, and some were weaker. The excess pore water pressure increased over the course of the loading, but in an irregular manner. As the excess pore pressure approached 100 kPa (at which point initial liquefaction will occur), it periodically dropped for short instances of time. These drops were the result of dilation of the soil when the effective stress path was above the phase transformation line. The stress-strain curve showed clear evidence of dilation as manifested in the increasing stiffness of the soil as the shear strain reached relatively high levels.

The response of the shear strain time history was also of note. The shear strains in Figure 6.28 were observed to be very small prior to the time at which the pore pressure ratio became large. As the excess pore pressures approached the level of initial liquefaction, the cyclic strain amplitudes increased quickly to approximately eight percent for the example shown. This observation reinforces the need to further develop the framework described in Chapter 4, as it

appears that the effects of liquefaction, as expressed in terms of soil deformations, are more closely related to the loading that occurs after liquefaction has been initiated.

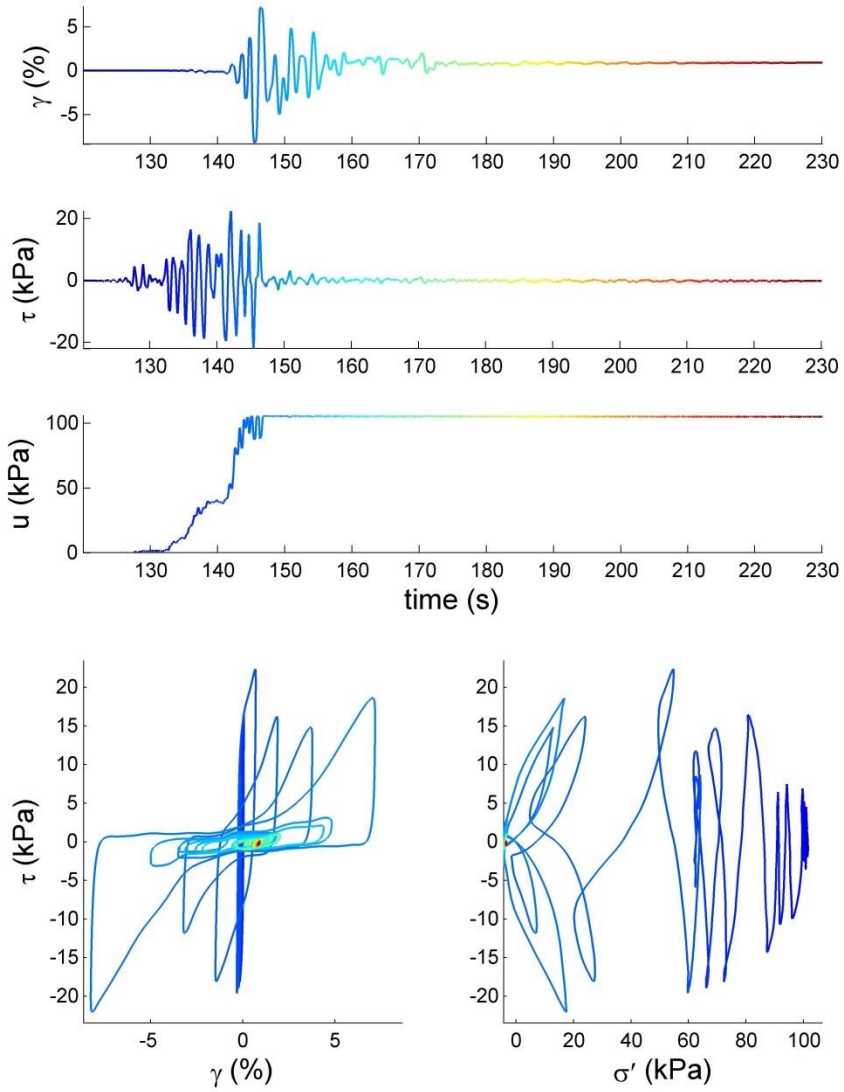


Figure 6.28: Example results from a transient CSS test.The upper three plots show the shear strain, shear stress and excess pore pressure time histories, respectively. The lower plots show the stress-strain and stress path response of the sample. Color changes with time for each plot.

The example shown in Figure 6.28 shows the results of a test that reached initial liquefaction during the transient loading portion of the history. However, this was not the case for all tests. As described in Section 6.4.1.4, tests that did not liquefy during the initial transient portion were subjected to a ramped sine wave applied while the sample was still in an undrained state. An example of the results for a test that did not liquefy during the transient portion of the test are shown in Figure 6.29. The transient loading history, from its beginning up to about 250 s,

induced a pore pressure ratio of about 0.5. After this time the shear stress returned to zero with the drainage valves closed and a ramped sine function load history was applied beginning at about 270 s. The sine loading began at an amplitude on the order of 2 kPa, and was increased linearly until the sample liquefied. As before it was observed that the strain levels remain very small until liquefaction was initiated. The strains that were observed prior to 320 s, when the pore pressure ratio was below 0.95, were very small. However, after 320 s, when the sample liquefied, the strain levels dramatically increased, and cyclic strains on the order of 10% were observed. See Kwan (2015) for further description and detail for all of the CSS tests performed at UT-Austin.

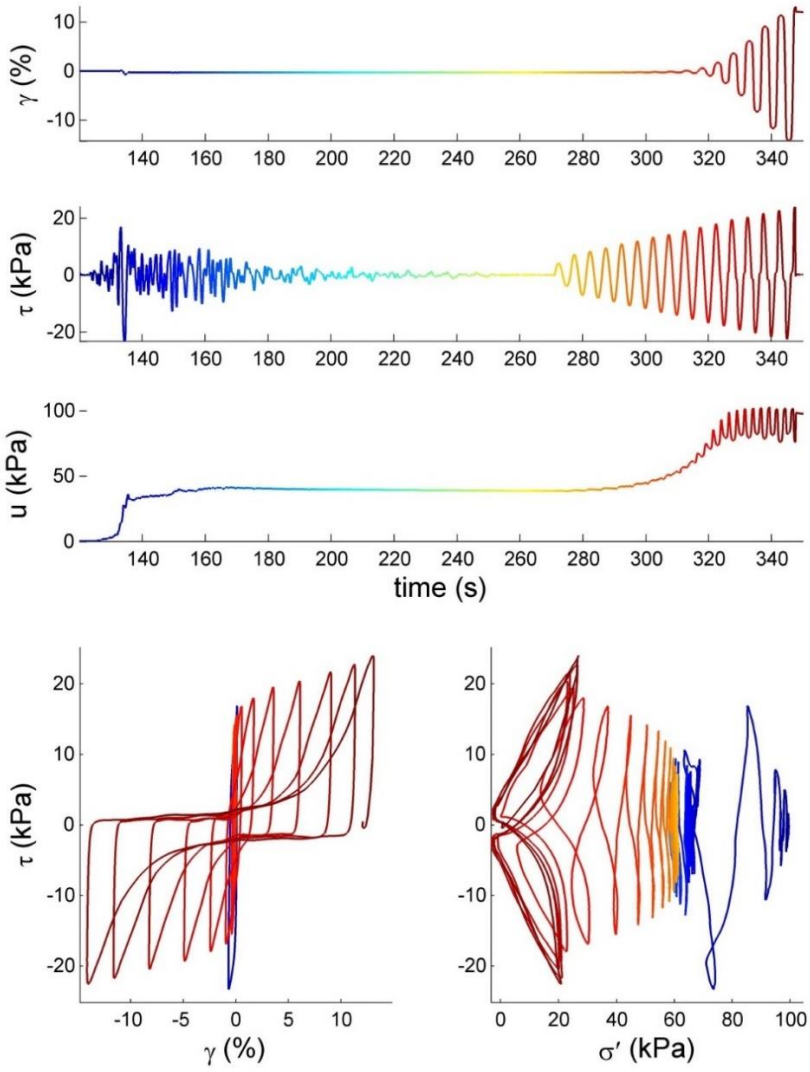


Figure 6.29: Example results from a transient CSS testing where liquefaction was not reached during the transient loading portion of the history.The upper three plots show the shear strain, shear stress and excess pore pressure time histories, respectively. The lower plots show the stress-strain and stress path response of the sample. Color changes with time for each plot.

6.4.3 *CSS Dataset Used to Analyze IM Efficiency*

The final CSS dataset used to analyze the efficiency of various IMs to predict the pore pressure response of the sample was derived from the 28 selected CSS tests performed under transient loading as described in Kwan (2015). The selected tests included 15 loose (less than 60% relative density) and 13 dense (greater than 70% relative density tests). Kwan (2015) used the following criteria to select the 28 tests:

1. None of the tests used the same input loading history for a given density range, and
2. Liquefaction was triggered near the end of the applied motion.

The first condition was employed so that there was no bias to any particular IM, since some of the motions were selected to be high with respect to a particular IM, while low with respect to another (Section 6.2). The second condition ensured that the majority of the time-domain characteristics of the selected motion are reflected in the data (Kwan, 2015). In addition, Kwan (2015) noted that the 28 selected tests were among the best tests ran during the testing program and were conducted after all the equipment modifications had been made and the pluviation techniques standardized.

A summary of the 28 selected tests is presented in 6.3 and summary plots for each of the tests are provided in Appendix A. 6.3 presents the Test ID, relative density, Skempton's B-value, the motion used in the test, and a reference number used to identify each individual test in scatter plots presented later in this document. For this study tests where the B-value fell below 0.9 were removed from the dataset.

Each test was inspected to determine whether the stress-strain and pore pressure response was considered representative of the response of liquefiable soils based on soil mechanics and the literature review presented previously. One of the selected tests, Test 130115, showed inconsistent behavior and a directional bias, and was subsequently removed from the data set. The results of Test 130115 are shown in Figure 6.30. The motion had a very long duration, and the majority of the pore pressure is developed at the beginning and end of the time history. Excess pore pressure did not develop between 80 to 160 seconds into the motion despite significant stress cycles during that portion of the time history, including the peak stress amplitude at about 95 seconds. Figure 6.31 shows the same plot as Figure 6.30 but focused on the interval from 60-120 seconds into the record. The stress-strain and stress path response appear to show a directional bias, with the soil behaving stiffer in the negative direction and

softer in the positive direction. The source of this bias is unknown, and this behavior was not observed in other tests in the dataset. As a result, Test 130115 was removed from the database.

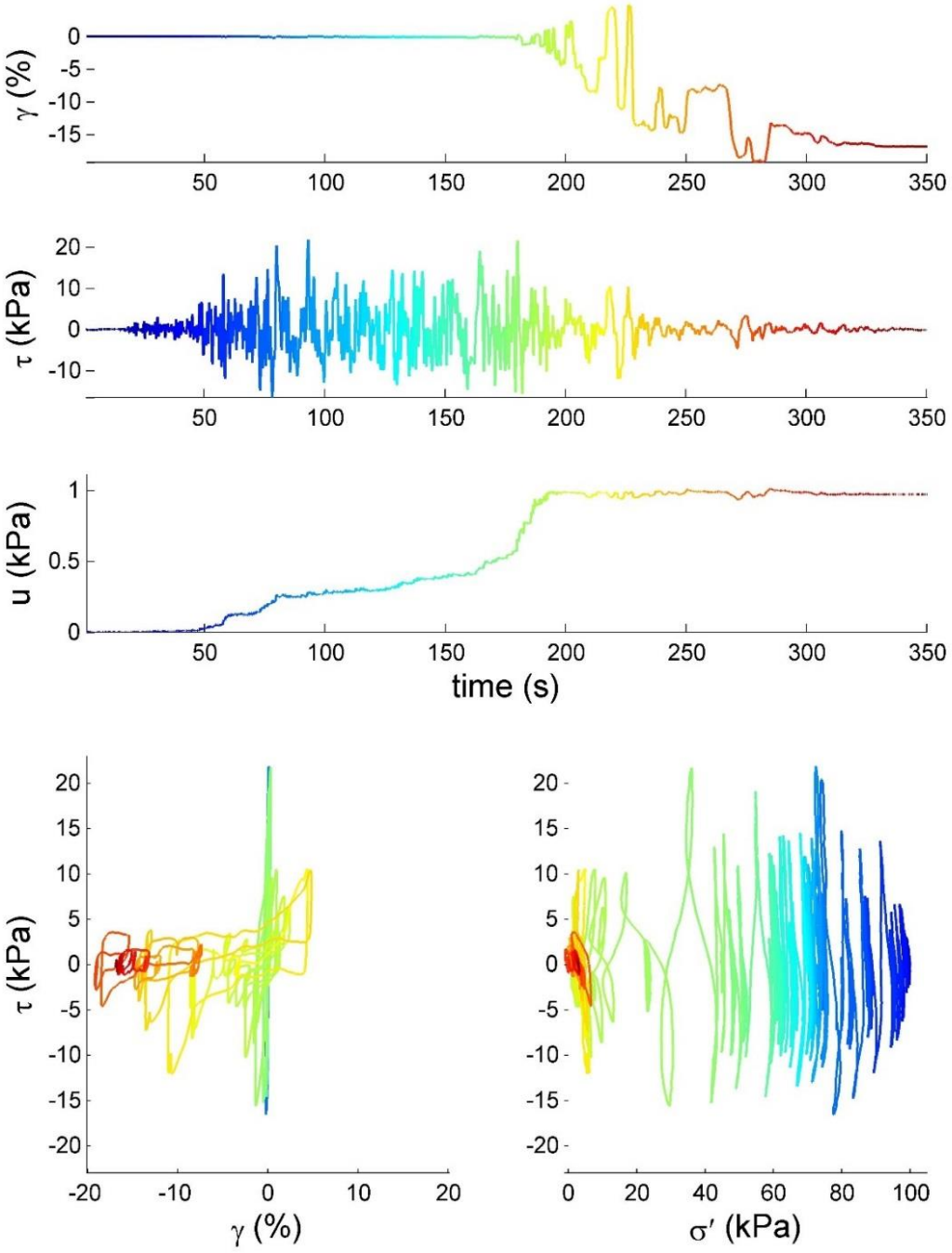


Figure 6.30: Results from CSS Test 130115.

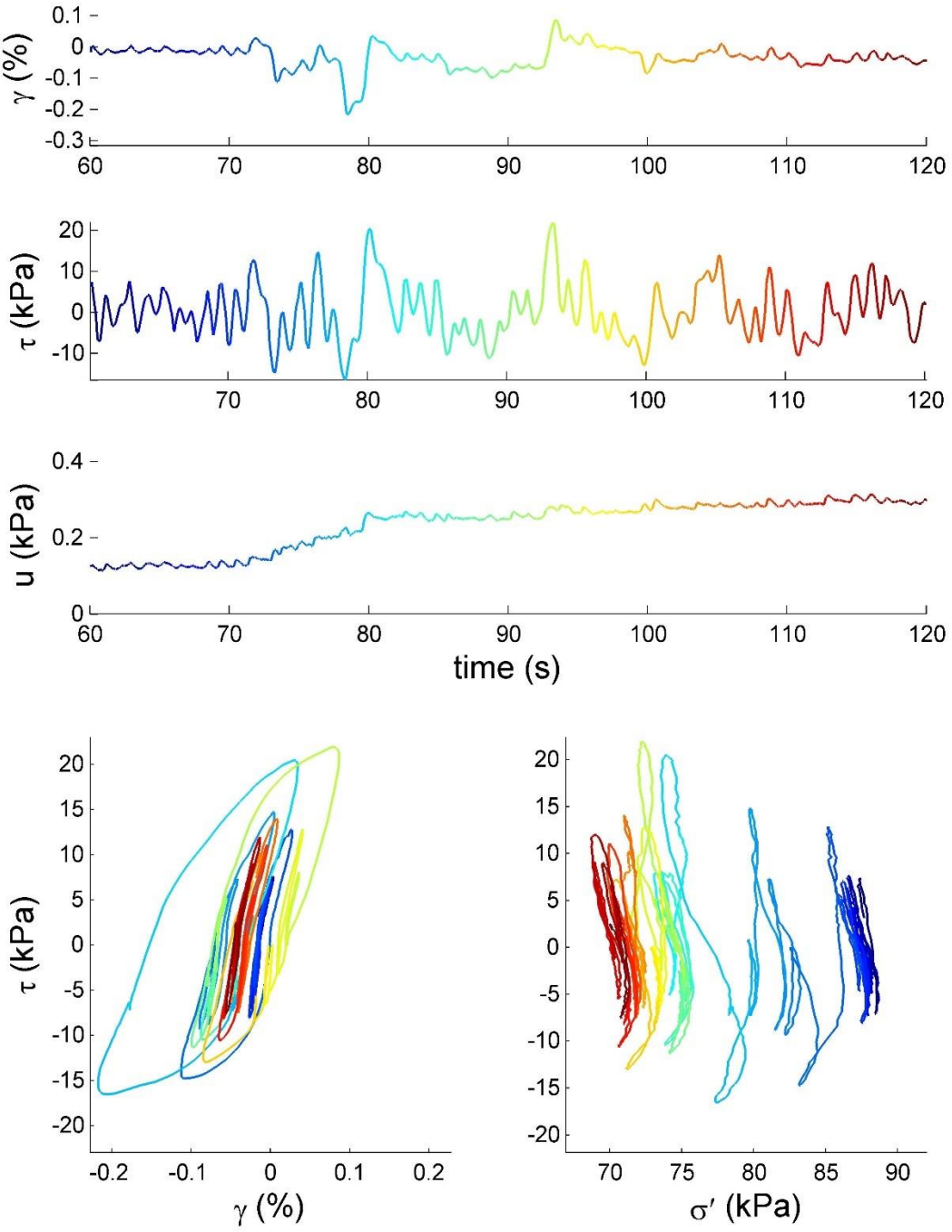


Figure 6.31: Results from CSS Test 130115 over the interval of 60-120 seconds.

The tests that were removed, whether due to low B-values, or inconsistent behavior, are highlighted in Table 6.3. The final CSS test dataset used in this research included 21 total tests. Eleven of the 21 tests were performed on loose samples, and ten tests were performed on dense

samples using a threshold of 55% relative density to distinguish between loose and dense sand samples. Table 6.3 includes the Test ID used by Kwan (2015), the reported relative density, the B-value, and the motion name. In addition, each of the 21 tests used in this study was assigned a reference ID number, provided in the table. This reference ID number is used in figures that are presented in the efficiency evaluation (Section 6.5) to identify the response from individua tests.

Table 6.3: Summary of the 28 selected CSS tests from Kwan (2015).Highlighted tests were not included in the final analyses due to low B-values or inconsistent stress-strain behavior.

Test ID	Dr (%)	B-Value	Motion	Reference ID
130115	43	0.94	NGA_no_1534_TCU107-N.AT2	-
130118	41	0.93	NGA_no_484_PLK-NS.AT2	1
130119	37	0.94	NGA_no_1157_CNA000.AT2	2
130209	47	0.91	NGA_no_249_l-FIS090.AT2	3
130215	50	0.87	NGA_no_695_A-RO3000.AT2	-
130215-02	47	0.91	NGA_no_1792_12543090.AT2	4
130306	40	0.91	NGA_no_527_MVH135.AT2	5
130401	37	0.96	NGA_no_107_B-OAP180.AT2	6
130628	43	0.91	NGA_no_288_A-BRZ000.AT2	7
130916	47	0.95	7030_1A	16
130921	44	0.93	6530_1B	17
130923	49	0.85	7030_2B	-
130924	41	0.91	7030_2A	18
130925	55	0.90	6530_2B	19
131001	50	0.87	6530_2A	-
130711-02	78	0.94	NGA_no_724_B-PLS135.AT2	8
130726-02	72	0.99	NGA_no_988_CCN360.AT2	9
130727	84	0.94	NGA_no_755_CYC195.AT2	10
130809-02	74	0.93	NGA_no_587_A-MAT083.AT2	11
130821	80	0.90	7030_2A	12
130826-02	89	0.88	7030_1A	-
130827-02	89	0.92	6530_2A	13
130829-02	81	0.91	7030_2B	14
130905-02	86	0.94	6530_1B	15
131008	73	0.93	NGA_no_484_PLK-NS.AT2	20
131009	72	0.92	NGA_no_527_MVH135.AT2	21
131009-02	71	0.85	NGA_no_880_MCF000.AT2	-
131106-02	74	0.89	NGA_no_1157_CNA000.AT2	-

6.4.4 *Computing Accelerations from CSS Shear Stress Histories*

The goal of the testing program was to correlate pore pressure generation and the initiation of liquefaction to an evolutionary IM which is calculated from an acceleration time history. Since acceleration is not recorded during the CSS testing process, the recorded shear stress time history must be converted to an equivalent acceleration time history. This was accomplished using an equivalent linear analysis program developed specifically for this research project.

The analysis was performed using the soil profile shown in Figure 6.26, which is the same profile used to develop the shear stress time histories and in the numerical analyses by Abegg (2010). The dynamic properties of all the sand layers were modeled using the Seed upper bound curves for the modulus reduction and the Seed lower bound curves for the damping ratio. All of the sand layers were assigned a uniform density, corresponding to the average density of the soil sample reported for a given CSS test. Shear wave velocity was computed by correlating the relative density to an equivalent blow count using the correlation of Idriss and Boulanger (2008), then computing the shear wave velocity based on Ohta and Goto (1976). The base of the model was modeled as rigid using linear dynamic properties and 2% damping ratio. The equivalent linear program computed a transfer function relating the shear stress at the depth of interest to the acceleration at the same depth. The actual shear stress history as recorded by the laboratory test was then applied, and the resulting acceleration time history was extracted and used to calculate the various evolutionary IMs included in the corresponding investigation. A further description of the equivalent-linear program used for in this project is provided in the following subsection.

6.4.4.1 Shear Stress-based Equivalent-linear Program Description

The equivalent-linear program used to obtain acceleration time histories from the shear stress input time histories was based on the assumption that each of the soil layers behaves as a Kelvin-Voigt solid. Using this assumption, the solution to the general one-dimensional wave equation can be expressed as

$$\rho\frac{\partial^2 u}{\partial t^2} = G\frac{\partial^2 u}{\partial z^2} + \eta\frac{\partial^3 u}{\partial z^2 \partial t} \tag{6.4}$$

where ρ, G, and η are the density, shear modulus and viscosity of the material the waves are travelling in, u is the displacement, and z and t represent the depth and time, respectively. The solution to the wave equation is of the form

$$u(z,t) = Ae^{i\left(\omega t + k^* z\right)} + Be^{i\left(\omega t - k^* z\right)} \tag{6.5}$$

where u(z, t) is the displacement at depth z and time t, A and B represent the amplitudes of the waves travelling in the upward (-z) and downward directions (+z) directions, respectively. ω is the circular frequency of the waves and k^* represents the complex wave number ($k^* = \frac{w}{v_s}(1 - i\xi)$, where ξ is the damping ratio of the material). Based on this solution, the shear stress can be expressed as the product of the complex shear modulus, $G^* = G + i\omega\xi$, and the shear strain, $\gamma = {\partial u}/{\partial z}$, as

$$\tau(z,t) = G^*\gamma = G^*\frac{\partial u}{\partial z} = ik^* G^*\left(Ae^{ik^* z} - Be^{-ik^* z}\right)e^{i\omega t} \tag{6.6}$$

By introducing a local coordinate system for each layer, as shown in Figure 6.32, the displacement at the top and bottom of each layer can be expressed as

$$u(z_m = 0,t) = (A_m + B_m)e^{i\omega t} \tag{6.7}$$

$$u(z_m = h_m,t) = \left(A_m e^{ik^*_m h_m} + B_m e^{-ik^*_m h_m}\right)e^{i\omega t} \tag{6.8}$$

and the shear stresses at the same locations can be similarly expressed as

$$\tau(z_m = 0,t) = ik^*_m G^*_m (A_m - B_m)e^{i\omega t} \tag{6.9}$$

$$\tau(z_m = h_m,t) = ik^*_m G^*_m\left(A_m e^{ik^*_m h_m} - B_m e^{-ik^*_m h_m}\right)e^{i\omega t} \tag{6.10}$$

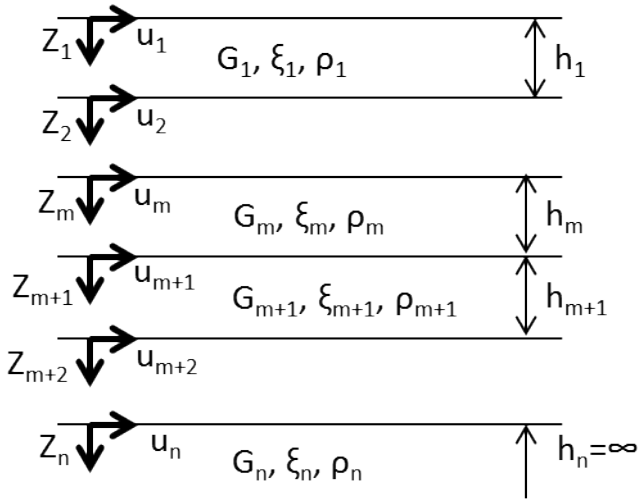


Figure 6.32: Schematic of layered soil deposit for equivalent-linear calculations

Using the formulations for displacement and shear stress shown in Equations 6.7 to 6.10, and noting that the displacements and stresses must be consistent at the layer boundaries, the values for the amplitudes of the upward and downward travelling waves in layer m+1 can be expressed as

$$A_{m+1} = \frac{1}{2}A_m\left(1+\alpha_m^*\right)e^{ik_m^* h_m} + \frac{1}{2}B_m\left(1-\alpha_m^*\right)e^{-ik_m^* h_m} \tag{6.11}$$

$$B_{m+1} = \frac{1}{2}A_m\left(1-\alpha_m^*\right)e^{ik_m^* h_m} + \frac{1}{2}B_m\left(1+\alpha_m^*\right)e^{-ik_m^* h_m} \tag{6.12}$$

where α_m^* is the complex impedance ratio between layers m and m+1

$$\alpha_m^* = \frac{k_m^* G_m^*}{k_{m+1}^* G_{m+1}^*} = \frac{\rho_m\left(v_s^*\right)_m}{\rho_{m+1}\left(v_s^*\right)_{m+1}} \tag{6.13}$$

In addition, the shear stress must go to 0 at the ground (free) surface, which based on Equation 6.9 implies that $A_1 = B_1$. Using this observation and recursively solving Equations 6.11 and 6.12 for layers 1 through m, functions relating the displacement amplitudes between layer m and layer 1 can be expressed as

$$A_m = a_m(\omega)A_1 \tag{6.14}$$

$$B_m = b_m(\omega)B_1 \tag{6.15}$$

Using these results, a transfer function relating the displacement amplitude between layers *i* and *j* can be derived as

$$TF_{ij}(\omega) = \frac{|u_i|}{|u_j|} = \frac{a_i(\omega) + b_i(\omega)}{a_j(\omega) + b_j(\omega)} \tag{6.16}$$

In the case of harmonic motion, the displacements, velocities and accelerations are related based on the circular frequency, ω, such that $|\ddot{u}| = \omega|\dot{u}| = \omega^2|u|$, therefore Equation 6.16 also describes the amplification of the acceleration and velocity between layers *i* and *j*. Using Equation 6.16, the motion at any layer in the soil profile can be used to determine the motion in any other layer in the soil profile.

Determining the acceleration time history from a given shear stress time history as input requires a transfer function between the shear stress time history and the acceleration time history. The acceleration can be derived from the displacement as expressed in Equation 6.5 as

$$a(z,t) = \frac{\partial^2 u(z,t)}{\partial t^2} = -\omega^2\left(Ae^{ik^* z} + Be^{-ik^* z}\right)e^{i\omega t} \tag{6.17}$$

Using the definition of the shear stress as shown in Equation 6.6 and the definitions for A_m and B_m seen in Equations 6.14 and 6.15, the transfer function relating the shear stress in layer *i* to the acceleration in layer *i* was derived as

$$TF_{a_i\tau_i}(\omega) = \frac{-\omega^2\left(a_i(\omega)e^{ik^*_i z} + b_i(\omega)e^{-ik^*_i z}\right)}{ik^*_i G^*_i\left(a_i(\omega)e^{ik^*_i z} - b_i(\omega)e^{-ik^*_i z}\right)} \tag{6.18}$$

At the top of each layer, z = 0 so Equation 6.18 is reduced to

$$TF_{a_i\tau_i}(\omega) = \frac{-\omega^2(a_i(\omega) + b_i(\omega))}{ik^*_i G^*_i\left(a_i(\omega) - b_i(\omega)\right)} \tag{6.19}$$

Equivalent-linear analysis can be conducted using a shear stress time history at a given depth as input by initially assuming small strain shear modulus and damping values to compute the acceleration time history at the same depth using Equation 6.18 and the shear stress input time history. Then the motion is deconvolved to determine the acceleration time history at the base of the profile using Equation 6.16. Next, a standard equivalent linear analysis is conducted using the deconvolved base motion as input. The strain results from the analysis are then used to determine the shear modulus and damping values for the following iteration and the analysis is repeated until the strain results from successive analyses are identical.

6.4.4.2 Validation and Results of the Shear Stress-based Equivalent Linear Program

The shear stress-based equivalent-linear code was validated through comparisons with the equivalent-linear site response analysis program ProSHAKE. The soil profile shown in Figure 6.26 was modeled in both programs using a variety of relative density values for the upper sand layers. A base motion was applied to the ProSHAKE model and the resulting shear stress time history in the critical layer was extracted and used as input into the project-specific equivalent linear code.

The results, in terms of acceleration time histories and shear stress to acceleration transfer functions show that results from the two codes provided consistent results. Examples of these results are provided in Figures 6.33 and 6.34, which show plots of the acceleration time histories and frequency domain shear stress to acceleration transfer functions, respectively for both ProSHAKE and the project-specific equivalent linear code. The response in both the time and frequency domain between the two codes was nearly identical. Reasons for the slight differences in the results from the two codes include differences between the iteration algorithms and minute differences in the damping and modulus reduction curves used to define the dynamic properties of the soil.

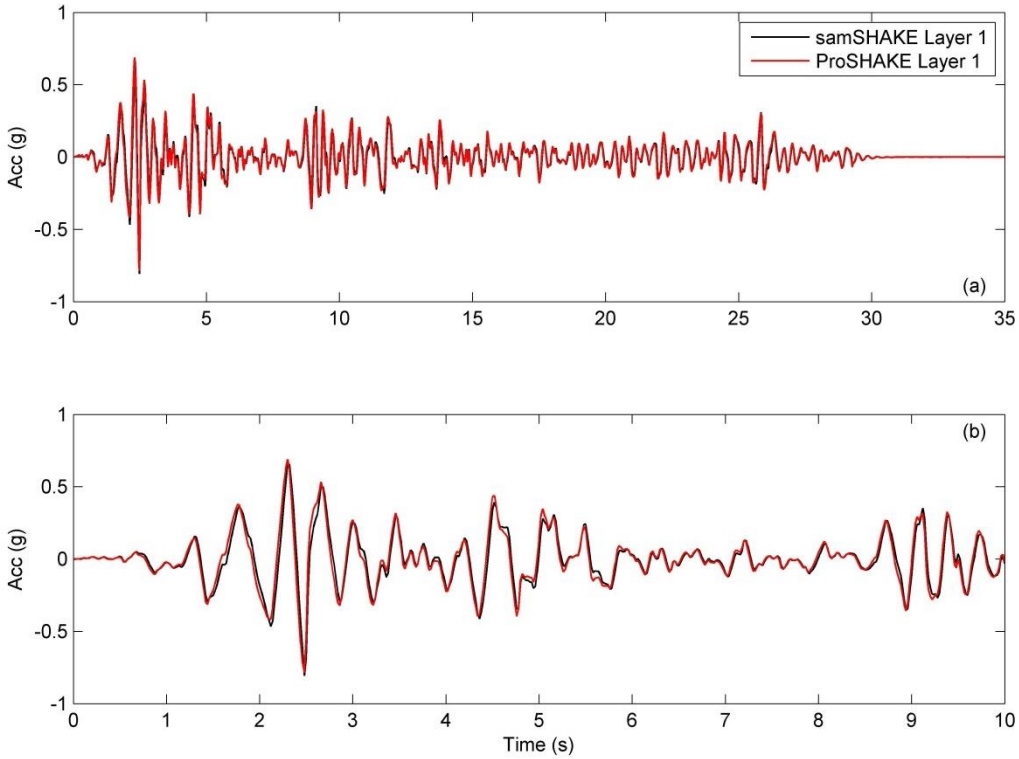


Figure 6.33: Acceleration time histories comparing ProSHAKE to the shear stress-based equivalent linear code written for this project (a) the entire time history and (b) zoomed in on the first 10 seconds of the time history.

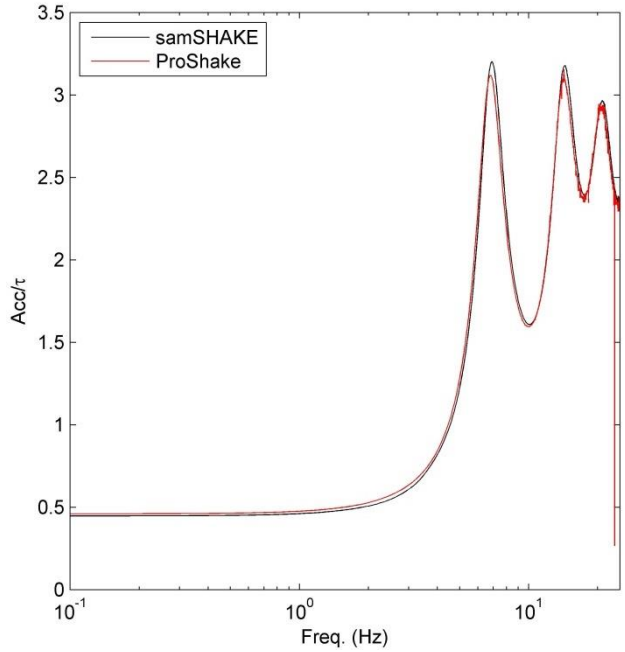


Figure 6.34: Transfer function between shear stress and acceleration for both ProSHAKE and the shear stress-based equivalent linear code.

Figure 6.35 shows an acceleration time history obtained using the equivalent-linear analysis program with a shear stress time history recorded during CSS testing as input. As discussed previously, because the input soil profile is relatively thin, the computed transfer functions used in the equivalent-linear process predominantly affect high frequencies and the resulting acceleration time history is very similar in shape to the shear stress input history. The derived acceleration time histories were then used to evaluate the efficiency of various evolutionary intensity measures to predict the initiation of liquefaction.

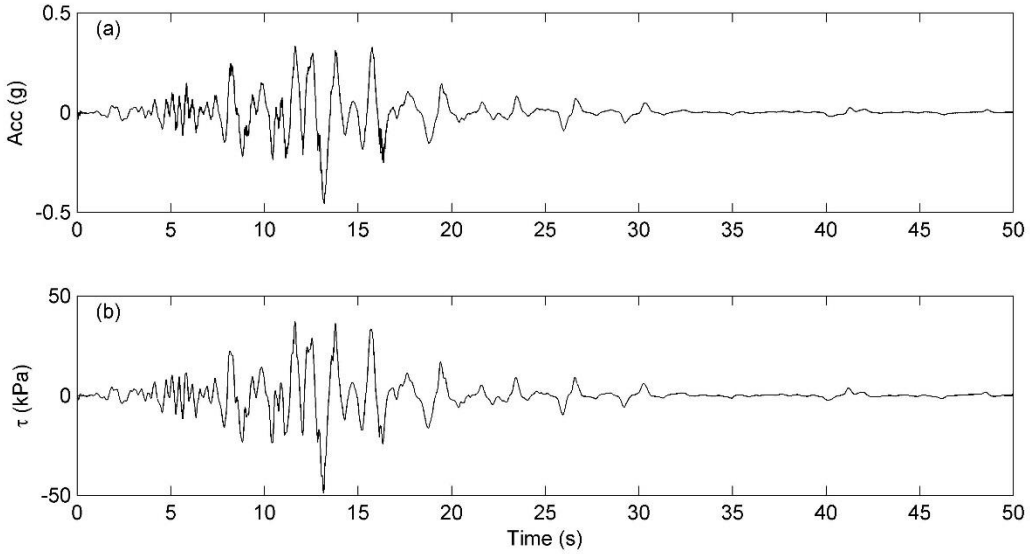


Figure 6.35: (a) Acceleration response at 5.5 m depth derived using shear stress-based equivalent-linear analysis using the soil profile shown in Figure 6.26 and (b) shear stress input time history.

6.5 Relationship Between Pore Pressure and Standard Intensity Measures

As outlined previously, each transient shear stress loading history was converted to a corresponding acceleration time history using equivalent linear analysis methods. The acceleration time history was then used to assess the efficiencies with which various IMs were able to predict the excess pore pressure response measured during testing with the goal of identifying the most efficient IM for predicting the triggering of liquefaction for use in the timing-based framework described in Chapter 4 (i.e. IM^{trig}). This section investigated the ability of conventional IMs to predict the pore pressure response of the CSS tests. Conventional, or standard, IMs investigated as part of this study were PGA_m, I_A, CAV and CAV_5. As described in Chapter 4, PGA_m was computed using both the Liu et al. (2001) and the density-independent

formulation of the Boulanger and Idriss (2014) methods, referred to as PGA_{mL} and PGA_{mB}, respectively. The following sections outline the methodology and results of the efficiency evaluation using the standard IMs.

6.5.1 *Surface Fitting Methodology*

In the conventional presentation of the PBEE framework, the engineering demand parameter, EDP, is calculated directly from an IM, and the efficiency of the IM is expressed as the dispersion in the EDP|IM relationship. However, since liquefaction is a transient process and the behavior of a soil deposit before and after liquefaction is significantly different, a timing-based framework was developed, as presented in Chapter 4, which allows for multiple IMs to be used to evaluate the EDP of interest. The triggering IM, IM^{trig}, is used to evaluate if liquefaction will occur. If liquefaction will occur, IM^{trig} is used to estimate the amount of post-triggering loading that remains in the time history, quantified by an IM used to evaluate the effects of liquefaction, IM^{eff}_P. Then the EDP is computed using a relationship between IM^{eff}_P and the EDP. The focus of this study is on evaluating the most efficient triggering IM. As shown in Chapter 4.5.1, the uncertainty in the triggering relationship is expressed as the dispersion in IM^{trig} at the initiation of liquefaction. Therefore, in this study, efficiency was evaluated as the uncertainty in the IM|r_u relationship. The following sections describe the surface fitting methodology used in this study.

6.5.1.1 General Functional Form

Figure 6.36 shows an example of a hypothetical transient CSS test result expressed in terms of an acceleration, r_u, and a generic evolutionary IM time history. The r_u time history included local negative incremental fluctuations due to dilation, which were particularly apparent as r_u became greater than approximately 0.6. The r_u time history used to evaluate the efficiency of the IM|r_u relationship was processed to remove these transient fluctuations. The processed r_u time history is shown in red in Figure 6.36b. The pore pressure ratio and evolutionary IM time histories can be directly compared by plotting the evolutionary IM as a function of the r_u, as shown in Figure 6.37, which includes both the raw and processed r_u histories. If r_u and IM were a perfectly correlated the r_u and IM curves would have identical shapes and a plot of IM vs. r_u would be a straight line.

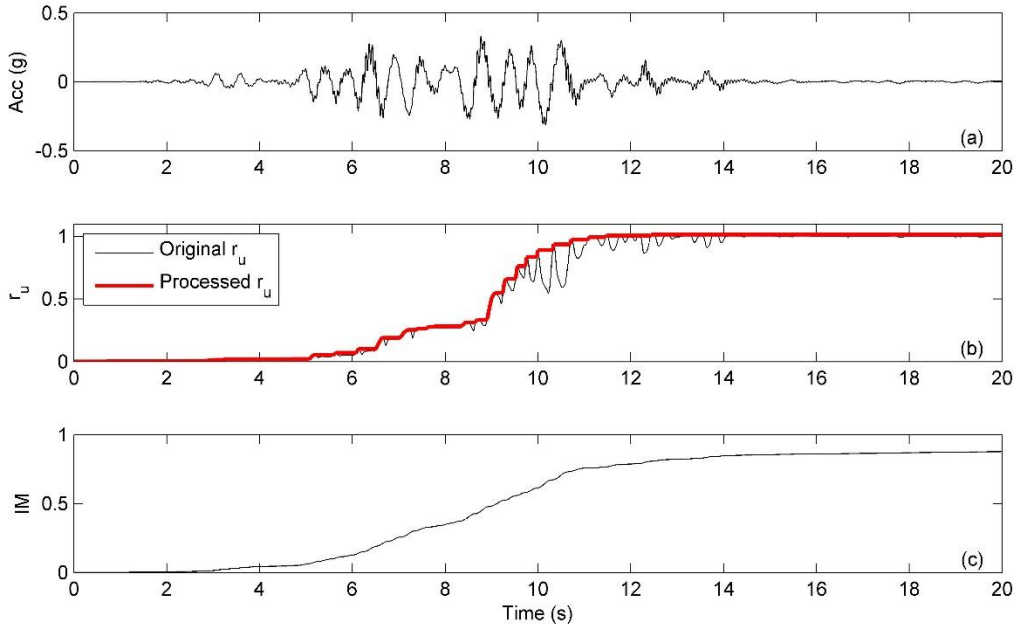


Figure 6.36: Example of hypothetical test results showing (a) Pore pressure ratio, (b) acceleration and (c) evolutionary IM time histories generated by CSS or centrifuge test.

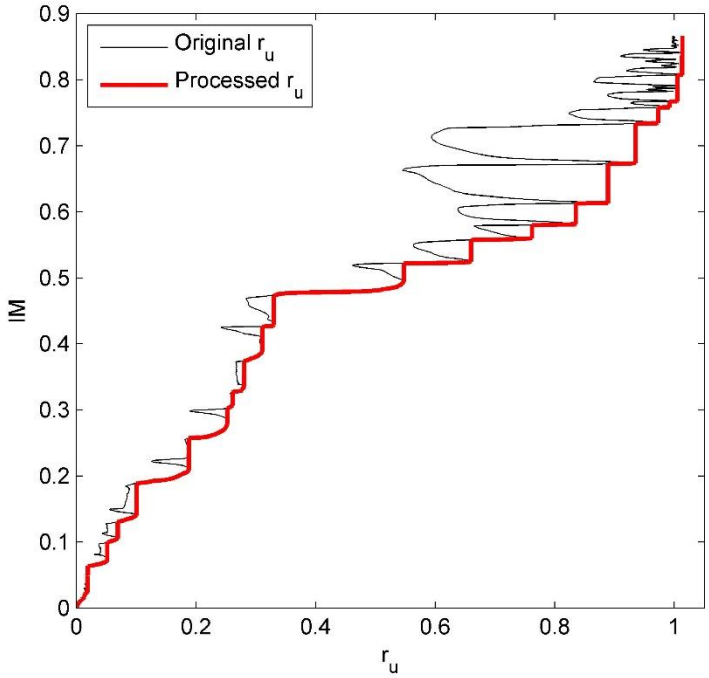


Figure 6.37: Example of a hypothetical pore pressure ratio-IM plot.If the IM were a perfect predictor of pore pressure ratio the data would plot as a straight line.

In addition to the intensity of the loading history, the relationship between excess pore pressure generation and the loading intensity is also a function of the relative density of the liquefiable soil. The slopes of the linear curves for IM|r_u that would be expected for a perfect IM would then be expected to increase with increasing relative density. The relationship between pore pressure ratio, relative density, and the intensity of the loading (expressed as an IM) can be displayed using a three-dimensional plot as shown in Figure 6.38a.

The process used to evaluate the efficiency of a generic evolutionary IM is illustrated schematically in Figure 6.38. A three-dimensional plot of the evolutionary IM as a function of r_u and relative density for a single test is shown in Figure 6.38a. With additional tests that span a range of densities, all of the results can be plotted together, as shown in Figure 6.38b. Efficiency can be evaluated by fitting a three-dimensional surface to the data and examining the residuals between the measured and predicted values. An example of a surface fit to the schematic data is shown in Figure 6.38c. An alternative way to view the three-dimensional surface formed by the IM-r_u-D_r relationship is to look at a plot of the IM as a function of D_r for various contours of constant r_u, as shown in Figure 6.38d. In Figure 6.38d the fitted values are shown as the solid lines. The two-dimensional representation is analogous to the liquefaction resistance curves from the various simplified procedures described in Section 2.3.3.1, where the value of the IM required to trigger liquefaction (r_u=1.0) is plotted as a function of a parameter to describe the initial state of the soil.

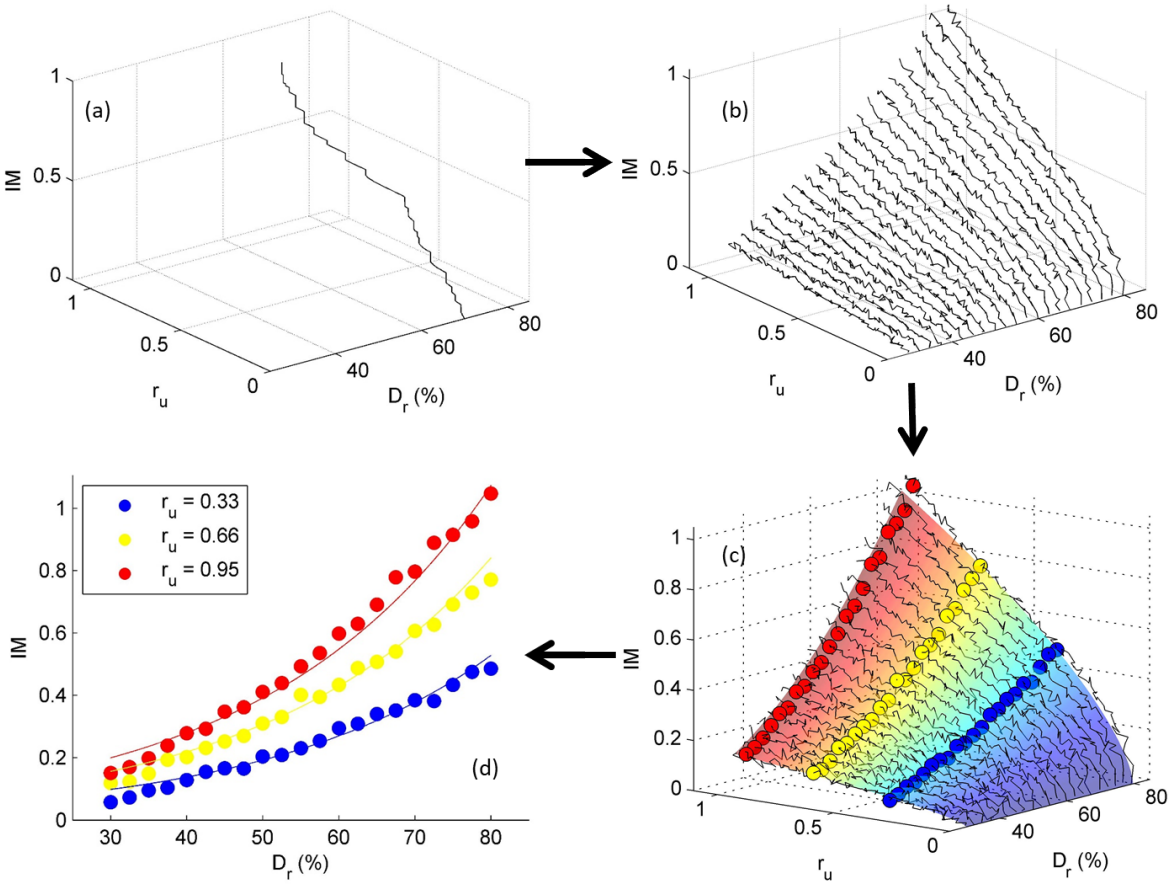


Figure 6.38: Schematic of hypothetical experimental data analysis to illustrate the proposed method.(a) Example of an evolutionary IM as a function r_u and of relative density for a single test. (b) Additional tests are performed at various relative densities. (c) IM-Dr relationship is investigated at various levels of pore pressure by looking at "slices" of the data to produce the relationships shown in (d), the dispersion in these relationships can be used to evaluate the efficiency of the IM given r_u across a range of relative densities and r_u amplitudes

The form of the IM-D_r-r_u surface function was assumed to be the product of a function that accounts for the relative density of the soil, f(D_r), and a function based on the given r_u level, f(r_u), such that,

$$IM = f(D_r) \cdot f(r_u) \tag{6.20}$$

The functional form of f(D_r) was assumed to be an exponential function,

$$f(D_r) = \beta_1 \cdot \exp(\beta_2 \cdot D_r) \tag{6.21}$$

This functional form was selected because it is simple and provides a reasonable approximation to the IM-D_r curves used in each of the simplified liquefaction triggering procedures calibrated against case history data presented in Section 2.3.3.1. However, no such guidance exists for the

form of $f(r_u)$ for transient loading histories. The following section discusses the development of the functional form for $f(r_u)$.

6.5.1.2 Development of the Relationship between IM Versus Pore Pressure Ratio

The parameter r_u is bounded between the values of 0 and 1.0, therefore the function $f(r_u)$ needed to be such that $f(r_u) = 0$ at $r_u = 0$ and $f(r_u) = 1$ at $r_u = 1$ so that the surface function starts at a value of 0 and converges to the liquefaction triggering curve at the initiation of liquefaction. To determine the functional form of $f(r_u)$, the Equations 6.20 and 6.21 were combined and rearranged such that,

$$IM = f(D_r) \cdot f(r_u) \rightarrow f(r_u) = \frac{IM}{f(D_r)} = \frac{IM}{\beta_1 \cdot \exp(\beta_2 \cdot D_r)} \qquad 6.22$$

The values for β_1 and β_2 were determined by fitting the IM-D_r relationship at the initiation of liquefaction (assumed to be at $r_u = 0.99$) for each of the standard IMs discussed previously. The results of this analyses are presented in Figure 6.39. Each plot shows the value of the given IM at liquefaction for each test, and each individual test is identified using the reference number listed in 6.3. The fit result is shown in the lower right-hand corner of each plot. The results shown in Figure 6.39 confirmed that the general form for $f(D_r)$ could suitably capture the IM-D_r response. However, these initial results showed that Test 8 was a significant outlier for PGA_{mL}, I_A, CAV, and CAV_5, but the same test was not an outlier for PGA_{mB}. The single outlier did not impact the decisions made with respect to the functional form of the IM-D_r-r_u surface function, so it was included in the analyses presented in this section. A further discussion regarding that test is provided in Section 6.5.2.

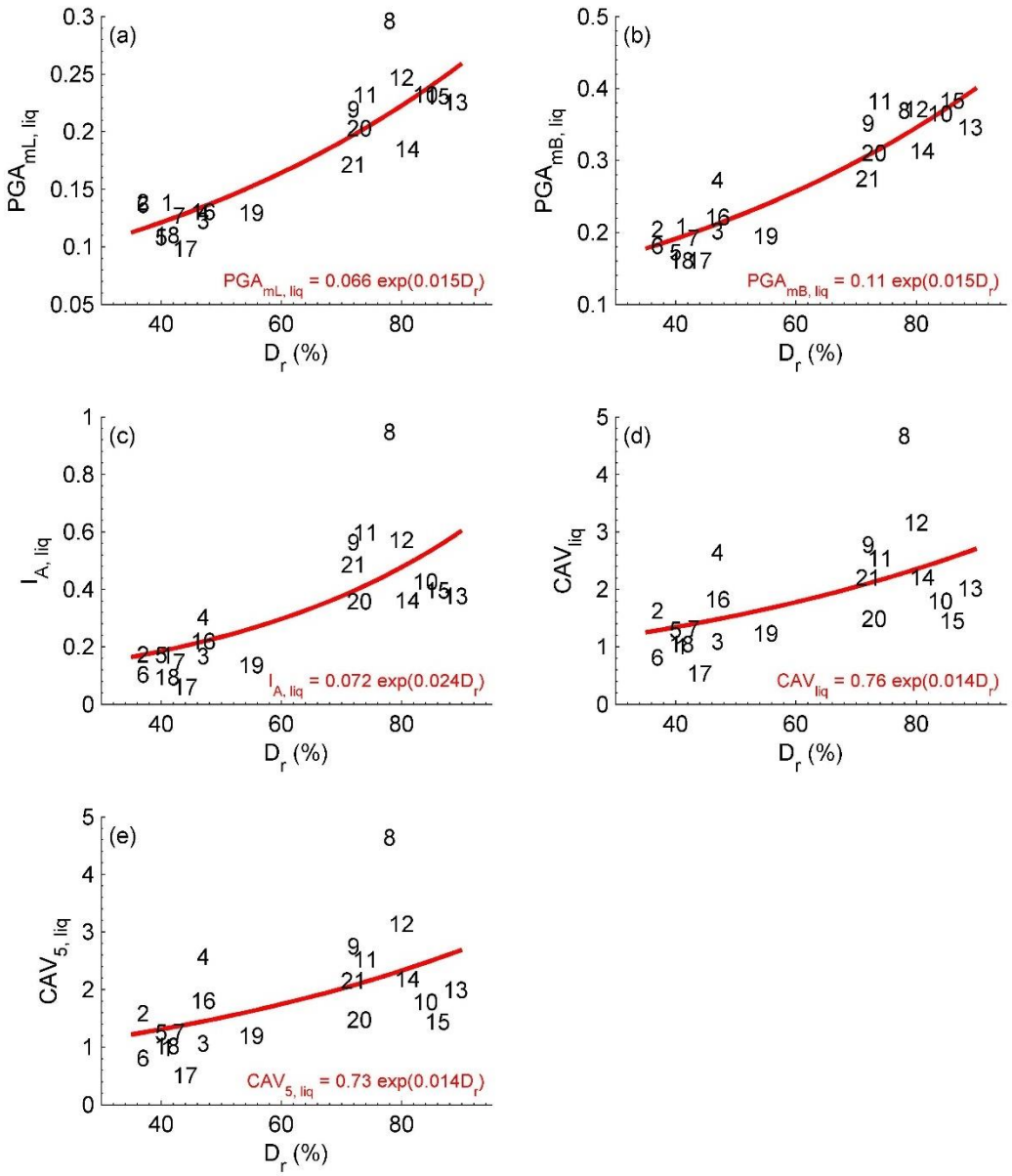


Figure 6.39: IM-D_r fit at the time of liquefaction (r_u = 0.99) for the Standard IMs(a) PGA_{mL}, (b) PGA_{mB}, (c) I_a, (d) CAV, and (e) CAV_5. The fitted IM-D_r relationship is provided in the lower right-hand corner of each plot. The numbers indicate the test reference ID.

Using the results of the IM-D_r fit at the time of liquefaction (Figure 6.39), the function presented in Equation 6.22 was plotted to investigate the form of $f(r_u)$. So that the surface fit was not affected be extremely low values of r_u, values below 0.05 were not considered in this study. The results are shown in Figure 6.40 for each of the standard IMs.

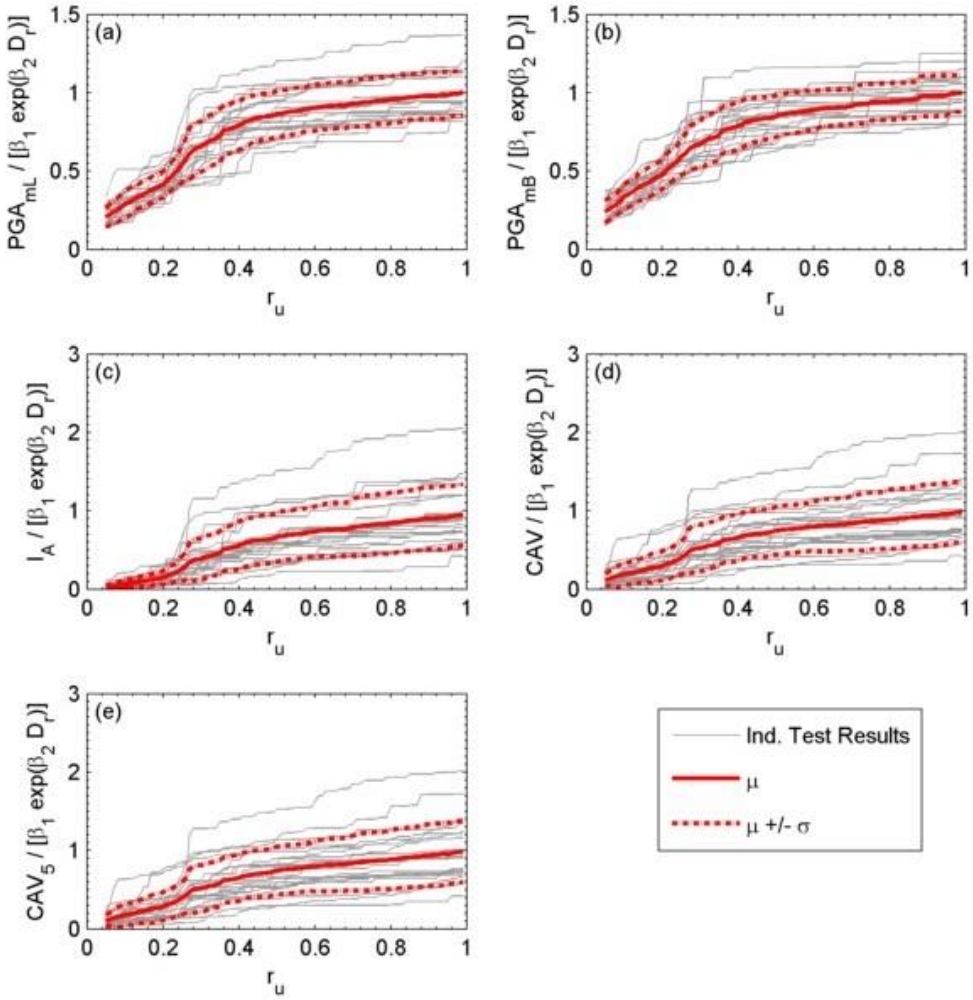


Figure 6.40: Investigation of the shape of the r_u function based on the evolutionary IM normalized by an initial estimate of the IM at the time of liquefaction (Equation 6.22) for the standard IMs(a) PGA_{mL}, (b) PGA_{mB}, (c) I_a, (d) CAV, and (e) CAV_5. The individual test data is shown in grey and the average and standard deviation are provided in red.

For a perfect IM, the shapes of the normalized IM vs. r_u relationship would be linear. However, as shown in Figure 6.40, the shape of the normalized IMs vs. r_u curves for each of the standard IMs were generally sigmoidal with an inflection point at around $r_u = 0.3$. In addition, the rate of increase in normalized IM tended to decrease with increasing r_u for each of the IMs. This rate increase is attributed to phase transformation behavior. As discussed in Section 6.3 with the harmonic loading, phase transformation behavior dramatically alters the relationship between the loading history and the corresponding pore pressure response.

An example of phase transformation behavior using a transient loading history is provided in Figure 6.41 for Test 130925 (Ref. ID. 19). In this test, the initial low amplitude

cycles applied in the first eight seconds of the record generated negligible amounts of excess pore pressure. The local peak at 8.5 seconds had an amplitude of about 8 kPa (CSR = 0.08), which was significantly greater than the PPA, and resulted in an increase in r_u of approximately 0.1. Subsequent cycles between 9 and 28 seconds into the record (light blue to the green-yellow transition) were did not exceed the PPA and generated comparably less excess pore pressure due to the shielding effect discussed previously. Between 28 and 31 seconds into the record (yellow), larger pulses that exceeded the PPA (with amplitudes of approximately 13 kPa or CSR = 0.13) were applied and the rate of pore pressure generation again increased. The pulses applied between 31 and 32 seconds into the record (light orange) had relatively significant amplitudes of approximately 11 kPa, however, these amplitudes were less than the PPA and the pore pressure response was negligible. At 32.5 seconds a downward pulse with an amplitude of 20 kPa (CSR = 0.2) was applied, which was followed by an upward pulse with a similar amplitude. This cycle was significantly larger than the PPA at this time and this cycle led to an increase in r_u of approximately 0.2. In addition, phase transformation behavior was initiated during the upward (positive) pulse, as seen by the closed loop in the stress-path response when the vertical effective stress was just below 60 kPa. Note that the pulses before (28 to 32 seconds, yellow to orange) and after (33.5 to 37 seconds, orange to red) the peak stress cycle that induced phase transformation behavior had similar amplitudes, but the increments of excess pore pressure generated by each were dramatically different. The eight pulses applied between 28 to 32 seconds had amplitudes between 6 and 13 kPa (CSR = 0.06 to 0.13) and generated a cumulative increase in r_u of only about 0.125, while the five pulses applied between 33.5 and 37 seconds had amplitudes between 10 and 13 kPa (CSR = 0.1 to 0.13) and generated an increase in r_u of approximately 0.5.

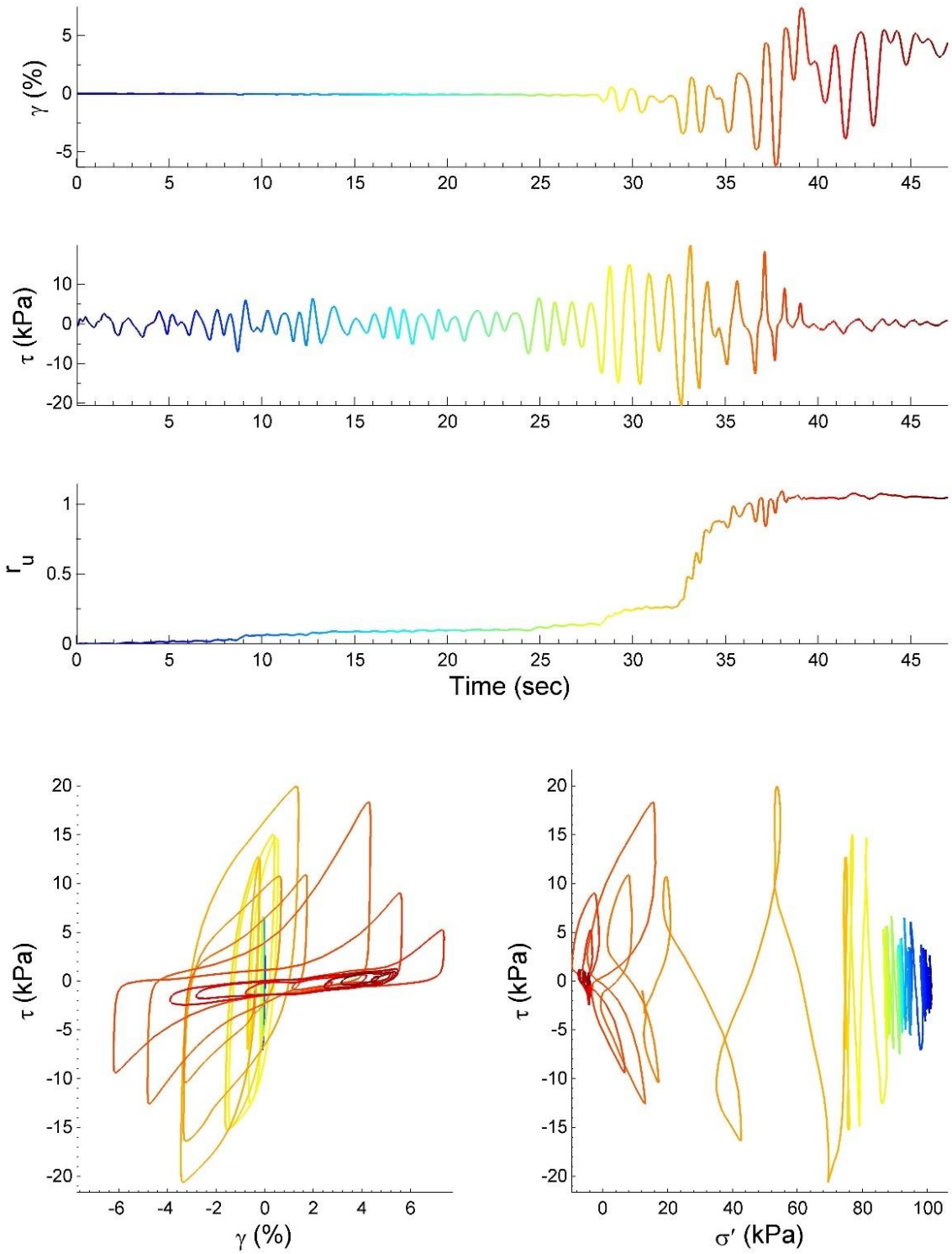


Figure 6.41: Results from a transient CSS test 130925.The upper three plots show the shear strain, shear stress and excess pore pressure time histories, respectively. The lower plots show the stress-strain and stress path response of the sample. Color changes with time for each plot. Note the dramatic change in behavior after phase transformation, observed at approximately 34 seconds into the time history.

Figure 6.42 illustrates how phase transformation behavior impacts the IM-r_u relationship and shows plots of the acceleration, r_u, and standard IM time histories for the same test shown in Figure 6.41 (Test 130925). The lower left plot in Figure 6.42 shows the response of each of the standard intensity measures normalized by the peak value (Norm. IM) as a function of r_u, and the lower right plot shows the stress path. All of the normalized IMs showed similar behavior with respect to r_u – the IMs increased at a relatively constant rate with r_u prior to the initiation of phase transformation behavior which occurred at an r_u level of about 0.4 in the given test. After phase transformation behavior was initiated at approximately 33 seconds into the record, r_u increased at a much faster rate than any of the normalized IMs. None of the IMs were able to capture the rapid increase in excess pore pressure generation due to phase transformation and, as a result, the rate of increase in the IMs was modest compared to the increase in r_u during that portion of the test. This behavior is shown in the normalized IM vs r_u figure as the relatively flat portion of the curves at high r_u levels. This post-phase transformation behavior was consistent for all tests and all the standard IMs.

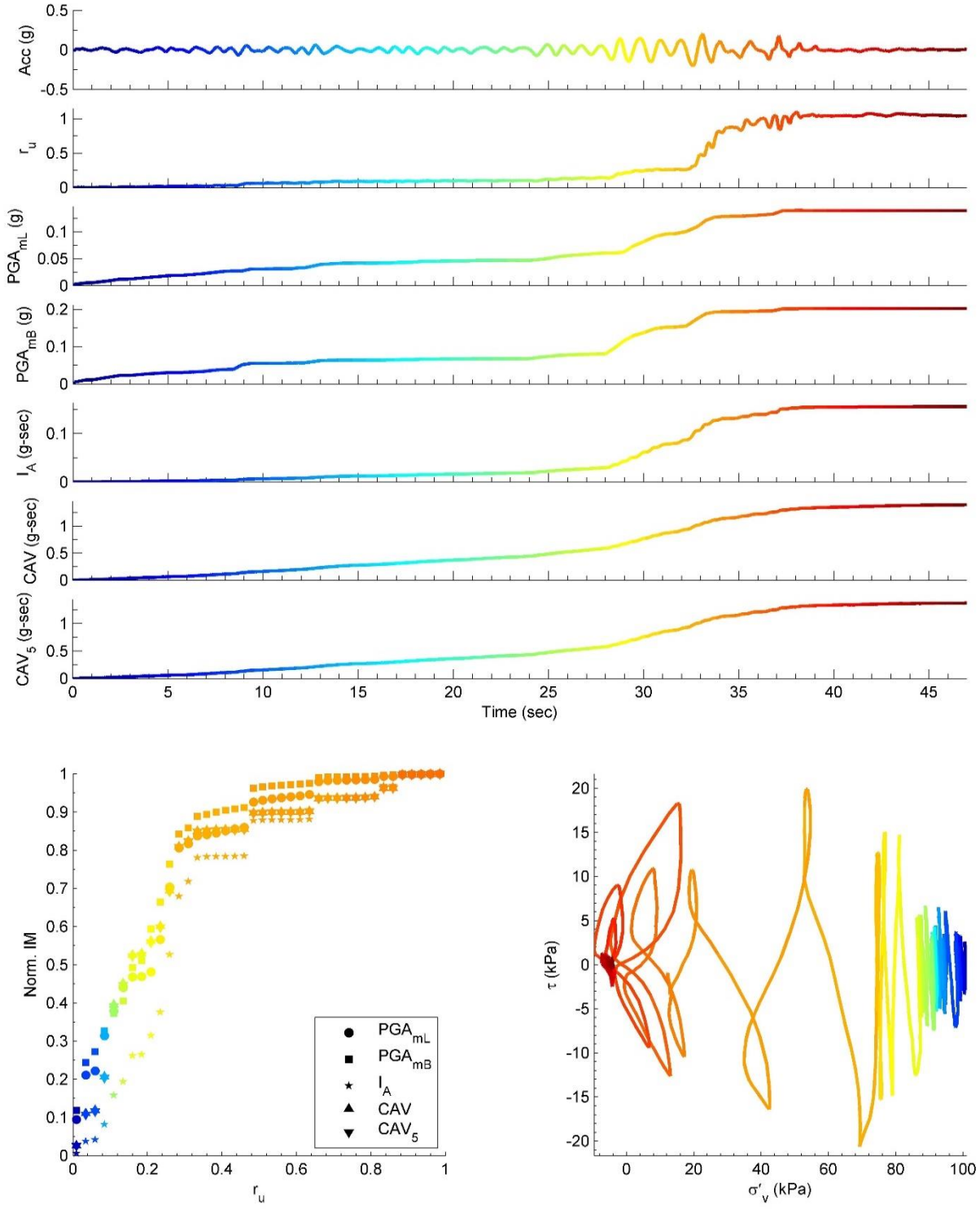


Figure 6.42: Results from Test ID 130925 (Test 18) showing the acc, r_u, and standard IM time histories, a plot of the normalized standard IM vs r_u, and the stress path.All plots are colored with respect to time.

Based on the shape of the normalized IM-r_u relationship provided in Figure 6.40, the functional form of $f(r_u)$ was approximated as,

$$f(r_u) = \frac{1 + \alpha_1}{1 + \alpha_1 \cdot r_u^{\alpha_2}} \qquad 6.23$$

where α_1 and α_2 are constants. This function was selected because it was reasonably simple, converged to values of 0 and 1 at r_u values of 0 and 1, respectively, and had a flexible shape that could approximate a wide range of behavior. Figure 6.43 shows the same results as provided in Figure 6.40, but includes the results of the $f(r_u)$ fit from Equation 6.23 to the mean of the data. The results provided in Figure 6.43 show that the assumed r_u function could provide a reasonable fit to the observed response.

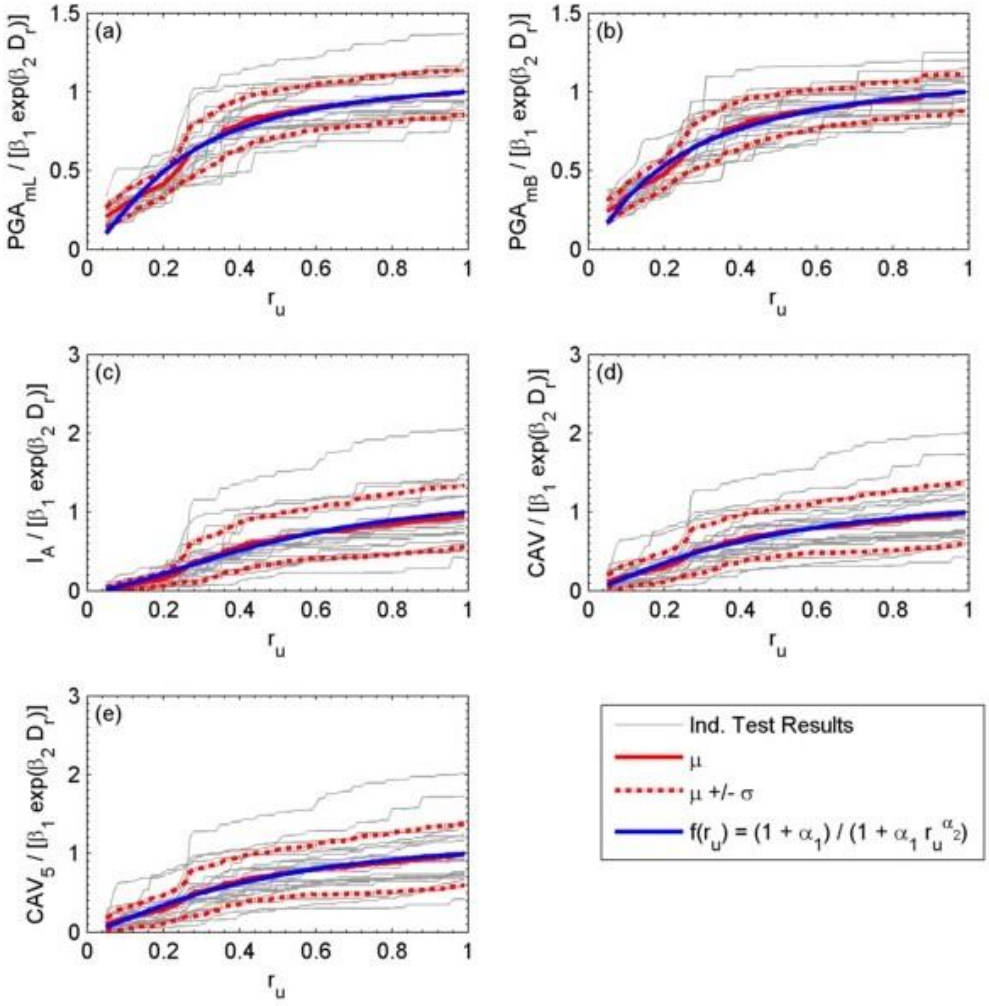


Figure 6.43: Investigation to the shape of the r_u function based on IM normalized by an initial estimate of the IM at the time of liquefaction (Equation 6.22) with a fit provided in Equation 6.23 shown for (a) PGA_{mL}, (b) PGA_{mB}, (c) I_a, (d) CAV, and (e) CAV_5

Substituting Equations 6.23 and 6.21 into 6.20 yields the final form of the IM-D_r-r_u equation

$$IM = \beta_1 \cdot \exp\left(\beta_2 \cdot D_r\right) \frac{1 + \alpha_1}{1 + \alpha_1 \cdot r_u^{\alpha_2}} \qquad 6.24$$

The functional form summarized in Equation 6.24 was relatively simple, versatile, and effectively captured the IM-D_r-r_u response at levels above r_u greater than 0.05, which are the r_u levels of engineering interest. In this study the efficiency of a given IM was evaluated based on the uncertainty in the IM = f(D_r, r_u) relationship shown in Equation 6.24. As discussed previously, this definition is due to how uncertainty is propagated through each step of the timing-based framework as presented in Section 4.5.

To evaluate the efficiency of the standard IMs to predict the pore pressure response, the surface fit described in Equation 6.24 was determined using non-linear least squares estimation (i.e. Weisberg, 2005) implemented using the `fit` function in MATLAB. Since the purpose of this study is to determine optimal evolutionary IMs to predict the triggering of liquefaction, only the portion of the time history up to the initiation of liquefaction was used in the curve fitting process. In this study, liquefaction was assumed to be triggered once the recorded r_u exceeded 0.99.

6.5.2 *Results of Surface Fitting Using Standard Intensity Measures*

The results of the surface fitting are summarized in Figures 6.44 through 6.48. The figures show plots of the computed and fitted IM values, a histogram of the residuals, denoted as ε (computed with respect to natural log of the given IM minus the natural log of the fitted IM), the IM versus D_r contour at liquefaction, the normalized IM versus r_u, and ε as a function of D_r and r_u. The efficiency of a given IM to evaluate the generation of pore pressure was evaluated using the standard deviation of the natural log residuals, σ_ε. The computed values of σ_ε are summarized in Table 6.4 and are also provided in the upper left-hand corner of the histogram plots shown in the surface fitting summary figures. The analysis showed that the two PGA_m formulations performed significantly better than the three integral based IMs. Of the PGA_m formulations, PGA_{mB} performed better than PGA_{mL}. The σ_ε for the integral IMs ranged from 0.58 to 0.82.

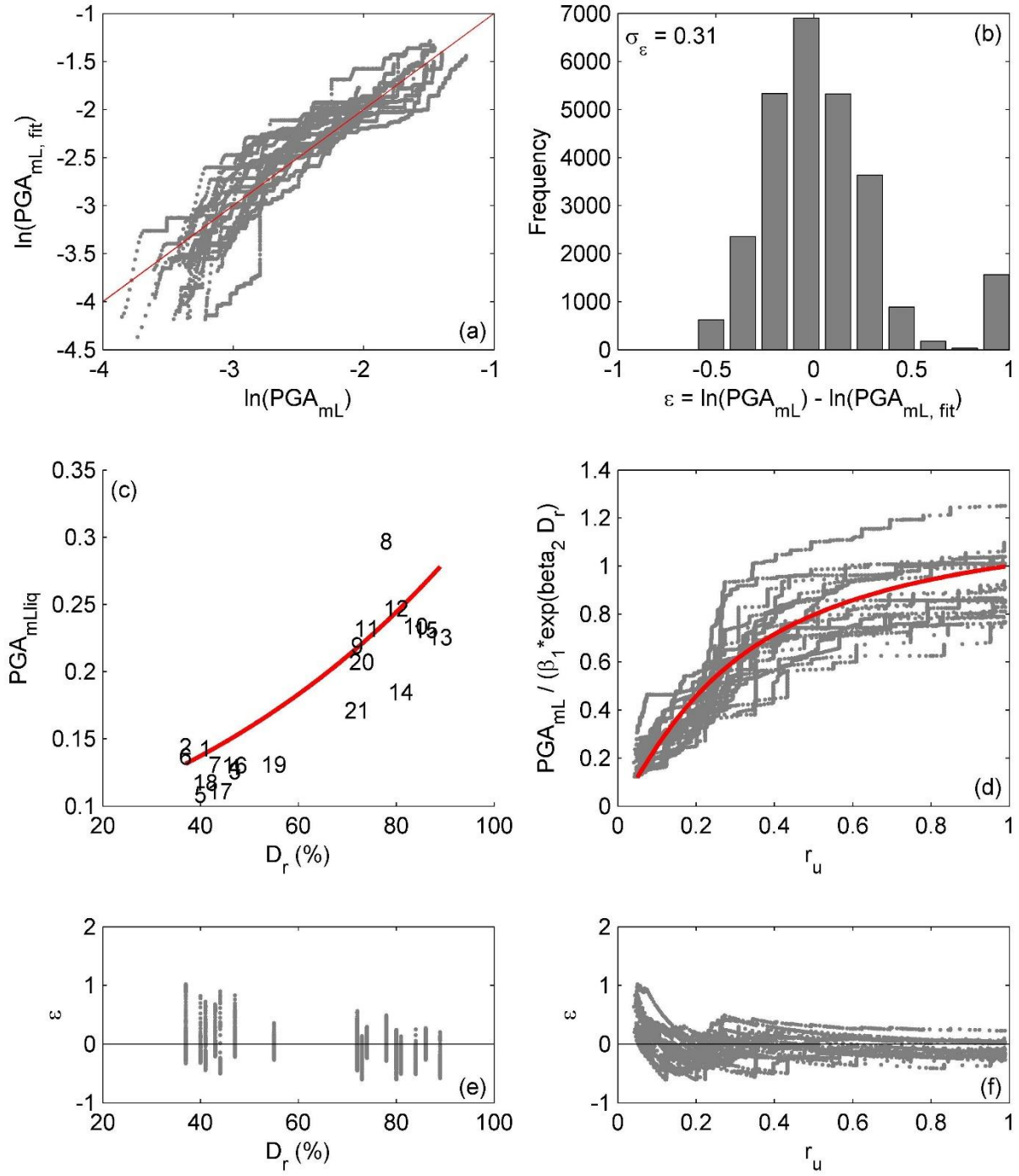


Figure 6.44: Summary of the surface fit results of PGA_{mL}(a) plot of the fitted and computed IM values, (b) histogram of the log residuals, (c) IM vs D_r contour at the initiation of liquefaction, (d) plot of the r_u function vs. IM normalized by $f(D_r)$, (e) the log residuals vs relative density, and (f) the log residuals vs. r_u.

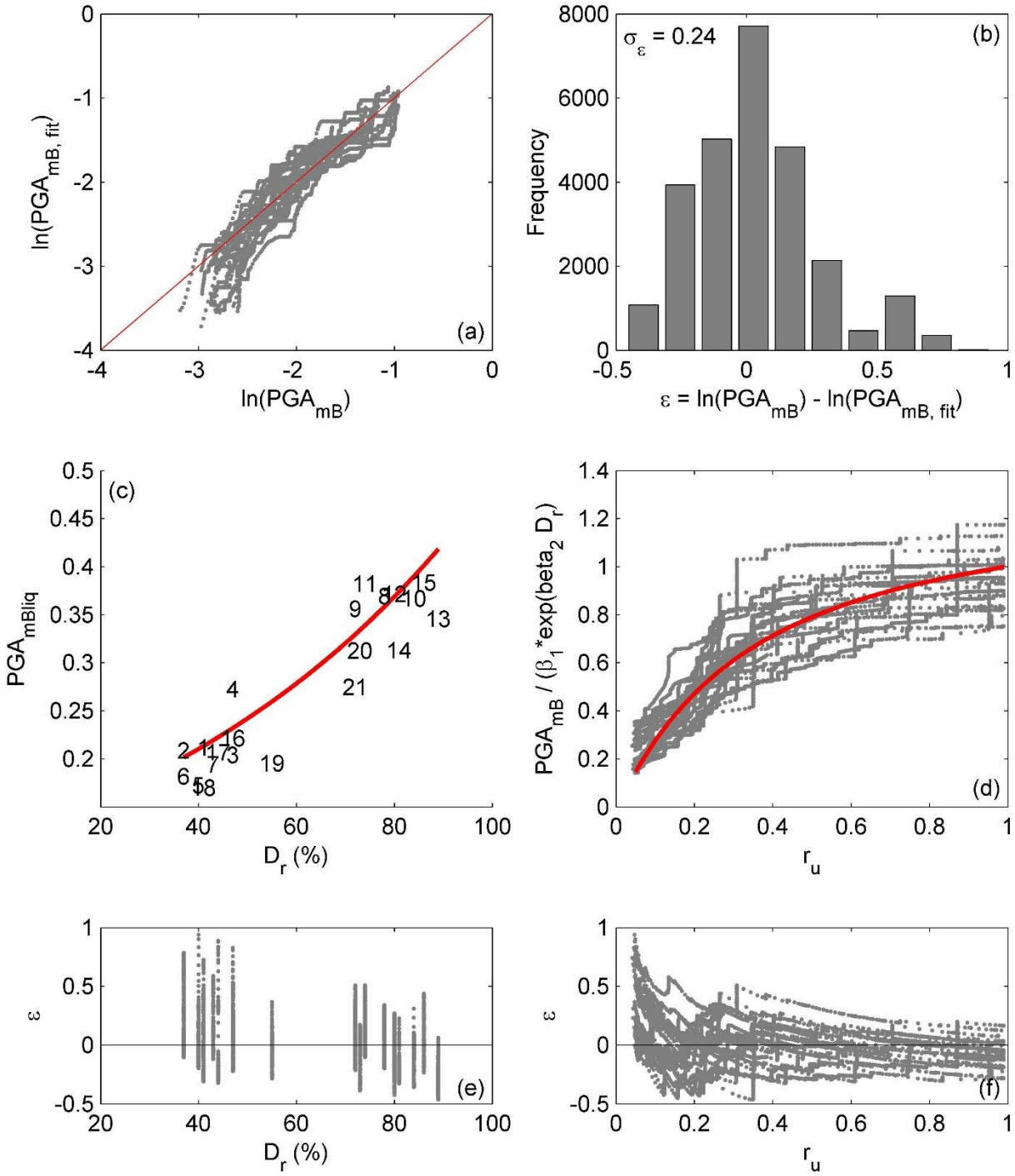


Figure 6.45: Summary of the surface fit results of PGA_{mB}(a) plot of the fitted and computed IM values, (b) histogram of the log residuals, (c) IM vs D_r contour at the initiation of liquefaction, (d) plot of the r_u function vs. IM normalized by $f(D_r)$, (e) the log residuals vs relative density, and (f) the log residuals vs. r_u.

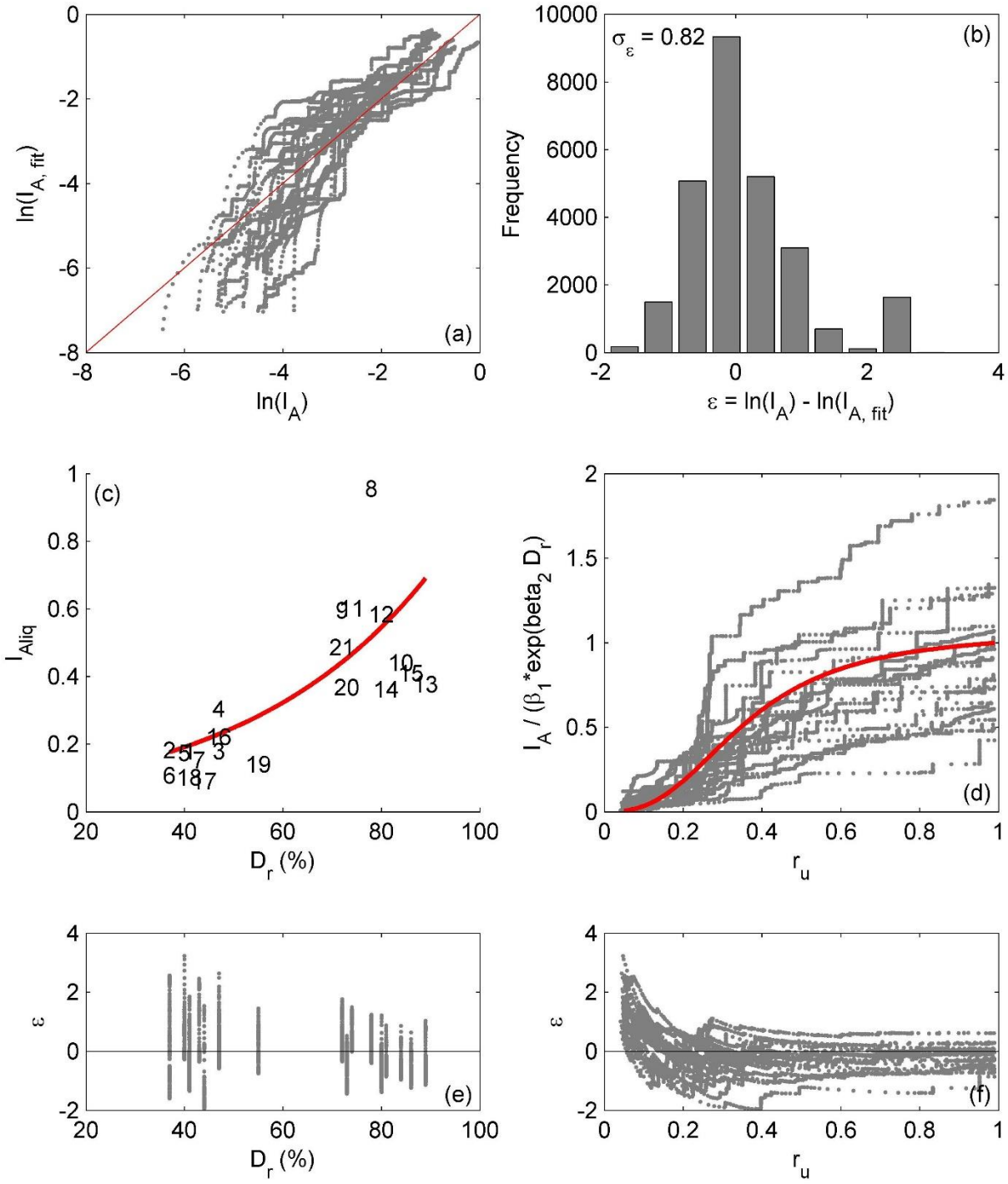


Figure 6.46: Summary of the surface fit results of I_A(a) plot of the fitted and computed IM values, (b) histogram of the log residuals, (c) IM vs D_r contour at the initiation of liquefaction, (d) plot of the r_u function vs. IM normalized by f(D_r), (e) the log residuals vs relative density, and (f) the log residuals vs. r_u.

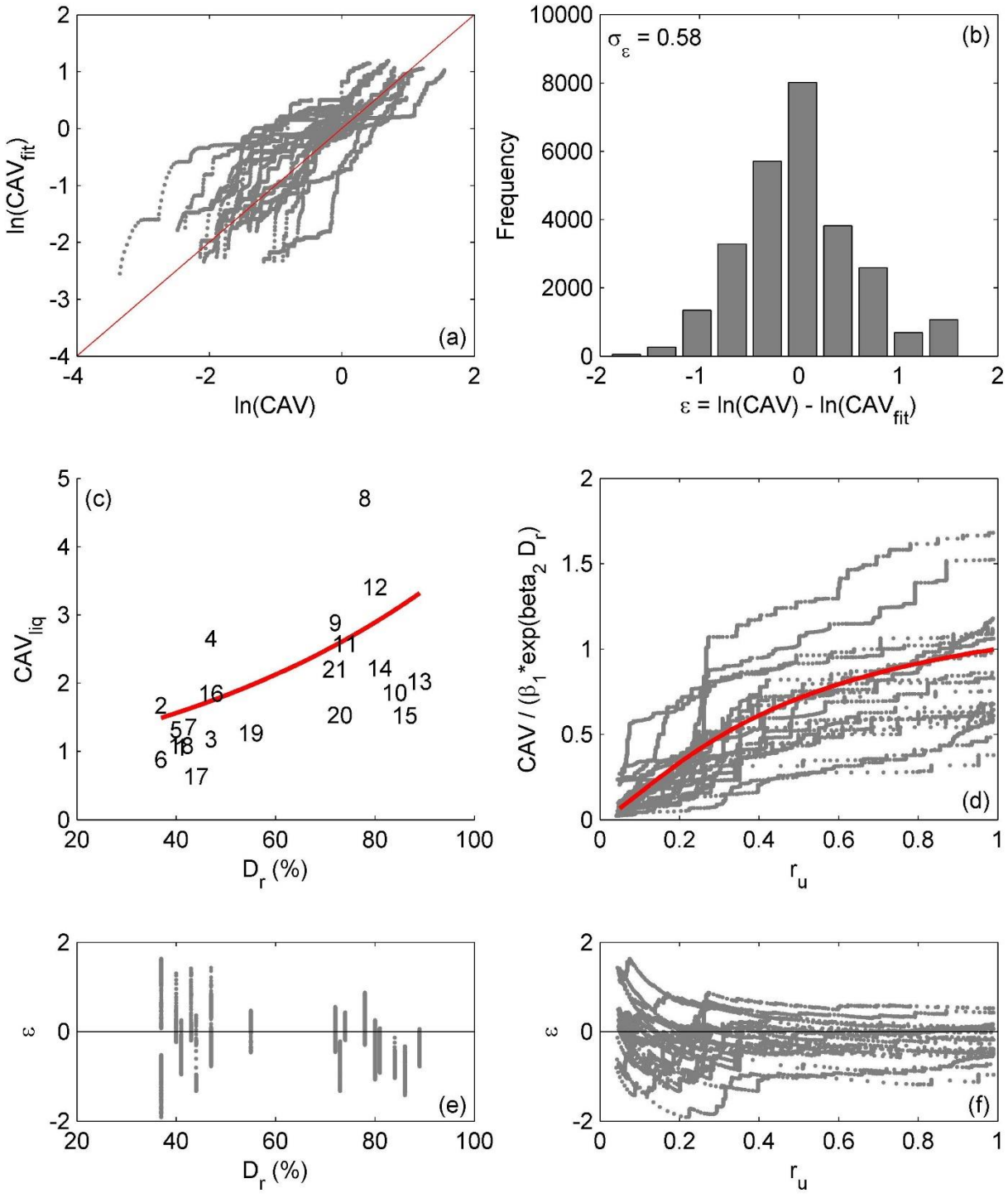


Figure 6.47: Summary of the surface fit results of CAV(a) plot of the fitted and computed IM values, (b) histogram of the log residuals, (c) IM vs D_r contour at the initiation of liquefaction, (d) plot of the r_u function vs. IM normalized by $f(D_r)$, (e) the log residuals vs relative density, and (f) the log residuals vs. r_u.

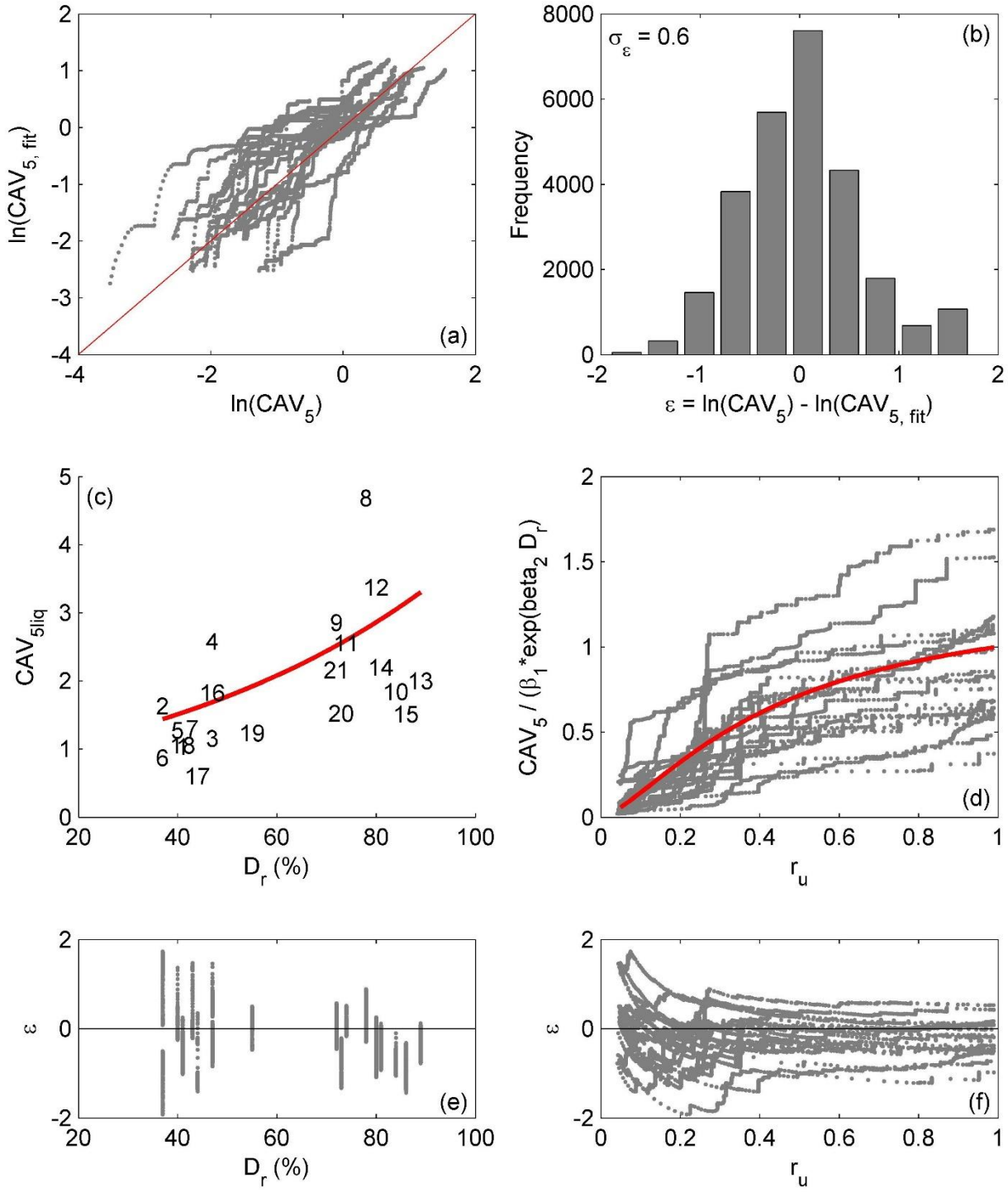


Figure 6.48: Summary of the surface fit results of CAV_5(a) plot of the fitted and computed IM values, (b) histogram of the log residuals, (c) IM vs D_r contour at the initiation of liquefaction, (d) plot of the r_u function vs. IM normalized by $f(D_r)$, (e) the log residuals vs relative density, and (f) the log residuals vs. r_u.

Table 6.4: Standard deviation of the log residuals, σ_ε, for each of the five standard IMs computed using the fit for r_u values ranging from 0.05 to 0.99.

IM	σ_ε
PGA_{mL}	0.31
PGA_{mB}	0.24
I_A	0.82
CAV	0.58
CAV_5	0.6

As noted previously, the cycle counting-based PGA_m formulations performed better than the integral-based IMs. One of the main distinctions between a cycle counting-based IM and an integral IM is that the cycle counting-based IMs are independent of the frequency of the loading, while the integral-based IMs are significantly influenced by the frequency content of the loading history. As shown by Riemer et al. (1994), liquefaction resistance is independent of frequency over the range of frequencies of interest in earthquake engineering. An IM that is influenced by aspects of the loading history that excess pore pressure generation is insensitive to will introduce additional uncertainty, which was reflected by large σ_ε values for the integral-based IMs, as shown in Table 6.4.

Another interesting observation from the standard IM results was that Test 130115 (Ref. No. 8) was a significant outlier for the integral IMs and PGA_{mL} but was not an outlier with respect to PGA_{mB}. The test results are shown in Figure 6.49. The initial portion of the loading, up until approximately 20 seconds into the loading history (transition from blue to light blue), included stress cycles that gradually increased in amplitude until a local peak of approximately 25 kPa (CSR = 0.25) was reached. During this period the PPA was being consistently exceeded as the loading amplitudes grew larger and the excess pore pressure ratio gradually increased to a value of approximately 0.3. This response was similar to the behavior observed in taper-up modulated harmonic tests. After the local peak, from 20 to 38 seconds into the record, the loading included significant stress cycles with amplitudes above 20 kPa (CSR = 0.2), however, these cycles contributed very little to the r_u response of the sample. This shielding effect, where cycles with shear stress amplitudes less than the PPA generated relatively little excess pore pressure, was also observed during the irregular and modulated harmonic tests. Between 38 and 44 seconds into the loading history the stress cycles exceeded the PPA and the excess pore

pressure again began to increase. During this time phase transformation behavior was observed. Subsequent large stress cycles that were applied beginning at 48 seconds into the record caused the excess pore pressure to increase rapidly until liquefaction was observed at approximately 55 seconds into the record. The behavior of this test was consistent with the observations from the harmonic test program. In addition, the stress path and stress-strain plots do not show any odd behavior or directional bias. Therefore, this test was not judged to be an outlier due to errors in sample preparation or malfunctions in the testing apparatus, but rather was an outlier due to inefficiencies in some of the standard IMs to capture important aspects of liquefiable soil behavior.

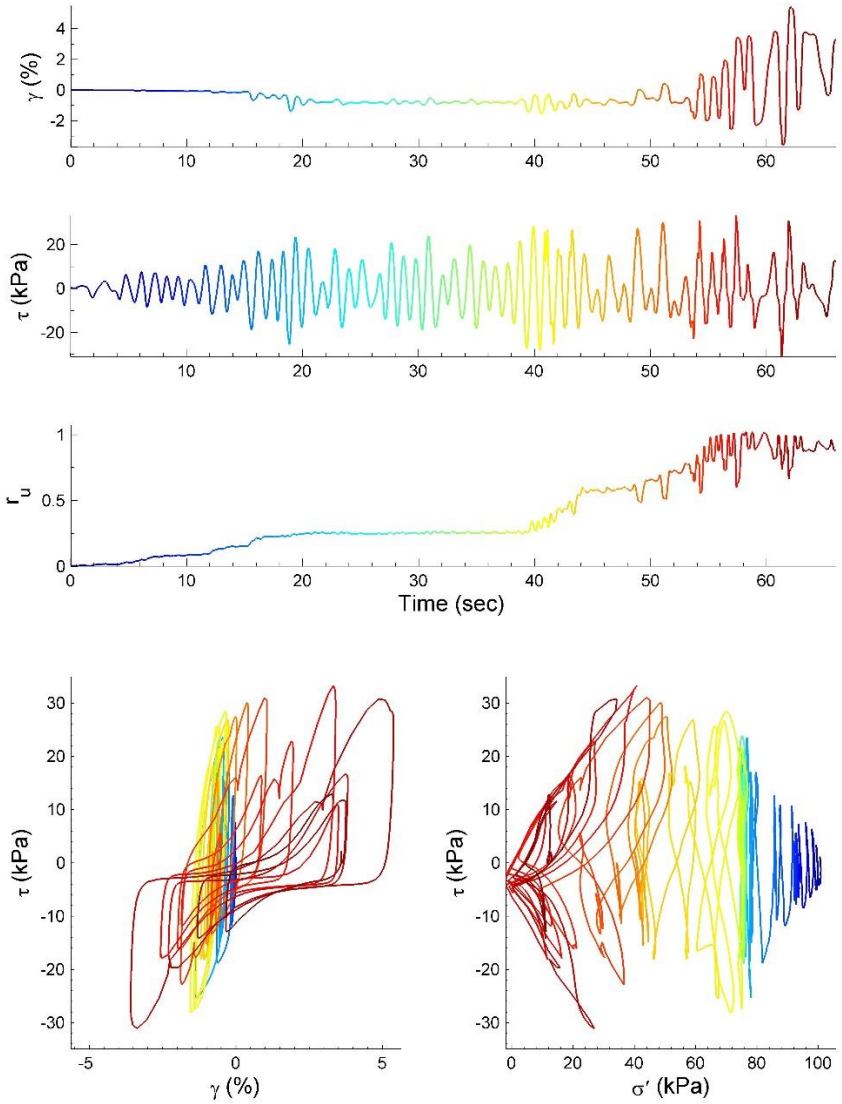


Figure 6.49: Summary response of Test 130711-02 (Ref. No. 8)with plots of the shear strain, CSR, and r_u time histories, stress path and stress-strain response. The lines in each plot are colored with respect to time.

Figure 6.50 compares the evolution of the most efficient cycle counting-based IM, PGA_{mB}, to the most efficient integral-based IM, CAV, for test 130711-02. Note the behavior of N and MSF (Figure 6.50d and e, respectively) include local dips when a new PGA value was encountered. This was because N was computed based on a reference amplitude equal to 65% of PGA. As the PGA increased the reference amplitude increased and the corresponding number of equivalent cycles decreased. These local drops are reflected in the MSF time history that is computed using N. However, as shown in Figure 6.50e, PGA_{mB} computed as the PGA divided by MSF was constantly increasing, this was because the small momentary drops in MSF were counteracted by the increase in PGA. The general shape of PGA_{mB} was similar to the shape of the evolutionary PGA. However, PGA_{mB} increased during the constant PGA portions of the record due to the accumulation of N. CAV on the other hand, was observed to increase at a nearly linear rate over the duration of loading.

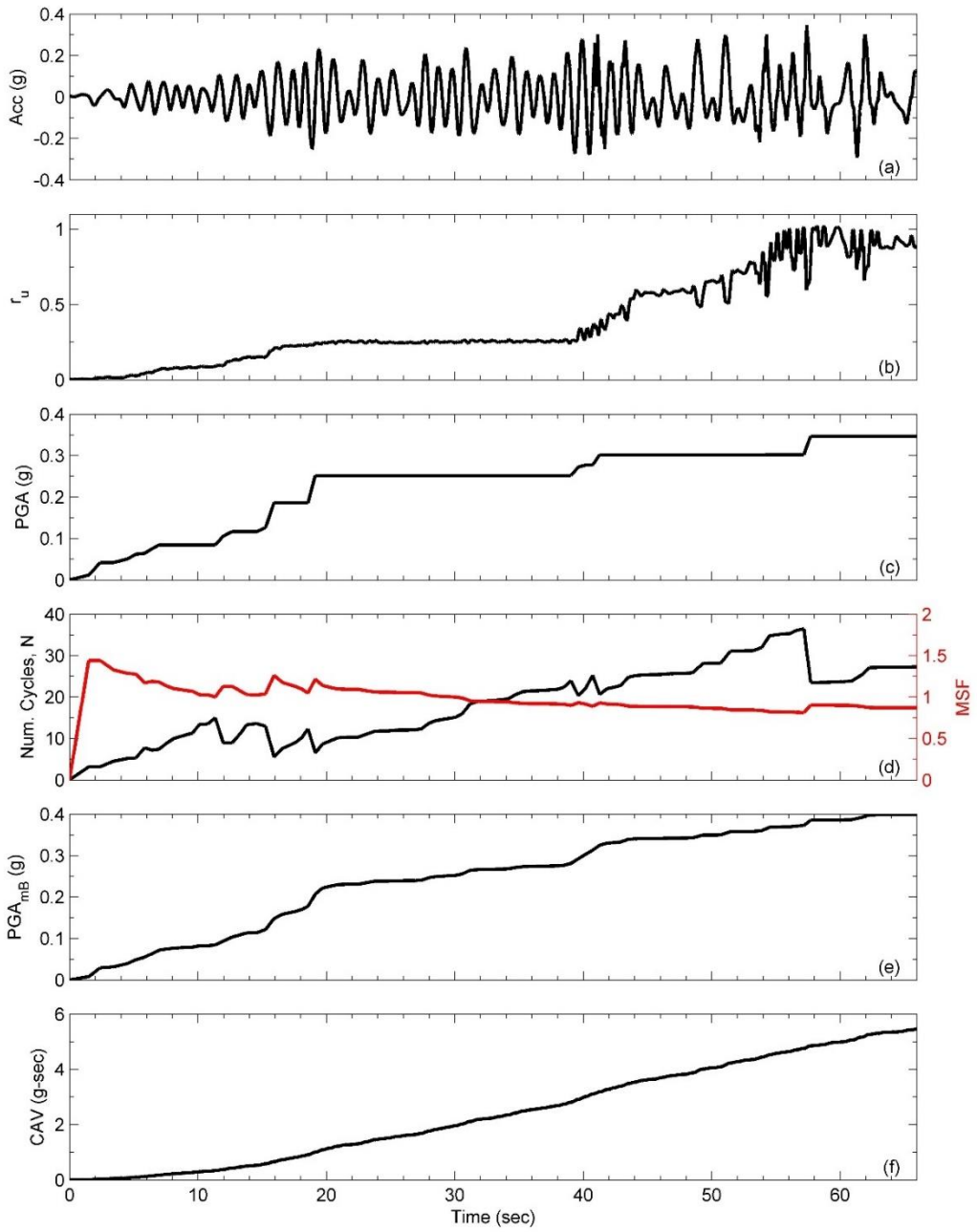


Figure 6.50: Summary of the acceleration and IM behavior for Test 130711-02(a) acceleration, (b) r_u, (c) PGA, (d) number of cycles, N, and MSF, (e) PGA_{mB}, and (f) CAV time histories. PGA_{mB} was computed as the PGA divided by the MSF time histories shown in (c) and (d), respectively.

A further comparison between the r_u and IM time histories is provided in Figure 6.51. A plot of the r_u and the normalized PGA_{mB} and CAV time histories are provided in Figure 6.51a. Figure 6.51b, c, and d show plots of the rate of change for r_u, PGA_{mB}, and CAV, respectively. To compute the rate of change in r_u, the processed r_u time history (see Section 6.5.1.1) was smoothed using cubic smoothing spline fit with a smoothing parameter of 0.75 (e.g. 'csaps'

function in MATLAB). During the first 18 seconds of the time history, both IMs and r_u increase at relatively constant (but different) rates. Between 18 and 38 seconds the r_u plateaued, and the rate of change went to 0. While PGA_{mB} did not plateau to the same degree as the r_u time history, the rate of increase slowed significantly during this time. CAV on the other hand, continued to increase at a relatively constant rate. At approximately 38 seconds into the record the r_u time history showed a sudden increase that was also captured in the PGA_{mB} time history. The CAV time history showed an increase as well, although it was not as distinct as was observed in r_u and PGA_{mB}. At 48 seconds into the record the r_u time history began to increase rapidly due to phase transformation behavior, which was not reflected in PGA_{mB} or CAV.

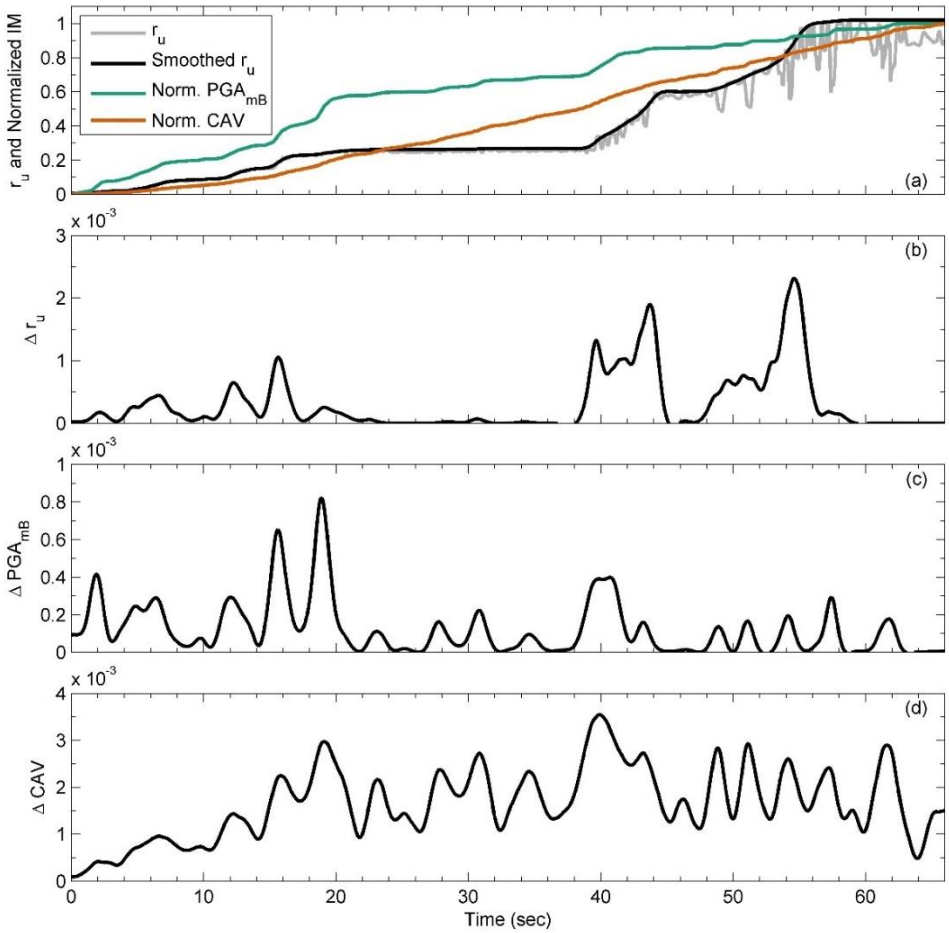


Figure 6.51: Rate of change of r_u, PGA_{mB}, and CAV for Test 130711-02(a) r_u, smoothed r_u, and normalized PGA_{mB} and CAV, and the rate of change of (b) r_u, (c) PGA_{mB}, and (d) CAV as a function of time.

6.5.3 *Efficiency of Standard Intensity Measures for Prediction of Initiation of Liquefaction*

While the ideal IM would be able to accurately predict an entire r_u time history, the goal of this research is to identify the most efficient IM for predicting the triggering of initial liquefaction, taken here as $r_u = 0.99$. When creating a surface fit over the entire range of r_u values, the predicted IM at the initiation liquefaction (plot c in Figures 6.44-6.48) was generally slightly larger than the observed values (see Figures Figures 6.44c-6.48c).

To determine the most efficient IM for predicting the triggering of liquefaction, regression analyses were performed based on the IM value taken at the initiation of liquefaction (denoted using the subscript liq) using the exponential function presented in Section 6.5.1. The results of these analyses are presented in Figure 6.52, which provides the fitted trend line. The efficiency of each fit is summarized using the standard deviation of the residuals computed using the difference between the natural logarithm of the IM and the natural logarithm of the fitted value, $\sigma_{\varepsilon,liq}$. The computed $\sigma_{\varepsilon,liq}$ value for each of the IMs are provided in the bottom right-hand corner of each plot shown in Figure 6.52 and are summarized in Table 6.5. The results provided in Figure 6.52 and Table 6.5 were in agreement with the findings from the evaluations that used the entire r_u time history, in that the two PGA_m formulations, PGA_{mL} and PGA_{mB} are much more efficient than the integral-based IMs at predicting the initiation of liquefaction, with PGA_{mB} having the lowest $\sigma_{ln,liq}$ value (0.12) of all the IMs. Each of the integral-based IMs performed similarly, and had $\sigma_{ln,liq}$ values between 0.37 and 0.39.

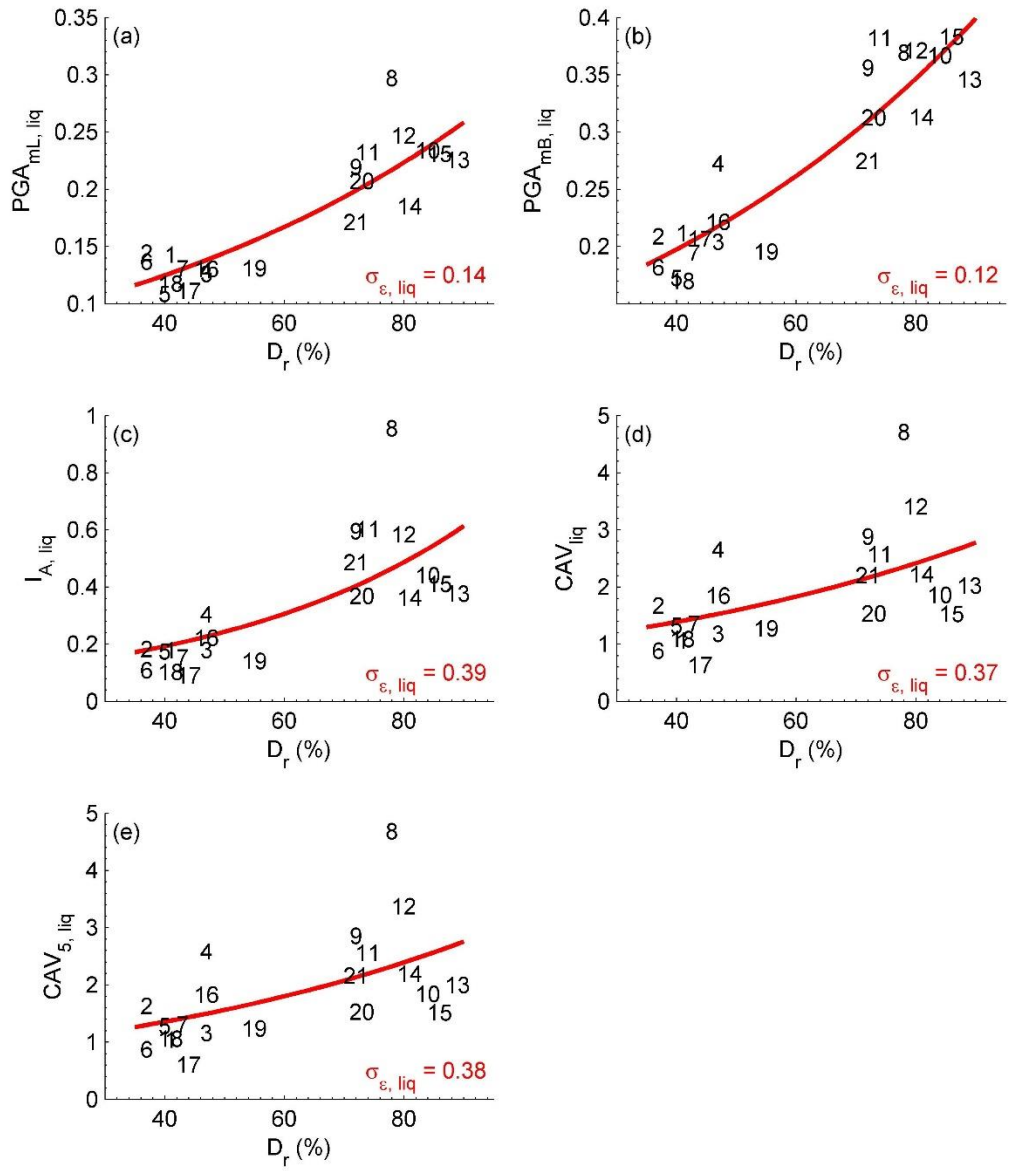


Figure 6.52: Measured and fitted values of (a) PGA_{mL}, (b) PGA_{mB}, (c) I_A, (d) CAV, and (e) CAV_5 at the initiation of liquefaction ($r_u = 0.99$) as a function of relative density.

Table 6.5: Standard deviation of the log residuals, σ_{ln}, for the IM-D_r fit at the initiation of liquefaction ($r_u = 0.99$) for each of the five standard IMs.

IM	$\sigma_{ln,\ liq}$
PGA_{mL}	0.14
PGA_{mB}	0.12
I_A	0.39
CAV	0.37
CAV_5	0.38

As noted in Sections 6.1.5.2 and 6.5.2 the relationship between the generation of excess pore pressure and the loading history were quite different before and after the onset of phase transformation behavior. Prior to phase transformation behavior, while the soil is in a contractive state, the excess pore pressure response is primarily a function of the loading history and behaves in a relatively predictable manner. However, after phase transformation behavior, the soil alternates between contractive and dilative behavior and the pore pressure response becomes a function of not only the loading history, but also the stress-path dependent soil response. An IM computed from an acceleration time history is unable to account for the change in behavior due to phase transformation and this aspect is a source of epistemic uncertainty inherent in the IM-D_r-r_u relationship.

Phase transformation behavior has been shown to dramatically increase the rate of excess pore pressure generation of the soil. The CSS test results showed that, once phase transformation behavior was initiated, samples would tend to liquefy after only a few additional cycles of loading. Therefore, it is reasonable to expect that IM value at the onset of phase transformation behavior and would be correlated to the IM value at the initiation of liquefaction. Since an IM is only capable of predicting the r_u response prior to phase transformation, one would expect that the most efficient IM for predicting the initiation of liquefaction would be the IM that is most efficient at predicting the onset of phase transformation behavior.

To test this theory, the time of the onset of phase transformation behavior was identified in each of the transient CSS tests as the time that dilation was first observed and the rate of excess pore pressure generation changed dramatically. Examples of how this time was evaluated were provided in the discussion related to Figures 6.41 and 6.49. Figure 6.53 shows the recorded r_u history plotted as a function of PGA_{mB} and CAV with the IM value at the onset of phase transformation behavior identified in each plot as red scatter points. The tests have been grouped into loose and dense tests using a cutoff relative density of 55%. The r_u was plotted on the y-axis to highlight the rapid increase in r_u relative to the increase in the IMs after the onset of phase transformation, as indicated by a near vertical response in $r_u|IM$. As shown in Figure 6.53, the relationship with relative density was most apparent for PGA_{mB}, where the relationship between IM and r_u were distinctly different between the loose and dense groups. This relationship was not as apparent in the plot for CAV. In addition, the PGA_{mB} appeared to be a better predictor of the initiation of phase transformation, which was initiated between PGA_{mB} values of 0.15 and 0.2 for

the loose tests and 0.22 to 0.32 for the dense tests. Similar observations could not be visually identified from the CAV plot.

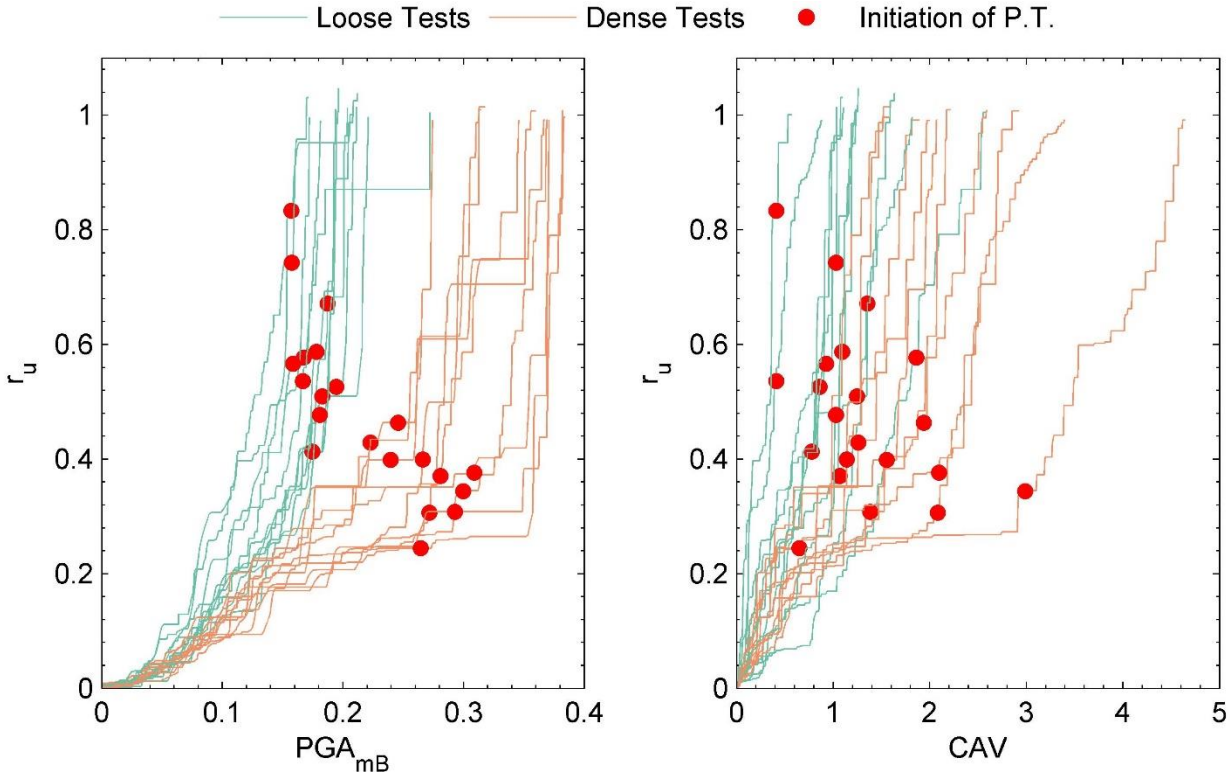


Figure 6.53: Relationship between r_u and PGA_{mB} and CAV with the time of initiation of phase transformation indicated as red scatterpoints.

The correlation between the IM value at the onset of phase transformation (IM_{PT}) and the IM value at the initiation of liquefaction (IM_{liq}) was evaluated as shown in Figure 6.54. For each of the standard IMs, IM_{liq} was found to be highly correlated with IM_{PT}, as indicated by the correlation coefficients which ranged from 0.90 to 0.94 (provided in Figure 6.54). This finding substantiates the theory that, since an IM based on the loading history alone is incapable of accurately accounting for the dramatic increase in the generation of excess pore pressure following liquefaction, an IM that can accurately predict the onset of phase transformation should be the most efficient IM at predicting the initiation of liquefaction.

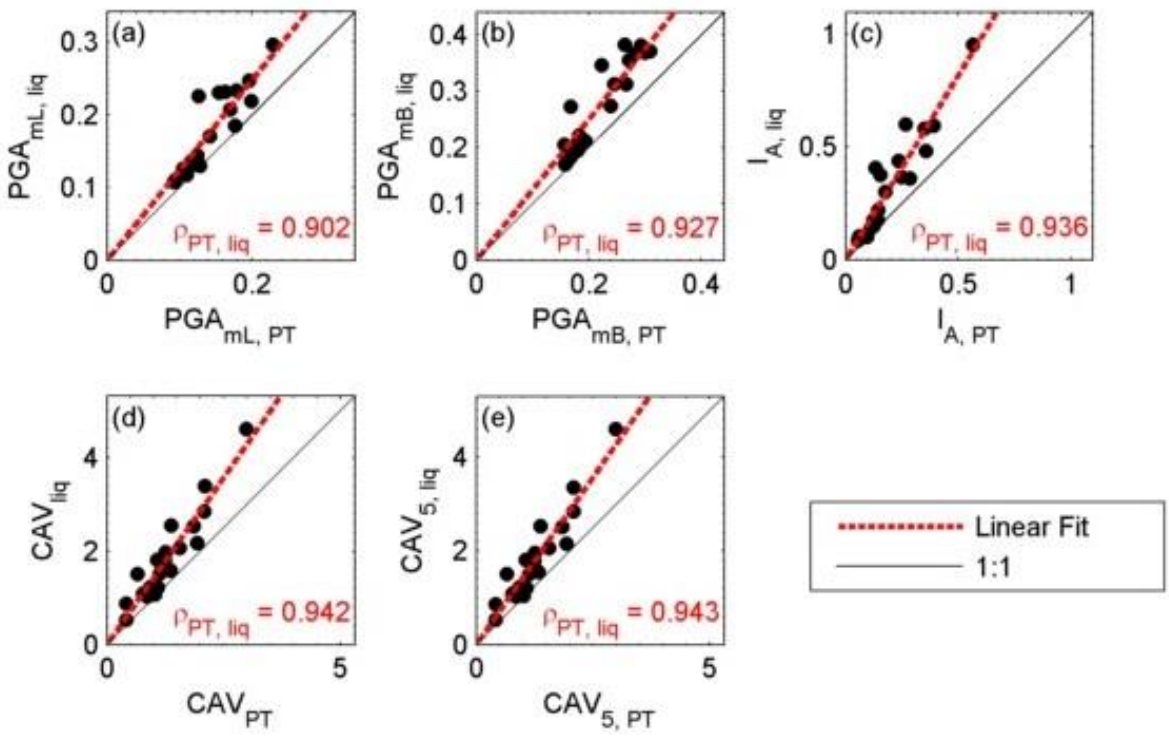


Figure 6.54: Correlation between the IM value at the onset of phase transformation and the IM value at the initiation of liquefaction for (a) PGA_{mL}, (b) PGA_{mB}, (c) I_A, (d) CAV, and (e) CAV_5

To investigate the dependence of the $IM_{liq}|IM_{PT}$ correlation on variables such as relative density and the loading history, a function of the form $IM_{liq} = c \cdot IM_{PT}$, was fit to the $IM_{liq}|IM_{PT}$ data. The residuals from this fit were plotted as a function of the relative density of the test and the magnitude of the loading that occurred between the onset of phase transformation behavior and the initiation of liquefaction. The loading magnitude was evaluated using the difference in the Husid parameter (Equation 6.3) computed at the onset of phase transformation (H_{PT}) and the initiation of liquefaction (H_{liq}). These results are shown in Figure 6.55, and indicate the residuals of $IM_{liq}|IM_{PT}$ are strongly related to both the relative density and the magnitude of the loading that occurs between the onset of phase transformation and the initiation of liquefaction. However, this result was not unexpected. The amount of loading that occurs between the onset of phase transformation and the initiation of liquefaction should be related to the residuals of the $IM_{liq}|IM_{PT}$ relationship, since IMs are computed based on the applied load. The density dependence can be explained by the relationship between relative density and the amount of loading between the onset of the phase transformation and the initiation of liquefaction, shown in Figure 6.56. In general, following the onset of phase transformation, loose soils required less

additional loading before initial liquefaction was observed than dense soils, which is consistent with our general understanding of liquefiable soil behavior.

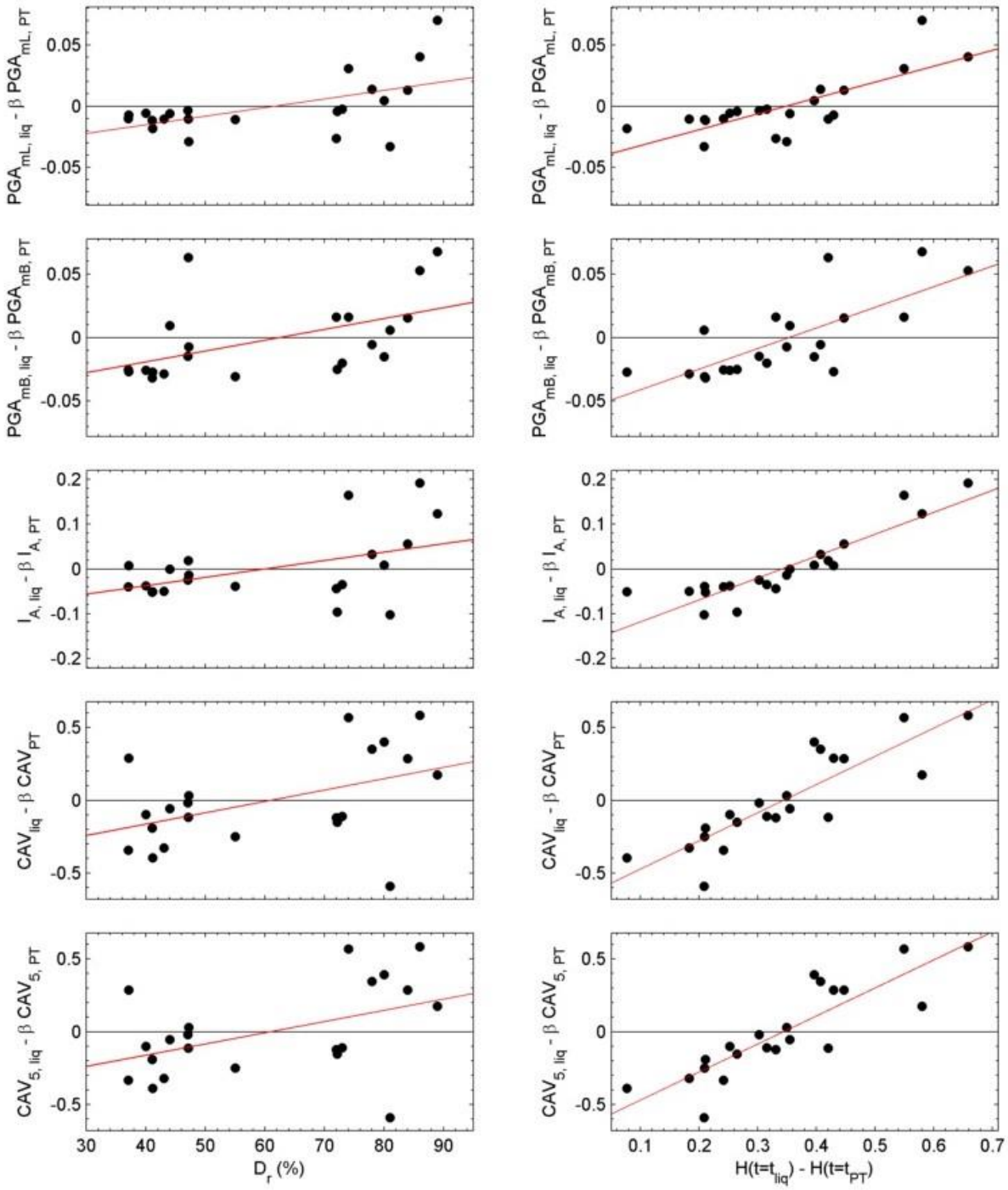


Figure 6.55: Residuals of the $IM_{liq}|IM_{PT}$ fit as a function of relative density and the difference in the Husid parameter between the onset of phase transformation and the initiation of liquefaction.

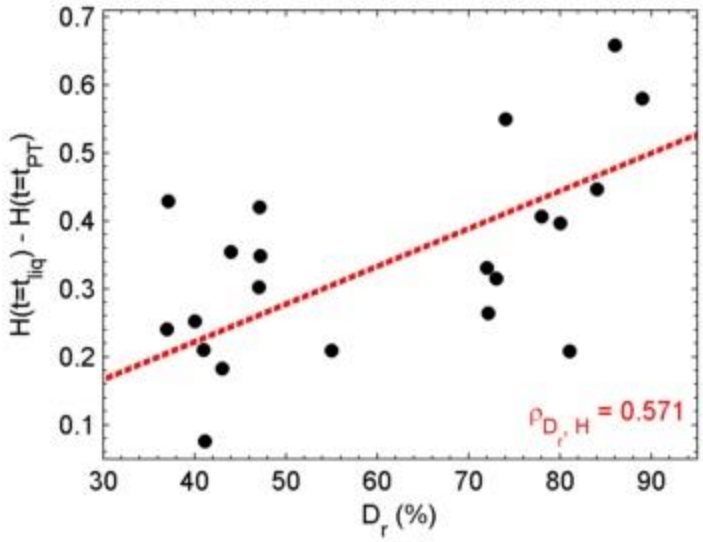


Figure 6.56: Correleation between relative density and the amount of loading betwee the onset of phase transformation and the initiation of liquefaction as evaluated using the Husid parameter.

The CSS data showed that IM_{PT} and IM_{liq} are highly correlated, therefore, the IM that is most efficient at predicting the onset of liquefaction should be the IM that is most efficient at predicting the initiation of liquefaction. To evaluate the efficiency of each of the IMs at predicting the onset of phase transformation behavior, IM_{PT} was plotted as a function of relative density for each test and an exponential function of the form presented in Equation 6.21 was fit to the data. The results of these analyses are shown in Figure 6.57 for each of the five standard IMs. The efficiency of each of the five standard IMs was summarized using the standard deviation of the residuals computed using the difference between the natural logarithm of the IM at the initiation of phase transformation and the natural logarithm of the fitted value, $\sigma_{\varepsilon,PT}$. The computed $\sigma_{\varepsilon,PT}$ values for each of the IMs are provided in the bottom right-hand corner of each plot shown in Figure 6.57 and are summarized in Table 6.6. The results based on the onset of phase transformation behavior were similar to the findings based on the initiation of liquefaction. The two PGA_m formulations, PGA_{mL} and PGA_{mB} were much more efficient than the integral-based IMs at predicting the onset of phase transformation, with PGA_{mB} having the lowest $\sigma_{ln,liq}$ value (0.11) of all the standard IMs. Each of the integral-based IMs performed essentially the same, and had $\sigma_{ln,liq}$ values of 0.45, which was approximately 20% larger than the $\sigma_{\varepsilon,liq}$ values evaluated at the initiation of liquefaction. This finding supports the theory that the most efficient

IM for predicting the initiation of liquefaction is the IM that is most efficient at predicting the onset of phase transformation behavior.

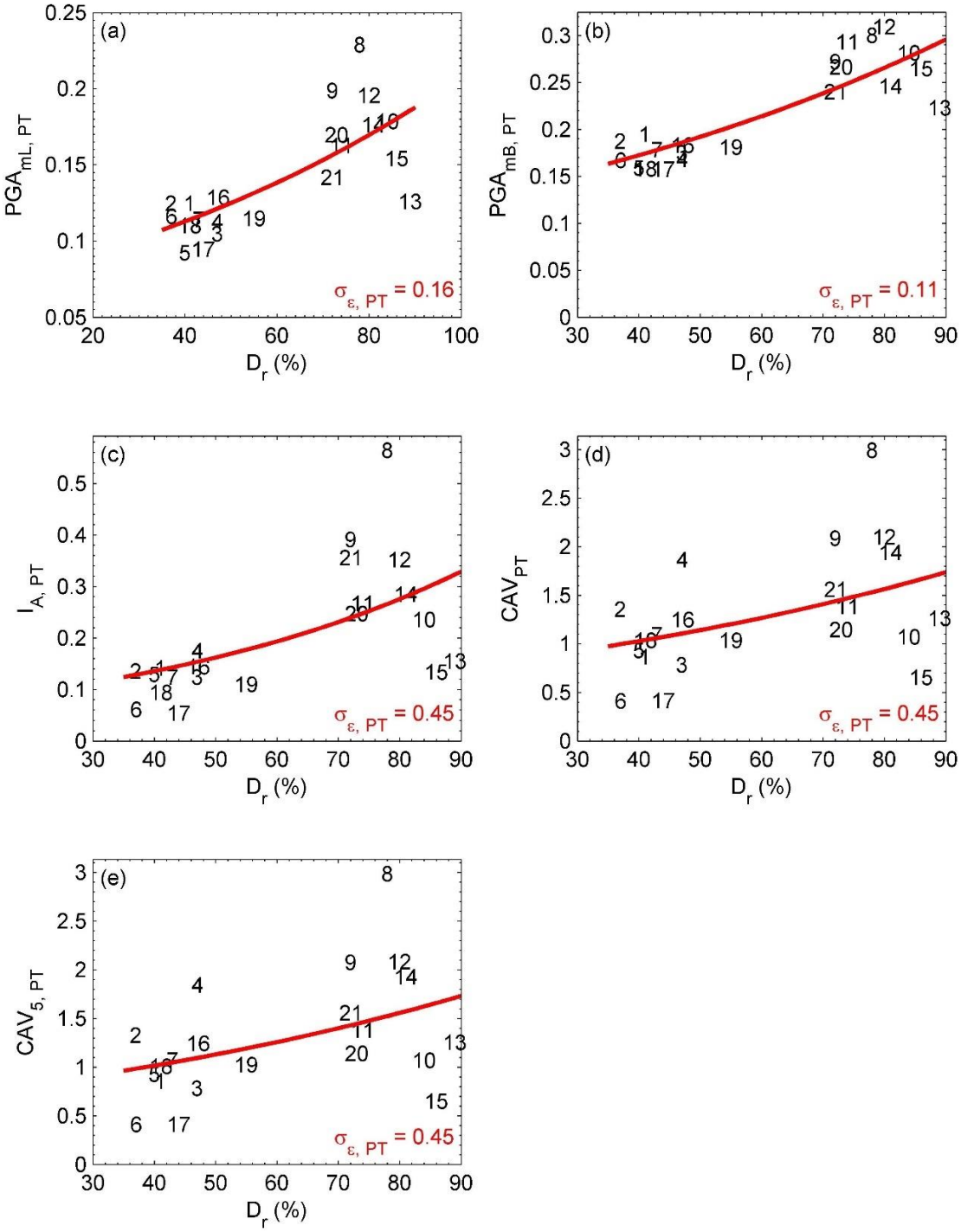


Figure 6.57: Measured and fitted values of (a) PGA_{mL}, (b) PGA_{mB}, (c) I_A, (d) CAV, and (e) CAV_5 at the onset of phase transformation behavior as a function of relative density.

Table 6.6: Standard deviation of the log residuals, σ_{ln}, for the IM-D_r fit at the onset of phase transformation behavior for each of the five standard IMs.

IM	$\sigma_{\varepsilon, PT}$
PGA_{mL}	0.16
PGA_{mB}	0.11
I_A	0.45
CAV	0.45
CAV_5	0.45

6.5.4 *Discussion*

The transient CSS data presented in Section 6.4 was used to evaluate the efficiency of the standard IMs for use in the liquefaction triggering relationship which is the first step in the timing-based liquefaction hazard evaluation framework. The efficiency was evaluated using the standard deviation of the natural log residuals from the IM-D_r-r_u relationship using both the entire r_u history and at the initiation of liquefaction. The standard IMs investigated included two cycle counting-based IMs, PGA_{mL} and PGA_{mB} and three integral-based IMs, I_A, CAV, and CAV_5.

The analyses showed that the cycle counting-based IMs performed much better than the integral-based IMs considering both the entire r_u time history and only the values at the initiation of liquefaction; PGA_{mB} was observed to perform slightly better than PGA_{mL}. These findings differed from those of Kramer and Mitchell (2006) and Abegg (2010), which found that CAV_5 and I_A were the most efficient IMs based on numerical analyses. However, there are three distinct reasons why the cycle counting-based IM, PGA_m, performed better than the integral-based IMs:

1. PGA_m, like r_u, is insensitive to the frequency content of the applied loading,
2. PGA_m is more efficient at predicting the onset of phase transformation behavior, and
3. The r_u response from the CSS data showed a dependence on the order of cycles and was highly sensitive to local peak amplitudes. This effect was not captured in the in the numerical analysis of Kramer and Mitchell (2006) and Abegg (2010). Due to the cycle-weighting and MSF formulations used in both definitions of PGA_m, PGA_m is able to capture these effects in a manner that is consistent with the observed r_u response.

Item 1 has been discussed previously, both in this document and in previous studies (e.g. Riemer et al. 1976, Green and Terri; 2005, National Academies of Sciences, Engineering, and Medicine; 2016, etc.). Item 2 was discussed in Section 6.5.3, which presented the hypothesis that because (a) the excess pore pressure increases rapidly during phase transformation behavior and (b) this response is unpredictable using an IM based on the loading history alone, the IM that is best correlated with the initiation of phase transformation behavior should be the IM that is best correlated with the initiation of liquefaction. This hypothesis was supported using analyses from the transient CSS test database. Item 3 is related to relationship between the generation of excess pore pressure and the prior peak amplitude, or PPA, that was discussed extensively throughout this chapter. The CSS data consistently showed that:

a) Large increases in pore pressure are associated with loading pulses that exceed the PPA.
b) Minimal amounts of pore pressure are generated by subsequent cycles that are less than the PPA.

As shown in Figure 6.50 for PGA_{mB}, the PGA_m formulations also show large increases when the acceleration time history exceeds the previous peak acceleration amplitude and are relatively insensitive to amplitudes less than the peak. Therefore, PGA_m evolves in a manner that is consistent with the r_u response during the CSS tests. This point can be clearly illustrated using the irregular harmonic loading as an example.

Figure 6.58 shows the development of PGA_{mB} and CSR for the irregular harmonic load tests. The peak r_u values from these tests were relatively low and the response was not impacted by phase transformation behavior. Figure 6.58a and b show the time histories of CSR and r_u respectively. The development of PGA_{mB} computed using the CSR time history is shown in Figures 6.58c through f, which show time histories of the peak CSR (c), number of equivalent cycles (d), the MSF (e), and PGA_{mB} computed as the peak CSR divided by MSF (f). Figure 6.58g shows CAV computed using the CSR time history. The peak CSR time histories began at 0, increased to a value of 0.075 during the initial half-cycle of loading after which they remained constant until increasing to the peak CSR of 0.15 that was encountered during the 2^{nd}, 4^{th}, 6^{th}, 8^{th}, and 10^{th} loading cycles for Tests A through E, respectively. After the 0.15 CSR half-cycle the peak amplitudes remained constant for the remainder of the loading history for each test. The time histories for the number of cycles, N, all increased at a linear rate during the lower amplitude portion of the loading history; however, once the peak CSR cycle was reached the

number of cycles dropped due to the increase in reference amplitude. Because the amplitude of the large amplitude cycle is significantly greater than the lower amplitude cycle, once the peak CSR was reached the subsequent lower amplitude cycles contributed very little to the cumulative number of equivalent cycles, and correspondingly to MSF. Due to the formulation of MSF (Equation 2.8), during the constant amplitude portion of the loading when the accumulation of N was linear, the evolution of MSF was nonlinear and the rate of change in MSF was greater at low values of N than at large values of N. This behavior was reflected in PGA_{mB}, which increased at a fast rated during the initial cycle of load and at a slower rate during subsequent cycles. This effect is most apparent in the plot for Test E, where the largest cycle was not applied until the end of the record. The evolution of CAV was observed to be very different. CAV increased at a nearly constant rate throughout the duration of the test, and the location of the peak amplitude cycle was not as apparent in the CAV time history as it was in the PGA_{mB} time history.

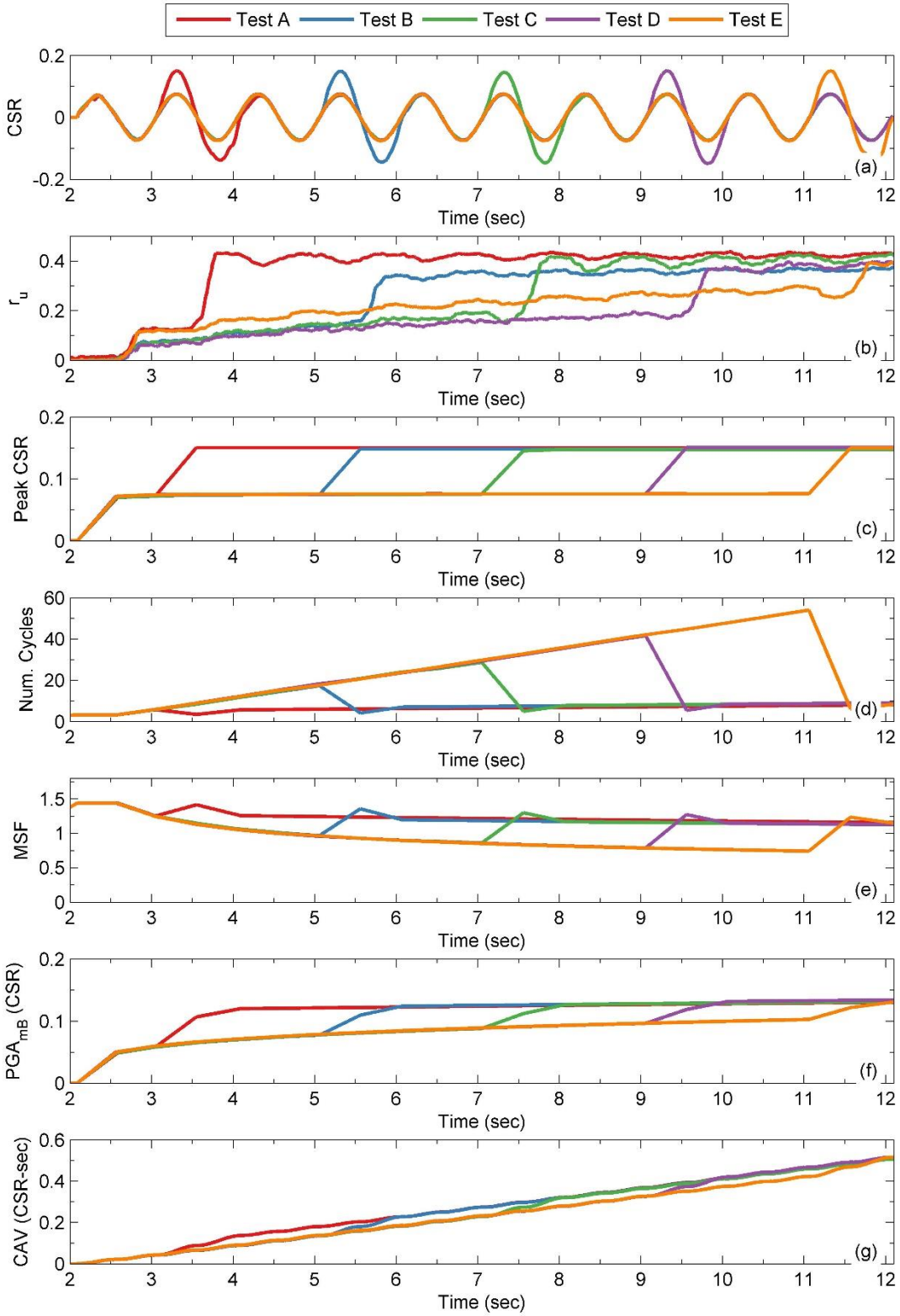


Figure 6.58: Development of cycle counting- and integral-based IMs for irregular harmonic loading showing time historiesof (a) CSR, (b) r_u, (c) Peak CSR, (d) number of cycles, (e) magnitude scaling factor, (f) PGA_{mB} in units of CSR and computed as the product of (c) and (e), and (g) CAV computed using the CSR time history and in units of CSR-seconds.

As shown in Figure 6.58, the shape of PGA_{mB} was much more representative of the shape of the r_u time history than CAV. To provide a direct comparison, Figure 6.59 provides a comparison of the normalized r_u, PGA_{mB}, and CAV for Test A and E. In both instances, CAV plotted as a nearly linear line, with a slight increase during the large amplitude cycle applied between 3 and 4 seconds for Test A and between 11 and 12 seconds for Test B. In general, CAV plotted below the normalized r_u time history until the end of the record. On the other hand, while PGA_{mB} tended to overpredict the initial increase in r_u, it was more effective in capturing the general shape of the r_u time history than CAV.

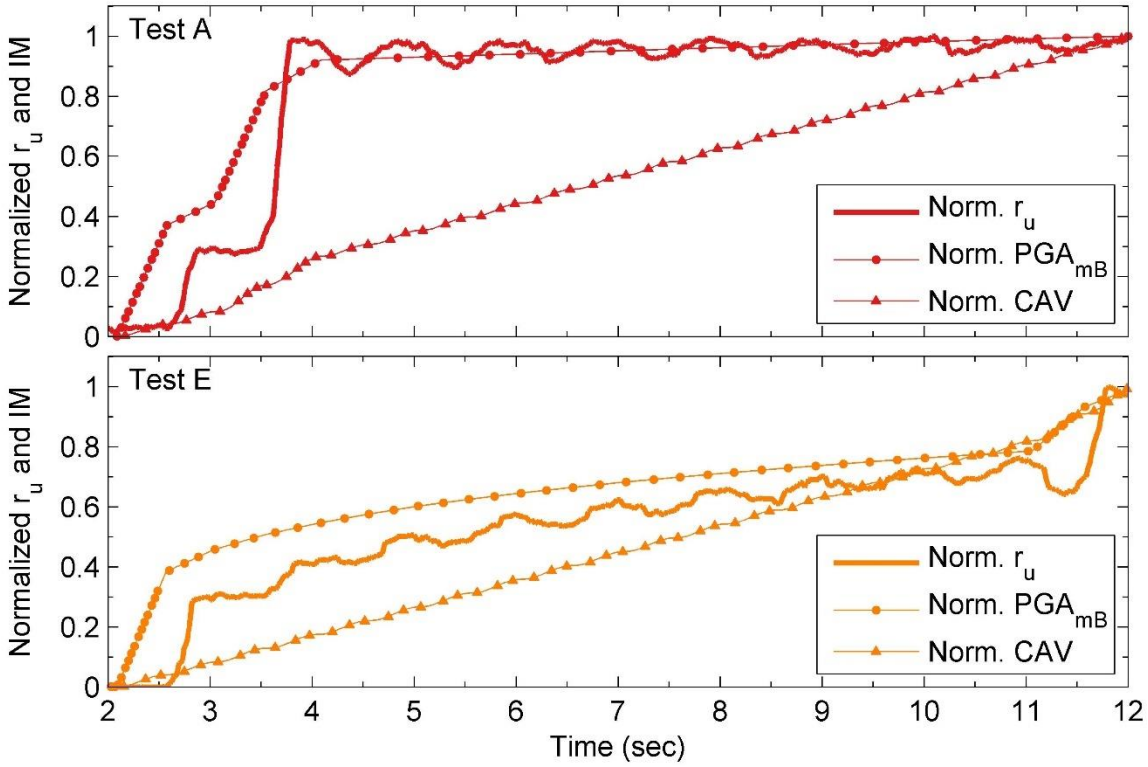


Figure 6.59: Comparison of normalized r_u and normalized PGA_{mB} and CAV for irregular harmonic Tests A (top) and E (bottom).

The fact that PGA_m is insensitive to frequency content, is able to reproduce the general trends seen in the r_u time history, and can reliably predict the initiation of phase transformation behavior was likely why PGA_{mB} was the most efficient of the standard IMs as identified using both the entire r_u time history and at the time of liquefaction triggering. The next section presents a brief review of the results from torsional ring shear tests to investigate if the behavior observed in section was unique to CSS testing.

6.6 LIQUEFACTION-SPECIFIC INTENSITY MEASURE

In addition to the standard IMs investigated in the previous section, a new, liquefaction-specific intensity measure or LIM, was developed as part of this study. The premise of the LIM is to tailor an IM that captures the components of a loading history that are most closely related to the generation of excess pore pressure prior to phase transformation behavior as observed during the CSS test program. These observations have been reiterated throughout Sections 6.3 through 6.5. Specifically, the LIM should

1. Capture the amplitude and duration of the loading history,
2. Be insensitive to the frequency of the loading history,
3. Reflect the stress-history dependent behavior of excess pore pressure generation (early cycles tend to generate more excess pore pressure than later arriving cycles of the same amplitude), and
4. Account for the relative amplitude and phasing of the loading history.

The following sections detail the development, implementation, and evaluation of LIM using the CSS test database.

6.6.1 *Development of a Liquefaction-specific Intensity Measure*

The four main observations listed at the beginning of this section formed the basis for the development of a liquefaction-specific intensity measure. The process to develop a liquefaction-specific intensity measure, or LIM, that captures each component began by investigating the most efficient standard IM, PGA_{mB}, which was shown to effectively capture most of the important trends listed above.

As presented in Sections 2.3.3.1 and 4.1, the formulation of PGA_{mB}, computed as the peak acceleration divided by a magnitude scaling factor, accounts for the amplitude and duration of the loading history (Item 1). In addition, because the magnitude scaling factor is computed using the number of equivalent cycles, which are calculated using the absolute peak amplitude between zero-crossings, PGA_{mB} is insensitive to the frequency of the loading history (Item 2). Lastly, as shown in Section 6.5.4, due to the formulation of MSF, PGA_{mB} evolves in a similar manner to r_u prior to phase transformation behavior (Item 3). From the evolutionary definition of PGA_{mB} and substituting Equation 2.6 into Equation 4.2

$$PGA_{mBj} = \frac{PGA_j}{MSF_j} = \frac{PGA_j}{\left(N_{ref}/N_j\right)^b} = PGA_j\left(\frac{N_j}{N_{ref}}\right)^b \tag{6.25}$$

where PGA_{mBj} is the value of PGA_{mB} at peak j, PGA_j is the maximum peak amplitude through peak j, MSF_j was defined previously in Table 4.1, N_{ref} is the reference number of cycles defined by Boulanger and Idriss (2014) as 15 cycles, N_j is the number of equivalent cycles through peak j, and b is the scaling exponent which was equal to 0.236 (see Section 4.1). As described in Section 2.3.3.1, N_j is equal to the sum of the number of equivalent cycles for each peak through peak j

$$N_j = \sum_{i=1}^{j} N_i \tag{6.26}$$

From Equation 2.7 and assuming a reference amplitude of 0.65·PGA, the number of equivalent cycles for peak i, N_i, is evaluated as

$$N_i = \frac{1}{2}\left(\frac{pk_i}{0.65 \cdot PGA_j}\right)^{1/b} \tag{6.27}$$

where pk_i is the amplitude of the i^{th} peak. Note that the factor of ½ is applied to N_i because pk_i is defined as the peak amplitude between successive zero crossings and therefore represents a half-cycle of loading. Substituting Equations 6.26 and 6.27 into Equation 6.25 results in

$$\begin{aligned} PGA_{mBj} &= PGA_j\left[\frac{\sum_{i=1}^{j}\frac{1}{2}\left(\frac{pk_i}{0.65 \cdot PGA_j}\right)^{1/b}}{N_{ref}}\right]^b \\ &= \frac{PGA_j}{{N_{ref}}^b}\left[\frac{1}{2}\left(\frac{1}{0.65 \cdot PGA_j}\right)^{1/b} \cdot \sum_{i=1}^{j} {pk_i}^{\frac{1}{b}}\right]^b \\ &= \frac{1}{0.65 \cdot {N_{ref}}^b} \cdot \left(\frac{1}{2}\right)^b \left(\sum_{i=1}^{j} {pk_i}^{1/b}\right)^b \end{aligned} \tag{6.28}$$

Noting that N_{ref} is a constant, Equation 6.28 becomes

$$PGA_{mBj} = c \cdot \left(\sum_{i=1}^{j} pk_i^{1/b} \right)^b \tag{6.29}$$

where c is equal to 0.694 when N_{ref} is assumed to be 15 and b = 0.236. Therefore, PGA_{mB} reduces to the summation of the individual peak amplitudes that are adjusted by the exponent 1/b that controls the contribution of each individual peak, the quantity of which is raised to the exponent b that controls the general shape of PGA_{mB}, all of which is then multiplied by an arbitrary constant, c. Equation 6.29 served as the basis for the liquefaction-specific intensity measure, LIM. A preliminary version of LIM, LIM_o, was developed by allowing the exponent outside the quantity, b, and the exponent within the summation, 1/b, to be independent variables θ_1 and θ_2, respectively,

$$LIM_{0j} = \left(\sum_{i=1}^{j} pk_i^{\theta_2} \right)^{\theta_1} \tag{6.30}$$

Noting that LIM_0 reduces to PGA_{mB} when $\theta_1 = b$ and $\theta_2 = 1/\theta_1$.

LIM_0 is a more flexible representation of PGA_{mB}, which was shown to capture the general trends observed in the CSS test data. However, Equation 6.30 does not explicitly account for the phasing of the loading history. All peaks are treated the same whether they exceed the PPA, in which case they would be anticipated to generate large amounts of pore pressure, or less than the PPA, where the pore pressure response should be severely diminished. Therefore, to allow for LIM to capture the relative amplitude of a given cycle, and scale up peaks that exceed the PPA while reducing the contribution for peaks that are less than the PPA, a cycle ratio factor was added to Equation 6.30. The peak ratio factor, r, was of the form

$$r_i = \frac{2}{1 + \left(\frac{pk_i}{PGA_{i-1}} \right)^{\theta_3}} \tag{6.31}$$

where PGA_{i-1} is the peak amplitude of the loading history for all the peaks preceding pk_i (i.e. the PPA) and θ_3 is a constant that controls the rate of change of r. Note that in Equation 6.31 the constant θ_3 needs to be negative to produce a ratio term that increases when the current peak amplitude exceeds the previous peak amplitude. This functional form was selected because it was flexible and constrains the peak ratio factor to a maximum value of 2 which prevents the peak ratio factor from taking on unreasonably large values during the initial portion of the

transient loading histories when PGA_{i-1} approaches zero. As will be shown in the final form of LIM, if the numerator in Equation 6.31 is defined as a constant value, its value is arbitrary. A value of 2.0 was selected so that the cycle ratio factor computed from Equation 6.31 produced values between 0 and 1.0 for peak ratios ≤ 1.0 and values between 1.0 and 2.0 for peak ratios ≥ 1.0. This symmetry was judged to be desirable from a conceptual standpoint. The behavior of the peak ratio factor for a range of θ_3 values is shown in Figure 6.60. As θ_3 becomes more negative, the slope of the cycle ratio factor at cycle ratios near 1.0 increase. At a value of θ_3 equals zero the ratio factor is a flat line at a value of 1.0.

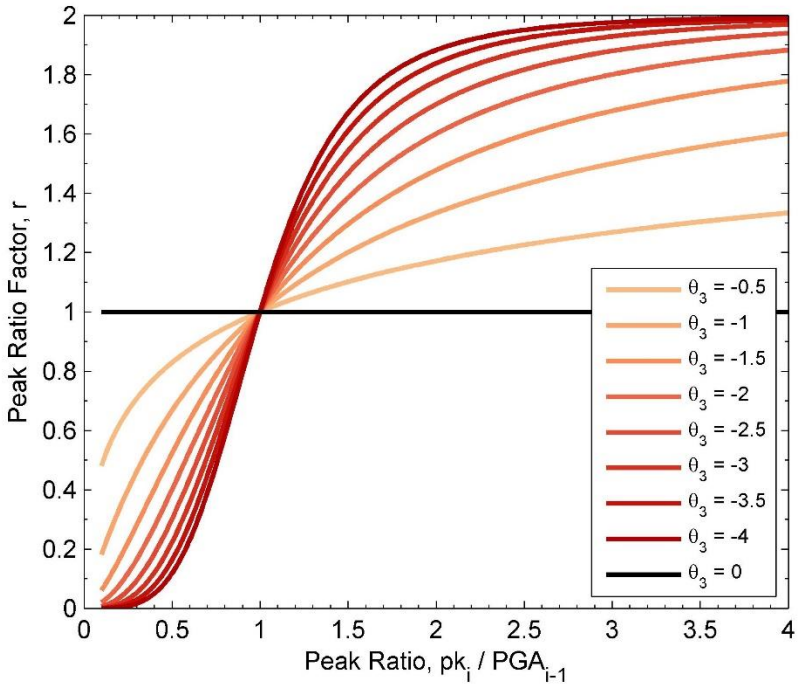


Figure 6.60: General behavior of the cycle ratio factor for different values of the exponent θ_3

Incorporating the cycle ratio factor (Equation 6.31) into LIM_0 (Equation 6.30), the final form of the LIM was derived as

$$LIM = \left[\sum_{i=1}^{j}\left(pk_i \cdot \frac{2}{1+\left(\frac{pk_i}{PGA_{i-1}}\right)^{\theta_3}}\right)^{\theta_2}\right]^{\theta_1} \qquad 6.32$$

Note that per Equation 6.32 the constant in the numerator of the peak ratio factor, c (shown in Equation 6.32 as c = 2.0), merely works to scale LIM by a factor of $c^{\theta 1 * \theta 2}$ and is arbitrary. A value of c = 2 was selected based on the reasons conceptual reasons provided previously.

The LIM as defined in Equation 6.32 is able to capture each of the four critical items relating the loading history to excess pore pressure generation prior to phase transformation behavior as specified previously. LIM function scales a given peak by a ratio factor that captures the amplitude of that peak relative to the PPA. The scaled peak is then modified by an exponent, θ_2 that, when greater than one, reduces the influence of low amplitude loading and increases the influence of high amplitude loading. The exponent, θ_1, allows for the rate of increase of LIM to be altered based on the cumulative load, which serves as a proxy for the stress history. When θ_1 is less than 1.0, LIM increases faster during the initial loading cycles and the rate of change of LIM decreases as more loading is accumulated. This is similar to how the excess pore pressure is generated prior to phase transformation behavior as noted in Sections 6.3 and 6.5.

Figure 6.61 shows the behavior of LIM for a uniform harmonic loading history. For uniform loading, LIM is insensitive to θ_3 because the ratio of pk_i to PGA_{i-1} is always equal to 1.0. In addition, while θ_2 will affect the amplitude of LIM for uniform harmonic loading, the general shape of LIM from a normalized perspective is insensitive to θ_2 because the term within the summation is constant, and the cumulative summation of a constant produces a uniformly spaced series. For uniform harmonic loading and when LIM is normalized, the behavior is entirely controlled by θ_1, which was varied from 0.1 to 0.5 in the example provided in Figure 6.61. As θ_1 increases the color of the lines go from light blue to dark purple. The plot includes the response for $\theta_1 = b = 0.236$ shown as a heavy black line to allow for comparison with PGA_{mB}. The parameter θ_1 controls the general shape or "backbone" behavior of LIM during uniform harmonic loading. Low values of θ_1 cause the initial portion of LIM to be steep during the first cycle of loading. Increasing the value of θ_1 decreases the initial value of LIM and increases the rate that LIM accumulates as more loading cycles were applied.

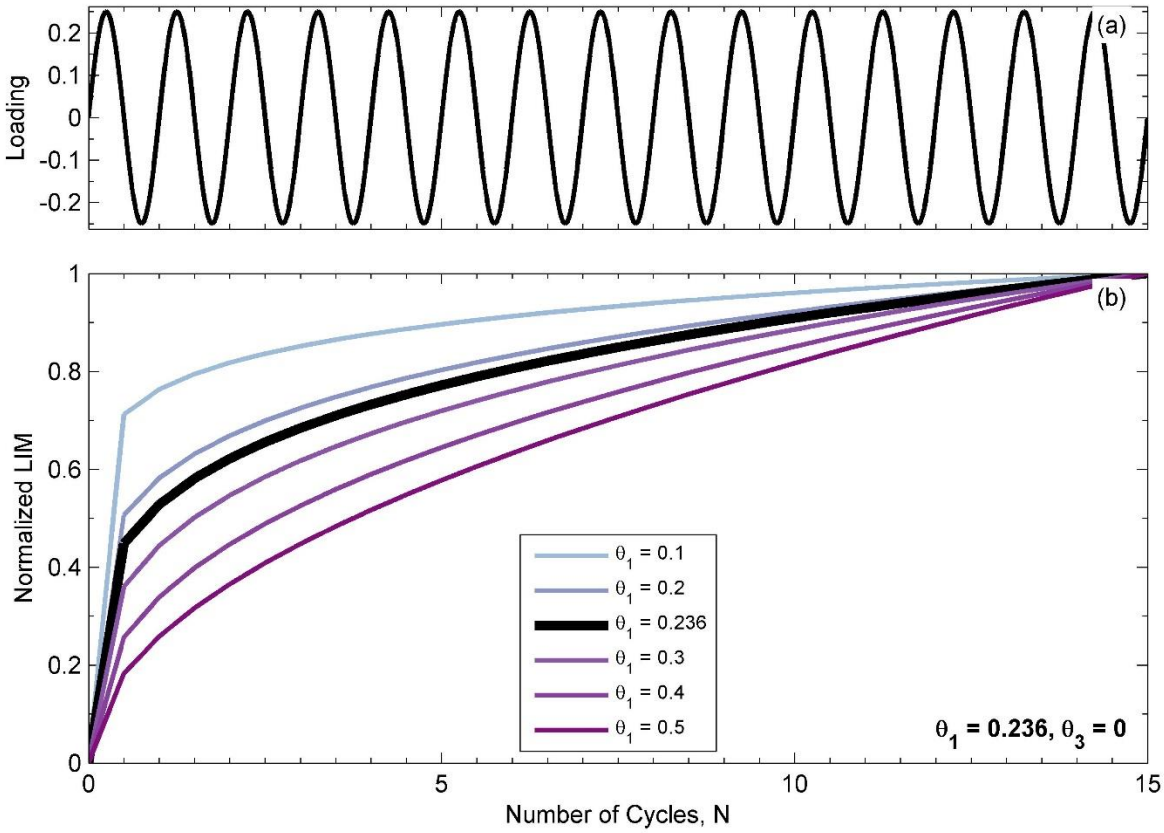


Figure 6.61: Behavior of normalized LIM with a constant amplitude harmonic loading for various values of θ_1.Note that for harmonic load the values of θ_2 and θ_3 are arbitrary when LIM is normalized since all the peak values are the same amplitude. The upper plot shows the loading history and the lower plot shows the evolution of LIM.

To illustrate how the combination of θ_1 and θ_2 impact the amplitude of LIM, Figure 6.62 shows the true, non-normalized response of LIM for constant amplitude harmonic loading using various combinations of θ_1, θ_2, and θ_3. The loading history is shown in Figure 6.62a. Figure 6.62b shows the response of LIM using a range of θ_1 values from 0.1 to 0.4 while holding θ_2 and θ_3 constant. The value of θ_2 was 0.236, which is equal to the b value used in the formulation of PGA_{mB}. The value of θ_3 was set to 0 to remove any effect of the ratio scaling factor. Figure 6.62c shows the response of LIM to various values of θ_2 values while holding θ_1 constant at $\theta_1 = 1/b = 4.23$ and setting $\theta_3 = 0$. Figure 6.62d shows the response of LIM to various values of θ_3 while keeping θ_1 and θ_2 constant at $\theta_1 = 1/b$ and $\theta_2 = b = 0.236$. The heavy black lines in all the plots show the equivalent PGA_{mB} formulation. Note that θ_3 was varied in the example provided in Figure 6.62, however for uniform harmonic loading the peak ratio term has no effect on the

behavior of LIM. When the product of θ_1 and θ_2 is less than 1.0 the response of LIM is greater than the equivalent PGA_{mB} formulation ($\theta_1 = 1/\theta_2 = 0.236$ and $\theta_3 = 0$), and less than the PGA_{mB} formulation when the product is greater than 1.0.

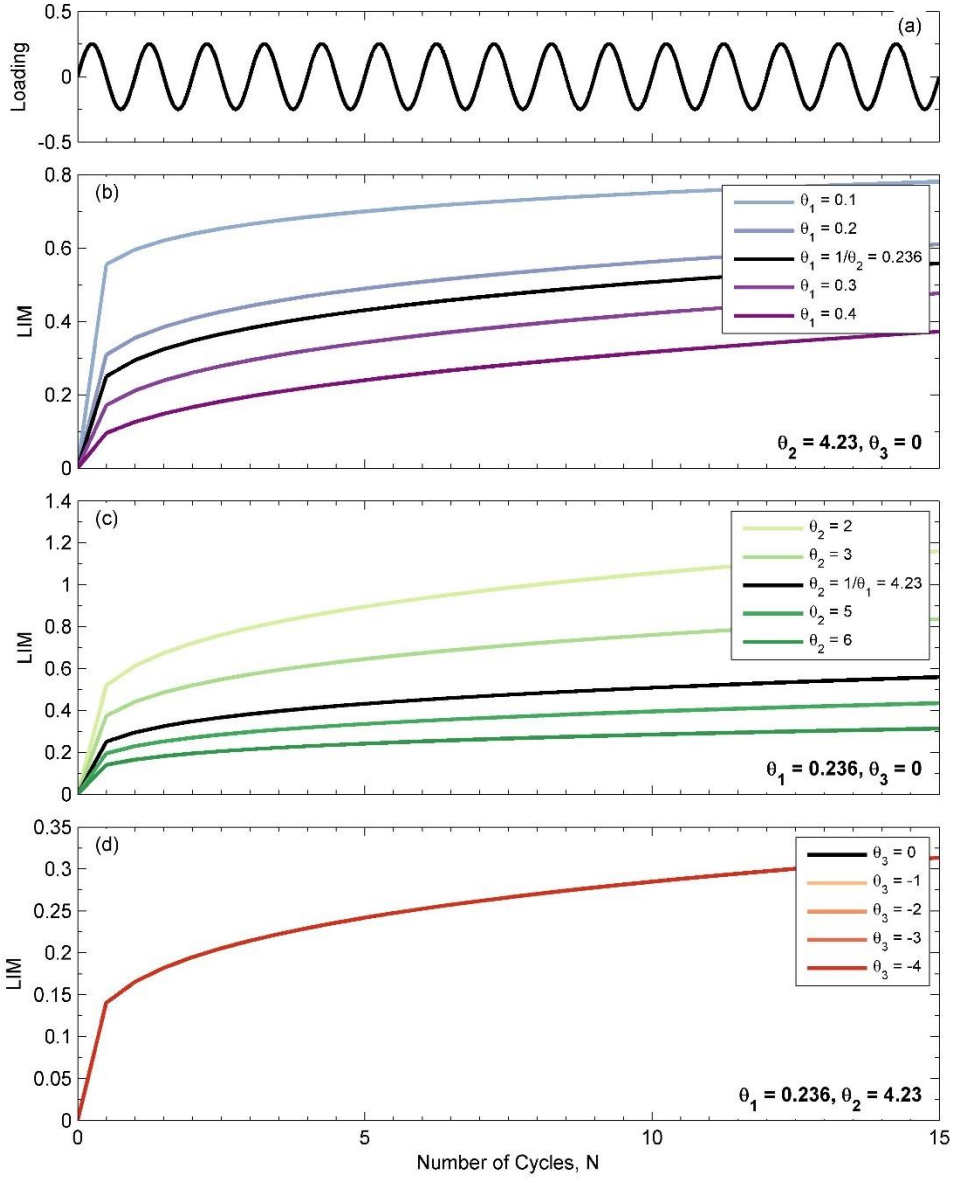


Figure 6.62: Behavior of LIM_0 with constant amplitude harmonic loading.The loading history is shown in (a). Plot (b) shows the behavior of LIM_0 while holding θ_2 constant at 0.236, equal to the parameter b used to compute PGA_{mB}. Plot (c) shows the behavior of LIM_0 while holding θ_1 constant at 4.23, equal to 1/b.

Figure 6.63 shows the behavior of LIM with respect to a linearly increasing harmonic load using the same values for θ_1, θ_2, and θ_3 and format as shown in Figure 6.62. Figure 6.63b

and c show that increasing θ_1 or θ_2 decreases the initial values of LIM when N is small and increases the slope of the LIM versus N when N is large. Due to the form of LIM (Equation 6.32) fully decoupling the response of θ_1 and θ_2 was not possible. Figure 6.63 clearly shows that LIM is very sensitive to both θ_1 and θ_2. For the linearly increasing loading history example shown, LIM was not as sensitive to the cycle ratio factor as it was to θ_1 and θ_2. However, Figure 6.63d clearly illustrates that LIM increased as the coefficient θ_3 became more negative.

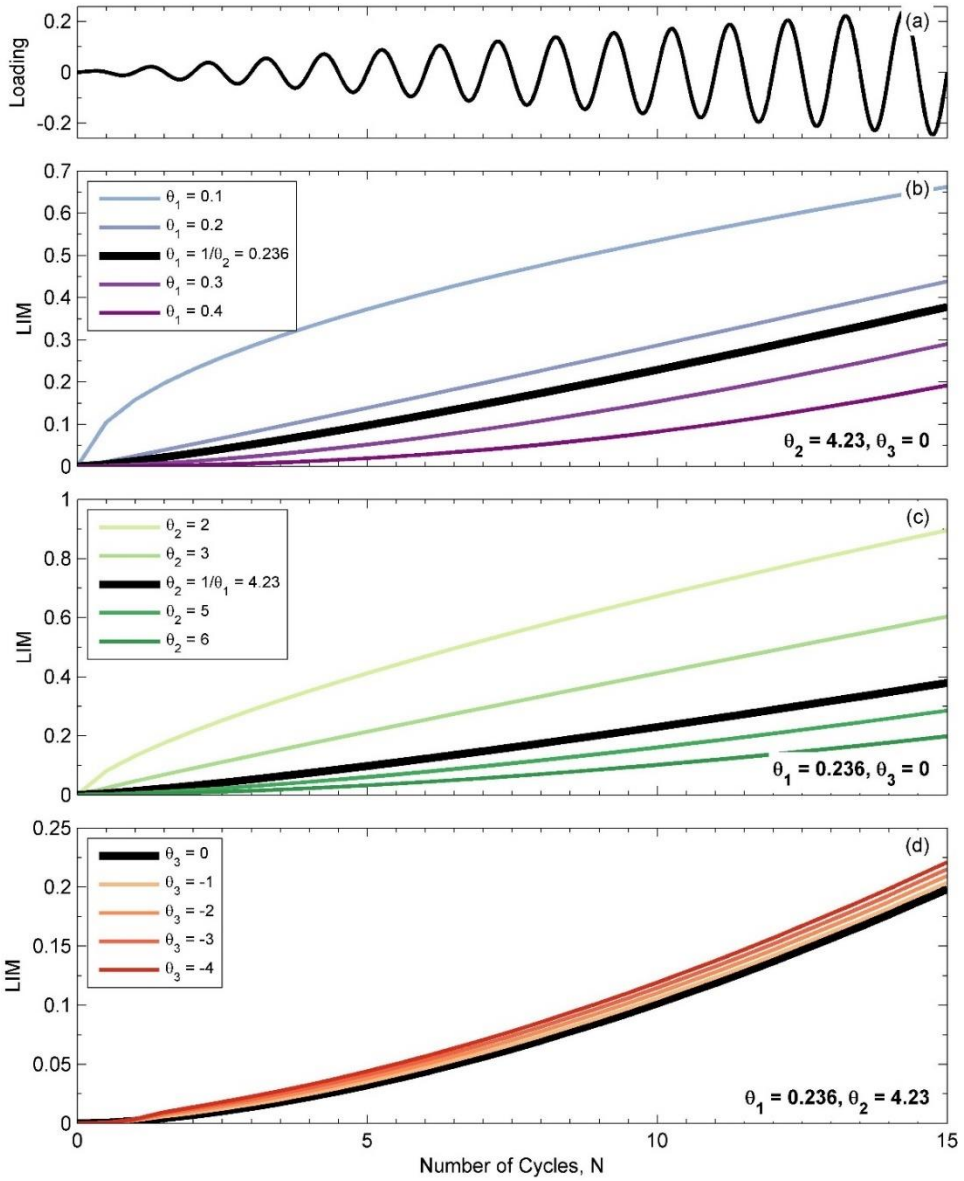


Figure 6.63: Behavior of LIM_0 with a linearly increasing harmonic loading.The loading history is shown in (a). Plot (b) shows the behavior of LIM_0 while holding θ_2 constant at 0.236, equal to the parameter b used to compute PGA_{mB}. Plot (c) shows the behavior of LIM_0 while holding θ_1 constant at 4.23, equal to 1/b.

Figure 6.64 shows the behavior of LIM in response to a linearly decreasing loading history using the same values for θ_1, θ_2, and θ_3 and format as shown in Figure 6.63. Figures 6.64b and c show that the response of LIM for the case of a linearly decreasing loading history was similar to the response shown for the linearly increasing load. In addition, even without considering the ratio factor, LIM was not very sensitive to loads less than the peak value, as illustrated by the relatively flat response for all of the curves when N was large and the cycle amplitudes were low. As with the linearly increasing loading history, LIM appeared to be slightly very sensitive to both θ_1 and θ_2, as indicated by the spread of the curves provided in Figures 6.64b and c. For this example, the effect of the ratio factor is more pronounced, and shows that as θ_3 became more negative, the influence of the low amplitude cycles on LIM became essentially negligible.

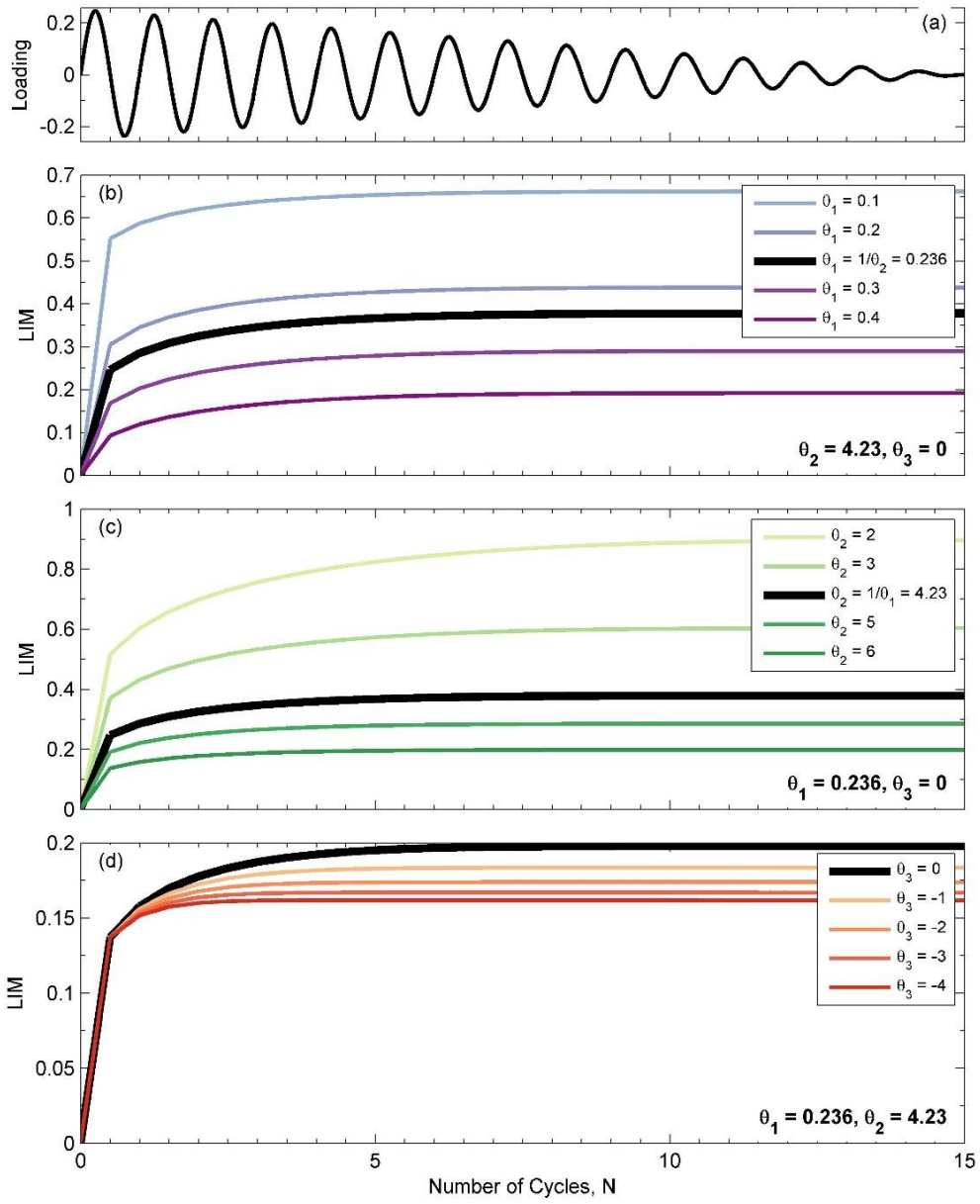


Figure 6.64: Behavior of LIM_0 with a linearly decreasing harmonic loading.The loading history is shown in (a). Plot (b) shows the behavior of LIM_0 while holding θ_2 constant at 0.236, equal to the parameter b used to compute PGA_{mB}. Plot (c) shows the behavior of LIM_0 while holding θ_1 constant at 4.23, equal to 1/b.

The formulation of LIM incorporated each of the four important facets relating a loading history to the generation of excess pore pressure prior to phase transformation behavior. Figures 6.61 through 6.64 used simple harmonic loading histories to illustrate the flexibility of LIM, which is capable of producing a wide range of responses depending on the values of the

coefficients θ_1, θ_2, and θ_3. The values of the coefficients were determined using the transient CSS test database, as detailed in the following section.

6.6.2 *Implementation of the Liquefaction-specific Intensity Measure*

The transient CSS test data was used to determine the LIM coefficients θ_1, θ_2, and θ_3 using a constrained optimization routine. A constrained optimization was performed because there is some theoretical basis for the parameters θ_1 and θ_2, which are related to the parameter b from the liquefaction resistance relationship for uniform harmonic tests. Based on the literature review by Boulanger and Idriss (2014), the b value for clean sands typically ranges from 0.14 to 0.54. Therefore, θ_1, which is equal to b in the PGA_{mB} formulation, was constrained to values between 0.15 and 0.55 for the optimization process. In the formulation of PGA_{mB} the value of θ_2 is equal to 1/b. To be consistent with the theoretical basis for PGA_{mB}, while allowing some additional flexibility in the cycle scaling coefficient θ_2, θ_2 was constrained to be within 0.7 to 1.4 times the value of $1/\theta_1$. There was no theoretical guidance for the ratio factor coefficient θ_3 other than it should be less than or equal to zero. Based on engineering judgement the value of θ_3 was constrained to be between values of 0 (i.e. the cycle ratio factor is not considered) and -5.0, which would greatly reduce small amplitude cycles that followed larger cycles and greatly amplify the effect of cycles that represented the PPA.

The constrained optimization process to determine the coefficients θ_1, θ_2, and θ_3 was performed as follows:

1. Select initial values of θ_1, θ_2, and θ_3 that conform to the constraints listed above,
2. Compute LIM for the acceleration time history from each test,
3. Create vectors of LIM, recorded r_u, and D_r,
4. Compute the IM-D_r-r_u surface fit as described in Section 6.5.1,
5. Compute the sum-of-squared errors between the natural logarithm of LIM determined using the acceleration time histories and the natural logarithm of the fitted value, and
6. Select new values of θ_1, θ_2, and θ_3 and repeat steps 1 through 5.

The constrained optimization routine, `fminsearchbnd`, in Matlab, which is based on the simplex search algorithm of Lagarias et al. (1998), was used to determine the values of θ_1, θ_2, and θ_3 that minimized the error computed in step 5.

6.6.3 *Results of Liquefaction-specific Intensity Measure Optimization*

The optimization process described in Section 6.6.3 was used to determine the optimum values of the LIM coefficients θ_1, θ_2, and θ_3. The final values of each coefficient are shown in Table 6.7. A summary of the surface fit, including the fit of LIM at the time of liquefaction, is provided in Figure 6.65. Figure 6.65 can be compared to Figure 6.45, which presents the same data for the best standard liquefaction intensity measures, PGA_{mB}. The efficiency of LIM over the entire range of r_u values from 0.05 to liquefaction ($r_u = 0.99$) can be characterized by $\sigma_\varepsilon = 0.16$. This represents a reduction of 33% compared to the σ_{ln} of the most efficient standard IM, PGA_{mB}, for which the equivalent $\sigma_\varepsilon = 0.24$. The efficiency of LIM to predict the initiation of liquefaction was evaluated using the standard deviation of the log residuals for the IM at $r_u = 0.99$, $\sigma_{ln,\,liq}$ and is summarized in Figure 6.65c. The $\sigma_{ln,\,liq}$ value for LIM was computed as 0.11, which was only an 8% reduction as compared to the $\sigma_{ln,\,liq}$ for PGA_{mB}.

Table 6.7: LIM coefficients determined using constrained optimization to the transient CSS test data.

Coefficient	Value
θ_1	0.298
θ_2	2.53
θ_3	2.91

.

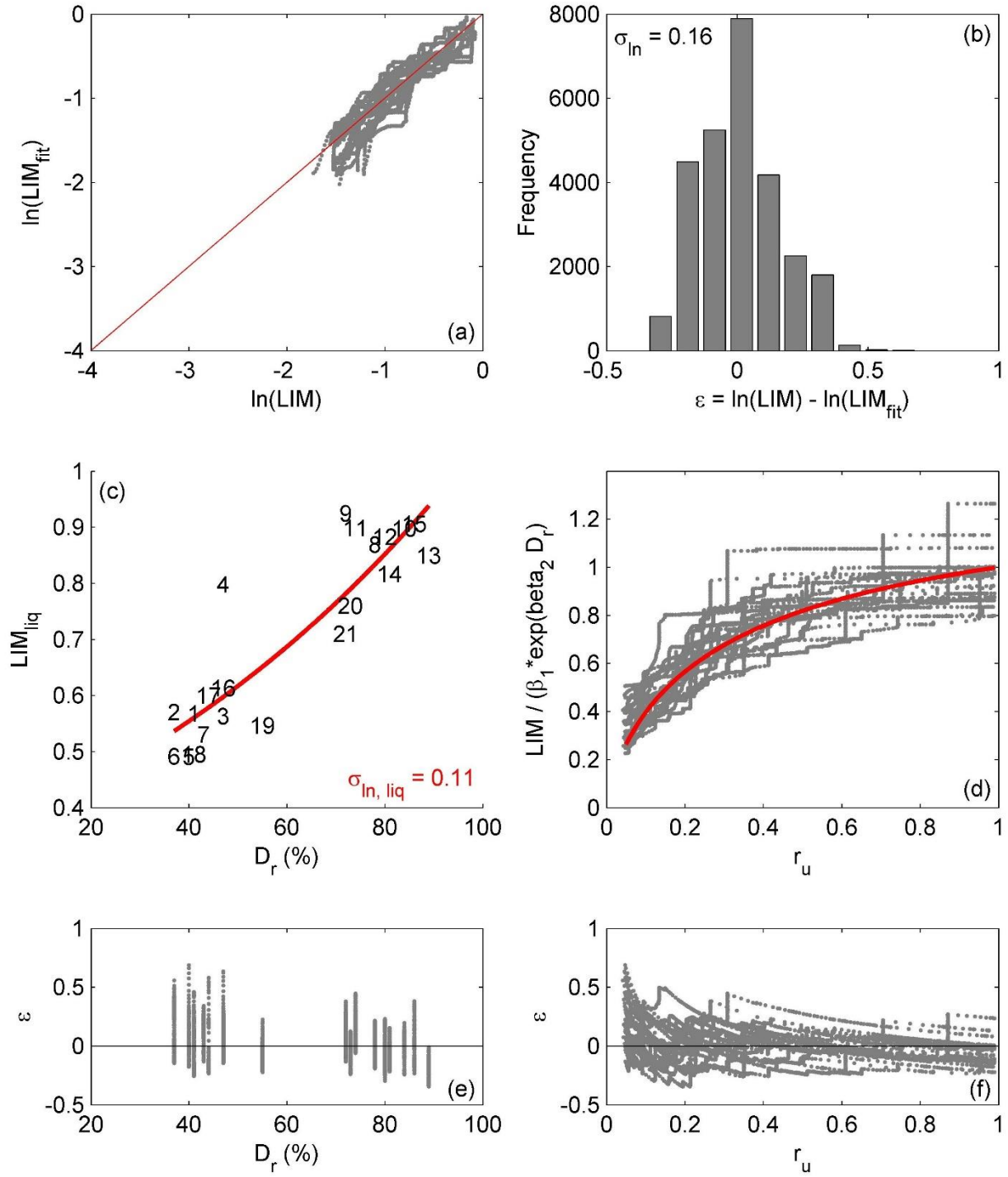


Figure 6.65: Summary of the surface fit results of LIM(a) plot of the fitted and computed IM values, (b) histogram of the log residuals, (c) IM vs D_r contour at the initiation of liquefaction, (d) plot of the r_u function vs. IM normalized by $f(D_r)$, (e) the log residuals vs relative density, and (f) the log residuals vs. r_u.

The results of the efficiency evaluations for LIM summarized in Figure 6.65 show that LIM offers a significant improvement in evaluating the uncertainty in IM|r_u across the range of r_u from 0.05 to liquefaction, but provides only a marginal improvement in reducing the uncertainty in evaluating the value of the IM at the initiation of liquefaction. Upon inspection of Figure 6.65c, the dispersion in LIM at the time of liquefaction appeared to be heavily influenced by a single test, Test 130215-02 (Ref. Num. 4). The response for this test is shown in Figure 6.66, a unique and notable feature of this test was that there was a large acceleration pulse that was applied just prior to the initiation of liquefaction at approximately 70 seconds into the record when the r_u level was approximately 0.85. This pulse induced dilation, as indicated by the large negative dip in the r_u time history. Following this dilation spike, the r_u time history increased rapidly to liquefaction. Therefore, two factors caused this response to be an outlier. The first is that the r_u response was influenced by phase transformation, which has been discussed extensively and cannot be predicted by an IM computed based solely on the loading history. The second is that, by definition, r_u is constrained to values between zero and 1.0, and as a result the amount of excess pore pressure that a given cycle can generate is limited based on the difference between the current pore pressure ratio and 1.0. This limitation cannot be fully approximated by an IM computed solely as a function of the loading history and is another source of uncertainty in the IM-D_r-r_u relationship.

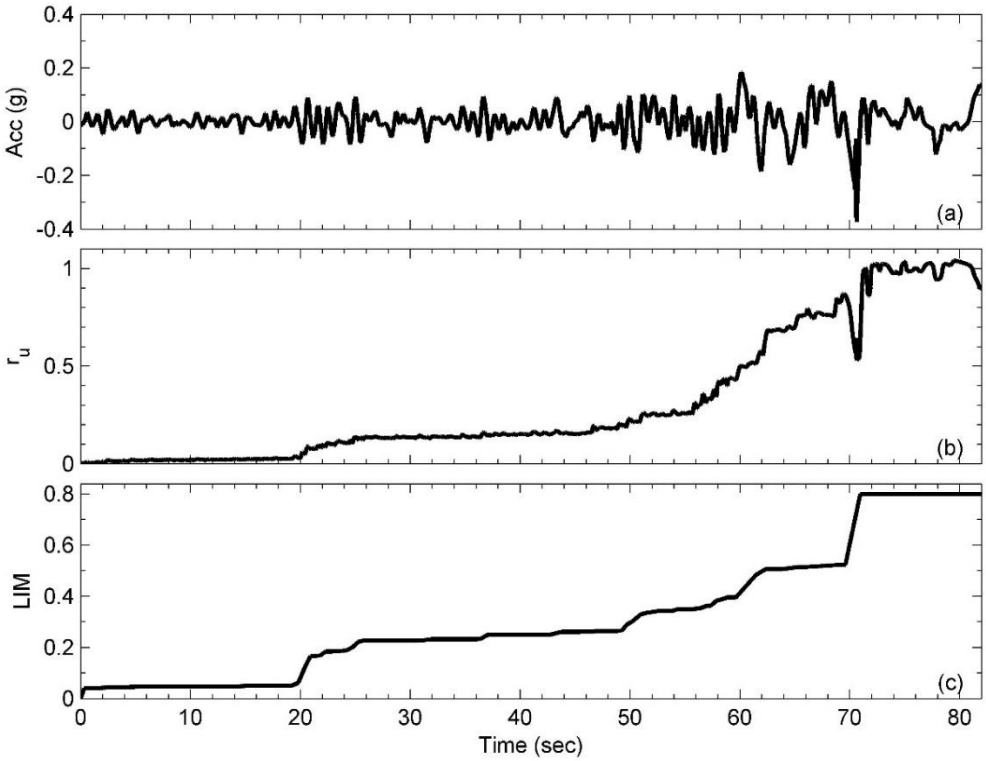


Figure 6.66: Plots of the acceleration, r_u, and LIM time histories for Test 130215-02.

LIM was developed based on the formulation of PGA_{mB} to capture the aspects of a loading history that are related to the generation of excess pore pressure prior to the onset of phase transformation behavior, which is the only portion of the soil response that can be reliably predicted using an IM computed using only an acceleration loading history. Section 6.5.3 showed that, because the excess pore pressures tended to increase rapidly following phase transformation behavior, the IM that is most efficient at predicting the initiation of liquefaction should be the IM that is most efficient at predicting the onset of phase transformation behavior. Figure 6.67 shows the value of LIM at the initiation of phase transformation behavior for each test plotted as a function of relative density. An exponential function was fit to the data and the efficiency was summarized using the standard deviation of the residuals computed using the difference between the natural logarithm of LIM at the initiation of phase transformation and the natural logarithm of the fitted value, $\sigma_{ln,PT}$. This analyses resulted in a $\sigma_{ln,PT}$ of 0.073 for LIM. This value is approximately 33% lower than the value computed using the most efficient standard IM, PGA_{mB}, and is significantly lower than $\sigma_{ln,liq}$ of 0.11 computed at the initiation of liquefaction. The additional uncertainty between LIM at the initiation of phase transformation

behavior and the initiation of liquefaction was attributed to the dramatic change in soil properties that occur following initiation of phase transformation behavior that cannot be accounted for in LIM.

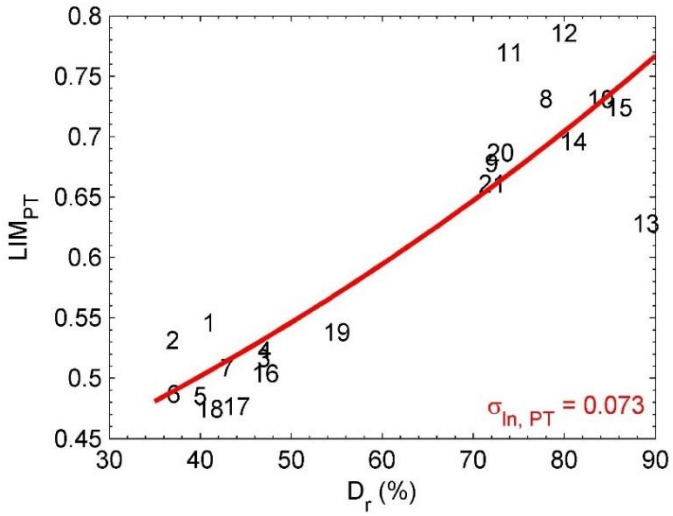


Figure 6.67: Measured and fitted values of LIM at the onset of phase transformation behavior as a function of relative density.

Figure 6.68 compares the evolutionary response of LIM at PGA_{mB} for Test 130215-02 (Ref. Num. 4, shown previously in Figure 6.66). This figure includes plots of the acceleration time history (Figure 6.68a), the time histories of r_u and each IM normalized by its value at the time of initiation of liquefaction (Figure 6.68b) and at the time of phase transformation (Figure 6.68c). In plot c the onset of phase transformation behavior is indicated by the thin vertical red line. Plots d, e, and f show the change in the smoothed r_u time history (smoothed using a cubic smoothing spline function as described in Section 6.5.2), PGA_{mB}, and LIM, respectively. As expected given their near identical formulations, PGA_{mB} and LIM show very similar evolutionary behavior and tend to overpredict the r_u response at low r_u values, and underpredict the r_u response following phase transformation behavior. LIM shows a slight improvement in predicting the low r_u response because the cycle ratio factor works to decrease the influence of the very small cycles applied in the first 20 seconds of the time history. The general shape of both PGA_{mB} and LIM were in agreement with the shape of the r_u time history prior to phase transformation behavior. This is corroborated by plots d, e, and f, which show that the locations of the peak rate of change in PGA_{mB} and LIM align with the peak rate of change in the r_u time history.

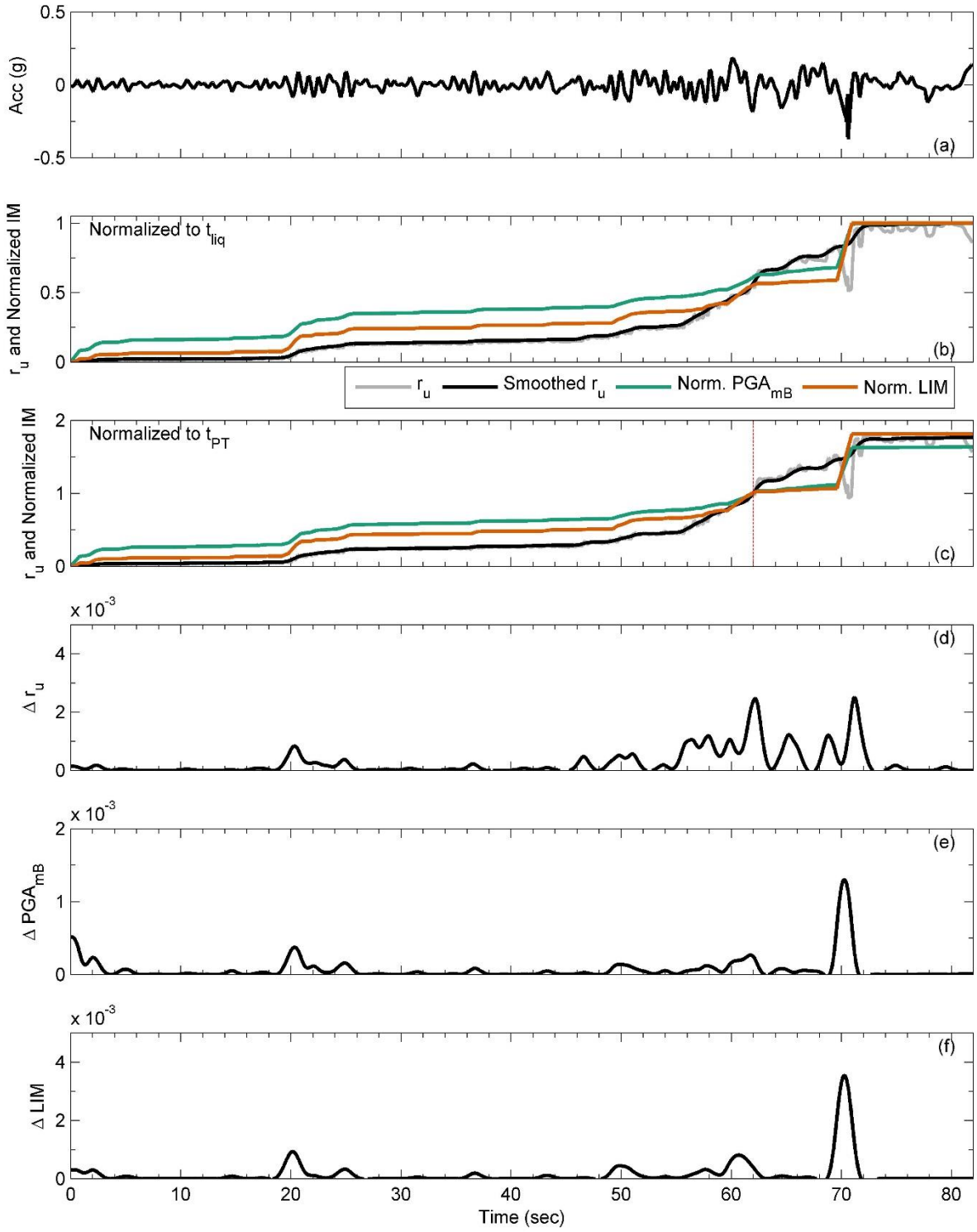


Figure 6.68: Comparison of the evolutionary response of PGA_{mB} and LIM for Test 130215-02(a) acceleration, (b) r_u, PGA_{mB}, and LIM normalized by the value at the initiation of liquefaction (t_{liq}) (c) r_u, PGA_{mB}, and LIM normalized by the value at the initiation of phase transformation behavior (t_{PT}) indicated with the vertical red line, (d) the time history of the change in the smoothed r_u, (e) the time history of change in PGA_{mB}, and (f) the time history of the change in LIM.

Figure 6.69 provides the same plots as shown in Figure 6.68, but using the results of Test 130711-02 (Ref. Num. 8). The response was similar to that observed in Figure 6.68 (Test 130215-02). Both LIM and PGA_{mB} had similar evolutionary behavior, and effectively captured the trends in the r_u time history prior to phase transformation. The incorporation of the cycle ratio factor led to a slight improvement in the fit between LIM and r_u when normalized at the time phase transformation behavior was initiated (plot c), apparent between 14 to 20 seconds into the time history. In addition, the cycle ratio factor reduced the contribution of the pulses between 22 and 38 seconds into the record to LIM as compared to PGA_{mB}, as indicated by the rate of change plots shown in plots e and f for PGA_{mB} and LIM, respectively. These pulses did not contribute to the generation of excess pore pressure, as indicated by the rate of change of r_u shown in plot d.

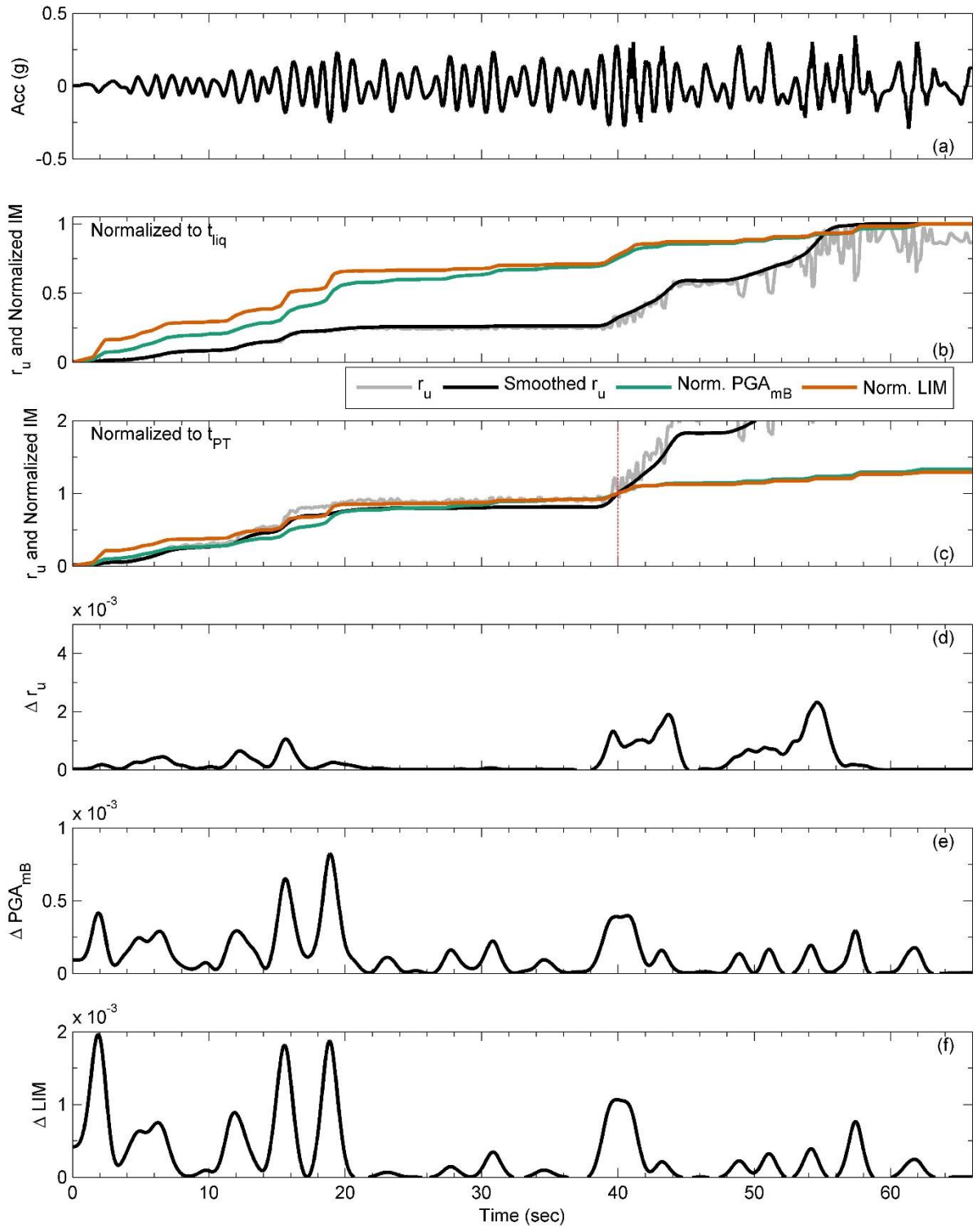


Figure 6.69: Comparison of the evolutionary response of PGA_{mB} and LIM for Test 130711-02(a) acceleration, (b) r_u, PGA_{mB}, and LIM normalized by the value at the initiation of liquefaction (t_{liq}) (c) r_u, PGA_{mB}, and LIM normalized by the value at the initiation of phase transformation behavior (t_{PT}) indicated with the vertical red line, (d) the time history of the change in the smoothed r_u, (e) the time history of change in PGA_{mB}, and (f) the time history of the change in LIM.

The analyses presented in this section show that a modified version of PGA_{mB}, termed LIM here, was more efficient than the five standard IMs at capturing the excess pore pressure behavior using the CSS test database. However, the improvements relative to PGA_{mB} for predicting the initiation of liquefaction were fairly moderate. This finding suggests that PGA_{mB}, the IM used in the stress-based methods that are prevalent in practice, is a fairly robust IM that is efficient at predicting the onset of liquefaction.

6.7 NUMERICAL MODELING OF TRANSIENT CSS TESTS

For high-risk projects, numerical modeling using finite element (e.g. OpenSees, McKenna et al., 2000) or finite difference (e.g. FLAC, Itasca, 2016) methods is commonly performed to evaluate the initiation and effects of liquefaction. While the focus of this research is on the identification of efficient evolutionary IMs for the prediction of the initiation of liquefaction, the data and observations that were generated from the CSS testing program presented in this document and in Kwan (2015) can also be used to calibrate and refine constitutive models for liquefiable soils. In particular, the CSS test data showed that the excess pore pressure response was sensitive to the PPA and loading amplitudes that were less than the PPA were shielded and generate relatively little excess pore pressure. To investigate if this behavior is captured by numerical models, single-element simulations using the transient CSS test data were performed using the Pressure Dependent Multi-yield 02 (PDMY02) model implemented in OpenSees (Elgamal et al., 2002; Yang et al., 2003; Yang et al., 2008) and the PM4Sand model (Boulanger and Ziotopoulou, 2017) implemented in FLAC. The results from the numerical simulations were compared to the test results to evaluate the ability of the constitutive models to capture the generation of excess pore pressure and the initiation of liquefaction from the CSS tests.

6.7.1 *Constitutive Models and Model Calibration*

PDMY02 is an elastic-plastic material model based on the nested yield surface plasticity framework (Prevost, 1985; Yang et al. 2003). This model uses a series of nested yield surfaces with a non-associative flow rule to simulate the contractive and dilative behavior of a liquefiable sand under cyclic shear loading. A detailed description of the PDMY02 material model and input parameters are provided in Yang et al. (2003; 2008).

PM4Sand is a stress-ratio controlled, critical state compatible, bounding-surface plasticity model (Boulanger and Ziotopoulou, 2016). The model is based on the framework presented by Manzari and Dafalias (1997) and Dafalias and Manzari (2004) with modifications to improve the ability of the model to approximate the behavior of cyclically loaded liquefiable soils as observed in the laboratory and in the field (Boulanger and Ziotopoulou, 2016; Ziotopoulou and Boulanger, 2016). A thorough description of the PM4Sand model formulation and input parameters are provided in Boulanger and Ziotopoulou (2016).

In order to compare the two constitutive models, both were calibrated to the liquefaction triggering relationship of Idriss and Boulanger (2014) using single-element direct simple shear simulations of a sample consolidated at a confining stress of 100 kPa (1 atm) and subjected to constant amplitude harmonic loading. To determine the target CSR, the relative density was converted to a corrected SPT blow count using the relationship presented in Boulanger and Idriss (2014). The model input parameters were adjusted so that liquefaction was observed after 15 cycles at the target CSR value, with liquefaction defined as the instance that r_u was greater than 0.95 and the single-amplitude shear strain was greater than 3%.

For the PDMY02 model, the calibrated parameters presented in Khosravifar (2012) were used to match the target triggering relationship at relative densities of 33, 57, 74, and 87% using the procedure described above. The PDMY02 input parameters at intermediate relative densities were evaluated using linear interpolation. The inputs from Khosravifar (2012) and the interpolation technique used in this study was verified and the results are shown in Figure 6.70. The figure shows that the calibrated parameters were able to reproduce the target liquefaction triggering curve.

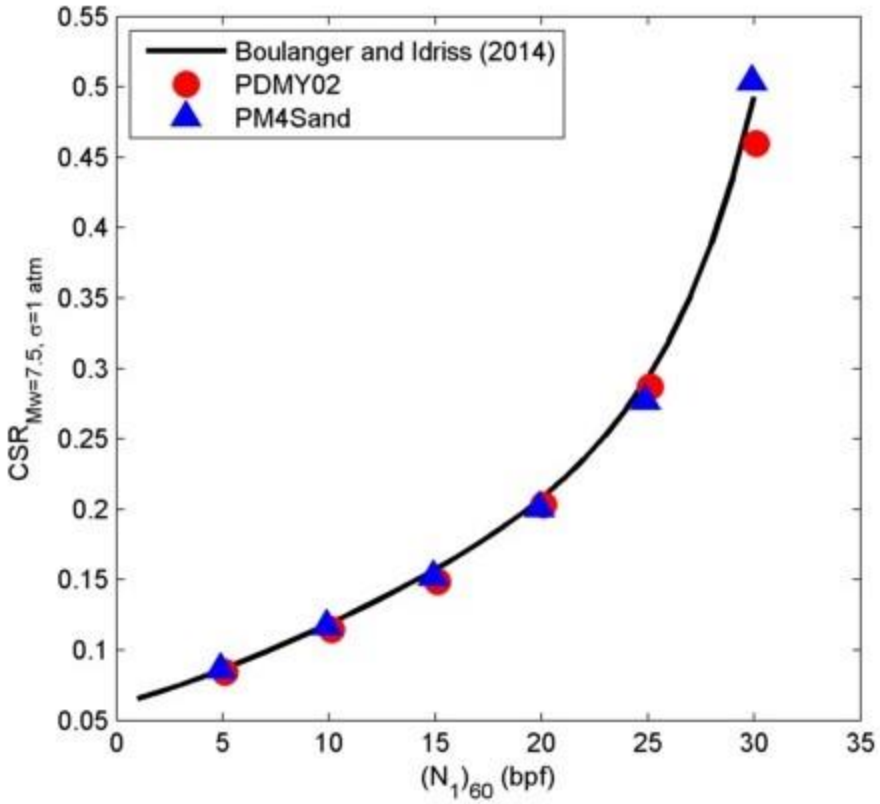


Figure 6.70: Calibration results for PDMY02 and PM4Sand compared to the Boulanger and Idriss (2014) liquefaction triggering curve.

The PM4Sand model inputs were calibrated as part of this study. PM4Sand has three primary input parameters and 21 secondary parameters. The primary input parameters are relative density, D_r, the shear modulus coefficient, G_o, and the contraction rate parameter, h_{po}. The values of D_r and G_o are both related to the corrected SPT blow count as detailed in Boulanger and Ziotopoulou (2016). The relationship between D_r, corrected SPT blow count, and G_o were maintained in this study. The 21 secondary parameters were left at the default values recommended by Boulanger and Ziotopoulou (2016). The contraction rate parameter was calibrated to match the target triggering curve using the method described previously. The results of the calibration process are provided in Figure 6.70 which shows the calibrated PM4Sand model was able to reproduce the target liquefaction triggering curve.

6.7.2 *Relative Density Calibration*

The constitutive models were calibrated to match the liquefaction triggering curve from Idriss and Boulanger (2014), which is based on case history data. The soil fabric and insitu stress

conditions in the field often differ from what can be reproduced in the laboratory. Therefore, in order to directly compare the pore pressure response from the numerical simulations with the CSS test results, the numerical models were further calibrated by evaluating an apparent relative density for each test. The apparent relative density was computed as the relative density used to define the model input parameters that produced the best fit to the measured r_u response as evaluated using the sum-of-squared error between the computed r_u values and the measured response. The results of all of the simulations using the transient CSS test data are presented in Appendix B. The figures provided in Appendix B show the reported test relative density and the apparent relative density used in the numerical simulations. The following section presents a discussion of the results.

6.7.3 *Results*

To simulate the transient CSS test results, the shear stress that was measured during the CSS tests were used to define the stress-controlled single-element numerical simulations. The excess pore pressure and shear strain response were obtained from the simulations and used to compare the model response with the behavior recorded during each test.

In general, the numerical simulations were able to provide a good approximation of the CSS test results. A comparison of the numerical simulations and the recorded test data is shown in Figure 6.71 for Test 130118. The test was performed on a sample with a relative density of 41%. The calibrated apparent relative densities that provided the best fit to the measured r_u response were evaluated as 48 and 52% for PDMY02 and PM4Sand, respectively. This test provides an example where the numerical models performed well in comparison to the recorded response. Both numerical models captured the generation of excess pore pressure as the loading amplitudes increased between 8 and 18 seconds. From 18 to 21 seconds, the amplitudes were below the PPA, and the shielding effect was observed in the recorded r_u time history. During this time, the r_u computed from the calibrated PM4Sand model was practically identical to the recorded time history. The PDMY02 model on the other hand, continued to increase and did not fully capture the reduction in the pore pressure response for pulses with amplitudes well below the PPA. As the amplitudes exceeded the PPA, at approximately 21.5 seconds, both the test data and PM4Sand showed a rapid increase in r_u. The PDMY02 model response showed a more gradual increase in r_u than was observed in the measured test result.

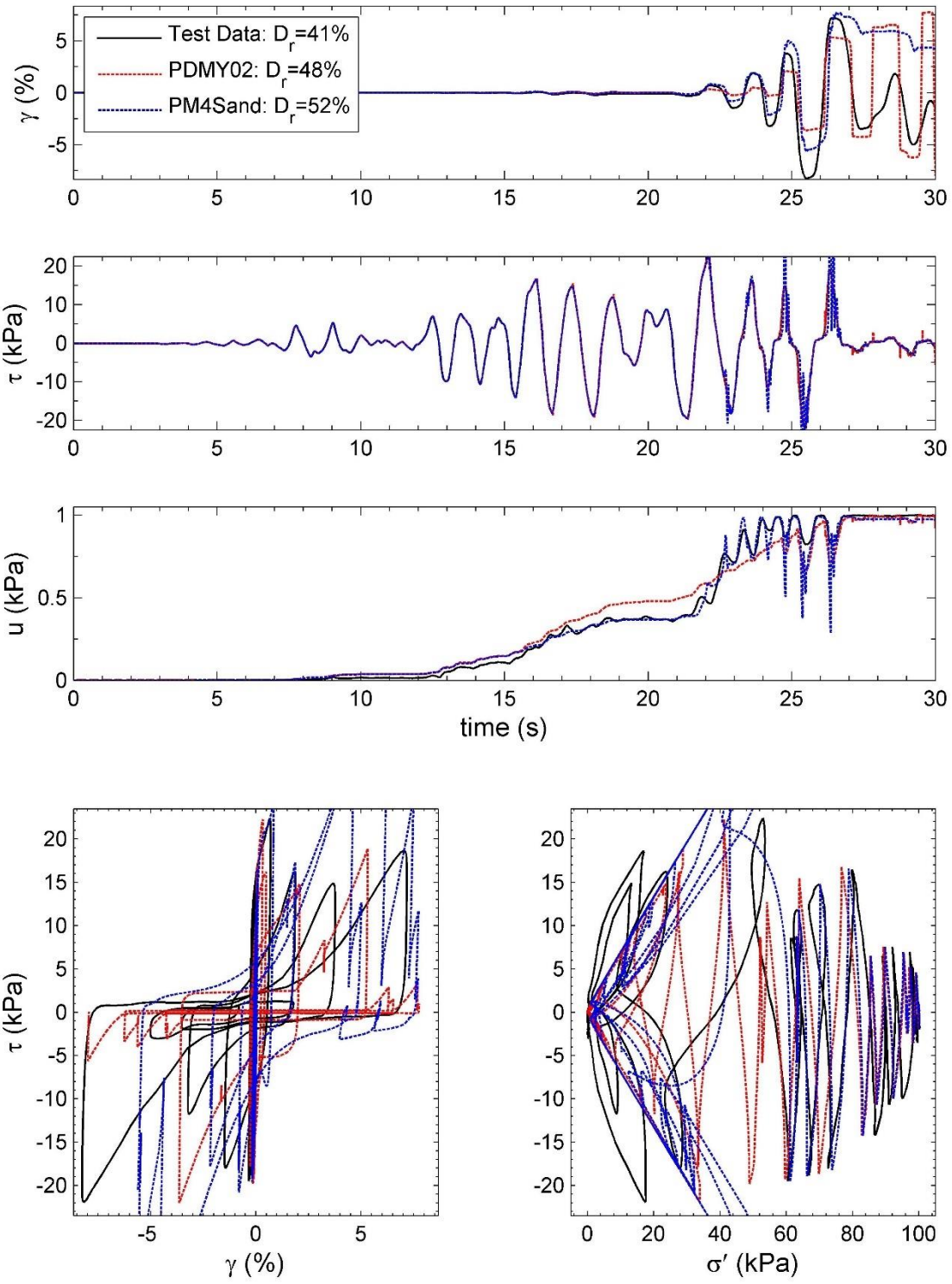


Figure 6.71: Comparison of CSS test data and numerical simulations using PDMY02 and PM4Sand for Test 130118the figure includes plots showing the strain, stress, and r_u time histories as well as stress-strain and stress path response.

The response for Test 130711-02 is shown in Figure 6.72. As discussed previously, the numerical simulations generally do a good job of approximating the recorded r_u response. However, for this test, neither of the numerical models were able to fully reproduce the shielding effect or the rapid increase in r_u associated with large peaks that significantly exceed the PPA. The relative denity of the test was 78%, and the calibrated apparent relative densities for the numerical models were 73 and 70% for PDMY02 and PM4Sand, respectively. From 20 to 36 seconds the recorded r_u and the computed r_u from the numerical models increased as the loading amplitudes increased. The PM4Sand r_u response increased in a very gradual manner, while the recorded and PDMY02 r_u response generally showed sudden increases in r_u at the location of local peaks in the shear stress time history. From 36 to approximately 57 seconds, the shear stress loading history included pulses with amplitudes that were near the PPA, however they did not exceed the PPA and the recorded r_u response was essentially constant. During this time both numerical models computed a slight increase in r_u. From 57 to 60 seconds the loading amplitudes exceeded the PPA and the recorded r_u response again began to increase. The numerical models also showed an increase during this time, but the incremental increase in r_u from the numerical models were lower than the recorded response. Between 61 and 66 seconds the loading amplitudes were significantly lower than the PPA, and the numerical models were able to capture the shielding behavior observed in the recorded r_u time history. After 70 seconds phase transformation behavior was observed and the r_u quickly up to initial liquefaction ($r_u > 0.99$). This behavior was also captured by both numerical models, but the response was slightly delayed with respect to the recorded r_u time history.

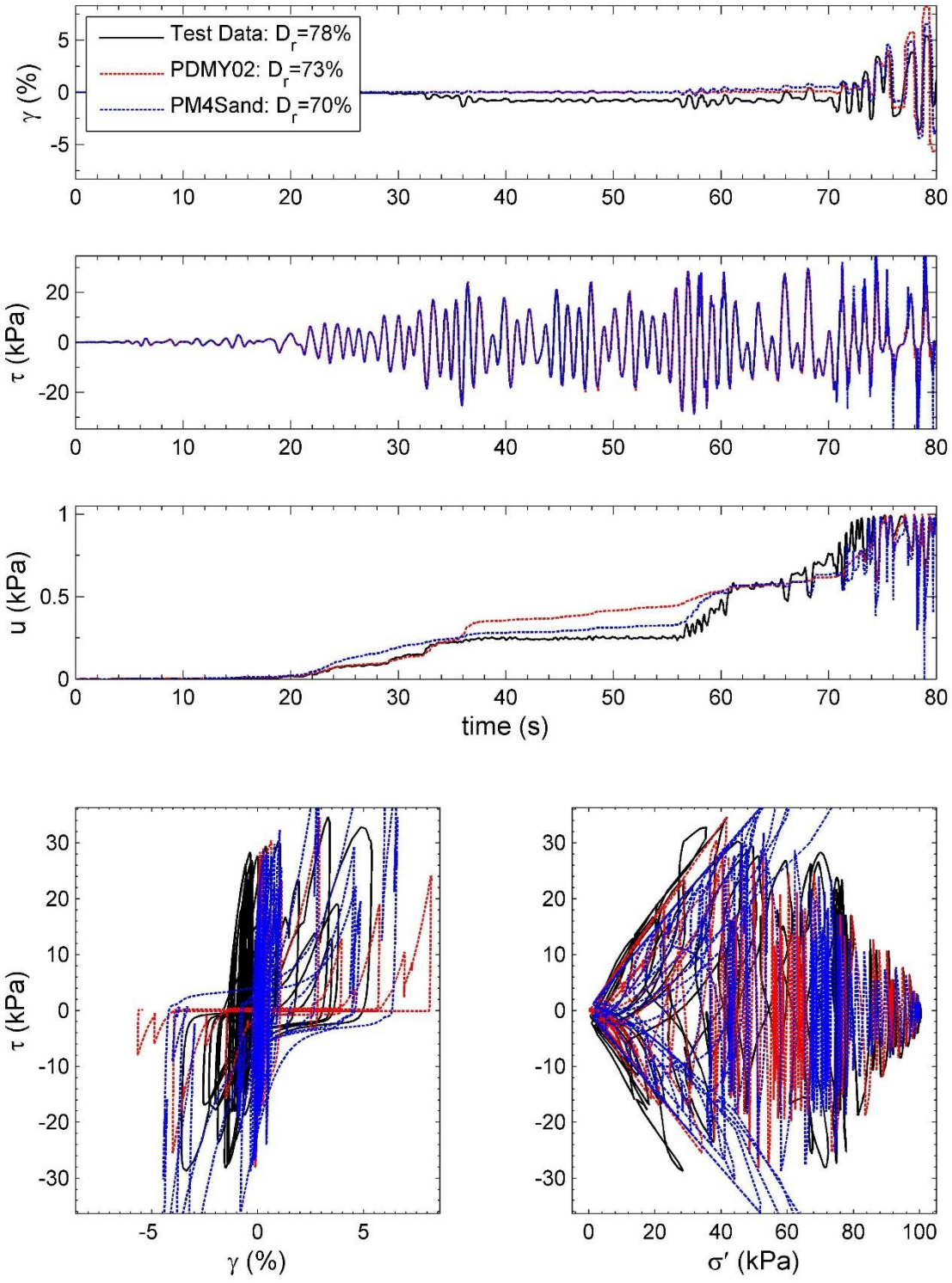


Figure 6.72: Comparison of CSS test data and numerical simulations using PDMY02 and PM4Sand for Test 130711-02the figure includes plots showing the strain, stress, and r_u time histories as well as stress-strain and stress path response

From the example shown in Figure 6.72, it appears as though the numerical models can effectively capture the shielding effect when the loading amplitudes are significantly lower than the PPA (i.e. from 61 to 66 seconds in Figure 6.72), but are not as effective at simulating the shielding behavior that was observed when the loading amplitudes are just below the PPA (i.e. 20 to 36 seconds).

Figure 6.73 shows the recorded and simulated response for Test 130119 and provides another example where the numerical models are not able to fully account for the shielding of cycles that are close to, but less than, the PPA. For this example, the relative density of the test was 37% and the calibrated apparent density of the numerical models were 52 and 49% for PDMY02 and PM4Sand, respectively. The loading amplitudes in the first 20 seconds of the record were low and generated minimal amounts of excess pore pressures. Both numerical models overpredicted the r_u response during this time. The loading between 20 and 24 seconds included slightly larger amplitude stress pulses that exceeded the PPA, and the r_u showed a small increase. This increase was also observed in the numerical models. The loading history between 24 and 54 seconds included pulses with amplitudes that were close to, but did not exceed, the PPA and the sample did not generate any additional excess pore pressure. However, the numerical models showed a slight increase during this time. While the magnitude of the computed r_u response was low (below 0.25), both numerical models computed r_u values that were over double the recorded response. From 56 to 64 seconds the loading amplitudes increased significantly and the recorded and computed r_u values increased rapidly. However, the recorded r_u response increased at a faster rate than the simulated response and appeared to be more sensitive to the high amplitude loading pulses.

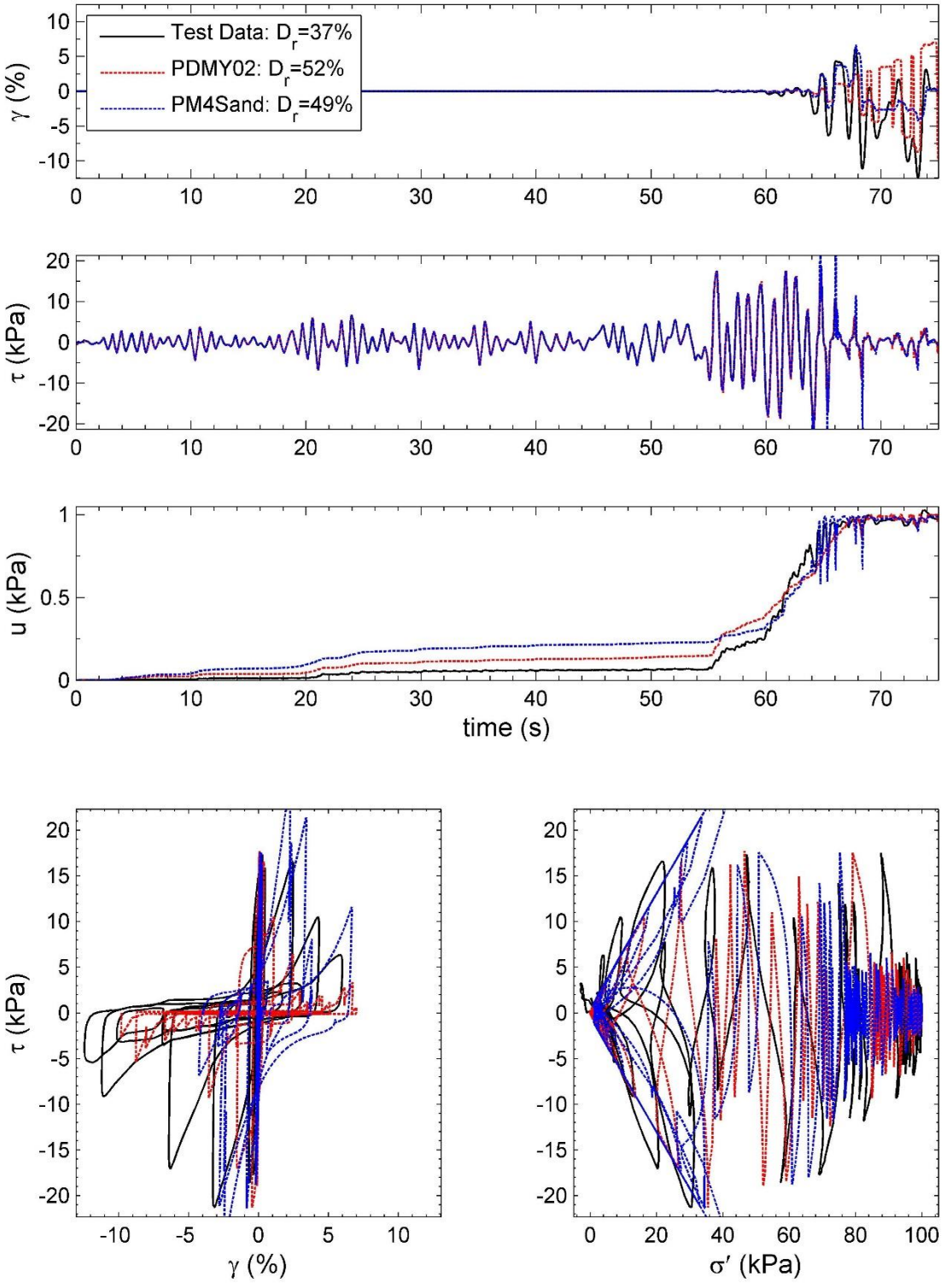


Figure 6.73: Comparison of CSS test data and numerical simulations using PDMY02 and PM4Sand for Test 130119the figure includes plots showing the strain, stress, and r_u time histories as well as stress-strain and stress path response

6.7.4 *Discussion*

While the focus of this research is on the identification of efficient evolutionary IMs for the prediction of the initiation of liquefaction, numerical modeling is becoming increasingly popular in engineering practice for the prediction of the initiation and effects of liquefaction. The CSS data presented in this study and in Kwan (2015) provides valuable data for the calibration of these models. A brief study was performed to investigate the behavior of two existing constitutive models for liquefiable soils, and to evaluate their performance considering the observations made during the CSS test program. The numerical models generally performed well and were able to effectively approximate the general trends in the recorded r_u response. However, while the numerical models were able to capture the shielding effect when there was a significant reduction in the loading amplitudes with respect to the PPA, they were not as effective at capturing the response when the differences were slight. In addition, the recorded r_u was observed to be extremely sensitive to pulses with large peak amplitudes and showed rapid increases in excess pore pressure that the numerical models were not able to fully simulate.

6.8 DISCUSSION

This chapter described the methods, materials, and results of the CSS testing program, which constituted the first step in a two-stage experimental process. The goal of the CSS testing program was to systematically identify which characteristics of an earthquake loading history are best correlated with the generation of excess pore pressure and the initiation of liquefaction and to assess the efficiency of evolutionary IMs to predict the pore pressure response of an element of soil subjected to transient loading. To accomplish this goal, two CSS test programs were performed, a harmonic loading program (Section 6.3) that used relatively simple loading histories to attempt to isolate important characteristics of the loading history that are related to excess pore pressure generation, and a transient test program (Sections 6.4 and 6.5) that used loading histories derived from actual earthquake records to evaluate the efficiency of various IMs to predict the generation of excess pore pressure and the onset of liquefaction. Important observations from the harmonic test program included

- The generation of excess pore pressure is related to the amplitude and duration of the applied load,

- The generation of excess pore pressure is insensitive to frequency content within the range of interest for earthquake engineering,
- Prior to phase transformation behavior, the generation of excess pore pressure is related to the stress history and the relative amplitude or phasing of the loading history. The prior peak amplitude, or PPA, was found to be an influential aspect of the pore pressure response of a sample in that
    a. Large increments of pore pressure generation are associated with shear stress pulses that exceed the PPA and,
    b. Shear stress pulses that are lower than the PPA generate significantly less pore pressure than if they had not been preceded by a larger amplitude pulse.
- The onset of phase transformation behavior significantly alters the relationship between the loading history and the generation of excess pore pressure. Furthermore, this relationship cannot be accurately predicted using an IM computed based only on the loading history.

The transient test program used loading histories were derived from time histories selected from the NGA Ground Motion Database (Chiou et al. 2008). A diverse suite of transient loading histories was used. The suite of loading histories was composed of three groups of ground motions selected with respect to:

- The behavior with respect to the four standard evolutionary IMs, PGA_m, I_A, CAV and CAV_5 (high with respect to one IM, low with respect to another)
- The rate of energy buildup
- The difference between the acceleration and shear stress time histories from equivalent linear analyses.

In order to compare evolutionary intensity measures calculated from acceleration time histories to the pore pressure response of samples subjected to shear stress loading histories, an equivalent linear program was created to convert the shear stress values to acceleration. The efficiencies of the various IMs in predicting the pore pressure response was evaluated using the standard deviation of the residuals from an IM-D_f-r_u surface fit. The dataset used consisted of 21 tests from the database provided by Kwan (2015) selected to encompass a wide range of relative density values (37-89%), reach a final pore ratio above 0.99, and reflect the diverse suit shear

stress loading histories. The results using the five standard evolutionary IMs indicated that the cycle counting-based IMs, PGA_{mL} and PGA_{mB}, were much more efficient than the integral-based IMs, I_A, CAV, and CAV_5. In particular, PGA_{mB} was shown to be the most efficient IM both when considering both the entire range of r_u values from 0.05 to liquefaction, and at the initiation of liquefaction. This result contradicts the findings of Kramer and Mitchell (2005) and Abegg (2010), which found CAV_5 and I_A to be the most efficient based on numerical analyses. However, the formulation of the two PGA_m IMs have a theoretical basis for being more efficient with respect to predicting the onset of liquefaction than the integral-based methods because,

- PGA_m, like r_u, is insensitive to frequency,
- PGA_m is more efficient at predicting the onset of phase transformation behavior, and
- The r_u response from the CSS data showed a dependence on the order of cycles and was highly sensitive to local peak amplitudes in the loading history. These effects were not captured in the in the numerical analysis of Kramer and Mitchell (2006) and Abegg (2010). Due to the cycle-weighting and MSF formulations used in both definitions of PGA_m, PGA_m is able to capture these effects in a manner that is consistent with the observed r_u response

Any integral-based IM is inherently sensitive to the frequency content of the loading history, while the generation of excess pore pressure is not. Therefore, an integral-based IM will include a degree of uncertainty that will always exist regardless of its formulation. Also, because the onset of phase transformation behavior generally leads to a rapid increase in the generation of excess pore pressure that cannot be accurately accounted for using an IM based on the loading history alone, it was hypothesized that the IM that could best predict the initiation of phase transformation behavior should be the IM that could best predict the onset of phase transformation behavior. Subsequent analyses substantiated this hypothesis and showed that the IM value at the onset of phase transformation was highly correlated with the IM value at the initiation of liquefaction. In addition, these analyses showed that the cycle counting-based IMs were far more efficient at predicting both the onset of phase transformation behavior and the initiation of liquefaction than the integral IMs. In addition to predicting the onset of phase transformation behavior, PGA_{mB} was shown to evolve in a manner that was consistent with the generation of excess pore pressure prior to phase transformation behavior. These factors are

likely why PGA_{mB} was the most efficient IM with respect to the generation of excess pore press and the initiation of liquefaction.

Based on observations made during the harmonic and transient testing programs, a liquefaction-specific intensity measure, LIM, was formulated as a modified version of PGA_{mB} (Section 6.6). LIM differed from PGA_{mB} in that it allowed the stress-history and cycle-scaling factors to be independent and included a cycle ratio factor that explicitly accounted for the relative amplitude and phasing of the time history. The coefficients for LIM were determined from the transient CSS data using constrained optimization. The final form of LIM was shown to reduce the uncertainty in the IM-D_r-r_u relationship using the entire range of r_u values by approximately 33% as compared to the most efficient standard IM, PGA_{mB}. However, the reduction in the uncertainty when using the initiation of liquefaction was only 8%.

The CSS test program provided valuable insight into key aspects of the loading-excess pore pressure relationship. A significant and intrinsic source of uncertainty this relationship is that the behavior following phase transformation is impossible to predict using an IM based solely on the loading history. However, the analyses in this chapter showed that the IM that could best predict the onset of phase transformation and the generation of excess pore pressure prior to phase transformation behavior, PGA_{mB}, was also the most efficient at predicting the initiation of liquefaction. Analyses using a modified version of PGA_{mB}, LIM, only moderately improved the efficiency of the IM, which suggests that PGA_{mB} is a robust IM that can efficiently predict the initiation of liquefaction.

In addition to the IM efficiency evaluations described above, a brief study was performed to investigate the ability of two existing constitutive models to simulate the transient CSS test data. This study showed that the models, PDMY02 and PM4Sand, were able to approximate the generation of excess pore pressure very well in a general sense. However, there are areas where the models could be improved. These areas include (a) better capturing the shielding effect when the difference between the PPA and the subsequent loading amplitudes are slight, and (b) better capturing the rapid increase in r_u as a result of high amplitude stress loading. The CSS tests data from Kwan (2015) provides an excellent resource for numerical modelers to further refine these models. The next chapter will extend these findings using the second step in the experimental testing program, centrifuge testing. Centrifuge tests allow for observation of liquefiable soil behavior on a larger scale than was possible in the CSS testing program.

Chapter 7. CENTRIFUGE TESTING PROGRAM

The previous chapter described the CSS testing program. Gaining an understanding of the soil response at an elemental level provided valuable insight into the mechanisms of liquefaction and the pore pressure response to transient loading. While CSS tests are considered representative of the earthquake-induced shear loading conditions that a soil would experience in the field and can provide a level of detail that is not possible in large-scale tests, it has its limitations. Disadvantages of CSS testing include the development of non-uniform stress distributions due to a lack of complementary shear stresses at the lateral boundary of the test specimen, issues at large strains, and non-uniform sample preparation (Amer et al., 1986, Kishida and Uesugi, 1987).

Full-scale shake table tests likely provide the best simulation of the behavior of saturated soils in the field; however, the associated cost and effort required for those tests make them prohibitive for collecting large amounts of data spanning a wide range of initial soil conditions and transient loading histories. Another technique that simulates the behavior of saturated soils to transient loadings on a large scale in a controlled environment is centrifuge testing. Centrifuge testing provides a means for simulating life-sized events by subjecting scale models to higher gravitational fields. These models can be heavily instrumented and subjected to base shaking to simulate earthquake loading and can be reproduced more efficiently than full-scale testing. As such, centrifuge testing was selected for the second stage of the experimental testing program to evaluate the efficiency of evolutionary intensity measures to predict the pore pressure response of liquefiable soils.

7.1 INTRODUCTION

The underlying concept in centrifuge modeling is that a model built at a linear scale of 1:N, with N as the scale factor, subjected to an N-g gravitational field will feel the same stresses at the same locations in both the model and the (full-scale) prototype. This allows researchers to simulate an event on small, well instrumented models and produce results that are representative of the type of response that would be observed on a full-scale model. This is especially useful in the field of geotechnical engineering, as full-scale stress states can be generated on a model

constructed with well-defined soil properties. It provides advantages over full-scale testing, particularly in terms of cost and time (Gonzalez-Lagos et. al, 2007).

While the stresses seen in both a prototype and a centrifuge model are the same, other parameters that play an important role in liquefaction analyses do not scale at a 1:1 ratio between model and prototype. Table 7.1 lists a number of important factors (time, acceleration, etc.) along with their corresponding scaling factor.

Table 7.1: Centrifuge parameter scaling factors(from Steedman and Zeng, 1995)

Parameter	Prototype	Model
Stress	1	1
Strain	1	1
Displacement	1	1/N
Velocity	1	1
Acceleration	1	N
Time (dynamic)	1	1/N
Frequency	1	N
Time (consolidation)	1	$1/N^2$
Energy	1	$1/N^3$

With respect to the generation of excess pore pressures and the initiation of liquefaction, the time rate of consolidation, which affects the dissipation of excess pore pressures, is an important parameter. From Table 7.1, the time rate of consolidation between model and prototype differ by a factor of N^2. Therefore, excess pore pressures dissipate more rapidly in a centrifuge prototype than would be observed under similar conditions in the field provided the pore fluid is the same in both scenarios (i.e. water). To address this, prior studies (e.g. Stewart et al., 1998; Dashti et al., 2010a and 2010b; El-Sekelly et al., 2016; and Darby et al., 2019) have saturated the model with a solution of methylcellulose and water to increase the viscosity of the pore fluid and reduce the rate of consolidation in the centrifuge model. The pore fluid used in this study consisted solely of water. The goal of this study was to systematically identify optimal evolutionary IMs for the prediction of the initiation of liquefaction. To accomplish this goal, the centrifuge testing program involved subjecting the centrifuge models to repeated shaking events in order to capture as wide a range of IM and excess pore pressure response as possible. While using water as the pore fluid inevitably results in high rates of consolidation and can lead to partially drained conditions in the model, it also reduces the time it takes for excess pore

pressures to dissipate once the motion has ended. The current study included experiments where up to 68 base motions were applied to a single soil model. Before a new motion could be applied, the excess pore pressures generated during the previous test had to be allowed to dissipate. Therefore, water was selected as the pore fluid to allow for a large number of tests to be conducted in a reasonable amount of time.

The centrifuge testing for this research project was conducted at Rensselaer Polytechnic Institute (RPI) at the NEES Center for Earthquake Engineering Simulation (CEES) centrifuge facility. Technical specifications for the centrifuge can be found at http://homepages.rpi.edu/~dobryr/centrifuge2.html, and a photo of the centrifuge apparatus at RPI is shown in Figure 7.1. The radius of the centrifuge was 3-m as measured to the model platform.

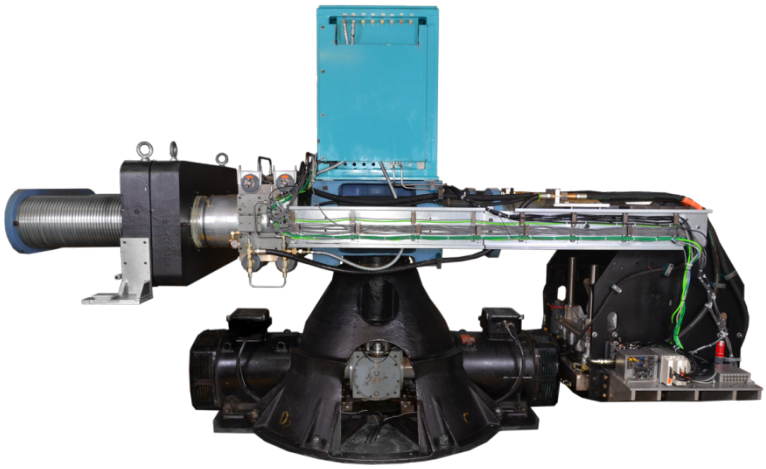


Figure 7.1: Side view of RPI centrifuge.

A total of six individual centrifuge experiments were performed. As described previously, each experiment consisted of numerous tests or trials, where a transient motion was applied to the model and the response was measured. After the excess pore pressures dissipated, another test was performed on the same model using a new base input motion. The following sections include a literature review of other centrifuge studies that involved multiple shaking events. The sections following the literature review provide further details on the centrifuge testing program. The sections include descriptions of the applied loading time histories, specifics of the testing program including model description, loading protocols and data processing, as well as the results of the centrifuge experiments.

7.2 Other Centrifuge Studies for Models Subjected to Multiple Shaking Events

This section describes two centrifuge studies, El-Sekelly et al. (2016) and Darby et al. (2019), that involved a level ground soil model subjected to multiple shaking events. Although published earlier, these tests were performed after the tests described later in this chapter. Both studies used constant amplitude harmonic input motions. The harmonic motions were scaled to different amplitudes and applied successively to the soil model. Insights from these studies can be used to inform the data processing and interpretation of the current centrifuge study, which used a suite of fully transient loading histories derived from actual earthquake records. A unique aspect of centrifuge experiments that include multiple shaking events is that the state of the soil is altered with each shaking event. During the review of each of these studies, special emphasis was placed on how the study quantified the change in soil conditions due to repeated shaking. Each study is presented individually in the following sections.

7.2.1 *El-Sekelly et al. (2016)*

El-Sekelly et al. (2016) performed centrifuge testing that used repeated sinusoidal loadings on a model composed of silty sand saturated with a viscous fluid. The tests were performed at the RPI centrifuge facility. The soil profile and sensor layout from El-Sekelly et al. (2016) is shown in Figure 7.2. The soil profile consisted of silty sand constructed at a target uniform relative density of 38%. The experiment was conducted at a centrifuge acceleration of 25 g, which corresponded to a prototype height of approximately 5.9 m. The sensors included accelerometers, pore pressure transducers, an LVDT at the ground surface, and bender elements.

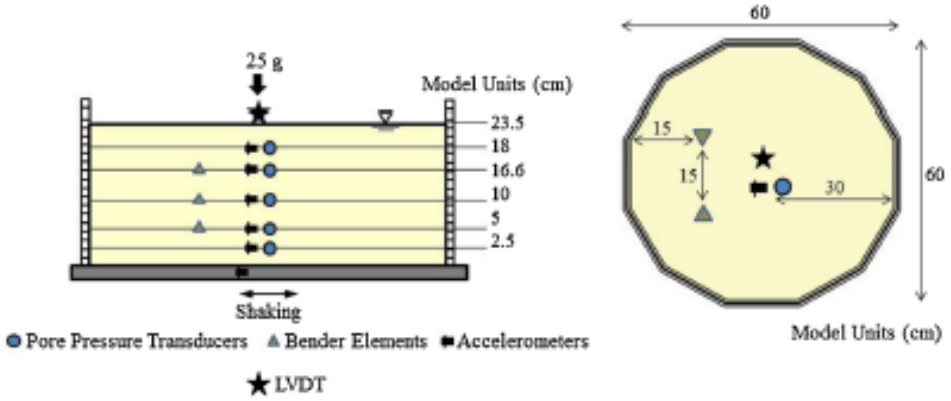


Figure 7.2: Centrifuge model and sensor layout from the study of El-Sekelly et al. (2016)note the provided units are in model scale.

The model was subjected to one-dimensional harmonic loadings applied at a frequency of 2 Hz (prototype scale). The loading histories included a series of weak shakings (Event A) performed between higher amplitude tests (Event B). Event A corresponded to 5 cycles at a target peak acceleration of 0.035 g and Event B corresponded to 15 cycles at a target peak acceleration of 0.04 g. For each motion, El-Sekelly et al. (2016) computed the CSR in the center of the profile using system identification procedures. The CSR for each event was then adjusted to account for the number of applied cycles, using a magnitude scaling factor, and for 2D effects in order to compare the centrifuge results to the field case history databases. Further details of the CSR computations are provided in El-Sekelly et al. (2016). A total of 66 motions were applied to the model, 60 of which used Event A as the base input motion, and 6 of which used Event B as the base input motion. Following each event, El-Sekelly et al. (2016) estimated the average change in relative density of the model based on measurements of the surface settlements and evaluated the change in shear wave velocity using bender elements.

El-Sekelly et al. (2016) found that the average relative density of the model, as determined using surface settlements, generally increased with each successive shaking event. In addition, the liquefaction resistance also generally increased with each successive event. However, strong events that induced high pore pressures in the model, Event B, tended to decrease the liquefaction resistance within the deposit for a subsequent Event A as compared to an Event A that was applied prior to Event B. This observation is summarized in Figure 7.3. Using shaking events 11, 12, and 13 as an example, note the peak r_u response for shaking number

11 (Event A) is approximately 0.4. Shaking number 12 (Event B), induced a large peak r_u of approximately 0.85. The peak r_u for shaking number 13 (Event A), produced an r_u of approximately 0.7, which was much larger than the peak r_u from shaking event 11 even though the loading histories were essentially the same. El-Sekelly et al. (2016) observed that this temporary reduction in liquefaction resistance diminished quickly as additional Event A motions were applied to the model.

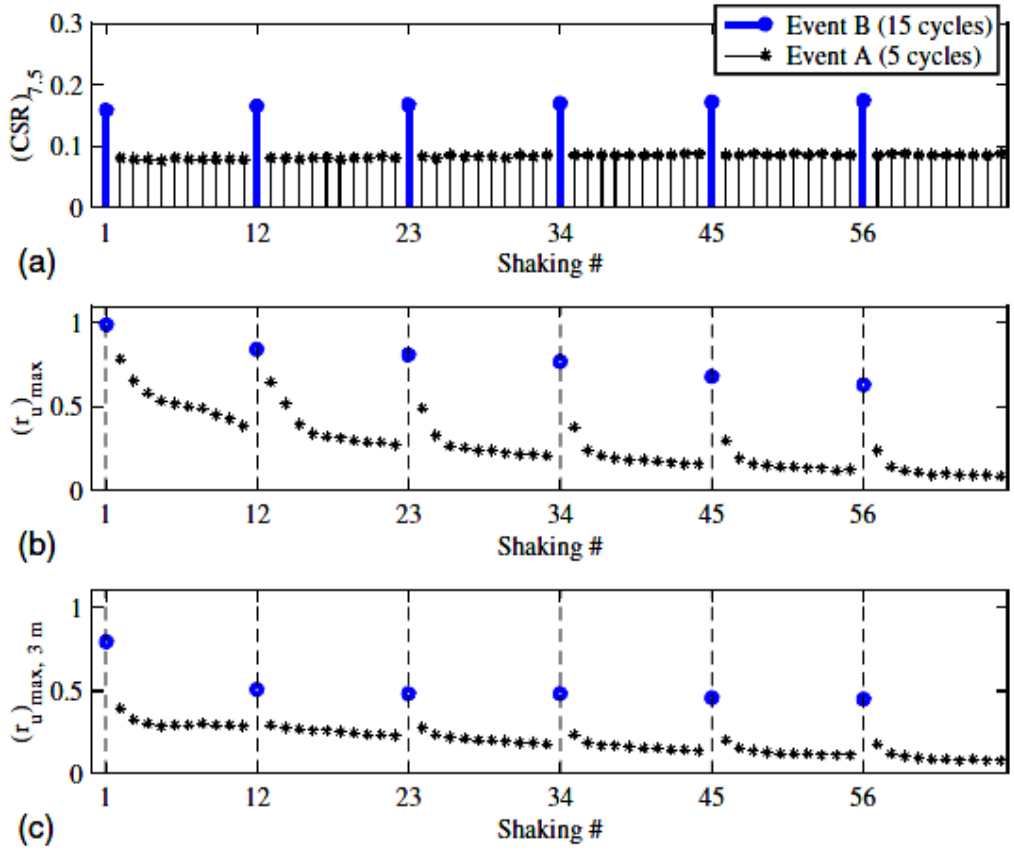


Figure 7.3: Excess pore pressure response from El-Sekelly et al. (2016) for a centrifuge model subjected to multiple shaking events.(a) The shaking sequence, with amplitudes presented in cycle-corrected CSR, (b) the maximum pore pressure ratio for the entire deposit, and (c) the maximum pore pressure ratio at a depth of 3 m.

After each test, El-Sekelly et al. (2016) evaluated the evolution of the normalized shear wave velocity, V_{s1}, using bender element measurements, and the average relative density, using the surface settlement. These results are provided in Figure 7.4. El-Sekelly et al. (2016) found that the normalized shear wave velocity measurements were relatively insensitive the amount of shaking that the model was subjected to and that shear wave velocity-based procedures did not

capture the increase in liquefaction resistance and relative density that was observed for models that have undergone multiple shaking events.

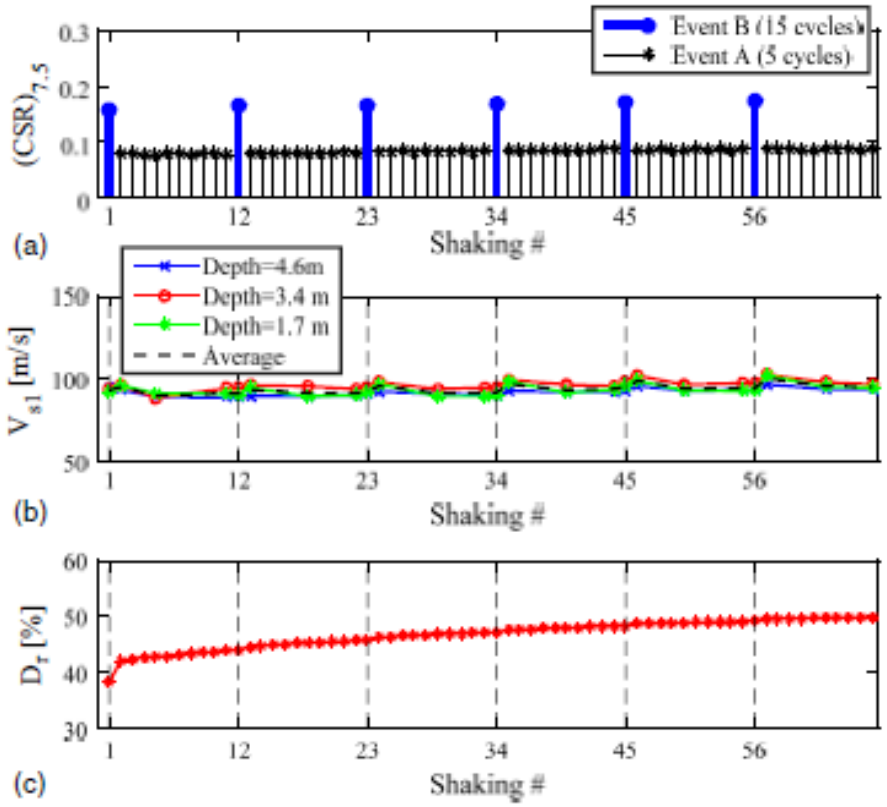


Figure 7.4: Change in V_{s1} and relative density from El Sekelly et al. (2016) for a centrifuge model subjected to multiple shaking events.The shaking magnitude in terms of cycle-corrected CSR, (b) the values of V_{s1} measured during the test, and (c) values of relative density computed from the surface settlements.

Figure 7.5 shows the relationship between the peak pore pressure response in the model (Figure 7.3b) as a function of the relative density and V_{s1} (Figures 7.4b and c, respectively) using the data provided in El-Sekelly et al. (2016). To account for the variation in loading intensity, Events A and B are distinguished individually in Figure 7.5. In addition, based on the observations from El-Sekelly et al. (2016), the first and second shaking Events A that followed the large amplitude Event B were also plotted using different colors and scatter point markers. This figure further illustrates the observations from El-Sekelly et al. (2016). As both V_{s1} and relative density increase, the peak r_u generally decreases. At similar values of V_{s1} and relative density, the larger amplitude loading generates higher pore pressure than the lower amplitude loading. In addition, a smaller amplitude event applied within the first two events following a

large amplitude event generated higher pore pressures than the subsequent small amplitude events. The relationship with peak r_u was observed to be stronger with respect to relative density than with V_{s1} and showed clear trends with respect to loading intensity and the shaking sequence. These results suggested that the relative density of the model was a more robust predictor of the liquefaction resistance of the model than shear wave velocity-based procedures.

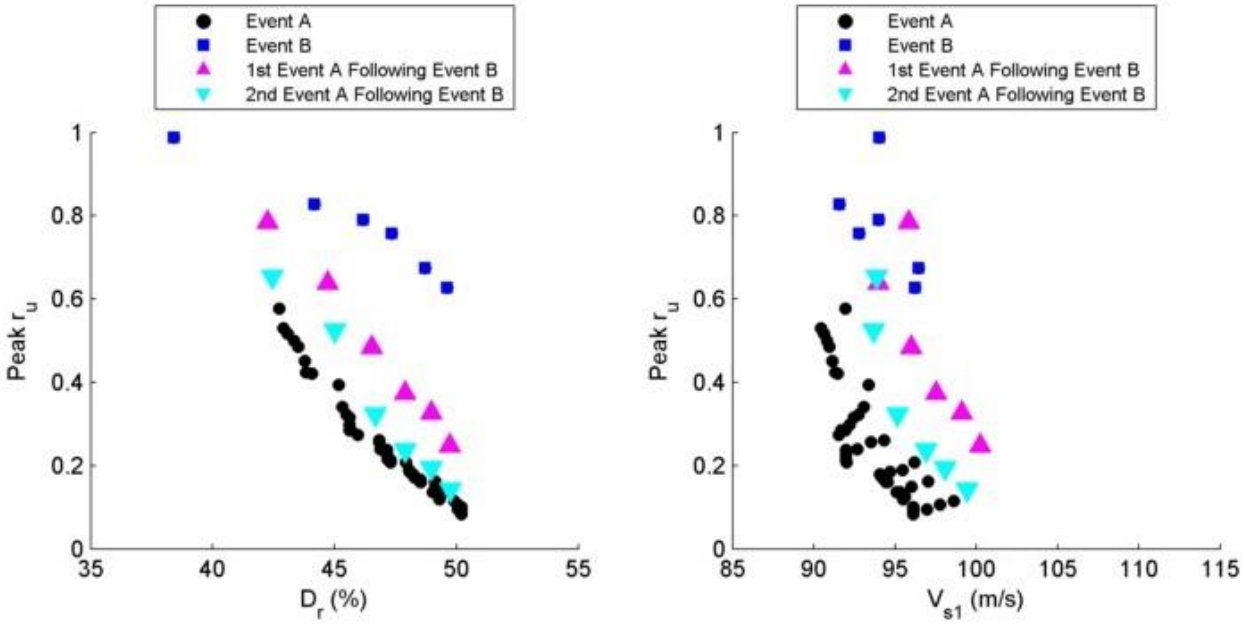


Figure 7.5: The peak r_u value as a function of relative density and V_{s1} (after El-Sekelly et al., 2016)

Another observation from El-Sekelly et al. (2016) was that the surface settlement (and correspondingly the change in relative density) was highly correlated to the peak r_u value, $(r_u)_{max}$, which generally occurred at shallow depths. The relationship between $(r_u)_{max}$ and the permanent vertical strain, $\Delta\varepsilon_v$, computed as the surface settlement divided by the height of the model, from El-Sekelly et al. (2016) is provided in Figure 7.6. This finding is consistent with laboratory- and empirically-based post-liquefaction settlement procedures (Ishihara and Yoshimine, 1992; Ishihara et al., 2016), which relate the liquefaction-induced volumetric strain to a factor of safety against liquefaction, noting that the factor of safety against liquefaction is related to the r_u value (e.g. Tokimatsu and Yoshimi, 1983).

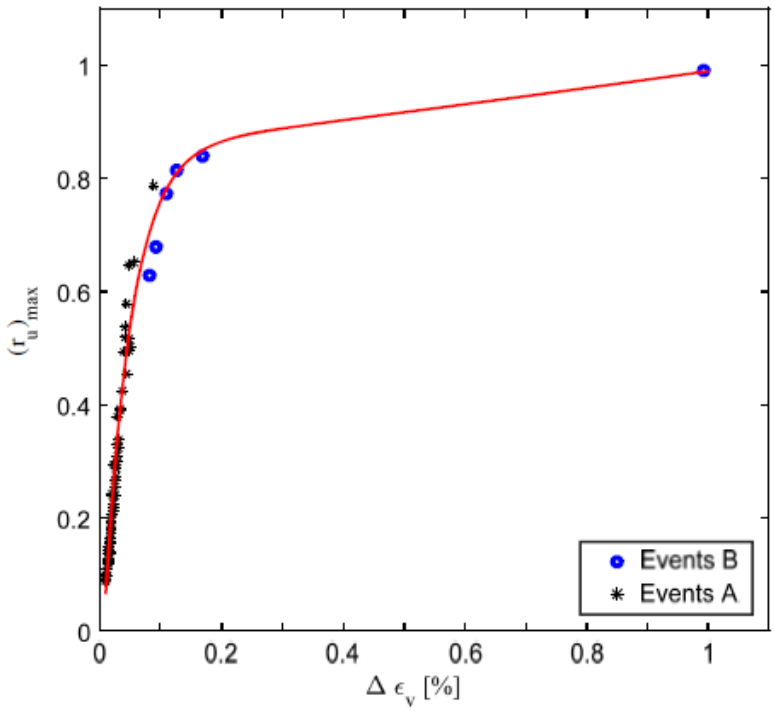


Figure 7.6: Relationship between maximum r_u and permanent vertical strain from El-Sekelly et al. (2016).

7.2.2 *Darby et al. (2017), Darby et al. (2018), and Darby et al. (2019)*

Darby et al. (2017; 2018; 2019) performed a series of three centrifuge tests on models composed of clean sand saturated with viscous fluid conducted at the University of California, Davis centrifuge facility. A schematic of the soil profile and sensor layout are provided in Figure 7.7. The model was tested at a centrifuge acceleration of 40 g. The soil profile in prototype units consisted of a 1.6 m thick gravel layer at the base of the model overlain by a 4 m thick layer of dense Monterey Sand placed at a target relative density of 85%. Above the dense Monterey sand layer, an Ottawa sand layer was constructed at target uniform initial densities of 43% (Model 1), 25% (Model 2), and 85% (Model 3). The model included interior accelerometers and pore pressure transducers, as well as four settlement pads located at the ground surface which measured the surface settlement using linear potentiometers. At intermittent points in the testing program, Darby et al. (2019) evaluated the soil conditions in the Ottawa sand layers using a mini-cone penetrometer (mini-CPT) device.

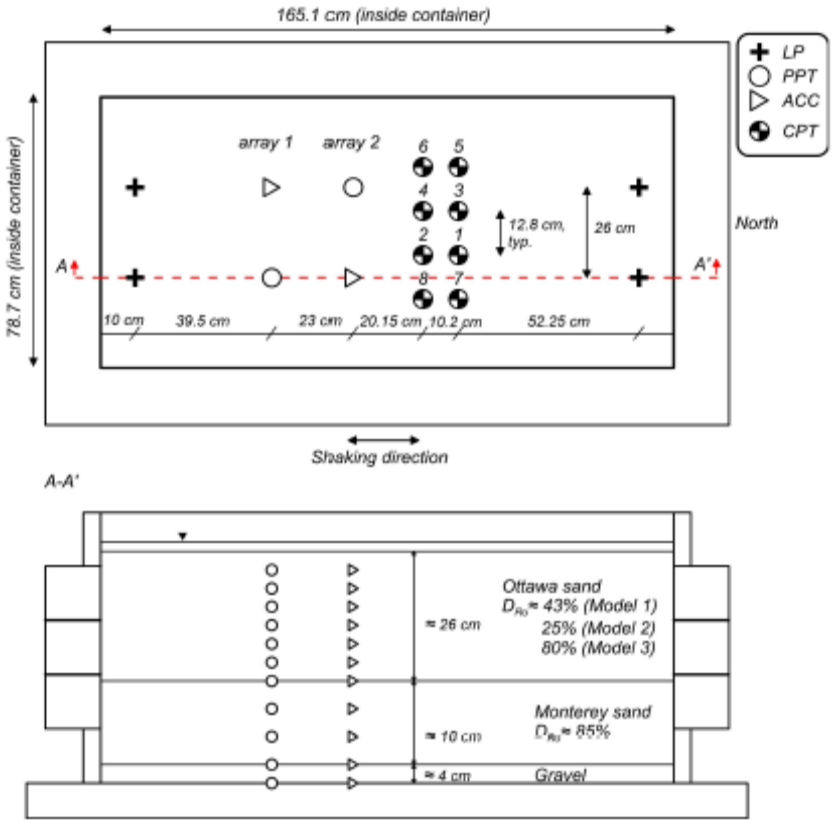


Figure 7.7: Centrifuge model and sensor layout from the study of Darby et al. (2019)note that the provided units are in model scale.

Each model was subjected to a series of one-dimensional shaking events. The base motions consisted of 15 uniform cycles applied at 1.0 Hz and scaled to various peak amplitudes. The shaking sequence consisted of amplitudes that progressively increased from a peak amplitude of 0.03 g for the first event to 0.25 g for the sixth event. This sequence was then repeated several times for each test. Towards the end of each experiment, as the model became very dense, the peak amplitude of the base motion was increased up to 0.55 g. The number of shaking events for each experiment were 29, 26, and 17 for Models 1 through 3, respectively. A summary of the results from Model 2 (D_r = 25%) are provided in Figure 7.8 which provides the peak base acceleration, peak r_u, and average volumetric strain (computed as the surface settlement divided by the thickness of the Ottawa sand layer) as a function of the shaking event.

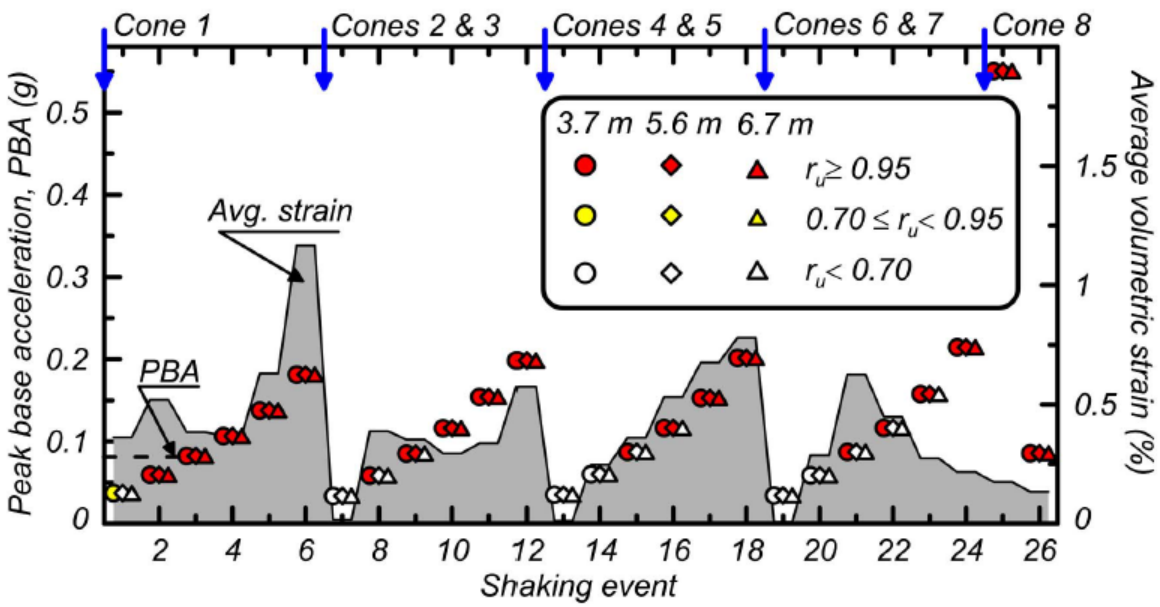


Figure 7.8: Test summary of Model 2 (D_r 25%) from Darby et al. (2019)summarizing the peak base acceleration, peak r_u, and average volumetric strain from each shaking event. The sequencing of the mini-CPT tests are provided at the top of the plot.

The results from Darby et al. (2019) were consistent with the findings from El-Sekelly et al. (2016) in that the resistance to liquefaction generally increased as successive motions were applied and the model densified. This behavior can be seen in Figure 7.8 by examining the results for shaking events 2, 8, and 14, which had the same peak base acceleration of approximately 0.05 g. Event 2 induced r_u values greater than 0.95 for each of the reported depths. In event 8, an r_u response greater than 0.95 was only observed at a depth of 3.7 meters, while in event 14 the peak r_u response was less than 0.7 at each of the sensor depths.

However, the decrease in liquefaction resistance following a very large event as noted in El-Sekelly et al. (2016) was not consistently observed in the experiments by Darby et al. (2019). In the example provided in Figure 7.8, shaking event 1 induced a peak r_u between 0.7 and 0.95 at a depth of 3.7 meters and less than 0.7 at all other depths. Shaking event 7, which had the same amplitude as event 1 and followed an event with a peak base acceleration of approximately 0.15 g that induced peak r_u values greater than 0.95 throughout the model, produced a peak r_u of less than 0.7 at all sensor depths. On the other hand, event 26, which had a peak base acceleration of 0.08 g and followed an event with a peak base acceleration of 0.55, which was the largest acceleration applied to the model by a factor of 2, induced r_u values greater than 0.95 throughout

the model. A similar event, Event 21 which followed a lower amplitude shaking event only induced a peak r_u greater than 0.95 in the uppermost sensor location. Darby et al. (2019) suggested that the differences in the observed responses between the two studies could have been due to the differences in relative densities, shaking intensity, and the sequencing of the applied motions.

As noted previously, Darby et al. (2019) evaluated the densification of the model due to successive shaking events using mini-CPT tests performed at the beginning and end of the tests, as well as at intermittent times between shaking events. The results of the mini-CPTs were correlated to relative density using a Monterey sand-specific correlation presented in Darby et al. (2019). An example of how the density of the soil evolved over the course of the testing program is provided in Figure 7.9 for Model 2 from Darby et al. (2017). The sequencing of the cone testing is as provided at the top of the plot shown in Figure 7.8. As shown in Figure 7.9, the model began at a fairly constant relative density, with the relative density slightly increasing with depth. The relative density of the liquefiable soils generally increased as the number of shaking events increased; however, the densification was not necessarily uniform with depth. The mini-CPT results showed that while the density at all depths tended to increase after each applied motion, the lower layers tended to densify more than the upper layers during the motions applied early in the testing program, while the upper layers tended to densify more during motions applied later in the testing program.

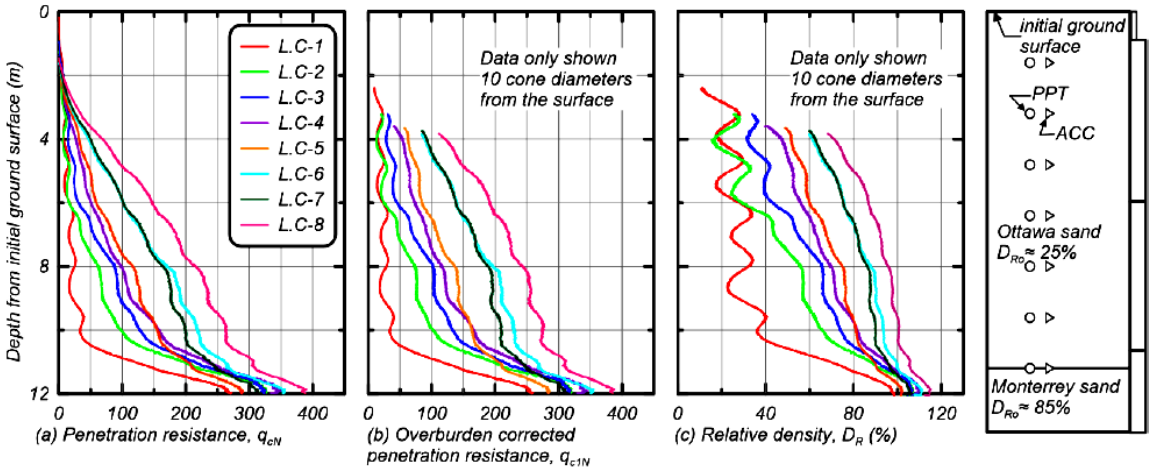


Figure 7.9: Example of model densification based on CPT tip resistances from Darby et al. (2017) for Model 2 (D_r = 25%).(a) measured tip resistance, (b) normalized penetration resistance, and (c) estimated relative density.

The results of the mini-CPT testing for Model 3 (D_r = 85%) from Darby et al. (2017) are provided in Figure 7.10. In Figure 7.10 the sequence of the cone testing was as follows:

- Cones 1 to 4 were performed prior to shaking,
- Cones 5 and 6 were performed after 6 shaking events,
- Cone 7 was performed after 12 shaking events,
- Cone 8 was performed after 13 shaking events,
- Cone 9 was performed after 16 shaking events, and
- Cones 10 and 11 were performed at the end of the test after 17 shaking events.

The cones performed prior to any Model 3 shaking events showed that the initial relative density profile was highly depth-dependent and varied from an initial relative density of 50% at the top of the profile to a relative density of 90% at the bottom of the profile. This contrasted with the initial relative density profile for Model 2, which only varied between 20% and 35% over the depth of the liquefiable layer. In addition, the increase in relative density due to shaking was more constant with depth than was observed in the initially loose model.

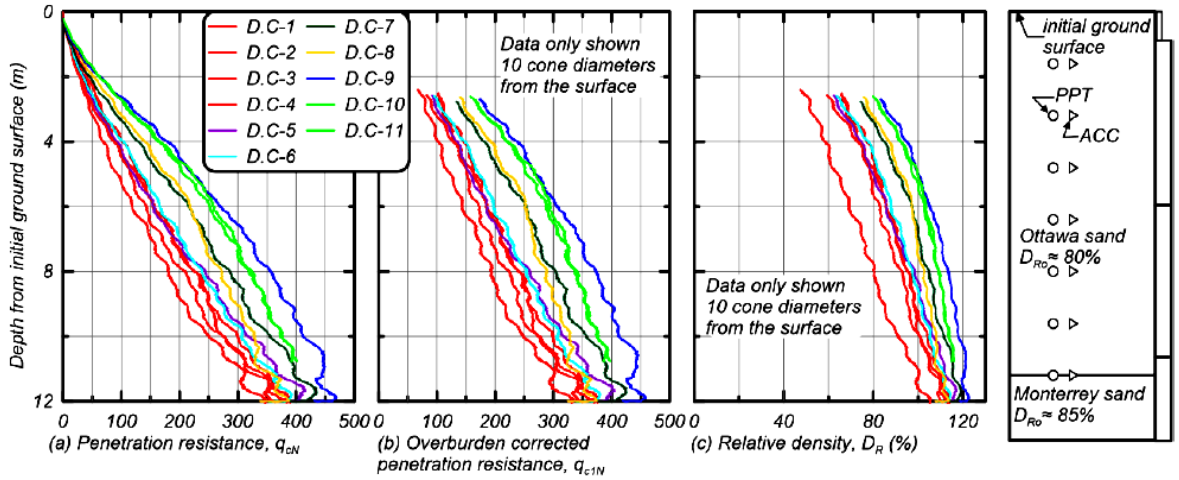


Figure 7.10: Example of model densification based on CPT tip resistances from Darby et al. (2017) for Model 3 (D_r = 85%).(a) measured tip resistance, (b) normalized penetration resistance, and (c) estimated relative density

Darby et al. (2017) noted that the average relative density as evaluated using the mini-CPT results were in reasonable agreement with the average relative density evaluated based on the surface settlement. Using the supplementary data provided by Darby et al. (2019) and the surface settlement data from Darby et al. (2018), a comparison was made between the average relative density computed using the surface settlement, and the density computed from the

average corrected cone tip resistances, q_{c1N}, for three locations within the liquefiable Ottawa sand layer (at 1/3, ½, and 2/3 H where H is the height of the liquefiable layer). Figure 7.11 shows the results of these analyses for each of the three centrifuge tests. The results show that the relative density computed using the average surface settlement was within the range of relative densities that were evaluated using the CPT data for each of the centrifuge models. However, there are some inconsistencies in the relative density estimate using the surface data. For Models 1 and 3 the estimate using the surface settlement was consistently on the upper bound of the CPT-based estimates, while for Model 2 the surface settlement estimates best approximated the lower bound CPT-based estimates. Darby et al. (2017) noted that the surface settlements can be influenced by liquefaction, which can result in tilting and burial of the settlement pads, and by strong shaking events that can cause the settlement monitoring instruments to stick when stressed laterally.

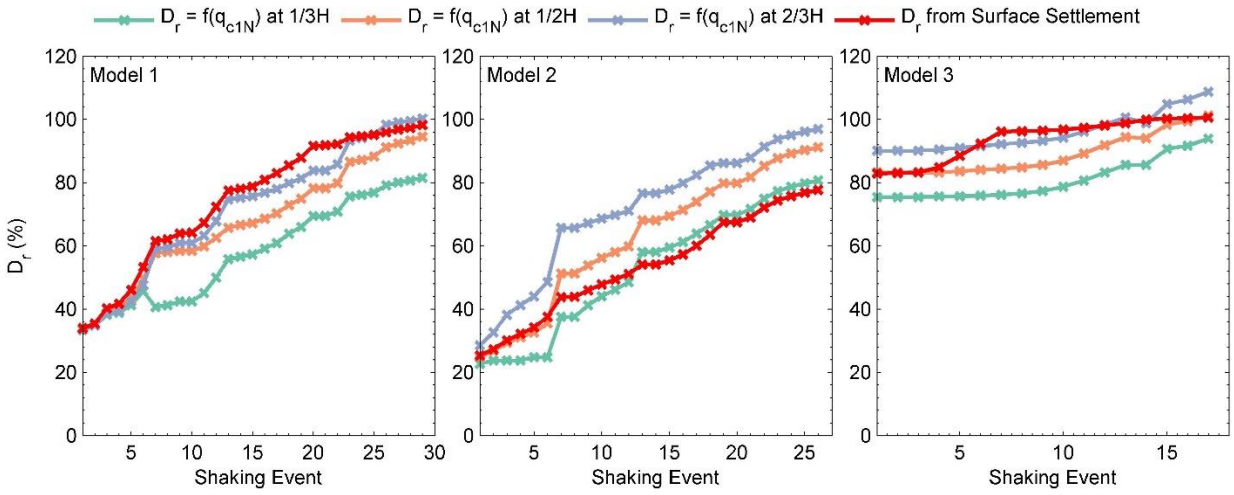


Figure 7.11: Comparison of relative density evaluated using mini-CPT data conducted during testing and the relative density estimated based on surface settlements for the 3 centrifuge models provided by Darby et al. (2019).

Like El-Sekelly et al. (2016), Darby et al. (2019) found that the increase in relative density due to repeated shaking led to a corresponding increase in liquefaction resistance. Darby et al. (2019) computed the corrected CPT tip resistance, q_{c1N}, and CSR values corrected to 15 uniform cycles and overburden pressure of one atmosphere for each shaking event and compared the results to the Boulanger and Idriss (2014) CPT-based liquefaction triggering procedure. Based on these analyses, Darby et al. (2019) found that the progressive increase in both the q_{c1N}

and the resistance to liquefaction as a result of successive shaking events generally followed the trends shown in the case history-based liquefaction triggering correlations.

7.2.3 *Discussion*

Previous studies by El-Sekelly et al. (2016) and Darby et al. (2017; 2018; 2019) found that successive shaking events generally increased both the density and liquefaction resistance of the centrifuge models. El-Sekelly et al. (2016) observed that the normalized shear wave velocity was not sensitive to the number of shaking events, and therefore was not a sufficient indicator of the model's resistance to liquefaction. Subsequent analyses using the data provided in El-Sekelly et al. (2016) showed that the average relative density as estimated using the surface settlement seemed to effectively capture the increase in liquefaction resistance due to successive shaking events when accounting for the intensity of the loading and the shaking sequence.

Darby et al. (2019), found that the increase in both q_{c1N} and the liquefaction resistance were consistent with the case history-based liquefaction triggering correlations. Darby et al. (2017) noted the relative density computed using the surface settlement and the average relative density computed using correlations with q_{c1N} data were generally in agreement. This further suggests that the average relative density of the model can be an effective indicator of the model's resistance to liquefaction. However, the settlement measurements can be affected by a number of factors which can lead to uncertainty in the relative density estimates.

Both studies observed that, in some instances, the model's resistance to liquefaction can be temporarily reduced following a very large event that causes extensive liquefaction; however, this phenomenon was not consistently observed in all of the centrifuge tests and is likely influenced by a number of factors including the soil density, the shaking amplitude, and the sequencing of the applied motions (Darby et al., 2019). The following sections present the details of the centrifuge testing program performed in this study. A notable difference between the present study and the studies performed by El-Sekelly et al. (2016) and Darby et al. (2019) is that as opposed to harmonic loading histories, the present study used a suite of transient input motions that were developed from actual recorded earthquake ground motions.

7.3 CENTRIFUGE LOADING HISTORIES

As with the CSS test program, due to time and budget constraints, it was important to carefully select motions that could distinguish between the predictive capabilities of various IMs as efficiently as possible. Two suites of input motions were developed and used as base input motions for the centrifuge test program. The first suite consisted of motions that were selected based on their behavior with respect to the IMs, while the second suite consisted of motions that were selected based on their rate of energy buildup. In order to diversify the motion suite and reduce the potential for bias, 24 new motions were selected from the database of Abegg (2010) based on their IM behavior using the same methodology described in Section 6.4.1.1. A detailed description of the development of the baseline ground motion database is provided in Abegg (2010).

A summary of these motions is shown in Table 7.2. Stacked acceleration time histories of the motions are shown in Figures 7.12 through 7.14. A scatter plot matrix showing the IM response of the selected motions is shown in Figure 7.15. Figures 7.12 through 7.15 show that the selected motions provided a diverse motion suite both in terms of temporal characteristics and their response with respect to the various standard intensity measures.

Table 7.2: Characteristics of input motions selected based on their IM behavior.

NGA #	Mag.	R_{JB} (km)	PGA (g)	PGA_M (g)	I_A (cm/s)	CAV_5 (cm/s)	NED	Motion Category	
614	5.99	15.29	0.422	0.255	73.0	328.8	2.58E-03	AVG CAV5	HIGH IA
568	5.80	7.93	0.517	0.262	116.0	358.9	1.26E-02	AVG CAV5	HIGH NED
626	5.99	21.26	0.526	0.257	67.7	363.8	3.41E-03	AVG CAV5	HIGH PGAM
1092	6.69	68.44	0.069	0.065	10.3	276.3	3.55E-05	AVG CAV5	LOW IA
1514*	7.62	107.04	0.068	0.051	14.0	367.0	3.40E-05	AVG CAV5	LOW NED
1167	7.51	147.89	0.053	0.044	9.4	313.2	2.15E-05	AVG CAV5	LOW PGAM
1538	7.62	46.32	0.088	0.094	32.1	631.3	1.40E-04	AVG IA	HIGH CAV5
33	6.19	40.26	0.383	0.174	31.5	209.8	1.58E-03	AVG IA	HIGH NED
1023	6.69	44.77	0.413	0.201	32.0	199.7	7.65E-04	AVG IA	HIGH PGAM
695	5.99	36.68	0.337	0.191	36.5	229.4	6.96E-04	AVG IA	LOW CAV5
310*	7.30	75.25	0.157	0.120	37.5	470.8	3.52E-04	AVG IA	LOW NED
1477	7.62	80.09	0.145	0.075	30.7	542.0	2.12E-04	AVG IA	LOW PGAM
1515	7.62	36.20	0.198	0.161	73.4	730.9	1.04E-03	AVG NED	HIGH CAV5
1462*	7.62	36.20	0.188	0.166	72.9	711.8	1.05E-03	AVG NED	HIGH IA
638	5.99	20.33	0.372	0.249	65.0	331.1	1.23E-03	AVG NED	HIGH PGAM
459	6.19	36.34	0.322	0.214	41.6	246.6	1.20E-03	AVG NED	LOW CAV5
3309	6.30	83.09	0.309	0.132	33.2	338.6	1.09E-03	AVG NED	LOW IA
338	6.36	38.54	0.280	0.131	48.0	457.1	1.22E-03	AVG NED	LOW PGAM
1547	7.62	33.80	0.139	0.114	65.3	838.1	4.47E-04	AVG PGAM	HIGH CAV5
732	6.93	63.49	0.239	0.120	57.6	439.2	8.88E-04	AVG PGAM	HIGH IA
784	6.93	91.68	0.258	0.114	37.3	370.4	8.25E-04	AVG PGAM	HIGH NED
1698	5.28	22.26	0.235	0.139	18.3	121.7	4.00E-04	AVG PGAM	LOW CAV5
34*	5.60	29.73	0.335	0.127	10.5	127.2	2.44E-04	AVG PGAM	LOW IA
672	5.99	38.38	0.176	0.138	18.7	180.5	2.06E-04	AVG PGAM	LOW NED

* from archived 2000 PEER Ground Motion Database

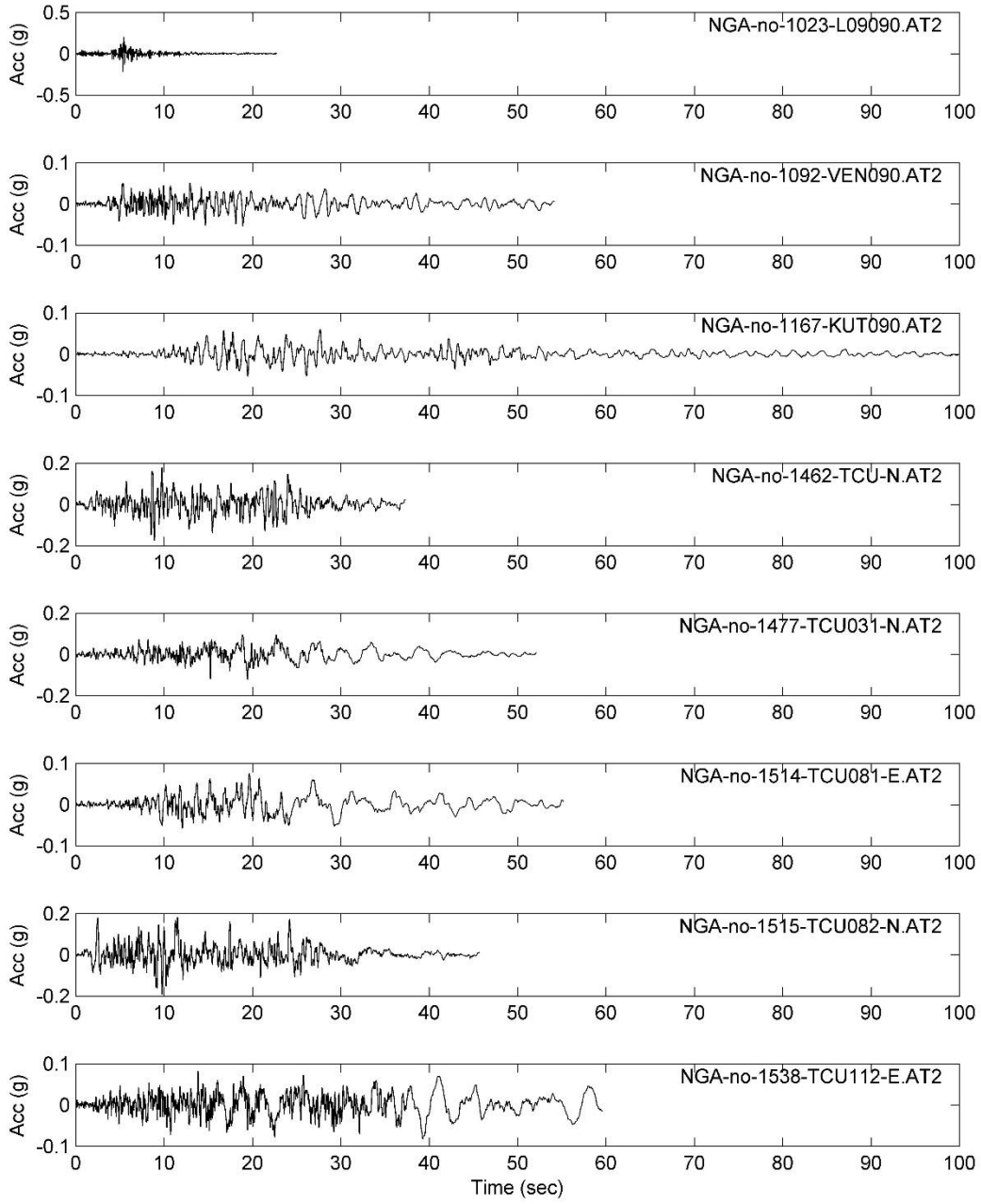


Figure 7.12: Motions selected for use in centrifuge testing based on IM behavior.

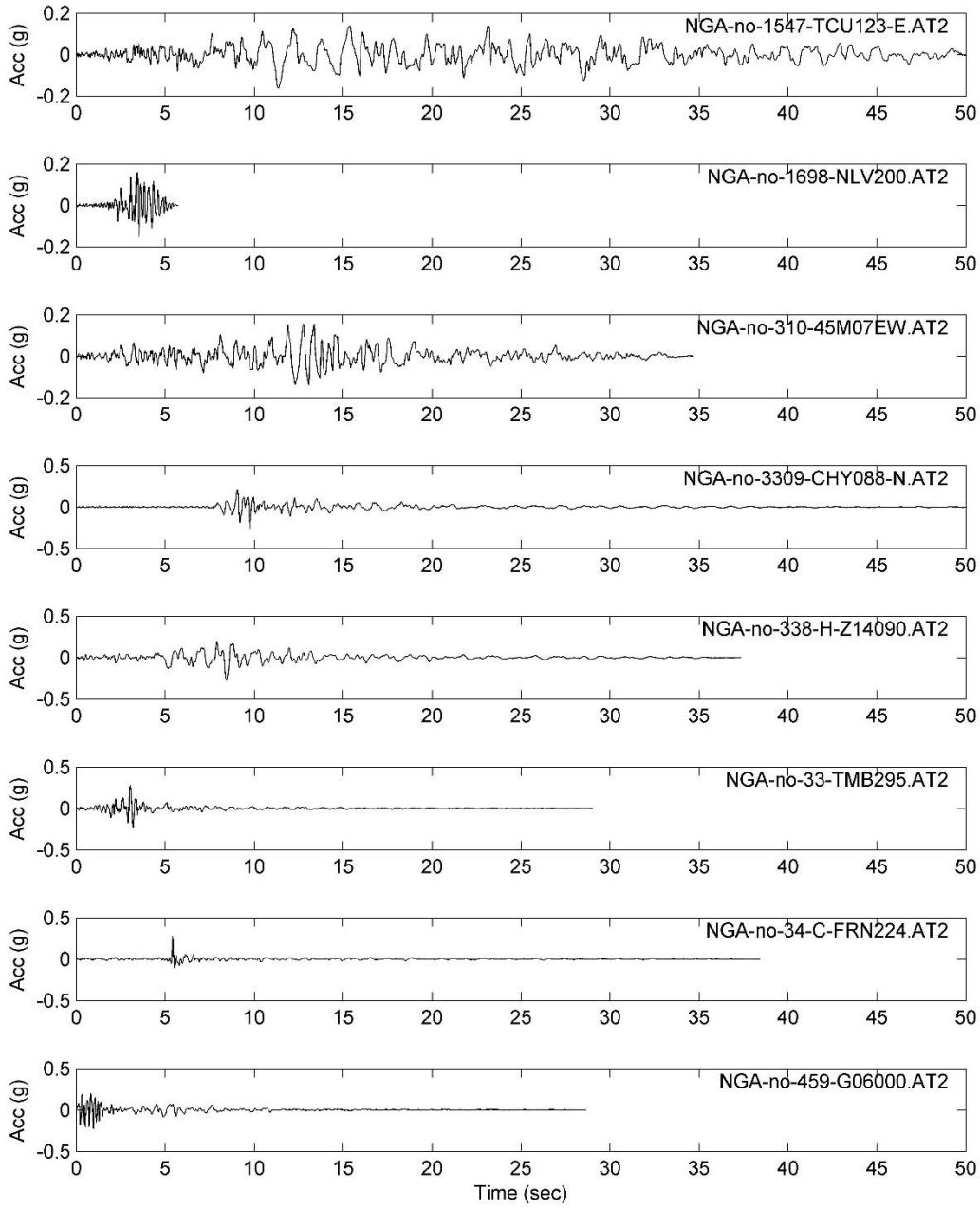


Figure 7.13: Motions selected for use in centrifuge testing based on IM behavior.

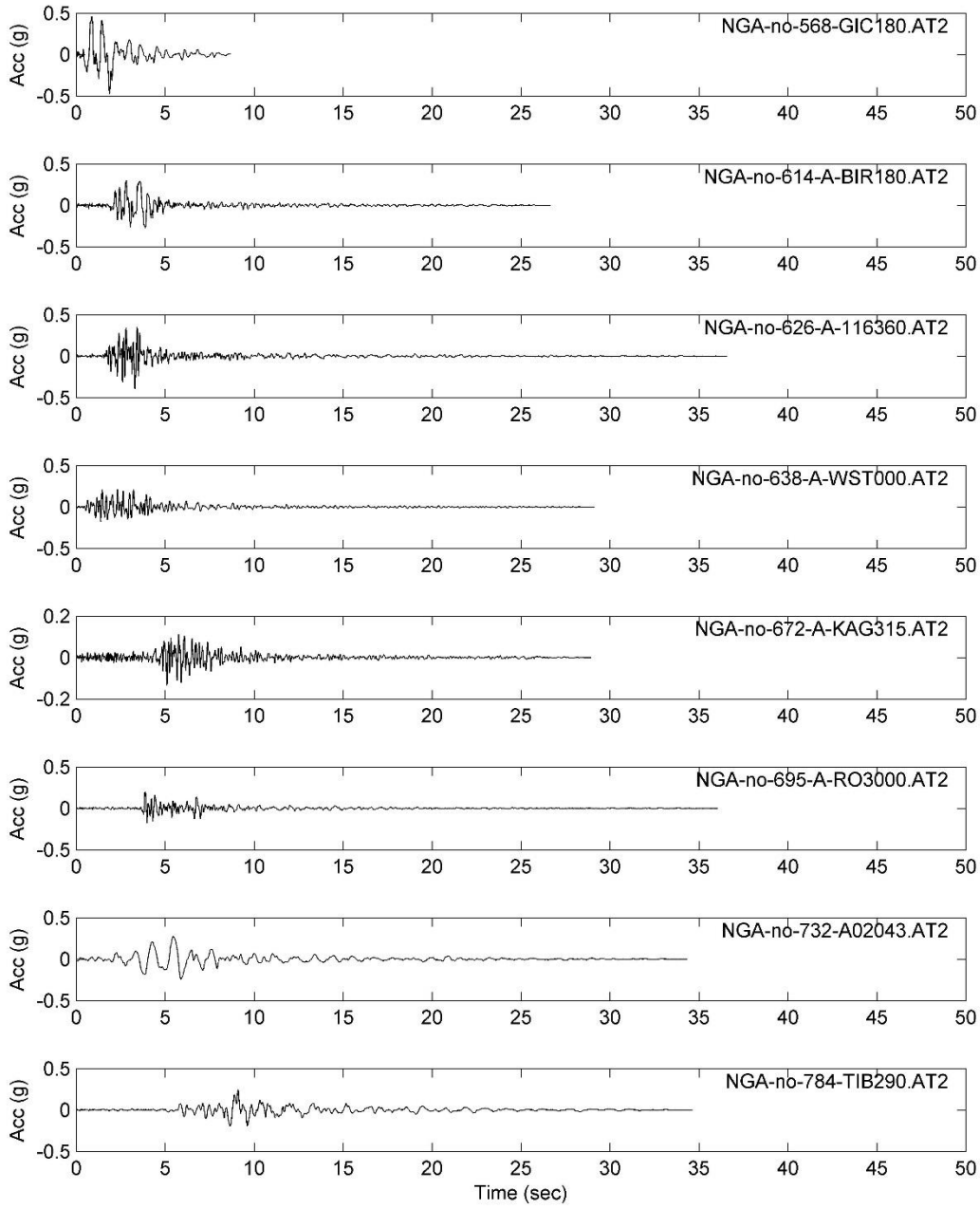


Figure 7.14: Motions selected for use in centrifuge testing based on IM behavior.

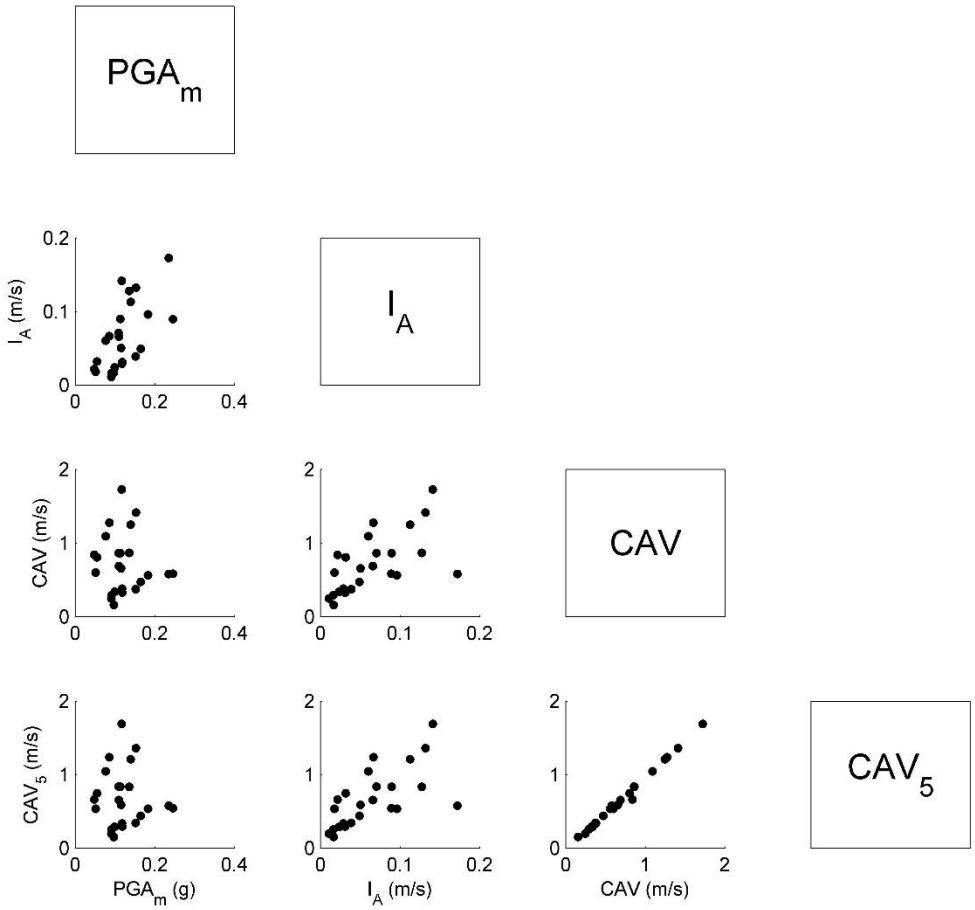


Figure 7.15: Scatterplot matrix showing the relationships of the IMs for the motions selected based on the IM behavior for use in centrifuge testing.

The second suite of motions were developed late in the centrifuge testing program based on observations made during the CSS testing, which identified that the relative amplitude and phasing of the loading history were related to the generation of excess pore pressure. Therefore, the six additional motions identified in Section 6.4.1.1 were also included in the centrifuge test program. Plots of the acceleration time histories for these motions were provided in Figure 6.24.

7.4 CENTRIFUGE EXPERIMENTAL TESTING PROGRAM

A total of six centrifuge experiments were conducted for this project. Each of the centrifuge experiments modeled a soil profile that was nearly identical to the profile shown in Figure 6.26, which was also used in the numerical analysis of Abegg (2010). The only difference between the

theoretical soil profile and the soil profile modeled in the centrifuge was that the ground water table for the centrifuge tests was located at the ground surface, which greatly simplified the model fabrication process. The goal for the centrifuge experiments was to physically model the one-dimensional behavior of a simple soil profile and record the pore pressure, displacement and acceleration response to a diverse set of input motions. Evolutionary IMs calculated from the recorded acceleration time histories were compared to the recorded pore pressure behavior to evaluate the ability of the various intensity measures to predict the generation of excess pore pressure and the triggering of liquefaction. A series of experiments were conducted using models constructed at different relative densities that were subjected to a diverse suit of motions applied to the base of the soil model.

The specifics, including model, material and equipment descriptions for each of the six centrifuge experiments have been archived on the National Hazards Engineering Research Infrastructure (NHERI) website. Both model reports and the data generated by the experiments can be accessed at https://www.designsafe-ci.org/data/browser/public/nees.public//NEES-2010-0957.groups/ as Experiments 1 through 6. A summary of the six experiments is provided in Table 7.3. Each of the experiments were conducted at a centrifuge acceleration of 22.5 g.

Table 7.3: Summary of centrifuge experiments.

NHERI Experiment Number	Test Dates	Initial Relative Density	Number of Applied Motions
1	2/4/2011 - 2/8/2011	100%	37
2	2/11/2011	50%	34
3	9/21/2010 - 9/23/2010	40%	62
4	9/13/2010 - 9/16/2010	70%	68
5	9/13/2013	40%	8
6	9/24/2013	40%	8

The purpose of the first four experiments was to generate as much data as possible using a diverse set of base input motions scaled to different amplitudes in order to capture the full range of pore pressure response, both low and high. The number of applied motions in these experiments ranged from 34 to 68. Despite the efforts made to measure the change in relative density of each of the models using settlement monuments, as described in Section 7.4.2, accurately measuring the change in density of an entire layer using a series of settlement

measurements proved difficult, as the monuments were subject to tilting and rocking during the shaking process. The difficulty was exacerbated by the large number of motions applied to the model. In addition, due to the large number of applied motions and the subsequent densification of the model, the motions applied towards the end of the testing program generated very little pore pressure despite the high amplitudes of the applied motions.

The last two centrifuge experiments, Experiments 5 and 6, incorporated fewer input motions (8), began at a low relative density, and had the goal of inducing large amounts of excess pore pressure. In this way each of the motions could, in theory, be applied to a model loose enough to generate high pore pressures, and with fewer motions applied, the confidence in the measured settlement, and resulting change in relative density, would increase. The following sections provide details on the process used to fabricate and instrument each of the centrifuge models, which were consistent for each of the six centrifuge tests.

7.4.1 *Centrifuge Model Construction*

All of the centrifuge tests featured the same geometry and fabrication process. Each model was constructed in a one-dimensional laminar box provided by RPI. A photo of the laminar box used in the centrifuge tests is shown in Figure 7.16. The box was rigid in the dimension perpendicular to the horizontally applied base motion, while the 9.35 mm tall laminar rings allowed the soil to move freely in the direction of the applied motion. Bearings were placed between each of the rings as well as between the rings and the rigid side walls to reduce the effect of friction. Further specifications of the RPI one-dimensional laminar box can be found at http://www.nees.rpi.edu/equipment/laminar-boxes/.

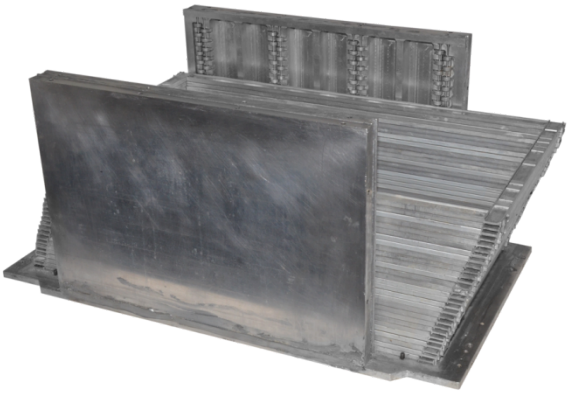


Figure 7.16: One-dimensional laminar box used in centrifuge tests.

The soil profile was 12.25” tall, at model scale, and was composed of seven 1.75” tall sub-layers. Each of the soil layers was constructed using Nevada sand. A cemented sand layer was constructed at the bottom of the profile by adding 6% by weight of QuickCrete to Nevada sand, and placed in four even lifts. Each lift was then sprayed with water until the entire lift was thoroughly damp. Once all four lifts were placed, the cemented layer was allowed to cure overnight prior to placement of the upper sand layers.

The upper six Nevada sand layers were placed in two 7/8-inch-thick lifts per layer. The layers were constructed by adding a specific weight of dry Nevada sand per lift. The weight per lift was calculated based on maximum and minimum density data provided by the RPI facilities (Table 7.4) and the inner dimensions of the laminar container to achieve a desired relative density for each sand layer. To create each lift, the soil was placed in a bucket and transferred to the container via a pluviating device. The device had nine rows of 40 holes of approximately 1/16” diameter, evenly spaced over a 3.75” by 6.75” area (Figure 7.17). Sand was dropped from a calibrated height and spread evenly over the entire area of the box. Tamping was performed when necessary to achieve the desired layer height. The sides of the container were marked in order to provide visual confirmation the layer was evenly placed. Once this was finished, the layer was smoothed using a straight edge to produce as uniform a lift as possible. After completion of each lift, sensors were placed as described in Section 7.4.2.

Table 7.4: Nevada sand relative density properties provided by RPI.

GeoTesting express
a subsidiary of Geocomp Corporation

Client:	Rensselaer Polytechnic Institute	Test Date:	11/25/09
Project Name:	Sand Testing	Tested By:	saa
Project Location:	---	Checked By:	mpd
GTX #:	9481		

Minimum Density of Soil by ASTM D 4254 and
Maximum Density of Soil Using a Vibratory Table by ASTM D 4253

Boring ID	Sample ID	Depth, ft	Visual Description	Minimum Density, lb/ft^3	Maximum Density, lb/ft^3
---	Nevada Sand 120	---	Dry, tan sand	94.5	106.7
---	Ottawa Sand F-55	---	Dry, white sand	93.85	105.20

Notes: Minimum density determined on a dry sample using Method A using a 0.100 cuft mold
Maximum density determined on a dry sample using Method 1A using a 0.100 cuft mold
The double amplitude of vertical vibration was the standard 0.013 ± 0.002 in.

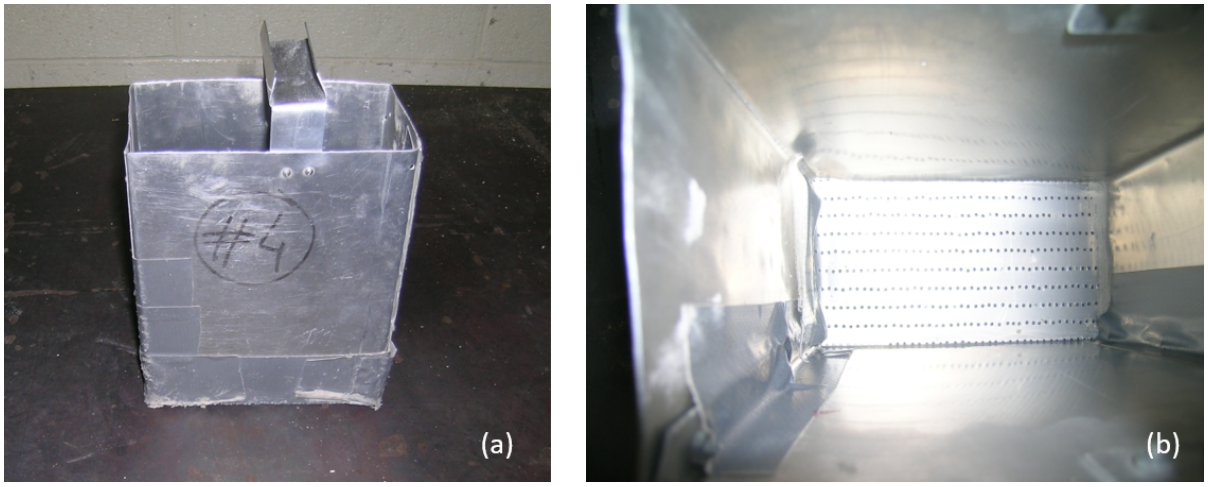


Figure 7.17: Pluviation device used to construct centrifuge models, (a) side view of device, (b) view of the holes drilled in bottom of device.

After the model was constructed and each of the interior sensors were placed, the entire model was carefully moved onto the centrifuge to begin the saturation process. To saturate the model, a cover was placed on the top of the model and secured in order to create an airtight seal. A vacuum was then applied to the interior of the model and the model was flushed with carbon dioxide (CO_2), which, being denser than air, was intended to displace the air within the voids of the soil. CO_2 is more soluble in water than air, which also helped to reduce the possibility of gas bubble entrapment within the model. Once this process was complete, water was introduced by

dripping onto sponges placed in the four corners of the model. The sponges prevented erosion of the ground surface, and introduction of water in the corners was intended to keep the level of the rising water surface lower in the center than on the sides and corners to reduce the potential for trapped gas bubbles in the center of the model. The vacuum was maintained until the water level reached the surface of the model. After saturation was complete the sensors were configured with the data acquisition system and the model was considered ready for testing.

7.4.2 *Centrifuge Model Sensors*

Three types of sensors were employed in the each of the centrifuge tests—one-dimensional accelerometers (ACCs), pore pressure transducers (PPTs) and linear variable displacement transformers (LVDTs). Sensors were placed both internally and externally in order to capture the response of the soil profile to the input base motions.

A total of 12 PPTs, 12 ACCs and six LVDTs were placed within the model, as shown in Figures 7.18 and 7.19. Each layer featured two PPTs, located between the first and second lifts at approximately the mid-depth of each layer, to measure the pore pressure response at the center of each soil layer. At the top of each layer, two accelerometers were oriented to capture the acceleration in the direction of the applied motion, along the long dimension of the laminar box. Settlement monuments were also placed at the top of each layer (same depth as the accelerometers) to measure the settlement (and corresponding change in relative density) of the layers after each applied motion in the testing program. The monuments were made of two acrylic pads connected by an aluminum rod (Figure 7.20). Each monument extended to the surface where it was connected to an LVDT attached to a steel bridge that spanned the short dimension of the laminar container. PPTs were placed at the mid-depth of each layer to measure the pore pressure response of the model. Photos showing the typical placement of the pore pressure transducers and accelerometers are shown in Figures 7.21 and 7.22, respectively. As seen in Figures 7.21 and 7.22, each sensor had to be placed so all of the connections were on the same side, to allow for configuration with the data acquisition system (DAQ).

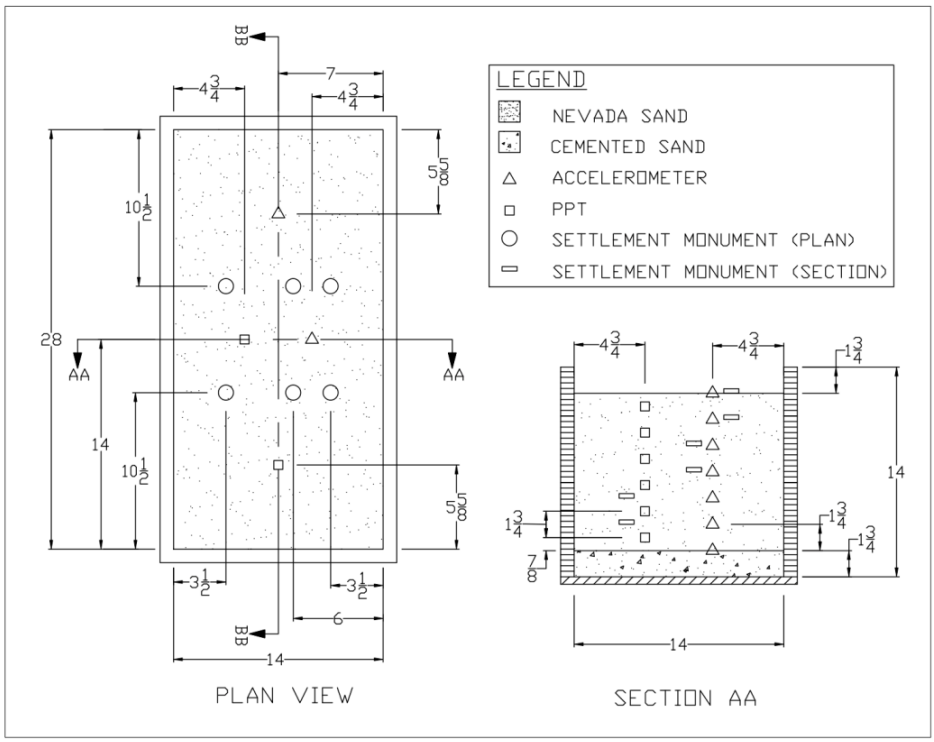


Figure 7.18: Interior centrifuge sensors, plan view and Section AA.

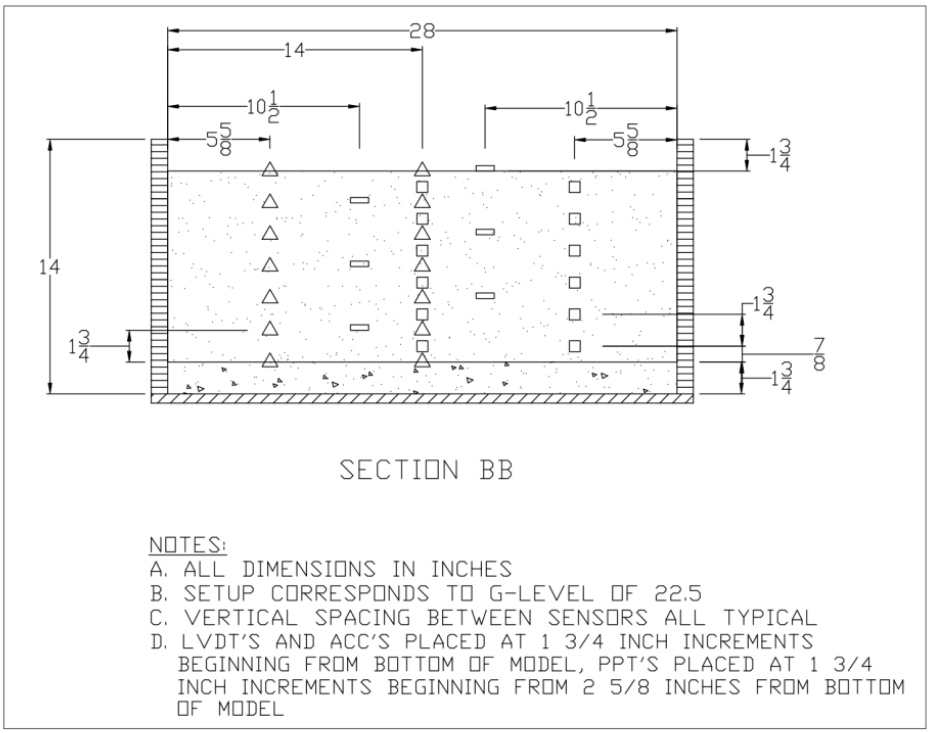


Figure 7.19: Interior centrifuge sensors Section BB.



Figure 7.20: Settlement monuments used in the centrifuge study.

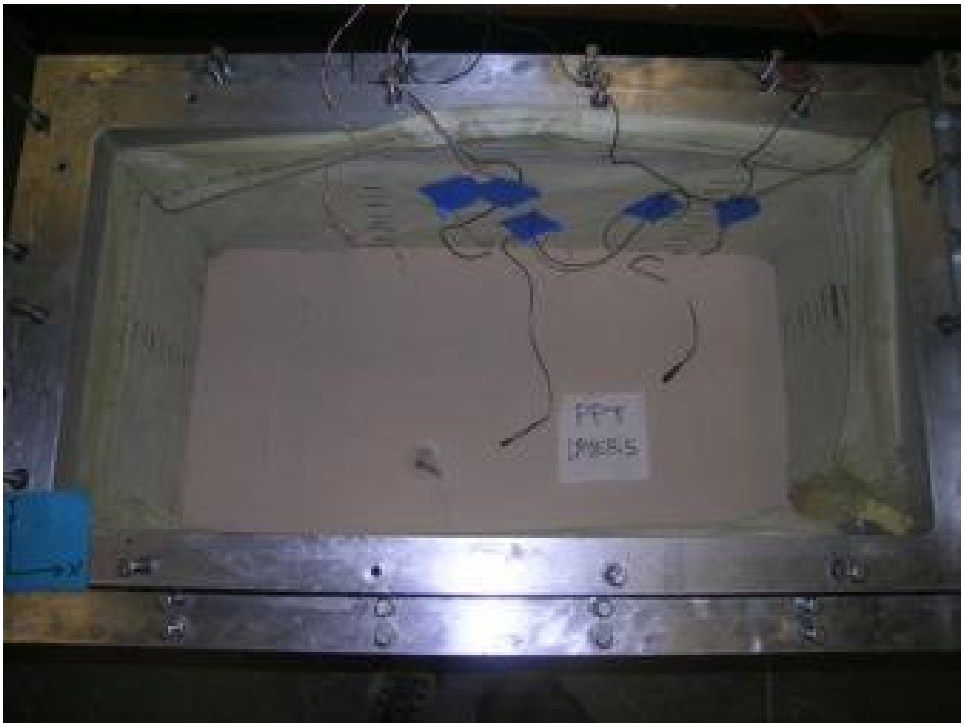


Figure 7.21: Typical placement of PPT in centrifuge model.



Figure 7.22: Typical placement of accelerometers and settlement monument in centrifuge model.

In addition to the interior sensors, ACCs and LVDTs were placed on the exterior of the model to capture the response of the actuator and horizontal displacement of the rings of the laminar box. Exterior accelerometers were placed on the rings of the laminar box, at the same elevations as the interior accelerometers to determine how coherently the layer responded to the input base motions. In addition, LVDTs were placed on the same rings as accelerometers corresponding to layers 7, 5, 3, and 1 (surface) to allow for comparison between the measured displacement time histories with displacement time histories obtained by double integration of the acceleration time histories.

Accelerometers oriented in the direction of the applied motion were also placed on the base plate, leveling plate and shaker. Finally, accelerometers oriented in the transverse and vertical directions were placed on both sides of the long dimension of the base plate in order to capture any unintended three-dimensional aspects of the input motions. The locations of the sensors placed on the rings and base plate are shown in Figures 7.23 and 7.24, respectively, while pictures of the typical sensor placement are shown in Figures 7.25 through 7.26.

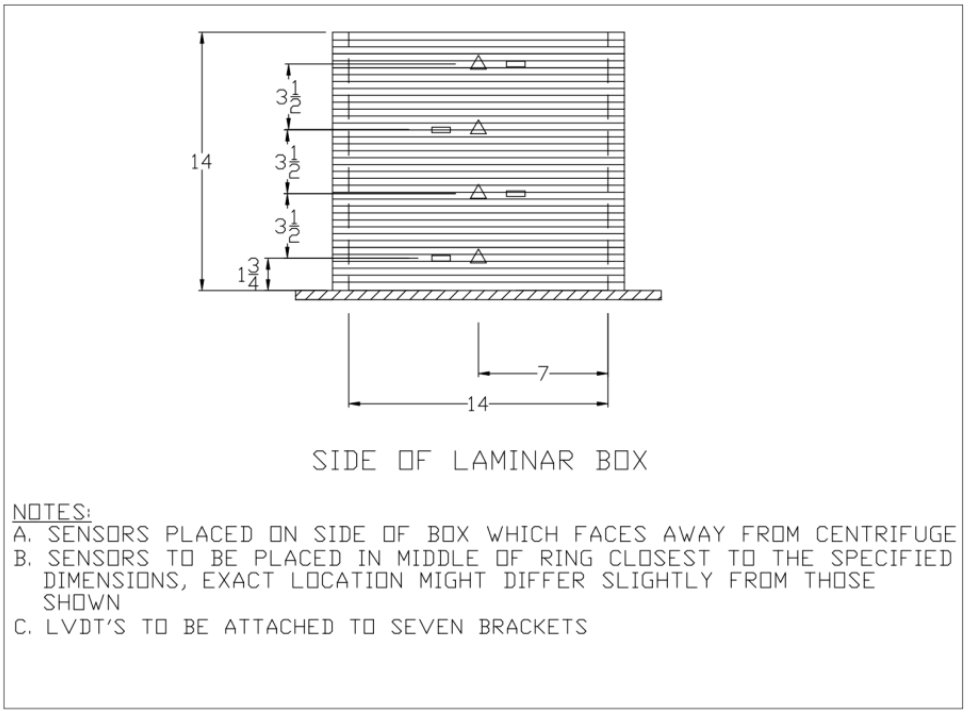


Figure 7.23: Sensors placed on exterior laminar rings of centrifuge model.

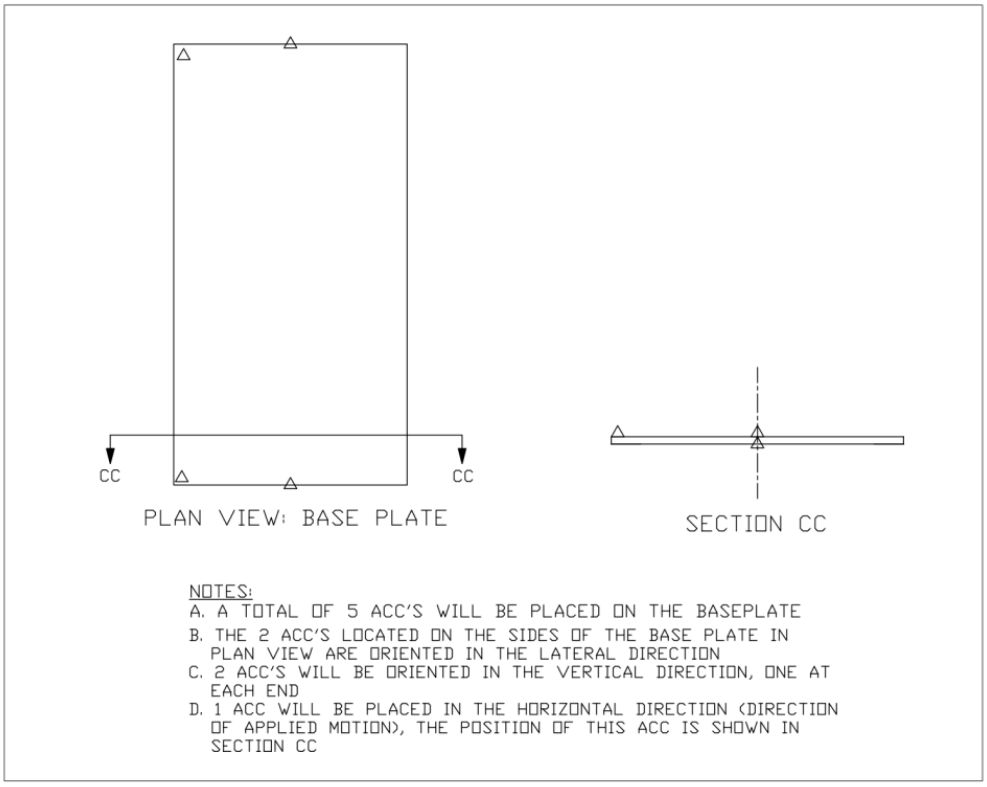


Figure 7.24: Sensors placed on baseplate of centrifuge model

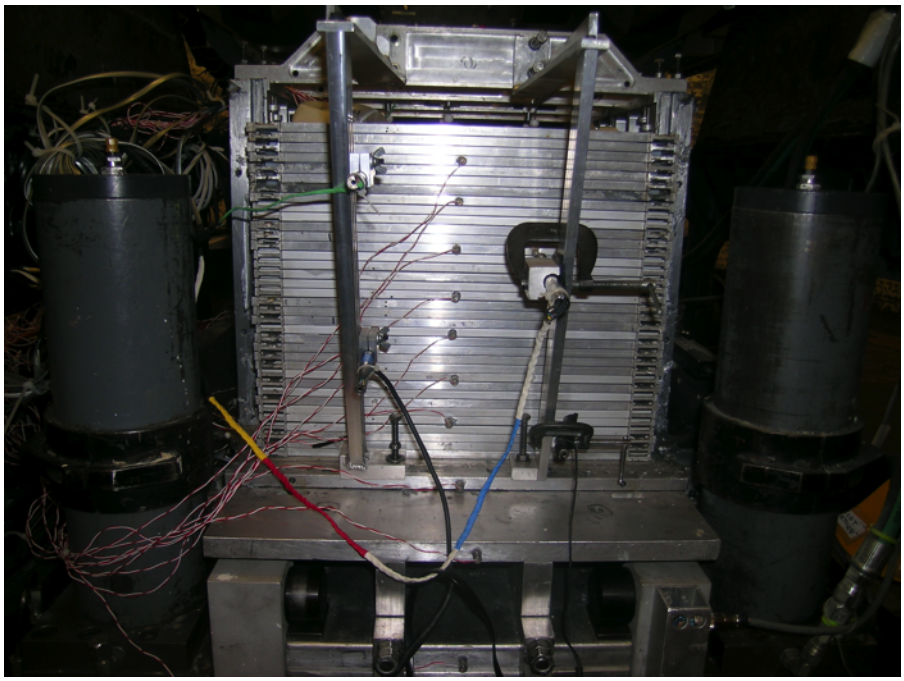


Figure 7.25: Typical placement of sensors on laminar ring and front of baseplate and actuator for centrifuge tests.

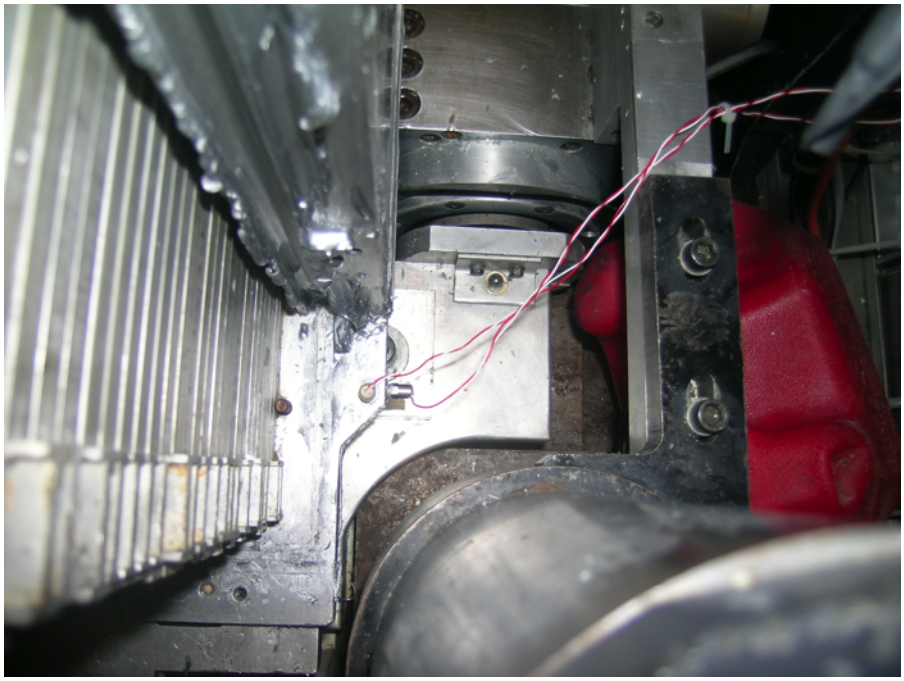


Figure 7.26: Accelerometers placed on baseplate to measure vertical and transverse response of the base input motion.

7.5 PROCESSING OF CENTRIFUGE DATA

During the centrifuge testing, an input motion was applied at the base of the model and the pore pressure, acceleration, and displacement response was recorded. Multiple motions were applied to each model. In this document, an experiment refers to a given model, and each test represents an individual base motion that was applied to the given model. To evaluate the results of each test, all data was converted to prototype scale based on the scaling laws presented in Table 7.1. The following sections describe the analyses performed to process the recorded data and the methodology used to evaluate how the relative density of the model evolved throughout the testing process. The general methodology presented in these sections were common to each of the six centrifuge experiments. Following these sections, the aspects of the data processing that were unique to each of the six centrifuge experiments are discussed individually.

7.5.1 *Processing of acceleration, pore pressure, and settlement data*

After the conversion of the recorded test data to prototype scale, additional processing of the acceleration, pore pressure, and settlement data was performed as described in this section. Unless otherwise noted, all units for the centrifuge data are presented in prototype scale. Each of the seven one-meter thick layers in the model are referred to as Layers 1 through 7, with Layer 7 representing the cemented sand layer at the base of the model, and Layer 1 corresponding to the saturated sand layer at the top of the model.

The acceleration data was processed using an 8-pole, Butterworth filter with cutoff frequencies of 0.1 Hz (high-pass) and 35 Hz (low-pass) filter. The filtering was applied in order to remove sensor noise from the acceleration time history. The filter cutoff frequencies were selected in order to span the frequency range of the input base motions and were found to effectively remove sensor noise based on trial and error. The pore pressure and LVDT time histories were filtered with a low-pass, 8-pole, Butterworth filter with a cutoff frequency of 35 Hz at prototype scale. A high-pass filter was not applied to the pore pressure or LVDT time histories to avoid filtering out long-period behavior, such as pore pressure dissipation or permanent displacements, that were considered true aspects of the model behavior.

As with the CSS testing program, the occurrence of liquefaction was evaluated using the pore pressure ratio, r_u. To evaluate r_u, an estimate of the initial overburden effective stress, σ'_{v0}

was required. Unlike the CSS testing, the stresses in the model were not measured parameters and had to be calculated based on an estimate of the soil's unit weight, the depth of the groundwater table, and the depth of the PPT. The soil's unit weight was computed using the relative density of the soil and the dry densities provided in Table 7.4. The depth of the groundwater was assumed to be at the ground surface per the model saturation procedure described in Section 7.4.1. As noted in Darby et al. (2019), interior model sensors can move during model construction and testing. To account for this movement, the depth of each PPT was back-calculated based on the measured hydrostatic water pressure prior to each test. From this estimate of depth, the initial vertical effective stress, σ'_{v0}, was then computed for each PPT individually.

7.5.2 *Development of Acceleration and Pore Pressure Time History Data for Analyses*

To create a centrifuge dataset that could be used to assess the efficiency of evolutionary intensity measures to predict the generation of excess pore pressure and the triggering of liquefaction, additional processing steps had to be performed. These steps included interpolation to generate sets of acceleration and r_u time histories at specific depths in the model and evaluating the partial drainage that occurred during shaking. Each of these steps are discussed in the following sections.

7.5.2.1 Development of Acceleration and Excess Pore Pressure Time History Pairs

Based on examination of the centrifuge test data, the acceleration response was found to be very similar for the side and center transducers located at the same depth. An example is provided in Figure 7.27 which shows the processed acceleration, velocity, and displacement time histories from Experiment 3 Test 3. This test was selected as an example because all the interior ACCs were functioning, and it was the first test in the experiment that generated significant excess pore pressures. The processed side and base acceleration, velocity, and displacement time histories were observed to be essentially identical for each side and center ACC pair located at the same depth for layers 4 through 7, located at depth. Slight differences were observed in the response of the upper saturated sand layers (Layers 1 to 3), which is most apparent in the displacement time histories that included slight phasing and amplitude differences between side and center

transducers. However, the difference was minor and likely due to the generation of excess pore pressures in the upper soil layers, as will be shown later.

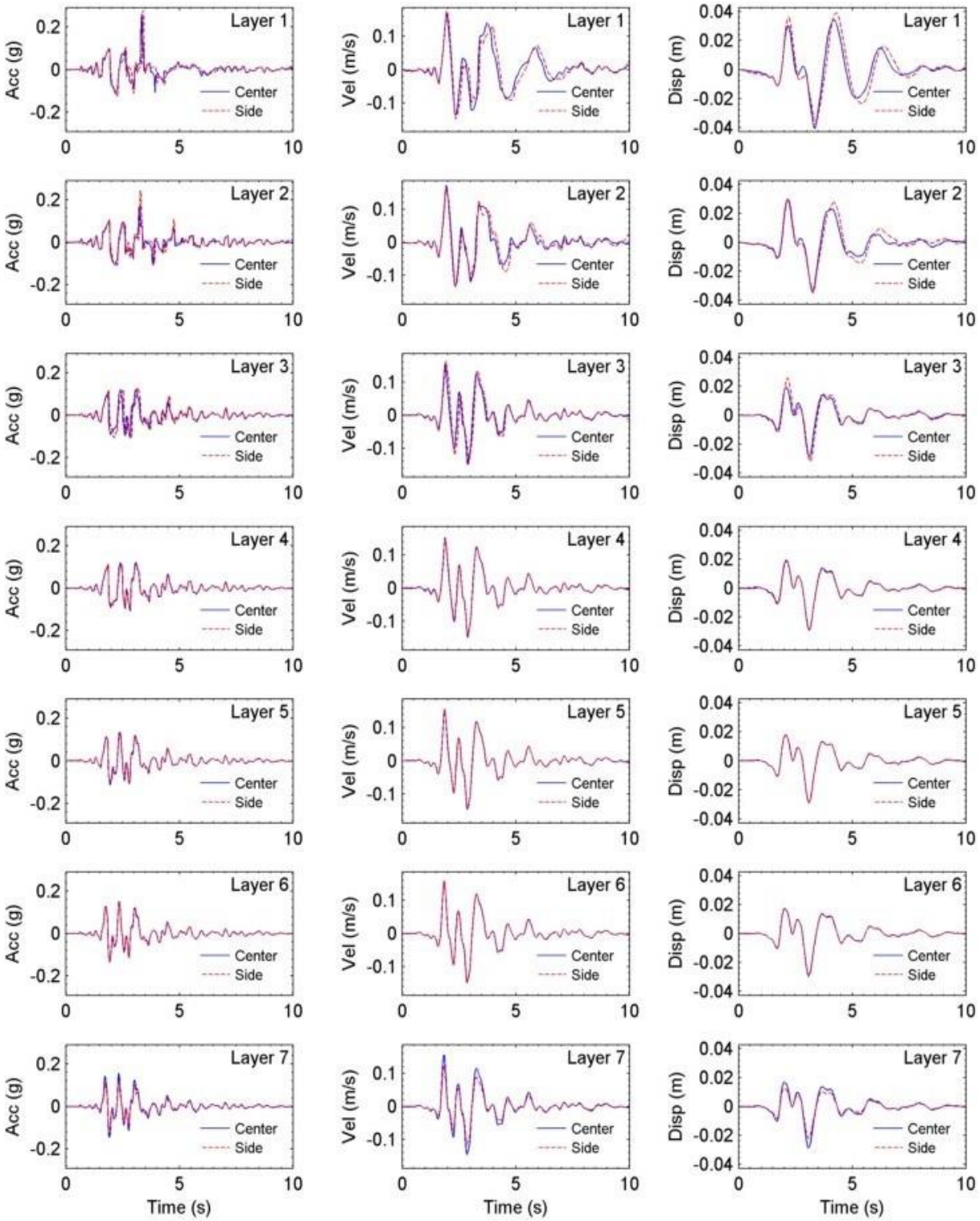


Figure 7.27: Example of the recorded acceleration, and computed velocity, and displacement response from interior ACCs during Experiment 3 Test 3.

In the subsequent analyses, when both ACCs at a given depth were functioning, the response from the center ACC was used to analyze the loading intensity. Preference was given to the center ACC because the soil response recorded in the center of the model was assumed to be less influenced by boundary effects from the model container than the side ACC (Teymur and Madhabushi, 2003). If the center ACC was observed to be malfunctioning, the side ACC was used. The performance of each of the interior sensors is noted in the discussion provided for each individual experiment (Sections 7.5.4 through 7.5.9).

Similar to acceleration, the pore pressure response was also found to be relatively consistent for PPTs located at the same depth. Figure 7.28 shows an example of the processing performed to evaluate the pore pressure response from Experiment 3 Test 3. Plots of the recorded pore pressure (u) time histories show that the response for each layer was similar for both the side and center PPTs, particularly for the deeper soil layers (Layers 3 through 6). Slight differences were observed in the upper two layers of the model, Layers 1 and 2. The differences observed in Layers 1 and 2 were primarily due to the slight differences in the depth of the sensors, potential boundary effects, and the fact that the pore pressure is limited to the value of the total vertical stress, σ_v, at which point liquefaction is initiated. Based on the initial pore pressure reading and the estimate of the hydrostatic pore water pressure, u_h, a depth for each sensor was computed as shown in Figure 7.28b, which also provides the estimate of the total vertical stress, σ_v. In this example, liquefaction was initiated in Layers 1 and 2 for both side and center PPTs.

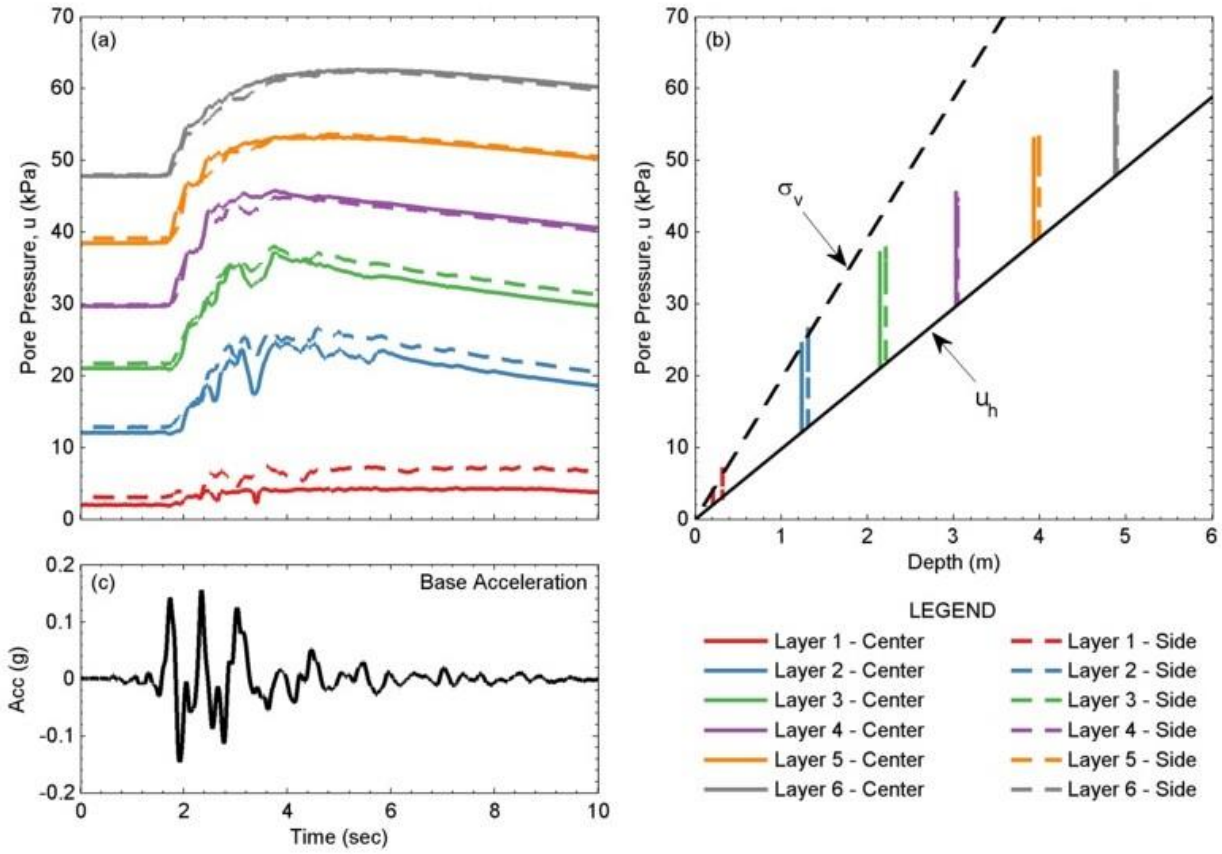


Figure 7.28: Example of the recorded pore pressure response for Experiment 3 Test 3.The recorded pore pressures are provided in (a). Using the initial pore pressure reading the depth was computed based on the hydrostatic pressure, u_h, shown in (b), which also provides an estimate of the total overburden pressure, σ_v. The base input acceleration time history is shown for comparison in (c).

The r_u time histories computed using the pore pressures shown in Figure 7.28a are provided in Figure 7.29, and show that in terms of the peak pore pressure ratio, r_u, the response for the side and center of each layer are in good agreement, particularly for Layers 3 through 6. The r_u time histories for the upper two layers still show some differences in response, especially in Layer 1 which featured temporary reductions in r_u caused by dilation that differed between the side and center PPTs. These differences were likely due to spatial variability of the soil profile or possible boundary effects. Another notable characteristic of the r_u time histories shown in Figure 7.29 was that the rate of pore pressure dissipation was nonuniform with depth. This was most apparent in the response of the upper three layers, Layers 1 to 3. The pore pressures began to dissipate in Layers 2 and 3, as indicated by the negative slope of the r_u time history, after about 4 seconds into the record; however, the r_u time history in Layer 1 remained essentially constant until about 9 seconds. This suggests that there was an upward flow of pore water into Layer 1

from lower layers. Quantifying the flow and drainage characteristics of the model is discussed further in Section 7.5.2.2.

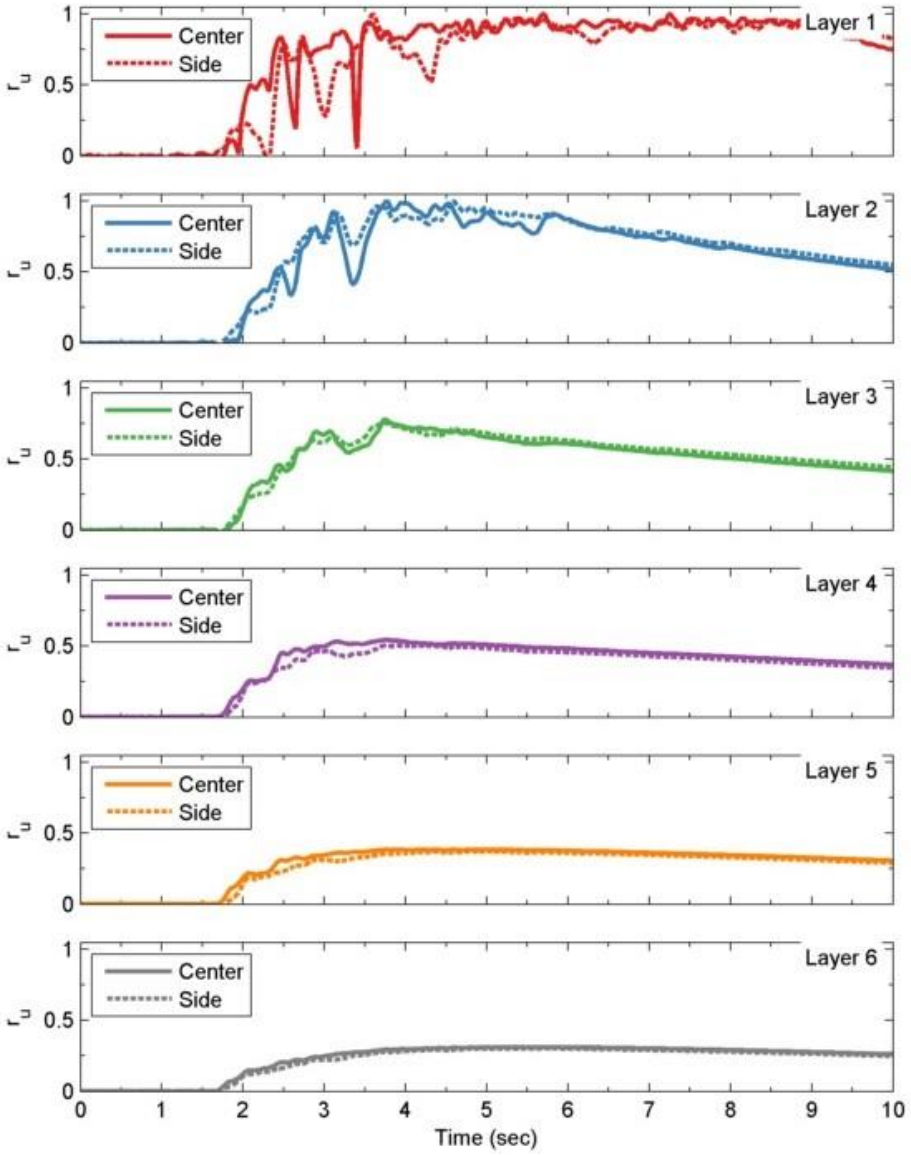


Figure 7.29: Example of r_u time histories from Experiment 3 Test 3

As noted in Section 7.4.2, the centrifuge model included a dense array of ACCs, PPTs, and LVDTs which measured the acceleration, pore pressure, and displacement response of the model, respectively. To avoid overcrowding the model, the interior ACCs and PPTs were staggered with respect to depth. To estimate the r_u time history at the depth of each acceleration record, the excess pore pressure, u_e, response at the depth of each ACC was estimated by

interpolation at each time step. Interpolation was performed on u_e, as opposed to r_u directly because u_e was also used to evaluate the hydraulic gradients and drainage response of the model as described in Section 7.5.2.2. In addition, because u_e is related to r_u by the initial vertical effective stress, σ'_{v0}, which is constant at each depth, interpolating on u_e and then computing r_u is equivalent to interpolating on r_u directly. The functional form of the u_e interpolation was,

$$u_e(z) = a_0 z^5 + a_1 z^4 + a_2 z^3 + a_3 z^2 + a_4 z \quad (7.1)$$

where z is depth and a_0 through a_4 are fitting constants. Equation 7.1 was based on similar analyses by Darby et al. (2018). This functional form was selected because it satisfied the boundary condition of $u_e = 0$ at the ground surface and was highly flexible. This flexibility was desired because the excess pore pressure response with depth was unknown and expected to vary considerably from test to test. Given the depth profile of u_e at each time step, the r_u response at a given depth can be computed by dividing the time history of u_e at depth z, $u_e(z)$, by the initial vertical effective stress at depth z, $\sigma'_{v0}(z)$.

An example of this interpolation is provided in Figure 7.30. The figure shows isochrones of excess pore pressure as a function of depth and includes both the fitted response from Equation 7.1 as well as scatter points of the excess pore pressure response computed from each individual PPT. The results show that the polynomial function is capable of accurately approximating the excess pore pressure response with depth, and that the excess pore pressure response recorded by the side and center PPTs were generally in good agreement. The isochrones illustrate the pore pressure generation and dissipation characteristics of the model. In the example provided, the excess pore pressure increases throughout the model during the first 3.5 seconds of the record, where the motion was strongest. As the amplitude of the loading history subsides the pore pressure began to dissipate. However, this dissipation was not uniform. The excess pore pressure dissipated more rapidly at depths between 1.5 and three meters than at shallower and deeper depths.

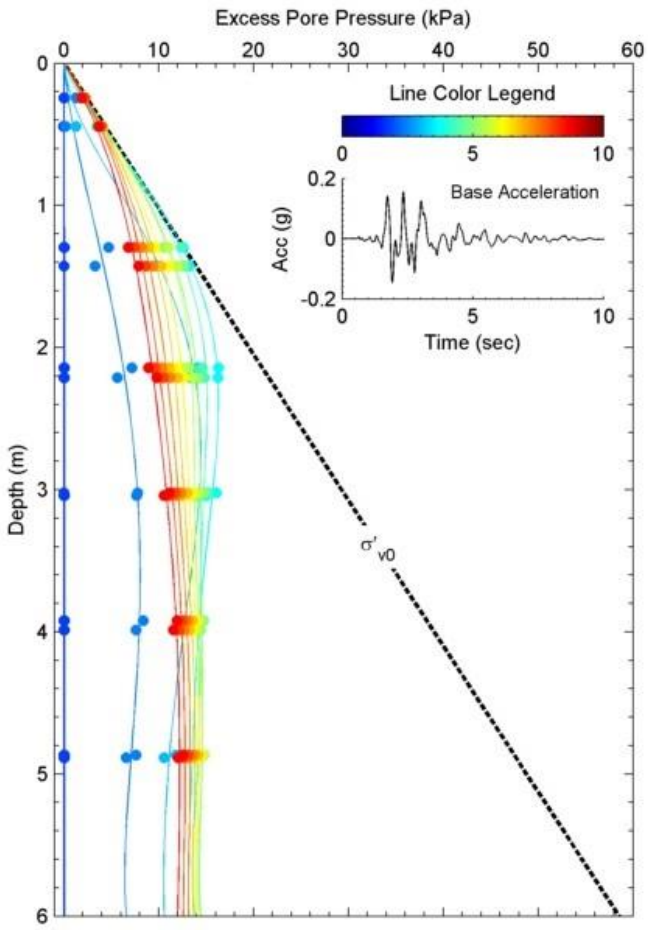


Figure 7.30: Isochrones of excess pore pressure as a function of depth for Experiment 3 Test 3.The color of the isochrones represent time. The line color legend is provided in the upper right corner along with the base acceleration loading time history for comparison.

From the interpolated excess pore pressure response, r_u time histories at any depth can be computed. Continuing with the example results from Experiment 3 Test 3, Figure 7.31 shows a colormap of r_u as computed from the excess pore pressure isochrones as a function of depth and time. This figure includes the base and surface acceleration time histories for comparison. Values of r_u in the shallow soils began to increase rapidly following the first cycle of large amplitude loading between 1.5 and 2.0 seconds into the record. Near the ground surface liquefaction was initiated at about 2.5 seconds into the record. By 3.0 seconds into the record, all of the soil in the upper 2.5 meters of the profile had reached a peak r_u value near 1.0. The r_u values decreased intermittently due to dilation, which was particularly noticeable at approximately 3.4 seconds into the record in the upper 2.5 meters of the soil profile. The dilatative response was also

observed in the surface time history, which shows a large amplitude, high frequency pulse at this time that was not observed in the base acceleration time history.

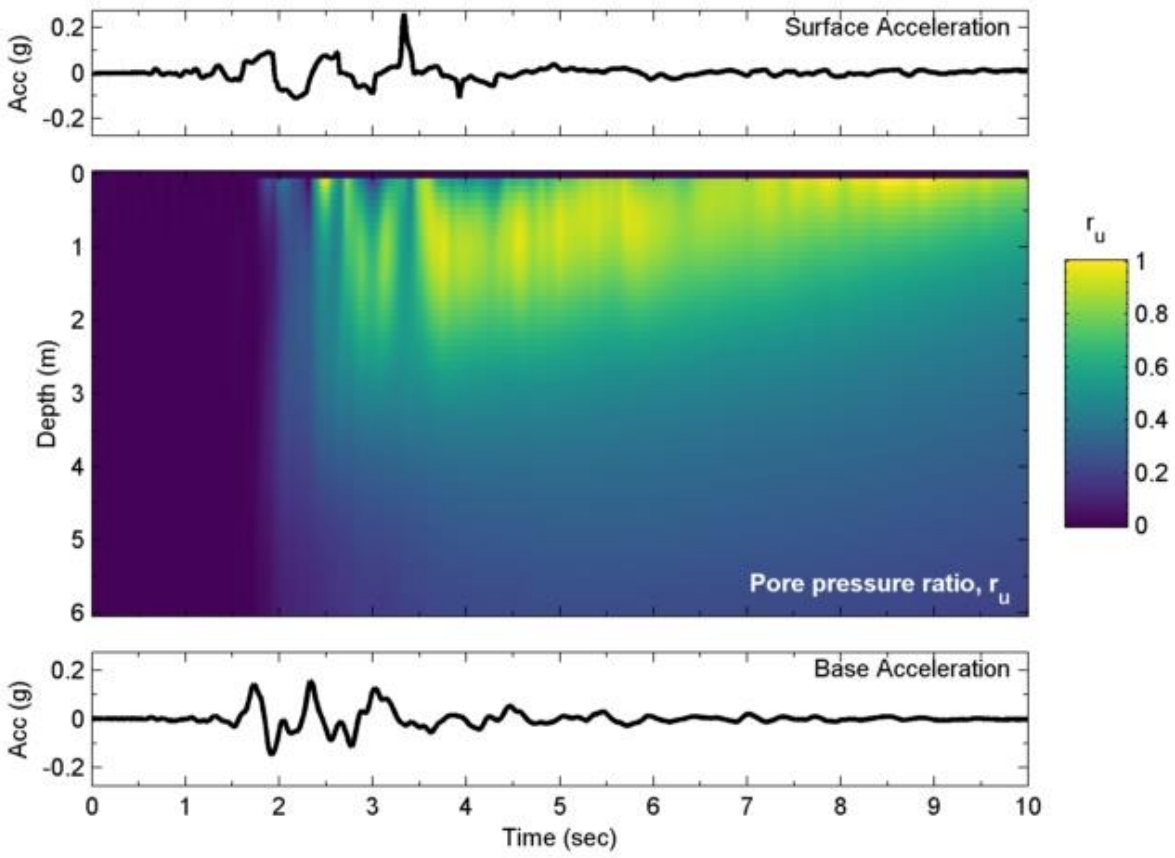


Figure 7.31: Plots of the base and surface acceleration time histories, and a colormap of the r_u as a function of depth and time for Experiment 3 Test 3.

As noted previously the excess pore pressure response was affected by the drainage characteristics of the model in addition to the intensity of the applied loading. The following section describes the interpretation of the diffusion of excess pore pressure in the centrifuge experiments. The purpose of this interpretation is to identify times when the generation of excess pore pressure was primarily influenced by the flow of pore water as opposed to the intensity of the loading history in order to reduce the influence of the drainage characteristics of the model on the evaluation of IM efficiency.

7.5.2.2 Evaluation of Ground Water Flow

The response of liquefiable soils depends on the drainage characteristics of the model in addition to the soil properties and the loading intensity. The evaluation of the diffusion of excess pore

pressures during and after shaking were conducted using the methods of Malvick et al. (2008) and Darby et al. (2018). As the centrifuge model was shaken and excess pore pressures were generated, hydraulic gradients developed in the soil profile. The hydraulic gradient, i, is defined as the change in total head divided by a unit of length. In this centrifuge study the velocity component of head was neglected, and the hydraulic gradient reduces to,

$$i = \frac{\partial u_e}{\partial z} \frac{1}{\gamma_w} \tag{7.2}$$

where γ_w is the unit weight of water. In a permeable material with a free drainage boundary condition, as was the case for the centrifuge experiments, flow will occur when there is a difference in head, i.e. when the hydraulic gradient takes on a value other than zero. With the definition of hydraulic gradient defined in Equation 7.2, a hydraulic gradient greater than zero indicates upward groundwater flow, while a hydraulic gradient less than zero indicates downward flow.

The velocity, or rate of flow, is related to the hydraulic gradient. In the case of laminar flow, Darcy's law applies. The flow velocity is then directly proportional to the hydraulic gradient and is computed as the product of the hydraulic conductivity and the hydraulic gradient. Per Arumoli et al. (1992), the hydraulic gradient of Nevada sand was generally on the order of 0.002 to 0.006 cm/s depending on the relative density of the sample. Multiplying by the model scale factor of 22.5, the prototype hydraulic conductivity was computed as 0.045 to 0.135 cm/s. Given that the prototype hydraulic conductivity was large, the assumption of laminar flow at large values (in an absolute sense) of hydraulic gradient may be invalid. However, the purpose of these analyses was to identify when the generation of excess pore pressure was primarily influenced by the diffusion of excess pore pressures as opposed to the intensity of the loading history. The general premise that as the hydraulic gradient deviates from zero the flow velocity increases generally holds true regardless of the laminar flow assumption.

To investigate the partial drainage characteristics of the model, the hydraulic gradient was evaluated using the fitted excess pore pressure isochrones at each time step to produce a colormap of hydraulic gradient as a function of time and depth. This plot is shown in Figure 7.32 for Experiment 3 Test 3 and includes plots of the acceleration and r_u time histories for each of the liquefiable layers in the model. A hydraulic gradient developed in the model soon after excess pore pressures began to generate, at about two seconds into the record. The gradient was not

uniform and implied both upward and downward dissipation of excess pore pressures. The effect of the drainage characteristics of the model can be observed in the r_u time histories. As the strong shaking subsides at about four seconds into the time history, the r_u time histories in Layers 3 and 4, near the center of the model have a downward slope which indicated that the excess pore pressures had begun to dissipate. The r_u response above and below these layers were either relatively constant or increased as a result of the flow of pore water from the center of the model. The r_u time history near the top of the model, in Layer 1, sustained high pore pressures until the end of the record as the excess pore pressure dissipated towards the ground surface. This is shown in the gradient colormap, where a positive gradient was observed in the upper 1.5 meters of the profile during the 2 to 10 second time period.

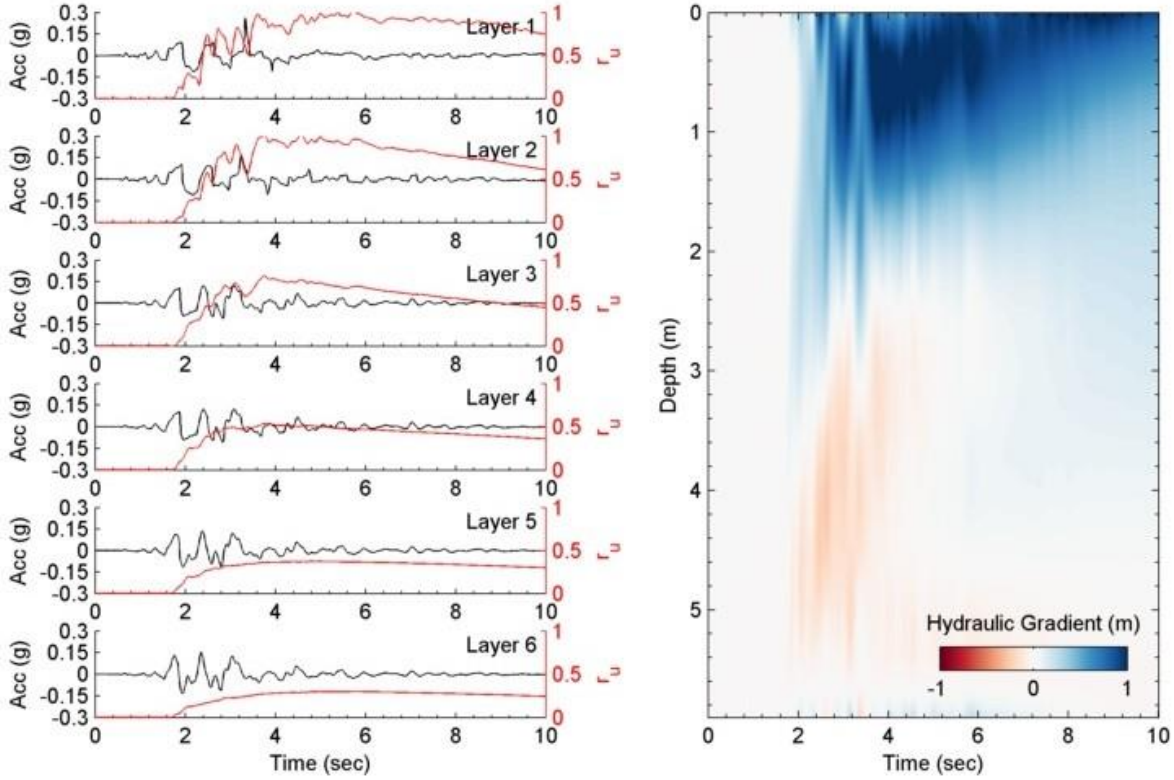


Figure 7.32: Acceleration and r_u time histories and colormap of hydraulic gradient as a function of time and depth for Experiment 3 Test 3.

The peak r_u value in Layer 1 occurred at about 5.5 seconds, after the strong shaking portion of the record had subsided. Observations from the CSS testing program, which were performed on an element of soil during undrained conditions, showed that the generation of excess pore pressures were highly correlated with the peak amplitudes in the loading history. In

addition, prior to phase transformation behavior, loading amplitudes less than the PPA were shielded and generally contributed very little to the pore pressure response of the sample. From Figure 7.32, the peak amplitude occurred between 2.4 and 3.3 seconds into the record (depending on the soil layer), and the loading amplitudes after 3.3 seconds were significantly lower than the PPA. In an undrained scenario, these later arriving, extremely low amplitude cycles would not be expected to generate significant excess pore pressures, and the peak r_u value at 5.5 seconds was due to the drainage characteristics of the model as opposed to the applied loading.

Similar behavior, where surficial soils showed an increase in r_u after strong shaking had ended, was also observed in the centrifuge study by Darby et al. (2019). Given that the centrifuge models were highly permeable, and hydraulic gradients developed soon after excess pore pressures began to develop, fully decoupling the excess pore pressure response due to the loading intensity and the response due to pore water flow is not possible based solely on observations from the processed data. As described in Section 7.5.2.3 an attempt was made to correct the pore pressure time histories for the effect of drainage. However, the drainage characteristics of a centrifuge model are highly complex and have been shown to change with time as excess pore pressures are developed (Shair et al., 2011), and the correction was only useful for qualitative purposes. Therefore, this study used an approach similar to the approach used by Darby et al. (2019), where increases in excess pore pressure that occurred after strong shaking had ended were not included in the evaluation of IM efficiency. The portions of the r_u time history that were primarily influenced by the flow of pore water were evaluated on a test-by-test basis using plots of the acceleration and r_u time histories and colormaps of the hydraulic gradient as a function of depth and time, as shown in Figure 7.32. For the example provided in Figure 7.32, the r_u response after approximately 3.8 seconds was assumed to be a due to the drainage characteristics of the model, as opposed to the loading intensity.

Appendix C provides summary figures for each centrifuge test, an example of which is provided below. These figures include plots of the acceleration and r_u time history pairs for each layer, profiles of the recorded (scatter points) and fitted excess pore pressure isochrones at evenly spaced time intervals, and stacked plots showing the measured surface settlement, colormaps of the hydraulic gradient as a function of depth and time, and the input base motion. The r_u time histories include a scatter point that indicates the peak r_u value during the portion of the record where the r_u response was assumed to be primarily a function of the loading history as

opposed to the flow of pore water. The acceleration and r_u time histories up to this point were used to evaluate the IM efficiency presented later in this chapter.

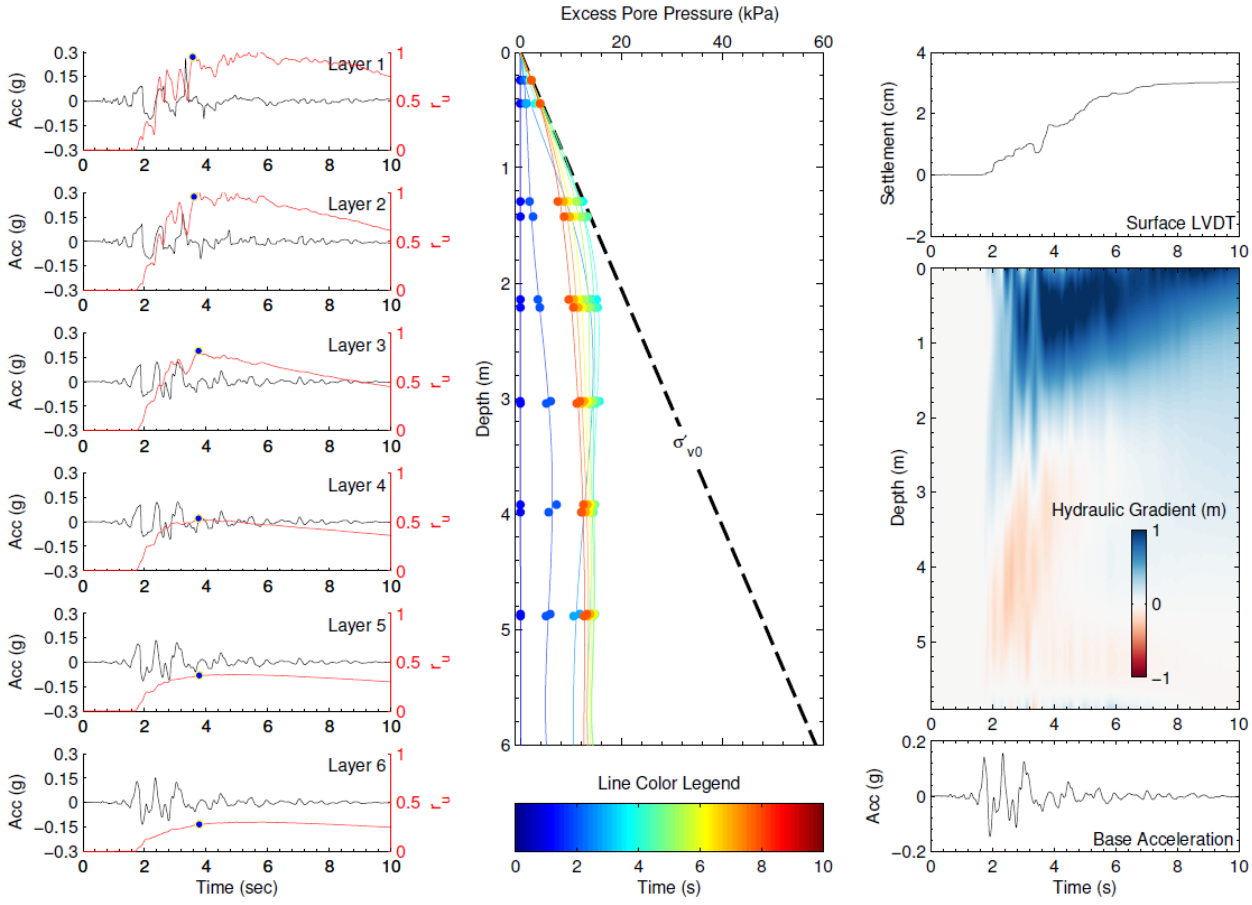


Figure 7.33: Centrifuge test summary plot for Experiment 3 Test 3. The stacked plots on the left side of the figure provide the acceleration and r_u time histories at each of liquefiable soil layers. The scatter points in these plots represent the peak r_u value during the portion of the r_u time history where the r_u response was assumed to be primarily due to the loading intensity as opposed to the flow of pore water. The center plot shows the recorded (scatter points) and fitted excess pore pressure isochrones at evenly spaced time intervals. The stacked plots of the surface settlement, hydraulic gradient vs time and depth, and the base input acceleration time history.

7.5.2.3 A Qualitative Correction Procedure to Account for the Dissipation of Excess Pore Pressures during Shaking

As noted previously, the pore pressure response of the centrifuge experiments was influenced by the redistribution of excess pore pressures due to the free-drainage boundary at the model surface. From the centrifuge scaling relationships (Table 7.1), the time rate of consolidation between model and prototype differed by a factor of N^2 and the permeability at prototype-scale

was greater than the permeability at model-scale by a factor of N where N is the centrifugal acceleration in units of g. Due to the drainage characteristics of the centrifuge models, the flow of pore water and the redistribution of exess pore pressures occurred both during shaking and after the applied motion had ended. These observations were consistent with other centrifuge experiments tha investigated liquefiable soils (e.g., Dashti et al., 2010a, 2010b; Darby et al. 2019).

The CSS program involved highly controlled tests on an element of soil during undrained conditions. During undrained conditions, reductions in the excess pore pressure (or r_u) are interpretted as dilation. However, during partially drained conditions, reductions in excess pore pressure can occur due to drainage. To distinguish between the two phenomenon and allow for a consistent qualitative comparison between the results from the two test programs, a procedure was developed to adjust the recorded pore pressure time histories from the centrifuge tests to reflect an undrained condition. Due to the highly complex nature of the redistribution of excess pore water pressures during seismic excitation, fully decoupling the generation and dissipation of excess pore pressure in a centrifuge experiment was not possible at this time. These complications included,

- The drainage characteristics of a liquefiable soil have been shown to be dependent on the relative density, effective stress, and pore pressure ratio (Seed et al., 1975; Brennan and Madabhushi, 2010; Shahir et al., 2012), and therefore vary both with time and depth in the soil profile.
- The soil properties may vary laterally and localized drainage paths can develop under high hydraulic gradients which can occur during shaking (Dashti et al., 2010a, 2010b).
- The ACC and PPT sensors and their associated wires can lead to localized high or low permeability zones.

Previous studies have been performed that modeled the reconsolidation of a liquefied soil deposit (Brennan and Madabhushi, 2010) and evaluated the change in the permeability of a liquefiable soil during shaking to provide better agreement between numerical models and the results of centrifuge tests (Shahir et al., 2012). However, these studies did not provide a fully verified methodology to compute the theoretical undrained response of a partially drained

centrifuge experiment. Therefore, this study introduces a simple first-order method to approximate the amount of pore pressure that was dissipated during shaking.

The qualitative procedure used in this study was based on Terzaghi's 1-dimensional consolidation theory (Terzaghi, 1925) which expresses the flow of excess pore water with time and depth as

$$\frac{\partial u_e}{\partial t} = c_v \frac{\partial u_e^{\,2}}{\partial z^2} \tag{7.3}$$

where c_v is the coefficient of consolidation. Equation 7.3 assumes:

A. The soil is homogenous and completely saturated,
B. Darcy's law governs the flow of pore water,
C. Small-strain consolidation theory, and
D. The flow of pore water and volumetric strains only occur in the vertical (z) direction.

Analytical solutions for Equation 7.3 exist for specific cases that use idealized drainage boundary conditions and initial excess pore water pressure distributions (e.g. Holtz and Kocavs, 1981). For situations where these idealized scenarios do not apply, as was the case for the centrifuge model, Equation 7.3 can be evaluated numerically using finite-difference methods as described in Harr (1966). The pore pressure correction procedure used in this study was based on a finite-difference solution to Equation 7.3 assuming free-drainage at the top of the model and an impervious base. The pore pressure correction procedure was as follows:

1. Estimate a value of c_v, which was assumed to be constant with time and depth, by evaluating a best fit of the theoretical finite difference solution to Equation 7.3 and the recorded time history of excess pore pressure during dissipation. The dissipation portion of the excess pore pressure time history was taken as the portion of the time history after shaking had ended at time $t = t_{diss}$. The theoretical estimate of the pore pressure dissipation was computed assuming an initial excess pore water pressure profile equal to the excess pore pressure isochrone at $t = t_{diss}$. The value for c_v was evaluated as the c_v that produced the lowest sum of squared error between the theoretical and recorded pore pressures.
2. Using the estimated c_v from Step 1, compute the pore pressure increment due to dissipation, Δu_{diss}, for each time step, Δt, over the entire time history. The pore pressure

increment due to dissipation is the amount of pore pressure that would be dissipated between time $t = t_i$ and time $t = t_i + \Delta t$. This procedure assumes that additional pore pressures are not generated during the time step and the change in excess pore pressure during the time increment was solely due to the drainage characteristics of the model. To compute Δu_{diss}, at each time t_i the excess pore pressure isochrone at t_i was used to define the initial excess pore pressure profile and Equation 7.3 was used to compute the excess pore pressure profile at time $t_i + \Delta t$. The Δu_{diss} at t_i, $\Delta u_{diss,i}$ was computed as the difference in the two excess pore pressure profiles.

3. Determine a cumulative history of the theoretical dissipated excess pore pressure u_{diss} by summing $\Delta u_{diss,i}$ for each time step.
4. Add the theoretical dissipated excess pore pressure to the recorded excess pore pressure time history to estimate the adjusted excess pore pressure response assuming the model was undrained.

Because the coefficient of consolidation is known to vary both spatially (due to initial effective stress and relative density) and temporally (due to the accumulation of r_u), Steps 1 through 4 were performed for each individual layer in the liquefiable soil profile. Example results of the c_v fitting process (Step 1) for Experiment 3 Test 3 are shown in Figure 7.34. The figure shows the theoretical and recorded excess pore pressure response after the shaking had subsided (t_{diss} = 10 seconds). The best-fit c_v values ranged from 0.222 in Layer 1 to 0.50 for Layers 3 and 4. The analyses using constant c_v values, unique for each layer, are shown to provide a reasonable approximation of the recorded pore pressures during dissipation, particularly for Layers 2 to 6. The relatively poor fit for Layer 1 was not unexpected, because at low confining pressures the small strain assumption in Terzaghi's 1-D consolidation theory can be violated and finite strain theory may be more appropriate (i.e. Gibson et al., 1967).

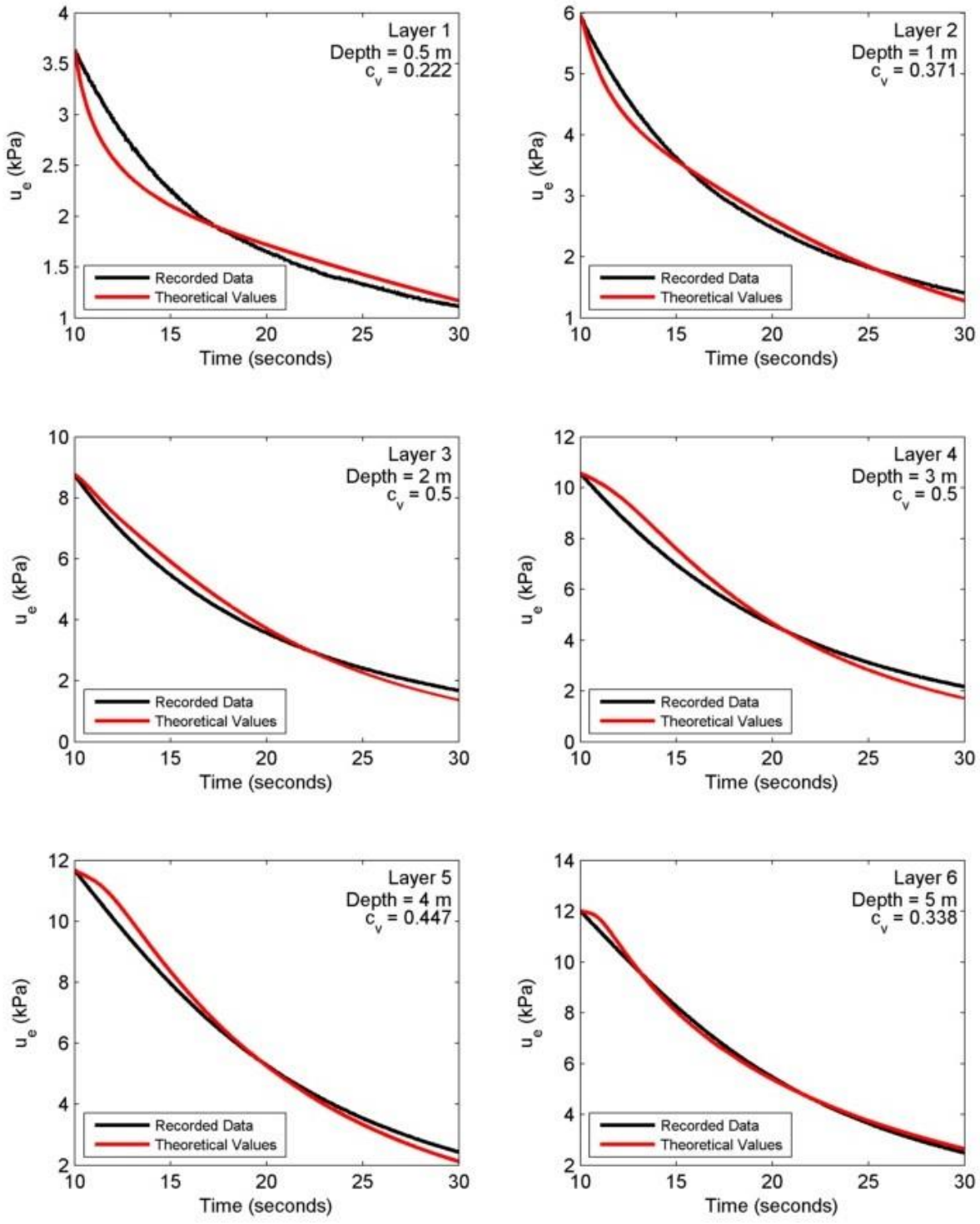


Figure 7.34: Determination of c_v for each individual layer based on the dissipation portion of the pore pressure time history (Step 1) for Experiment 3 Test 3.Individual c_v values were evaluated for each liquefiable soil layer, the c_v that produced the best fit for each layer are provided in the upper right hand corner of each subplot.

Using the c_v values developed in Step 1, the amount of excess pore pressure dissipated at each time step (Step 2) was computed and the cumulative sum of the dissipated pore pressure increments (Step 3) was added to the recorded time history (Step 4). This process is illustrated in Figure 7.35 which shows plots of the recorded excess pore pressure, the computed dissipated pore pressure (u_{diss}), and the adjusted excess pore pressure time histories for each layer. The general trends in u_{diss} time histories can vary greatly between layers. For Layers 2 and 3 the theoretical u_{diss} began to accumulate soon after excess pore pressures were generated (about 2 seconds into the record) and consistently increased with time. Layers 1 and 4-6 featured local decreases in u_{diss} between 4 and 7 seconds. These local decreases suggested that pore water was flowing into these layers during this time. Based on the hydraulic gradient plots presented earlier (7.32), the temporary decrease in u_{diss} for Layer 1 was likely due to the upward dissipation of excess pore pressure from Layer 2, while the temporary decrease in u_{diss} for Layers 4-6 was likely a result of the downward dissipation of excess pore pressures from Layer 3. After 8 seconds, the u_{diss} time histories for all of the layers were increasing with respect to time, which suggested a consistent upward dissipation of excess pore pressure. These observations were consistent with the behavior of the hydraulic gradient shown in Figure 7.32.

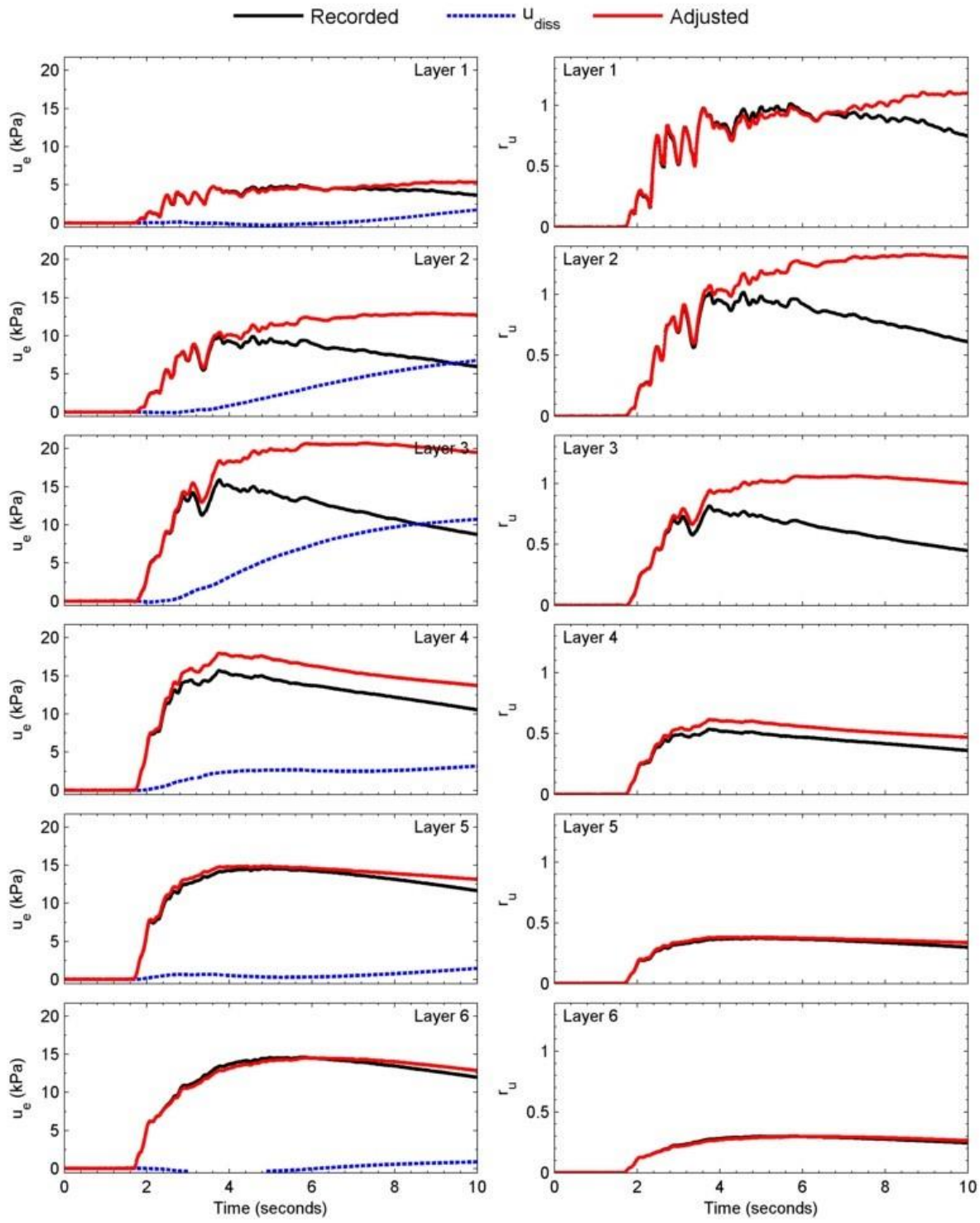


Figure 7.35: Adjustment of excess pore pressures based on theoretical dissipation time histories for Experiment 3 Test 3. The plots on left show the recorded excess pore pressure, the computed dissipated pore pressure, u_{diss}, and the adjusted pore pressure time histories. The plots on the right show the r_u histories using the recorded and adjusted excess pore water pressures.

The pore pressure correction procedure used in this study was able to capture the general trends of the u_{diss} response in a manner that was consistent with the hydraulic gradients computed from the measured pore pressures. However, due to the numerous simplifying assumptions outlined previously, the correction procedure is only approximate. The approximate nature of the proposed excess pore pressure correction procedure was especially apparent when the adjusted excess pore pressures were converted to r_u time histories (Figure 7.35).

For Layer 1 the corrected and recorded r_u time histories were practically identical until 7 seconds, when the adjusted r_u time history began to increase relatively rapidly and reached an r_u of 1.1 at 10 seconds. As shown in Figure 7.32, at this time the amplitude of the motion was very low and an increase in excess pore pressure was not anticipated. The increase in the adjusted r_u was likely a numerical artifact; however, as noted previously the assumption of Terzaghi's 1-D consolidation theory is likely not appropriate at very low confining pressures, therefore the odd behavior for Layer 1 was not unexpected. The response for Layer 2 appeared reasonable with respect to excess pore pressure, however when converted to r_u, the adjustment was observed to overpredict the dissipated excess pore pressures and led to adjusted r_u values as high as 1.3. Brennan and Madabhushi (2010) show that c_v is related to r_u and that as r_u approaches 1.0 c_v can be as much as three times lower than the c_v value computed during dissipation. Therefore, the assumption of a constant c_v based on a fit to the pore pressure response during dissipation likely led to the overprediction of the dissipated excess pore pressure during shaking.

Layer 3 appeared to provide a reasonable response both with respect to excess pore pressure and r_u. The excess pore pressure response was fairly constant after strong shaking had subsided, which is the expected response during undrained condition. For the same reasons as noted above for Layer 2, the r_u value implied by the adjusted excess pore pressure may not be representative of the actual r_u value that would be obtained had the test been undrained; however, the general trends in the r_u time history from a qualitative standpoint appeared to be consistent with an undrained condition.

For Layers 4 through 6 the correction procedure was not able to fully remove the negative slope in the excess pore pressure and r_u time histories that are most notable after 6 seconds into record. However, in each layer the adjustment procedure did generally reduce the flatten the slope in the excess pore pressure and r_u time histories near the end of the record when the shaking amplitudes were low. This response was more consistent with the anticipated

behavior had the test been undrained. This suggested that the adjustment procedure was able to capture the general trends in the dissipation behavior of the model, but only in an approximate manner.

Due to the limitations of the adjustment procedure, the r_u values used in the efficiency evaluations in Section 7.7 were based on r_u computed from the measured (uncorrected) pore pressure response. Portions of the record that were judged to be influenced by flow were not included in the evaluation of the IM-r_u response. However, for specific layers the adjustment procedure did appear to provide a reasonable approximation of an undrained response and can allow for a consistent qualitative comparison of behavior in the centrifuge (where flow could occur) to the element tests (where flow could not occur). From the example provided previously, Layer 3 was selected as a good candidate for this comparison, and plots of the acceleration, r_u, and the dissipation-corrected r_u time histories are provided in Figure 7.36.

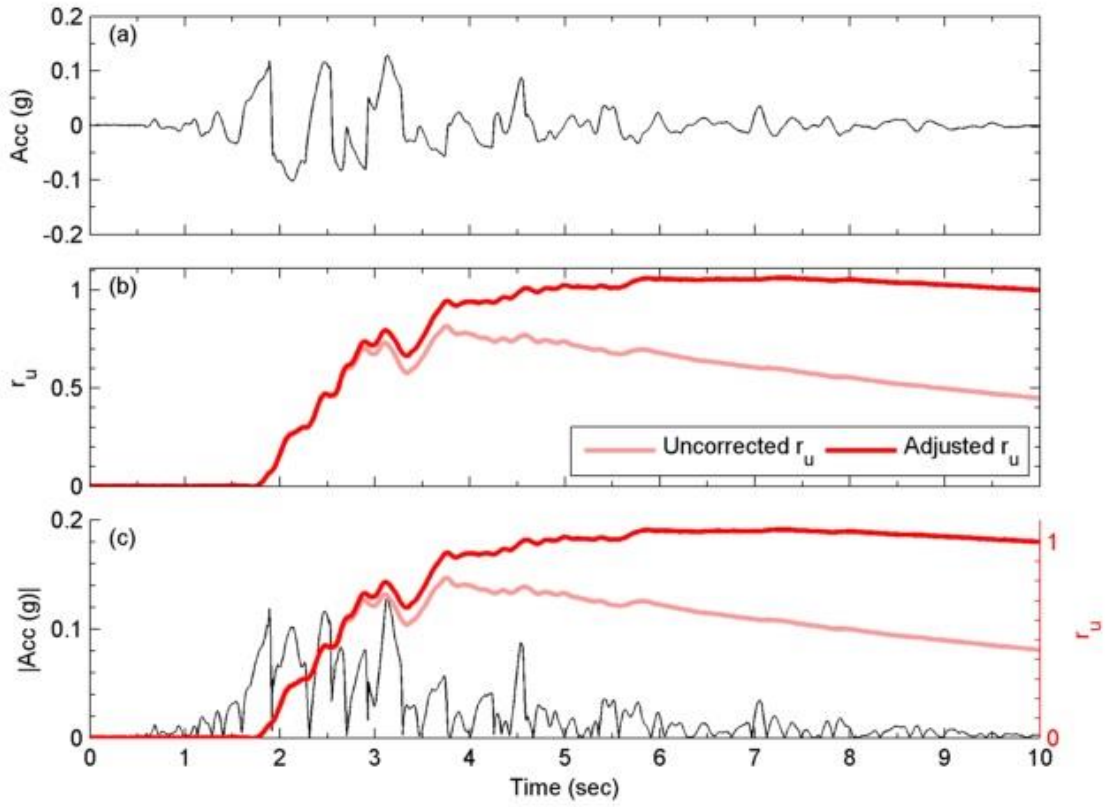


Figure 7.36: Comparison of the recorded acceleration, r_u, and drainage-corrected r_u time histories for Layer 3 in Experiment 3 Test 3.The acceleration record is shown in (a) and both r_u time histories are shown in (b). A comparison with the absolute value of acceleration and both r_u time histories are shown in (c).

Both the adjusted and uncorrected r_u time histories showed that the majority of the excess pore pressure was developed from 1.5 to 3.5 seconds into the record when the acceleration amplitudes were large. Following the large amplitude acceleration pulse just after 3 seconds, the uncorrected r_u time history showed a local reduction in r_u between 3 and 3.5 seconds. This local decrease in r_u was also observed in the adjusted r_u time history. This observation implied that the reduction in r_u at 3.5 seconds was likely due to dilation and phase transformation behavior as opposed to solely dissipation. After 3.5 seconds the uncorrected r_u time history steadily decreases for the remainder of the time history with the exception of a few minor positive fluctuations. These positive fluctuations generally coincided with local peaks in the acceleration time history, as seen at approximately 4.5 seconds. The steady decrease in the uncorrected r_u was due to drainage and was not observed in the adjusted r_u time history. The excess pore pressure contributions from the loading that occurred after 3.5 seconds was more apparent in the adjusted r_u time history but were very small as compared to the excess pore pressures that were generated between 1.5 and 3.5 seconds.

Chapter 6 discussed a number of important observations from the CSS test program, including the theory that the generation of excess pore pressure is related to the prior peak amplitude or PPA, and that loading that was less than the PPA contributes very little to the pore pressure response. The acceleration pulses between 1.5 and 3.5 seconds included acceleration pulses that were either near or exceeded the PPA, while the loading cycles after 3.5 seconds were well below the PPA. The pore pressure response was observed to be in general agreement with the observations from the CSS data. However, the r_u response (both uncorrected and adjusted) showed an increase between 2.5 and 3 seconds when the acceleration amplitudes were less than the PPA. This observation may be due to a slight time lag in the pore pressure reading, which could occur if the sensors were not fully saturated. Section 7.6 provides an in-depth discussion on the relationship between the loading history and the pore pressure response, and utilizes the procedure described in this section.

7.5.3 *Estimation of Relative Density*

In each of the centrifuge experiments, a model was constructed at a uniform target relative density. The model was then subjected to repeated shaking events, which altered the density of the soil profile. Estimating how the soil density changed after being subjected to multiple

shaking events was an important component in evaluating the results of the centrifuge studies. Based on the literature review of previous centrifuge experiments that included multiple shaking events, the relative density of the liquefiable soil was found to be a more reliable indicator of liquefaction resistance than shear wave velocity. At the time the tests were performed, inflight measurements of the state of the soil using bender elements or mini-CPTs were not available at the RPI testing facility. Therefore, the experiments performed in this research used settlement monuments (Figure 7.20) placed at the top of each of the liquefiable soil layers during model fabrication to quantify the change in the soil relative density as multiple tests were performed on the same model.

The settlement recorded by each monument, δ_i, (where i is the layer number) represented the settlement of the soil from the depth of the monument down to the top of the cemented sand layer (Layer 7) just above the base of the profile. The settlement of the cemented sand layer was assumed to be zero. The settlement of each layer for each test was calculated as the difference in the LVDT reading at the beginning of the test (prior to application of the base motion) and the LVDT reading at the end of the test after the excess pore pressure had fully dissipated.

The purpose of including a settlement monument at the top of each liquefiable soil layer was to allow for the estimation of a depth-dependent relative density profile. However, due to complications that arose during the testing process, developing a reasonable estimate of the depth-dependent relative density profile was not possible and the relative density of the model was evaluated as constant with depth using an average value computed from the surface settlement. These complications included tilting of the settlement monuments, loss of connection between the settlement pads and the LVDT, and inconsistent results. To illustrate the difficulty in developing a depth-dependent density profile, and to clarify why a constant average value of relative density was used to evaluate the liquefaction resistance of the model, the full density estimation procedure for Experiment 3 is presented in detail. The lack of direct measurement (such as the mini-CPT as used by Darby et al., 2019) of the state of the soil during tested is a significant, and noted, limitation in the current centrifuge study.

7.5.3.1 Example Calculations of Relative Density

To determine the relative density of each layer, the change in height of each layer i, ΔH_i, was computed as

$$\Delta H_i = \delta_i - \delta_{i+1} \tag{7.4}$$

Using the change in height for the given layer, in addition to the height of the layer prior to applied motion, the width and length of the laminar box, and the weight of soil placed in each layer during model construction, the density of each layer was computed. The density was then converted to a relative density using the data provided in Table 7.4.

An example of the cumulative settlement and the cumulative vertical strain for Experiment 3 is provided in Figure 7.37. The cumulative vertical strain for each layer was computed as the cumulative settlement for the layer divided by the height of the soil from the top of the cemented sand layer to the initial position of the settlement monument. The settlements and vertical strain for each layer evolved in relatively consistent manner and, as expected, both the settlement and the vertical strain generally increased as the number of applied motions increased. However, the magnitude of the measured settlement for each layer displayed unexpected behavior. Generally the settlement the largest settlements and strains are anticipated to occur near the ground surface, however the cumulative settlement for Layer 4 was greater than the cumulative settlement for Layer 3 for all tests and was larger than the cumulative settlement recorded in Layer 2 between Test 23 and 36. The vertical strain in Layer 4 was the largest that was observed in any of the layers from Test 19 through the end of the experiment. Several potential explanations for the high settlement response in Layer 4 were investigated, as discussed subsequently.

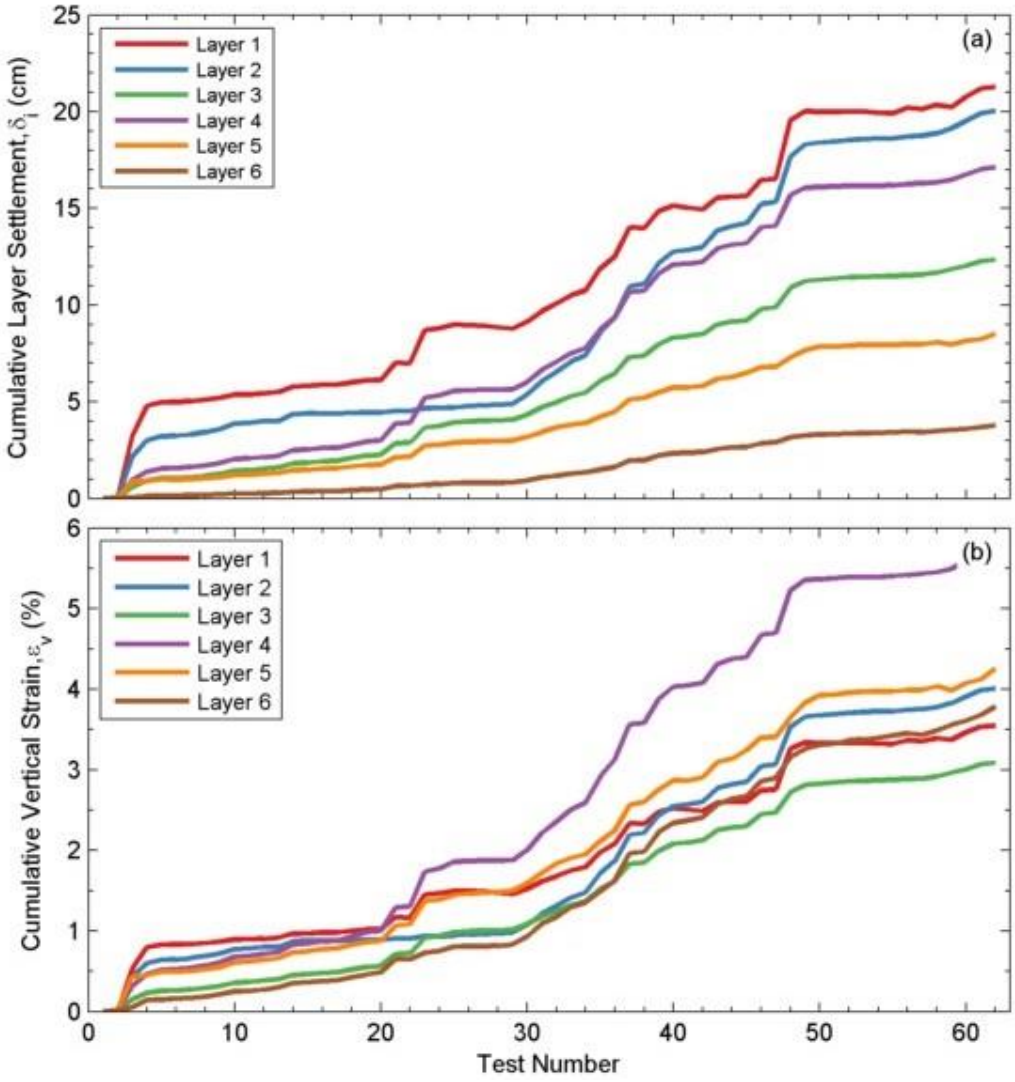


Figure 7.37: Total settlement (a) and total vertical strain (b) as a function of test number for Experiment 3.

The reason for the large vertical strains measured in Layer 4 was unknown. From El-Sekelly et al. (2016) and the laboratory and empirical liquefaction settlement procedures (e.g. Ishihara et al., 2016), the seismic settlement should be related to the peak excess pore pressure ratios and peak cyclic shear strains that were developed during shaking. However, as shown in Figure 7.38, larger excess pore pressure ratios were generated in the portion of the soil profile above Layer 4 (particularly Layers 1 and 2) than in the lower portions of the profile (Layers 4 through 6). This observation that high r_u values tended to develop at shallow depths was consistent with observations made by El-Sekelly et al. (2016) and Darby et al. (2019).

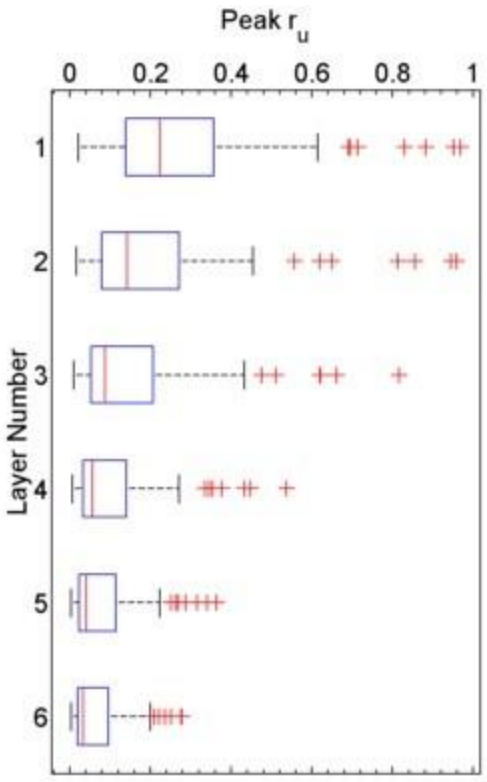


Figure 7.38: Box plots of the peak pore pressure developed in each layer during Experiment 3.

Figure 7.39 shows the vertical strains for Layers 1 and 4 for each test as a function of the average peak r_u and the average peak shear strain values computed for the layers underlying the settlement monument (i.e. for Layer 4 the average peak r_u was computed using the peak r_u values from Layers 4, 5, and 6). The cyclic shear strains were estimated as the difference in the computed displacement time histories for each successive layer divided by the distance between the two sensors. The plots include power function fits to each set of test data. The results show that the vertical strain was correlated with both r_u and the peak shear strain. However, the vertical strain was more closely related to r_u than shear strain based on the standard deviation of the residuals, σ_ε, between the measured verical strain and the fitted value. The σ_ε values for the vertical strain – peak r_u relationship were 0.034 and 0.045 for Layers 1 and 4 respectively. These values were approximately half of the σ_ε computed using the vertical strain – peak shear strain relationship (σ_ε of 0.065 and 0.085 for Layers 1 and 4, respectively). The additional scatter in the volumetric strain-shear strain relationship was likely because there is more uncertainty in estimating shear strains from acceleration records (Conti and Viggiani, 2012) than there is in estimating r_u based on directly measured pore pressure data. In addition, the r_u-vertical strain

relationship from this experiment was not as strong as the results presented in El-Sekelly et al. (2016), likely because of the diverse suite of input motions that were used in this study as compared to El-Sekelly et al. (2016). Note that for a given average peak r_u or peak shear strain value, the vertical strain computed in Layer 4 was larger than Layer 1, particularly with respect to r_u. These observations were inconsistent with the results of previous studies. Possible explanations for this behavior include:

- Spatial variation in the soil properties, which could occur during model construction and due to shaking and the generation and dissipation of excess pore pressures,
- Tilting of the settlement monument,
- Sensor malfunction or miscalibration, and
- Downdrag forces on the settlement monuments due to the settlement of the surrounding soil.

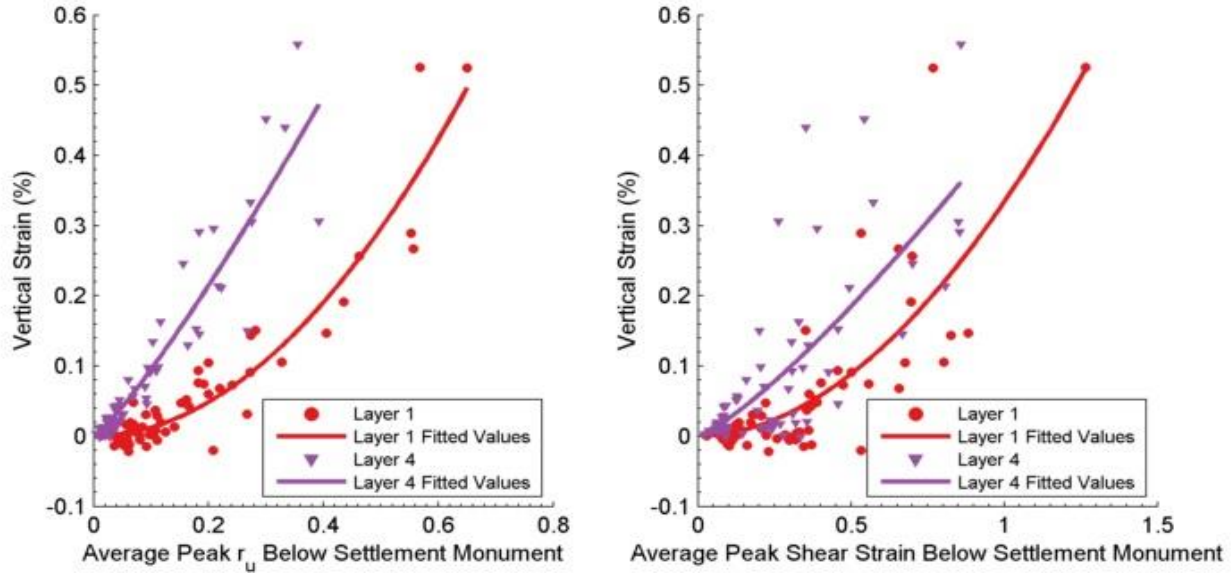


Figure 7.39: Relationship between vertical strain and the average r_u and peak shear strain for Layers 1 and 4 from Experiment 3.

Assuming all the settlement measurements are accurate, per Equation 7.4, if the settlement of an underlying layer (δ_{i+1}) was greater than the settlement in Layer i, then the change in height of the layer is negative which results in a reduction in the relative density for the layer. Figure 7.40 shows the computed change in layer height and the relative density for each layer as a function of the test number. The bottom plot of the figure shows the shaking intensity of the input motion expressed in terms of PGA_{mb} for comparison. The relative densities

of Layers 4, 5, and 6 consistently increased throughout the duration of the test, and reached final relative densities of approximately 115, 80, and 72%, respectively. Layer 3 generally decreased in relative density and, using the procedure described previously, the relative density at the end of testing was computed as approximately zero percent. The relative densities for Layers 1 and 2 evolved in an irregular manner and included local peaks and valleys in response to the different input motions used in the individual tests.

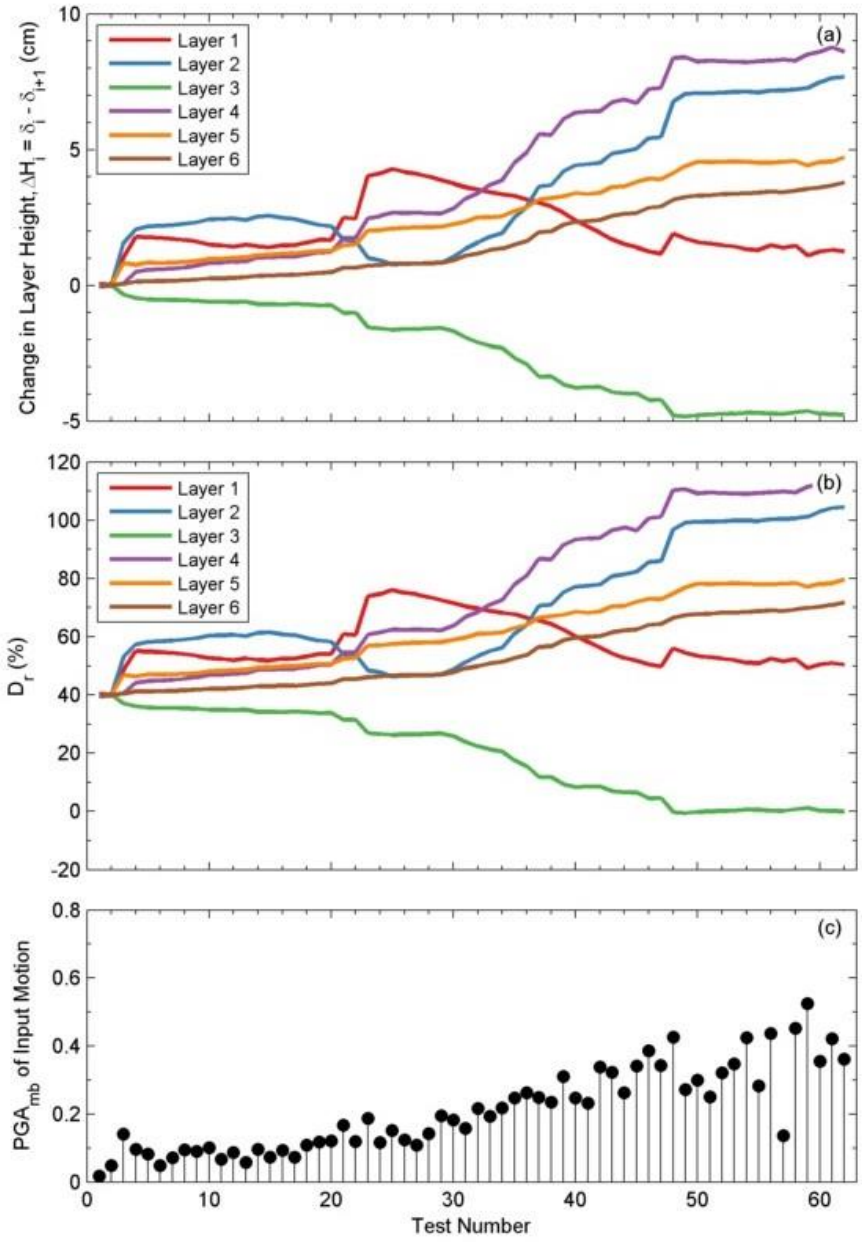


Figure 7.40: Change in layer height (a), relative density (b), and input base motion amplitude with respect to PGA_{mb} (c) as a function of test number for Experiment 3.

The relative density profiles computed using the settlement response of each layer are shown in Figure 7.41. The profiles reflect the observations made above and highlight the inconsistent apparent relative density response in Layers 1 through 4. The irregular relative density response with depth is inconsistent with the density profiles from Darby et al. (2017; 2018; 2019) which generally increased as a function of depth and the number of applied motions. The density estimates from Darby et al. (2017; 2018; 2019) were evaluated using direct measurements with a mini-CPT device. In contrast, due to limitations of the available equipment at the time the tests were performed, the relative density profile from this study was initially computed based on a change in layer height computed using the difference in the settlement measurements from successive layers. This method was extremely sensitive to the recorded settlement in each layer. There is, however, a large amount of uncertainty in settlement measurements from dynamic centrifuge experiments, as noted in previously and described in Darby et al. (2018). Inaccurate settlement data for a single layer can result in a highly irregular relative density profile as shown in Figure 7.41.

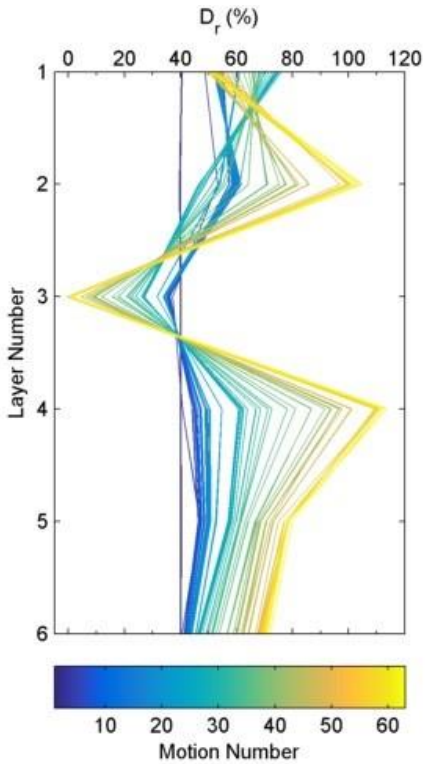


Figure 7.41: Relative density profiles for Experiment 3 using all of the recorded settlement data.

Repeating the analyses assuming the settlement response for Layer 4 was the same as Layer 3 produces the settlement profile shown in Figure 7.42. Relative to the results using all of the settlement data, the profile provided in Figure 7.42 provides a more reasonable density profile, however the profile is still irregular and inconsistent with the mini-CPT studies from Darby et al. (2017 and 2019). The results shown in Figures 7.41 and 7.42 suggested that Layer 2 had a significantly higher final relative density than all of the other liquefiable soil layers.

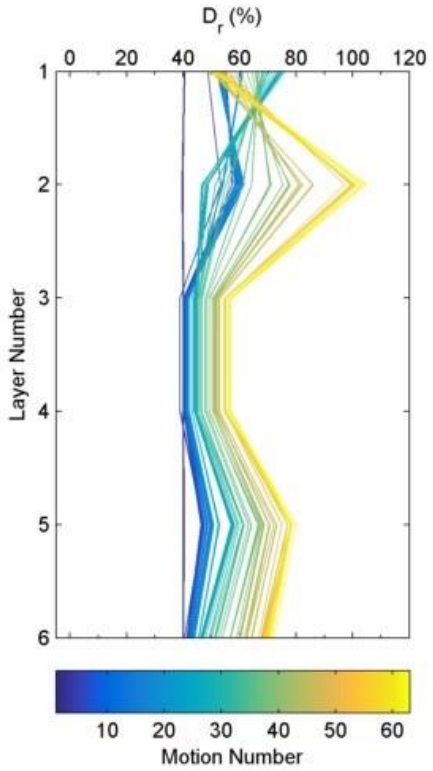


Figure 7.42: Relative density profiles for Experiment 3 excluding the recorded settlement from Layer 4.

An alternative to computing the relative density for each individual soil layer was to use the surface settlement and the entire height of the liquefiable soil layer to estimate an average relative density for the soil profile. This method was used in El-Sekelly et al. (2016) and was shown to provide an estimate of relative density that was generally within the range of values that were computed using CPT-based procedures in Darby et al. (2017) and Darby et al. (2019). Figure 7.43 shows the average relative density computed using the surface settlement from Experiment 3 as a function of the test number. For comparison, the plot also includes the estimated relative density of the individual layers from Figure 7.40. The average relative density evolved in a steady manner and generally increased as the number of applied motions increased,

consistent with the previous centrifuge studies. Therefore, the average relative density computed with the surface settlement was used for all layers when evaluating the IM efficiencies.

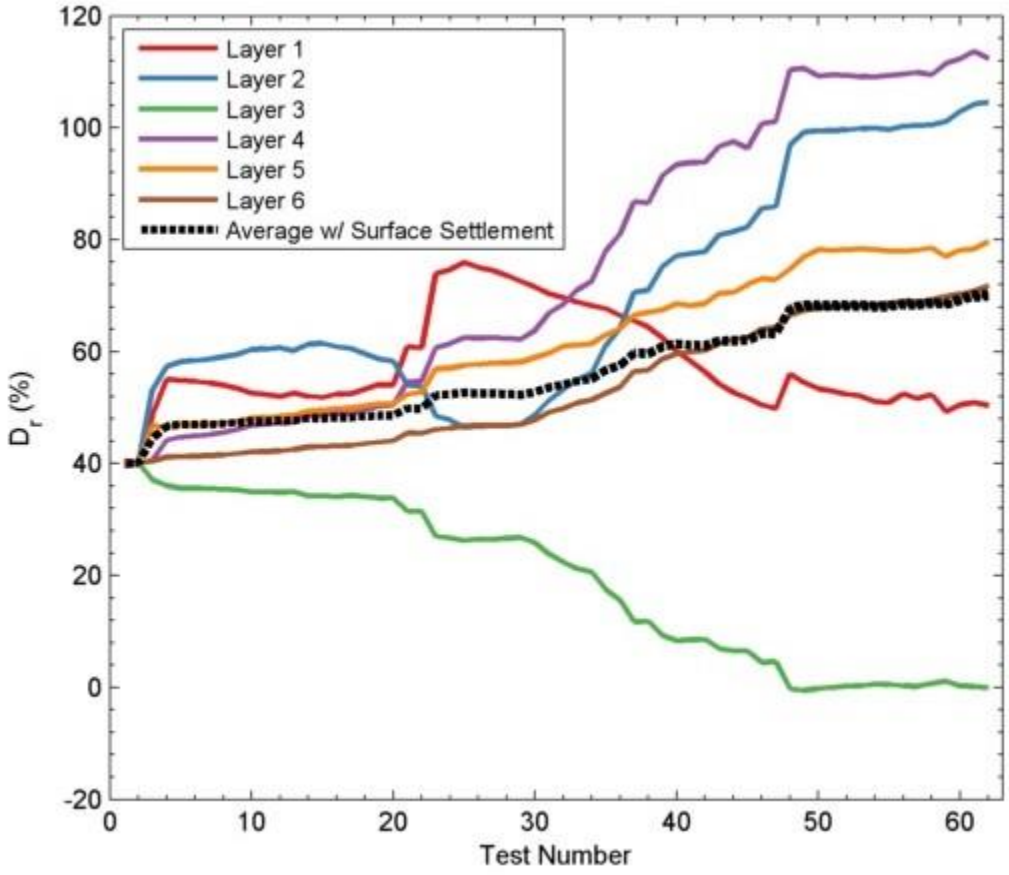


Figure 7.43: Comparison of relative density computed for each individual layer and the average relative density of the entire profile using the surface settlement for Experiment 3.

7.5.3.2 Discussion

Computing the change in relative density at each depth in the soil profile requires consistent and accurate measurements of the settlement at the top of each layer. Numerous potential complications are associated with recording settlement during dynamic centrifuge testing. Even relatively minor errors in the settlement measurements can lead to density estimates that are inconsistent with direct measurements made in similar studies, the observations made during model excavation, and our understanding of liquefiable soil behavior. Alternatively, the average density of the soil, computed based on the surface settlement provided a simple and comparatively more robust method to estimate the average liquefaction resistance of the soil.

Using the published data from El-Sekelly et al. (2016), the average relative density of the soil profile, computed from the surface settlement, was shown to provide a reasonable estimate

of the soil's resistance to liquefaction (Figure 7.5). In addition, based on data from Darby et al. (2017; 2018; 2019) the average relative density from the surface settlement was shown to be in general agreement with the relative density derived from mini-CPT data (Figure 7.11). Therefore, the average relative density computed using surface settlements was used in this study to evaluate the efficiencies of the IMs for predicting pore pressure generation and the triggering of liquefaction. The actual distribution of density with depth could not be accurately determined using the available equipment at the time the tests were performed. As will be shown during the efficiency evaluations presented in Section 7.7, the overburden stress term in the analyses showed behavior that implied a variable density profile. A further investigation of this behavior is provided in Section 7.7.2.2.

For unique cases the surface settlement measurement were not reliable due to tilting or shifting of the surface settlement monument. For these tests the settlement and average change in relative density was estimated using alternative methods on a case-by-case basis and will be discussed as needed in the following sections that detail the individual centrifuge experiments.

7.5.4 *Experiment 1 Data Processing*

The liquefiable soil layers (Layers 1 through 6) for Experiment 1 were placed at a target relative density of 100%. The model was subjected to 37 motions to generate a wide range of pore pressure response, both low and high. The model response was recorded by the interior and exterior sensors as described in Section 7.4.2. Summary plots for each test are provided in Appendix C and the raw data is archived on the NHERI website provided previously. The following sections describe the details of the sensors and relative density estimates for Experiment 1.

7.5.4.1 Sensors

Data for the sensors placed inside the model are provided in Table 7.5. The table includes the sensor type (ACC, PPT, or LVDT), layer number, lateral location (side or center), column number of the sensor output in the raw data file, the initial location of the sensor as placed during model construction, and the final location of the sensor as measured during model excavation following the conclusion of the experiment. All the location data is provided in inches at model scale as measured from the bottom corner of the model. The x- and y-axes represent the long and

short dimensions of the container, respectively, and the z-axis represents the height as measured from the bottom of the container. Data for the sensors placed on the exterior of the model are provided in Table 7.6, and include a description of the sensor, the column number of the sensor output in the raw data file, and a qualitative description of the sensor location.

Table 7.5: Experiment 1 Interior Sensor Data

Layer Num.	Sensor	Raw Data Output Col. Num.	Placement			Excavation		
			X (in)	Y (in)	Z (in)	X (in)	Y (in)	Z (in)
1	Acc Center	45	13.75	9	11.375	14	10.25	11
1	Acc Side	28	23.5	7.5	11.375	23.5	7.5	11.5
1	PPT Center	2	14	7	11.375	14	5	11.25
1	PPT Side	8	4	5	11.375	5	5.5	11.5
1	Sett. Mon.	39	16.25	7	11.375	16.175	11.5	11.5
2	Acc Center	46	14	7	10.5	13.5	7.25	10.75
2	Acc Side	29	23.5	8	10.5	24	8	10.5
2	PPT Center	3	14	6.5	9.5	14	7.5	9.75
2	PPT Side	9	5	6	9.5	5.5	8	9.75
2	Sett. Mon.	40	11.25	7	10.5	11.175	10.5	10.375
3	Acc Center	47	14	7	8.75	14	7.5	9.25
3	Acc Side	30	24	6.25	8.75	24	7	8.25
3	PPT Center	4	14	4	7.875	14	4.25	8
3	PPT Side	10	5	5.5	7.75	5.5	6	7.5
3	Sett. Mon.	41	16.25	11.5	8.75	16.25	11.5	8.875
4	Acc Center	48	13.5	7.5	7	13	7.5	7
4	Acc Side	31	23.5	7.5	7	23	7	7
4	PPT Center	5	14.5	8	6.125	15	8	6.5
4	PPT Side	11	5.5	6.5	6.125	5.5	6	6.25
4	Sett. Mon.	42	11.25	11.5	7	11.375	11.5	7
5	Acc Center	49	15	6.5	5.25	15	6.5	5.5
5	Acc Side	32	23.5	8	5.25	23.5	8	5.5
5	PPT Center	6	15.5	3.5	4.5	15.5	4	4.75
5	PPT Side	12	4	5	4.5	4	5.5	4.5
5	Sett. Mon.	43	16.25	2.5	5.25	16.25	2.5	5.5
6	Acc Center	50	15	7	3.5	15	7	3.5
6	Acc Side	33	22.5	7	3.5	22.5	7	3.5
6	PPT Center	7	16	6.25	2.675	15.5	6.25	2.75
6	PPT Side	13	5	5	2.75	5	5	3
6	Sett. Mon.	44	11.25	2.5	3.5	11.25	2.5	3.375
7	Acc Center	51	13.75	9	1.75	13.75	9	1.75
7	Acc Side	34	22	6.75	1.75	22	6.75	1.75

Table 7.6: Experiment 1 Exterior Sensor Data

Sensor	Raw Data Output Col. Num.	Location Description
Acc Base Long.	21	Front of base plate in direction of motion
Acc Base Near Vert.	24	Left front of base plate in vertical direction
Base Far Vert.	26	Left rear of base plate in vertical direction
Acc Base Near Tran.	25	Left front of base plate perpendicular of applied motion
Acc Base Far Tran.	27	Left rear of base plate perpendicular of applied motion
Acc Leveling Plate Hor.	22	Front of Leveling plate in direction of applied motion
Acc Shaker Hor.	23	Front of shaker in direction of applied motion
Acc Layer 7 Rings	20	Front of rings for Layer 7 (1.75" up from of base plate)
Acc Layer 6 Rings	19	Front of rings for Layer 6 (3.5" inches up from base plate)
Acc Layer 5 Rings	18	Front of rings for Layer 5 (5.25" up from base plate)
Acc Layer 4 Rings	17	Front of rings for Layer 4 (7" up from base plate)
Acc Layer 3 Rings	16	Front of rings for Layer 3 (8.75" up from base plate)
Acc Layer 2 Rings	15	Front of rings for Layer 2 (10.5" up from base plate)
Acc Layer 1 Rings	14	Front of rings for Layer 1 (12.25" up from base plate)
LVDT Layer 7 Rings	38	Front of rings for Layer 7 (1.75" up from base plate)
LVDT Layer 5 Rings	37	Front of rings for Layer 5 (5.25" up from base plate)
LVDT Layer 3 Rings	36	Front of rings for Layer 3 (8.75" up from base plate)
LVDT Layer 1 Rings	35	Front of rings for Layer 1 (12.25" up from base plate)

Based on a review of the test data, it was observed that the Layer 6 accelerometers located on the side, center, and exterior rings of the model malfunctioned and were not able to provide meaningful data for any of the tests performed in Experiment 1. In addition, following Test 10 the accelerometers in Layer 3 (both interior and exterior) were observed to malfunction during the experiment. Due to the lack of reliable acceleration time histories, the IM-r_u response for Layer 6 and for Layer 3 following Test 10 were not included in the efficiency evaluations presented later in this chapter. All other central ACCs function throughout the duration of the test.

The side PPTs for Layers 4 and 5 produced erratic pore pressure readings and showed initial stress conditions that were not consistent with the depth at which the sensors were placed. The pore pressure response from the side PPTs in Layers 4 and 5 were therefore not considered during the evaluation of the hydraulic gradient and calculation of r_u during the processing of the centrifuge test results for Experiment 1.

Review of the acceleration-r_u response from Experiment 1 showed that there was a noticeable lag between the excess pore pressure response and the peak amplitudes in the recorded acceleration time history. A similar lag was also observed in Experiment 2; however, this response was not observed in the other four centrifuge experiments or in the CSS test data. An example of delayed pore pressures response is shown in Figure 7.44 for Experiment 1 Test 2. The figure shows plots of the acceleration and r_u time histories at each of the six liquefiable soil layers. The peak acceleration occurred at approximately 6.5 seconds into the record for each of the layers. However, the excess pore pressures were essentially 0 until approximately 7 seconds. The peak pore pressure response was observed at approximately 9.0 seconds into the record, when the amplitude of the recorded motion was low. This delay in the pore pressure response was observed at all depths within the model.

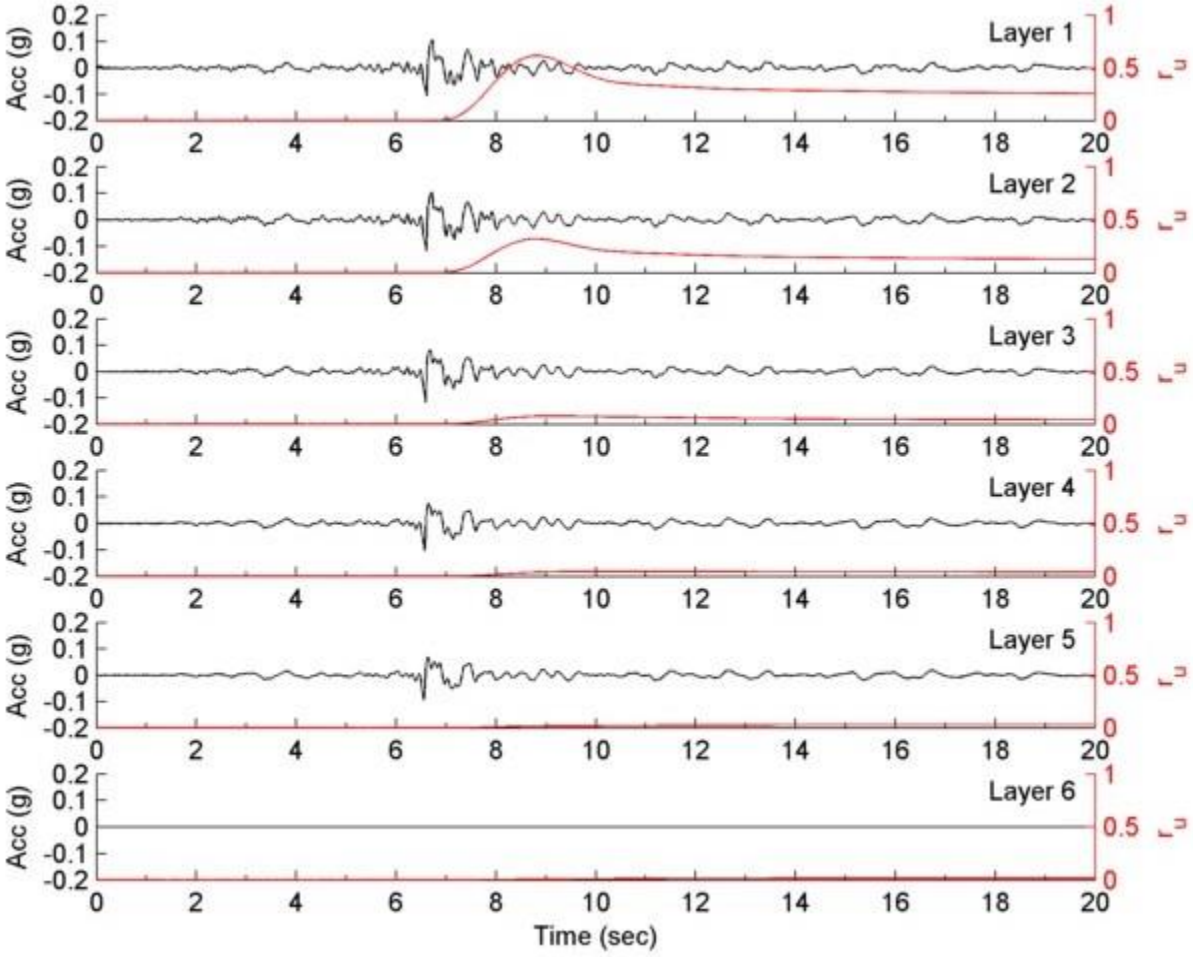


Figure 7.44: Acceleration and r_u response for each of the six liquefiable soil layers for Experiment 1 Test 2.

Figure 7.45 shows plots of the acceleration and pore pressure response for Layer 2, as well as the surface settlement time history for Experiment 1 Test 2. In Figure 7.45 the acceleration time history is shown in terms of the absolute value of the acceleration record to help distinguish the peak amplitudes in the time history. The data used to create the pore water pressure time history plot was taken directly from the raw data file and does not include any post processing. The pore pressure response was noticeably delayed with respect to the peak amplitudes of the acceleration time history. This contradicts the observations made during CSS testing, where the generation of excess pore pressure coincided with the peaks in the loading history. In addition, the CSS test data (and the results of the other centrifuge tests as illustrated in Section 7.6) suggested that later-arriving, lower-amplitude cycles that were less than the PPA should be shielded and should not contribute to the generation of pore pressures. Also, even though the pore pressure time history was taken directly from the raw data file and does not include any filtering, the time history was alarmingly smooth, and did not include any high frequency characteristics.

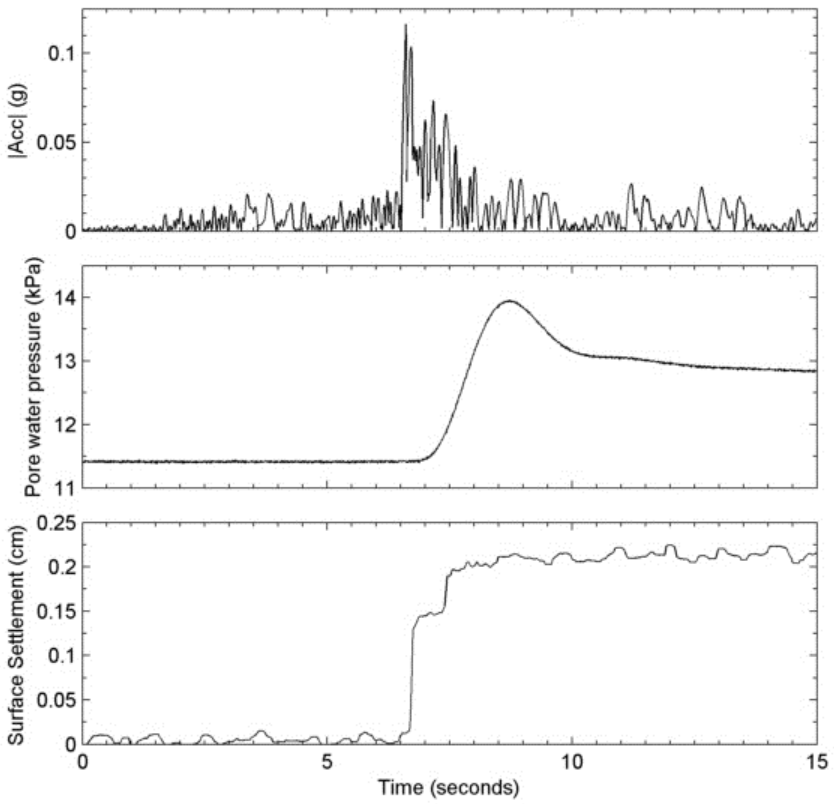


Figure 7.45: Comparison of the absolute value of the recorded acceleration time history, the pore water pressure from the raw data file, and the recorded surface settlement for Experiment 1 Test 2.

The pore pressure response was also delayed in comparison to the surface settlement time history. The surface settlement time history showed two noticeable jumps that occurred shortly after the large acceleration cycles at approximately 6.5 and 7.5 seconds into the record. In addition, the surface settlement was essentially constant from 9.5 seconds on when the pore pressure time history indicated that dissipation was occurring. For comparison, Figure 7.46 shows the same plots as Figure 7.45 using the response in Layer 2 from Experiment 3 Test 3. In this test the initial increase in pore pressure generally coincided with the first large amplitude acceleration pulses that were recorded 1.6 seconds into the time history. While the pore pressure response does not include as much high frequency fluctuations as the acceleration time history (as expected), it does include local peaks and valleys that correspond to dilation. Comparing the pore pressure response to the surface settlement the time history, the two time histories appeared to be roughly in phase. In addition, the settlement was observed to increase when the pore pressures were dissipating at the end of the record, which was consistent with consolidation settlement theory.

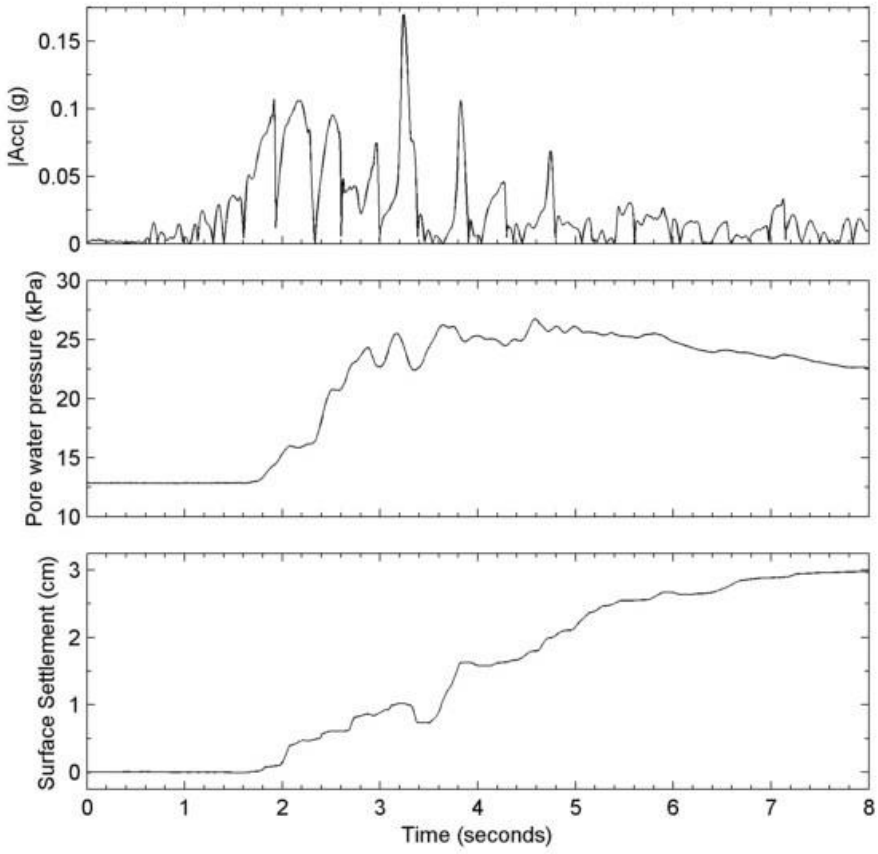


Figure 7.46: Comparison of the absolute value of the recorded acceleration time history, the pore water pressure from the raw data file, and the recorded surface settlement for Experiment 3 Test 3

The observed lag in the pore pressure response was consistent across all of the PPTs and all of the tests from Experiment 1. The reason for the delay was unknown. Potential explanations for the delay could be clogging of the sensors due to the dense placement of the soils, inadequate saturation of the PPTs, or residual viscous fluid from previous centrifuge experiments. Flow of the pore water during the test could also have been a factor, although flow was also observed in the other centrifuge experiments which did not show as significant a time lag. While the delay in the pore pressure readings was not consistent with observations from CSS testing or Experiments 3 through 6, given the consistency of the measured response and the complex behavior of a partially drained centrifuge experiment with liquefiable soils, the data generated by Experiment 1 was considered in the efficiency evaluations presented later in Section 7.7. The efficiency analyses included performing regression analyses on datasets that both included and excluded the results from this experiment to investigate the effect of the delayed pore pressure response that was observed in this experiment.

7.5.4.2 Evolution of Relative Density

The change in relative density following each test was estimated from the surface settlement data using the procedures described in Section 7.5.3. The evolution of the average relative density of the entire profile is provided in Figure 7.47. The figure also includes a plot summarizing the intensity of the input motion, evaluated with respect to PGA_{mb}. The average relative density computed using the surface settlement evolved in a consistent manner and increased as the number of shakings increased. The relative density at the conclusion of the experiment, i.e. after application of 37 motions, was estimated to be approximately 123%.

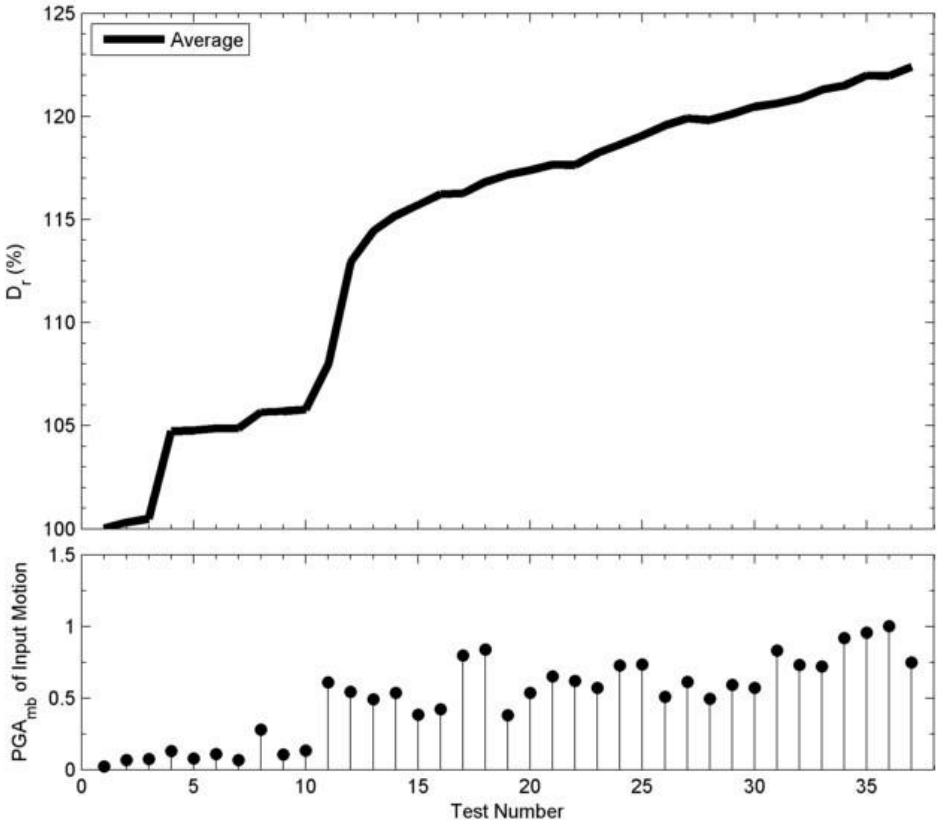


Figure 7.47: Evolution of relative density as a function of test number for Experiment 1

As the model densified during shaking, the liquefiable layer became increasingly dilative and the delay in the excess pore pressure response appeared to increase. As shown in Figure 7.47, Tests 11 through 13 included large amplitude base motions. Due to these motions, the estimated average relative density of the model increased from approximately 106% to approximately 115%. The tests that followed Test 13 showed highly dilative behavior and generated relatively little excess pore pressure despite extremely large amplitude applied loads. The tests performed after Test 13 were not included in the IM efficiency evaluation (Section 7.7.2) because at this stage in the experiment the model was essentially non-liquefiable and was unable to generate significant pore pressures.

7.5.5 *Experiment 2 Data Processing*

The liquefiable soil layer for Experiment 2 was placed at an initial target relative density of 50%. The model was subjected to 34 motions with the model response recorded by the sensors described in Section 7.4.2. Summary plots for each test are provided in Appendix C and the raw

data is archived on the NHERI website provided previously. The following sections describe the sensors and estimate of relative density for centrifuge Experiment 2.

7.5.5.1 Sensors

Data for the sensors placed inside the model are provided in Table 7.7, which includes the sensor type, layer number, a description of the lateral location (side or center), column number of the sensor output in the raw data file, and the initial (placement) and final (excavation) sensor locations. All the location data is provided in inches at model scale as measured from the bottom corner of the model using the same x-y-z coordinate system as Experiment 1. Data for the sensors placed on the outside of the model are provided in Table 7.8, and include a description of the sensor, the column number of the sensor output in the raw data file, and a qualitative description of the sensor location.

Table 7.7: Experiment 2 Interior Sensor Data

Layer Num.	Sensor	Raw Data Output Col. Num.	Placement			Excavation		
			X (in)	Y (in)	Z (in)	X (in)	Y (in)	Z (in)
1	Acc Center	46	15.25	9	11.375	15.5	8.375	11
1	Acc Side	28	23.5	8	11.375	23.25	7.875	11
1	PPT Center	2	15.25	4.75	11.375	15.25	4.5	10.875
1	PPT Side	8	4	6	11.375	4	6.25	11
1	Sett. Mon.	40	16.25	7	11.375	16.175	11.5	11.625
2	Acc Center	47	15	9.5	10.5	14.5	9.5	10
2	Acc Side	29	22.25	6.25	10.5	22.5	7.5	10.25
2	PPT Center	3	13.25	4	9.625	13	4	9.375
2	PPT Side	9	7	7.5	9.625	7	7	9.375
2	Sett. Mon.	41	11.25	7	10.5	11.175	10.5	9.875
3	Acc Center	48	15.5	8	8.75	15	8	8.625
3	Acc Side	30	23	7.5	8.75	23	7	8.625
3	PPT Center	4	14	4	7.875	14	4	7.875
3	PPT Side	10	4	7	7.875	4	6.5	7.875
3	Sett. Mon.	42	16.25	11.5	8.75	16.25	11.5	8.625
4	Acc Center	49	14	6.25	7	14	7.25	7
4	Acc Side	31	24	6.25	7	24	7.25	6.875
4	PPT Center	5	15.25	6	6.125	15	5.5	6.125
4	PPT Side	11	5	5.5	6.125	5	6.25	6.125
4	Sett. Mon.	43	11.25	11.5	7	11.375	11.5	7
5	Acc Center	50	14	9	5.375	14	9	5.25
5	Acc Side	34	23	6	5.25	23	7.25	5.25
5	PPT Center	6	15	5.5	4.375	15	5.5	4.375
5	PPT Side	12	5	6	4.375	5	6	4.375
5	Sett. Mon.	44	16.25	2.5	5.25	16.25	2.5	5
6	Acc Center	51	14.5	8	3.5	14.5	8.5	3.75
6	Acc Side	32	22	6	3.5	22	7.25	3.75
6	PPT Center	7	14	7.25	2.625	14	7	3.25
6	PPT Side	13	4.25	3	2.625	4.25	2.75	3.25
6	Sett. Mon.	45	11.25	2.5	3.5	11.25	2.5	4
7	Acc Center	52	14	9	1.875	14	9	2.25
7	Acc Side	33	24	7.75	1.875	24	7.75	2.25

Table 7.8: Experiment 2 Exterior Sensors

Sensor	Raw Data Output Col. Num.	Location Description
Acc Base Long.	21	Front of base plate in direction of motion
Acc Base Near Vert.	24	Left front of base plate in vertical direction
Base Far Vert.	26	Left rear of base plate in vertical direction
Acc Base Near Tran.	25	Left front of base plate perpendicular of applied motion
Acc Base Far Tran.	27	Left rear of base plate perpendicular of applied motion
Acc Leveling Plate Hor.	22	Front of Leveling plate in direction of applied motion
Acc Shaker Hor.	23	Front of shaker in direction of applied motion
Acc Layer 7 Rings	20	Front of rings for Layer 7 (1.75" up from of base plate)
Acc Layer 6 Rings	19	Front of rings for Layer 6 (3.5" inches up from base plate)
Acc Layer 5 Rings	18	Front of rings for Layer 5 (5.25" up from base plate)
Acc Layer 4 Rings	17	Front of rings for Layer 4 (7" up from base plate)
Acc Layer 3 Rings	16	Front of rings for Layer 3 (8.75" up from base plate)
Acc Layer 2 Rings	15	Front of rings for Layer 2 (10.5" up from base plate)
Acc Layer 1 Rings	14	Front of rings for Layer 1 (12.25" up from base plate)
LVDT Layer 7 Rings	38	Front of rings for Layer 7 (1.75" up from base plate)
LVDT Layer 5 Rings	37	Front of rings for Layer 5 (5.25" up from base plate)
LVDT Layer 3 Rings	36	Front of rings for Layer 3 (8.75" up from base plate)
LVDT Layer 1 Rings	35	Front of rings for Layer 1 (12.25" up from base plate)

The PPTs located in the center of the model for Layers 1 and 4, and in the side of the model in Layer 5 were observed to provide erratic pore pressure time histories and included initial pore pressure readings that were not consistent with the known depths at which the sensors were placed. The output from these sensors were not included in the processing and interpretation of the results from Experiment 2. All central ACCs were functioning throughout the experiment and were used to evaluate the acceleration time histories and IM response for each layer.

As discussed further in the next section, the surface LVDTs for all soil layers lost connection with the settlement monuments during Test 6. The loss of connection was due to large transient displacements of the soil model and tilting of the settlement monuments due to widespread liquefaction and elevated pore pressure ratios throughout the model. The peak r_u in every liquefiable soil layer for this test was greater than 0.6 and exceeded 0.9 in the upper 4 m of the soil profile. Following this test, the centrifuge was spun down and the settlement monument at the ground surface was readjusted to be in contact with the surface LVDT. The settlement

monuments for the lower soil layers were not replaced because moving the monuments could have created voids in the model and induced stresses within the soil which could have comprised the response of the adjacent ACCs and PPTs. Therefore, for the remaining tests, the tilted monuments were left in place and only the surface settlement was measured

As with Experiment 1, a lag was observed between the peaks in the acceleration time history and the recorded pore pressure response. These observations were inconsistent with the findings from the CSS test program and the other centrifuge tests. An example response from Experiment 2 is provided in Figure 7.48 which shows plots of the acceleration and r_u response at each layer for Test 4. The peak acceleration occurred at approximately 8.5 seconds into the record at all depths in the profile. However, at the time the peak acceleration was reached, the excess pore pressures were essentially 0. The peak pore pressure response occured at approximately 12.0 seconds into the record, when the amplitude of the recorded motion was low. The delayed pore pressure response was consistently observed throughout all depths in the profile.

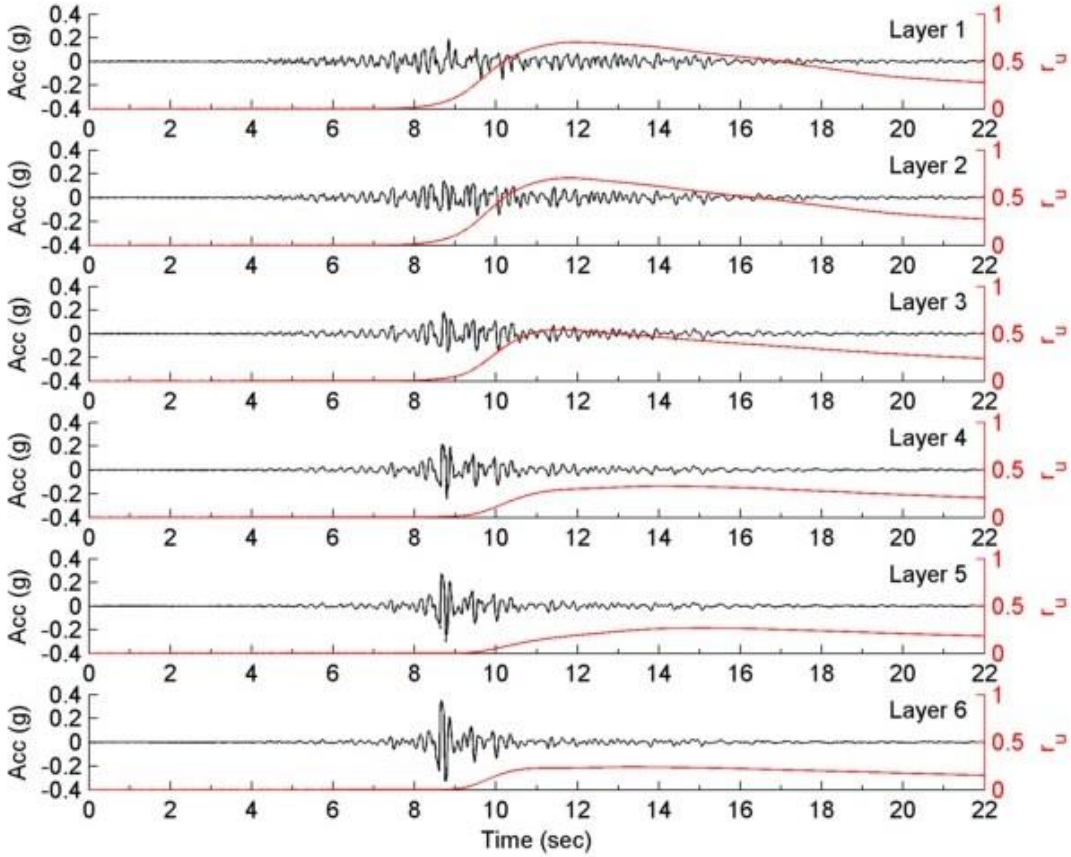


Figure 7.48: Acceleration and r_u response for each of the six liquefiable soil layers for Experiment 2 Test 4.

Time histories of the absolute value of acceleration and the raw pore pressure for Layer 2, and the recorded surface settlement are shown in Figure 7.49 for Experiment 2 Test 4. The acceleration time history featured large amplitude pulses between 8 to 10 seconds. The pore pressures began to increase at approximately 8 seconds, but in a very slow and gradual manner. The pore pressures continued to increase until approximately 11.5 seconds into the record, when the amplitudes of the acceleration history were relatively low. At this time the acceleration amplitudes were significantly less than the PPA which occurred at approximately 8.5 seconds into the record. The CSS test data, and the results from the other centrifuge experiments (Section 7.6) would suggest that the loading cycles that were less than the peak should not significantly contribute to the generation of pore pressure. As compared to Experiment 1, the pore pressure time history was better correlated with the surface settlement response. However, the majority of the settlement had already occurred prior to the time the PPT record showed signs of dissipation. The pore pressure time history was extraordinarily smooth and does not contain any of the high frequency characteristics observed in the acceleration time history.

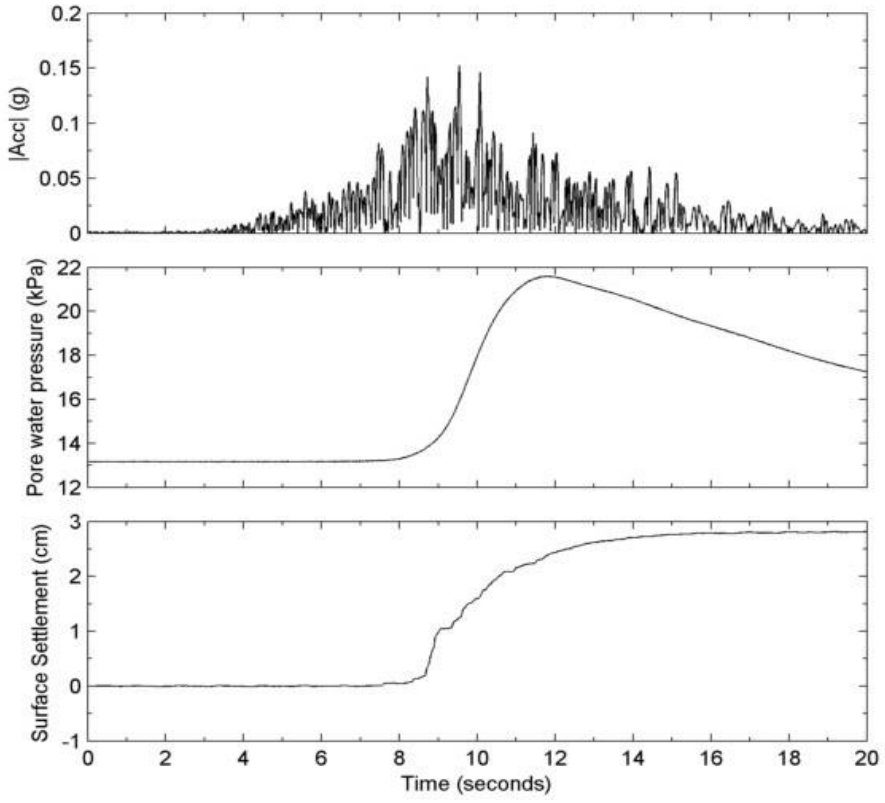


Figure 7.49: Comparison of the absolute value of the recorded acceleration time history, the pore water pressure from the raw data file, and the recorded surface settlement for Experiment 2 Test 4.

The observed lag in the pore pressure response was consistent across all of the PPTs and all of the tests from Experiment 2. As with Experiment 1, the reason for the delay was unknown. Potential explanations for the delay were presented in Section 7.5.4.1. While the delay in the pore pressure readings was not consistent with observations from CSS testing or Experiments 3 through 6, given the consistency of the measured response throughout all of the PPTs, and the complex behavior of a partially drained centrifuge experiment with liquefiable soils, the data generated by Experiment 2 was not disregarded and the data was considered in the efficiency evaluations presented later in this Chapter.

7.5.5.2 Evolution of Relative Density

As noted previously, during Test 6 all the settlement LVDTs became dislodged from the monuments and direct measurement of the settlement and corresponding change in relative density for this test was not possible. Following this test, the surface settlement monument was replaced and the testing continued. When the surface settlement measurement was available (i.e. Tests 1 through 5 and 7 to 34) the change in average relative density following each test was estimated using the procedures described in Section 7.5.3 based on the surface settlement.

To estimate the settlement that occurred during Test 6, the average vertical strain (computed as the surface settlement divided by the total height of the liquefiable layer) was plotted as a function of the average peak r_u and the average peak shear strain in the liquefiable layer, as shown in Figure 7.50. The average peak r_u and peak shear strain were computed in the same manner as described in Section 7.5.3.1. The figure also includes a fitted power function for each relationship and the fitted parameters are provided in the legend. The efficiency of each vertical strain relationship was evaluated using the standard deviation of the residuals, σ_ε, between the measured volumetric strain and the fitted value. The σ_ε values were computed as 0.083 and 0.14 for the average peak r_u and the average peak shear strain, respectively. The finding that the vertical strain was more strongly correlated with r_u than shear strain was consistent with the analyses presented in Section 7.5.3.1. For Test 6 the average peak r_u was computed as 0.85 and the average peak shear strain was evaluated as 3.9%. Extrapolating the relationships presented in Figure 7.50, the estimated vertical strain for Test 6 was 0.94 and 4.32% using the r_u and peak shear strain relationships, respectively.

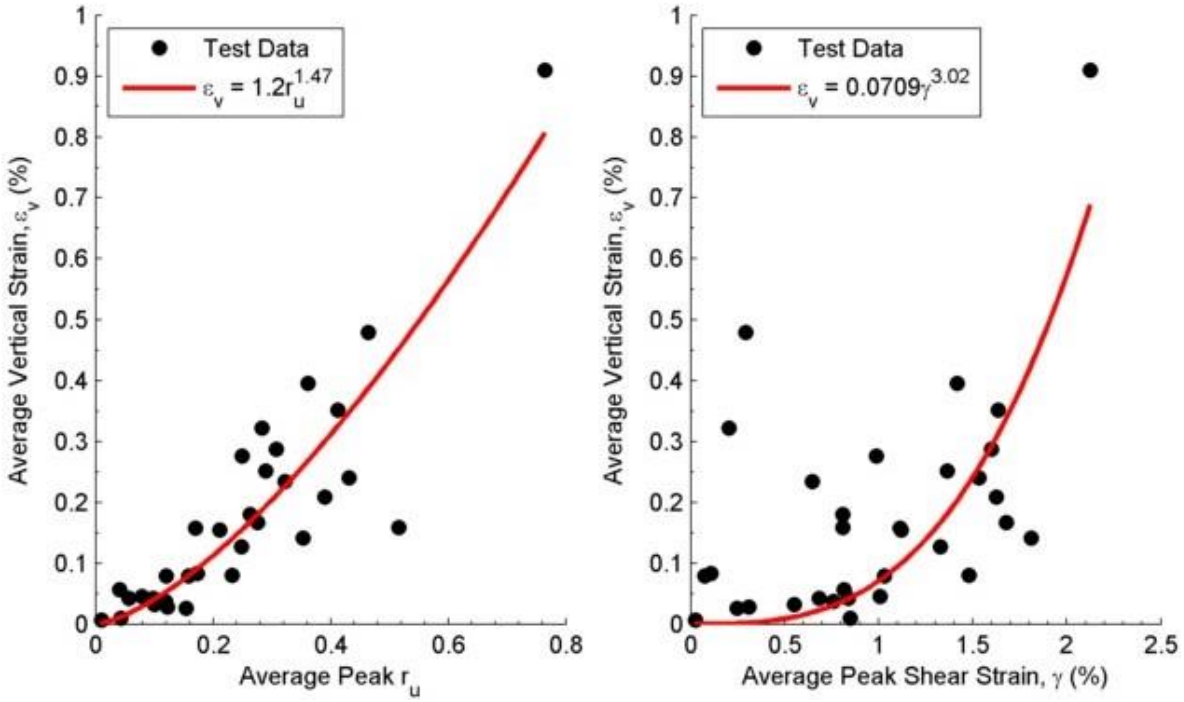


Figure 7.50: Average vertical strain as a function of average peak r_u and average peak shear strain for Experiment 2.

The estimated vertical strain using the average peak shear strain relationship for Test 6 was much larger than the observed settlements from other centrifuge experiments both from this study and from El-Sekelly et al. (2016) and Darby et al. (2019). The observed vertical strains from each of these studies were generally less than 1%. Figure 7.51 provides a plot of the volumetric strain due to liquefaction as a function of the peak shear strain and relative density from Ishihara and Yoshimine (1992). Using the computed average peak shear strain of 3.9% from Test 6 and assuming a relative density between 50 and 60%, the design chart from Ishihara and Yoshimine (1992) predicts a volumetric strain between approximately 1.2 and 1.6%. This estimate was relatively consistent with the estimate based on extrapolation of the fit from the r_u data presented in Figure 7.50. A vertical strain of 1.25% was selected for Test 6 because this value was consistent with both the experiment-specific vertical strain-r_u relationship (see Figure 7.52) and with the volumetric strain-peak shear strain relationship of Ishihara and Yoshimine (1992). The settlement and change in relative density for Test 6 was computed using the estimate of the vertical strain and the height of the liquefiable soil layer. However, basing the liquefaction resistance on a relative density computed from an estimated settlement imposes significant

uncertainty on the interpretation of the results from this experiment. This additional uncertainty is discussed further during the evaluation of IM efficiency presented later in this chapter.

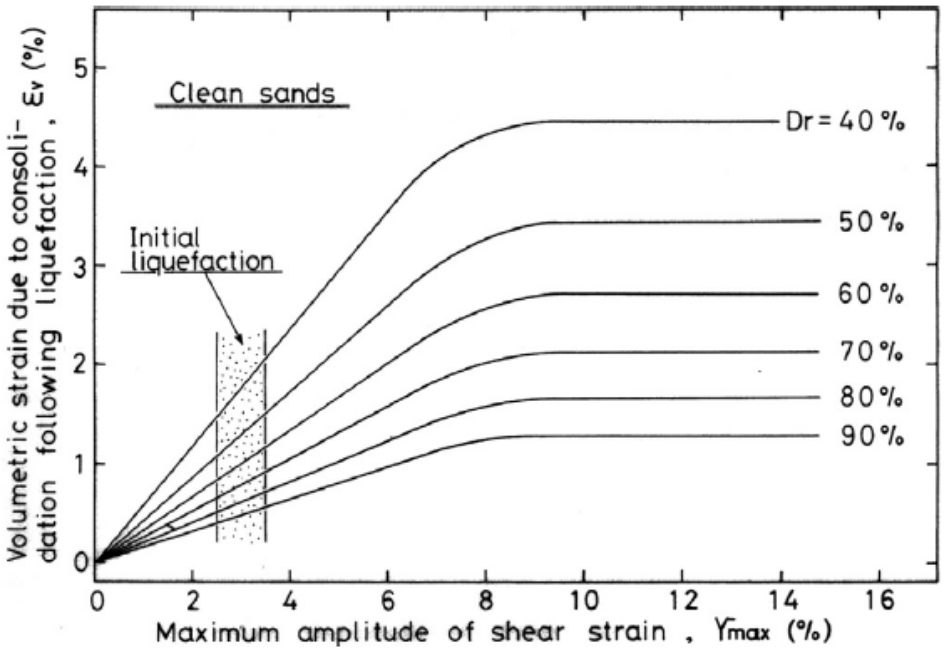


Figure 7.51: Volumetric strain as a function peak shear strain and relative density from Ishihara and Yoshimine (1992)

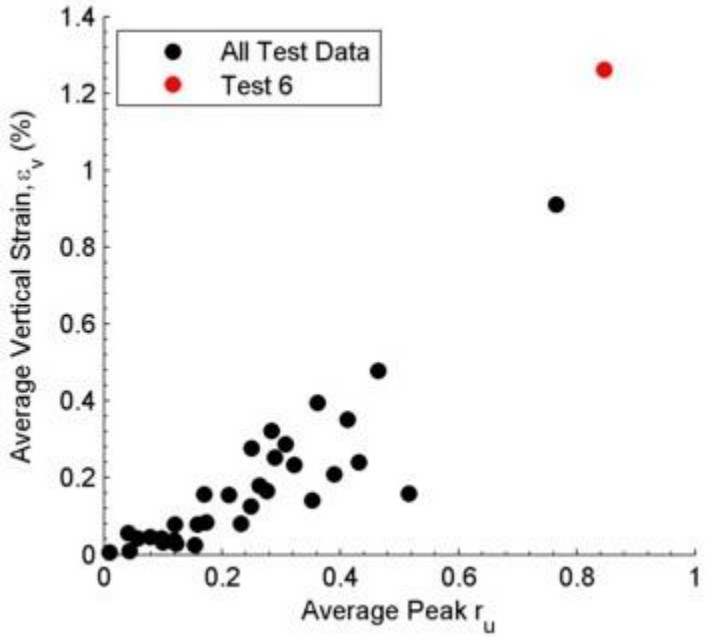


Figure 7.52: Average vertical strain as a function of average peak r_u including the estimated vertical strain for Experiment 2 Test 6.

Using the surface settlement data from Tests 1-5, an estimate of the surface settlement from Test 6, and the measured surface settlements from Test 7 to the end of the experiment, the evolution of the average relative density was computed and shown in Figure 7.53. The figure also includes a plot of the base motion intensity evaluated using PGA_{mb} for comparison. The average relative density evolved in a consistent manner and increased after each shaking event. Tests 6 and 7 induced very large settlements and the relative density increased from approximately 57% following Test 5 to 75% following Test 7. Interestingly, the PGA_{mb} of the base input motion for Test 6 was lower than the PGA_{mb} from Test 4. This suggests that PGA_{mB} computed from the total base motion may not be the most efficient IM at predicting the consolidation settlement of a liquefiable soil profile.

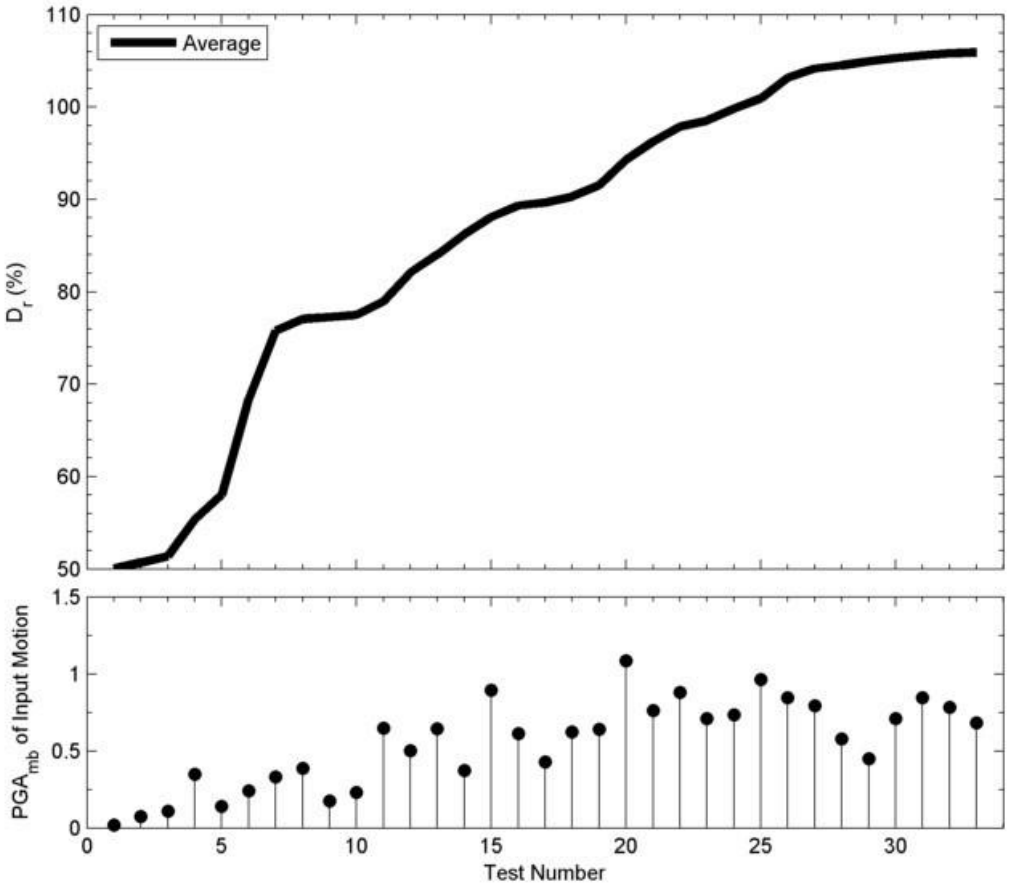


Figure 7.53: Evolution of relative density as a function of test number for Experiment 2

As the model densified during shaking the liquefiable layer became increasingly dilative, as indicated by large negative fluctuations in r_u, and the delay in the excess pore pressure response appeared to increase relative to the high amplitude portion of the acceleration loading

history (see Appendix C). Following Test 14 the model began to show highly dilative behavior and generated low excess pore pressures despite the large amplitudes of the input motions. As shown in Figure 7.53, the estimated density of the model was approximately 85% following Test 14, which was larger than the initial density of the model by a factor of 1.7. At this stage in the experiment the model was essentially non-liquefiable and was unable to generate significant pore pressures, therefore only Tests 1 through 14 were considered in the efficiency evaluation presented in Section 7.7.2.

7.5.6 *Experiment 3 Data Processing*

The liquefiable soil layer for Experiment 3 was placed at an initial target relative density of 40%. The model was subjected to 62 motions with the model response recorded by the sensors described in Section 7.4.2. Summary plots for each test are provided in Appendix C and the raw data is archived on the NHERI website. The following sections describe the sensors and estimate of relative density for centrifuge Experiment 3.

7.5.6.1 Sensors

Data for the sensors placed inside the model are provided in Table 7.9, and include the sensor type, layer number, a description of the lateral location (side or center), column number of the sensor output in the raw data file, and the initial (placement) and final (excavation) sensor locations. All the location data is provided at model scale using the same x-y-z coordinate system described previously. Data for the sensors placed on the exterior of the model are provided in Table 7.10, and include a description of the sensor, the column number of the sensor output in the raw data file, and a qualitative description of the sensor location. All of the interior sensors were functioning during this experiment and were used to process the centrifuge data as described in Sections 7.3.2.

Table 7.9: Experiment 3 Interior Sensor Data

Layer Num.	Sensor	Raw Data Output Col. Num.	Placement			Excavation		
			X (in)	Y (in)	Z (in)	X (in)	Y (in)	Z (in)
1	Acc Center	18	14	8	11.375	13.5	9	11.25
1	Acc Side	25	4	7.25	11.375	3.75	6.75	11.035
1	PPT Center	36	14	3.75	11.375	13	3.5	11.375
1	PPT Side	30	21.5	6.75	11.375	22	6.75	11.75
1	Sett. Mon.	45	15	9.625	12.25	15	9.625	12.125
2	Acc Center	19	14	8	10.375	13.5	8	10.25
2	Acc Side	10	4.5	6.75	10.375	4.5	6.5	10.25
2	PPT Center	37	14	4	10.125	13.5	4	10
2	PPT Side	31	21.25	6.75	10.125	21.5	6.5	10
2	Sett. Mon.	48	12	7.5	10.375	12	7.5	10.25
3	Acc Center	20	13	9.5	8.875	13	9.5	8.875
3	Acc Side	11	5.5	6.5	8.875	5	6.5	8.875
3	PPT Center	38	14	4.5	8.5	14	4.5	8.25
3	PPT Side	32	23.5	7	8.5	23.5	7	8.25
3	Sett. Mon.	47	15	3	8.625	15	3	8.75
4	Acc Center	21	13.5	8	7.125	13	7.75	7
4	Acc Side	12	5.5	7	7.125	5.5	7	7
4	PPT Center	39	13.5	4.25	6.625	13	4	6.625
4	PPT Side	33	22.5	6	6.625	22.5	6	6.625
4	Sett. Mon.	44	12	11.5	7.125	12	11.5	7.125
5	Acc Center	22	12.5	8.5	5.875	12	8	5.75
5	Acc Side	13	5	7	5.875	4.75	7	5.75
5	PPT Center	41	14	5	5.125	13.5	4.75	5
5	PPT Side	34	22.5	6.5	5.125	22	6.5	4.875
5	Sett. Mon.	46	15	11.5	5.125	15	11.5	5.5
6	Acc Center	23	13	10	4.25	12.75	10	4
6	Acc Side	14	5.5	6.75	4.25	5.25	6.5	4
6	PPT Center	40	13	4	3.125	12.75	4	3.25
6	PPT Side	35	22.5	6.75	3.125	22.25	6.75	3.25
6	Sett. Mon.	49	12	3.5	4.25	12	3.5	4.125
7	Acc Center	24	14	10	2.5	14	10	2.5
7	Acc Side	15	5	6.5	2.5	5	6.5	2.5

Table 7.10: Experiment 3 Exterior Sensor Data

Sensor	Raw Data Output Col. Num.	Location Description
Acc Base Long.	2	Front of base plate in direction of motion
Acc Base Near Vert.	5	Left front of base plate in vertical direction
Base Far Vert.	16	Left rear of base plate in vertical direction
Acc Base Near Tran.	6	Left front of base plate perpendicular of applied motion
Acc Base Far Tran.	17	Left rear of base plate perpendicular of applied motion
Acc Leveling Plate Hor.	3	Front of Leveling plate in direction of applied motion
Acc Shaker Hor.	4	Front of shaker in direction of applied motion
Acc Layer 7 Rings	7	Front of rings for Layer 7 (1.75" up from of base plate)
Acc Layer 6 Rings	8	Front of rings for Layer 6 (3.5" inches up from base plate)
Acc Layer 5 Rings	9	Front of rings for Layer 5 (5.25" up from base plate)
Acc Layer 4 Rings	26	Front of rings for Layer 4 (7" up from base plate)
Acc Layer 3 Rings	27	Front of rings for Layer 3 (8.75" up from base plate)
Acc Layer 2 Rings	28	Front of rings for Layer 2 (10.5" up from base plate)
Acc Layer 1 Rings	29	Front of rings for Layer 1 (12.25" up from base plate)
LVDT Layer 7 Rings	43	Front of rings for Layer 7 (1.75" up from base plate)
LVDT Layer 5 Rings	42	Front of rings for Layer 5 (5.25" up from base plate)
LVDT Layer 3 Rings	51	Front of rings for Layer 3 (8.75" up from base plate)
LVDT Layer 1 Rings	50	Front of rings for Layer 1 (12.25" up from base plate)

7.5.6.2 Evolution of Relative Density

The change in relative density following each test for the 40% D_r Experiment 3 was described in detail in Section 7.5.3.1. The summary of the average relative density as a function of test number was provided in Figure 7.43. As the model densified during shaking the liquefiable layer became increasingly dilative. Following Test 49 the model began to show highly dilative behavior and generated low excess pore pressures despite the large amplitudes of the input motions. At this stage in the experiment the model was essentially non-liquefiable and was unable to generate significant pore pressures, therefore only Tests 1 through 49 were considered in the efficiency evaluation presented in Section 7.7.2.

7.5.7 *Experiment 4 Data Processing*

The liquefiable soil layer for Experiment 4 was placed at an initial target relative density of 70%. The model was subjected to 68 motions with the model response recorded by the sensors described in Section 7.4.2. Summary plots for each test are provided in Appendix C and the raw data is archived on the NHERI website. The following sections describe the sensors and estimate of relative density for centrifuge Experiment 4.

7.5.7.1 Sensors

Data for the sensors placed inside the model are provided in Table 7.11, and include the sensor type, layer number, a description of the lateral location (side or center), column number of the sensor output in the raw data file, and the initial (placement) and final (excavation) sensor locations. All the location data is provided at model scale using the same x-y-z coordinate system as the previous centrifuge experiments. Data for the sensors placed on the exterior of the model are provided in Table 7.12, and include a description of the sensor, the column number of the sensor output in the raw data file, and a qualitative description of the sensor location.

Table 7.11: Experiment 4 Interior Sensor Data

Layer Num.	Sensor	Raw Data Output Col. Num.	Placement			Excavation		
			X (in)	Y (in)	Z (in)	X (in)	Y (in)	Z (in)
1	Acc Center	20	13.25	9	11.375	13.25	9	11.5
1	Acc Side	14	6	6.75	11.35	6.125	6.5	10.75
1	PPT Center	39	15	4.25	11.375	14.5	4.25	11.5
1	PPT Side	31	23.75	7	11.375	23.75	6.5	11
1	Sett. Mon.	41	17	3	12	17	3.25	11.75
2	Acc Center	19	15	10	10.375	15	10	10.25
2	Acc Side	13	4.5	7	10.375	5	7.25	9.75
2	PPT Center	38	13.75	4	9.325	13.75	4	9.5
2	PPT Side	30	23	6.5	9.325	23	6	9.25
2	Sett. Mon.	40	10.5	11	10.375	10.5	11.125	10.25
3	Acc Center	18	15	10.75	8.625	15	10.75	8.25
3	Acc Side	12	5	6.5	8.625	5	7	8.25
3	PPT Center	37	14.5	4.5	7.75	14	4.5	7.5
3	PPT Side	29	21.25	6.5	7.75	21.75	6.25	7.75
3	Sett. Mon.	42	17	8	8.75	17	8	8.5
4	Acc Center	17	14	9	7.125	14	9	6.75
4	Acc Side	11	5.5	7.25	7.125	5.5	7.25	6.75
4	PPT Center	36	14.125	4.25	6.25	14.25	4.25	6
4	PPT Side	28	23.5	7	6.25	23	7	6
4	Sett. Mon.	43	10.5	8	7.125	10.5	8	6.75
5	Acc Center	16	14	13	5.125	14	13	5.25
5	Acc Side	10	5.75	6.5	5.125	6	6.25	5.25
5	PPT Center	33	14.5	4.875	4.25	14.5	4.75	4.5
5	PPT Side	27	22	7.75	4.25	22	7.75	4.5
5	Sett. Mon.	44	17	11	5.125	17	11	5.25
6	Acc Center	15	12	12	3.625	12	12	3.25
6	Acc Side	9	6.25	7	3.625	6.125	7	3.5
6	PPT Center	32	13.5	5	2.5	13.5	5	2.5
6	PPT Side	26	22	7	2.5	22	7	2.5
6	Sett. Mon.	45	10.5	3	3.625	10.5	3	3.25

Table 7.12: Experiment 4 Exterior Sensor Data

Sensor	Raw Data Output Col. Num.	Location Description
Acc Base Long.	4	Front of base plate in direction of motion
Acc Base Near Vert.	5	Left front of base plate in vertical direction
Base Far Vert.	7	Left rear of base plate in vertical direction
Acc Base Near Tran.	6	Left front of base plate perpendicular of applied motion
Acc Base Far Tran.	8	Left rear of base plate perpendicular of applied motion
Acc Leveling Plate Hor.	3	Front of Leveling plate in direction of applied motion
Acc Shaker Hor.	2	Front of shaker in direction of applied motion
Acc Layer 7 Rings	35	Front of rings for Layer 7 (1.75" up from of base plate)
Acc Layer 6 Rings	34	Front of rings for Layer 6 (3.5" inches up from base plate)
Acc Layer 5 Rings	25	Front of rings for Layer 5 (5.25" up from base plate)
Acc Layer 4 Rings	24	Front of rings for Layer 4 (7" up from base plate)
Acc Layer 3 Rings	23	Front of rings for Layer 3 (8.75" up from base plate)
Acc Layer 2 Rings	22	Front of rings for Layer 2 (10.5" up from base plate)
Acc Layer 1 Rings	21	Front of rings for Layer 1 (12.25" up from base plate)
LVDT Layer 7 Rings	49	Front of rings for Layer 7 (1.75" up from base plate)
LVDT Layer 5 Rings	48	Front of rings for Layer 5 (5.25" up from base plate)
LVDT Layer 3 Rings	47	Front of rings for Layer 3 (8.75" up from base plate)
LVDT Layer 1 Rings	46	Front of rings for Layer 1 (12.25" up from base plate)

All of the interior ACCs and PPTs functioned properly during this experiment, with the exception of the center PPT for layer 5. The response recorded by that transducer was erratic, and the initial pore pressure corresponded to a sensor depth that was significantly different than the depth the sensor was placed at during model construction. Note that accelerometers were not placed in Layer 7 (cemented sand layer) during this experiment. The response at Layer 7 was estimated using the ACCs located on the rings of the laminar container.

7.5.7.2 Evolution of Relative Density

The change in relative density following each test was estimated using the procedures described in Section 7.5.3 based on the data from the settlement monuments. The evolution of the average relative density of the liquefiable soil layers are provided in Figure 7.54. The figure also includes a plot summarizing the intensity of the input motion with respect to PGA_{mb} for comparison. The average relative density computed using the surface settlement layer evolved in a steady manner and increased as the number of shakings increased up to a final relative density of approximately

106%. Note the large increase in relative density due to Test 34. The motion applied in that test was very large and induced high excess pore pressures throughout the model. In addition, the actuator used to apply the input motion broke during this test. Following Test 34, the centrifuge was spun down, the exterior sensors were detached from the model and the model was removed from the centrifuge to allow for maintenance on the actuator. Once the actuator was fixed, the model was placed back on the centrifuge and the experimental program resumed. However, the process of removing and placing the centrifuge model and reconnecting the surface LVDT could have altered the density of the model. The degree to which the model density was impacted was unknown and could not be measured or inferred. As a result, the tests performed following Test 34 include additional uncertainty in their estimated densities and were not included in the efficiency evaluations performed later in Section 7.7.

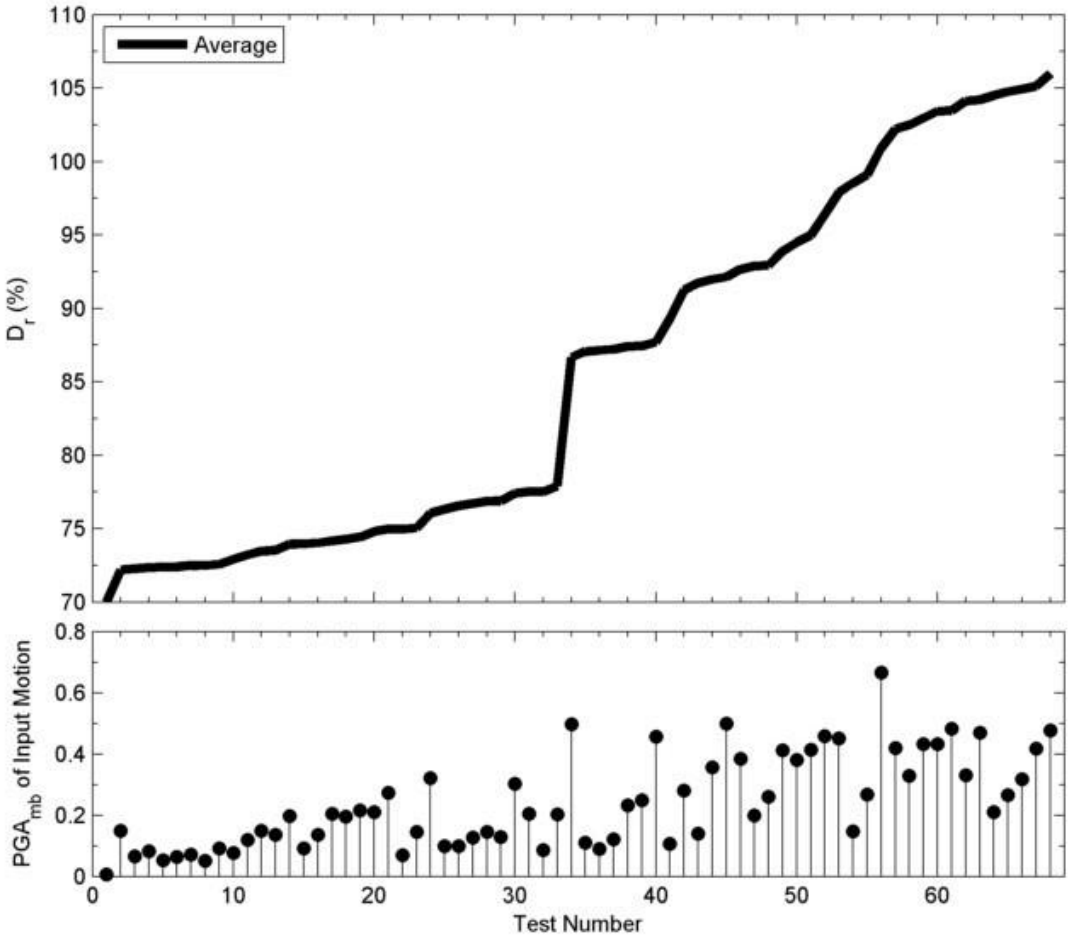


Figure 7.54: Evolution of relative density as a function of test number for Experiment 4

7.5.8 *Experiment 5 Data Processing*

The liquefiable soil layer for Experiment 5 was placed at an initial target relative density of 40%. The experimental procedure for Experiment 5 differed from Experiments 1 through 4 in that a smaller number of high amplitude base input motions were applied with the intent of generating large excess pore pressures in each test. The model was subjected to eight motions and the model response was recorded by the sensors as described in Section 7.4.2. Summary plots for each test are provided in Appendix C and the raw data is archived on the NHERI website. The following sections describe the sensors and estimate of relative density for centrifuge Experiment 5.

7.5.8.1 Sensors

Data for the sensors placed inside the model are provided in Table 7.13, and include the sensor type, layer number, a description of the lateral location (side or center), column number of the sensor output in the raw data file, and the initial (placement) and final (excavation) sensor locations. All the location data is provided at model scale using the same x-y-z coordinate system as the previous centrifuge experiments. Data for the sensors placed on the exterior of the model are provided in Table 7.14, and include a description of the sensor, the column number of the sensor output in the raw data file, and a qualitative description of the sensor location. In Experiment 5, the LVDTs used to measure the displacement of the settlement monuments were replaced with photoelectric laser sensors. The laser sensors were considered superior to the LVDTs for measuring surface settlement because they do not require a physical connection between the sensor and the settlement monument which can impose lateral stresses in the LVDT due to friction at the LVDT-monument interface.

Table 7.13: Experiment 5 Interior Sensor Data

Layer Num.	Sensor	Raw Data Output Col. Num.		Placement			Excavation		
		Test 1 to 3	Rest	X (in)	Y (in)	Z (in)	X (in)	Y (in)	Z (in)
1	Acc Center	22	23	14	13.5	11.25	14	13.5	12.13
1	Acc Side	2	2	5.5	7	11.4	5	7	12
1	PPT Center	9	9	14	5.5	11.5	14	5.5	11.5
1	PPT Side	29	30	24.7	8.5	11.25	24.5	8.5	12.1
1	Sett. Mon.	16	22	9	8.75	11	9	8.75	12
2	Acc Center	23	24	14.25	9	10.5	14.5	9	10.8
2	Acc Side	3	3	4.3	7.2	10.45	4.25	7.2	11
2	PPT Center	10	10	14	5	9.7	13.8	5	9.9
2	PPT Side	30	31	23.2	7.1	9.6	23.5	7.1	10
2	Sett. Mon.	17	16	18	8.75	10.6	18	8.75	10.8
3	Acc Center	24	25	14	8.25	8.8	14	8.25	9.4
3	Acc Side	4	4	5.1	6.5	8.8	5.25	6.5	9
3	PPT Center	11	11	14	7	7.9	14	7	8.5
3	PPT Side	31	32	23.8	6.9	7.8	23.75	6.9	8.5
3	Sett. Mon.	18	17	18	13.5	8.8	18	13.5	9.1
4	Acc Center	25	26	14	9	6.9	14	9	7.75
4	Acc Side	5	5	5.1	5.5	6.9	5	5.5	7.5
4	PPT Center	12	12	13.8	5	6	14	5	6.75
4	PPT Side	32	33	24.5	6.5	6.1	24.5	6.5	7
4	Sett. Mon.	19	18	9	13.5	7	9	13.5	7.25
5	Acc Center	26	27	15.2	10.5	5.1	15	10.5	5.75
5	Acc Side	6	6	6.7	6.5	5.2	6.5	6.5	5.6
5	PPT Center	13	13	14	5	4.4	14	5	5
5	PPT Side	33	34	23.1	7	4.4	23	7	5.2
5	Sett. Mon.	20	19	9	11.75	5.2	9	11.75	5.25
6	Acc Center	27	28	14.15	9.2	3.3	14	9	2.9
6	Acc Side	7	7	5.5	6.9	3.4	5.7	6.5	2.7
6	PPT Center	14	14	14	5.6	2.6	14	5.5	2.63
6	PPT Side	34	35	22.3	7.1	2.63	22.25	7	2.6
6	Sett. Mon.	21	20	18	11.75	3.4	18	11.75	4
7	Acc Center	28	29	14	9.3	1.75	13.9	9.4	1.8
7	Acc Side	8	8	5.6	7	1.75	5.6	6.9	1.75

Table 7.14: Experiment 5 Exterior Sensor Data

Sensor	Raw Data Output Col. Num.		Location Description
	Tests 1 and 2	Tests 3 to 8	
Acc Base Near Hor.	48	49	Left front of base plate in vertical direction
Base Far Hor.	50	51	Left rear of base plate in vertical direction
Acc Base Near Tran.	49	50	Left front of base plate perpendicular of applied motion
Acc Base Far Tran.	51	52	Left rear of base plate perpendicular of applied motion
Acc Leveling Plate Hor.	47	48	Front of Leveling plate in direction of applied motion
Acc Shaker Hor.	46	47	Front of shaker in direction of applied motion
Acc Layer 7 Rings	45	46	Front of rings for Layer 7 (1.75" up from of base plate)
Acc Layer 6 Rings	44	45	Front of rings for Layer 6 (3.5" inches up from base plate)
Acc Layer 5 Rings	43	44	Front of rings for Layer 5 (5.25" up from base plate)
Acc Layer 4 Rings	42	43	Front of rings for Layer 4 (7" up from base plate)
Acc Layer 3 Rings	41	42	Front of rings for Layer 3 (8.75" up from base plate)
Acc Layer 2 Rings	40	41	Front of rings for Layer 2 (10.5" up from base plate)
Acc Layer 1 Rings	39	40	Front of rings for Layer 1 (12.25" up from base plate)
LVDT Layer 7 Rings	38	39	Front of rings for Layer 7 (1.75" up from base plate)
LVDT Layer 5 Rings	37	38	Front of rings for Layer 5 (5.25" up from base plate)
LVDT Layer 3 Rings	36	37	Front of rings for Layer 3 (8.75" up from base plate)
LVDT Layer 1 Rings	35	36	Front of rings for Layer 1 (12.25" up from base plate)

Note that the raw data output column number for Tests 1 and 2 is different than for Tests 4 to 8 for most sensors. During testing, it was observed that the output for the surface settlement was behaving inconsistently and included erroneous settlement readings and drift during the portion of the record prior to the application of the base motion. The centrifuge was spun down and after inspection of the sensors the cause of the issue was identified as the connection from the sensor to the DAQ. The subsequent reconfiguring of the sensor connection to the DAQ led to a shift in the raw data output columns shown in Tables 7.13 and 7.14. The estimation of the surface settlement for Layer 1 during Tests 1 and 2 is described in the next section.

All of the interior ACCs and PPTs were functioning during this experiment, with the exception of the center ACC for Layer 5 and the side PPT for Layer 1. The center ACC for Layer 5 showed long period drift and did not record the high frequency acceleration response recorded in the other interior ACCs. The PPT for layer 1 showed negative pore pressure readings during the static portion of the record. These sensors were excluded from the subsequent data processing and interpretation of the results of Experiment 5.

7.5.8.2 Evolution of Relative Density

The change in relative density following each test was estimated using the procedures described in Section 7.5.3. As noted previously, the surface settlement readings for Tests 1 and 2 were not reliable due to sensor error. To estimate the surface settlement for these tests, the average vertical strain was plotted as a function of the average peak pore pressure ratio in the underlying layers for Layers 1 and 2, as shown in Figure 7.55. The vertical strain was observed to be highly correlated with the average peak pore pressure, as was observed in previous tests from this study and in El-Sekelly et al (2016). In addition, the relationship between vertical strain and r_u was reasonably consistent for both Layers 1 and 2. However, Test 7 was a notable outlier for both layers. The acceleration and r_u response of Layers 1 and 2 in Test 7 are shown in Figure 7.56. The input motion for Test 7 had a very long duration and included two large amplitude loading portions – from 25 to 40 seconds and from 75 to 90 seconds. During the lower amplitude loading between 40 and 75 seconds, pore pressures were dissipated. The generation, dissipation, and regeneration of excess pore pressures caused large settlements; however, this effect cannot be captured using single peak r_u value. Because Tests 1 and 2 were of shorter duration (less than 25 seconds total duration, see Appendix C), the settlement-r_u response of Test 7 was considered unrepresentative and was not considered in the evaluation of the settlement response for Tests 1 and 2. A fit to the vertical strain and the average peak r_u for the representative tests (Tests 3, 4, 5, 6, and 8 for Layer 1 and all tests except Test 7 for Layer 2) was performed and is shown on Figure 7.55. The fitted relationship was shown to provide a good match to the observed data.

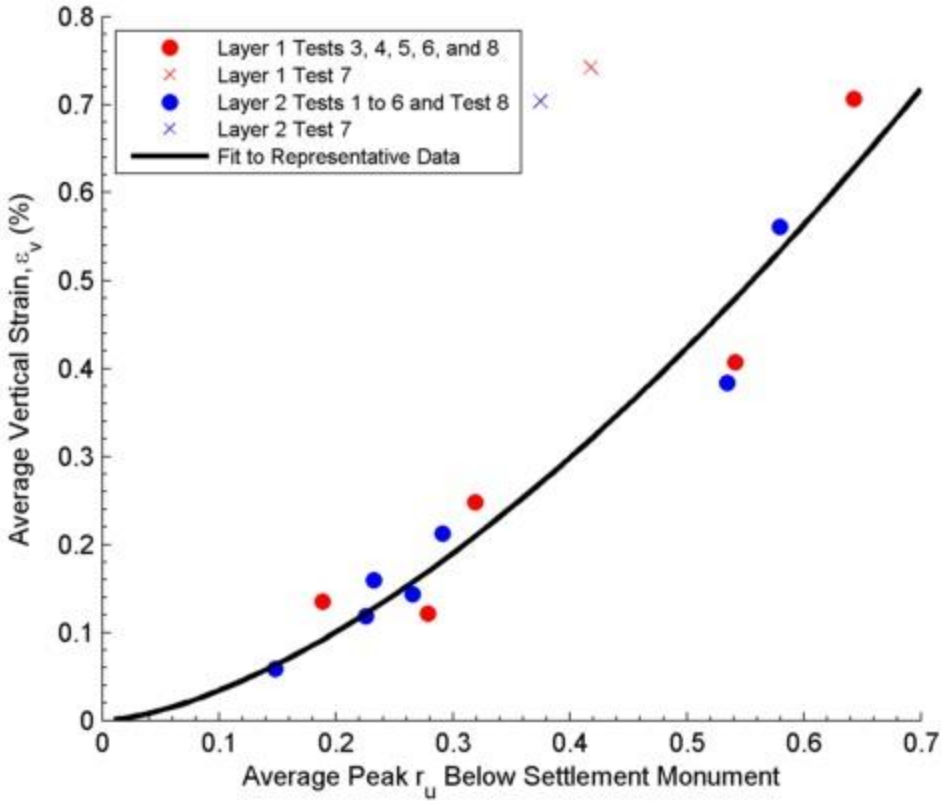


Figure 7.55: Average vertical strain as a function of the average peak r_u for Layers 1 and 2 in Experiment 5.The tests that are considered representative are plotted as filled circles. Tests 1 and 2 for Layer 1, where the surface settlement was unreliable due to sensor error shown as open circles. The response from Test 7, which was heavily impacted by drainage are shown as X-markers. The fitted line to the representative tests is provided in black.

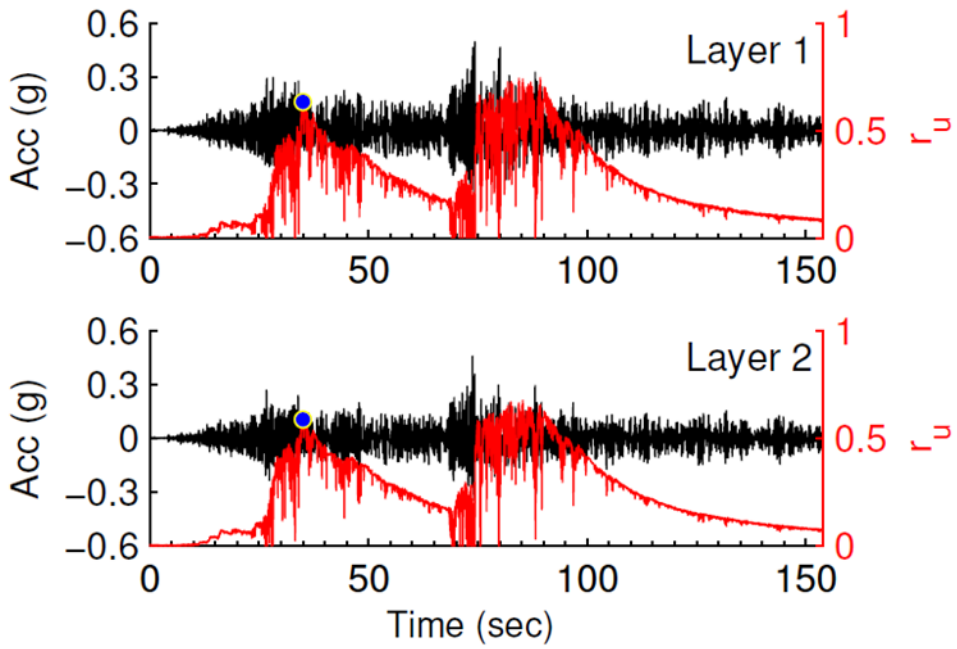


Figure 7.56: Acceleration and r_u response in Layers 1 and 2 for Experiment 5 Test 7

The surface settlements for Tests 1 and 2 were evaluated using height of the liquefiable layer and an estimate of the vertical strain using the fitted vertical strain – average peak r_u relationship provided in Figure 7.55. Based on the estimated surface settlements from Tests 1 and 2, and the recorded surface settlement from Tests 3 to 8, the evolution of the average relative density of the entire profile is provided in Figure 7.57. The figure also includes a plot summarizing the intensity of the input motion with respect to PGA_{mb} for comparison. The estimated average density profile increases as the number of shakings increase and reached a final value of approximately 67% at the end of the test.

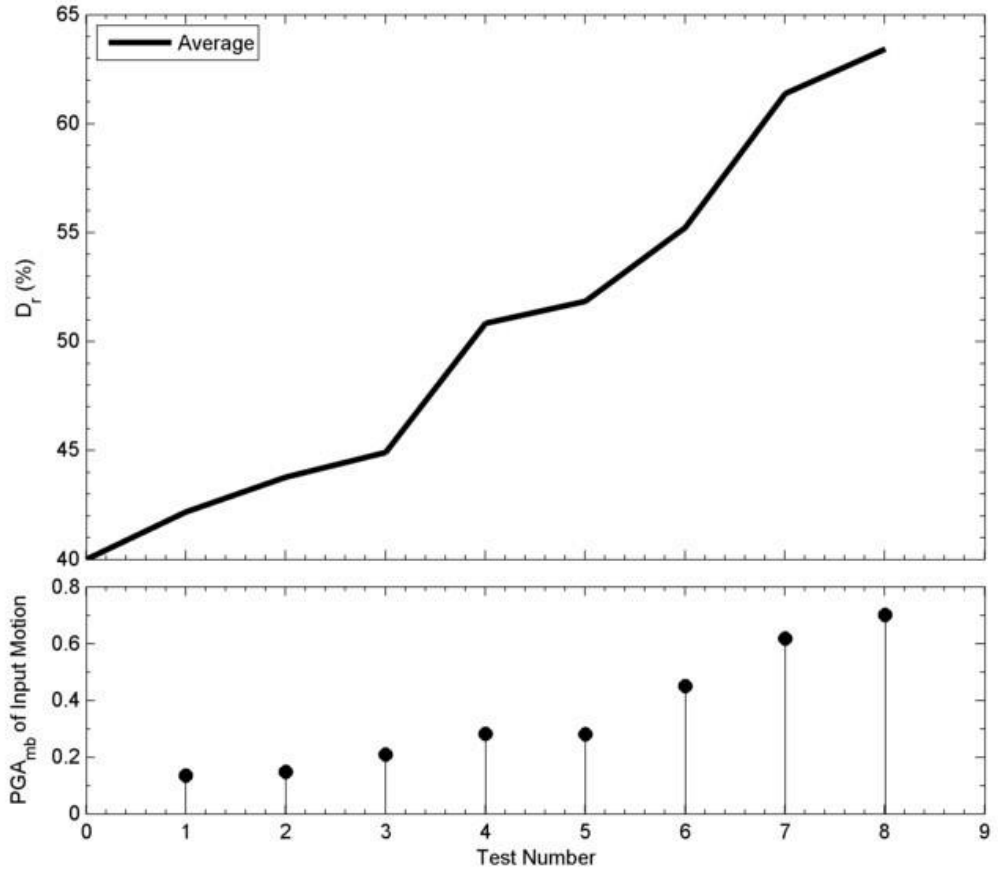


Figure 7.57: Evolution of relative density as a function of test number for Experiment 5

7.5.9 *Experiment 6 Data Processing*

The liquefiable soil layer for Experiment 6 was placed at an initial target relative density of 40%. Experiment 6 used the same experimental procedure used in Experiment 5. The model was subjected to 8 motions with the intent of generating large excess pore pressures in each test. The model response was recorded by the sensors as described in Section 7.4.2. Summary plots for each test are provided in Appendix C and the raw data is archived on the NHERI website. The following sections describe the sensors and estimate of relative density for centrifuge Experiment 6.

7.5.9.1 Sensors

Data for the sensors placed inside the model are provided in Table 7.15, and include the sensor type, layer number, a description of the lateral location (side or center), column number of the

sensor output in the raw data file, and the initial (placement) and final (excavation) sensor locations. All the location data is provided at model scale using the x-y-z coordinate system described for the previous centrifuge experiments. Data for the sensors placed on the exterior of the model are provided in Table 7.16, and include a description of the sensor, the column number of the sensor output in the raw data file, and a qualitative description of the sensor location.

Table 7.15: Experiment 6 Interior Sensor Data

Layer Num.	Sensor	Raw Data Output Col. Num.	Placement			Excavation		
			X (in)	Y (in)	Z (in)	X (in)	Y (in)	Z (in)
1	Acc Center	39	15	9	11.3	16	9	11.5
1	Acc Side	46	7	7	11.45	7	7.25	11.5
1	PPT Center	13	14.2	5	11.45	15.25	6	11.5
1	PPT Side	29	23.3	6.9	11.4	No Data		
1	Sett. Mon.	15	18.5	7.3	12.2	18.85	7.25	12.05
2	Acc Center	40	14.5	9.5	10.5	14.5	9.5	10.4
2	Acc Side	47	5.5	7.25	10.45	5.5	7.25	10.4
2	PPT Center	8	16	5.7	9.5	16	5.7	9.95
2	PPT Side	30	24.2	7	9.6	24.2	7	9.85
2	Sett. Mon.	16	9.1	7.5	10.55	9.1	8.5	10.75
3	Acc Center	41	13.5	9.75	8.75	13.5	9.75	8.85
3	Acc Side	48	7	7.8	8.7	7	7.75	8.75
3	PPT Center	9	13.9	5	7.65	13.9	6	8.15
3	PPT Side	31	22	7.3	7.75	22	8.3	8.25
3	Sett. Mon.	18	9	3.2	8.7	9	3.25	8.75
4	Acc Center	42	12.25	9.9	7.1	12.25	9.9	7.25
4	Acc Side	49	5.6	6.8	7.1	5.6	6.8	7.15
4	PPT Center	10	13.1	6.7	6.15	13.1	7.7	6.55
4	PPT Side	32	22.9	4.5	6.15	22.9	5.5	6.5
4	Sett. Mon.	21	18.5	3.4	6.95	18.5	4.4	7.15
5	Acc Center	43	13.8	10	5.2	13.8	10	5.35
5	Acc Side	50	5.3	7.05	5.3	5.3	7.1	5.35
5	PPT Center	11	13.3	4.8	4.35	13.3	5.8	4.85
5	PPT Side	33	21.2	7.1	4.35	21.2	8	4.75
5	Sett. Mon.	19	8.9	12.25	5.25	8.9	12.25	5.35
6	Acc Center	44	13.4	9.8	3.5	13.4	9.8	3.6
6	Acc Side	51	5.6	7.15	3.55	5.5	7.1	3.65
6	PPT Center	12	14.1	5	2.65	14.1	7	3.05
6	PPT Side	34	23	7.3	2.6	23	8.3	3.05
6	Sett. Mon.	17	18.4	12.5	3.45	18.4	13	3.5
7	Acc Center	45	5.25	7.1	1.75	5.25	7.1	1.85
7	Acc Side	52	13	9.1	1.8	13	10.1	1.95

Table 7.16: Experiment 6 Exterior Sensor Data

Sensor	Raw Data Output Col. Num.	Location Description
Acc Base Long.	3	Front of base plate in direction of motion
Acc Base Near Long.	5	Left front of base plate in vertical direction
Base Far Long.	7	Left rear of base plate in vertical direction
Acc Base Near Tran.	6	Left front of base plate perpendicular of applied motion
Acc Base Far Tran.	8	Left rear of base plate perpendicular of applied motion
Acc Leveling Plate Hor.	4	Front of Leveling plate in direction of applied motion
Acc Layer 7 Rings	28	Front of rings for Layer 7 (1.75" up from of base plate)
Acc Layer 6 Rings	27	Front of rings for Layer 6 (3.5" inches up from base plate)
Acc Layer 5 Rings	26	Front of rings for Layer 5 (5.25" up from base plate)
Acc Layer 4 Rings	25	Front of rings for Layer 4 (7" up from base plate)
Acc Layer 3 Rings	24	Front of rings for Layer 3 (8.75" up from base plate)
Acc Layer 2 Rings	23	Front of rings for Layer 2 (10.5" up from base plate)
Acc Layer 1 Rings	22	Front of rings for Layer 1 (12.25" up from base plate)
LVDT Layer 7 Rings	38	Front of rings for Layer 7 (1.75" up from base plate)
LVDT Layer 5 Rings	37	Front of rings for Layer 5 (5.25" up from base plate)
LVDT Layer 3 Rings	36	Front of rings for Layer 3 (8.75" up from base plate)
LVDT Layer 1 Rings	35	Front of rings for Layer 1 (12.25" up from base plate)

All the interior ACCs and PPTs functioned properly during this experiment, except for the Layer 2 side ACC, which did not register a response above the baseline noise. The location of the side PPT for Layer 1 during excavation was not provided because the sensor was accidentally removed from the model during the process of detaching the model from the centrifuge platform.

7.5.9.2 Evolution of Relative Density

The change in relative density following each test was estimated using the procedures described in Section 7.5.3. The evolution of the average relative density of the liquefiable soil layers are provided in Figure 7.58. The figure also includes a plot summarizing the intensity of the input motion with respect to PGA_{mb} for comparison. The average relative density computed using the surface settlement layer evolved in a steady manner and increased as the number of shakings increased up to a final relative density of approximately 77%.

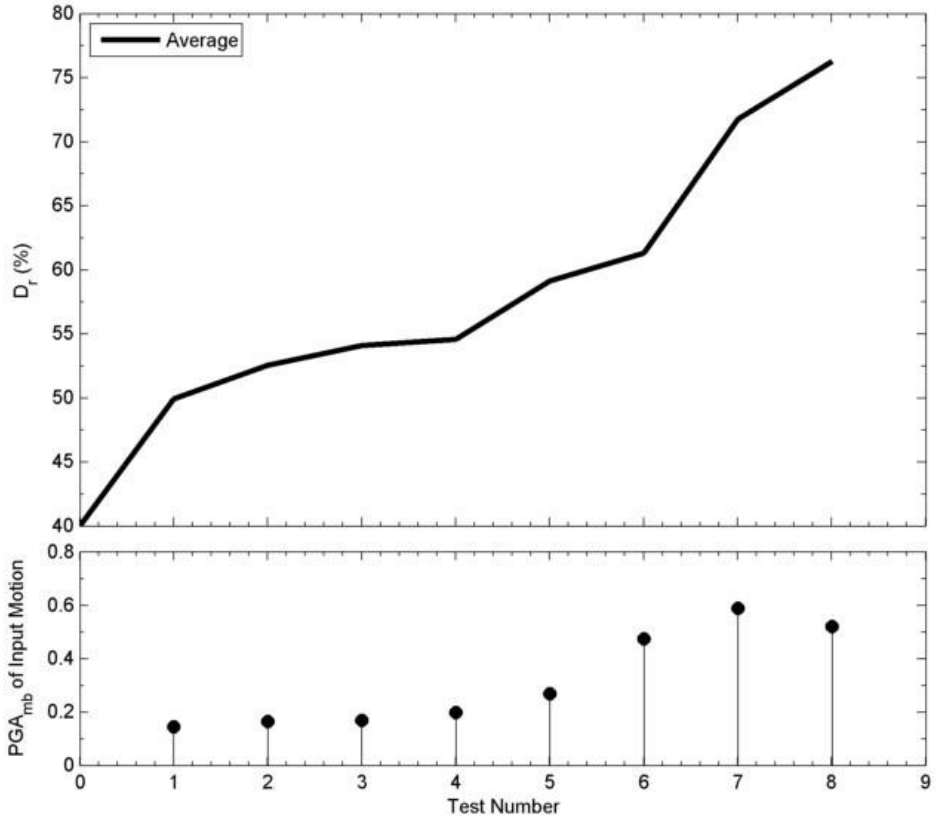


Figure 7.58: Evolution of relative density as a function of test number for Experiment 6

7.5.10 *Uncertainties in centrifuge modeling*

Centrifuge modeling contains a number of uncertainties, most of which are not able to be quantified with a high degree of accuracy. For the experiments performed as part of this study, the largest source of uncertainty was attributed to the evaluation of relative density due to repeated shaking, which has been discussed extensively. Other common sources of error include spatial variability of the soil characteristics and interior sensor migration during testing. The vertical migration of the PPTs can be estimated using the hydrostatic pore pressure measured prior to shaking during each test. Unfortunately, no such method exists for the ACCs. During model excavation, it was observed that in a few instances the ACCs migrated by as much as 0.5 inches at model scale, which corresponds to approximately 0.3 m in prototype units. Estimating the interior ACC locations following each applied motion was not possible; therefore, when computing the acceleration-r_u time history pairs for evaluating the IM efficiencies, the ACCs were assumed to be fixed at their original locations.

Uncertainties in the spatial uniformity of the soil properties and sensor migration are not unique to this study and are an inherent part of dynamic centrifuge experiments; however, they are uncertainties the reader should be aware of. Despite these uncertainties, the centrifuge experiments performed as part of this study provide a unique and valuable dataset that is representative of the general behavior of a liquefiable soil subjected to 1-dimensional shaking using a diverse set of transient base motions. The following sections present observations from the centrifuge study and an evaluation of the efficiency of evolutionary IMs to predict the generation of excess pore pressures and the initiation of liquefaction.

7.6 Observations from Centrifuge Testing Program

The CSS test program presented in Chapter 6 methodically investigated the response of a liquefiable soil subjected to transient loading. The CSS tests allowed the behavior of a liquefiable soil to be observed at a level of detail that was not possible in the centrifuge. These tests provided valuable insight into key aspects of the relationship between the loading history and the generation of excess pore pressure. Some of these insights included well-known characteristics of liquefiable soil behavior, such as the fact that the generation of excess pore pressure is related to the amplitude and duration, and relatively insensitive to the frequency content, of the applied load. A unique observation from this study was the notion that the phasing of the loading history can dramatically impact the pore pressure response. A theory was presented that states the amount of pore pressure generated by a given pulse of loading is a function of both the amplitude of the pulse and the ratio of the pulse amplitude to the prior peak amplitude, or PPA. Loading pulses that exceeded the PPA tended to generate large increments of excess pore pressure, while pulses with amplitudes lower than the PPA generated significantly less pore pressure than if they had not been preceded by a larger amplitude pulse. Incorporating this effect into a new intensity measure, LIM, was shown to reduce the uncertainty in the IM-D_r-r_u relationships. This section provides a qualitative investigation of the centrifuge test data to evaluate to extent to which the behavior that was observed in the CSS test program is also applicable to the large-scale centrifuge experiments.

The impact of drainage on the pore pressure response of the centrifuge model has been discussed extensively. In order to make a qualitative comparison between the observations from the centrifuge, which included the drainage effects, to observations from the undrained CSS

tests, a pore pressure adjustment procedure was developed as presented in Section 7.5.2.3. Due to the highly complex drainage behavior of the centrifuge model, fully decoupling the pore pressure response due to shaking with the response due to drainage was not possible. Given the approximate nature of the adjustment procedure, the discussions presented in the following section include both the adjusted and uncorrected r_u time histories.

7.6.1 *Relationship Between the Loading History and Excess Pore Pressure*

This section presents the results of select tests from the centrifuge experimental program to evaluate the relationship between the loading history, in terms of acceleration, and the generation of excess pore pressure. The tests presented in this section represent a wide range of loading characteristics and were selected with the purpose of evaluating the PPA-based pore pressure generation theory from the CSS test program. The selected tests include tests with unique and interesting loading histories and cover a representative range of pore pressure responses. The acceleration and r_u time histories for all of the centrifuge tests are provided in Appendix C.

7.6.1.1 Experiment 6 Test 2

Figure 7.59 shows the response of Layer 2 during Experiment 6 Test 2. Plots 7.59a, b, and c are the same as presented in Figure 7.36, and show the acceleration time history, uncorrected and adjusted r_u time histories, and the absolute value of acceleration and r_u time histories plotted on the same axis, respectively. This test was selected because of its similarity to the modulated harmonic loading histories from the CSS test program (Section 6.3.3). The acceleration time history from this test was fairly symmetric. The amplitudes of the acceleration time history gradually increased with time from the beginning of the record up until the maximum peak acceleration just after 8 seconds and decreased at a similar rate following the maximum peak. The portion of the time history from 0 to 8 seconds resembled the taper-up modulated harmonic loading histories from the CSS test program (Sections 6.3.3.1 and 6.3.3.3), while the portion of the time history after 8 seconds resembled the taper-down modulated harmonic loading (Section 6.3.3.2).

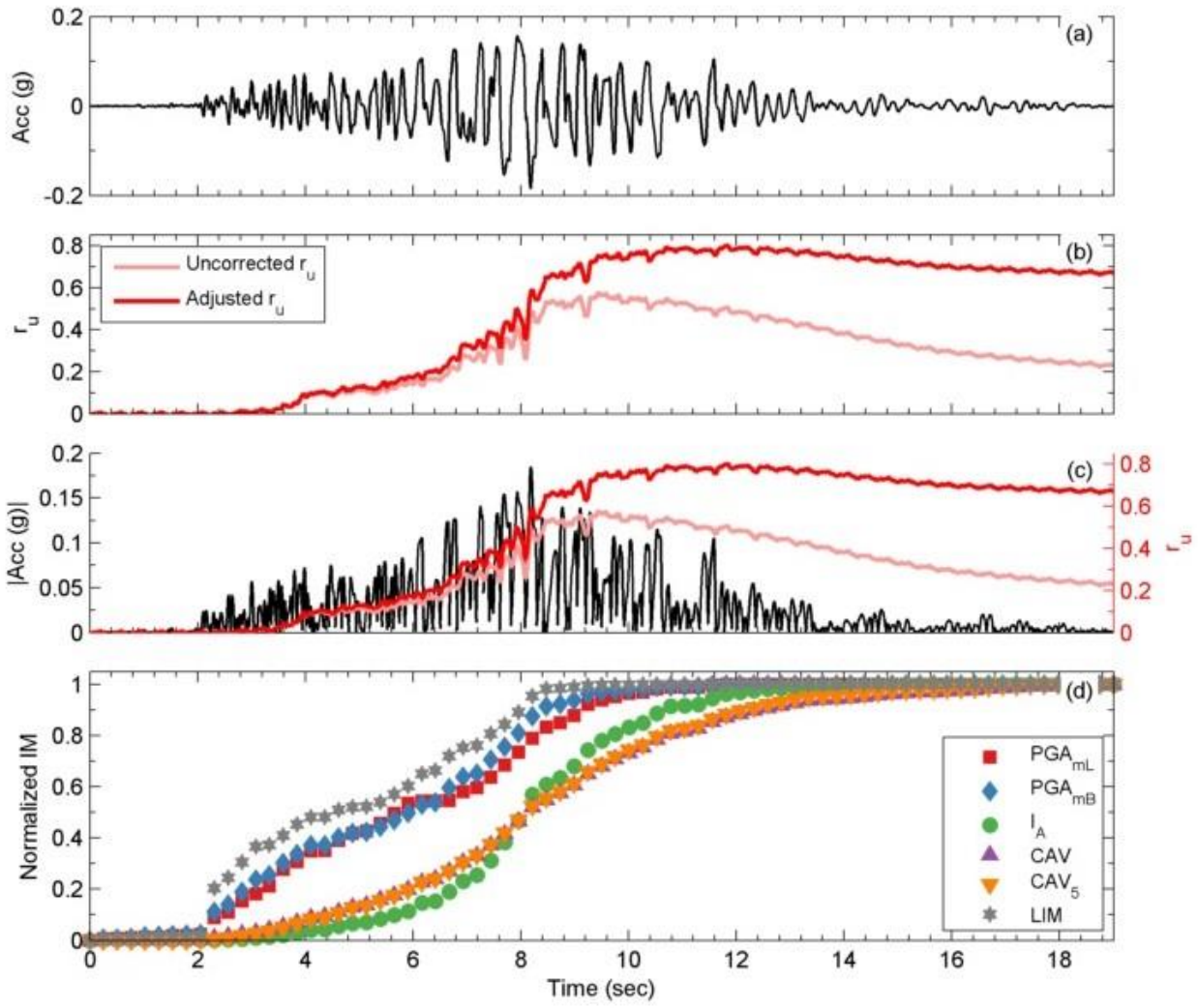


Figure 7.59: Comparison of the acceleration time history, excess pore pressure, and evolutionary IM response for Experiment 6 Test 2 Layer 2. (a) the acceleration time history, (b) the uncorrected and adjusted r_u time histories, (c) the absolute value of the acceleration time history and the r_u time histories, and (d) time histories of the normalized evolutionary IMs computed as the evolutionary IM time history divided by the value of the IM at the end of the record.

It was observed that while the amplitudes of the loading history were fairly symmetric, the r_u response was not. During the initial 3.2 seconds of the record, the acceleration amplitudes and derived shear strains were low (less than 0.01%) and pore pressures were not generated. After approximately 3.2 seconds, as the acceleration amplitudes began to increase, the pore pressures increased rapidly. After 8 seconds, when all of the subsequent acceleration pulse amplitudes were considerably less than the PPA, additional increments of excess pore pressure were not generated. These observations were consistent with the observations made during CSS

testing. From 0 to 8 seconds the PPA was successively exceeded as the loading amplitudes increased, and as observed in the taper-up CSS tests, the pore pressures increased at a similar rate as the loading amplitudes. Note that both the uncorrected and adjusted r_u time histories are practically identical during this portion of the time history.

After the peak amplitude pulse, at about 8 seconds, the rate of pore pressure slowed considerably, even though the acceleration amplitudes before and after the maximum peak pulse were similar. In the uncorrected r_u time history, the pore pressures were practically constant from 8 to 9 seconds. After 9 seconds the excess pore pressure began to dissipate. The adjusted r_u time history showed a similar response and included only minor increases in r_u following the peak amplitude pulse at about 8 seconds. This response was similar response to the taper-down CSS tests, where cycles that were less than the PPA generated relatively little excess pore pressure and were effectively shielded by the previously applied higher amplitude pulse.

Figure 7.59d shows a plot of the six evolutionary IMs discussed in Chapters 6 (PGA_{mL}, PGA_{mB}, I_A, CAV, and CAV5, and LIM). Each IM was normalized by its value at the end of the record to compare the evolutionary IM response to the r_u time histories. The time histories for the integral IMs (I_A, CAV, and CAV_5) highlight the symmetry of the acceleration time history. At approximately 8 seconds each of the integral IMs were at approximately half of their final value. For the first 8 seconds of the record the rate of increase for each of the integral IMs resembles the shape of the r_u time histories, however the integral IMs continued to increase after the maximum peak amplitude at 8 seconds, when the r_u time histories were at (uncorrected r_u) or near (adjusted r_u) their peak value. The cycle counting-based procedures, PGA_{mL}, PGA_{mB}, and LIM, increased steadily from 2 to 8 seconds into the record, and like the r_u time history, reached their peak values at or shortly after the maximum peak acceleration pulse at 8 seconds. While the cycle counting-based IMs increased at a faster rate than r_u during the initial loading pulses, these IMs evolved in a manner that was consistent with the r_u time history and reached a peak value at a similar time.

7.6.1.2 Experiment 4 Test 26

Figure 7.60 shows the response of the model in Layer 2 during Experiment 4 Test 26. The test was selected because the acceleration loading history had similar characteristics as the irregular sine CSS tests (Section 6.3.2). The acceleration time history included two relatively large

acceleration pulses of approximately 0.15 g as observed at approximately 14 and 18.5 seconds, respectively. The acceleration time history prior to 14 seconds, between 14 and 18.5 seconds, and after 18.5 seconds included a number of pulses with amplitudes of approximately 0.075 g.

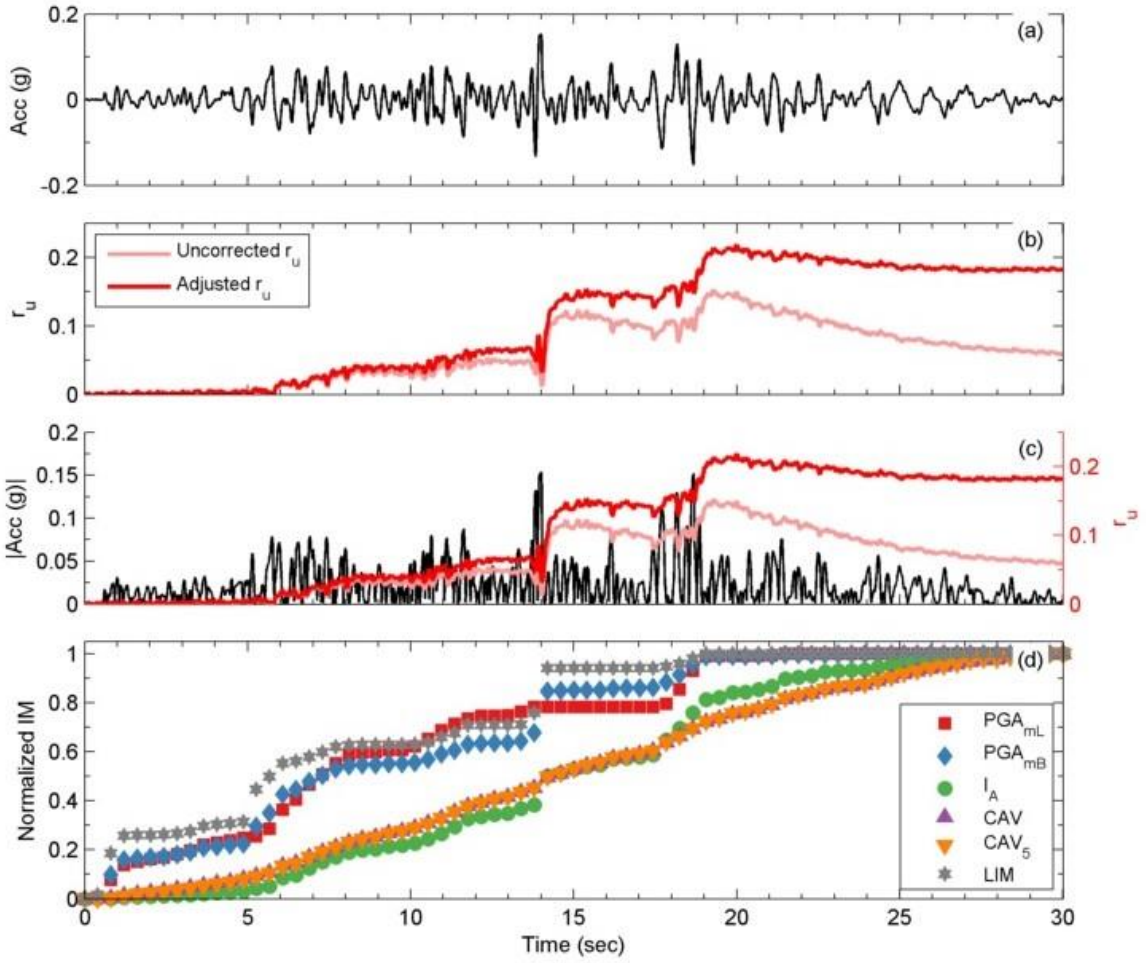


Figure 7.60: Comparison of the acceleration time history, excess pore pressure, and evolutionary IM response for Experiment 4 Test 26 Layer 2. (a) the acceleration time history, (b) the uncorrected and adjusted r_u time histories, (c) the absolute value of the acceleration time history and the r_u time histories, and (d) time histories of the normalized evolutionary IMs computed as the evolutionary IM time history divided by the value of the IM at the end of the record.

During the first 5 seconds of the record the acceleration, and hence shear strain, amplitudes were low and pore pressures were not generated. After 5 seconds the acceleration amplitudes increased and included multiple acceleration pulses with amplitudes near 0.075 g. During this time excess pore pressures began to develop. From 5 to 8 seconds the amplitude of the acceleration pulses were fairly constant and the pore pressures steadily increased. When the acceleration amplitudes dropped below the PPA of approximately 0.075 g from 8 to 10.5

seconds, additional excess pore pressures were not developed. The lack of pore pressure development could have been due to the low amplitude of the pulses (which were less than 0.05 g) or as a result of the shielding effect discussed previously. From 10.5 to 12 seconds, when the pulse amplitudes approached the PPA, the generation of excess pore pressure resumed. Prior to the large amplitude loading cycle observed at 14 seconds, the acceleration time history included eight 0.075 g pulses that generated an r_u of 0.07.

At approximately 14 seconds two successive 0.15 g pulses (i.e. one full 0.15 g cycle) was observed. These two pulses were double the PPA and generated as much pore pressure as all the previous lower amplitude pulses combined. The acceleration amplitudes between 14 and 18.5 seconds included a pulse with an amplitude of approximately 0.075 g (just after 16 seconds), however this pulse did generate any excess pore pressure. During this time the uncorrected r_u time history showed a steady decrease that was attributed to dissipation, and the adjusted excess pore pressure was relatively flat with the exception of a slight increase at approximately 17 seconds as a result of two acceleration pulses that featured amplitudes of about 0.12 g. Had these 0.12 g pulses occurred prior to the large amplitude pulse at 14 seconds, they would have been expected to generate more pore pressure than was observed. At 18.5 seconds an acceleration pulse with an amplitude that was nearly identical to the PPA generated an increase in r_u of approximately 0.05. For the remainder of the time history the acceleration amplitudes were below half of the PPA, and both the uncorrected and adjusted r_u time histories show that additional excess pore pressure was not generated after 18.5 seconds.

The relationship between the loading history and the r_u response in this example was consistent with the observations from the irregular sine CSS tests. Prior to the 0.15 g amplitude cycle at 14 seconds, the soil generated excess pore pressure for the lower amplitude 0.075 g acceleration pulses. However, following a large amplitude acceleration pulse, subsequent lower amplitude pulses were no longer able to generate excess pore pressure, and only cycles that were close to or exceeded the PPA contributed to the pore pressure response. This observation that the r_u response was highly sensitive to local peaks in the loading history was consistent with the CSS tests. Figure 7.60d shows the behavior of the evolutionary IMs. The cycle-counting based IMs are also very sensitive to local peaks, and the location of the local peaks can be clearly identified in the time histories of PGA_{mL}, PGA_{mB}, and LIM. The integral IMs, on the other hand, tended to

smooth over these local peaks and increased during portions of the record when the r_u response was either flat (adjusted) or decreasing due to dissipation (uncorrected).

7.6.1.3 Experiment 5 Test 7

Figure 7.61 shows the results from Layer 3 during Experiment 5 Test 7. The input motion for this test was based on a record from the 2011 Tohoku earthquake and had total duration of over 150 seconds. In addition, the motion had a unique shape that included two phases of strong ground motion centered at 26 (Phase 1) and 75 seconds (Phase 2). In general, this test reflected the same trends that have been observed throughout this study. Large increases in excess pore pressures were associated with cycles that exceeded the PPA, and subsequent pulses that were less than the PPA were shielded and generated relatively little excess pore pressure. The r_u response, both uncorrected and adjusted, was dominated by the high amplitude portion of the two phases, and even though the loading that occurred between Phases 1 and 2 and after Phase 2 included relatively large amplitudes (in excess of 0.15 g), the pore pressure response was negligible. Consistent with the other test results, the IM response from the cycle counting-based IMs provided a better representation of the r_u behavior than the integral based IMs, which increased considerably during the shielded portion of the record. However, when examined closely, the pore pressure was observed to increase after the PPA or local maxima in the two phases. This apparent delay was attributed to dilation and phase transformation behavior.

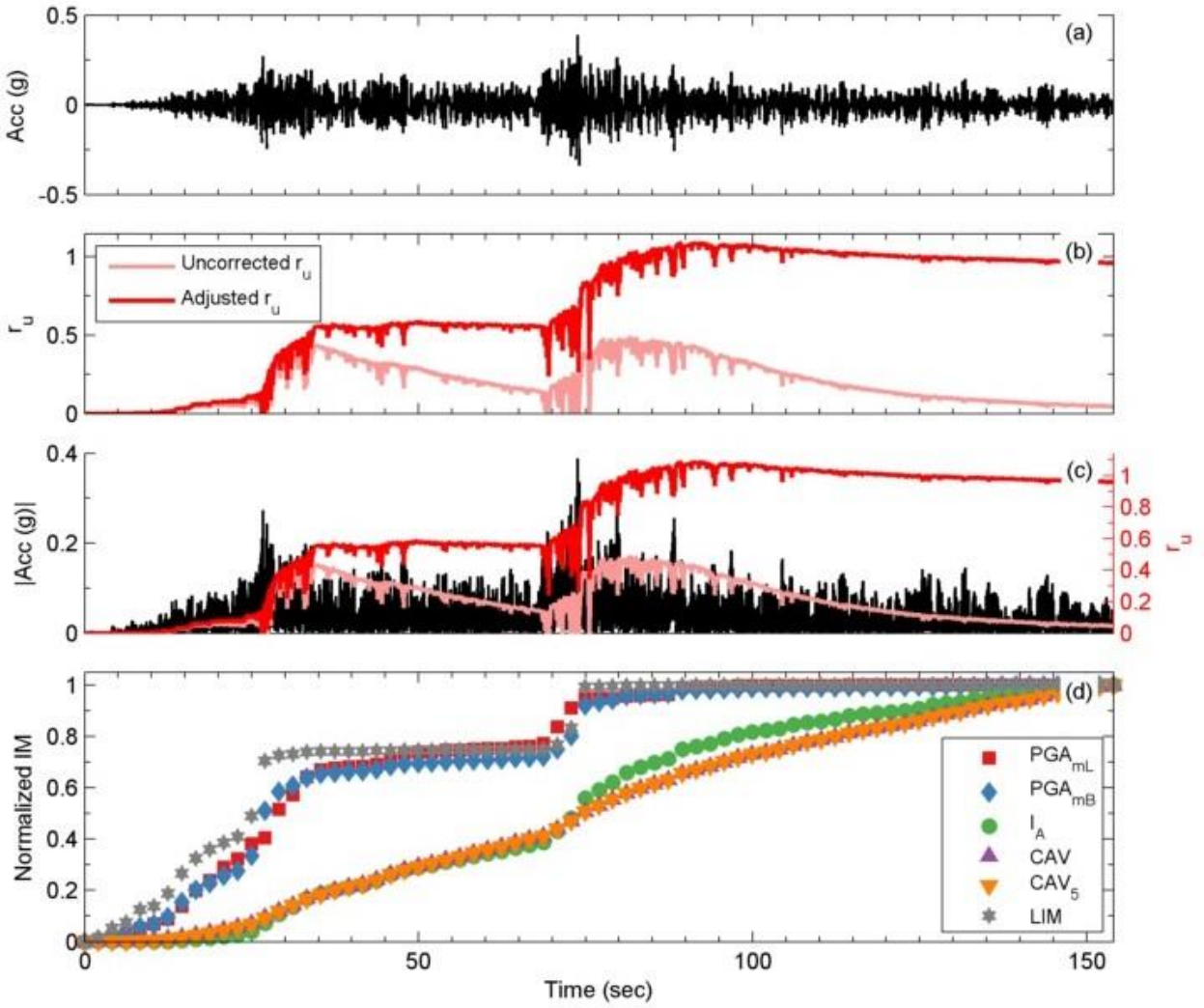


Figure 7.61: Comparison of the acceleration time history, excess pore pressure, and evolutionary IM response for Experiment 5 Test 7 Layer 3. (a) the acceleration time history, (b) the uncorrected and adjusted r_u time histories, (c) the absolute value of the acceleration time history and the r_u time histories, and (d) time histories of the normalized evolutionary IMs computed as the evolutionary IM time history divided by the value of the IM at the end of the record.

Figure 7.62 shows the acceleration and r_u response from 20 to 40 seconds to focus on the behavior during the large amplitude portion of the Phase 1 loading. The initial portion of the record up to 26 seconds generated low amounts of pore pressure up to an r_u level of approximately 0.1. Shortly after 26 seconds, a series of large amplitude pulses that exceeded the PPA were observed. During this time both r_u time histories showed a temporary reduction in r_u which suggested that the soil dilated. Following a reduction in r_u, the subsequent pulse produced an increase in pore pressure. This behavior was also observed in the CSS testing and was consistent with phase transformation behavior as described in Section 2.3.2.1. During CSS

testing, when a large amplitude stress pulse crossed the phase transformation line dilation would occur which increased the effective stress and reduced r_u. However, upon a stress reversal the soil would contract strongly, and excess pore pressures were generated at a relatively rapid rate. From the centrifuge data, the r_u generally increased from 26 to 34 seconds but included numerous local reductions in r_u followed by an increase in r_u. A large acceleration pulse would induce dilation; following dilation the r_u would increase when the direction of the load was reversed. This dilation-induced ratcheting effect could be what led to an overall increase in the r_u despite the loading amplitudes being less than the PPA. After 34 seconds the loading amplitudes were lower than the amplitudes required to induce dilation, and were significantly less than the PPA, and the generation of excess pore pressures stopped. The uncorrected r_u time history indicated that the excess pore pressures were dissipating during this time.

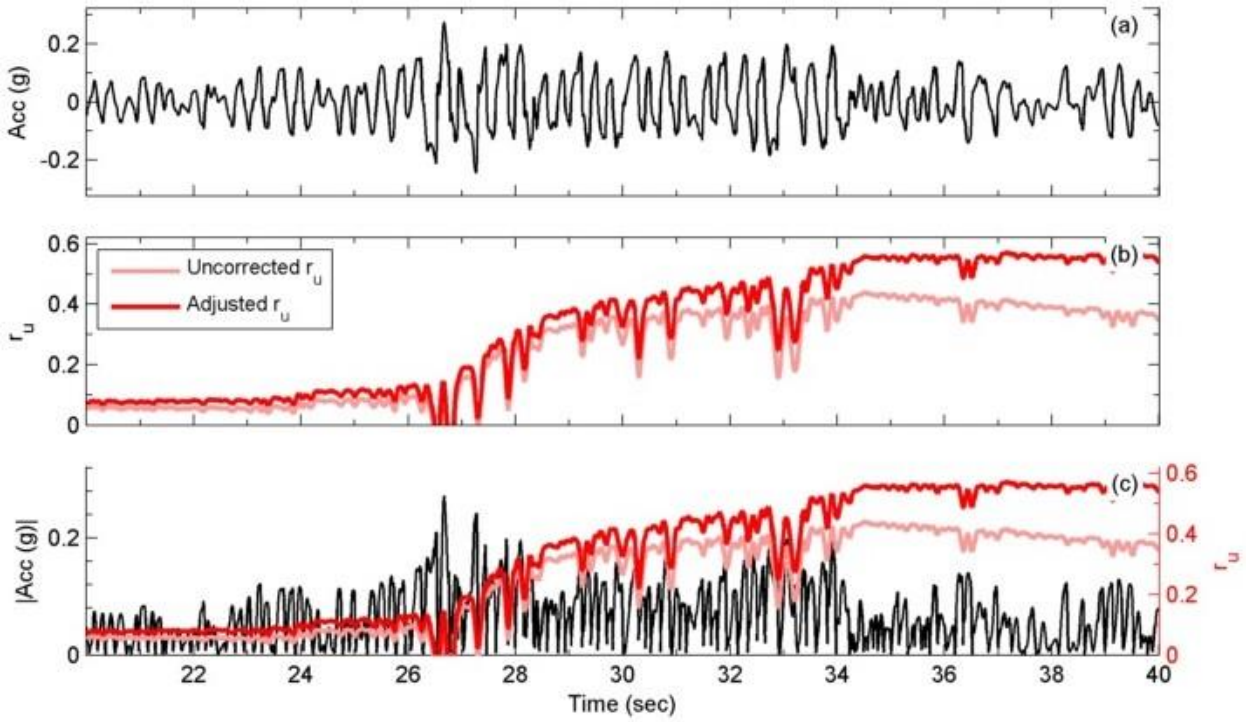


Figure 7.62: Comparison of the acceleration time history, excess pore pressure, and evolutionary IM response for Experiment 5 Test 7 Layer 3 from 20 to 40 seconds. (a) the acceleration time history, (b) the uncorrected and adjusted r_u time histories, (c) the absolute value of the acceleration time history and the r_u time histories.

Similar behavior was observed during Phase 2. Figure 7.63 shows the acceleration and r_u time histories between 55 and 90 seconds. From 34 to 69 seconds the uncorrected r_u indicated

that dissipation was occurring. The loading amplitudes during this time were significantly below the PPA, which was 0.27 g for this portion of the record. At 69.5 seconds dilation was induced by a 0.2 g acceleration pulse and the pore pressures increased slightly following load reversal. This pulse was much lower than the PPA and the increase in r_u was minimal. The largest increase in r_u during the Phase 2 loading occurred just after the maximum acceleration pulses observed at 74 seconds. These pulses included the maximum peak pulse of 0.37 g that greatly exceeded the PPA. During these large amplitude pulses the soil dilated, and the acceleration pulses that followed this dilation increased the r_u in both the uncorrected and adjusted time histories by 0.15. Following the maximum peak amplitude, a dilation-induced ratcheting effect as described previously for Phase 1 was observed. However, the increase in excess pore pressure response from pulses that were less than the PPA was minor in comparison to the increase in r_u associated with the pulses that exceeded the PPA.

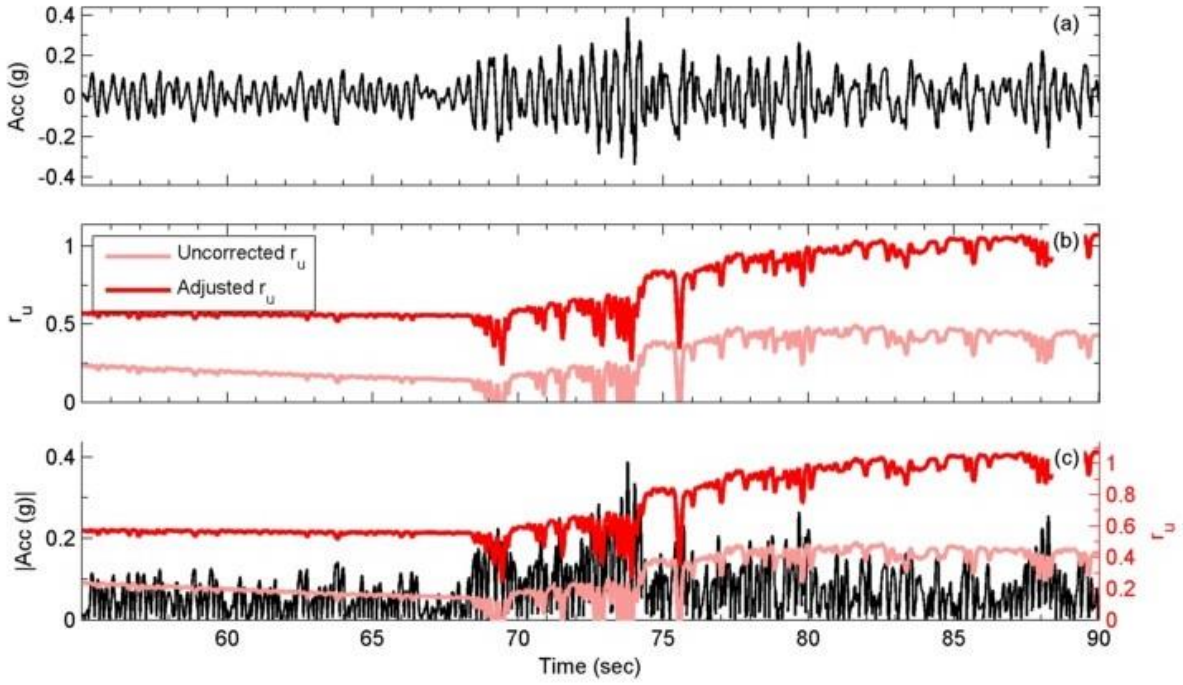


Figure 7.63: Comparison of the acceleration time history, excess pore pressure, and evolutionary IM response for Experiment 5 Test 7 Layer 3 from 55 to 90 seconds. (a) the acceleration time history, (b) the uncorrected and adjusted r_u time histories, (c) the absolute value of the acceleration time history and the r_u time histories.

This experiment highlighted the complexity associated with evaluating the response of a liquefiable soil due to transient loading during large-scale centrifuge testing. When the

acceleration and r_u time histories were observed on a small scale, on the order of seconds, the r_u response lagged behind the local peak accelerations, and excess pore pressures were generated after the PPA. However, this increase was attributed to alternation between dilative and contractive behavior that was consistent the observations from CSS tests.

7.6.1.4 Experiment 2 Test 9

The pore pressure response recorded during Experiments 1 and 2 were considered questionable due to an observed lag between the acceleration and pore pressure time histories. The reason for this time lag was unknown, and possible explanations for the lag were presented in Sections 7.5.4 and 7.5.5. The time lag complicated the interpretation of the results. However, these experiments still included examples of the trends described previously.

Figure 7.64 shows the response in Layer 3 during Experiment 2 Test 9. The loading history was similar to Experiment 6 Test 2 as described in Section 7.6.1.1. The acceleration time history was relatively symmetric, as observed in the plot of the absolute value of acceleration (Figure 7.64c) which shows acceleration pulses with comparable amplitudes on either side of the maximum peak amplitude at approximately 14.5 seconds.

The pore pressure response closely resembled the response observed in Experiment 6 Test 2, albeit with a slight lag in the pore pressure response. For example, the acceleration time history included a local low amplitude portion between 6 and 7 seconds into the record. During this time the acceleration amplitudes were both low in terms of their absolute amplitude and were less than the PPA. However, the excess pore pressure was observed to increase during this portion of the record. After 7 seconds, when the acceleration amplitudes began to increase, the excess pore pressure time history included a local plateau between 7 and 8.5 seconds before increasing again after 8.5 seconds in response to the higher amplitude loads. Observations from the CSS testing and other centrifuge experiments suggest that the local plateau in the pore pressure time history should have occurred during the local low amplitude portion of the record. When observed at a small time scale, on the order of seconds, the results from this experiment appeared to contradict the observations from the CSS test program.

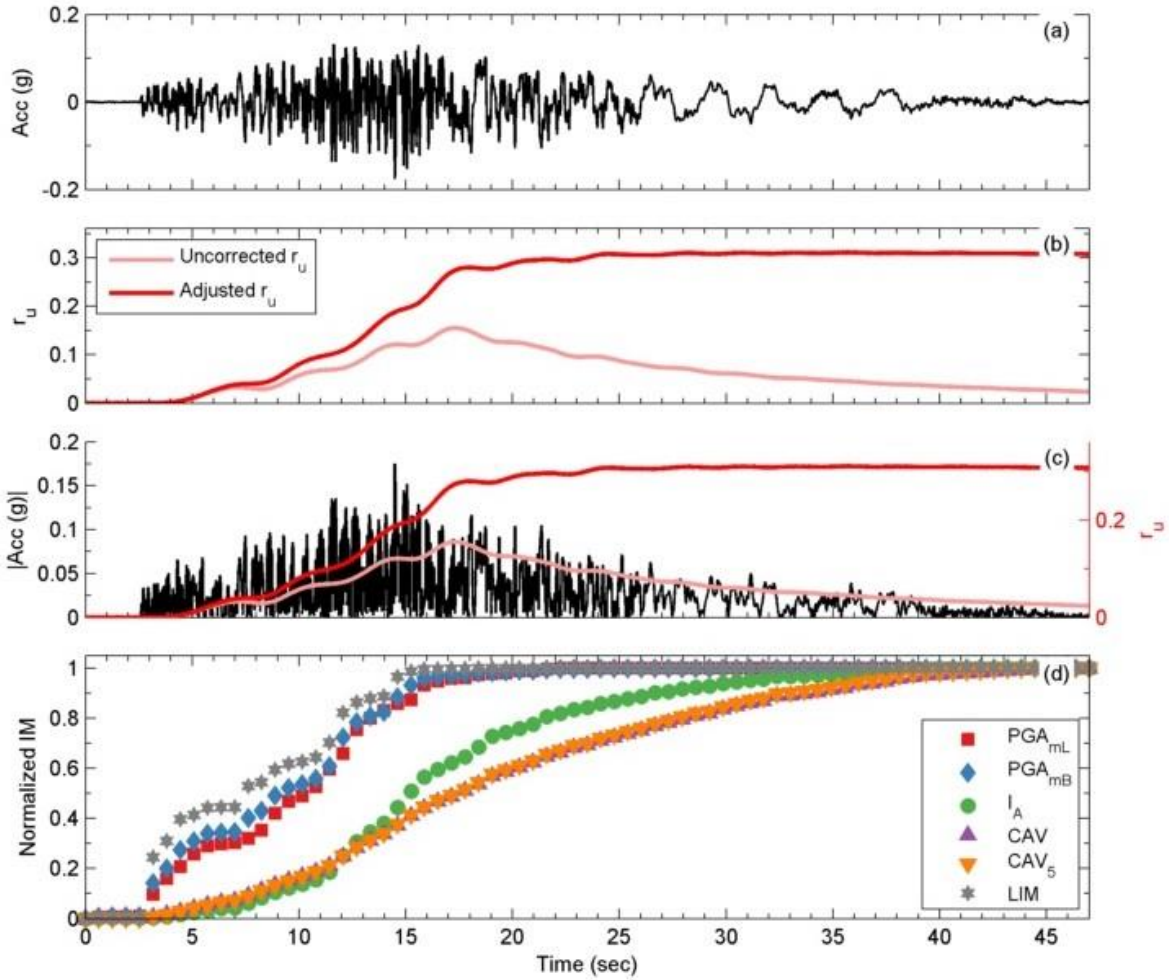


Figure 7.64: Comparison of the acceleration time history, excess pore pressure, and evolutionary IM response for Experiment 2 Test 9 Layer 3.(a) the acceleration time history, (b) the uncorrected and adjusted r_u time histories, (c) the absolute value of the acceleration time history and the r_u time histories, and (d) time histories of the normalized evolutionary IMs computed as the evolutionary IM time history divided by the value of the IM at the end of the record.

While the pore pressure response due to individual pulses may have been inconsistent with the observations discussed previously, the global response of these tests was similar to the other tests performed as part of this study. During the portion of the record prior to the maximum peak, between 3 and 14 seconds, the PPA was consistently being exceeded as the acceleration amplitudes increased, and the pore pressure generally increased as well. Following the maximum peak acceleration observed at 14.5 seconds, the pore pressure continued to rise for an additional 2 seconds. This delay was consistent with the delay observed in the local plateau discussed previously. After 16.5 seconds the rate of pore pressure generation decreased considerably, and

was either decreasing, as observed in the uncorrected r_u time history, or was essentially constant, as observed in the adjusted r_u time history.

As noted above, the loading that occurred after 16.5 seconds generated very little excess pore pressure; however, during this time the acceleration time history included relatively large loading amplitudes. For example, the loading that occurred between 18 and 21 seconds included multiple acceleration pulses with amplitudes above 0.1 g that generated relatively little excess pore pressure. Pulses with similar amplitudes that occurred between 7 and 11 seconds were observed to generate considerably more excess pore pressure. A notable difference between the acceleration pulses from 7 to 11 seconds and the pulses from 18 to 21 seconds was that the earlier pulses were at or near the PPA, while the later arriving pulses were significantly lower than the PPA. This behavior with respect to the PPA was consistent with the observations from the CSS test and other centrifuge experiments.

In terms of the response of the evolutionary IMs, due to the symmetry of the applied motion, the response of the integral IMs were relatively symmetric as well. This was particularly apparent for the response of CAV and CAV_5. On the other hand, the evolution of the cycle counting-based provided a better approximation of the r_u time history. These IMs reached their peak value near the peak amplitude of the loading history and were insensitive to acceleration pulses that occurred after the maximum peak value.

7.6.2 *Discussion*

The CSS tests allow for the response of a liquefiable soil to be observed during controlled conditions at a level of detail that was not possible in the centrifuge; specifically, the CSS tests were performed under totally undrained conditions in which the volume of the test specimen was not allowed to change. The centrifuge results are impacted by drainage which affected the measured pore pressures and resulted in flow and reconsolidation during shaking, which made the interpretation of the results difficult. However, even with these complications, the centrifuge experiments displayed the same general behavior as observed during the CSS testing. A series of examples were provided that showed that the pore pressure response was highly dependent on the phasing of the loading history. Acceleration amplitudes that were less than the PPA tended to generate relatively little pore pressure, while acceleration pulses that exceeded the PPA were generally associated with large increases in the excess pore pressure.

These examples showed that the cycle counting-based IMs, which are sensitive to the peak acceleration values, were able to capture the general shape of the r_u time history. Most notably, the cycle counting IMs were not sensitive to pulses in the record that occur after the maximum peak acceleration, which was consistent with the r_u response. The integral IMs tended to smooth over the peak amplitudes and were sensitive to later arriving low amplitude motion. As a result, they generally evolved in a manner that significantly differed from the r_u response. This observation was consistent with the findings from Chapter 6, where the cycle counting-based IMs, which were shown to be sensitive to the same loading characteristics as r_u, were found to be more efficient indicators of the generation of excess pore pressure and the onset of liquefaction than the integral-based IMs using CSS test data. The next section presents the results of the efficiency evaluation using the centrifuge test data to provide a qualitative assessment of the observations noted above.

7.7 Evaluation of IM Efficiency Using the Centrifuge Test Data

To extend the findings from the CSS test program, the paired acceleration and r_u records derived from the centrifuge experiments were used to evaluate how efficiently each of the IMs were able to predict the excess pore pressure response of the soil model. This section investigates the ability of the standard IMs from the CSS test program, and the new liquefaction-specific intensity measure, LIM, developed in Section 6.6, to predict the pore pressure response from the centrifuge tests. The following sections outline the methodology and results of the IM efficiency evaluation.

7.7.1 *Methodology to Evaluate IM Efficiency using Centrifuge Test Data*

The goal of this study is to evaluate the most efficient IM for the evaluation of liquefaction for use in the timing-based framework. As outlined in Section 6.5.1, due to the form of the timing-based framework the efficiency was evaluated based on the uncertainty in the IM|r_u relationship. The evaluation of efficiency using the CSS dataset utilized a surface function defined in Equation 6.24, where each IM was evaluated as a function of D_r and r_u. The efficiency was quantified in terms of the standard deviation of the natural log residuals between the IM computed from the converted acceleration time history and the fitted IM. A similar process was used to evaluate the IM efficiency using the centrifuge data, with the following modifications:

- The CSS test data was performed at a constant confining pressure. Therefore, the effect of overburden pressure (i.e., K_σ, see Section 2.3.3.1) could not be determined from the CSS data. The data from the centrifuge experiments included acceleration and r_u time histories recorded at multiple depths and confining pressures. Therefore Equation 6.24 was adjusted to account for the effect of confining pressure.
- Due to the centrifuge testing procedures and the distribution of the maximum r_u response generated by the centrifuge tests, the IM|r_u relationship for the centrifuge data was evaluated using the peak r_u value as opposed to the entire r_u time history.

Each of these items are discussed in further detail in the following subsections.

7.7.1.1 Functional Form of the IM-r_u Relationship

As noted in Section 2.3.3.1, laboratory tests have shown that resistance to liquefaction tends to decrease as the confining stress increases for a soil with a constant relative density. This finding has been substantiated by field case history data (e.g. Youd et al, 2001). To account for the affect of the effective overburden stress, σ'_v, a K_σ term with the functional form assumed by Youd et al. (2001) and Cetin et al. (2018) (Equation 2.14) was added to Equation 6.24 as follows

$$IM = \beta_1 \cdot \exp\left(\beta_2 \cdot D_r\right) \left(\frac{\sigma'_v}{p_a}\right)^{\beta_3} \frac{1 + \alpha_1}{1 + \alpha_1 \cdot r_u{}^{\alpha_2}} \tag{7.5}$$

where p_a is atmospheric pressure. The exponential term with the coefficients β_1 and β_2 applied to D_r represents the liquefaction triggering relationship. β_3 is a fitting coefficient that accounts for the overburden stress term, K_σ, and the r_u term scales the equation based on the given pore pressure response. The r_u term consists of the fitting coefficients α_1 and α_2 and was derived in Section 6.5.1.2 from the CSS test data. It is a flexible function that is capable of capturing a range of r_u behavior, and is constrained to a value of 1.0 when r_u = 1.0 such that Equation 7.5 reduces to the triggering relationship. Using regression analyses with the centrifuge test data, the fitting coefficients described in Equation 7.5 were evaluated and the natural log residuals were computed as the natural log of the IM computed from the recorded acceleration time history minus the natural log of the fitted IM. As was done for the CSS test data (Section 6.5.1), the efficiency of each IM was evaluated as the standard deviation of the natural log residuals (σ_ε). The effectiveness of Equation 7.5 to capture the IM-r_u relationship using the centrifuge test data is discussed further in Section 7.7.2.

7.7.1.2 Fitting Methodology

The CSS tests were performed on an element of soil under undrained conditions in a highly controlled setting. As discussed in Section 6.4.1.4, an iterative procedure was used to scale the input loading histories so that liquefaction was triggered toward the end of a given transient loading history. This generated a dataset that allowed for the systematic identification of what aspects of a loading history were most influential on the excess pore pressure response.

A similar iterative procedure was used in the centrifuge testing program. However, unlike the CSS tests program, which used newly constructed samples for each experiment, the centrifuge test program involved applying multiple loading histories to a single soil model. Each motion altered the density of the model, and consequently its resistance to liquefaction, in a manner that could not be quantified with significant accuracy using the equipment that was available at the time the tests were conducted. Therefore, the testing procedure used in the centrifuge involved scaling the transient loading histories to capture a broad range of pore pressure response based on observational methods during testing. Generally, a low amplitude motion was applied at the beginning of an experiment. Based on the r_u response of the first motion, the next motion was scaled to generate the r_u response of interest. This process was repeated until the conclusion of each of the experiment.

Careful sequencing and scaling of the applied motions was important. Applying too large a motion early in the testing process (i.e. Experiment 2 Test 6) could result in extensive liquefaction that could cause tilting of the settlement monuments and the temporary loss of density control, which added significant additional uncertainty to the interpretation of the results. Conversely, applying a large number of small amplitude motions could densify the model to the point that it is no longer able to generate significant excess pore pressures regardless of the amplitude of the applied loading.

A consequence of this procedure was that a large amount of low r_u data was generated. Figure 7.65 shows a histogram of the maximum excess pore pressure ratio generated in the liquefiable layer for all the centrifuge tests. The data is significantly skewed towards r_u values less than 0.4. Using the entire r_u time history would exacerbate this bias towards low r_u values. Therefore, only the peak r_u value (disregarding increases in r_u due to flow of excess pore pressures) and the IM computed up to the time the peak r_u value was reached, was used to evaluate the IM efficiency. In this way the bias towards low r_u values was reduced, while also

treating each test result equally. In addition, tests that produced a peak r_u value less than 0.05 were excluded from the analyses.

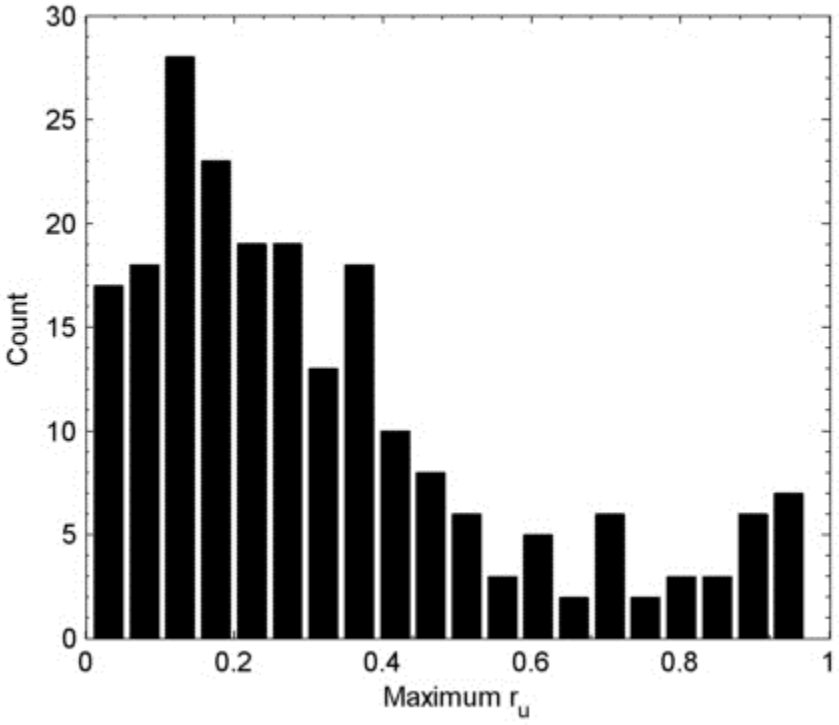


Figure 7.65: Histogram of maximum r_u generated within the liquefiable layer for all of the centrifuge tests

7.7.2 *Efficiency of Evolutionary Intensity Measures to Predict the Pore Pressure Response from Centrifuge Data*

The results of the regression analyses performed using the centrifuge data is provided in Appendix D. Initially, Equation 7.5 was fit to the centrifuge data, and the efficiency of each IM was evaluated. An example of the regression summary figures that are provided in Appendix D is shown in Figure 7.66 with respect to PGA_{mB} fit to the entire centrifuge dataset. Figure 7.66 includes plots of the fitted and computed IM, a histogram of the log residuals and the log residuals as a function of the various input parameters.

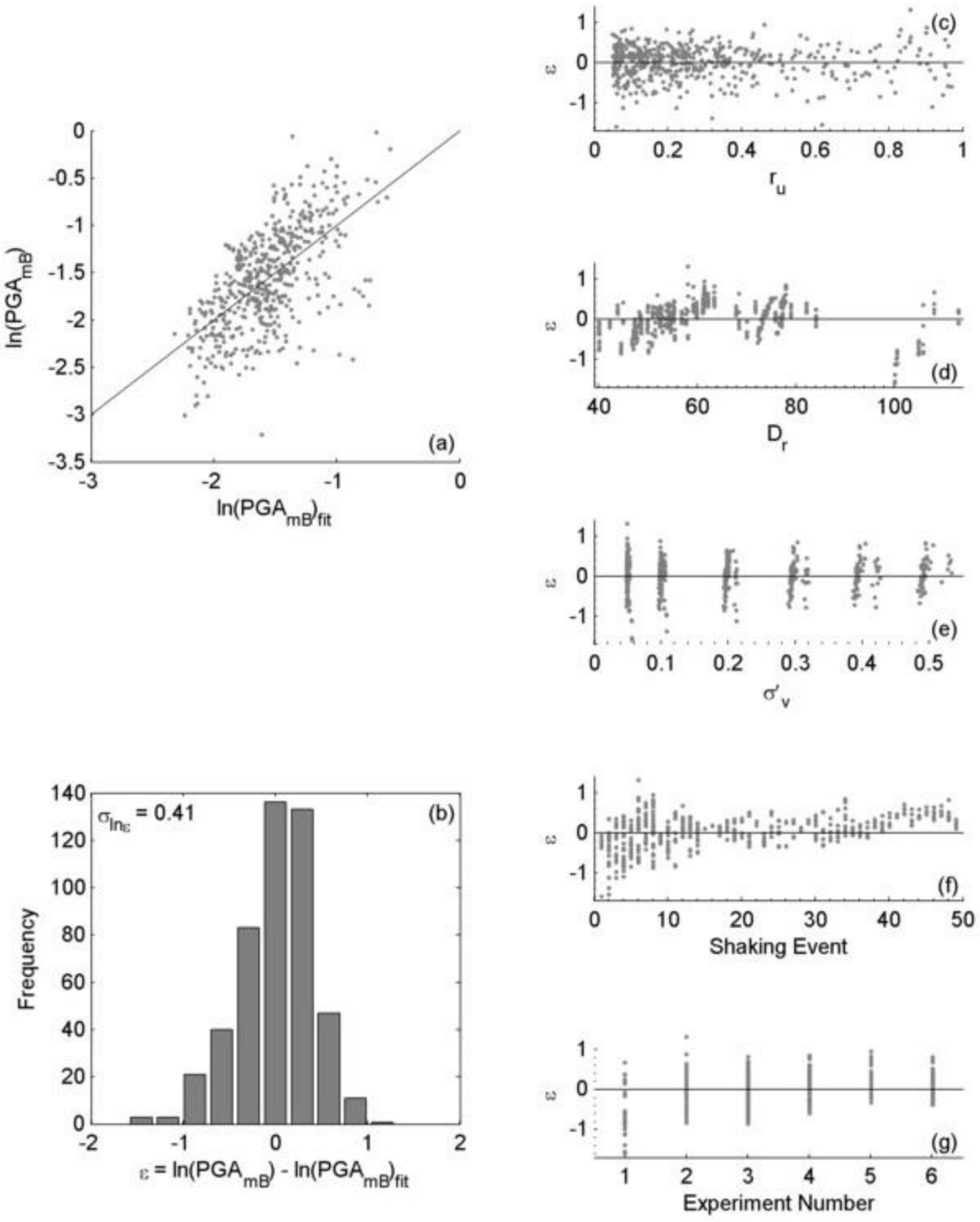


Figure 7.66: Results of regression analyses using Equation 7.5 and the entire centrifuge dataset for PGA_{mB}.The plots include (a) the computed and fitted IM response, (b) histograms of the log residuals, and plots of the log residuals as a function of (c) r_u, (d) relative density, (e) overburden effective stress, (f) the shaking event or motion number, and (g) the experiment number.

The results shown in Figure 7.66 indicated a high level of variability and the fit appears to be heavily influenced by a few large outliers. The plot of the log residuals as a function of the experiment number (Figure 7.66g) shows that Experiment 1, which was placed at an initial relative density of 100%, was a notable outlier and produced large negative residuals compared to the other experiments (i.e. the predicted IM was much larger than the IM computed from the recorded acceleration). To achieve the target relative density of 100%, Experiment 1 was constructed by pluviating the sand from a large drop height and additional densification was provided as needed via additional tamping. Experiments 2 and 4 also reached relatively high average relative density levels; however, the high relative densities that were observed in Experiments 2 and 4 occurred due to densification caused by repeated shaking of the model. These results suggested that the pore pressure response of a model that was constructed at a high initial relative density was different than the pore pressure response of a model that has densified due to shaking.

The difference in the liquefaction resistance between the initial tests in Experiment 1 and the tests performed late in Experiments 2 and 4 after the model had densified due to repeated shaking, was attributed to differences in the soil fabric or structure. The impact of the soil fabric on the liquefaction resistance of a soil has been studied extensively in the past (e.g. Seed, 1979; Dobry, 1982, etc.). Based on the results of the centrifuge experiments, a model that was densified by shaking appeared to be more resistant to the generation of excess pore pressures during seismic loading than a newly constructed model at a similar or higher relative density. This observation was consistent with the study of Mulilis, Chah, and Seed (1975) who found that the cyclic resistance to cyclic loading in a triaxial apparatus was higher for samples that were densified using high frequency vibrations than for samples at the same relative density that were constructed using alternative compaction procedures such as air-pluviated or most tamping. The soil fabric that was created via pluviation and dry tamping likely differed from the soil fabric that was created due to repeated shaking. Among other factors, the tests that densified due to repeated shaking likely had higher lateral stresses (i.e. higher K_0 values) than models initially placed at high densities. Higher K_0 conditions have been shown to increase the liquefaction resistance (e.g. Kokusho, 2016).

The effect of the increase in liquefaction resistance due to repeated shaking was reflected in Figure 7.66f, which shows the log residuals plotted as a function of the shaking event. The log

residuals computed from tests that were performed early in the experiment tended to have negative log residuals, while test that occurred later in the experiment, on average, tended to have positive log residuals. This observation indicated that there was an increase in the model's resistance to liquefaction that was not captured using estimates of relative density alone (as computed using the surface settlement).

This effect was also seen in the plot of the log residuals as a function of relative density (7.66f). A linear increase in the residuals can be observed between relative densities of approximately 50 to 65%, followed by a sudden decrease in the residuals near 70% relative density. The data in this density range was derived from experiments that were initially constructed at relative densities of 40 and 50% (Experiments 2, 3, 5, and 6) that had densified due to shaking. The decrease at approximately 70% relative density is due to data generated early in Experiment 4, which was initially placed at a 70% relative density.

To capture the effect of the number of shaking events on the soil's liquefaction resistance, Equation 7.5 was modified to include a term for the number of shaking events that the model had been subjected to, N_{test}. Based on examination of the log residuals as a function of the shaking event, the functional form of the number of shaking events term was evaluated using a power function and Equation 7.5 was modified as follows

$$IM = \beta_1 \cdot \exp\left(\beta_2 \cdot D_r\right)\left(\frac{\sigma'_v}{p_a}\right)^{\beta_3}\left(N_{test}\right)^{\beta_4}\frac{1+\alpha_1}{1+\alpha_1 \cdot r_u{}^{\alpha_2}} \tag{7.6}$$

The results of the PGA_{mB} regression using Equation 7.6 and the entire centrifuge dataset is provided in Figure 7.67. Including the N_{test} term reduced the σ_{ln} term from 0.41 (without the N_{test} term) to 0.28, a reduction of approximately 32%. In addition, the results from Experiment 1 were no longer as dramatic an outlier when N_{test} was included in the regression. However, even with the N_{test} term, the results from Experiment 1 still generally produced negative log residuals. Without direct measurement of the soil properties following spin-up and during testing, the actual relative density profile of the model was unknown and could not be accurately quantified using the available equipment at the time the centrifuge experiments were performed. The large degree of uncertainty associated with the relative density was a notable limitation of the centrifuge dataset. In addition to the large uncertainty in relative density, the pore pressure results from Experiments 1 and 2 showed a lag between the acceleration and the pore pressure time histories. However, while Experiment 1 tended to show negative log residuals, Experiment

2 tended to have positive log residuals. To investigate the robustness of the IM efficiency evaluation, regression analyses were performed on:

1. The entire centrifuge dataset,
2. The combined data from Experiments 1 and 2,
3. The combined data from Experiments 3 through 6, and
4. Each individual centrifuge experiment.

The results of each of the regression analyses are presented in the following sections. Summary plots for each regression analysis are provided in Appendix D.

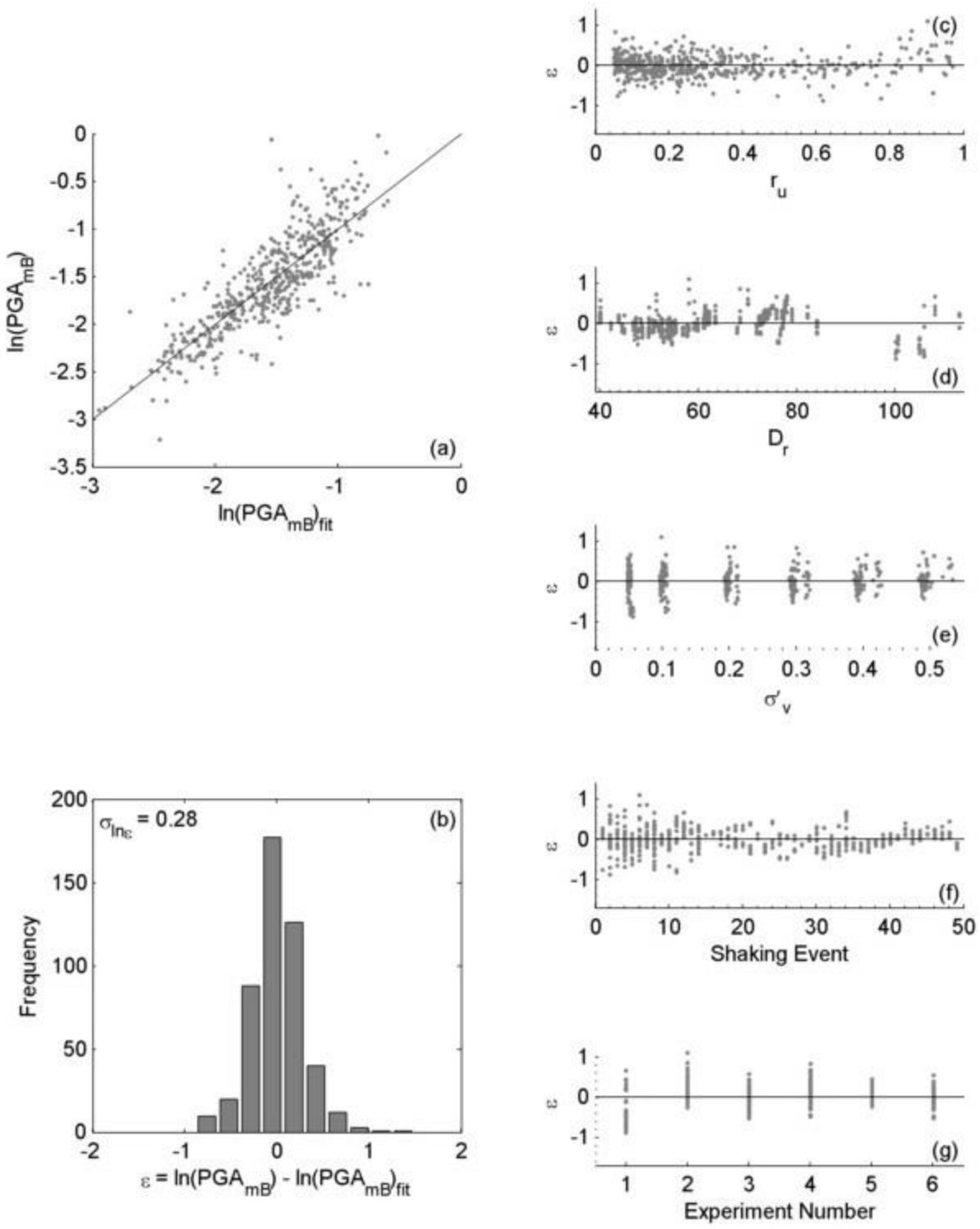


Figure 7.67: Results of regression analyses using Equation 7.6 and the entire centrifuge dataset for PGA_{mB}. The plots include (a) the computed and fitted IM response, (b) histograms of the log residuals, and plots of the log residuals as a function of (c) r_u, (d) relative density, (e) overburden effective stress, (f) the shaking event or motion number, and (g) the experiment number.

7.7.2.1 Evaluation of IM Efficiency Using the Entire Centrifuge Dataset

The efficiency of each of the IMs (PGA_{mL}, PGA_{mB}, I_A, CAV, CAV_5, and LIM) discussed in Chapter 6 were evaluated using regression analyses based on Equation 7.6 and the entire centrifuge dataset. Figures summarizing the results are provided in Appendix D for all of the regressions analyses conducted as part of this study. Values of the fitted coefficients and the standard deviation of the log residuals (σ_ε) are summarized in Table 7.17. The σ_ε values ranged from 0.217 for LIM to 0.619 for I_A. Of the conventional IMs, the PGA_m formulations performed the best, with PGA_{mB} performing slightly better than PGA_{mL}. However, the σ_{ln} value for PGA_{mB} was about 30% higher than the σ_{ln} value for LIM. These results were consistent with the findings from the CSS dataset which also found that the PGA_m formulations were significantly more efficient than the integral-based IMs. The σ_{ln} values from the CSS fit for the PGA_m formulations were approximately half the σ_{ln} from the most efficient integral-based IM (CAV), which was consistent with the results shown in Table 7.17. LIM was found to be the most efficient IM at predicting the r_u response using both the CSS and centrifuge datasets. Using the CSS test data, the σ_{ln} for LIM was a 50% lower than the σ_{ln} for PGA_{mB} as compared to approximately 30% using the centrifuge test data.

Table 7.17: Summary of regression analyses using entire centrifuge dataset

IM	β_1	β_2	β_3	β_4	α_1	α_2	σ_ε
PGA_{mL}	0.208	0.012	0.098	0.430	18.013	-0.319	0.309
PGA_{mB}	0.261	0.013	0.088	0.383	18.792	-0.284	0.279
I_A	0.180	0.026	0.275	1.014	21.704	-0.707	0.619
CAV	1.187	0.017	0.250	0.711	25.566	-0.513	0.577
CAV_5	1.216	0.018	0.261	0.738	21.293	-0.531	0.589
LIM	0.657	0.010	0.059	0.279	18.093	-0.213	0.217

7.7.2.2 Overburden Stress Factor

From Table 7.17, the coefficient, β_3, which represents the exponent in the K_σ term, was consistently positive for all the IMs and ranged from 0.059 to 0.274. If β_3 is positive, the overburden stress factor scales down the liquefaction resistance of soils near the ground surface, while scaling up the liquefaction resistance of deeper soils. This contradicts the theoretical basis for K_σ described in Section 2.3.3.1. Figure 7.68 shows a plot of K_σ computed using the exponent β_3 that from the regression analyses. Also provided in Figure 7.68 is the range of the

recommended K_σ relationships from the simplified liquefaction triggering relationships presented by Youd et al. (2001), Boulanger and Idriss (2014), and Cetin et al. (2018). The behavior of the overburden stress factor derived from the centrifuge data was directly opposite of the K_σ response computed from the relationships presented in literature.

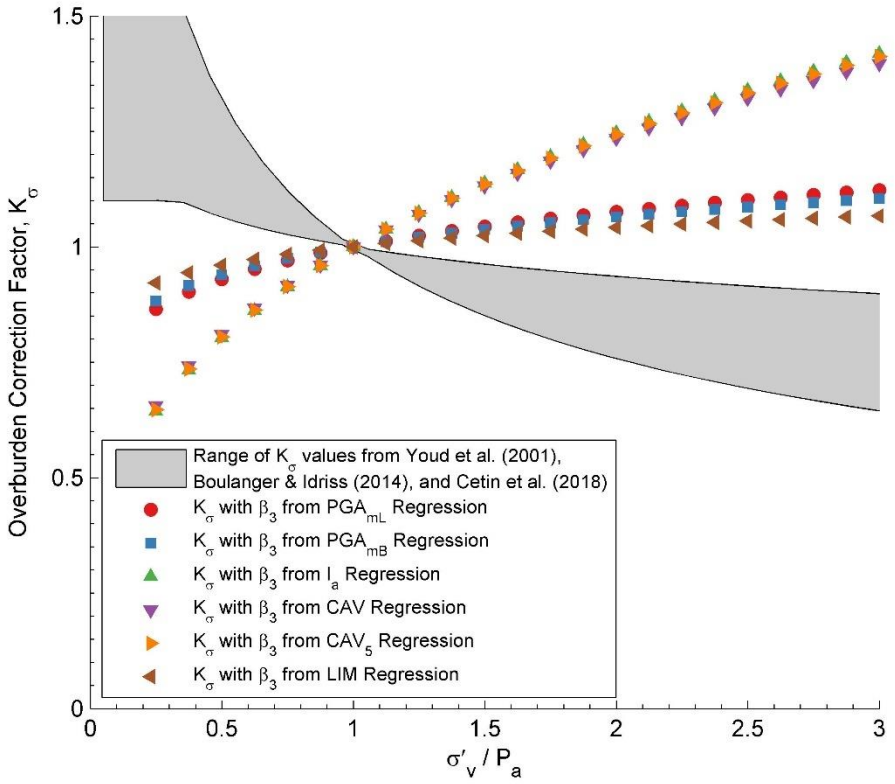


Figure 7.68: Comparison of K_σ from the simplified liquefaction triggering procedures and k_σ computed directly from the coefficient β_3 evaluated from the regression analyses for each IM.

However, as noted previously, equipment to accurately evaluate the relative profile (such as the mini-CPT) was not available at the time this study was performed. Therefore, the relative density of each experiment was evaluated using the surface settlement and was assumed to be constant throughout the liquefiable soil profile. As shown by Darby et al. (2019), the relative density profile in centrifuge experiments is often variable with depth even in soil layers that were placed at a constant relative density. As noted by Park and Byrne (2004), when constructing a centrifuge model, the soil is initially pluviated at very low confining stresses. As the model is subjected to higher gravitational fields during testing the overburden stress increases dramatically and this increase in overburden stress can cause the soil to densify. Park and Byrne

(2004) studied one-dimensional compression test data for eight different sand types, and found that the increase in relative density due to increases in vertical effective stress (σ'_v) was proportional to the square root of σ'_v. The basic form of the relationship proposed by Park and Byrne (2004) was of the form

$$D_r = D_{r0} + \alpha\sqrt{\sigma'_v} \tag{7.7}$$

where D_{r0} is the initial relative density (i.e., D_r prior to the change in vertical effective stress) and α is the coefficient of stress densification. Park and Byrne (2004) expressed α as a function of the maximum and minimum void ratio (e_{max} and e_{min}, respectively), D_{r0}, and a sand stiffness number, C, that was considered a material constant and independent of the void ratio, relative density, and stress conditions with the following relationship,

$$\alpha = \left(\frac{1 + e_{max}}{e_{max} - e_{min}} - D_{r0}\right)\frac{2(1.5 - D_{r0})}{C} \tag{7.8}$$

where D_{r0} in Equation 7.8 is expressed as a decimal. Park and Byrne (2004) found that this relationship was consistent for all of the sands included in their study. The relative density profiles from Darby et al. (2019) (Figures 7.9 and 7.10) that were evaluated using mini-CPT data appeared to confirm that the increase in relative density was proportional to the square root of effective stress.

If the relative density of the model was stress-dependent, than the coefficient β_3 evaluated from the regression analyses would include the effect of both K_σ and the stress-dependent aspect of relative density. Assuming the relative density of the centrifuge soil profile was proportional to the square root of σ'_v, the K_σ affect can be evaluated by subtracting 0.5 from the β_3 values computed from regression. Plots of the implied K_σ response using values of β_3 that were adjusted to remove the stress-dependent aspect of relative density are provided in Figure 7.69. After adjusting β_3 based on an assumed relationship for a stress-dependent relative density profile, the K_σ response from the centrifuge data was found to be in agreement with the K_σ relationships presented in literature. The implied K_σ response from cycle counting-based IMs were on the lower boundary of the range of the relationships presented in literature, while the implied K_σ response of the integral-based IMs were near the middle. Based on this simple correction, it appears that the discrepancy between the values of the β_3 coefficient from the regression and the known behavior of K_σ was due to uncertainties in the estimate of relative density.

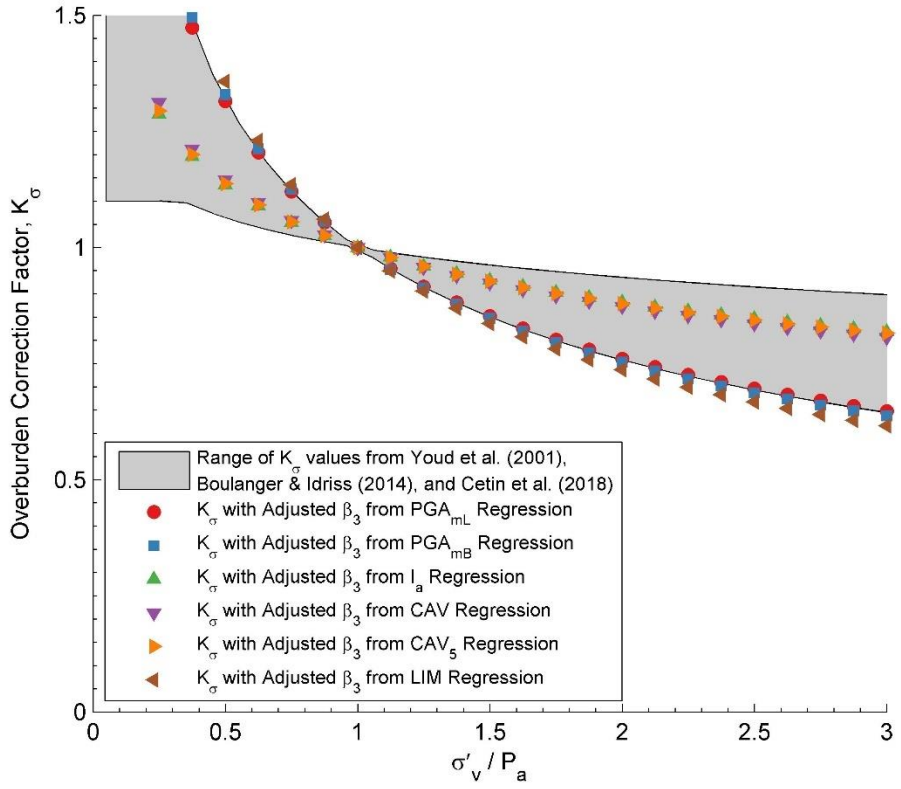


Figure 7.69: Comparison of K_σ from the simplified liquefaction triggering procedures and k_σ evaluated using a manually adjusted β_3 coefficient

To further investigate if the overburden stress term from the regression analyses was consistent with the known behavior of K_σ, the data from Darby et al. (2019) and Park and Byrne (2004) was used to develop an assumed stress-dependent relative density relationship and the regression analyses were repeated. The study of Park and Byrne (2004) included both Ottawa sand, which was used in Darby et al. (2019), and Nevada sand, which was used in this study. They found that Nevada sand was more susceptible to stress densification than Ottawa sand. Park and Byrne (2004) recommended a sand stiffness number, C, of 370 for Ottawa sand as compared to 220 for Nevada sand (noting that α is inversely proportional to C per Equation 7.8) However, the stress densification coefficient, α, from Park and Byrne (2004) was derived based on 1-D compression data, which may not represent the conditions in a centrifuge experiment that includes multiple shaking events. Therefore, the data from Darby et al. (2019) was used to compute a centrifuge-based α value, which was considered representative of Ottawa sand. Then the centrifuge-based Ottawa sand α value was adjusted for the differences between Nevada sand

and Ottawa sand using the ratio of C, which was defined as a material constant in Park and Byrne (2004).

The centrifuge-based Ottawa sand α value was evaluated using the supplemental data from Darby et al. (2019). This data included corrected CPT resistances, q_{C1N}, at 1/3, ½, and 2/3 H where H is the height of the liquefiable sand layer. The value of H varied between 8.1 and 12 m for the centrifuge experiments presented in Darby et al. (2019). The q_{C1N} values were used to compute a relative density using the correlation provided by Darby et al. (2019). The corresponding stress at each depth was estimated assuming a groundwater table above the ground surface and a constant unit weight. The unit weight was evaluated using the average relative density, e_{max} and e_{min} values of 0.83 and 0.51, respectively, as reported by Darby et al. (2017), and an assumed specific gravity of 2.67.

The overburden stress-dependent density profile was computed using Equation 7.7. The constant term, D_{r0}, was defined so that the average relative density computed using Equation 7.7 was consistent with the average relative density from the CPT data. Given that the top of the liquefiable layer was at the ground surface ($\sigma'_v = 0$ atm), D_{r0} was evaluated as

$$D_{r0} = \mu_{Dr} - {}^{2}/_{3}\alpha\sqrt{\sigma'_{v,max}} \tag{7.9}$$

where μ_{Dr} is the average relative density and $\sigma'_{v,max}$ is the effective stress at the bottom of the liquefiable layer. Combining Equations 7.7 and 7.9 the stress-dependent relative density profile was defined as

$$D_r = \mu_{Dr} - {}^{2}/_{3}\alpha\sqrt{\sigma'_{v,max}} + \alpha\sqrt{\sigma'_v} \tag{7.10}$$

From regression analyses using Equation 7.10 and the supplemental data from Darby et al. (2019), the centrifuge-based Ottawa sand α value was evaluated as 72. The results of the fitting are provided in Figure 7.70, which shows the quantity $D_r - \mu_{Dr}$ as a function of σ'_v. The results indicated that the assumed relationship was able to provide a reasonable approximation of the density profile from Darby et al. (2019).

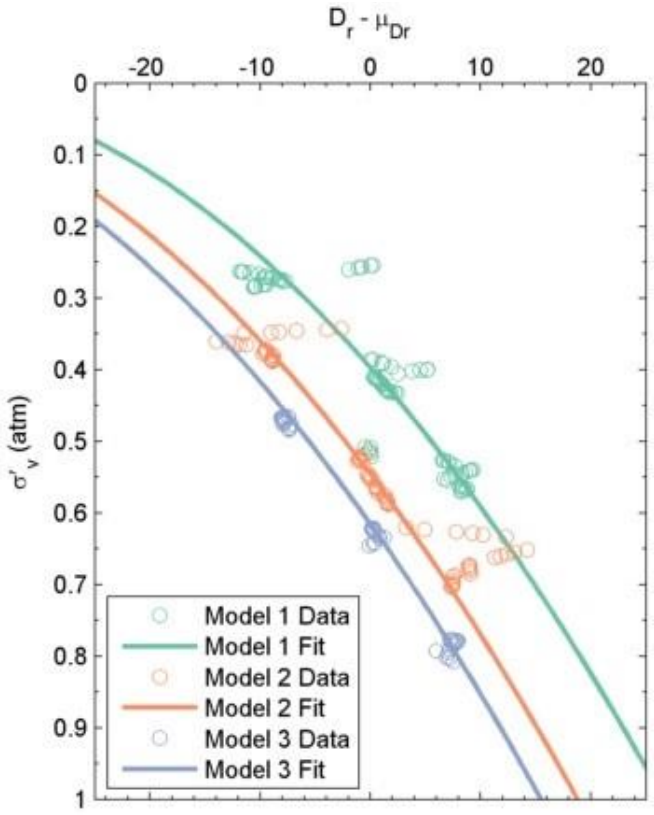


Figure 7.70: Regression results for stress-dependent density profile using the supplementary data from Darby et al. (2019).

The centrifuge-based Ottawa sand α value was adjusted to account to account for the differences in the stress densification properties between Ottawa and Nevada sand using the ratio of the sand stiffness number, C, reported by Park and Byrne (2004). The adjusted α value used to estimate the stress-dependent relative density relationship for the current study was computed as 121. The resulting stress-dependent relative density profiles are shown in Figure 7.71 for average relative densities of 40 and 70%. To prevent the relative density profiles from taking on unreasonably small values at low confining pressures the minimum relative density was prevented to go below 20%. Note that in this study the overburden effective stress ranged from a minimum of 0.48 atm in Layer 1 to a maximum of 0.54 atm in Layer 5.

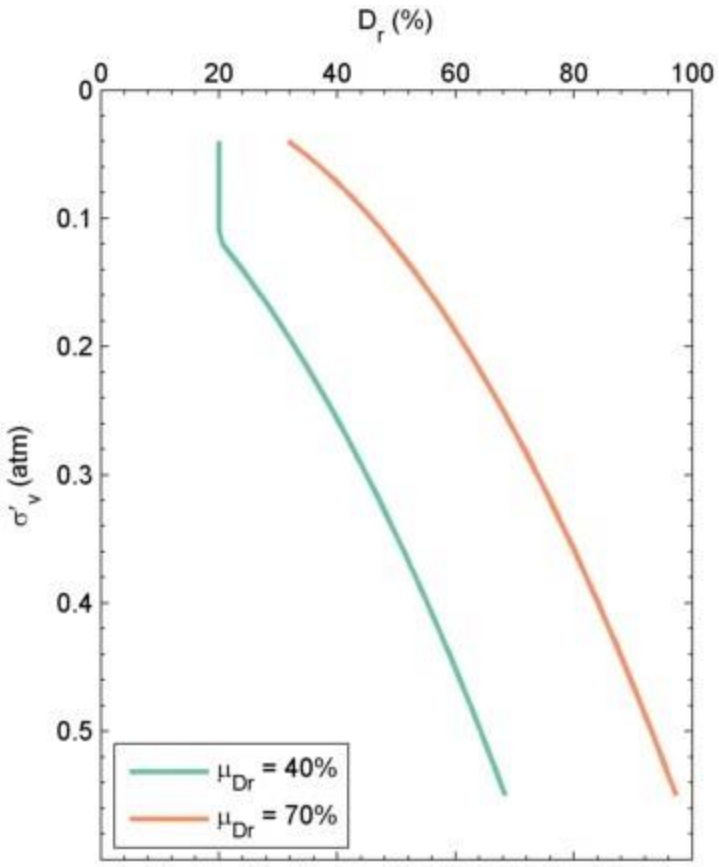


Figure 7.71: Assumed stress-dependent relative density profile, shown for average relative densities of 40 and 70%.The minimum relative density was capped at 20% to prevent unreasonably small values.

Regression analyses were performed using Equation 7.6 using the assumed stress-dependent relative density profile presented above and the entire centrifuge dataset. Values of the fitted coefficients and σ_ε are summarized in Table 7.18. Figures summarizing the regression results are provided in Appendix D. As expected, when compared to the values provided in Table 7.17, which assumed a constant relative density profile, the regression results assuming a stress-dependent relative density profile significantly changed the coefficients β_1 (the constant term) and β_3. The constant term was reduced by an average of 45% to reflect the lower relative density values in the upper layers. The overburden stress coefficient β_3 was found to be negative and within the range of the K_σ relationships from literature, as shown in Figure 7.72. The other coefficients, β_2, β_4, α_1, and α_2 were relatively insensitive to the assumed relative density profile and varied by less than 6% of the values provided in 7.17. Most significantly, the standard

deviation of the residuals, σ_{ln}, varied by less than 1.5% between the two analyses across all of the IMs.

Table 7.18: Summary of regression analyses using entire centrifuge dataset and an assumed stress-dependent relative density profile

IM	β_1	β_2	β_3	β_4	α_1	α_2	σ_{ln}
PGA_{mL}	0.129	0.012	-0.195	0.432	18.935	-0.315	0.311
PGA_{mB}	0.154	0.014	-0.232	0.385	18.659	-0.280	0.279
I_A	0.067	0.026	-0.355	1.019	22.353	-0.698	0.628
CAV	0.625	0.017	-0.160	0.713	23.877	-0.506	0.582
CAV_5	0.631	0.018	-0.160	0.741	22.118	-0.525	0.593
LIM	0.436	0.010	-0.189	0.280	19.208	-0.211	0.217

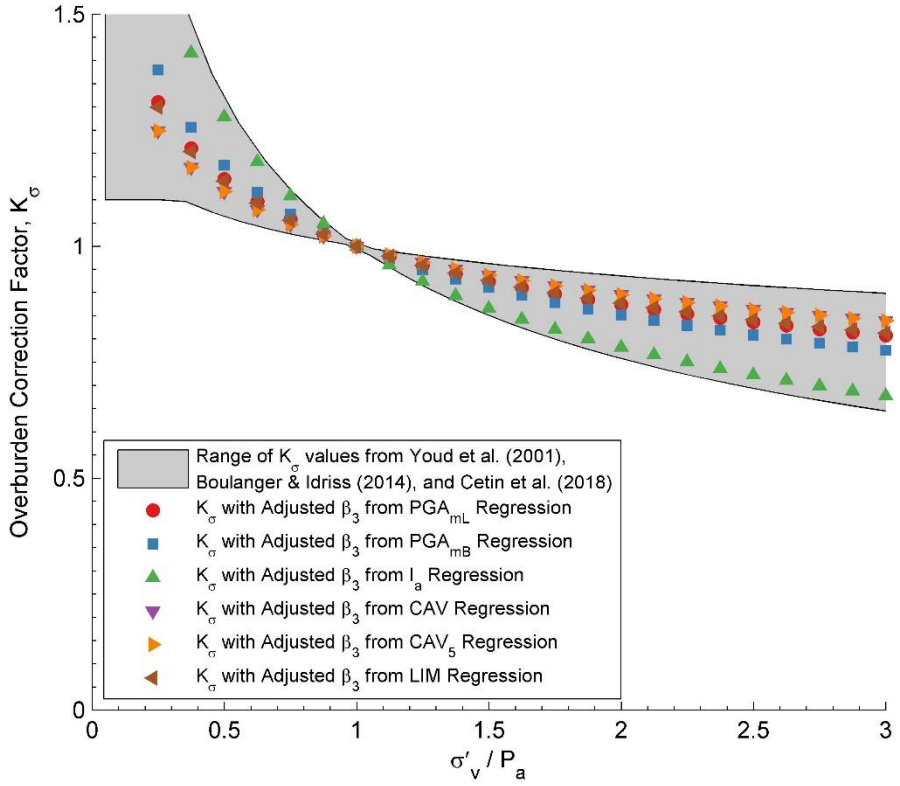


Figure 7.72: Comparison of K_σ from the simplified liquefaction triggering procedures and k_σ evaluated the coefficient β_3 evaluated from regression assuming a stress-dependent relative density profile.

The assumed density profile derived in this section combined the results of mini-CPT data from an experiment using Ottawa sand and the results of 1-D compression tests that included both Ottawa and Nevada sands. Even though both Ottawa and Nevada sand are

common testing sands, different batches of sand can include slight differences in gradation, particle shape, and other characteristics that can influence the e_{max}, e_{min}, compressibility, and other properties that can significantly influence the accuracy of the analyses performed above. The purpose of this analysis was to use known trends in the behavior of sands to provide confidence that the centrifuge dataset and regression analyses were capable of providing reasonable results. The regression analyses using an assumed stress-depended relative density profile was found to produce an overburden stress term, β_3 that was consistent with established K_σ relationships. However, the overall fit, evaluated using the standard deviation of the residuals, was essentially the same when a constant relative density profile was assumed. Therefore, the results of the regression analyses using the entire centrifuge database and an average relative density was judged to be reasonable, and the discrepancy in the β_3 coefficients from the regression and the known behavior of K_σ was due to uncertainties in the relative density profile. The uncertainty in both the average and the distribution of relative density is an acknowledged limitation of the centrifuge test data. The following section presents the results of the regression analyses using subsets of the centrifuge test data to substantiate the results using the entire test database.

7.7.2.3 Evaluation of IM Efficiency Using Subsets of the Centrifuge Database

As noted in Sections 7.5.4 and 7.5.5, the pore pressure response for Experiments 1 and 2 included a delay between the recorded pore pressure and acceleration time history. The reason for this delay was unknown and was inconsistent with observations from the CSS test program and the other centrifuge experiments. Therefore, in addition to analyses using the entire centrifuge dataset, regression analyses were also performed on subsets of the centrifuge data. These subsets included Experiments 1 and 2, Experiments 3 through 6, and each individual centrifuge experiment, to investigate if the analyses and conclusions summarized previously were consistent across each subset of the centrifuge test data.

Table 7.19 summarizes the σ_ε values computed from all of analyses using the subsets described above. The regression was performed assuming a constant relative density profile. Figure 7.73 shows a plot of the σ_ε values provided in Table 7.19. The results of the regression analyses performed on all the centrifuge data subsets were consistent with results using the regression analysis based on the entire centrifuge dataset. Of the standard IMs, both PGA_m

formulations showed lower σ_ε values than the integral-based IMs for both the combined subsets and for each individual experiment. PGA_{mB} generally performed better than PGA_{mL}, with the exception of the combined Experiment 1 and 2 dataset and using the Experiment 2 data alone. The integral IMs showed lower σ_ε values using the Experiment 1 and 2 dataset than for the dataset using Experiments 3 to 6. This response was opposite of the response observed for the PGA_m formulations and LIM. LIM consistently had the lowest σ_{ln} values compared to all of the other IMs for all of the efficiency analyses performed in this study.

Table 7.19: Summary of σ_{ln} from regression on each individual centrifuge experiment

	Standard Deviation of the Log Residuals, σ_{ln}								
IM	Exps 1 and 2	Exps 3 to 6	Exp 1	Exp 2	Exp 3	Exp 4	Exp 5	Exp 6	Mean of Ind. Exp
PGA_{mL}	0.303	0.257	0.311	0.264	0.189	0.263	0.153	0.191	0.229
PGA_{mB}	0.314	0.203	0.279	0.298	0.152	0.231	0.122	0.209	0.215
I_A	0.541	0.569	0.614	0.432	0.502	0.599	0.301	0.414	0.477
CAV	0.489	0.571	0.533	0.381	0.549	0.493	0.267	0.458	0.447
CAV_5	0.506	0.579	0.562	0.386	0.565	0.504	0.268	0.456	0.457
LIM	0.252	0.159	0.208	0.249	0.118	0.177	0.107	0.185	0.174

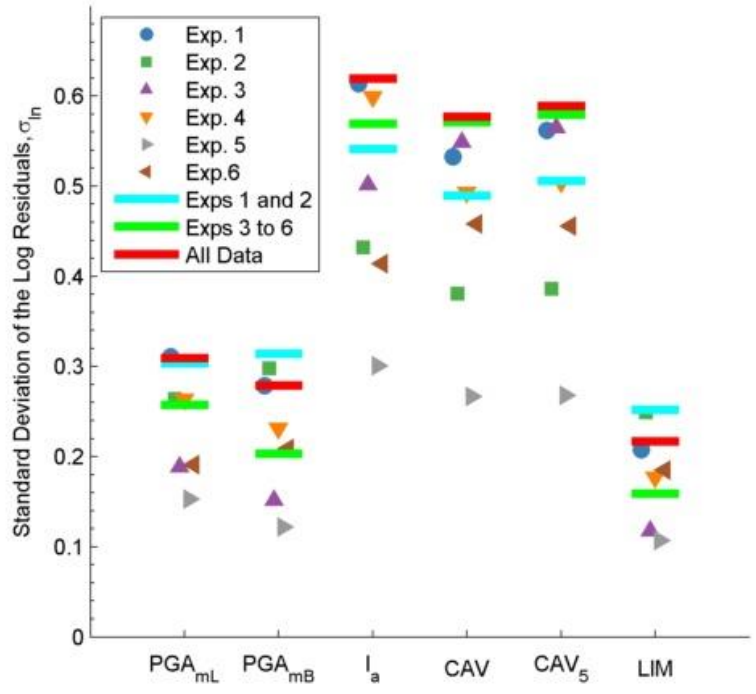


Figure 7.73: Summary of σ_{ln} from regression on each individual centrifuge experiment

7.7.2.4 Relationship Between Excess Pore Pressure and the Previous Peak r_u

El-Sekelly et al. (2016) observed a decrease in the liquefaction resistance of the soil model following an event that generated high excess pore pressures; however, this phenomenon was not consistently observed in the study of Darby et al. (2019). To investigate if this effect was significant in the current study, the residuals from the regression analysis performed on the entire centrifuge dataset were plotted as a function of the peak r_u value from the previous motion (Figure 7.74). The peak r_u value was evaluated on a layer-by-layer basis, i.e. in Figure 7.74 the regression residual for each layer was plotted as a function of the peak r_u value in the given layer from the prior test. These plots are provided for each of the IMs investigated in the current study. The plots include a linear fit of the residuals as a function of the peak r_u as well as the moving average using an 11-point-wide boxcar window function.

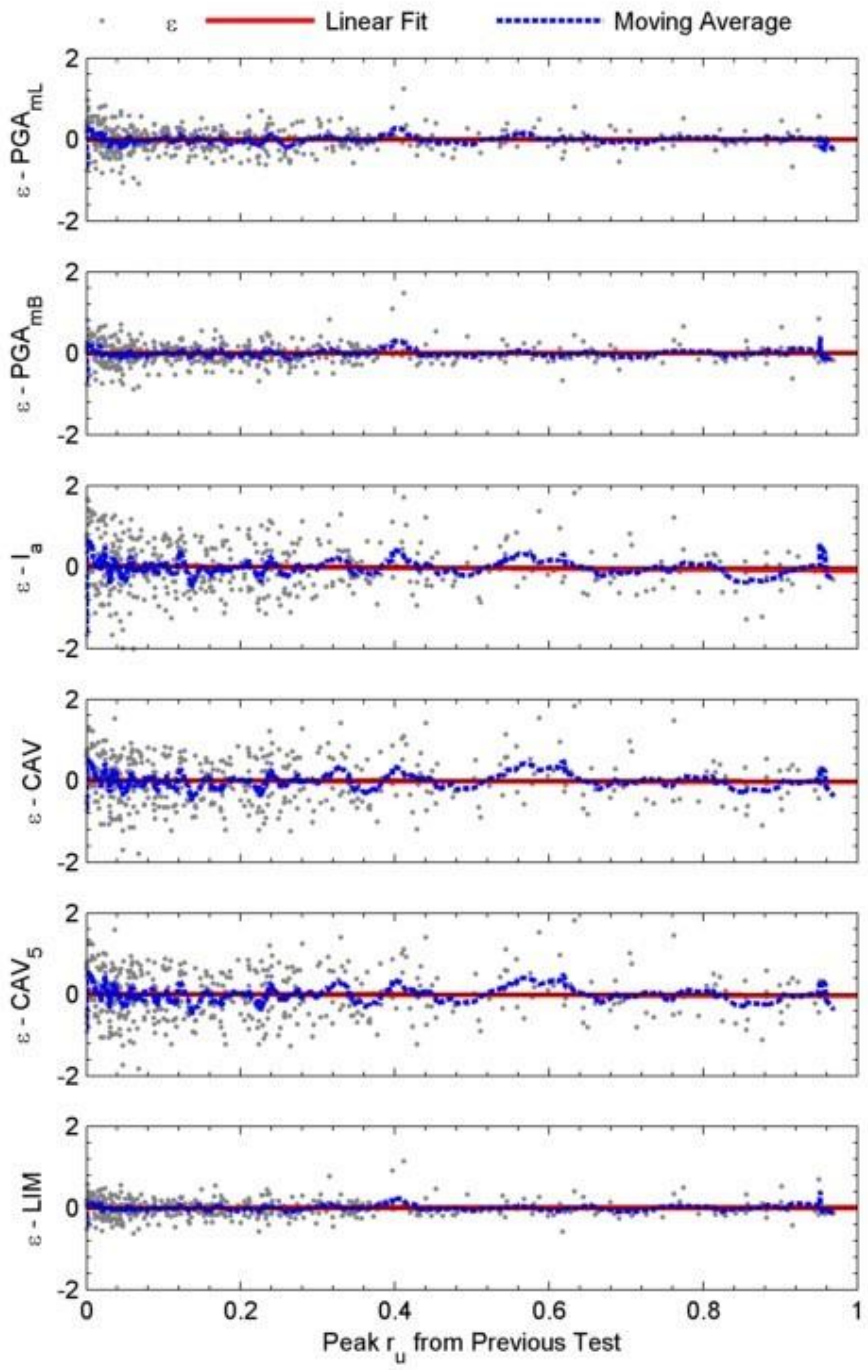


Figure 7.74: Log residuals from the regression analyses plotted as a function of the peak r_u within the given layer from the prior test

The results presented in Figure 7.74 did not show a noticeable trend with respect to the peak r_u generated by the previous motion. The linear regression fit is essentially flat and the moving average does not indicate any nonlinear trends with respect to the peak r_u. This finding

was consistent with the observations from Darby et al. (2019). El-Sekelly et al. (2016) suggested that the upward flow of water resulting from liquefaction has a quicksand effect that disturbs and loosens the upper layers of the deposit. However, both Darby et al. (2019) and the current study included motions that generated large excess pore pressures and a consistent reduction in the resistance to liquefaction following an event that generated high excess pore pressures was not observed.

A notable difference between the experiments of El-Sekelly et al. (2016) and Darby et al. (2019) and the current study was the grain size distributions of the liquefiable sands. Most notably, El-Sekelly et al. (2016) used a silty sand, with 21% fines content, while Darby et al. (2019) and the current study used clean sands. Potentially, the upward flow velocity during tests that generated high excess pore pressures could have been large enough to cause migration of the fines, which are lighter and more susceptible to migration than coarser sand particles. The migration of the fines could create additional voids in the liquefiable layer. These additional voids would make the soil more susceptible to contraction and the generation of excess pore pressure for the following event.

In addition, the study of El-Sekelly et al. (2016) used a loading sequence that included a series of 11 identical low-amplitude sinusoidal loading histories followed by a single large-amplitude sinusoidal loading history. This loading sequence was significantly different than the loading sequences used by Darby et al. (2019) and the current study. The difference in the observed response between El-Sekelly et al. (2016) and Darby et al. (2019) and the current study could be due to the differences in the gradation characteristics of the liquefiable soils, and/or differences in the shaking intensity and the sequencing of the applied motions.

7.8 DISCUSSION

Centrifuge tests were performed to substantiate the findings from the CSS test program. Centrifuge testing allows for the simulation of prototype-scale events by subjecting heavily instrumented scale models to higher gravitational fields. These tests can provide a more realistic representation of the behavior of saturated soil deposits in the field than CSS testing. However, the centrifuge experiments included a number of complicating factors, most notably the partial drainage conditions and the uncertainty in the evolution of relative density, that made the interpretation of the results difficult. Despite these complications, the centrifuge test program

was able to provide a useful dataset for the analysis of liquefiable soils subjected to transient loading histories derived from actual earthquake records.

Qualitative inspection of the relationship between the acceleration loading histories and the excess pore pressure response (Section 7.6) showed that the observations made during the CSS test program were also applicable in the centrifuge. These observations included:

- The generation of excess pore pressure is more strongly related to the peak amplitudes in the loading history.
- The phasing of the loading history and the order of the acceleration amplitudes is important. In particular, the concept of the peak prior amplitude, or PPA, introduced in Chapter 6 was observed to be a key component of the loading – r_u relationship as observed in the centrifuge. In general, excess pore pressures tended to build as the loading amplitude increased and the PPA was being repeatedly exceeded, while pulses that were less than the PPA were shielded and generated little or no pore pressure even if their magnitudes were relatively large.
- The cycle counting-based IMs (PGA_{mL}, PGA_{mB}, LIM) were able to visually capture the shape of the r_u time history, while the integral-based IMs (I_A, CAV, CAV_5) were sensitive to portions of the time history that did not contribute to the excess pore pressure response.
- Dilation and phase transformation-induced excess pore pressure generation is a complex phenomenon that an IM computed from the time history along is unable to fully capture.
- Of the standard IMs, the cycle counting-based IMs, particularly PGA_{mB}, were the most efficient at predicting the r_u response from the centrifuge.
- The IM developed based on observations from the CSS testing program, LIM, was found to reduce the uncertainty in regression relationship by 30% as compared to PGA_{mB}.

Regression analyses were performed to evaluate the efficiency of the evolutionary IMs to predict the generation of excess pore pressure. These analyses were performed using both the entire centrifuge dataset as well as subsets of the centrifuge data. The results of the efficiency evaluations from the centrifuge study were consistent across all of the centrifuge datasets. The efficiency evaluations consistently identified the cycle counting-based IMs as the most efficient. Of the cycle counting-based IMs, LIM, which explicitly accounts for the PPA in its formulation,

was found to be the most efficient IM. However, PGA_{mB}, the IM associated with the CSR-based liquefaction evaluation procedure widely used in practice, was also found to be an efficient and robust predictor of the pore pressure response in the centrifuge. These findings were consistent with the analyses using the CSS tests data and indicated that, based on experimental data, cycle counting-based IMs are more efficient predictors of the excess pore pressure than integral based IMs. In addition, LIM, which explicitly accounts for the phasing of the loading history, offers an improvement over the conventional PGA_m formulations that are prevalent in engineering practice.

.

[This page intentionally left blank]

Chapter 8. SUMMARY, CONCLUSIONS, AND RECOMMENDATIONS FOR FUTURE RESEARCH

The current procedures for evaluating the liquefaction hazard of a given soil deposit are generally based on comparing measures of seismic loading and a soil's capacity to resist that loading. These procedures have been modified and improved over the years, however, the same basic methods for liquefaction hazard evaluation commonly used in current design practice are nearly identical to those that were developed over 40 years ago. In particular, the method used to define the loading history has appeared to be a bit archaic given the numerous seismological and computation advancements that have been made since the inception of these procedures. For purposes of liquefaction hazard evaluation, earthquake loading is typically evaluated using a single point, the maximum value of ground surface acceleration, that is scaled to account for the duration of the event using a factor based on earthquake magnitude. Even though liquefaction is an inherently transient process in which a soil gradually softens due to the generation of excess pore pressures and reduction in effective stress that occurs over the course of the seismic loading history, current design methods use a static parameter calculated at a single point in the time history to evaluate the initiation and, often, the effects of liquefaction. These methods fail to acknowledge the drastically different dynamic characteristics of the soil before and after liquefaction has been initiated.

Based on the observed limitations in the current design procedures, Kramer et al. (2016) proposed a timing-based liquefaction hazard evaluation framework that explicitly accounts for the dramatic change in the characteristics of a soil before and after the initiation of liquefaction. The framework utilizes evolutionary intensity measures, or measures of the seismic loading that build up with time over the duration of an earthquake ground motion, to identify not only if, but when liquefaction will occur for a given design scenario. If liquefaction is triggered, the timing-based framework uses an estimate of the loading intensity that remains in the motion after liquefaction has been initiated to estimate the effects of liquefaction. The framework is relatively simple, highly flexible, built on concepts already familiar to practicing engineers, and can be implemented probabilistically. Preliminary work by Kramer et al. (2016) and Greenfield (2017) have shown that the timing-based framework can significantly improve the efficiency in

predictions of the effects of liquefaction, which has notable benefits in a probabilistic performance-based hazard analysis framework.

The objective of this research was to identify the most efficient evolutionary IMs at predicting the generation of excess pore pressure and the initiation of liquefaction, which is the first step of the timing-based liquefaction hazard evaluation framework. This study used both cyclic simple shear (CSS) and centrifuge testing to systematically investigate the response of liquefiable soils to fully transient earthquake loading histories in order to identify which aspects of an earthquake loading history are most closely related to excess pore pressure response. Based on the results and observations from the laboratory, this study identified evolutionary ground motion intensity measures that were the most efficient at predicting the occurrence and timing of liquefaction. The following sections provide a summary of the contents of this document, the conclusions from the current research effort, and recommendations for future research.

8.1 SUMMARY

This document contains eight chapters that provide a review of liquefiable soil behavior, the performance-based earthquake engineering framework, the timing-based framework that served as the motivation for this study, and recent research studies of evolutionary IMs for use in evaluating the potential for initiation of liquefaction. These chapters were followed by chapters that detailed the procedures and results of the experimental testing programs. Following the introduction provided in Chapter 1, a summary of the contents of this document is as follows:

- Chapter 2 presented the fundamental aspects of liquefiable soil behavior. This chapter described the complex mechanics of liquefiable soils subjected to cyclic shear loads. In addition, this chapter provided an overview of liquefaction hazard evaluation and included a review of the current liquefaction triggering evaluation procedures.
- Chapter 3 provided a summary of the performance-based earthquake engineering (PBEE) framework. The PBEE framework provides a rational, modular approach for the design of facilities that provides the facility stake-holders (owners, users, government, etc.) with performance metrics that are relevant to decision making for seismic risk mitigation, as opposed to satisfying minimum requirements outlined in building codes (Moehle and Deierlein, 2004). The PBEE framework allows for a probabilistic assessment of the seismic hazard to be extended to a probabilistic assessment of the building performance

in a robust and systematic manner. The PBEE framework served as the foundation for the timing-based liquefaction hazard evaluation framework that provided the motivation for this study.

- Chapter 4 included a detailed description of the timing-based liquefaction hazard evaluation framework. The timing-based framework decouples the ground motion intensity required to trigger liquefaction from the post-triggering intensity that drives the effects of liquefaction, such as permanent displacements (Greenfield 2017). This chapter included an overview of preliminary analyses by Kramer et al. (2016) and Greenfield (2017) that showed the potential benefits of the proposed framework. Step 1 of the framework, predicting the initiation and the timing of liquefaction using evolutionary intensity measures, was the focus of the work presented in this document.
- Chapter 5 provided an overview of recent studies that investigated the efficiency of evolutionary intensity measures the predict the initiation of liquefaction. These studies included Kramer and Mitchell (2006), Abegg (2010), and Dashti and Karimi (2017). Each of these studies utilized numerical analyses to evaluate the efficiency of various candidate IMs to predict the peak pore pressure response within a liquefiable soil layer. The results of these studies helped guide the experimental testing programs performed as part of this research project.
- Chapter 6 presents the CSS test program, and included descriptions of the CSS test apparatus, loading protocols, input shear stress loading histories, and the results and observations from the experimental study. The CSS test program included both simple transient shear stress histories based on sinewaves and fully transient shear stress histories derived from actual recorded earthquakes. The efficiency of standard IMs commonly associated with the liquefaction triggering procedures were evaluated with acceleration time histories derived from the applied shear stress record using equivalent linear analyses. In addition, this chapter established a new evolutionary IM, called the liquefaction-specific intensity measure, LIM, that was developed based on the observations from the CSS test program.
- Chapter 7 provides the results of the centrifuge test program, which consisted of six experiments where a soil model was subjected to repeated shaking using a diverse suit of input motions. This chapter provides a review of the centrifuge facility, model

characteristics, ground motion characteristics, a description of the publicly available data, and the efficiency evaluations performed using the centrifuge test data.

8.2 CONCLUSIONS

The literature review and experimental studies performed as part of this research project provided a number of unique and potentially valuable insights into the relationship between an earthquake loading history and the generation of excess pore pressures and the initiation of liquefaction. Some preliminary conclusions that were generated by this study include:

- Previous work has shown that the generation of excess pore pressure is related to the amplitude and duration, and relatively insensitive to the frequency content, of the loading history. These findings were consistent with the results of the CSS and centrifuge testing programs performed as part of this study.
- A unique observation from this study is that prior to phase transformation behavior, the generation of excess pore pressure is strongly influenced by the phasing and relative amplitudes of the loading history. This study presented the concept of the prior peak amplitude, or PPA. The pore pressure response was found to be related to the PPA in two distinct ways,
    a) The pore pressure response is highly correlated with local peaks in the loading history. Large increments of pore pressure generation are associated with loading pulses of amplitude that exceeds the PPA.
    b) Loading pulses of amplitude lower than the PPA appear to be "shielded" by the prior peak and generate significantly less pore pressure than if they had not been preceded by a larger amplitude pulse.

  These observations were consistently observed in both the CSS and centrifuge testing programs.
- The onset of phase transformation behavior significantly alters the relationship between the loading history and the generation of excess pore pressure. During phase transformation, the pore pressures increase rapidly during load reversals as the soil alternates between dilative and contractive behavior. Furthermore, this relationship cannot be directly predicted using an IM computed solely based on the loading history.

However, analyses using CSS test data showed that the IM value at the onset of phase transformation and the IM value at the initiation of liquefaction were highly correlated.

- Of the standard IMs (PGA_{mL}, PGA_{mB}, I_A, CAV, and CAV_5), the PGA_m formulations, particularly PGA_{mB}, were found to be the most efficient predictors of pore pressure generation and the initiation of liquefaction. This finding was consistent using both the CSS and centrifuge datasets, and contrasted with results of the numerical studies of Kramer and Mitchell (2006) and Abegg (2010). The explanation for this finding can be summarized as follows:
    a) PGA_m, like r_u, is insensitive to the frequency content of the applied loading.
    b) The r_u response from the CSS and centrifuge data showed a dependence on the order of cycles and was highly sensitive to local peak amplitudes. This effect was not captured in the in the numerical analyses of Kramer and Mitchell (2006) and Abegg (2010). Due to the cycle-weighting and MSF formulations used in both definitions of PGA_m, PGA_m is able to capture these effects in a manner that is consistent with the observed r_u response.
    c) PGA_m is very efficient at predicting the onset of phase transformation behavior which was found to be highly correlated with the initiation of liquefaction using the CSS test data.
- A new liquefaction-specific intensity measure, called LIM in this document, was developed. LIM was formulated to explicitly account for each aspect of a loading history that was found to significantly impact the pore pressure response in the CSS test program. LIM was formulated based on a derivation of PGA_{mB} and included a peak ratio term that scaled the amplitudes of individual pulses based on their amplitude relative to the PPA. Regression analyses using both the CSS and centrifuge test data showed that LIM was more efficient than any of the standard IMs at predicting the generation of excess pore pressure and the initiation of liquefaction based on the experimental databases.
- Two numerical models, PDMY02 and PM4Sand were used to simulate the response of the transient CSS tests. These results showed that calibrated numerical models can accurately predict the excess pore pressure response in a general sense. However, these models were not able to capture the shielding effect for pulses that were slightly below

the PPA and did not generate excess pore pressure as rapidly as the test data when subjected to high amplitude stress pulses.

8.3 Recommendations for Future Research

This motivation for this research was the development of the timing-based liquefaction hazard evaluation framework. This framework is relatively new and offers numerous avenues for future research. Even the most heavily researched component of the framework, the liquefaction triggering relationship, and the focus of this research still contains a number of areas that can be improved and is consistently being reviewed, scrutinized, and updated (e.g. Boulanger and Idriss, 2014; Cetin et al., 2018). Several specific studies that would improve our current understanding of liquefiable soil behavior and improve the timing-based liquefaction hazard evaluation framework include,

- This study included both CSS and centrifuge testing using a large suite of input ground motions that covered a wide range of earthquake mechanisms. However, no single study can incorporate the diverse and complex nature of liquefiable soil response to earthquake ground motion. This study was limited to one type of sand and used a simple, short, relatively stiff soil profile, therefore additional studies are needed to evaluate if the conclusions from this experimental program apply to:
    - Different sands with alternative gradation, particle shape, and other characteristics that may influence the pore pressure response.
    - Alternative soil profiles. Due to the dynamic characteristics of the soil profile used in this study, the acceleration and shear stress response were very similar. However, naturally occurring soil deposits can contain soft layers and impedance contrasts that would alter this relationship. Additional studies that include more realistic soil profiles are needed to verify these preliminary findings.
    - The density profile used in the centrifuge testing included large uncertainty due to limitations in the equipment at the time the test was performed. Currently, centrifuge facilities are able to directly measure the insitu properties of the model using devices such as the mini-CPT. Additional centrifuge studies using transient ground motions and insitu density measurements would provide valuable data to support the findings of this research study.

- In a performance-based framework the predictability of an IM is very important. As shown in Section 3.2 an IM with high uncertainty in its predictability can lead to a large increase in the corresponding hazard, even if it is can efficiently predict the EDP. This study did not evaluate the predictability of the IMs. Currently, PGA_m is evaluated using a joint hazard distribution of PGA and magnitude, and a GMPE that predicts PGA_m directly does not exist. The development of a full GMPE for PGA_m is required to properly evaluate its usefulness in the liquefaction hazard evaluation framework. Similarly, LIM showed promise as an efficient predictor of the initiation of liquefaction, but the predictability of LIM is unknown and the development of a GMPE is required to fully evaluate its utility in probabilistic applications.
- Numerical models offer an attractive method to evaluate the response of liquefiable soils under a wide range of applications. The brief study performed in this document showed that PDMY02 and PM4Sand provide reasonable estimates of the pore pressure response of the CSS tests. However, there is room for improvement. Virtually all numerical models for liquefiable soil are calibrated on the basis of harmonic loading tests where the shear stress amplitudes are constant. The CSS data from the transient loading tests presented here and in Kwan (2015) provide a useful resource for the further calibration of these models.
- Experimental and numerical studies are very useful and provide detailed insight that cannot be obtained from field studies. However, the soil fabric and stress states that exist in the field cannot be fully reproduced in the laboratory or modeled numerically to a high degree of certainty. Case histories that include sites where liquefaction was triggered near seismic ground motion recorders are invaluable for the development of the timing-based framework because they allow for the identification of the timing of liquefaction to be evaluated as described in Greenfield (2017). Greenfield (2017) noted several examples of these sites, and additional subsurface explorations and geotechnical characterization at these locations would be extremely beneficial. In addition, downhole arrays such as the Wildlife liquefaction, Port Island, and Seattle liquefaction arrays can provide vital data for researchers interested in the development of timing-based liquefaction hazard analysis procedures.

[This page intentionally left blank]

BIBLIOGRAPHY

Abegg, S. (2010). *Identification of optimal evolutionary intensity measures for evaluation of liquefaction hazards.* Masters thesis, University of Washington, Seattle WA.

Airy, D.W. and Wood D.M. (1987). An evaluation of direct simple shear testing on clay. *Geotechnique* vol. 37, no. 1, pp. 25-35.

Amer, M.I., Aggour, M.S. and Kovaks, W.D. (1986). Testing using a large-scale cyclic simple shear device. ASTM Geotechnical Testing Journal, vol. 9, no. 3, pp. 140-146

Ancheta, T.D., Darragh, R.B., Stewart, J.P., Seyhan, E., Silva, W.J., Chiou, B.S.J., Wooddell, K.E., Graves, R.W., Kottke, A.R., Boore, D.M., Kishida, T., and Donahue, J.L. (2013). PEER NGA-West2 Database, PEER 2013/03 – PEER, Pacific Earthquake Engineering Research Center, University of California, Berkeley.

Andrus, R.D. and Stokoe, K.H. (1997). Liquefaction resistance based on shear wave velocity. *Proceedings, NCEER Workshop on Evaluation of Liquefaction Resistance of Soils*, National Center for Earthquake Engineering Research, State University of New York, Buffalo, pp. 89-128.

Arango, I. (1996). Magnitude scaling factors for soil liquefaction evaluations. *Journal of Geotechnical Engineering*, vol. 122, no. 11, pp. 929-936.

Arias, A. (1970). A measure of earthquake intensity. *Seismic Design for Nuclear Power Plants*, R.J. Hansen (ed.), MIT Press, Cambridge, Massachusetts, pp. 438-483.

Arumoli, K., Muraleetharan, K., Hosain, M. and Fruth, L. (1992). VELACS laboratory testing program, soil data report. *Rep. to the National Science Foundation*, Earth Technology Program, Irvine, CA.

Bardet, J.P., Tobita, T., Mace, N. and Hu, J. (2002). Regional modeling of liquefaction-induced lateral spread, *Earthquake Spectra*, vol. 18, no. 1, pp. 19-46

Baska, D.A. (2002). *An analytical/empirical model for the prediction of lateral spread displacements*. PhD dissertation, University of Washington, Seattle, WA.

Benjamin, J.R. and Associates (1988). *A criterion for determining exceedance of the operating basis earthquake*, EPRI Report NP-5930, Electric Power Research Institute, Palo Alto, California.

Bennett, M.J., (1998). Sand boils and settlement on Treasure Island, The Loma Prieta earthquake of October 17, 1989—liquefaction. *USFS Professional Paper 1551-B*

Beroya, M.A.A., Aydin, A., and Katzenbach, R. (2009). Insight into the effects of clay minerology on the cyclic behavior of silt-clay mixtures, *Engineering Geology*, vol. 106, pp. 154-162.

Boore, D.M., Joyner, W.B., and Fumal, T.E., (1997). Equations for estimating horizontal response spectra and peak acceleration from western North American earthquakes: A summary of recent work, *Seismological Research Letters* vol. 68, no. 1, pp. 128-153.

Boulanger, R.W. and Idriss, I.M. (2004). State normalization of penetration resistance and effect of overburden stress on liquefaction resistance. *Proceedings, 11th International Conference on Soil Dynamics and Earthquake Engineering, and 3rd International Conference on Earthquake Geotechnical Engineering,* D.Doolin et al., eds., Stallion Press, Vol. 2, pp. 484-491.

Boulanger, R.W. and Idriss, I.M. (2006). Liquefaction susceptibility criteria for silts and clays. *Journal of geotechnical and geoenvironmental engineering*, ASCE vol. 132 no. 11, pp. 1413-1426.

Boulanger, R.W., and Idriss, I.M. (2012). Probabilistic SPT-based liquefaction triggering procedure. *J. Geotechnical and Geoenvironmental Engineering*, ASCE, vol. 138, no. 10 1185-1195.

Boulanger, R.W., and Idriss, I.M. (2014). CPT and SPT based liquefaction triggering procedures. Report No. UCD/CGM-14/01, Center for Geotechnical Modeling, UC Davis, Davis, California, 138 p.

Boulanger, R.W. and Seed, H.B. (1995). Liquefaction of sand under bi-directional monotonic and cyclic loading. *Journal of Geotechnical Engineering*, ASCE vol. 121, no. 12, 870-878.

Boulanger, R.W. and Truman, S.P., (1996). Void redistribution of in sand under post-earthquake loading. *Canadian Geotechnical Journal,* vol. 33, pp 829-834

Boulanger, R.W. and Ziotopoulou (2017). PM4Sand (version 3.1): A sand plasticity model for earthquake engineering applications. Report No. UCD/CGM-17/01, Center for Geotechnical Modeling, University of California, Davis, CA.

Brandenberg, S.J., Boulanger, R.W., Kutter, B.L., and Chang, D. (2005). Behavior of pile foundations in laterally spreading ground during centrifuge tests. *Journal of geotechnical and geoenvironmental engineering*, ASCE vol. 131, no. 11, pp. 1378-1391

Bray, J.D., Sancio, R.B., Riemer, M.F. and Durgunoglu, T. (2004). Liquefaction susceptibility of fine-grained soils. *Proc. 11th Int. Conf. on Soil Dynamics and Earthquake Engineering and 3rd Int. Conf. on Earthquake Geotechnical Engineering.* D. Doolin et al., eds., Stallion Press, Singapore, 655-662.

Brennan, A.J., and Madabhushi, S.P.G. (2010). Measurement of coefficient of consolidation during reconsolidation of liquefied sand. *Geotechnical Testing Journal*, vol. 34, no. 2, 139-146.

Campbell, K.W. and Bozorgnia, Y. (2010). A ground motion prediction equation for the horizontal component of cumulative absolute velocity (CAV) based on the PEER-NGA strong motion database. *Earthquake Spectra*, vol. 26, no. 3, pp. 635-650.

Campbell, K.W. and Bozorgnia, Y. (2012). A comparison of ground motion prediction equations for Arias intensity and cumulative absolute velocity developed using a consistent database and functional form, *Earthquake Spectra*, vol. 28, pp. 931-994

Campbell, K.W. and Bozorgnia, Y. (2014). NGA-West2 ground motion model for the average horizontal components of PGA, PGV, and 5% dampled linear acceleration response spectra, *Earthquake Spectra*, vol. 30, pp. 1087-1115.

Casagrande, A. (1936). Characteristics of cohesionless soils affecting the stability of slopes and earth fills. *Journal of the Boston Society of Civil Engineers*, reprinted in *Contributions to Soil Mechanics*. Boston Society of Civil Engineers, 1940, pp. 257-276

Casagrande, A. (1976). Liquefaction and cyclic mobility of sands: a critical review. *Harvard Soil Mechanics Series 88,* Harvard University, Cambridge, Mass.

Castro G, and Poulos, S.J. (1977). Factors affecting liquefaction and cyclic mobility. *Journal of the Geotechnical Engineering Division,* ASCE, vol.106, no. 6, pp. 501-506

Castro, G. (1969) Liquefaction of sands. *Harvard Soil Mechanics Series 87*, Harvard University, Cambridge, Mass.

Cetin, K.O., Seed, R.B., Kayen, R.E., Moss, R.E.S., Bilge, H.T., Ilgac, M., and Chowdhury, K. (2018). SPT-based probabilistic and deterministic assessment of seismic soil liquefaction triggering hazard. *Soil Dynamics and Earthquake Engineering*, vol. 115, pp. 698-709.

Chiou, B., Darragh, R. Gregor, N. and Silva, W. (2008). NGA project strong-motion database. *Earthquake Spectra*, vol., 24, 23-44.

Conti, R., and Viggiani, G.M.B. (2012). Evaluation of soil dynamic properties in centrifuge tests. *Journal of Geotechnical and Geoenvironmental Engineering*, vol. 138, no. 7, pp. 850-859.

Cornell, C.A. (1968). Engineering seismic risk analysis. *Bulletin of the Seismological Society of America*, vol. 58, no. 5, pp. 1583-1606.

Dafalias, Y.F., Manzari, M.T. (2004). Simple plasticity sand model for accounting for fabric change effects. *Journal of Engineering Mechanics,* ASCE, vol. 130, no. 6, pp. 622-634

Darby, K.M., Boulanger, R.W., and DeJong, J.T. (2017). Effect of multiple shaking events on cone penetration resistances in saturated sand. In *Proc., 3rd International Conf. on Performance-based Design in Earthquake Geotechnical Engineering*, edited by M. Taichat, et al., Vancouver, BC, Canada.

Darby, K.M., Boulanger, R.W., and DeJong, J.T., (2018). Volumetric strains from inverse analysis of pore pressure transducer arrays in centrifuge models. In *Proc. Geotechnical Earthquake Engineering and Soil Dynamics V*, edited by Brandenberg, S.J., and Janzaru, M.T., Austin, Texas, USA.

Darby, K.M., Boulanger, R.W., DeJong, J.T., and Bronner, J.D. (2019). Progressive changes in liquefaction and cone penetration resistance across multiple shaking events in centrifuge tests. *Journal of geotechnical and geoenvironmental engineering*, ASCE vol. 145, no. 3, 04018112.

Darragh, R.B., and Shakal, A.F., (1991). The site response of two rock and soil station pairs to strong and weak ground motion. *Bulletin of Seismological Society of America,* vol. 81, pp. 1885-1899

Dashti, S., Bray, J.D., Pestana, J.M., Riemer, M., and Wilson, D. (2010a). Centrifuge testing to evaluate and mitigate liquefaction-induced building settlement mechanisms. *Journal of Geotechnical and Geoenvironmental Engineering*, vol. 136, pp. 151-164.

Dashti, S., Bray, J.D., Pestana, J.M., Riemer, M., and Wilson, D. (2010b). Mechanisms of seismically-induced settlement of buildings with shallow foundations on liquefiable soil. *Journal of Geotechnical and Geoenvironmental Engineering*, vol. 136, pp. 151-164.

Dashti, S. and Karimi, Z. (2016). Ground motion intensity measure to evaluate I: the liquefaction hazard in the vicinity of shallow-founded structures. *Earthquake Spectra*, vol. 33, no. 1, pp. 241-276.

De Alba, P., Seed, H.B., and Chan, C.K. (1976). Sand liquefaction in large scale simple shear tests. *J. Geotechnical Eng. Div.,* ASCE vol. 102, no. GT9, 909-927.

Dobry, R., Ladd, R.S., Yokel, F.Y., Chung, R.M. and Powell, D. (1982). Prediction of pore water pressure buildup and liquefaction of sands during earthquakes by the cyclic strain method. *NBS Building Science Series 138*, National Bureau of Standards, Gaithersburg, Maryland.

Dobry, R., and Abdoun, T. (2015). 3rd Ishihara Lecture: An investigation into why liquefaction charts work: A necessary step toward integrating the states of art and practice. *Soil Dynamics and Earthquake Engineerin*, vol. 68, pp. 40-56.

EduPro Civil Systems, Inc. *ProShake: Ground response analysis program*. EduPro Civil Systems, Inc. Redmond, WA.

Elgamal, A., Yang, Z., and Parra, E. (2002). Computational modeling of cyclic mobility and post-liquefaction site response. *Soil Dynamics and Earthquake Engineering*. vol. 22, pp. 259-271.

El-Sekelly, W., Dobry, R., Abdoun., T., and Steidl, J.H. (2016). Centrifuge modeling of the effect of preshaking on the liquefaction resistance of silty sand deposits. *Journal of Geotechnical and Geoenvironmental Engineering*, ASCE vol. 142, no. 6, 04016012.

Evans, M.D. and Seed, H.B. (1987). Undrained cyclic triaxial testing of gravels: the effect of membrane compliance. *Report UCB/EERC-87/08*, Earthquake Engineering Research Center, University of California, Berkeley, California.

Gibson, R.E., England, G.L., and Hussey, M.J.L.. (1967). The theory of one-dimensional consolidation of saturated clays, I. Finite non-linear consolidation of thin homogenous layers, *Geotechnique*, vol. 17, pp. 261-273.

Gonzalez-Lagos, L.L., Abdoun, T. and Dobry, R. (2007). *Centrifuge modeling of permeability and pinning reinforcement effects on pile response to lateral spreading*. MCEER report MCEER-07-0020.

Green, R.A. (2001). Energy-based evaluation and remediation of liquefiable soils. PhD dissertation, Virginia Polytechnic and State University, Blacksburg, Virginia.

Green, R.A., and Terri, G.A. (2005). Number of equivalent cycles concept for liquefaction evaluations – Revisited, *Journal of Geotechnical and Geoenvironmental Engineering*, vol. 131, no. 4 477-488.

Greenfield, M.W. (2017). *Effects of long-duration ground motions on liquefaction hazards*, Ph.D. Dissertation, University of Washington, Seattle, WA, 478 pp.

Hanzawa, H., Itoh, Y., Suzuki, K., (1979). Shear characteristics of quick sand in the Arabian Gulf. *Soils and Foundations,* vol. 19, no. 4, pp. 1-15

Harr, M.E. (1966). *Foundations of theoretical soil mechanics*, McGraw-Hill Book Company, New York, 381 pp.

Holtz, R.D., and Kovacs, W.D. (1981). *An introduction to geotechnical engineering*. Prentice-Hall, Englewood Cliffs, N.J.

Hynes, M.E, and Olsen, R.S. (1999). Influence of confining stress on liquefaction resistance. *Proc. Int. Workshop on Phys. And Mech. Of Soil Liquefaction*, Balkema, Rotterdam, The Netherlands, 145-152.

Husid, L.R. (1969). Caracteristicas de teremotas. Analisis general. In *Revista del IDIEM 8*, pp. 21-42.

Idriss, I.M. (1990). Response of soft soil sites during earthquakes. *Proceedings, H. Bolton Seed Memorial Symposium*, Vol. 2, pp. 273-289, BiTech Publishers Ltd.

Idriss, I.M., and Boulanger, R.W., (2008) *Soil liquefaction during earthquakes.* Earthquake Engineering Research Institute, Oakland, California.

Idriss, I.M., and Boulanger, R.W., (2010). *SPT-based liquefaction triggering procedures*. Report No. UCD/CGM-10/02. Center for geotechnical modeling, University of California, Davis, California, 259 p.

Ishibashi, I., Sharif, M.A., and Tsuchiya, C. (1977). Pore-pressure rise mechanism and soil liquefaction. *Soils and Foundations*, vol. 17, no. 2, 17-27.

Ishihara, K. (1985). Stability of natural deposits during earthquakes. *Proceedings, 11th International Conference on Soil Mechanics and Foundation Engineering.* Vol. 1, pp.321-376

Ishihara, K. and Yoshimine, M. (1992). Evaluation of settlements in sand deposits following liquefaction during earthquakes. *Soils and Foundations*, vol. 32, no. 1, pp. 178-188.

Ishihara, K., Harada, K., Lee, W.F., Chan, C.C., and Safiullah, A.M.M. (2016). Post-liquefaction settlement analyses based on volume change characteristics of undisturbed and reconstituted samples. *Soils and Foundations*, vol. 56, no. 3, pp. 533-546.

Itasca (2016). FLAC – Fast Lagrangian Analysis of Continua, Version 8.0, Itasca Consulting Group, Inc., Minneapolis, Minnesota.

Jalayer, F. and Cornell, C.A. (2003). A technical framework for probability-based demand and capacity factor design (DCFD) seismic formats. PEER Report 2003/08, Pacific Earthquake Engineering Research Center, University of California, Berkely, CA.

Kammerer, A.M., Pestana, J. and Seed, R. (2002). Undrained response of Monterrey 0/30 sand under multidirectional cyclic simple shear loading conditions. In *Department of Civil and Environmental Engineering, 2002*. University of California, Berkeley. Berkeley, CA., pp. 459.

Karimi, Z., and Dashti, S. (2017). Ground motion intensity measures to evaluate II: the performance of shallow-founded structures on liquefiable ground. *Earthquake Spectra*. vol. 33, no. 1, pp. 277-298.

Kayen, R.E. and Mitchell, J.K. (1997). Assessment of liquefaction potential during earthquakes by Arias intensity. *Journal of geotechnical and geoenvironmental engineering*, ASCE vol. 123, no. 12, pp. 1162-1174

Kayen, R.E. and Mitchell, J.K. (1997). Assessment of liquefaction potential during earthquakes using Arias intensity. *Journal of Geotechnical and Geoenvironmental Engineering*, ASCE vol. 123, pp. 1162-1174.

Kayen, R., Moss, R.E.S., Thompson, E.M., Seed, R.B., Cetin, K.O., Der Kiureghian, A., Tanaka, Y., and Tokimatsu, K. (2013). Shear-wave velocity-based probabilistic and deterministic assessment of seismic soil liquefaction potential. *J. Geotechnical and Geoenvironmental Engineering*, ASCE vol. 139, no. 3, pp. 407-419.

Khosravifar, A. (2012). Analysis and design for inelastic structural response of extended pile shaft foundations in laterally spreading ground during earthquakes. Ph.D. Dissertation, University of California, Davis, California, 312 pp.

Kishida, H, and Uesugi, M. (1987). Tests of the interface between sand and steel in simple shear apparatus. Geotechnique vol 34, no. 1, pp. 45-52.

Kokusho, T. (2016). Major advances in liquefaction research by laboratory tests compared with in situ behavior. *Soil Dynamics and Earthquake Engineering*, vol. 91, pp. 3-22.

Konstandinou, M., and Georginnou, V.N. (2014). Prediction of pore water pressure generation leading to liquefaction under torsional cyclic loading. *Soils and Foundations*, 54(5) 993-1005.

Kramer, S.L. (1996). *Geotechnical earthquake engineering*. Prentice-Hall, Inc. Upper Saddle River, N.J.

Kramer, S.L. and Arduino, P., (1999), Constitutive modeling of cyclic mobility and implications for site response, *Proceedings, 2nd International Conference on Earthquake Geotechnical Engineering, Lisbon, Portugal*, Vol. 3, pp. 1029-1034.

Kramer, S.L. and Mitchell, R.A. (2006). An efficient and sufficient scalar intensity measure for soil liquefaction. *Earthquake Spectra*, vol. 22, no. 2, pp. 1-26.

Kramer, S.L., Sideras, S.S, and Greenfield, M.W. (2016). The timing of liquefaction and its utility in liquefaction hazard evaluation. *Soil Dynamics and Earthquake Engineering*, vol. 91, pp. 133-146.

Kramer, S.L. and Wang, C.H., (2015). Empirical model for estimation of the residual strength of liquefied soil. *Journal of Geotechnical and Geoenvironmental Engineering*, ASCE, vol. 141, no. 9.

Kwan, W.S. (2015). *Laboratory investigation into evaluation of sand liquefaction under transient loadings*. PhD dissertation, University of Texas, Austin, TX.

Liu, A.H., Stewart, J.P., Abrahamson, N.A. and Moriwaki, Y. (2001). Equivalent number of uniform stress cycles for soil liquefaction analysis. *Journal of Geotechnical and Geoenvironmental Engineering*, ASCE, vol. 127, no. 12, pp. 1017-1026.

Luco, N. and Cornell, C.A. (2007), Structure-specific scalar intensity measures for near-source and ordinary earthquake ground motions, *Earthquake Spectra*, vol. 23, no. 2, pp. 357-392.

Malvick, E.J., Kutter, B.L., and Boulanger, R.W. (2008). Postshaking shear strain localization in a centrifuge model of a saturated slope. *Journal of Geotechnical and Geoenvironmental Engineering*, ASCE vol. 134, no. 2, pp. 164-164.

Manzari, M.T., and Dafalias, Y.F. (1997). A critical state two-surface plasticity model for sands, *Geotechnique*, vol. 49, no. 2, pp. 252-272.

Mayfield, R.T. (2007). *The return period of soil liquefaction*. PhD dissertation, University of Washington, Seattle, WA.

McCaan, M.W., and Shah, H.C. (1979). Determining strong-motion duration of earthquakes. *Bulletin of the Seismological Society of America*, vol. 69, pp. 1253-1265.

McKenna, F., Fenves, G.L., Scott, M.H., and Jeremic, B. (2000). Open System for Earthquake Engineering Simulation (OpenSees), Pacific Earthquake Engineering Research Center, University of California, Berkeley, CA.

Middlebrooks, T.A. (1942). Fort Peck dam slide. *Transcations*, ASCE, vol. 107, pp. 723-764

Moehle, J. and Deierlein, G.G., (2004). A framework methodology for performance-based earthquake engineering, *Proceedings, 13th World Conference on Earthquake Engineering*, Vancouver, B.C. Paper No. 679.

Montgomery, J., Boulanger, R.W., and Harder, L.F., 2012. Examination of the K_σ Overburden Correction Factor on Liquefaction Resistance. Report No. UCD/CGM-12/02, Center for Geotechnical Modeling, University of California, Davis, California, 47 pp.

Moss, R.E.S., Seed, R.B., Kayen, R.E., Stewart, J.P., and Der Kiureghian, A. (2006). Probabilistic seismic soil liquefaction triggering using the CPT. *Journal of Geotechnical and Geoenvironmental Engineering*, ASCE, vol. 132, no. 8

Mulilis, J.P, Chan, C.K., and Seed, H.B. (1975). *The effects of method of sample preparation on the cyclic stress-strain behavior of sands*. Report No. EERC 75-18, Earthquake Engineering Research Center, University of California, Berkeley, Calif., July, 1975.

Nagase, H., and Ishihara, K. (1988). Liquefaction-induced compaction and settlement of sand during earthquakes. *Soils and Foundations*, Tokyo, Japan, vol. 28, no. 1, pp. 66-76.

National Academies of Sciences, Engineering, and Medicine (2016). State of the Art and Practice in the Assessment of Earthquake-Induced Soil Liquefaction and Its Consequences. Washington, DC: The National Academies Press. https://doi.org/10.17226/23474.

Nuttli, O. W. (1979) The relation of sustained maximum ground acceleration and velocity to earthquake intensity and magnitude. Geotechnical Laboratory (U.S.) United States Army Corps of Engineers, Vicksburg, Miss U.S. Army Engineer Waterways Experiment Station

Okamura, M., Ishihara, M., and Oshita, T. (2003). Liquefaction resistance of sand deposit improved with sand compaction piles. *Soils and Foundations,* Japanese Geotechnical Society, vol. 43, no. 5, pp. 175-187.

Olson, S.M. and Stark, T.D. (2002). Liquefied strength ratio from liquefaction flow case histories, *Canadian Geotechnical Journal*, vol. 39, pp.629-647.

Park, Y., Alfredo, H.S.A., and Wen, Y.K. (1985). Seismic damage analysis of reinforced concrete buildings. *Journal of Structural Engineering*, vol. 111, pp. 740-757.

Park, S.S., and Byrne, P.M. (2004). Stress densification and its evaluation. *Canadian Geotechnical Journal*, vol. 41, pp. 181-186.

Poulos, S.J. (1981). The steady state of deformation. *Journal of the Geotechnical Engineering Division,* ASCE, vol.107, no. GT5, pp. 553-562

Prevost, J.H. (1985). A simple plasticity theory for frictional cohesionless soils, *Soil Dynamics and Earthquake Engineering*, vol. 4, no. 1, 9-17.

Rauch, A.F., and Martin, J.R. (2000). EPOLLS model for predicting average displacements on lateral spreads, *Journal of Geotechnical and Geoenvironmental Engineering*, vol 126, no. 4, pp. 360-371.

Riemer, M.F., Gookin, W.B., Bray, J.D., and Arango, I. (1994). Effects of loading frequency and control on the liquefaction behavior of clean sands, Geotechnical Engineering Report No. UCB/GT/94-07, University of California, Berkeley, Calif.

Robertson, P.K. and Wride, C.E. (1998). Evaluating cyclic liquefaction potential using cone penetration tests. *Canadian Geotechnical Journal*, vol 35, no. 3, pp. 442-459.

Rollins, K.M. and Mchood, M.D. (1994). Ground response on Treasure Island. *The Loma Prieta, California, earthquake of October 17, 1989—strong ground motion*. USGS Professional Paper 1551-A, Borcherdt, ed.

Rollins, K.M., Mchood, M.D., Hryciw, R.D. and Homolka, M. (1994). The Loma Prieta, California, earthquake of October 17, 1989—strong ground motion. US Geological Survey Professional Paper 1551-A, R.D. Borcherdt ed., pp. A109-A121.

Sarma, S.K., and Yang, K.S. (1987). An evaluation of strong motion records and a new parameter A95, *Earthquake Engineering and Structural Dynamics*, vol. 15 pp. 119-132.

Seed, H.B. (1979). Soil liquefaction and cyclic mobility evaluation for level ground during earthquakes. *Journal of the Geotechnical Engineering Division*, vol. 105, no. GT2, pp. 210-255.

Seed, H.B. (1987). Design problems in soil liquefaction. *Journal of the Geotechnical Engineering Division*, ASCE vol. 103, no. GT7, pp. 757-768.

Seed, H.B. and Harder, L.F. (1990). SPT-based analysis of cyclic pore pressure degradation and undrained residual strength, *Proc. H.B. Seed Memorial Symposium*, Bi-Tech Publishing Ltd., Vol. 2, pp. 351-376

Seed, H.B and Idriss, I.M. (1971). Simplified procedure for evaluating soil liquefaction potential. *Journal of the Soil Mechanics and Foundations Division*, ASCE, vol. 93, no. 3, pp. 83-108

Seed, H.B, Idriss, I.M., Makdisi, F. and Banerjee, N. (1975). Representation of irregular stress time histories by equivalent uniform stress time series in liquefaction analysis. *Rep. No. UCB/EERC 75-29*, Earthquake Engineering Research Center, University of California, Berkeley, CA.

Seed, H.B. and Idriss, I.M. (1982). *Ground motions and soil liquefaction during earthquakes*. Earthquake Engineering Research Institute, Oakland, California.

Seed, H.B., Idriss, I.M., and Arango, I. (1983). Evaluation of liquefaction potential using field performance data. *Journal of Geotechnical Engineering*, ASCE vol. 109, no. 3.

Seed, H.B., and Lee, K.L., (1966). Liquefaction of saturated sands during cyclic loading. *Journal of the Soil Mechanics and Foundations Division,* ASCE, vol. 92, no., SM6, pp. 105-134

Seed, H. B., Martin, P. P., and Lysmer, J. (1975). The generation and dissipation of pore water pressures during soil liquefaction. Rep. No. EERC 75-26, Univ. of California, Berkeley, Calif.

Seed, H.B., Tokimatsu, K., Harder, L.F., and Chung, R. (1984). *The influence of SPT procedures on soil liquefaction resistance evaluations*, Report No. UCB/EERC-84/15, Earthquake Engineering Research Center, University of California, Berkeley, CA.

Shahir, H., Pak, A., Taibat, M., and Jeremic, B. (2011). Evaluation of variation of permeability in liquefiable soil under earthquake loading. *Computers and Geotechnics*, vol. 40, pp. 74-88.

Shnabel, P.B., Lysmer, J., and Seed, H.B. (1972). SHAKE: a computer program for earthquake response analysis of horizontally layered sites. Report No. UCB/EERC-72-12, Earthquake Engineering Research Center, University of California, Berkeley, CA

Skempton, A.W. (1957). Discussion on the planning and design of the new Hong Kong airport. *Proc. Inst. Civil Engrs*., vol. 7, pp. 305-307.

Steedman, R.S. and Zeng, X. (1995). Dynamics. *Geotechnical centrifuge technology*, R.N. Taylor, ed., Chapman and Hall, London, UK.

Stewart, D.P., Chen, Y.R., and Kutter, B.L. (1998). Experience with the use of methylcellulose as a viscous pore fluid in centrifuge models. *Geotechnical Testing Journal*, vol. 21, no. 4, pp. 365-369.

Terzaghi, K. (1925). Erdbaumechanik auf Bodenphysikalishcer Grundlage, Franz Deuticke, Liepzig, und Wein, 399 pp.

Teymur, B., and Madabhushi, S.P.G. (2003). Experimental study of the boundary effects in dynamic centrifuge modeling. *Geotechnique*, vol. 53, no. 7, pp. 655-663.

Tokimatsu, K., and Yoshimi, Y. (1983). Empirical correlation of soil liquefaction based on SPT N-value and fines content. *Soils and Foundations*, vol. 23, no. 4, pp. 56-74.

Tokimatsu K., and Seed, H.B. (1987). Evaluation of settlements in sands due to earthquake shaking. *Journal of the Geotechnical Engineering Division*, ASCE, vol. 113, no. 8, pp. 861-878.

Travasarou, T., Bray J.D. and Abrahamson, N.A. (2003). Empirical attenuation relationships for Arias intensity. *Earthquake Engineering and Structural Dynamics*, vol. 32, pp. 1133-1155.

Vaid, Y.P., and Chern, J.C. (1985). Cyclic and monotonic undrained response of saturated sands. *Soils and Foundations,* vol. 23, no. 1, pp.47-60

Yang, Z., Elgamal, A., and Parra, E. (2003). Computational model for cyclic mobility and associated shear deformation. *Journal of Geotechnical and Geoenvironmental Engineering*. vol 129, pp. 1119-1127.

Yang, Z., Lu, J., and Elgamal, A. (2008). *OpenSees Soil Models and Solid-Fluid Fully Coupled Elements: User's Manual*, Department of Structural Engineering, University of California, San Diego.

Youd, T.L. (1991). Mapping of earthquake-induced liquefaction for seismic zonation. *Proceedings, 4th International Conference on Seismic Zonation*, Earthquake Engineering Research Institute, Stanford University, vol. 1, pp. 111-147

Youd, T.L., Hansen, C.M., and Bartlett, S.F. (2002). Revised multilinear regression equations for prediction of lateral spread displacement, *Journal of Geotechnical and Geoenvironmental Engineering*, ASCE vol. 128, no. 12, pp. 1007-1017.

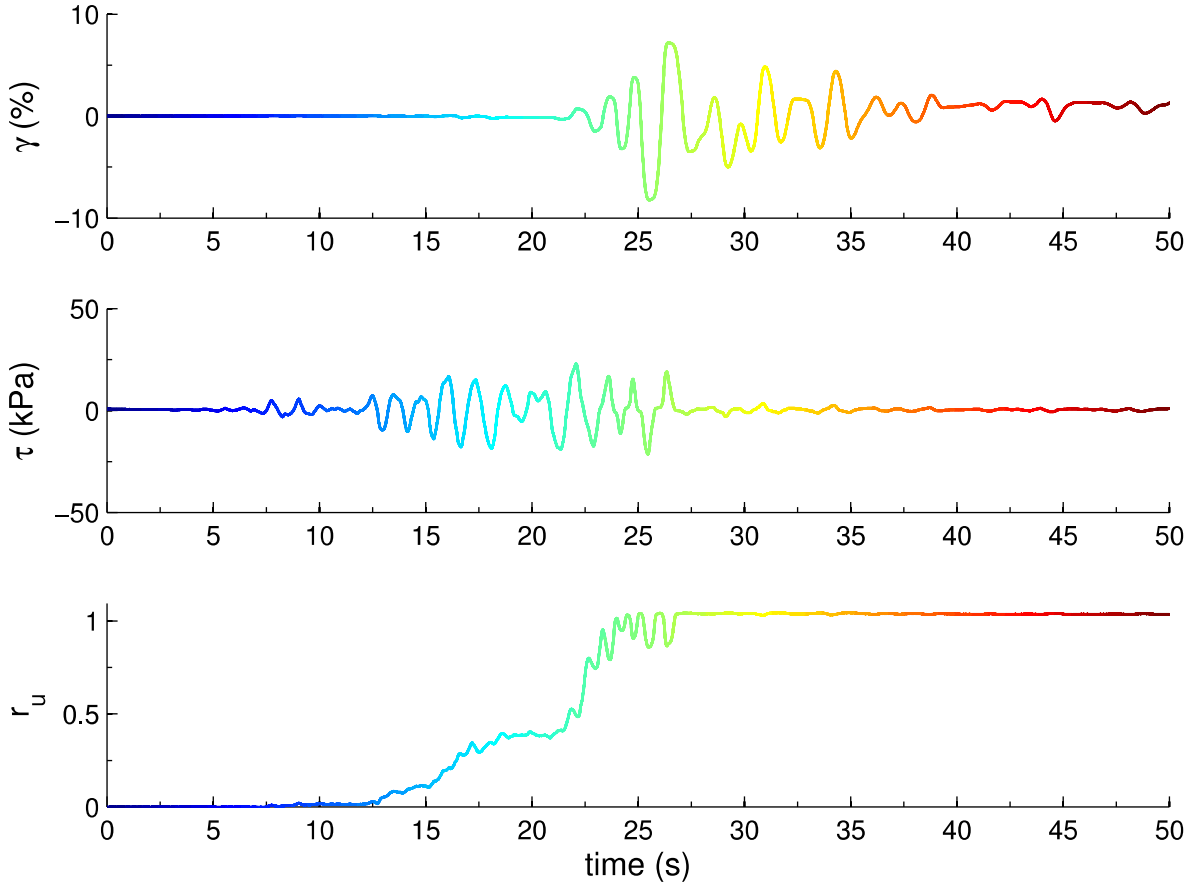
Youd, T.L., Idriss, I.M., Andrus, R.D., Arango, I., Castro, G., Christian, J.T., Dobry, R., Finn, W.D.L., Harder, L.F., Hynes, M.E., Ishihara, K., Koester, J.P., Liao, S.S.C., Marcuson, W.F., Martin, G.R., Mitchell, J.K., Moriwaki, Y., Power, M.S., Robertson, P.K., Seed, R.B. and Stokoe, K.H. (2001). Liquefaction resistance of soils: summary report from the 1996 NCEER and 1998 NCEER/NSF workshops on evaluation of liquefaction resistance of soils. *Journal of geotechnical and geoenvironmental engineering*, ASCE vol. 127, no. 10, pp.817-833.

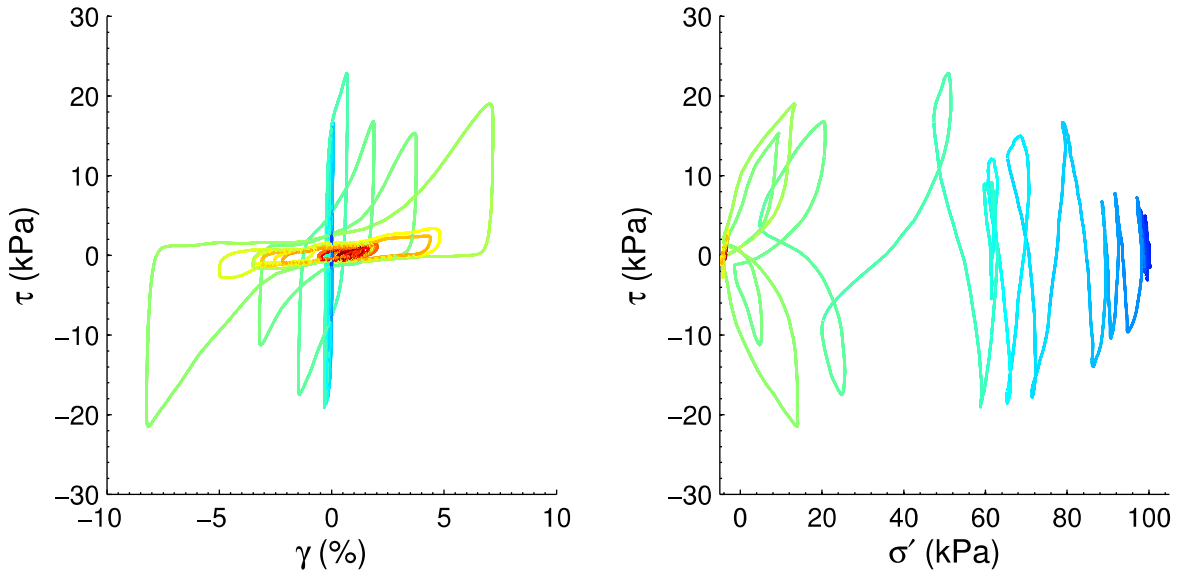
Zeghal, M., Elgamal, A.W., Parra, E. (1996). Identification and modeling of earthquake ground response—II. Site liquefaction. *Soil Dynamics and Earthquake Engineering*, vol. 15, pp.523-547.

Zhang, R.R., (2009). A recording based approach for identifying seismic site liquefaction and nonlinearity via HHT data analysis. *Advances in Adaptive Data Analysis,* vol. 1, no.1, 89-123.

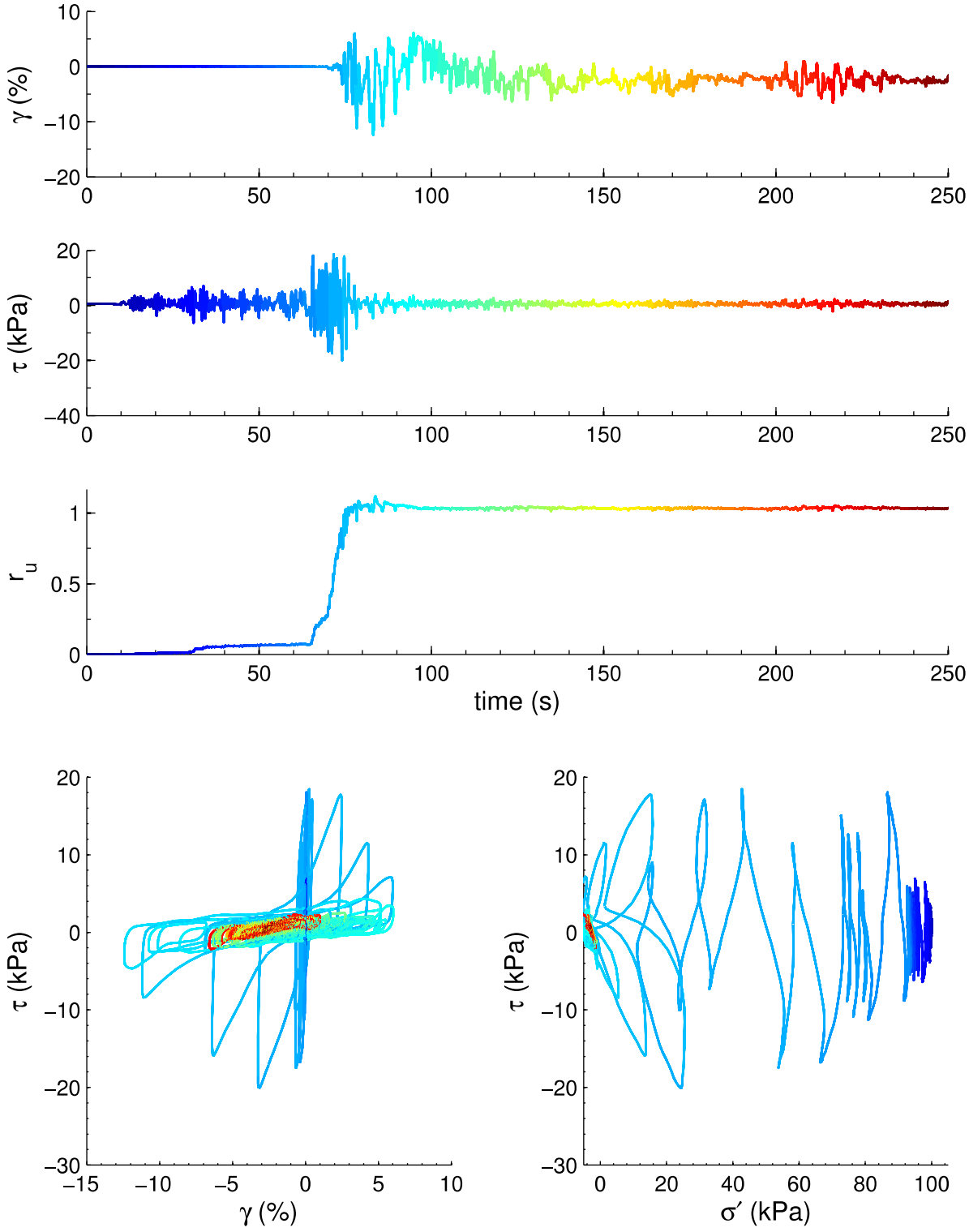
Ziotopoulou, K. and Boulanger, R.W. (2016). Plasticity modeling of liquefaction effects under sloping ground and irregular cyclic loading conditions. *Soil Dynamics and Earthquake Engineering*, vol. 84, pp. 269-283.

APPENDIX A: TRANSIENT CYCLIC DIRECT SIMPLE SHEAR TEST SUMMARIES

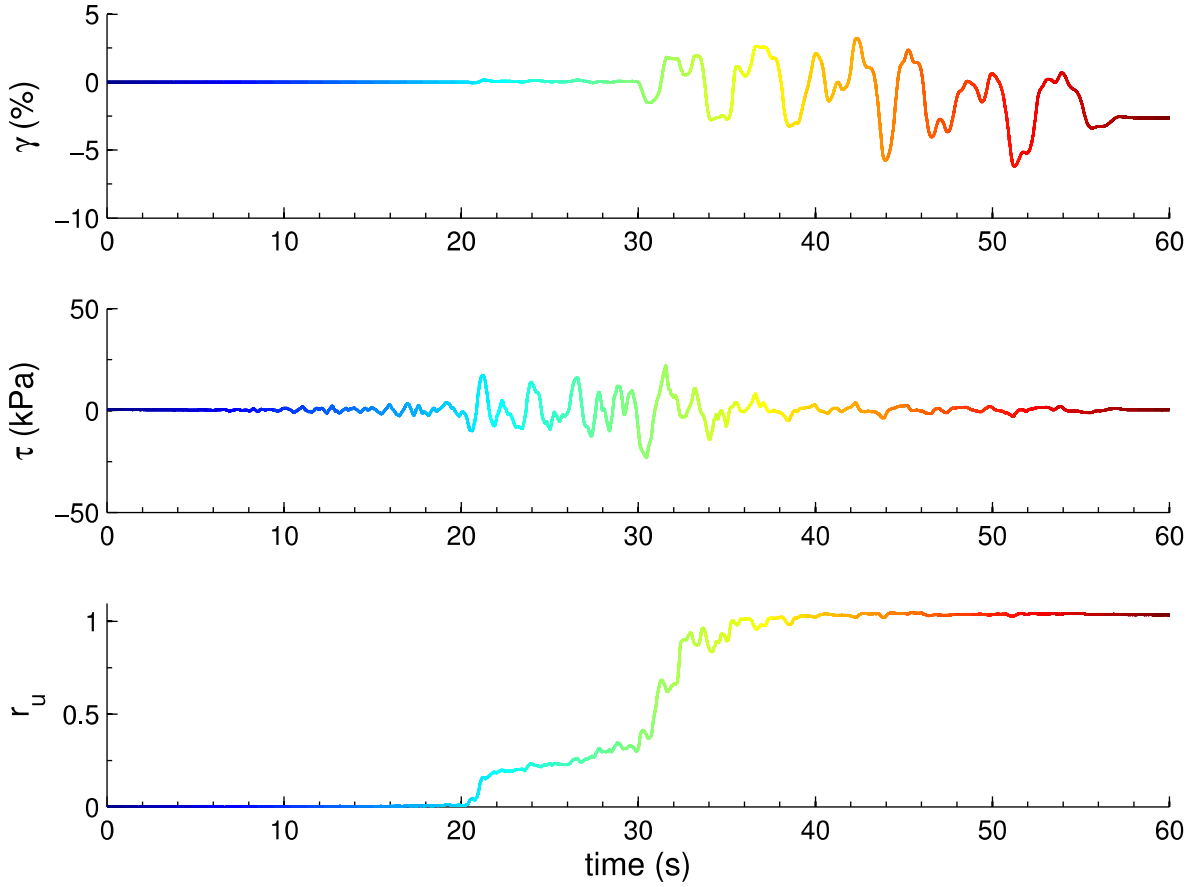


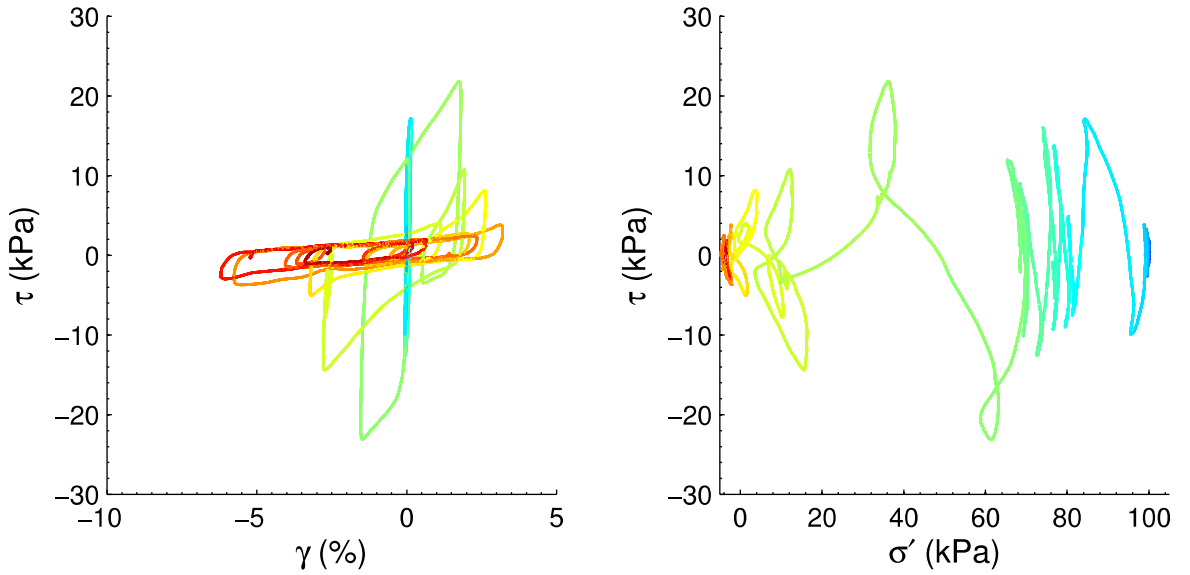


CSS Test 130118 – Data Summary Plot

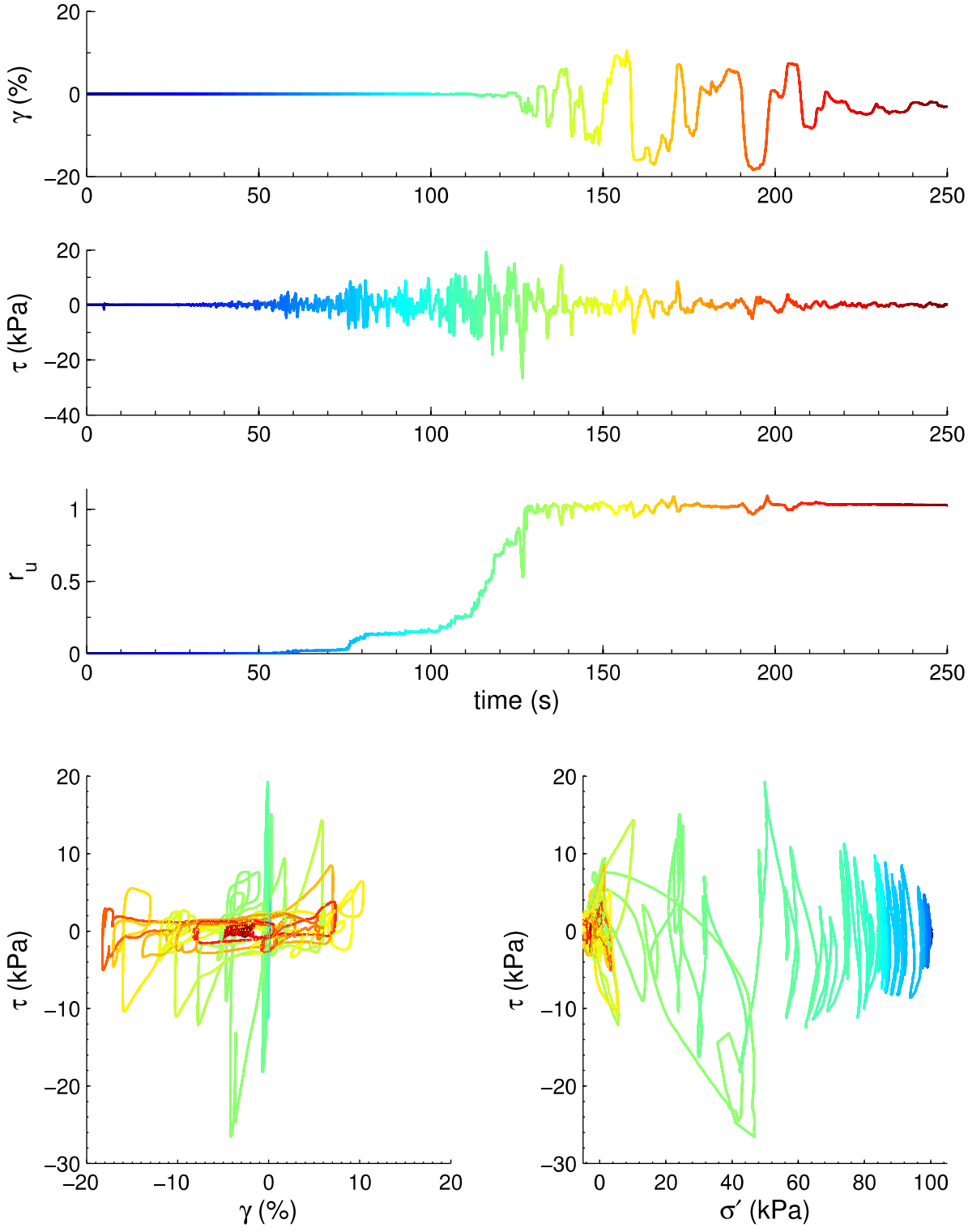


CSS Test 130119 – Data Summary Plot

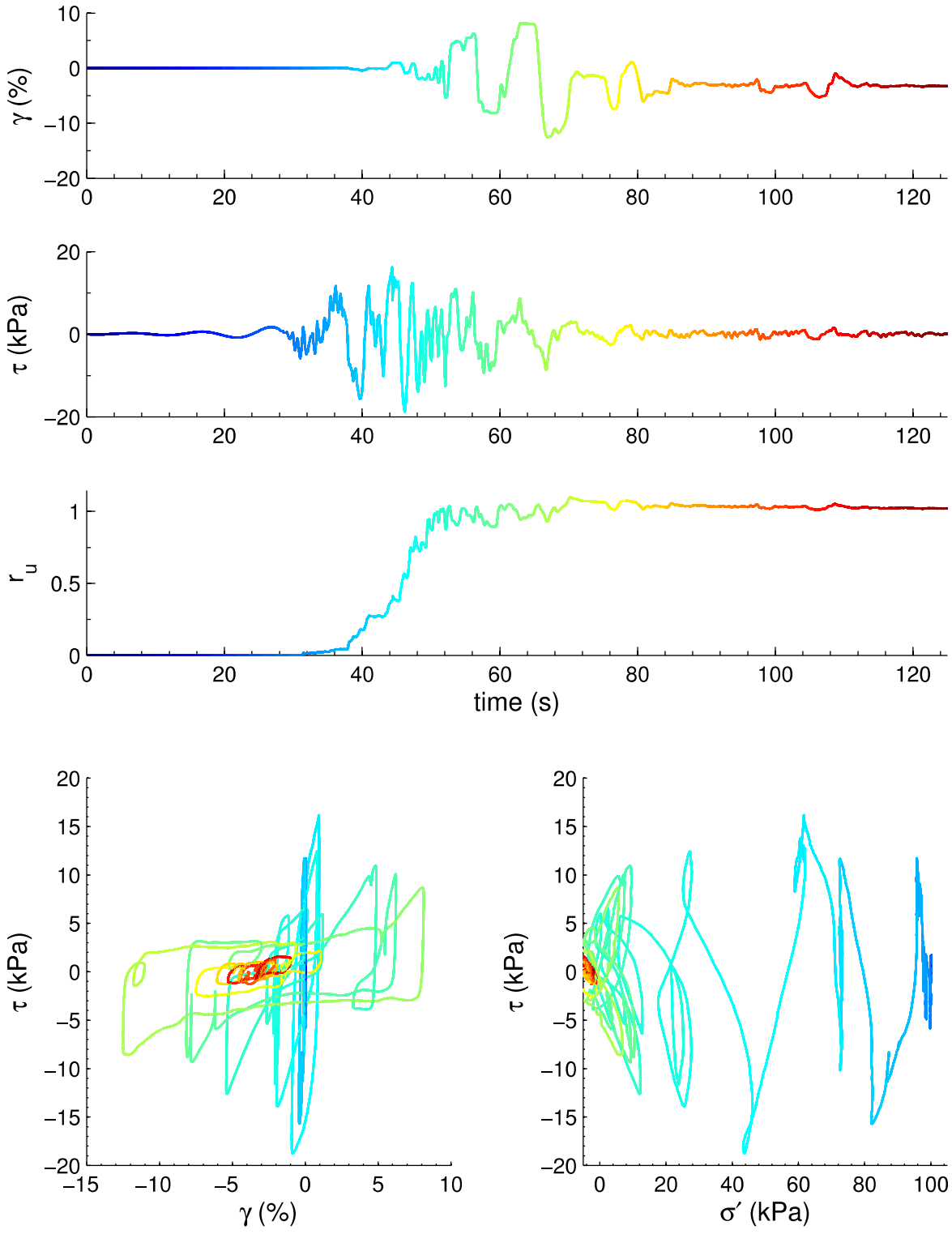




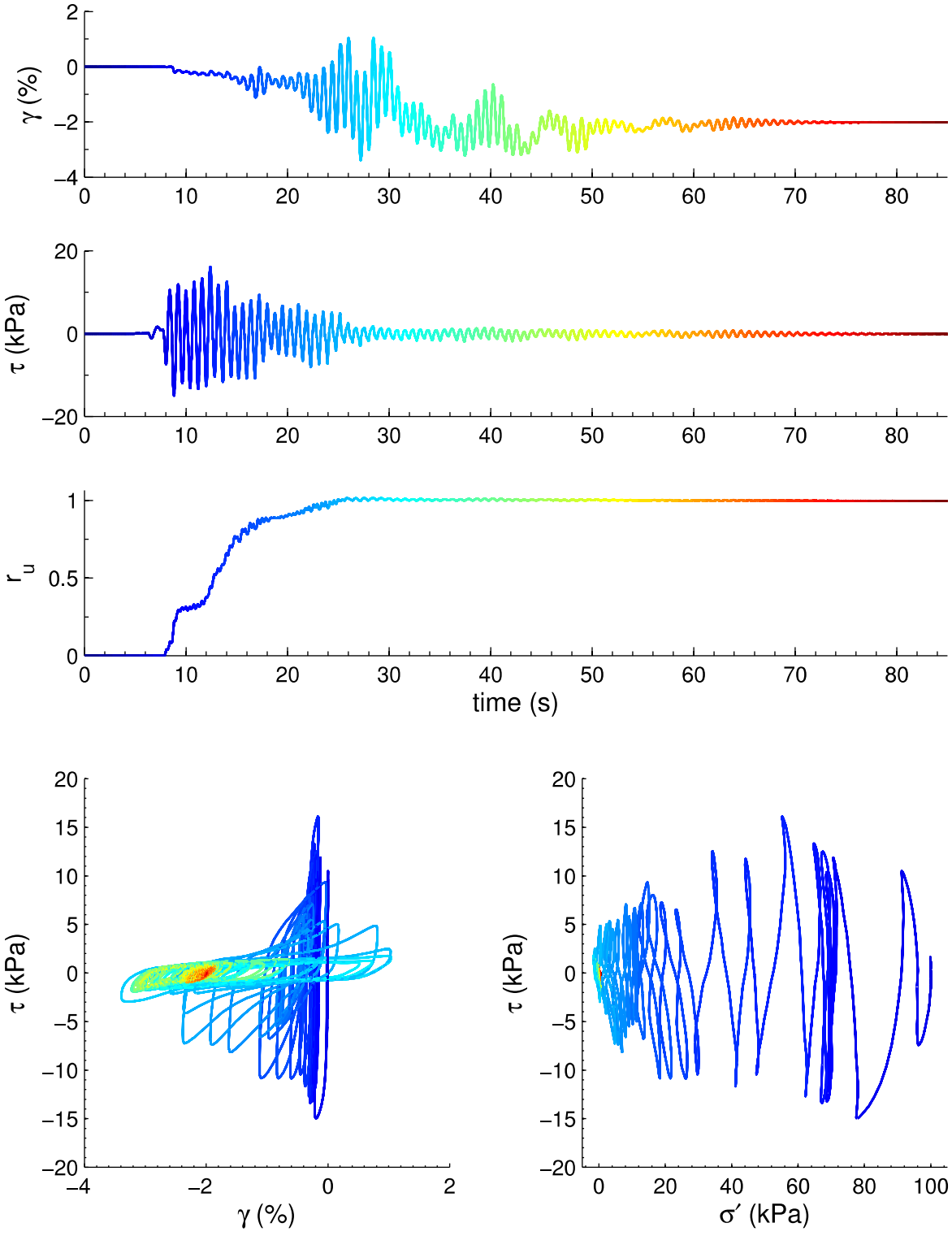
CSS Test 130209 – Data Summary Plot



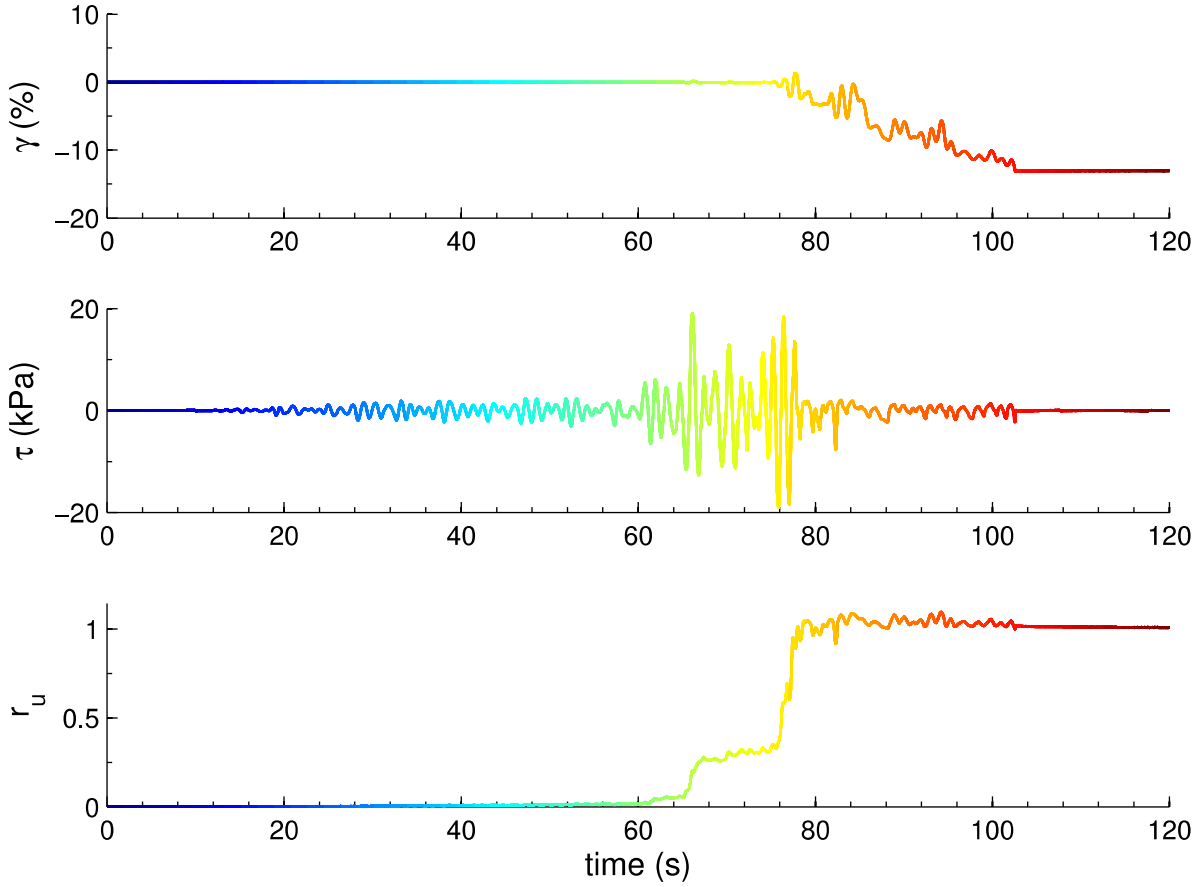
CSS Test 130215–02 – Data Summary Plot

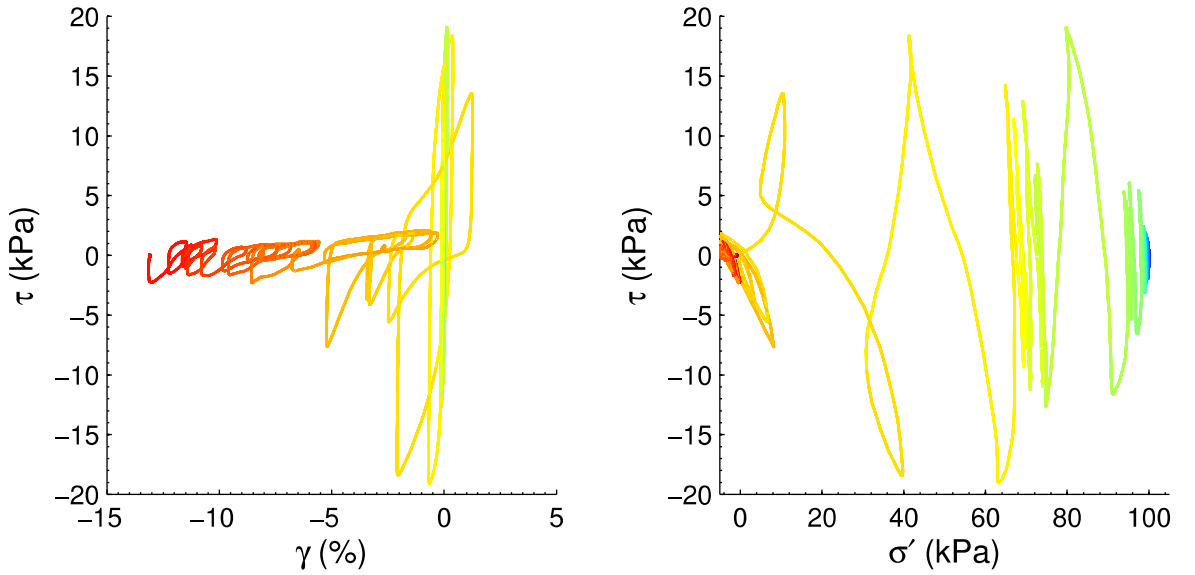


CSS Test 130306 – Data Summary Plot

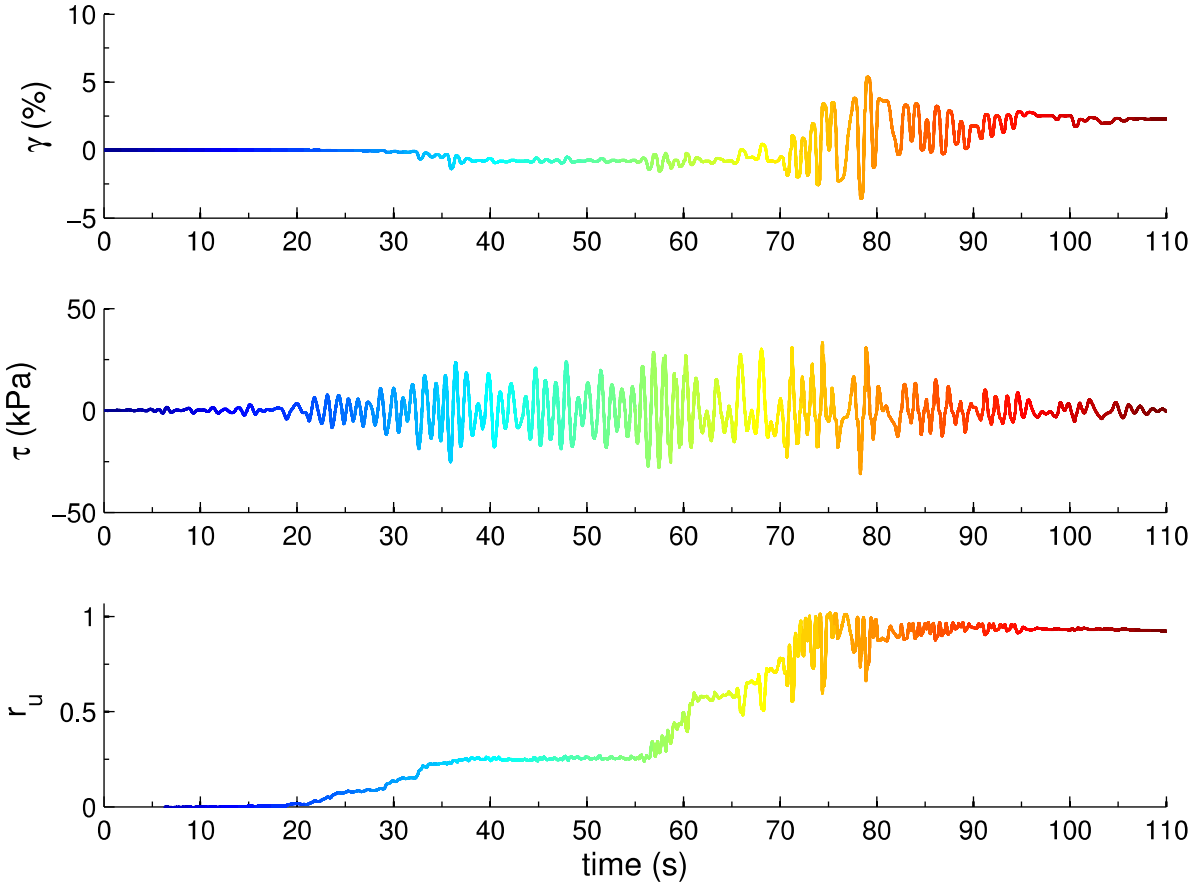


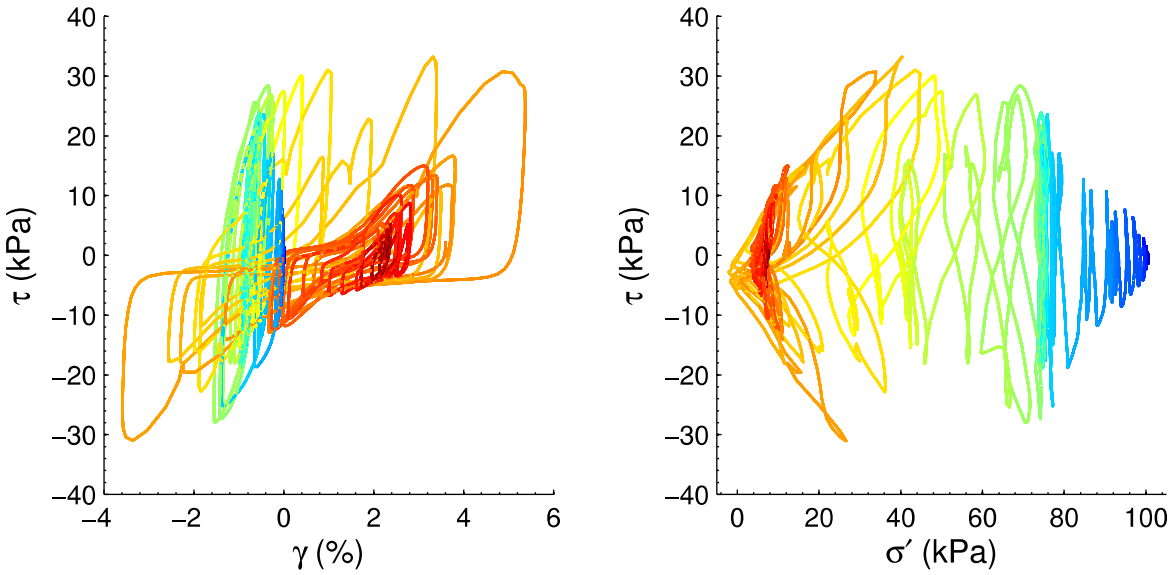
CSS Test 130401 – Data Summary Plot



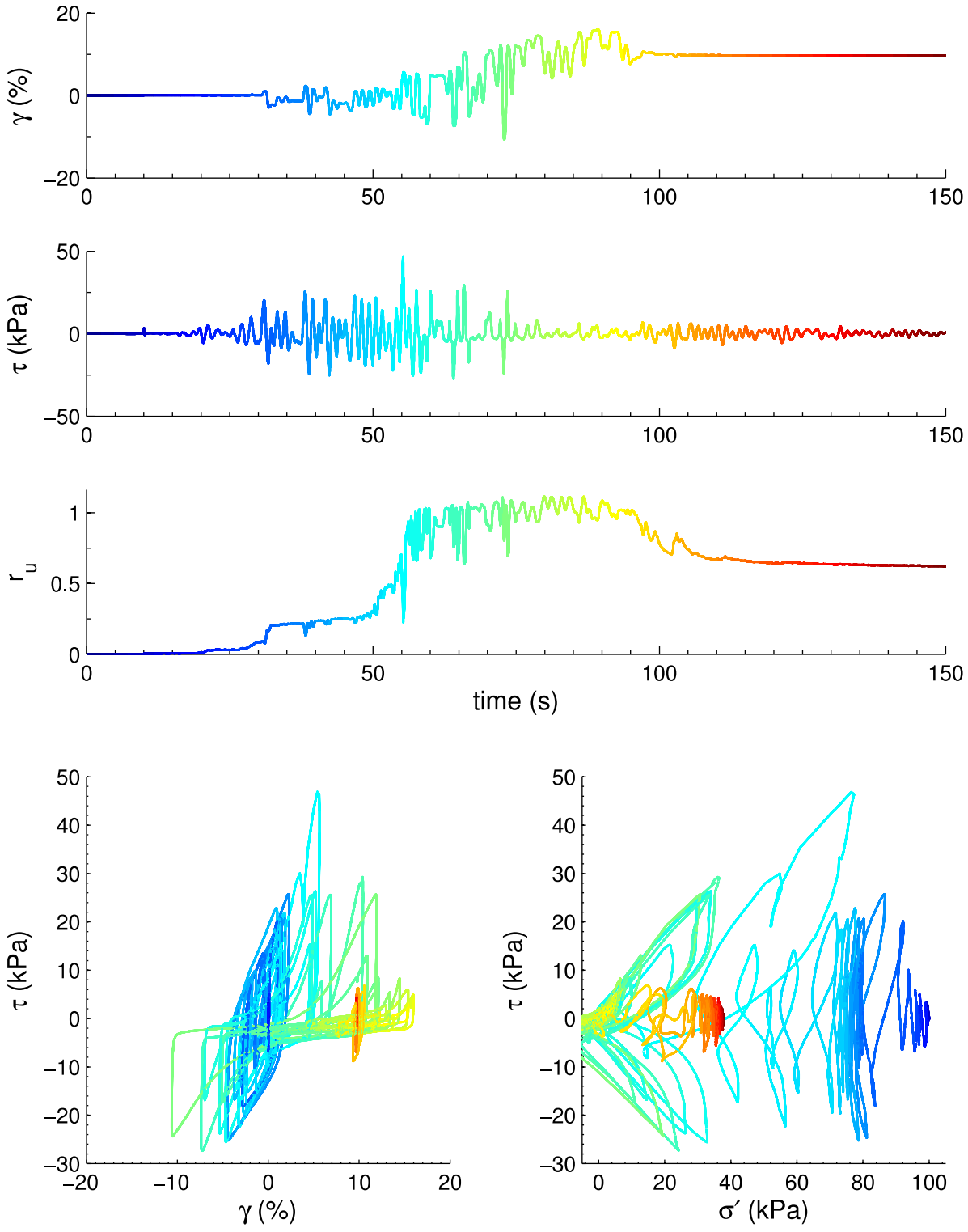


CSS Test 130628 – Data Summary Plot

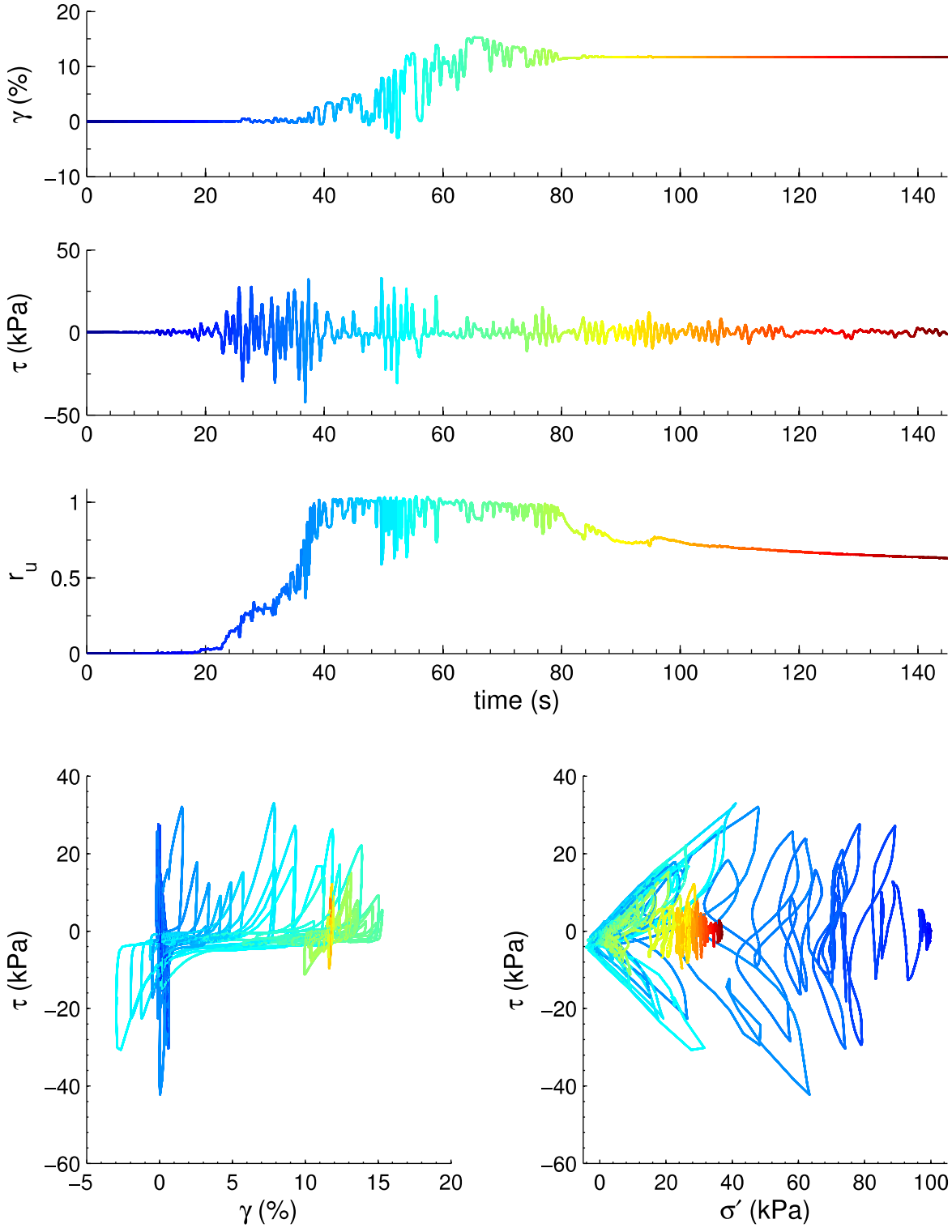




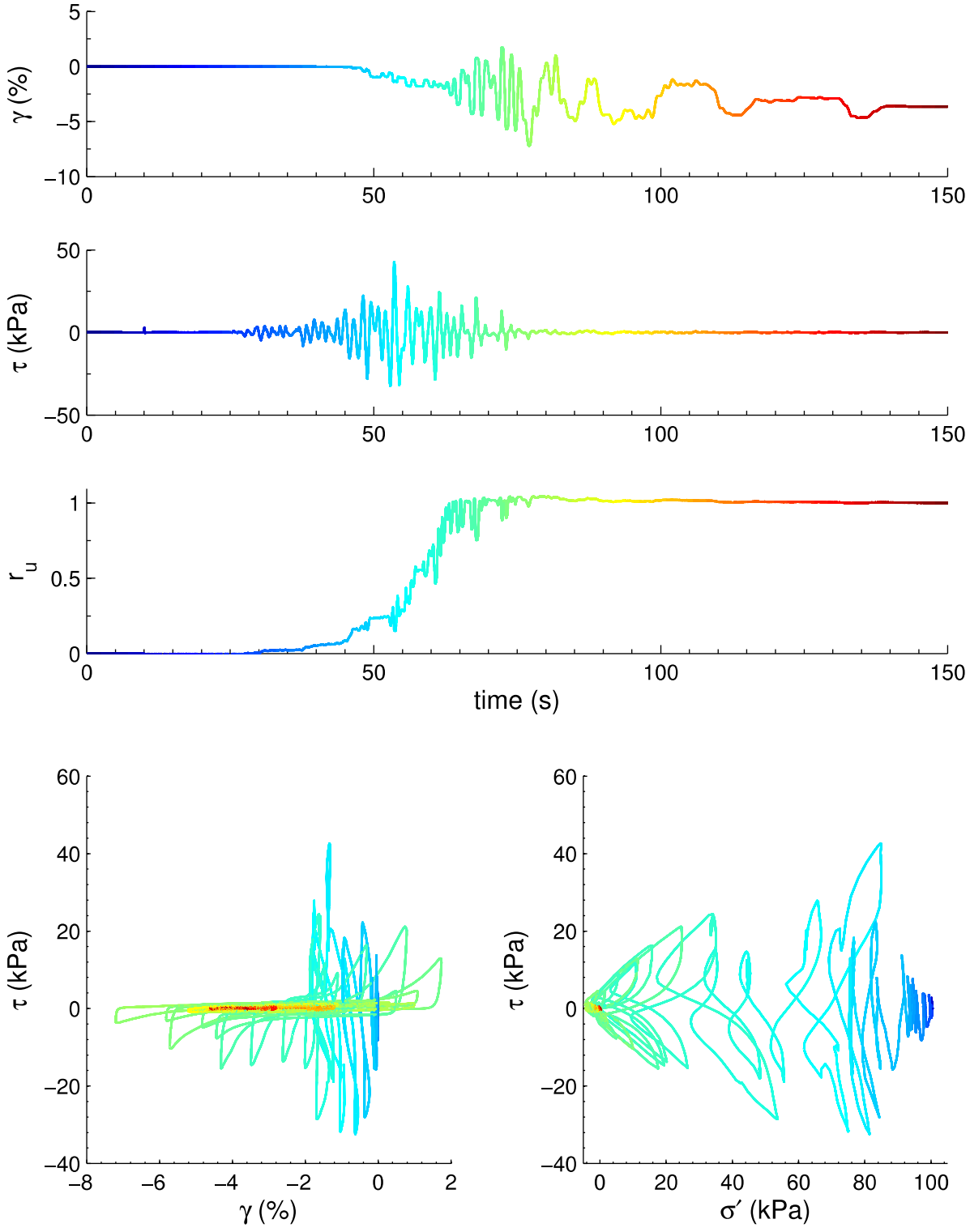
CSS Test 130711–02 – Data Summary Plot



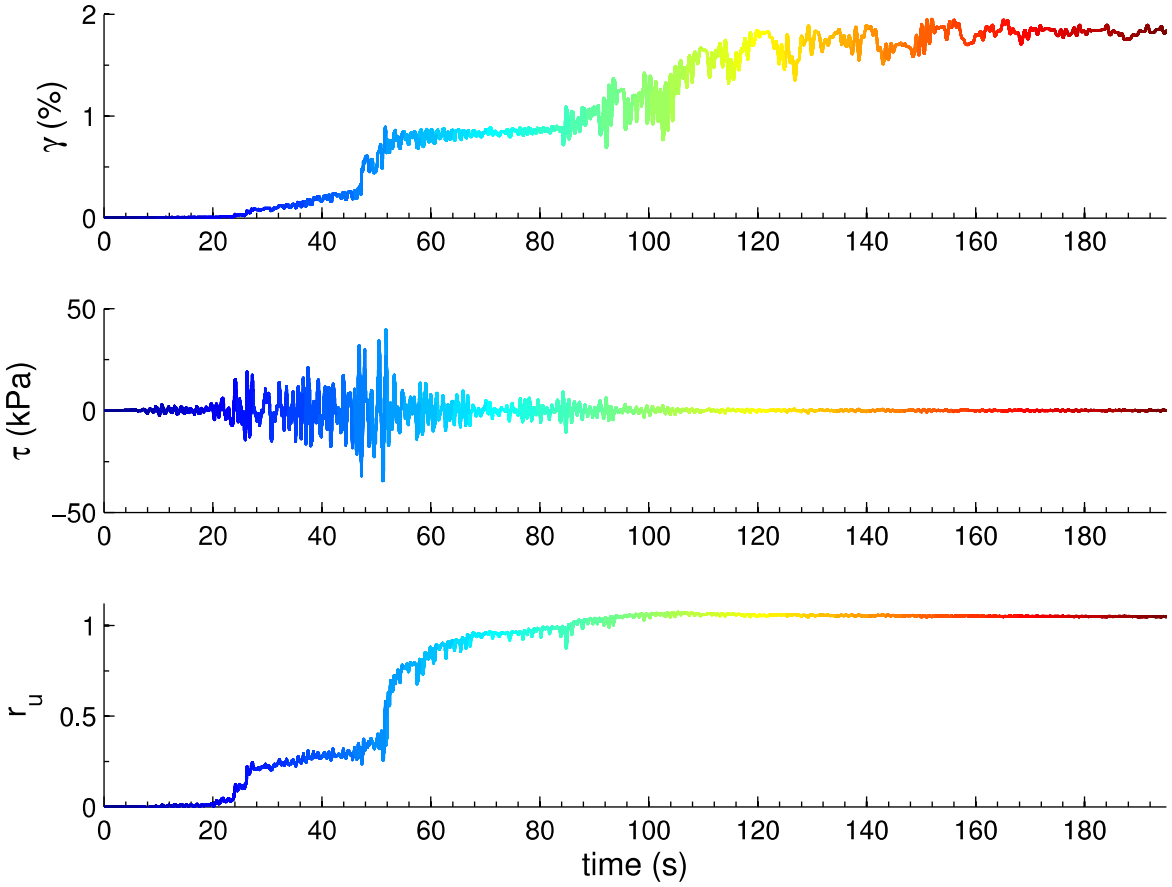
CSS Test 130726–02 – Data Summary Plot

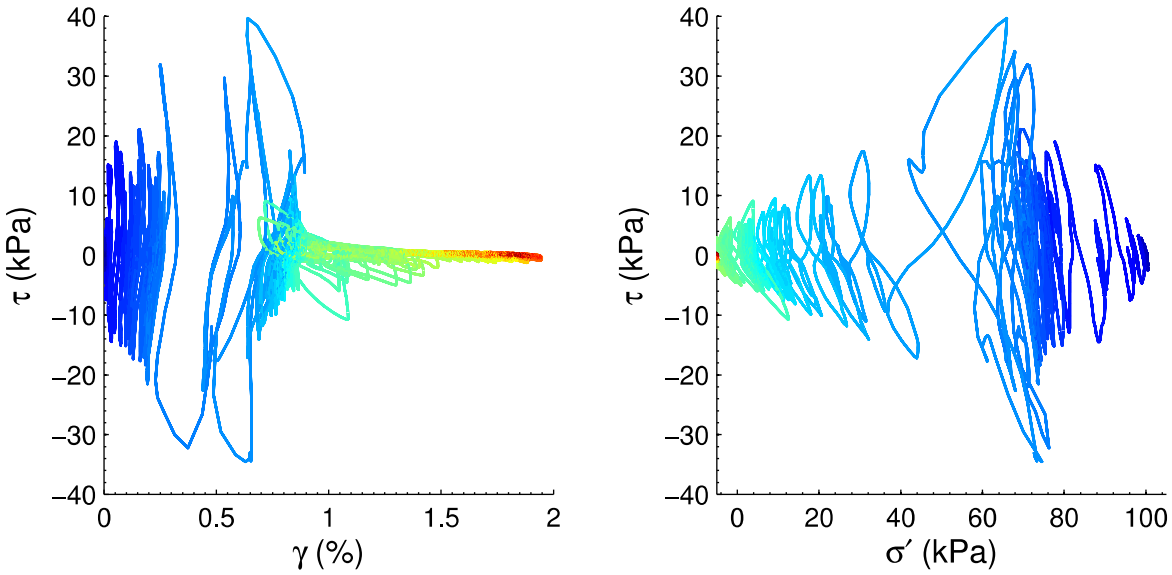


CSS Test 130727 – Data Summary Plot

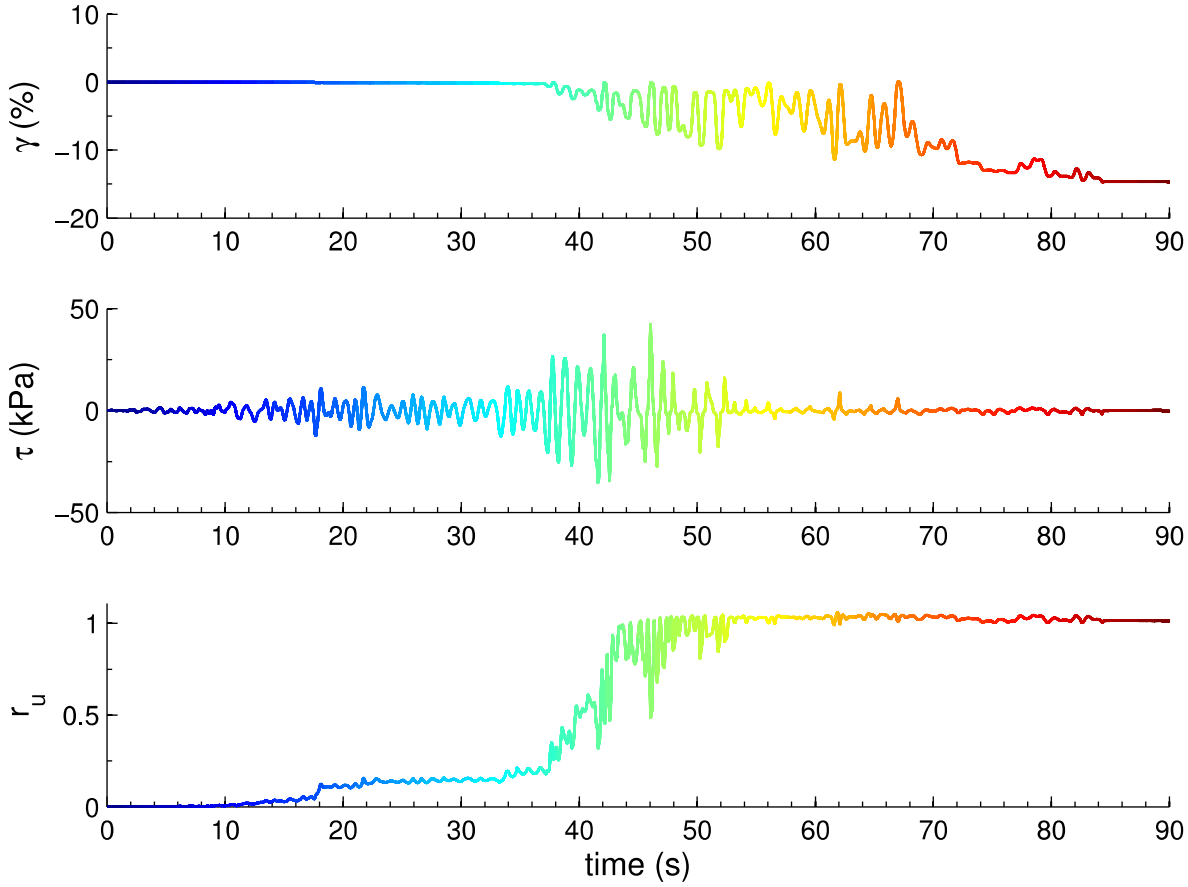


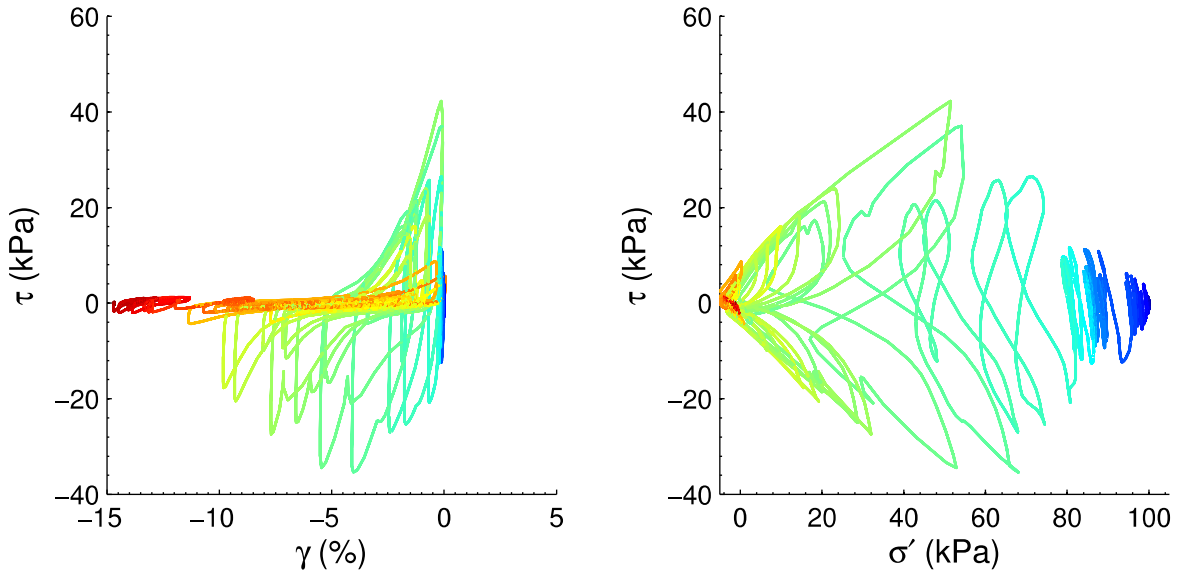
CSS Test 130809–02 – Data Summary Plot



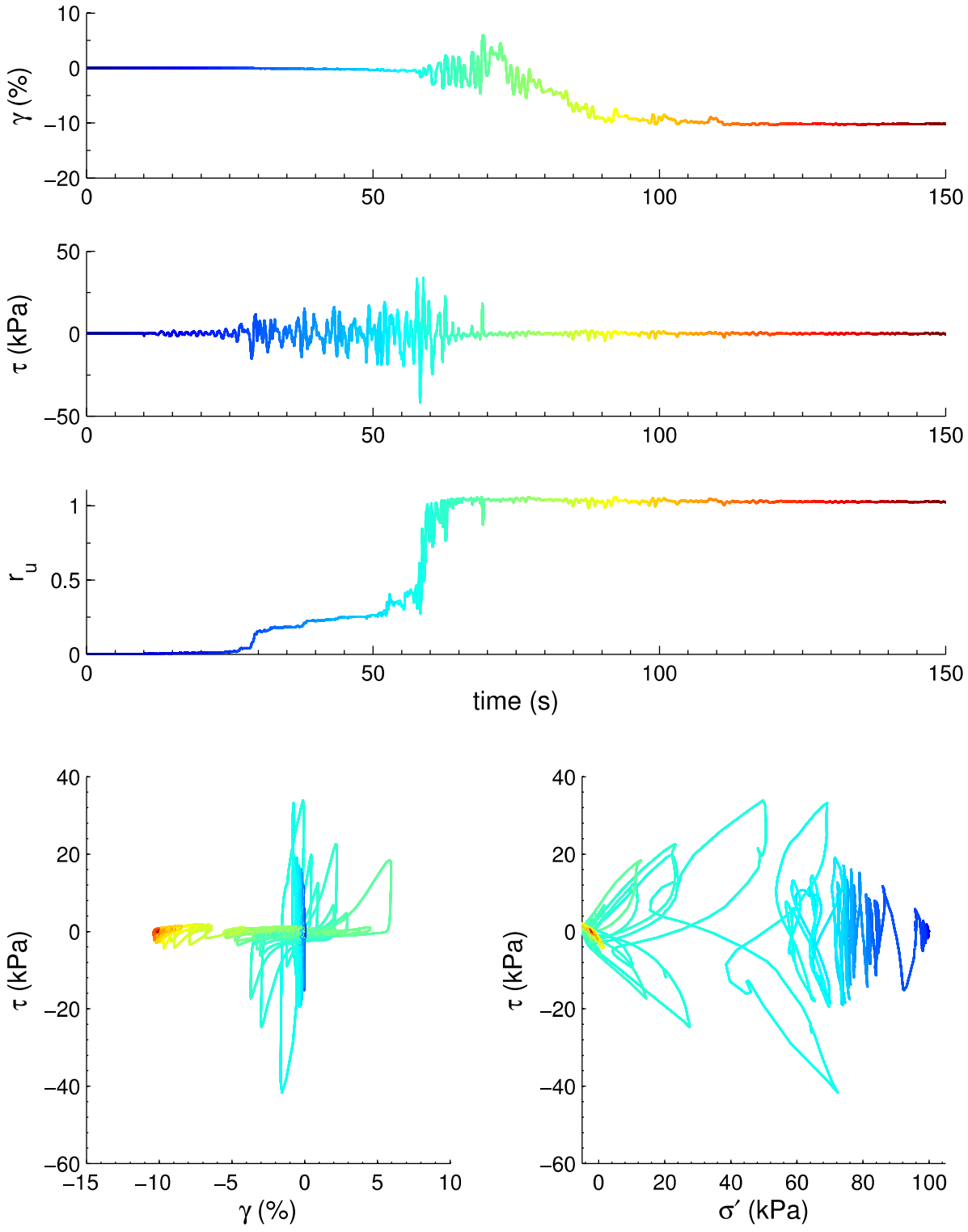


CSS Test 130821 – Data Summary Plot

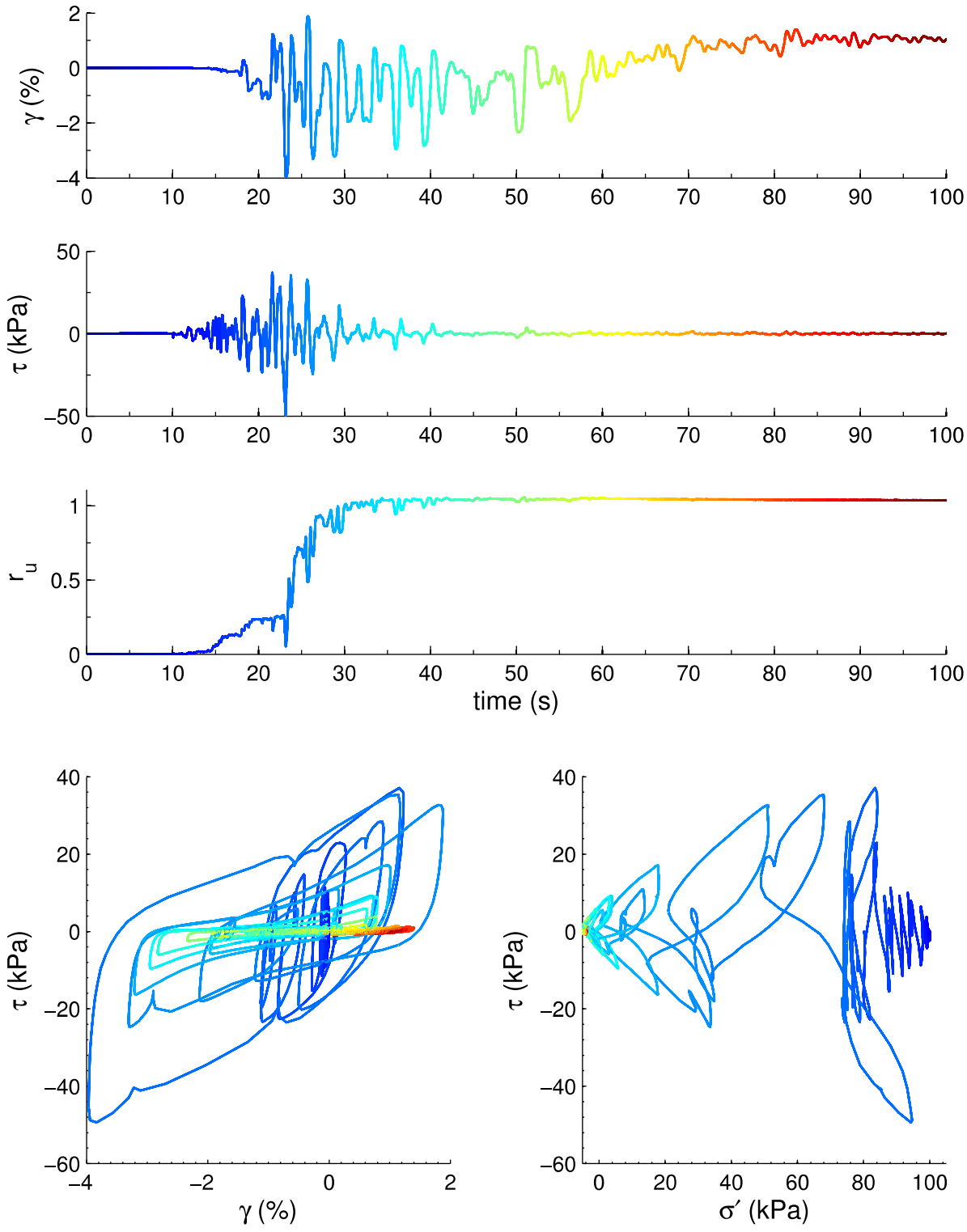




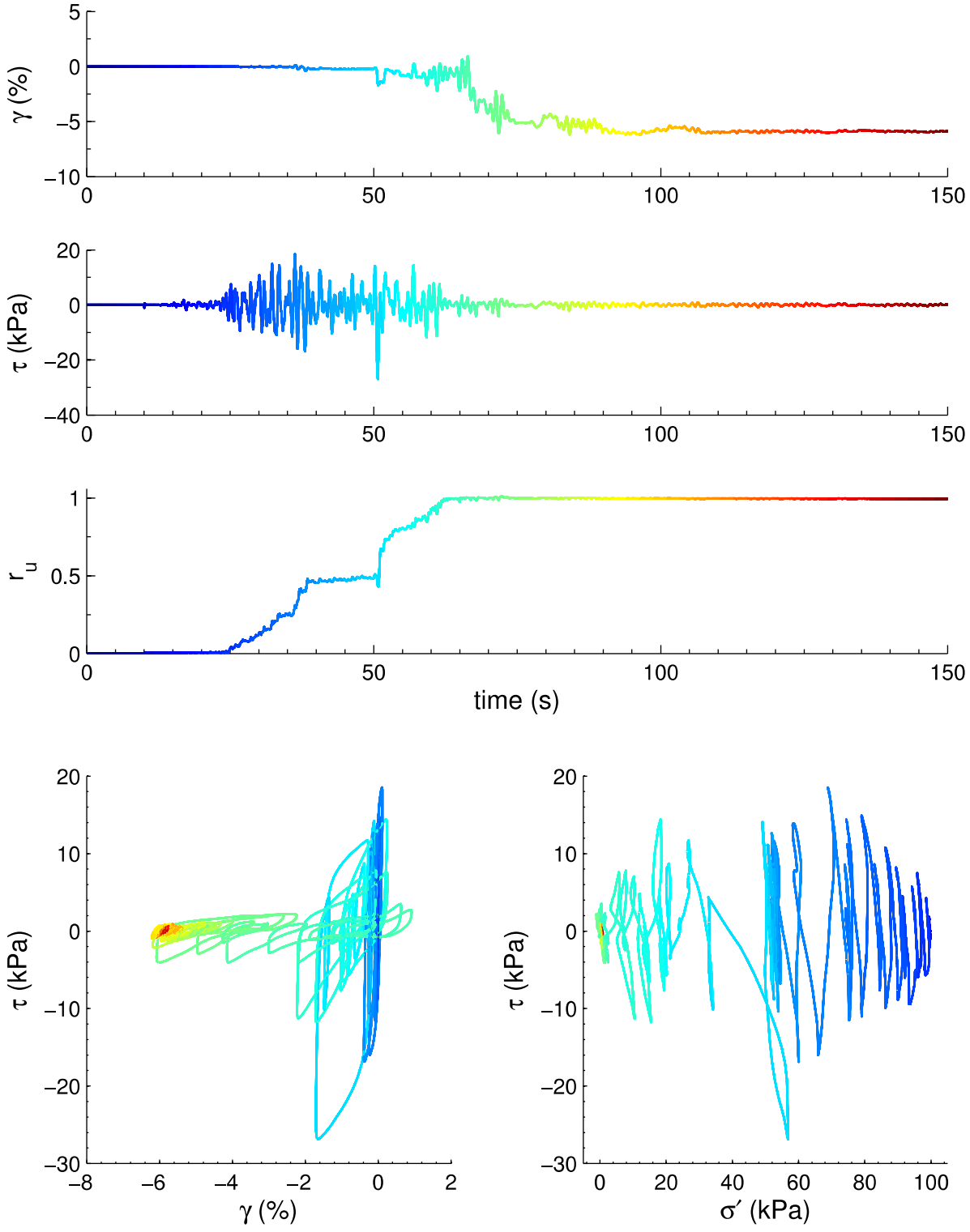
CSS Test 130827–02 – Data Summary Plot



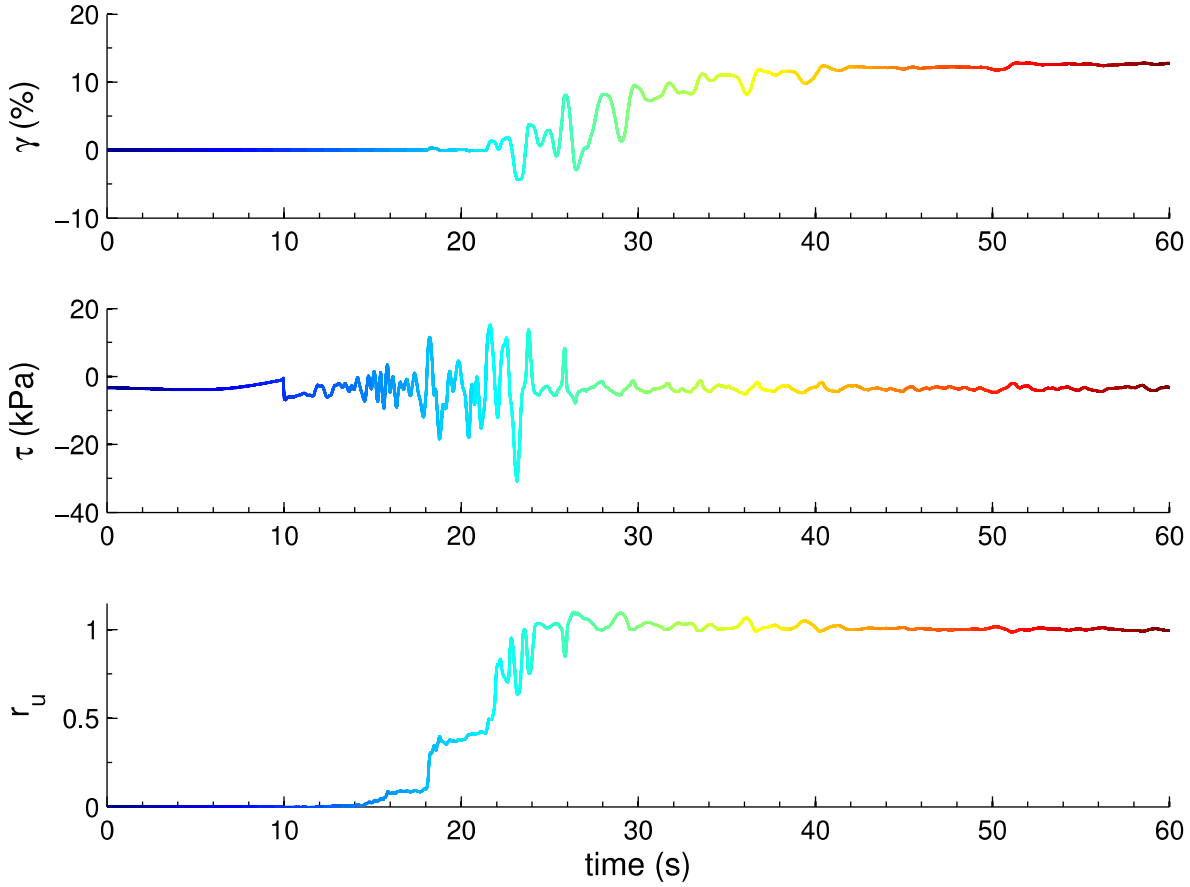
CSS Test 130829–02 – Data Summary Plot

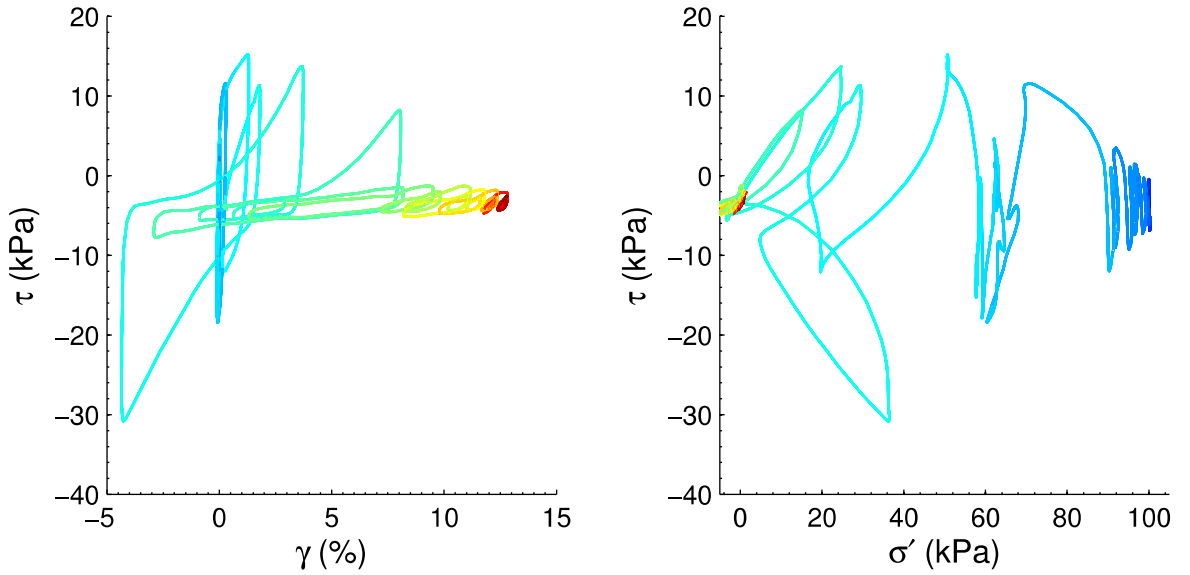


CSS Test 130905–02 – Data Summary Plot

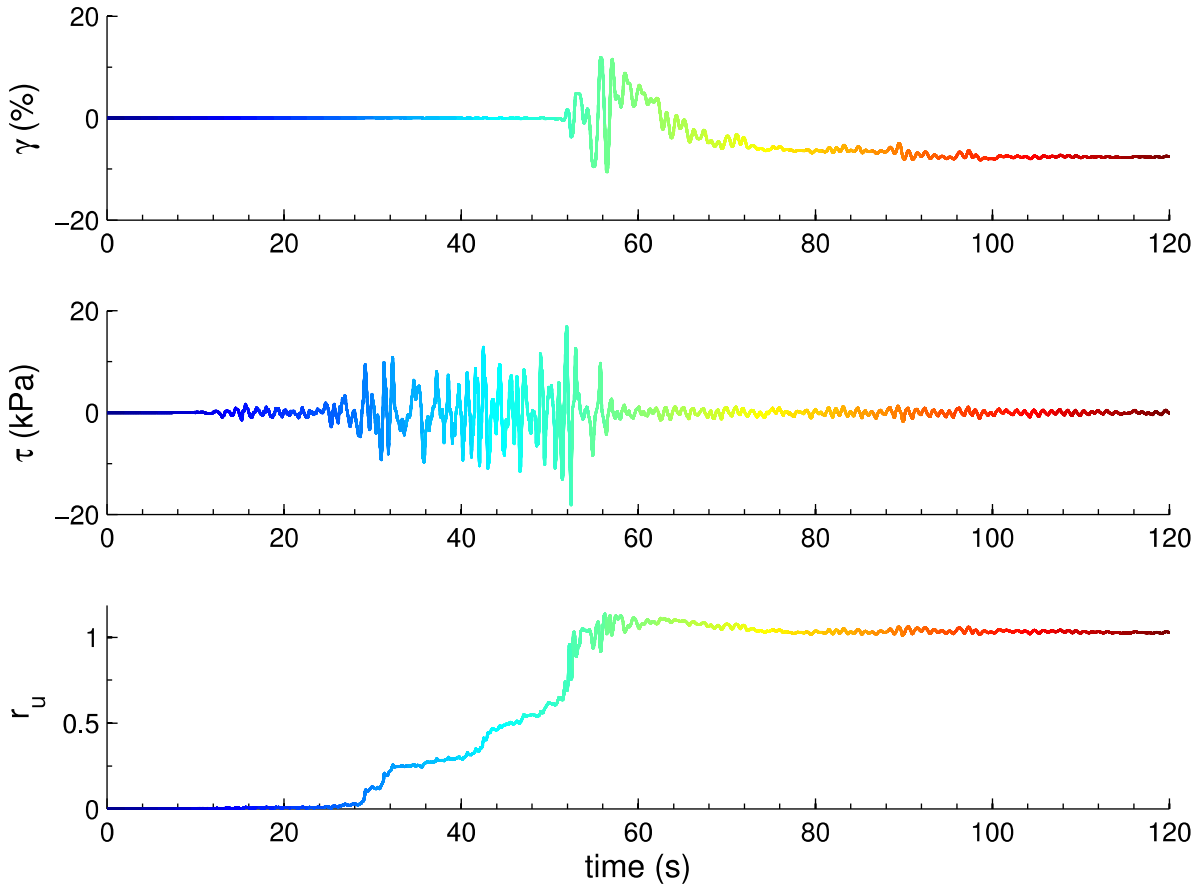


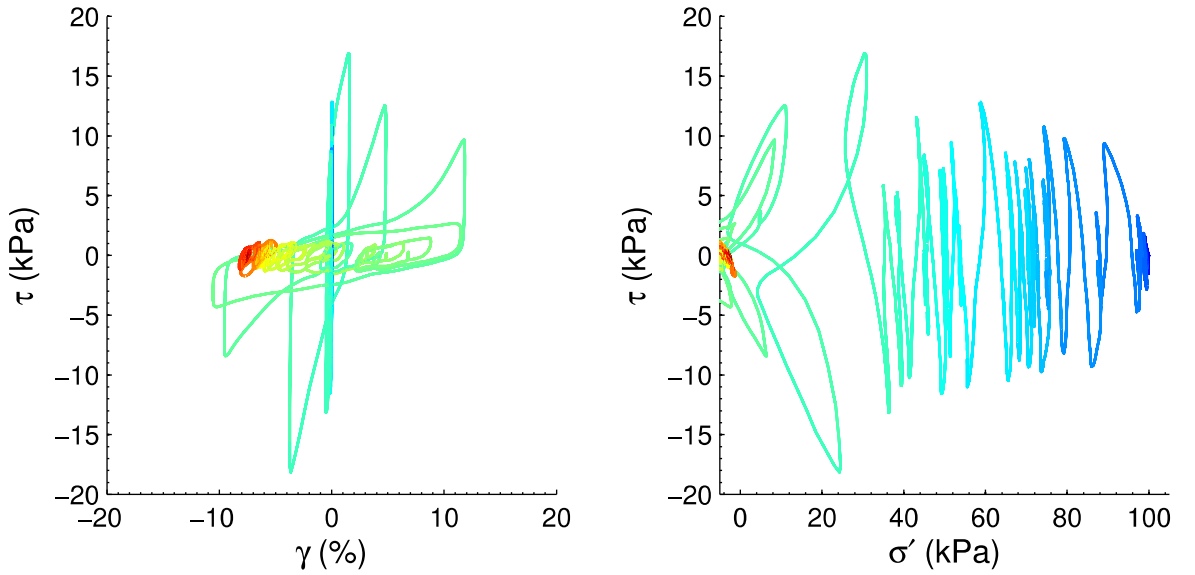
CSS Test 130916 – Data Summary Plot



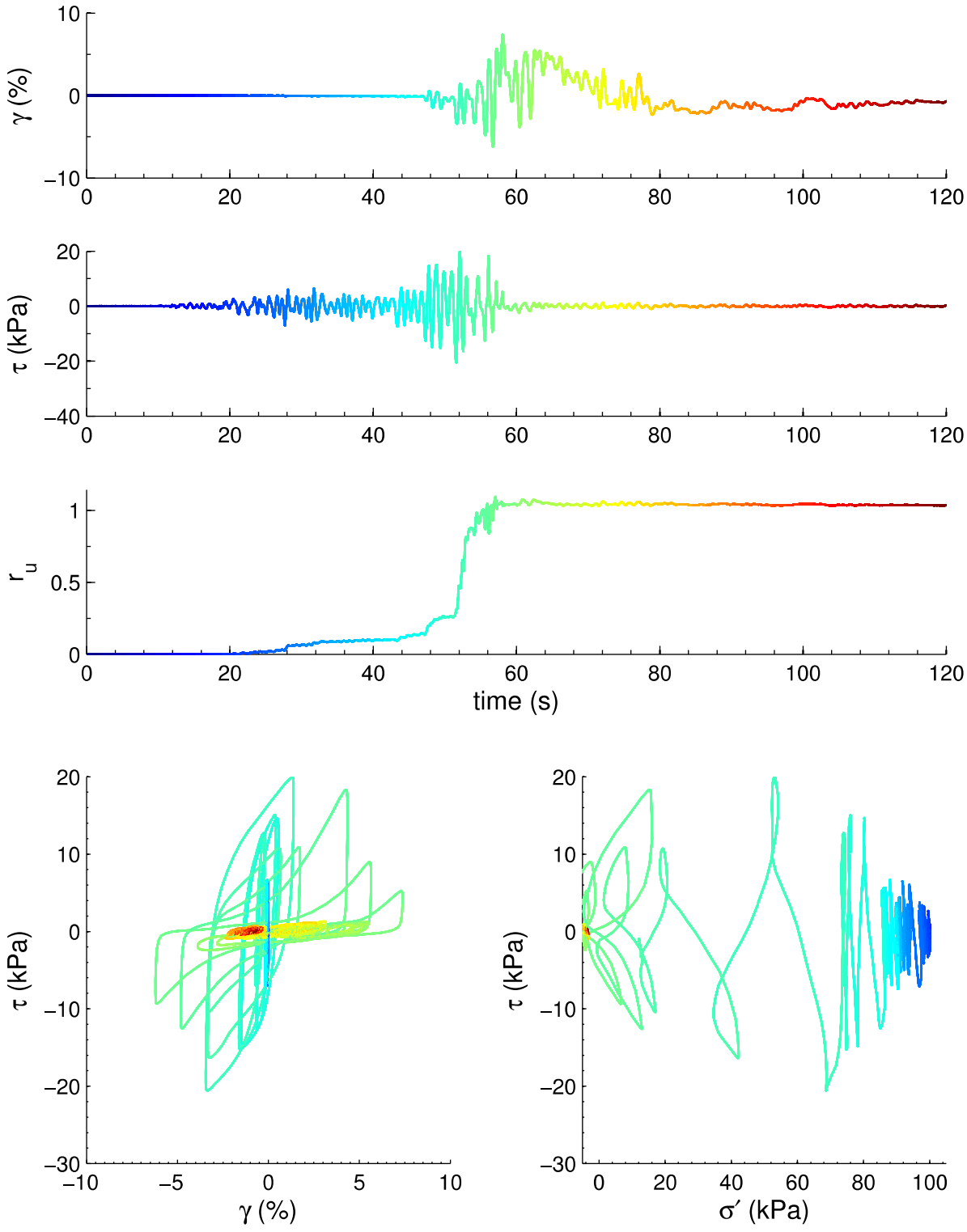


CSS Test 130921 – Data Summary Plot

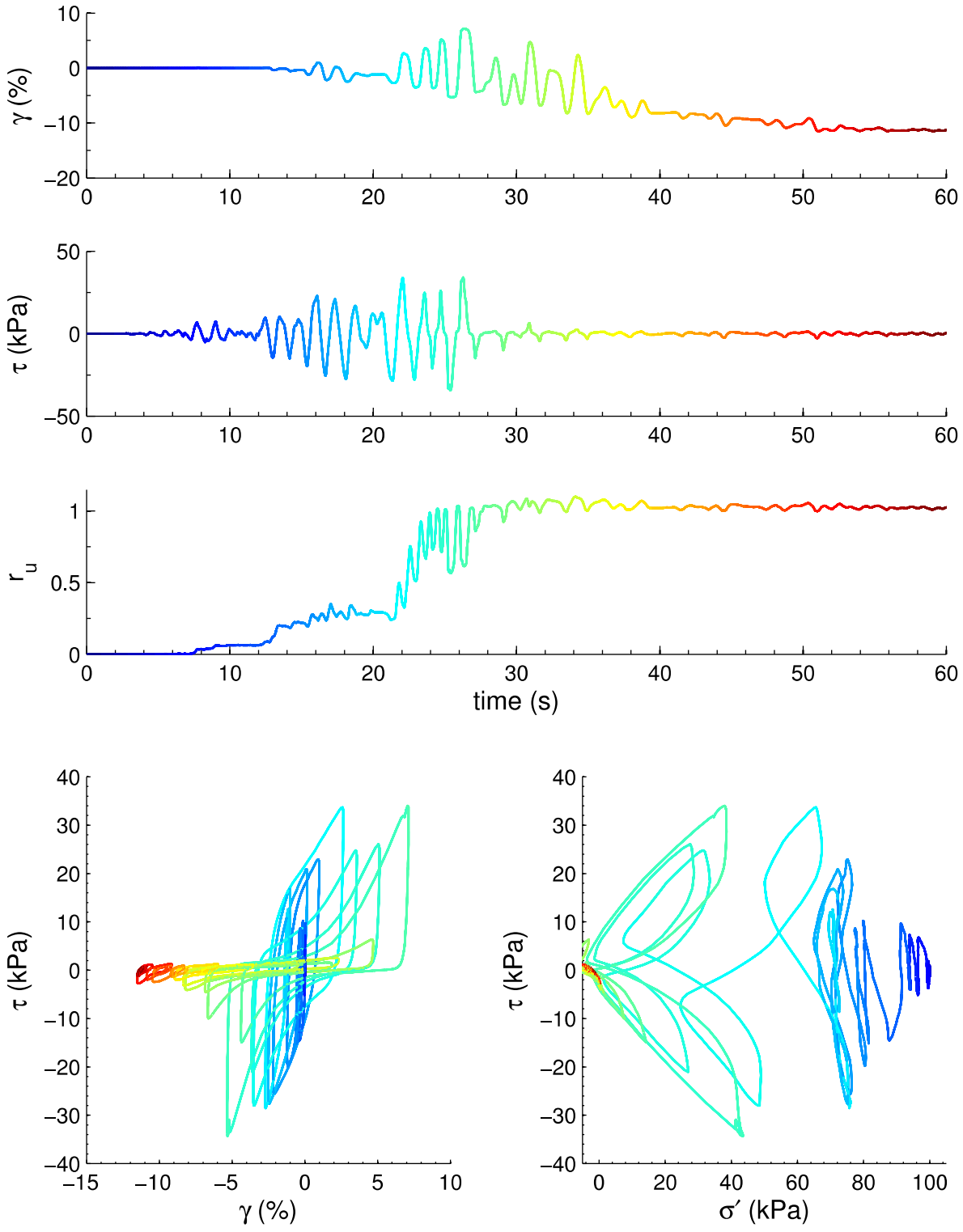




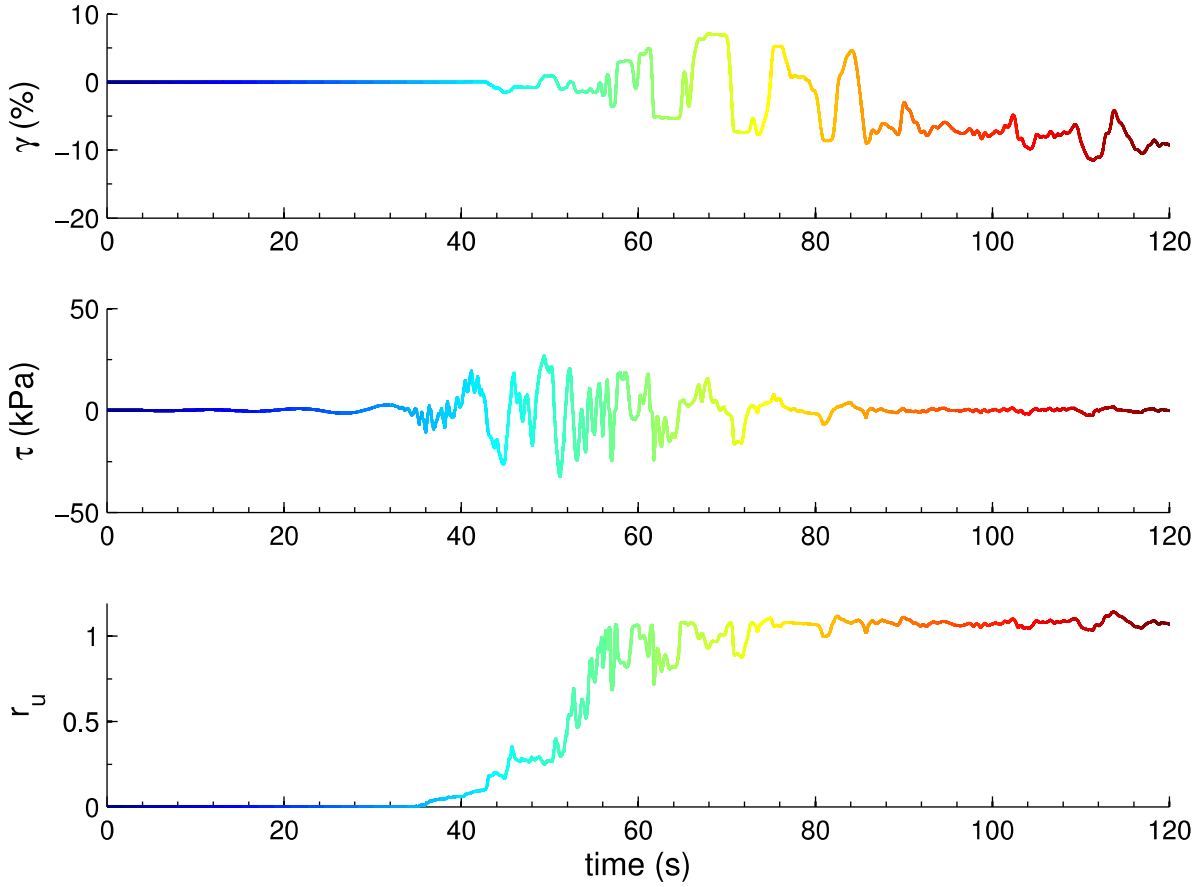
CSS Test 130924 – Data Summary Plot

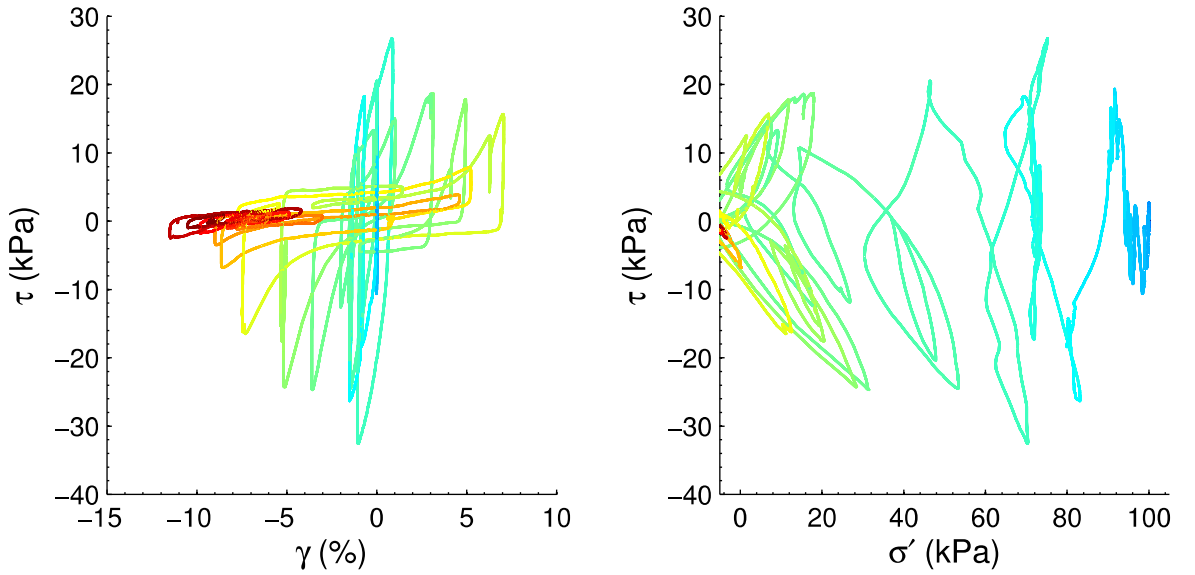


CSS Test 130925 – Data Summary Plot



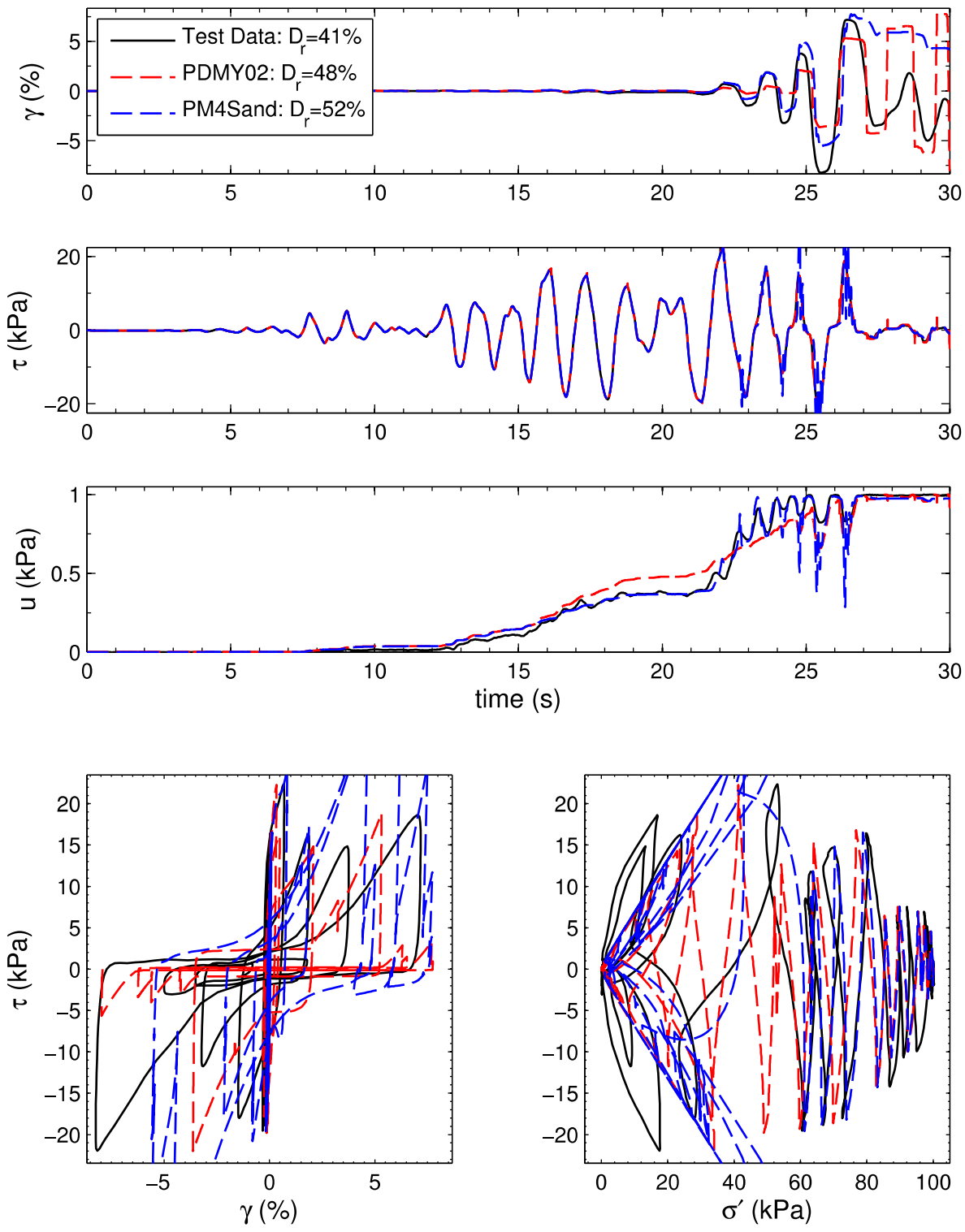
CSS Test 131008 – Data Summary Plot



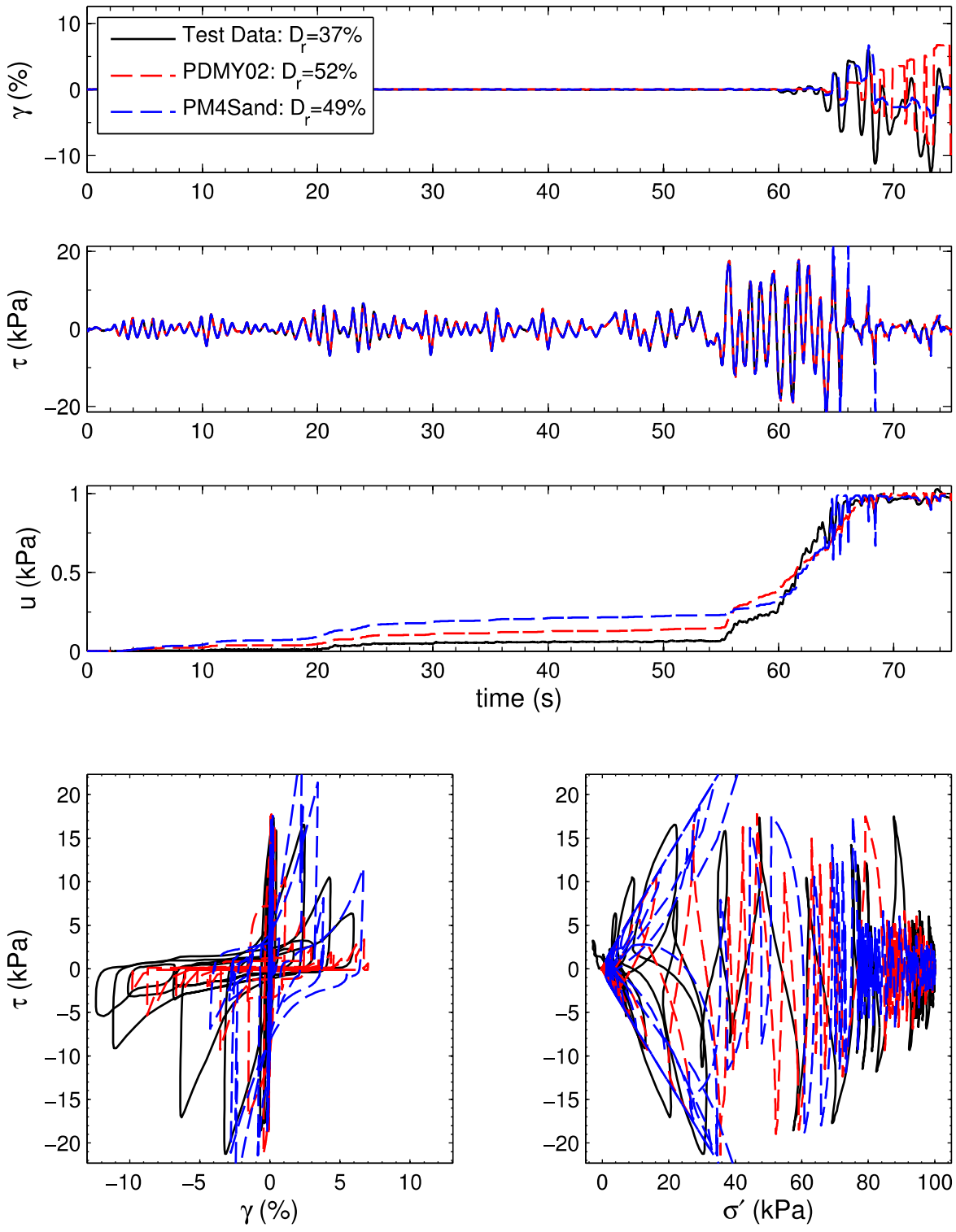


CSS Test 131009 – Data Summary Plot

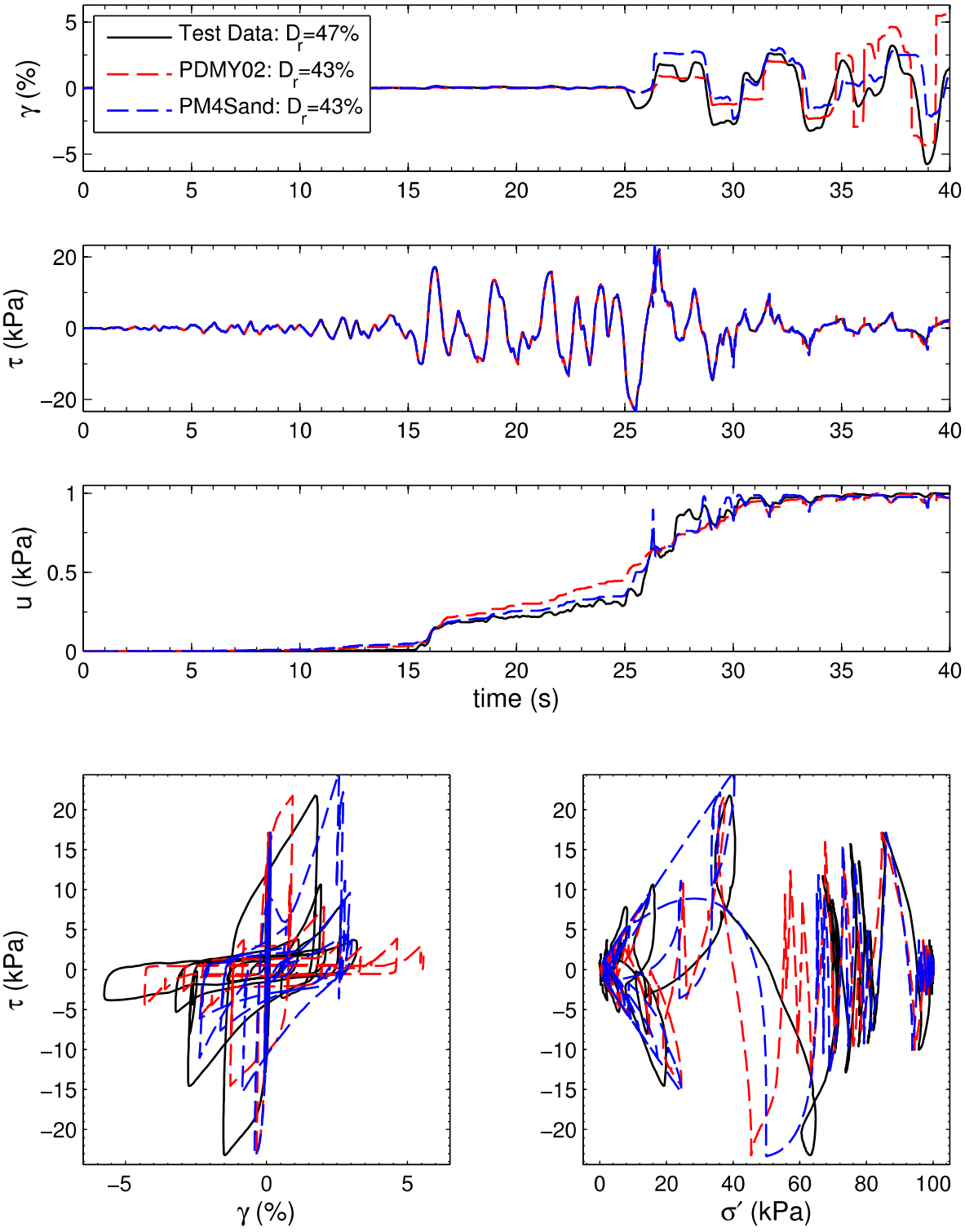
APPENDIX B: NUMERICAL ANALYSES OF TRANSIENT CYCLIC DIRECT SIMPLE SHEAR TESTS



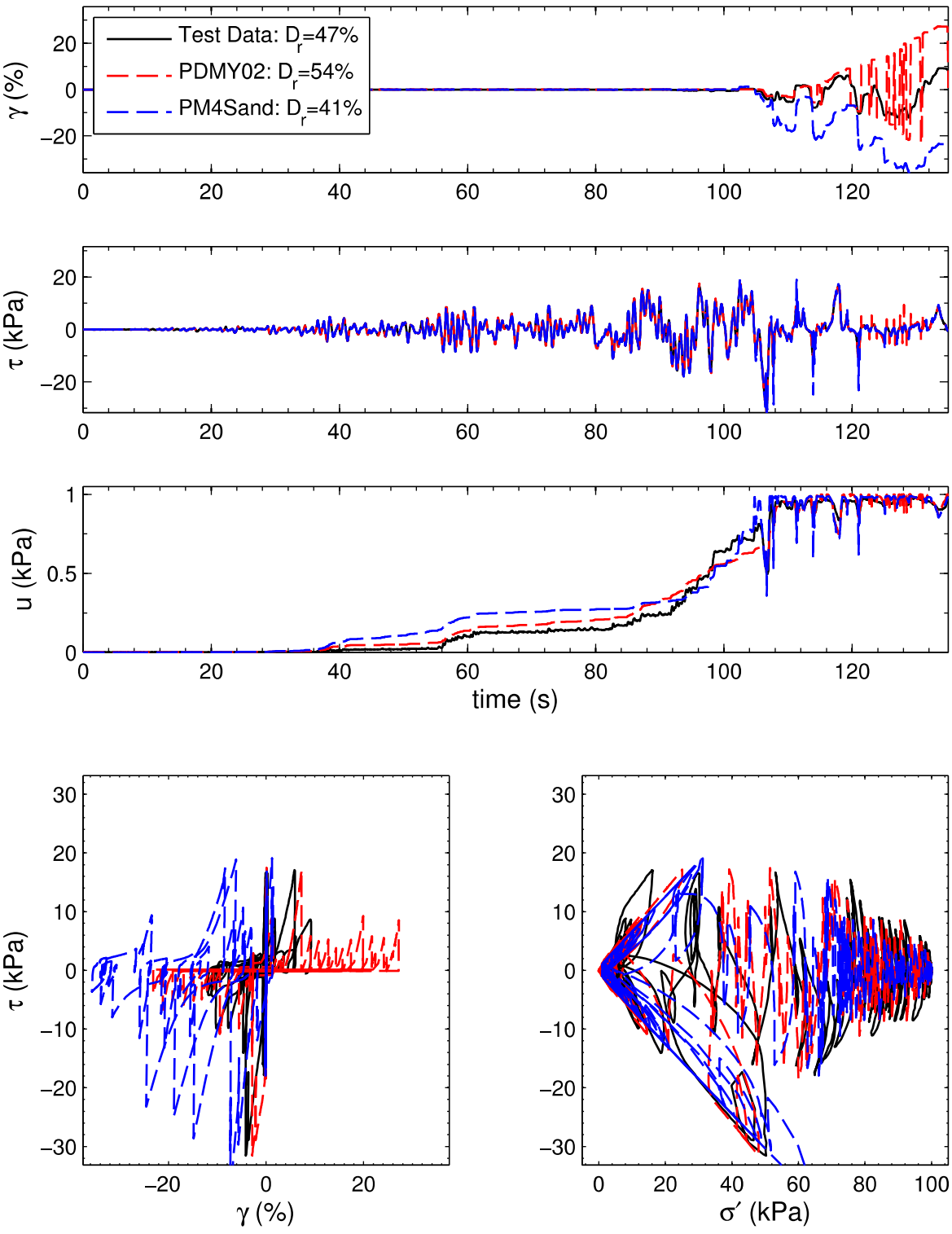
CSS Test 130118 – Comparison with Numerical Models



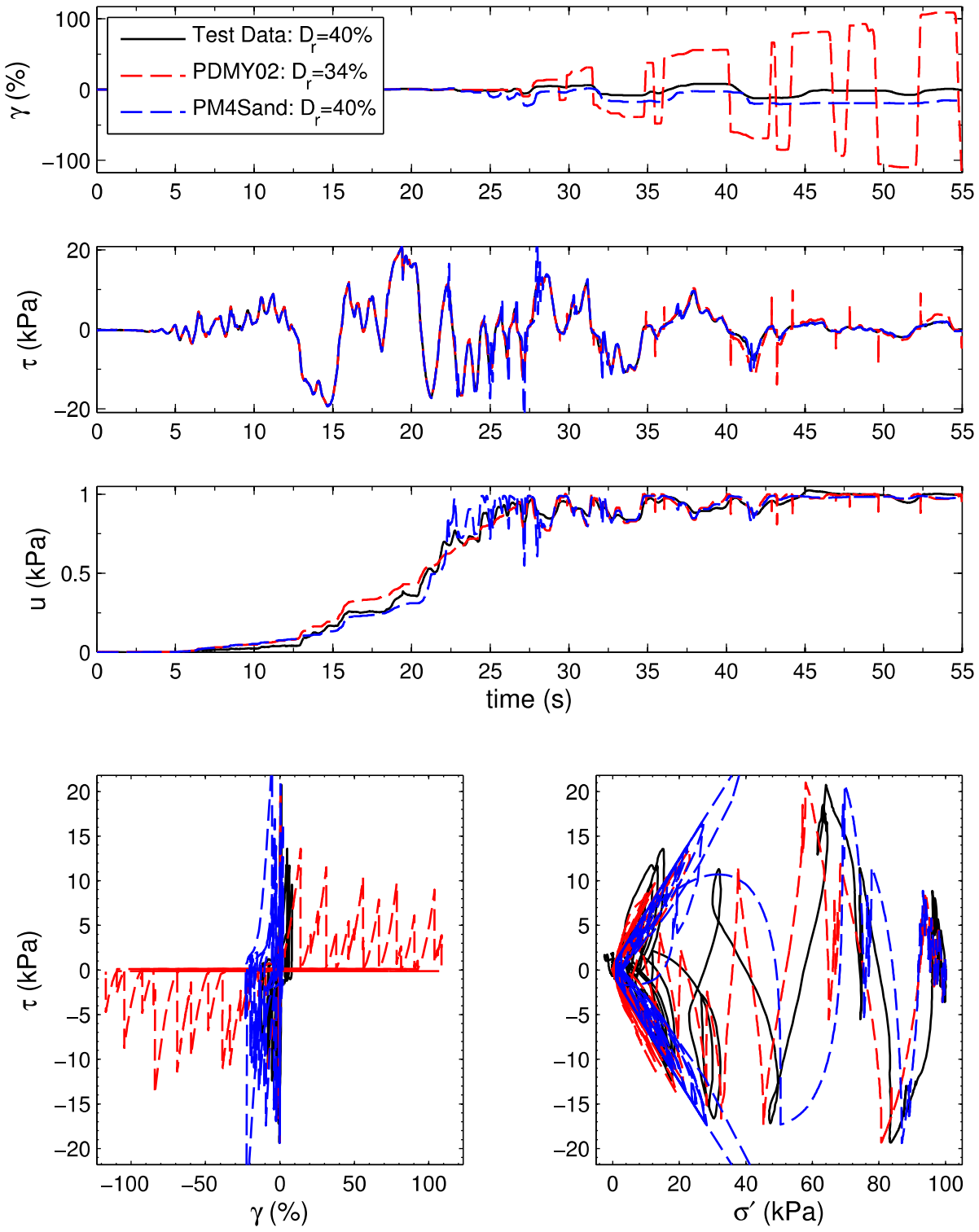
CSS Test 130119 – Comparison with Numerical Models



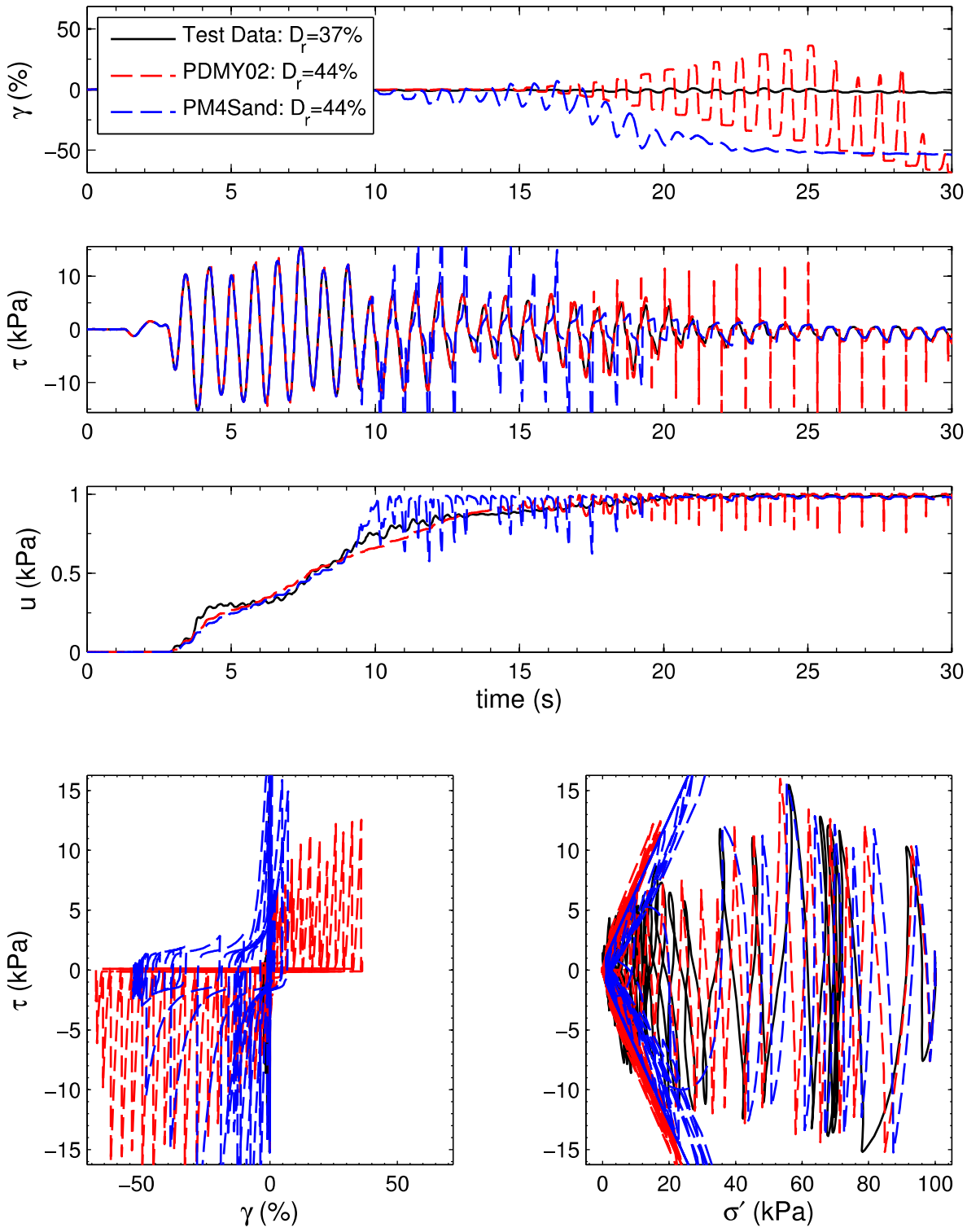
CSS Test 130209 – Comparison with Numerical Models



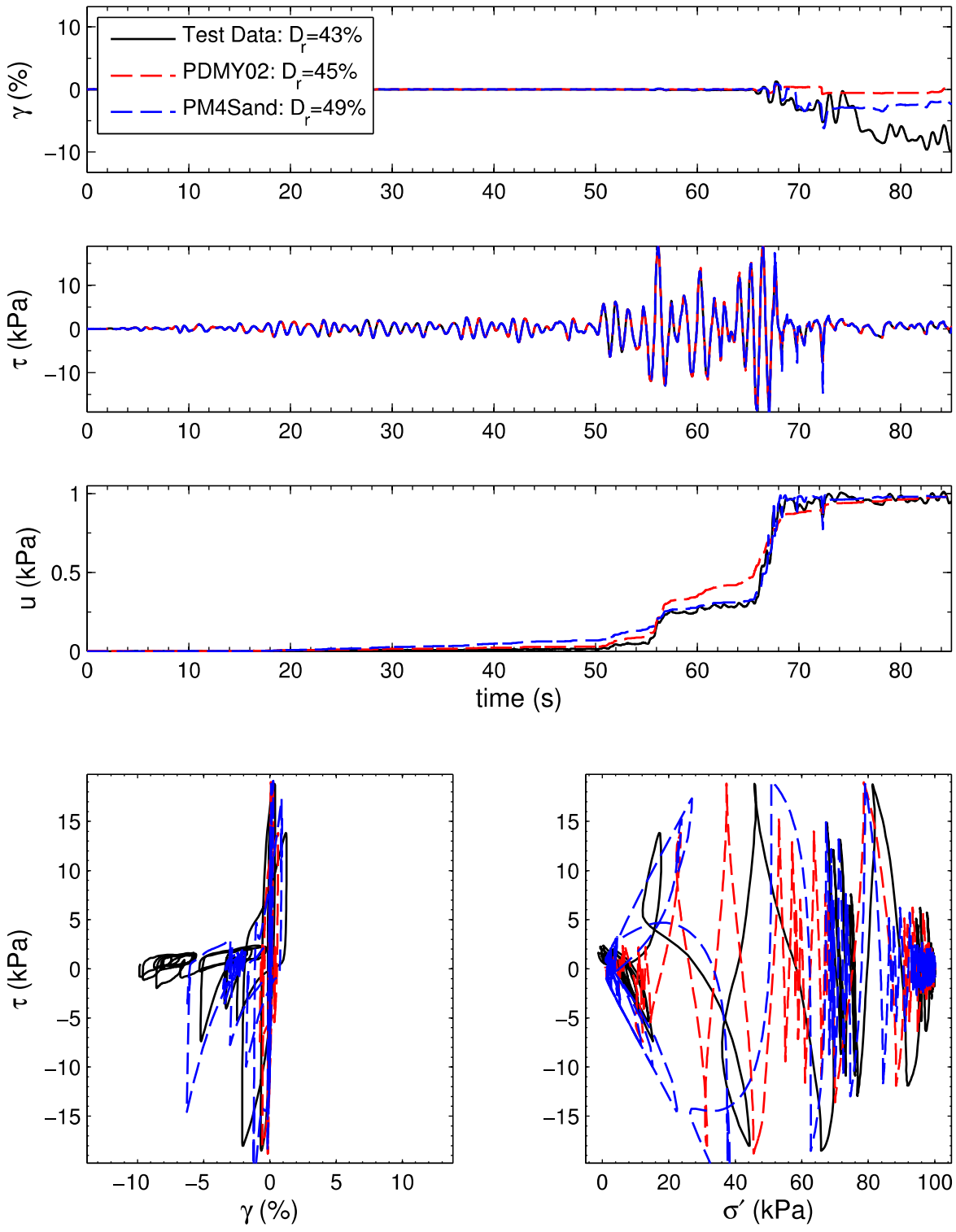
CSS Test 130215–02 – Comparison with Numerical Models



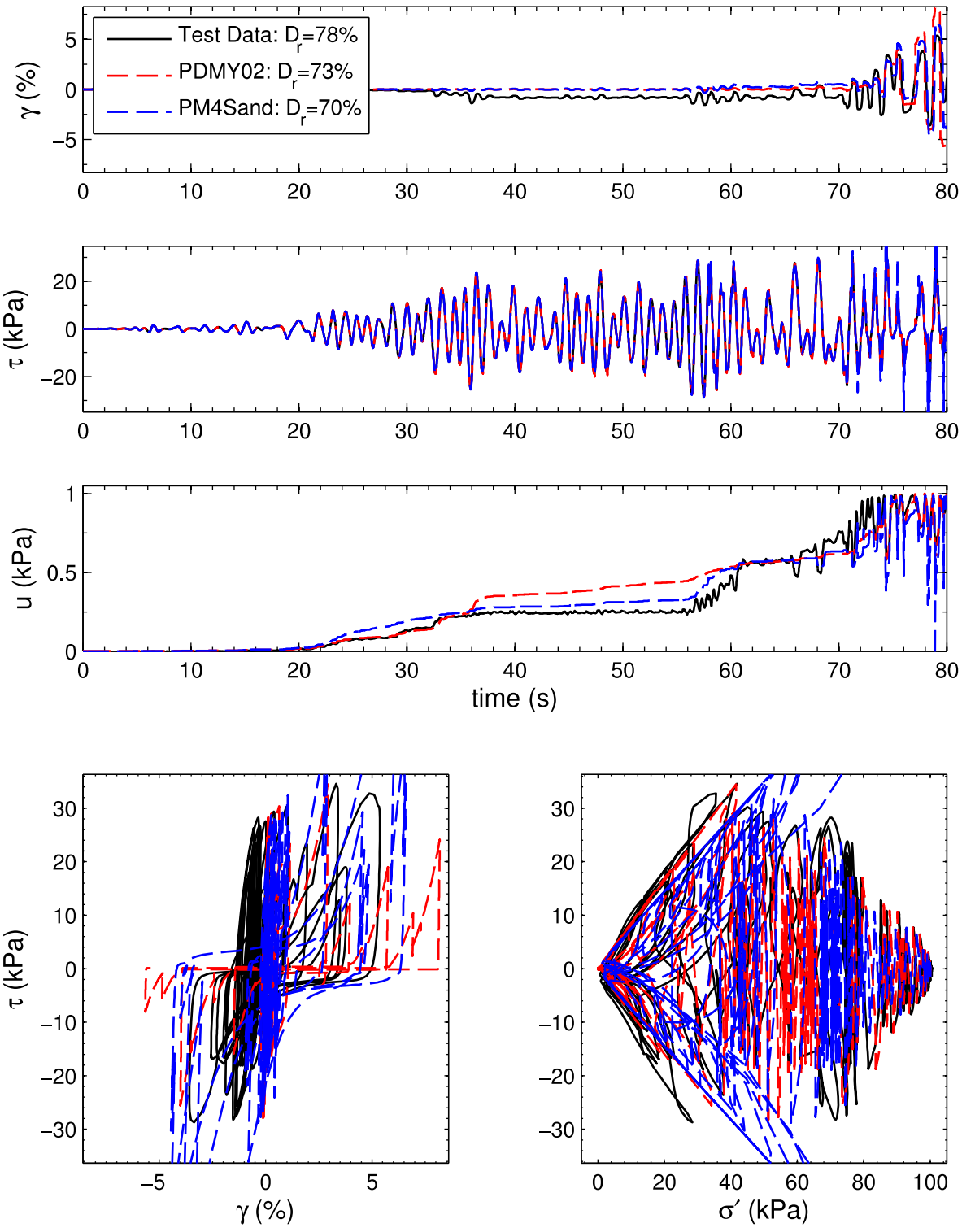
CSS Test 130306 – Comparison with Numerical Models



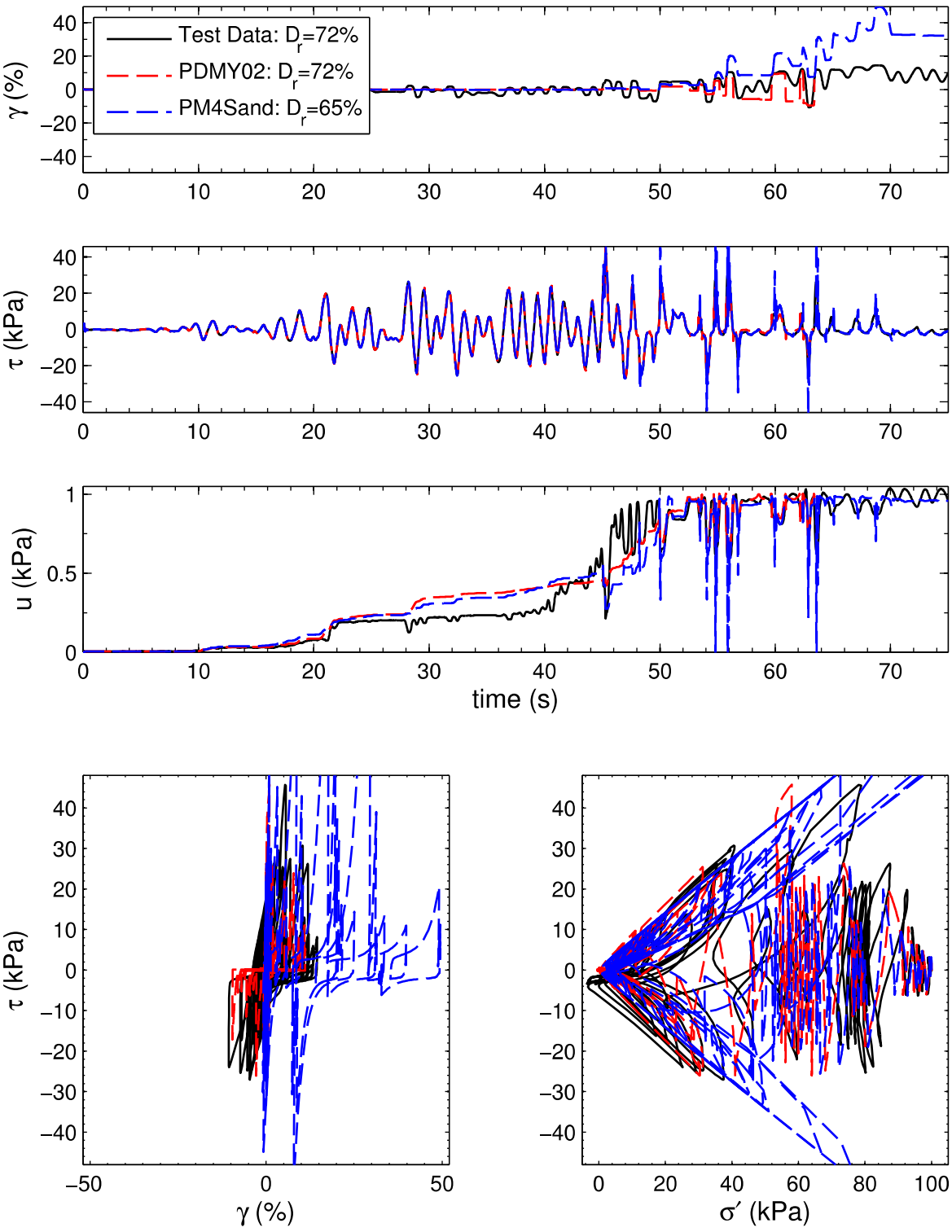
CSS Test 130401 – Comparison with Numerical Models



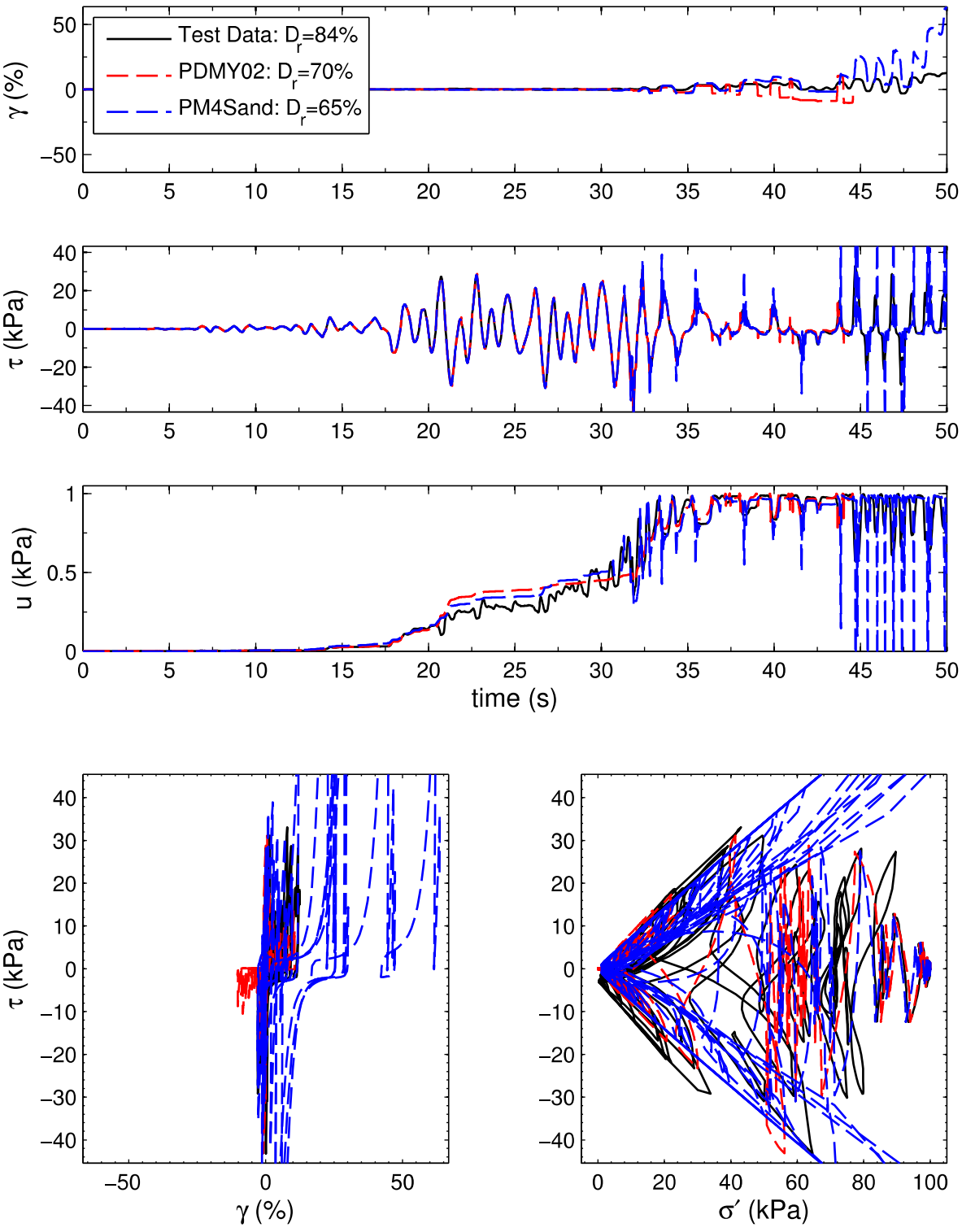
CSS Test 130628 – Comparison with Numerical Models



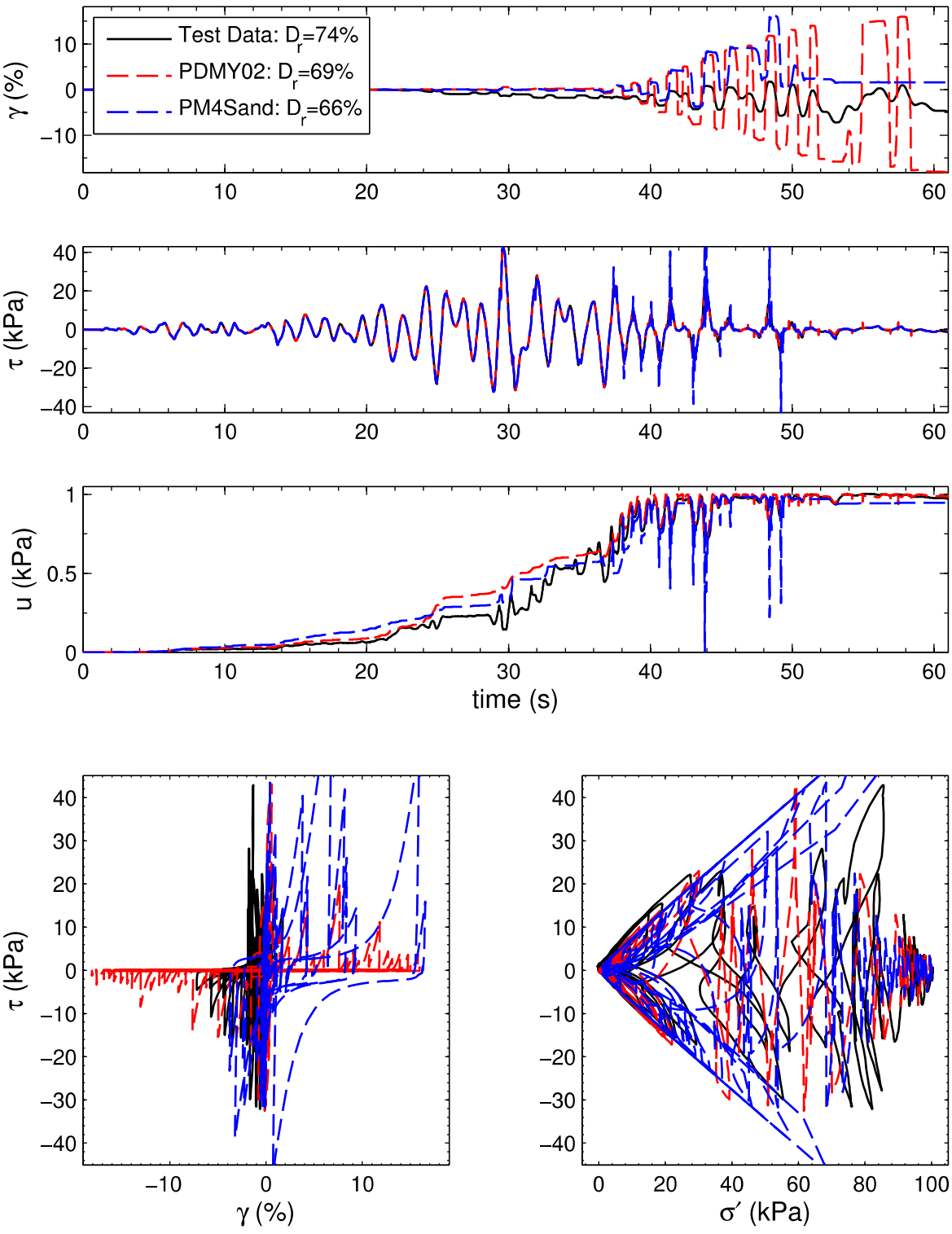
CSS Test 130711–02 – Comparison with Numerical Models



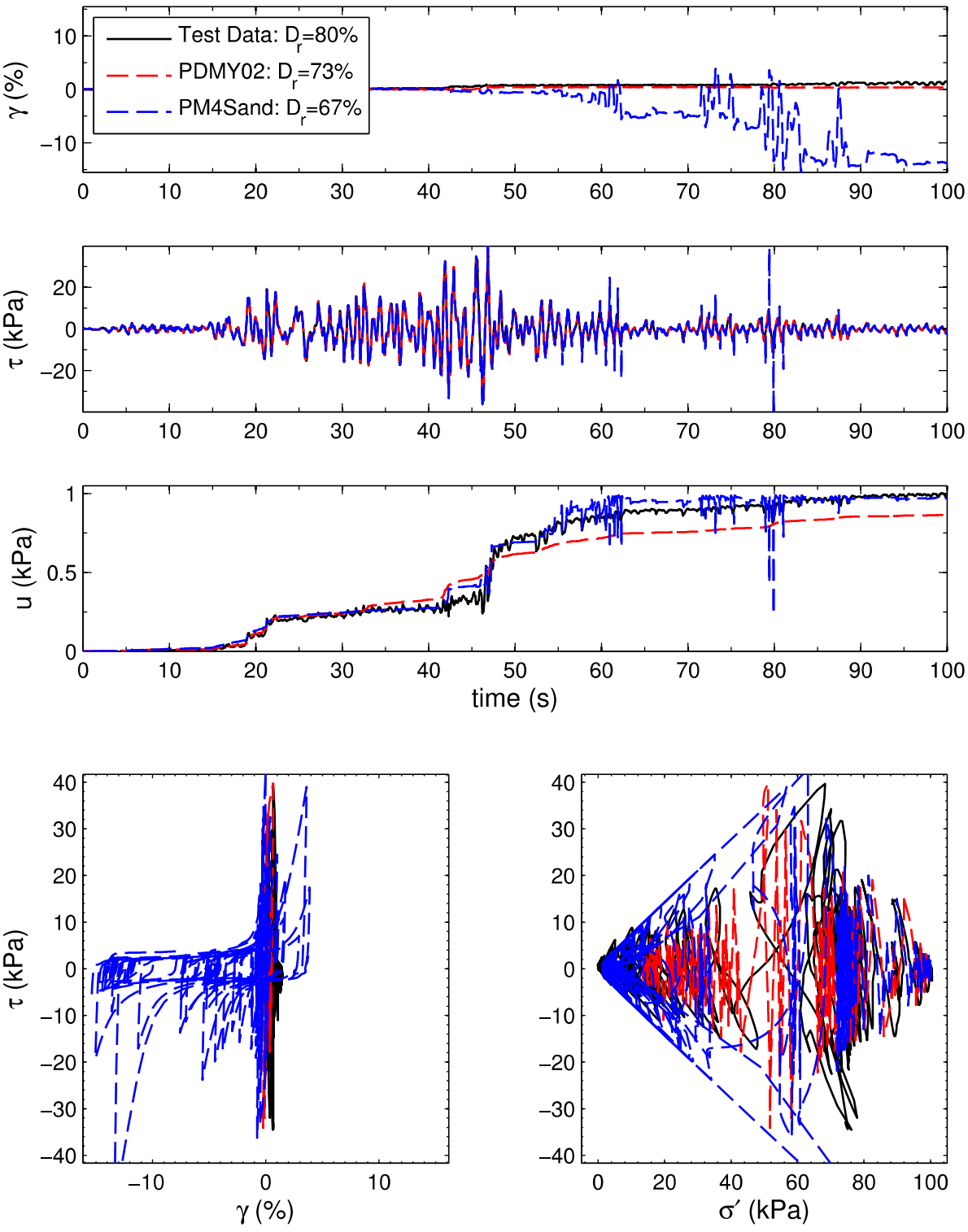
CSS Test 130726–02 – Comparison with Numerical Models



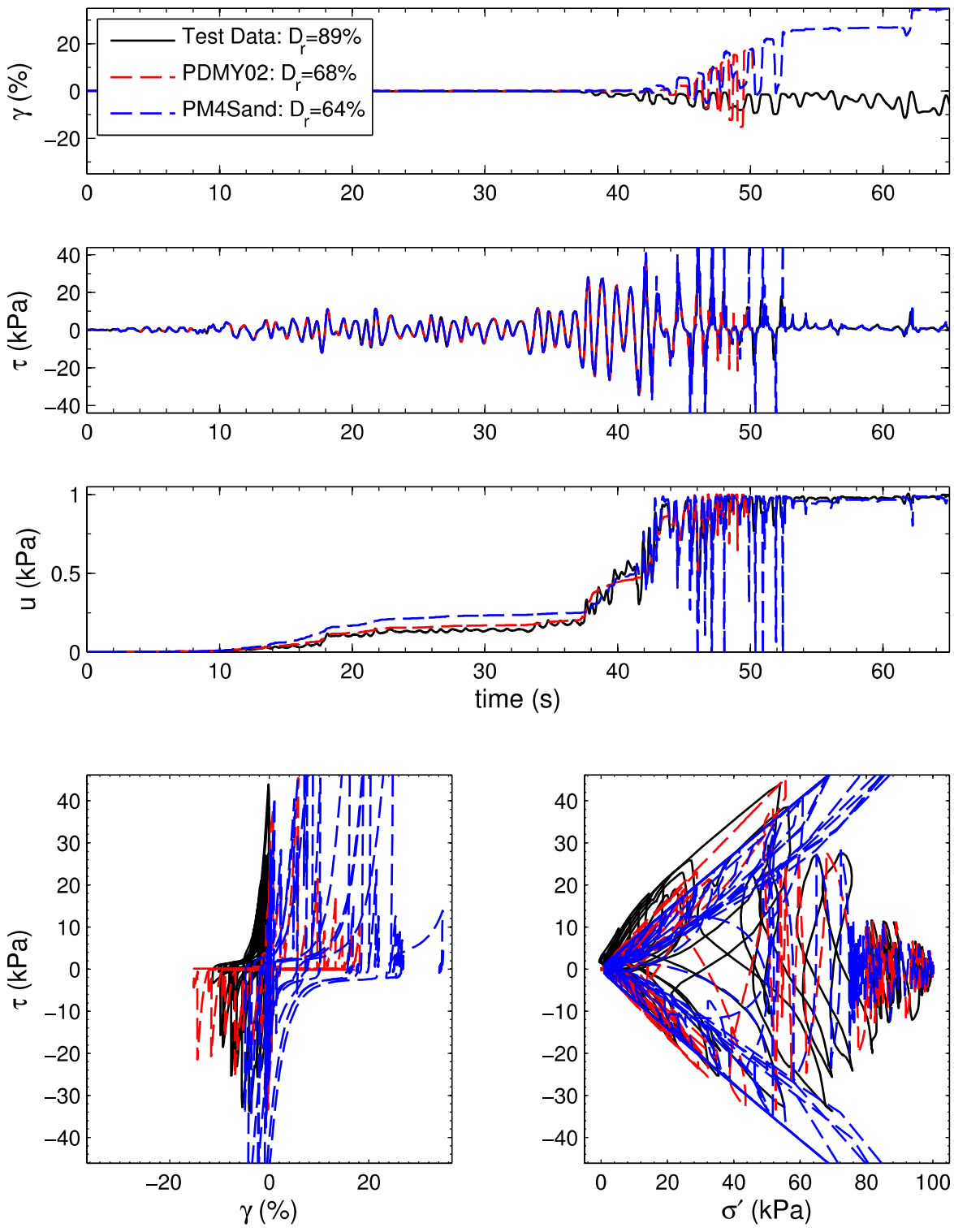
CSS Test 130727 – Comparison with Numerical Models



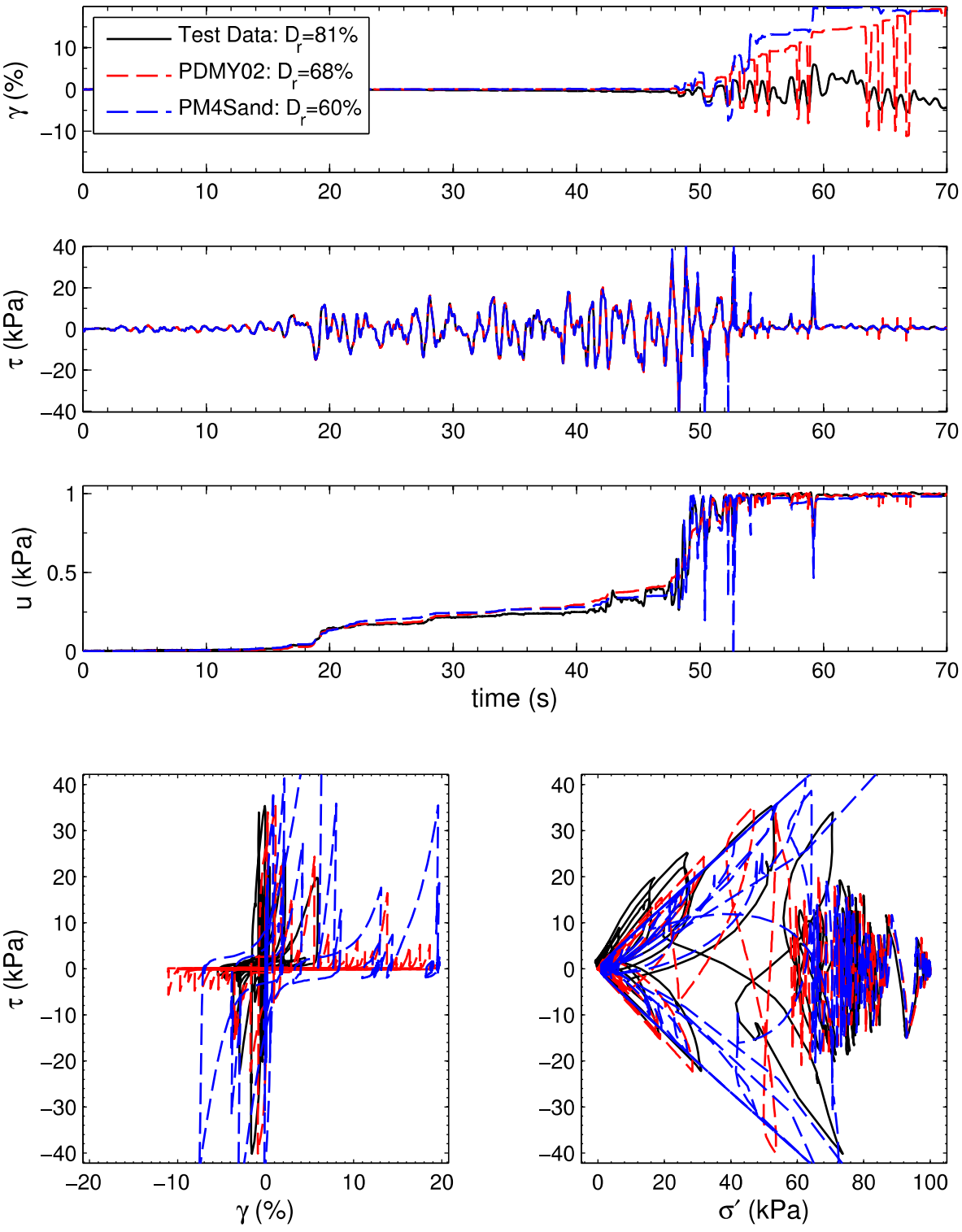
CSS Test 130809–02 – Comparison with Numerical Models



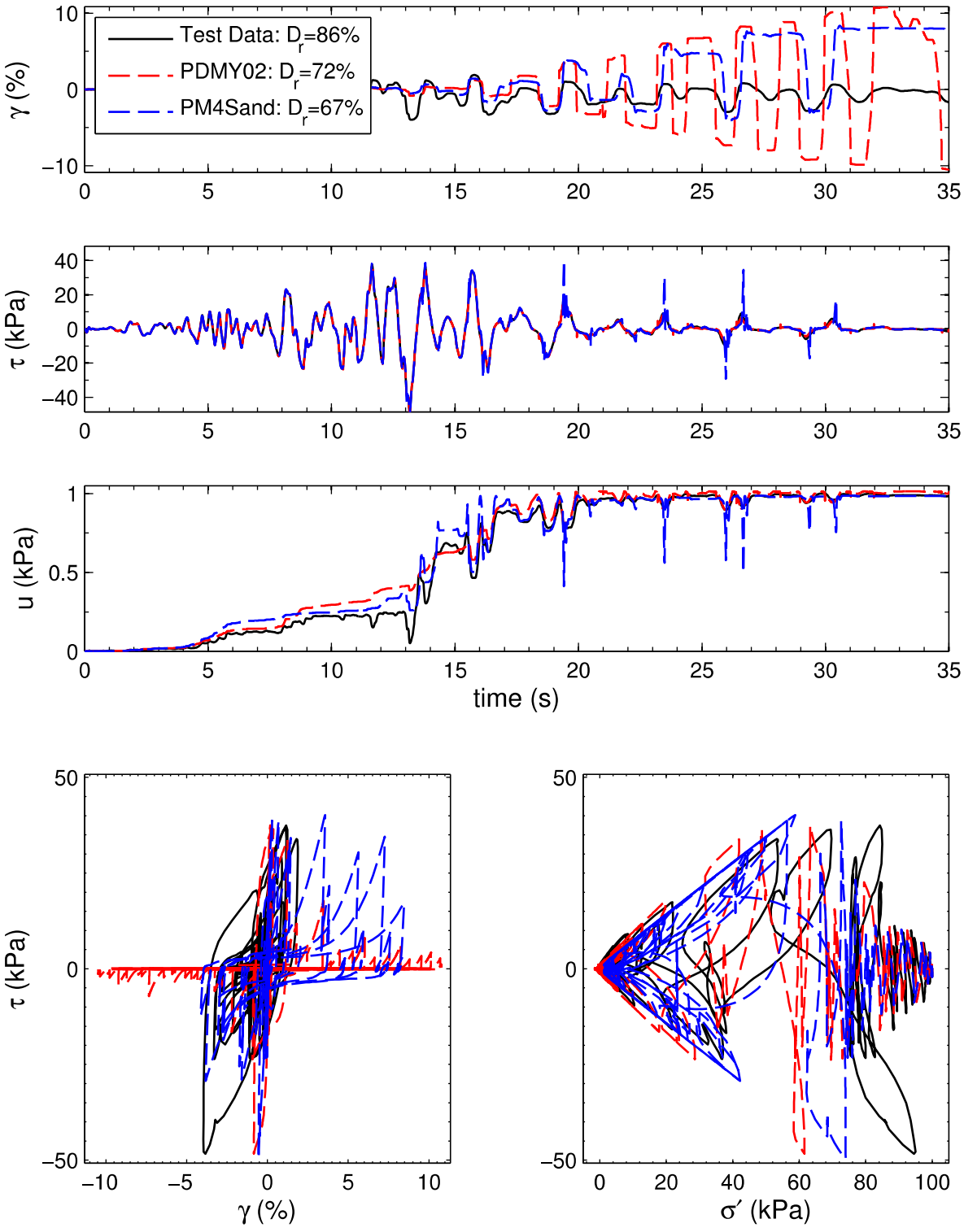
CSS Test 130821 – Comparison with Numerical Models



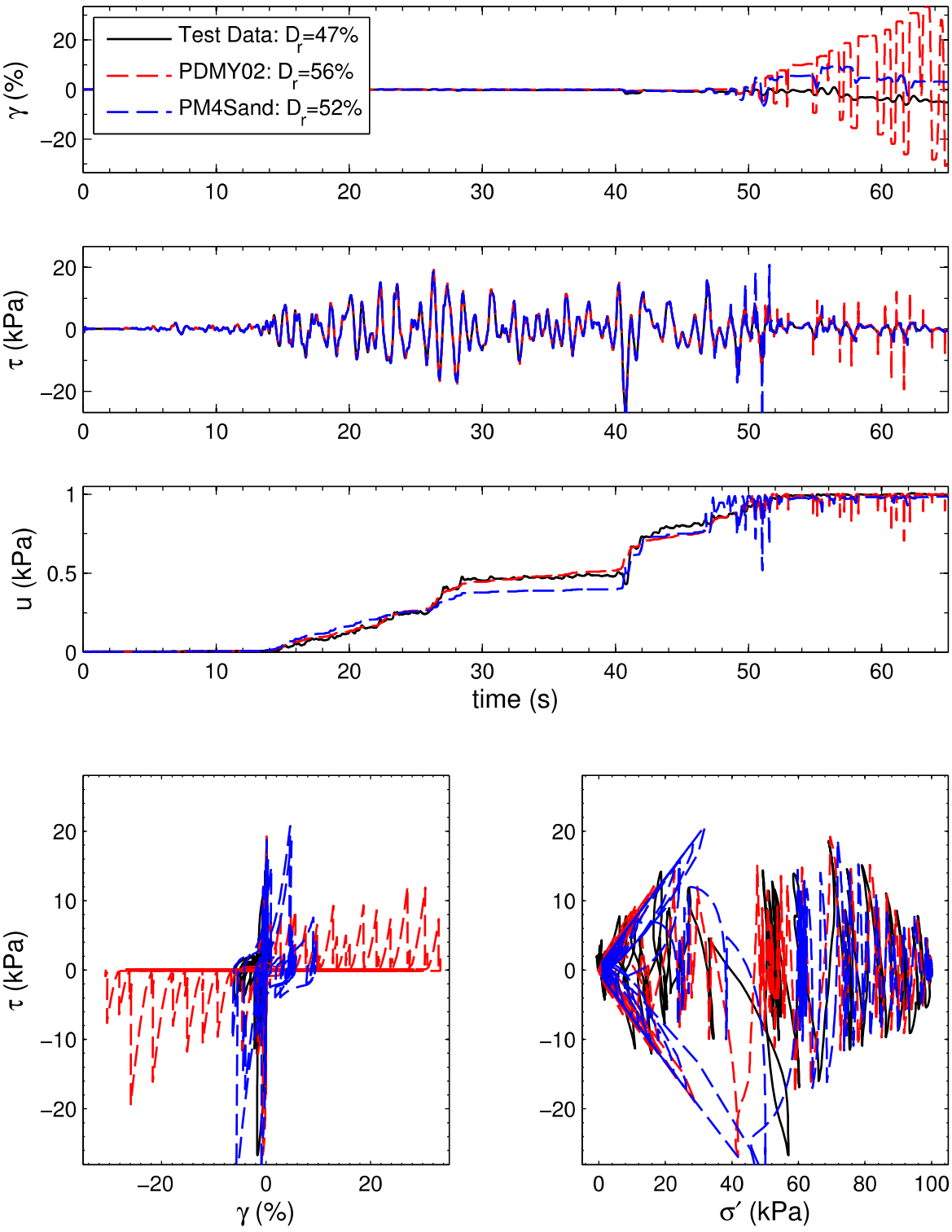
CSS Test 130827–02 – Comparison with Numerical Models



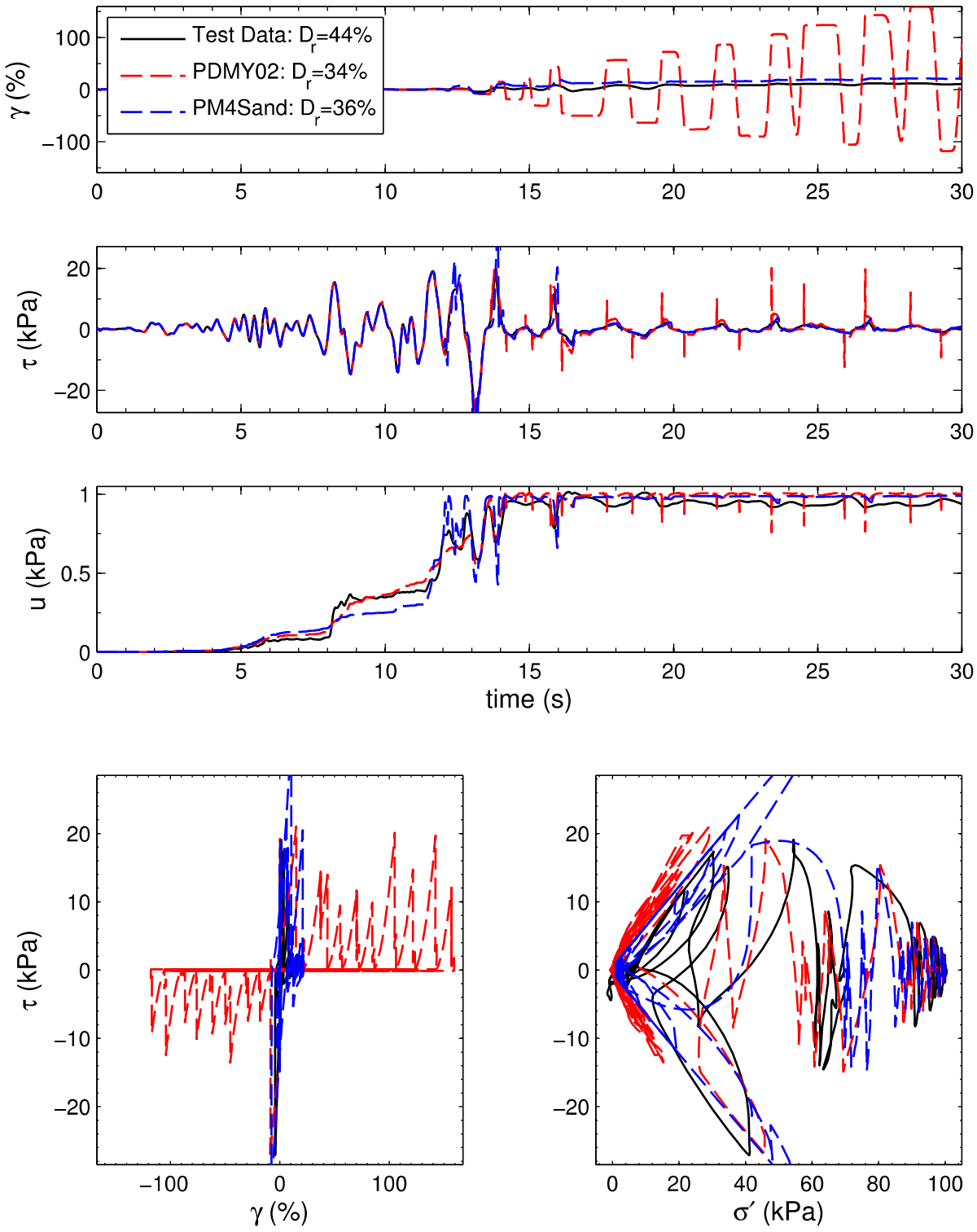
CSS Test 130829–02 – Comparison with Numerical Models



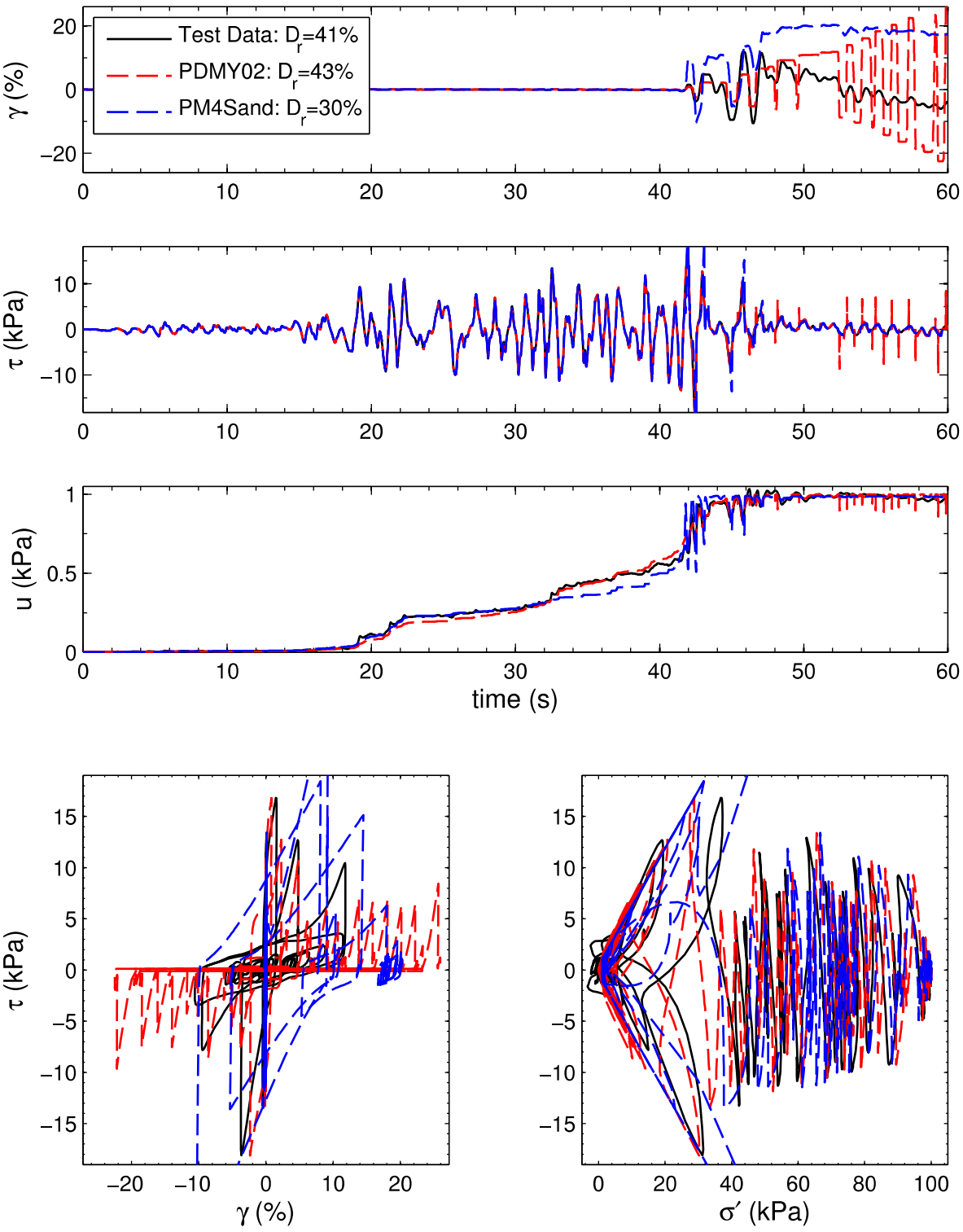
CSS Test 130905–02 – Comparison with Numerical Models



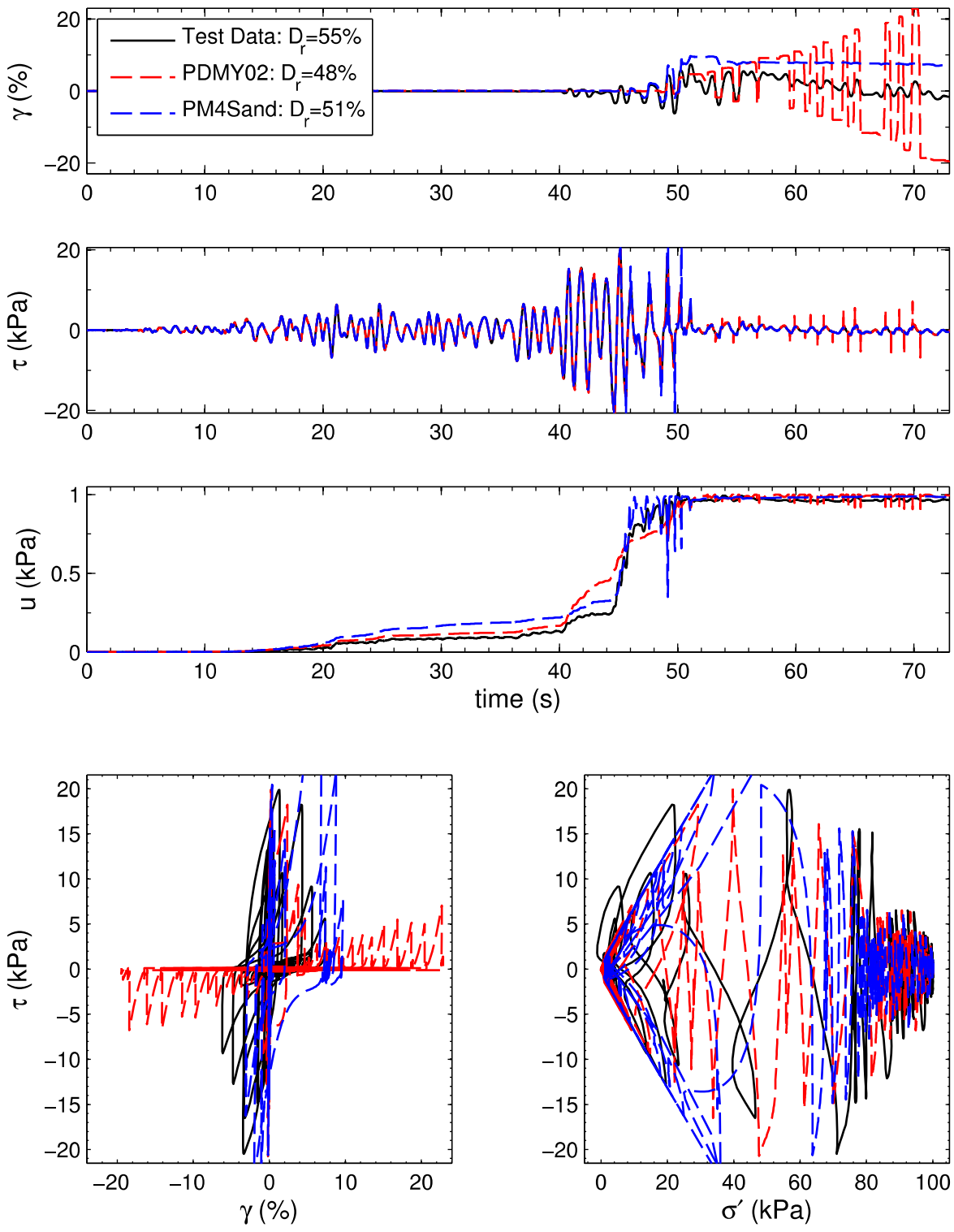
CSS Test 130916 – Comparison with Numerical Models



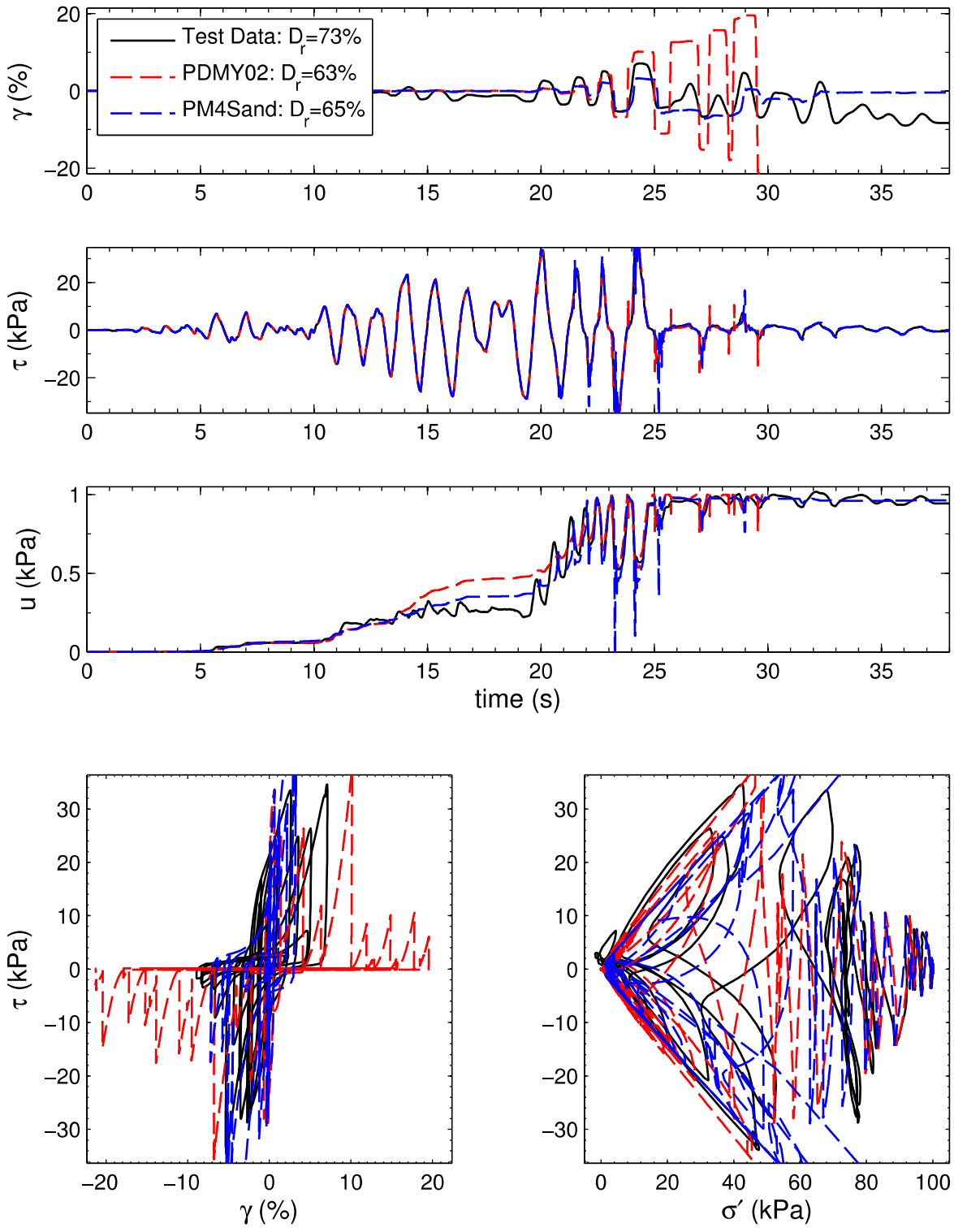
CSS Test 130921 – Comparison with Numerical Models



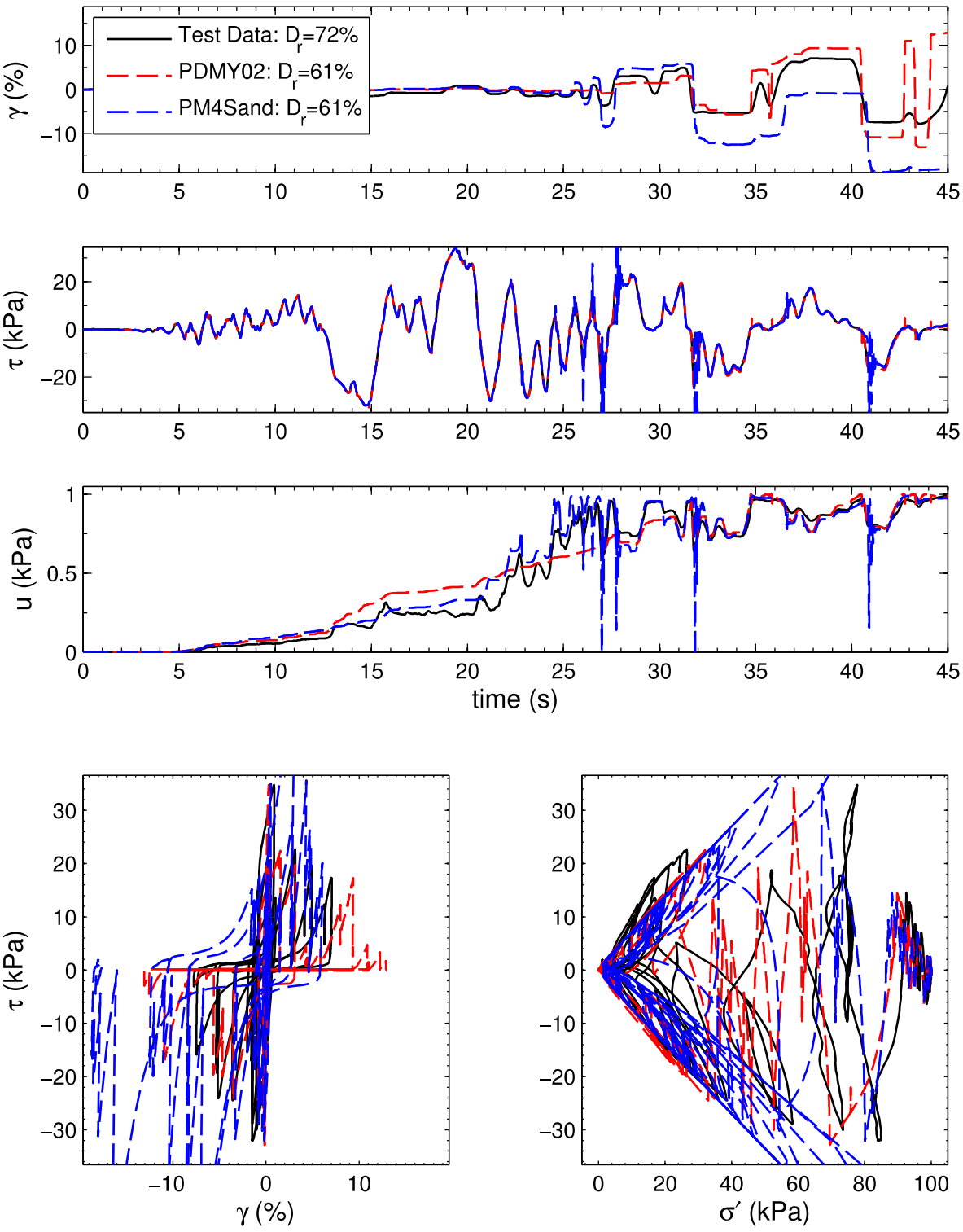
CSS Test 130924 – Comparison with Numerical Models



CSS Test 130925 – Comparison with Numerical Models

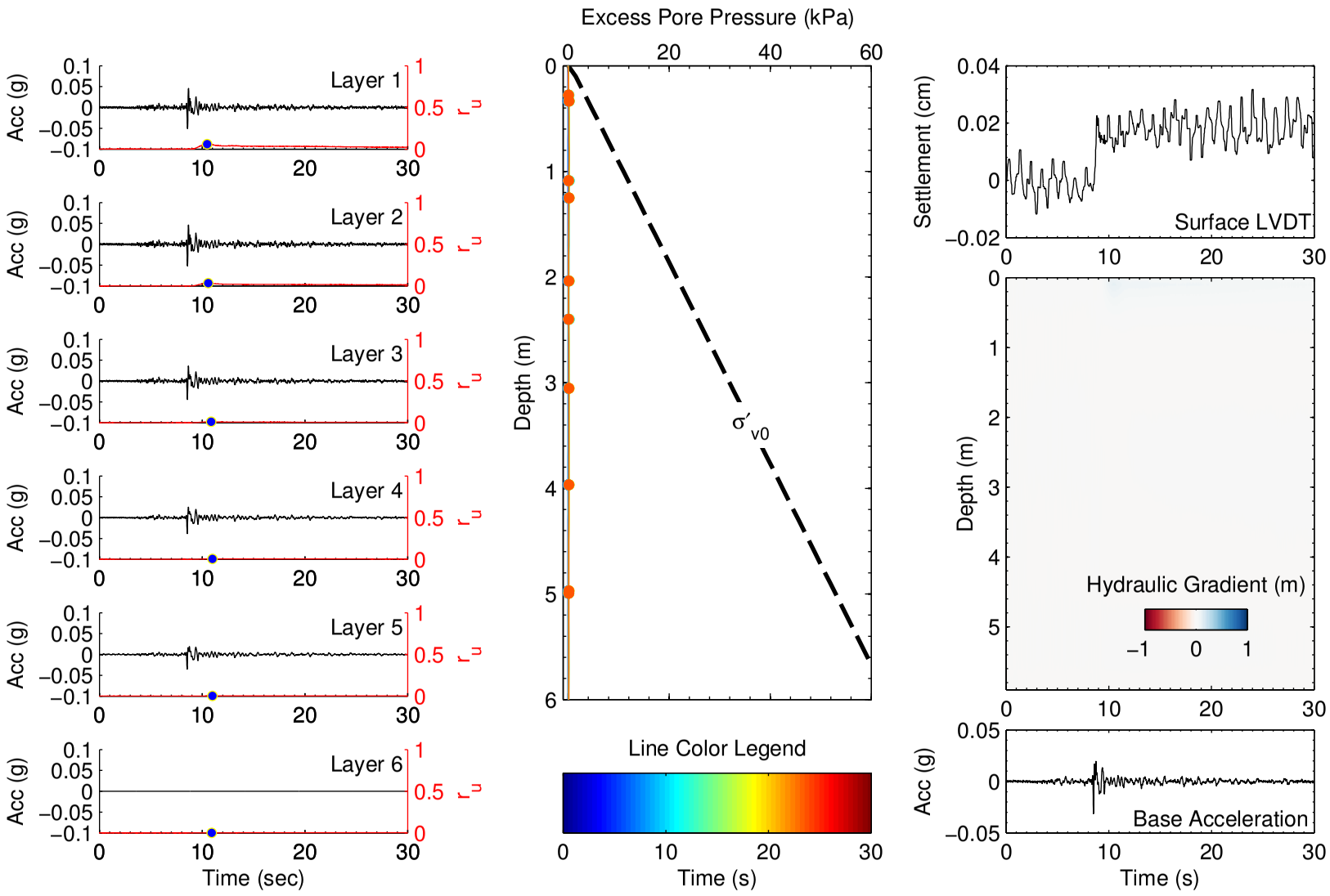


CSS Test 131008 – Comparison with Numerical Models

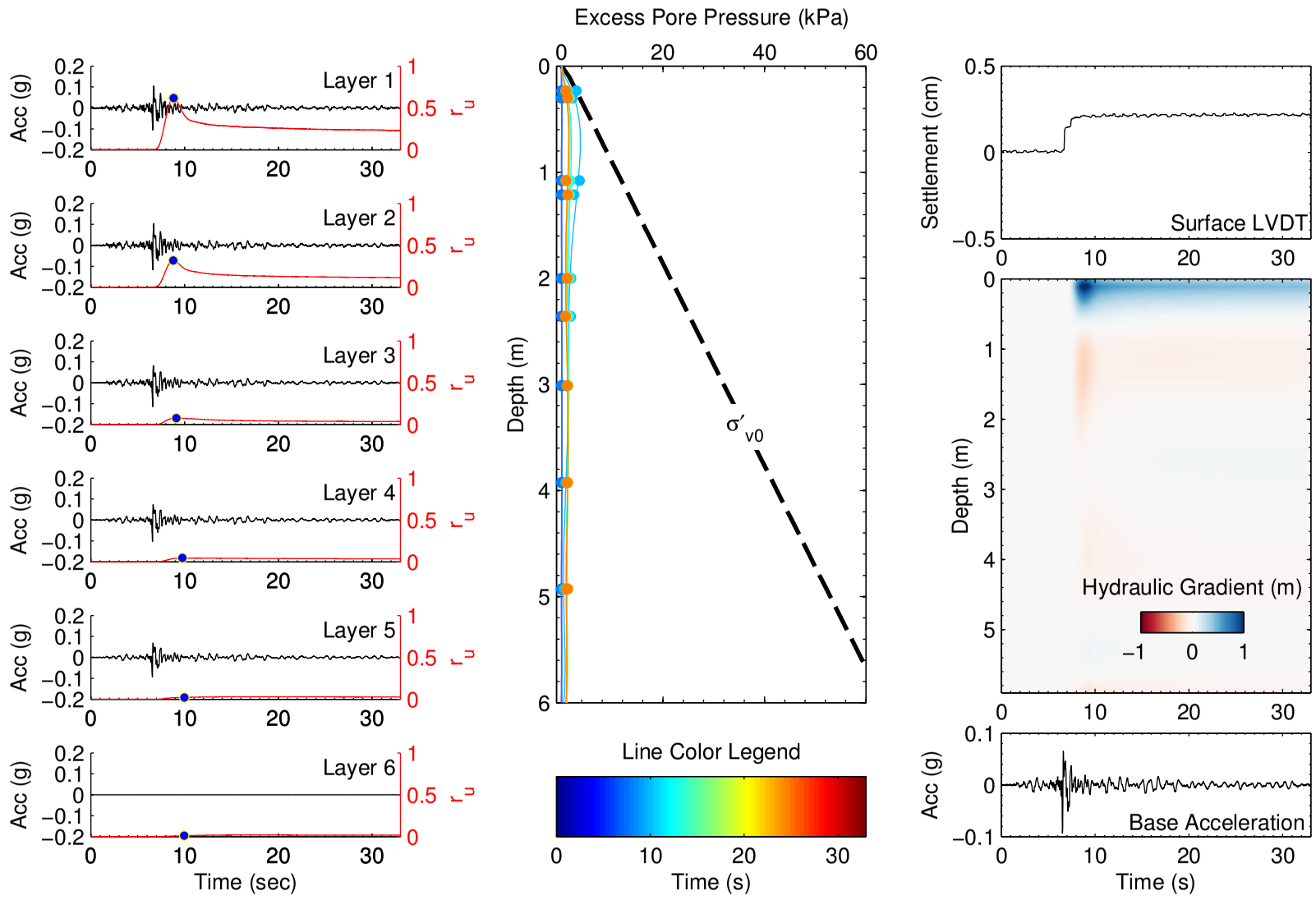


CSS Test 131009 – Comparison with Numerical Models

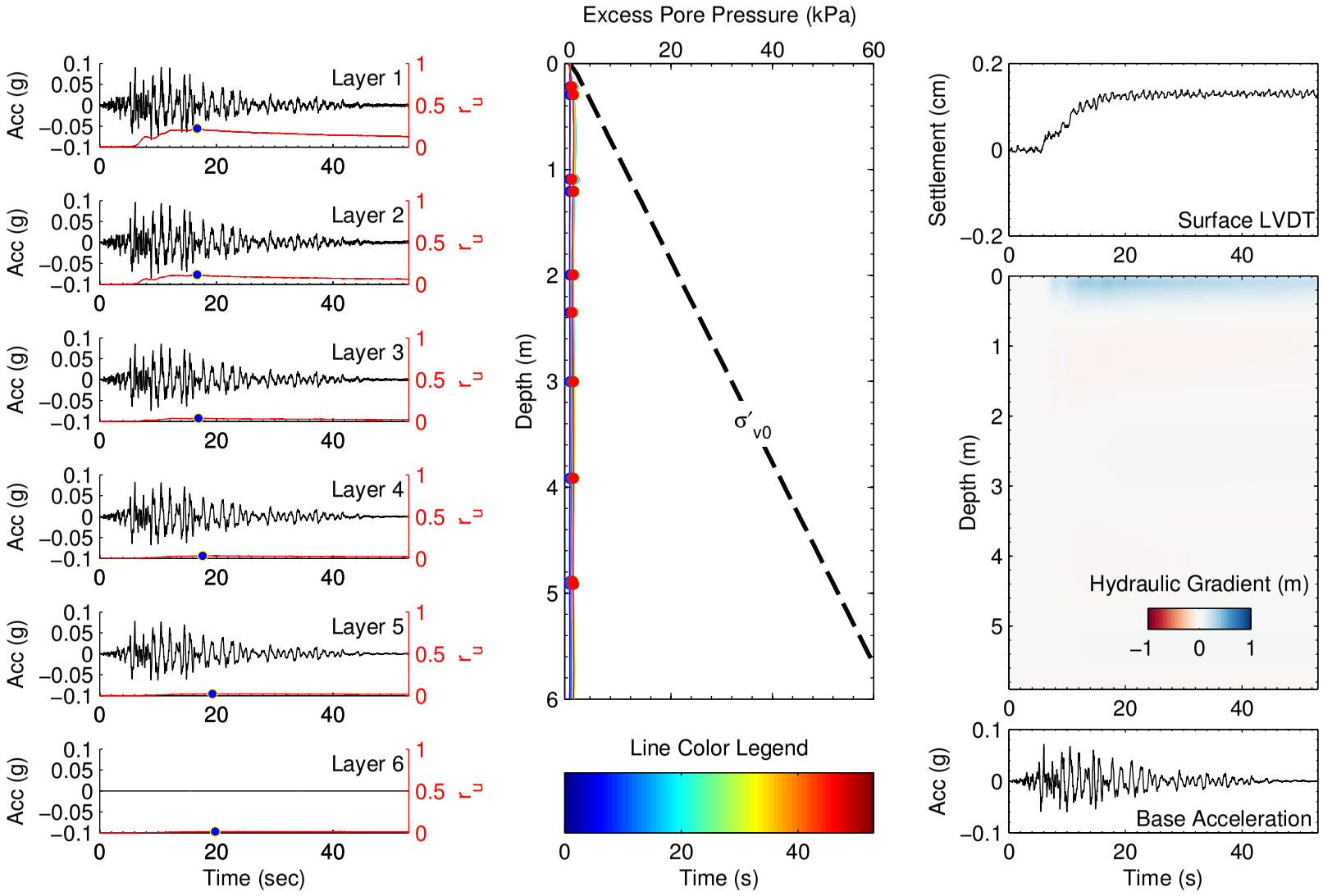
APPENDIX C: CENTRIFUGE TEST SUMMARIES



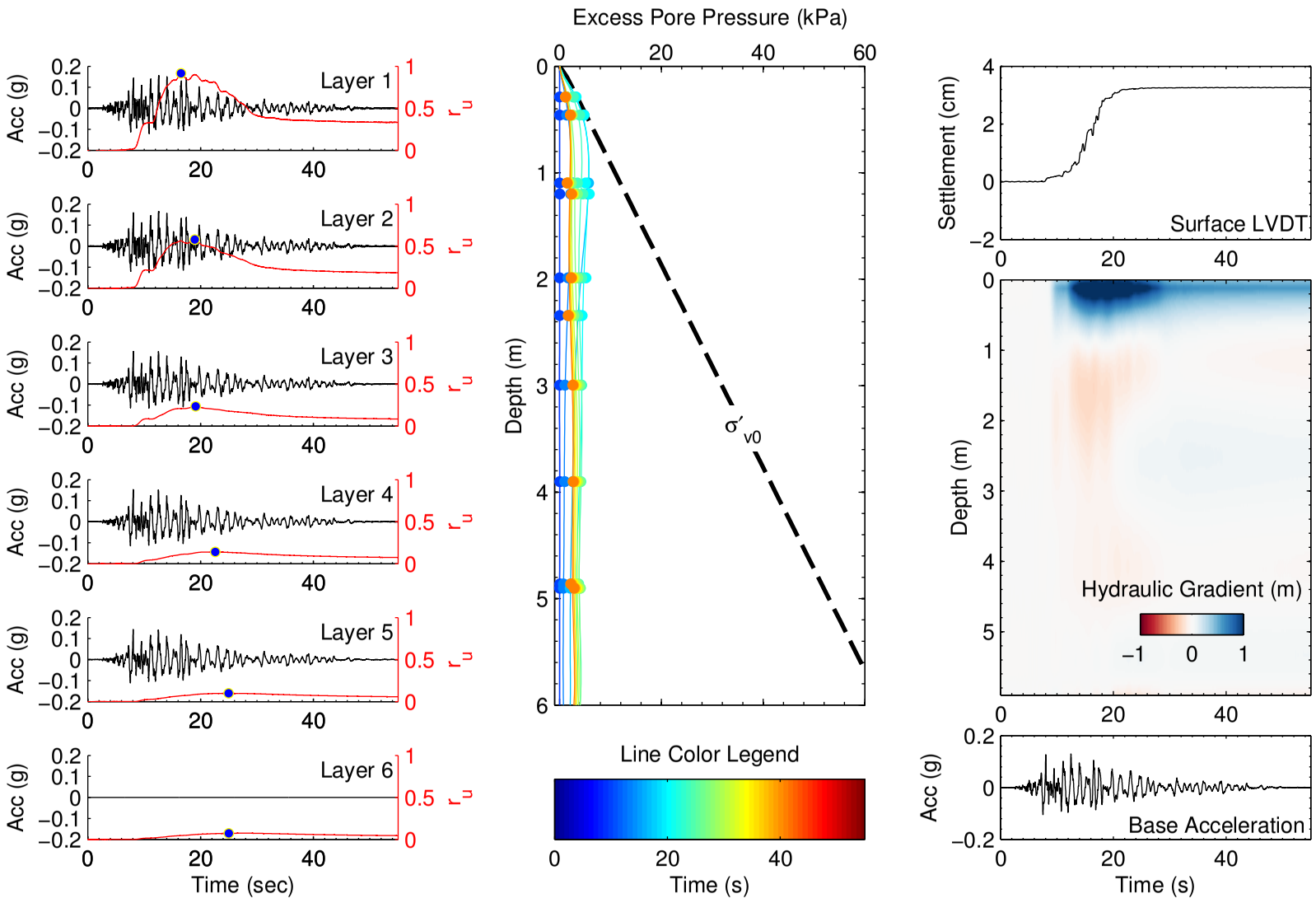
100% D_r Experiment 1 Test 1 – Data Summary Plot



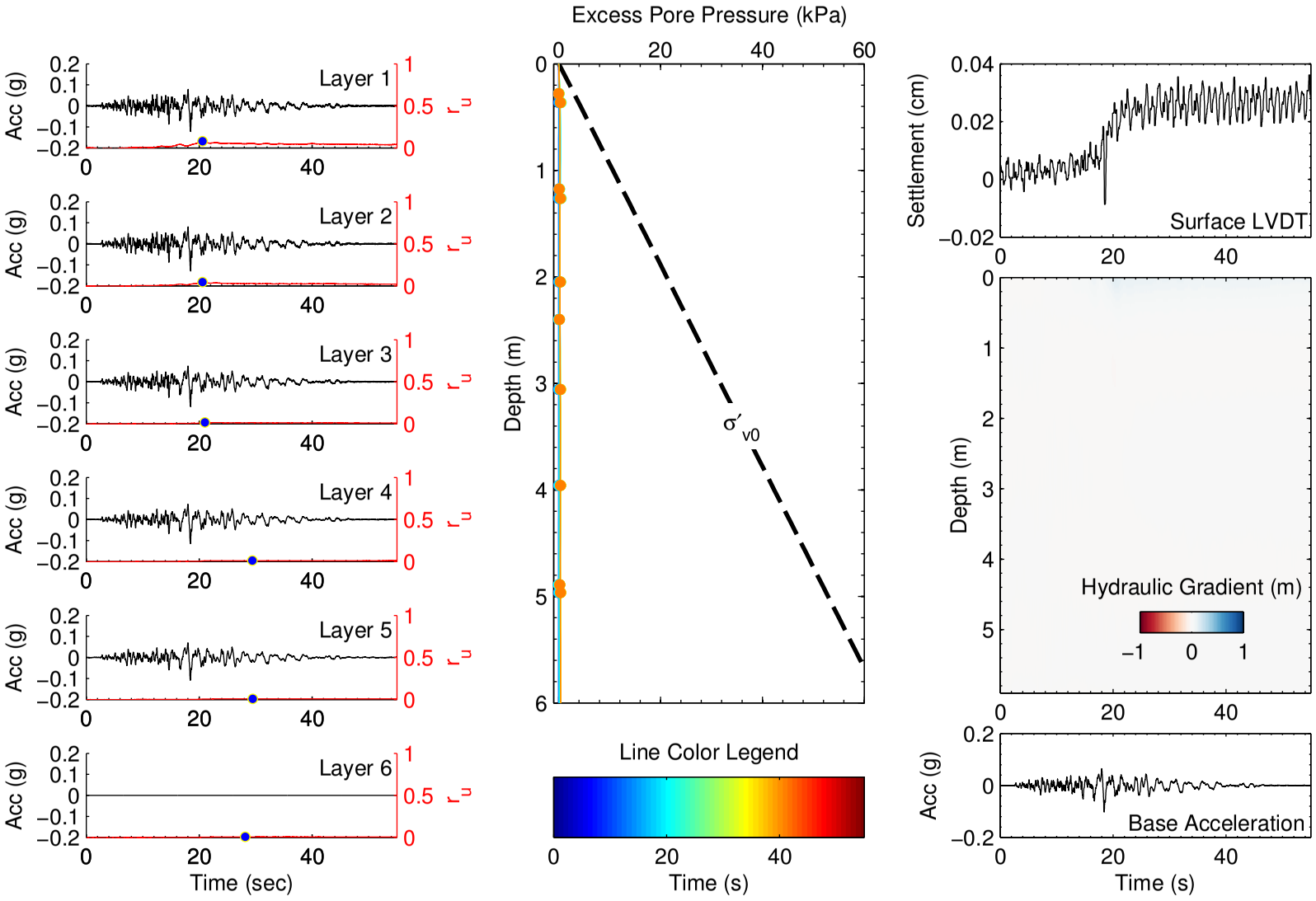
100% D_r Experiment 1 Test 2 – Data Summary Plot



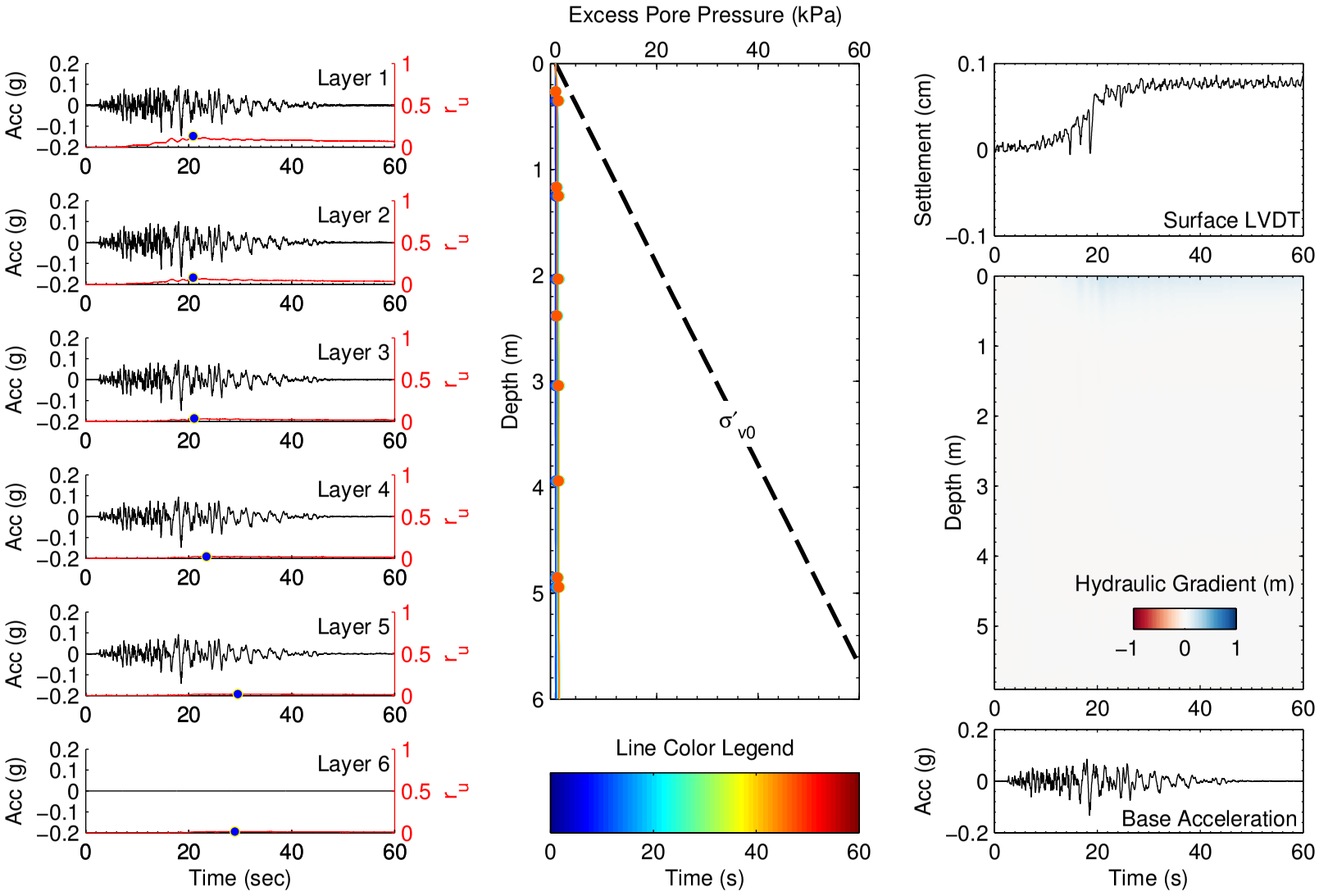
100% D_r Experiment 1 Test 3 – Data Summary Plot



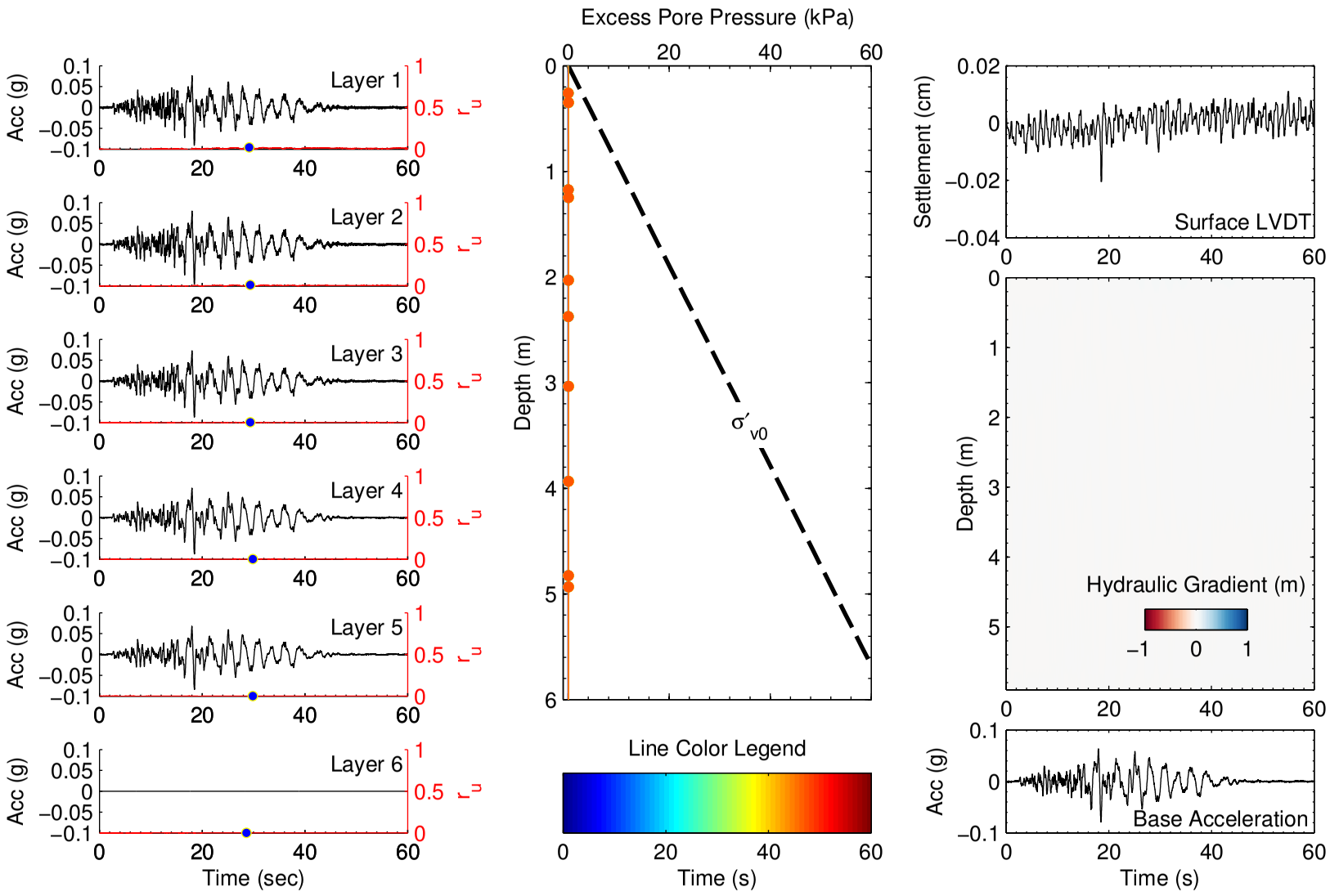
100% D_r Experiment 1 Test 4 – Data Summary Plot



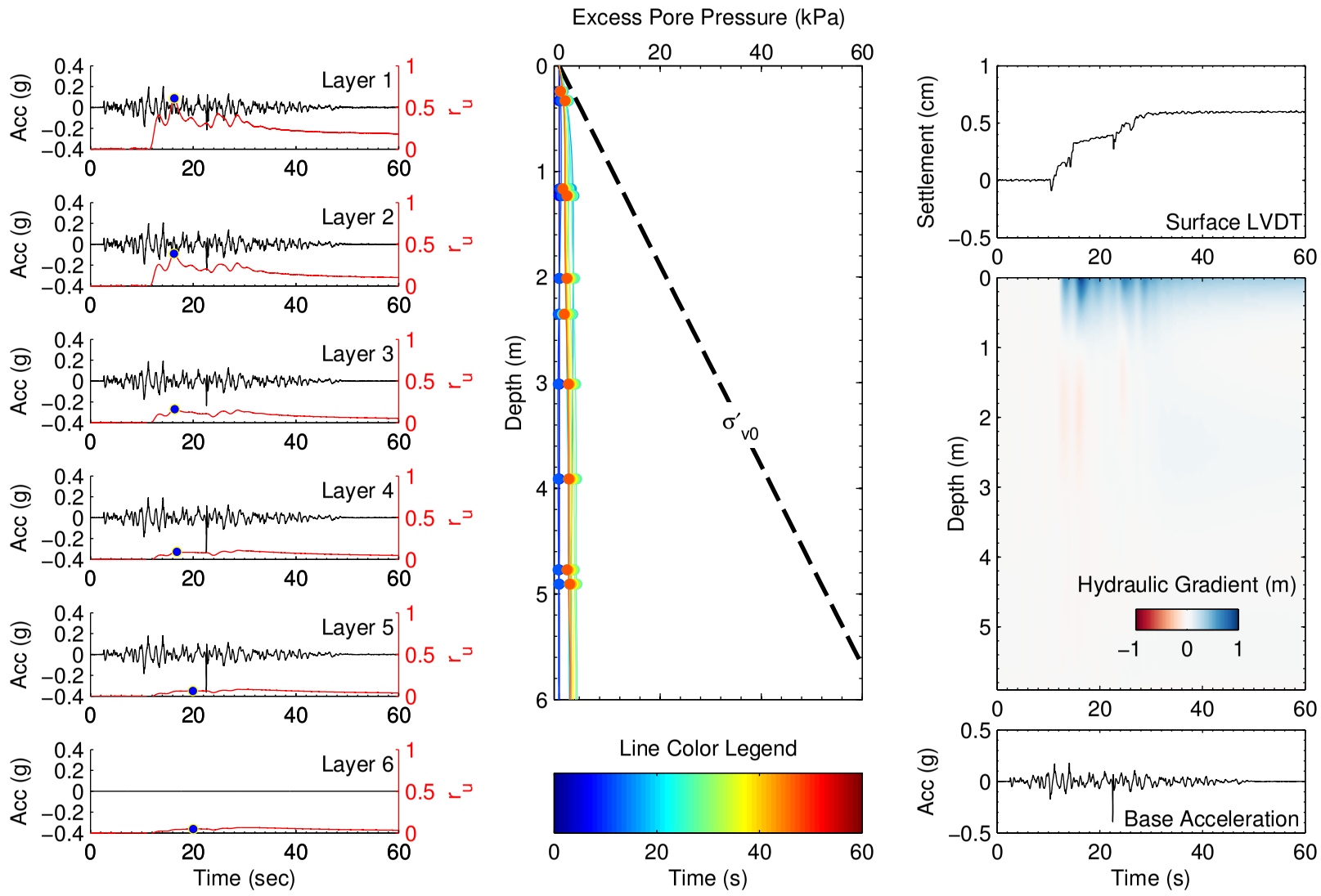
100% D_r Experiment 1 Test 5 – Data Summary Plot



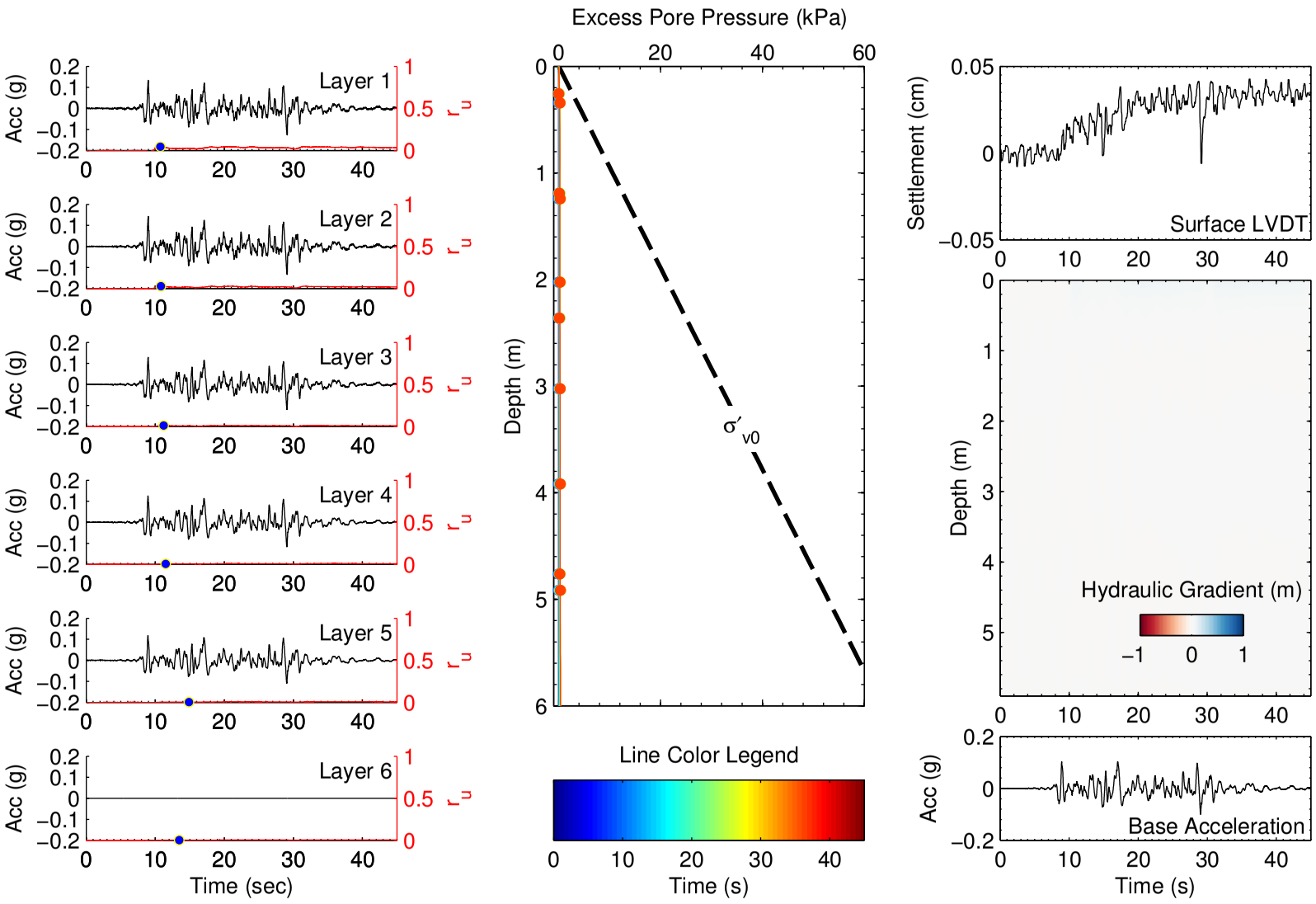
100% D_r Experiment 1 Test 6 – Data Summary Plot



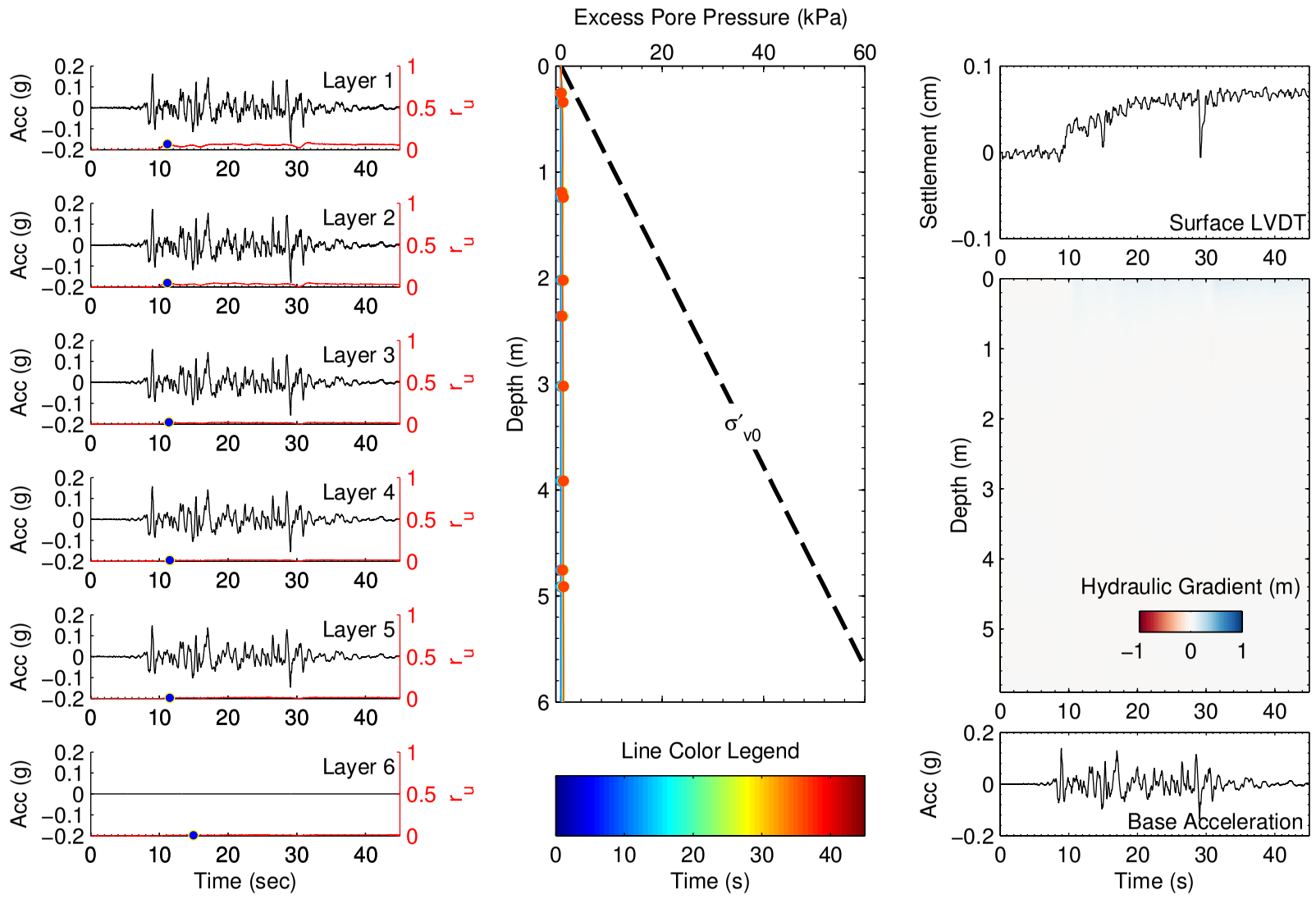
100% D_r Experiment 1 Test 7 – Data Summary Plot



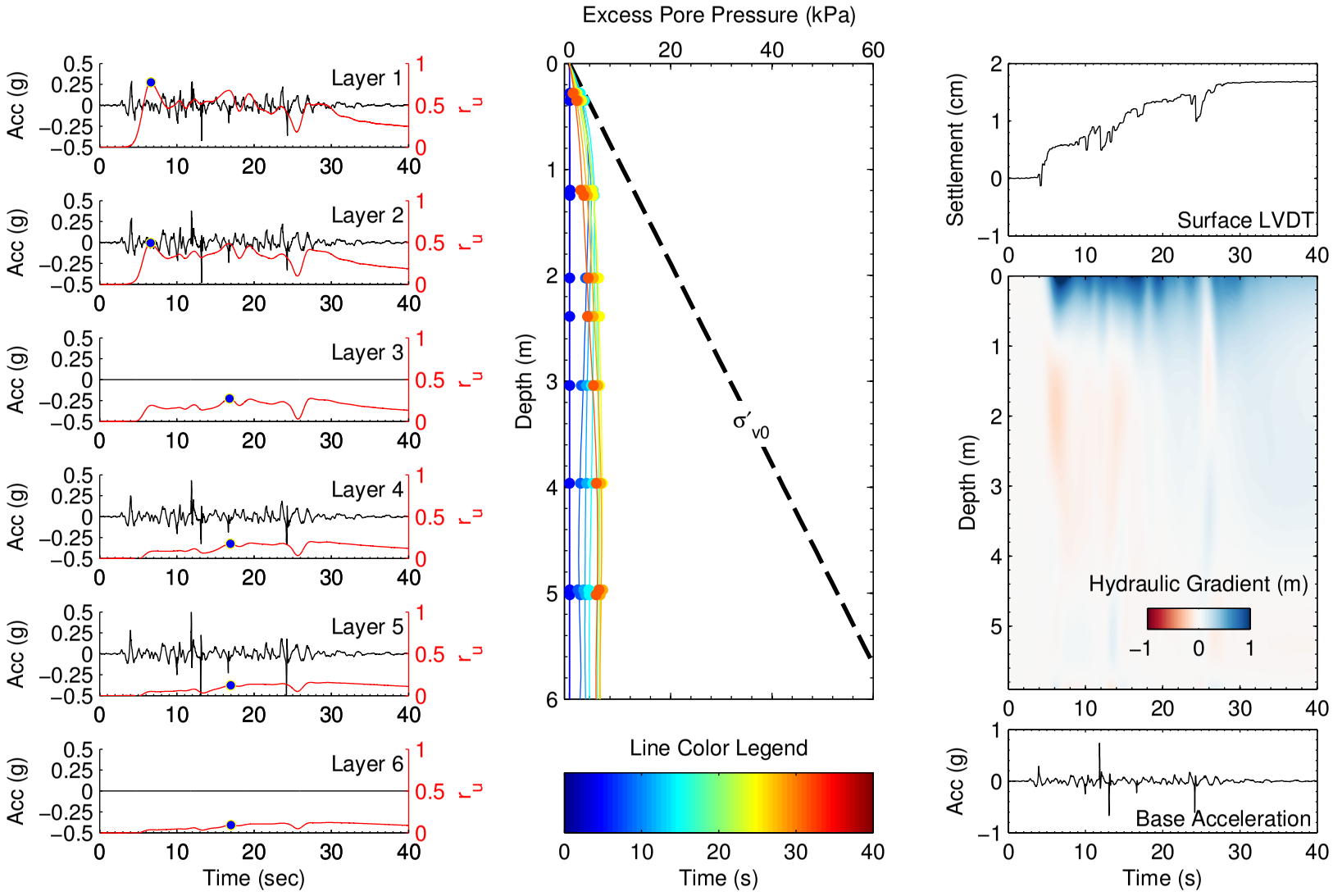
100% D_r Experiment 1 Test 8 – Data Summary Plot



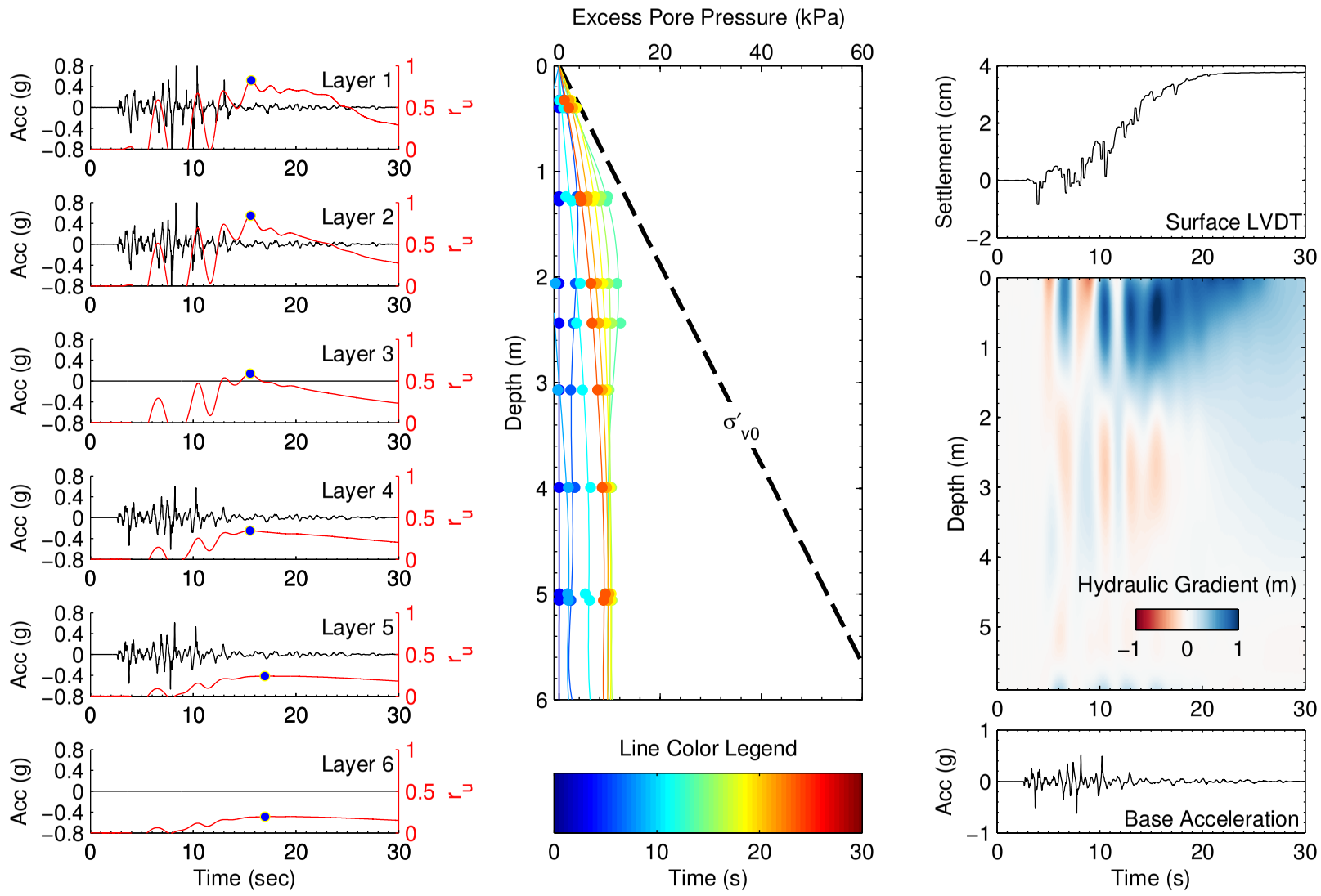
100% D_r Experiment 1 Test 9 – Data Summary Plot



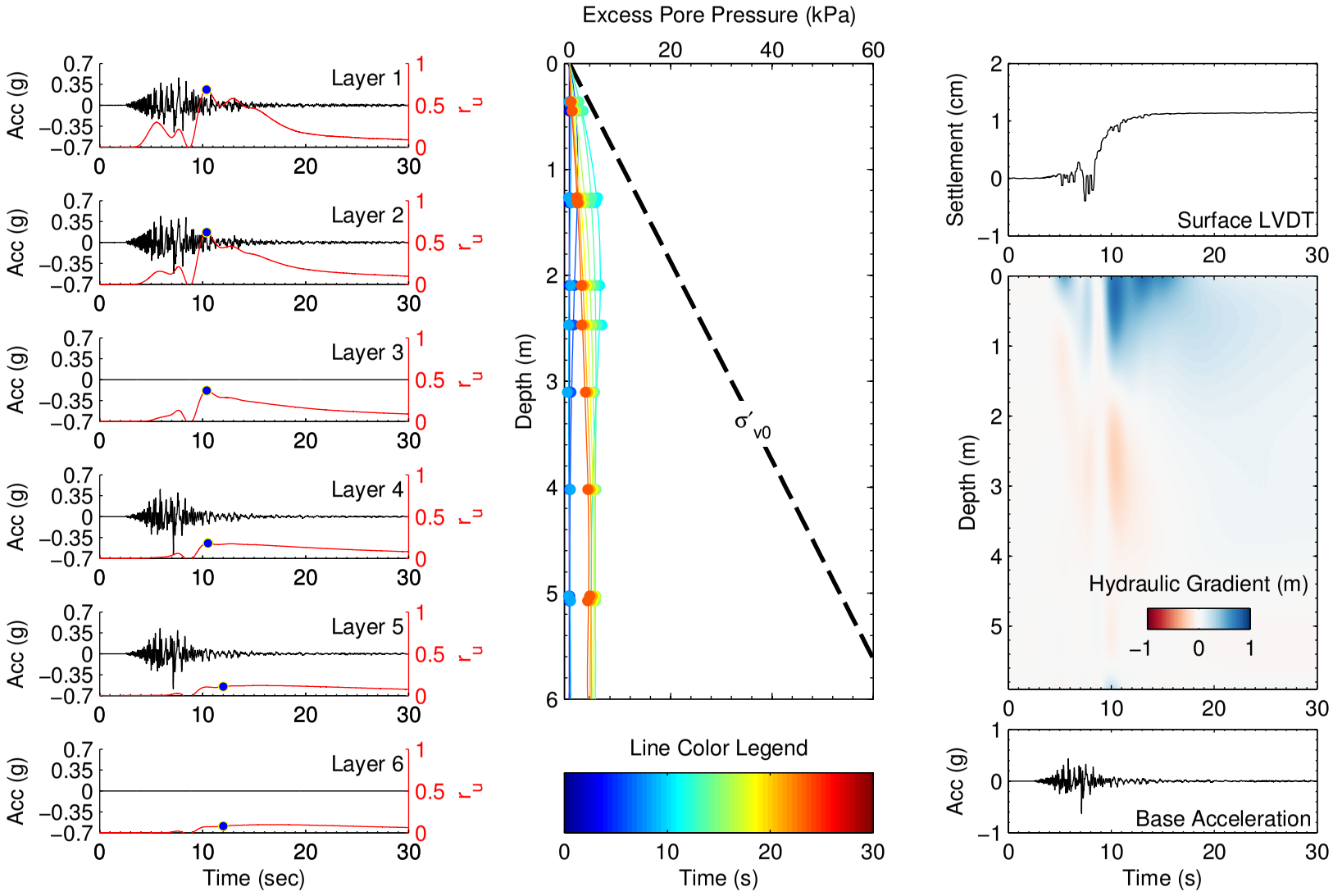
100% D_r Experiment 1 Test 10 – Data Summary Plot



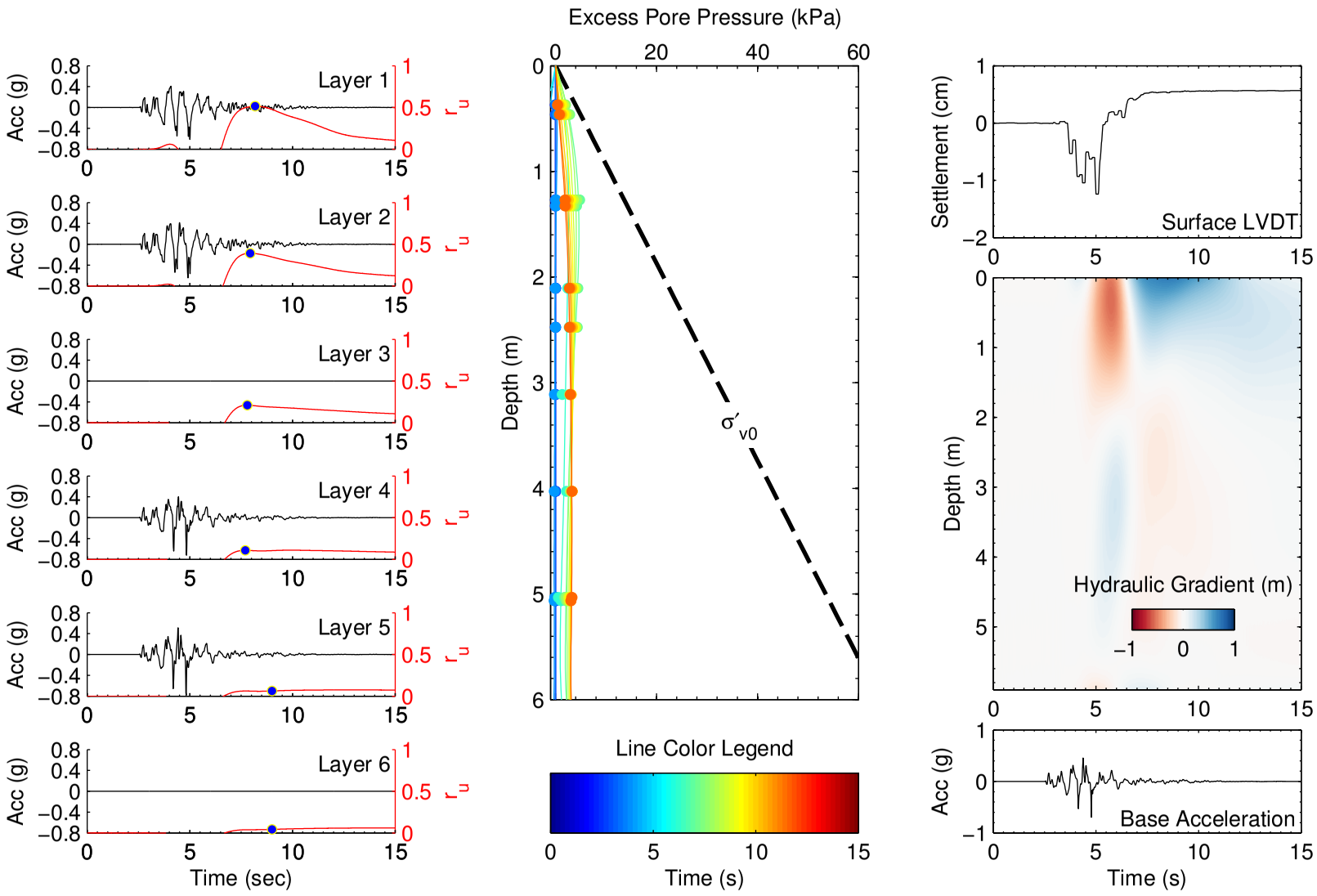
100% D_r Experiment 1 Test 11 – Data Summary Plot



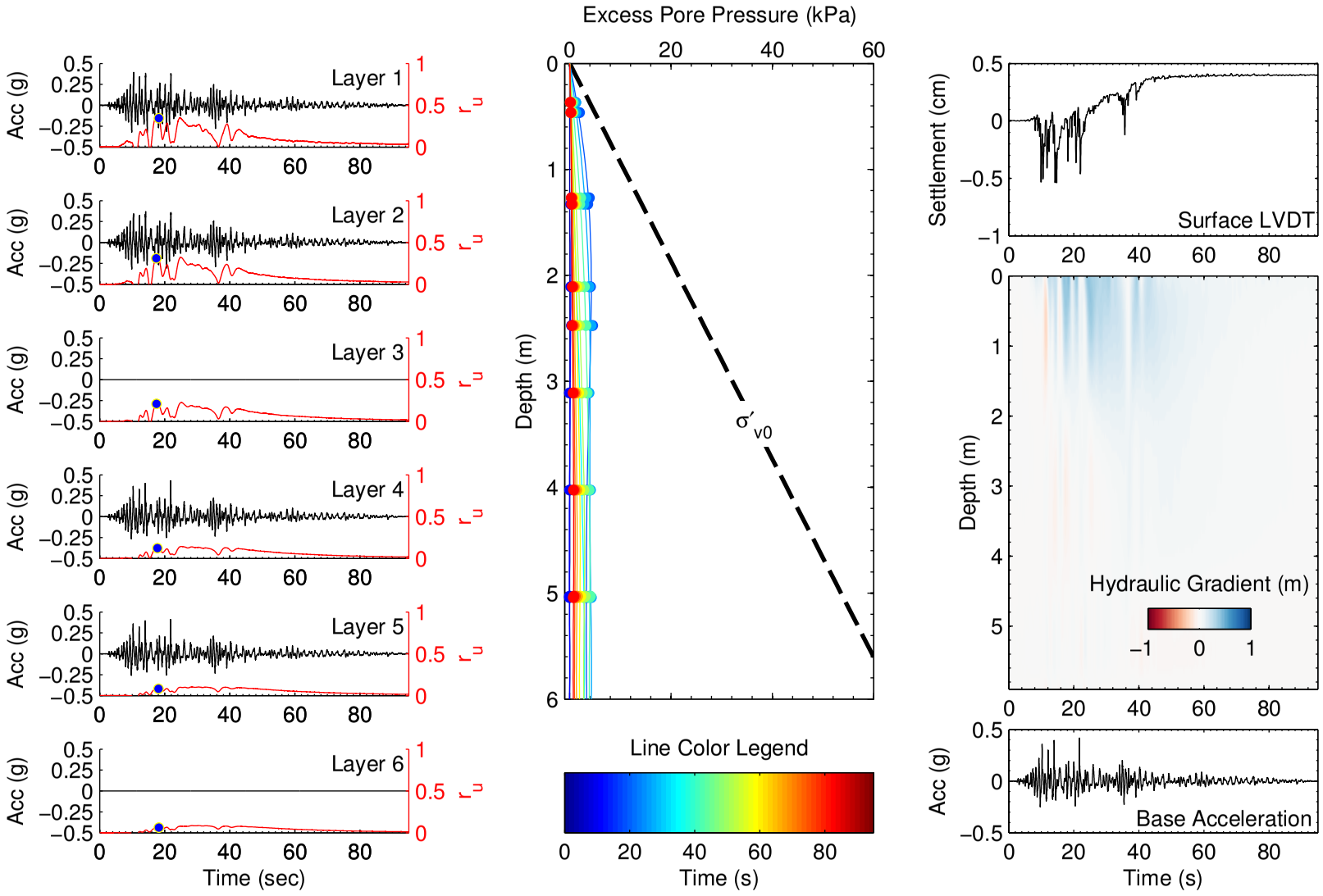
100% D_r Experiment 1 Test 12 – Data Summary Plot



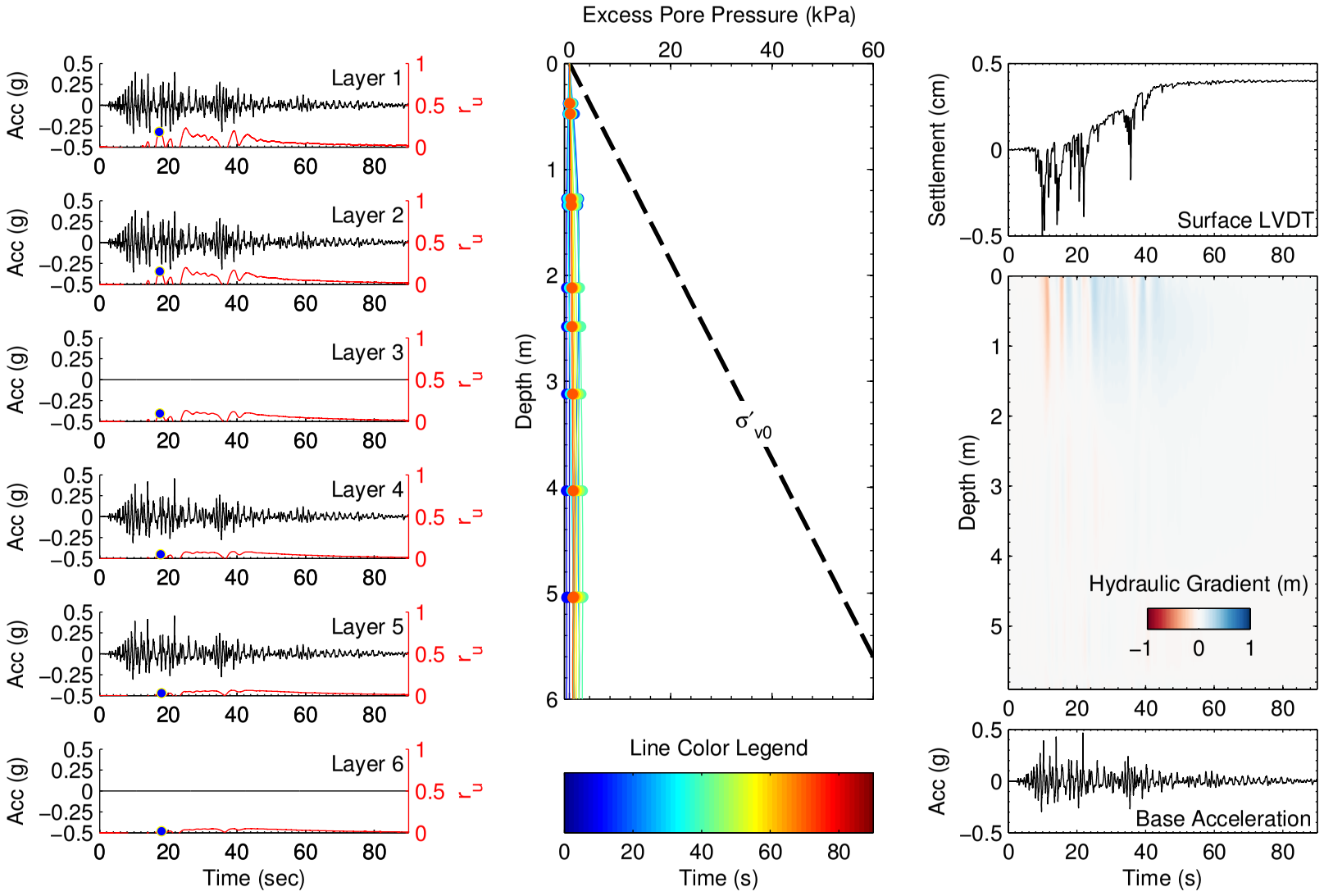
100% D_r Experiment 1 Test 13 – Data Summary Plot



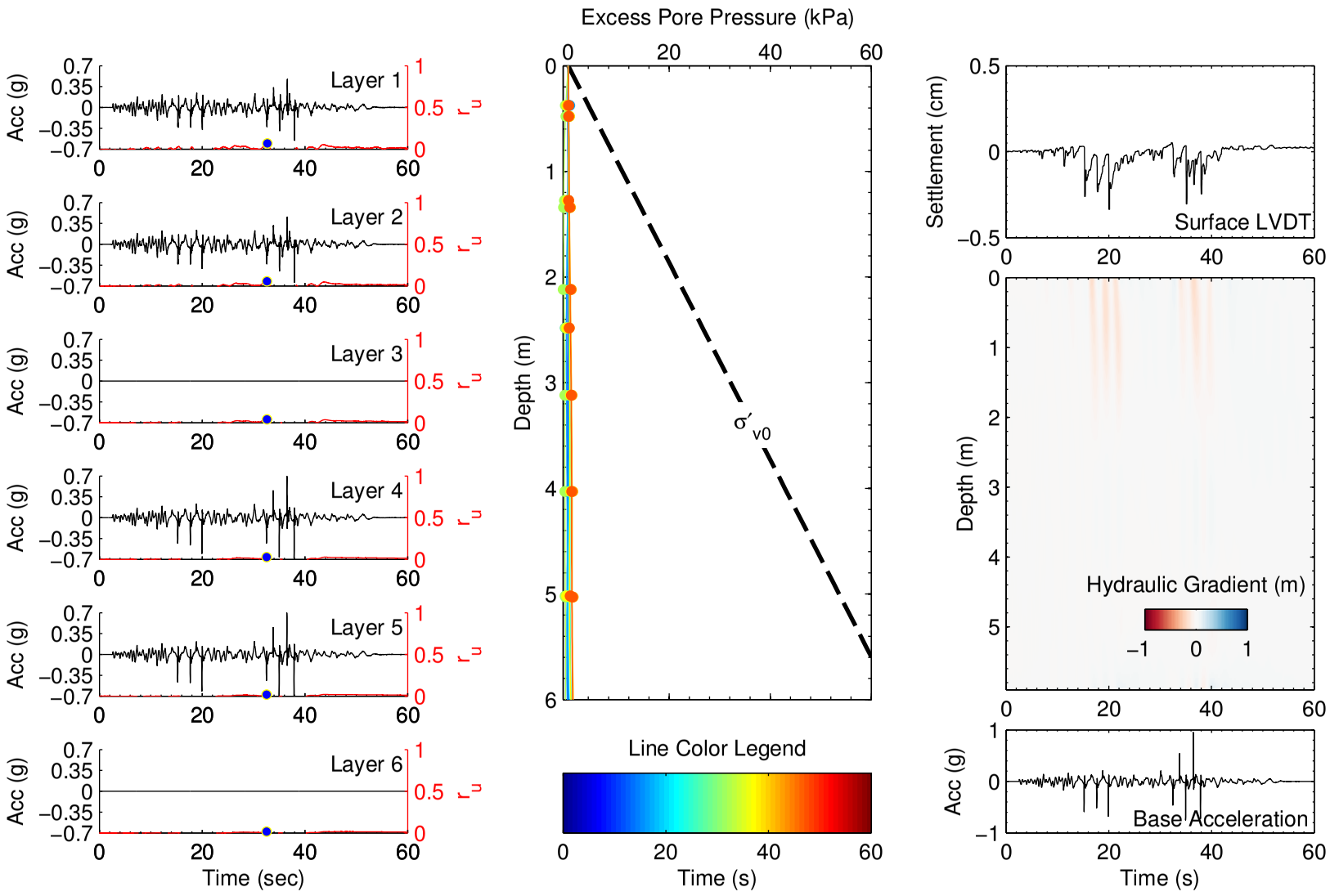
100% D_r Experiment 1 Test 14 – Data Summary Plot



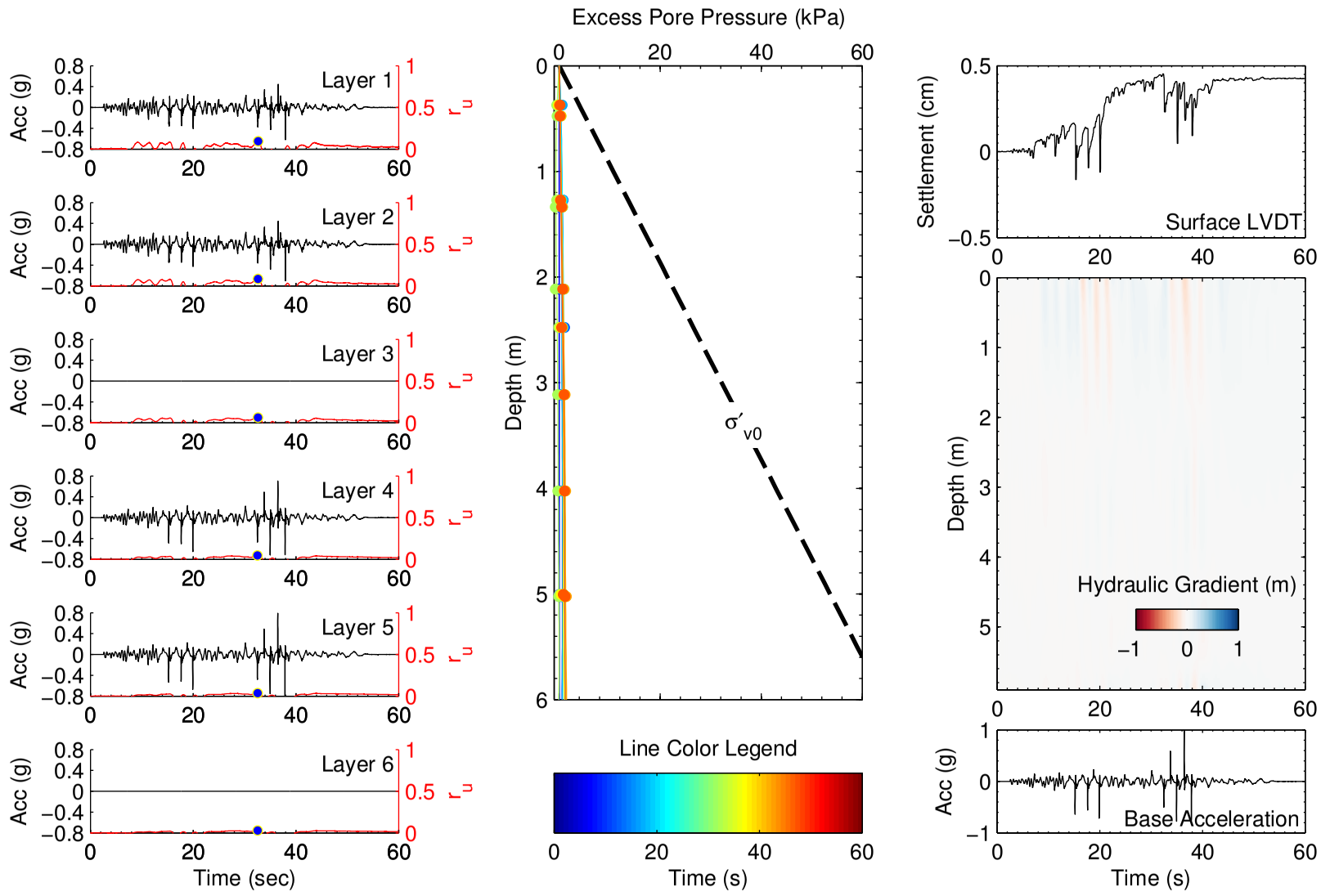
100% D_r Experiment 1 Test 15 – Data Summary Plot



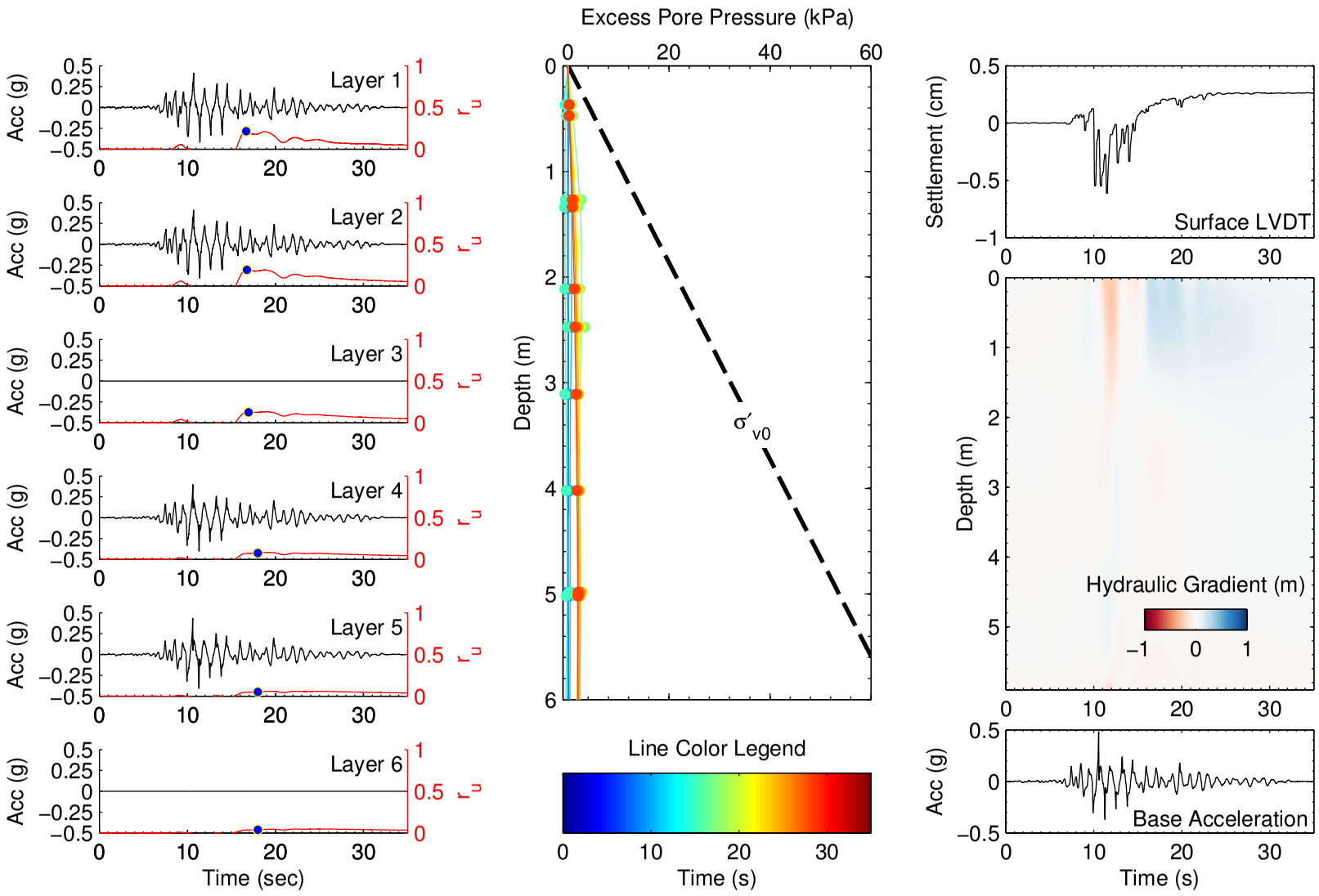
100% D_r Experiment 1 Test 16 – Data Summary Plot



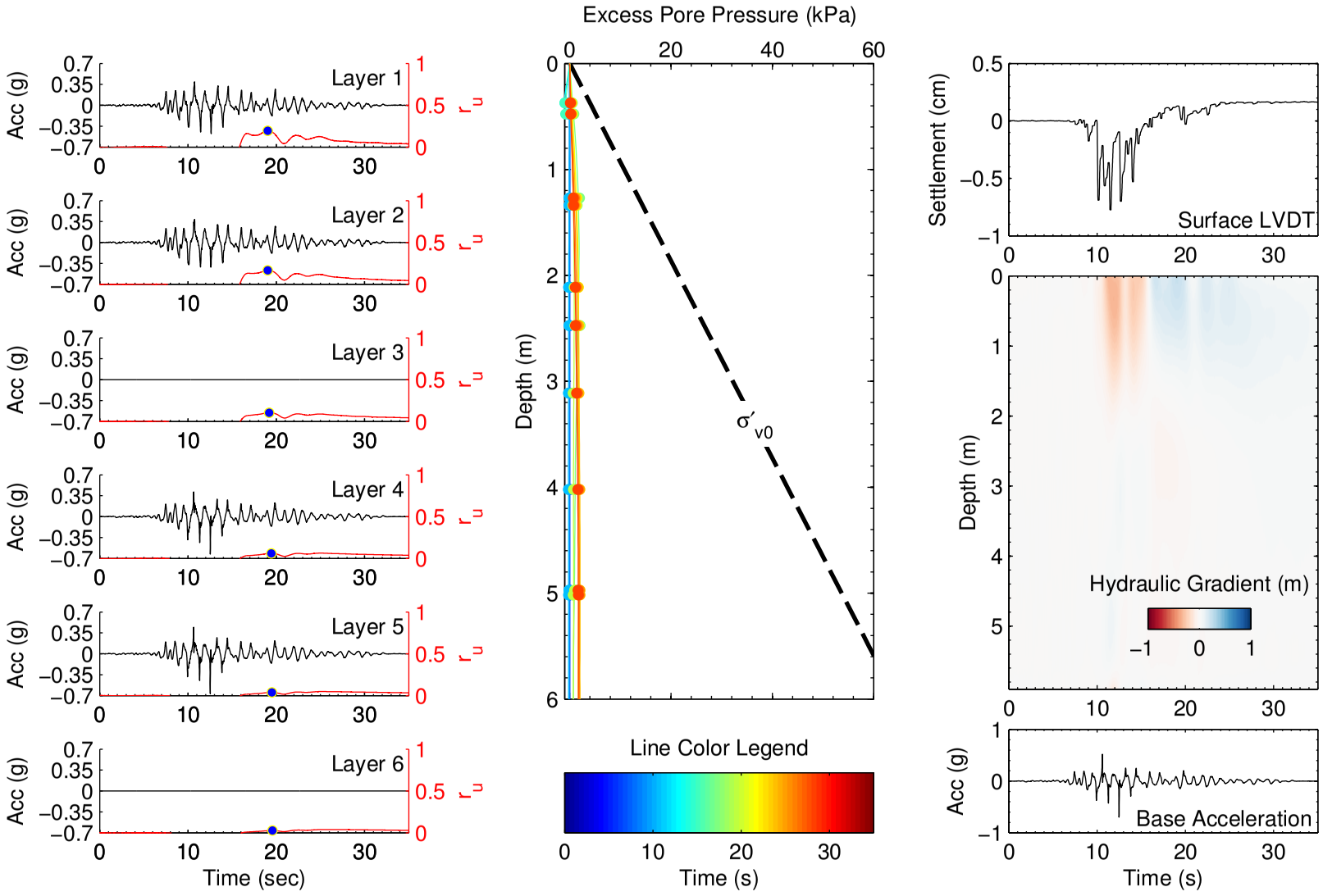
100% D_r Experiment 1 Test 17 – Data Summary Plot



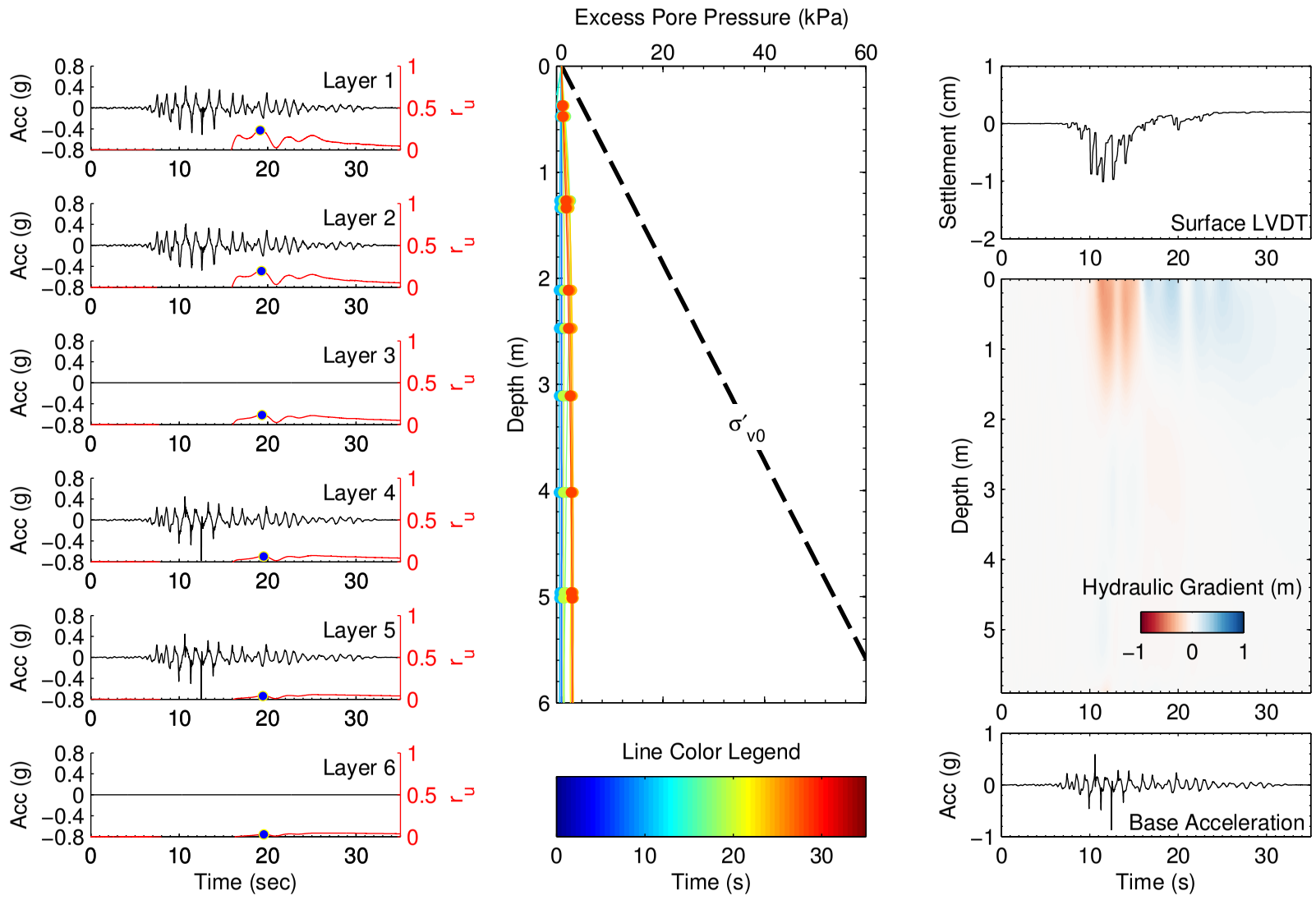
100% D_r Experiment 1 Test 18 – Data Summary Plot



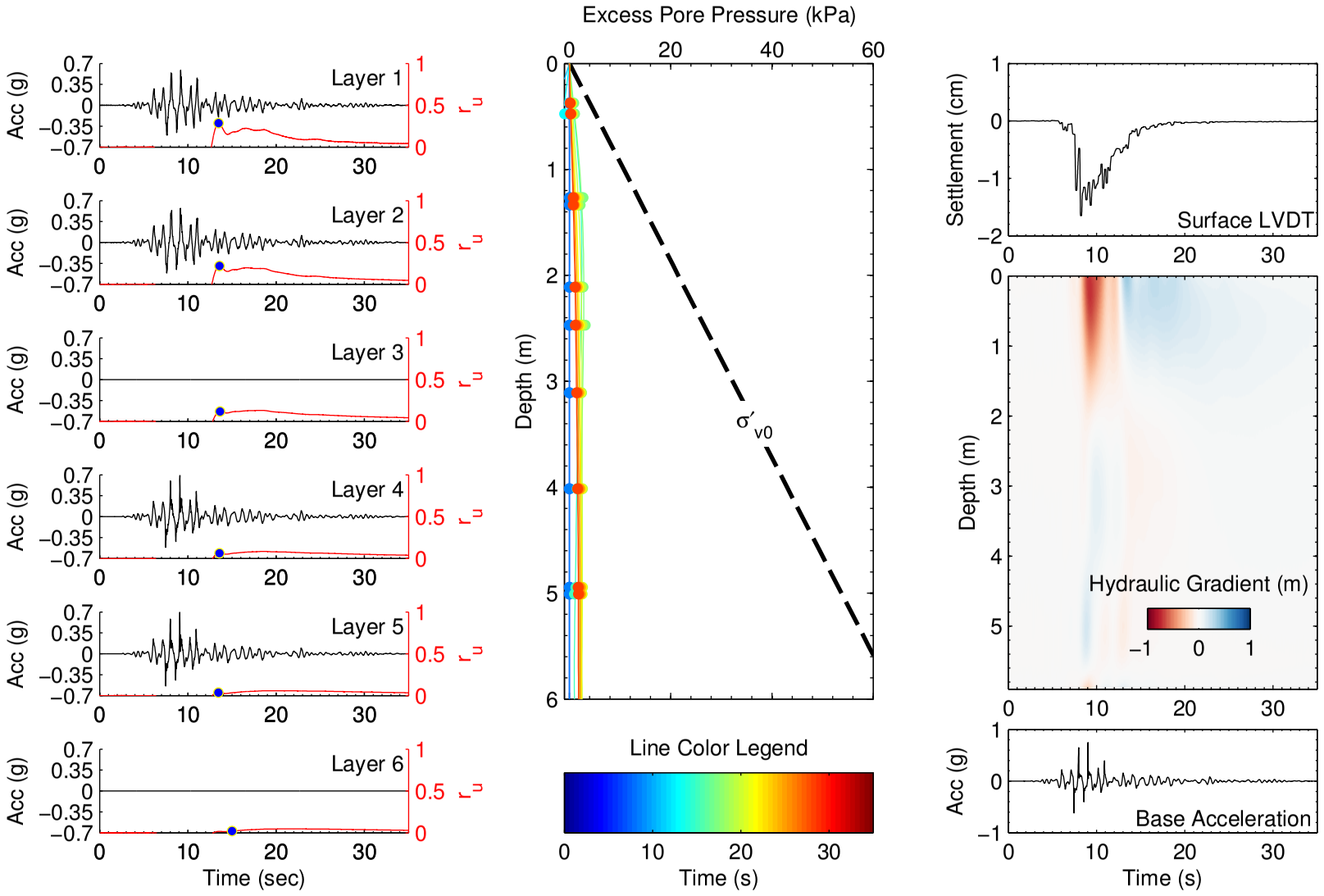
100% D_r Experiment 1 Test 19 – Data Summary Plot



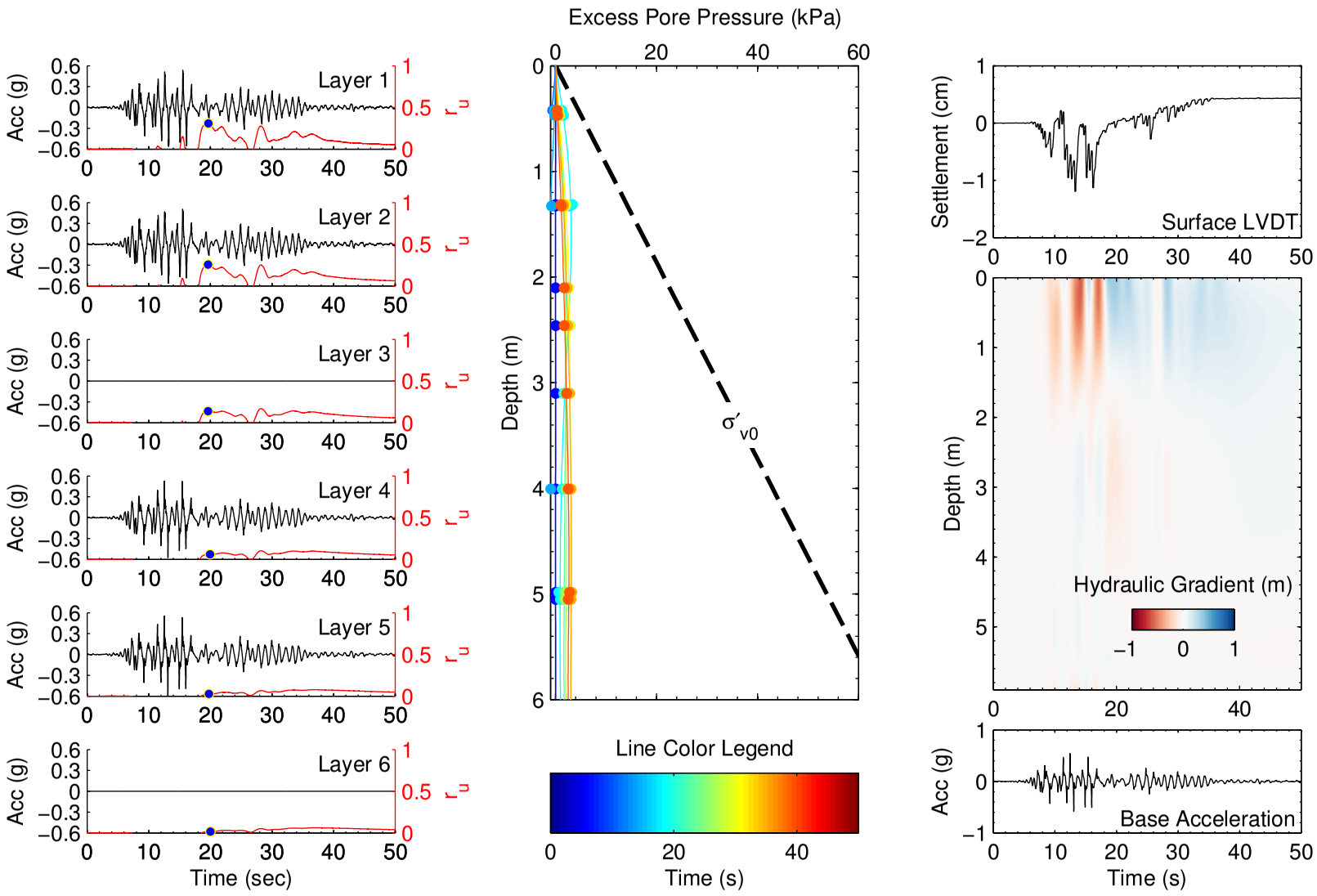
100% D_r Experiment 1 Test 20 – Data Summary Plot



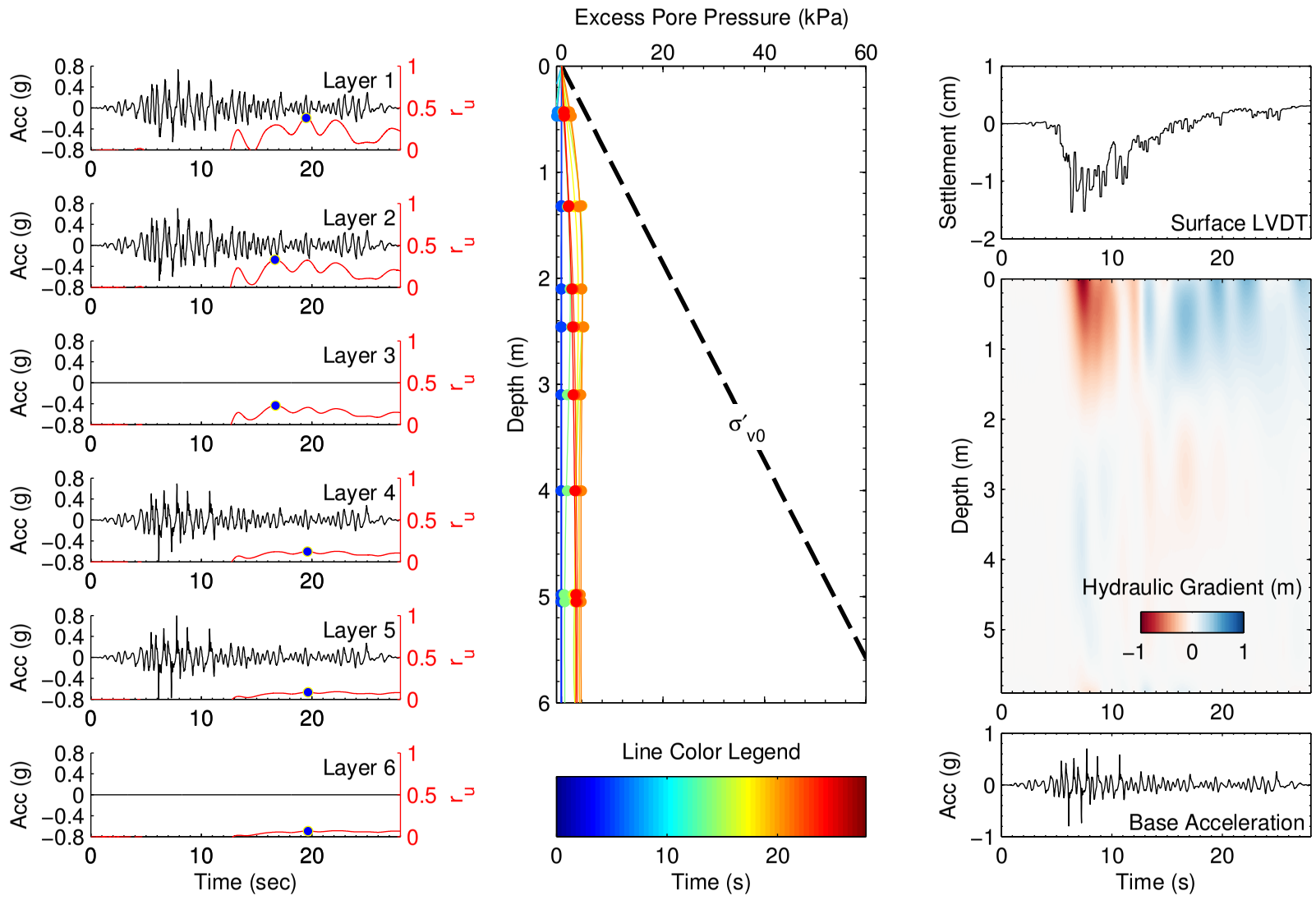
100% D_r Experiment 1 Test 21 – Data Summary Plot



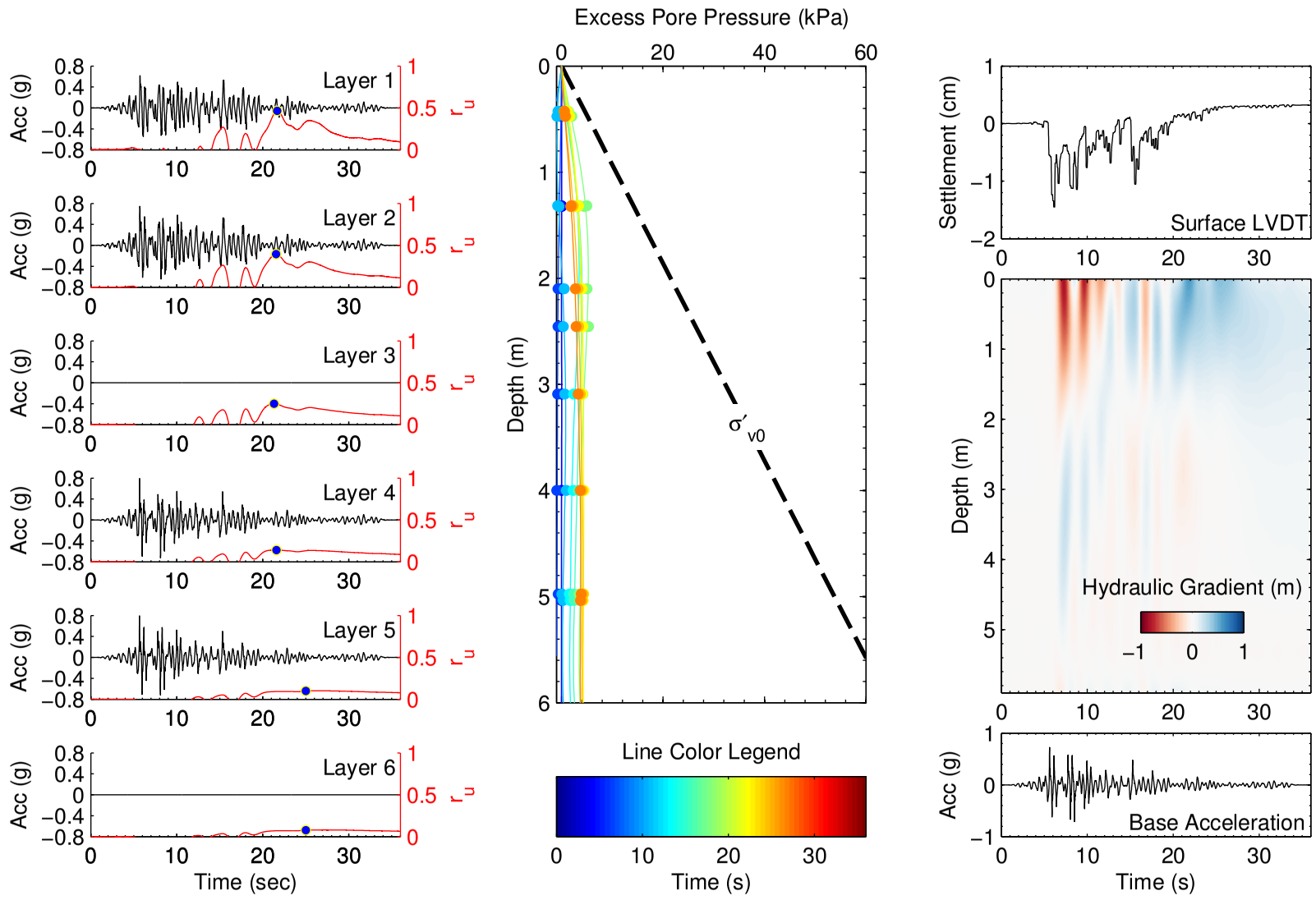
100% D_r Experiment 1 Test 22 – Data Summary Plot



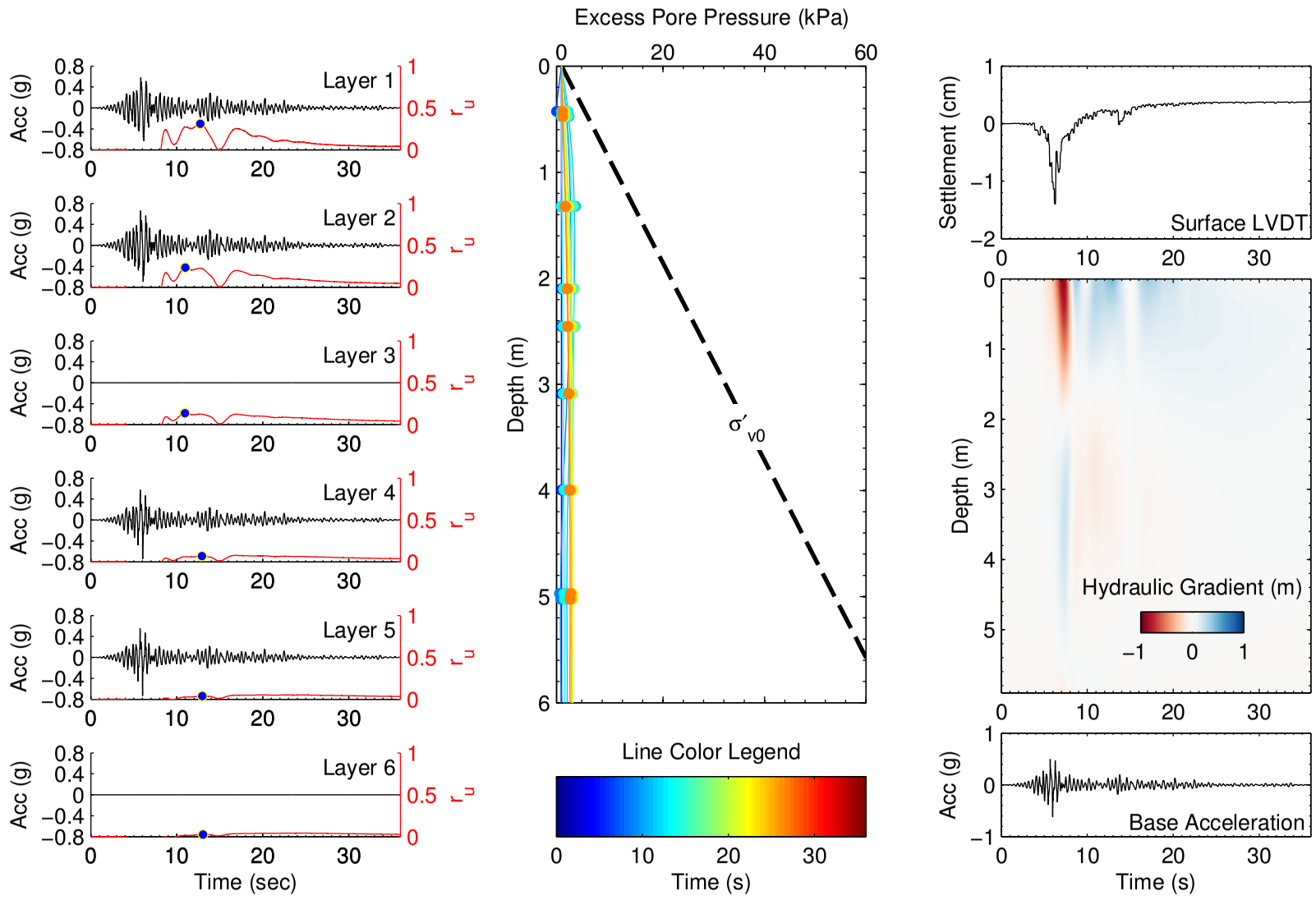
100% D_r Experiment 1 Test 23 – Data Summary Plot



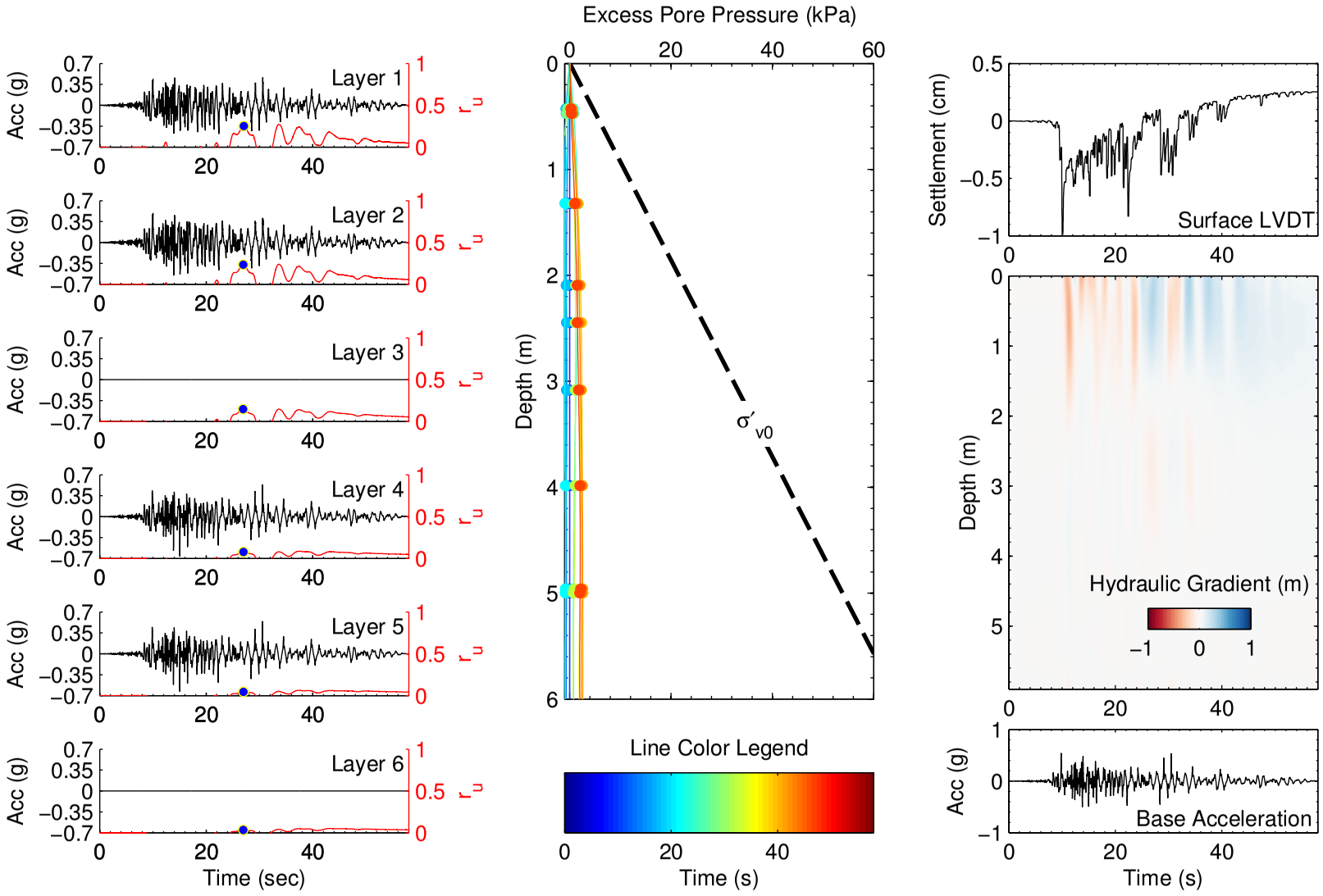
100% D_r Experiment 1 Test 24 – Data Summary Plot



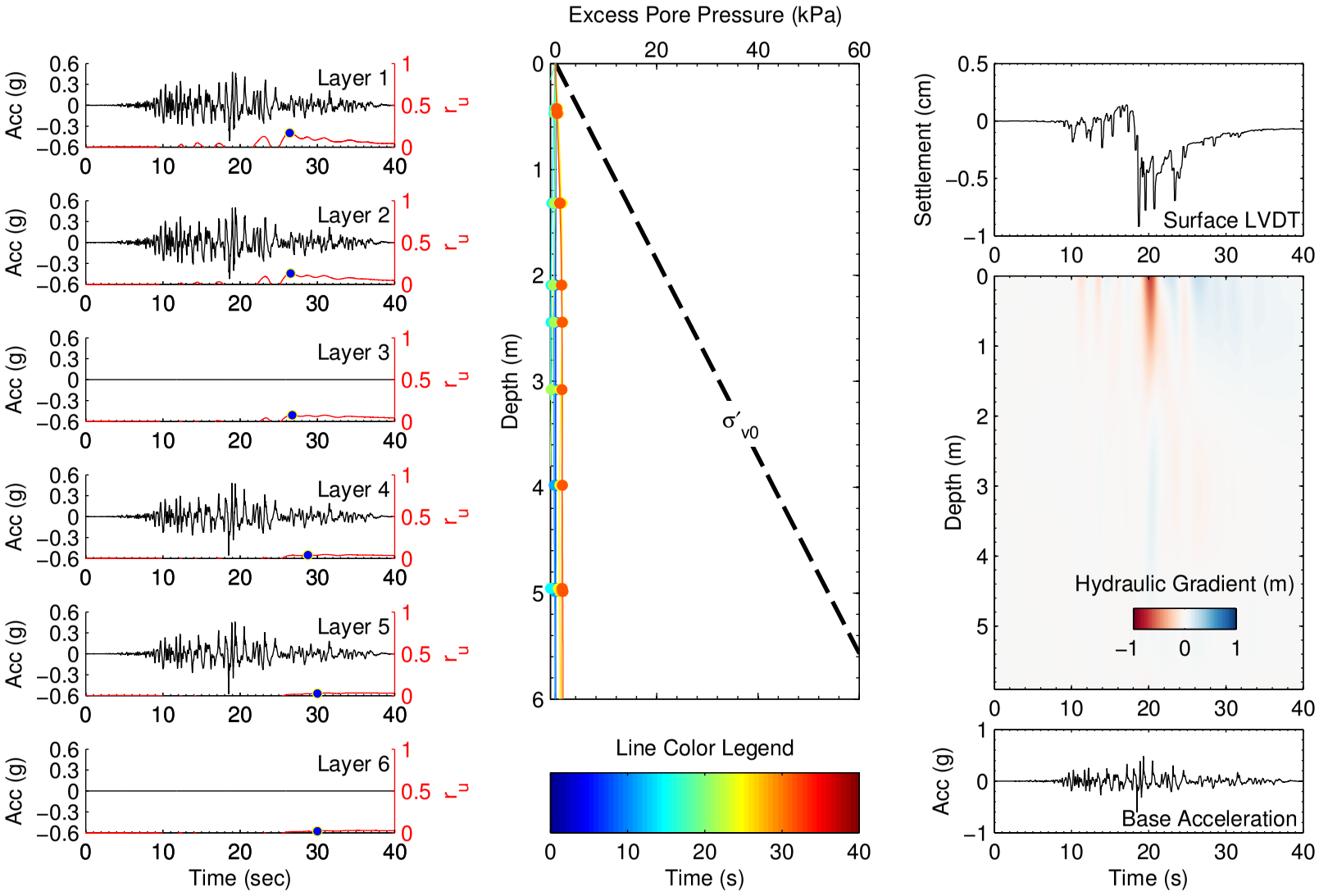
100% D_r Experiment 1 Test 25 – Data Summary Plot



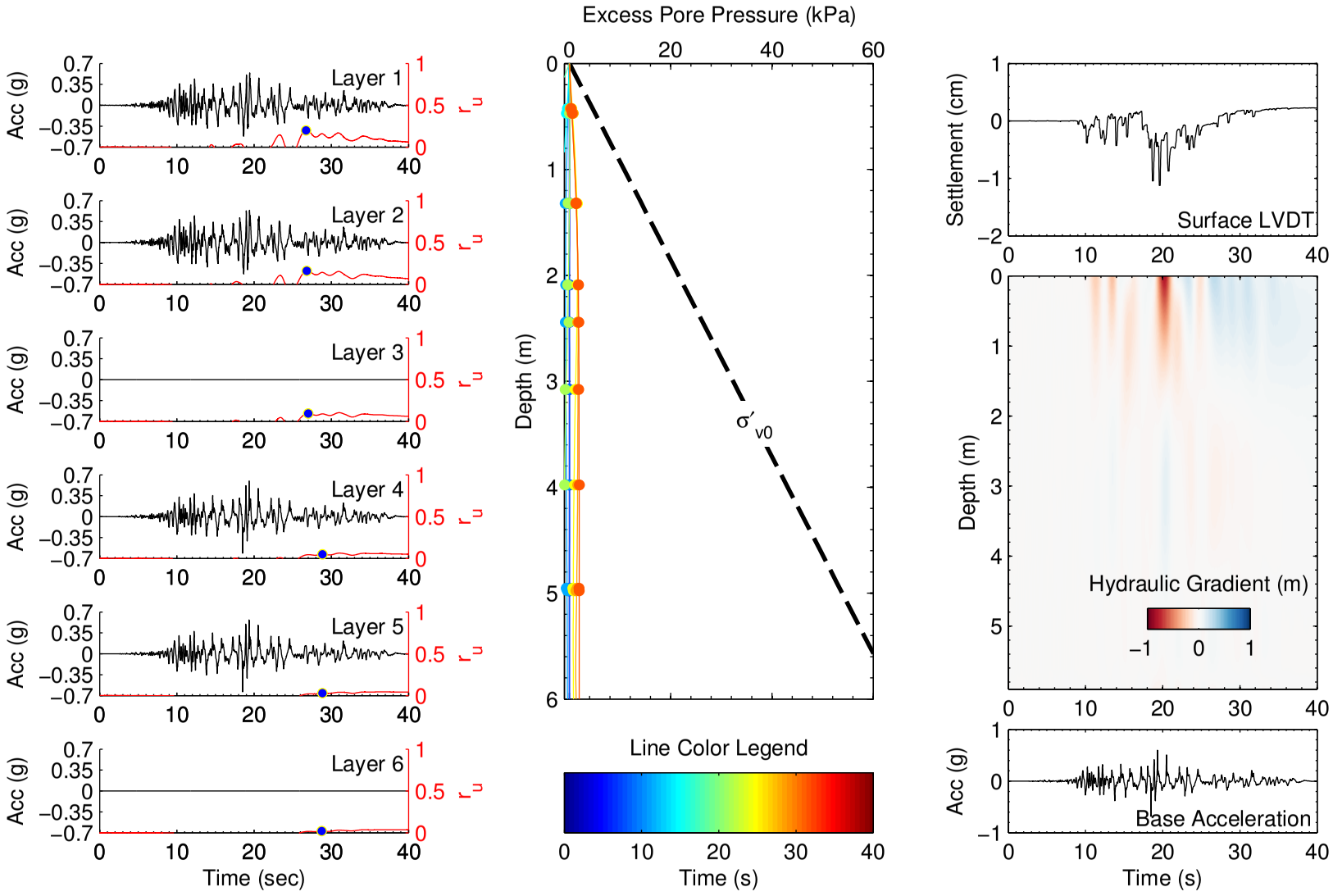
100% D_r Experiment 1 Test 26 – Data Summary Plot



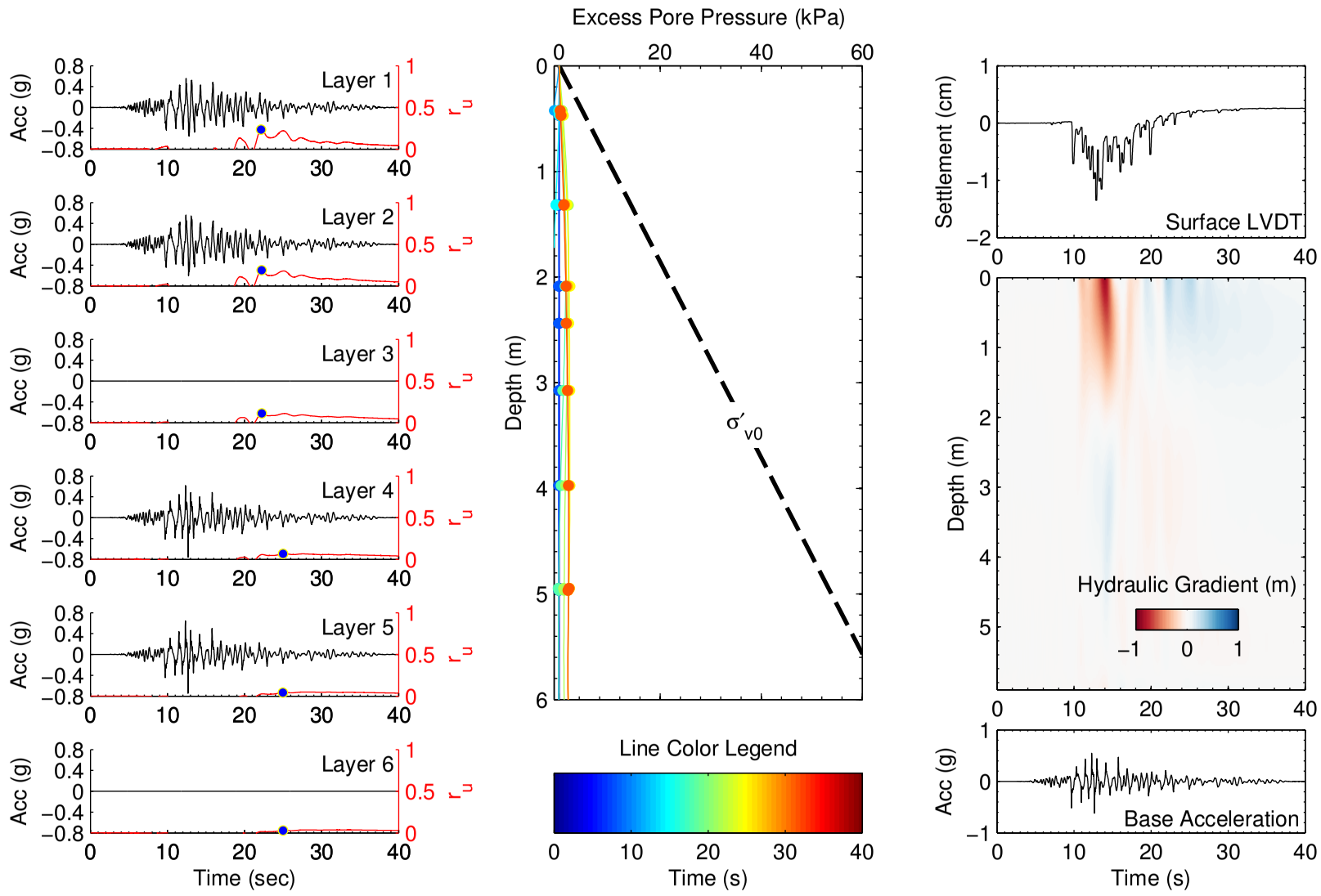
100% D_r Experiment 1 Test 27 – Data Summary Plot



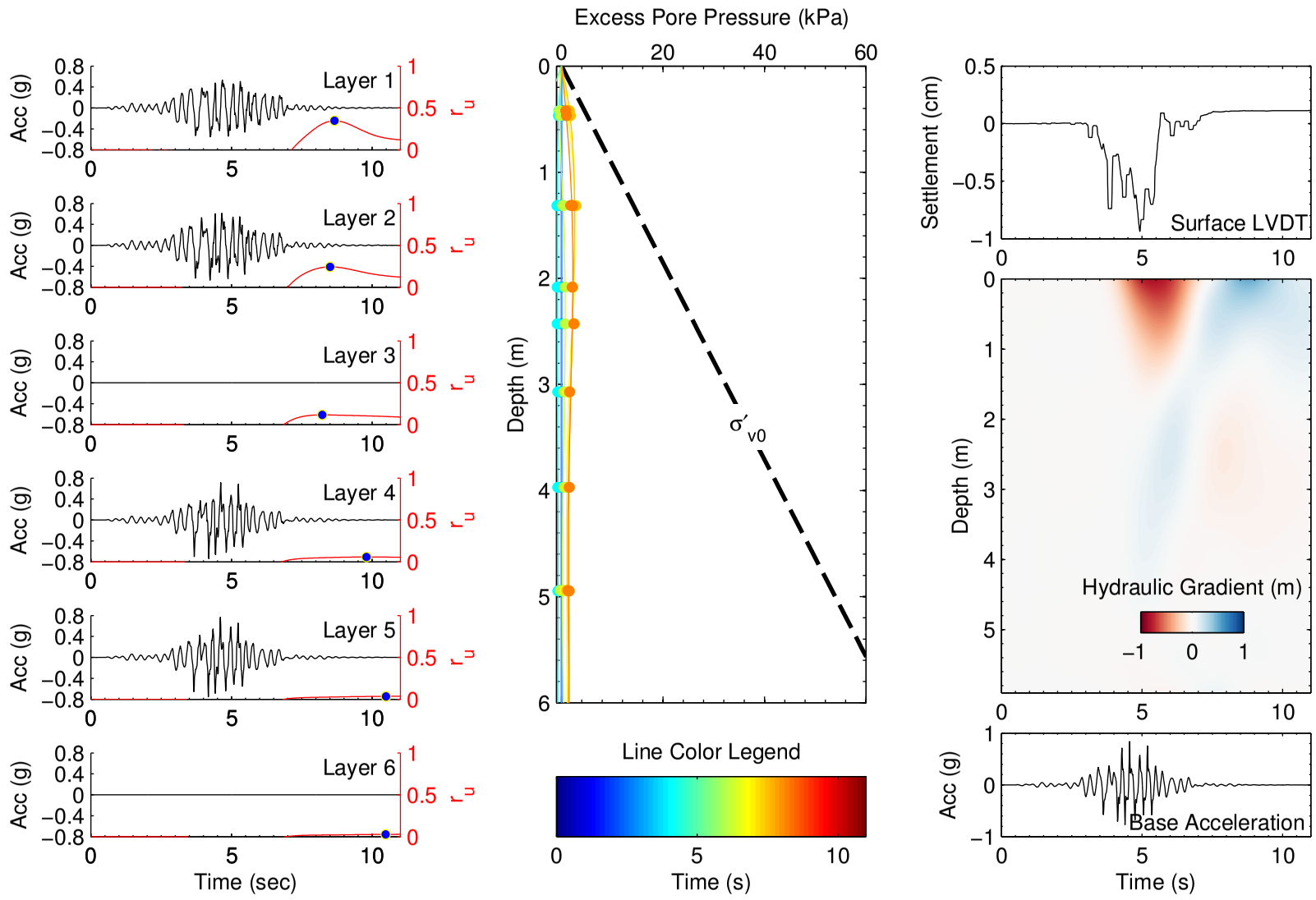
100% D_r Experiment 1 Test 28 – Data Summary Plot



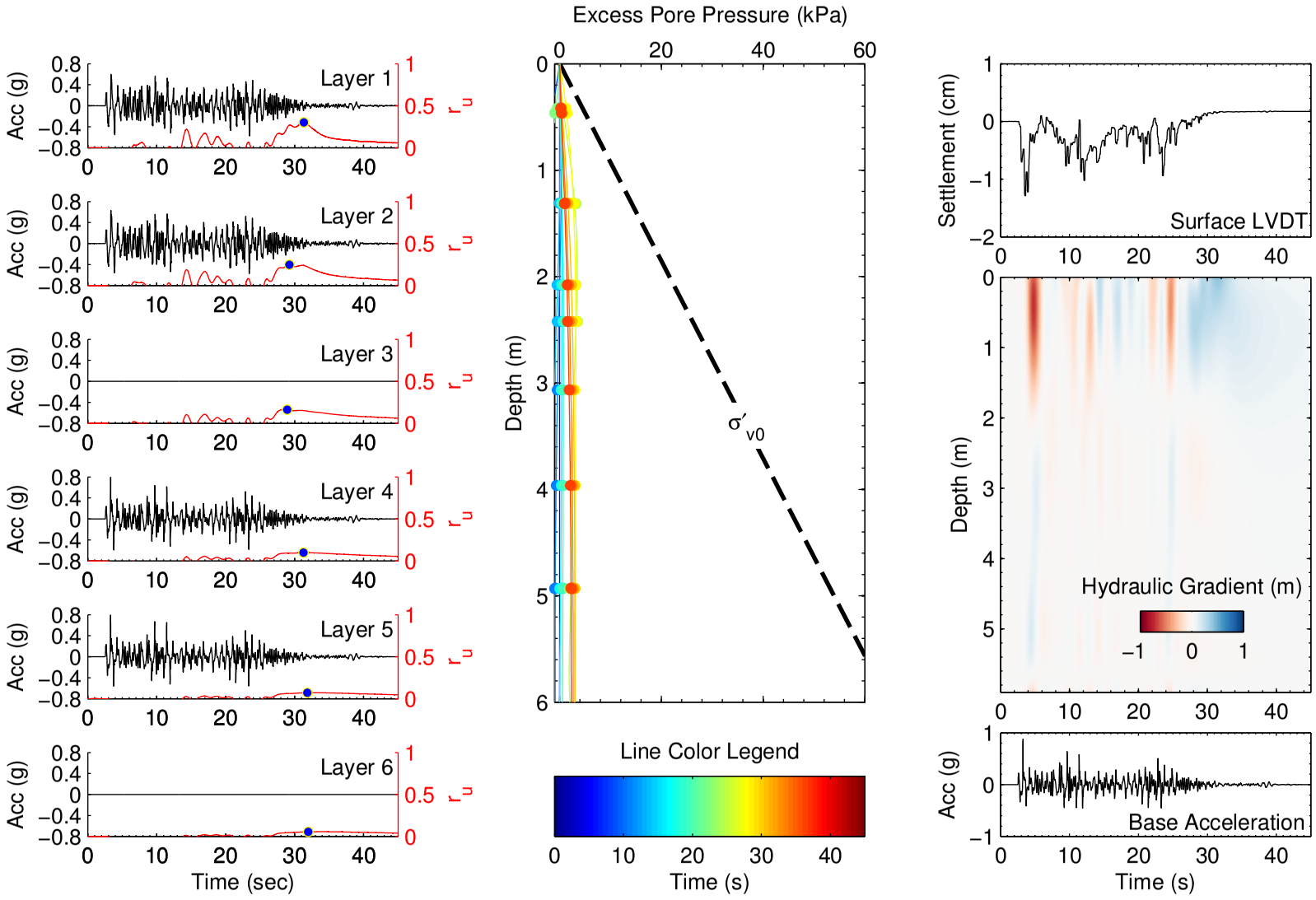
100% D_r Experiment 1 Test 29 – Data Summary Plot



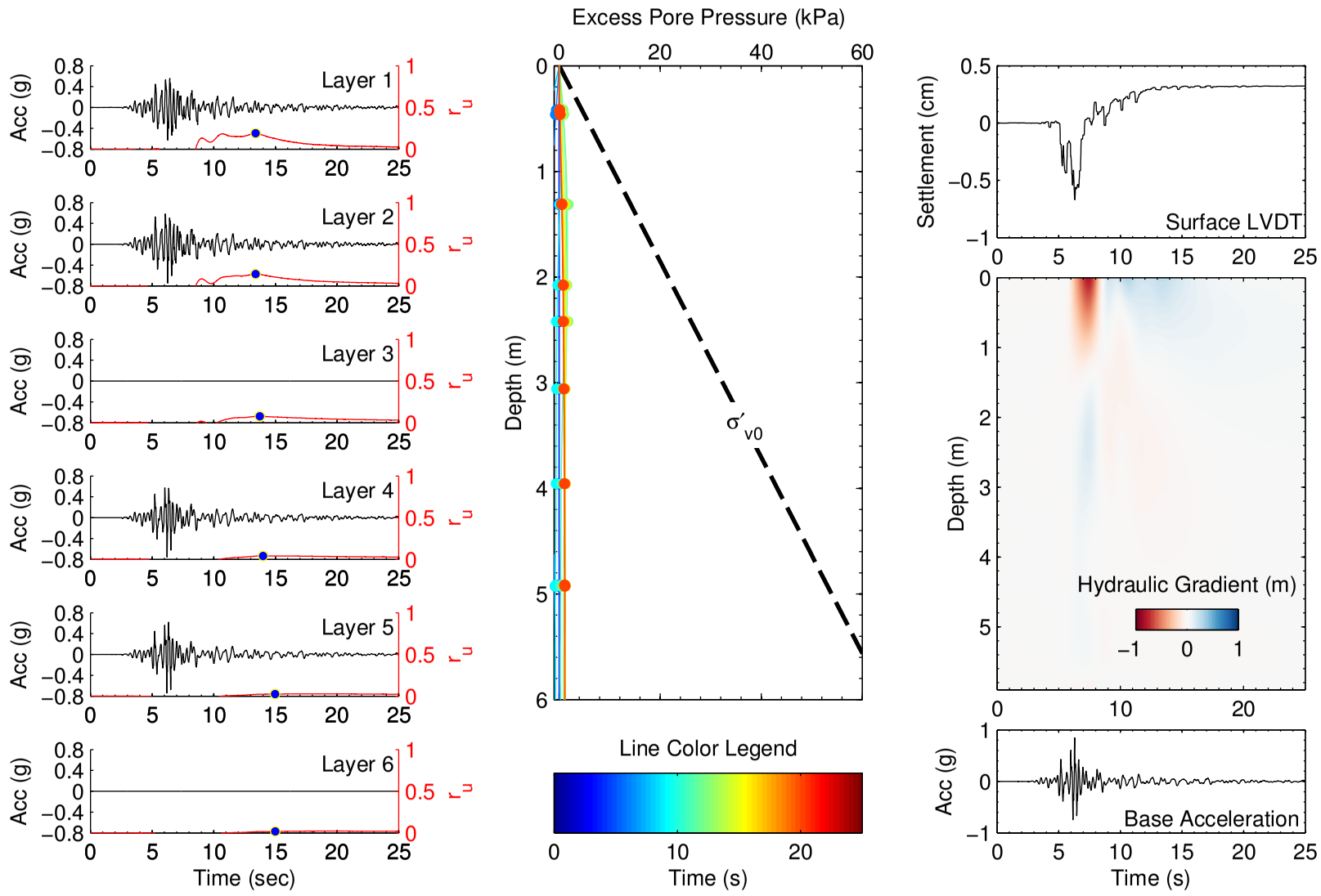
100% D_r Experiment 1 Test 30 – Data Summary Plot



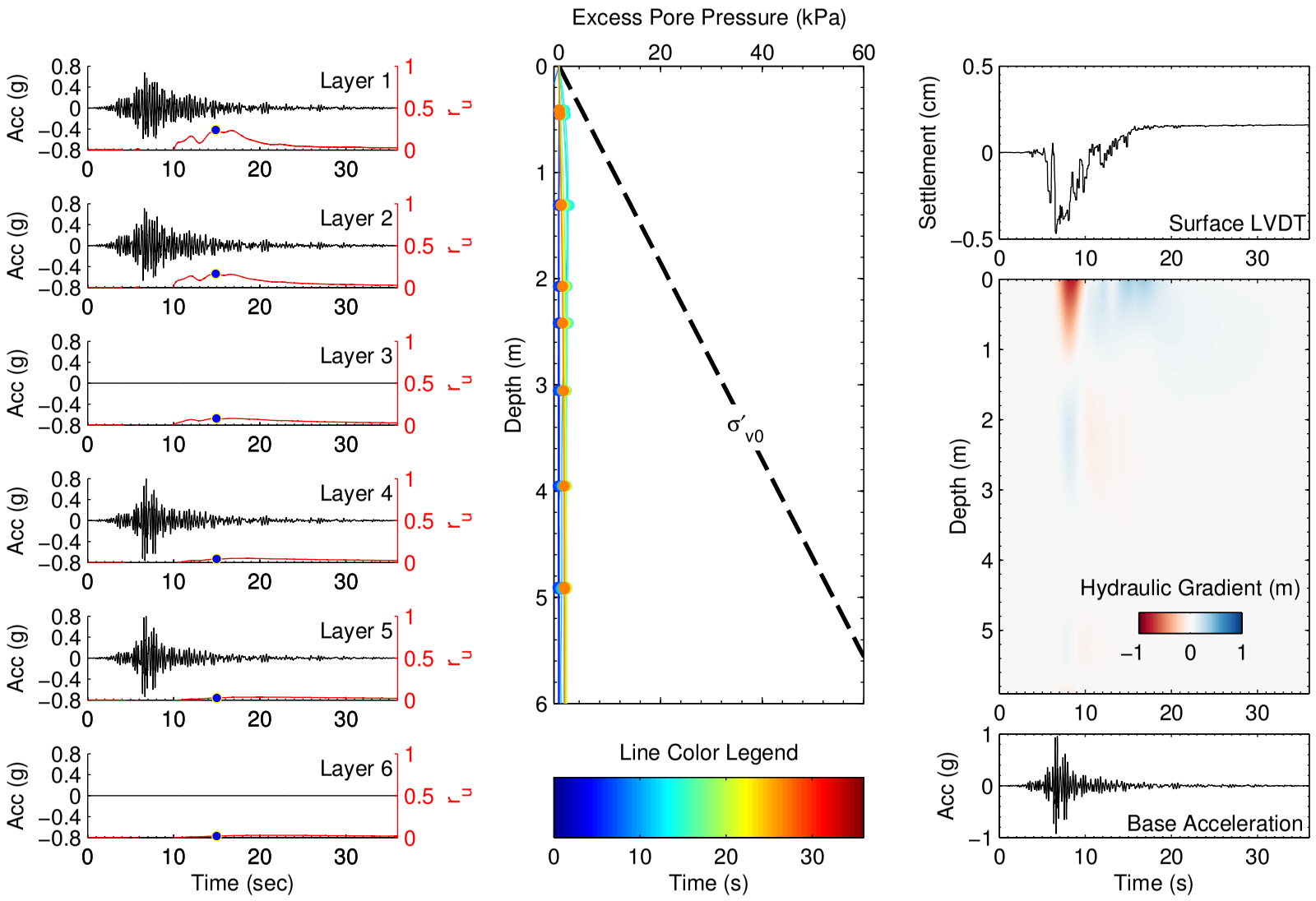
100% D_r Experiment 1 Test 31 – Data Summary Plot



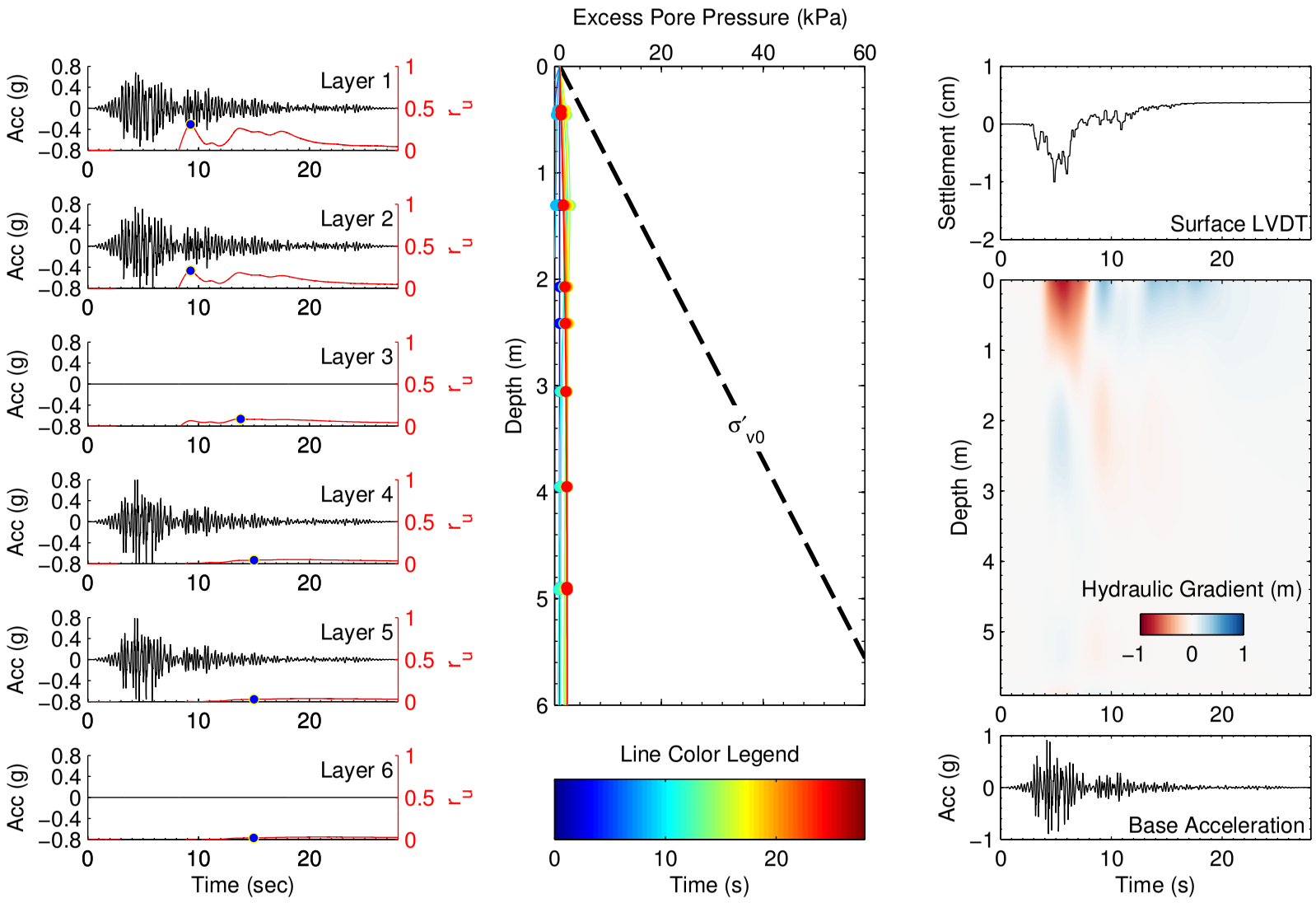
100% D_r Experiment 1 Test 32 – Data Summary Plot



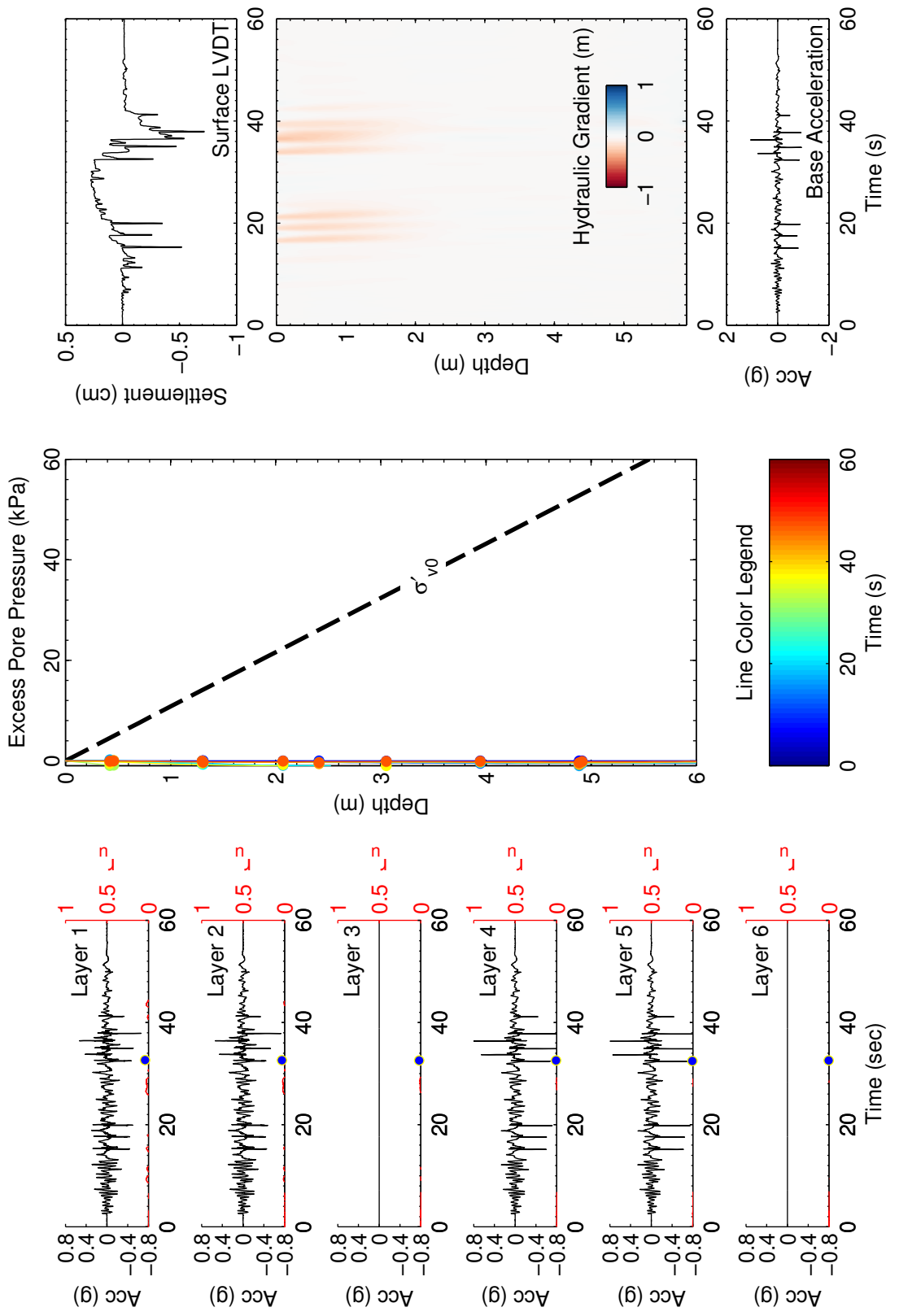
100% D_r Experiment 1 Test 33 – Data Summary Plot



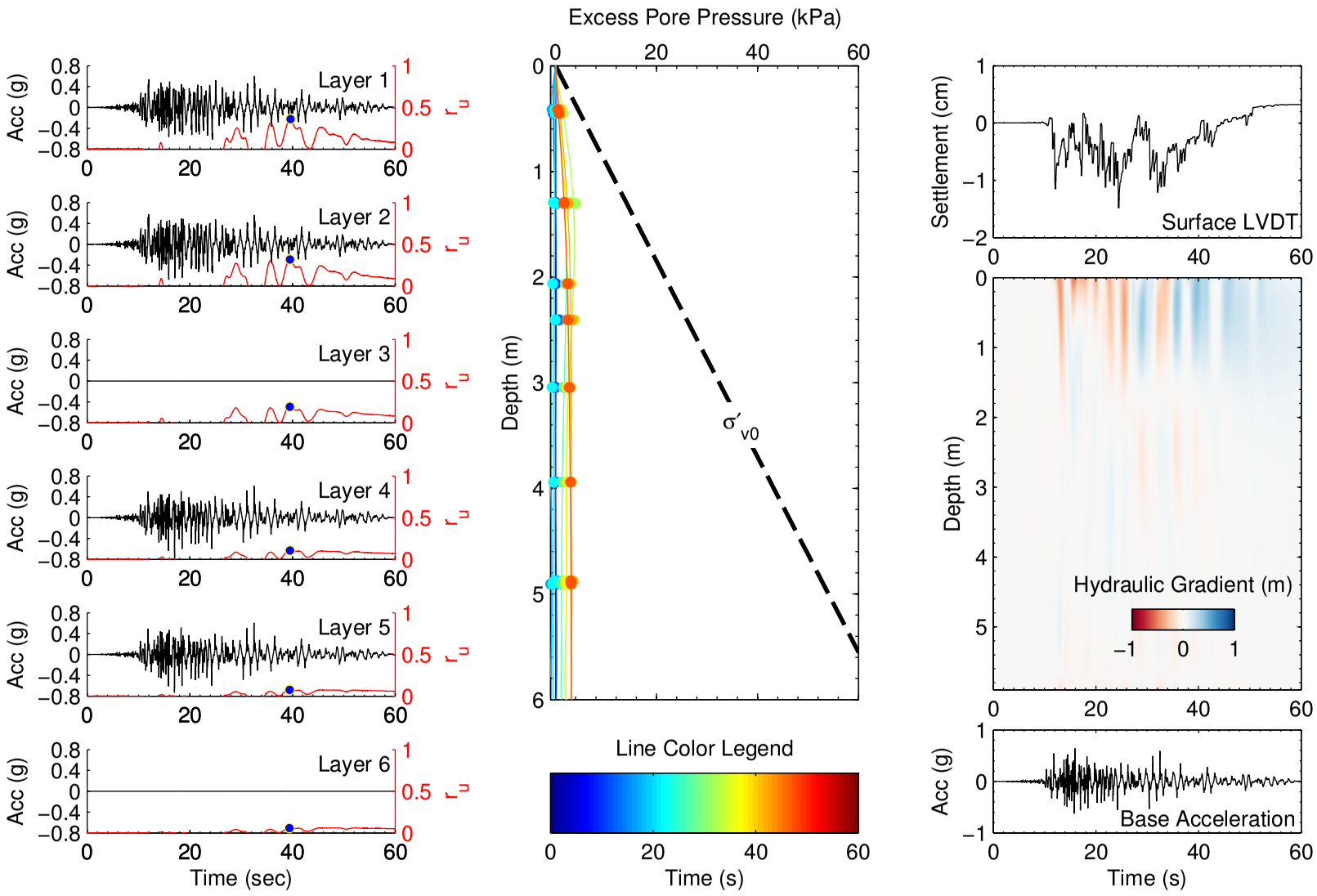
100% D_r Experiment 1 Test 34 – Data Summary Plot



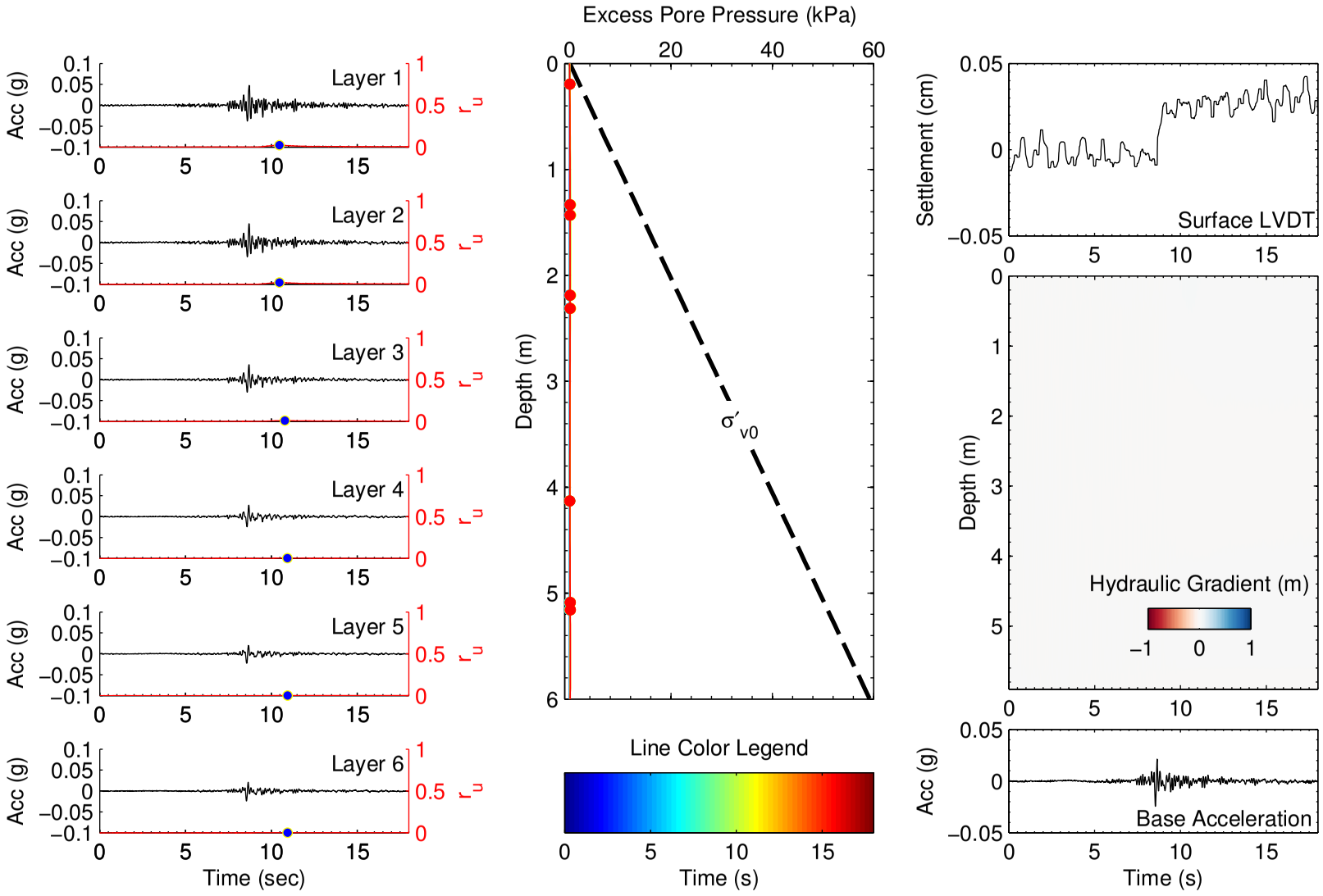
100% D_r Experiment 1 Test 35 – Data Summary Plot



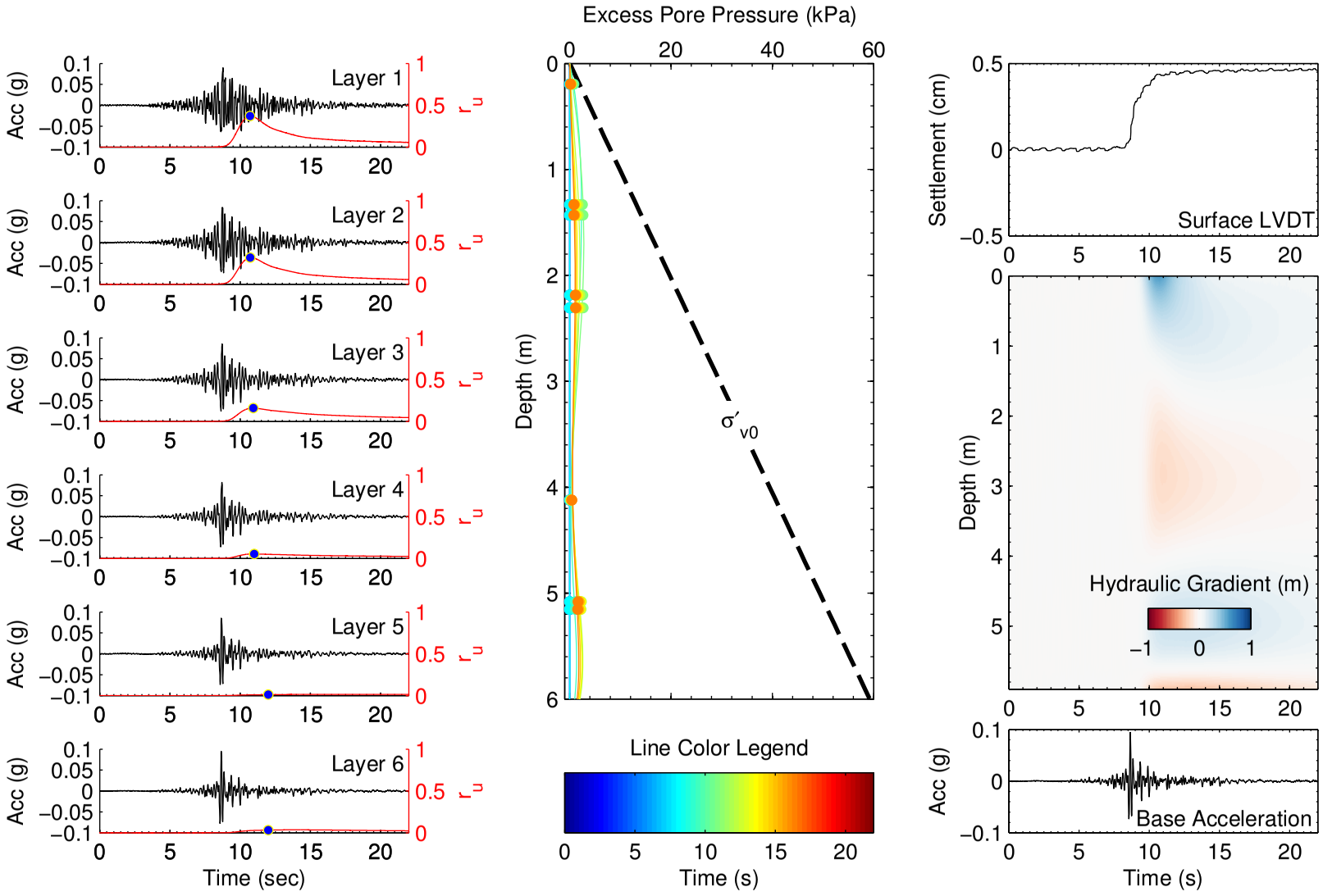
100% D_r Experiment 1 Test 36 – Data Summary Plot



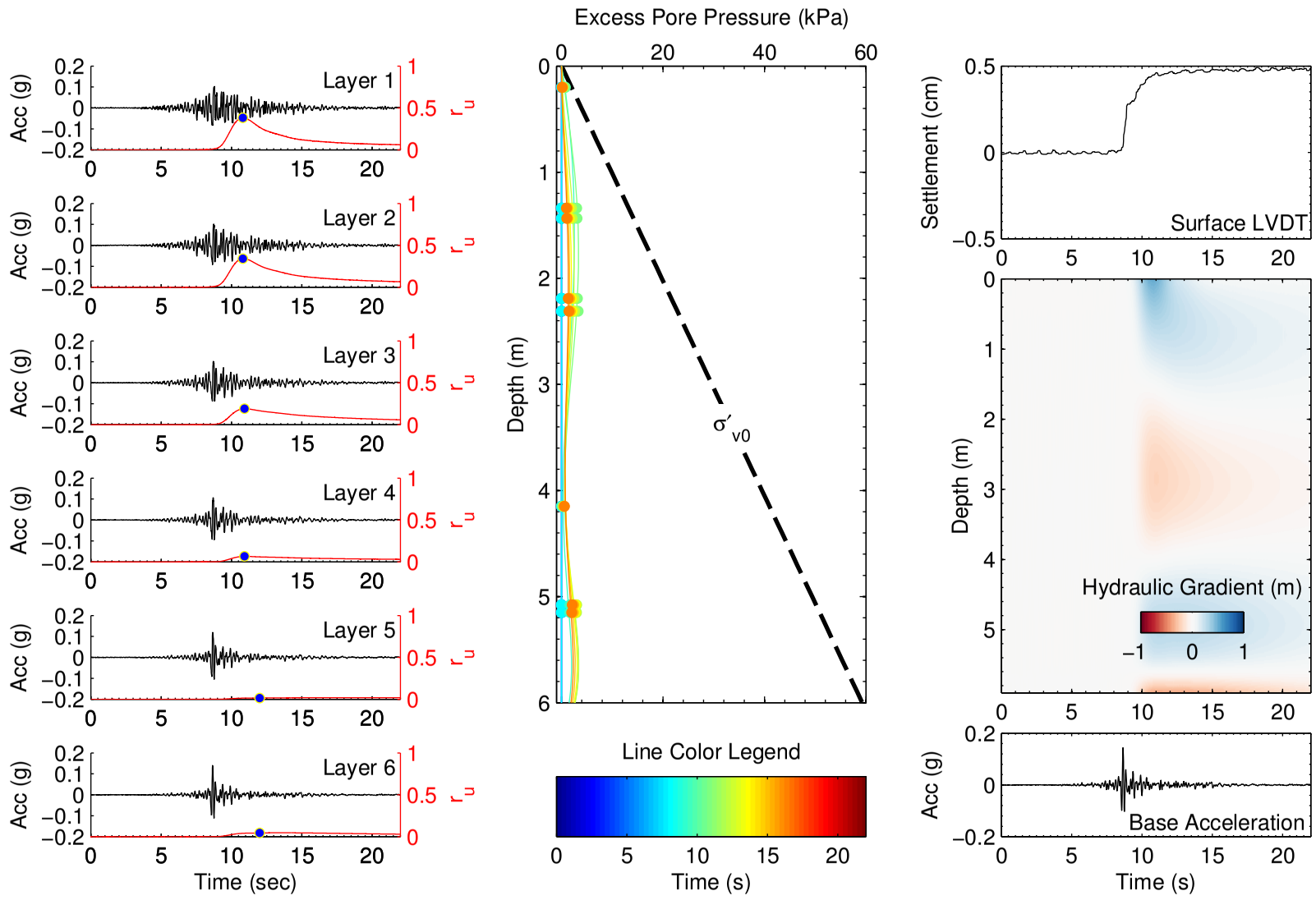
100% D_r Experiment 1 Test 37 – Data Summary Plot



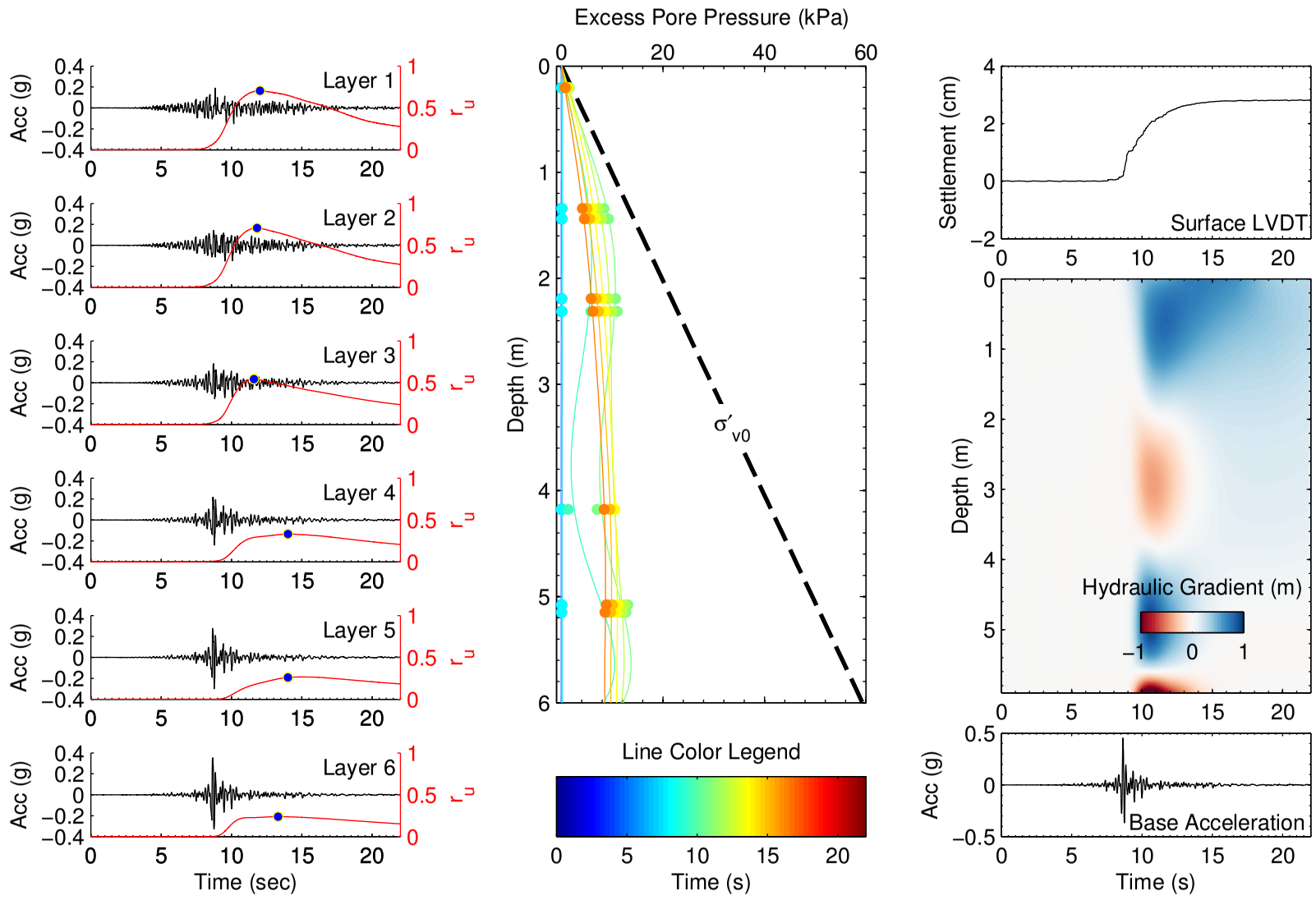
50% D_r Experiment 2 Test 1 – Data Summary Plot



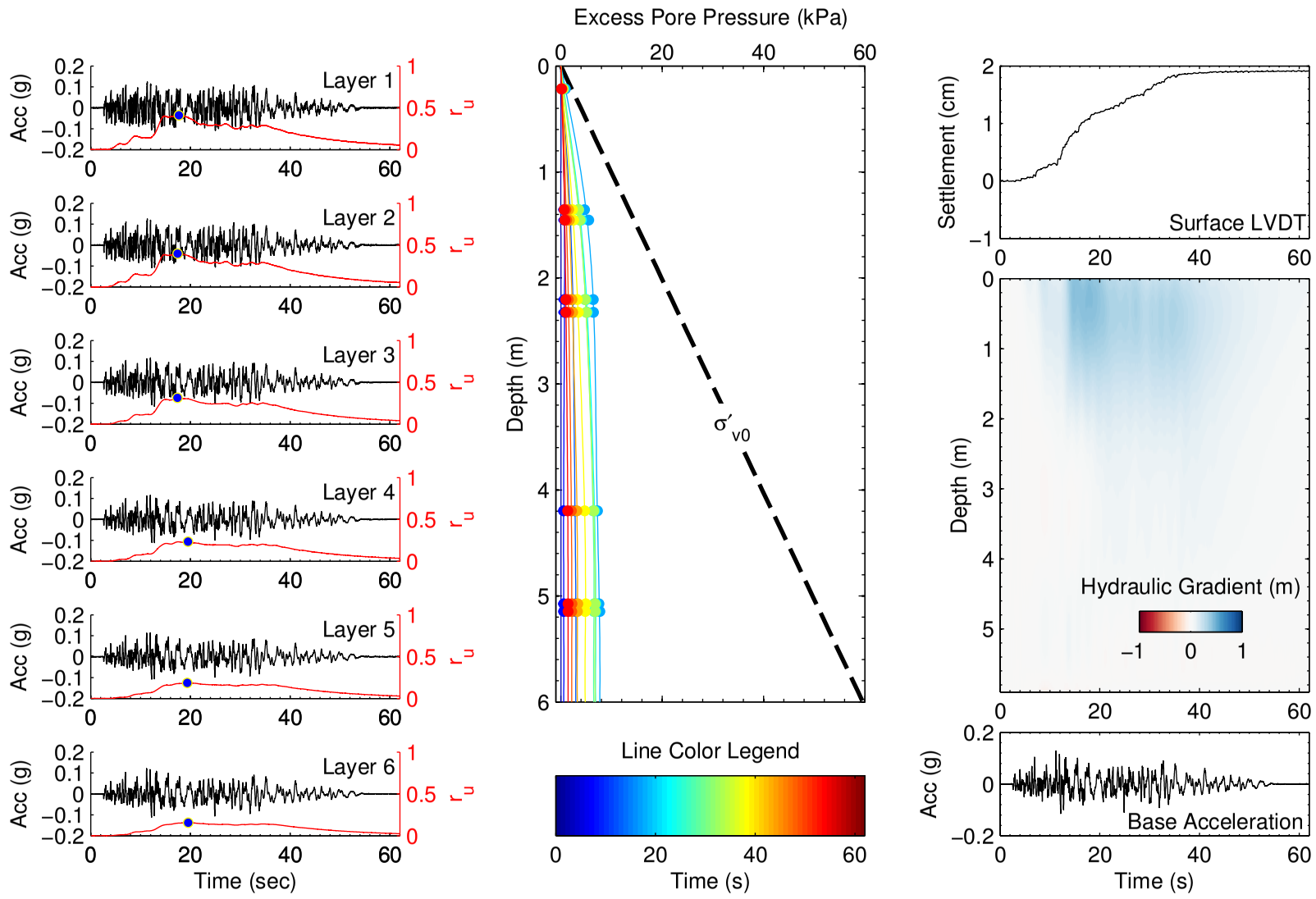
50% D_r Experiment 2 Test 2 – Data Summary Plot



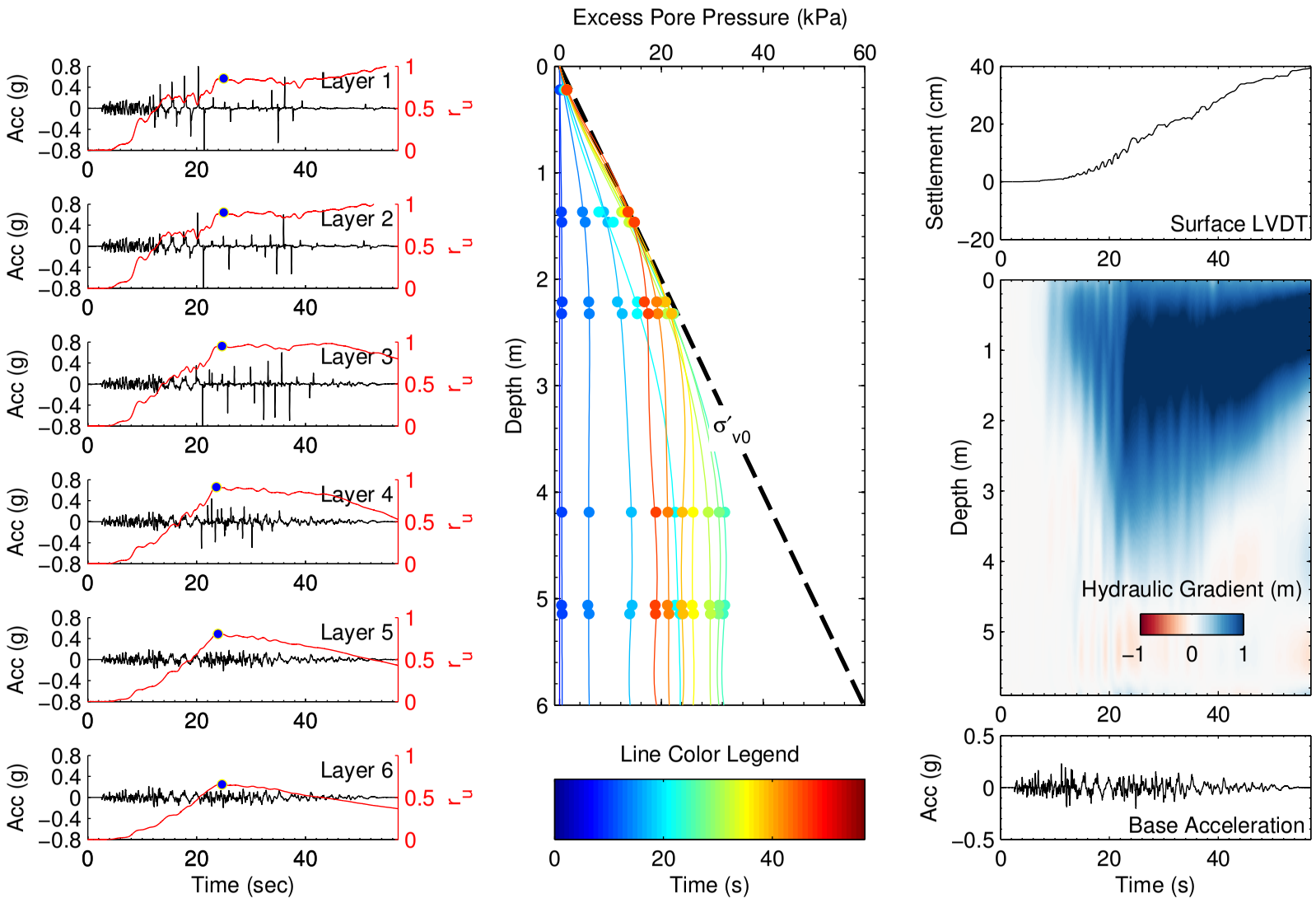
50% D_r Experiment 2 Test 3 – Data Summary Plot



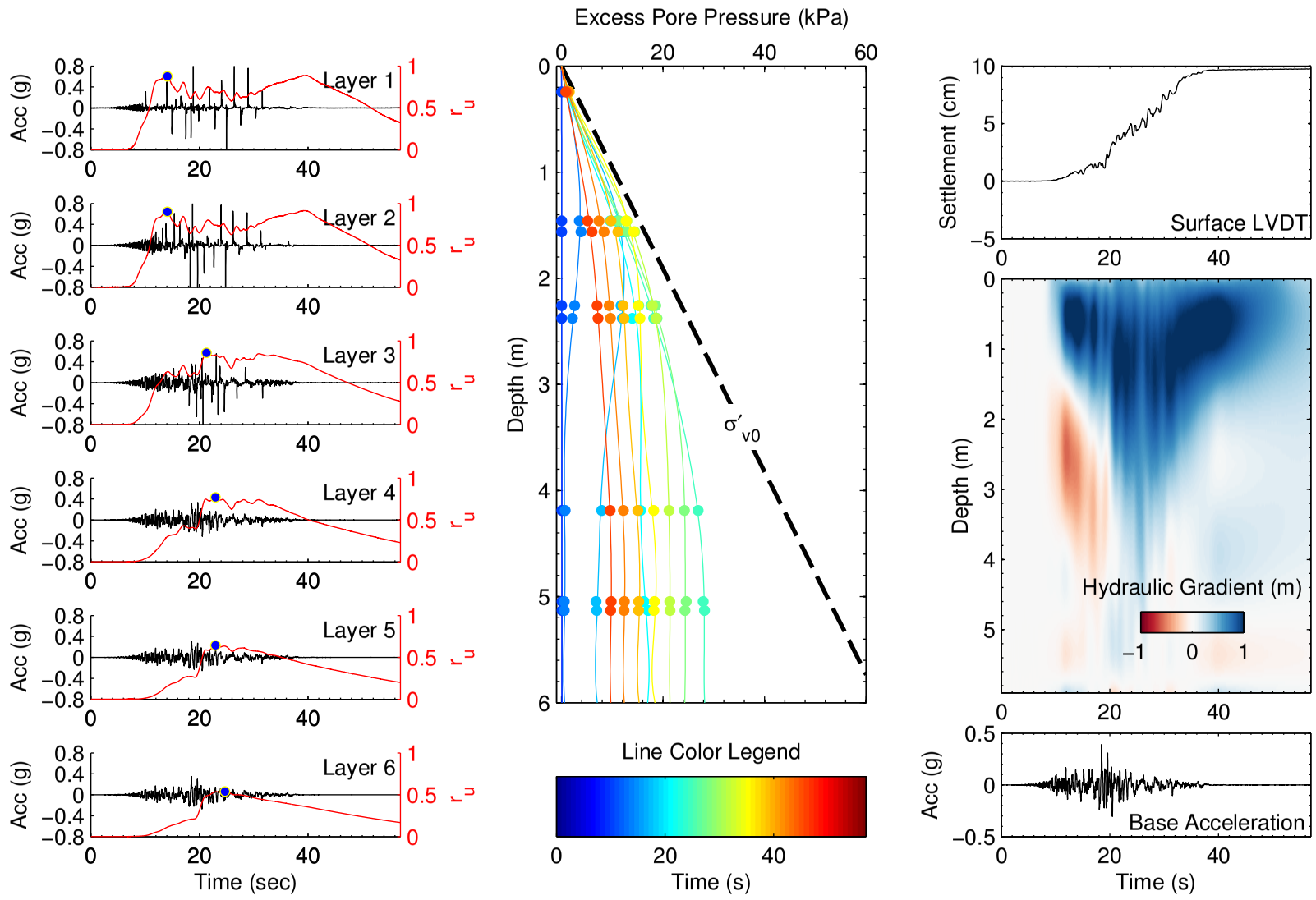
50% D_r Experiment 2 Test 4 – Data Summary Plot



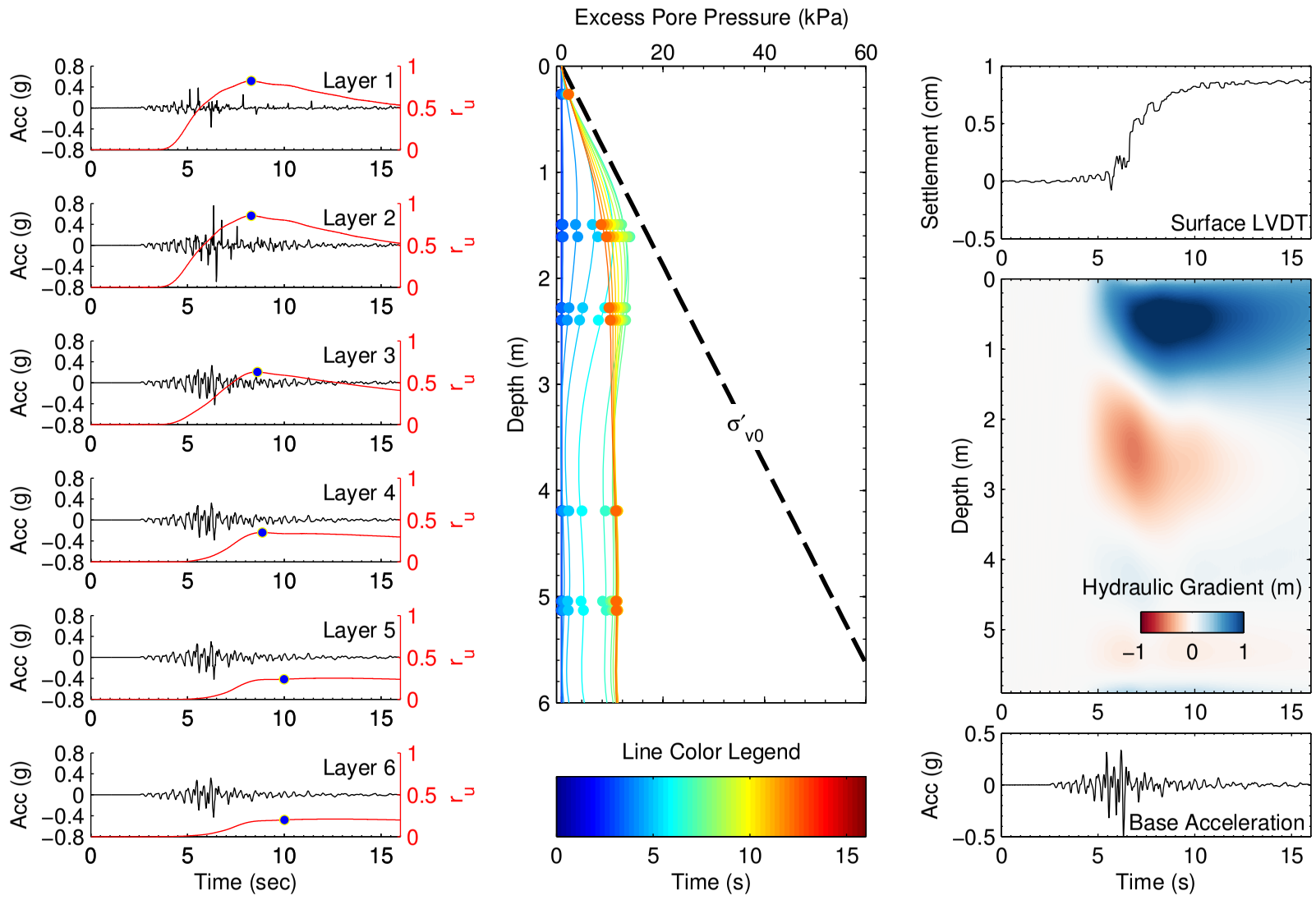
50% D_r Experiment 2 Test 5 – Data Summary Plot



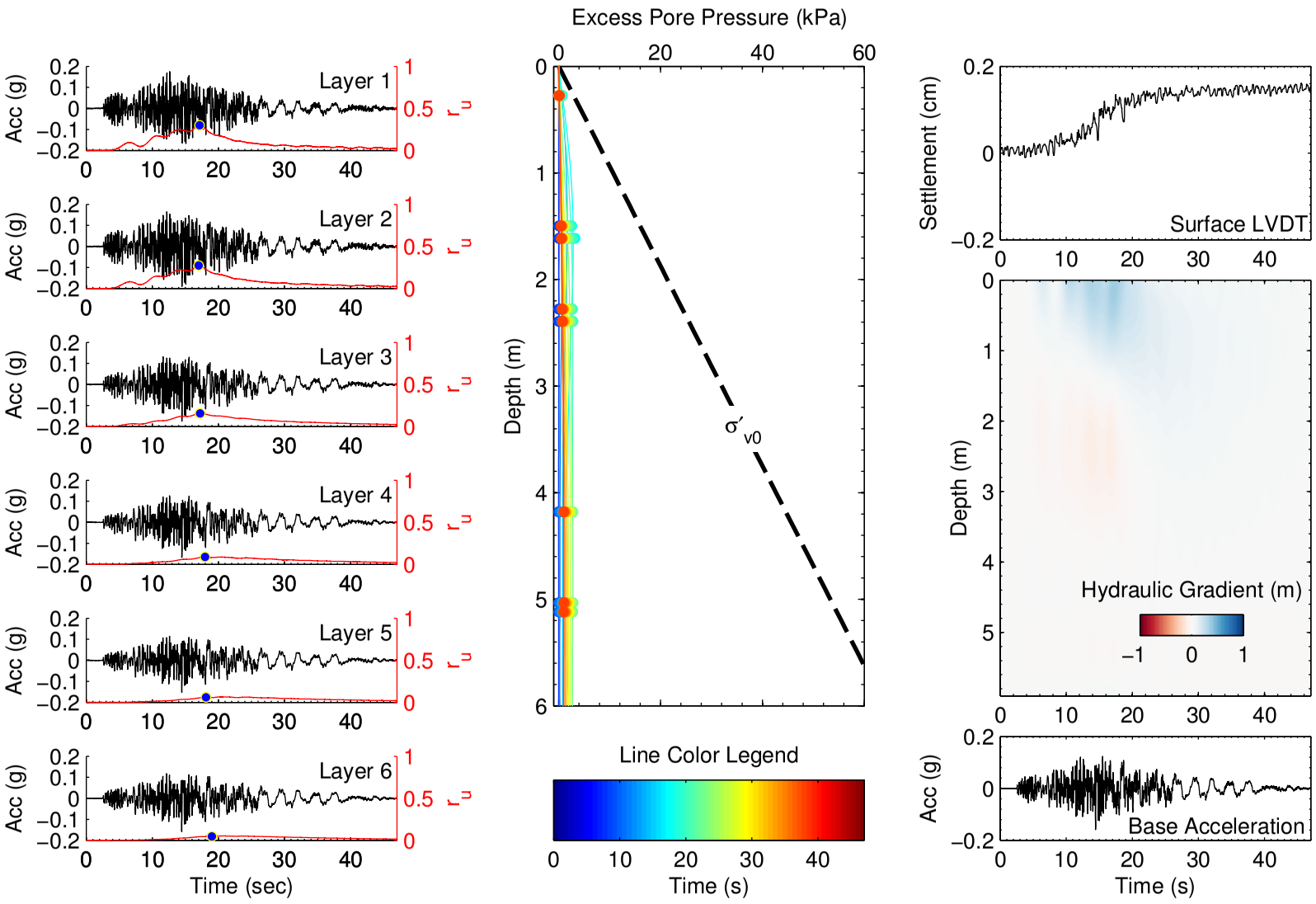
50% D_r Experiment 2 Test 6 – Data Summary Plot



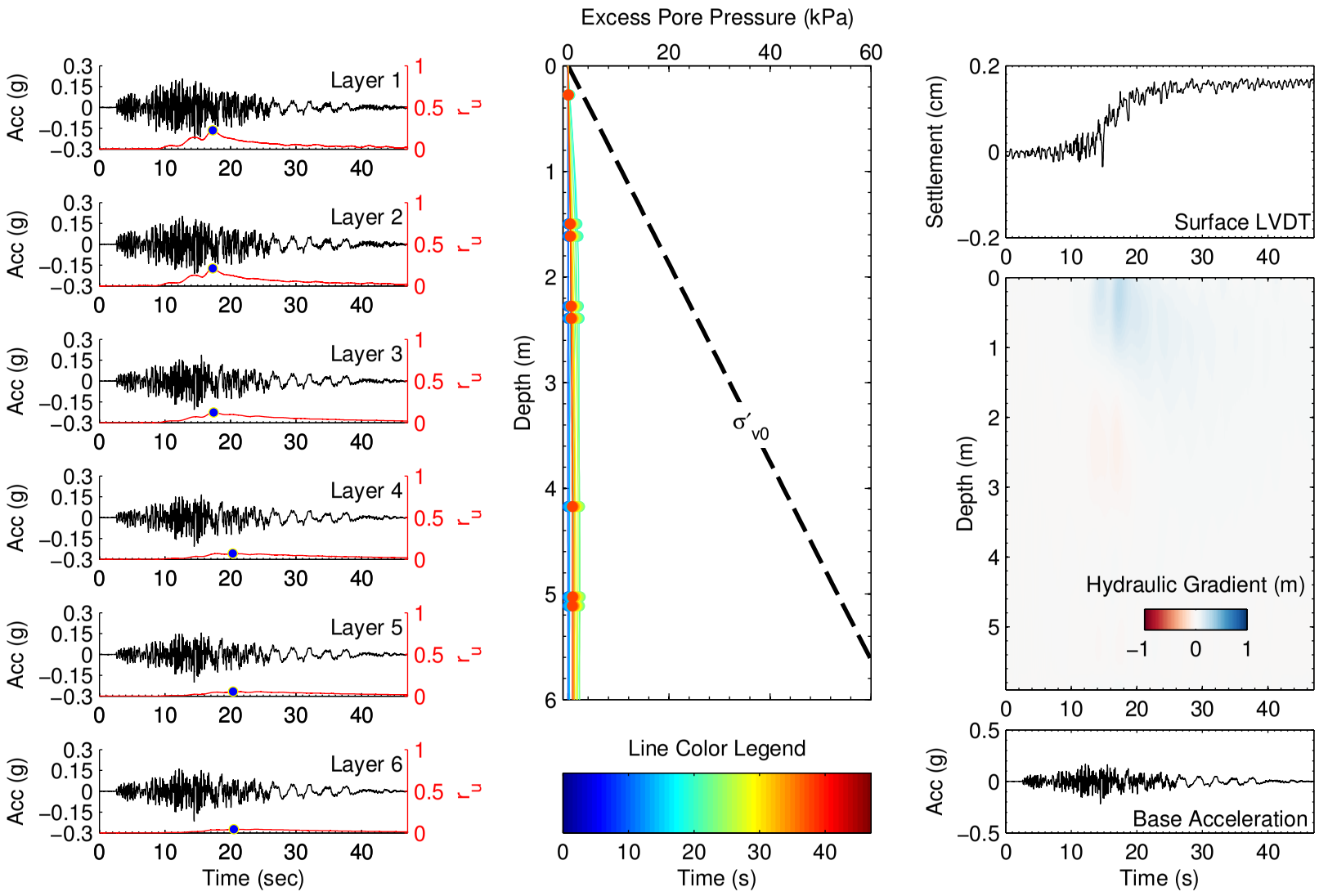
50% D_r Experiment 2 Test 7 – Data Summary Plot



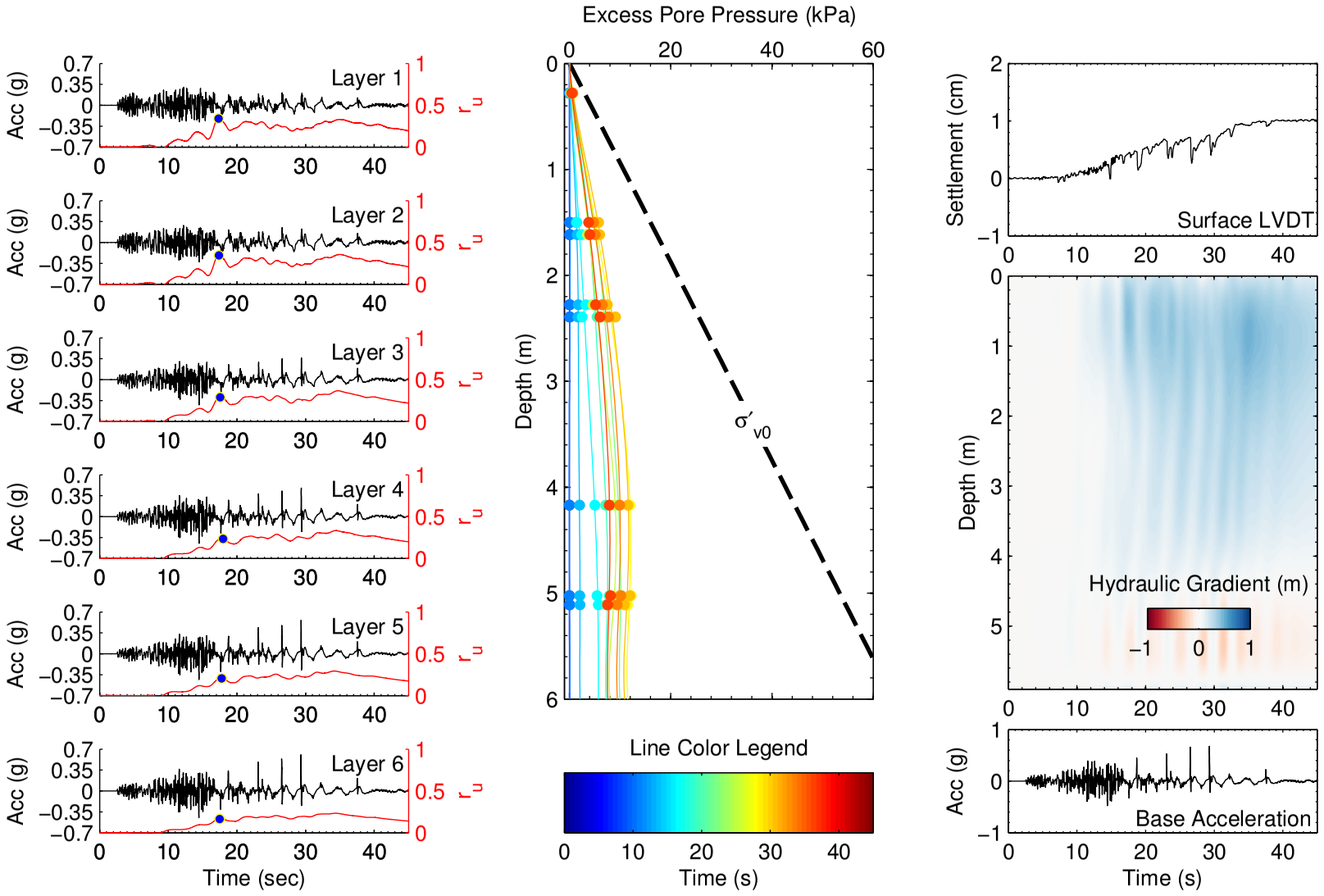
50% D_r Experiment 2 Test 8 – Data Summary Plot



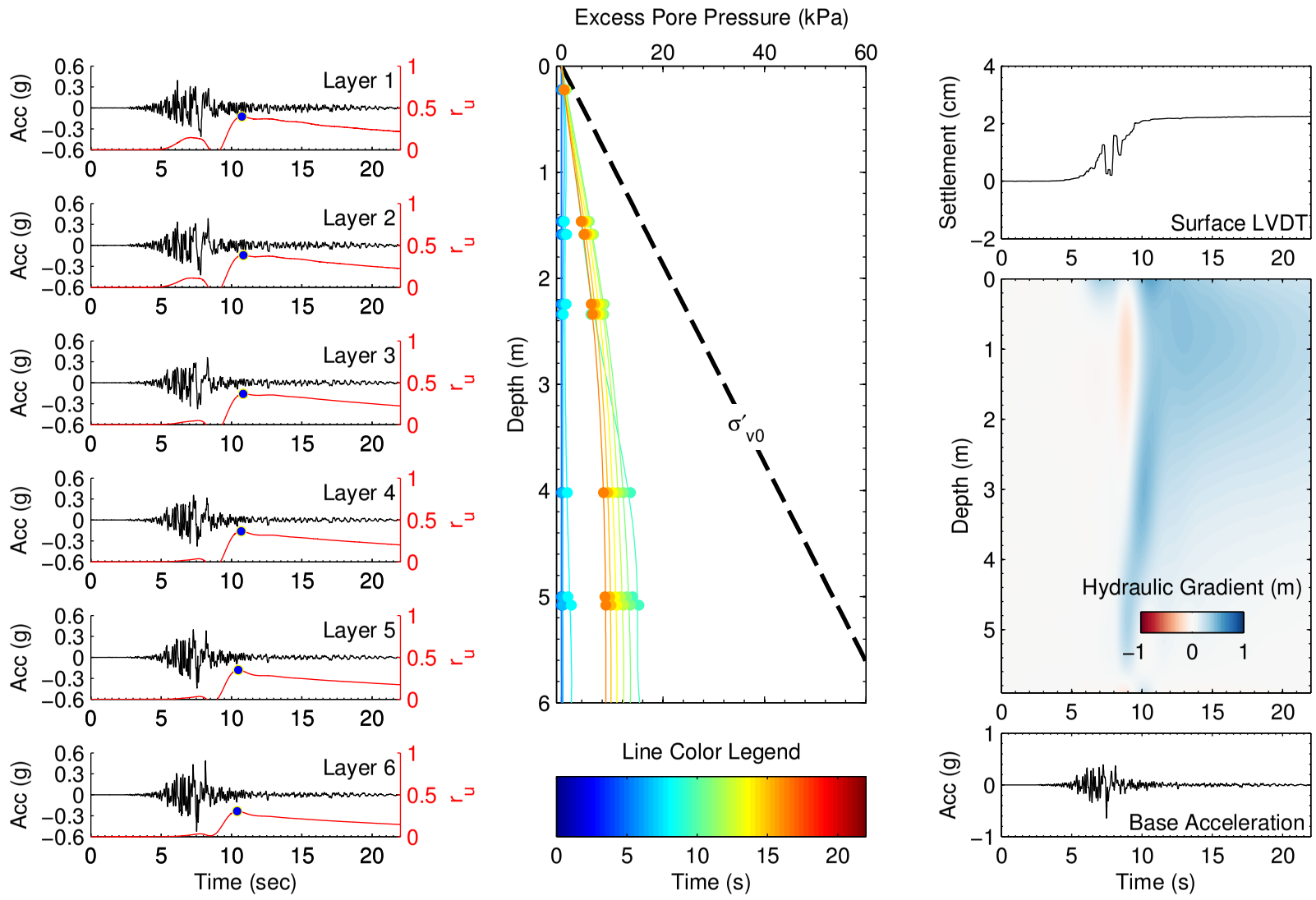
50% D_r Experiment 2 Test 9 – Data Summary Plot



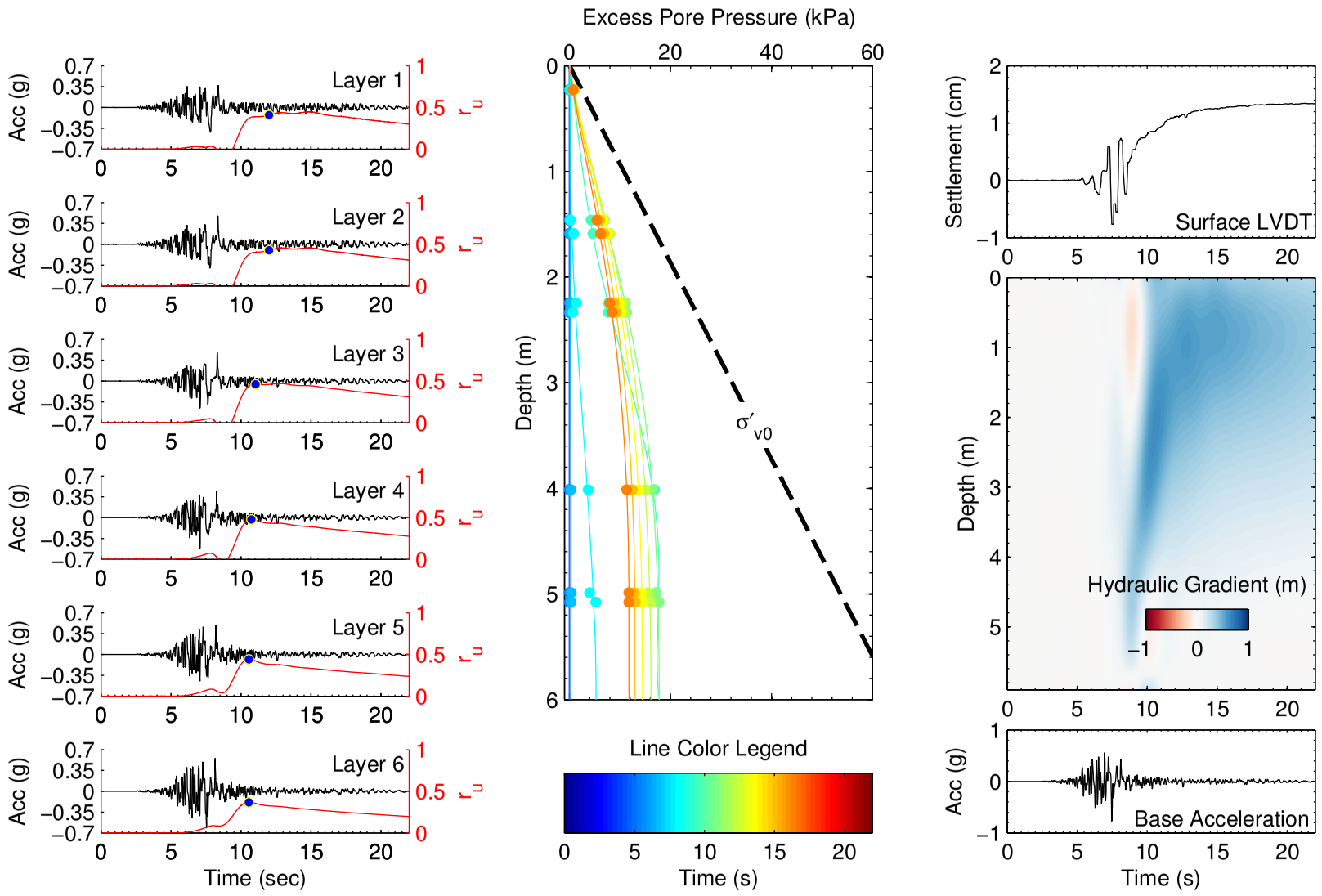
50% D_r Experiment 2 Test 10 – Data Summary Plot



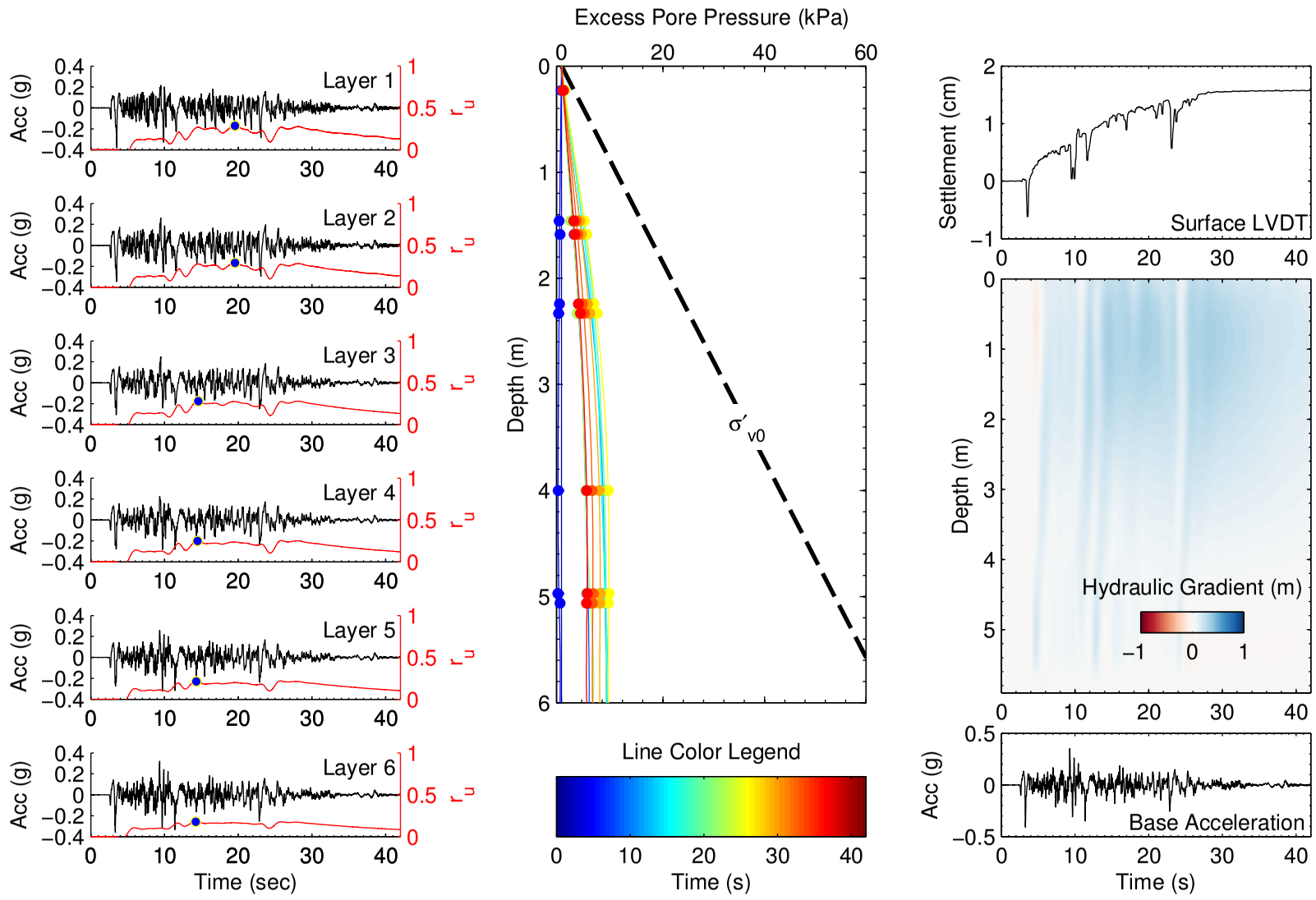
50% D_r Experiment 2 Test 11 – Data Summary Plot



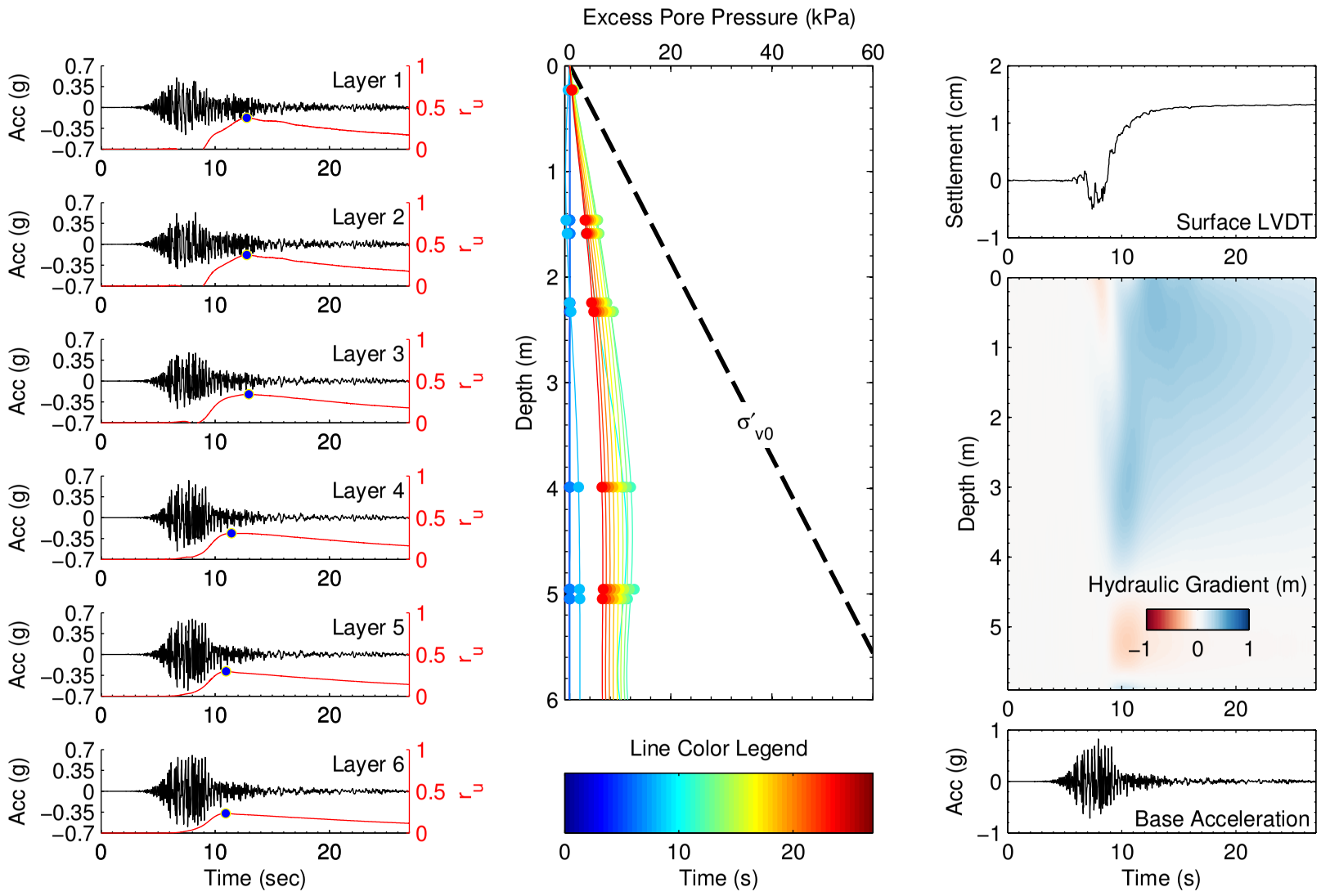
50% D_r Experiment 2 Test 12 – Data Summary Plot



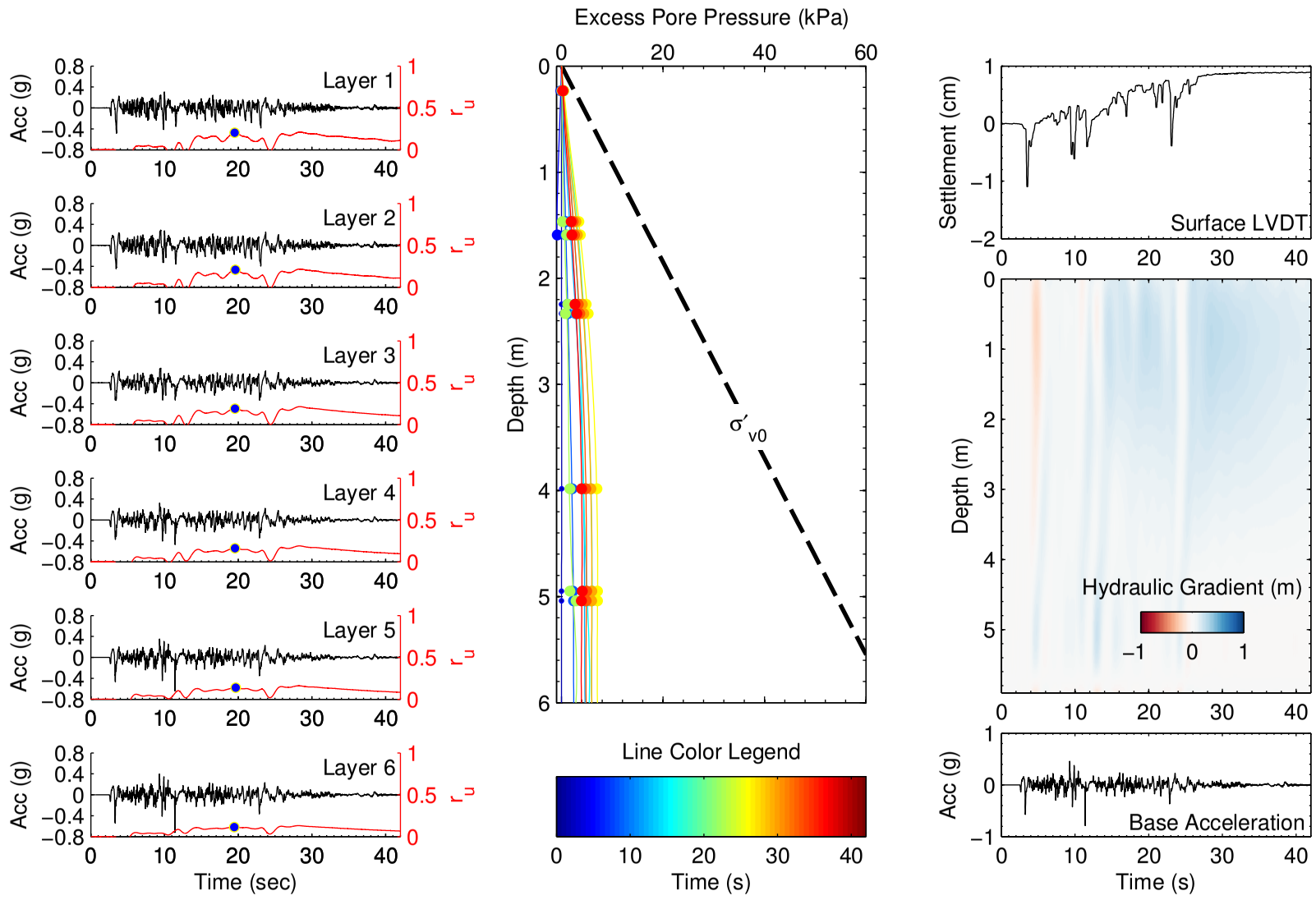
50% D_r Experiment 2 Test 13 – Data Summary Plot



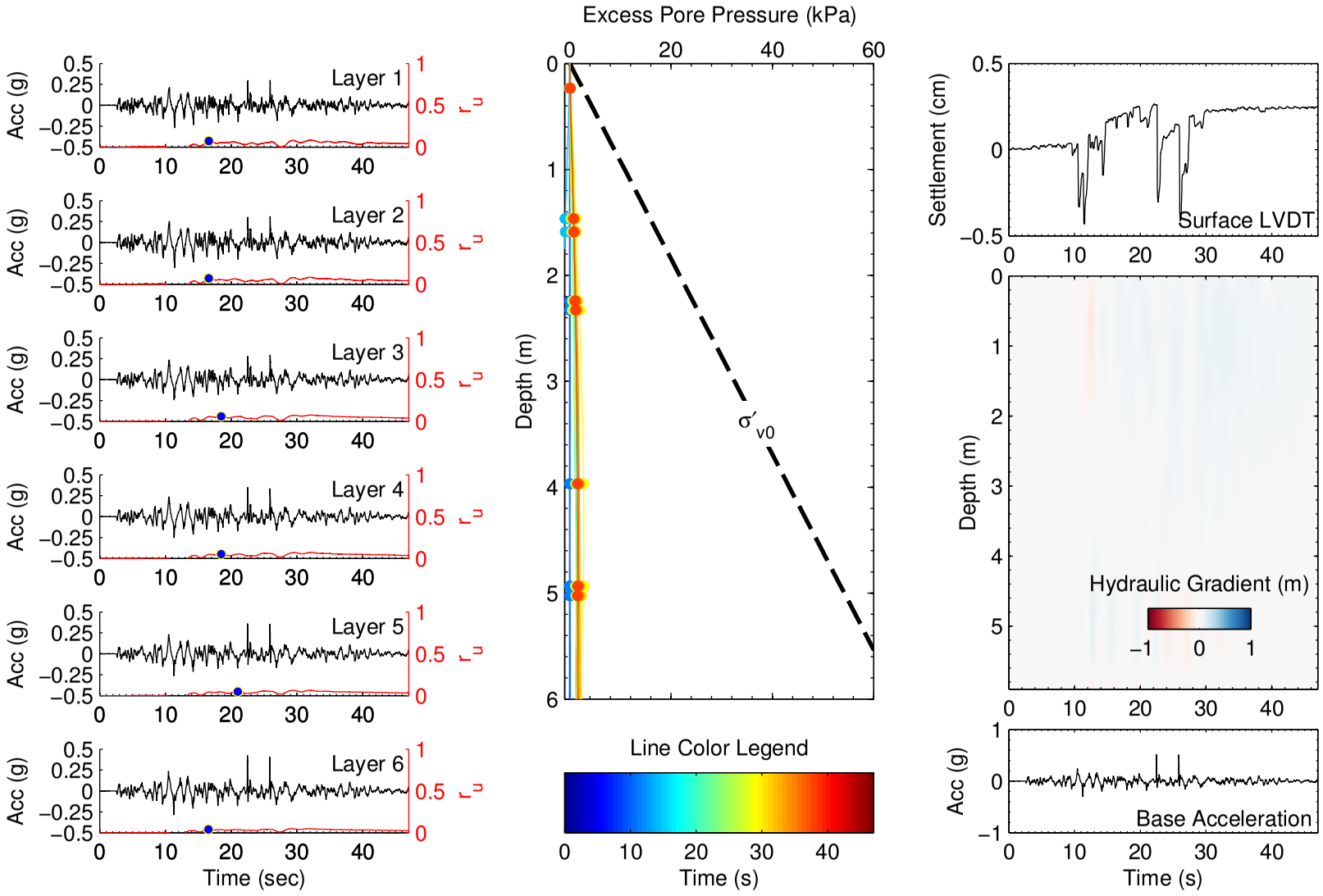
50% D_r Experiment 2 Test 14 – Data Summary Plot



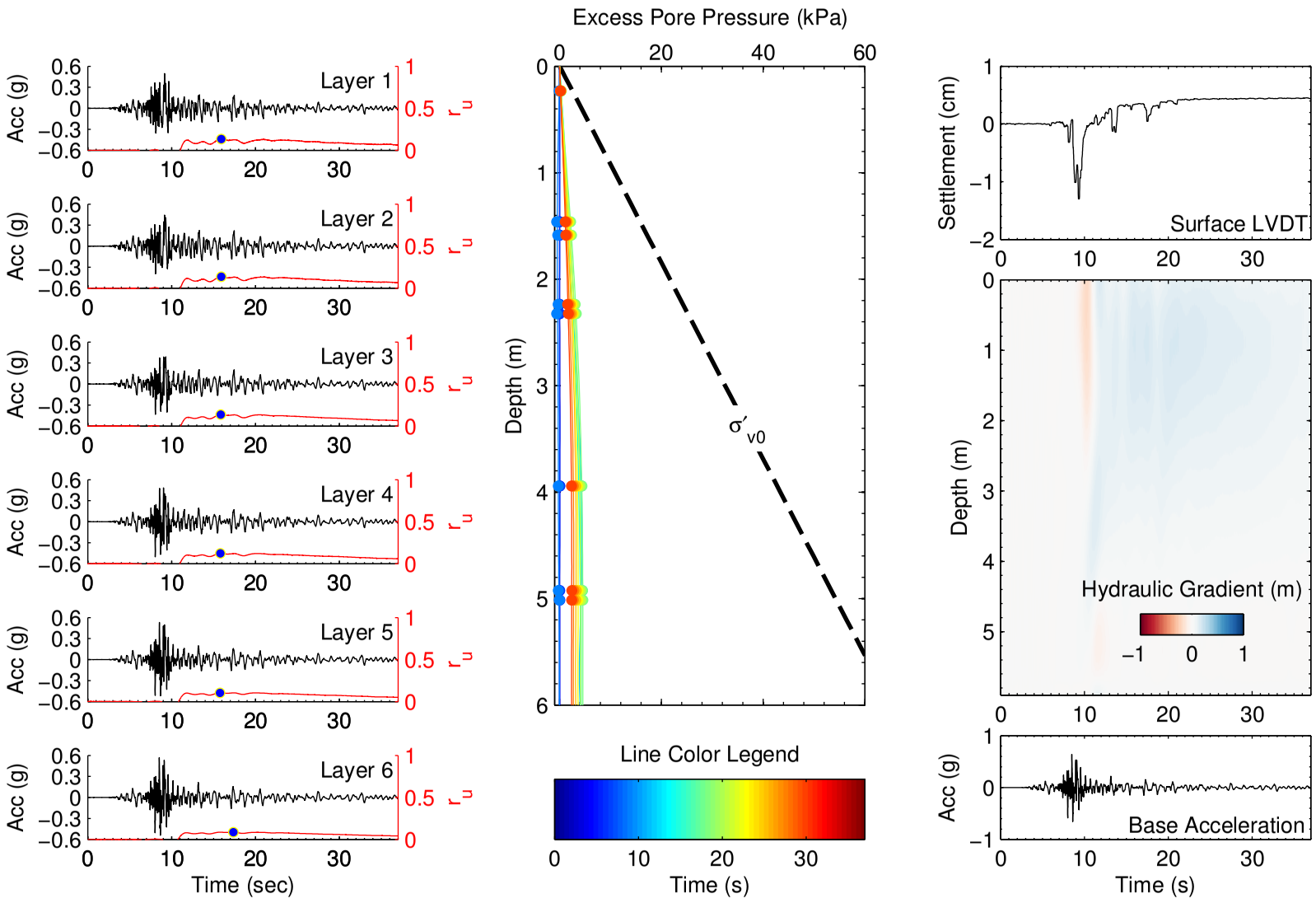
50% D_r Experiment 2 Test 15 – Data Summary Plot



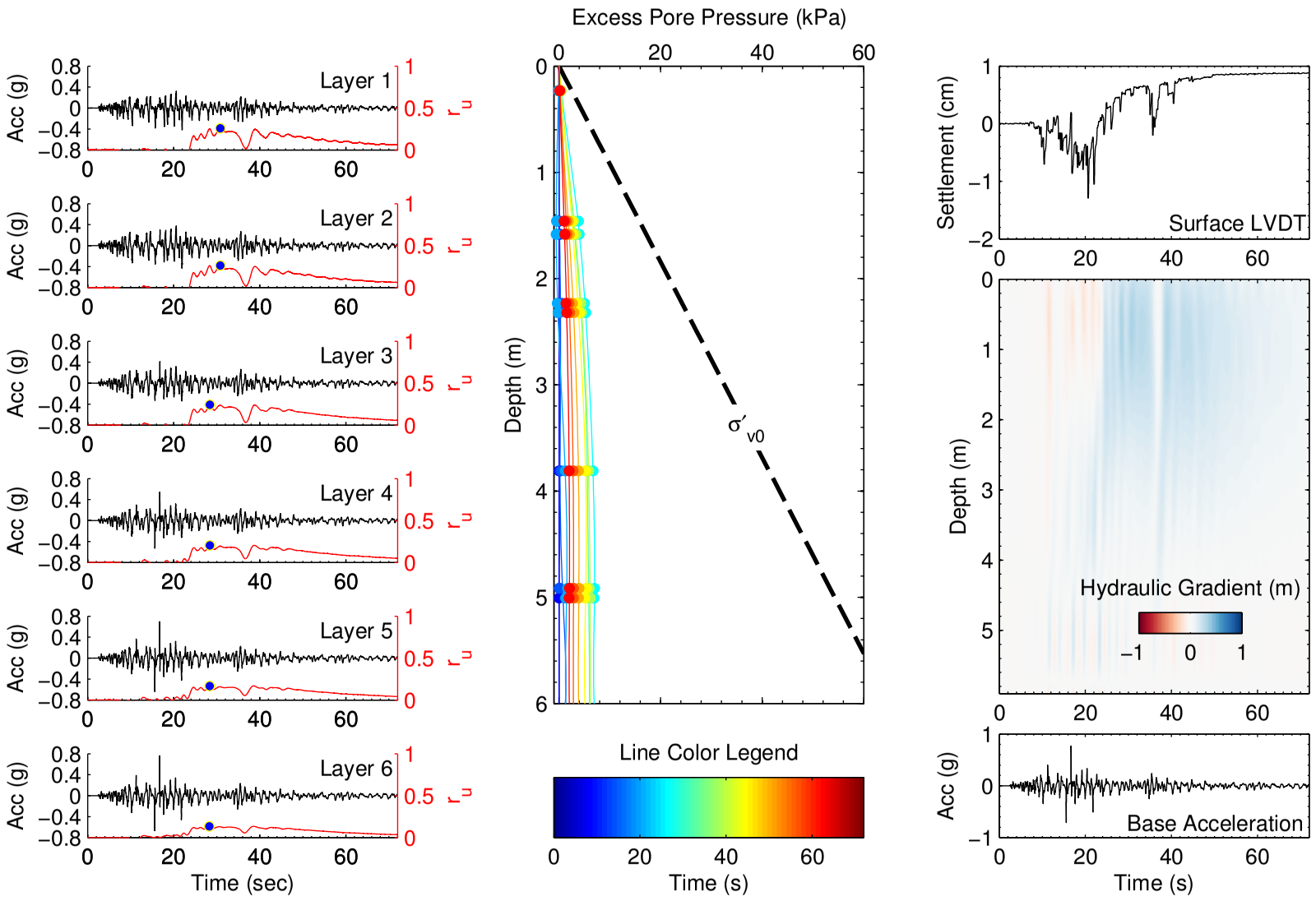
50% D_r Experiment 2 Test 16 – Data Summary Plot



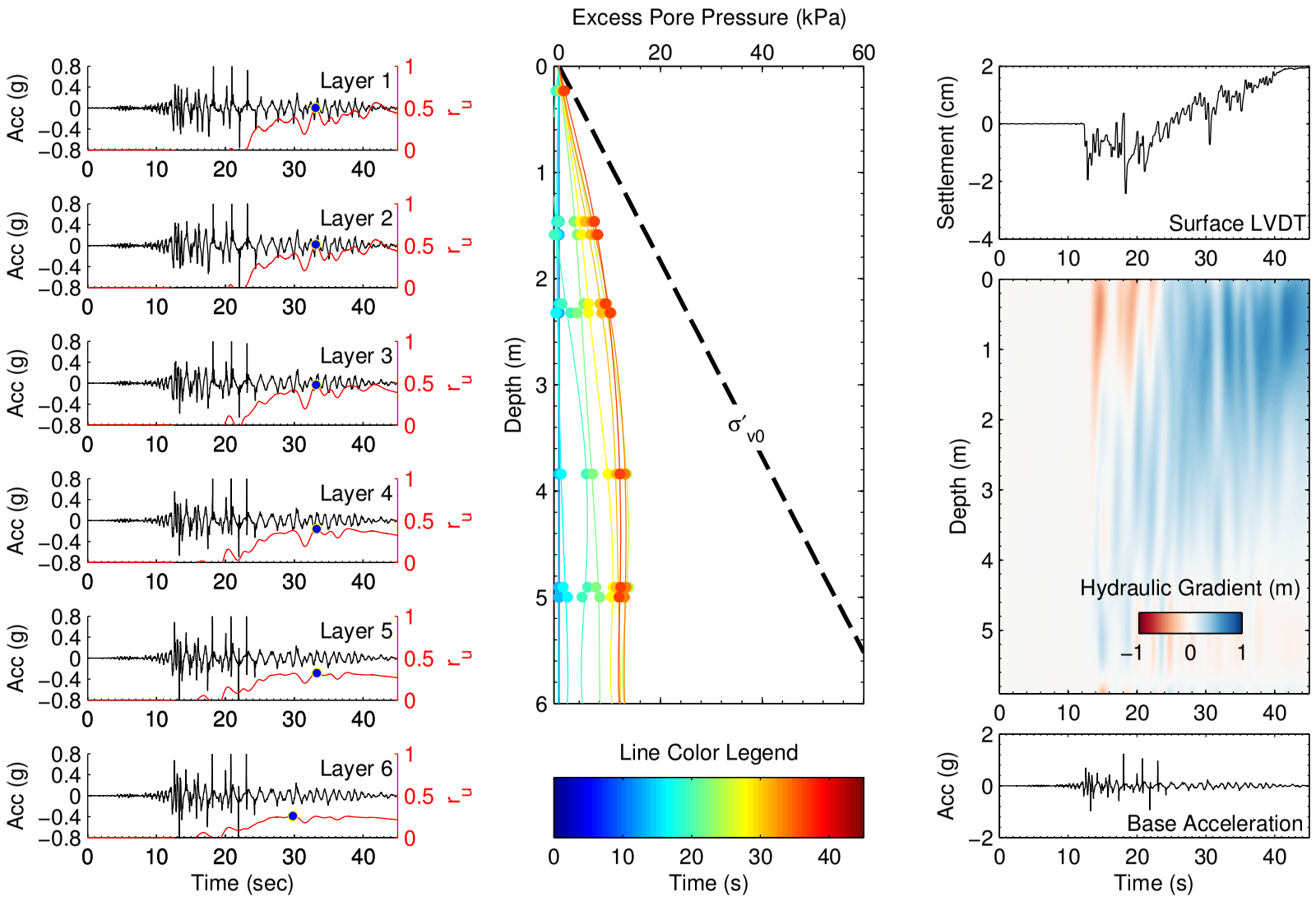
50% D_r Experiment 2 Test 17 – Data Summary Plot



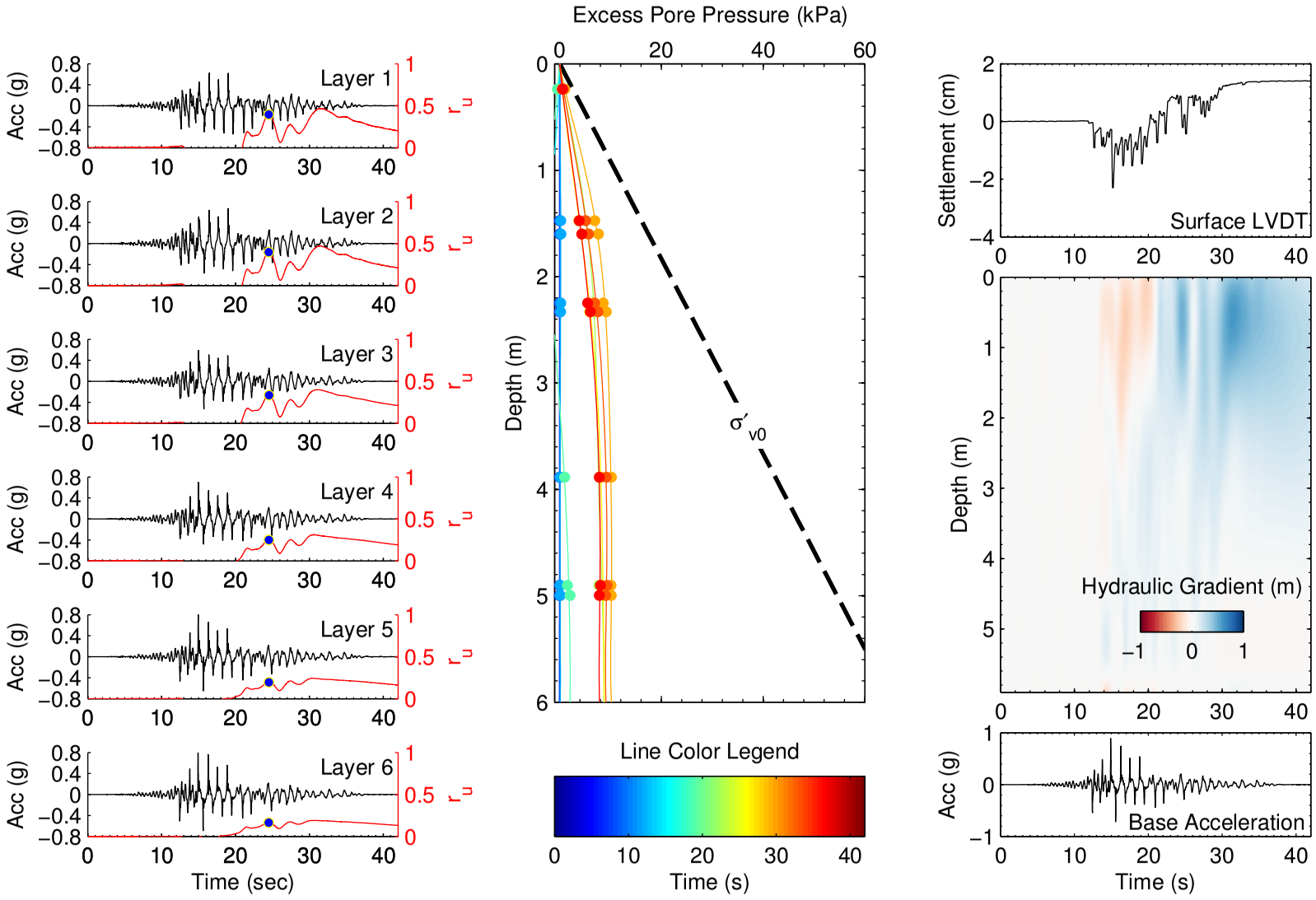
50% D_r Experiment 2 Test 18 – Data Summary Plot



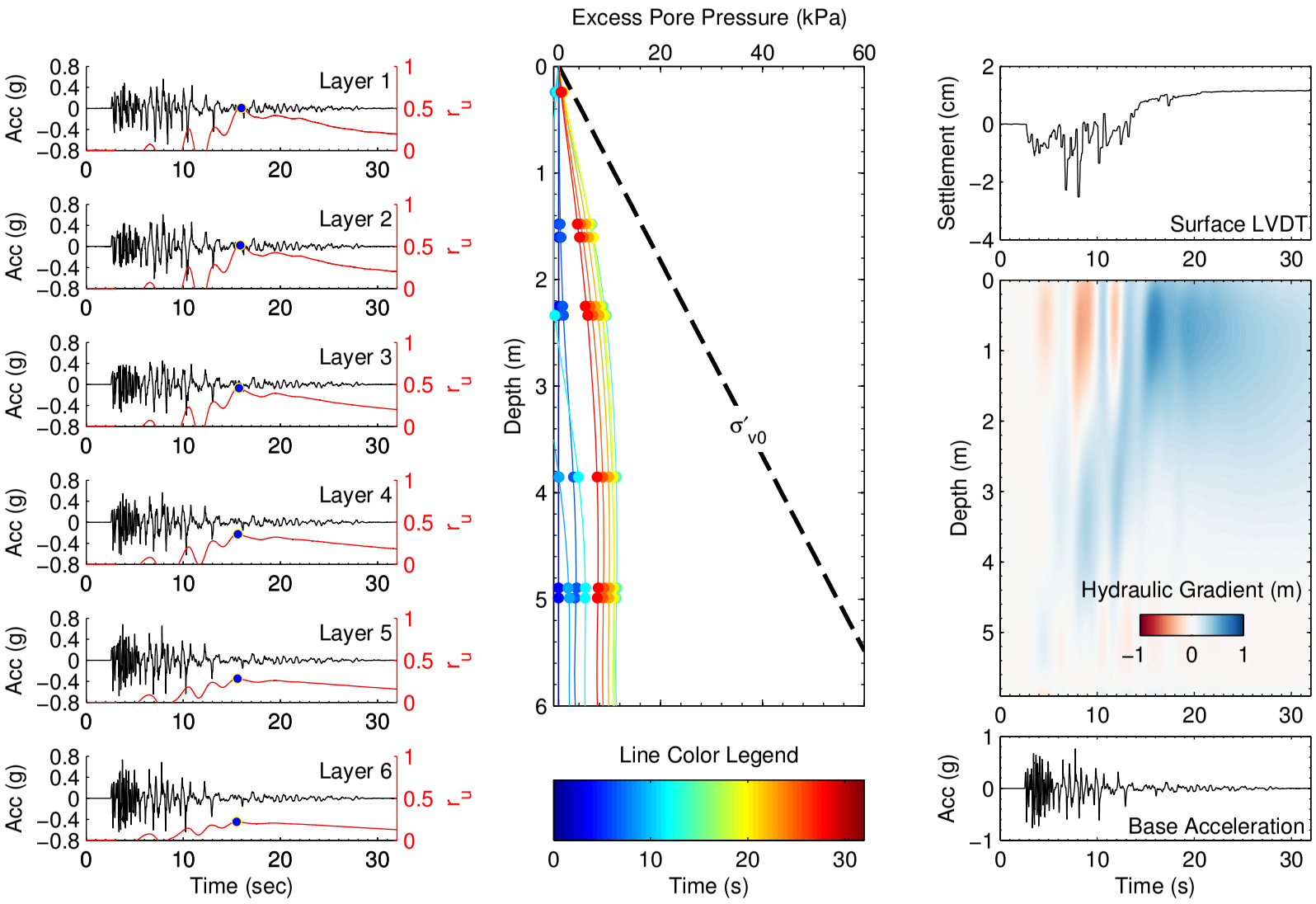
50% D_r Experiment 2 Test 19 – Data Summary Plot



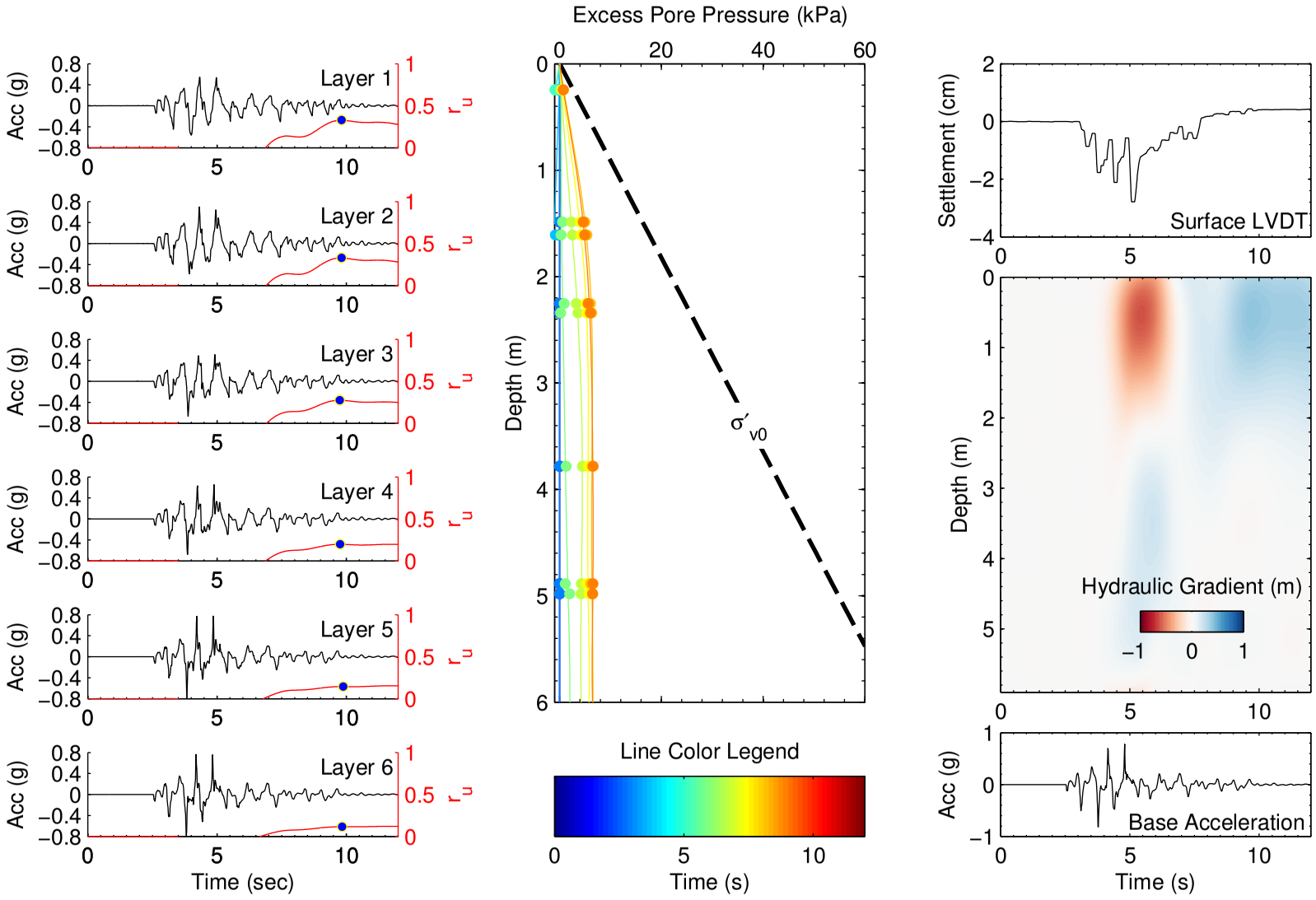
50% D_r Experiment 2 Test 20 – Data Summary Plot



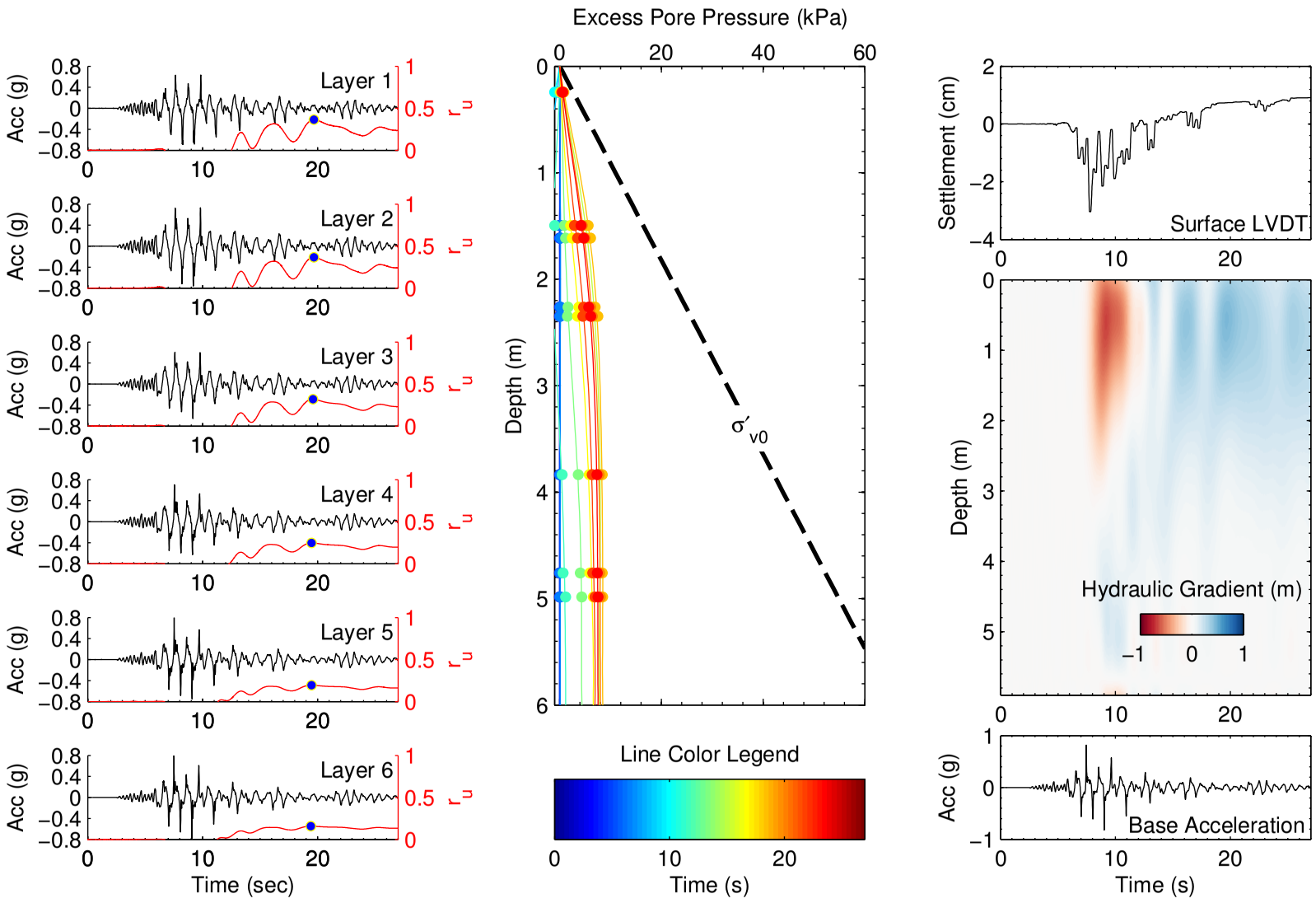
50% D_r Experiment 2 Test 21 – Data Summary Plot



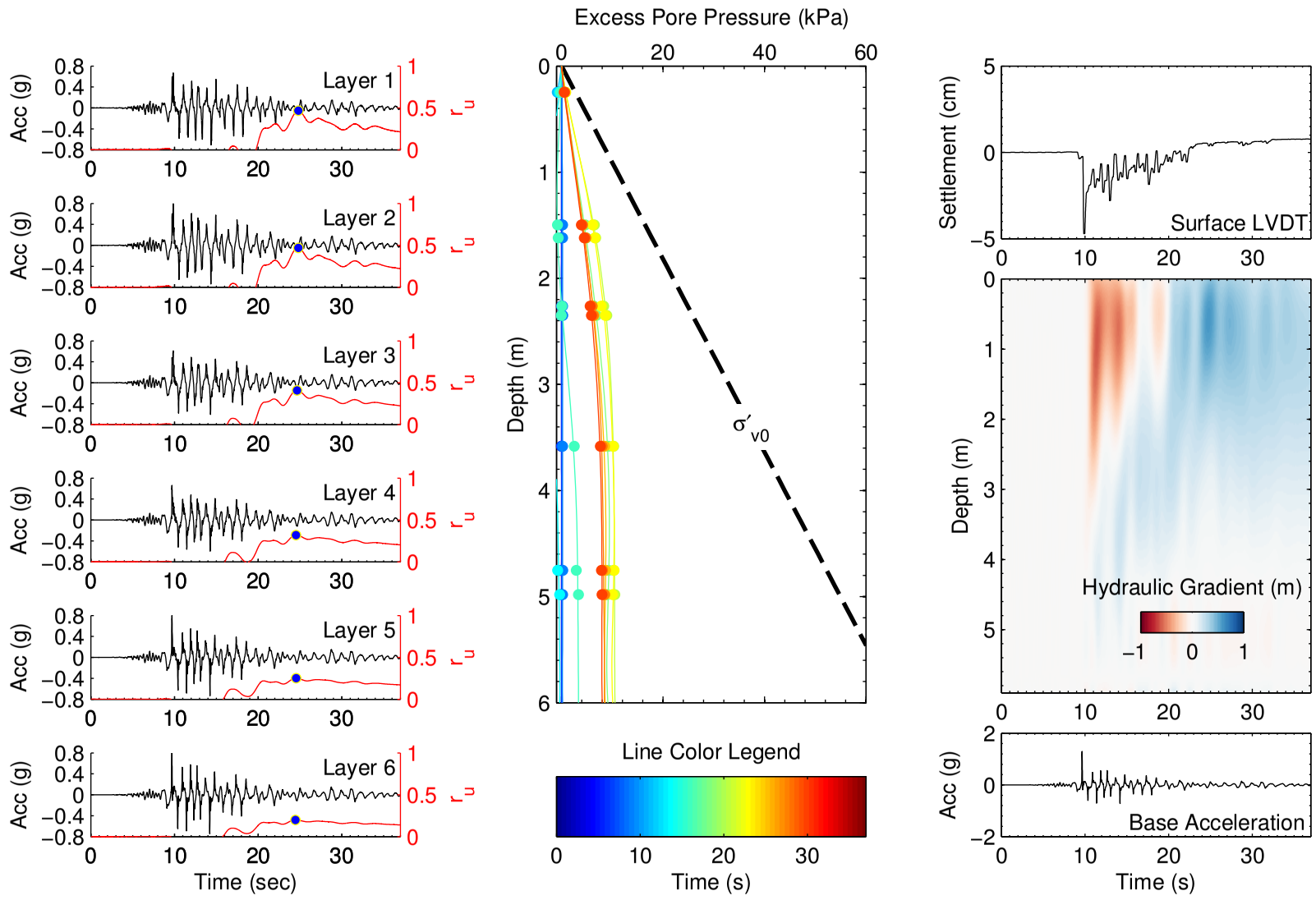
50% D_r Experiment 2 Test 22 – Data Summary Plot



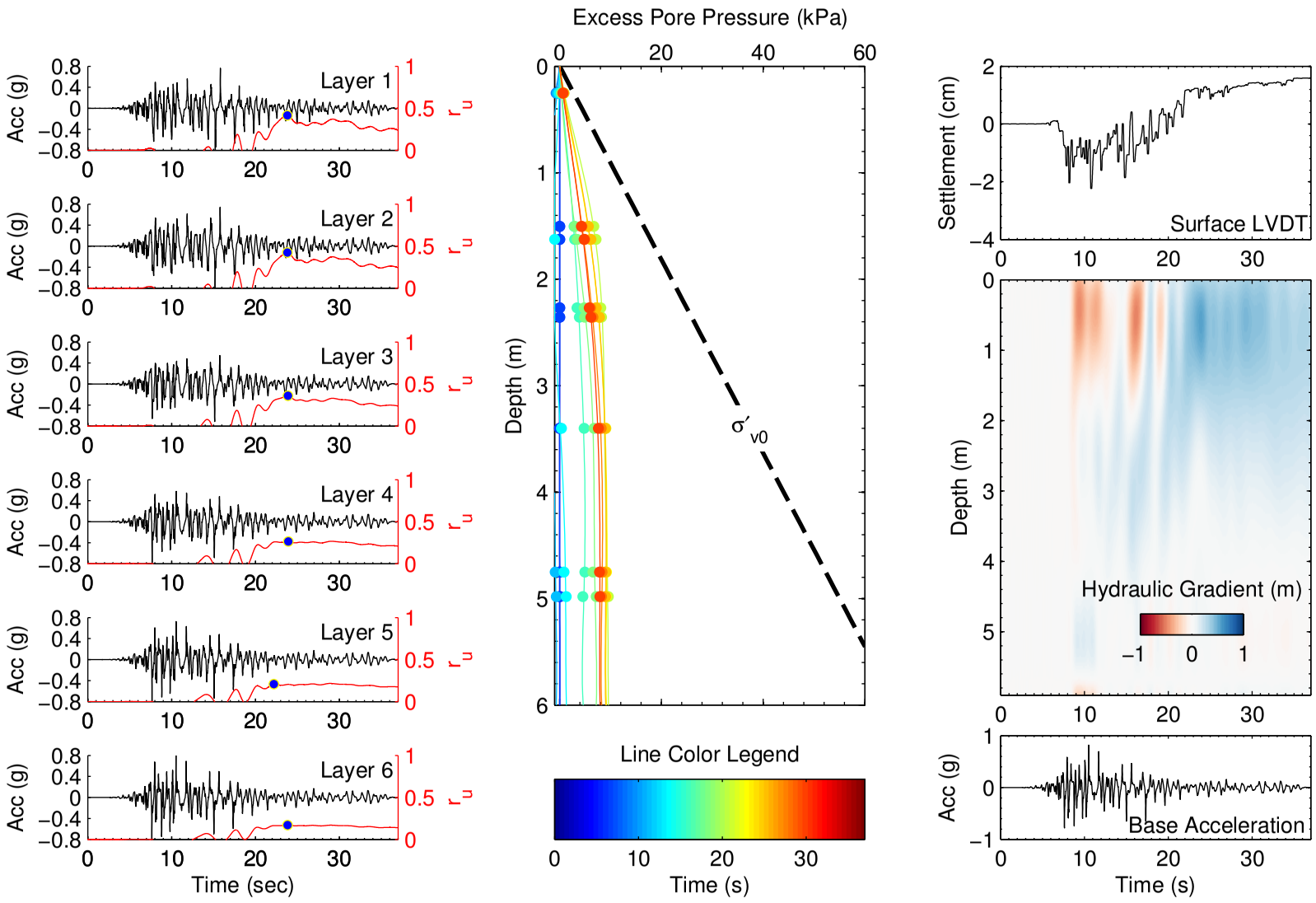
50% D_r Experiment 2 Test 23 – Data Summary Plot



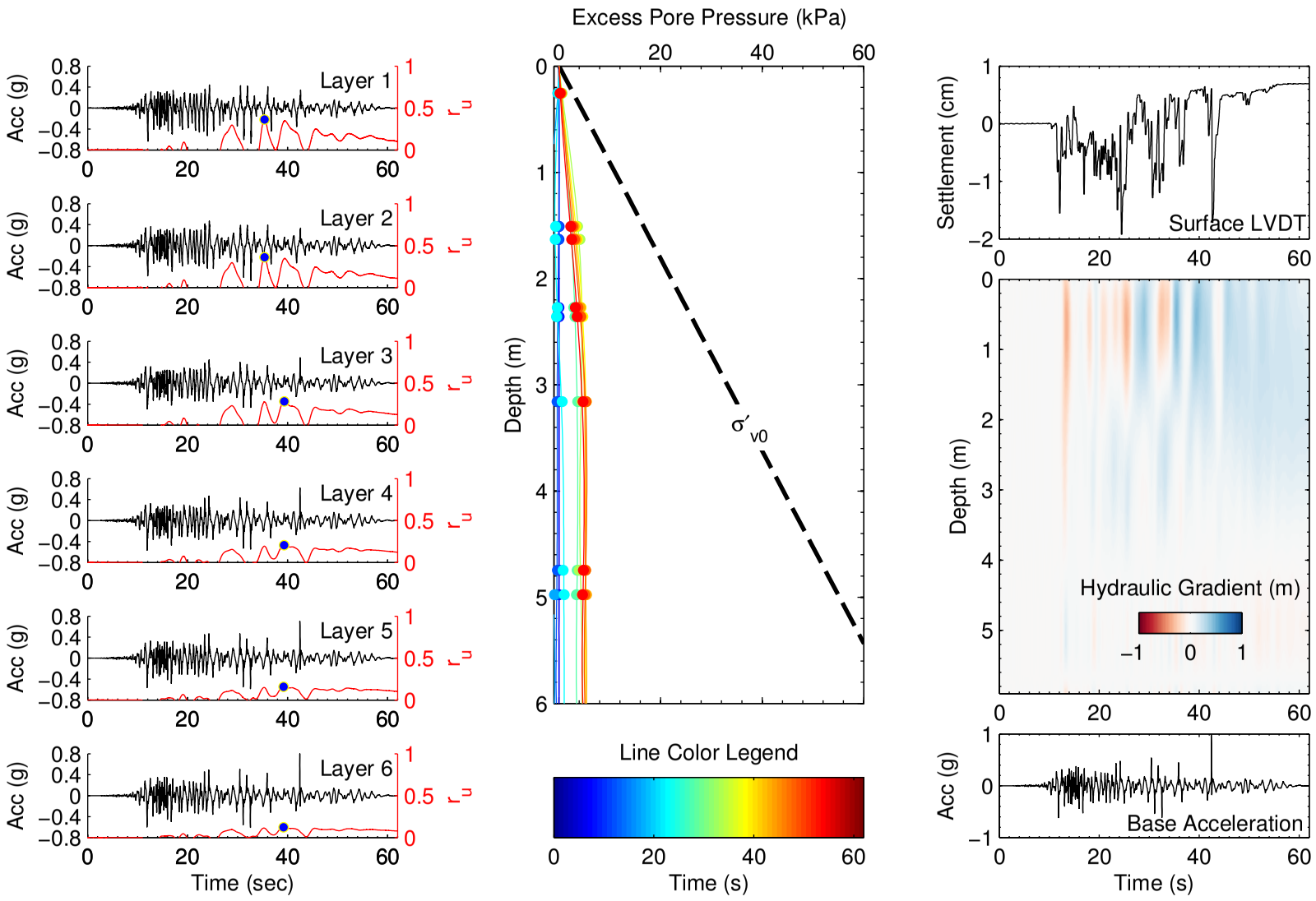
50% D_r Experiment 2 Test 24 – Data Summary Plot



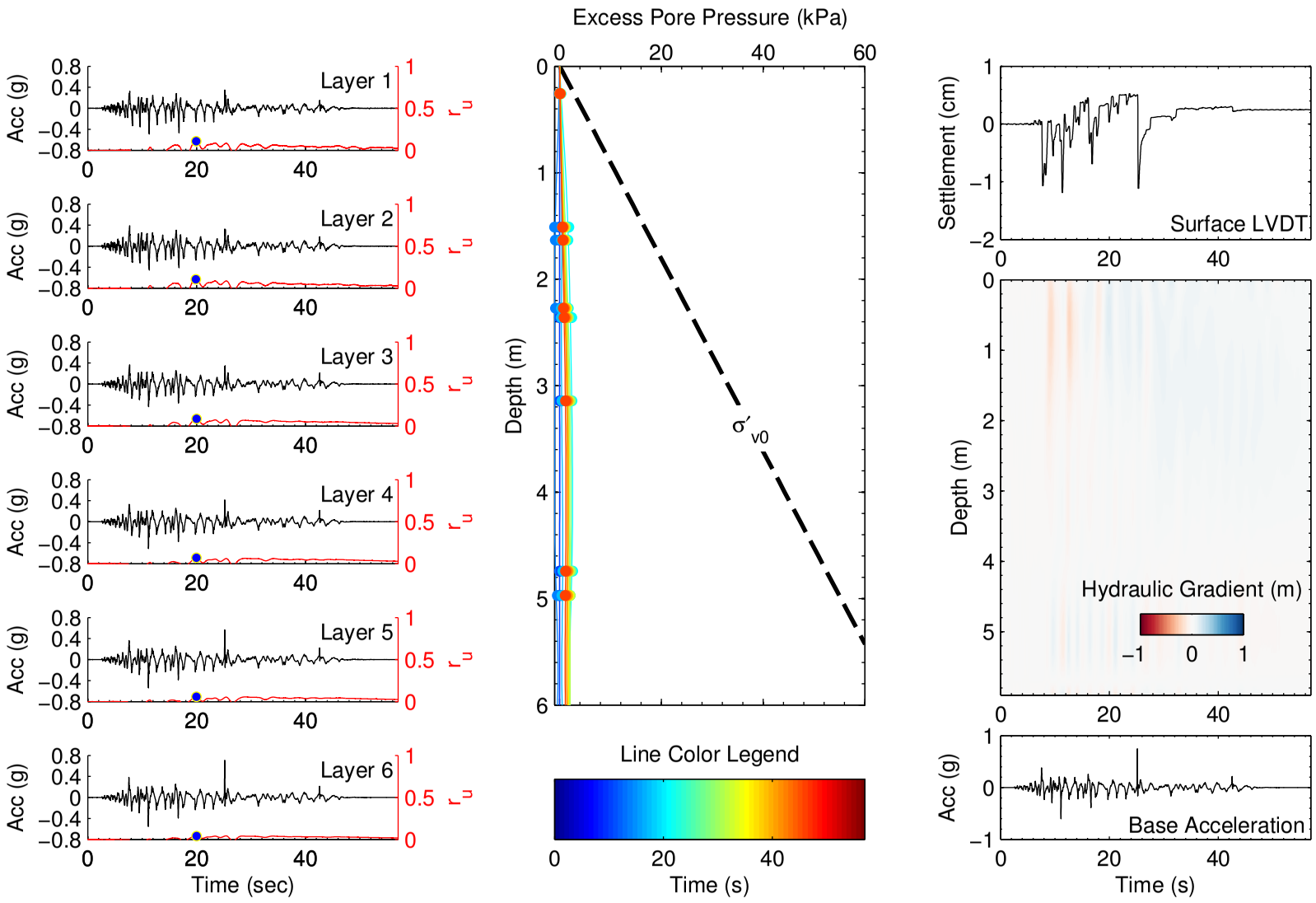
50% D_r Experiment 2 Test 25 – Data Summary Plot



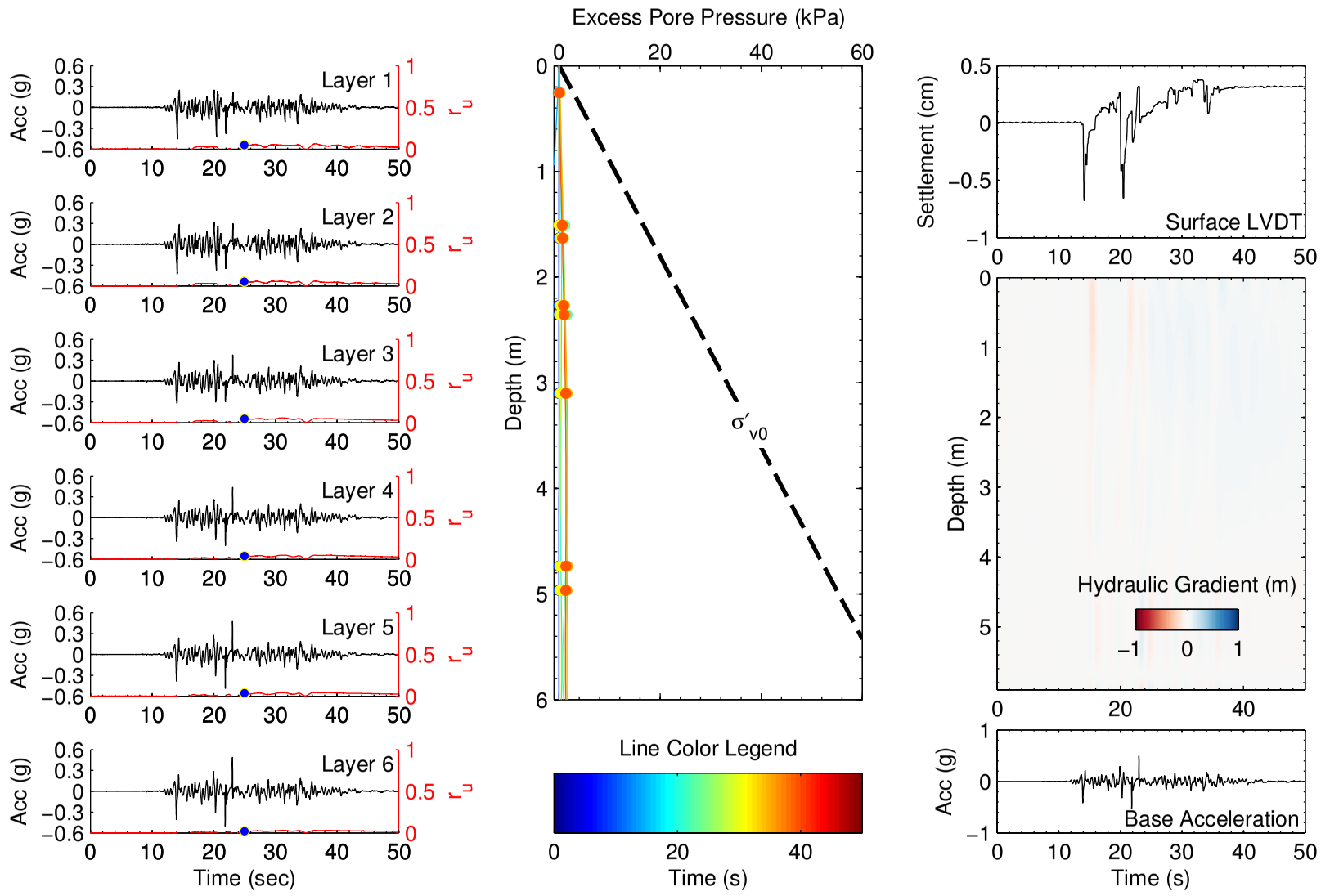
50% D_r Experiment 2 Test 26 – Data Summary Plot



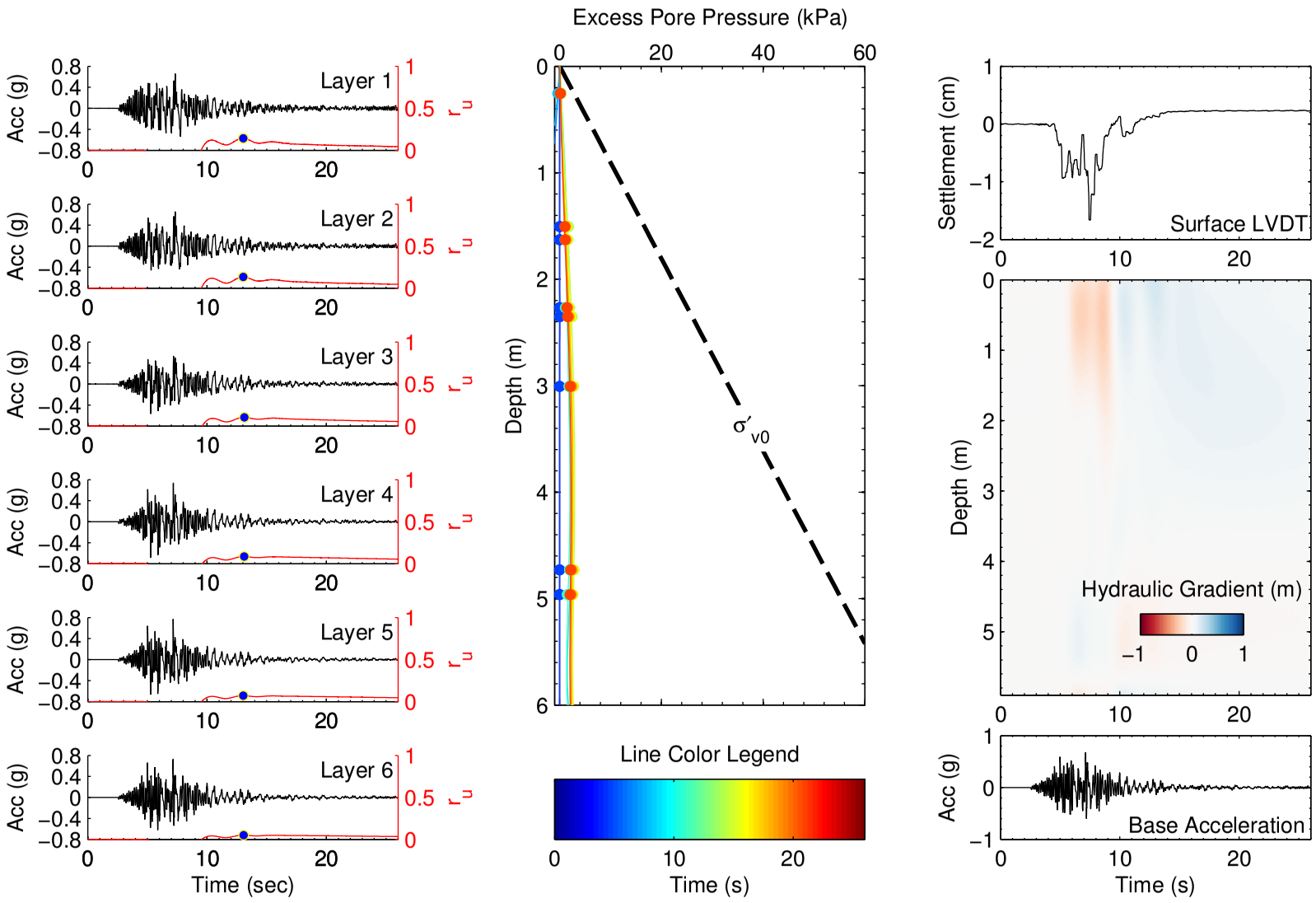
50% D_r Experiment 2 Test 27 – Data Summary Plot



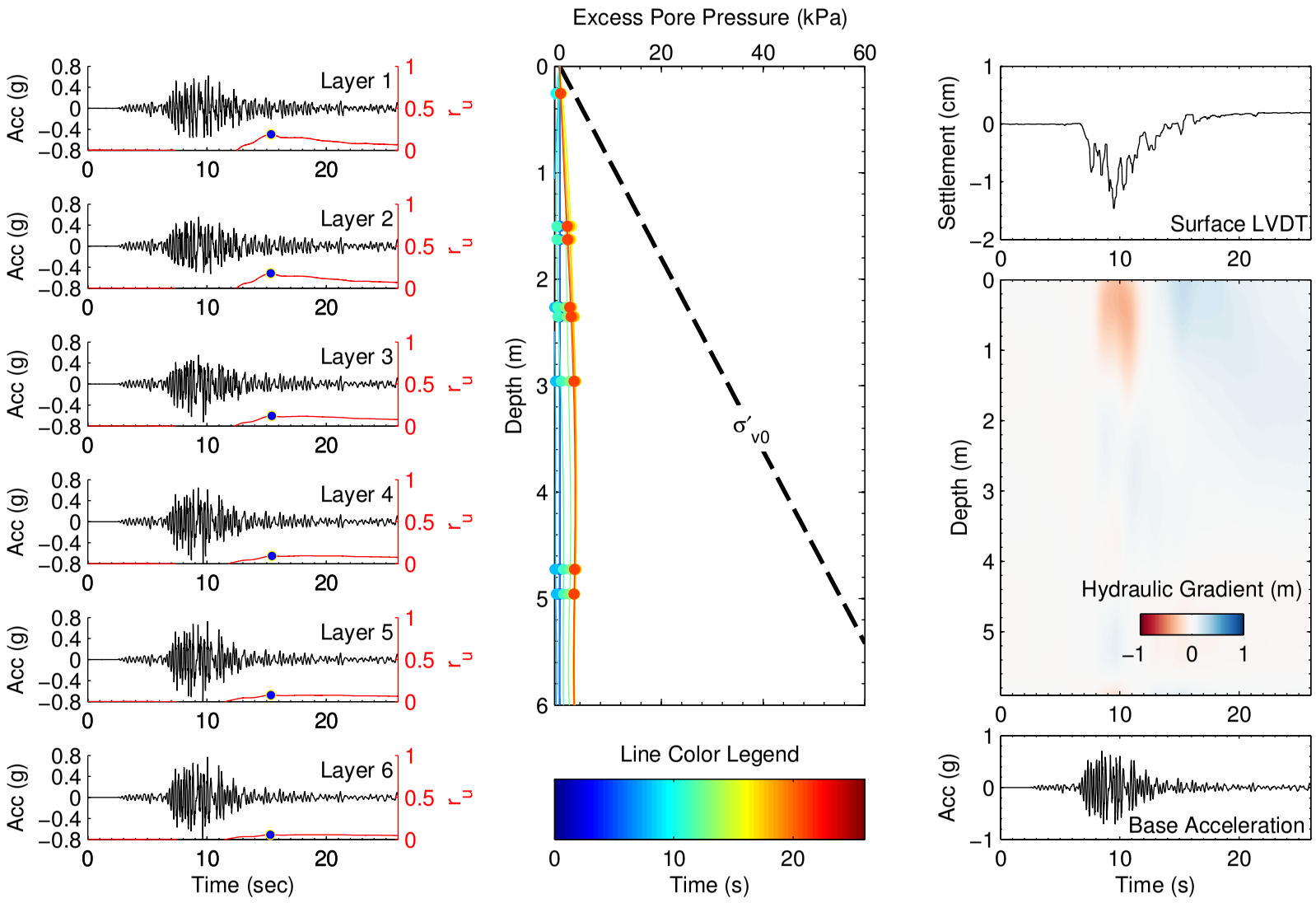
50% D_r Experiment 2 Test 28 – Data Summary Plot



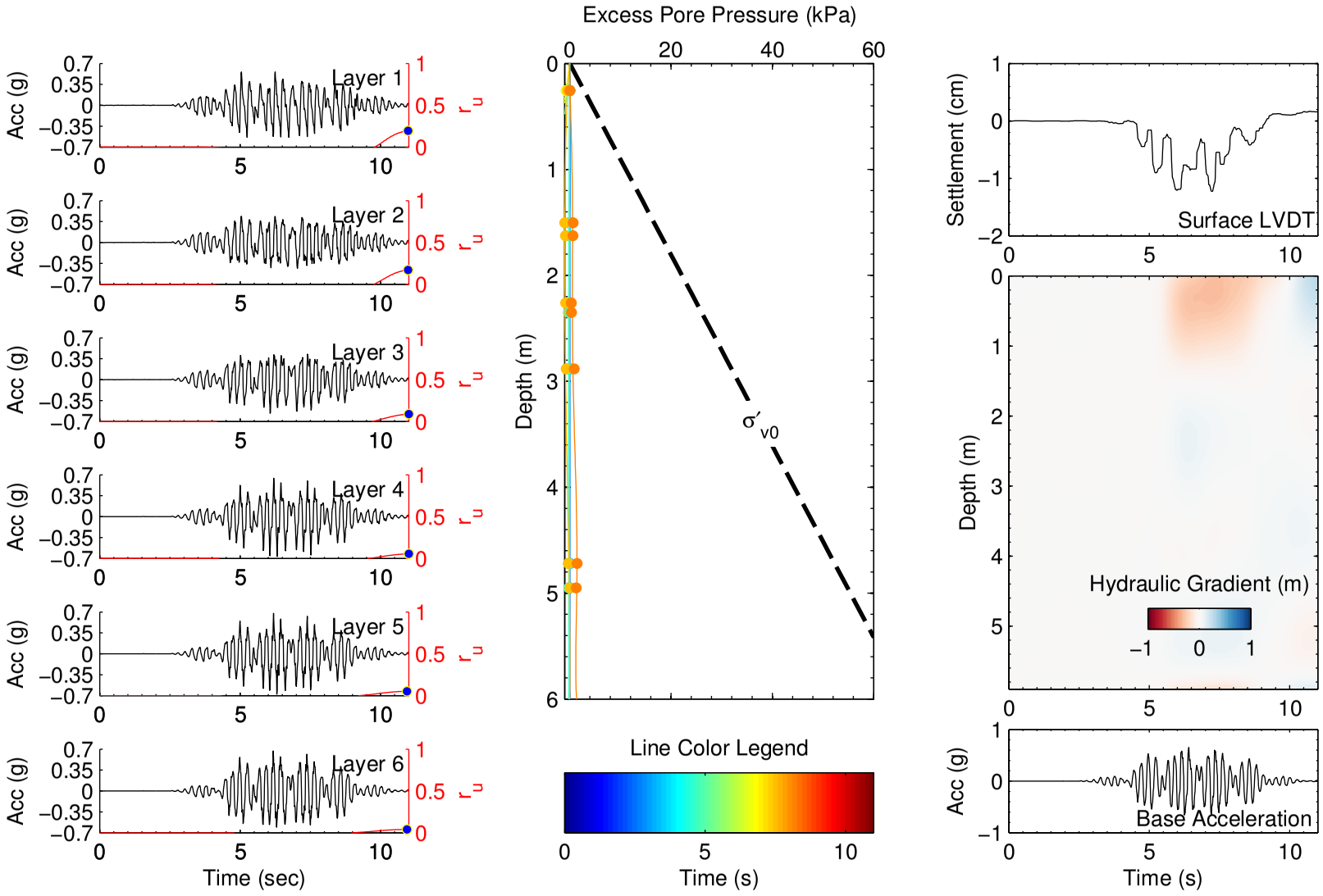
50% D_r Experiment 2 Test 29 – Data Summary Plot



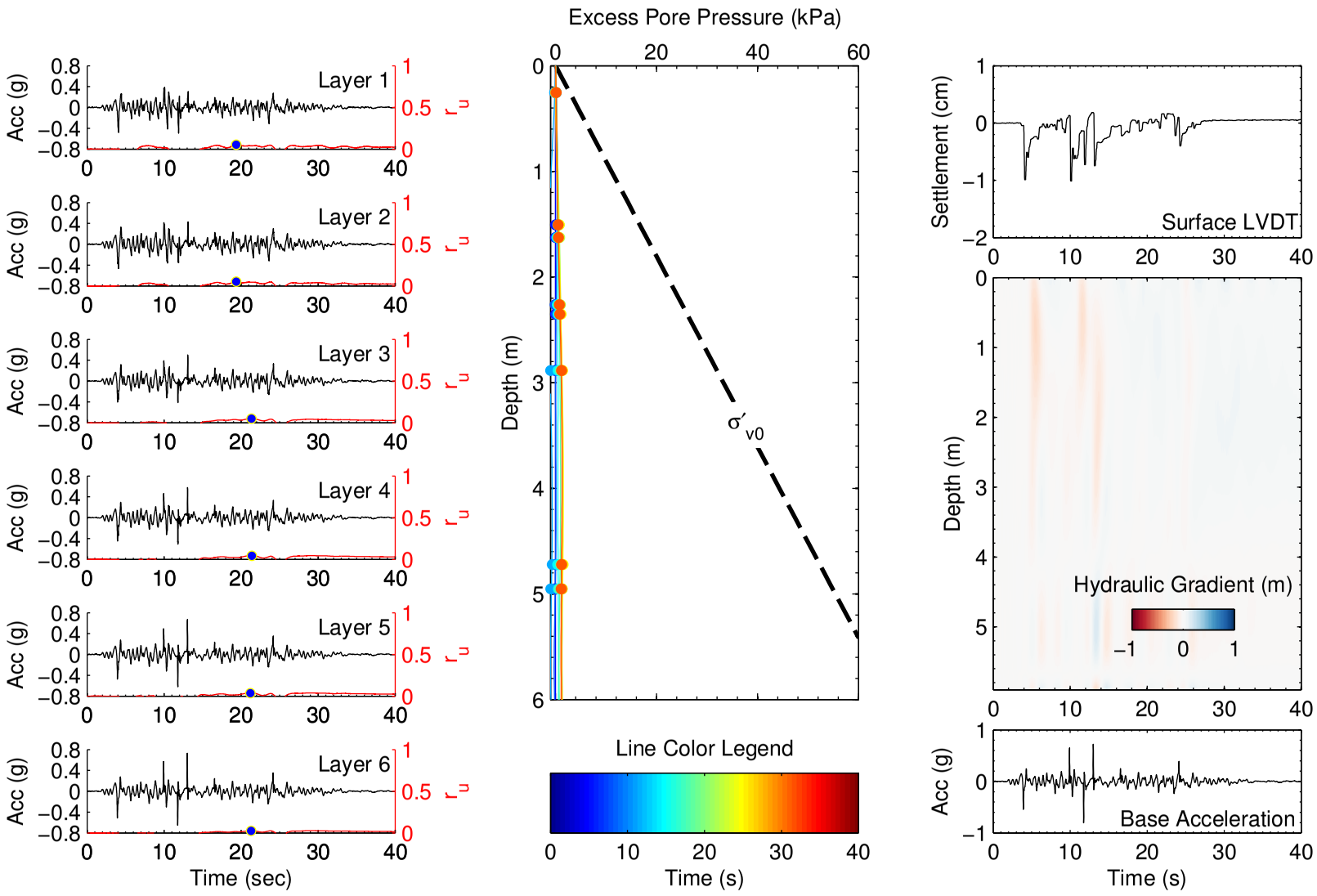
50% D_r Experiment 2 Test 30 – Data Summary Plot



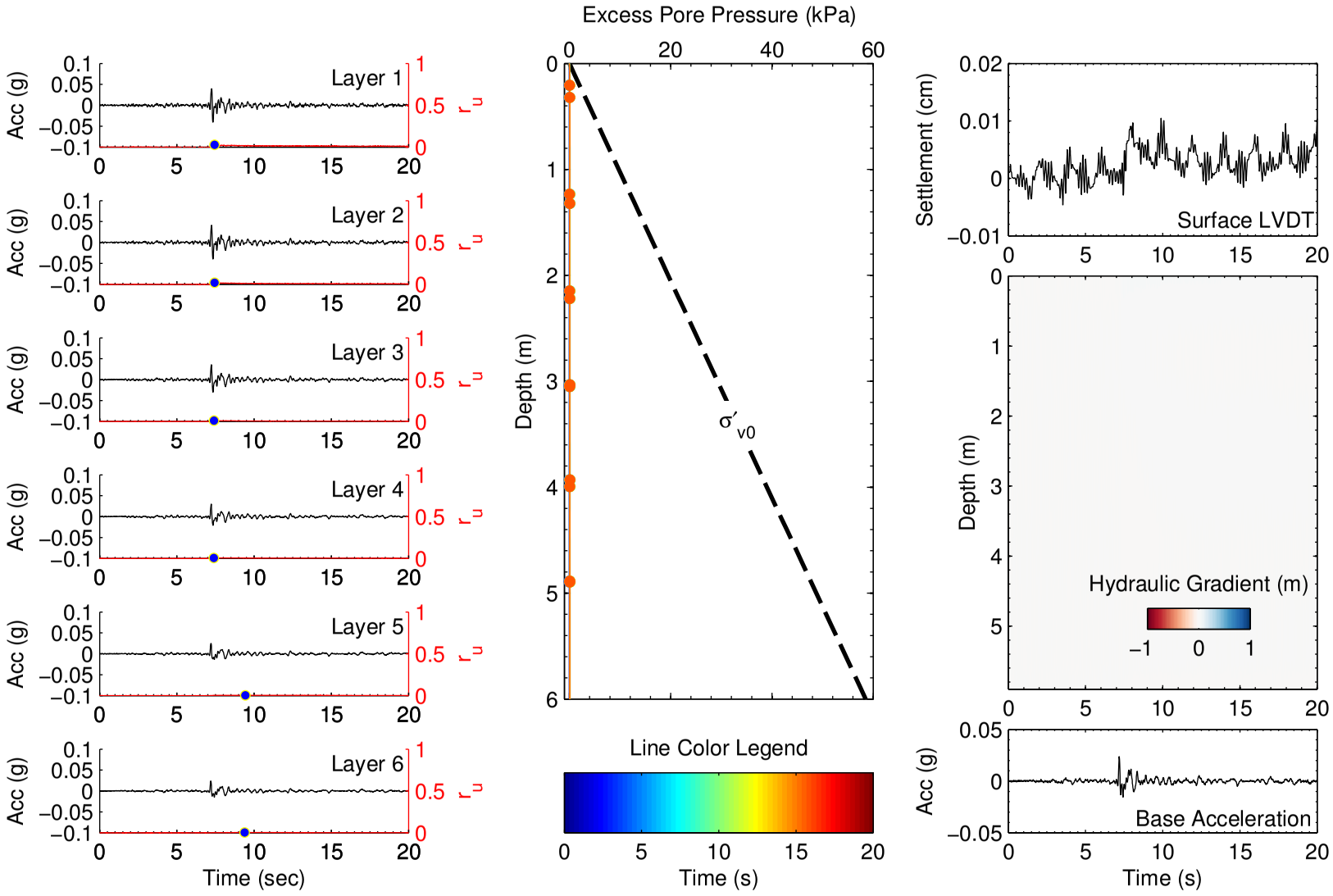
50% D_r Experiment 2 Test 31 – Data Summary Plot



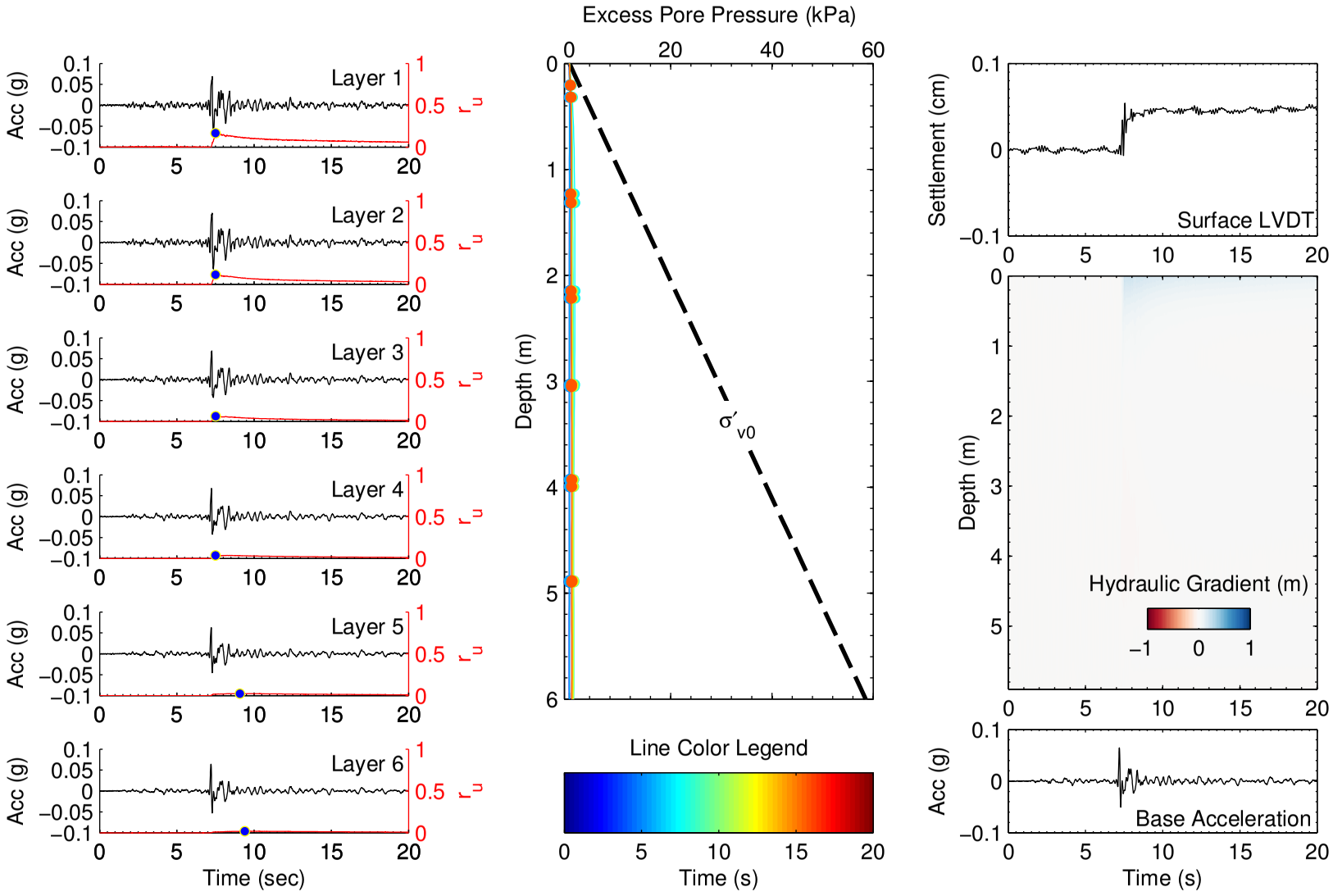
50% D_r Experiment 2 Test 32 – Data Summary Plot



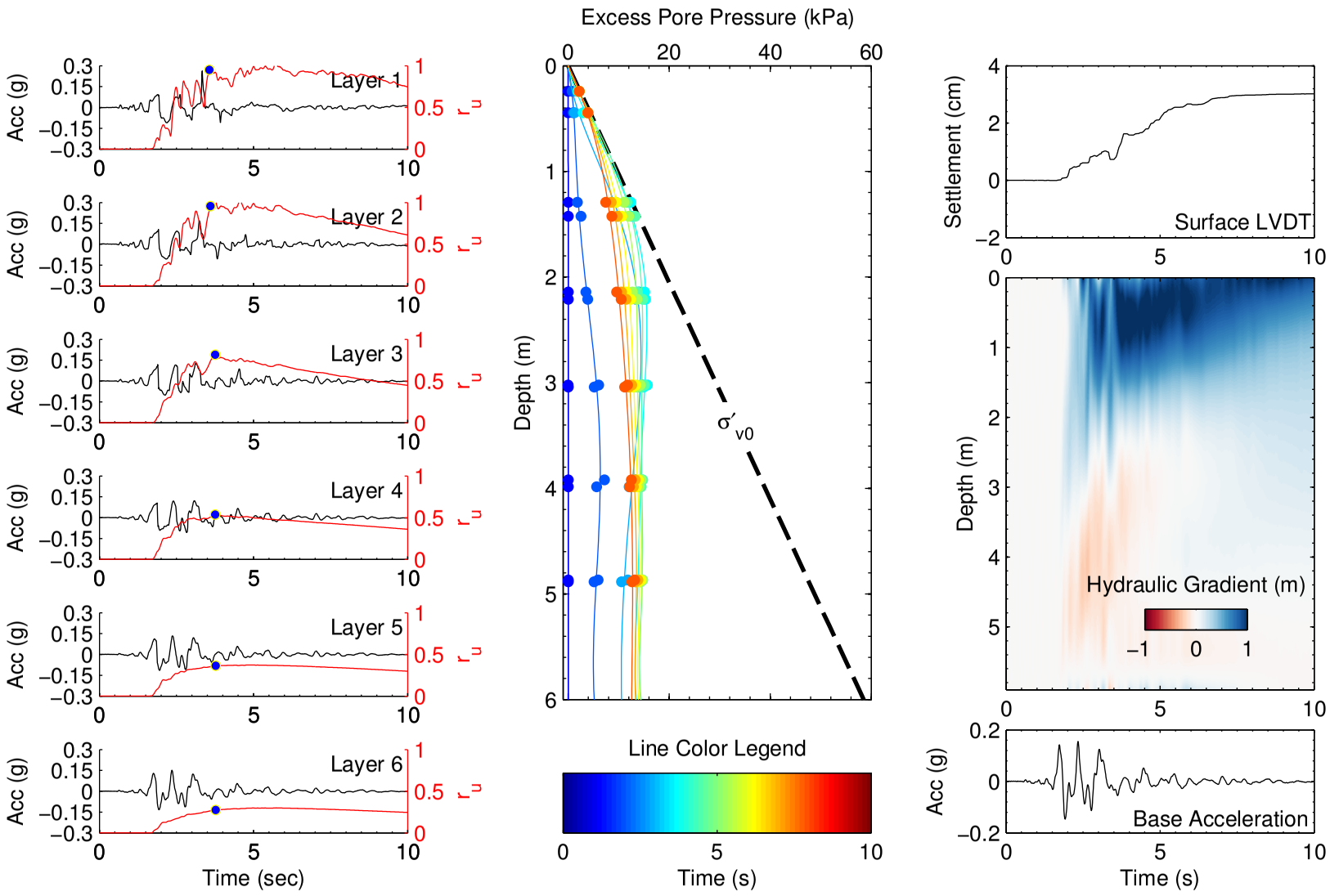
50% D_r Experiment 2 Test 33 – Data Summary Plot



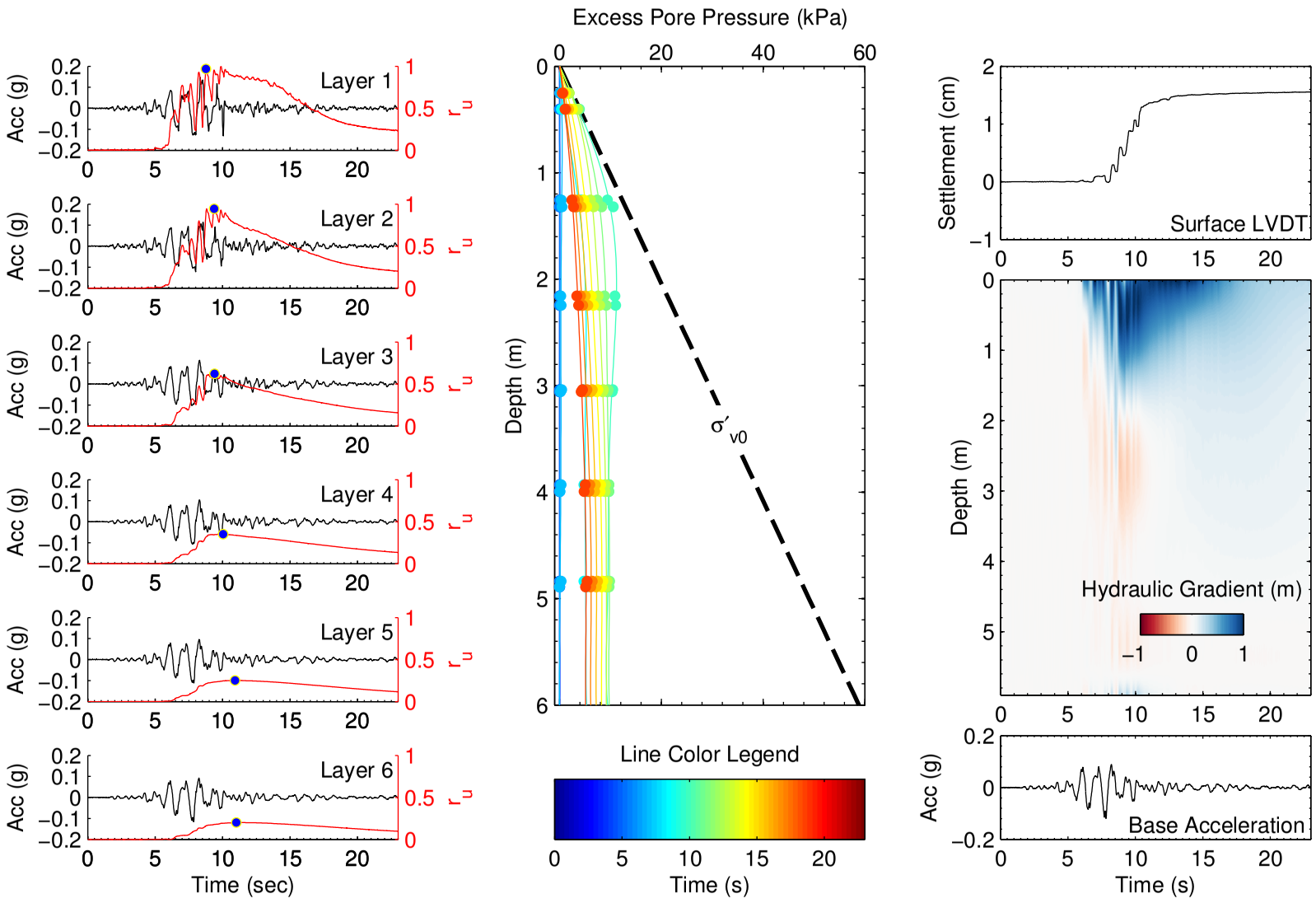
40% D_r Experiment 3 Test 1 – Data Summary Plot



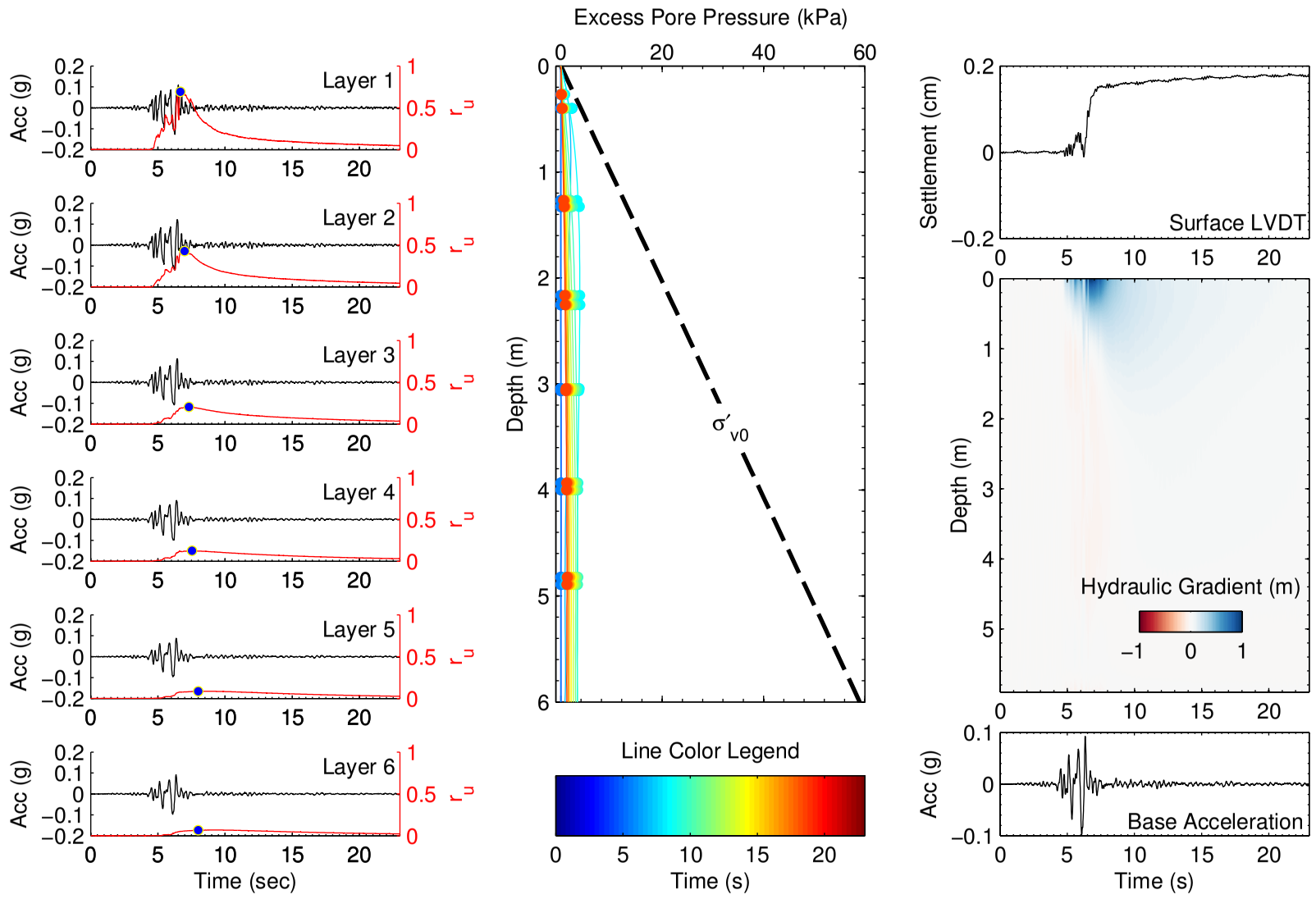
40% D_r Experiment 3 Test 2 – Data Summary Plot



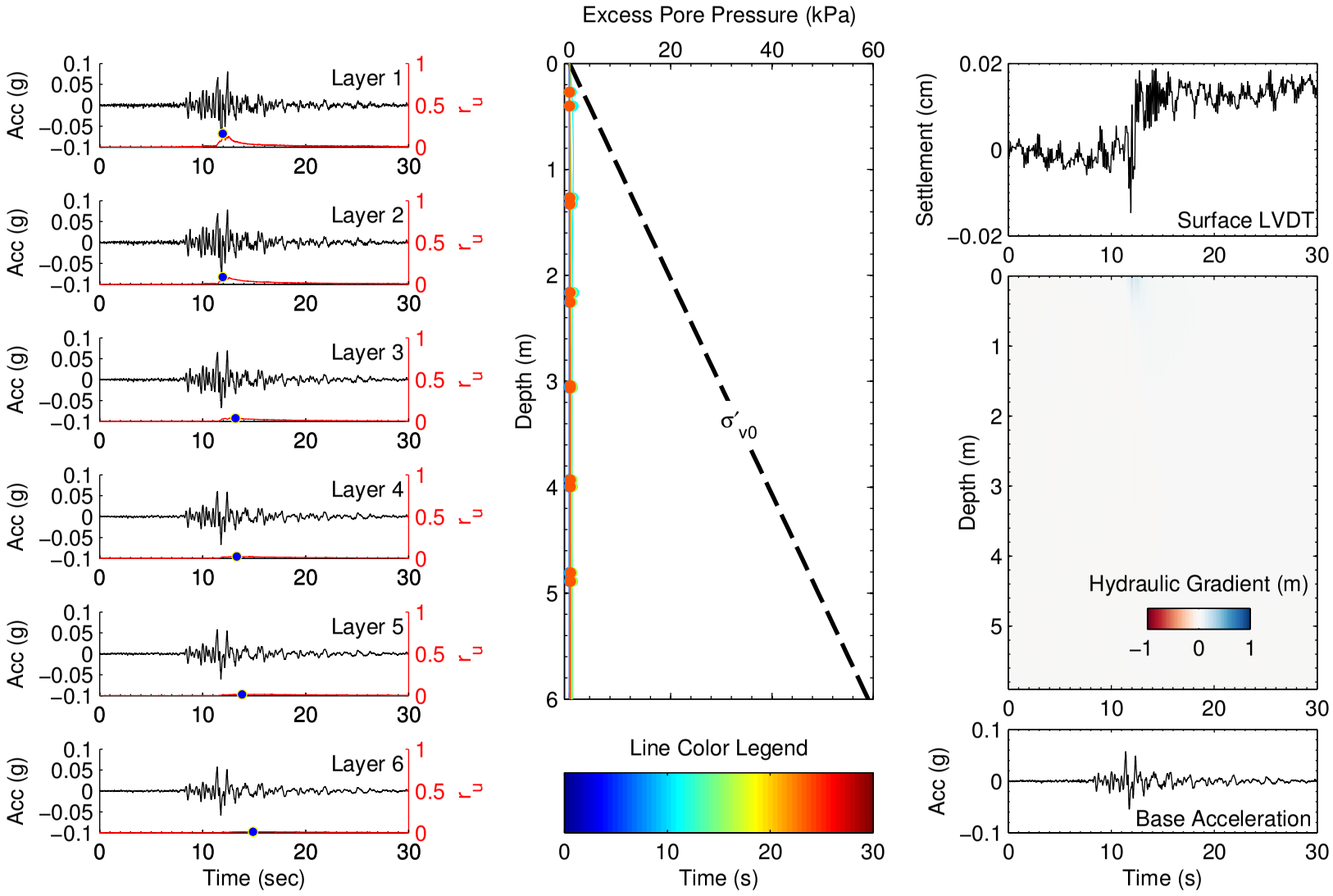
40% D_r Experiment 3 Test 3 – Data Summary Plot



40% D_r Experiment 3 Test 4 – Data Summary Plot

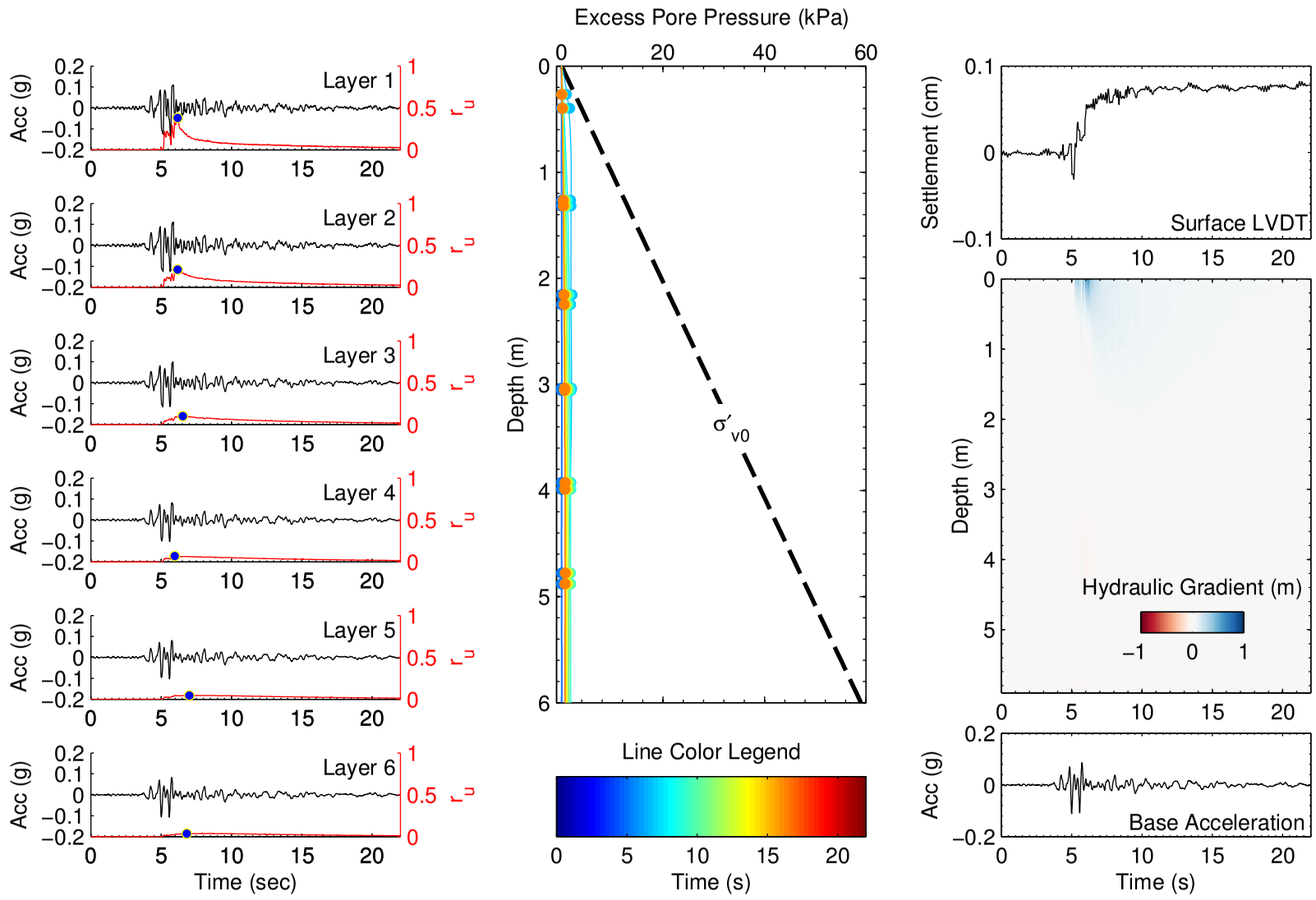


40% D_r Experiment 3 Test 5 – Data Summary Plot

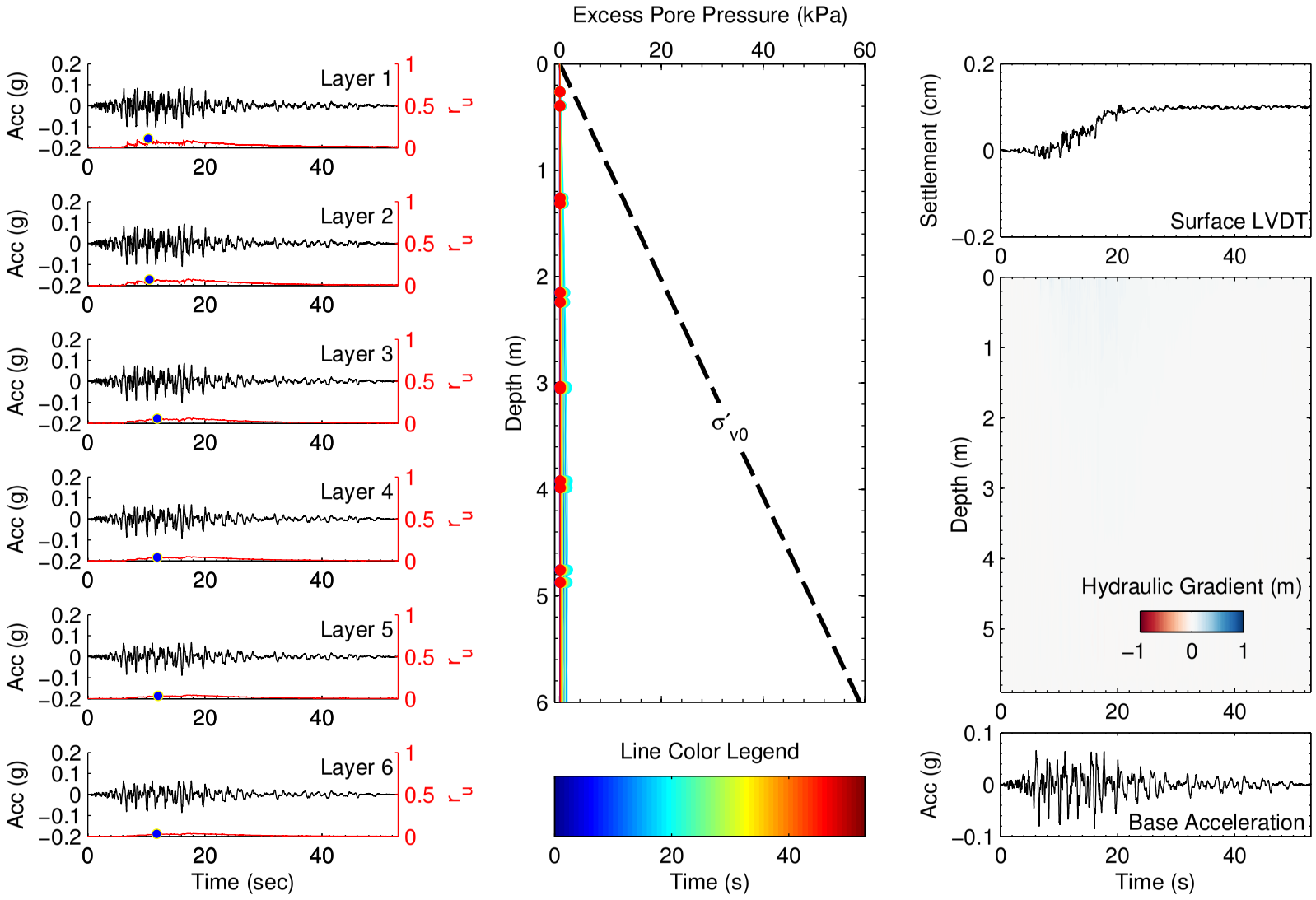


40% D_r Experiment 3 Test 6 – Data Summary Plot

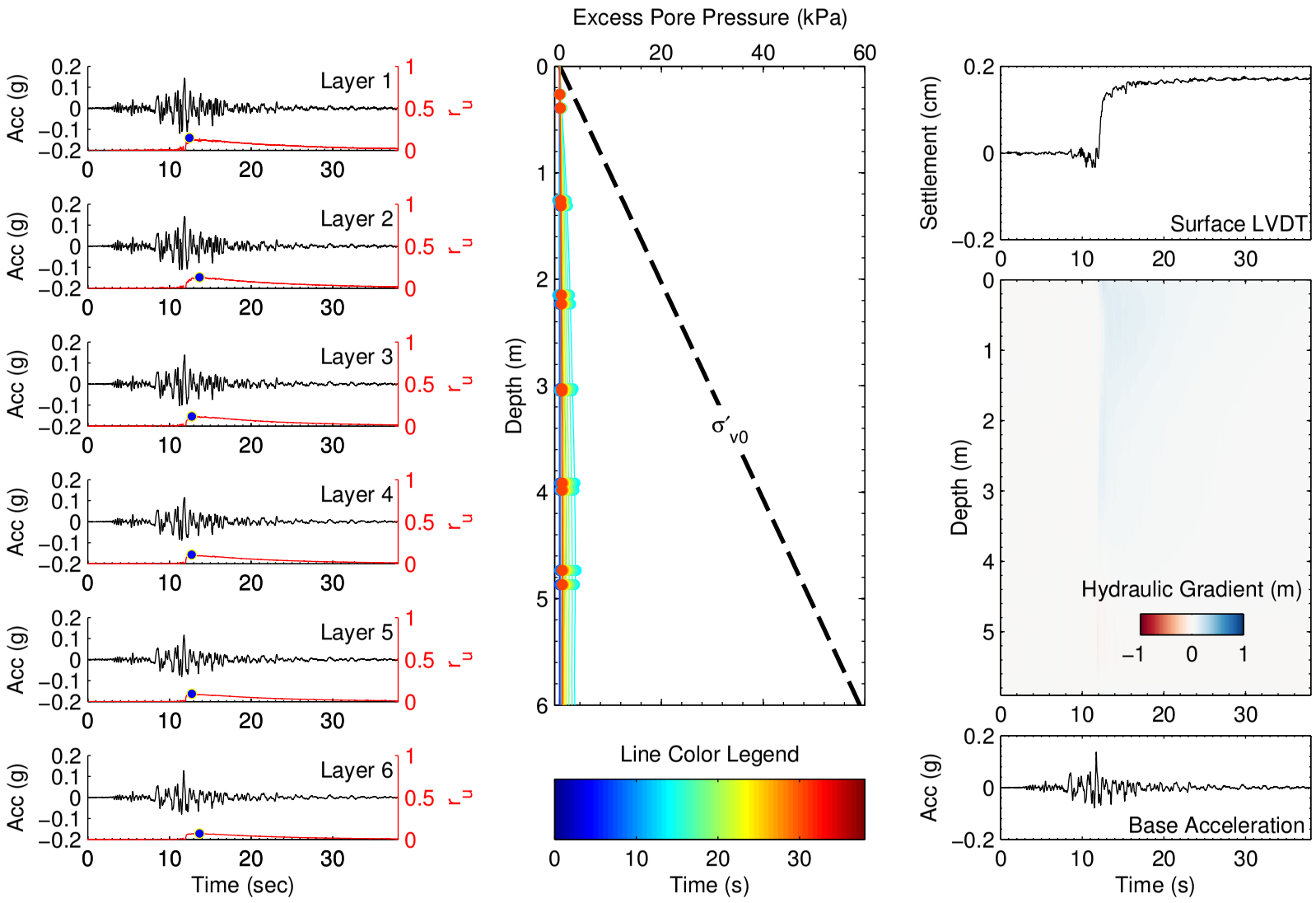
40% D_r Experiment 3 Test 7 – Data Summary Plot



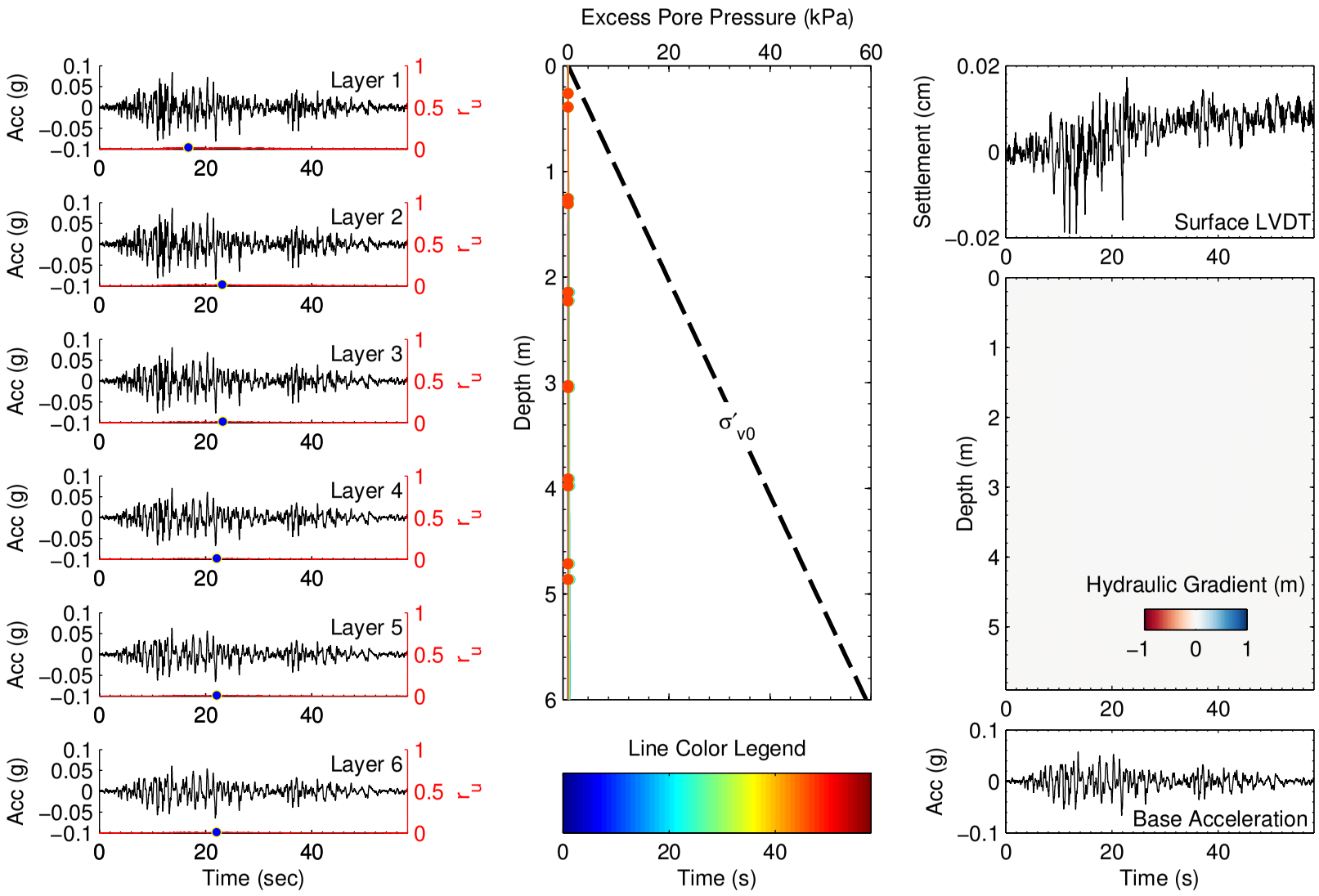
40% D_r Experiment 3 Test 8 – Data Summary Plot



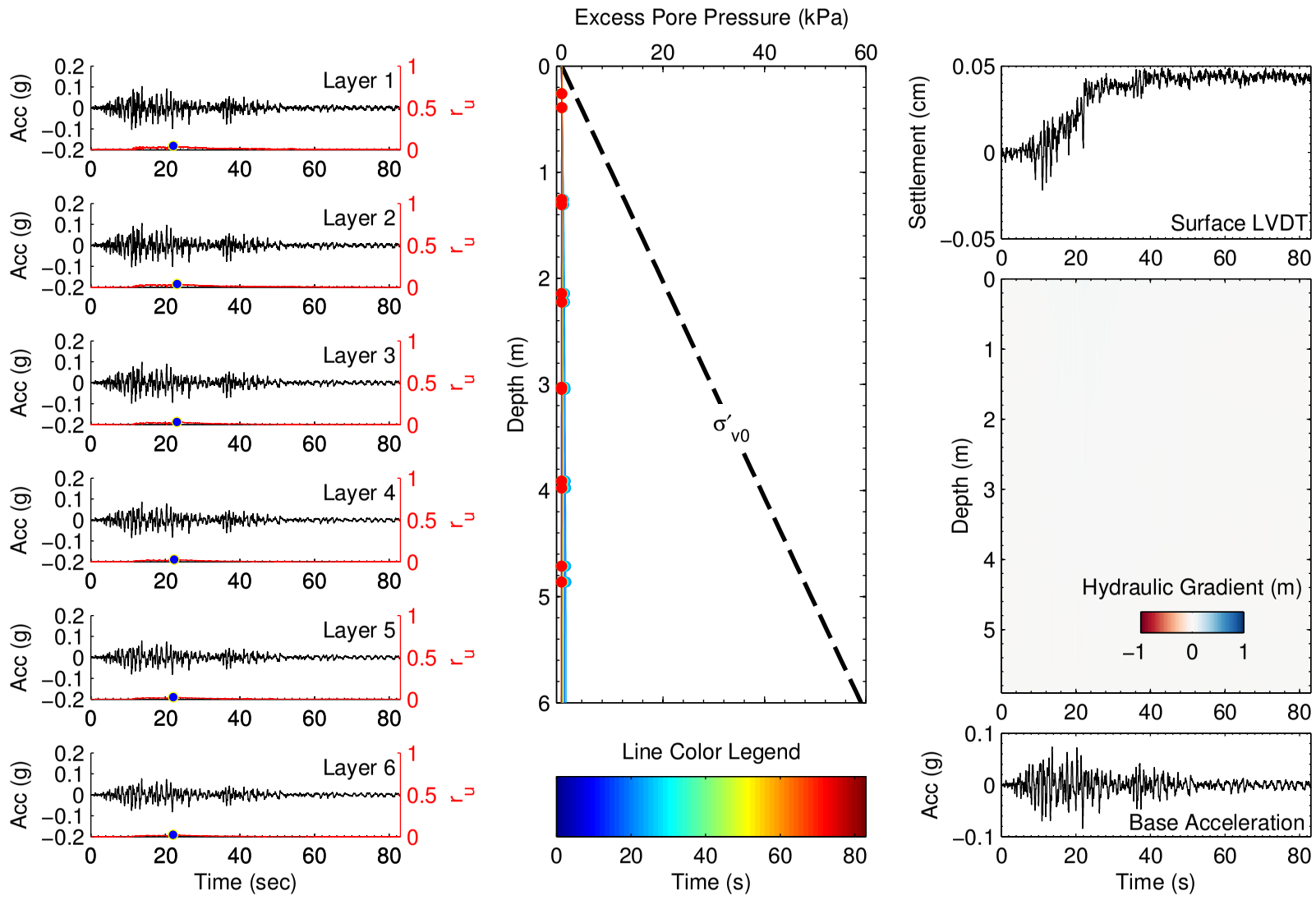
40% D_r Experiment 3 Test 9 – Data Summary Plot



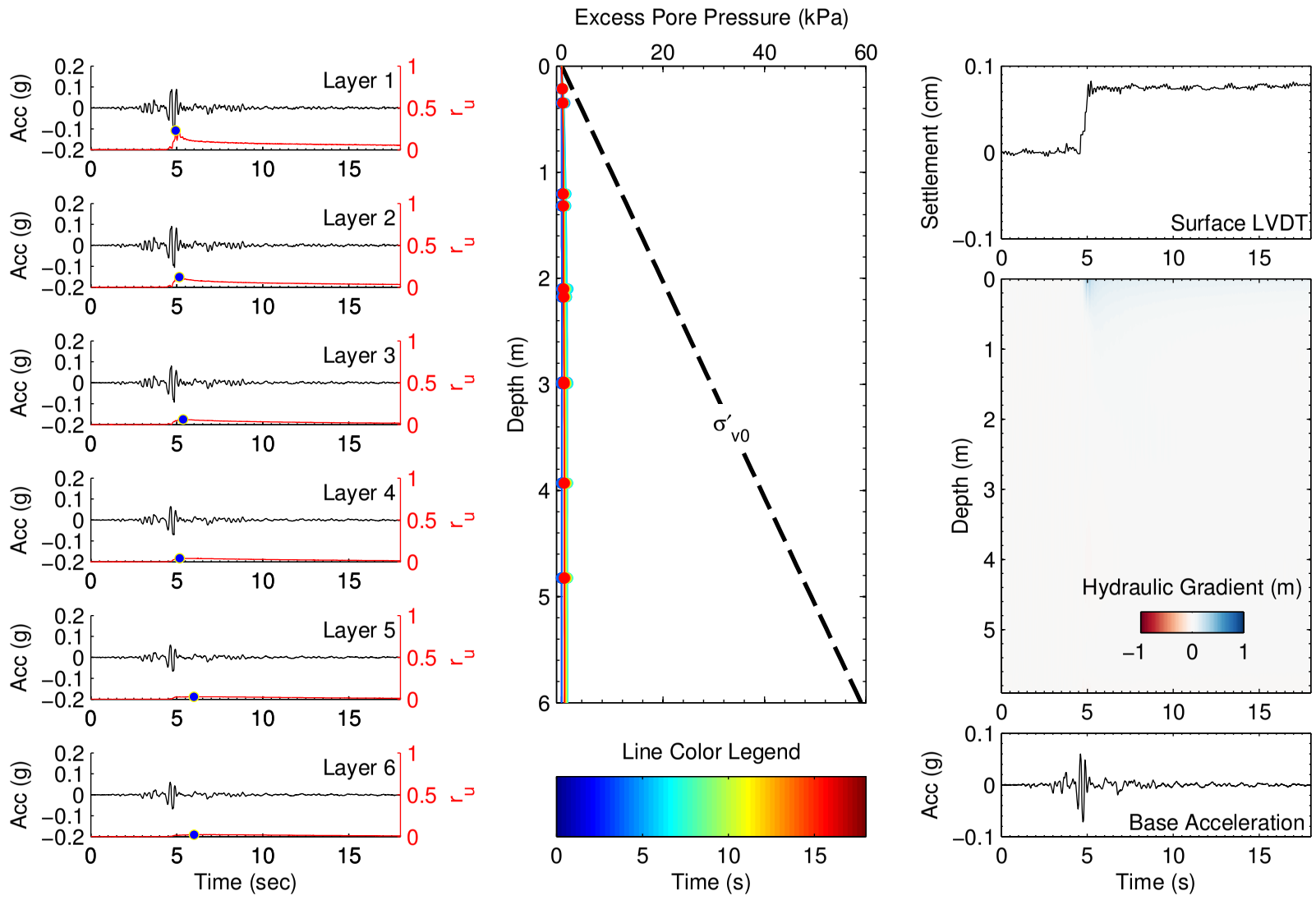
40% D_r Experiment 3 Test 10 – Data Summary Plot



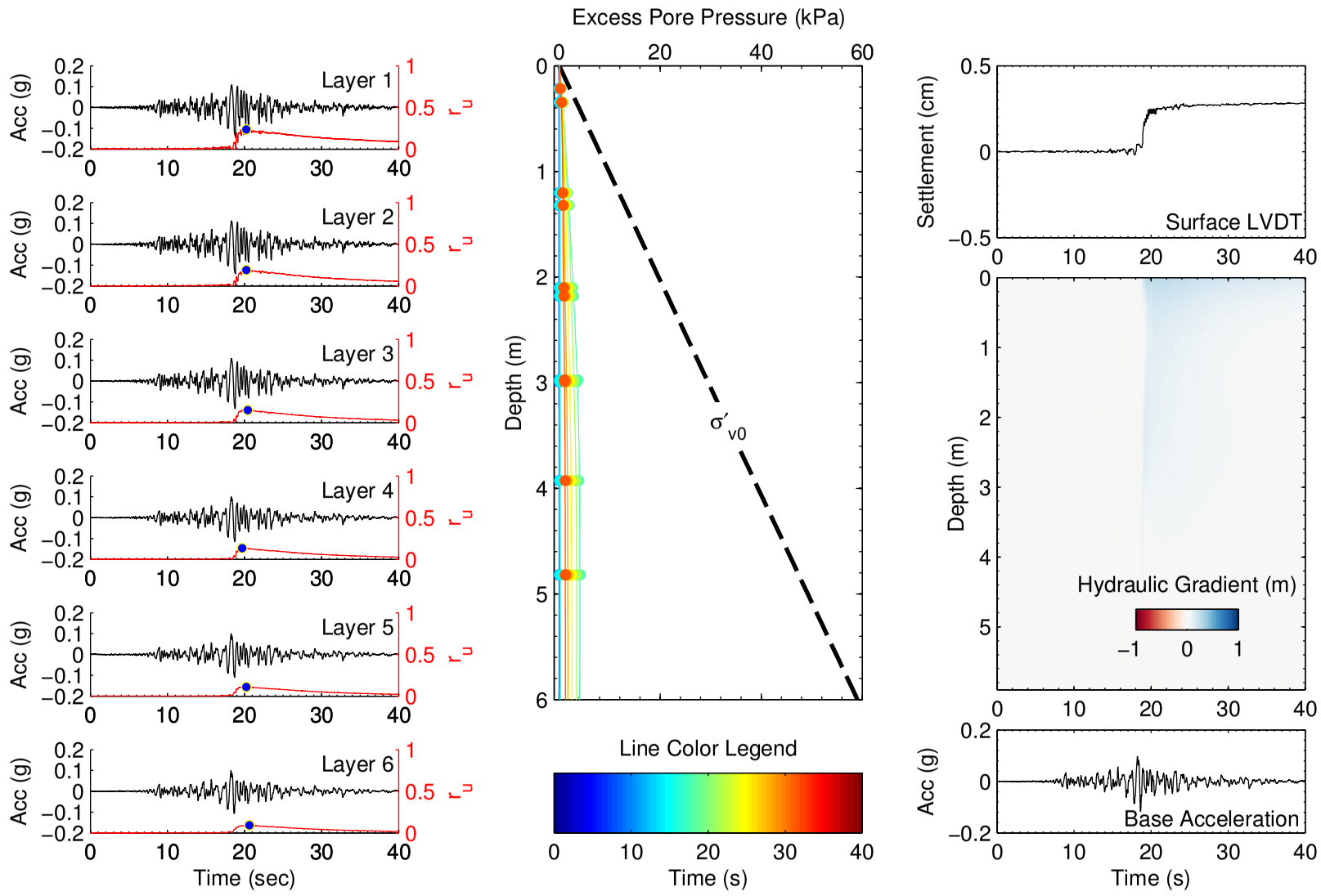
40% D_r Experiment 3 Test 11 – Data Summary Plot



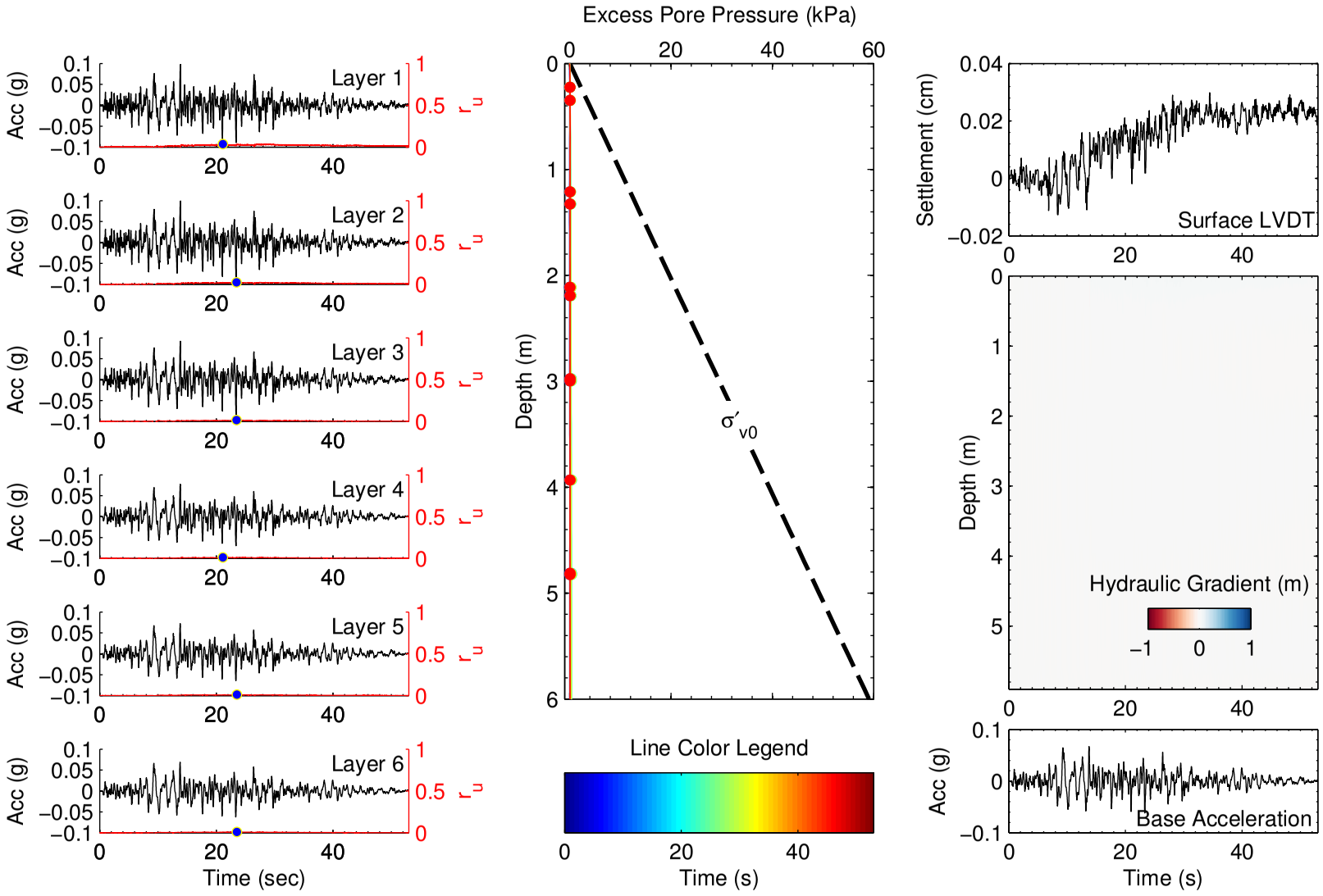
40% D_r Experiment 3 Test 12 – Data Summary Plot



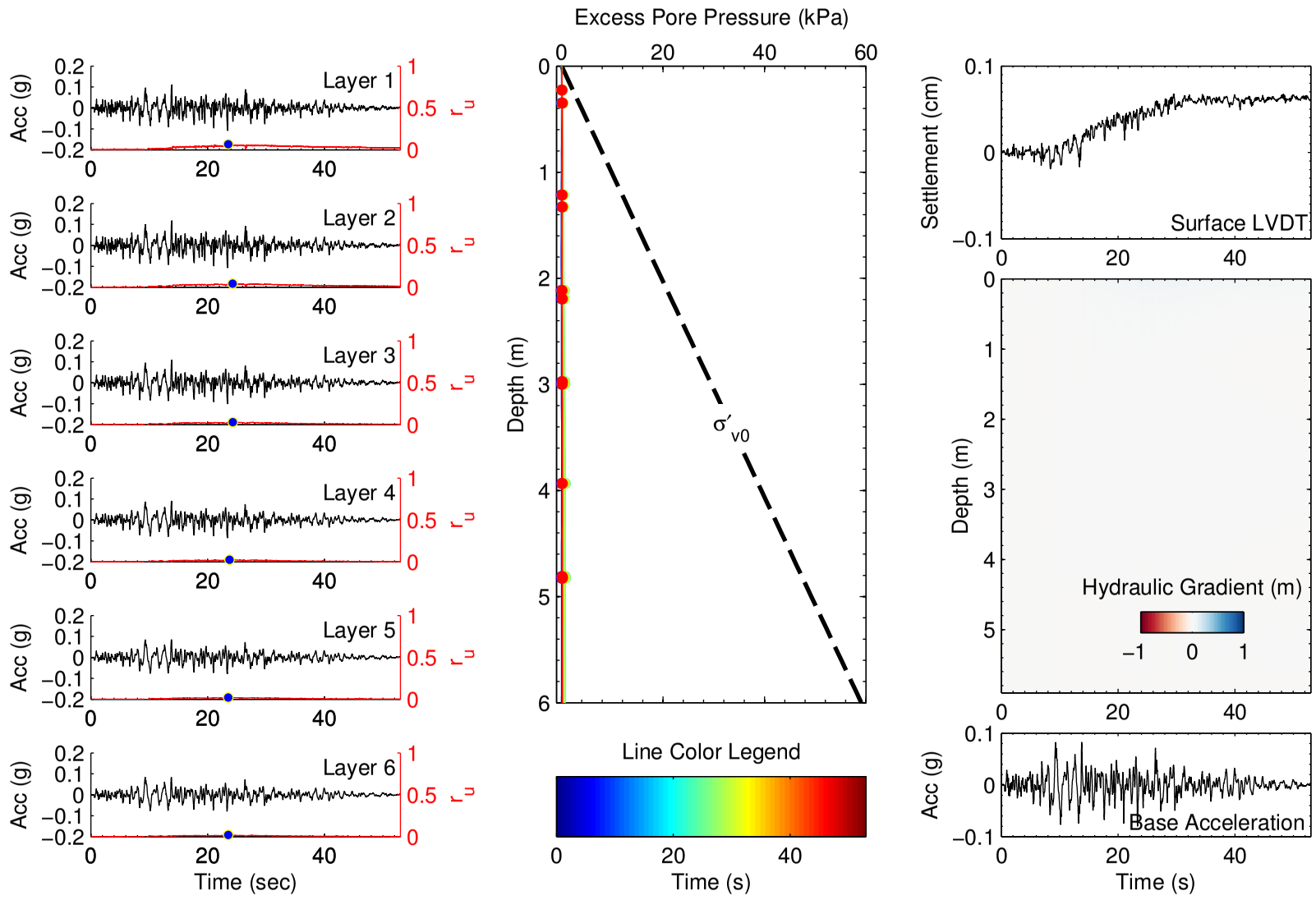
40% D_r Experiment 3 Test 13 – Data Summary Plot



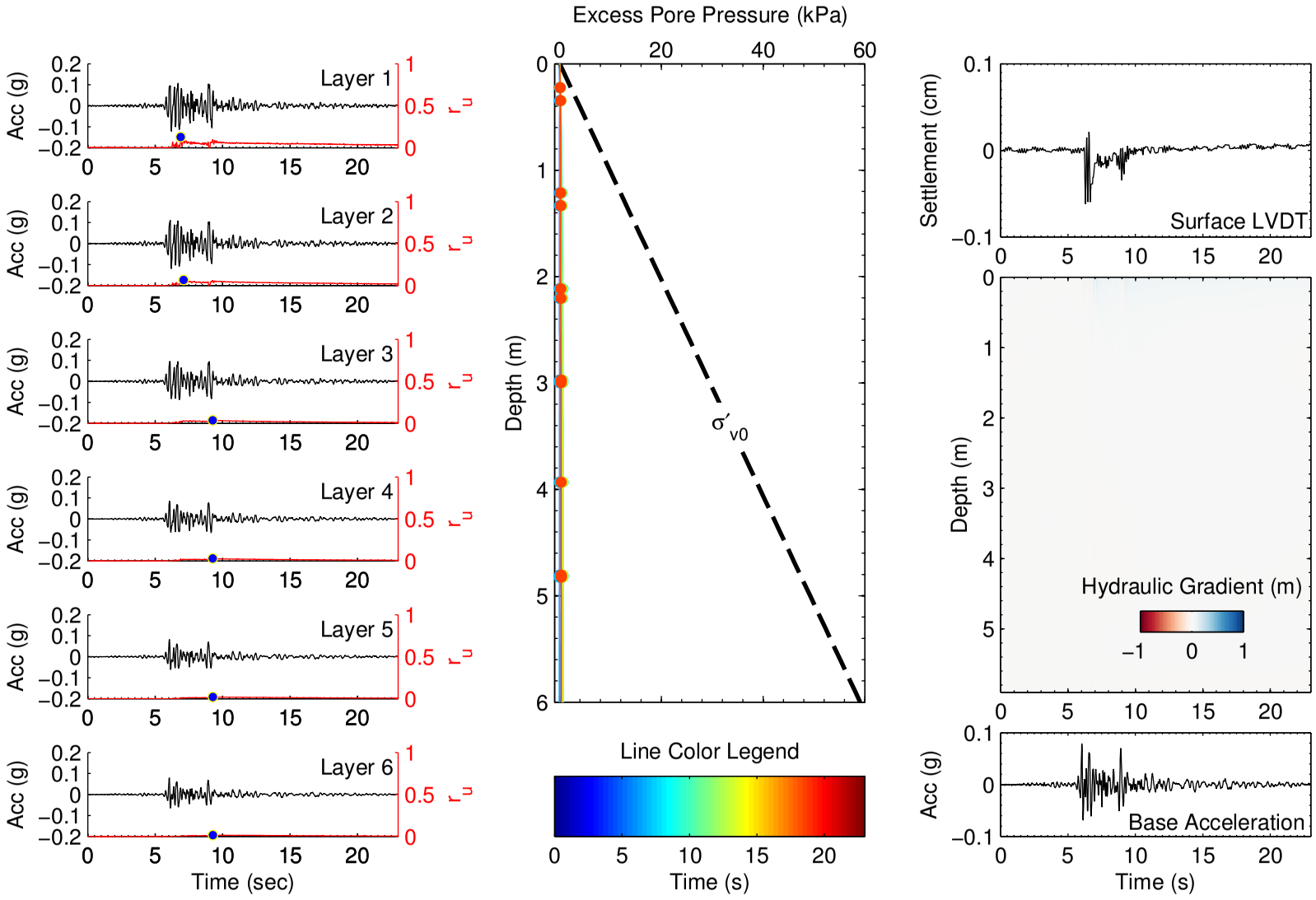
40% D_r Experiment 3 Test 14 – Data Summary Plot



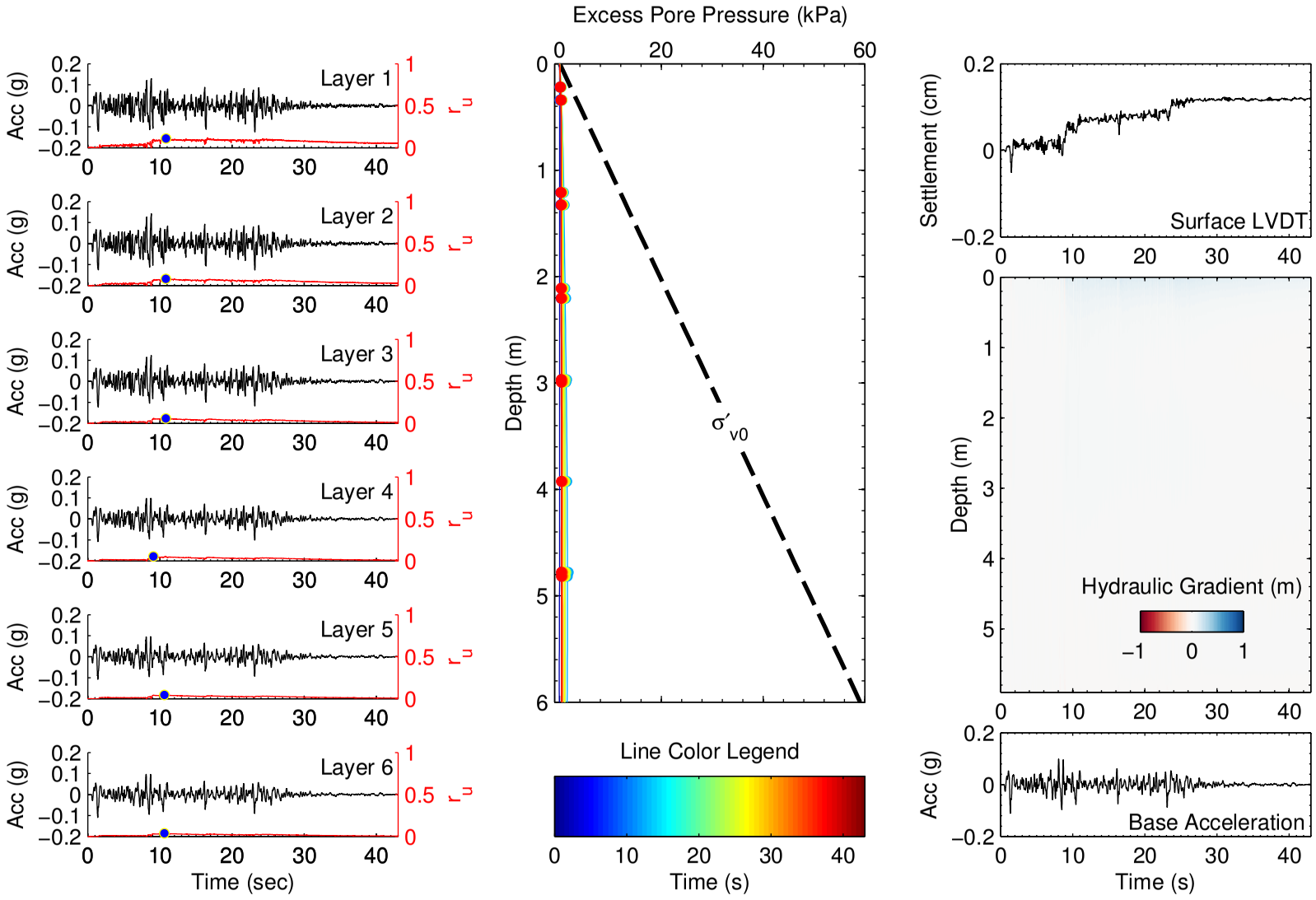
40% D_r Experiment 3 Test 15 – Data Summary Plot



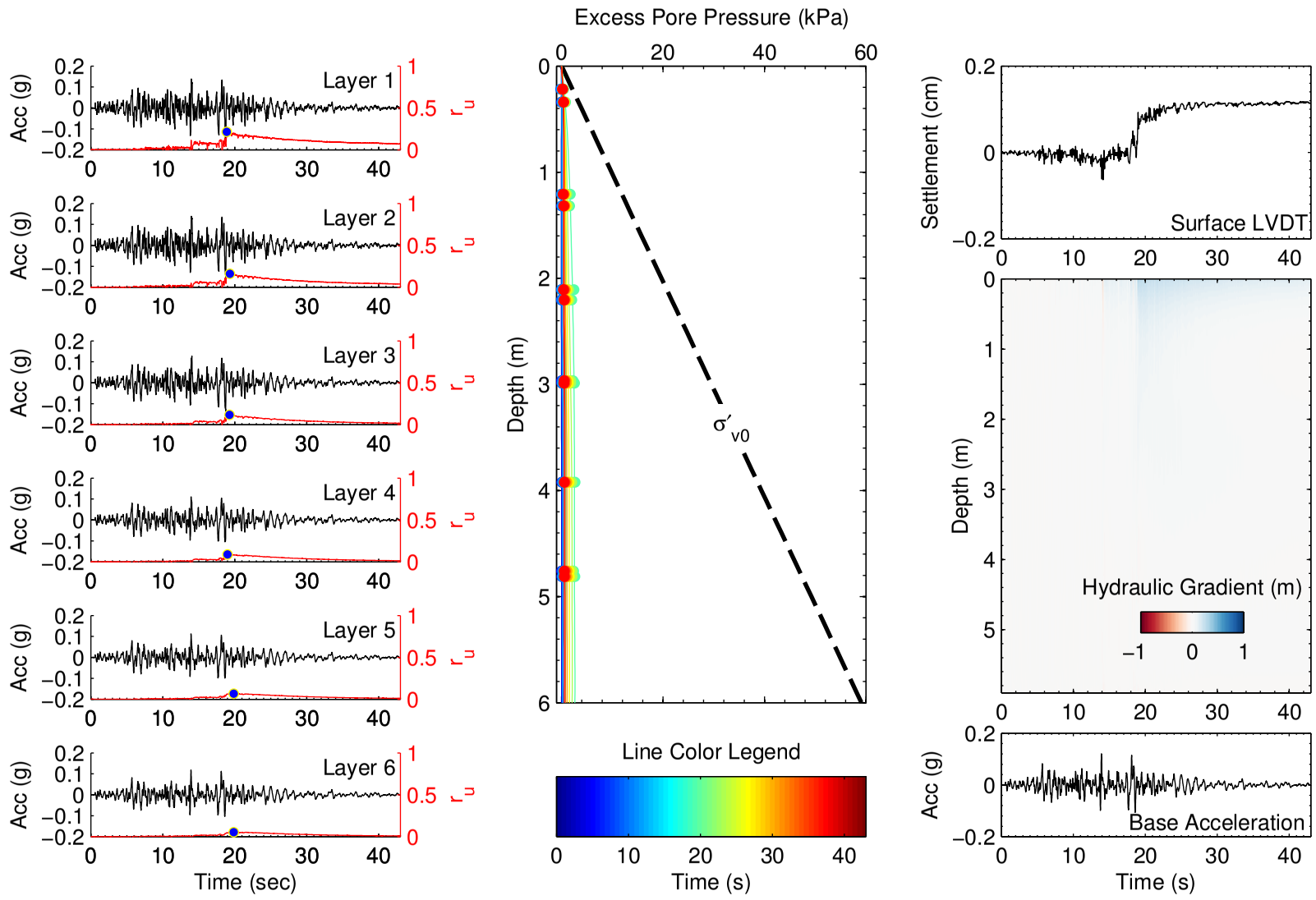
40% D_r Experiment 3 Test 16 – Data Summary Plot



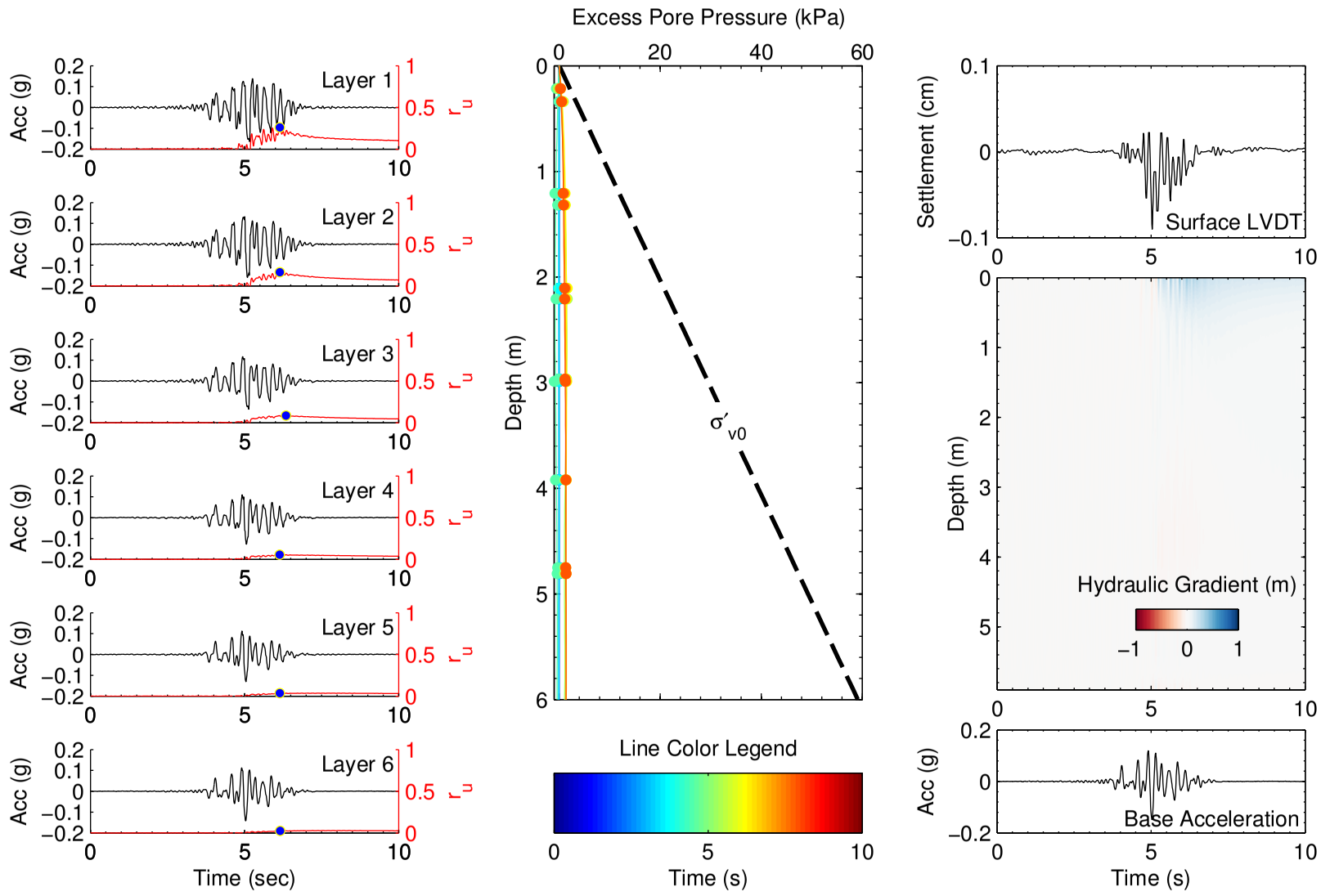
40% D_r Experiment 3 Test 17 – Data Summary Plot



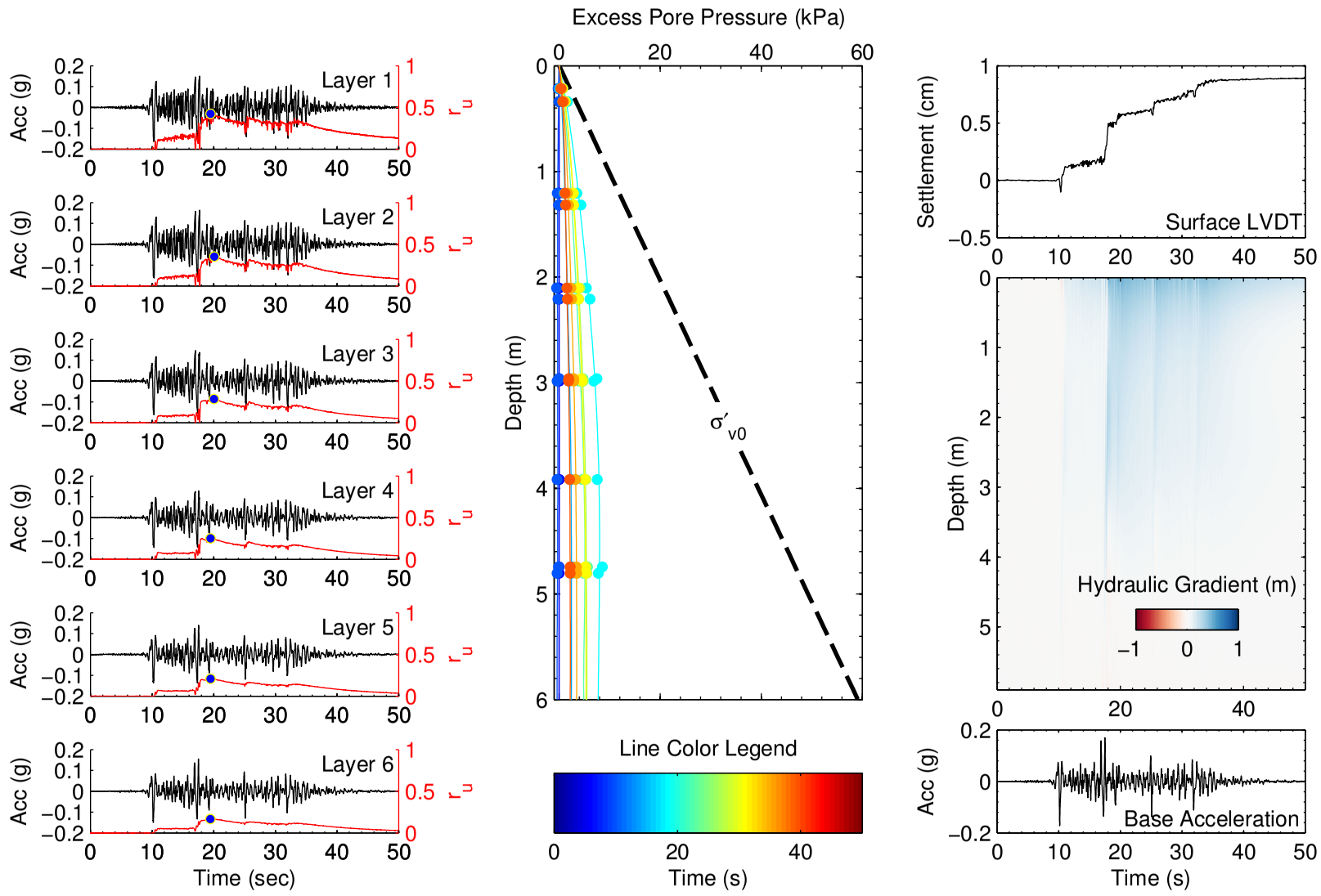
40% D_r Experiment 3 Test 18 – Data Summary Plot



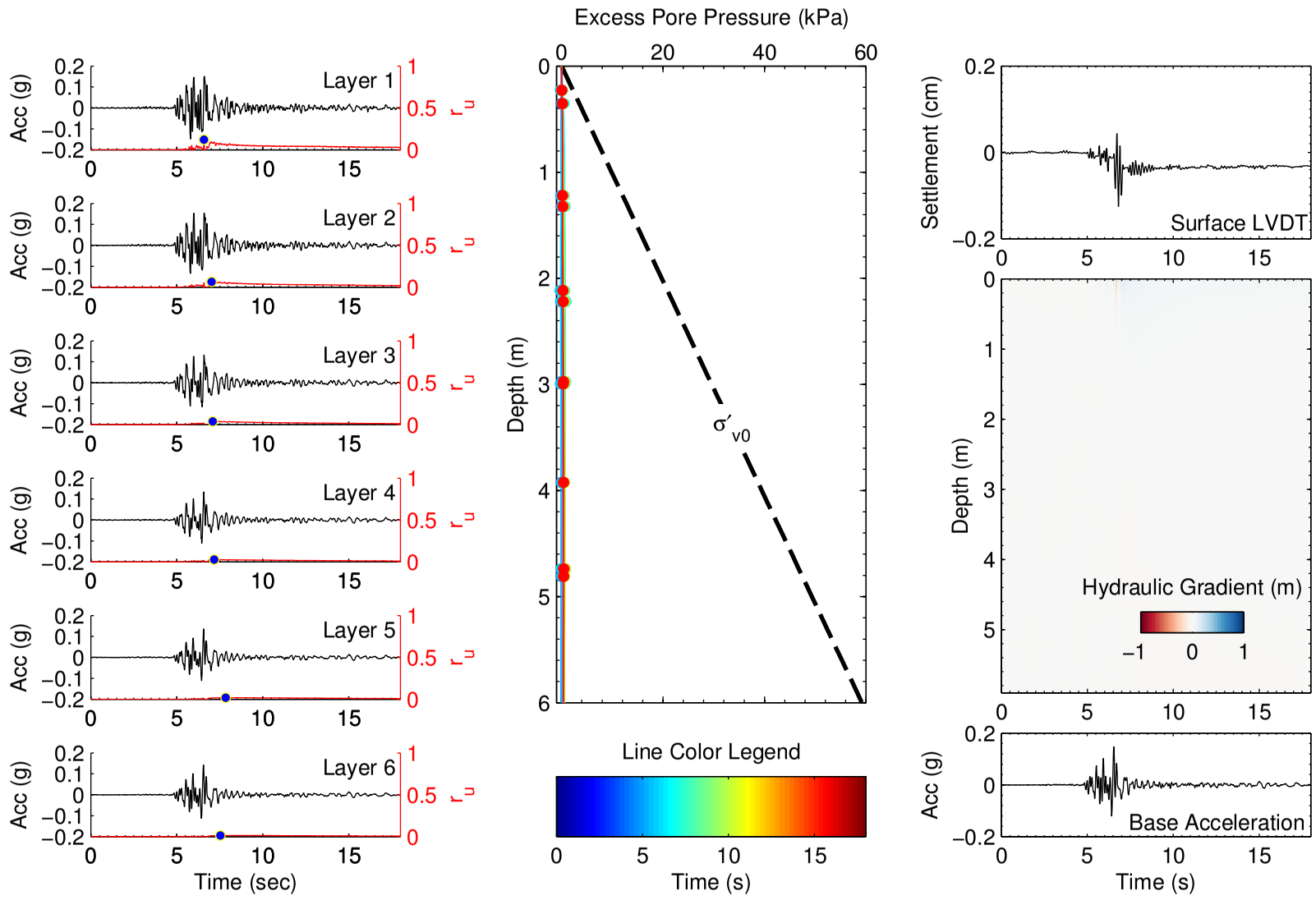
40% D_r Experiment 3 Test 19 – Data Summary Plot



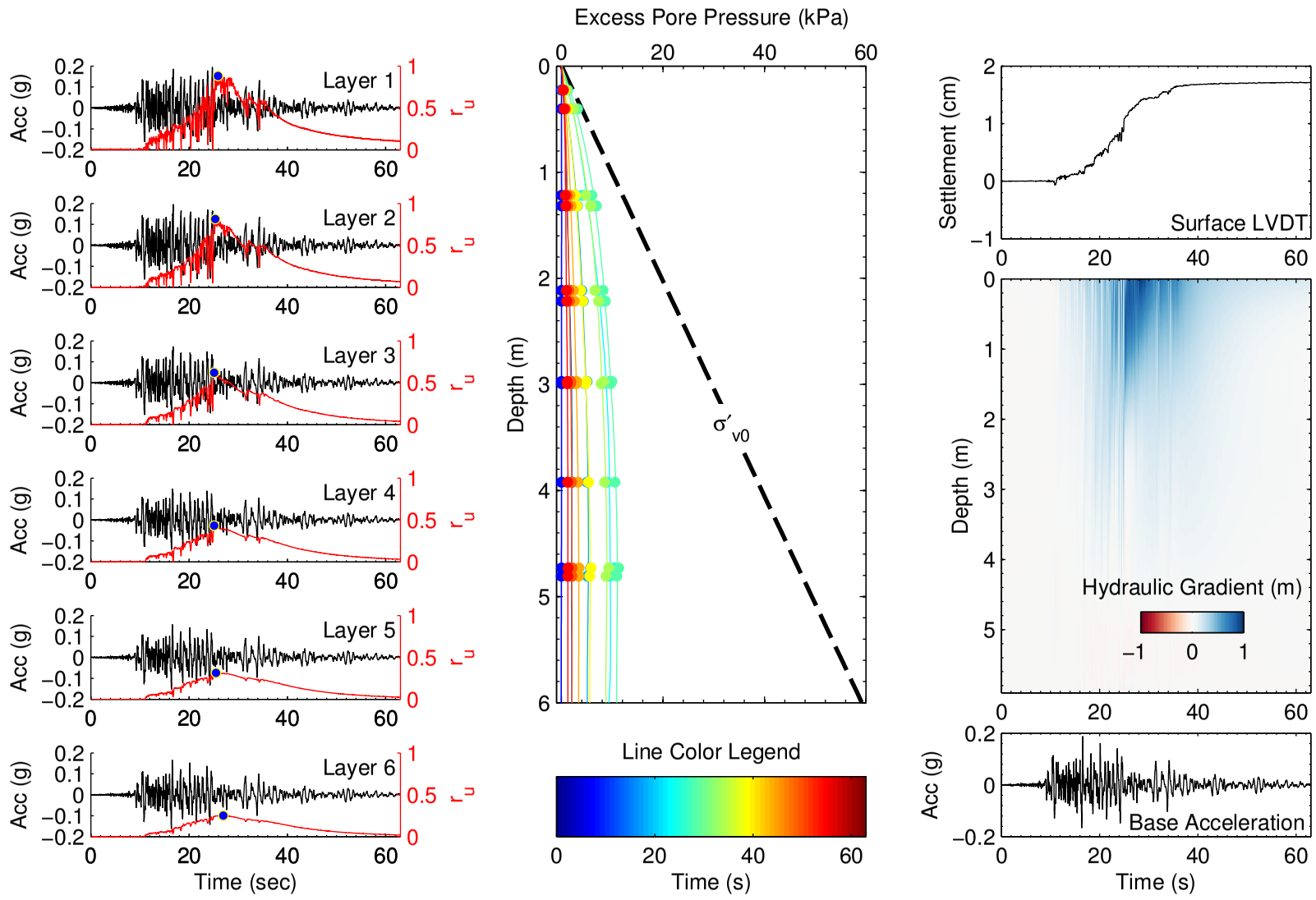
40% D_r Experiment 3 Test 20 – Data Summary Plot



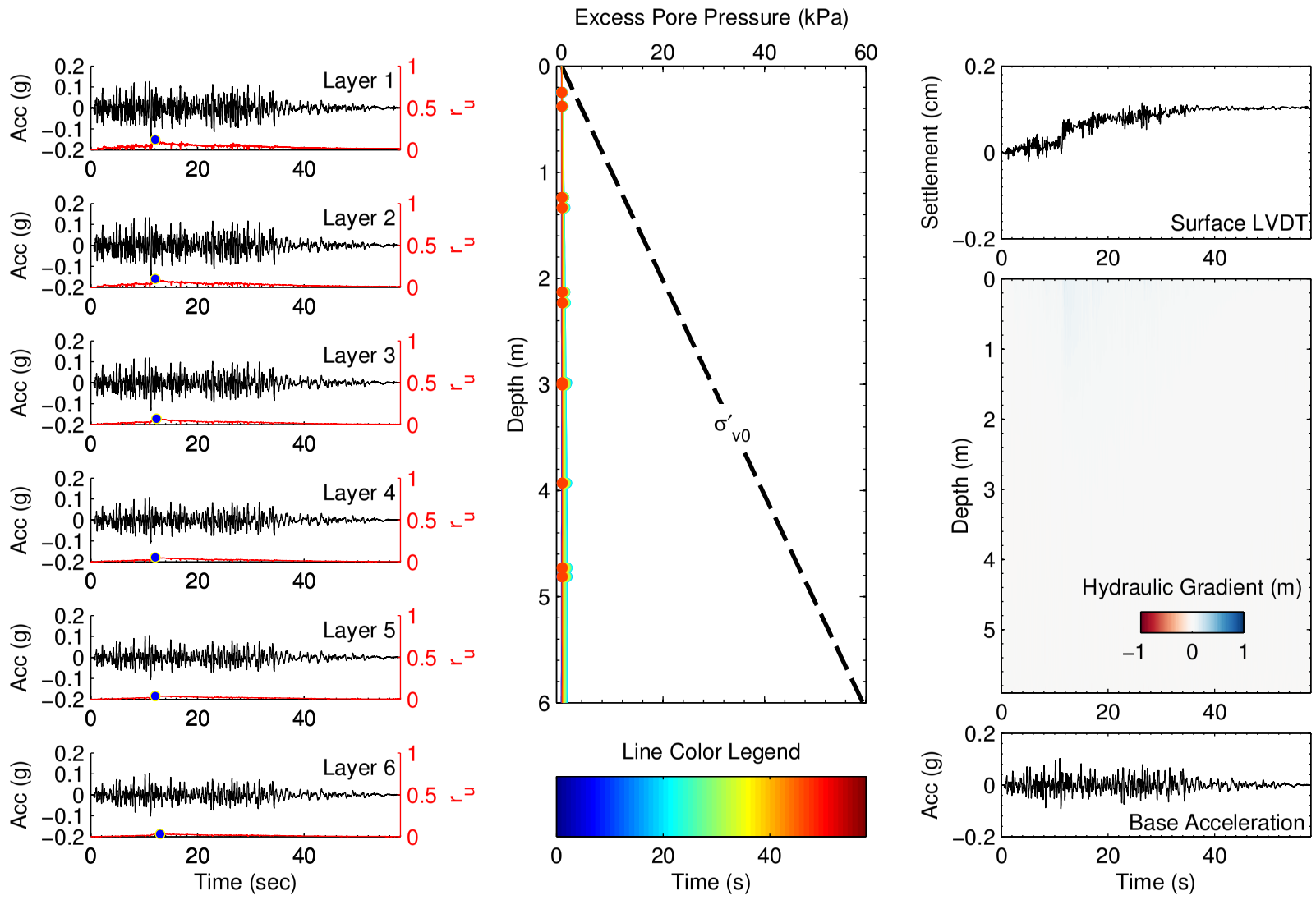
40% D_r Experiment 3 Test 21 – Data Summary Plot



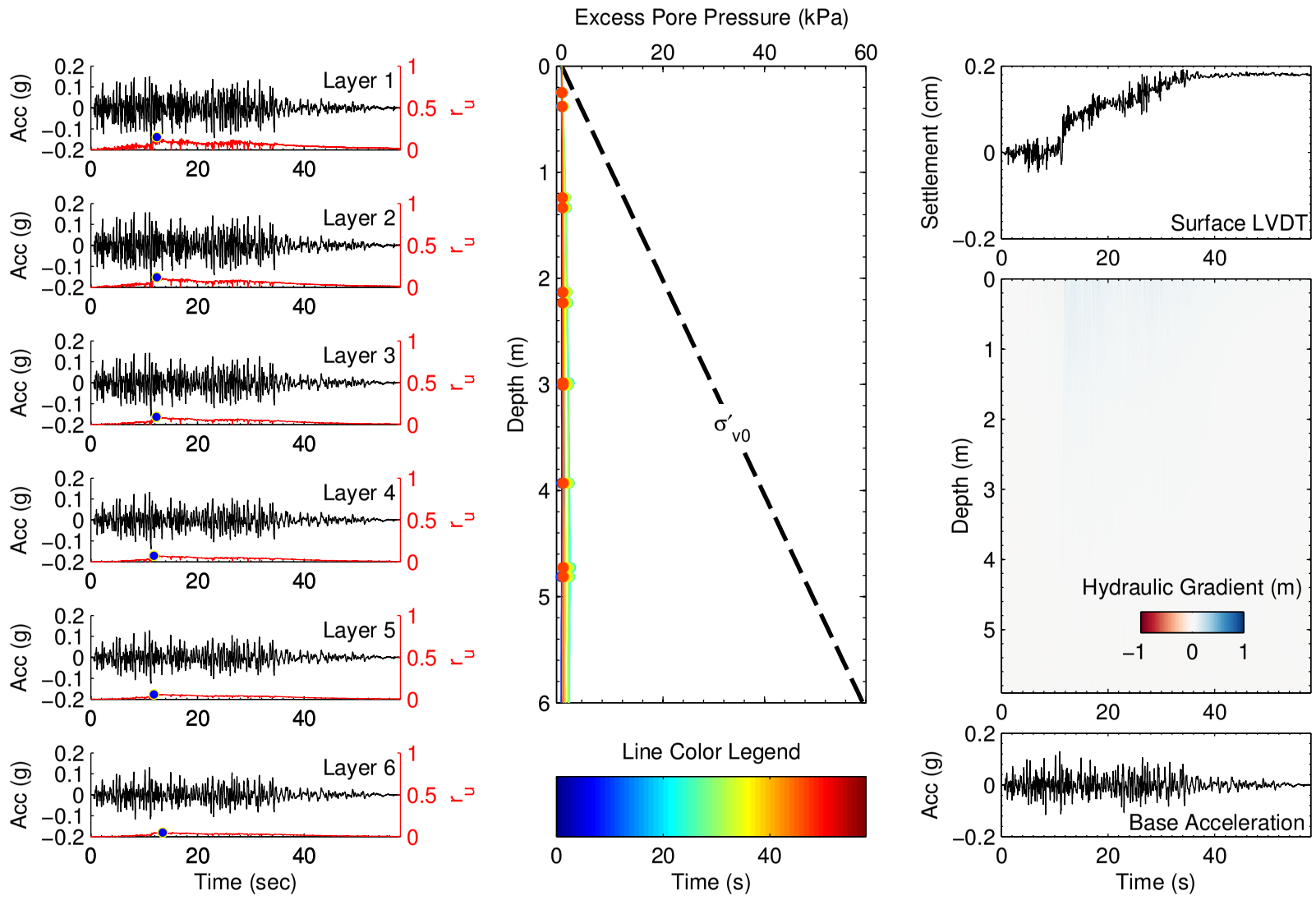
40% D_r Experiment 3 Test 22 – Data Summary Plot



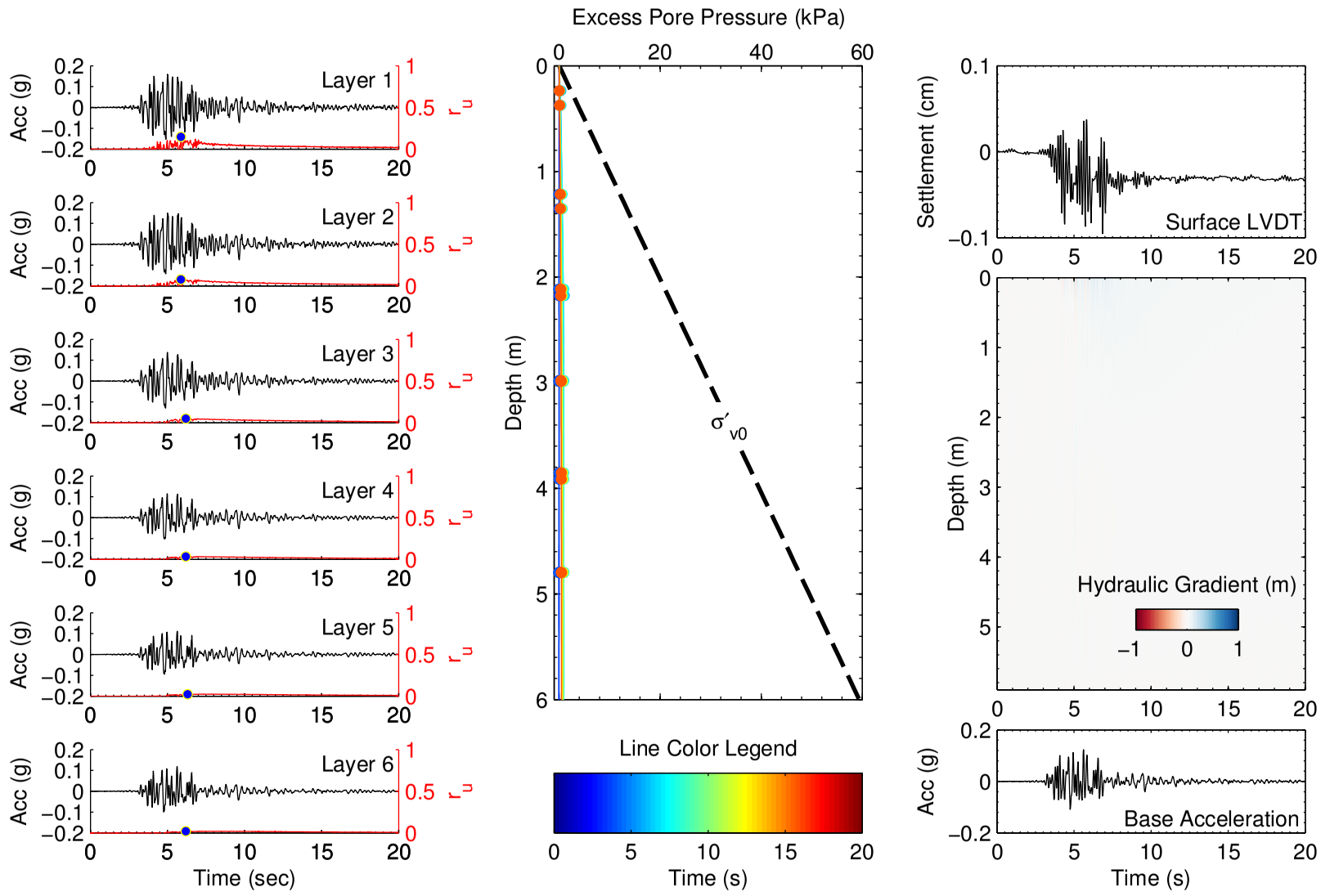
40% D_r Experiment 3 Test 23 – Data Summary Plot



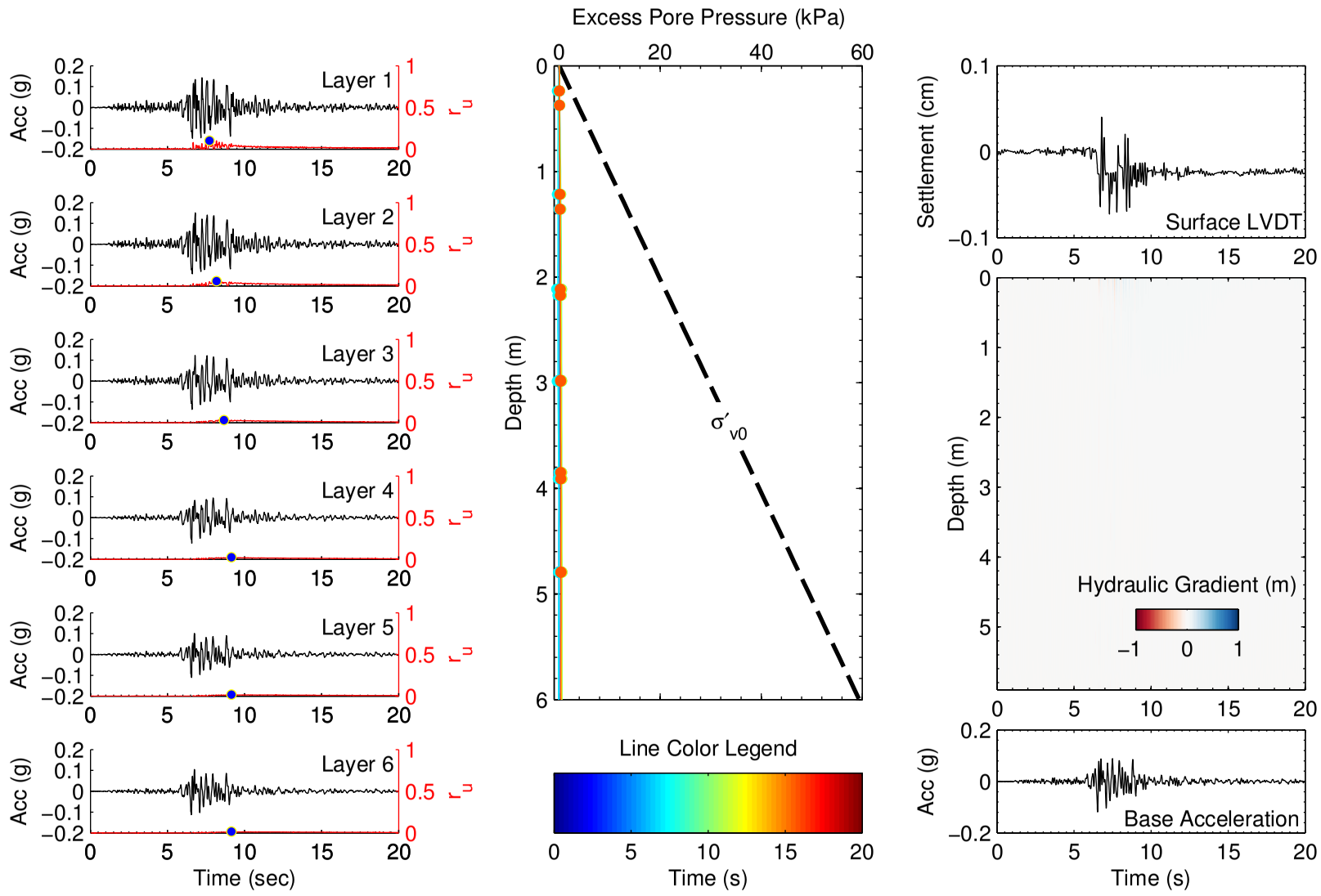
40% D_r Experiment 3 Test 24 – Data Summary Plot



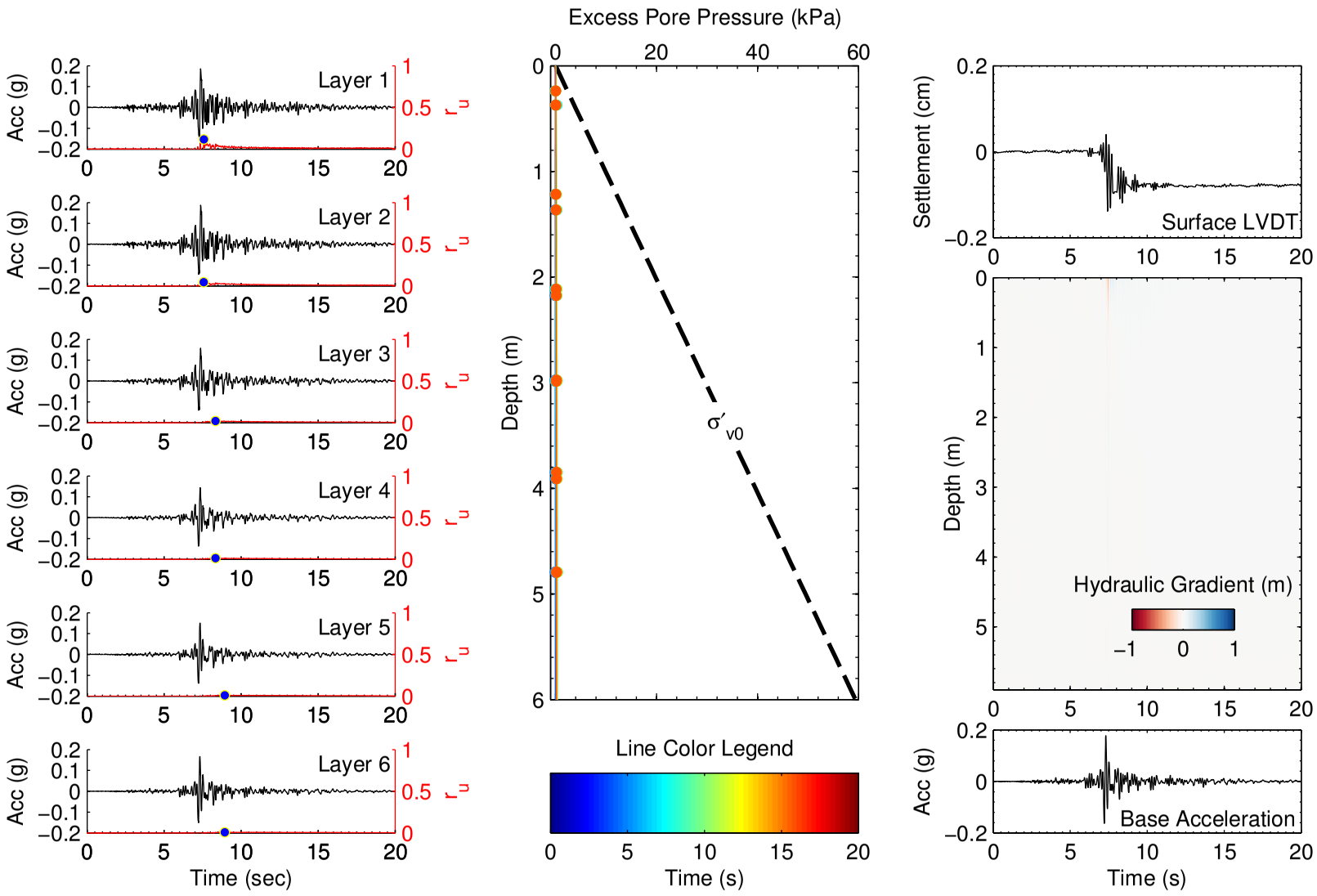
40% D_r Experiment 3 Test 25 – Data Summary Plot



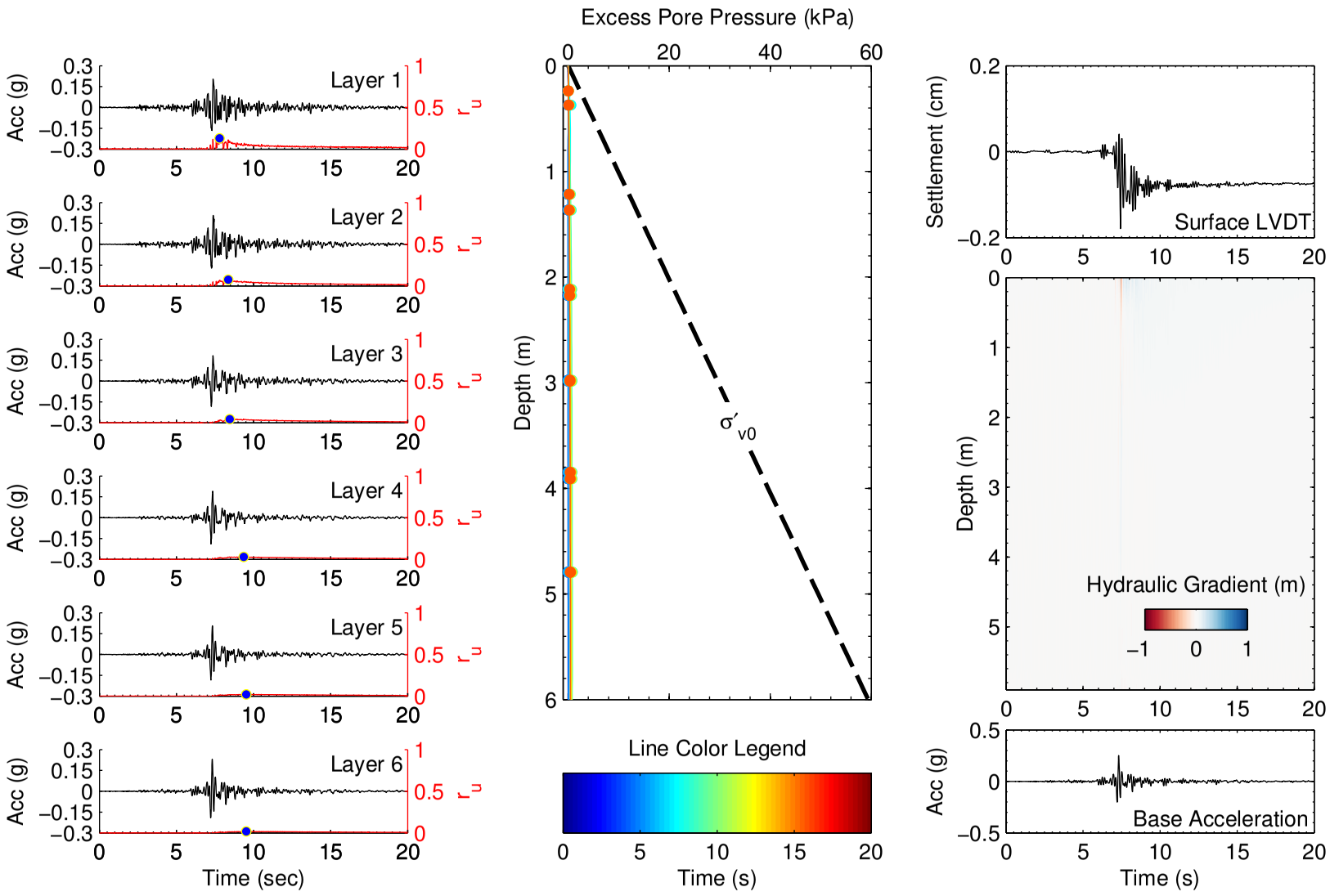
40% D_r Experiment 3 Test 26 – Data Summary Plot



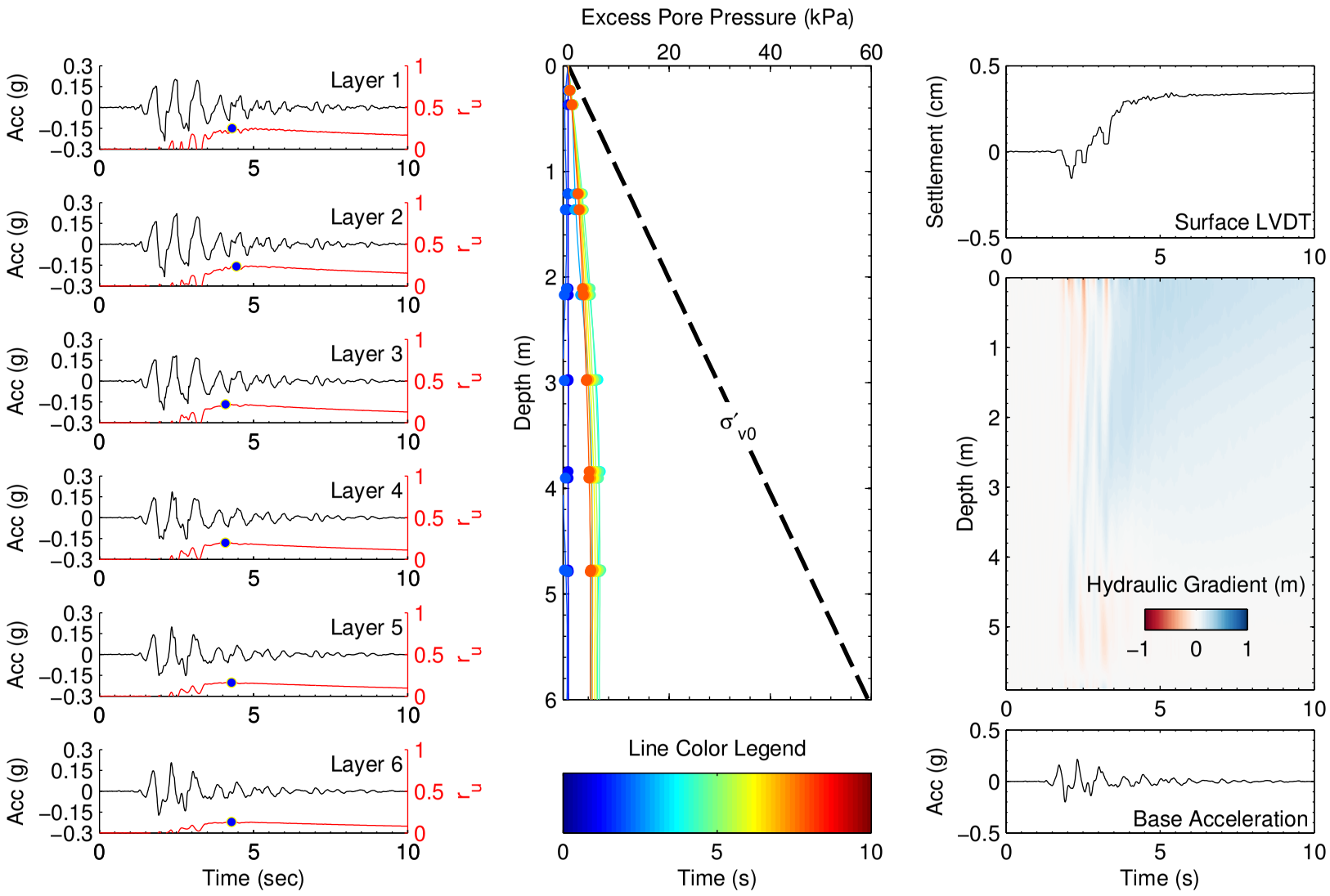
40% D_r Experiment 3 Test 27 – Data Summary Plot



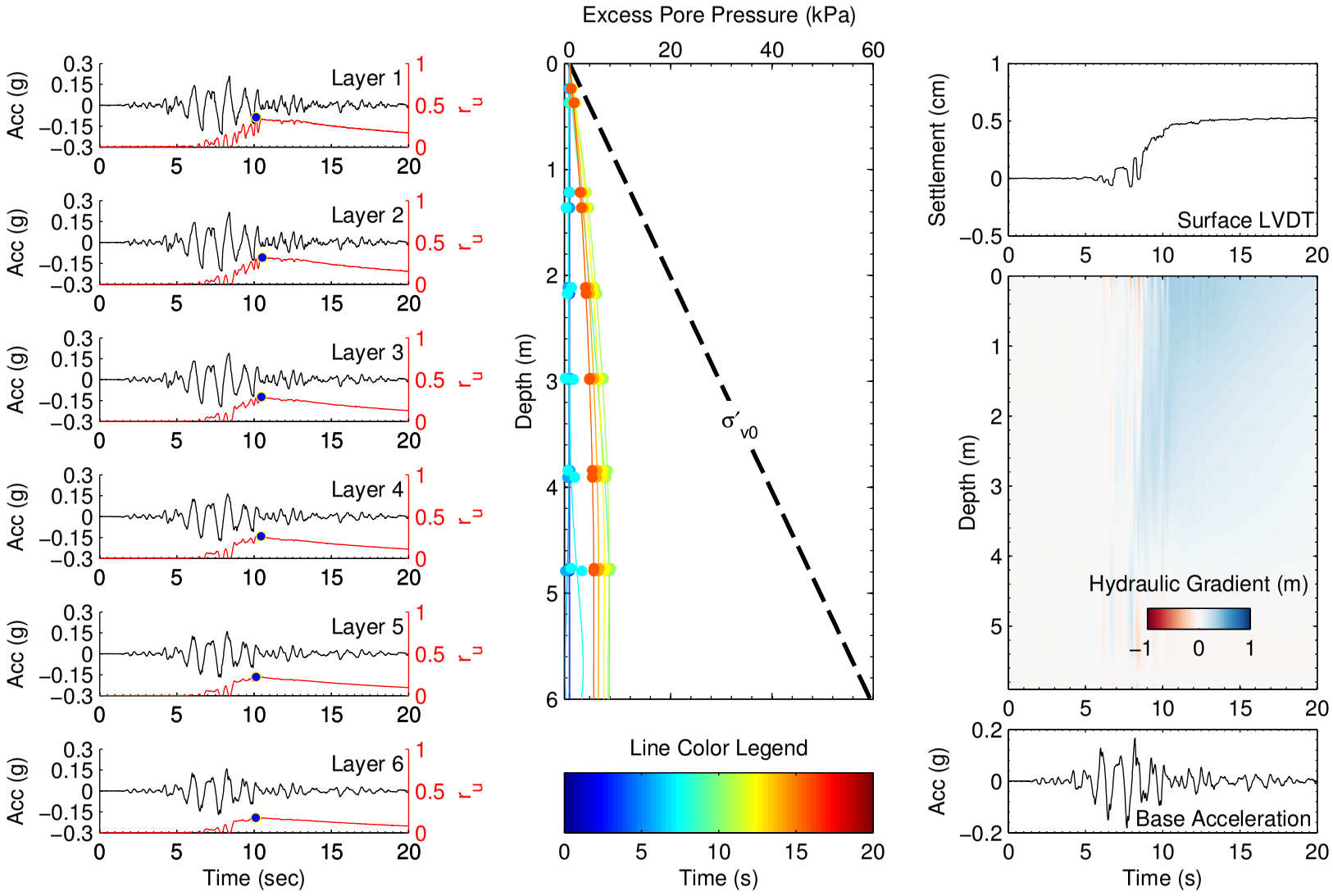
40% D_r Experiment 3 Test 28 – Data Summary Plot



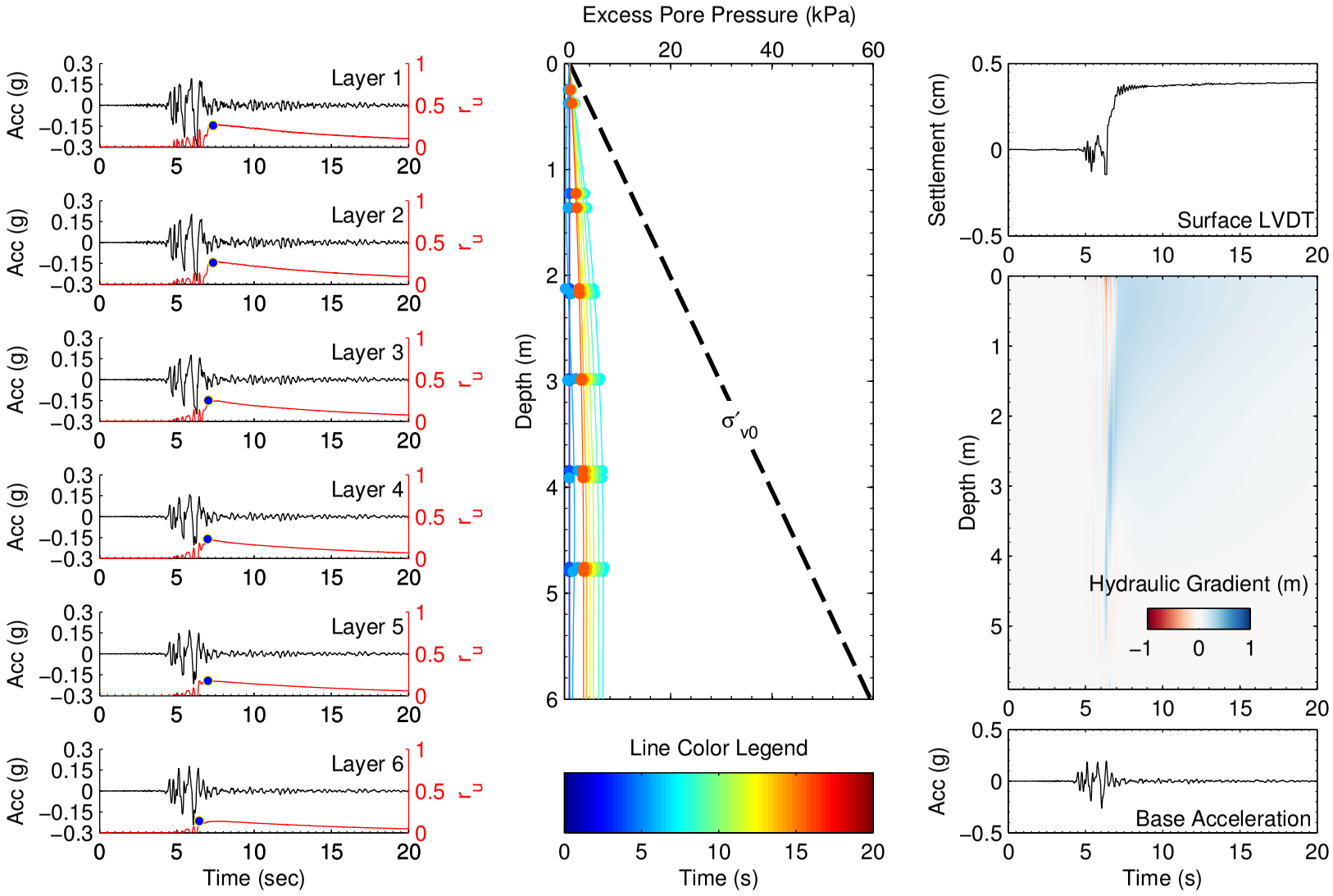
40% D_r Experiment 3 Test 29 – Data Summary Plot



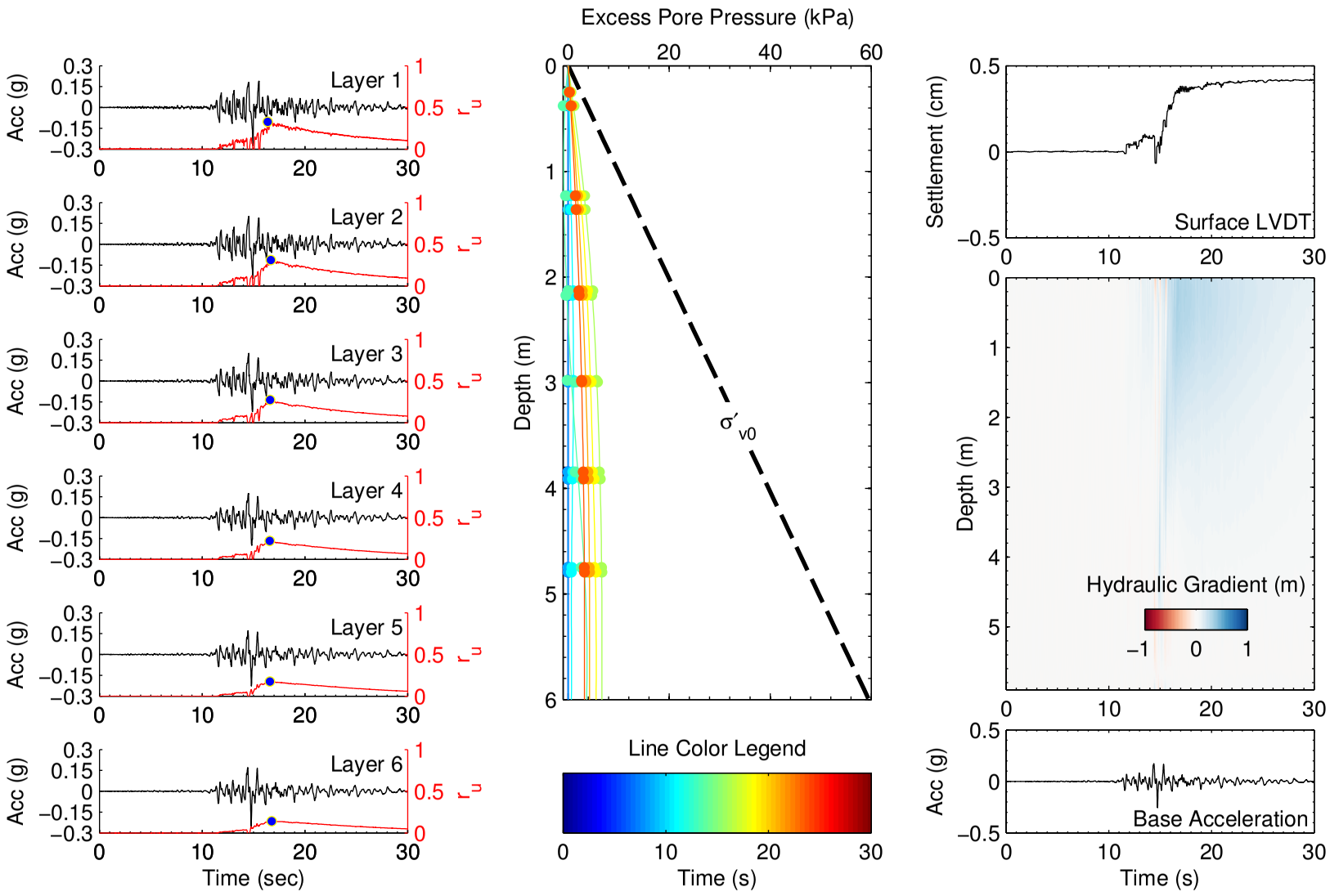
40% D_r Experiment 3 Test 30 – Data Summary Plot



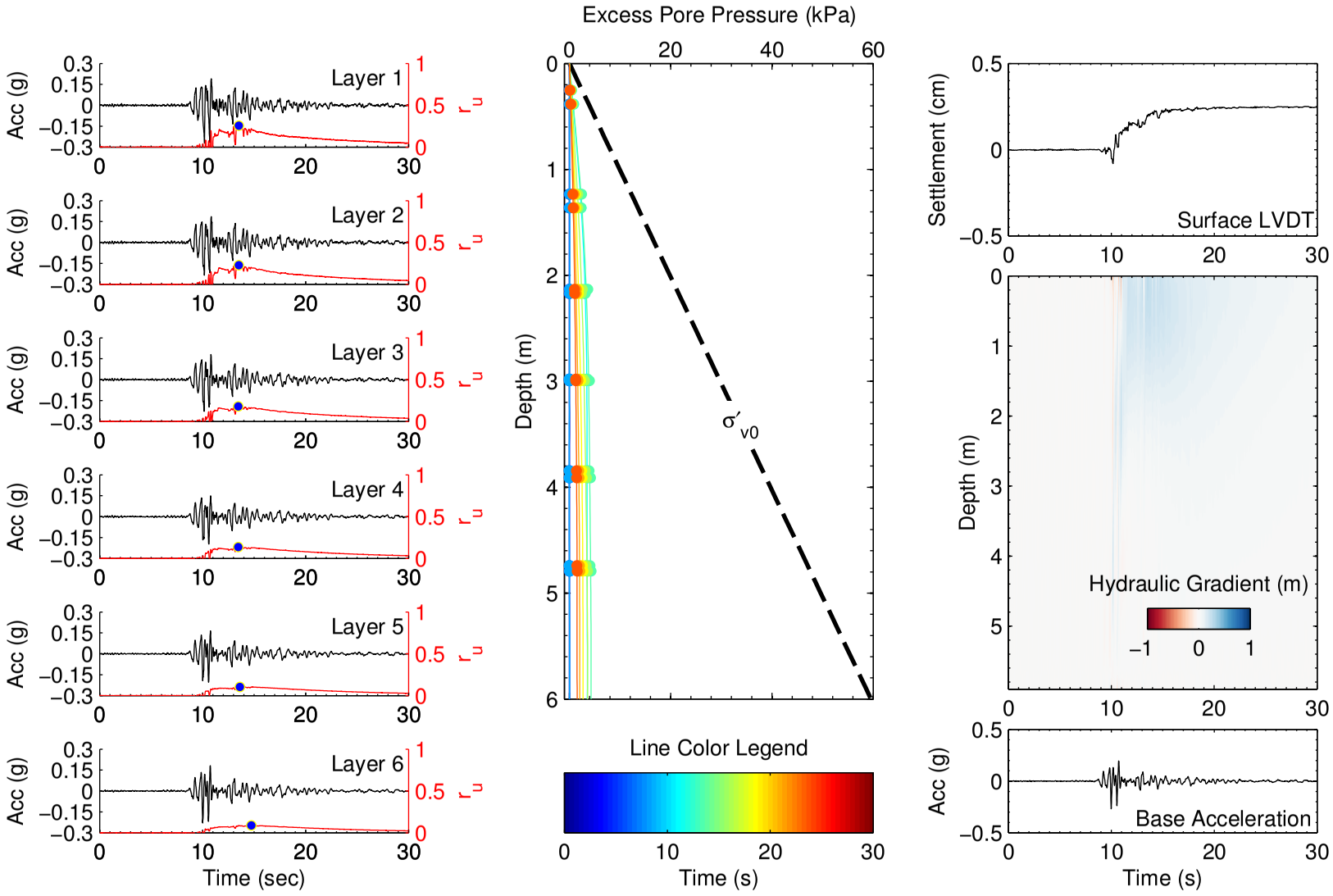
40% D_r Experiment 3 Test 31 – Data Summary Plot



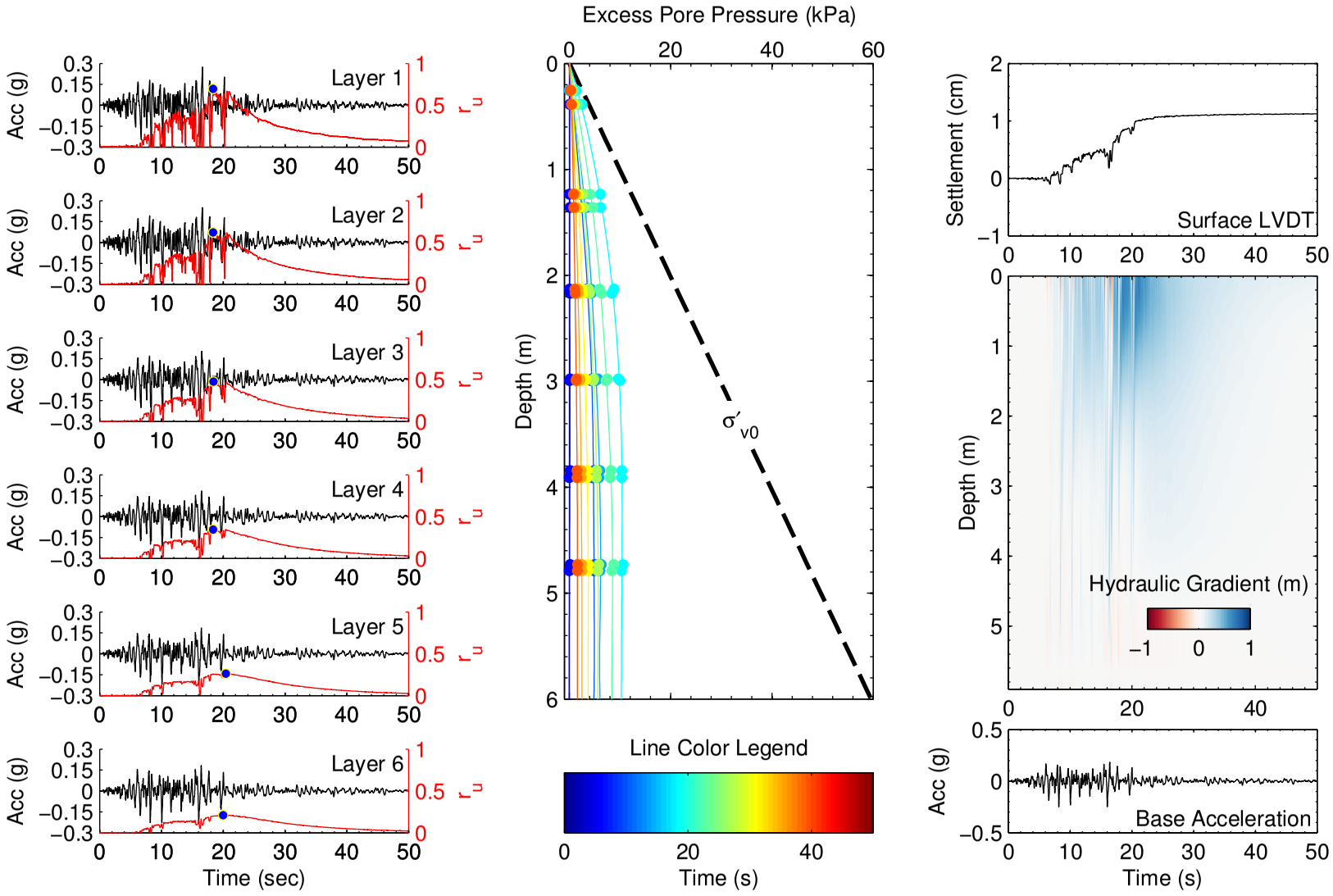
40% D_r Experiment 3 Test 32 – Data Summary Plot



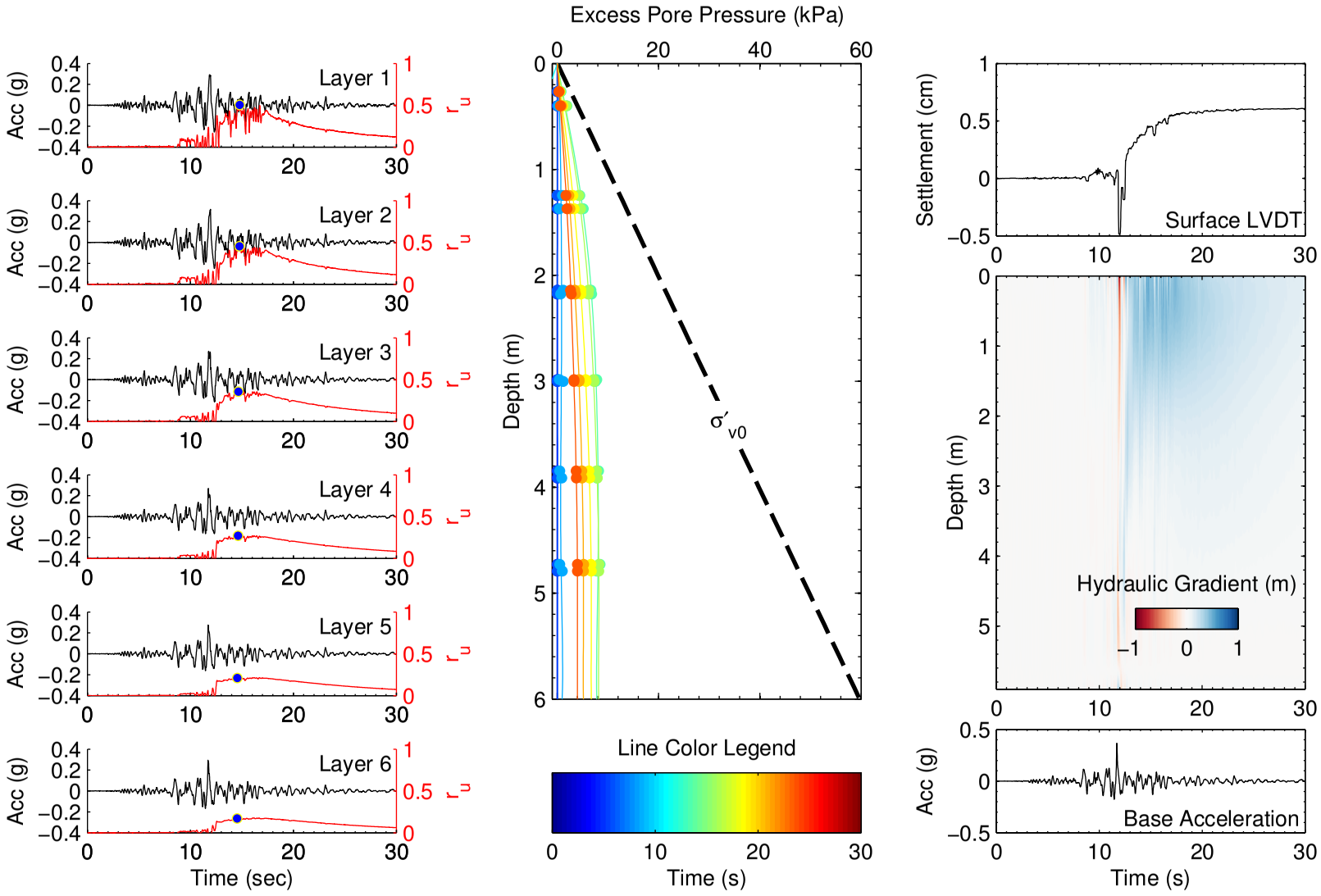
40% D_r Experiment 3 Test 33 – Data Summary Plot



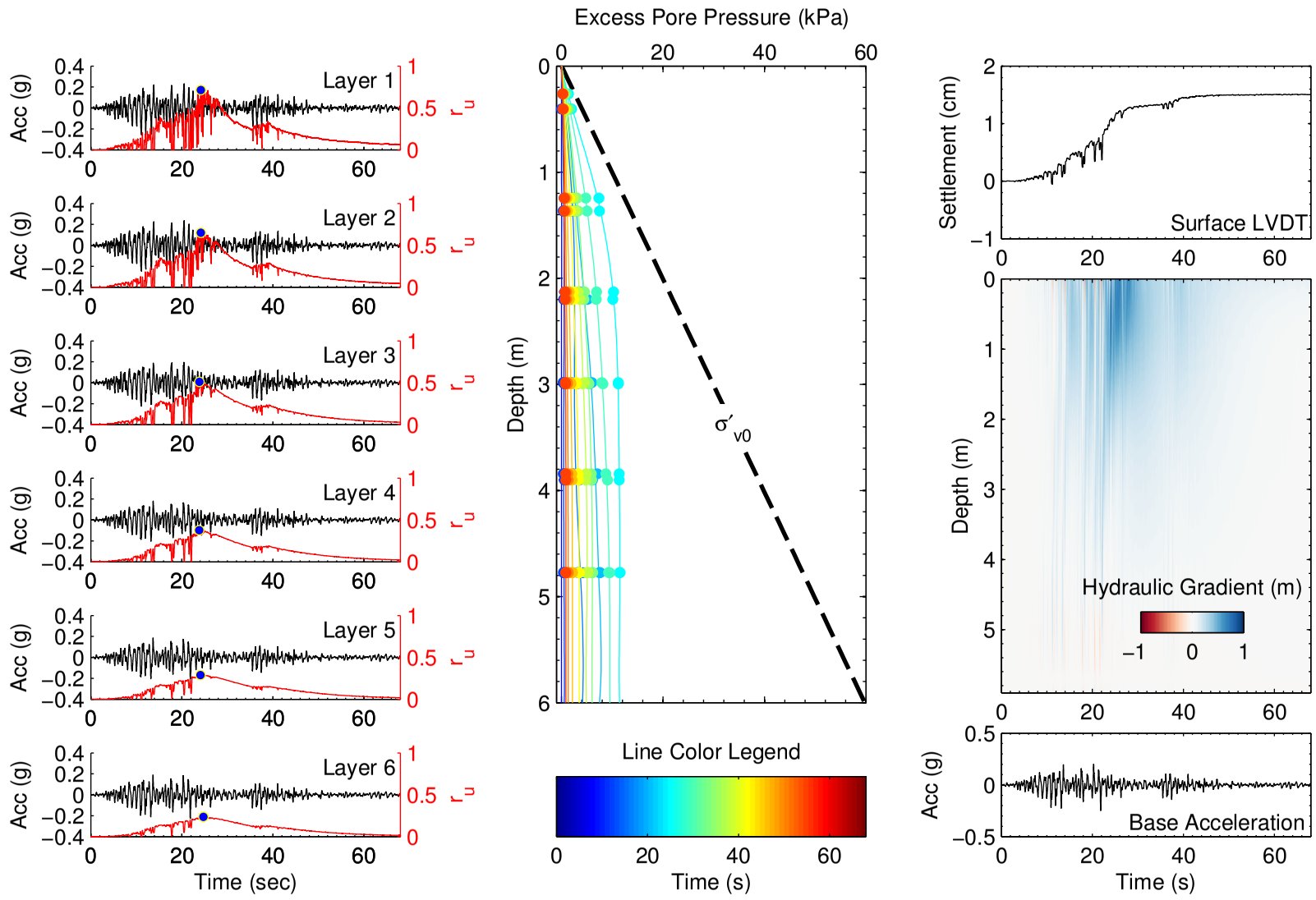
40% D_r Experiment 3 Test 34 – Data Summary Plot



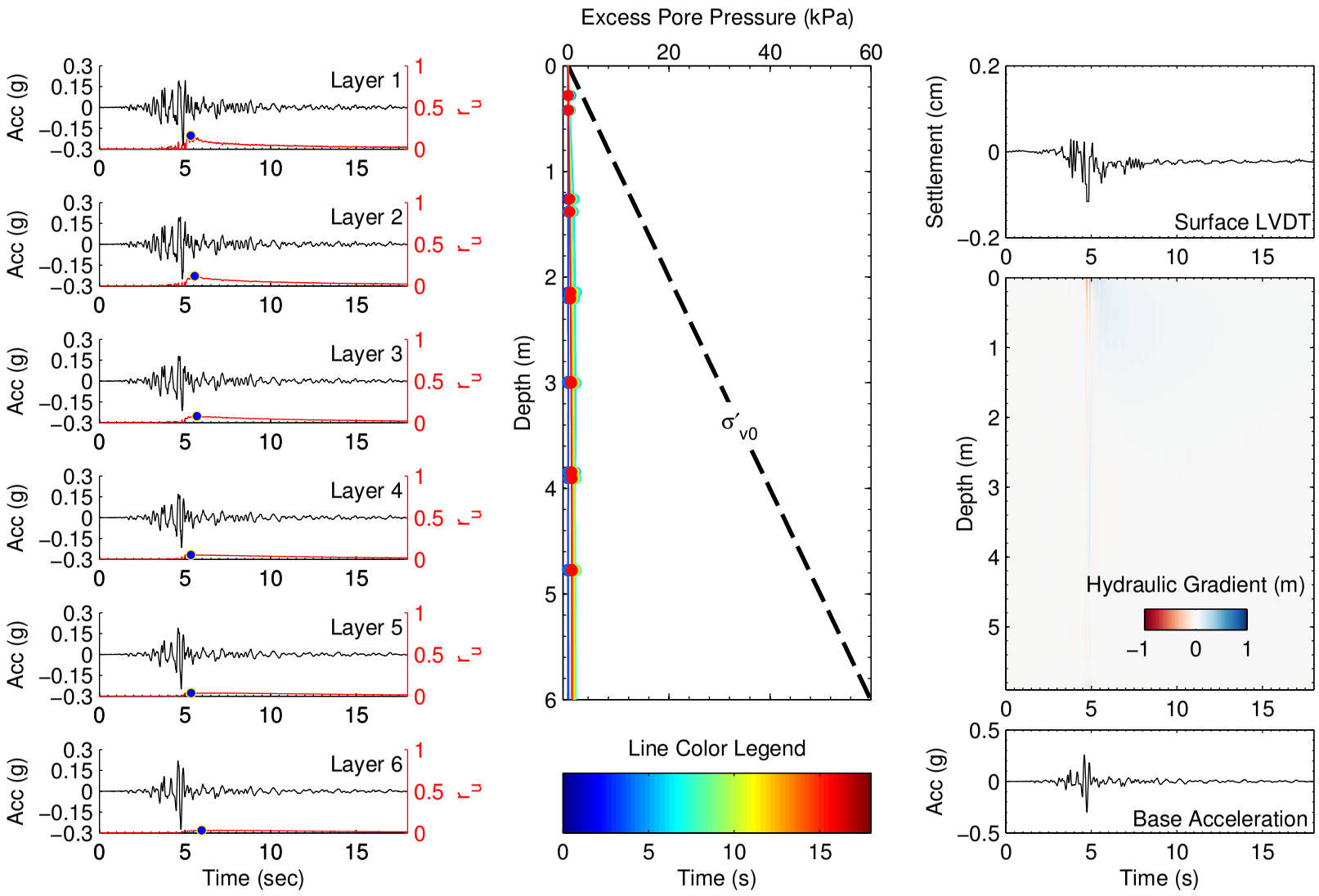
40% D_r Experiment 3 Test 35 – Data Summary Plot



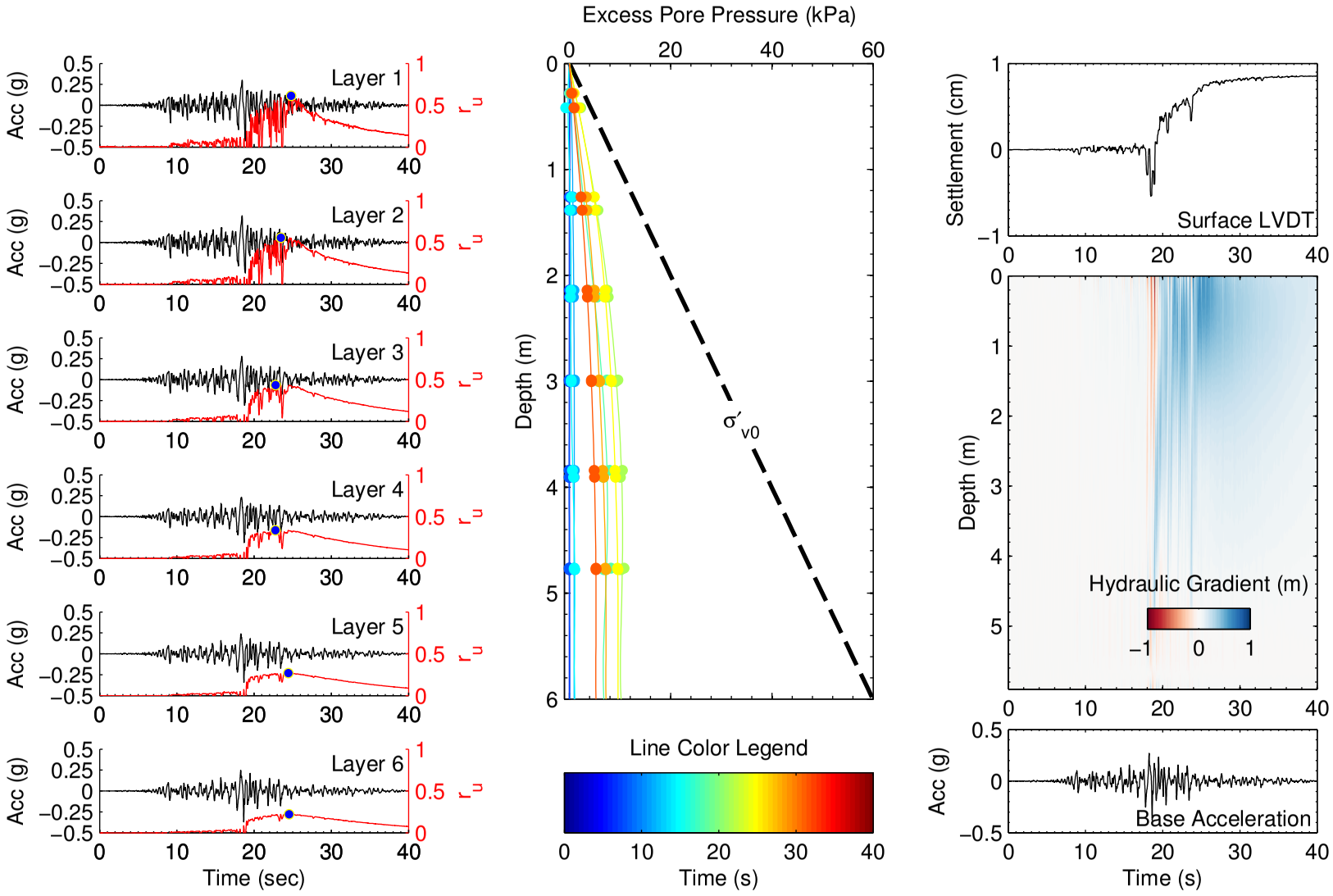
40% D_r Experiment 3 Test 36 – Data Summary Plot



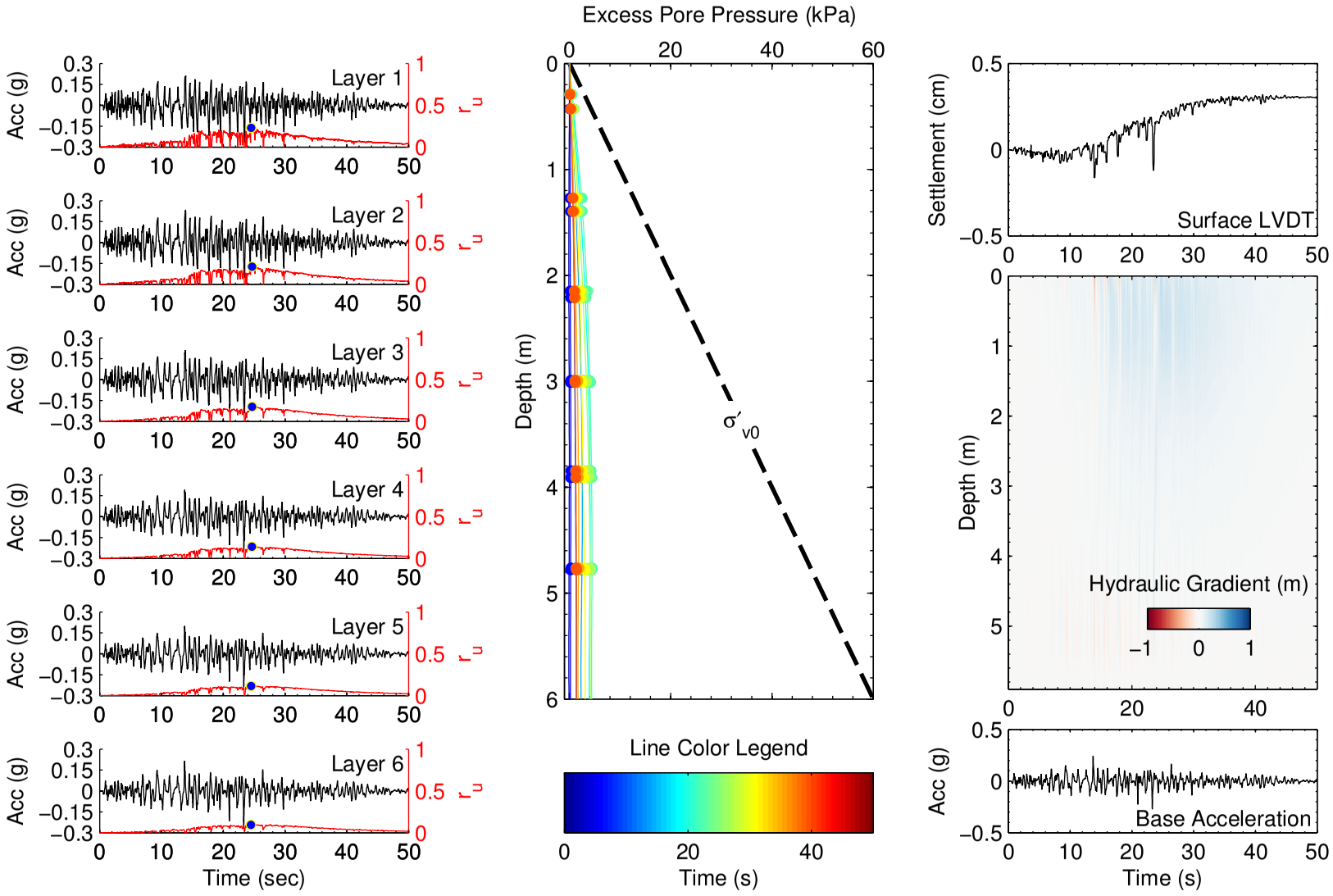
40% D_r Experiment 3 Test 37 – Data Summary Plot



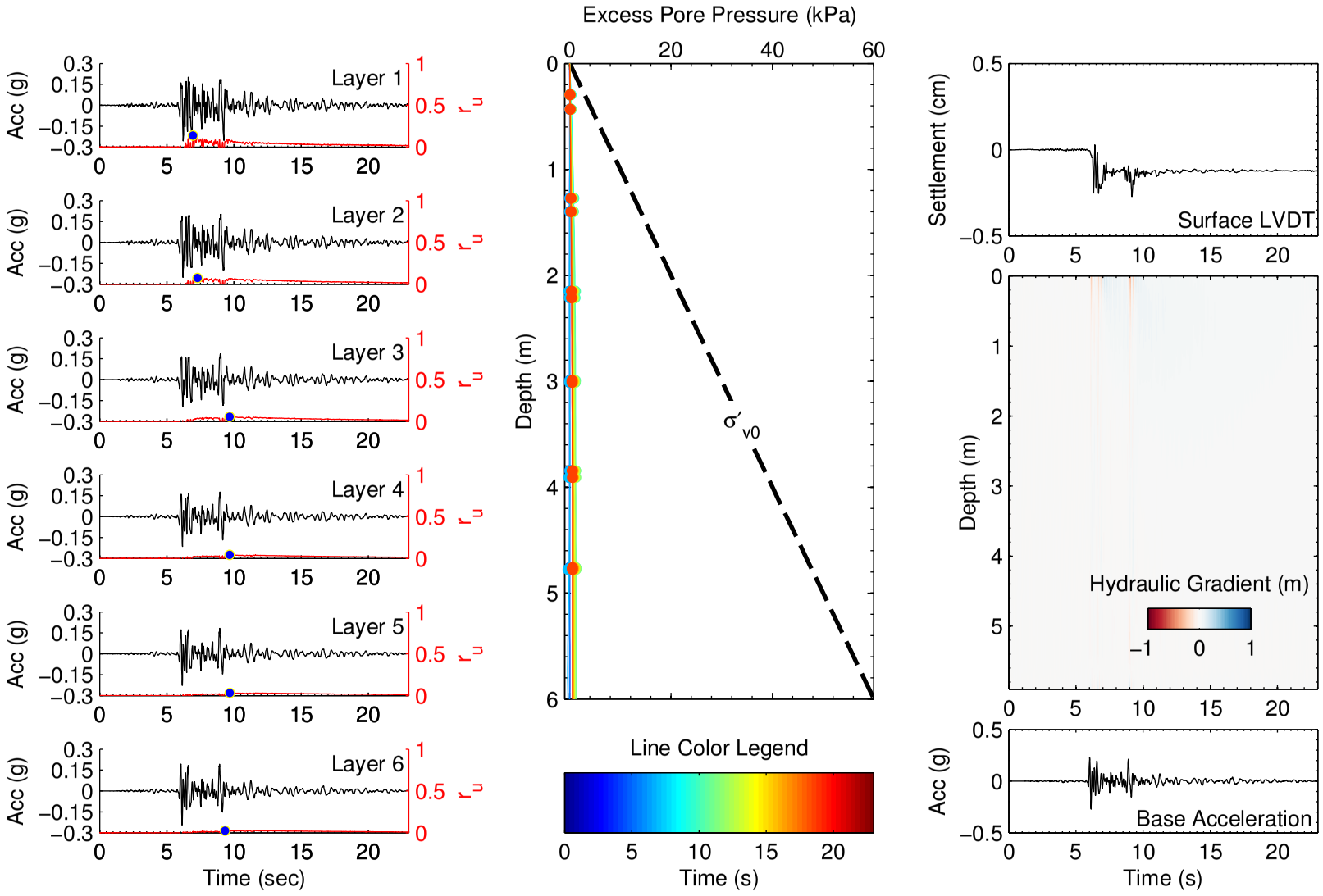
40% D_r Experiment 3 Test 38 – Data Summary Plot



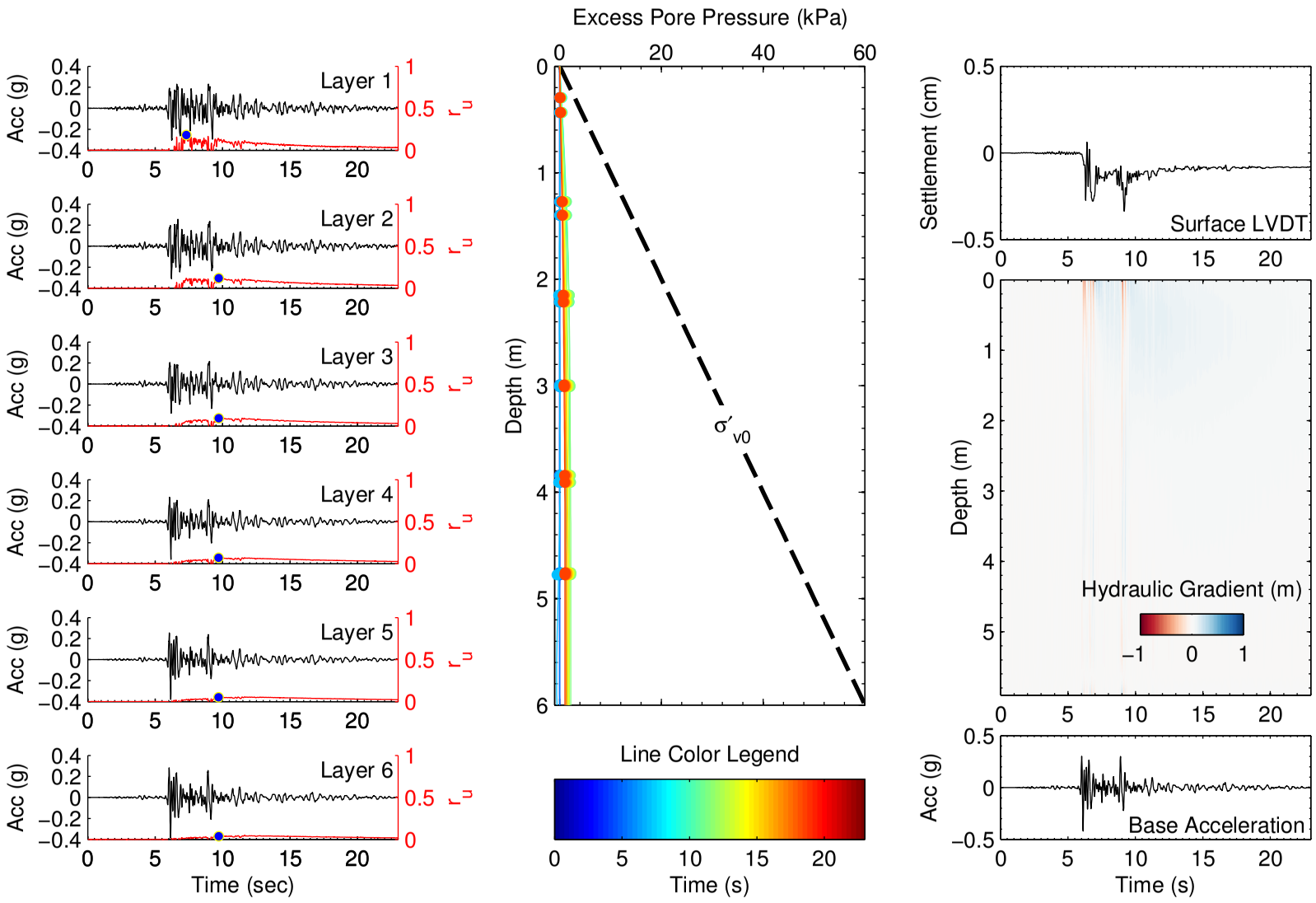
40% D_r Experiment 3 Test 39 – Data Summary Plot



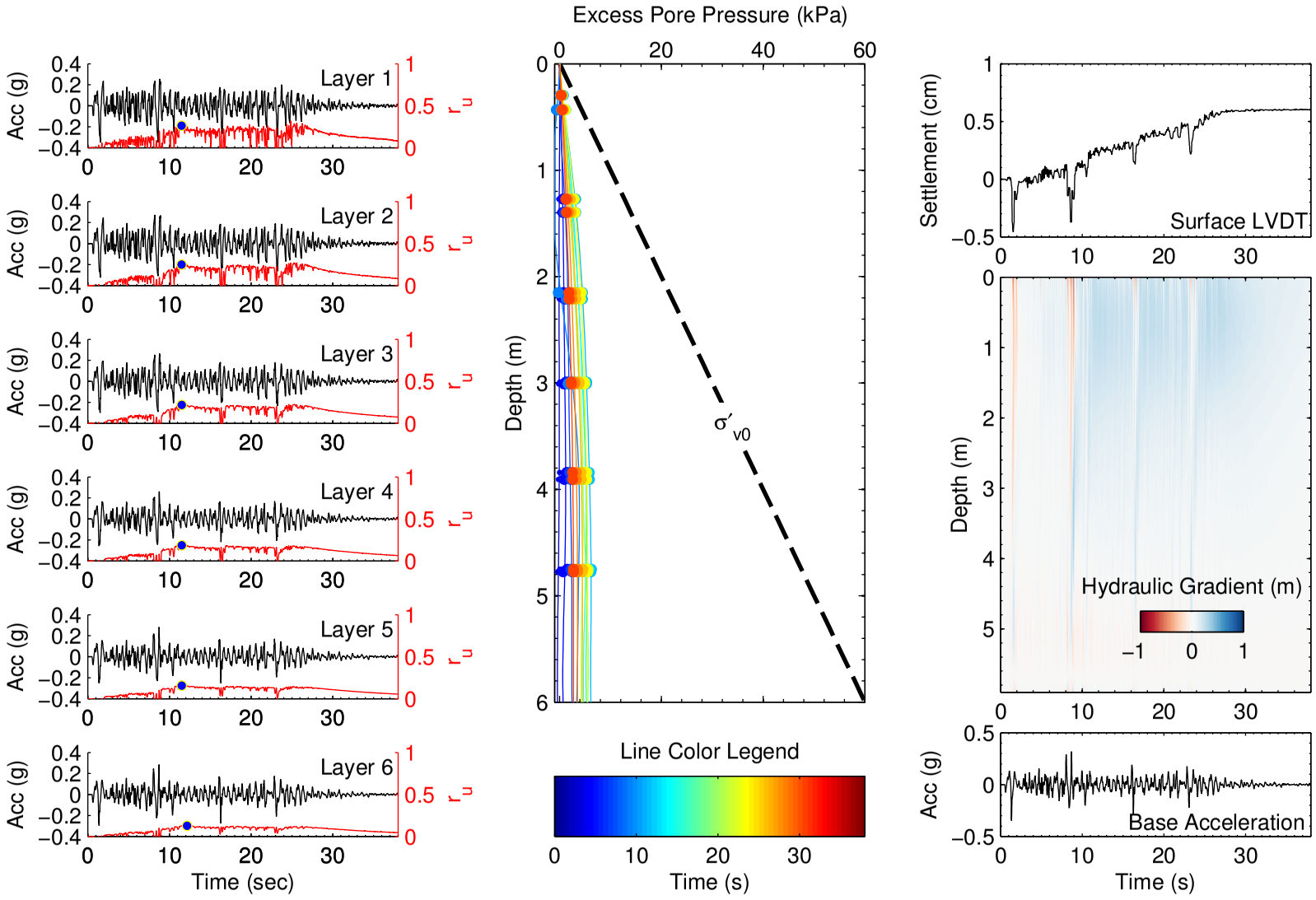
40% D_r Experiment 3 Test 40 – Data Summary Plot



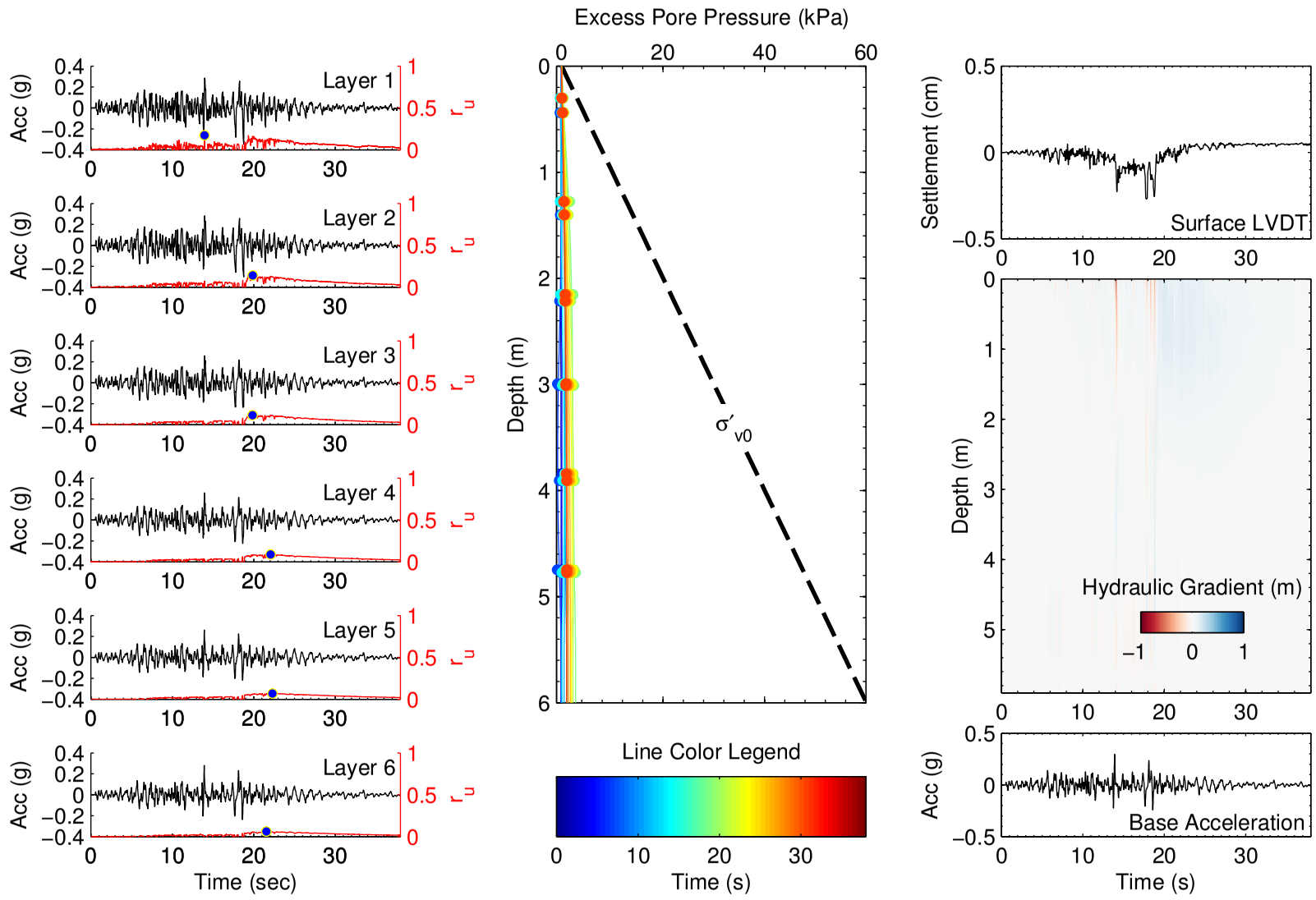
40% D_r Experiment 3 Test 41 – Data Summary Plot



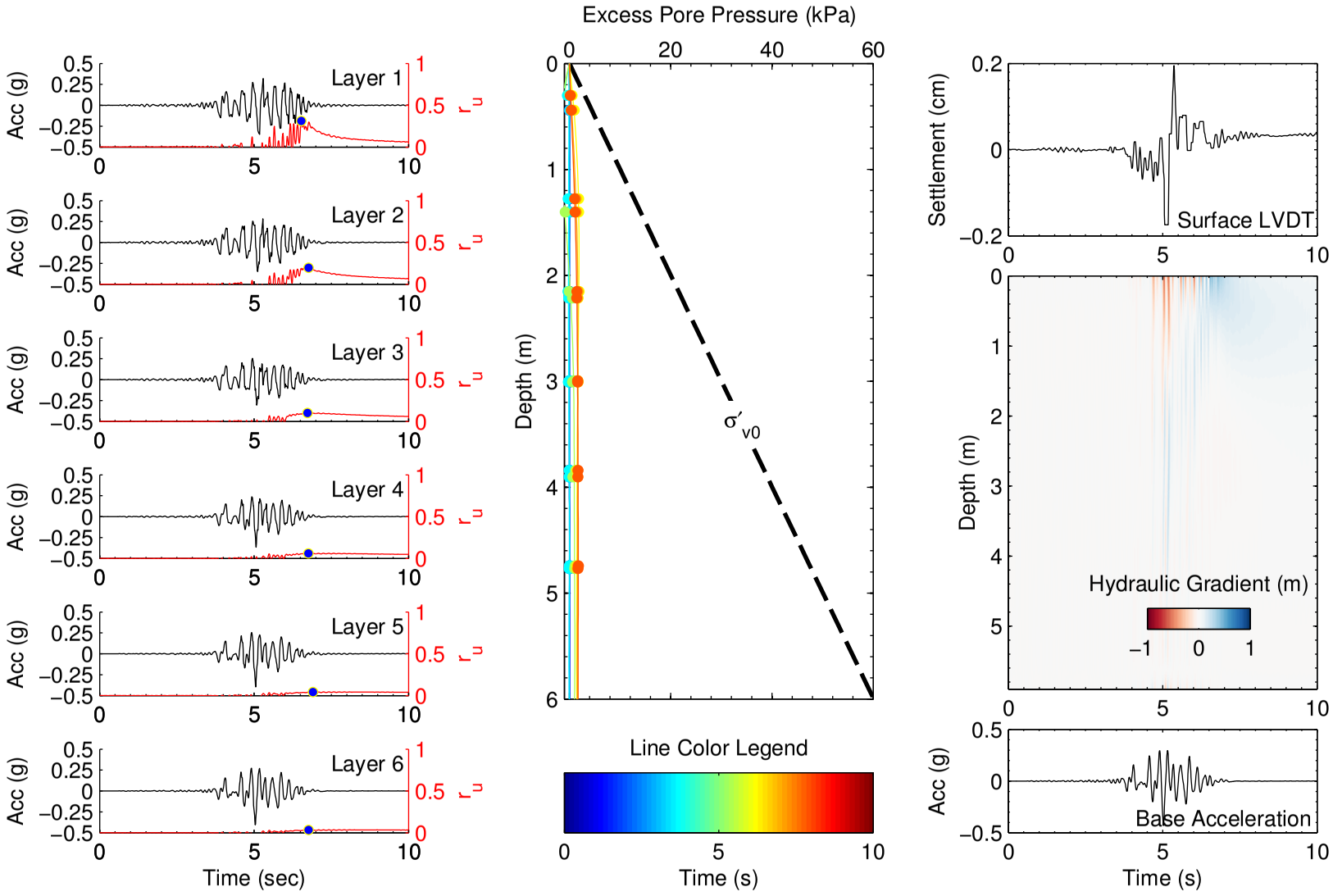
40% D_r Experiment 3 Test 42 – Data Summary Plot



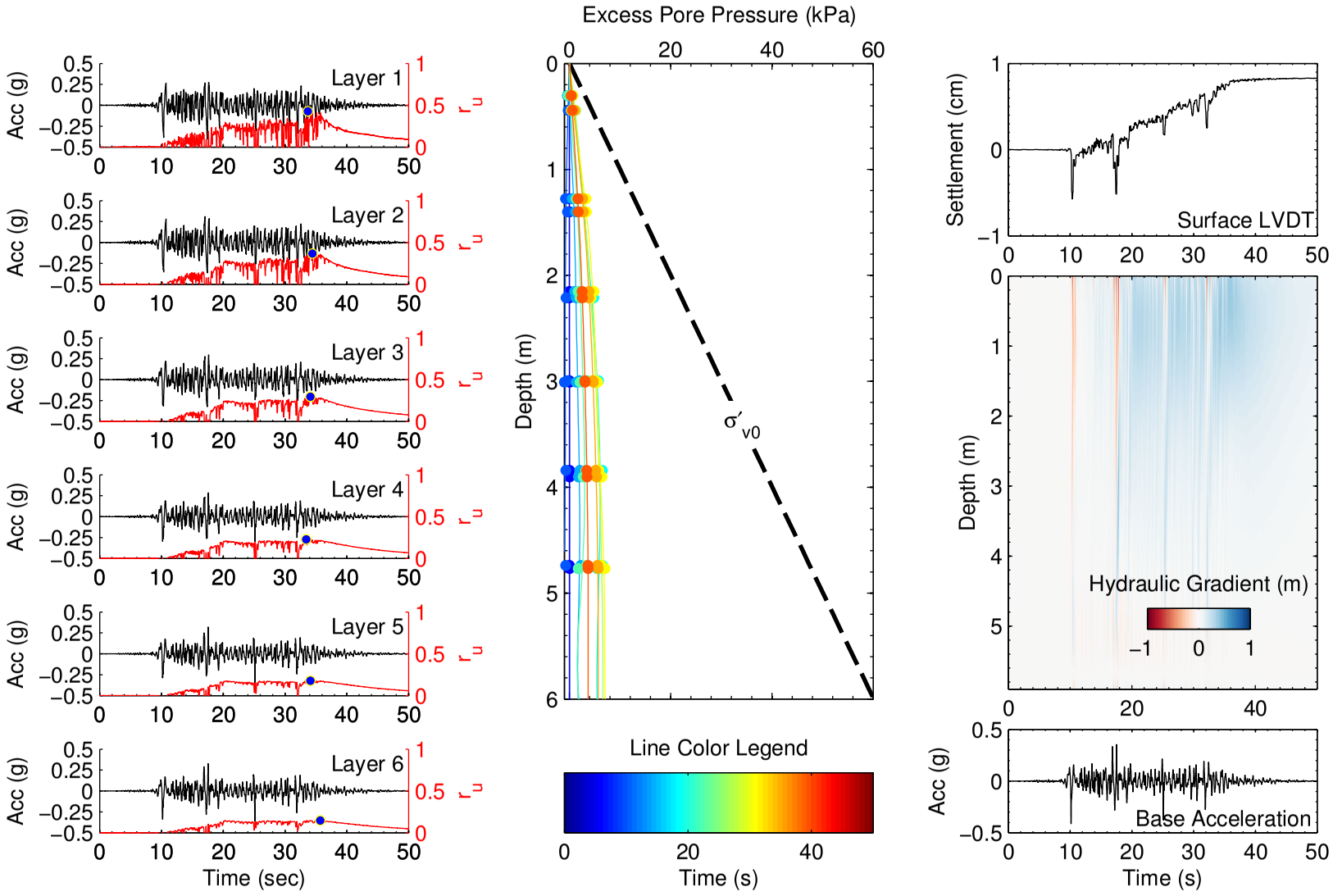
40% D_r Experiment 3 Test 43 – Data Summary Plot



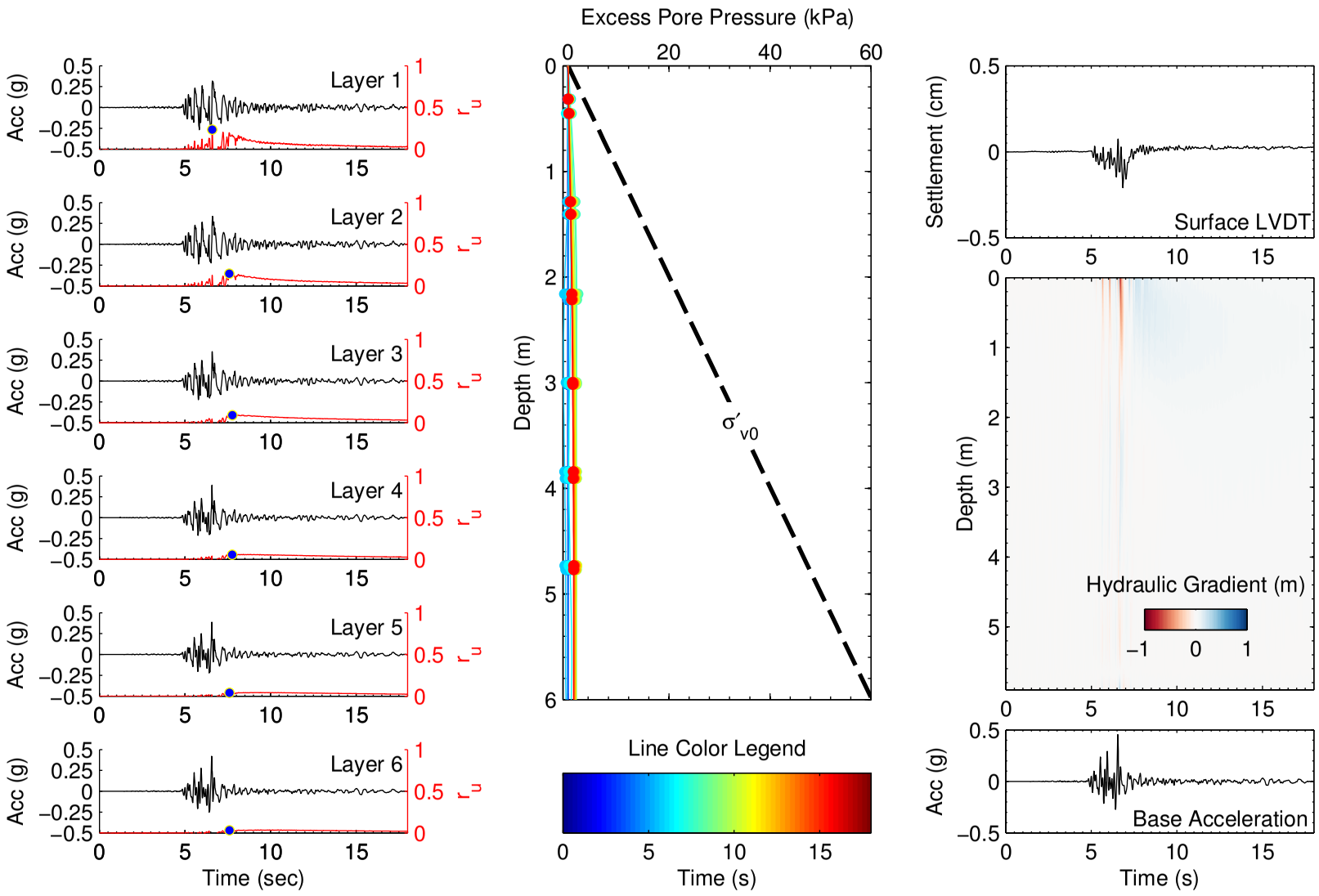
40% D_r Experiment 3 Test 44 – Data Summary Plot



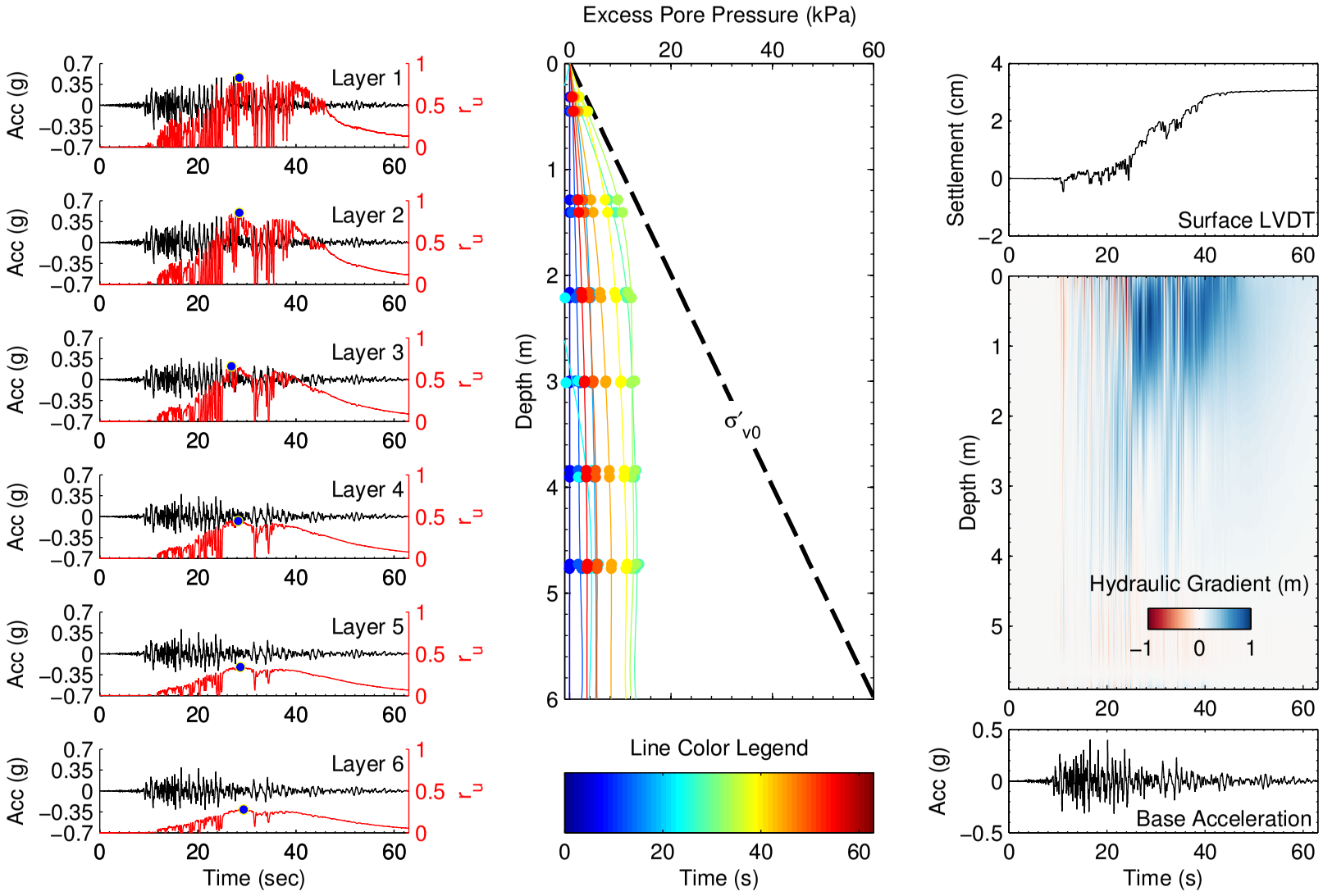
40% D_r Experiment 3 Test 45 – Data Summary Plot



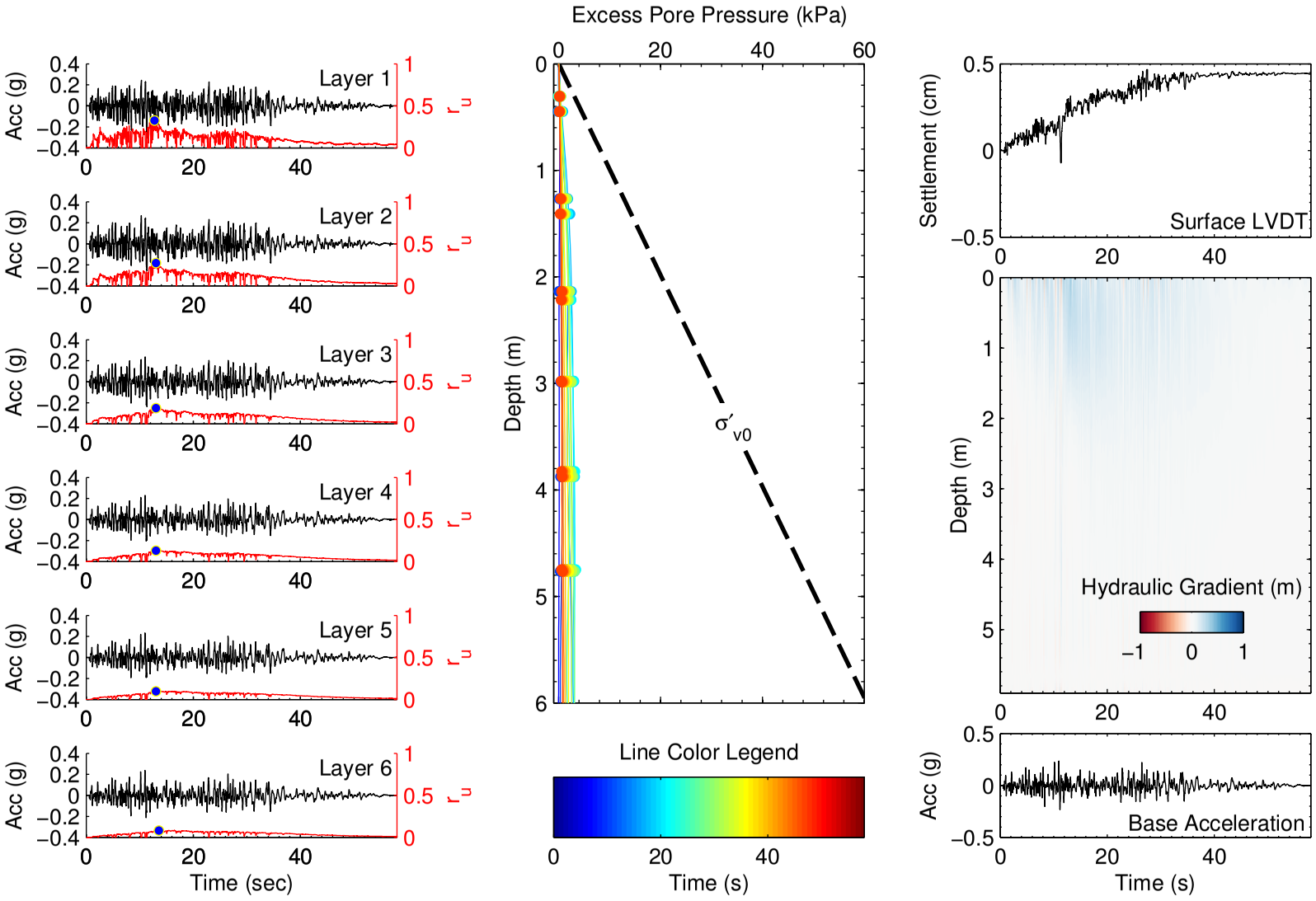
40% D_r Experiment 3 Test 46 – Data Summary Plot



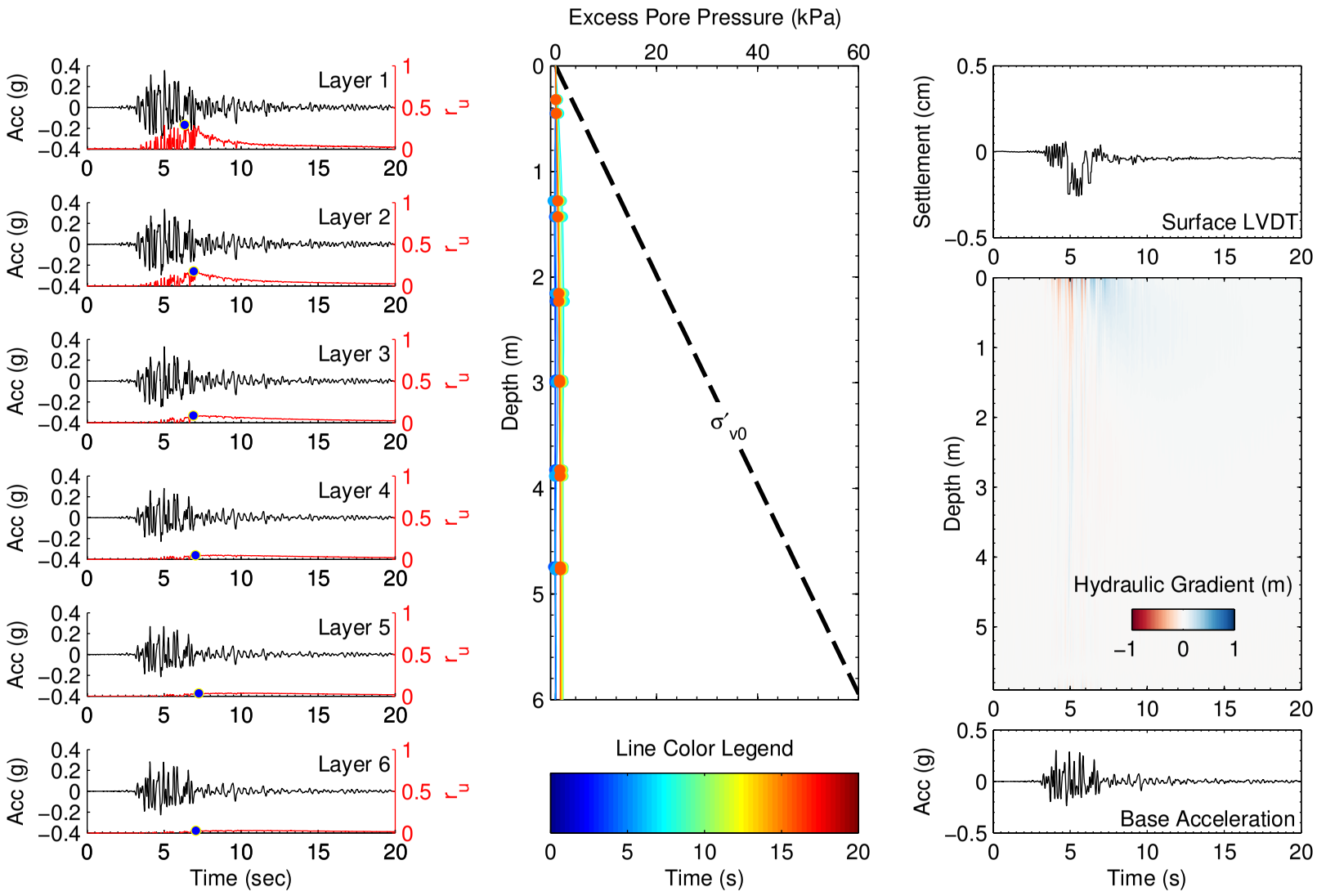
40% D_r Experiment 3 Test 47 – Data Summary Plot



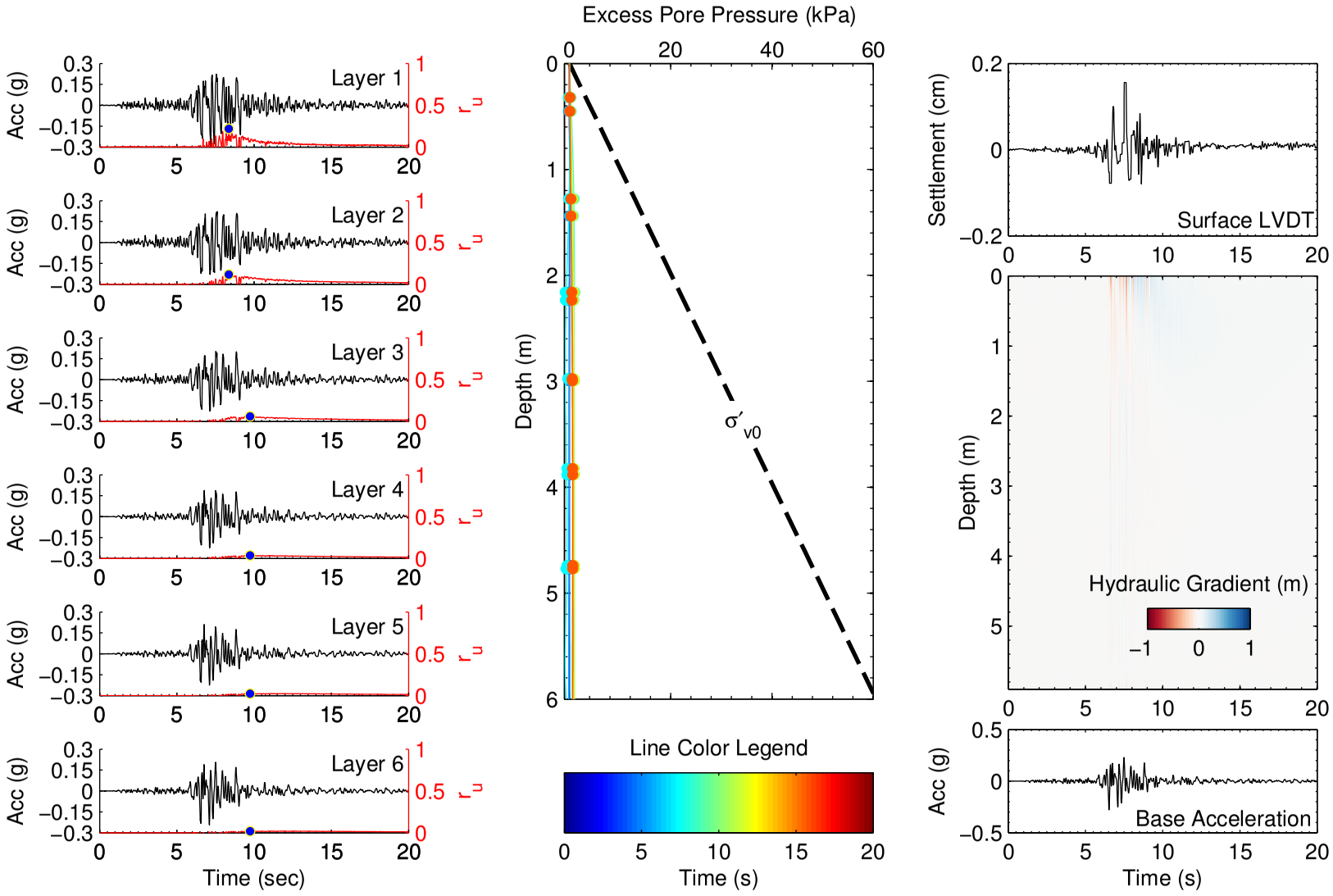
40% D_r Experiment 3 Test 48 – Data Summary Plot



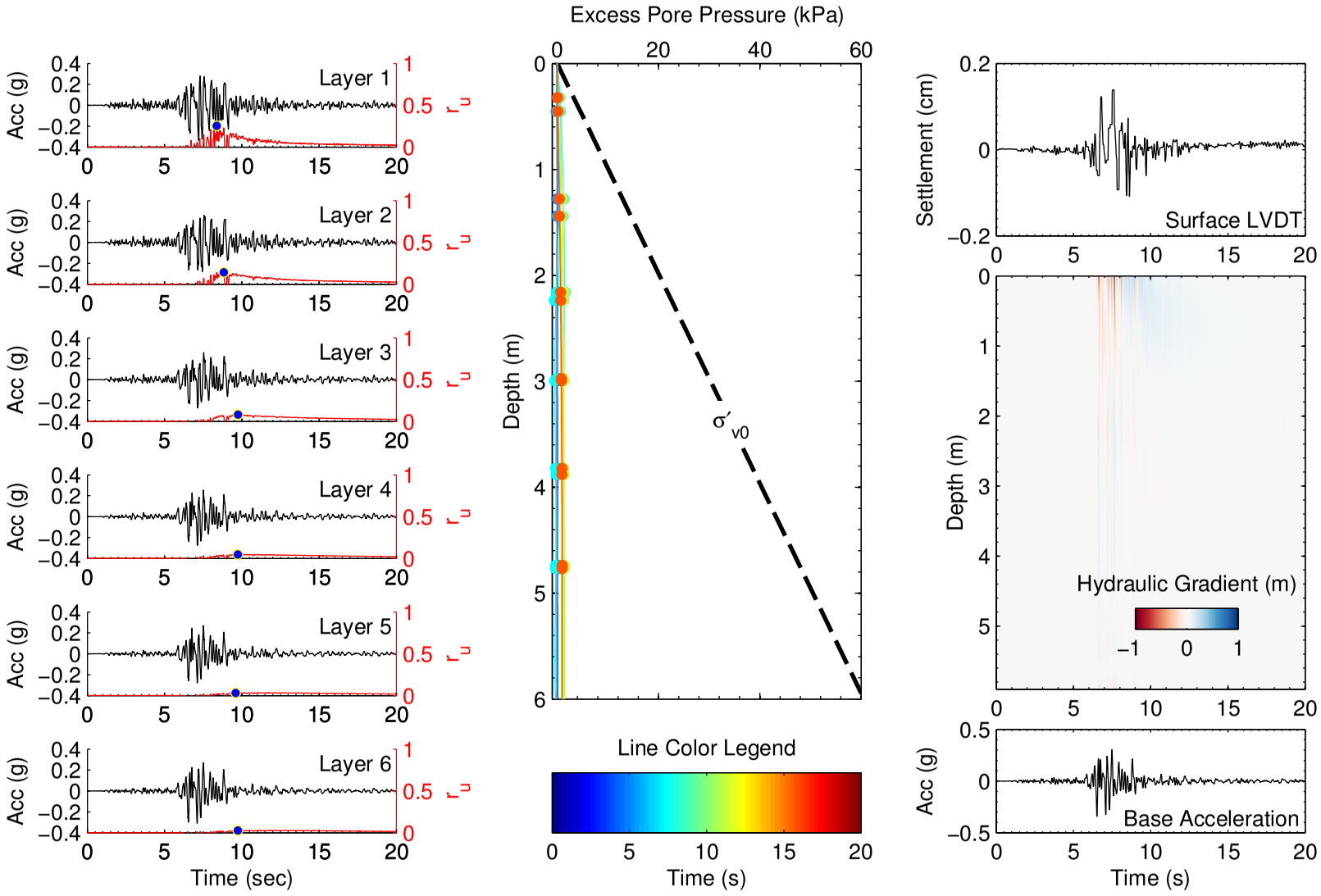
40% D_r Experiment 3 Test 49 – Data Summary Plot



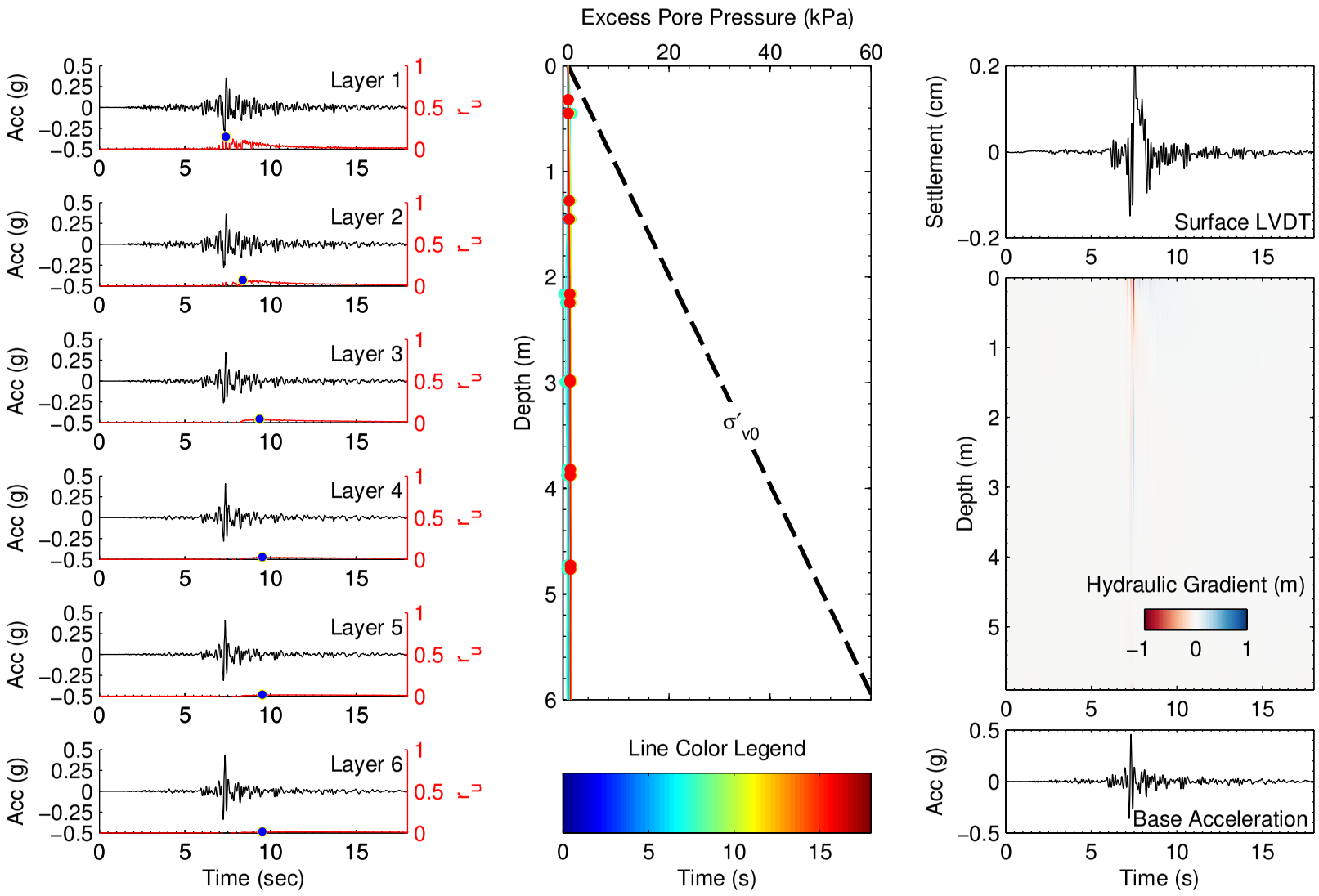
40% D_r Experiment 3 Test 50 – Data Summary Plot



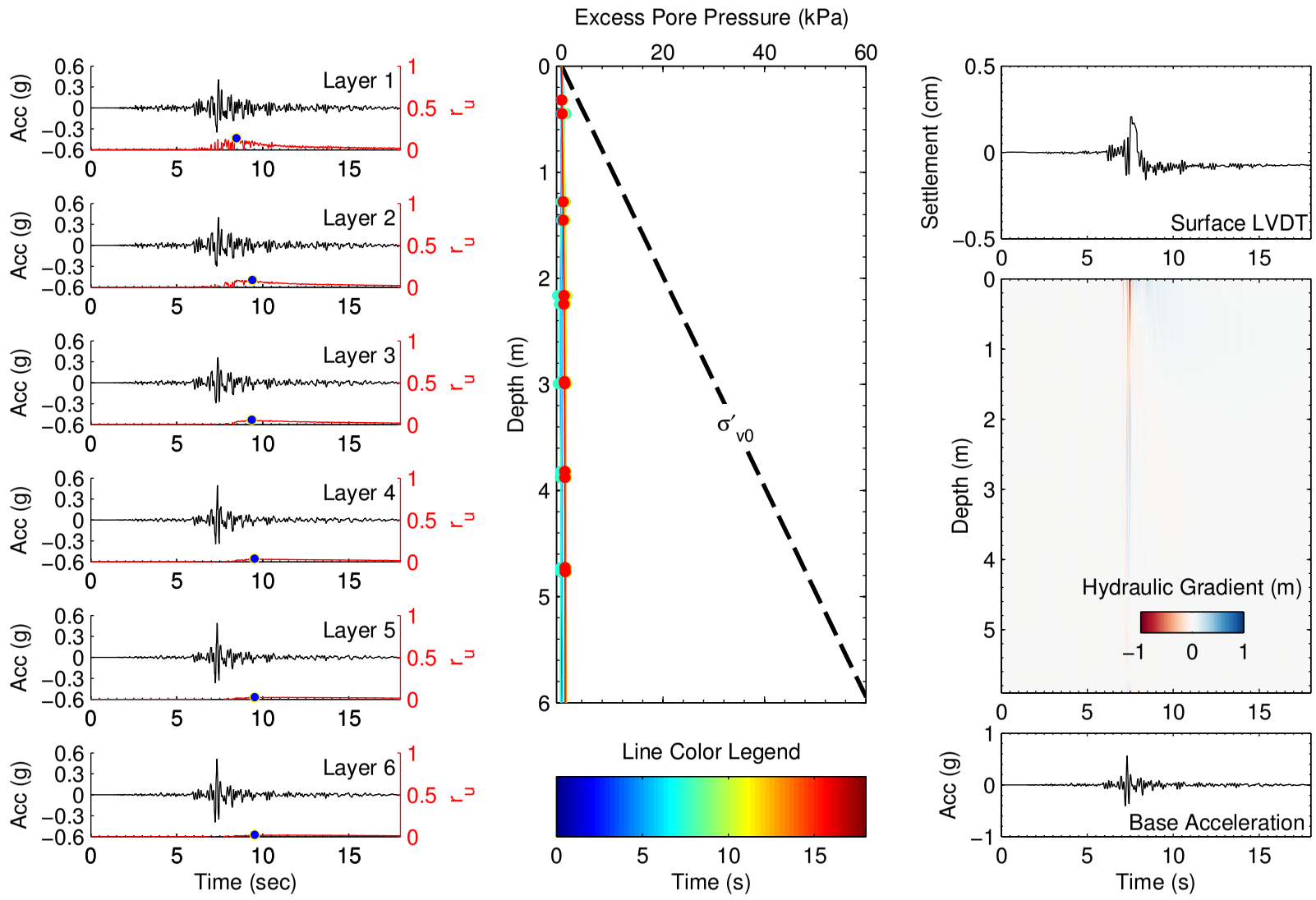
40% D_r Experiment 3 Test 51 – Data Summary Plot



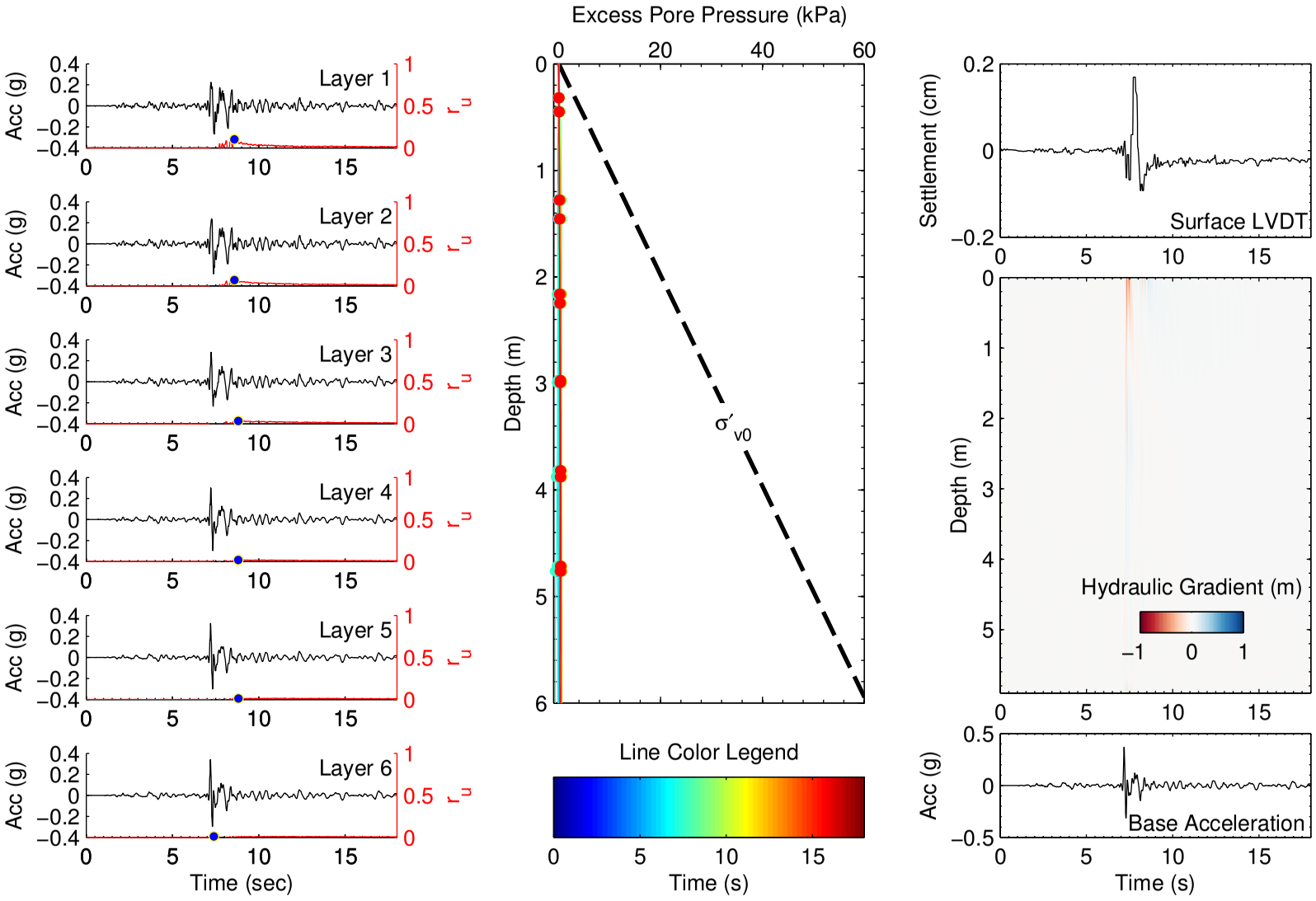
40% D_r Experiment 3 Test 52 – Data Summary Plot



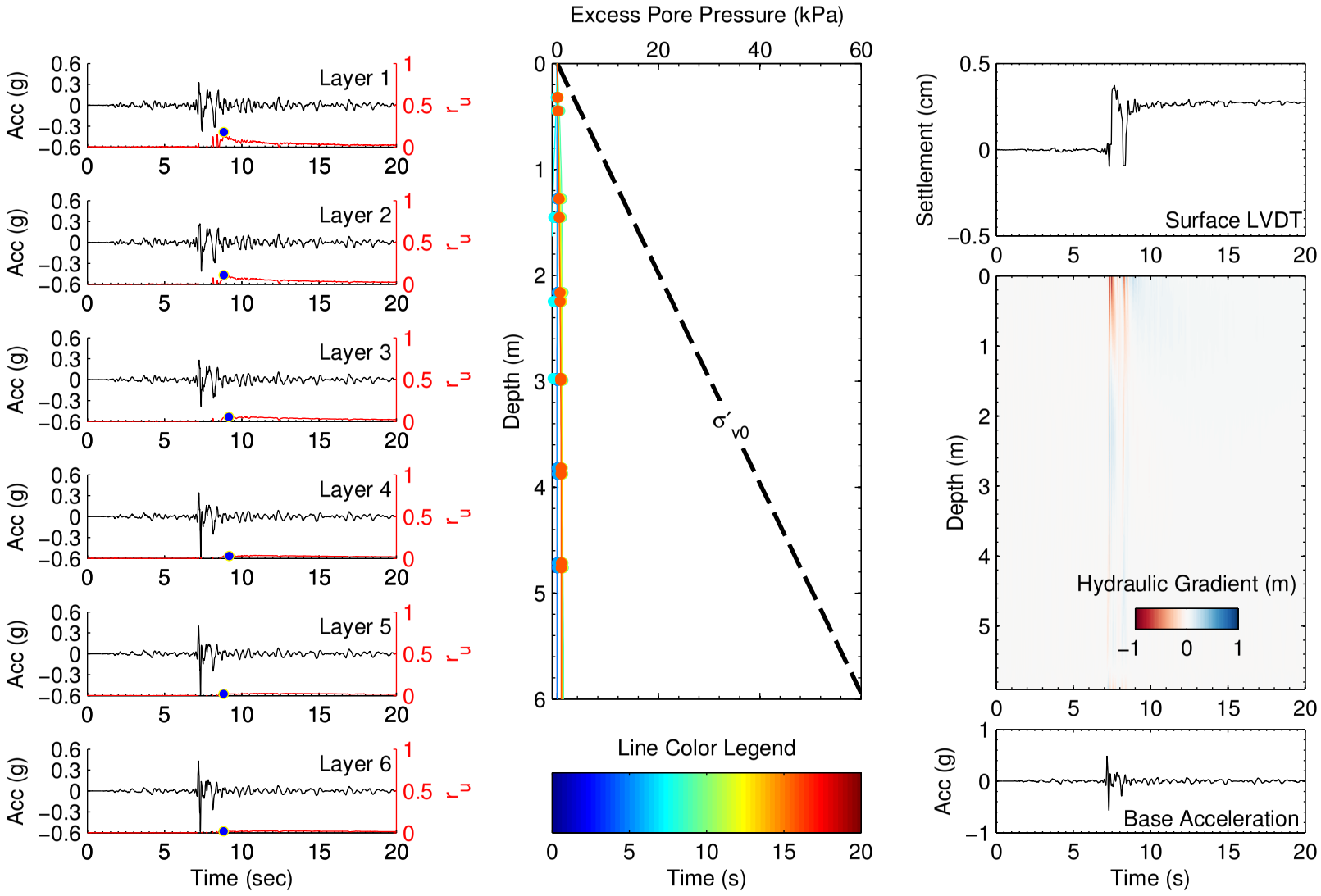
40% D_r Experiment 3 Test 53 – Data Summary Plot



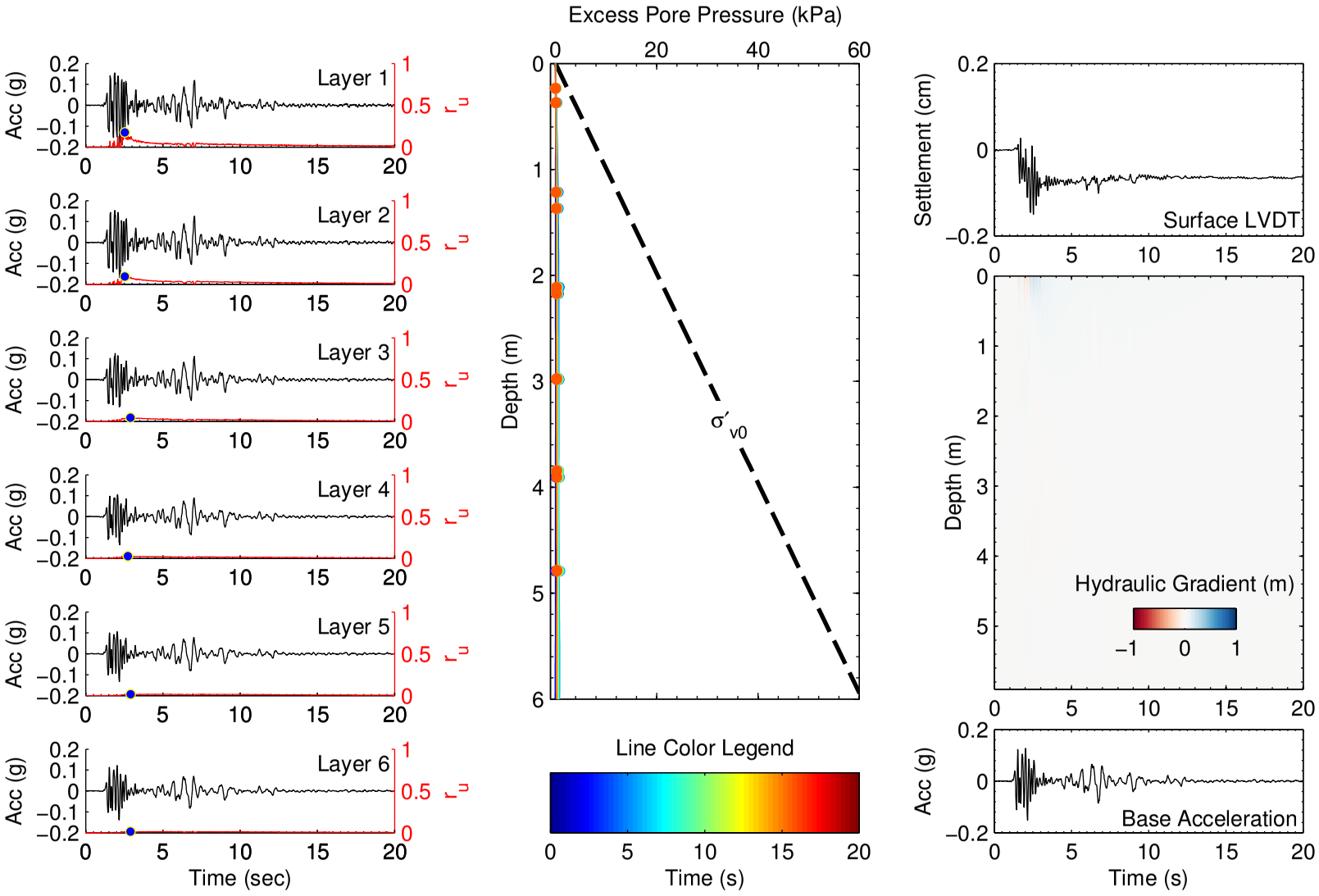
40% D_r Experiment 3 Test 54 – Data Summary Plot



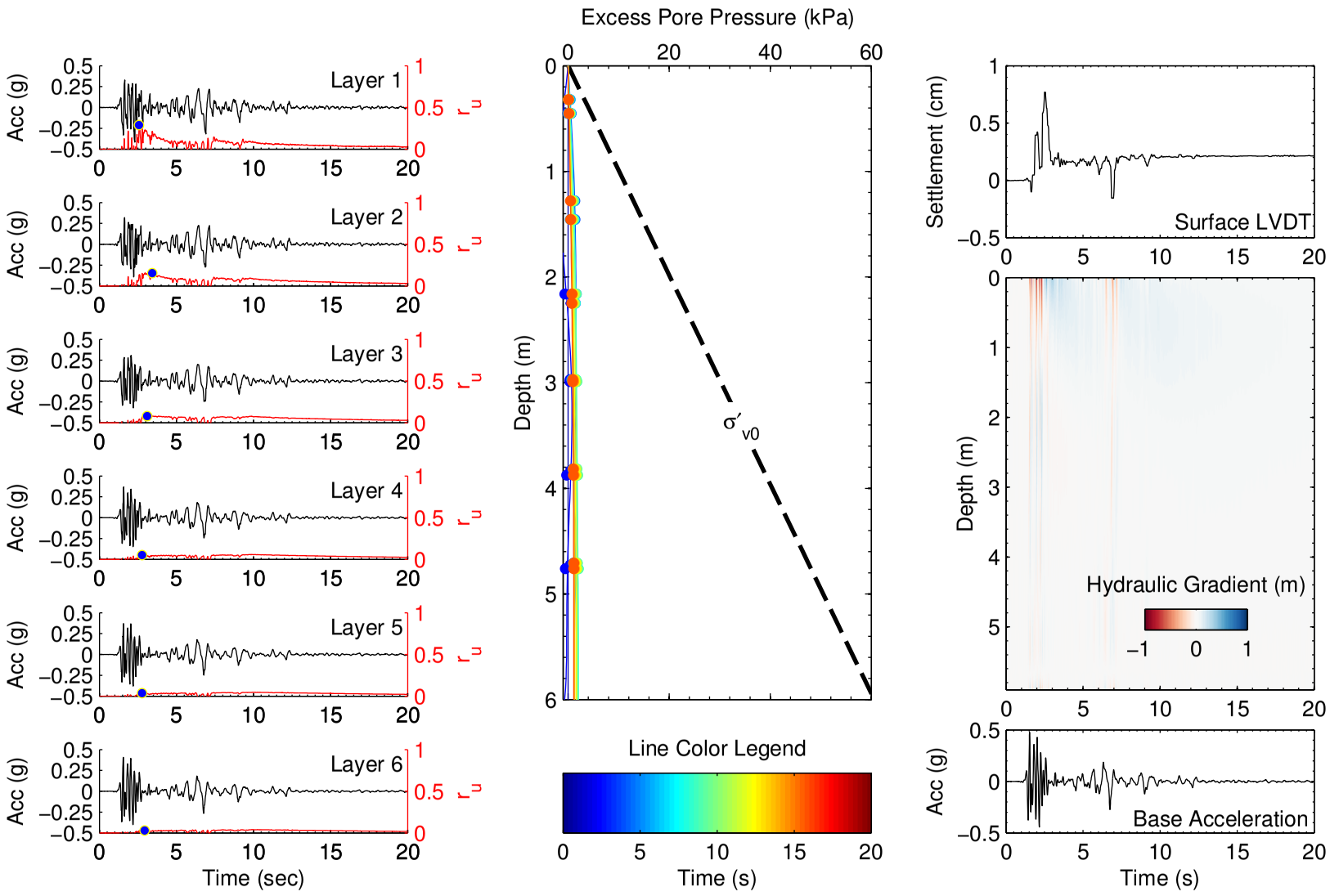
40% D_r Experiment 3 Test 55 – Data Summary Plot



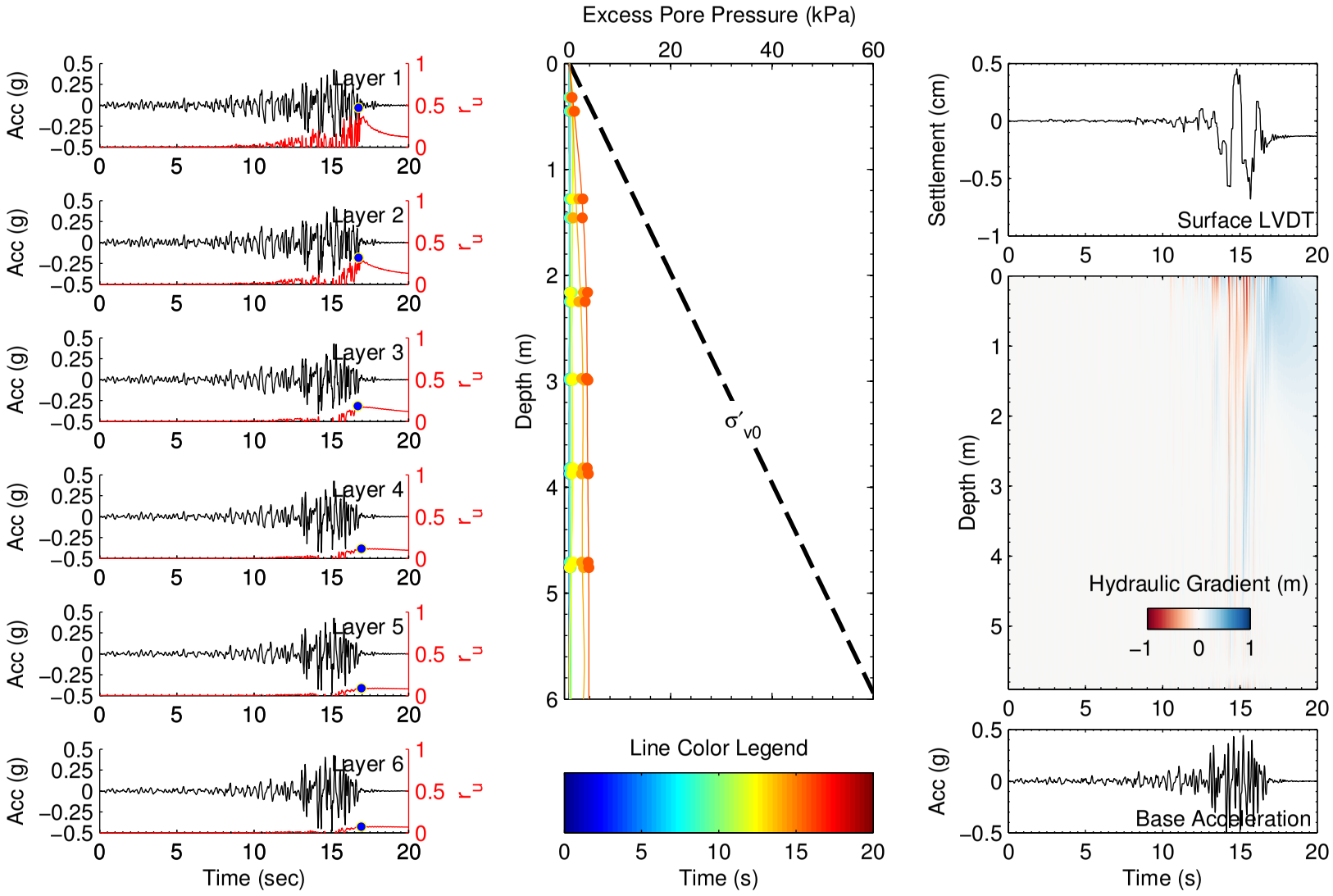
40% D_r Experiment 3 Test 56 – Data Summary Plot



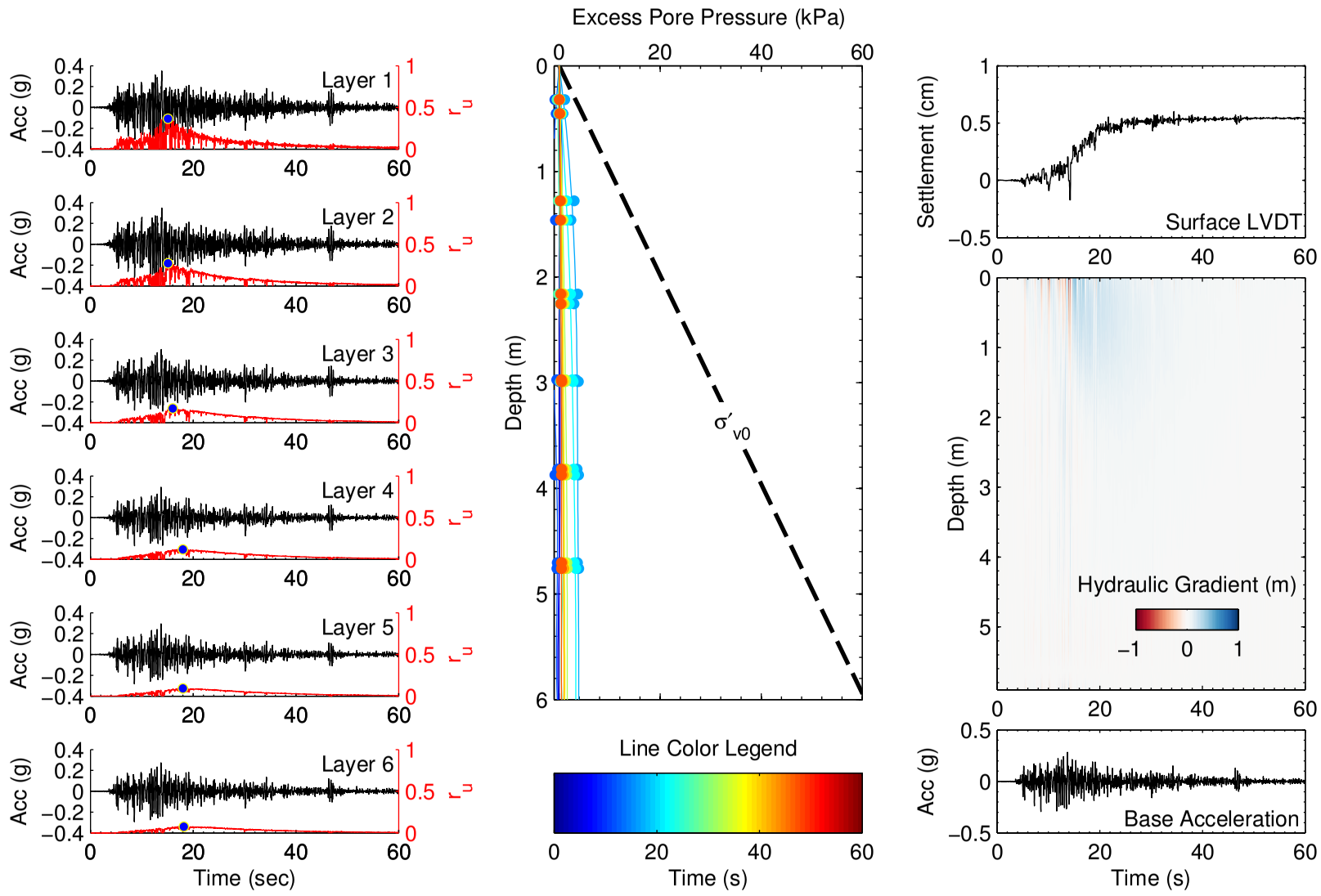
40% D_r Experiment 3 Test 57 – Data Summary Plot



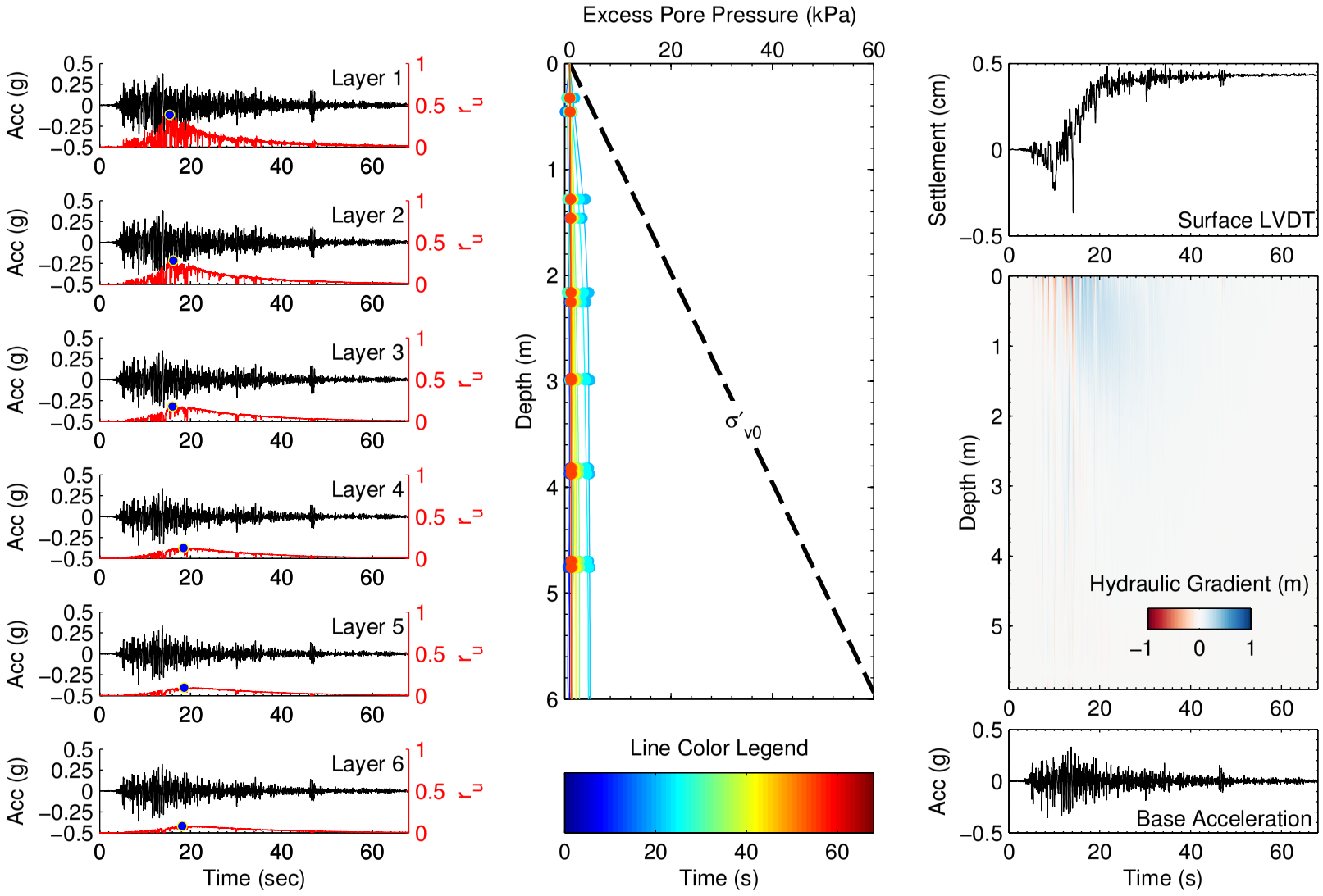
40% D_r Experiment 3 Test 58 – Data Summary Plot



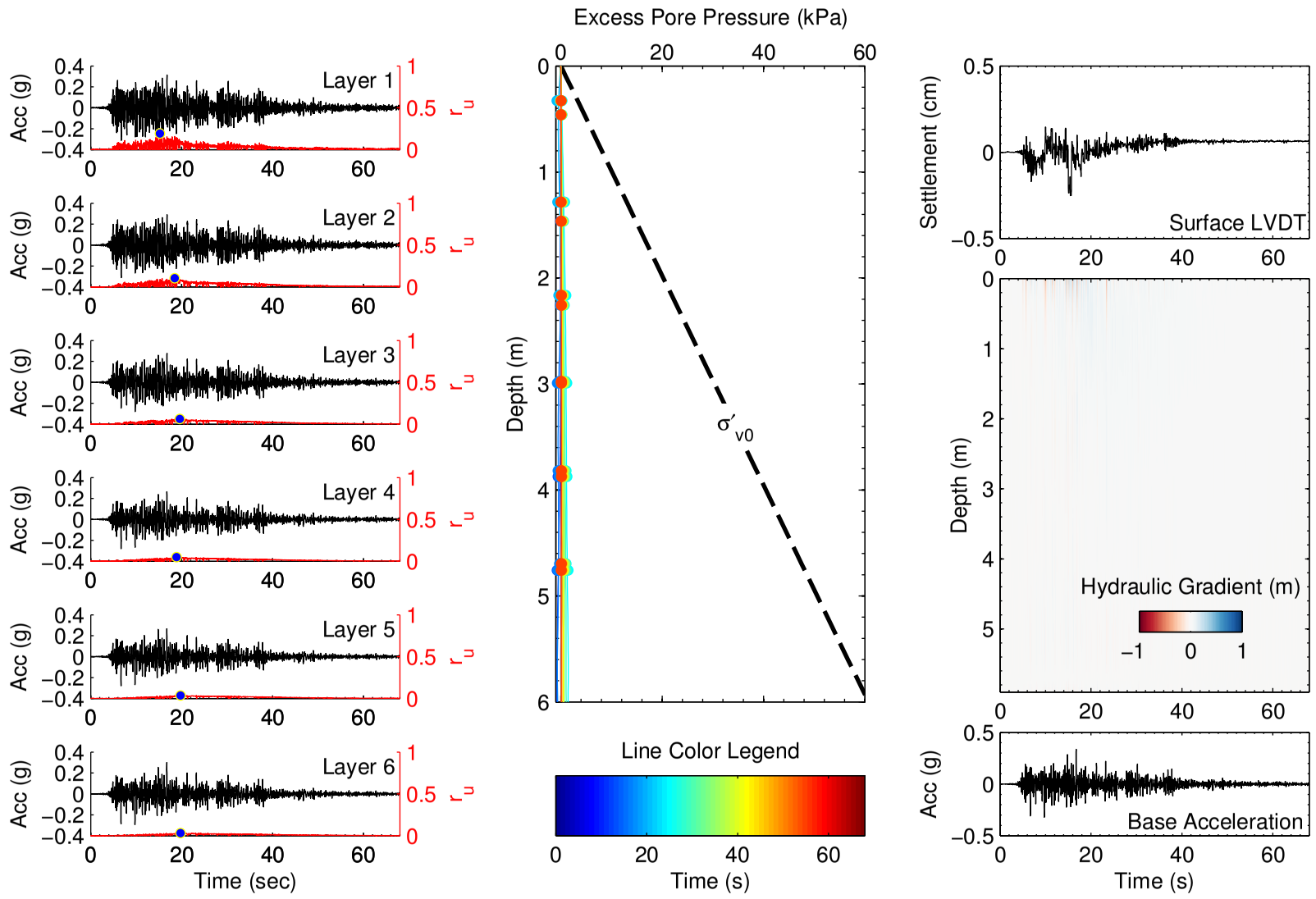
40% D_r Experiment 3 Test 59 – Data Summary Plot



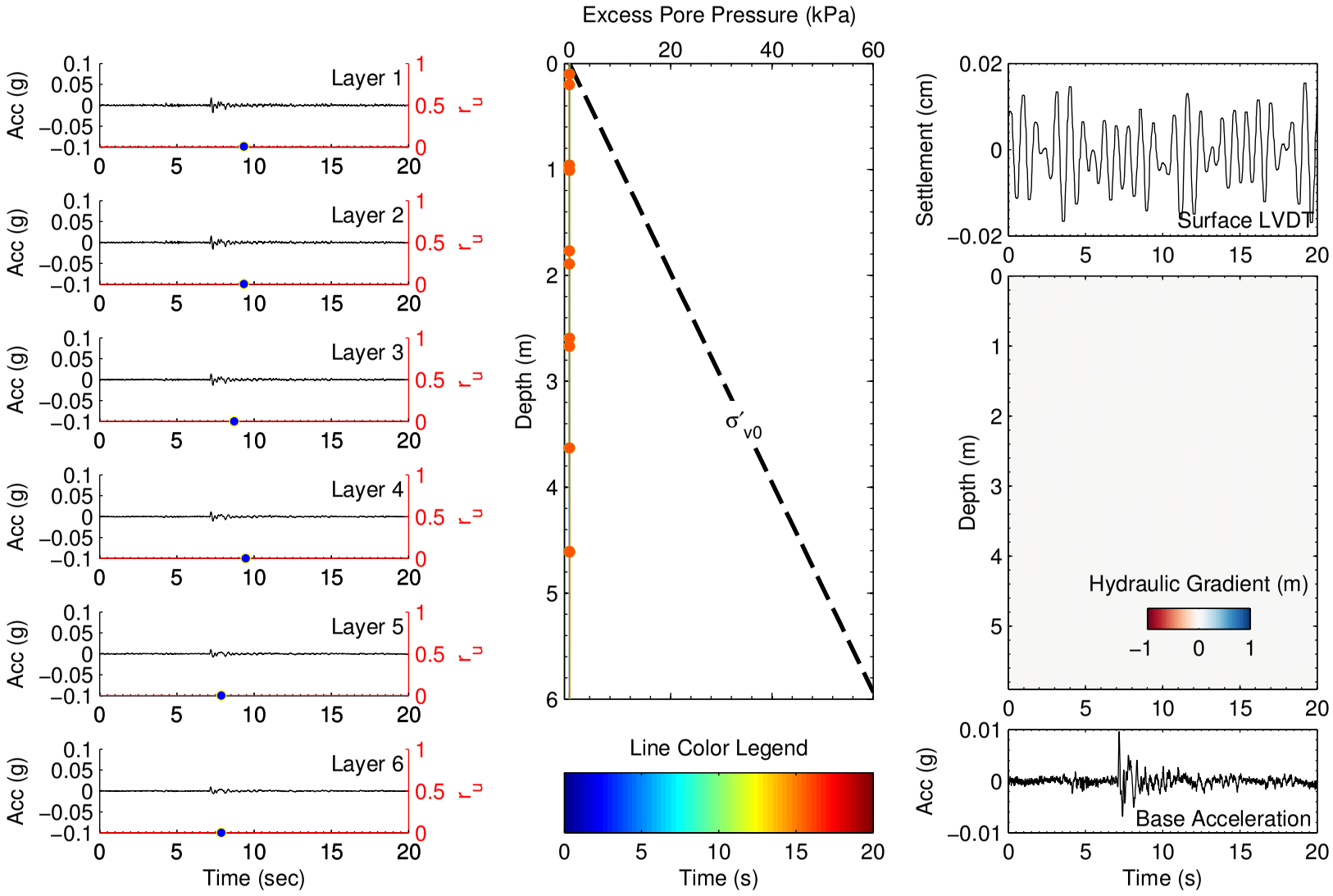
40% D_r Experiment 3 Test 60 – Data Summary Plot



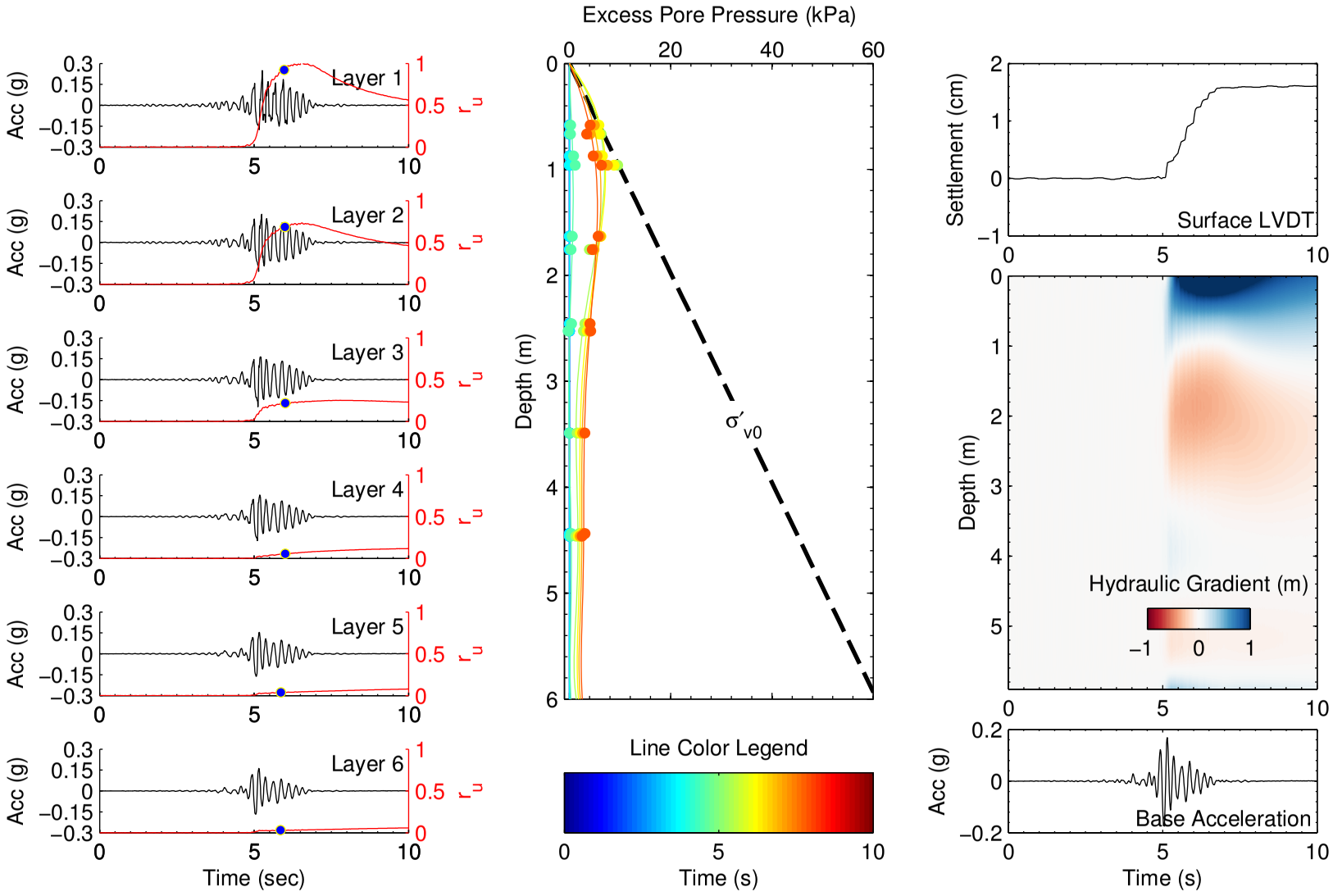
40% D_r Experiment 3 Test 61 – Data Summary Plot



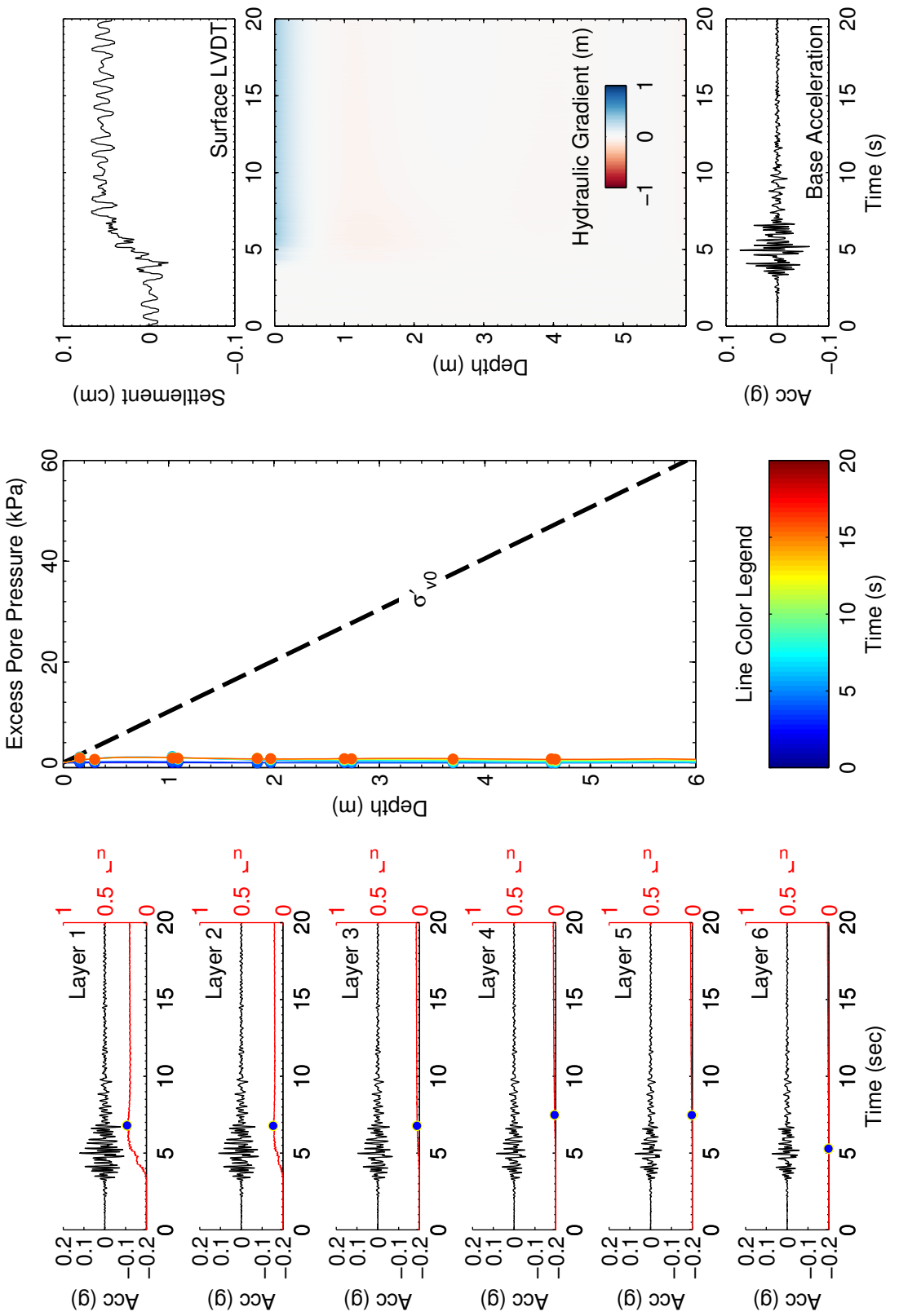
40% D_r Experiment 3 Test 62 – Data Summary Plot



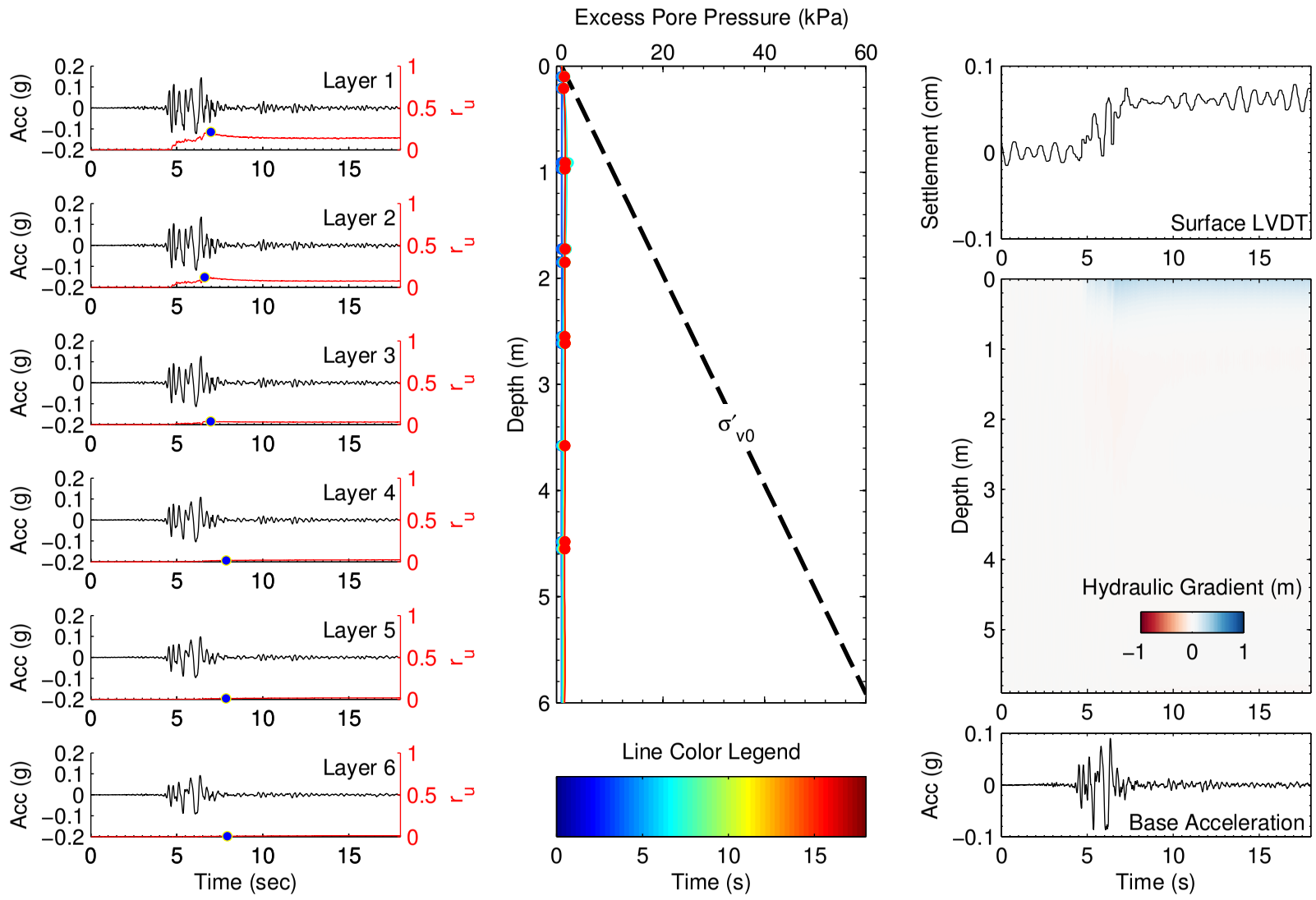
70% D_r Experiment 4 Test 1 – Data Summary Plot



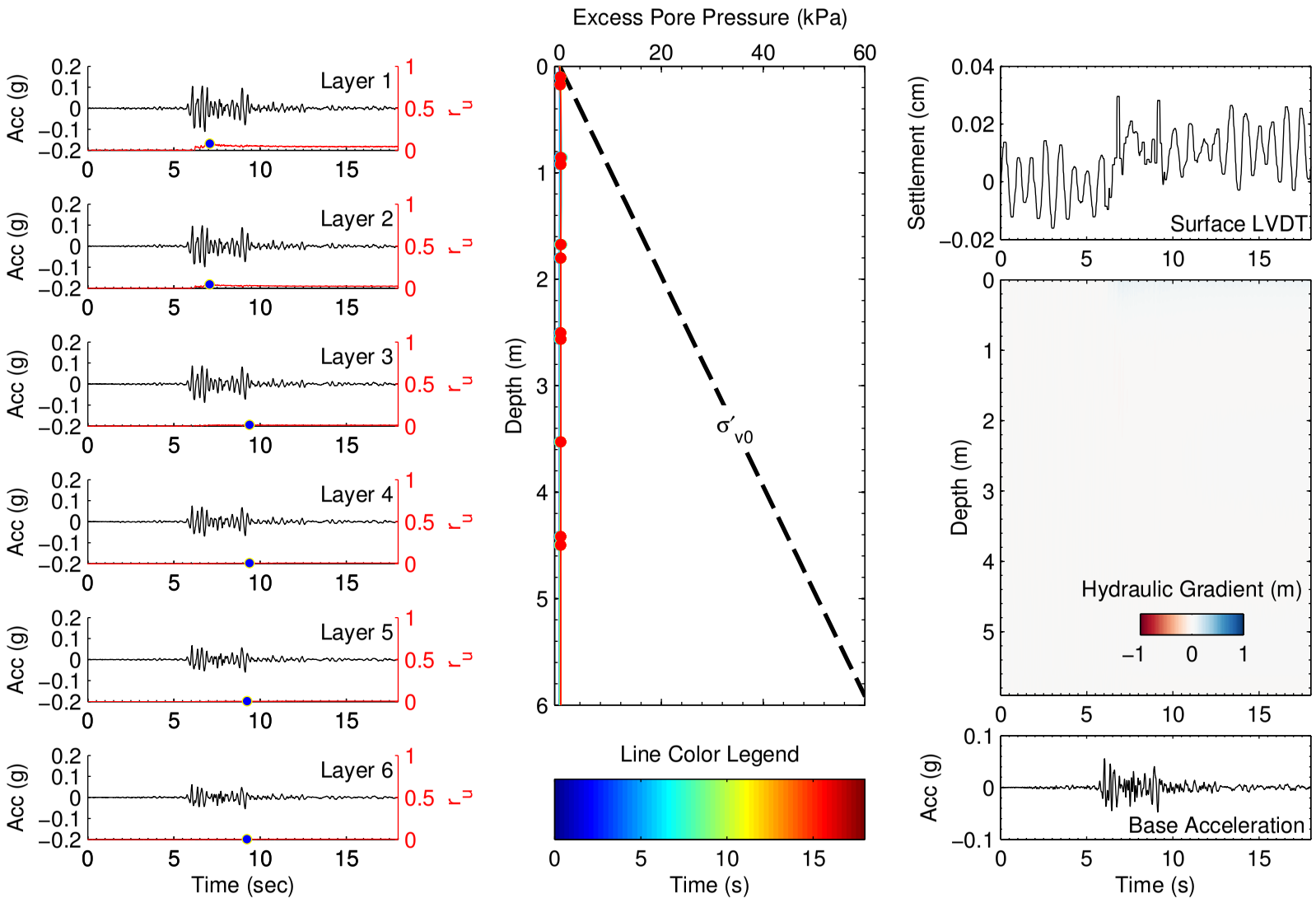
70% D_r Experiment 4 Test 2 – Data Summary Plot



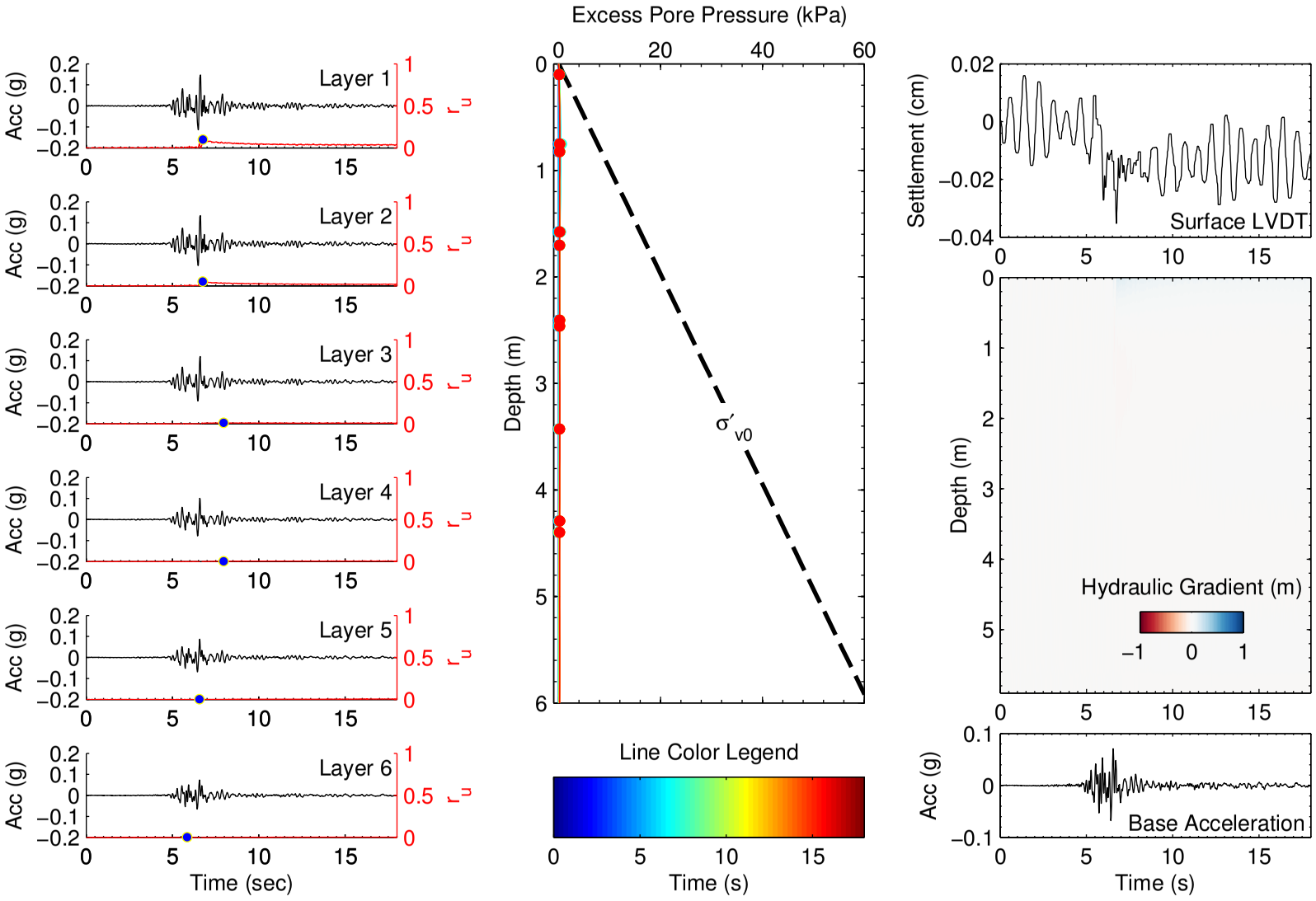
70% D_r Experiment 4 Test 3 – Data Summary Plot



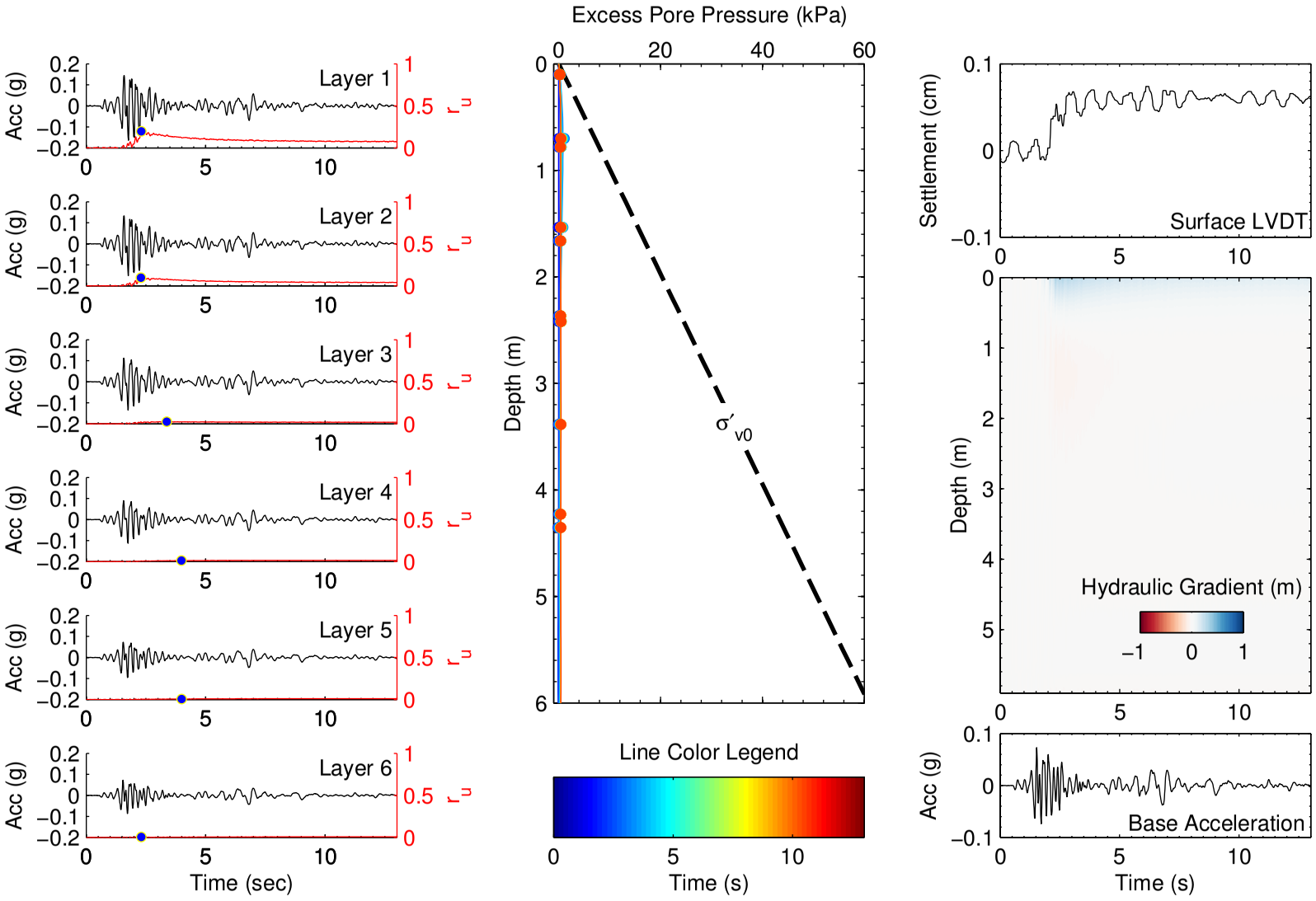
70% D_r Experiment 4 Test 4 – Data Summary Plot



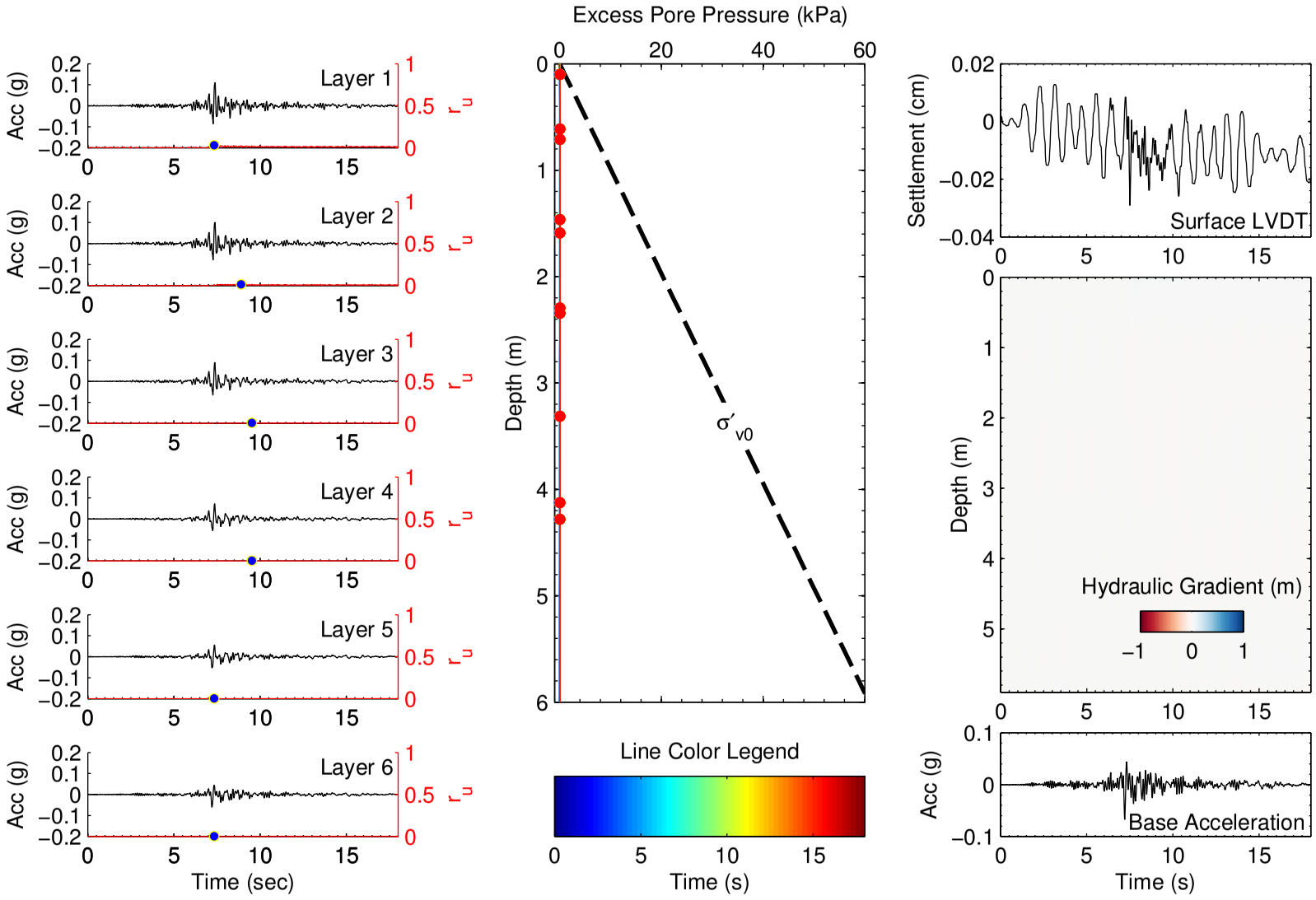
70% D_r Experiment 4 Test 5 – Data Summary Plot



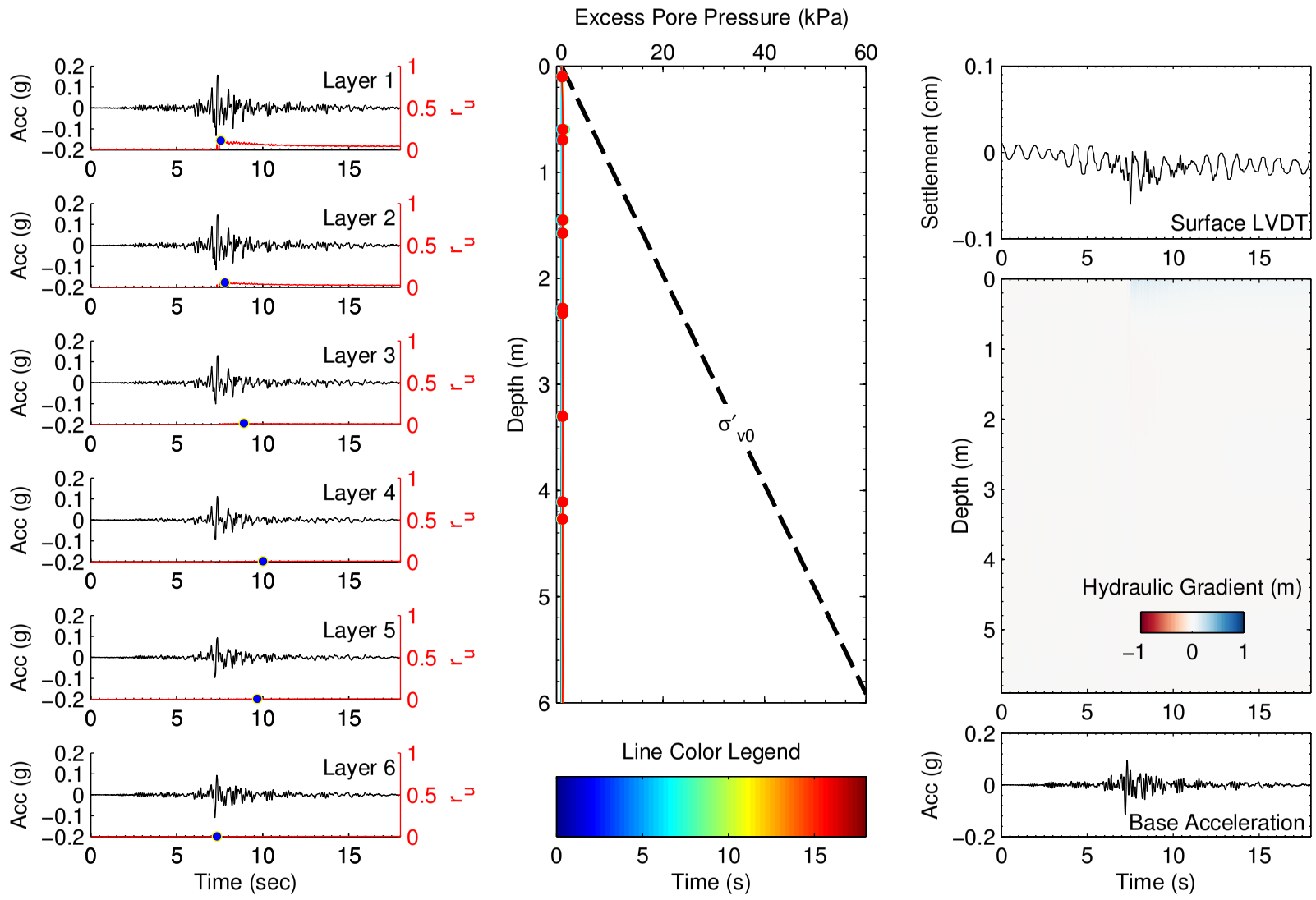
70% D_r Experiment 4 Test 6 – Data Summary Plot



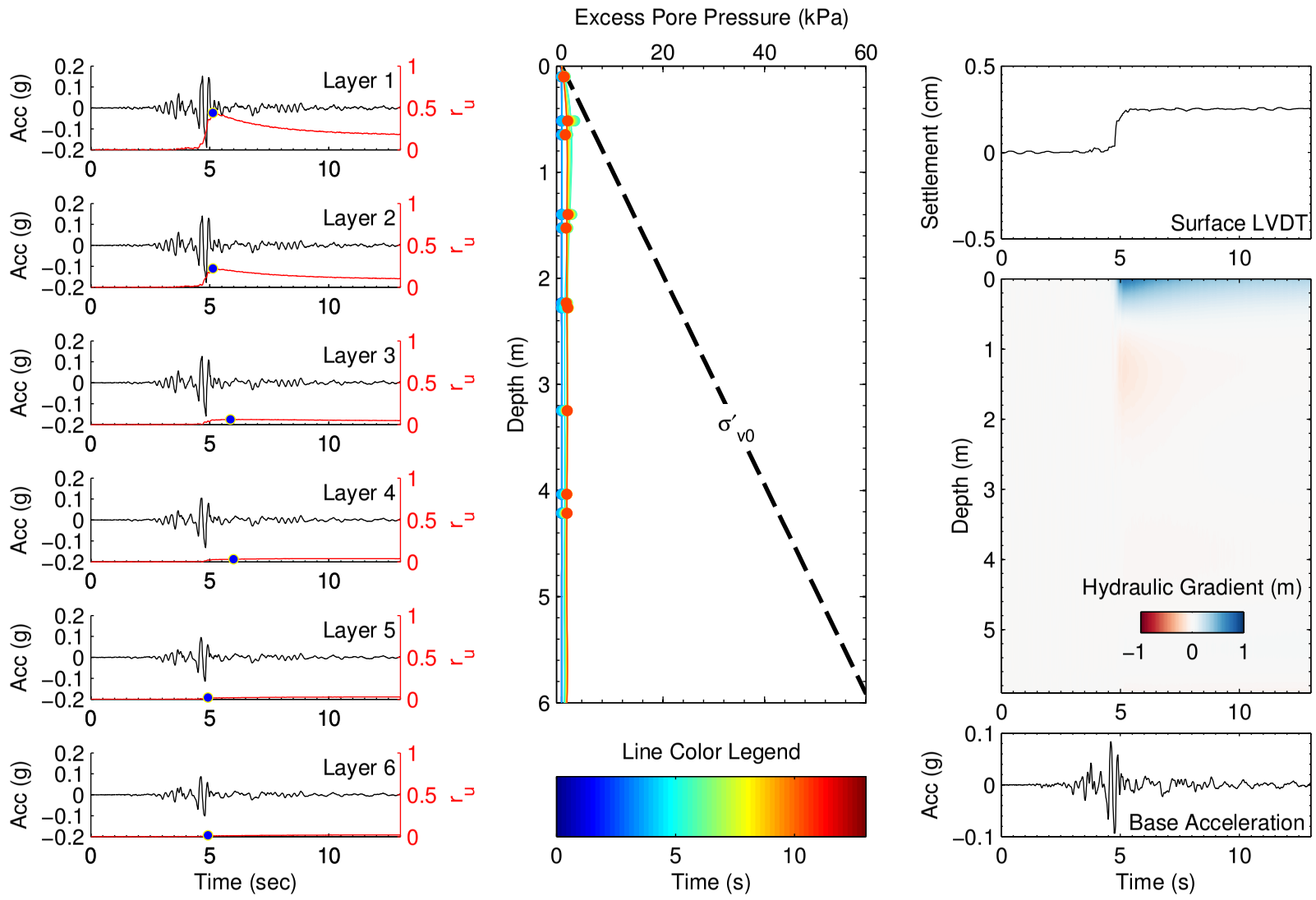
70% D_r Experiment 4 Test 7 – Data Summary Plot



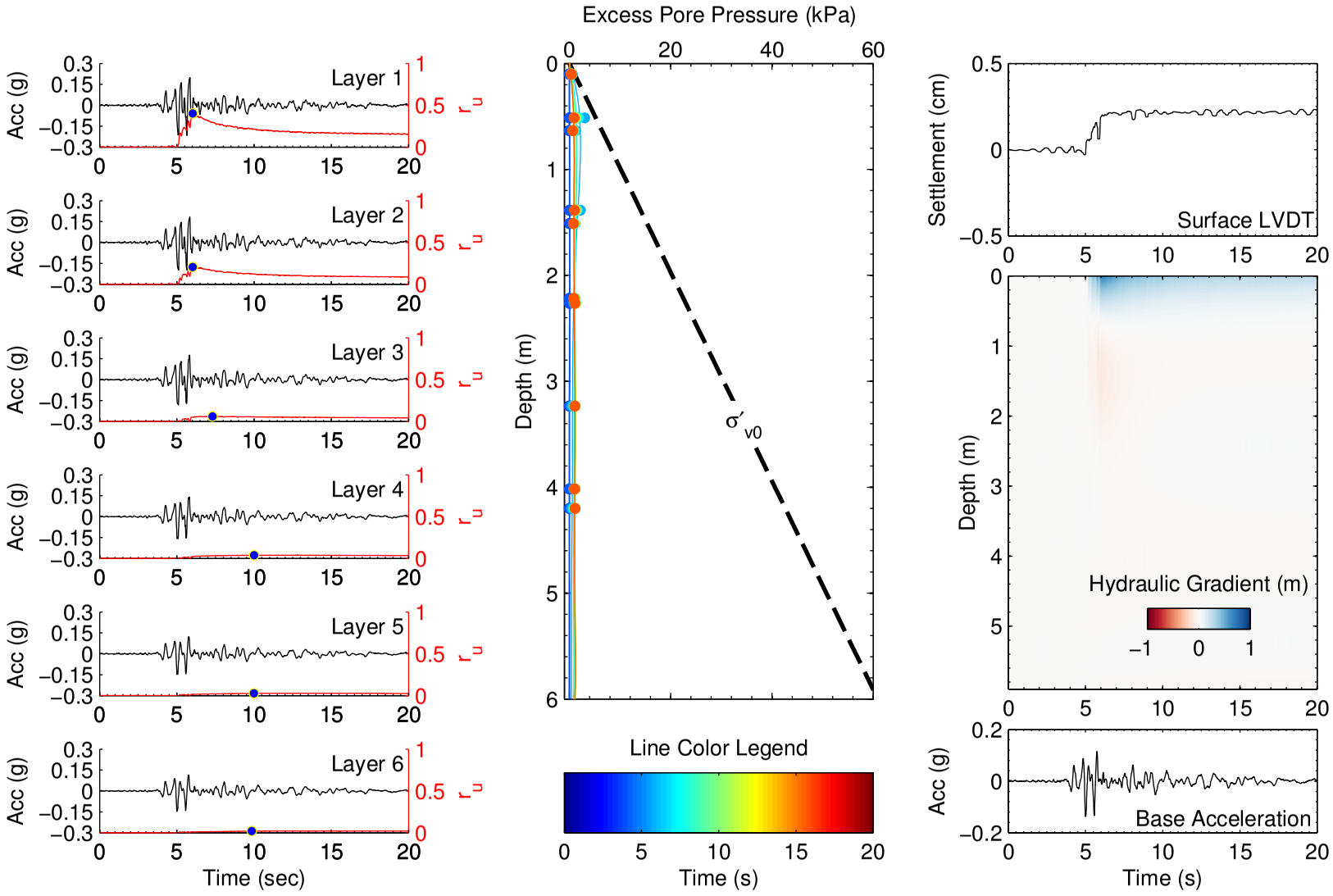
70% D_r Experiment 4 Test 8 – Data Summary Plot



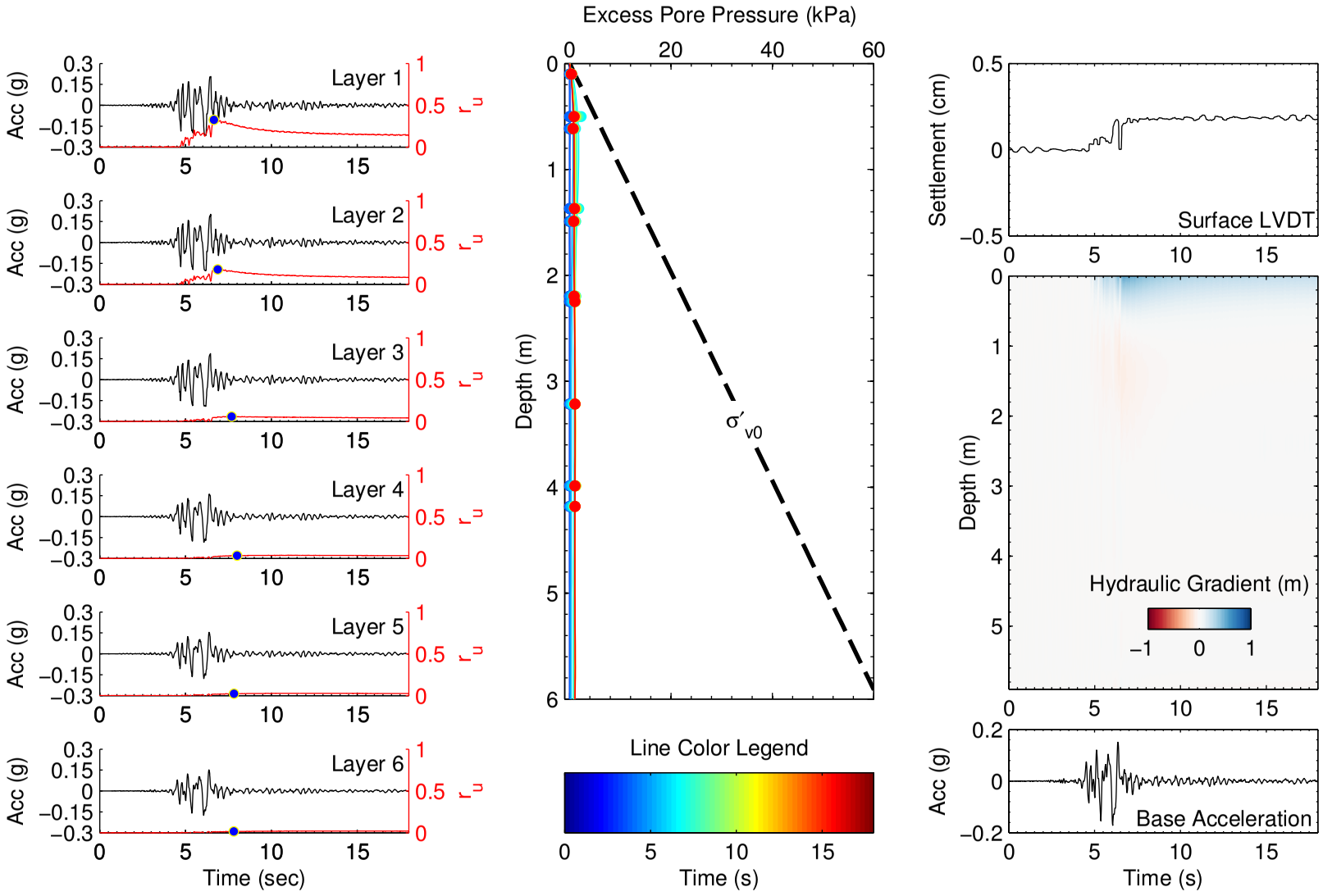
70% D_r Experiment 4 Test 9 – Data Summary Plot



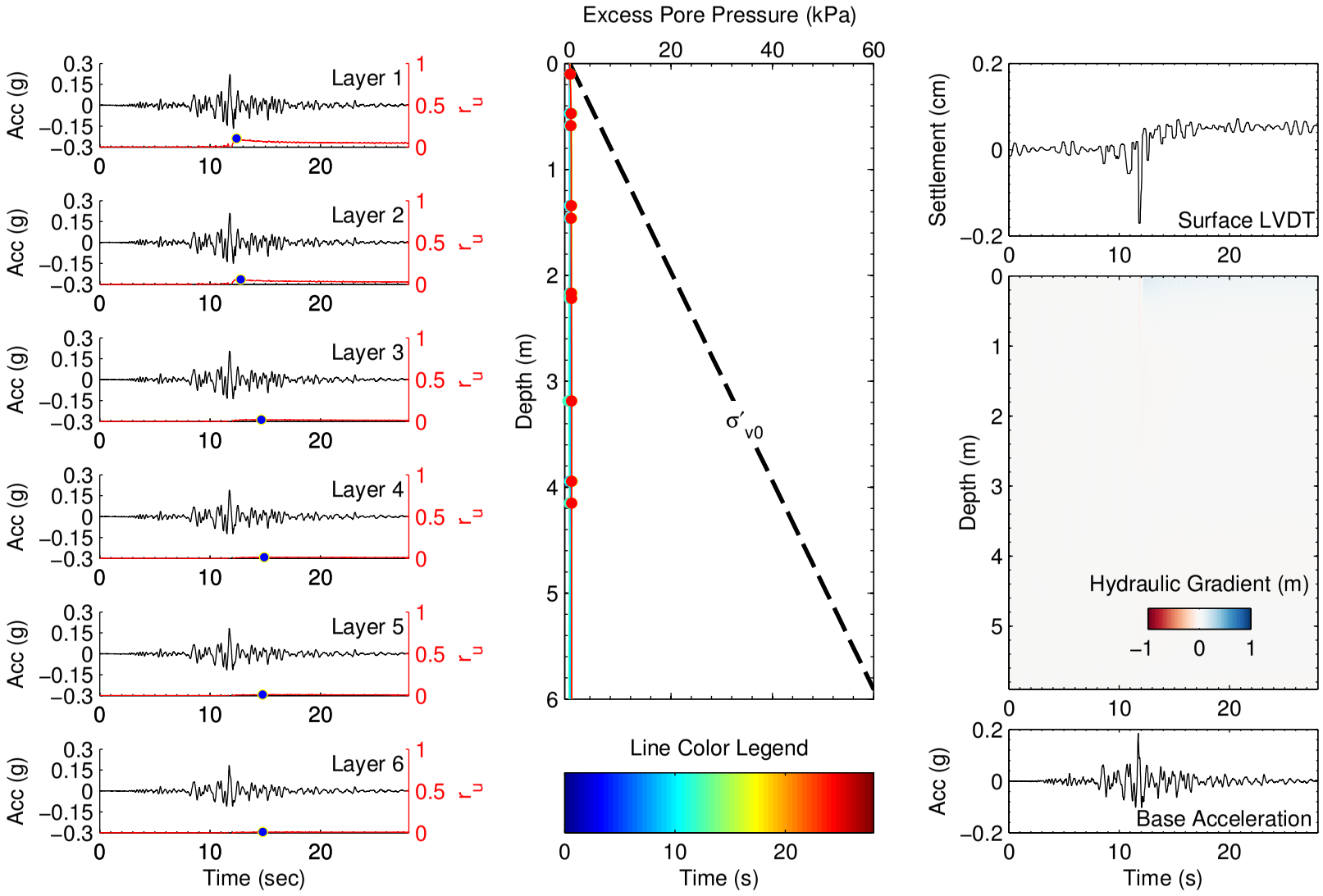
70% D_r Experiment 4 Test 10 – Data Summary Plot



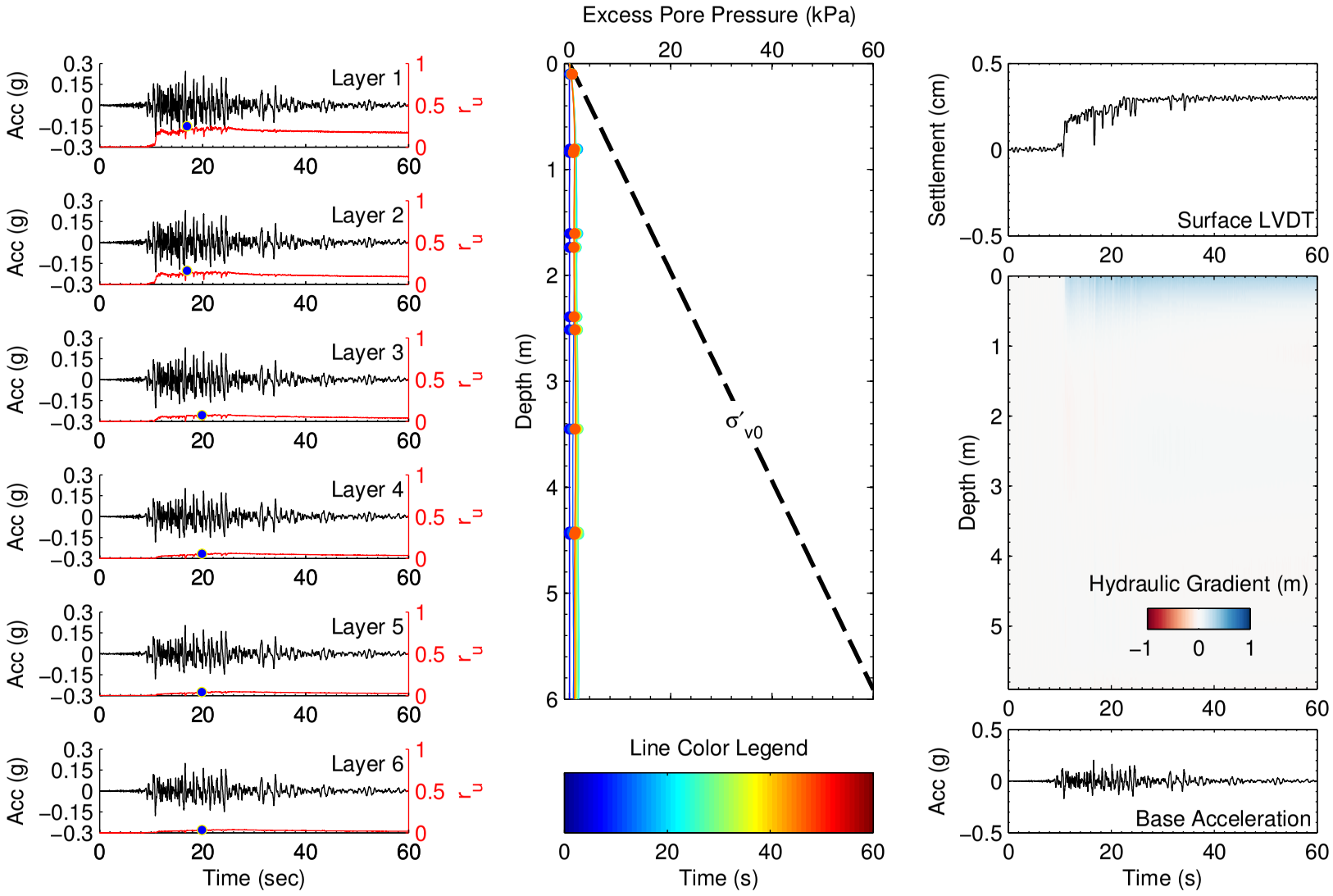
70% D_r Experiment 4 Test 11 – Data Summary Plot



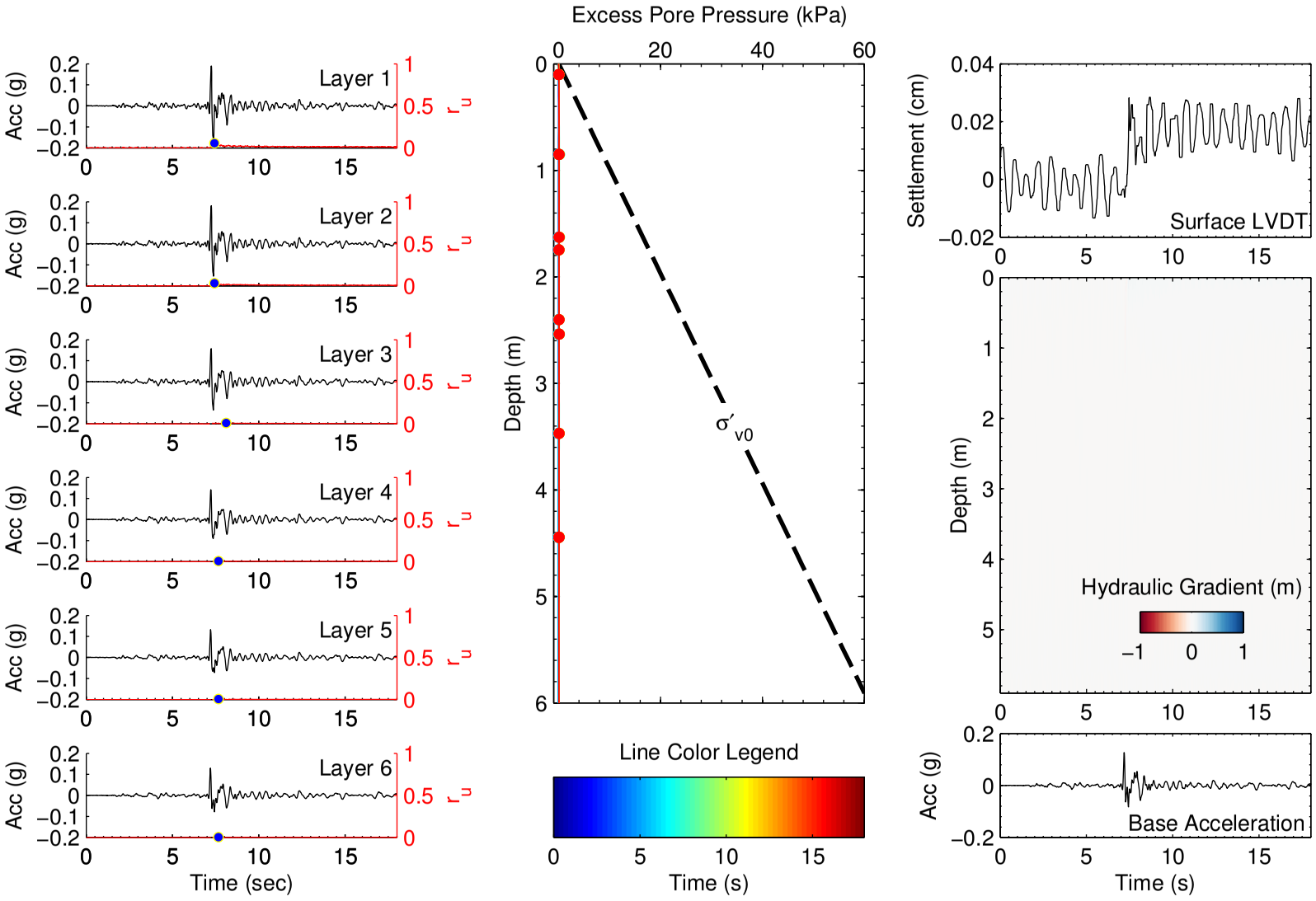
70% D_r Experiment 4 Test 12 – Data Summary Plot



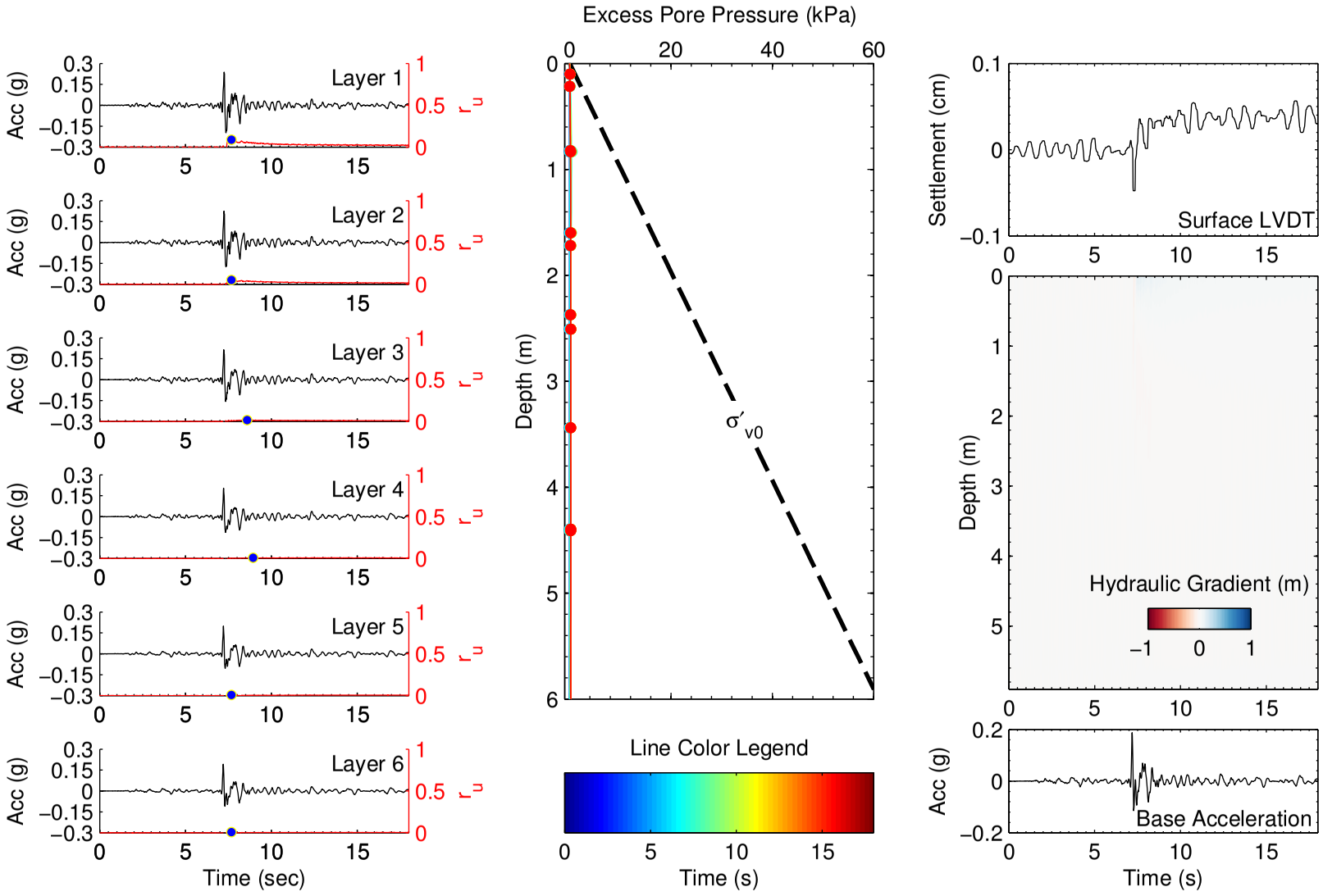
70% D_r Experiment 4 Test 13 – Data Summary Plot



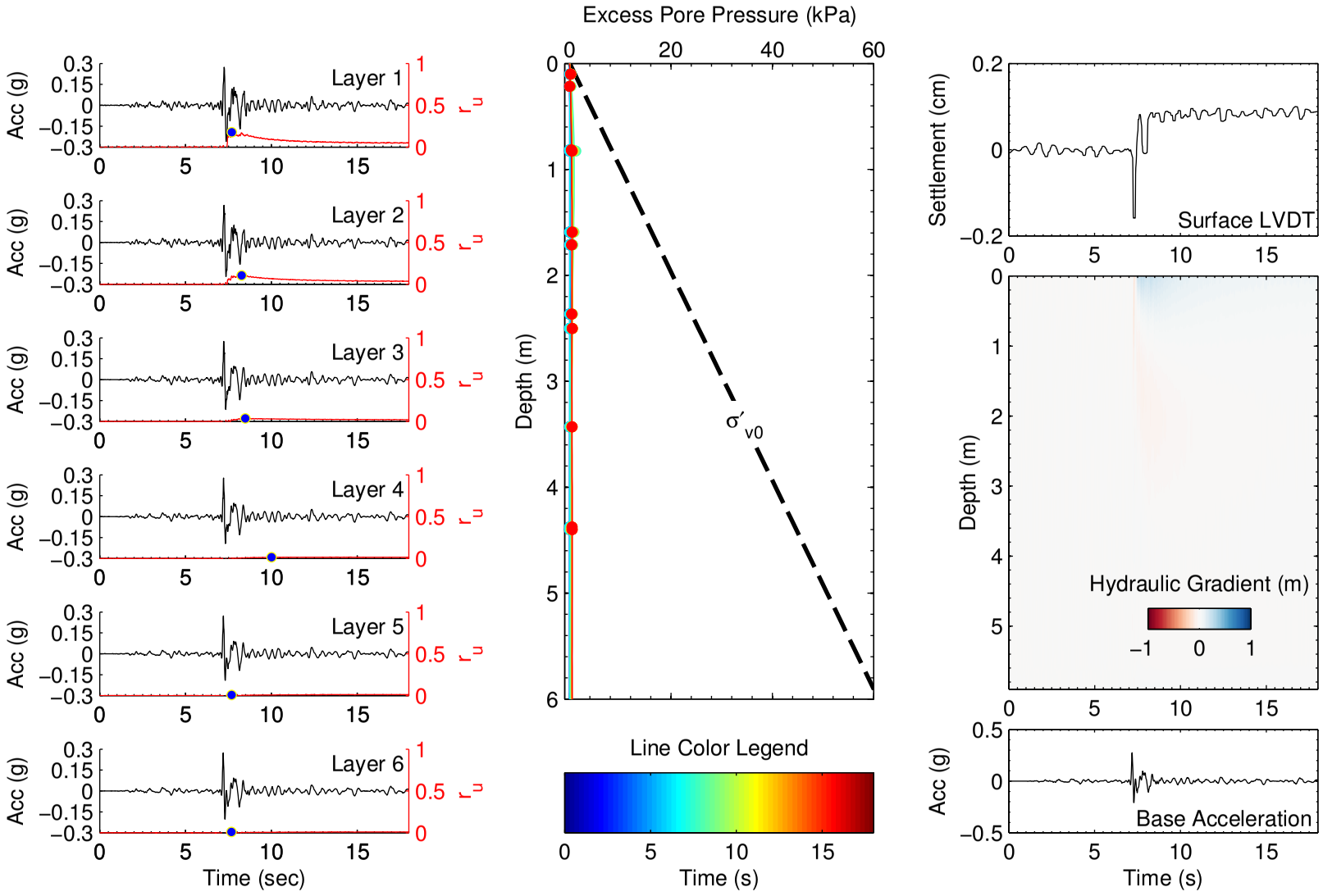
70% D_r Experiment 4 Test 14 – Data Summary Plot



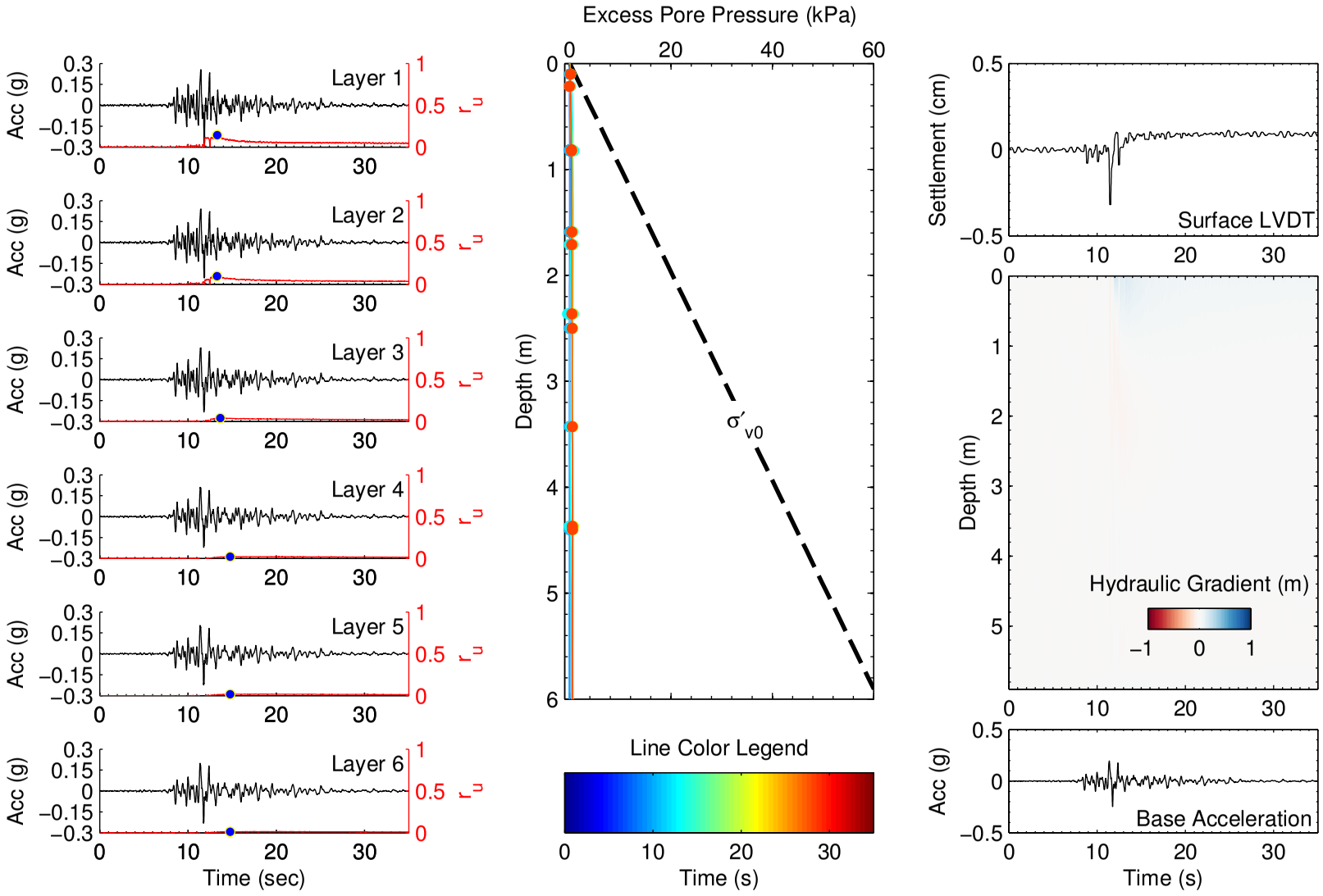
70% D_r Experiment 4 Test 15 – Data Summary Plot



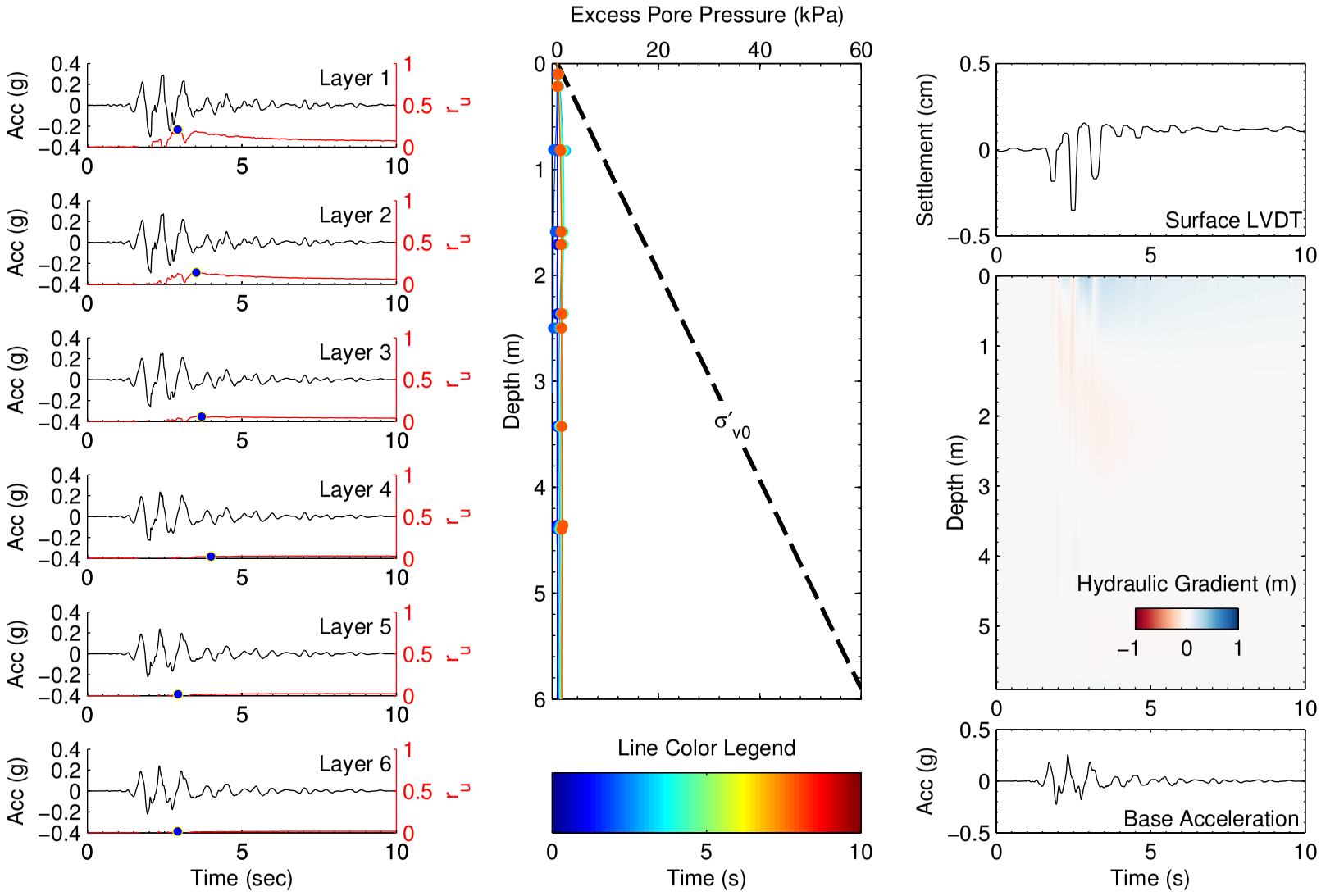
70% D_r Experiment 4 Test 16 – Data Summary Plot



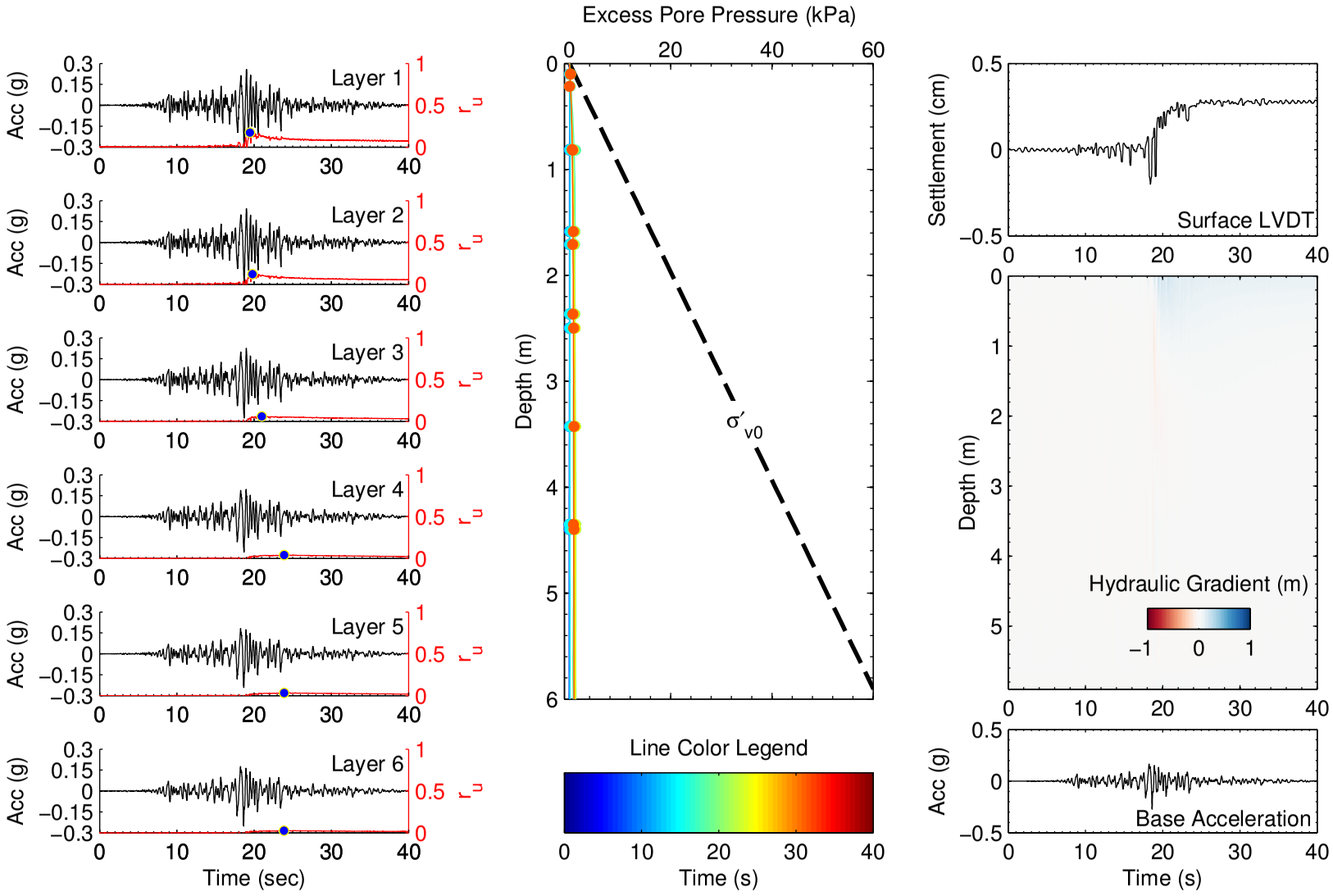
70% D_r Experiment 4 Test 17 – Data Summary Plot



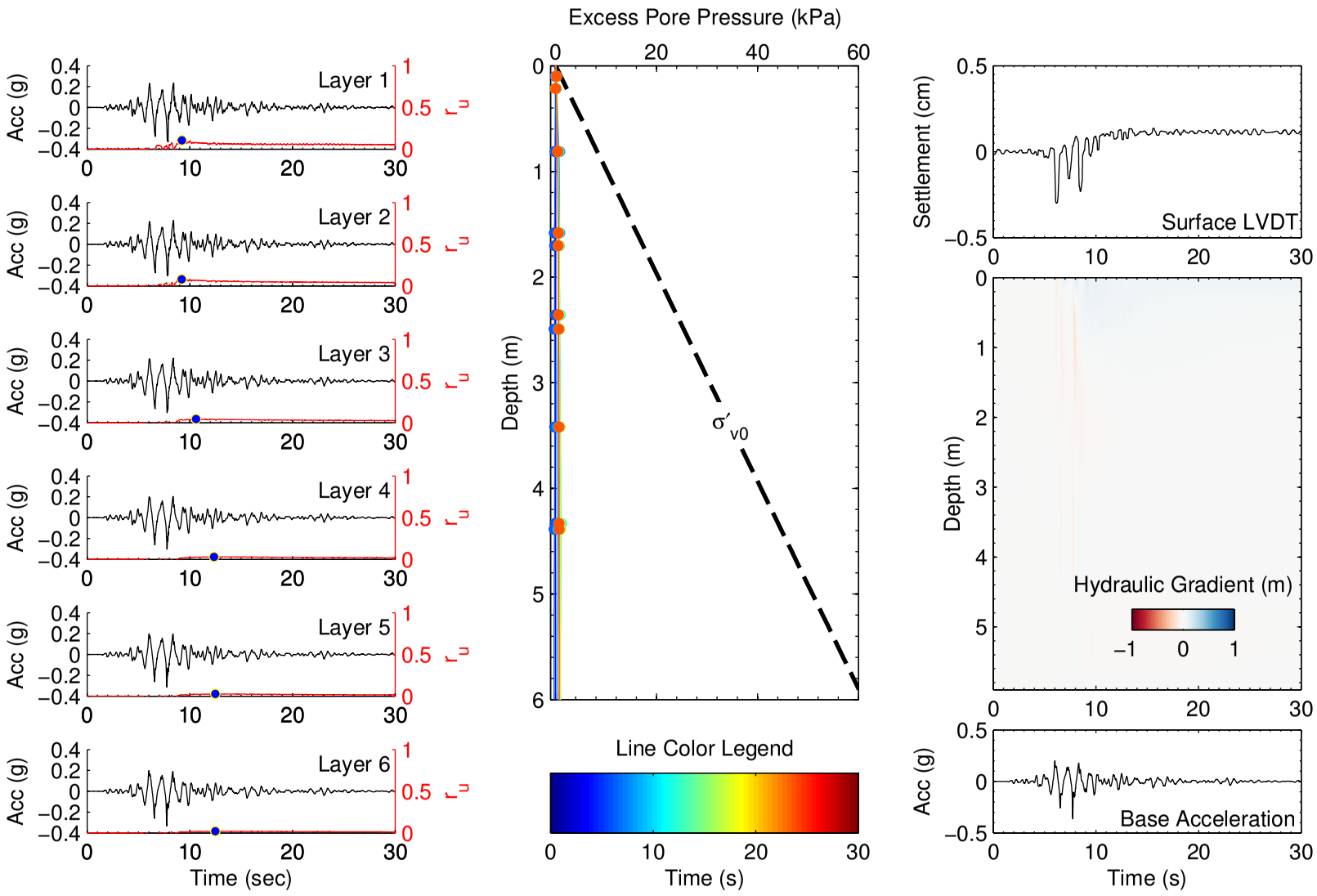
70% D_r Experiment 4 Test 18 – Data Summary Plot



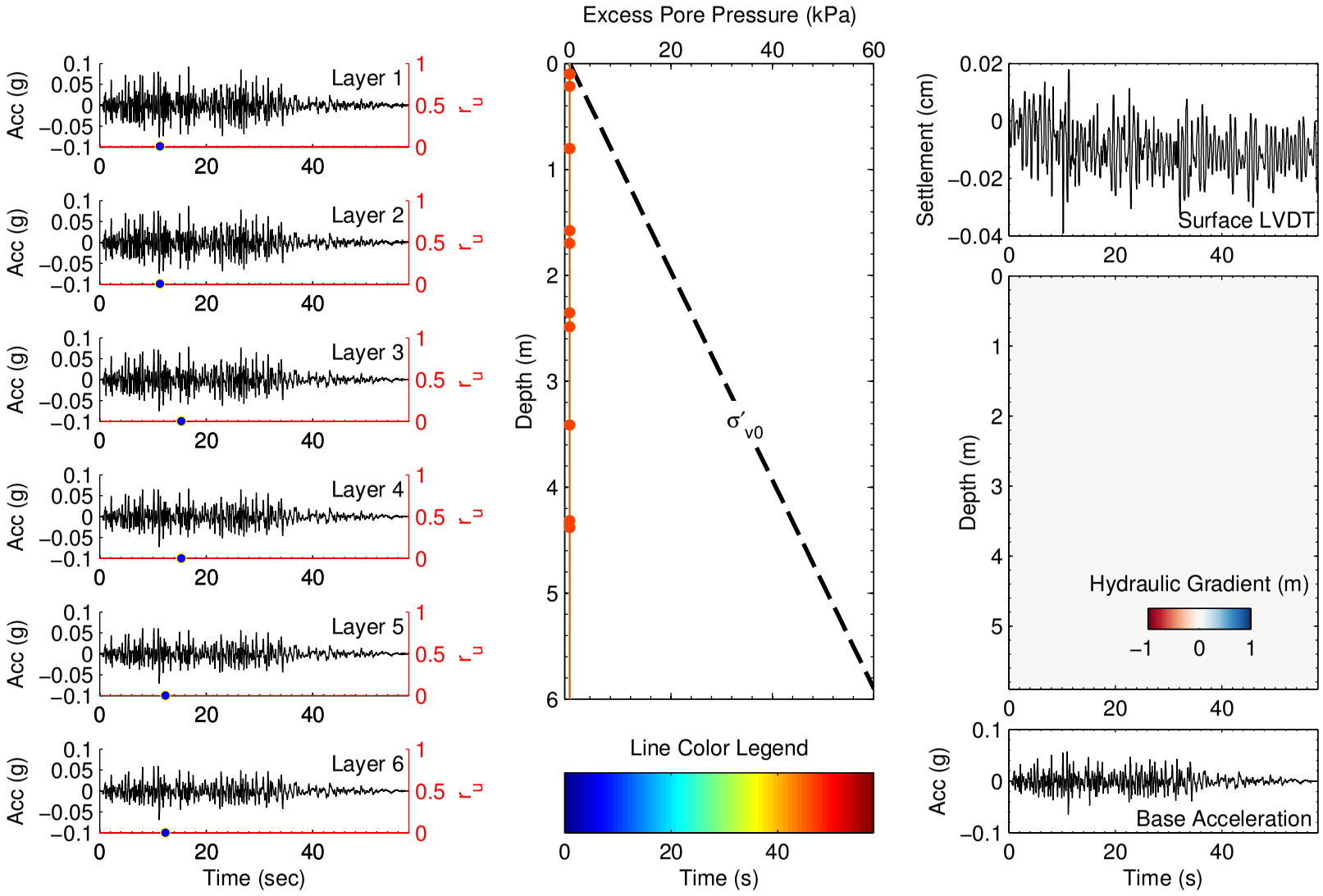
70% D_r Experiment 4 Test 19 – Data Summary Plot



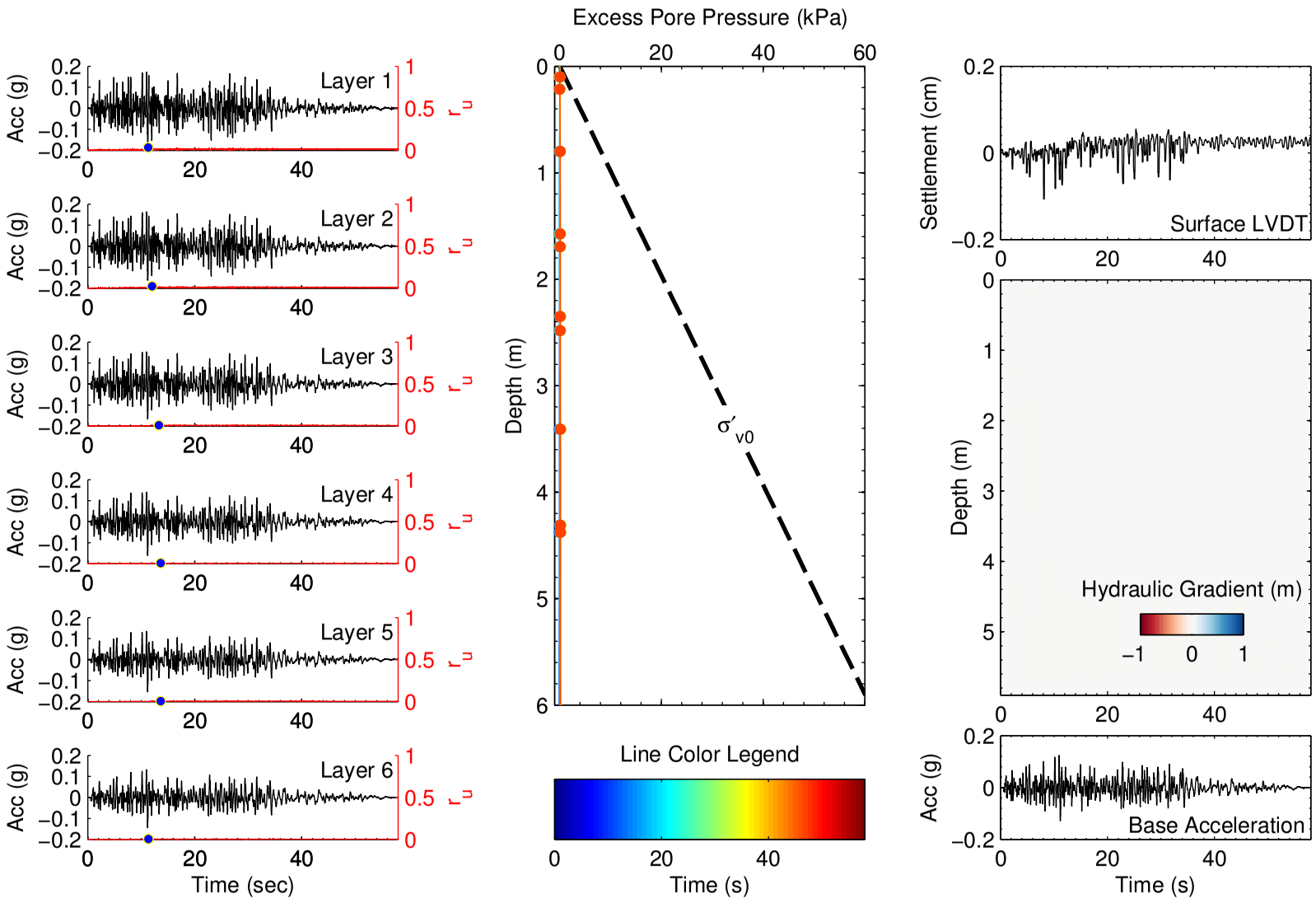
70% D_r Experiment 4 Test 20 – Data Summary Plot



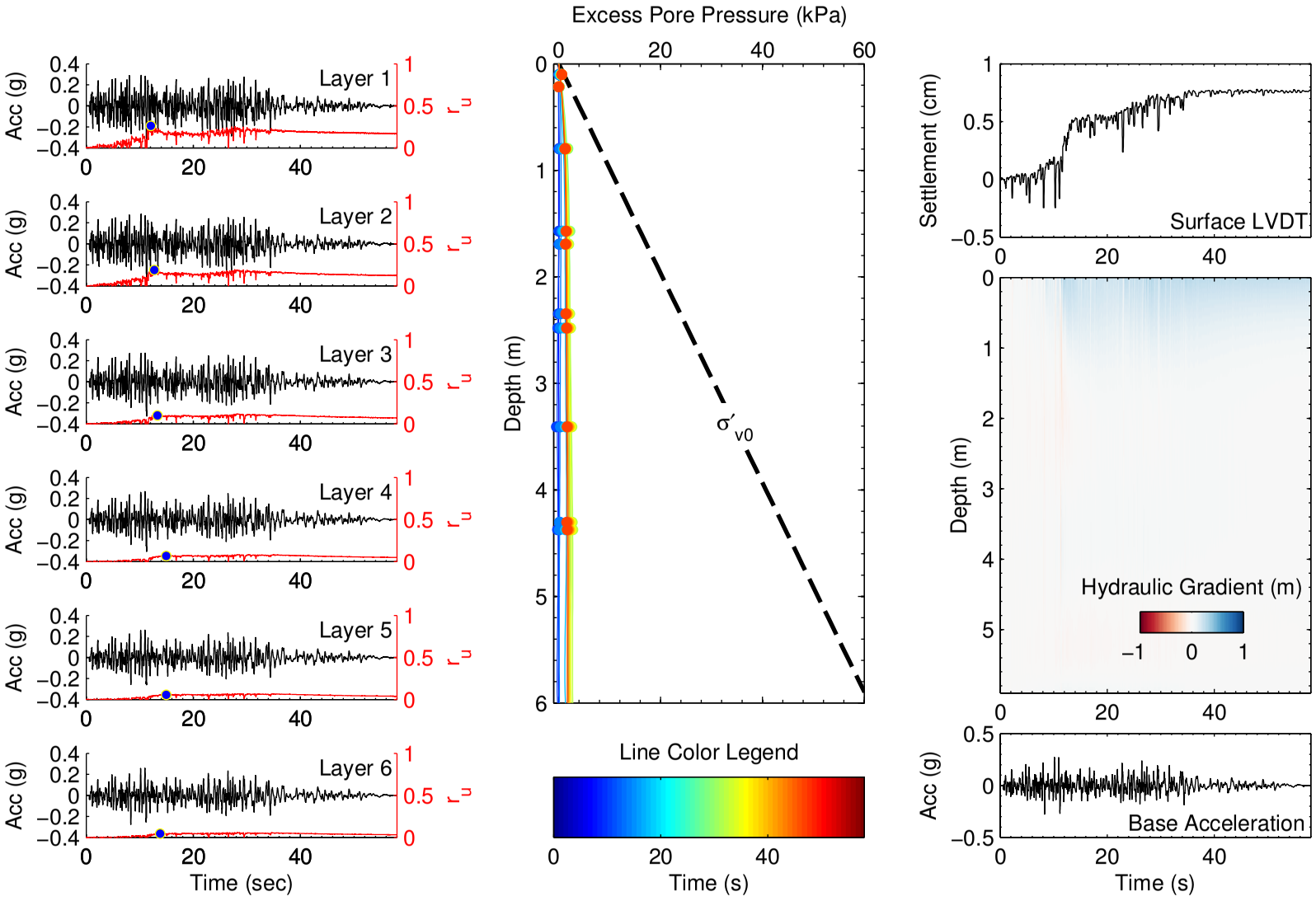
70% D_r Experiment 4 Test 21 – Data Summary Plot



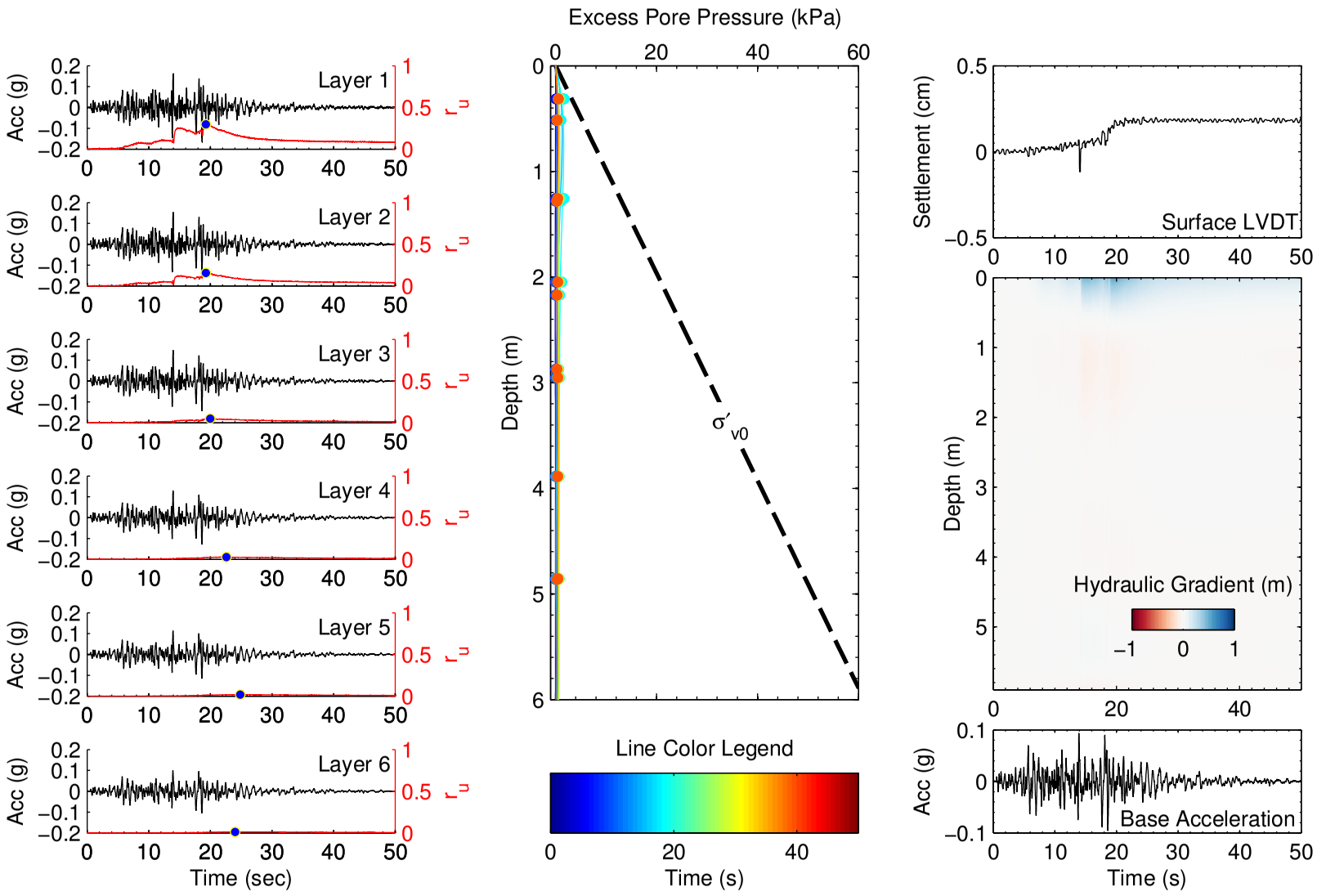
70% D_r Experiment 4 Test 22 – Data Summary Plot



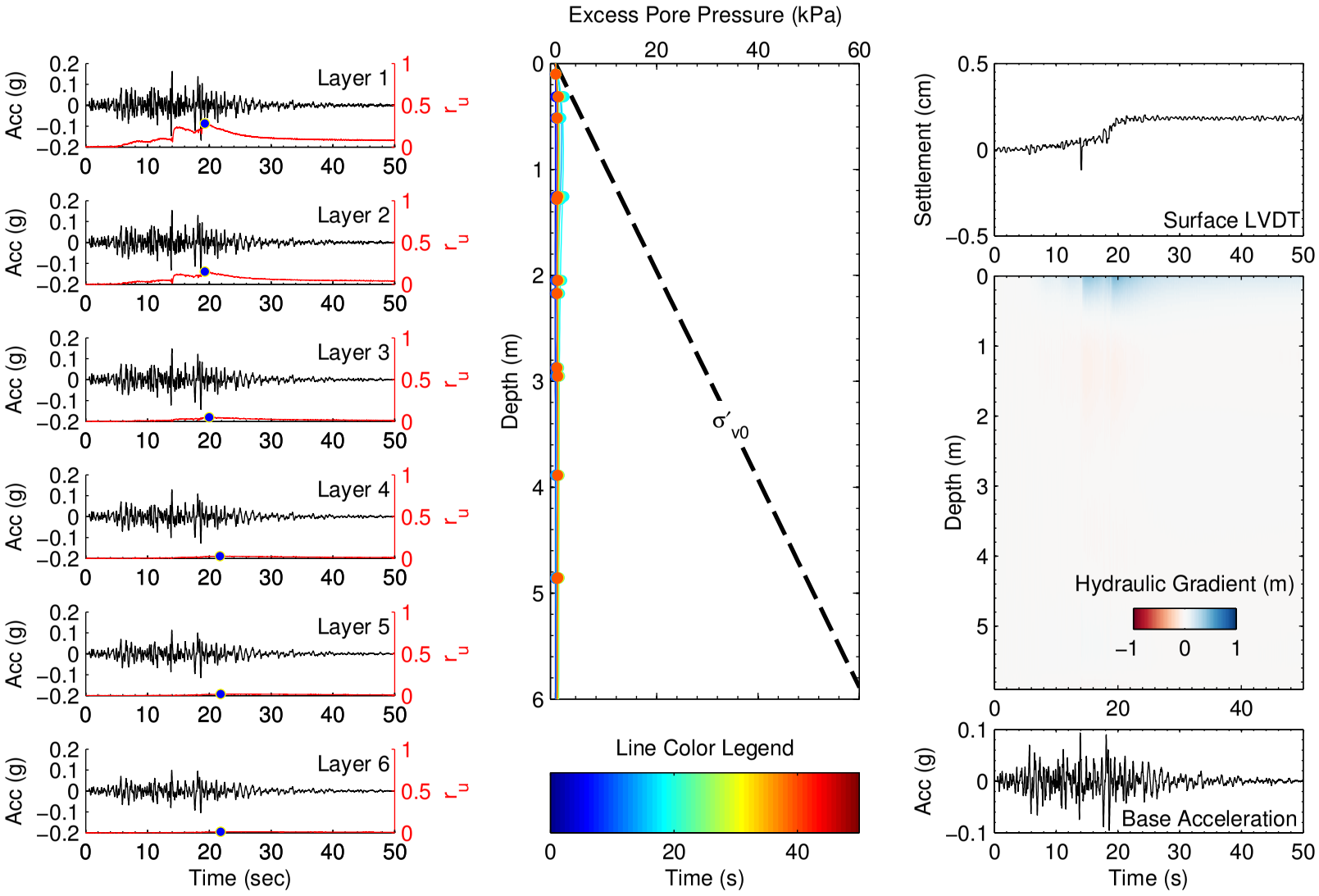
70% D_r Experiment 4 Test 23 – Data Summary Plot



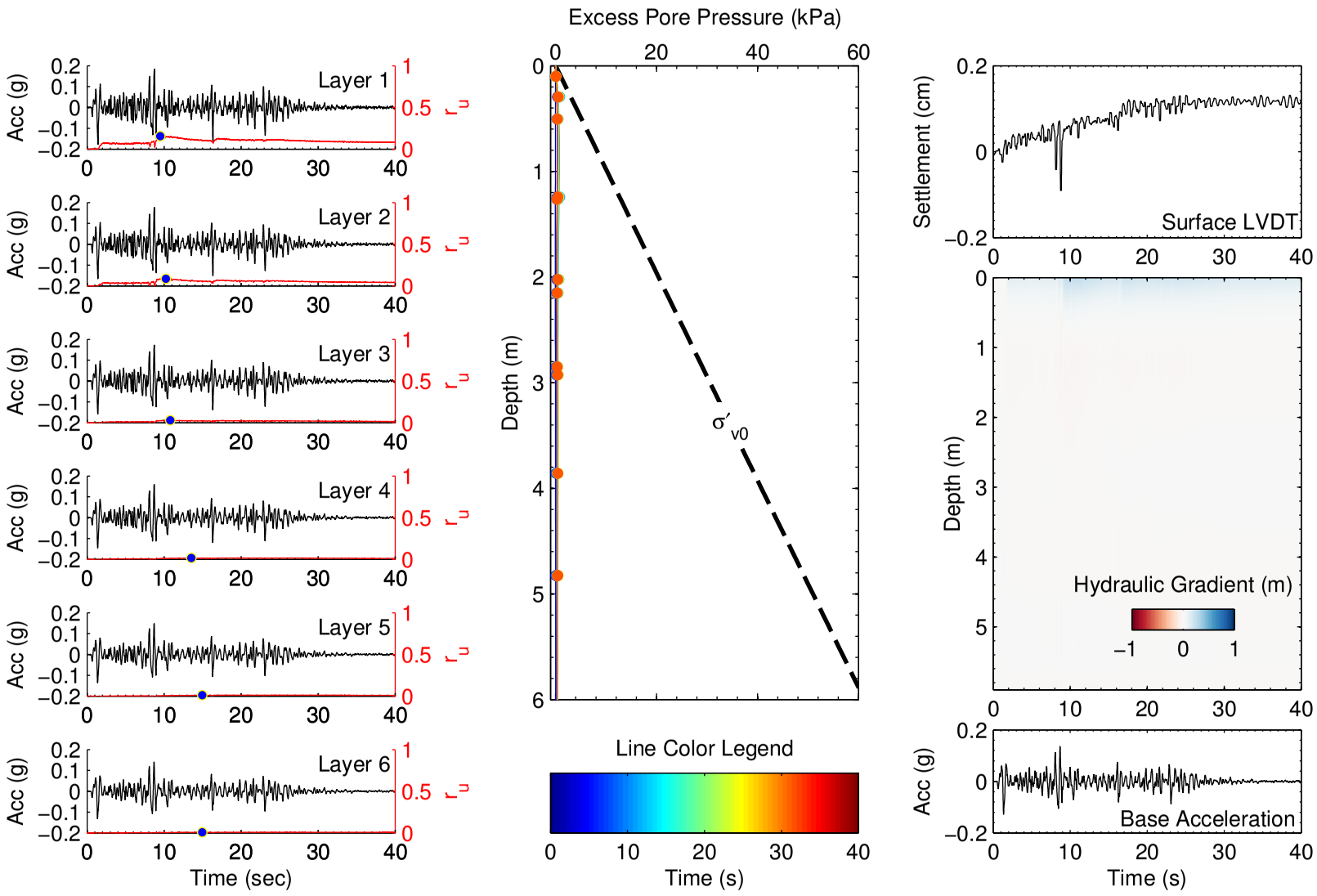
70% D_r Experiment 4 Test 24 – Data Summary Plot



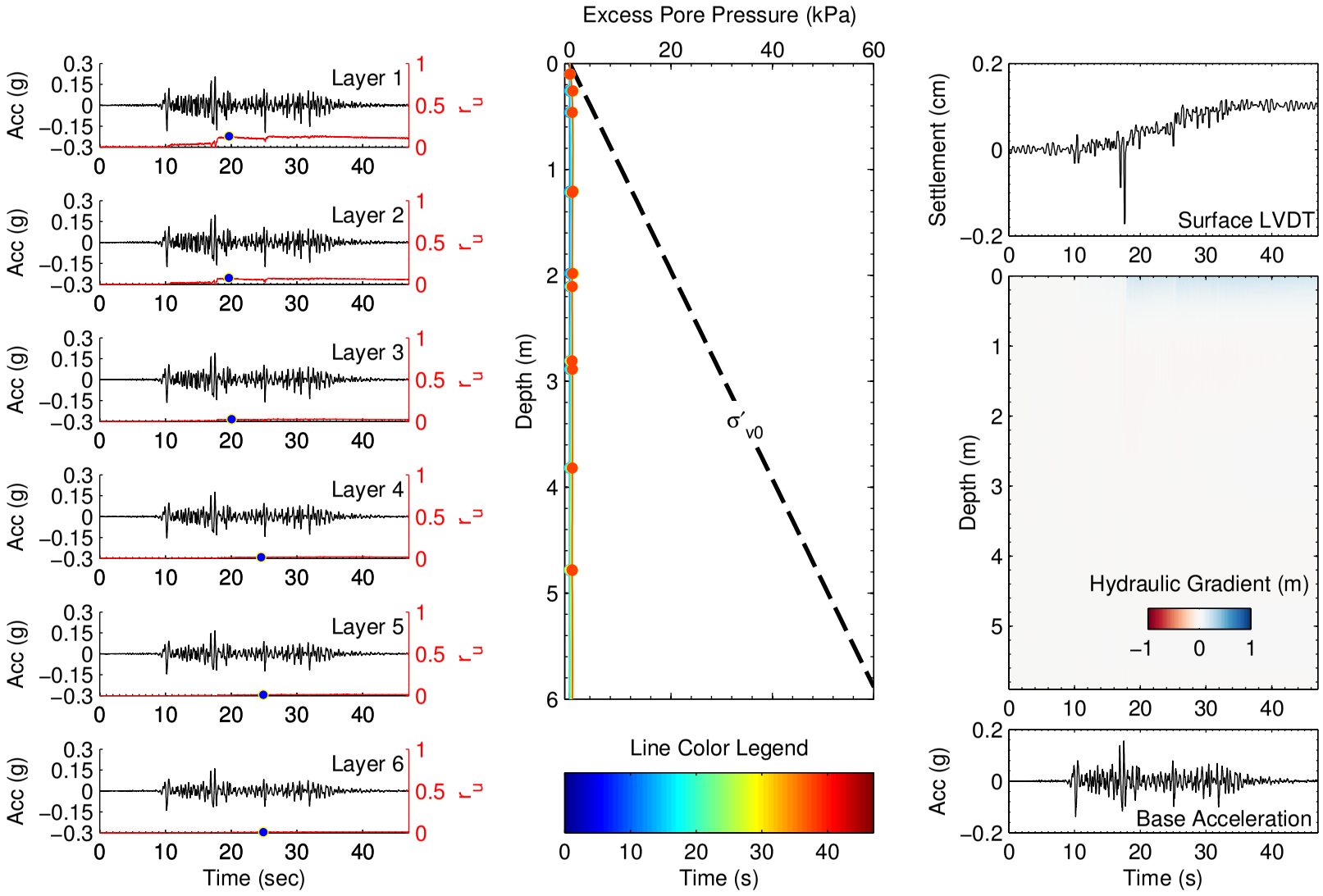
70% D_r Experiment 4 Test 25 – Data Summary Plot



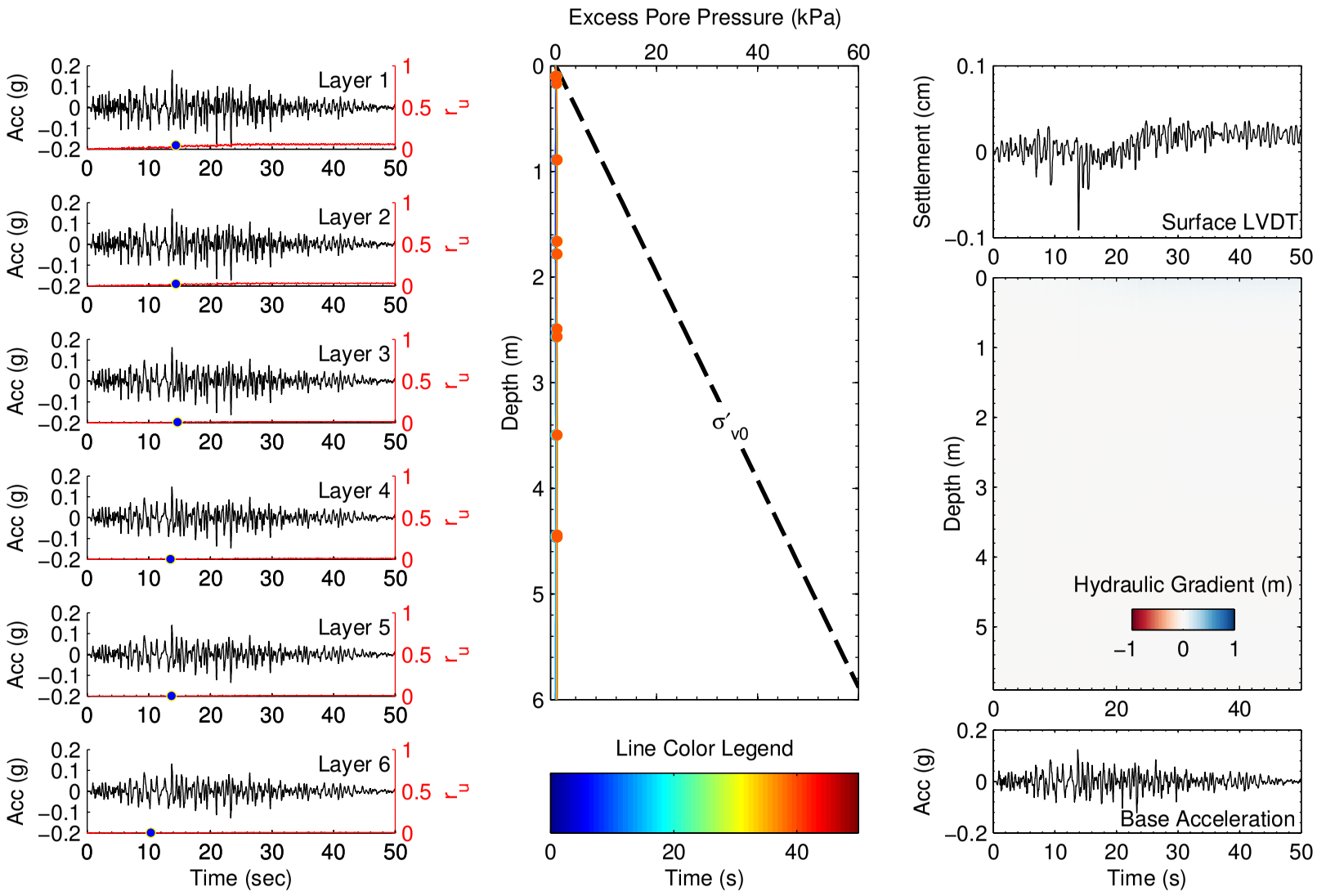
70% D_r Experiment 4 Test 26 – Data Summary Plot



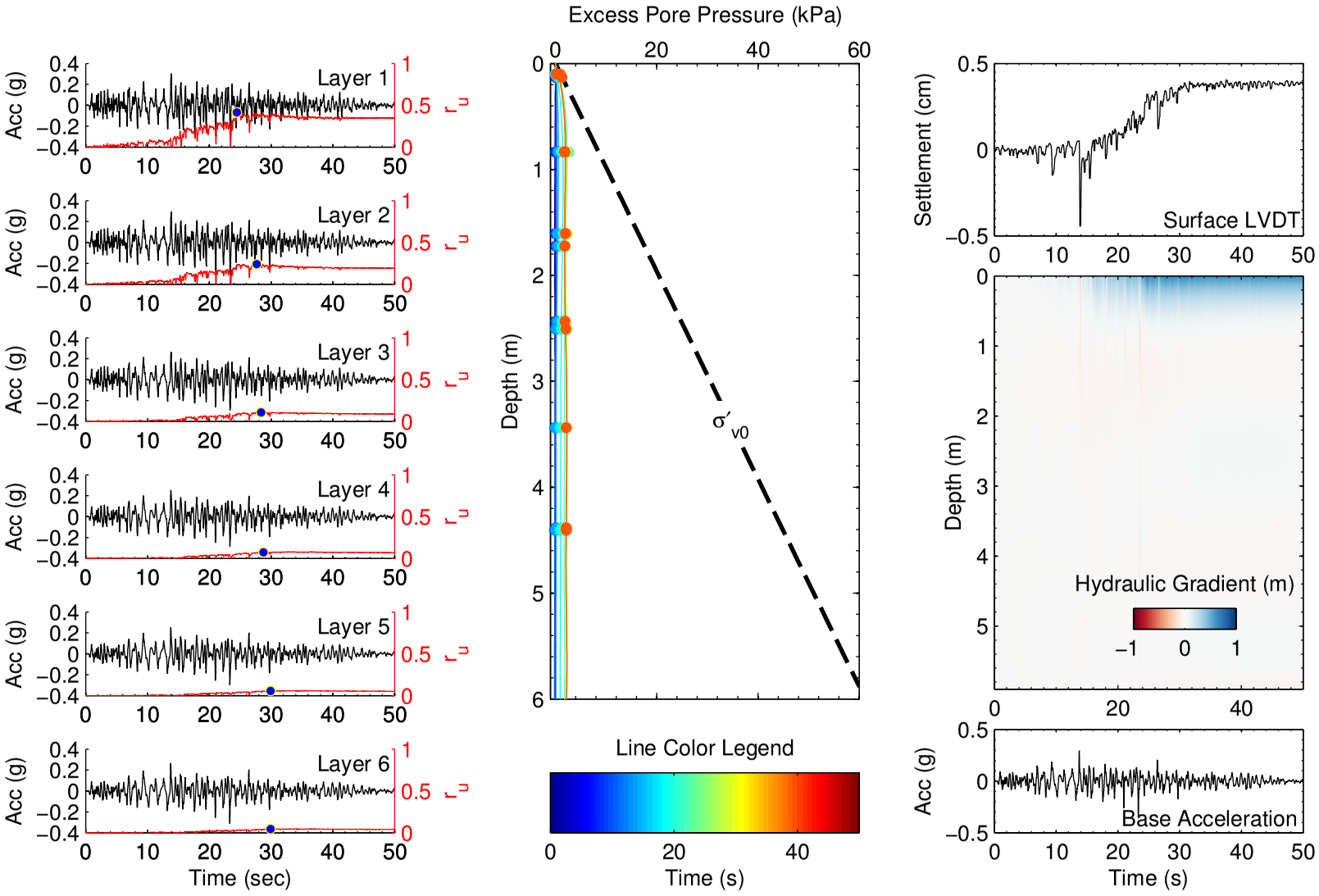
70% D_r Experiment 4 Test 27 – Data Summary Plot



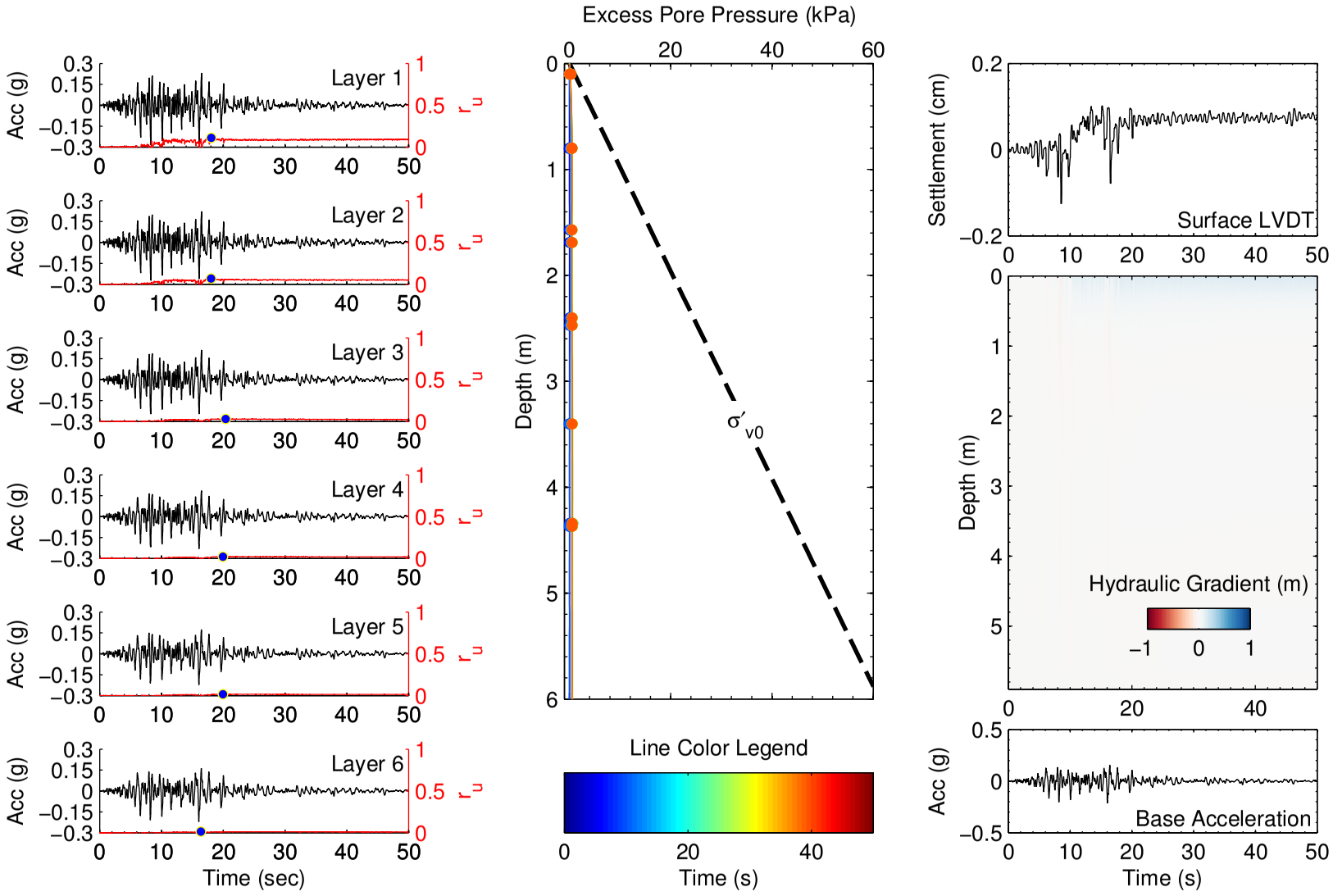
70% D_r Experiment 4 Test 28 – Data Summary Plot



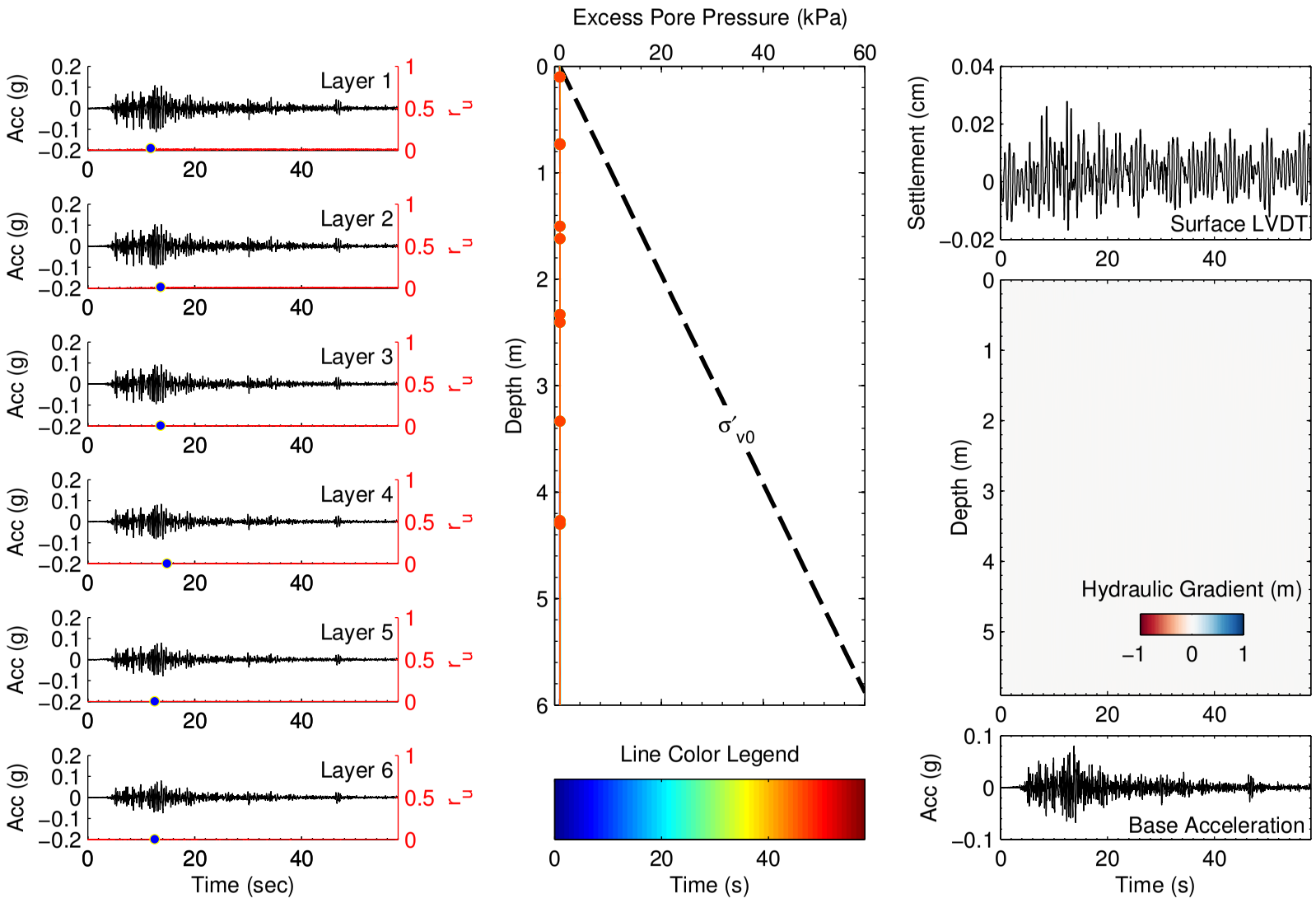
70% D_r Experiment 4 Test 29 – Data Summary Plot



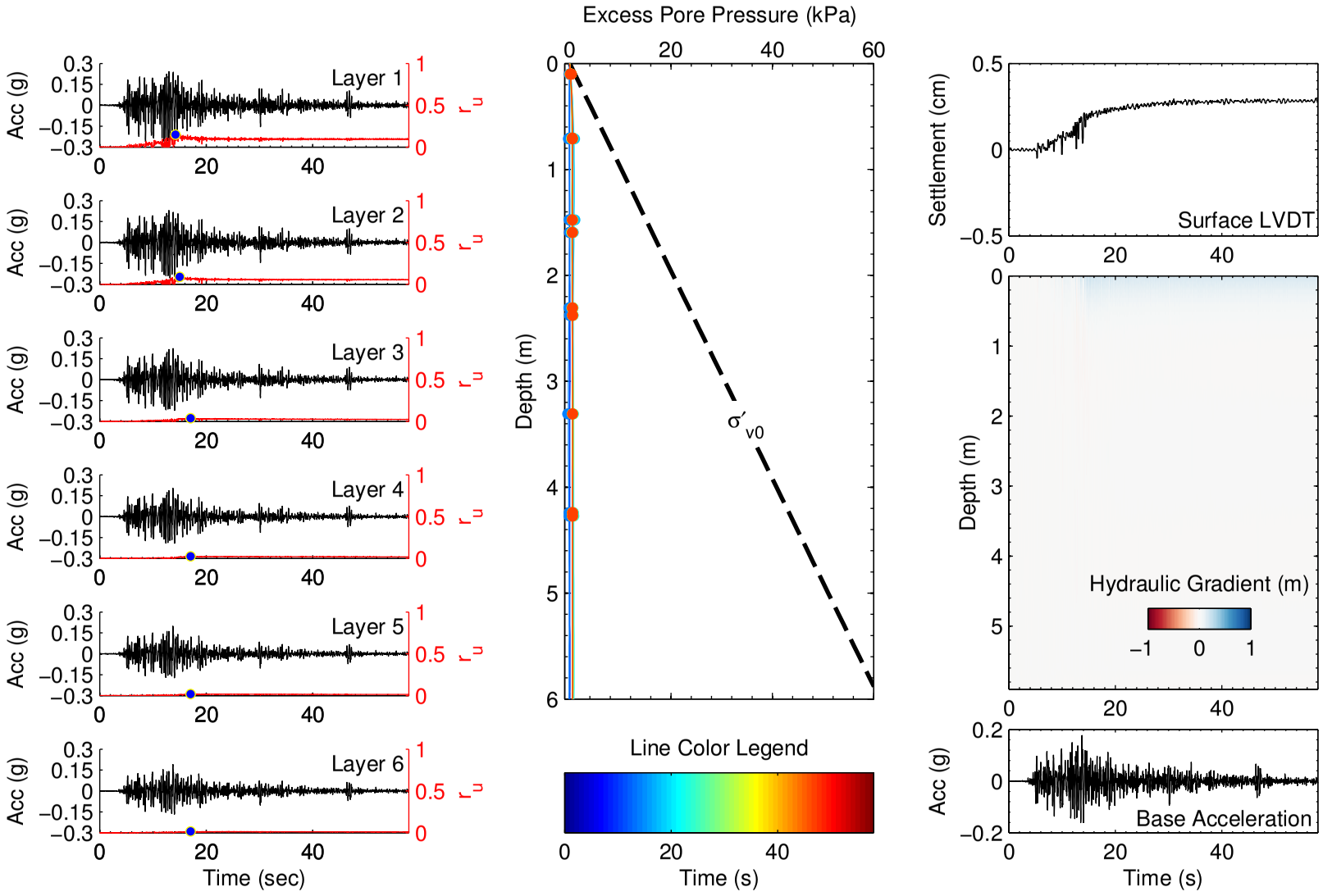
70% D_r Experiment 4 Test 30 – Data Summary Plot



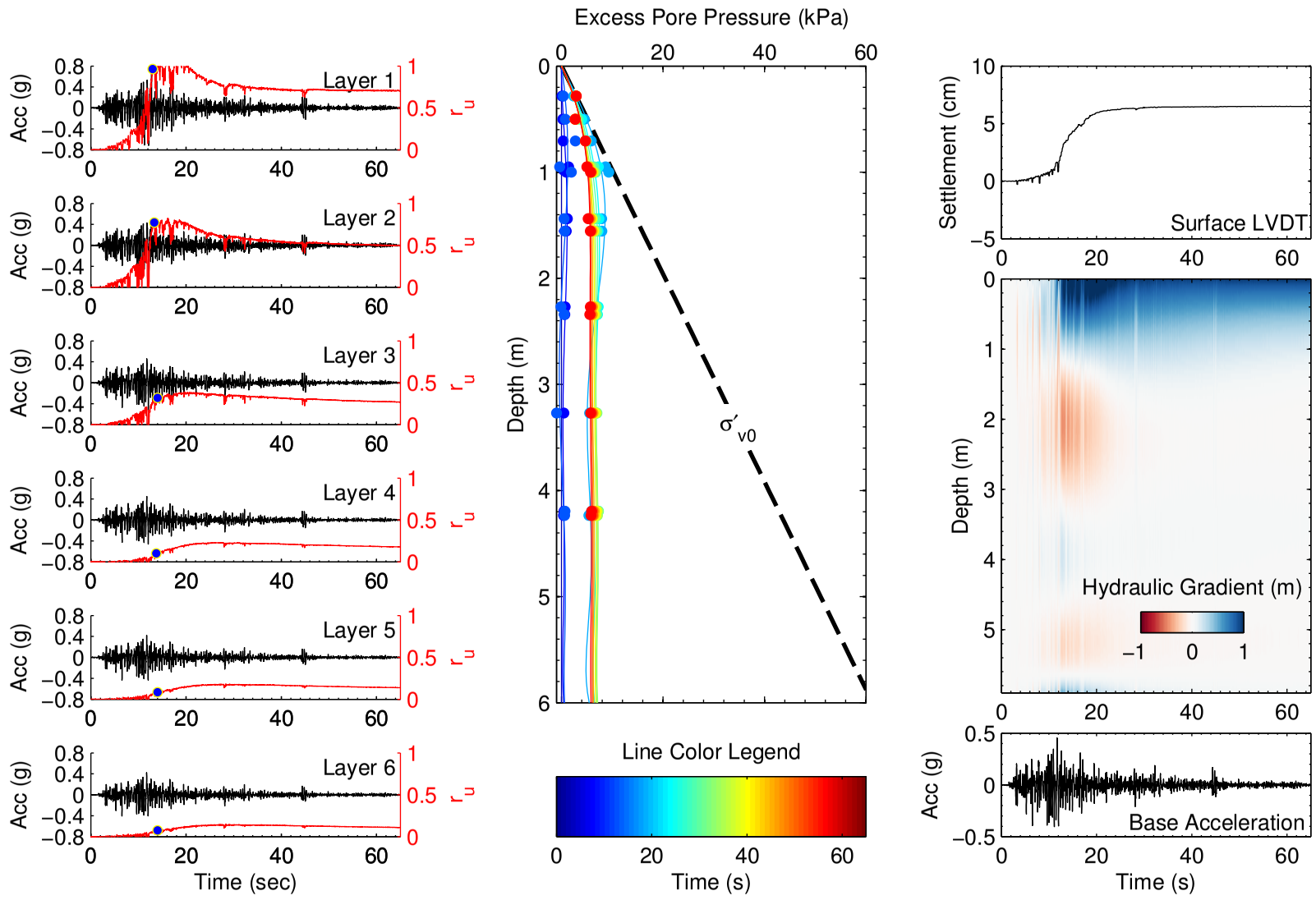
70% D_r Experiment 4 Test 31 – Data Summary Plot



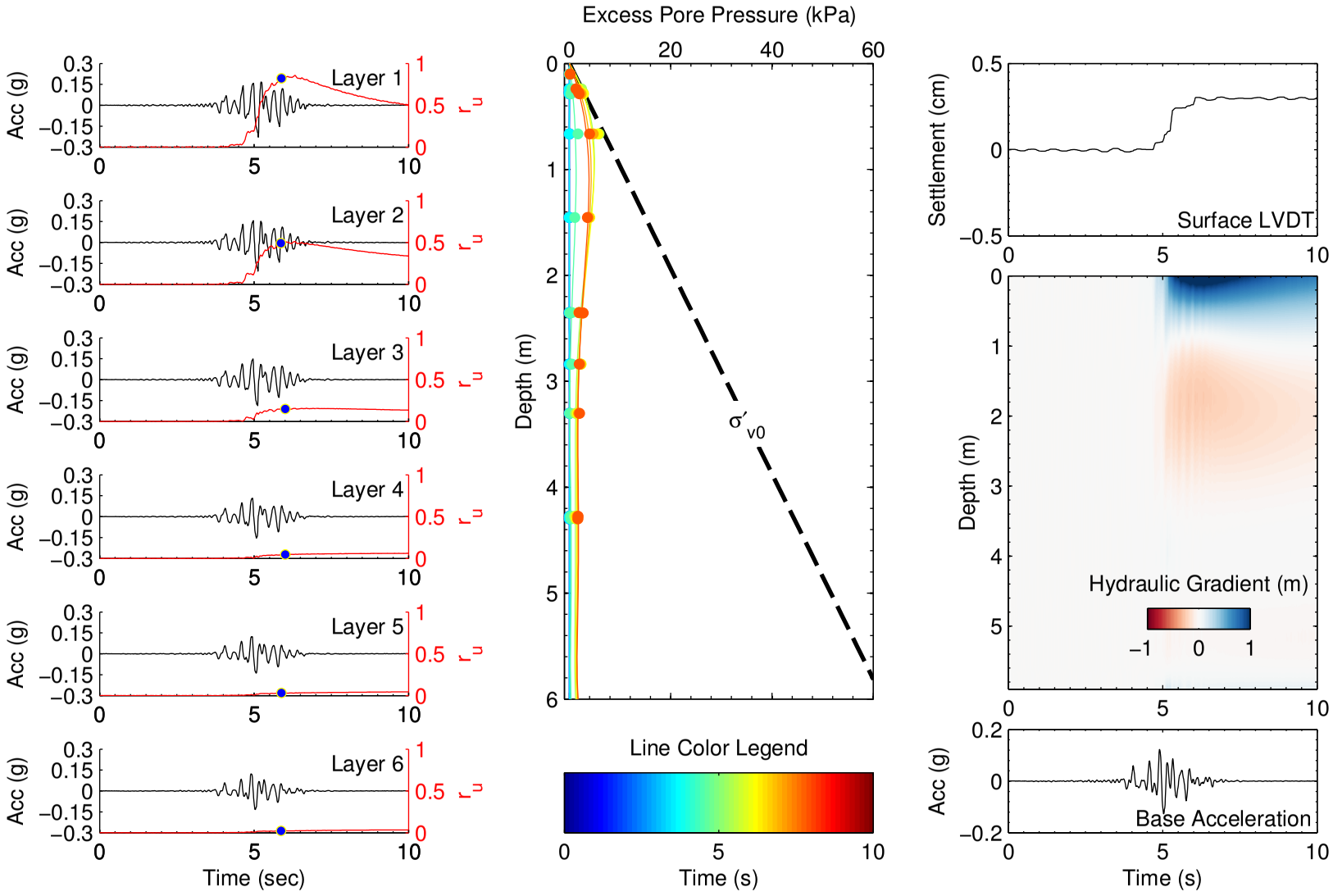
70% D_r Experiment 4 Test 32 – Data Summary Plot



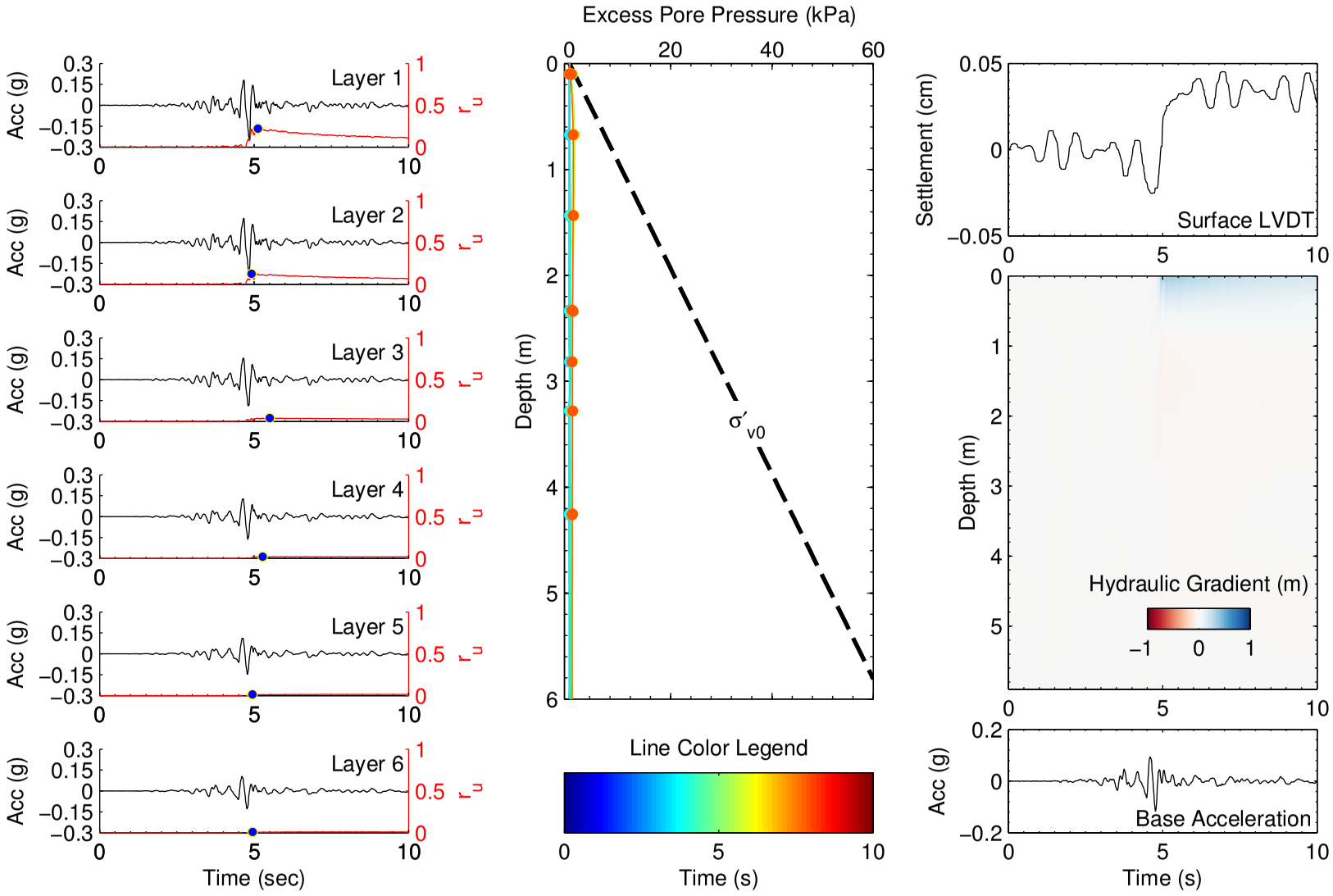
70% D_r Experiment 4 Test 33 – Data Summary Plot



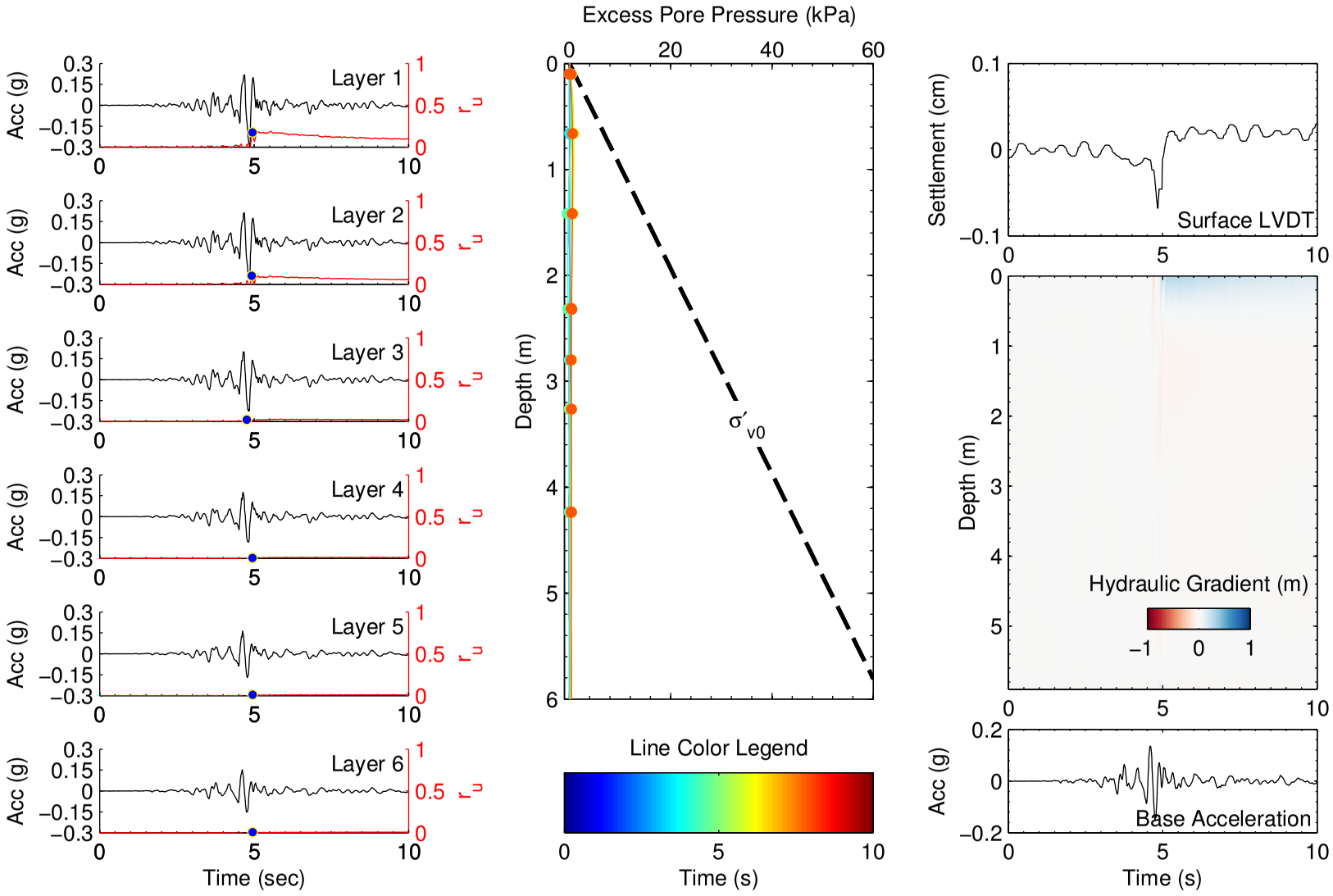
70% D_r Experiment 4 Test 34 – Data Summary Plot



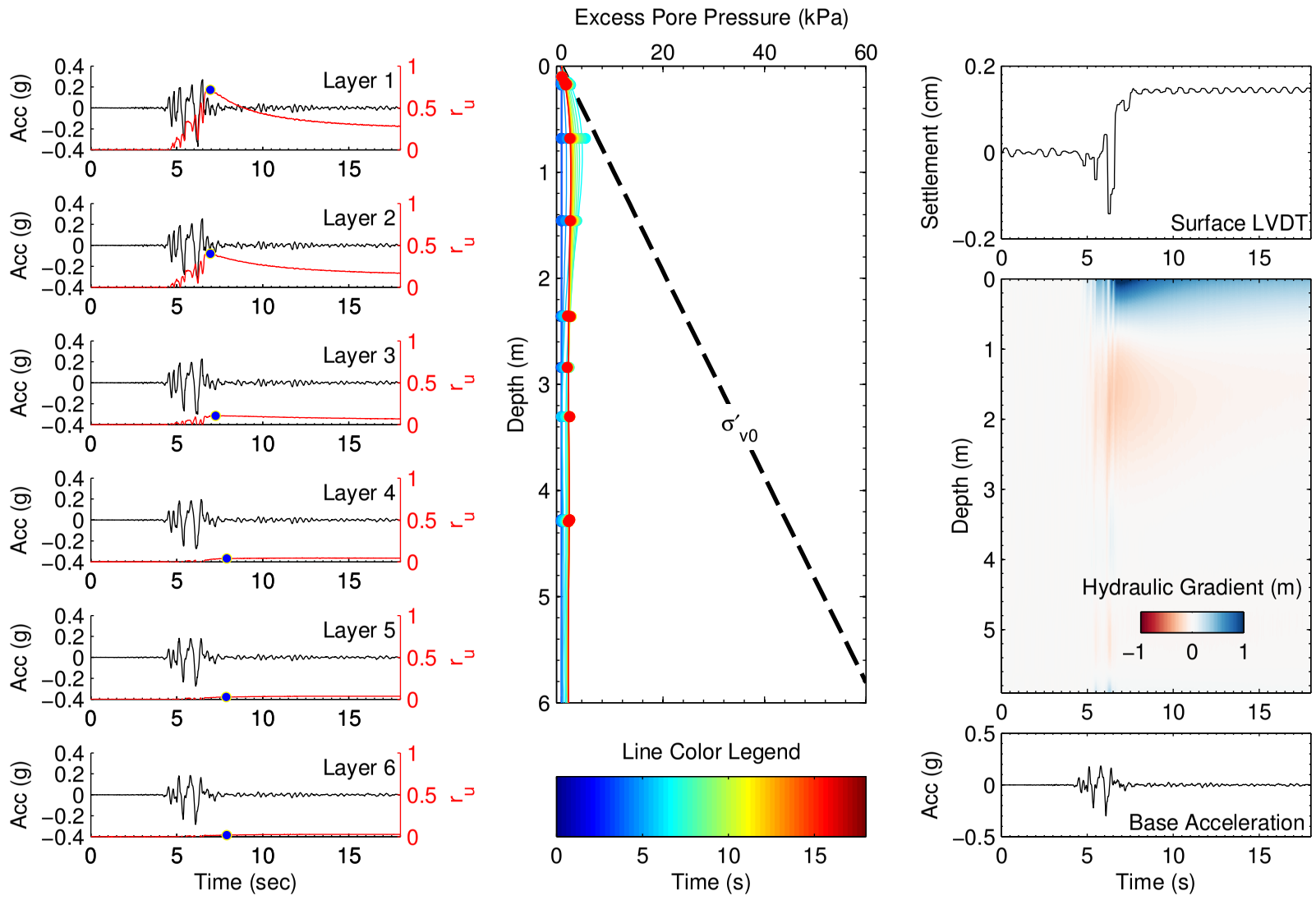
70% D_r Experiment 4 Test 35 – Data Summary Plot



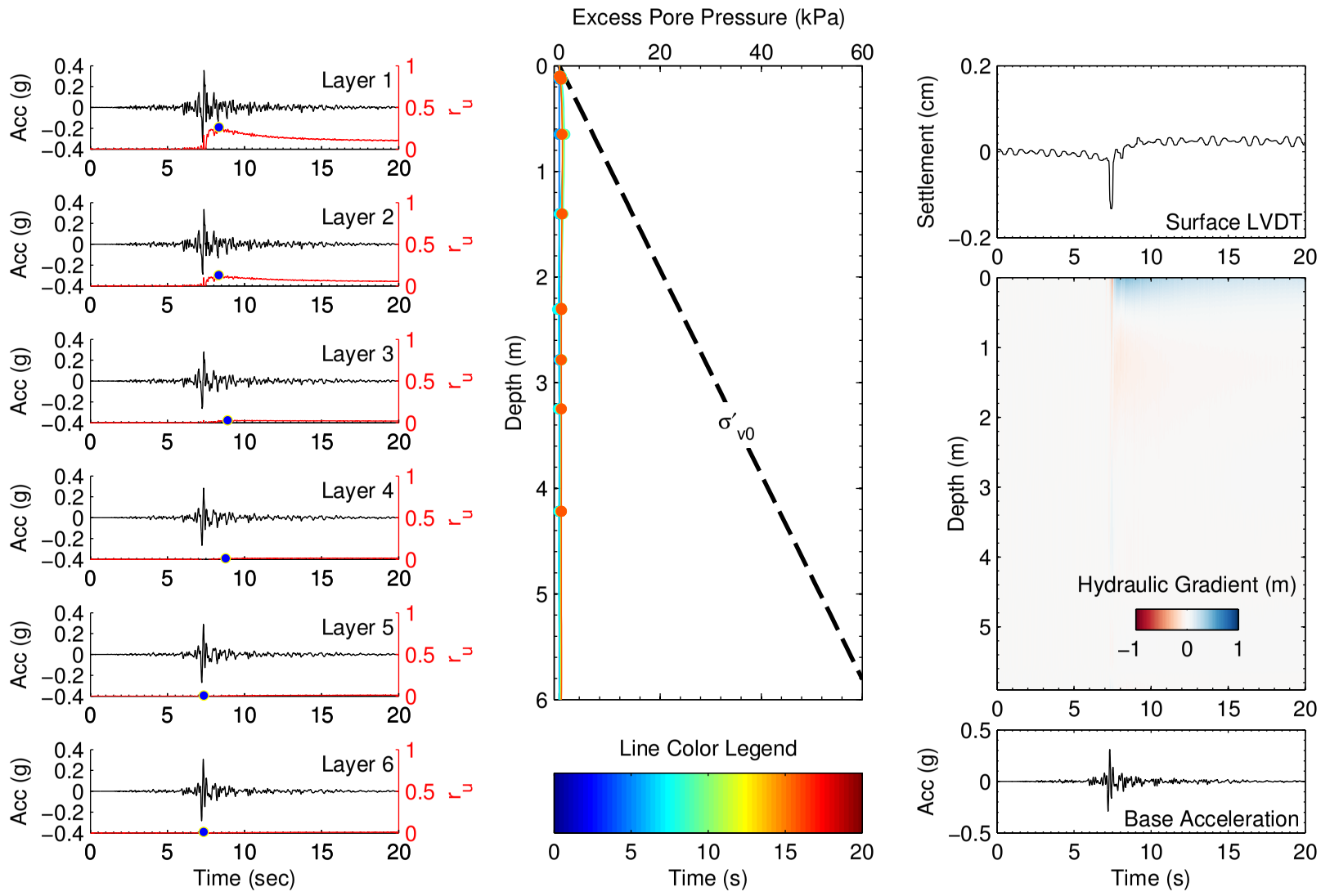
70% D_r Experiment 4 Test 36 – Data Summary Plot



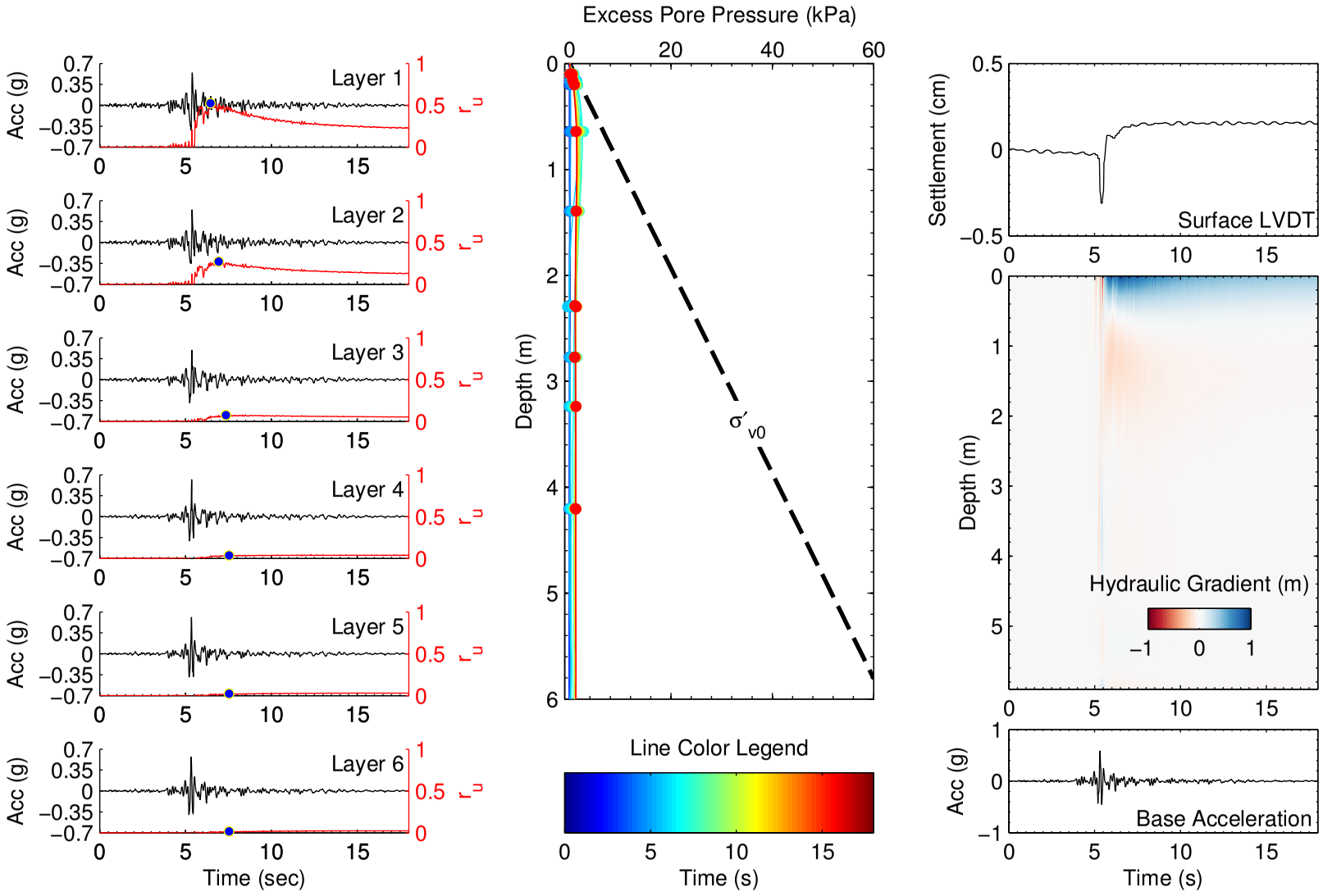
70% D_r Experiment 4 Test 37 – Data Summary Plot



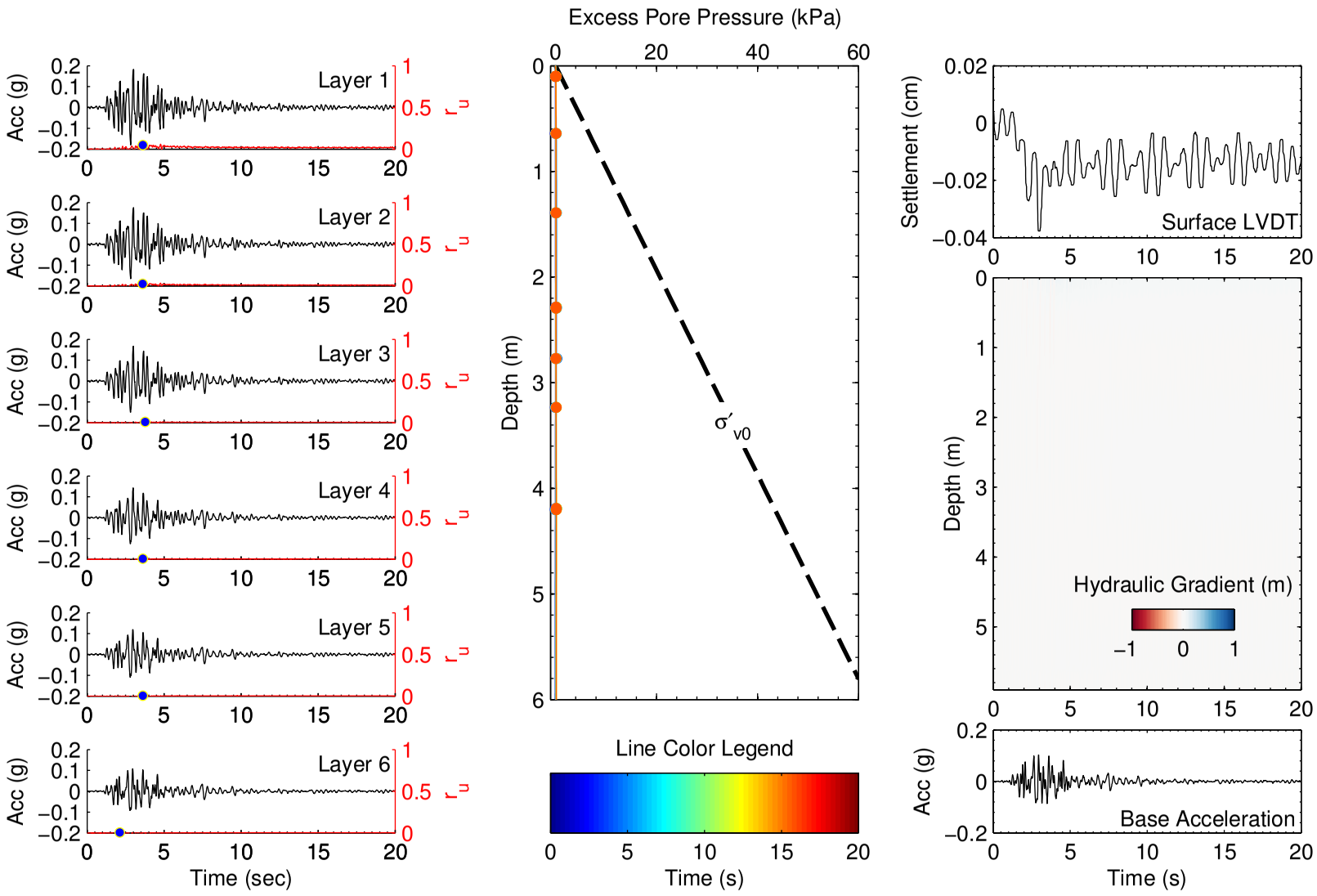
70% D_r Experiment 4 Test 38 – Data Summary Plot



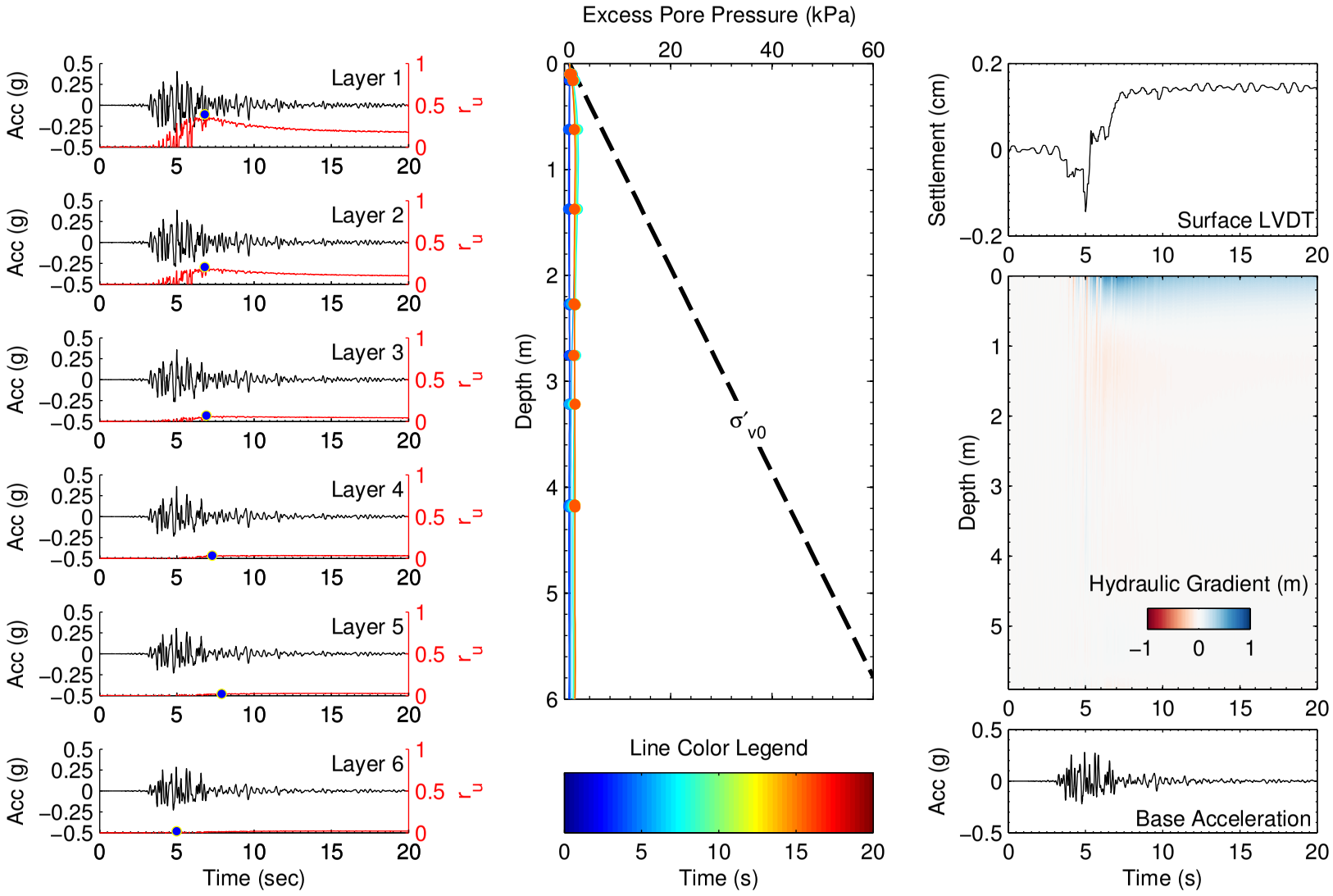
70% D_r Experiment 4 Test 39 – Data Summary Plot



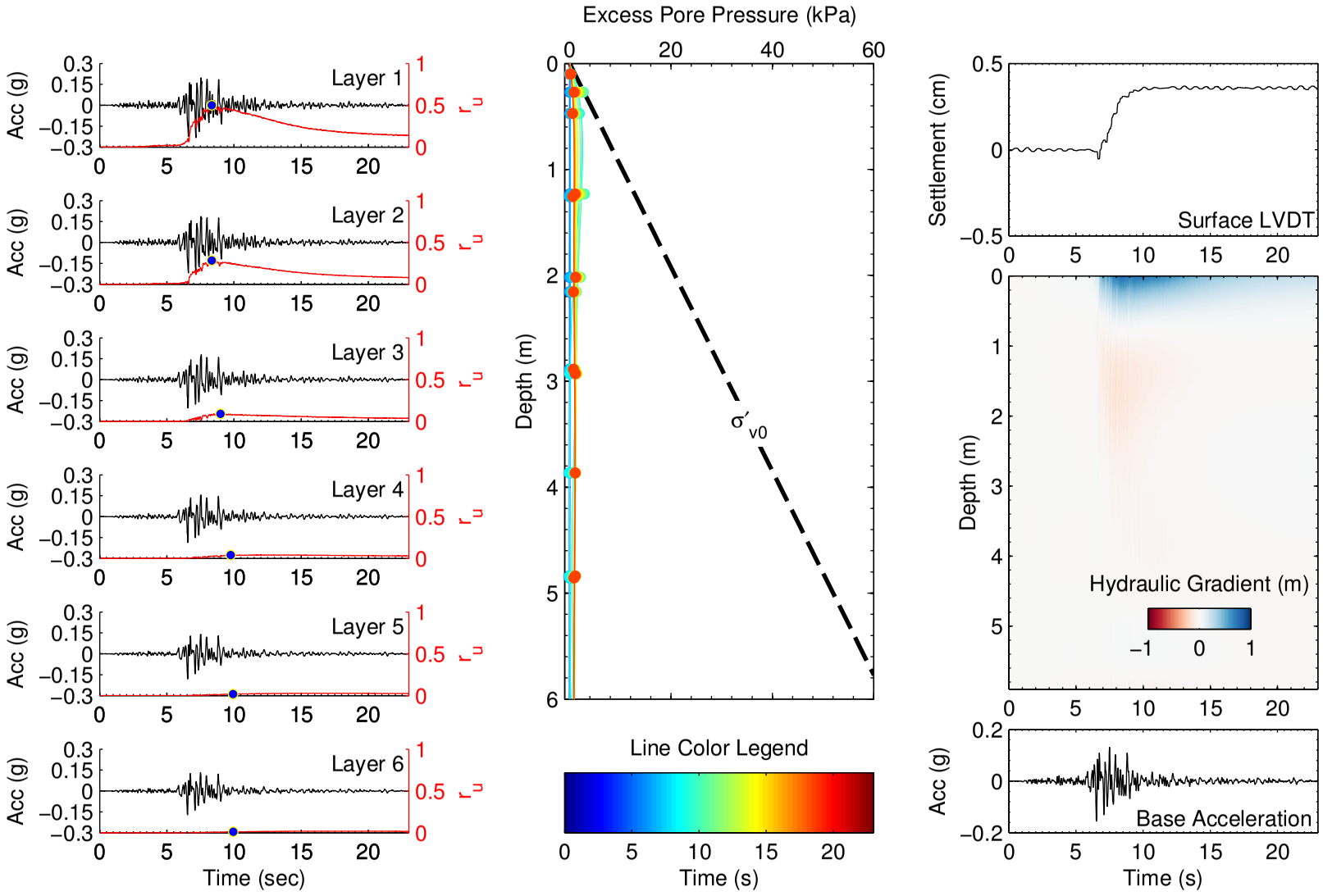
70% D_r Experiment 4 Test 40 – Data Summary Plot



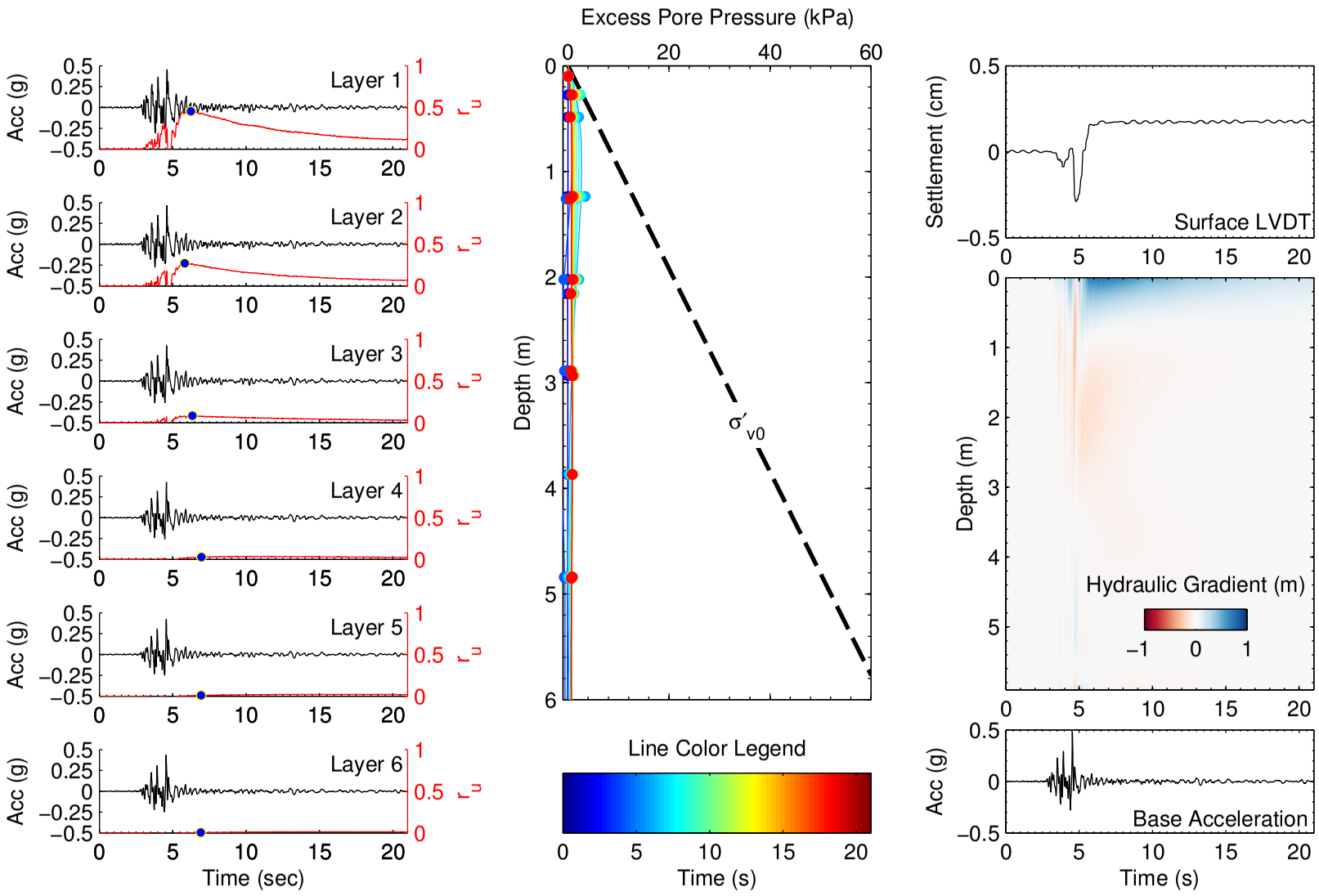
70% D_r Experiment 4 Test 41 – Data Summary Plot



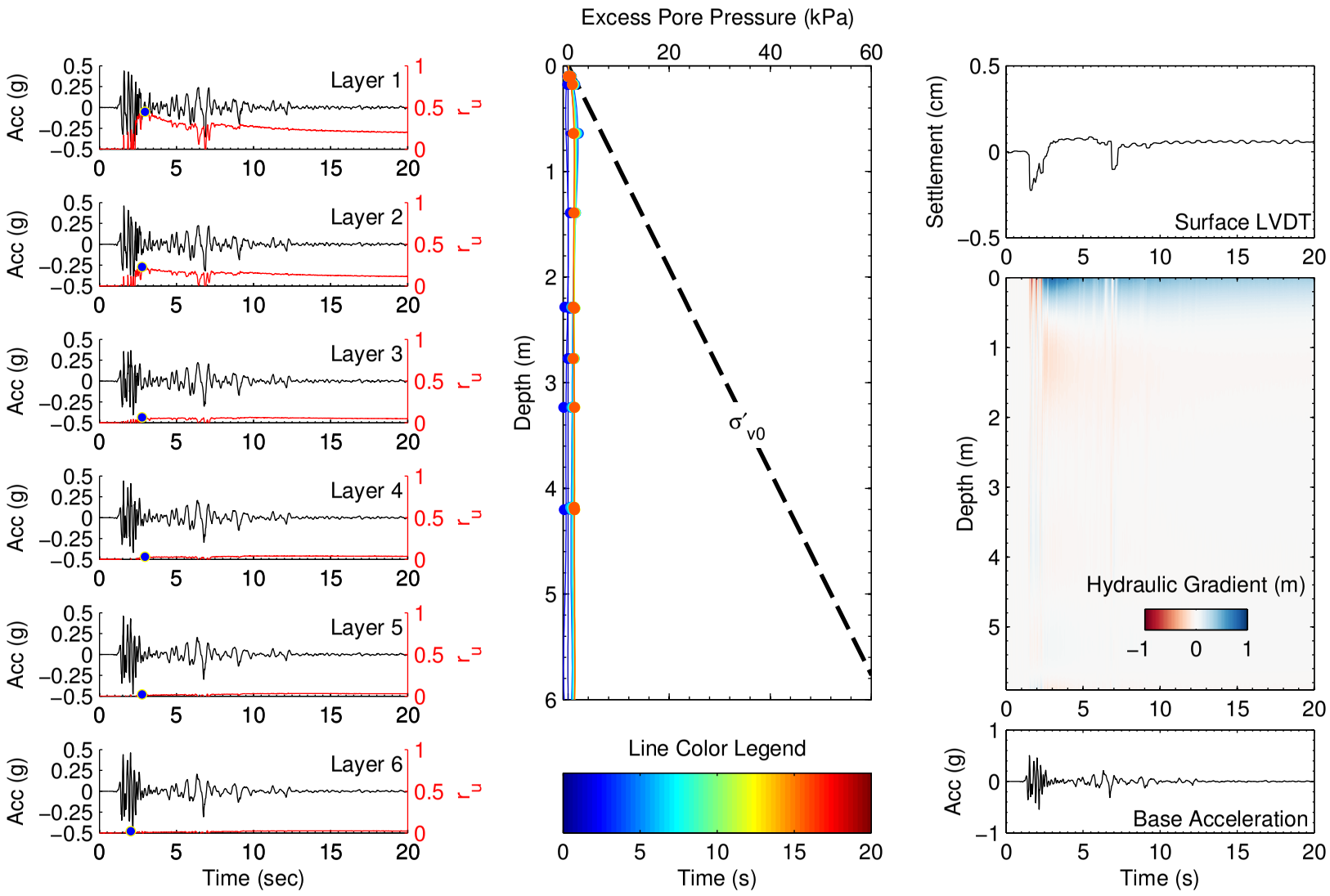
70% D_r Experiment 4 Test 42 – Data Summary Plot



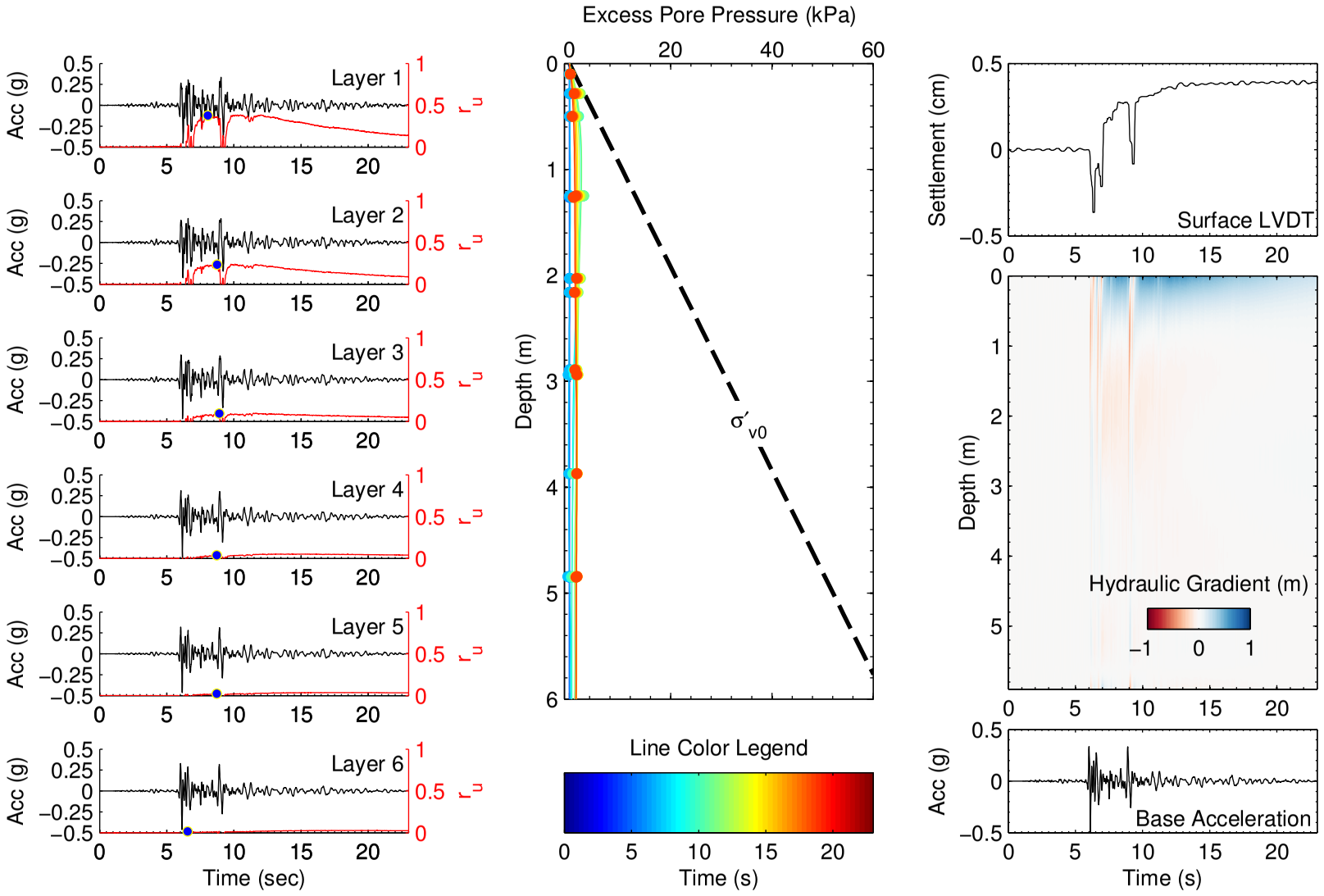
70% D_r Experiment 4 Test 43 – Data Summary Plot



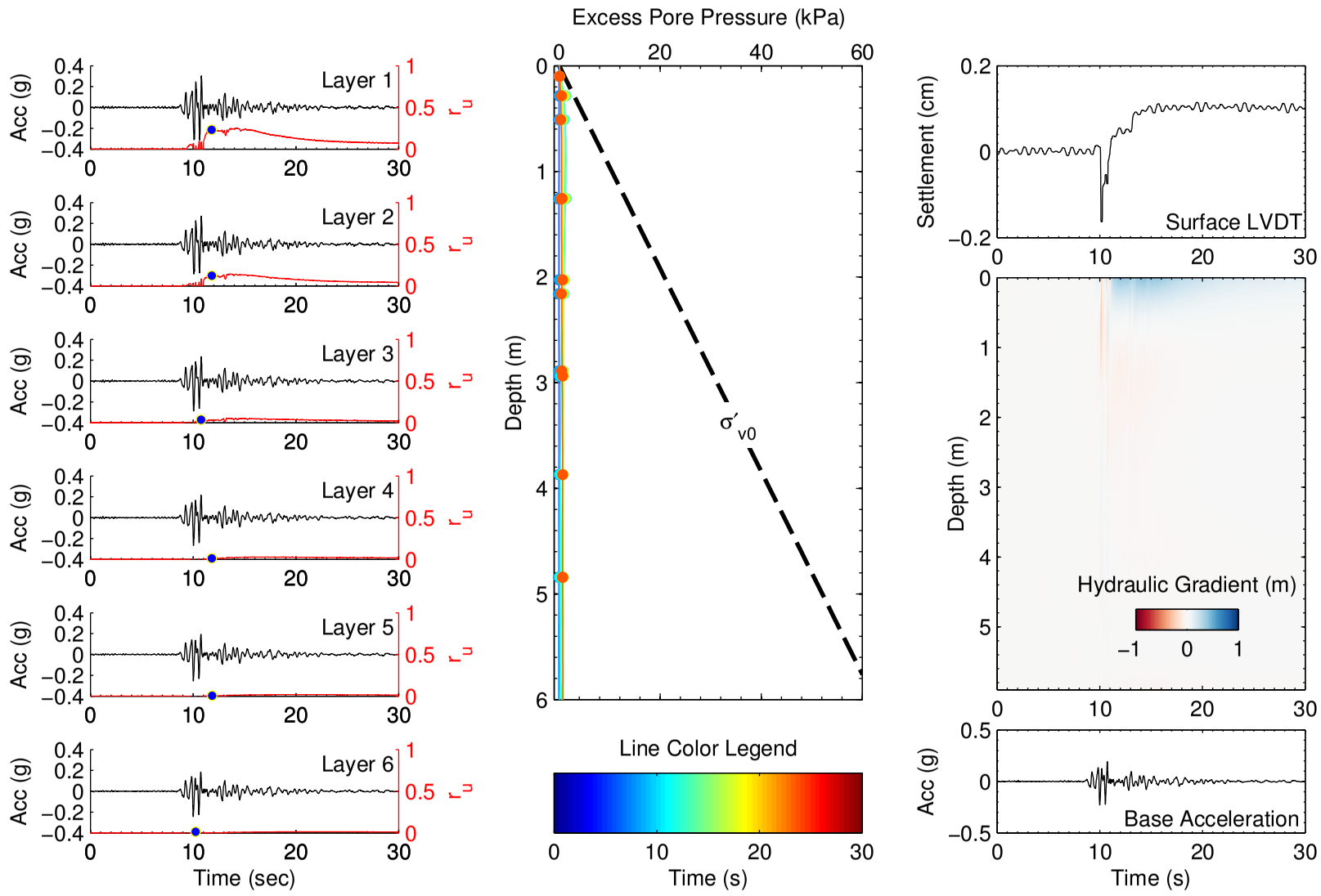
70% D_r Experiment 4 Test 44 – Data Summary Plot



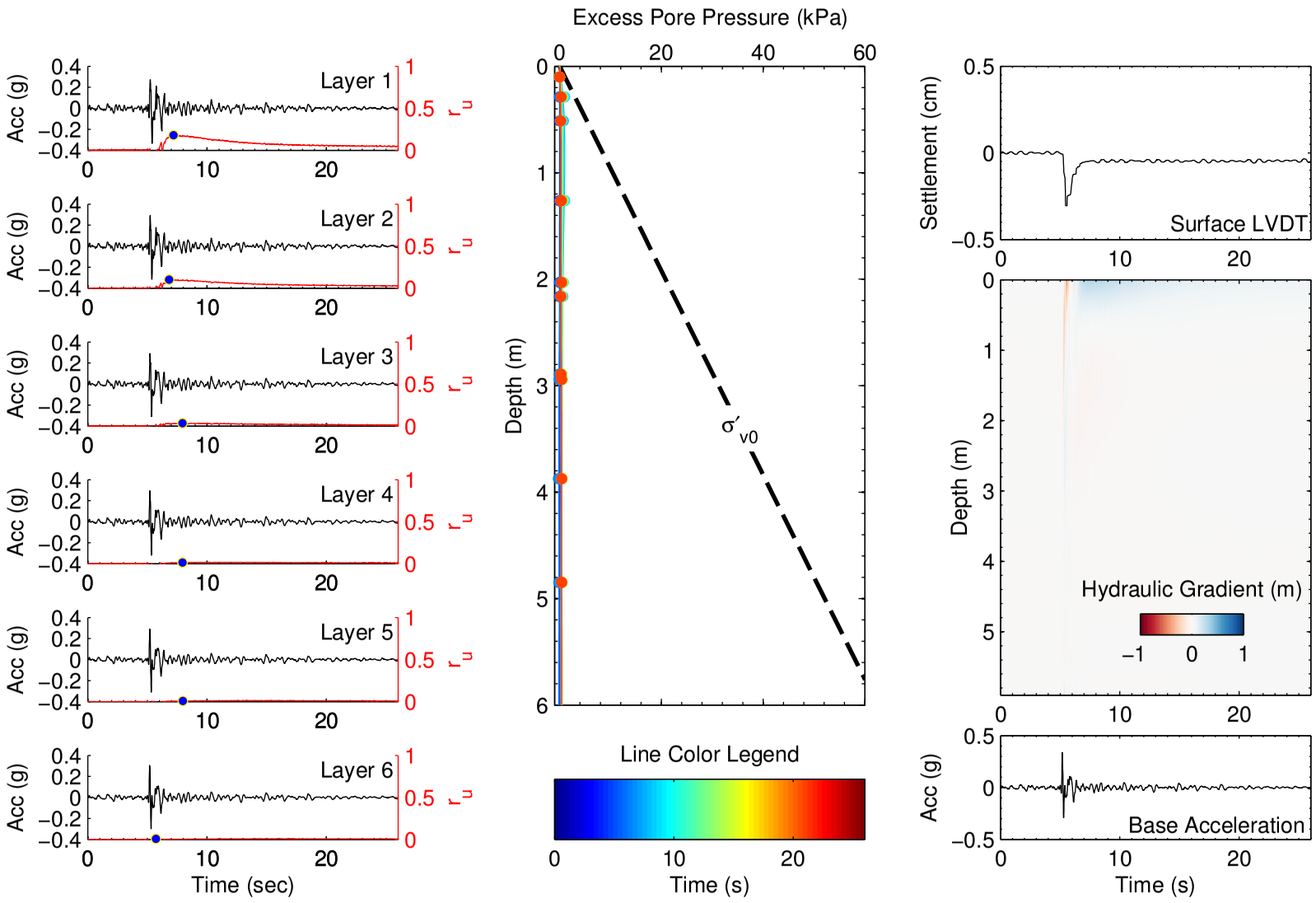
70% D_r Experiment 4 Test 45 – Data Summary Plot



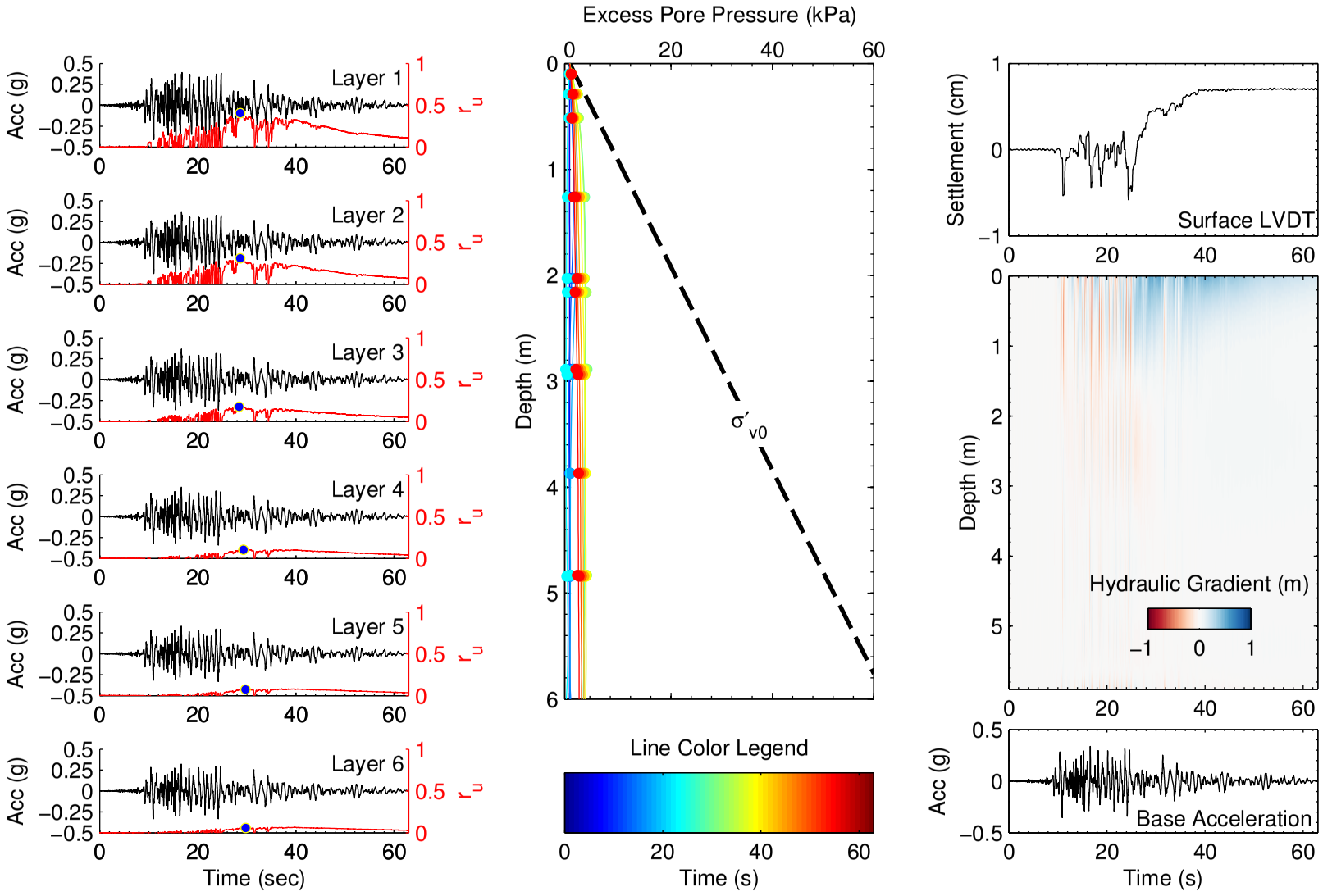
70% D_r Experiment 4 Test 46 – Data Summary Plot



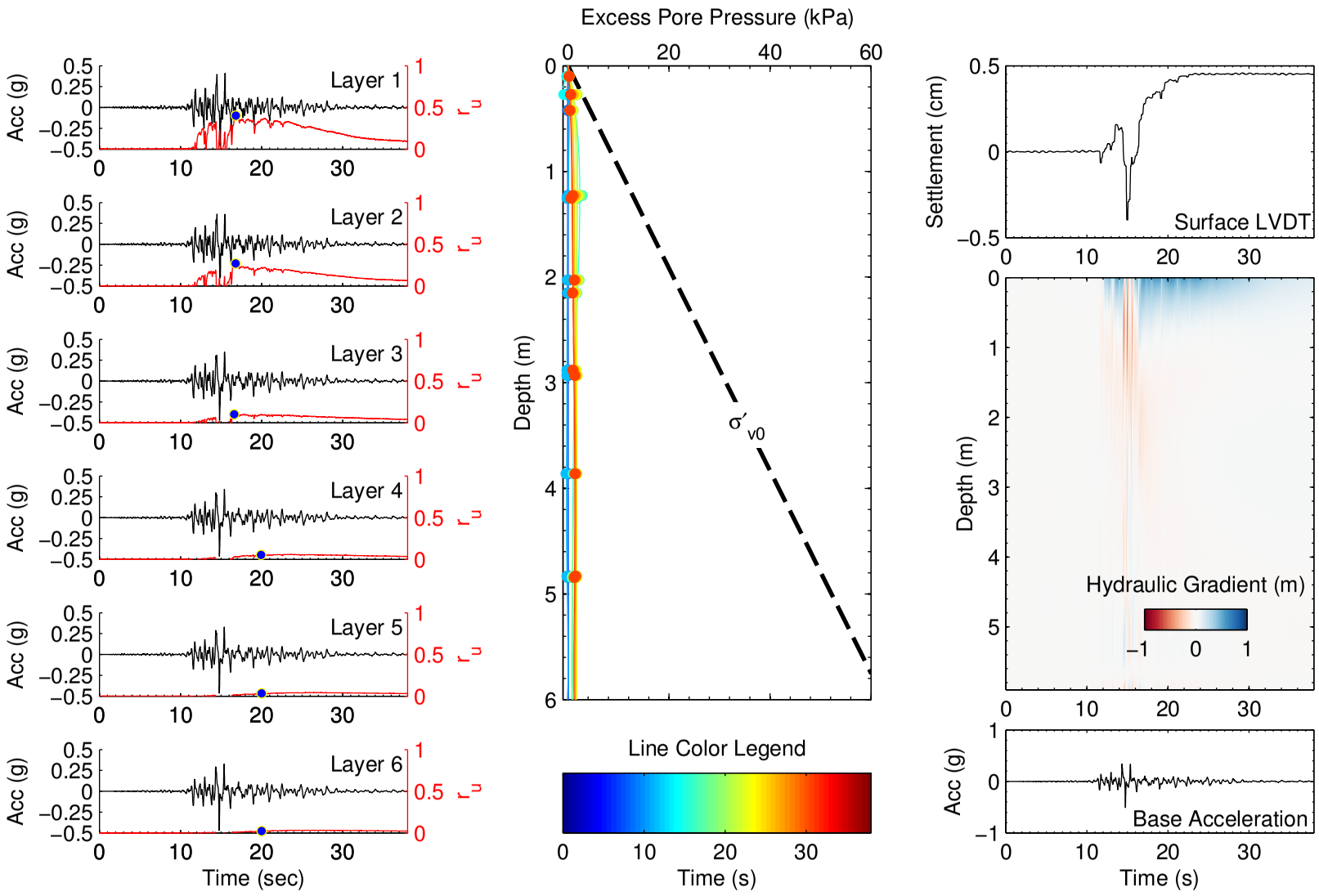
70% D_r Experiment 4 Test 47 – Data Summary Plot



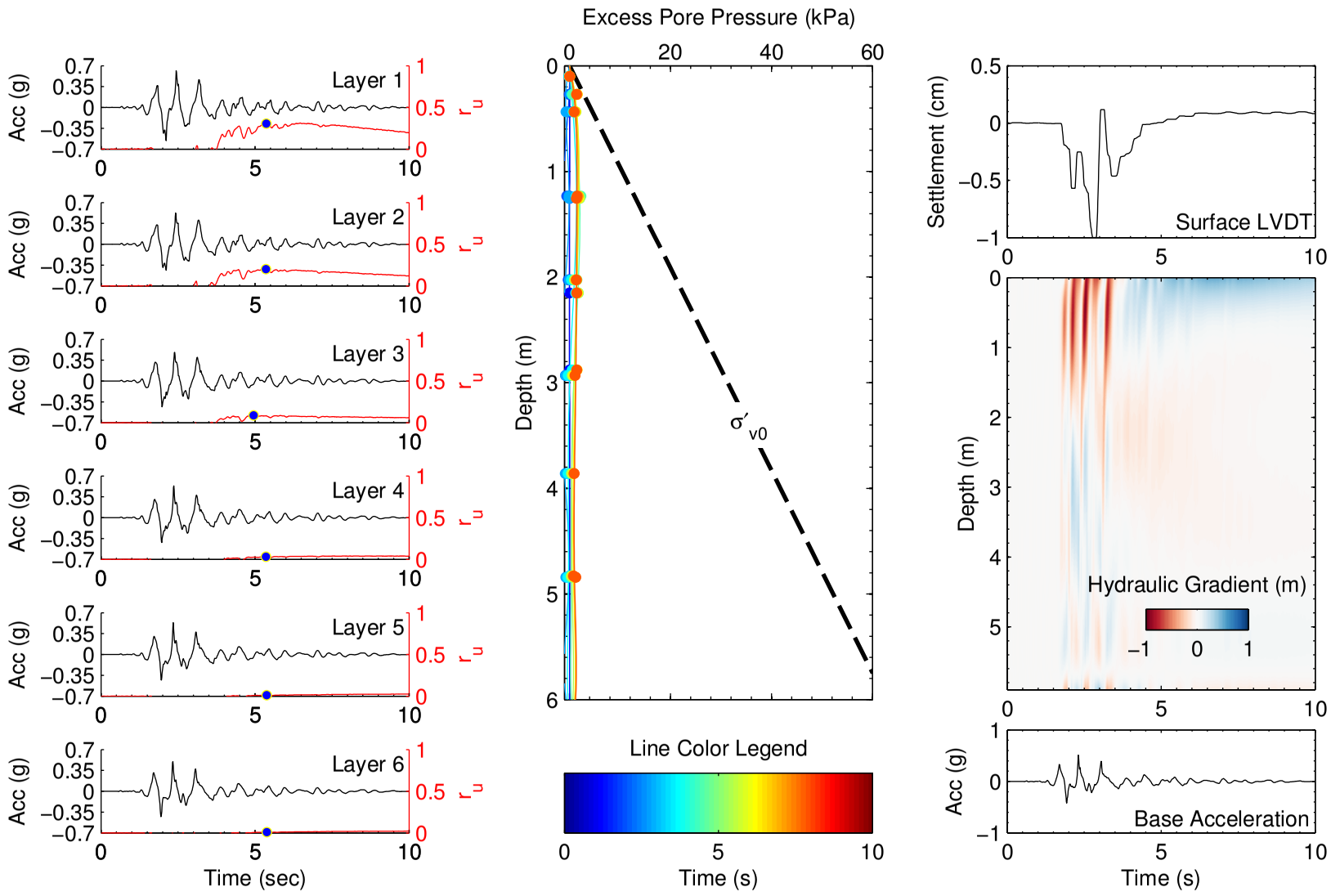
70% D_r Experiment 4 Test 48 – Data Summary Plot



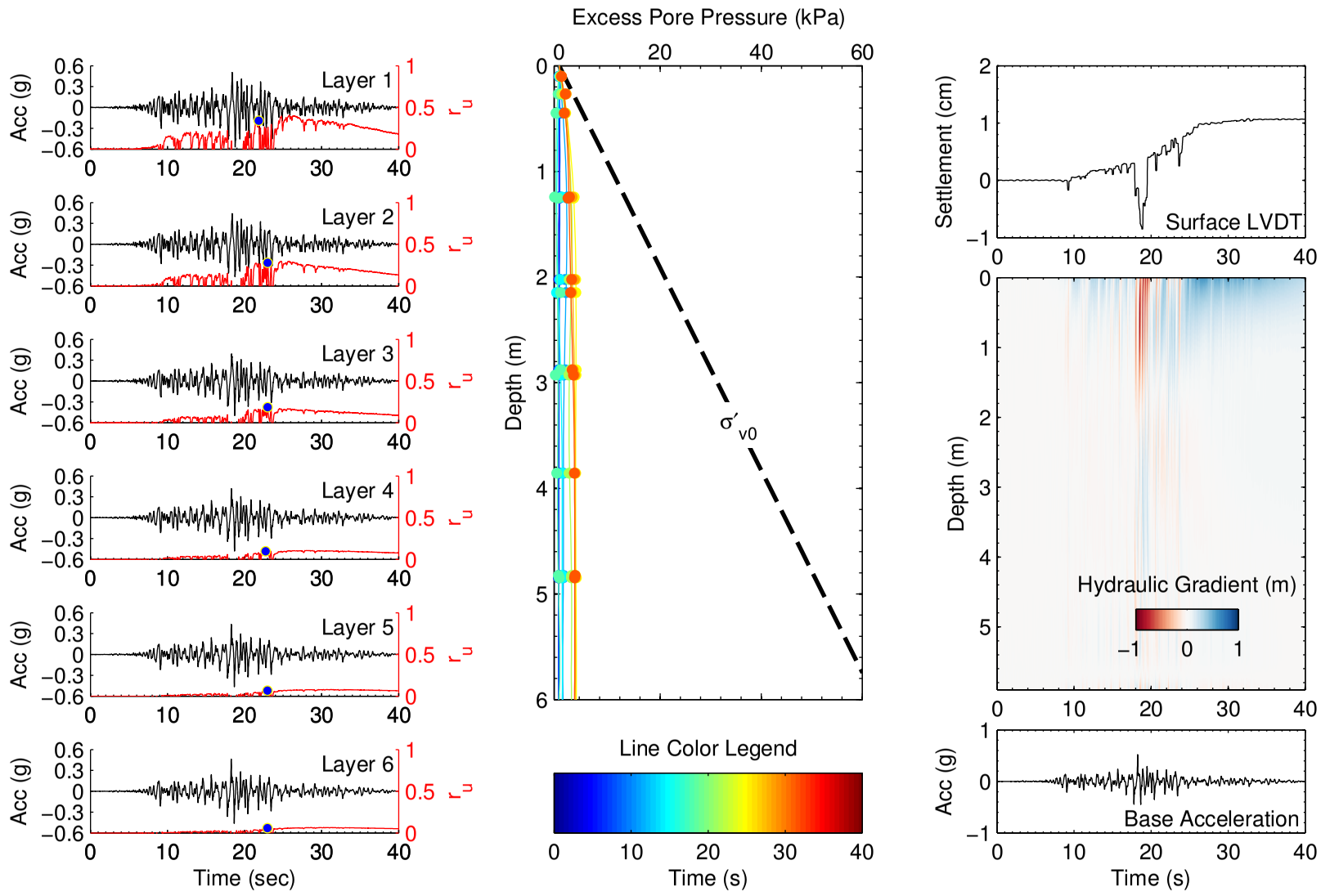
70% D_r Experiment 4 Test 49 – Data Summary Plot



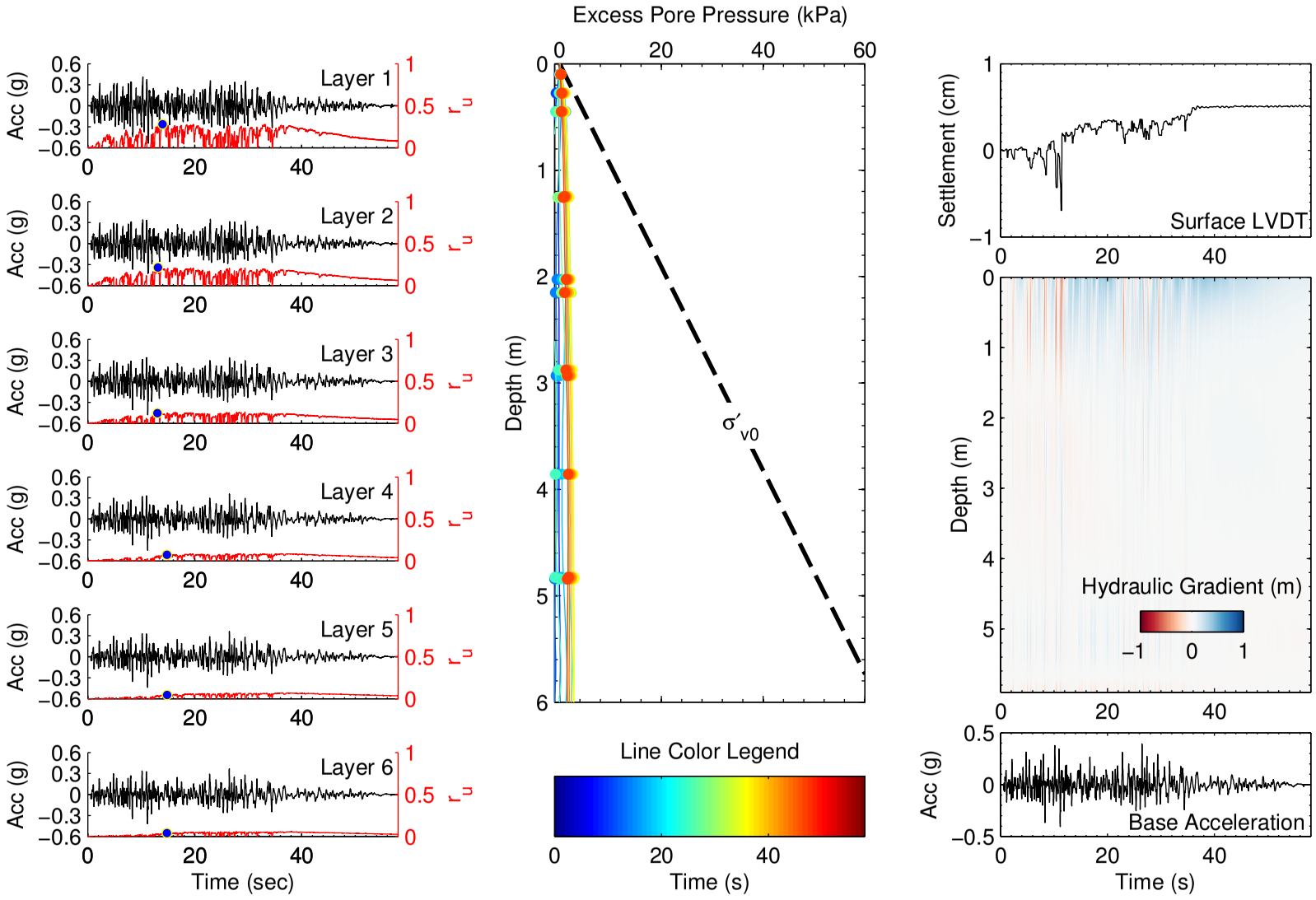
70% D_r Experiment 4 Test 50 – Data Summary Plot



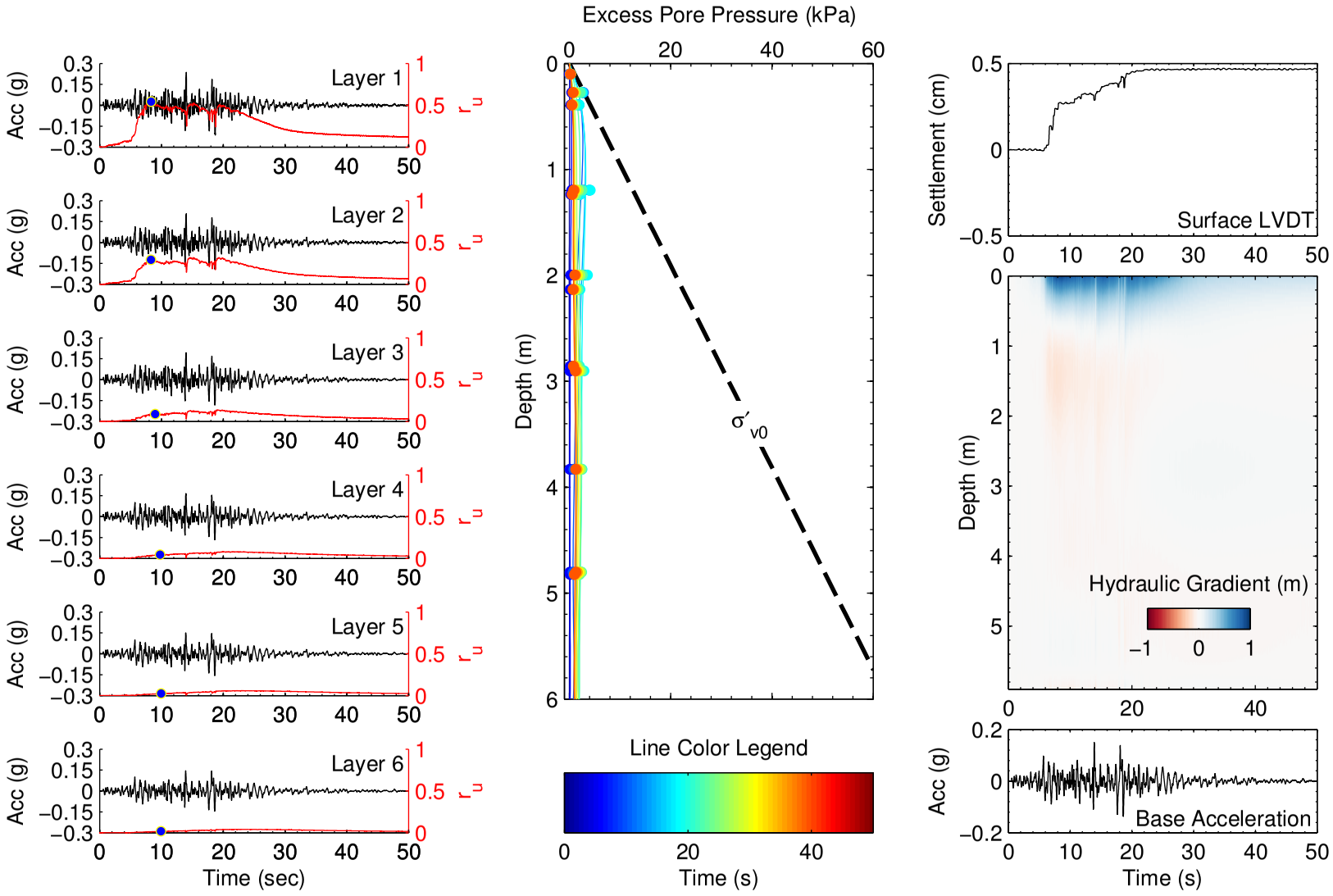
70% D_r Experiment 4 Test 51 – Data Summary Plot



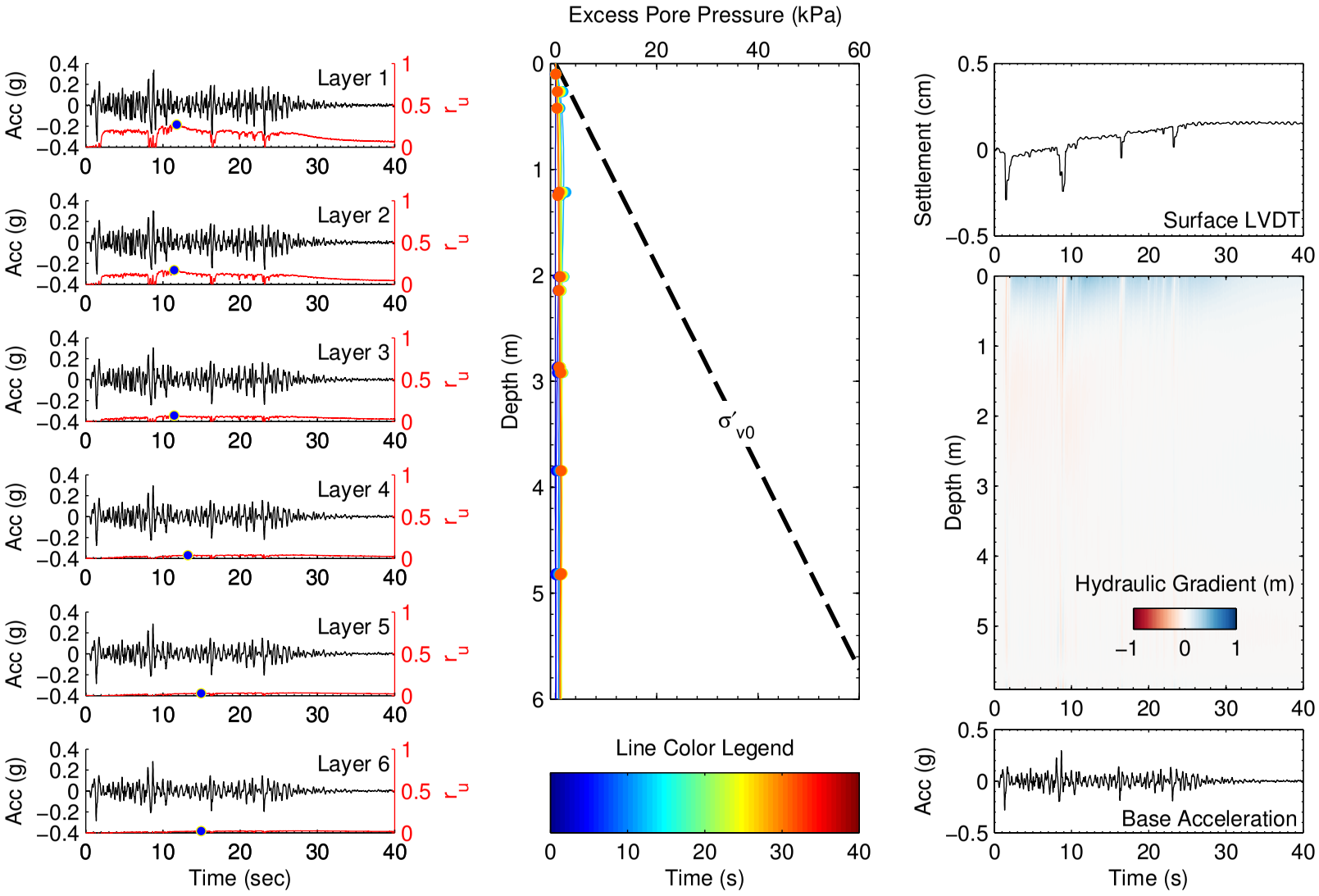
70% D_r Experiment 4 Test 52 – Data Summary Plot



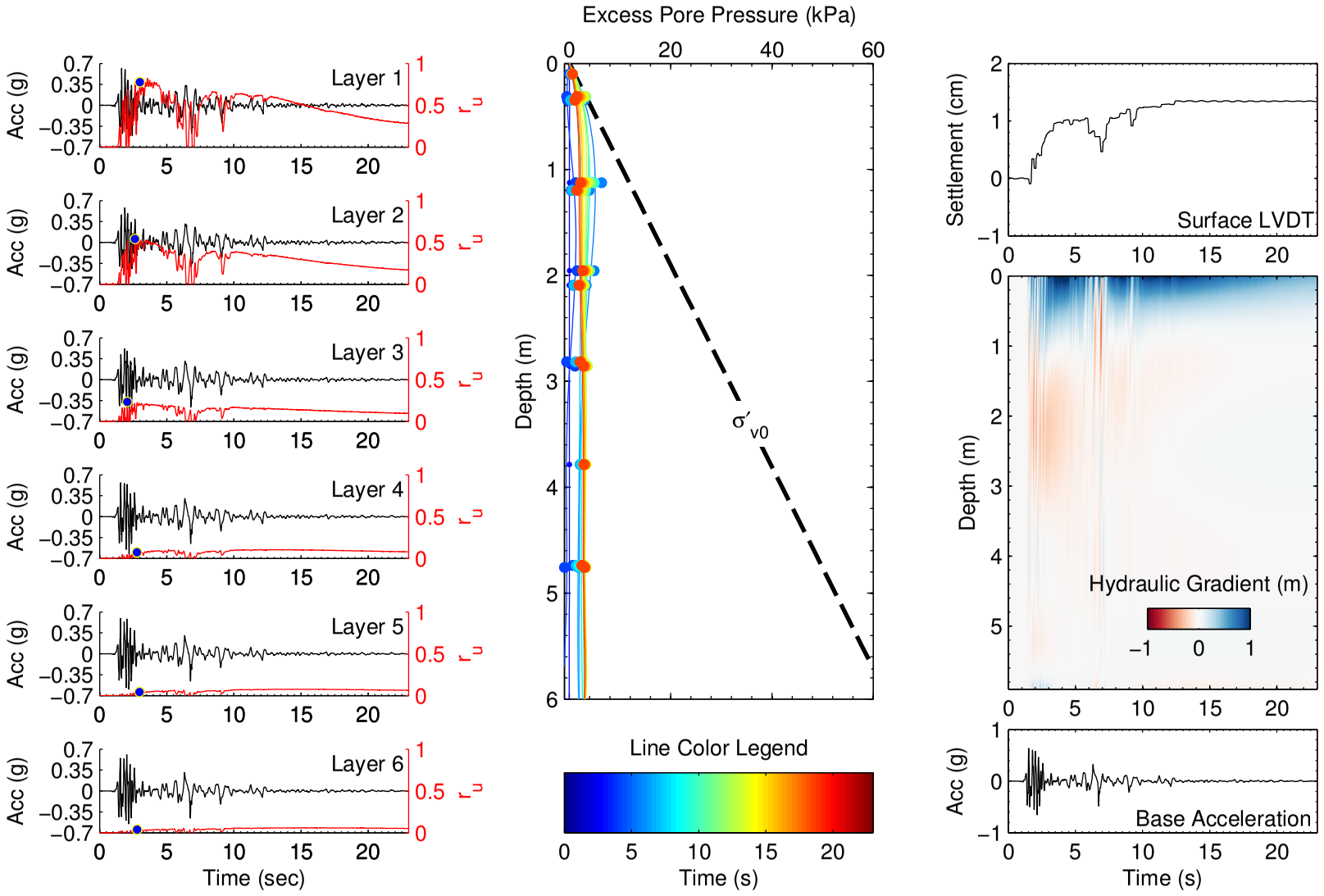
70% D_r Experiment 4 Test 53 – Data Summary Plot



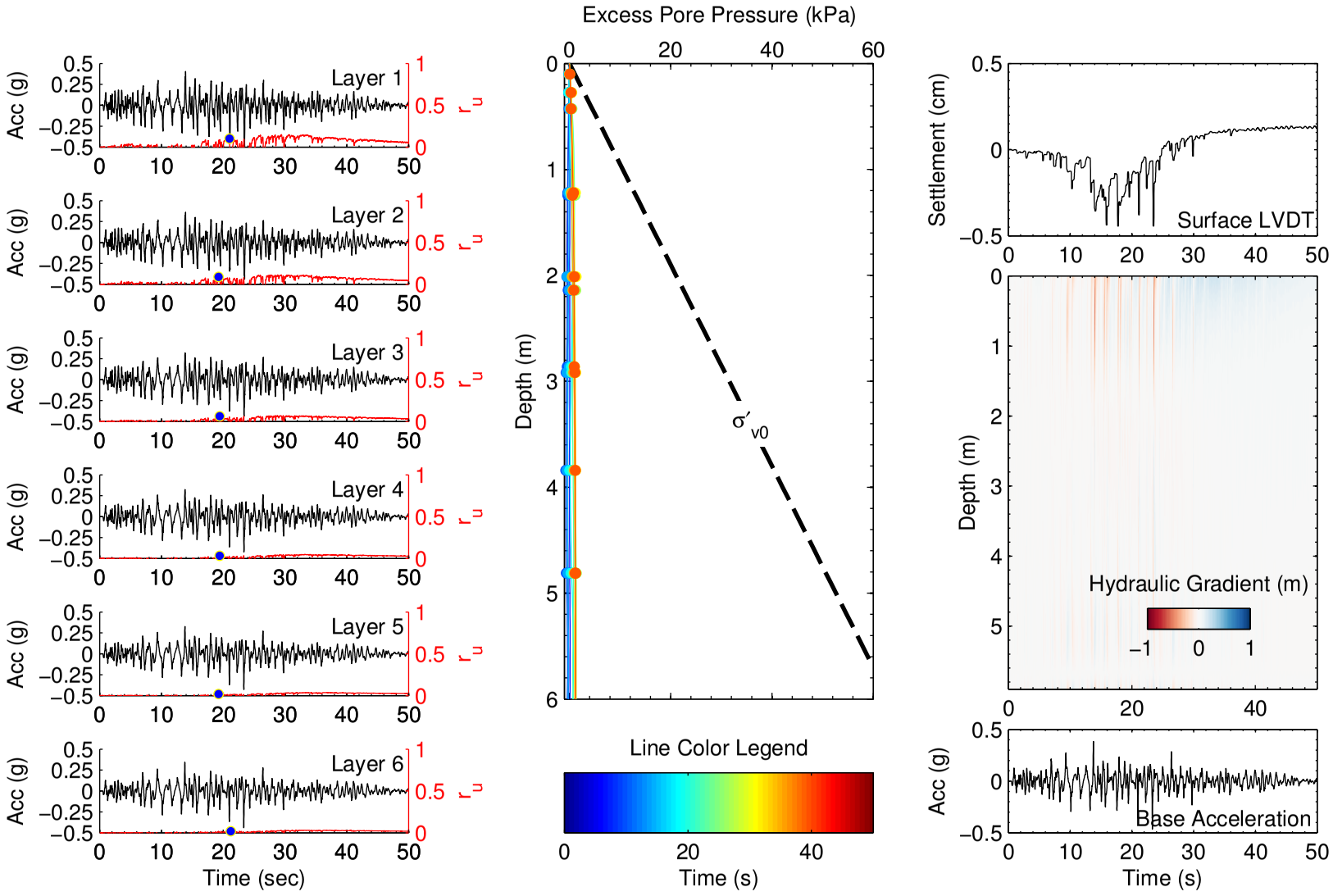
70% D_r Experiment 4 Test 54 – Data Summary Plot



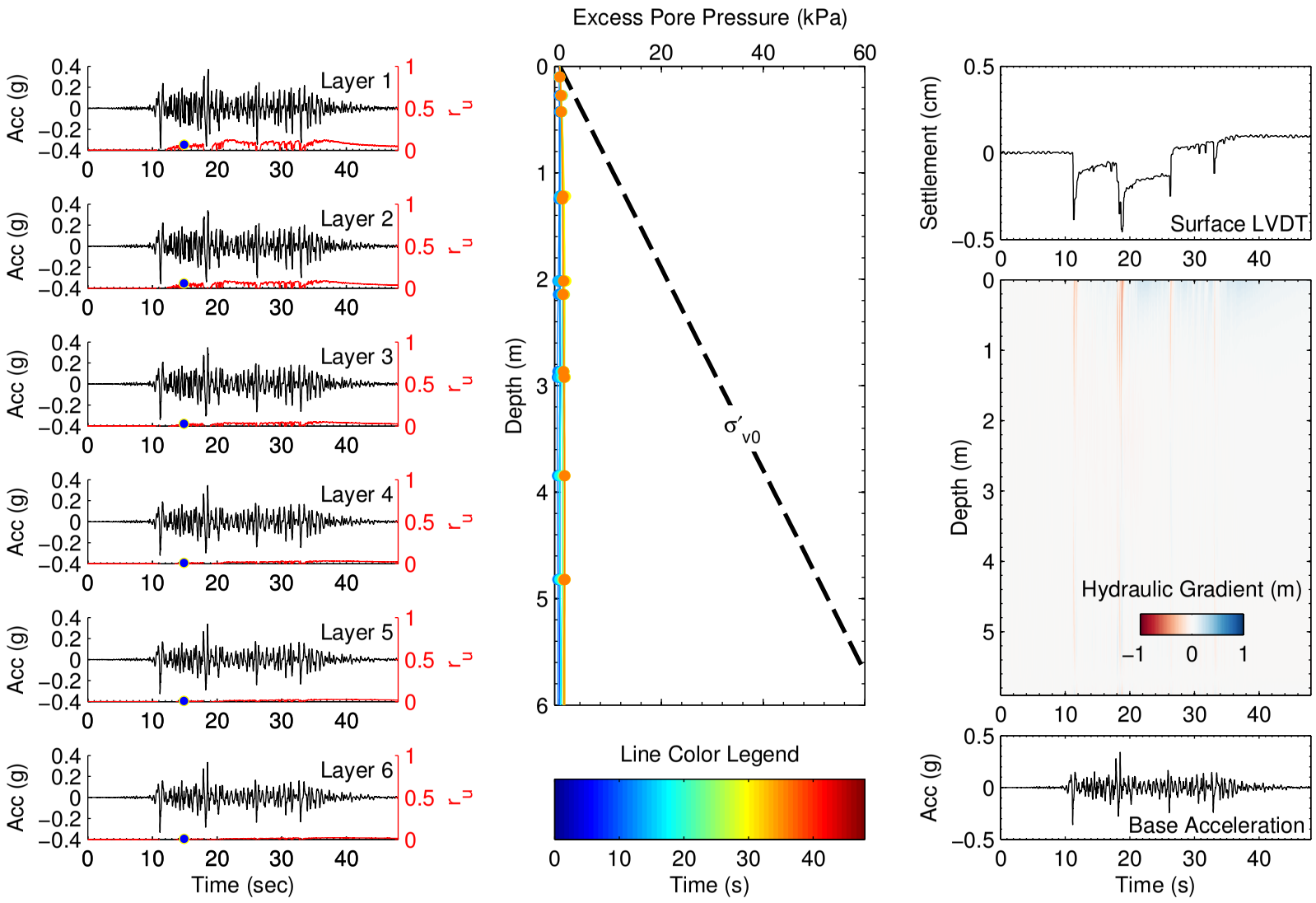
70% D_r Experiment 4 Test 55 – Data Summary Plot



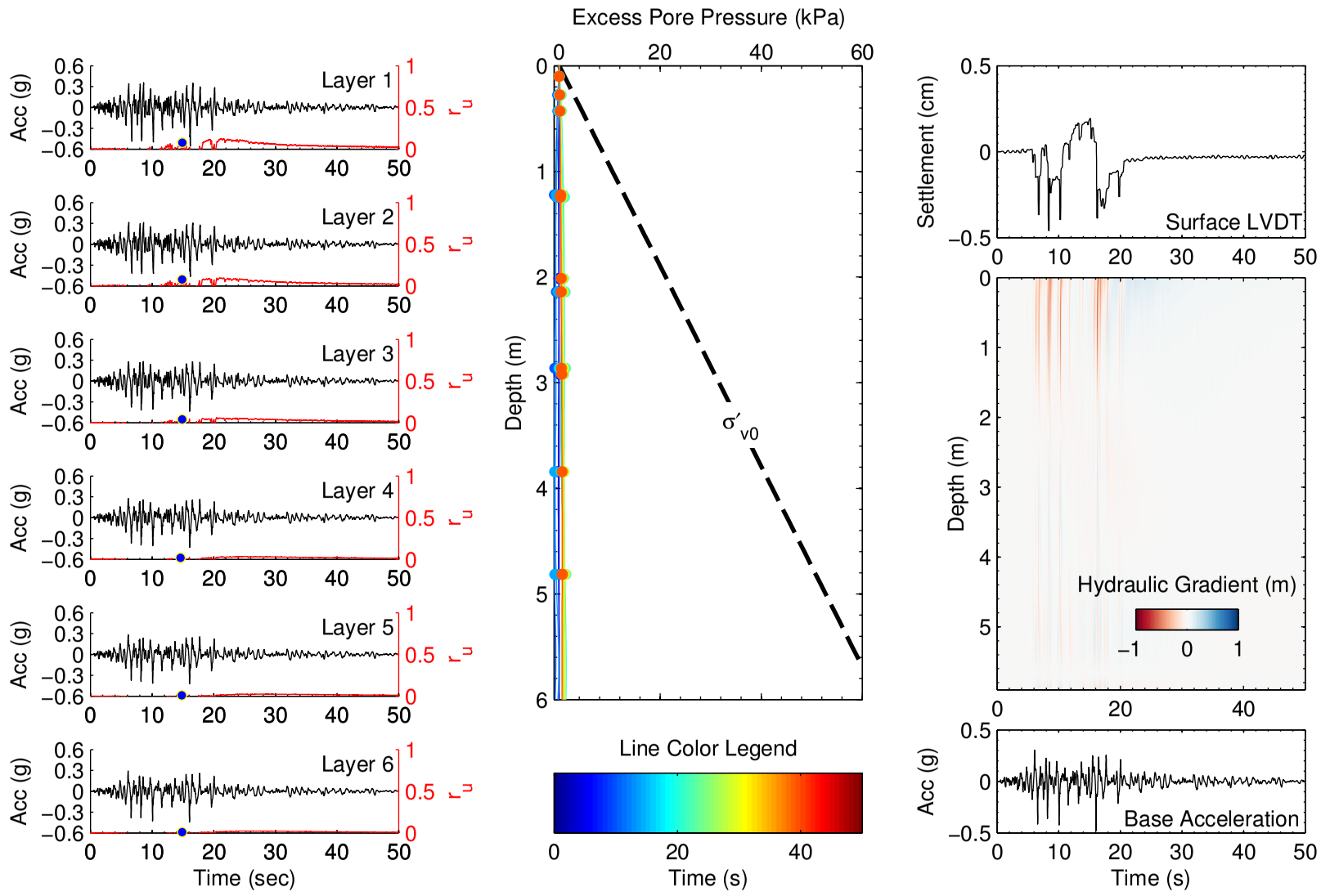
70% D_r Experiment 4 Test 56 – Data Summary Plot



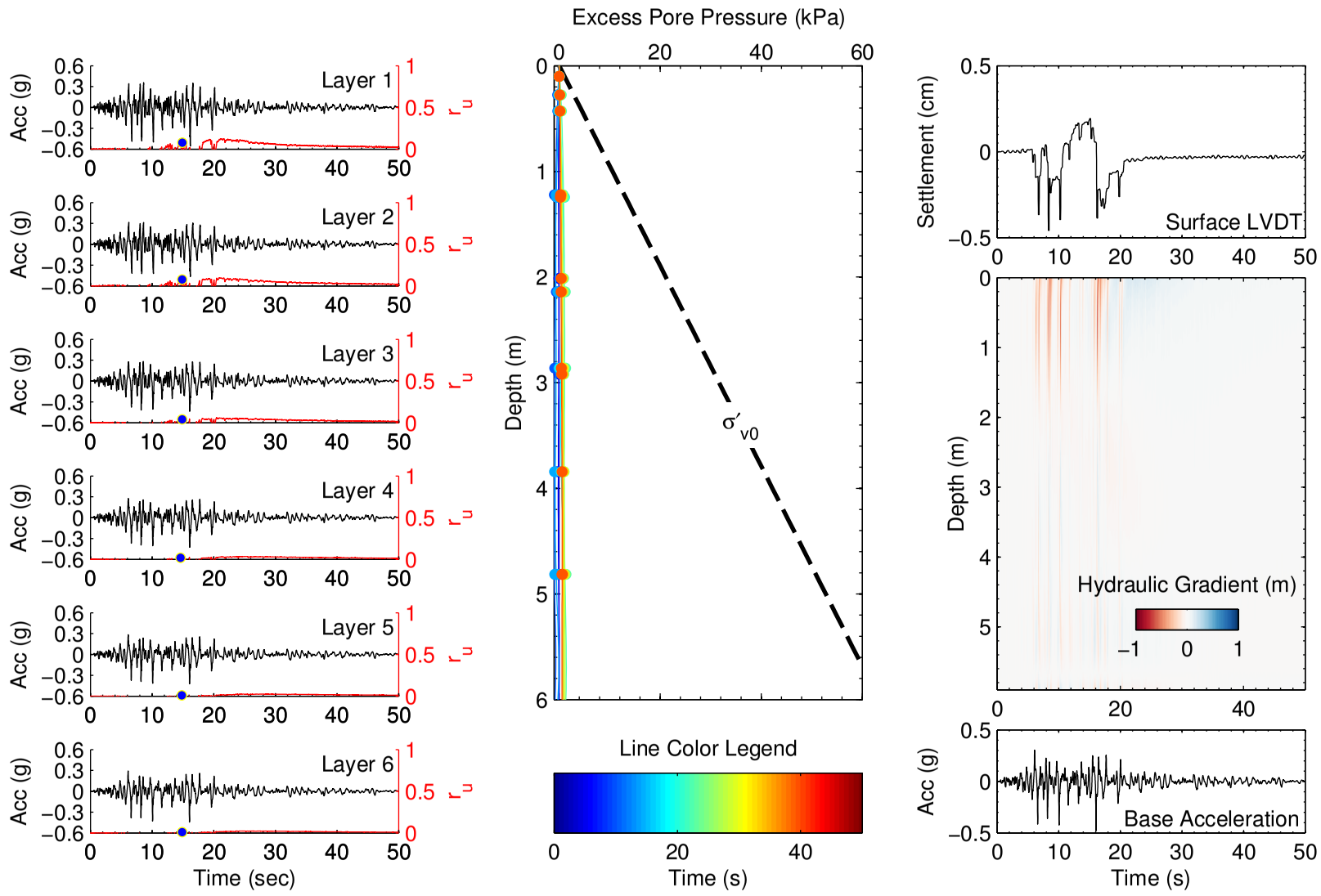
70% D_r Experiment 4 Test 57 – Data Summary Plot



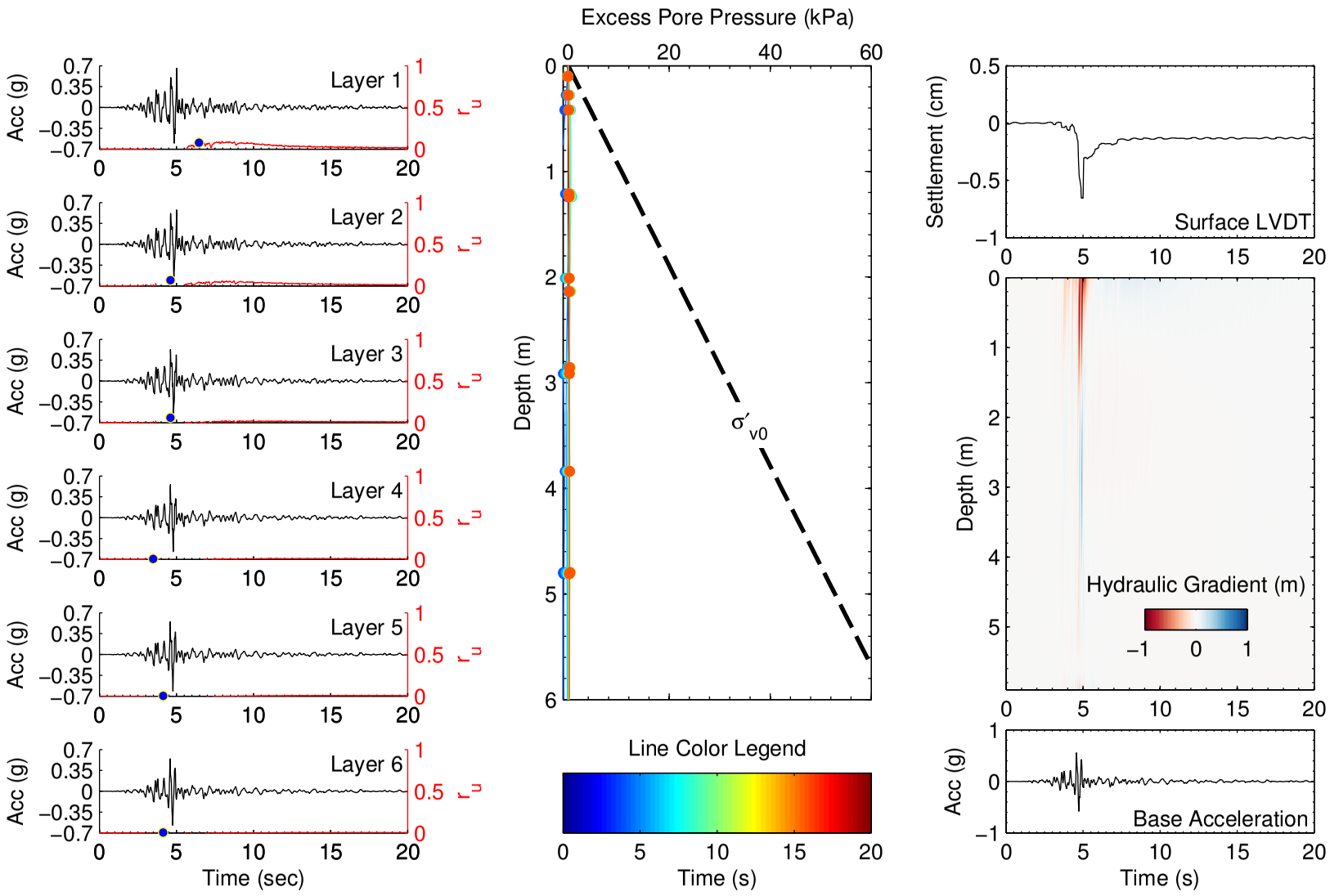
70% D_r Experiment 4 Test 58 – Data Summary Plot



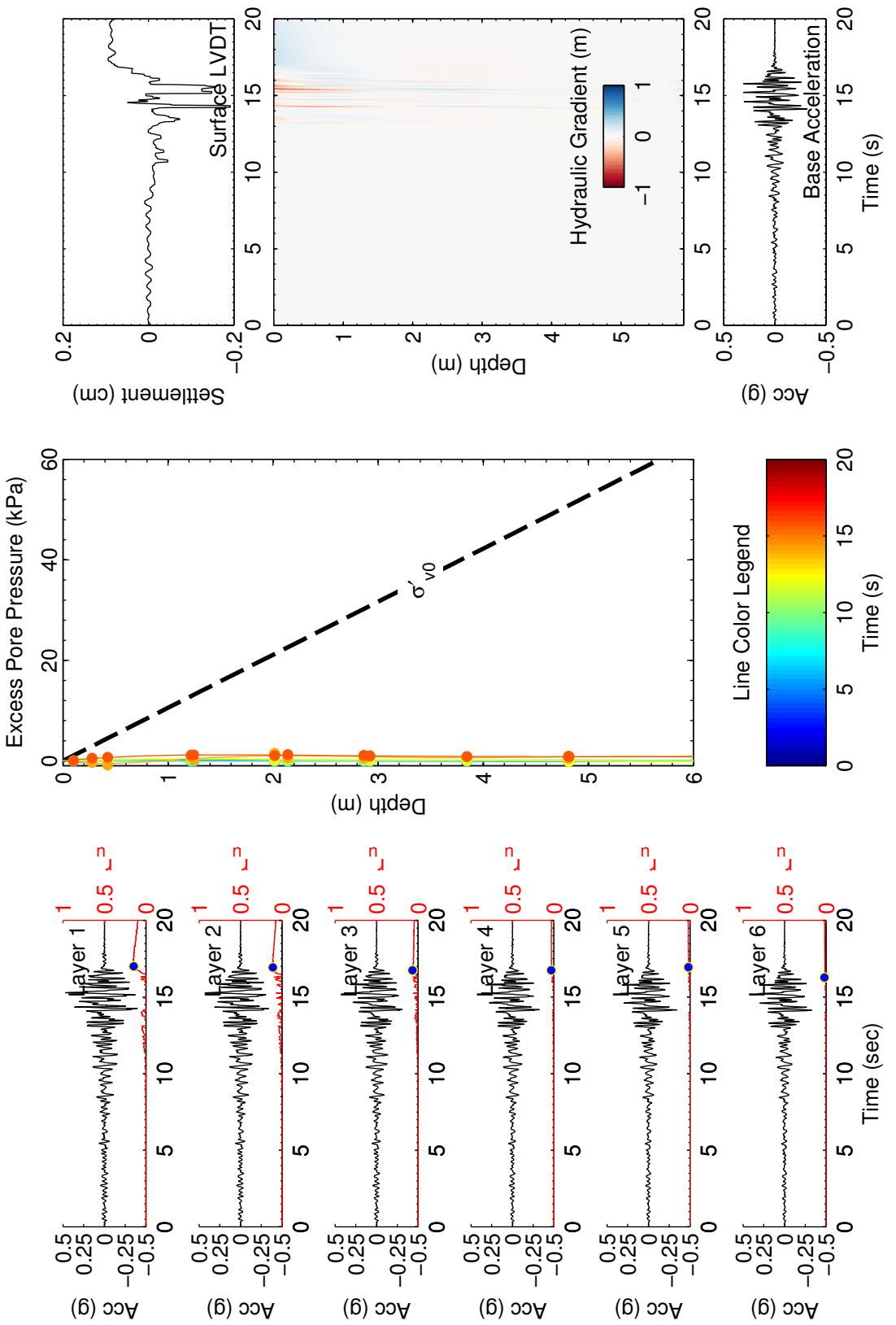
70% D_r Experiment 4 Test 59 – Data Summary Plot



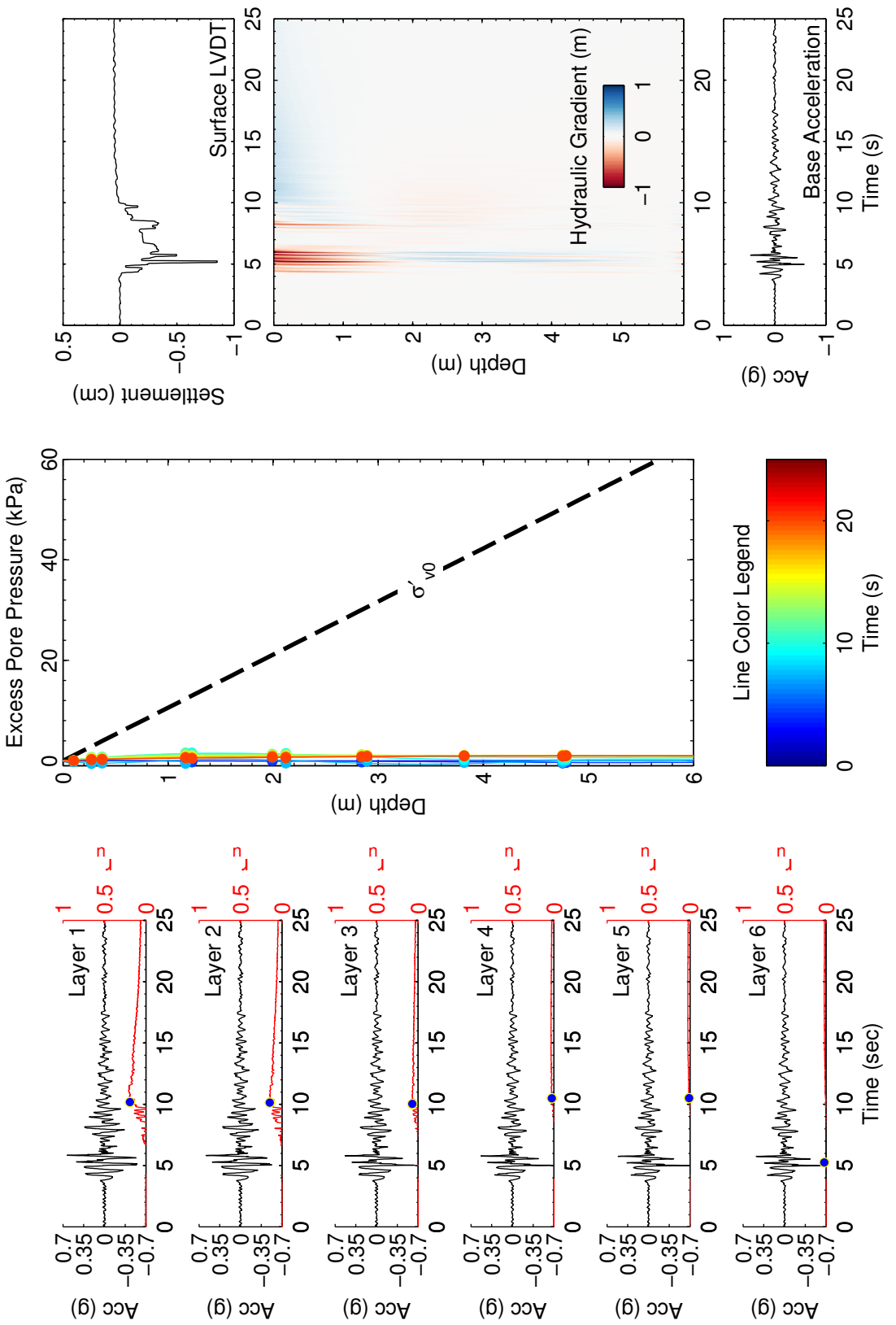
70% D_r Experiment 4 Test 60 – Data Summary Plot



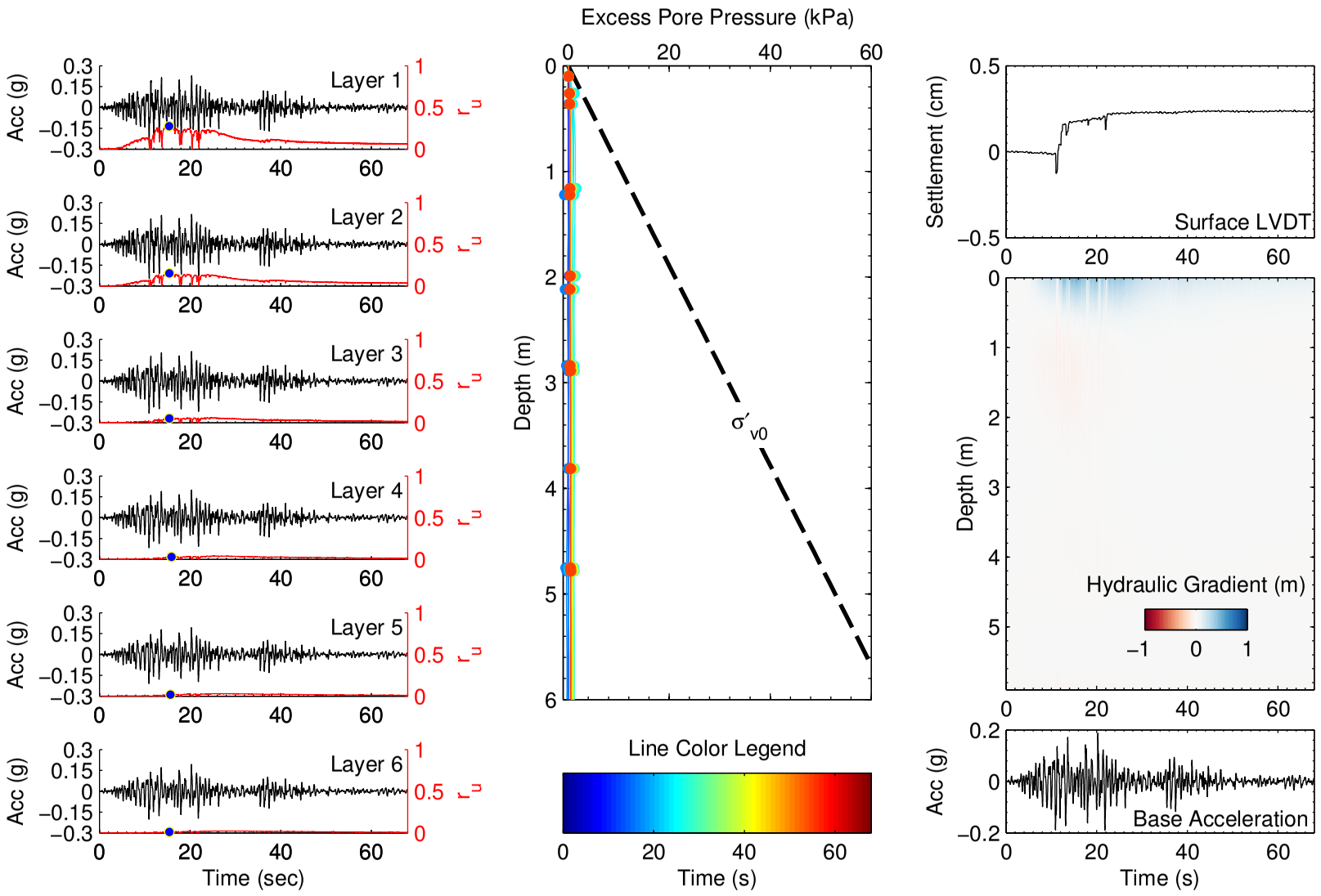
70% D_r Experiment 4 Test 61 – Data Summary Plot



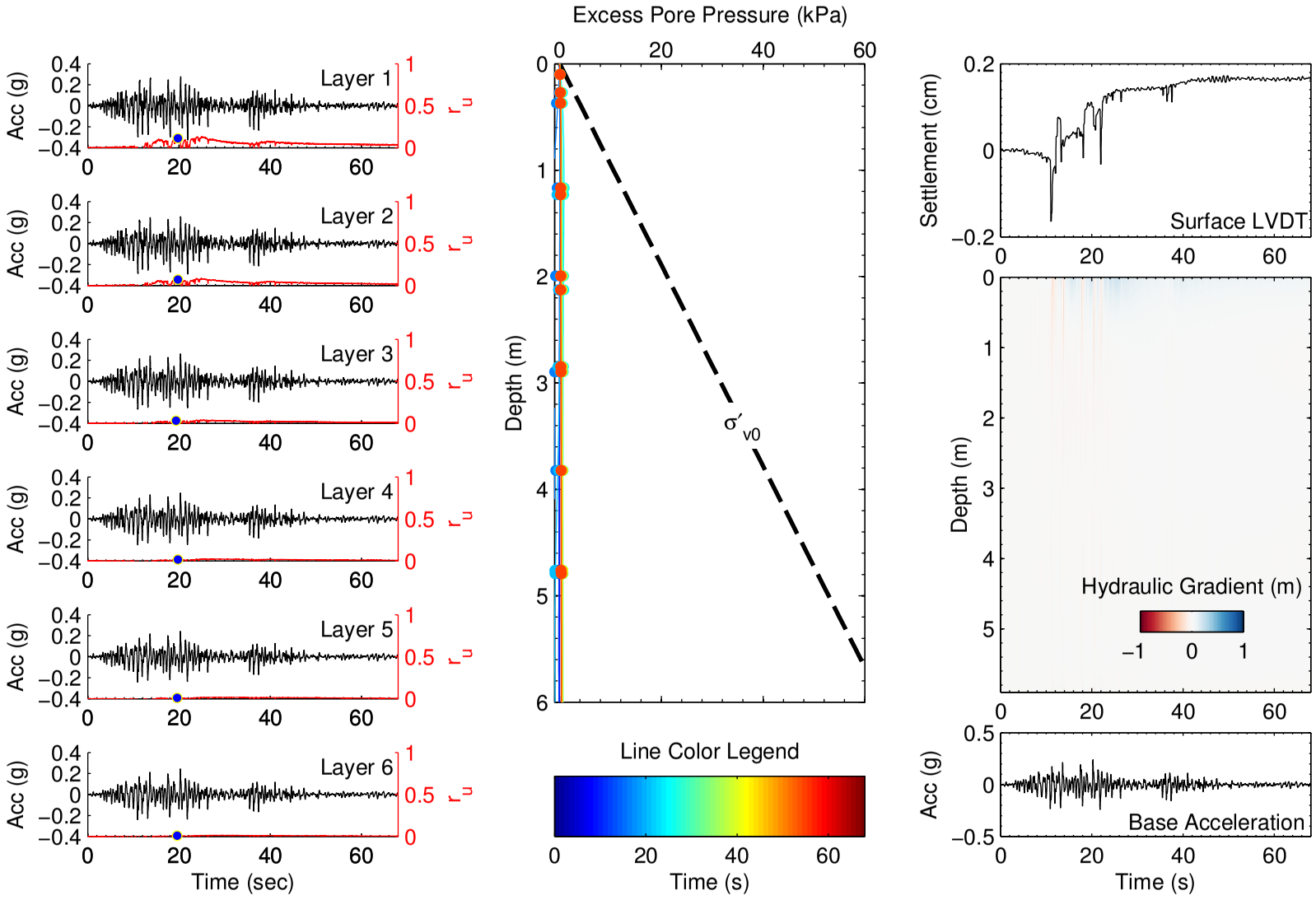
70% D_r Experiment 4 Test 62 – Data Summary Plot



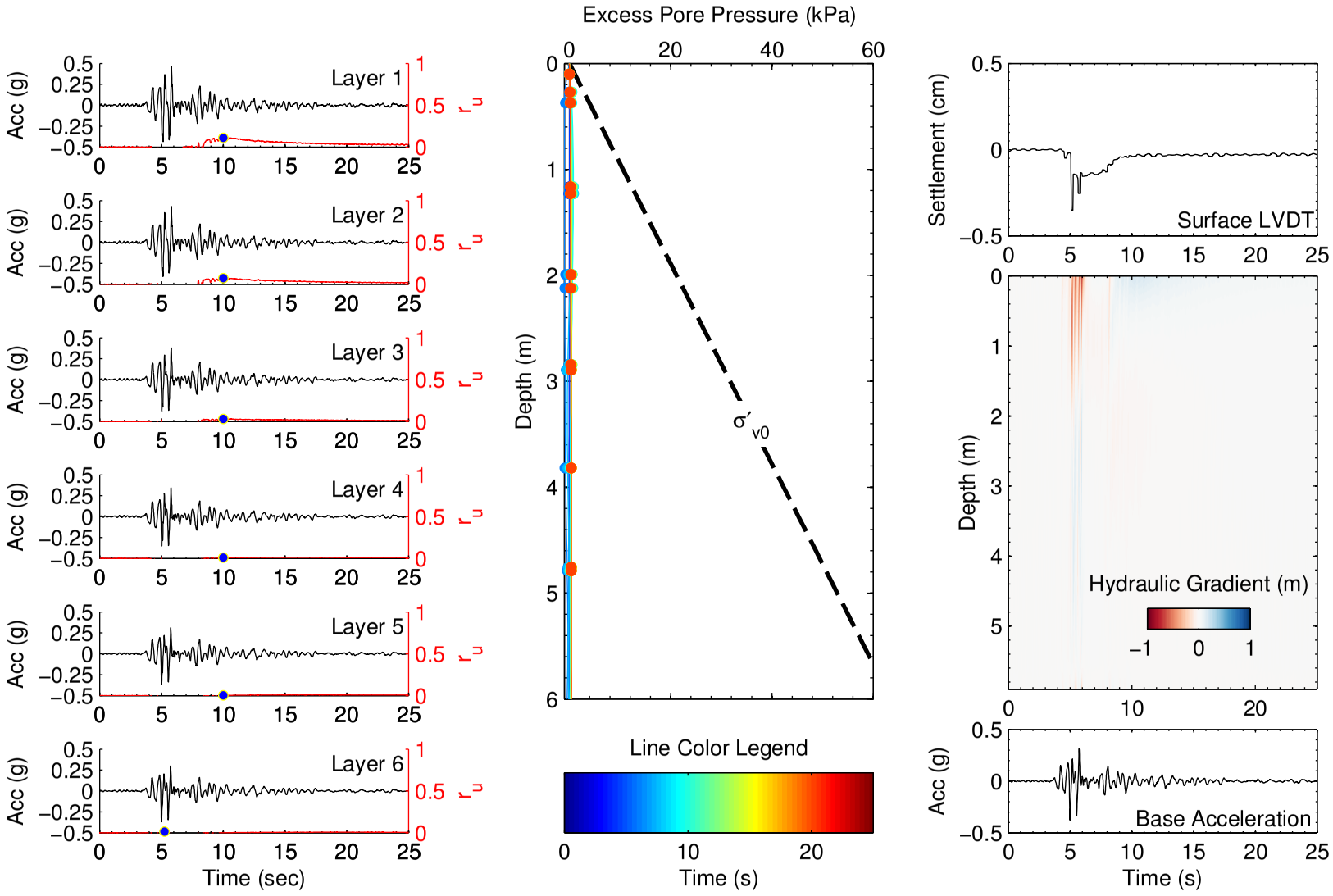
70% D_r Experiment 4 Test 63 – Data Summary Plot



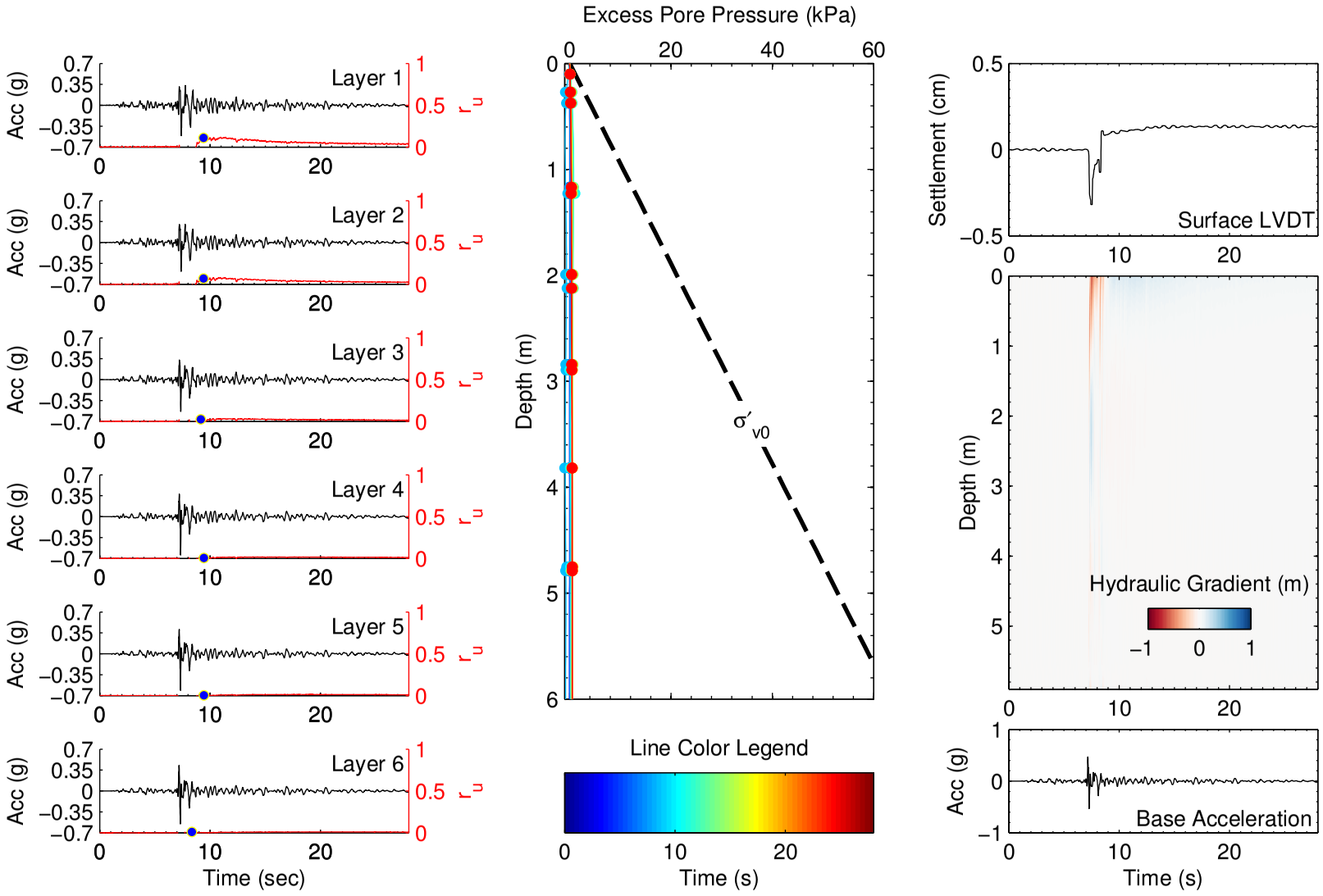
70% D_r Experiment 4 Test 64 – Data Summary Plot



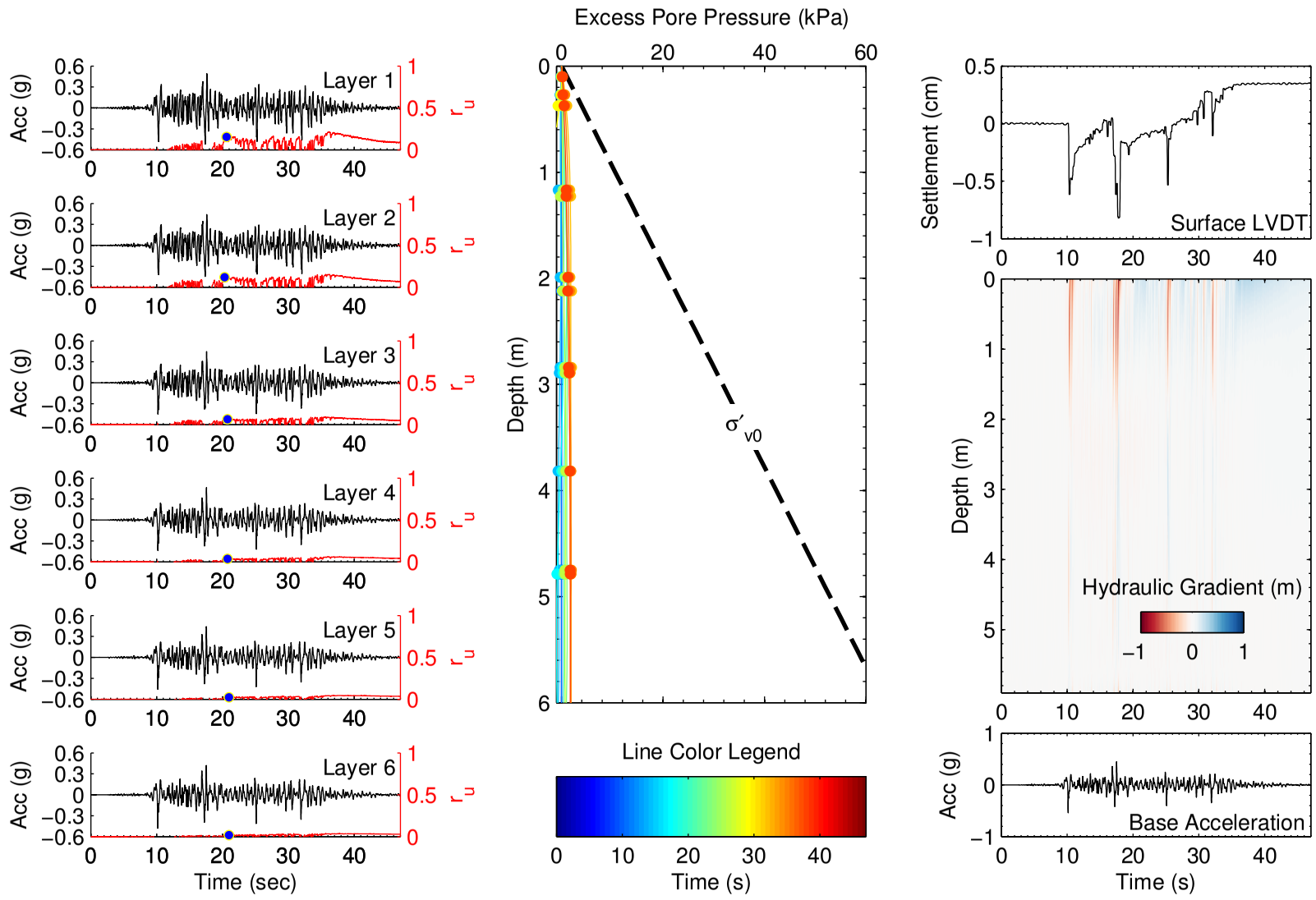
70% D_r Experiment 4 Test 65 – Data Summary Plot



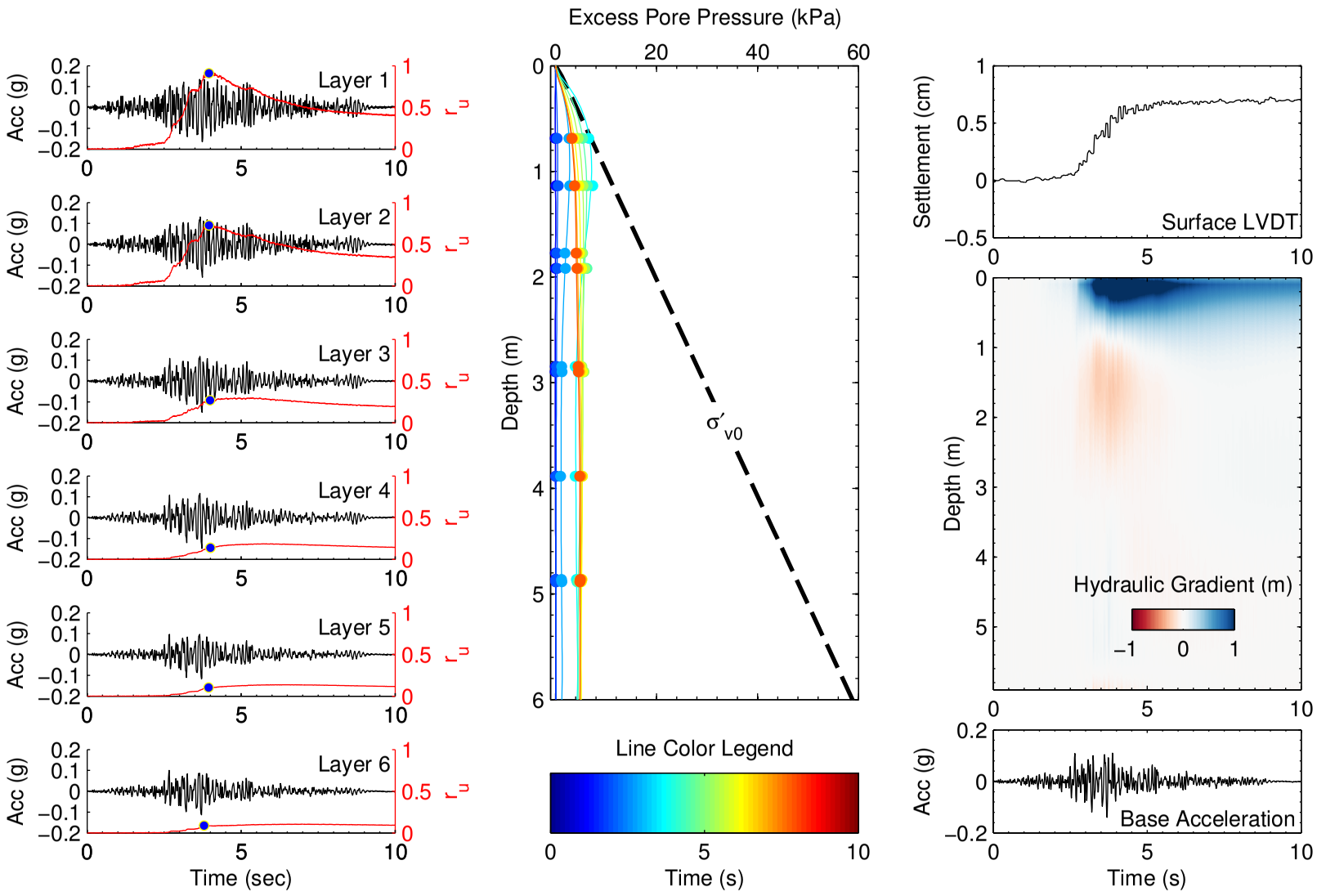
70% D_r Experiment 4 Test 66 – Data Summary Plot



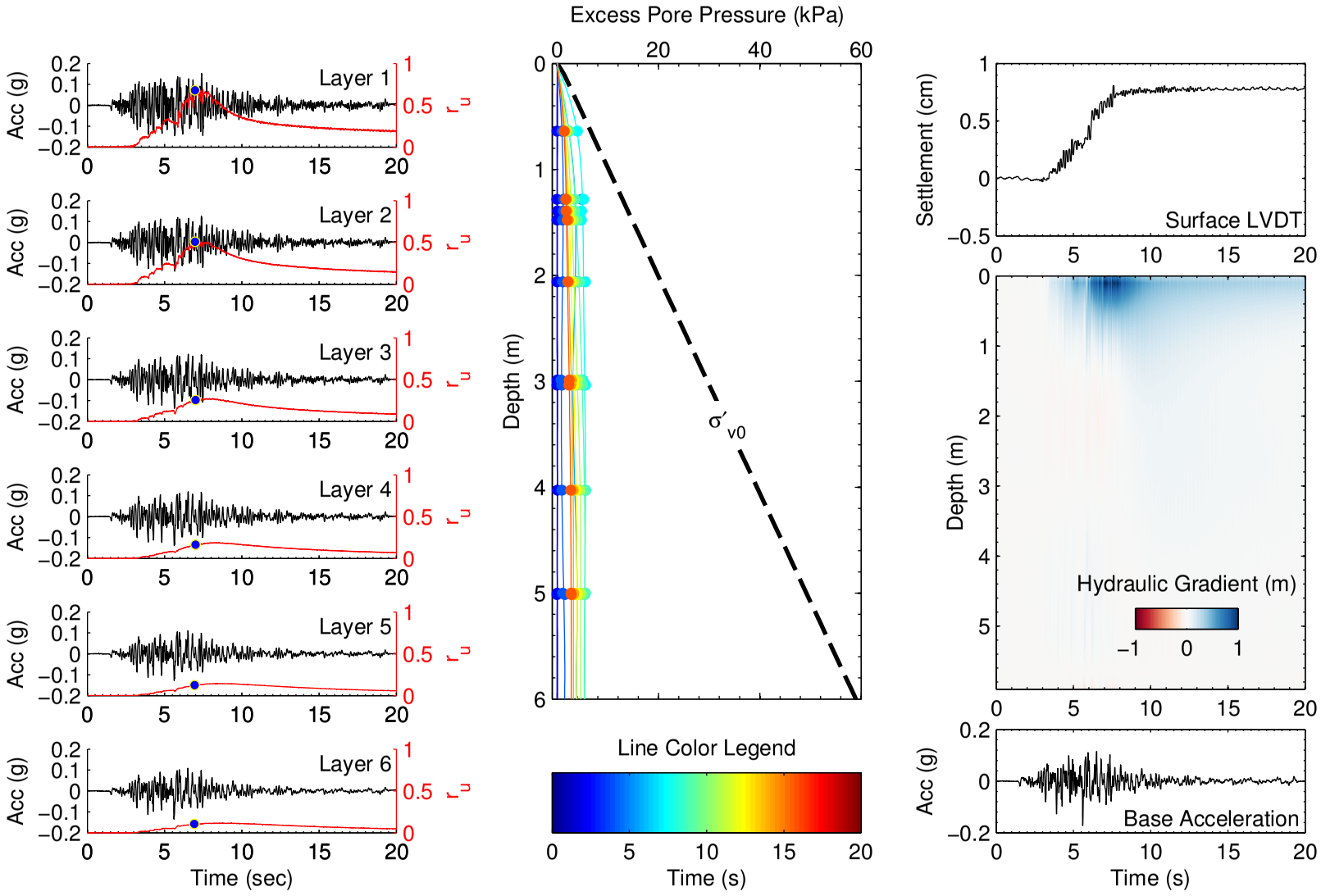
70% D_r Experiment 4 Test 67 – Data Summary Plot



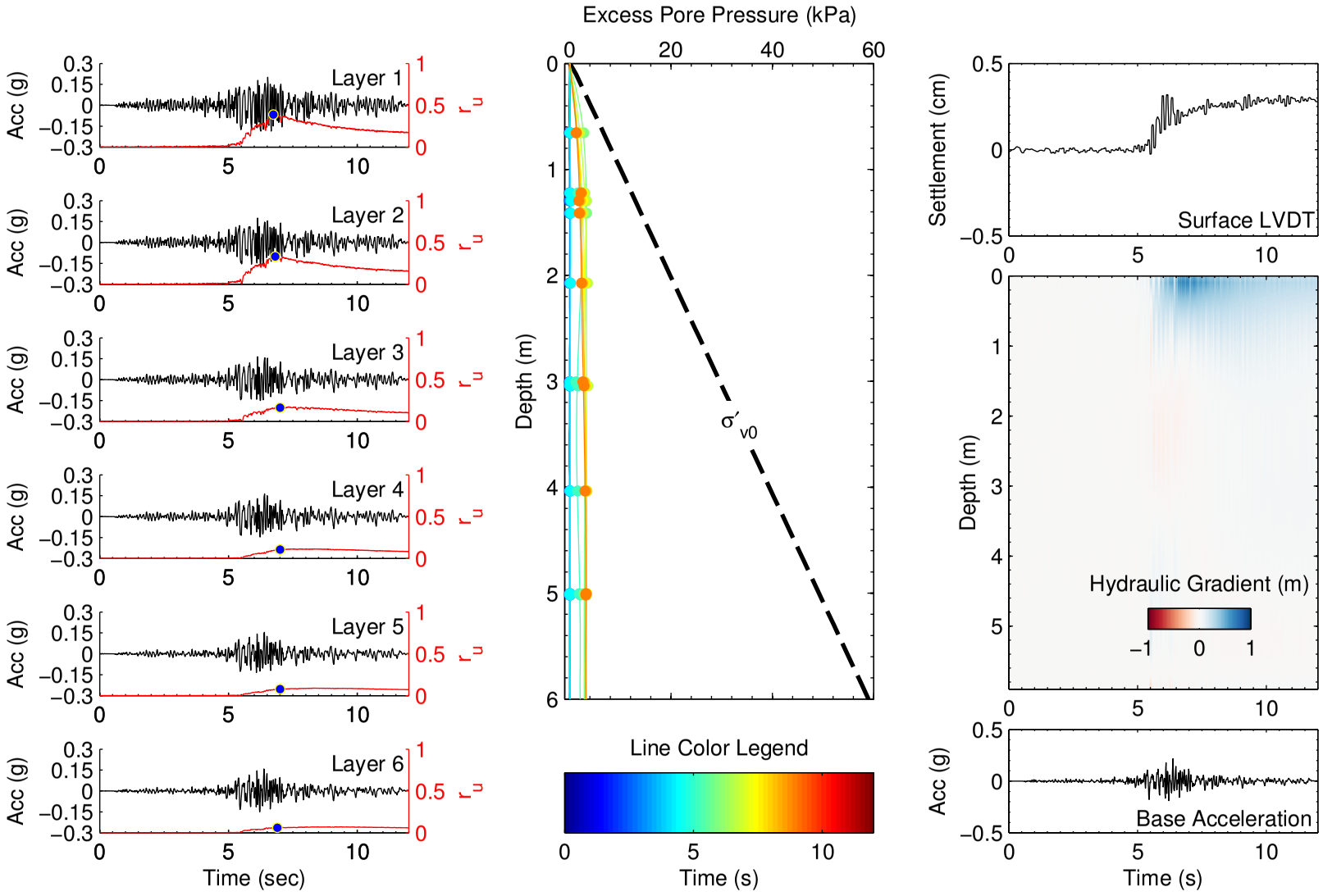
70% D_r Experiment 4 Test 68 – Data Summary Plot



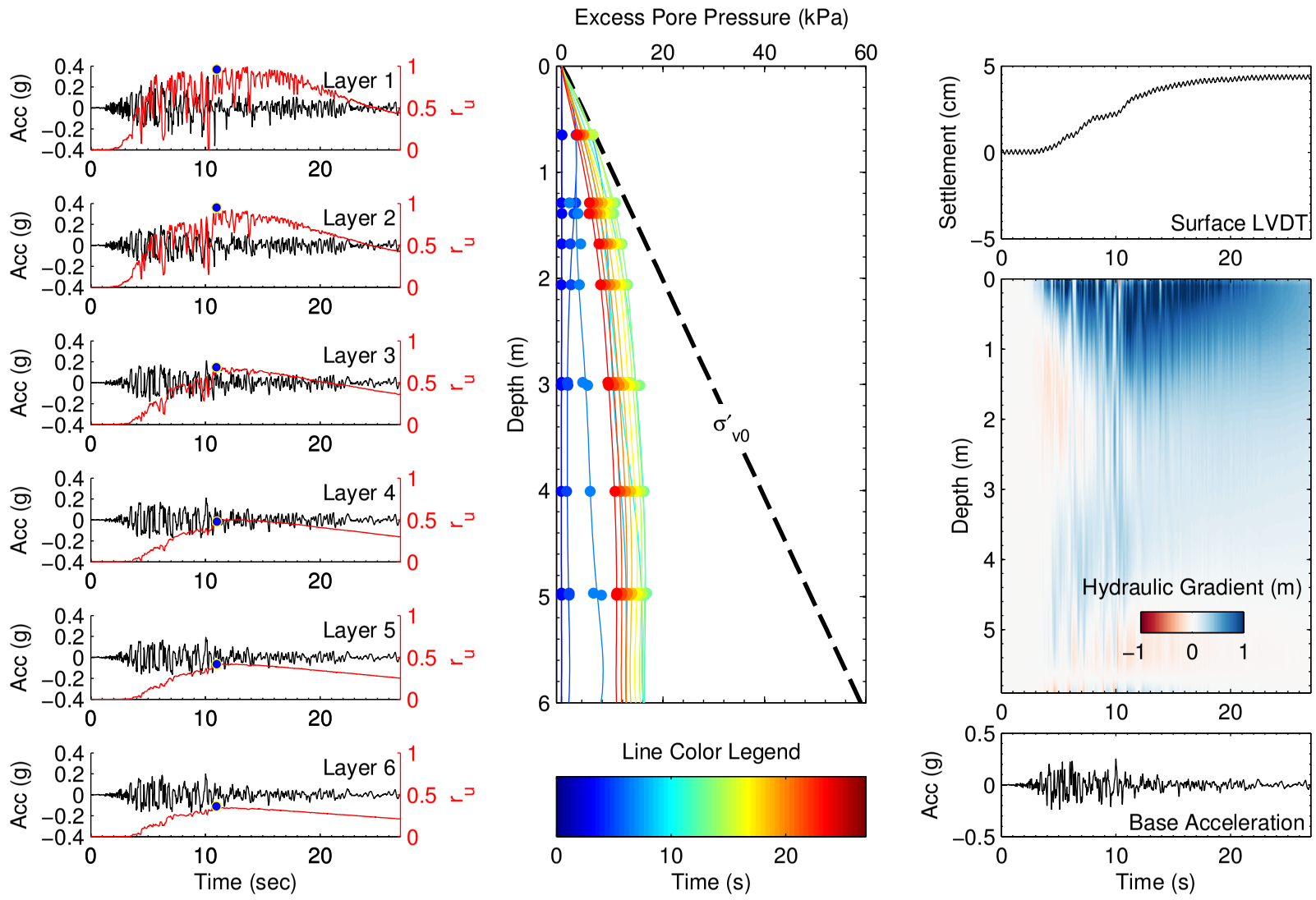
40% D_r Experiment 5 Test 1 – Data Summary Plot



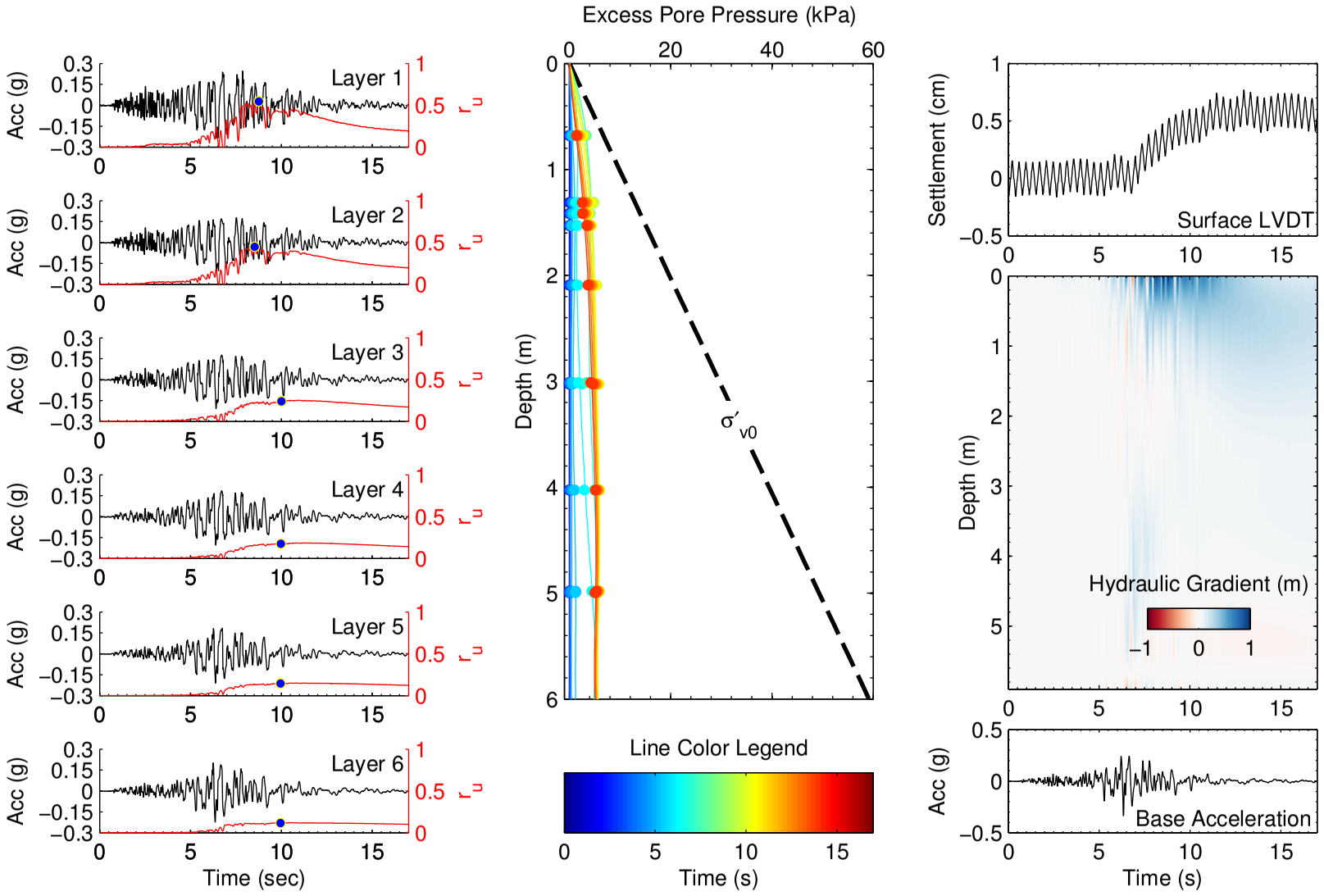
40% D_r Experiment 5 Test 2 – Data Summary Plot



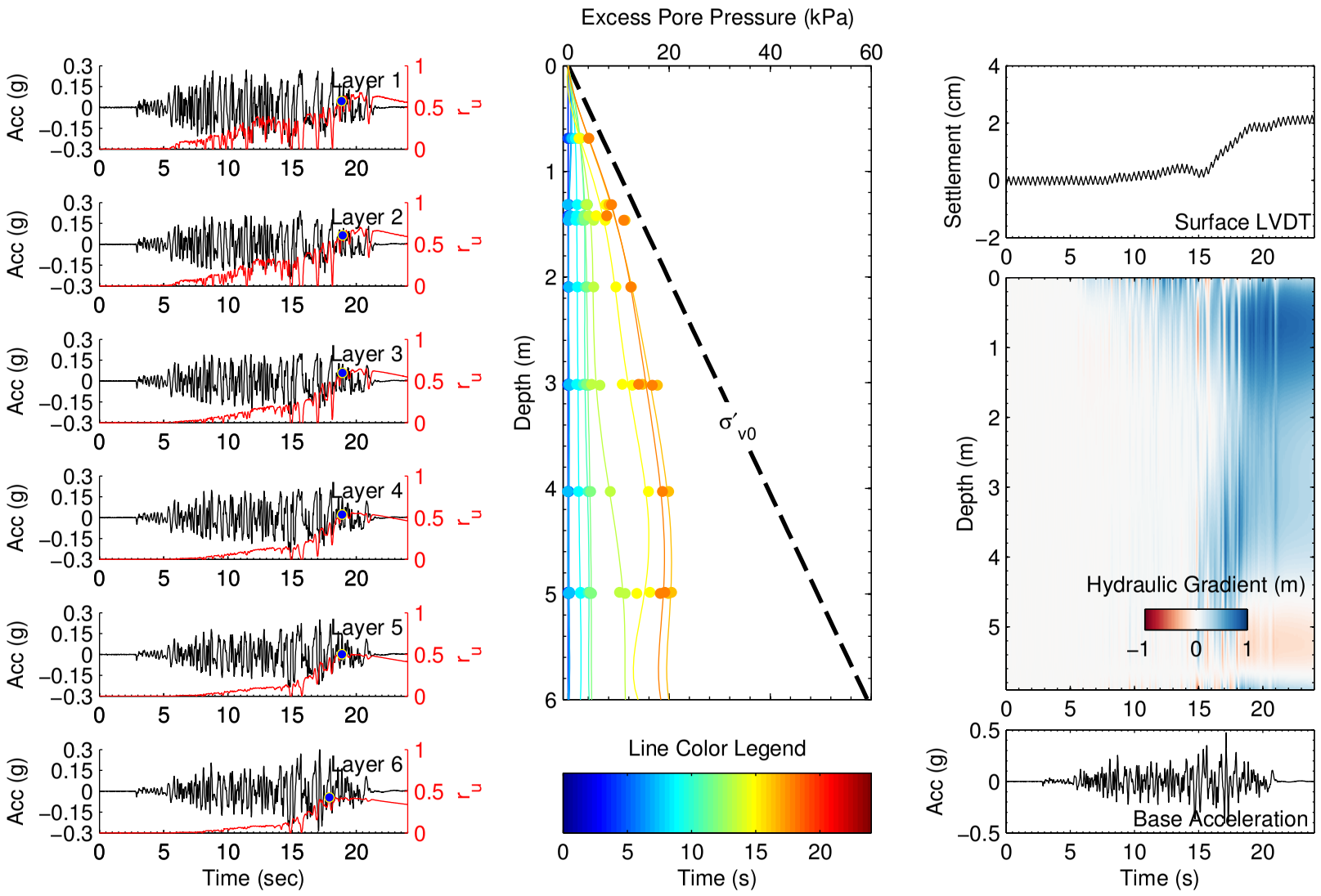
40% D_r Experiment 5 Test 3 – Data Summary Plot



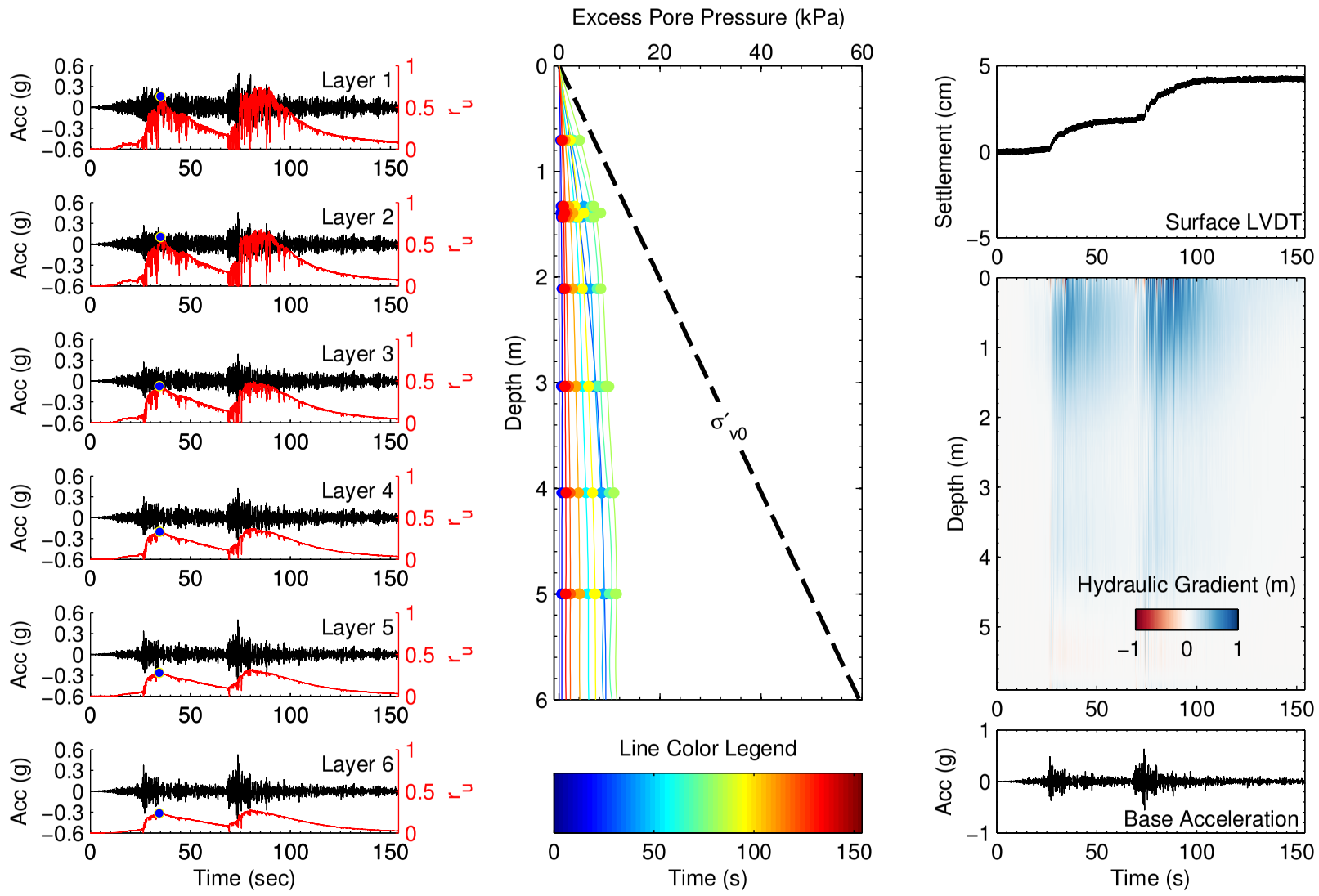
40% D_r Experiment 5 Test 4 – Data Summary Plot



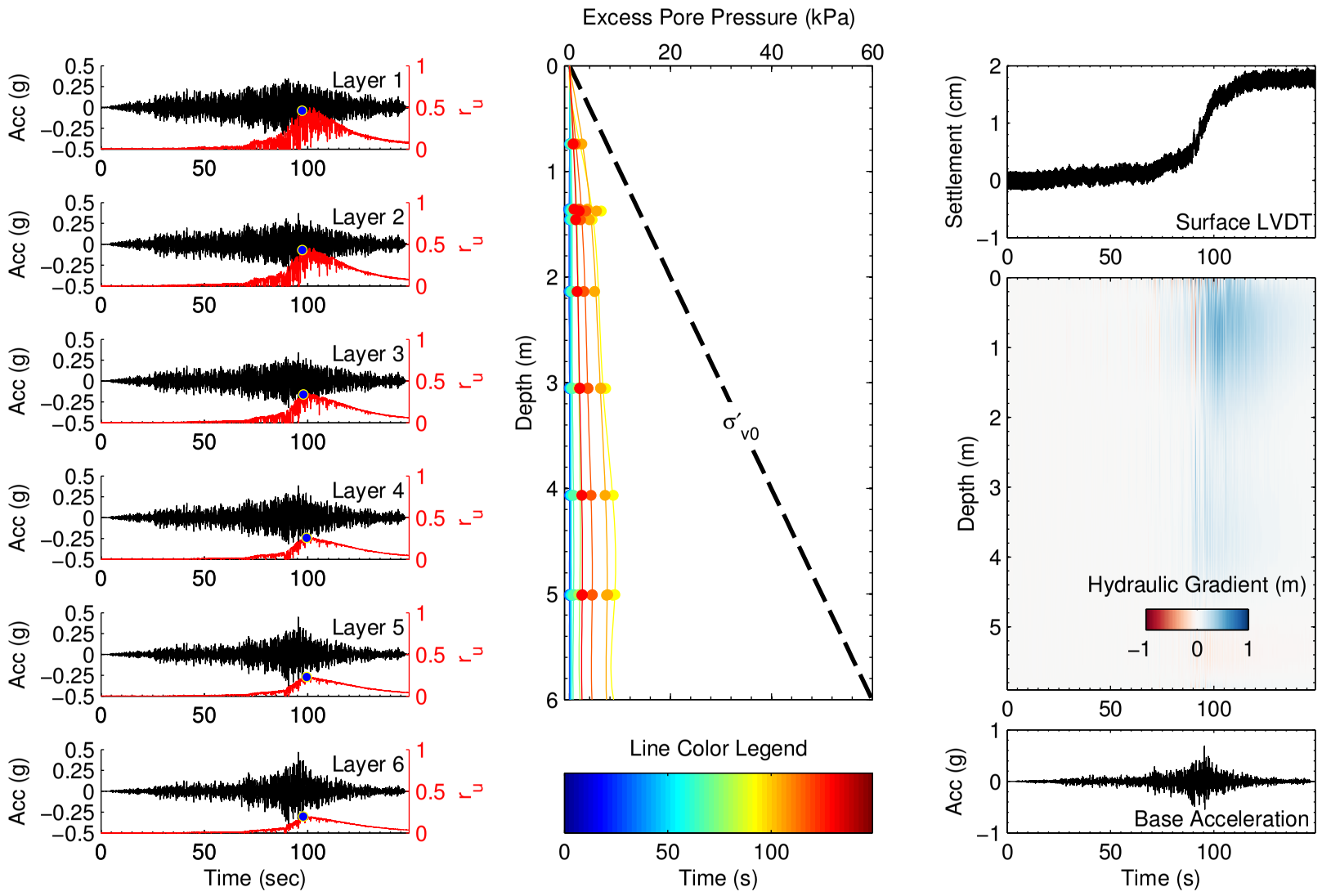
40% D_r Experiment 5 Test 5 – Data Summary Plot



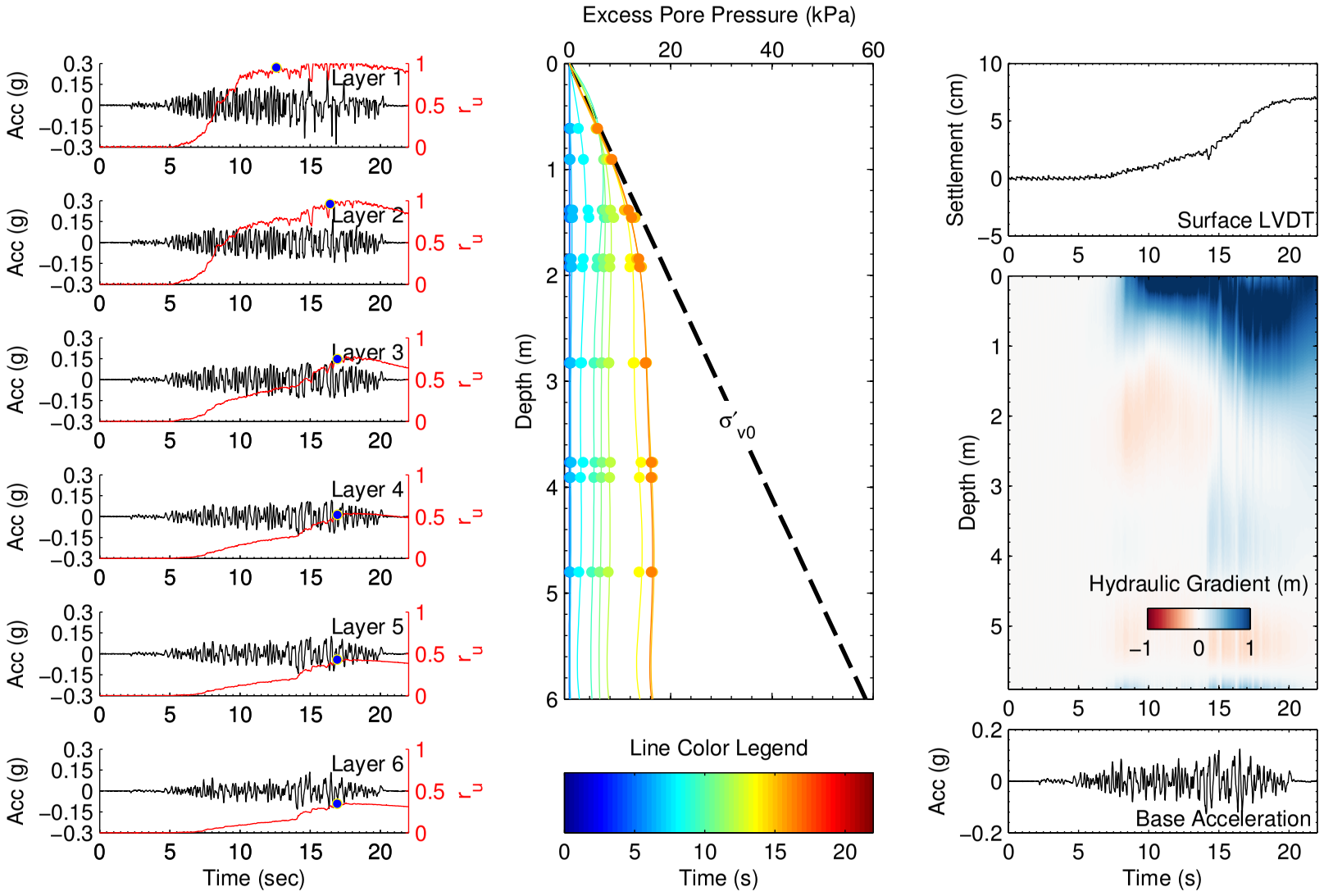
40% D_r Experiment 5 Test 6 – Data Summary Plot



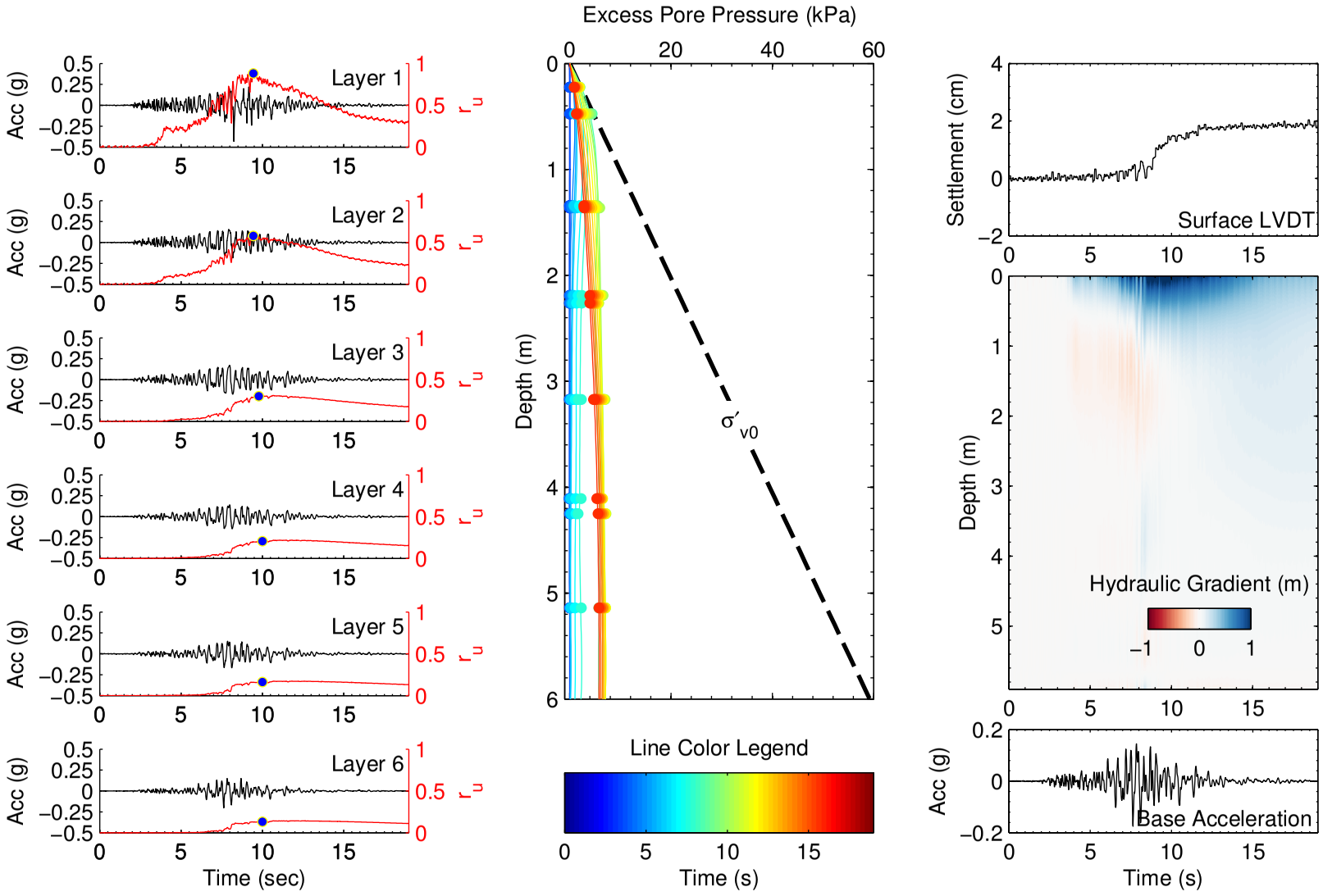
40% D_r Experiment 5 Test 7 – Data Summary Plot



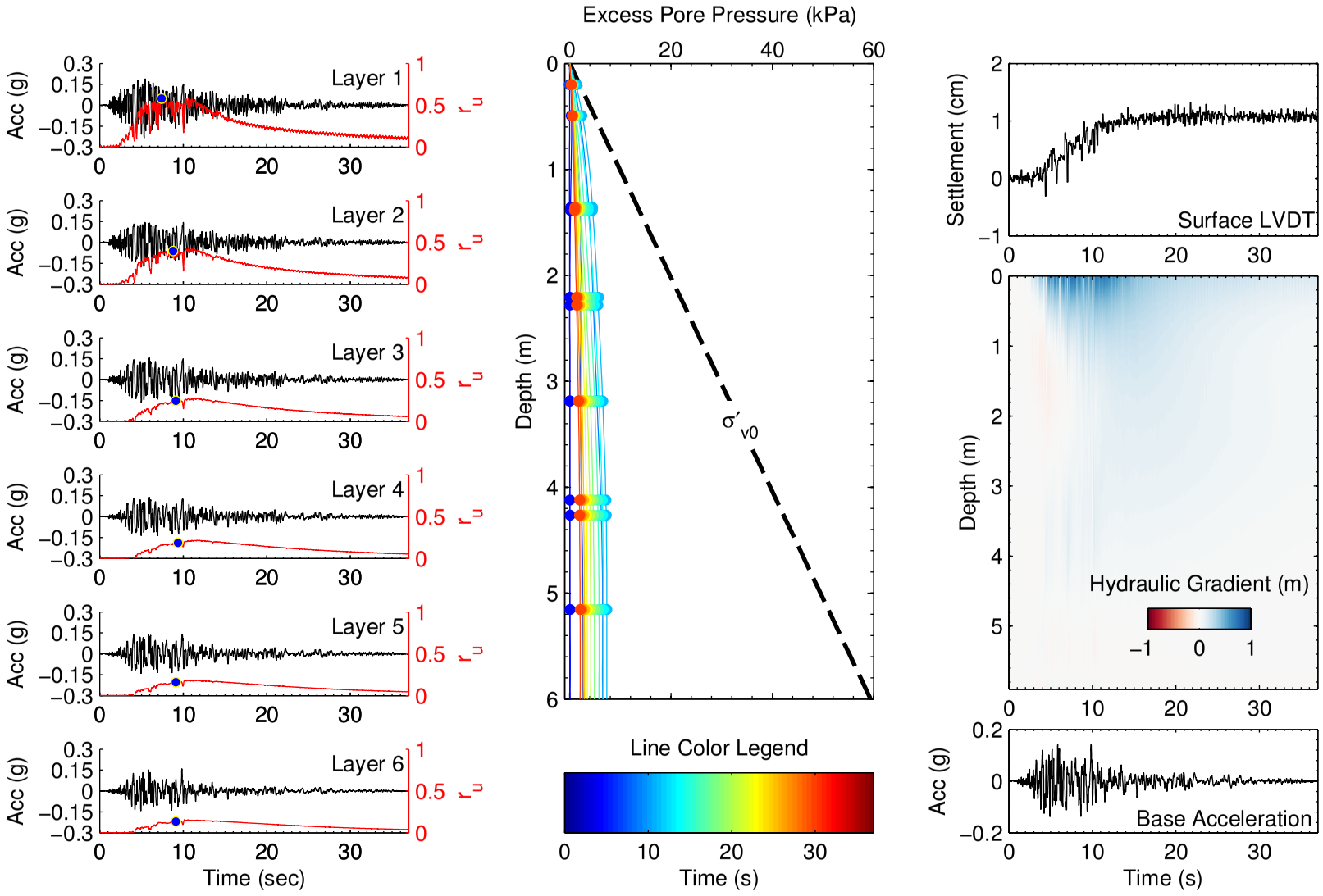
40% D_r Experiment 5 Test 8 – Data Summary Plot



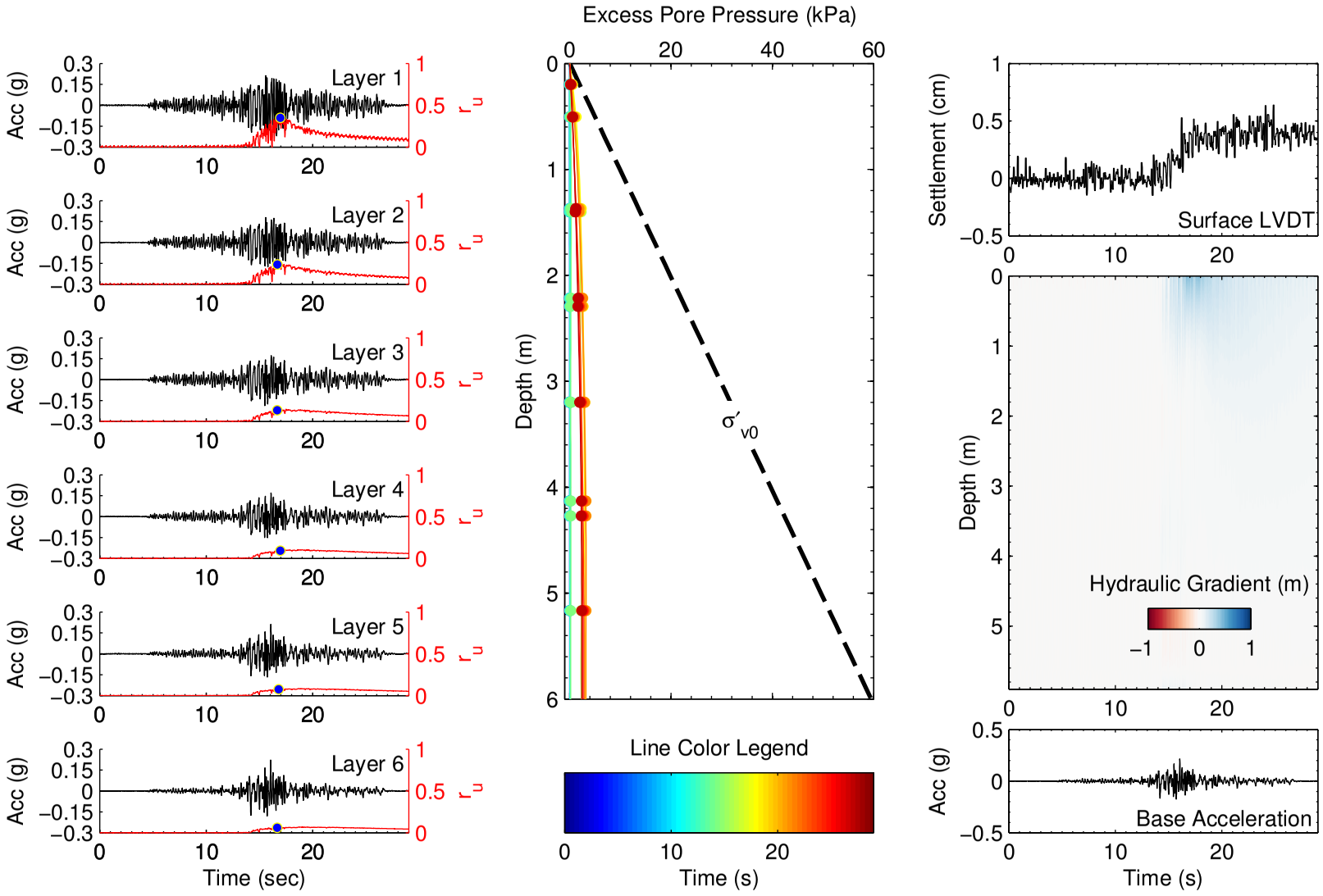
40% D_r Experiment 6 Test 1 – Data Summary Plot



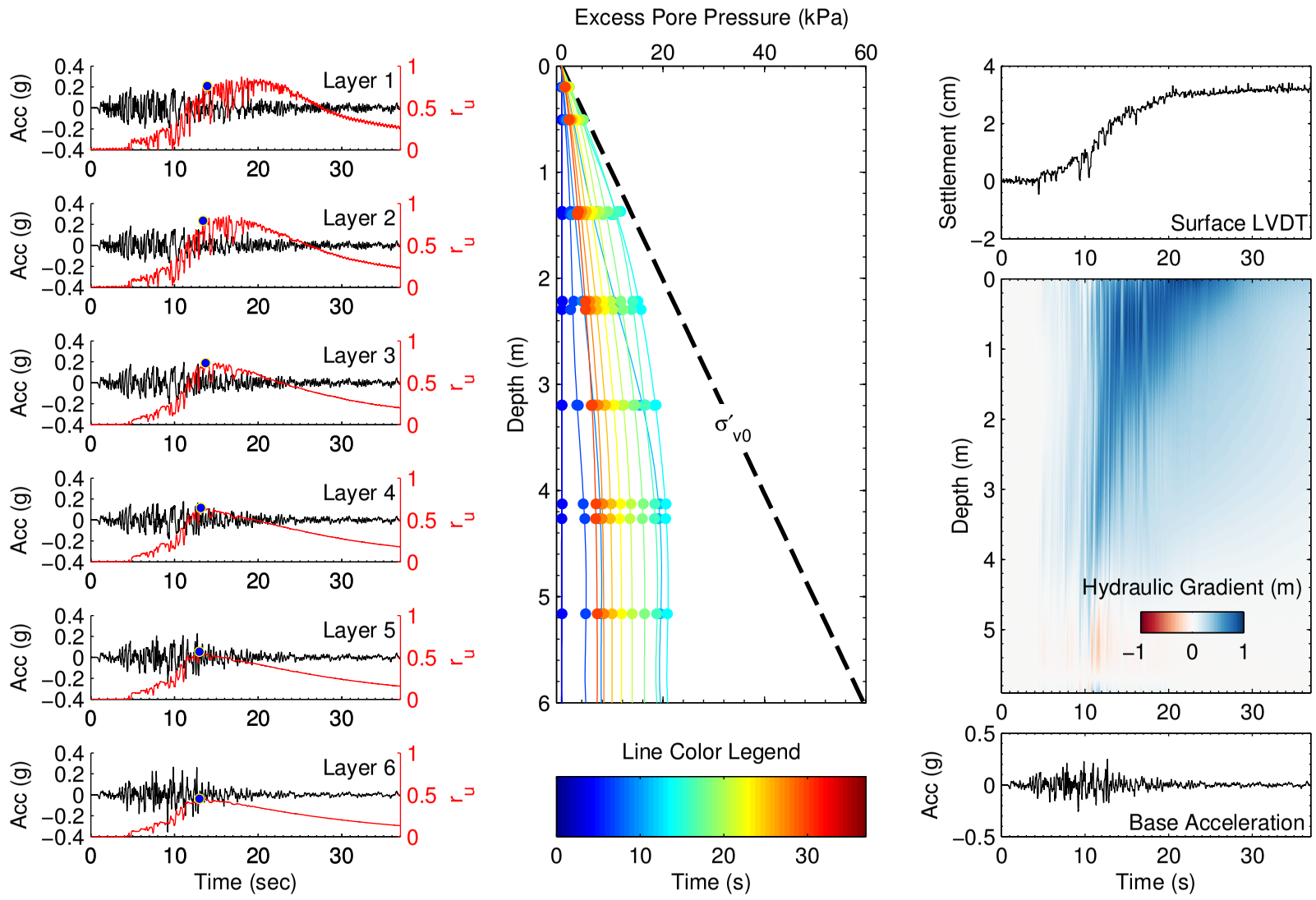
40% D_r Experiment 6 Test 2 – Data Summary Plot



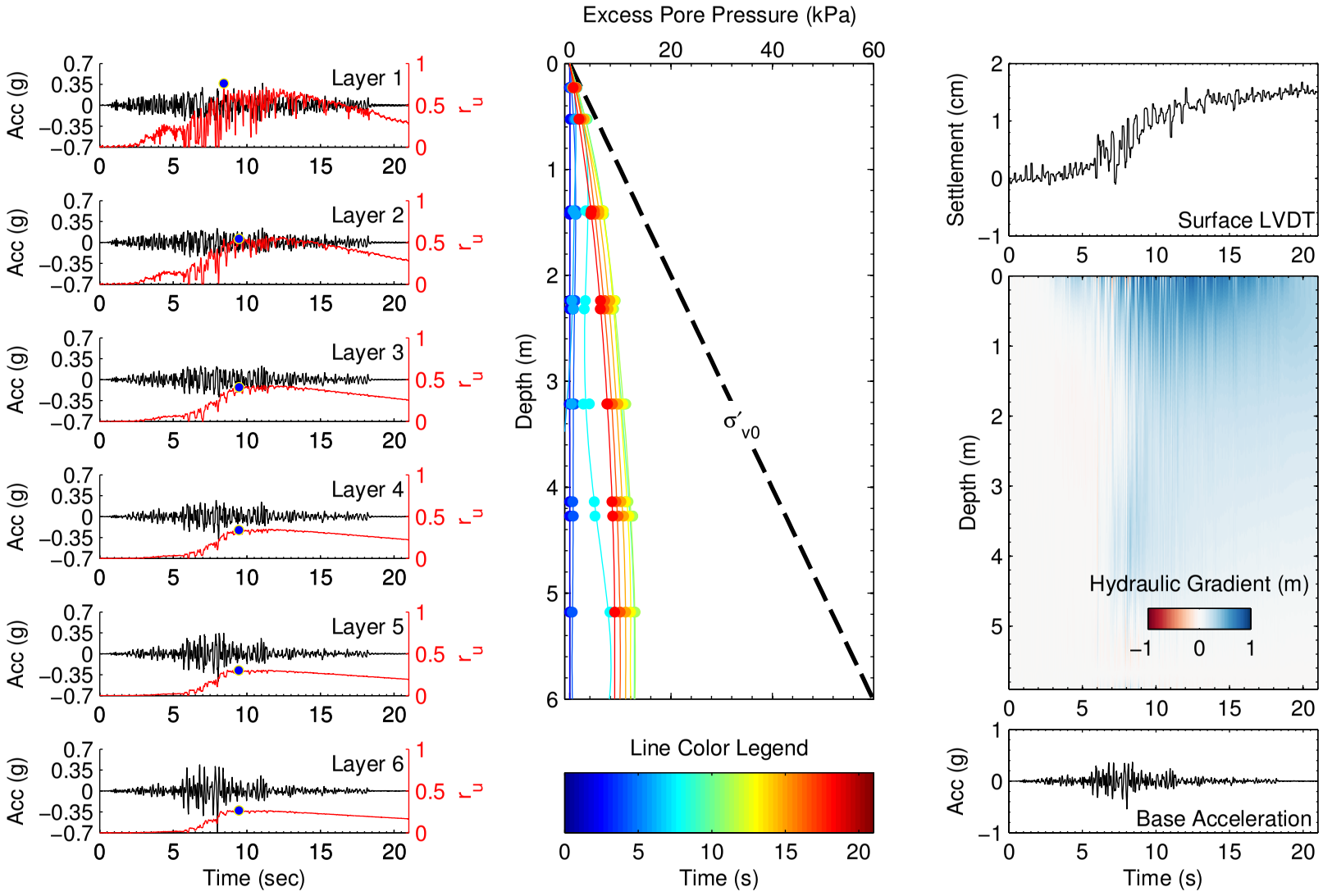
40% D_r Experiment 6 Test 3 – Data Summary Plot



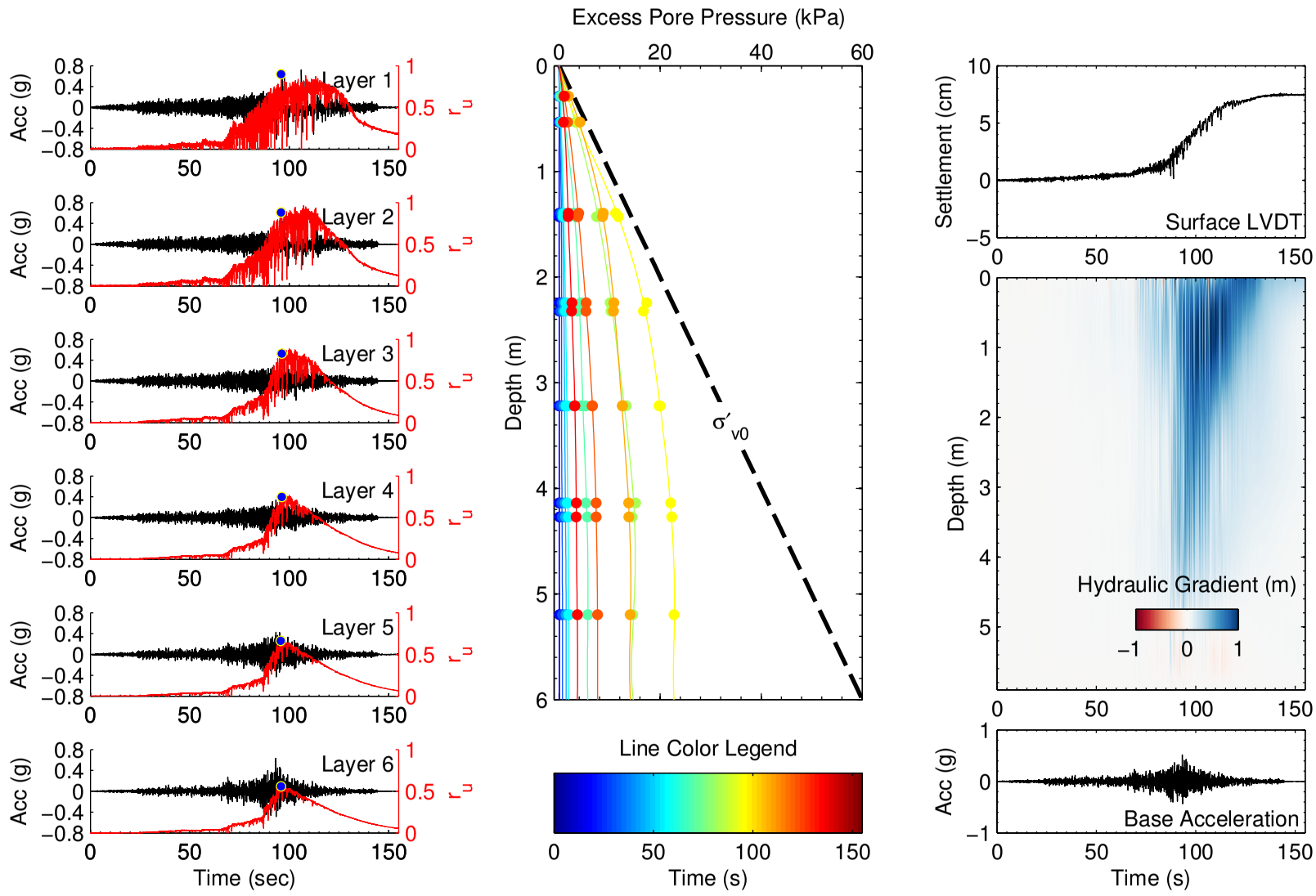
40% D_r Experiment 6 Test 4 – Data Summary Plot



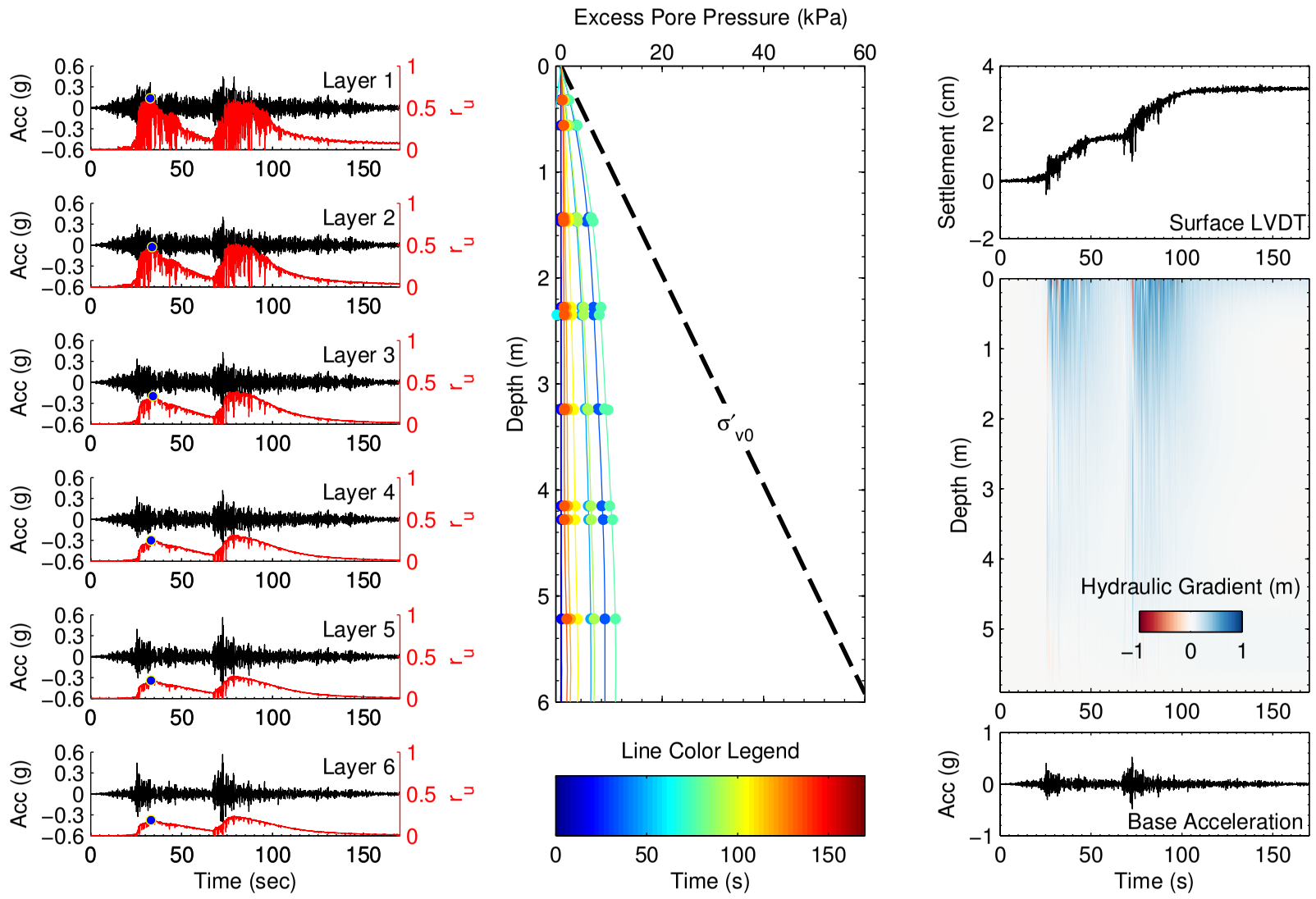
40% D_r Experiment 6 Test 5 – Data Summary Plot



40% D_r Experiment 6 Test 6 – Data Summary Plot



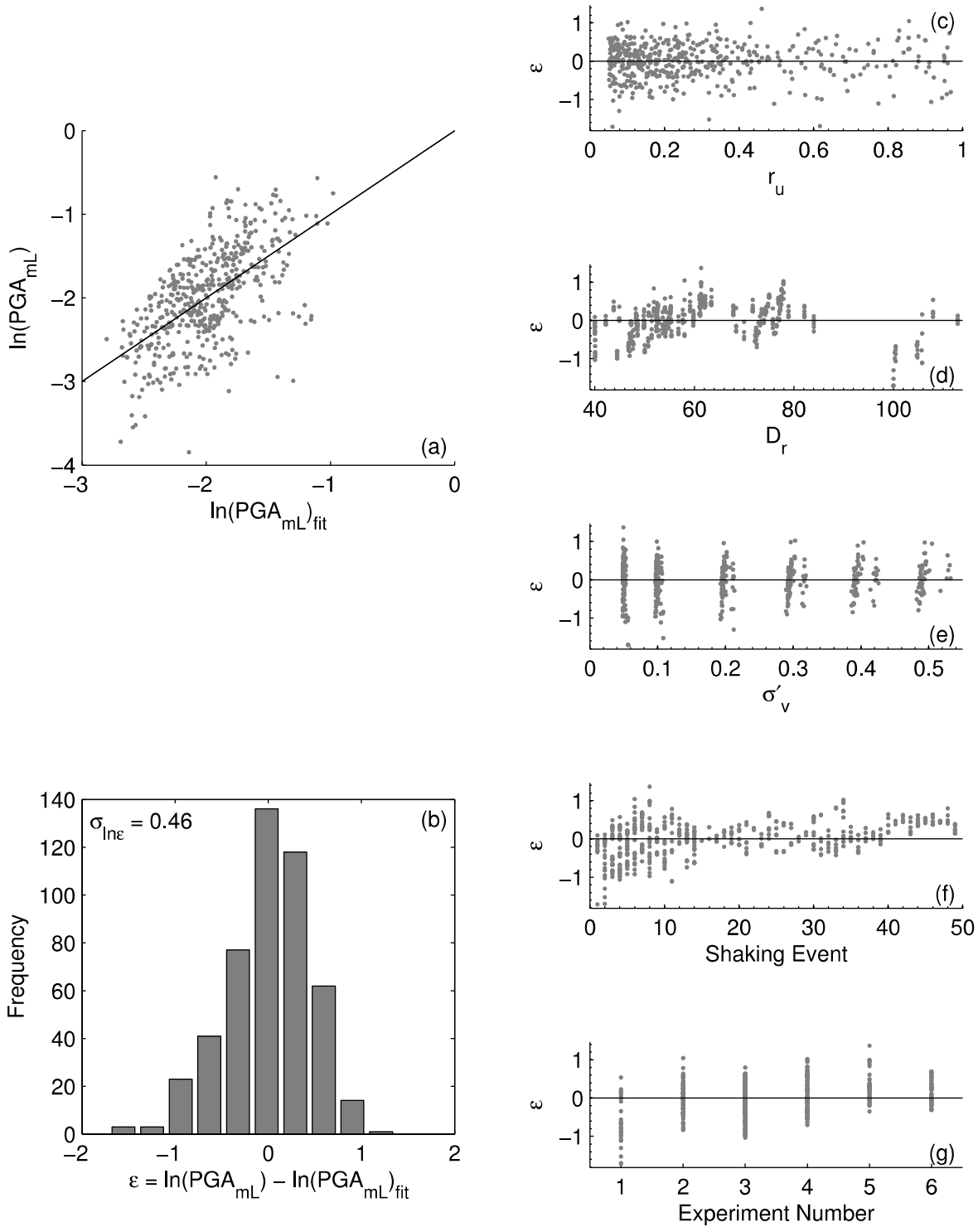
40% D_r Experiment 6 Test 7 – Data Summary Plot



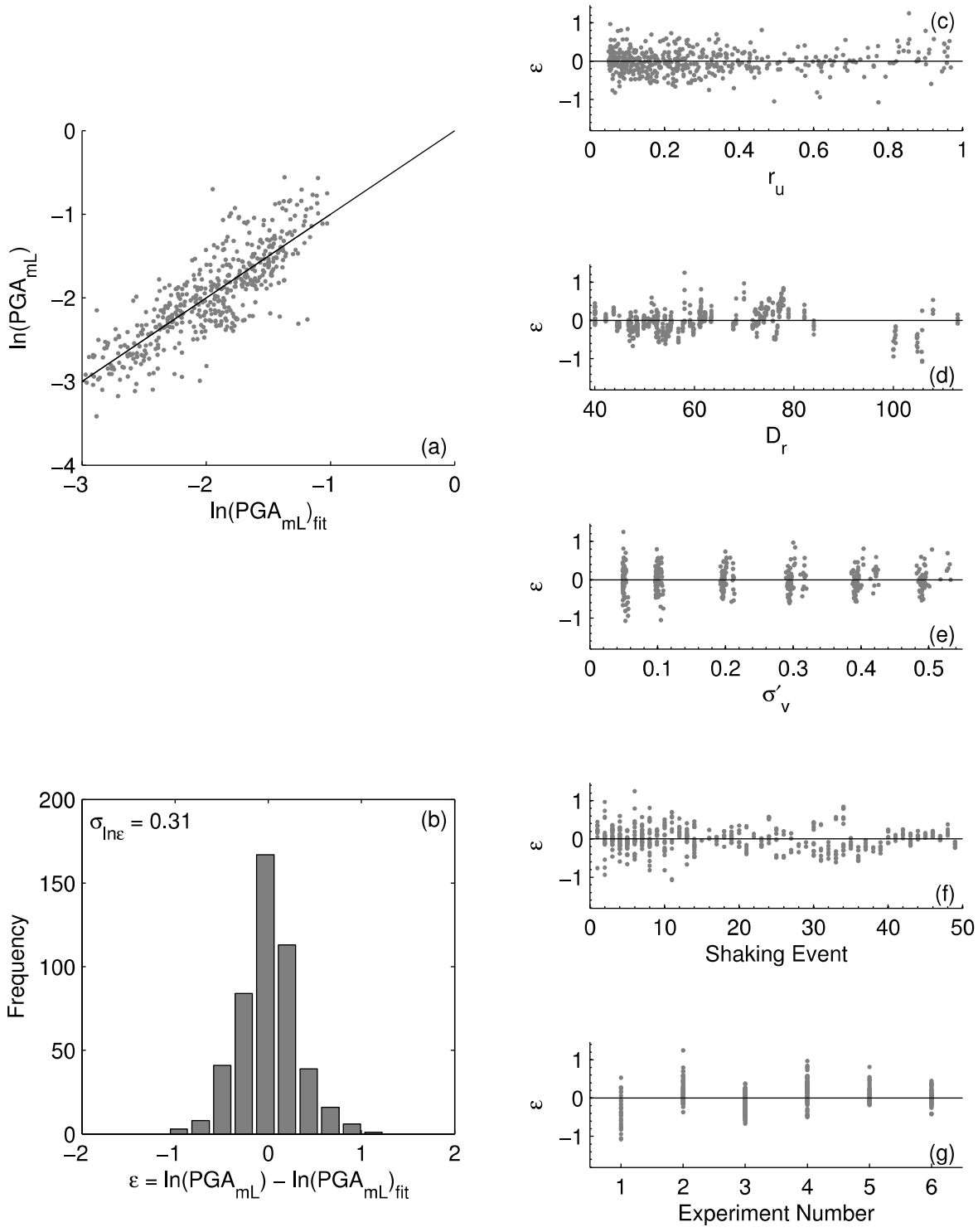
40% D_r Experiment 6 Test 8 – Data Summary Plot

[This page intentionally left blank]

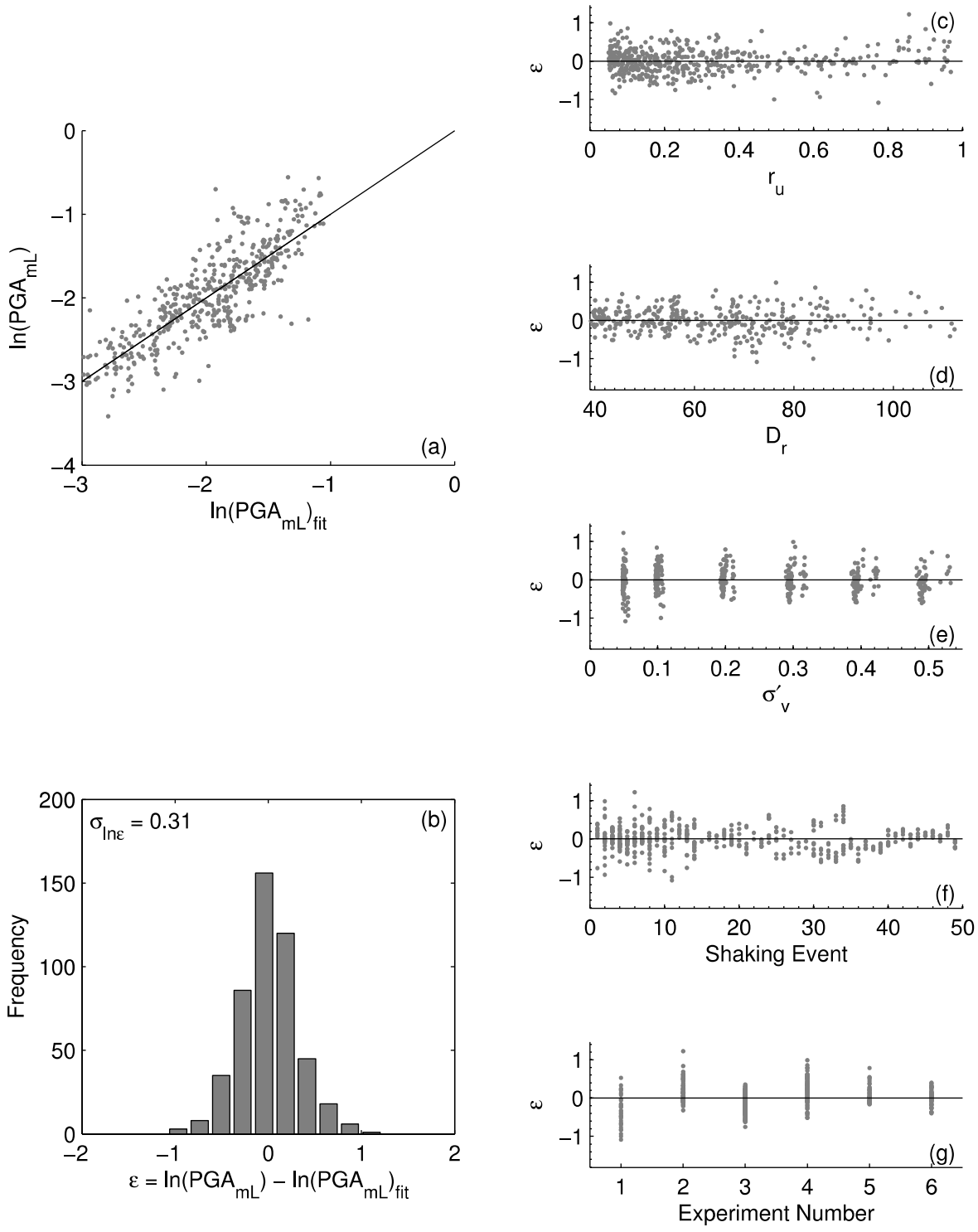
APPENDIX D: CENTRIFUGE TEST REGRESSION ANALYSIS SUMMARIES



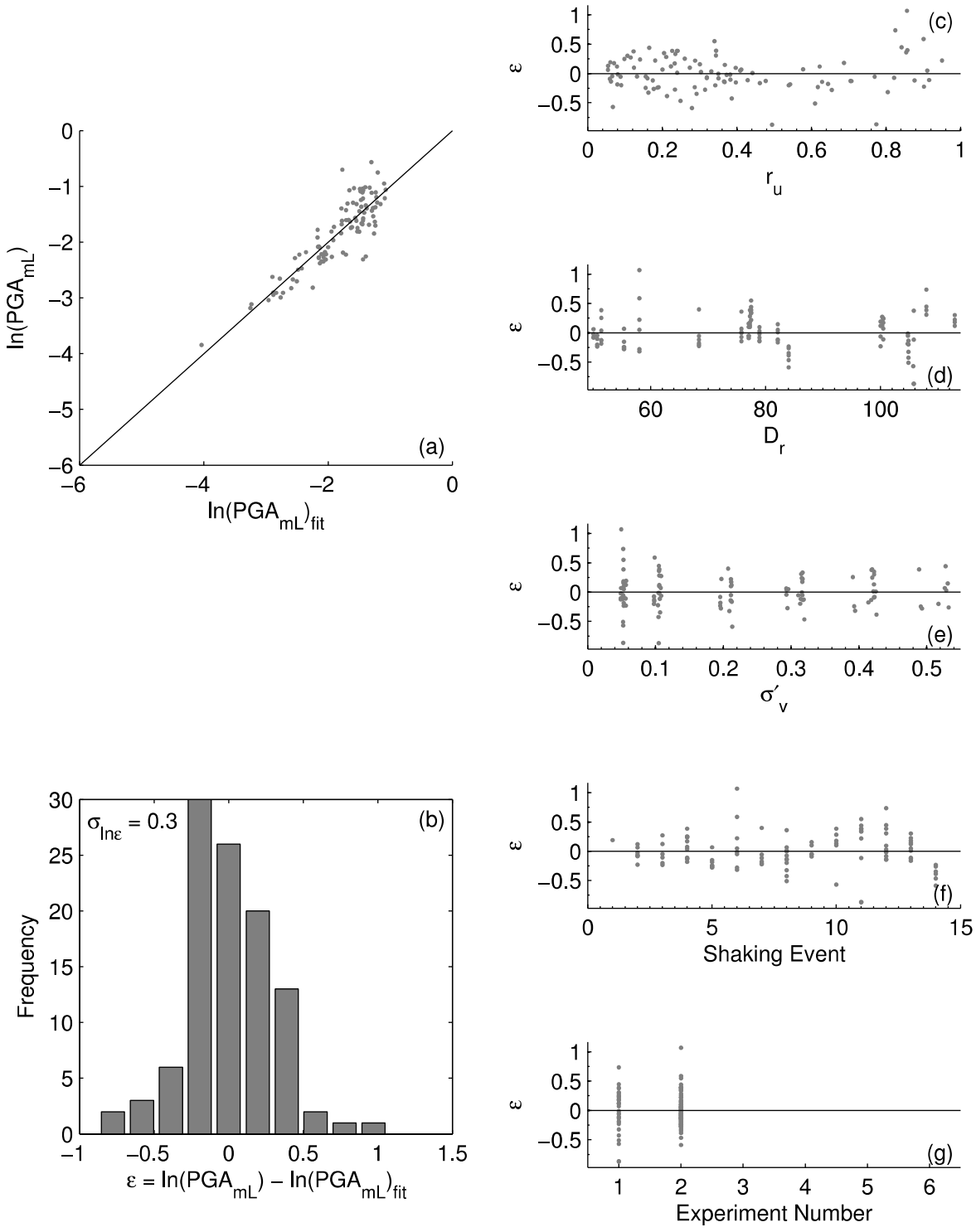
PGA_{mL} – Fit to All Centrifuge Experiments (Equation 7.5)



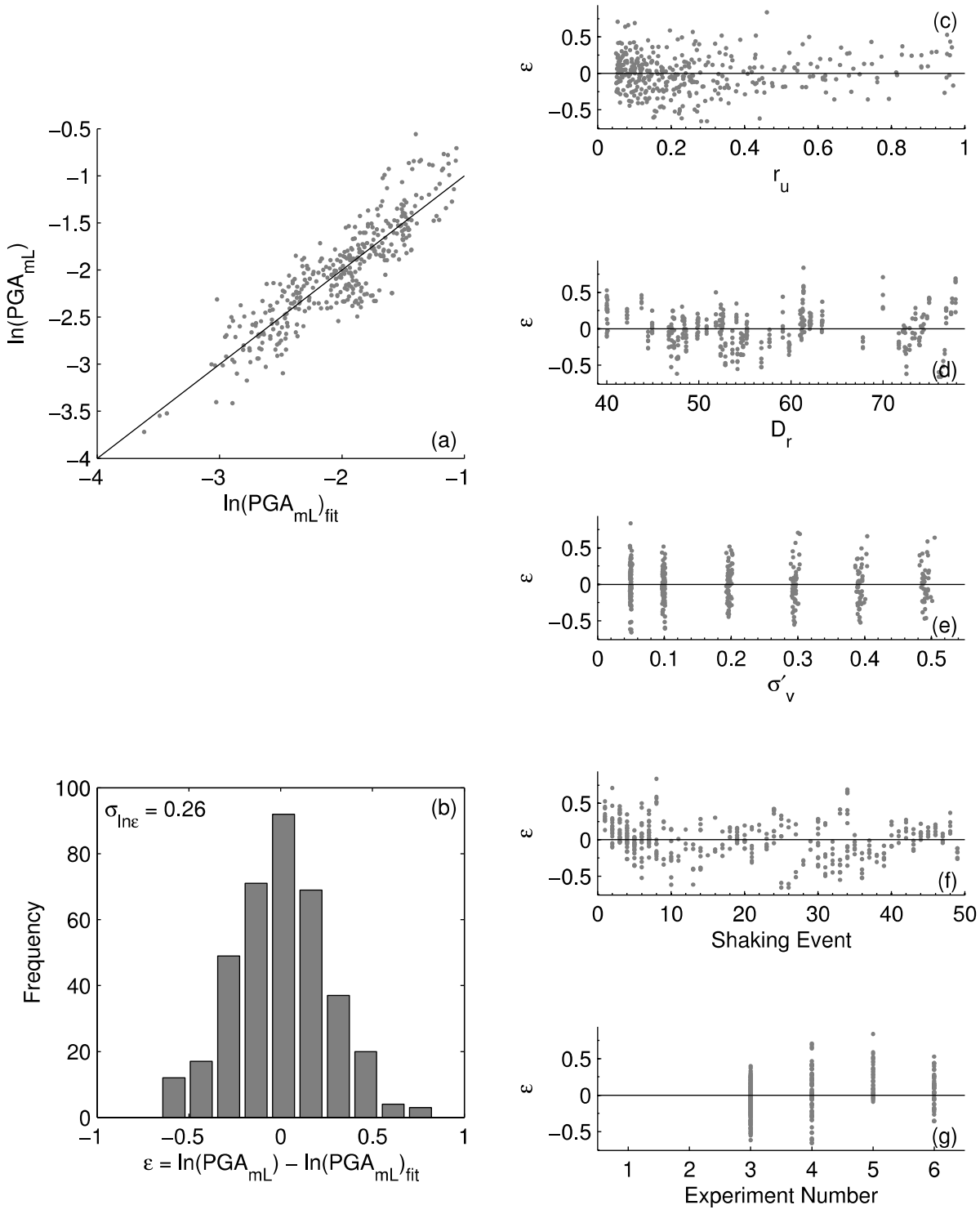
PGA_{mL} – Fit to All Centrifuge Experiments with N_{test} Term (Equation 7.6)



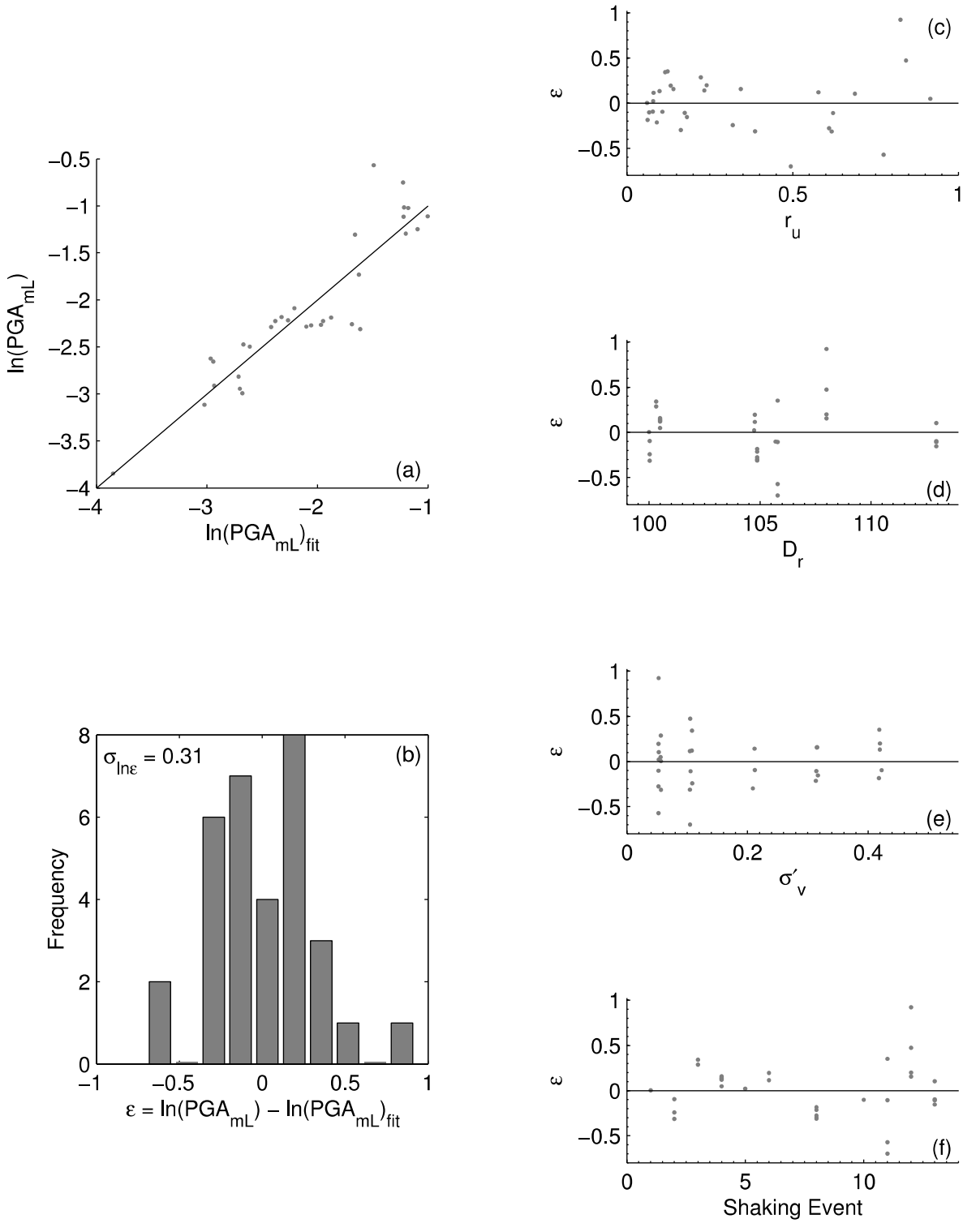
PGA_{mL} – Fit to All Centrifuge Experiments with Stress–Dependent D_r Profile and Including N_{test} Term (Equation 7.6)



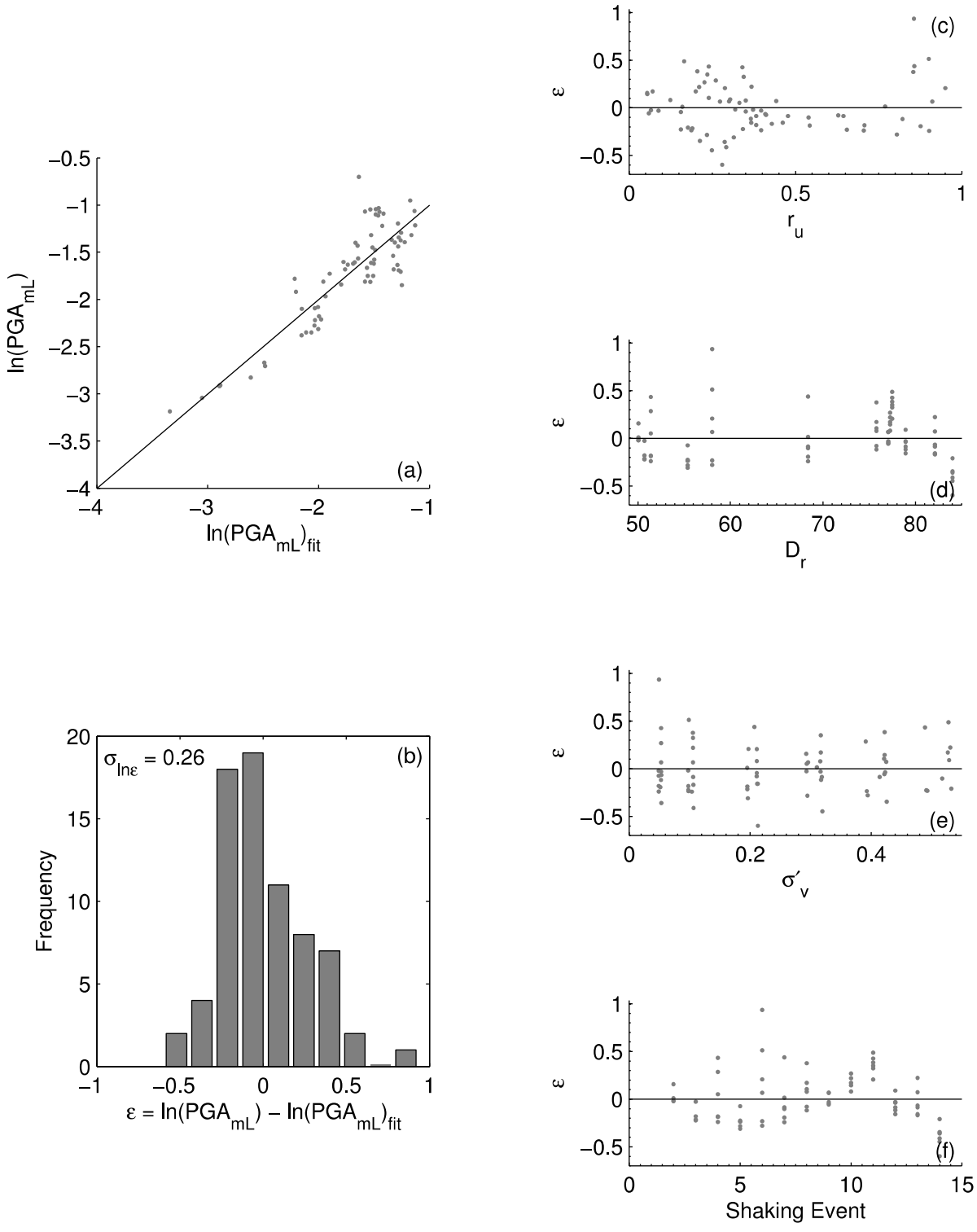
PGA_{mL} – Fit to Experiments 1 and 2 with N_{test} Term (Equation 7.6)



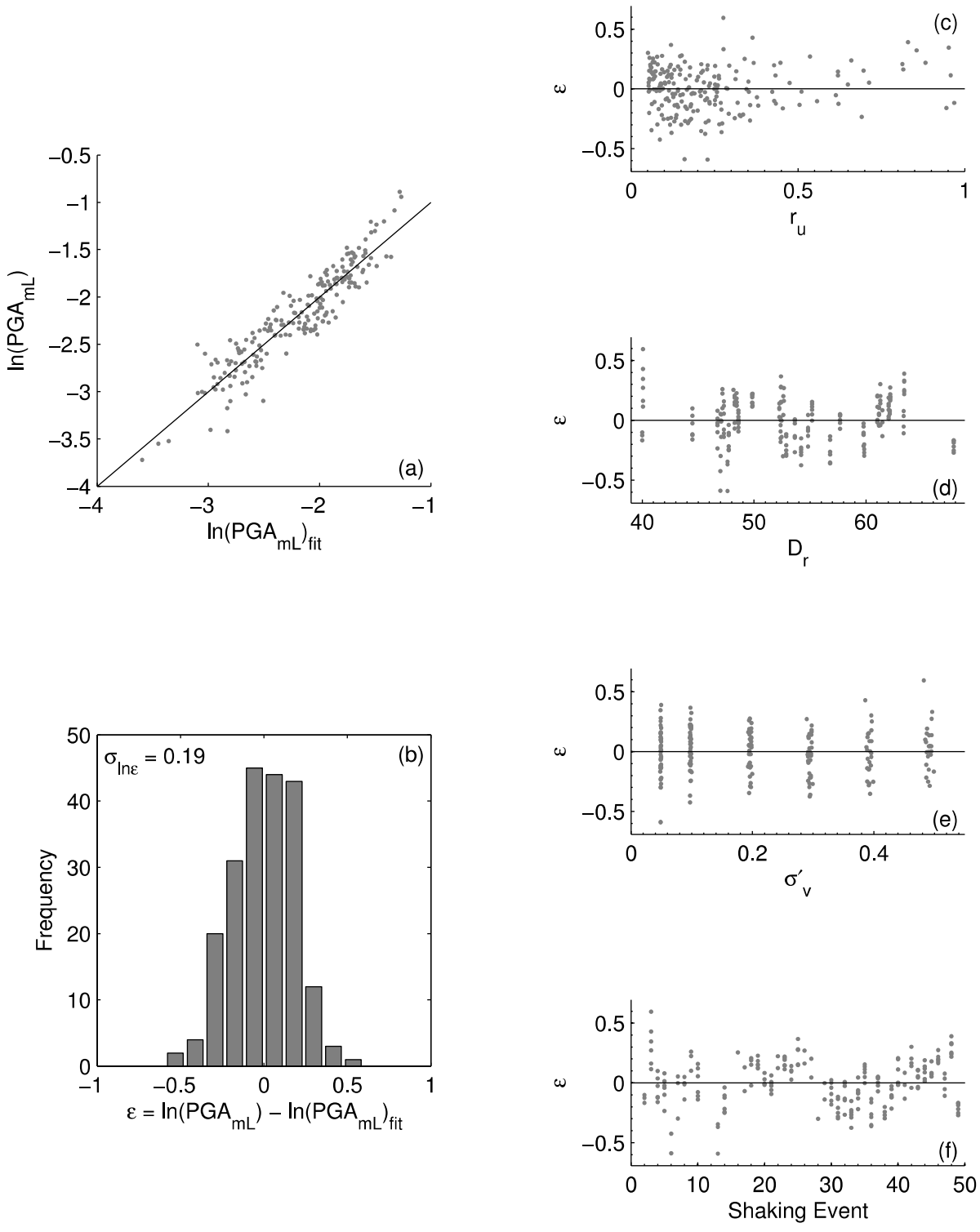
PGA_{mL} – Fit to Experiments 3 to 6 with N_{test} Term (Equation 7.6)



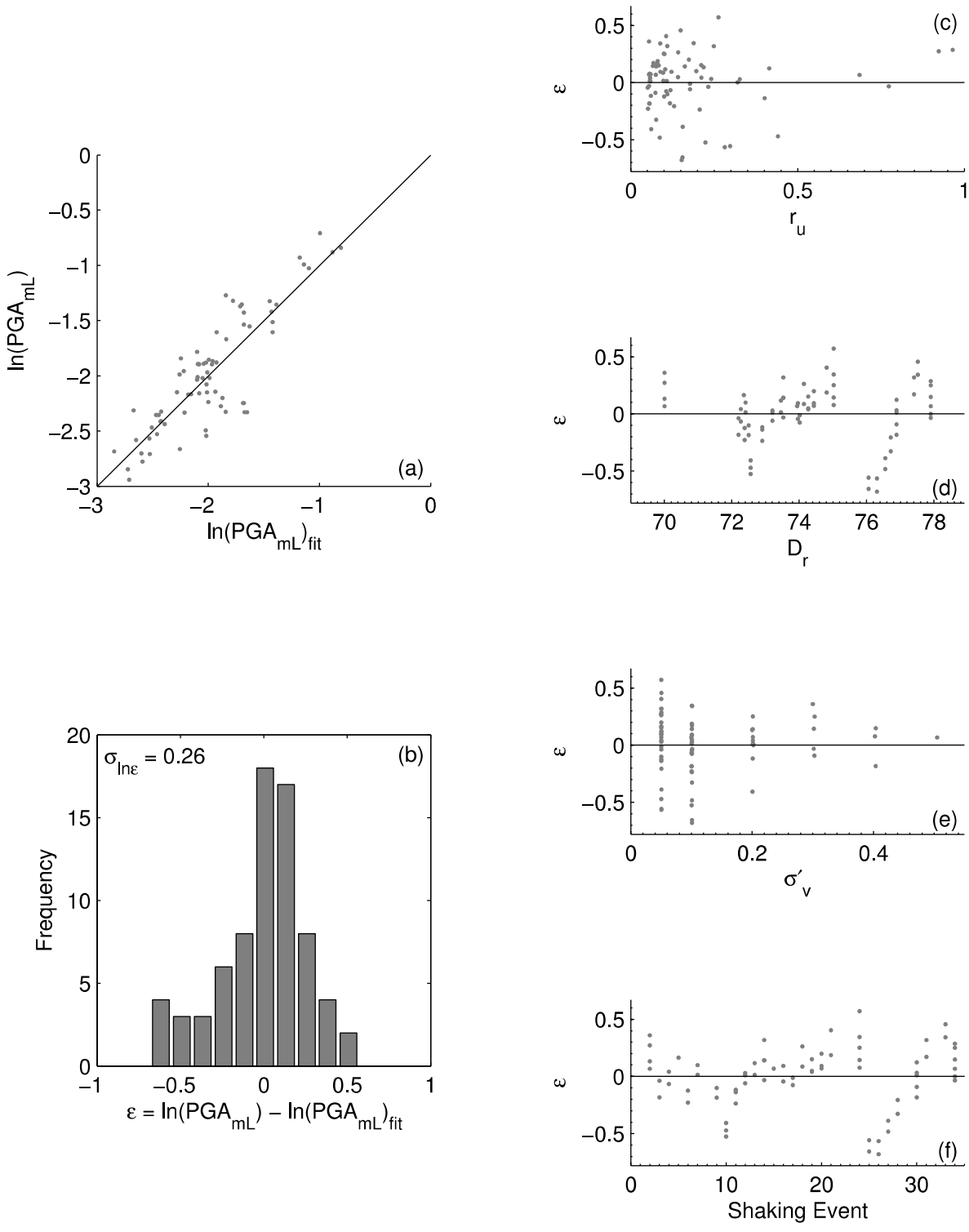
PGA_{mL} – Fit to Experiment 1 with N_{test} Term (Equation 7.6)



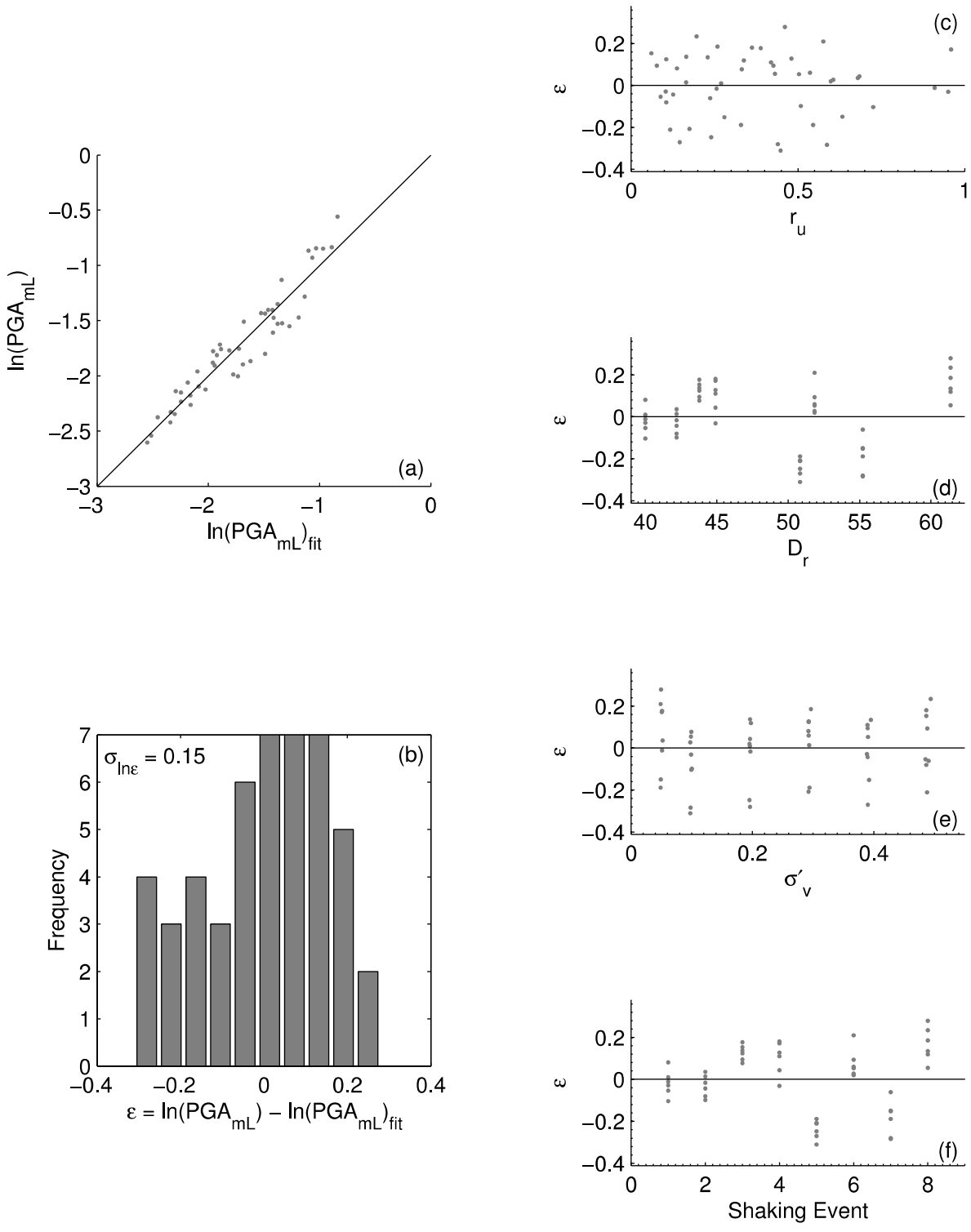
PGA_{mL} – Fit to Experiment 2 with N_{test} Term (Equation 7.6)



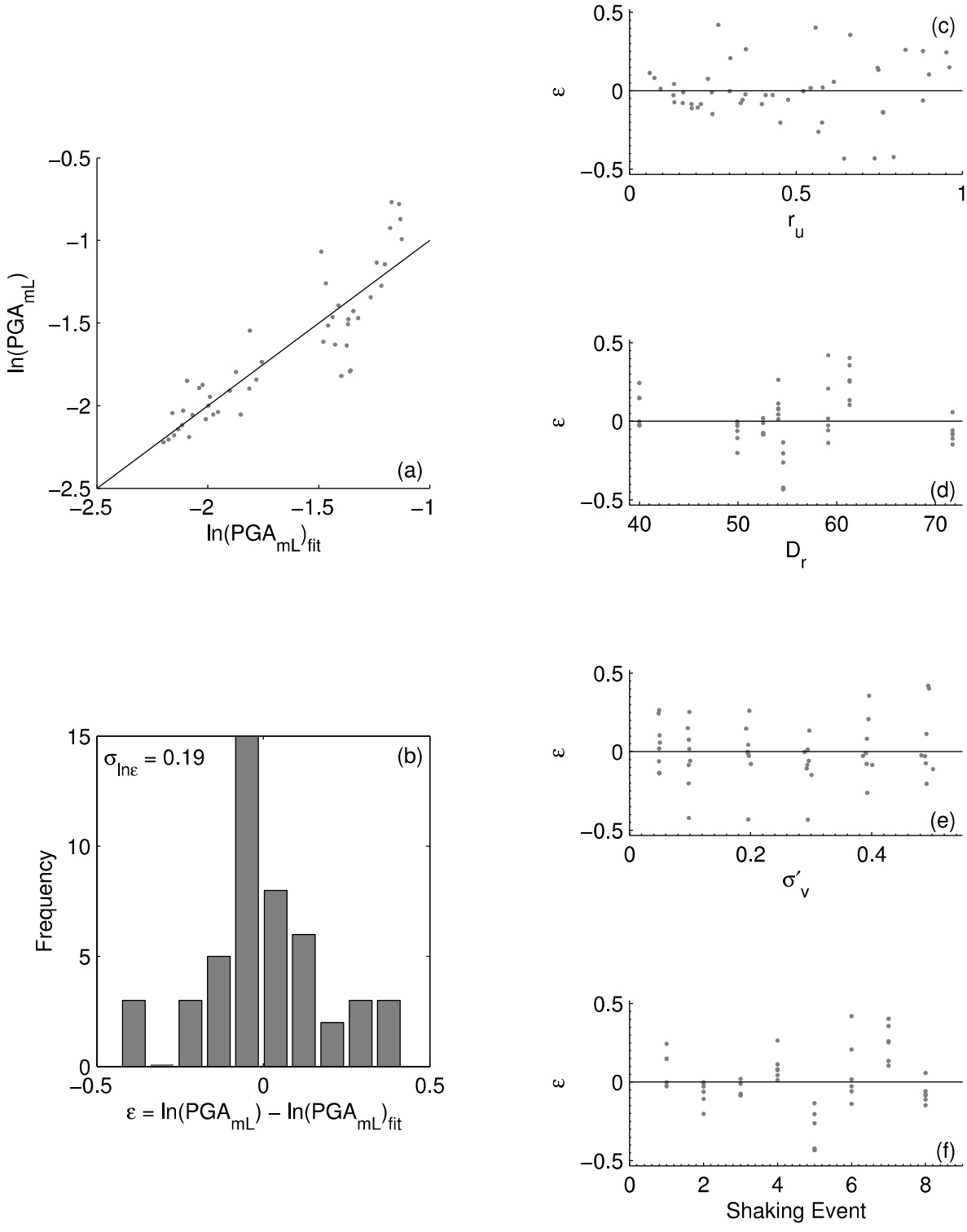
PGA_{mL} – Fit to Experiment 3 with N_{test} Term (Equation 7.6)



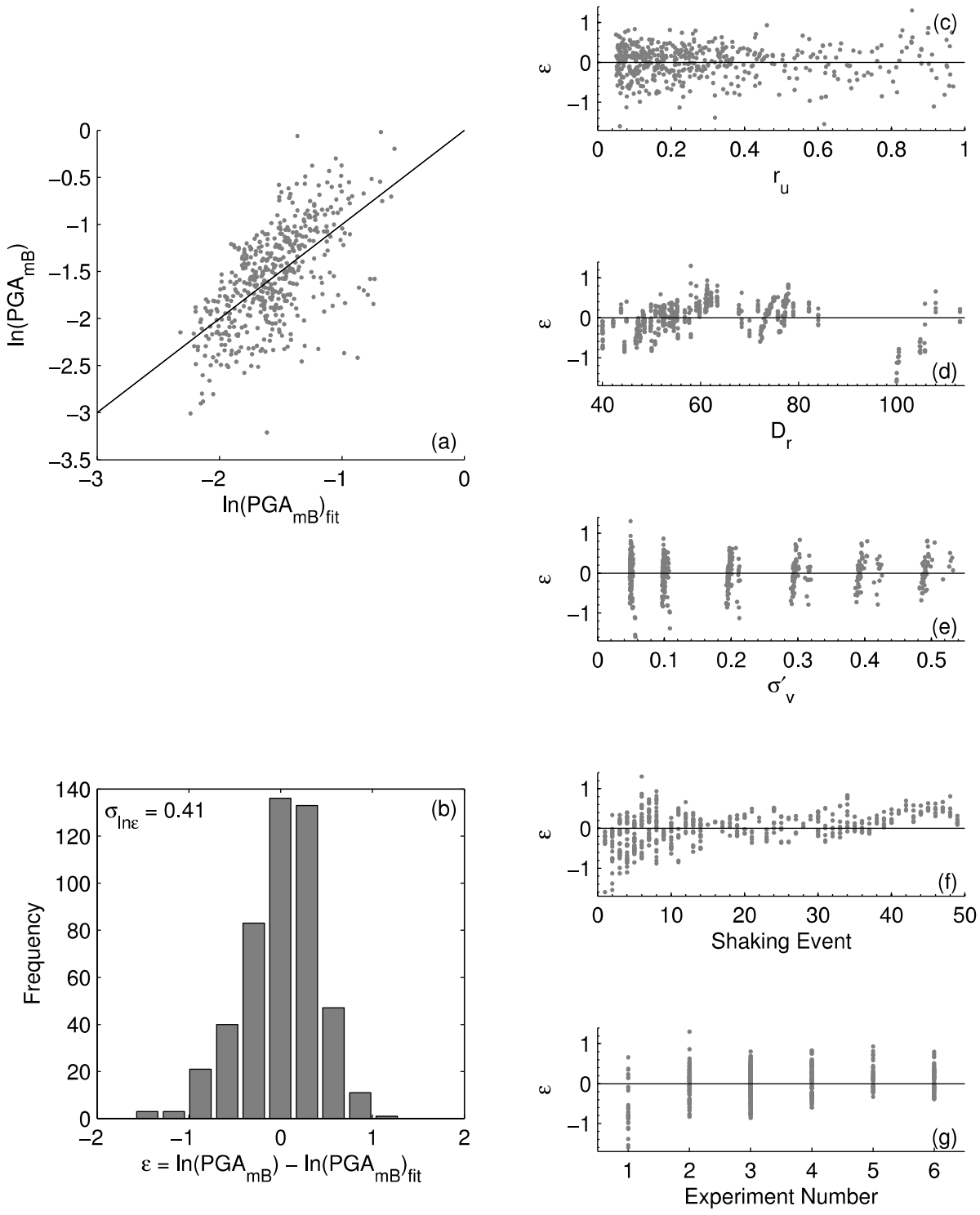
PGA_{mL} – Fit to Experiment 4 with N_{test} Term (Equation 7.6)



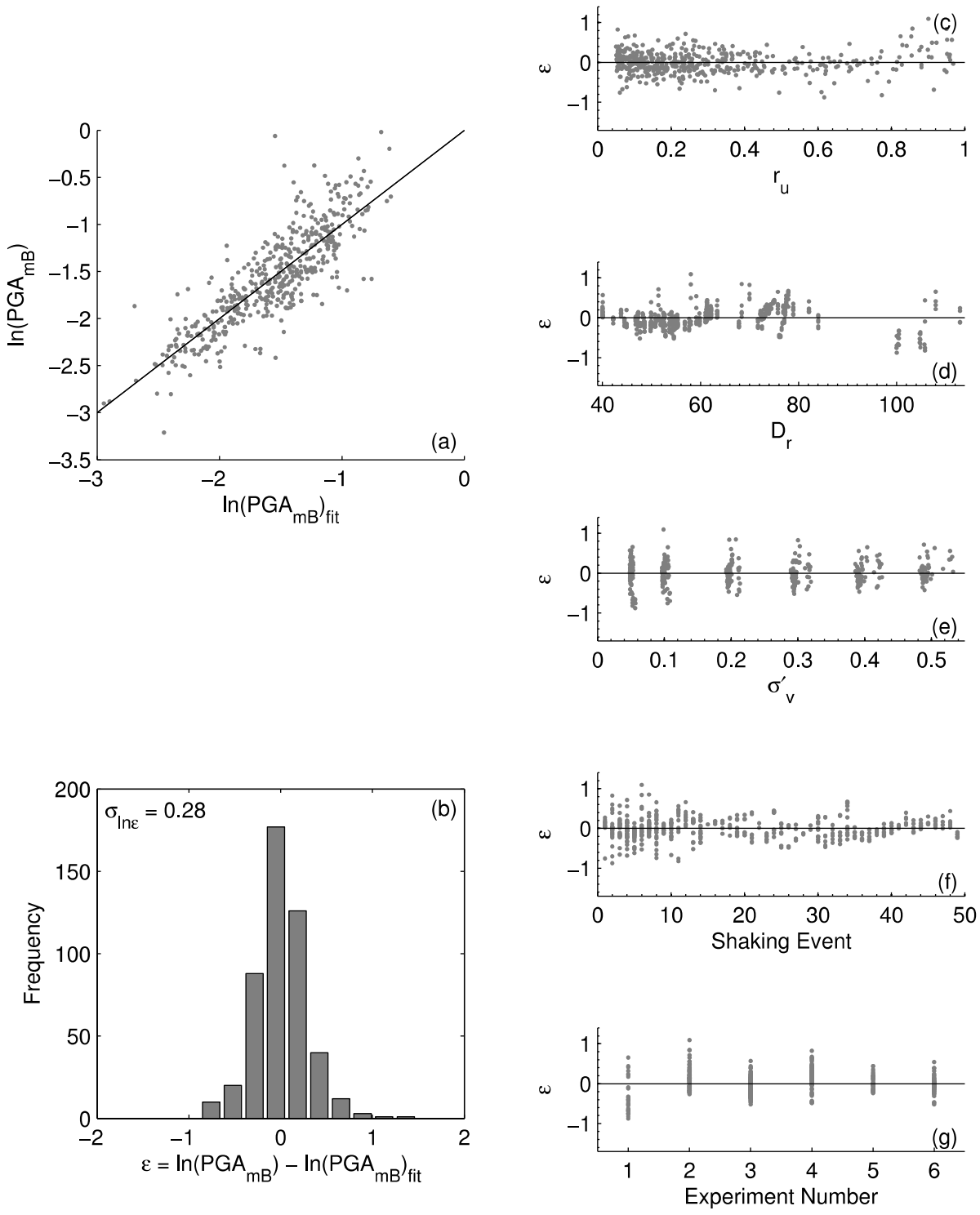
PGA_{mL} – Fit to Experiment 5 with N_{test} Term (Equation 7.6)



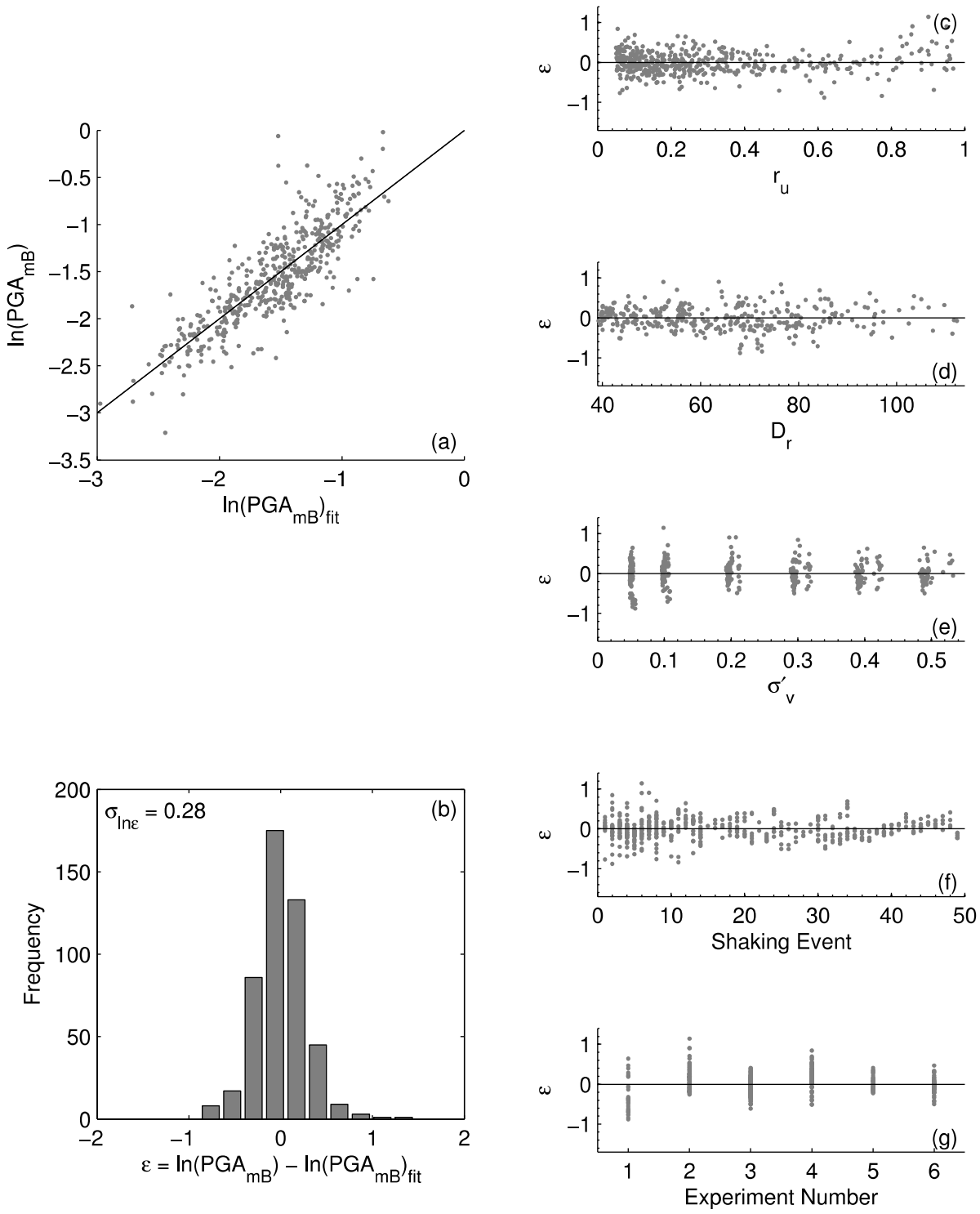
PGA_{mL} – Fit to Experiment 6 with N_{test} Term (Equation 7.6)



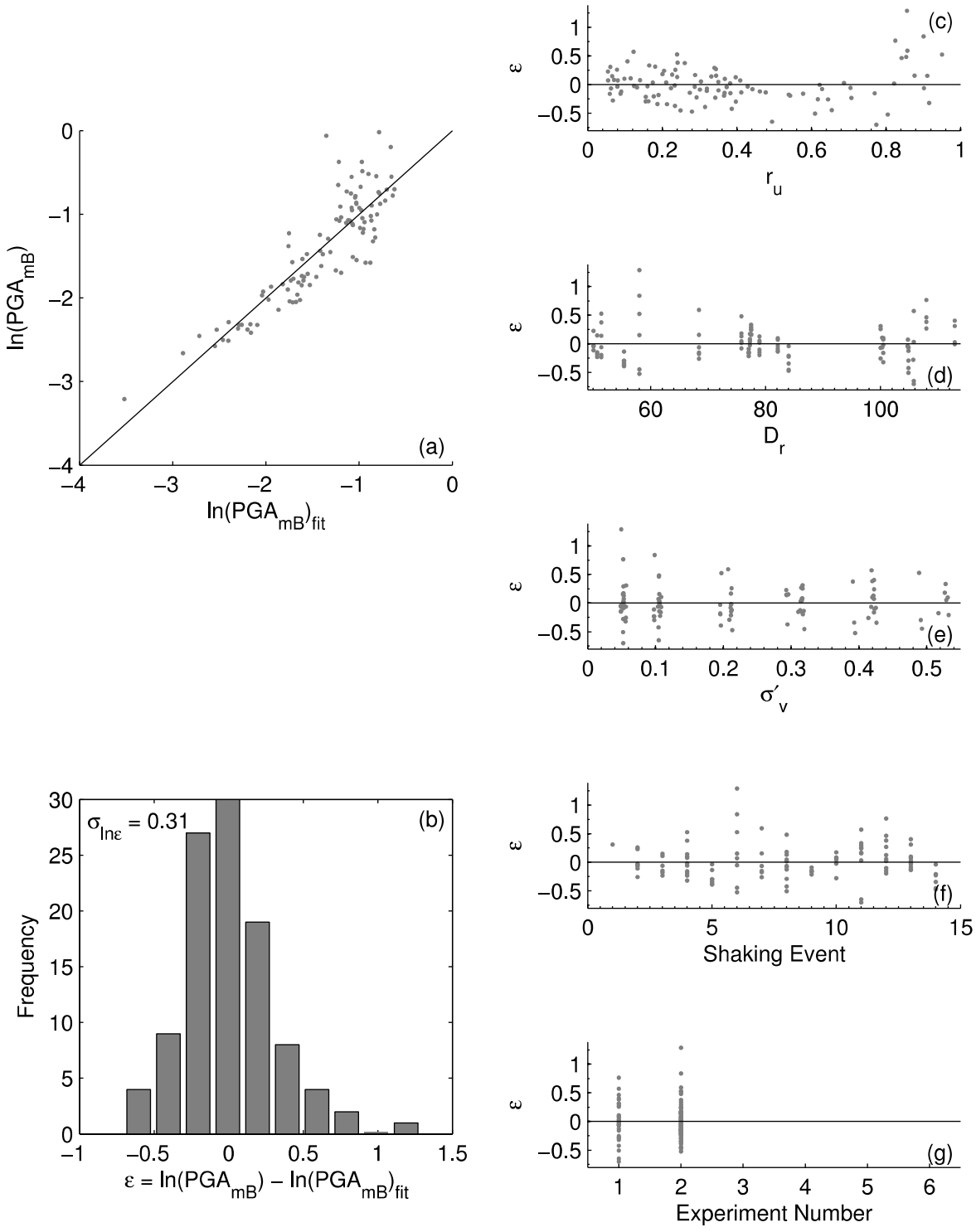
PGA_{mB} – Fit to All Centrifuge Experiments (Equation 7.5)



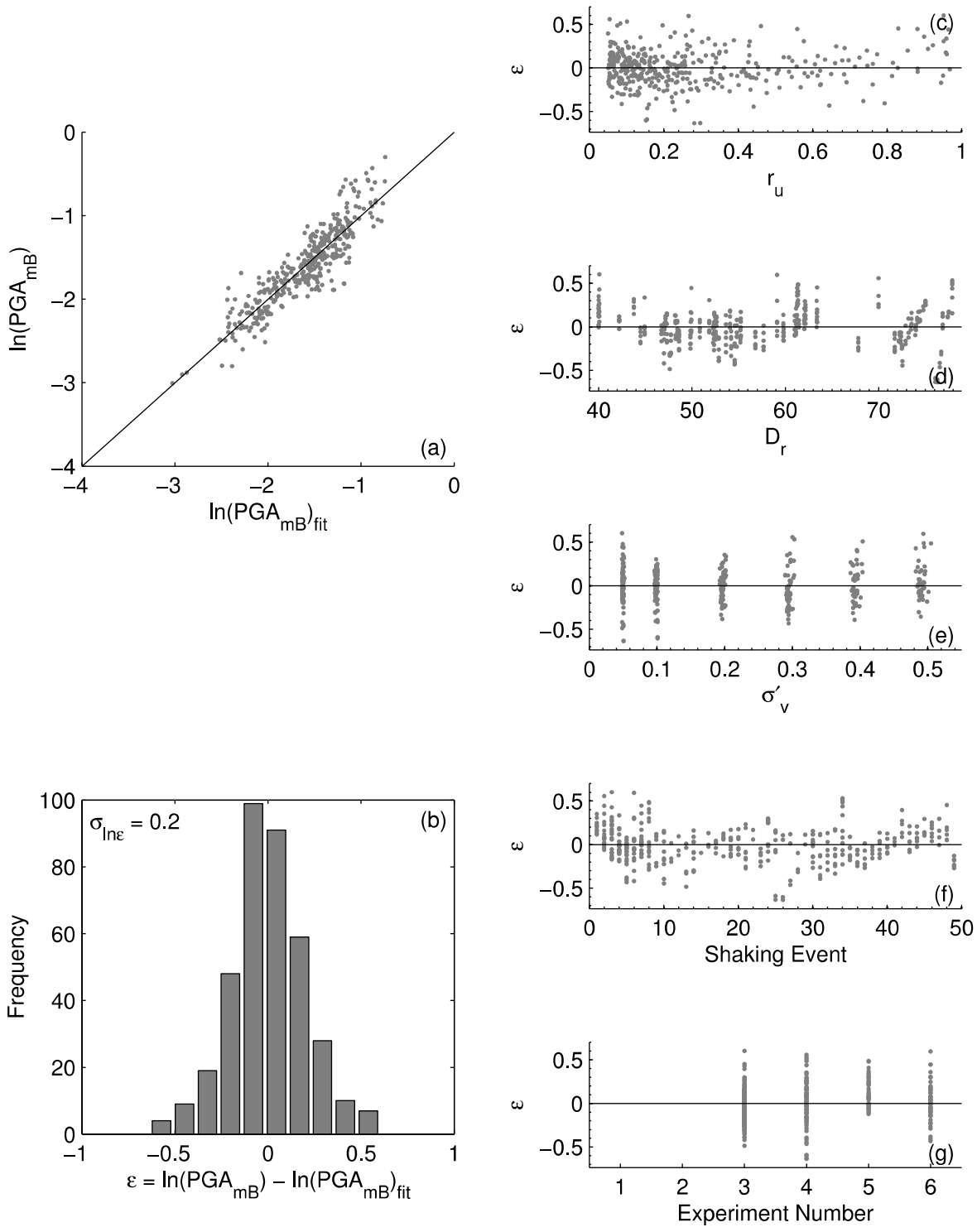
PGA_{mB} – Fit to All Centrifuge Experiments with N_{test} Term (Equation 7.6)



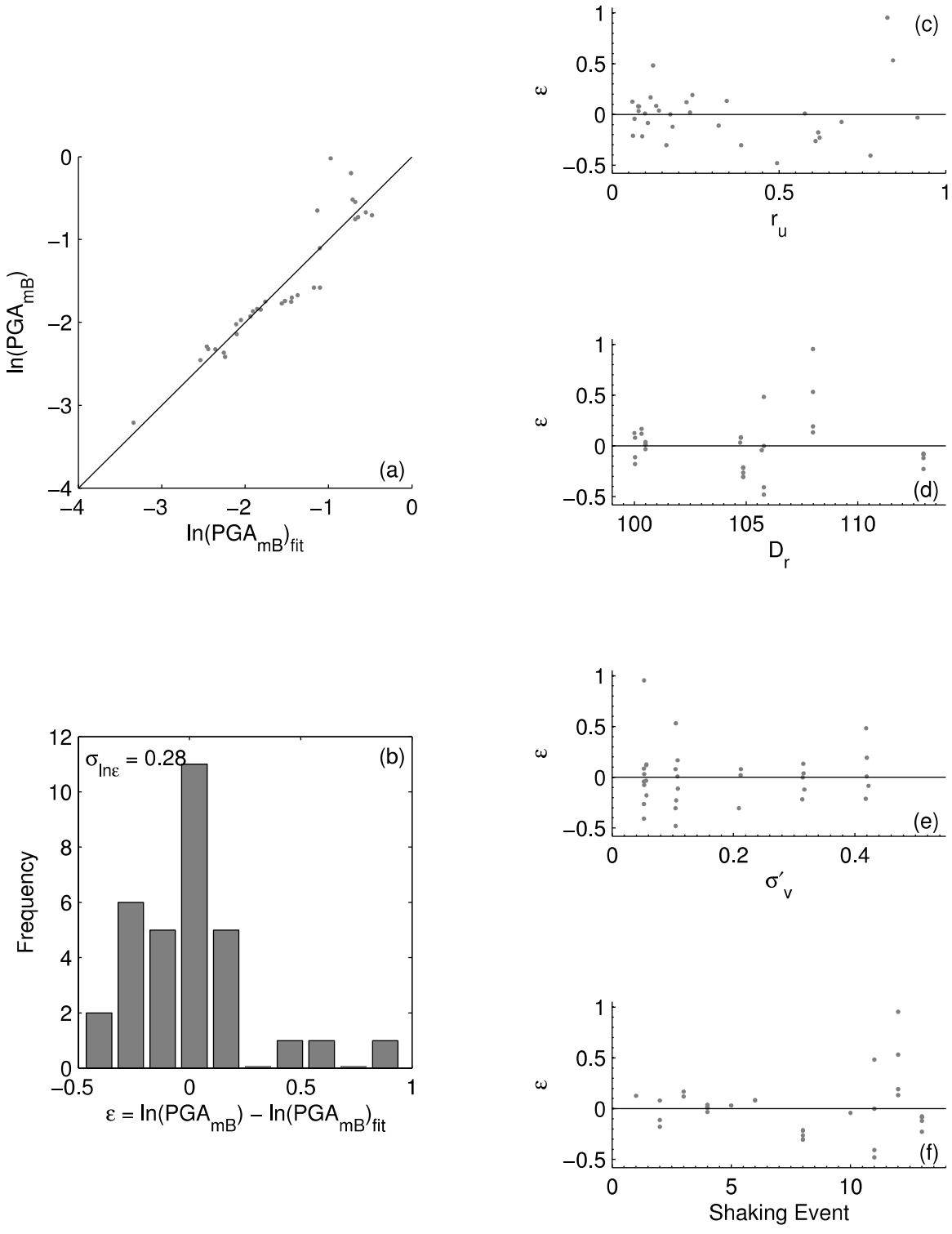
PGA_{mB} – Fit to All Centrifuge Experiments with Stress–Dependent D_r Profile and Including N_{test} Term (Equation 7.6)



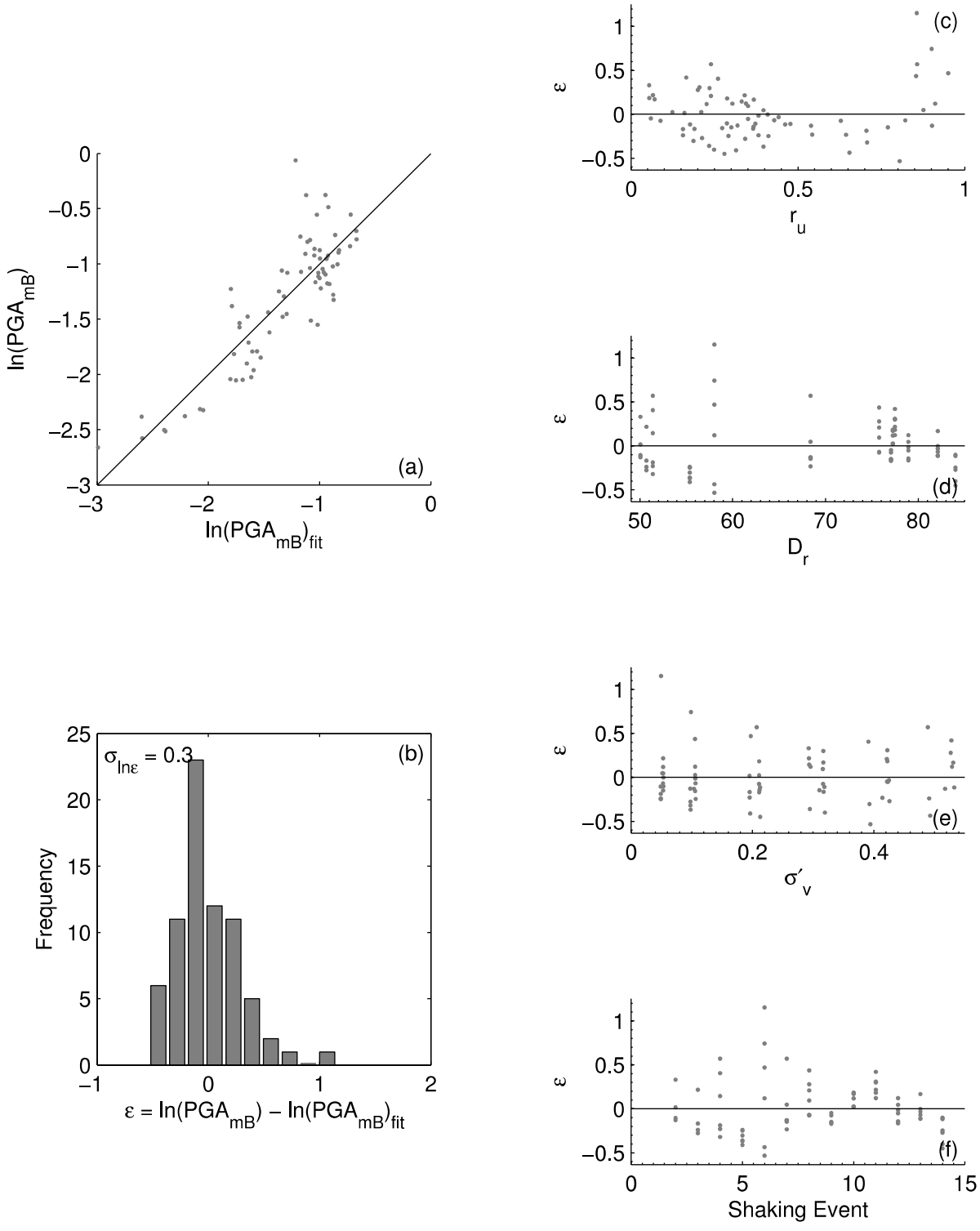
PGA_{mB} – Fit to Experiments 1 and 2 with N_{test} Term (Equation 7.6)



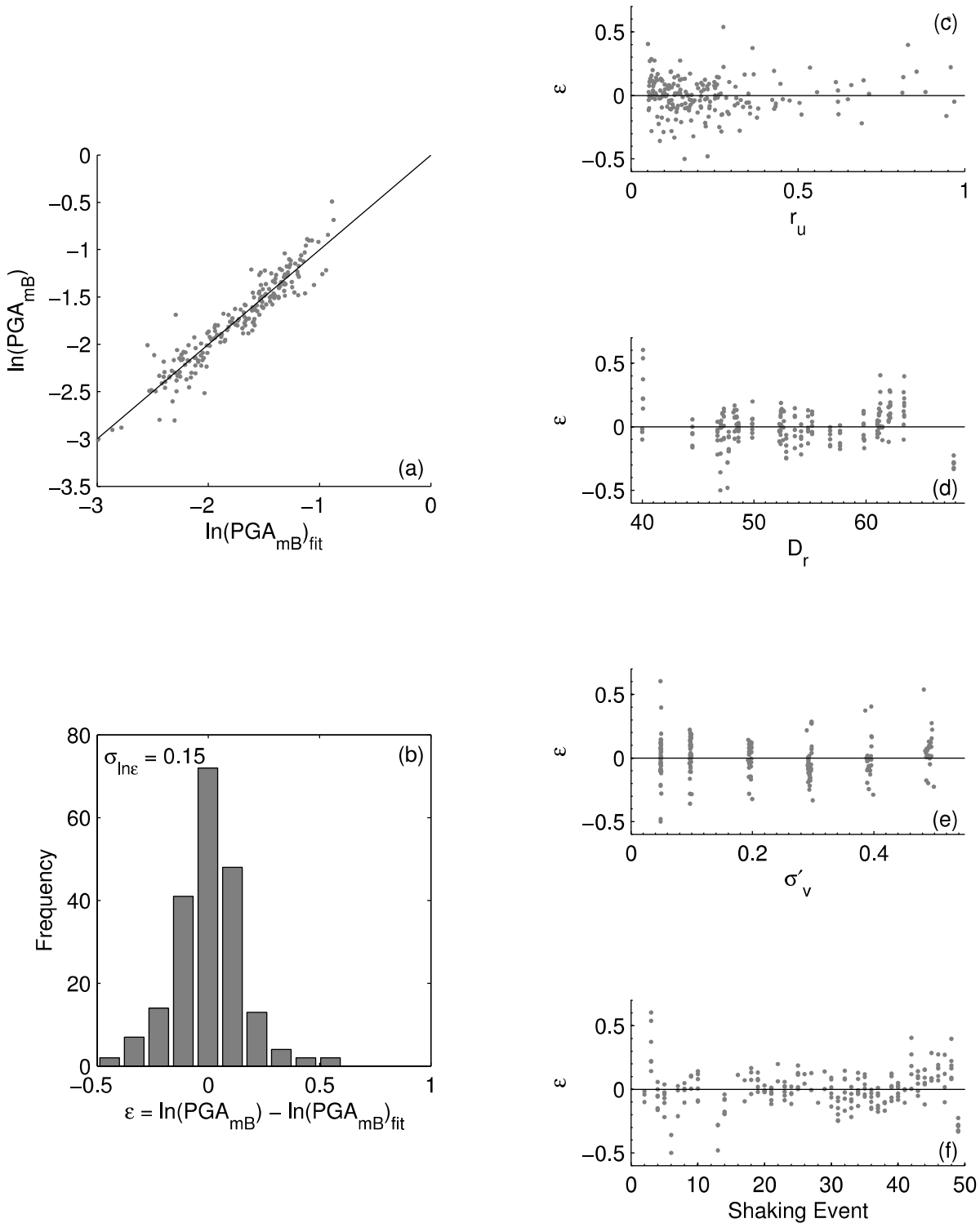
PGA_{mB} – Fit to Experiments 3 to 6 with N_{test} Term (Equation 7.6)



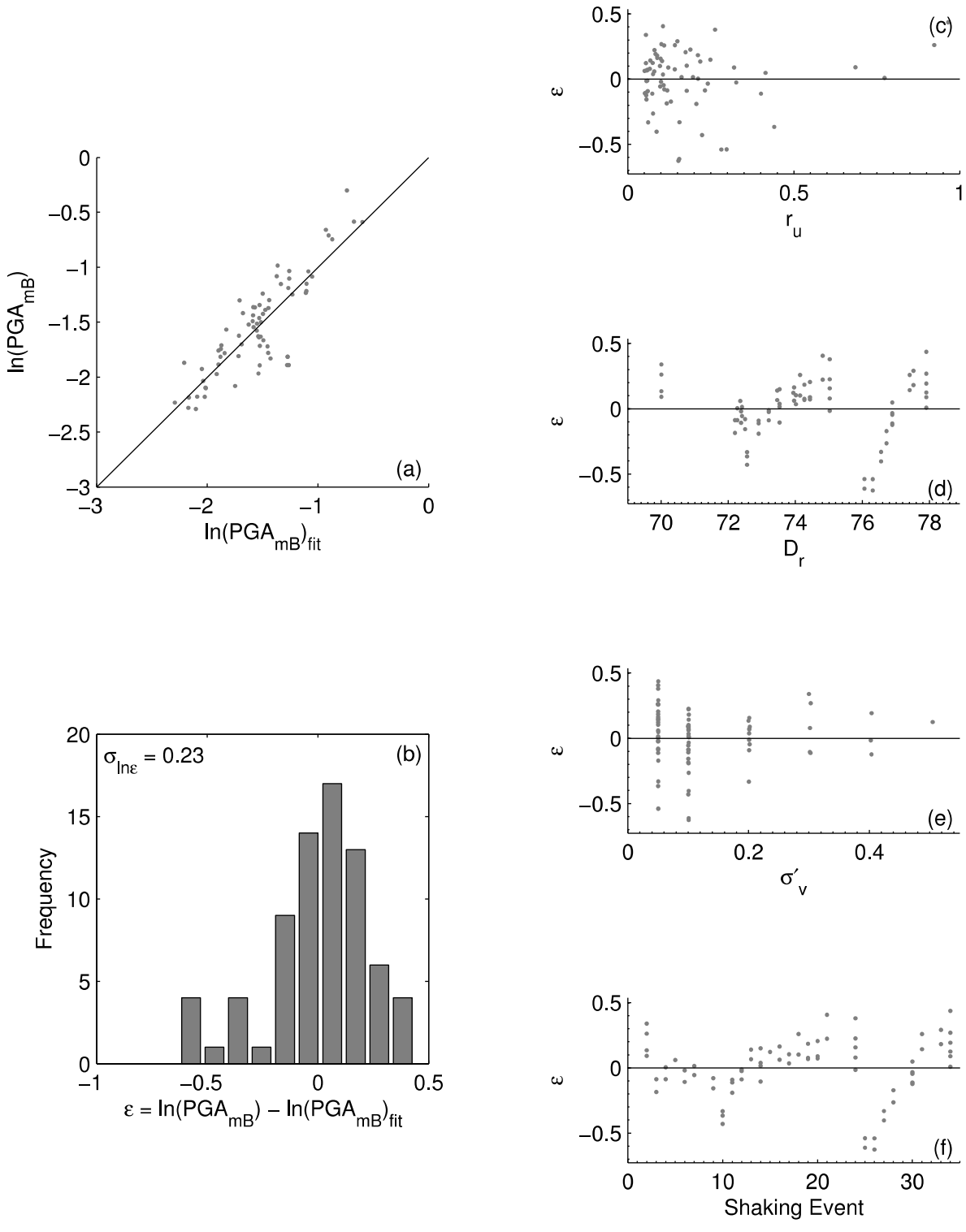
PGA_{mB} – Fit to Experiment 1 with N_{test} Term (Equation 7.6)



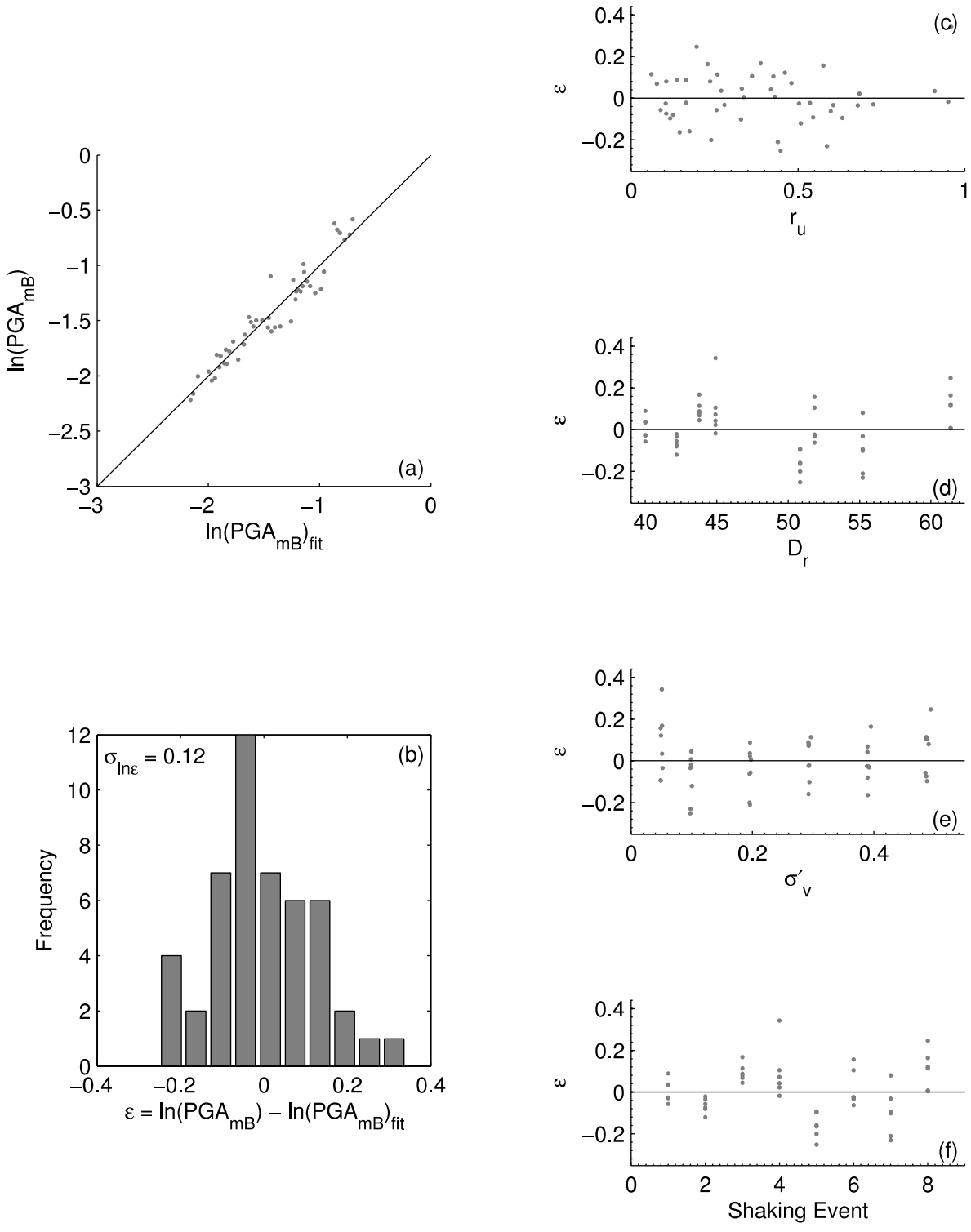
PGA_{mB} – Fit to Experiment 2 with N_{test} Term (Equation 7.6)



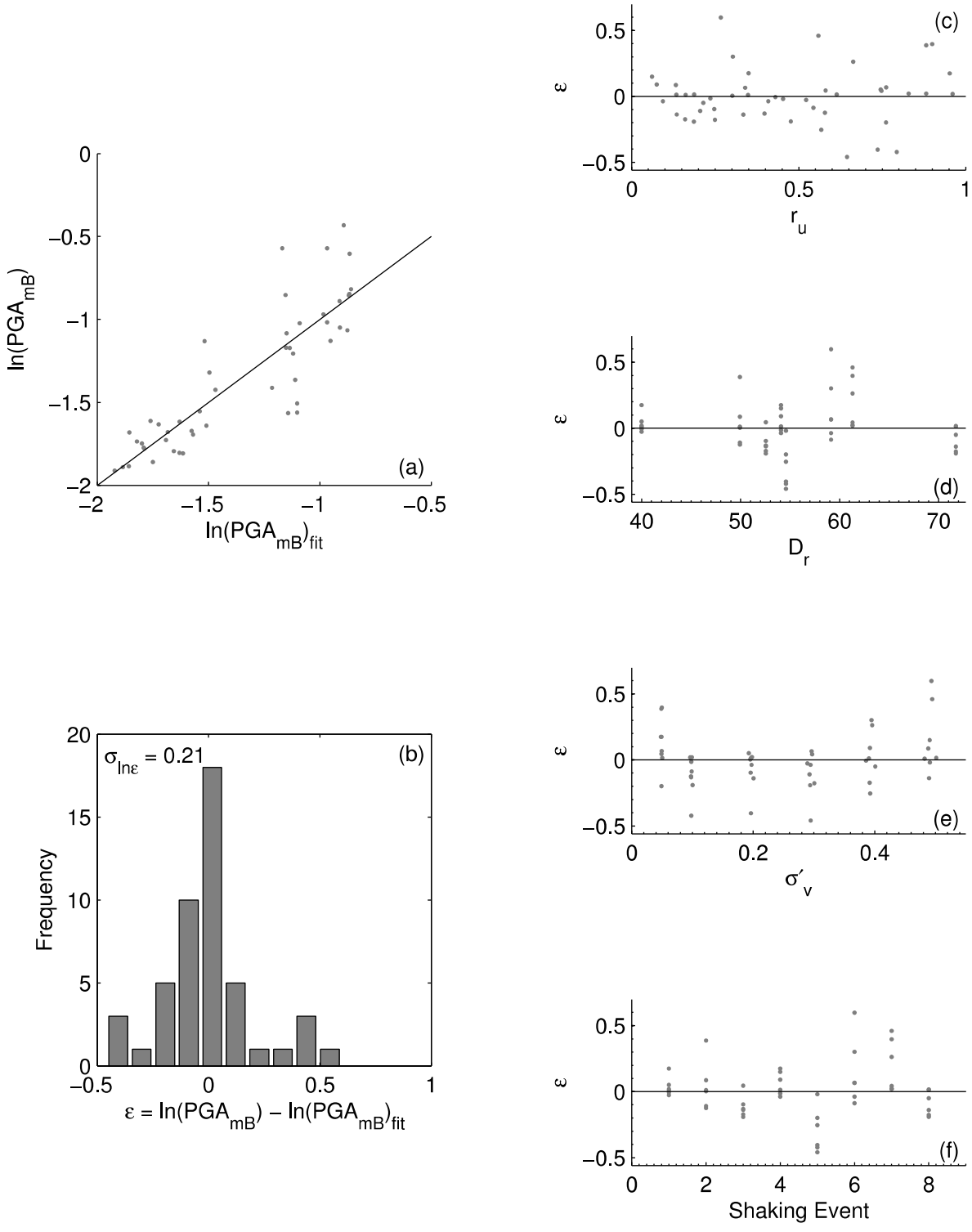
PGA_{mB} – Fit to Experiment 3 with N_{test} Term (Equation 7.6)



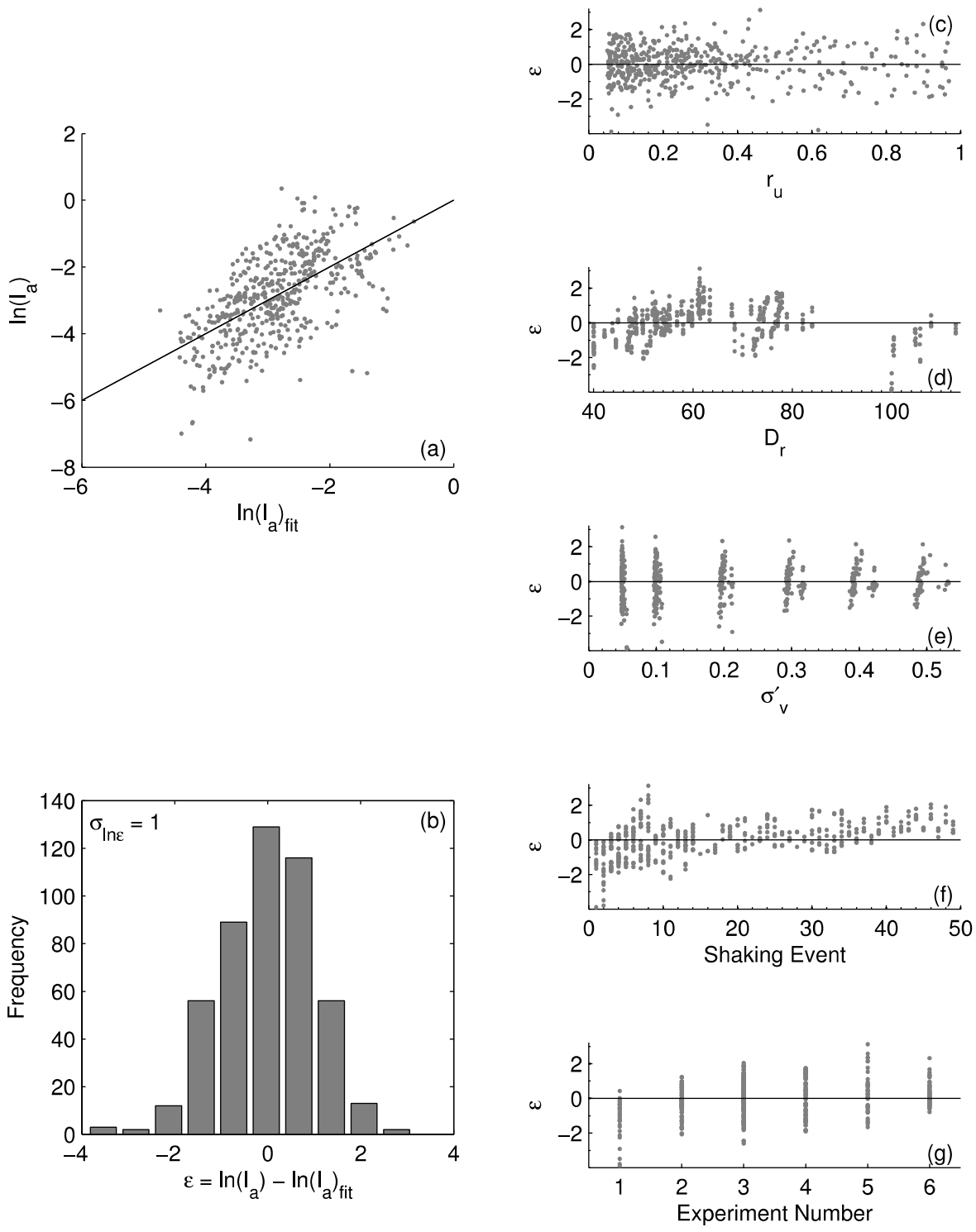
PGA_{mB} – Fit to Experiment 4 with N_{test} Term (Equation 7.6)



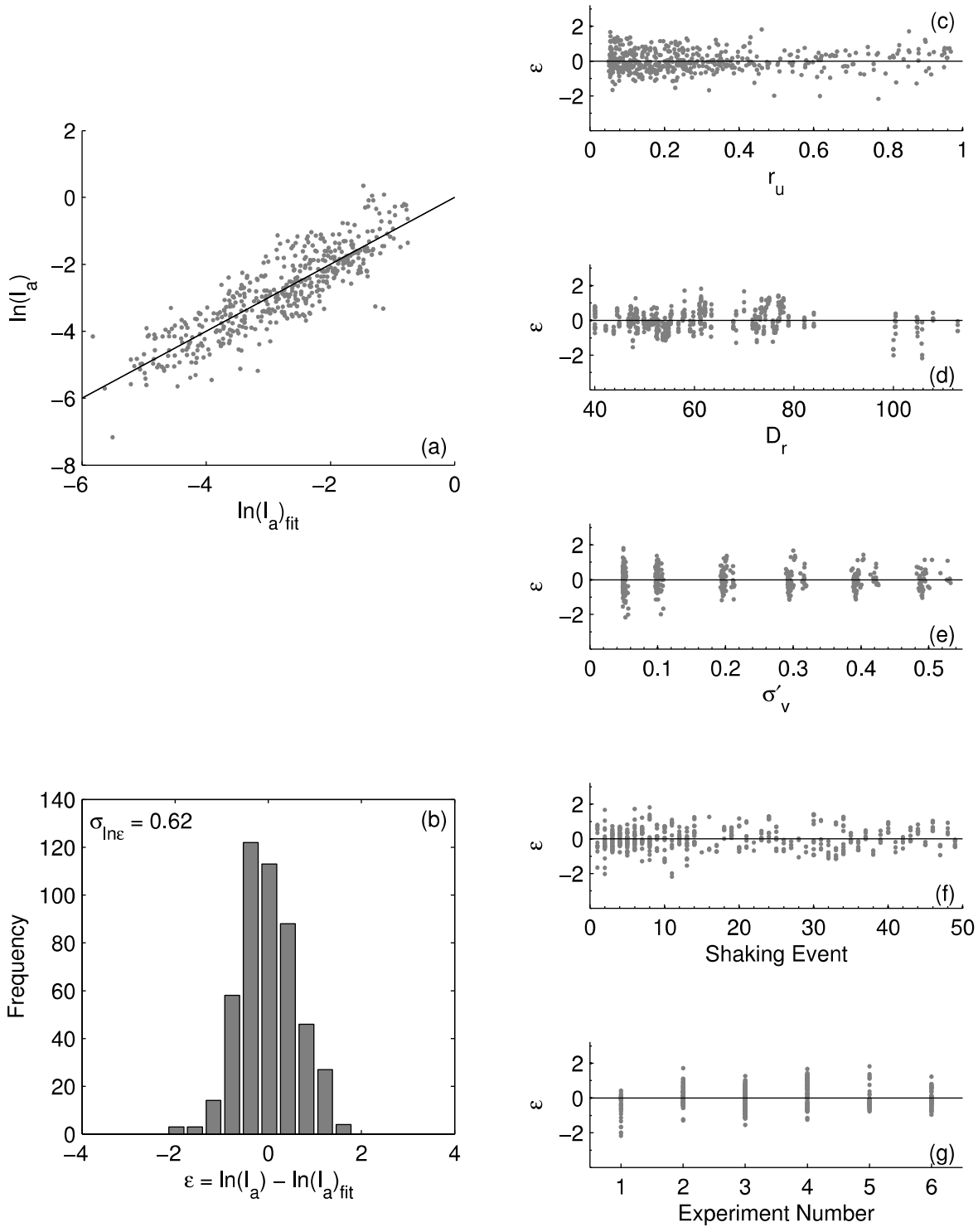
PGA$_{mB}$ – Fit to Experiment 5 with N$_{test}$ Term (Equation 7.6)



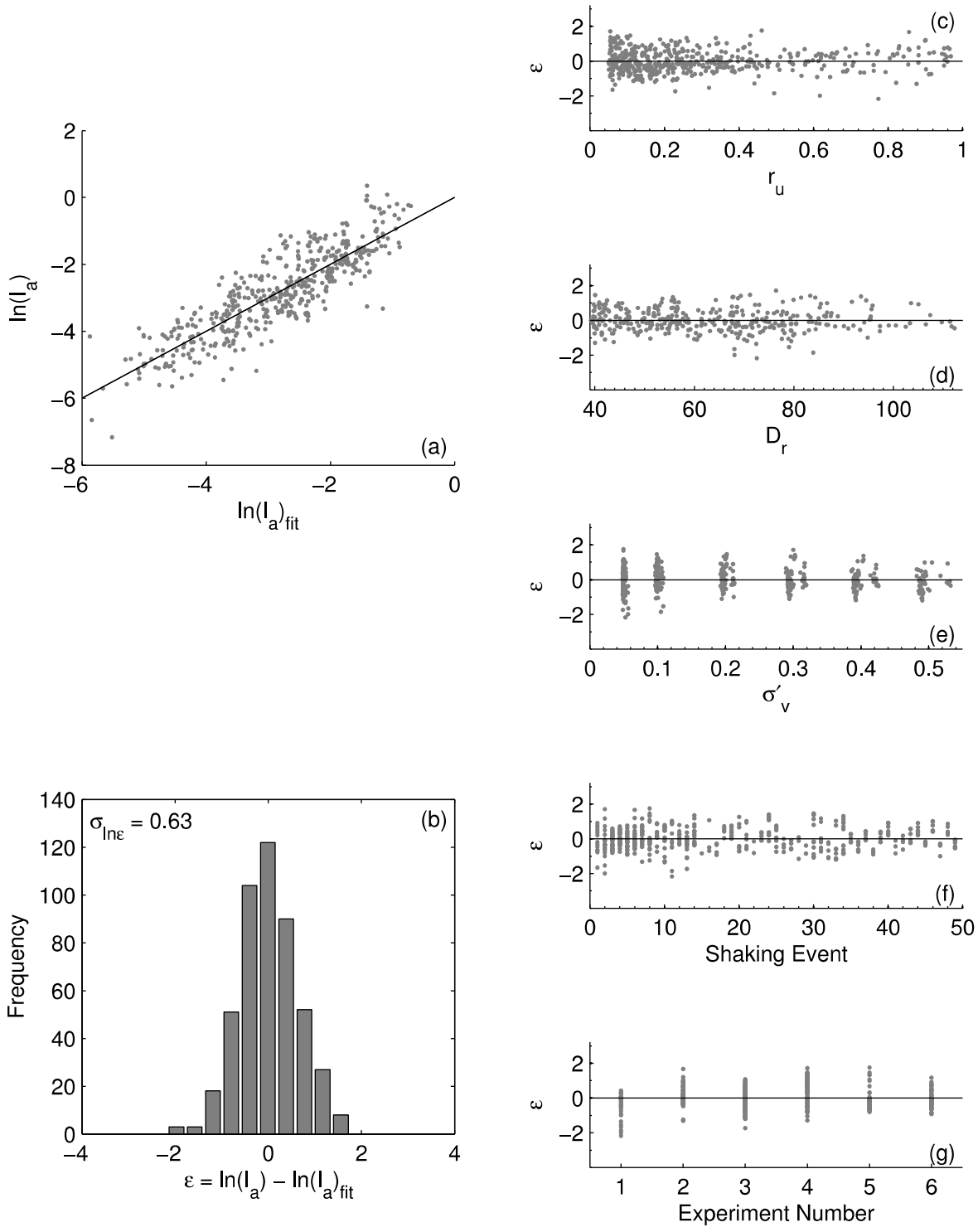
PGA$_{mB}$ – Fit to Experiment 6 with N$_{test}$ Term (Equation 7.6)



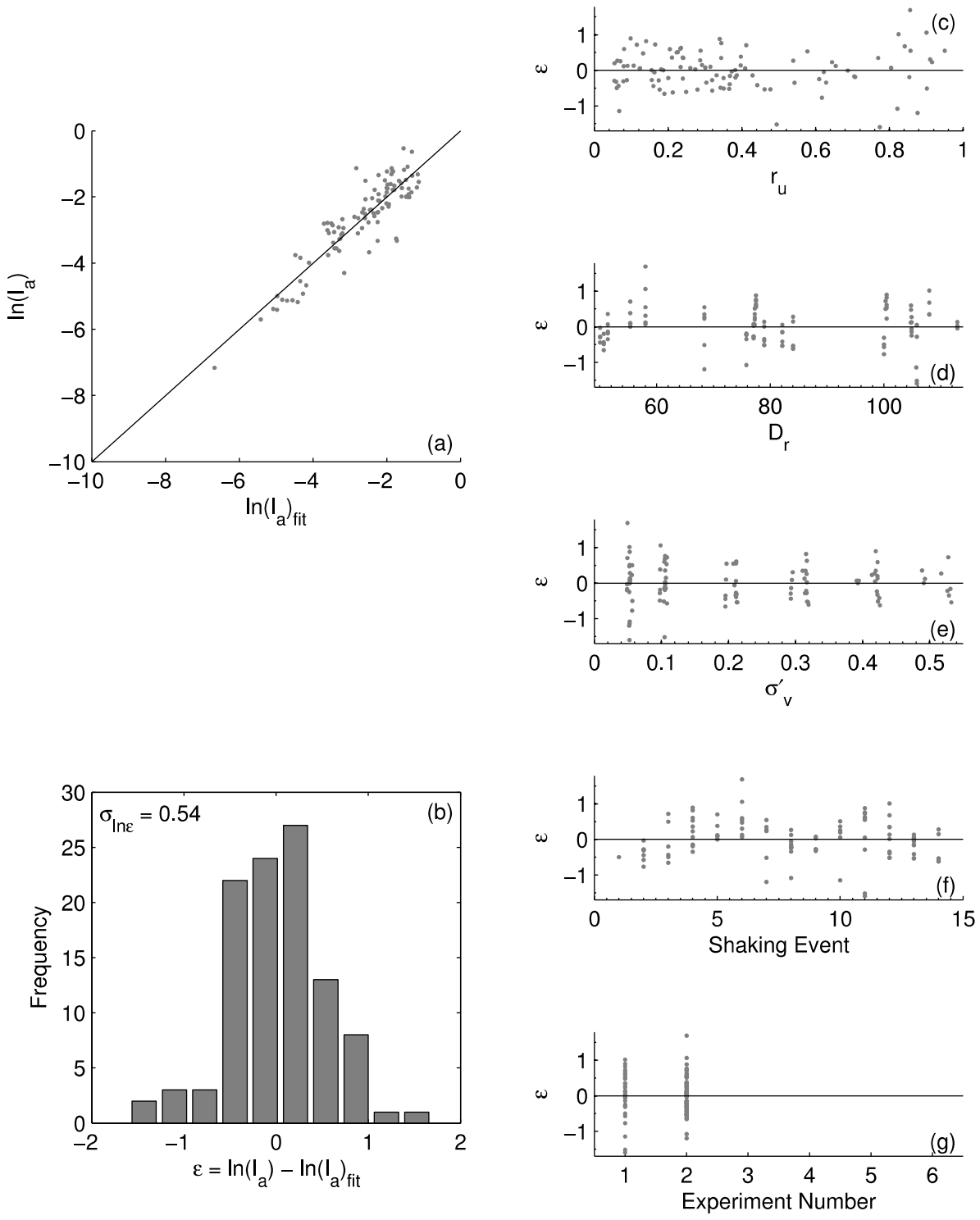
I_a – Fit to All Centrifuge Experiments (Equation 7.5)



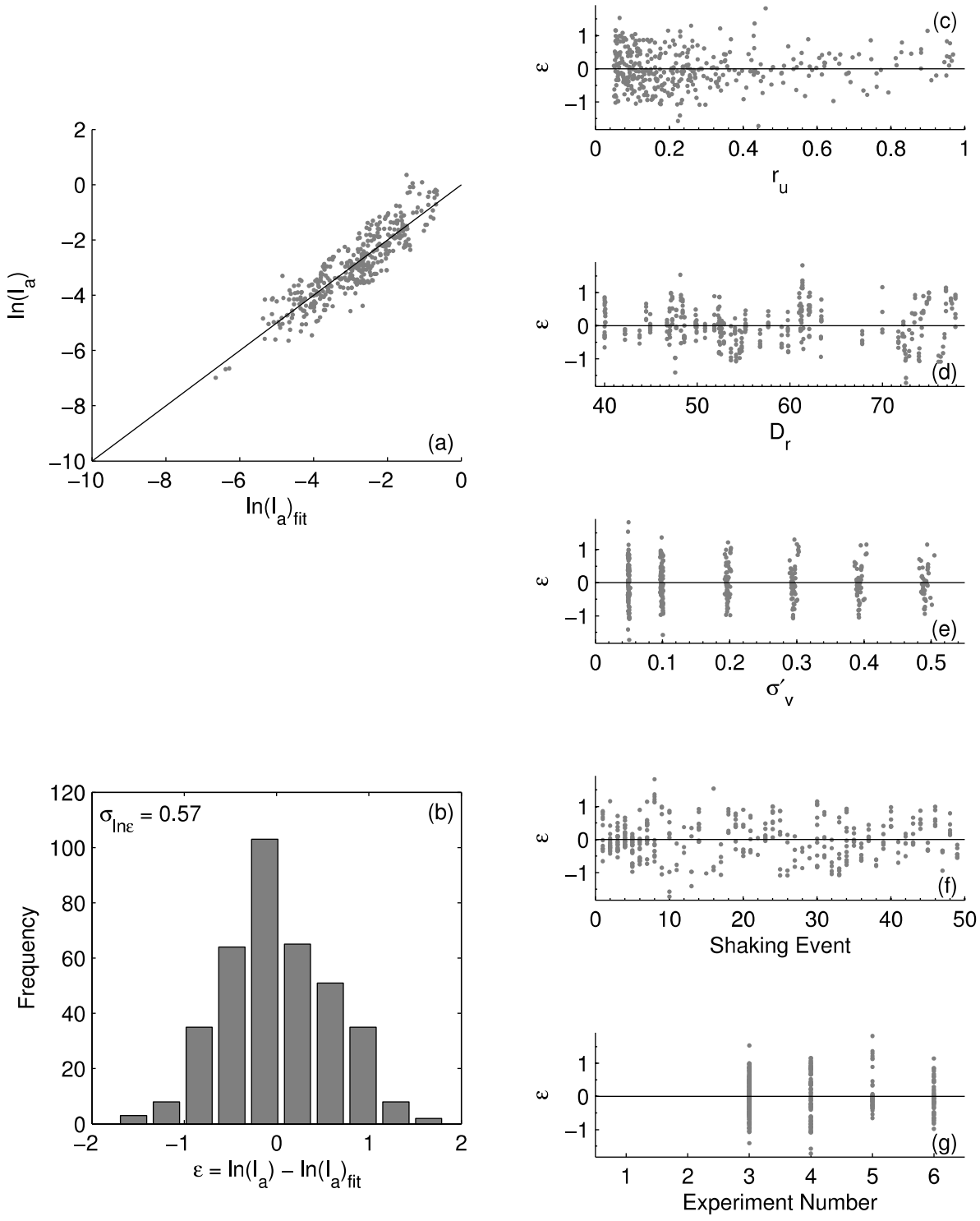
I_a – Fit to All Centrifuge Experiments with N_{test} Term (Equation 7.6)



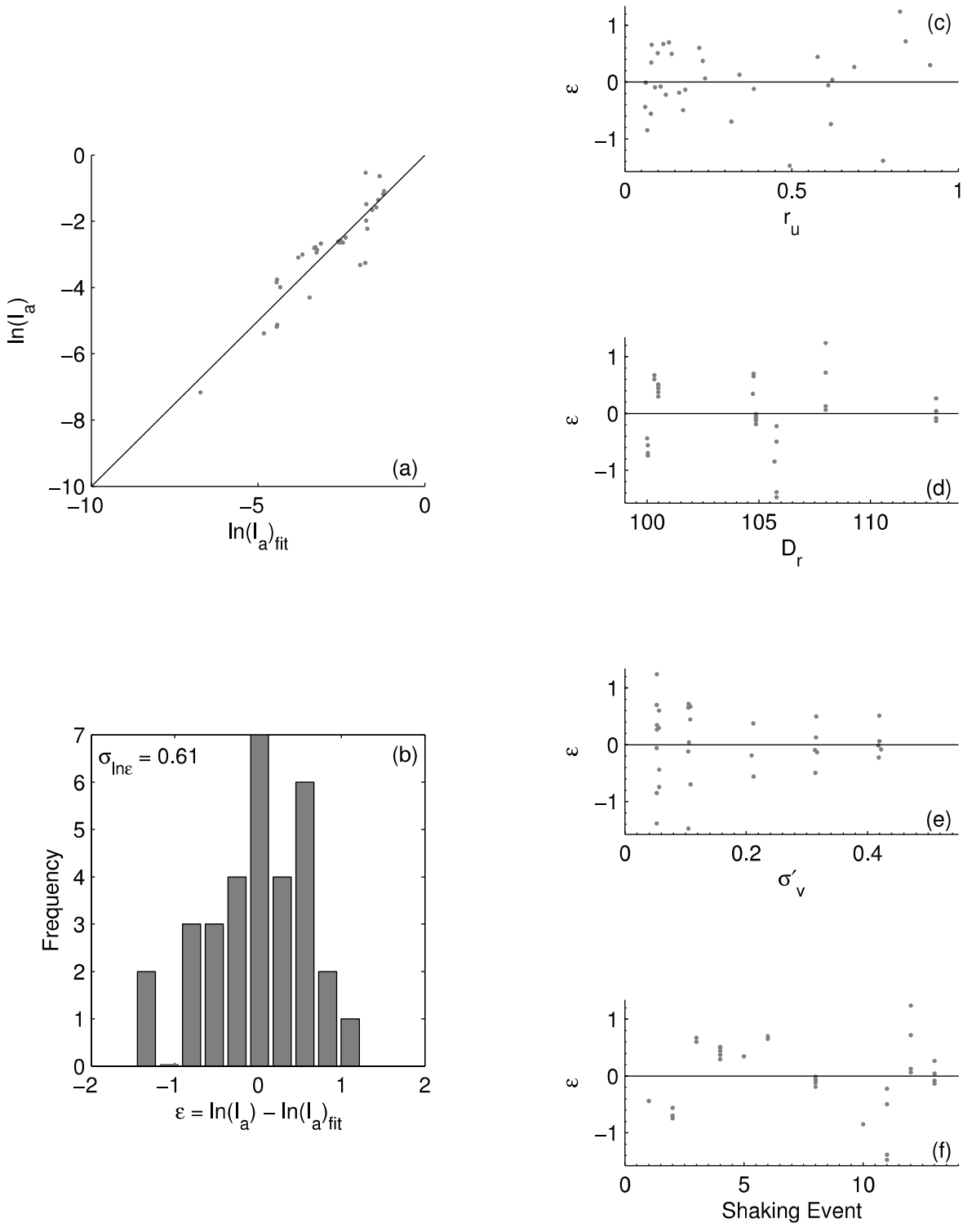
I_a – Fit to All Centrifuge Experiments with Stress–Dependent D_r Profile and Including N_{test} Term (Equation 7.6)



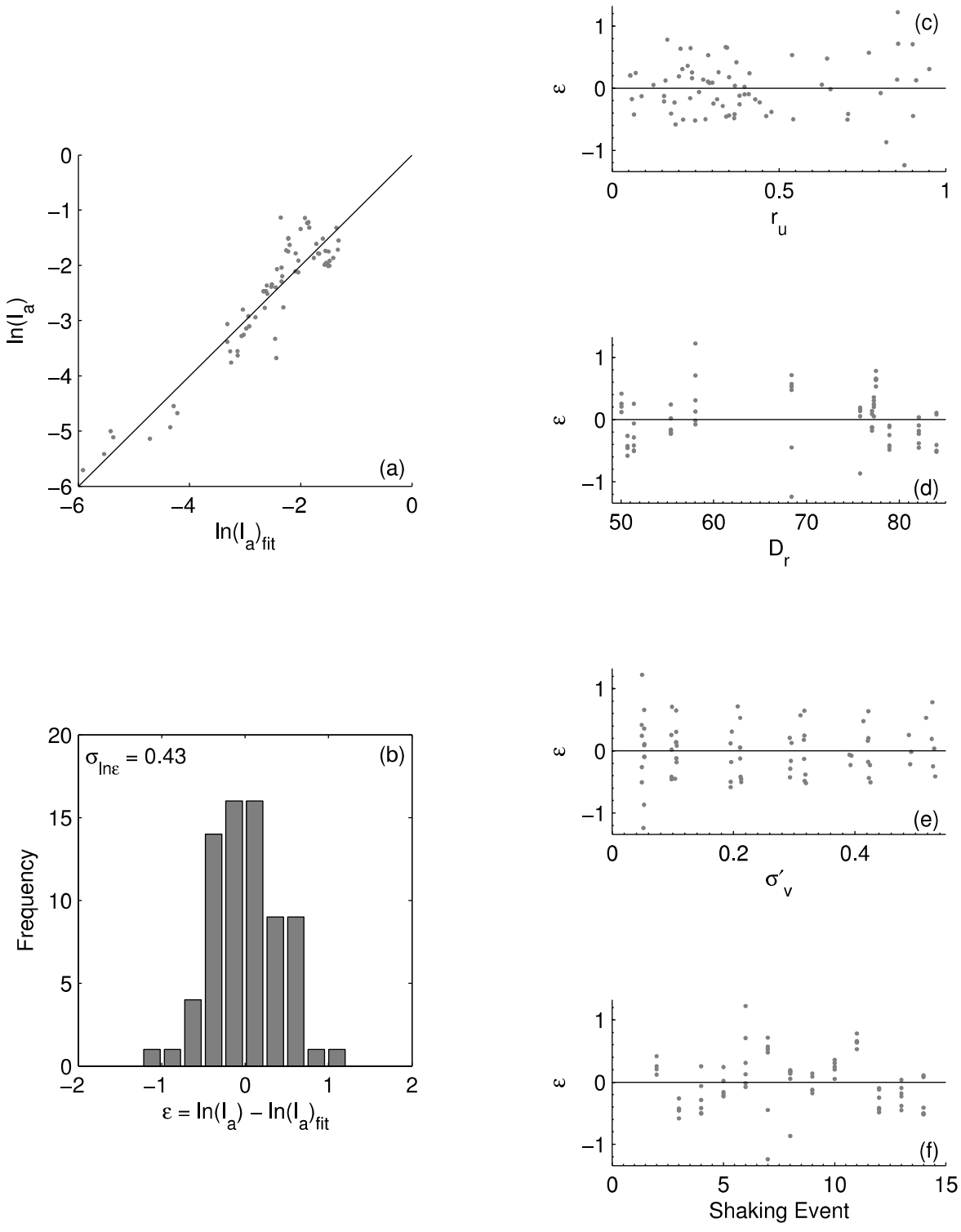
I_a – Fit to Experiments 1 and 2 with N_{test} Term (Equation 7.6)



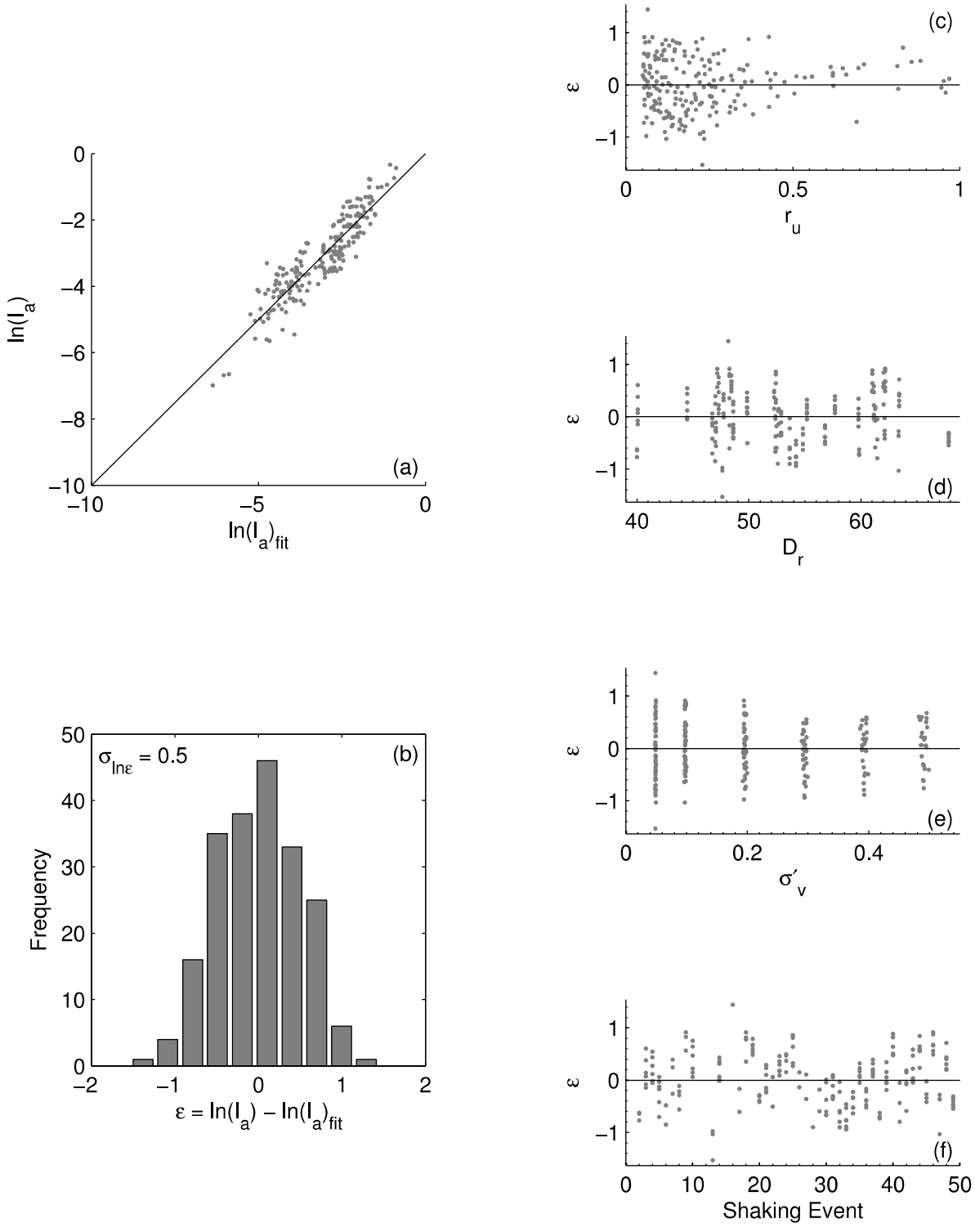
I_a – Fit to Experiments 3 to 6 with N_{test} Term (Equation 7.6)



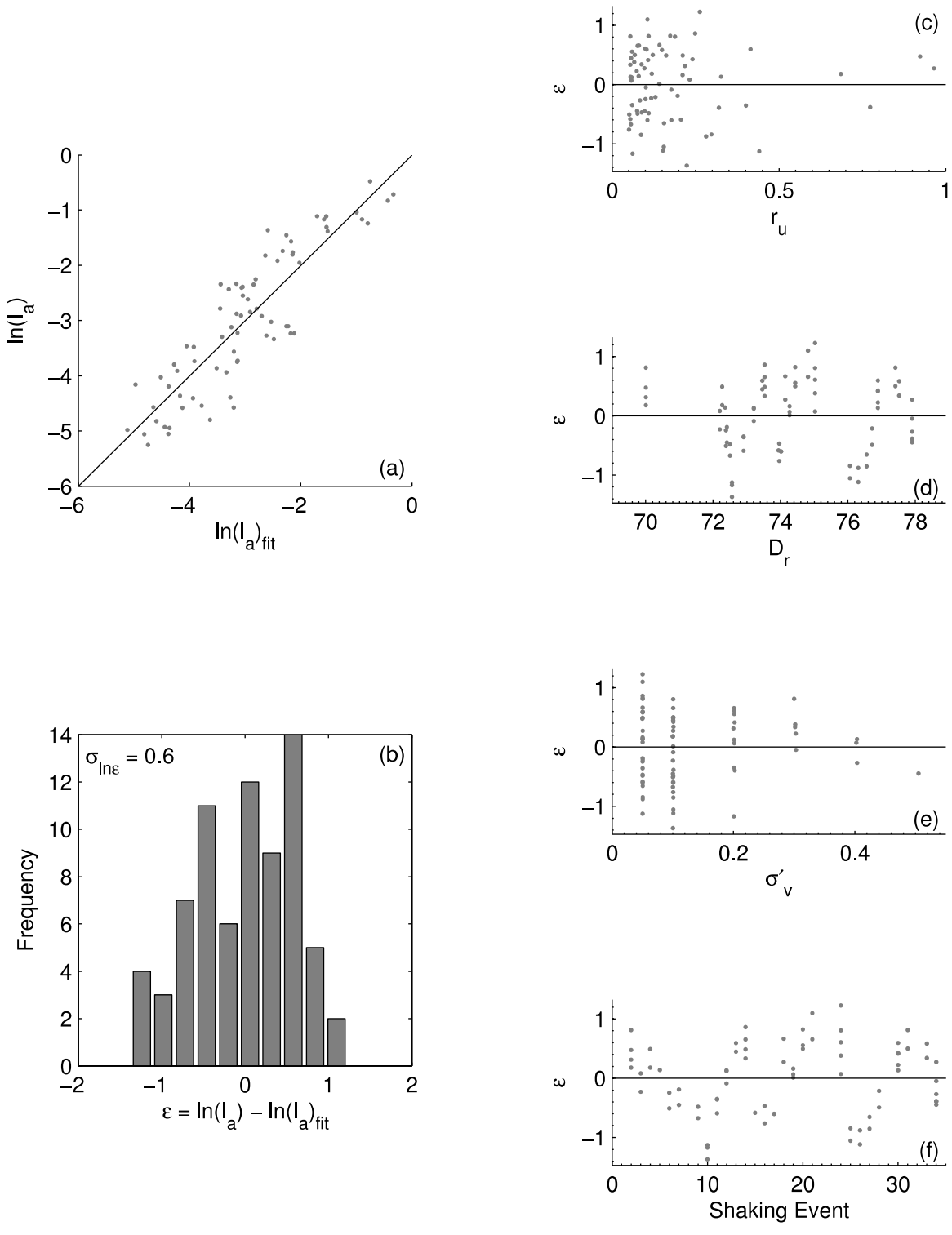
I_a – Fit to Experiment 1 with N_{test} Term (Equation 7.6)



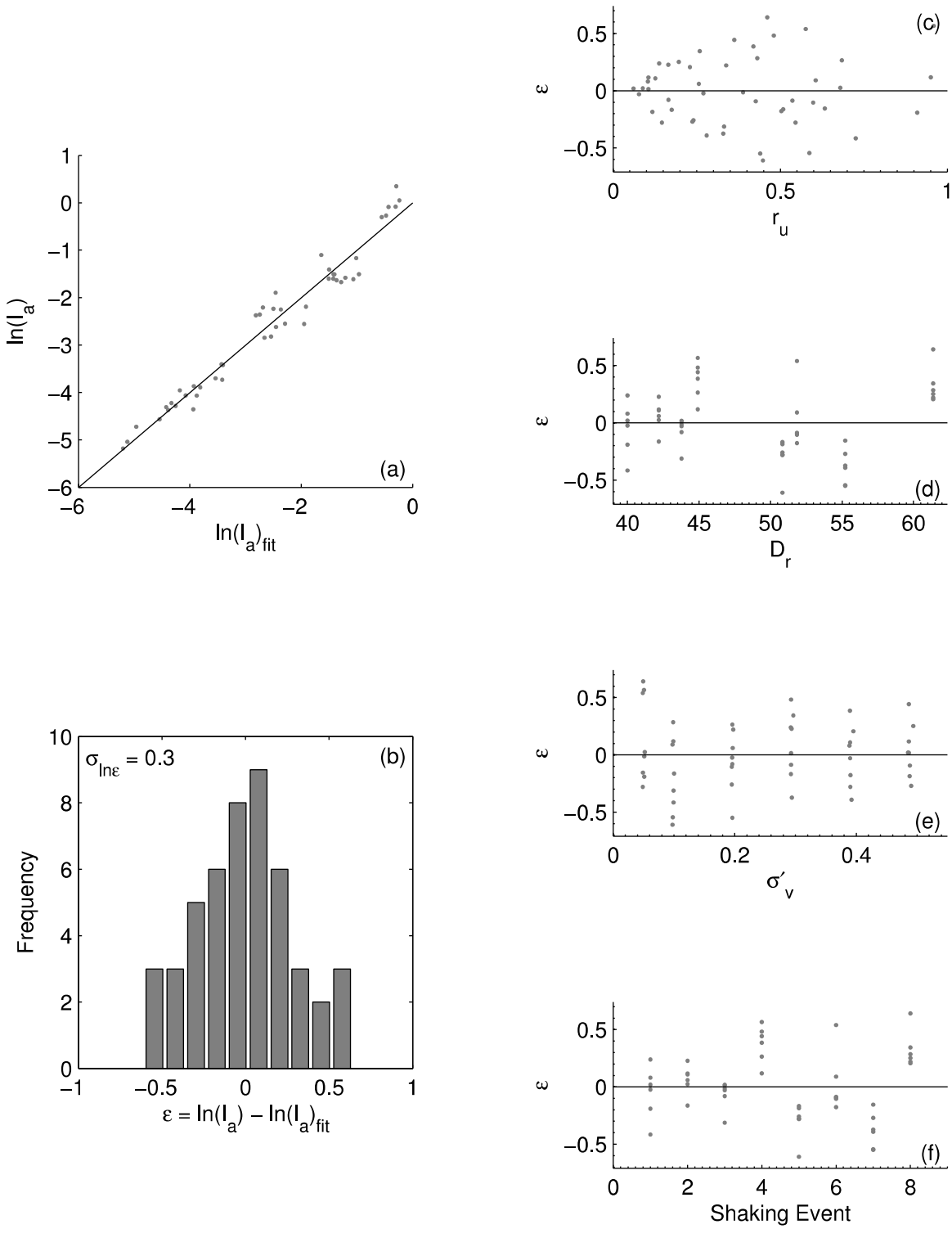
I_a – Fit to Experiment 2 with N_{test} Term (Equation 7.6)



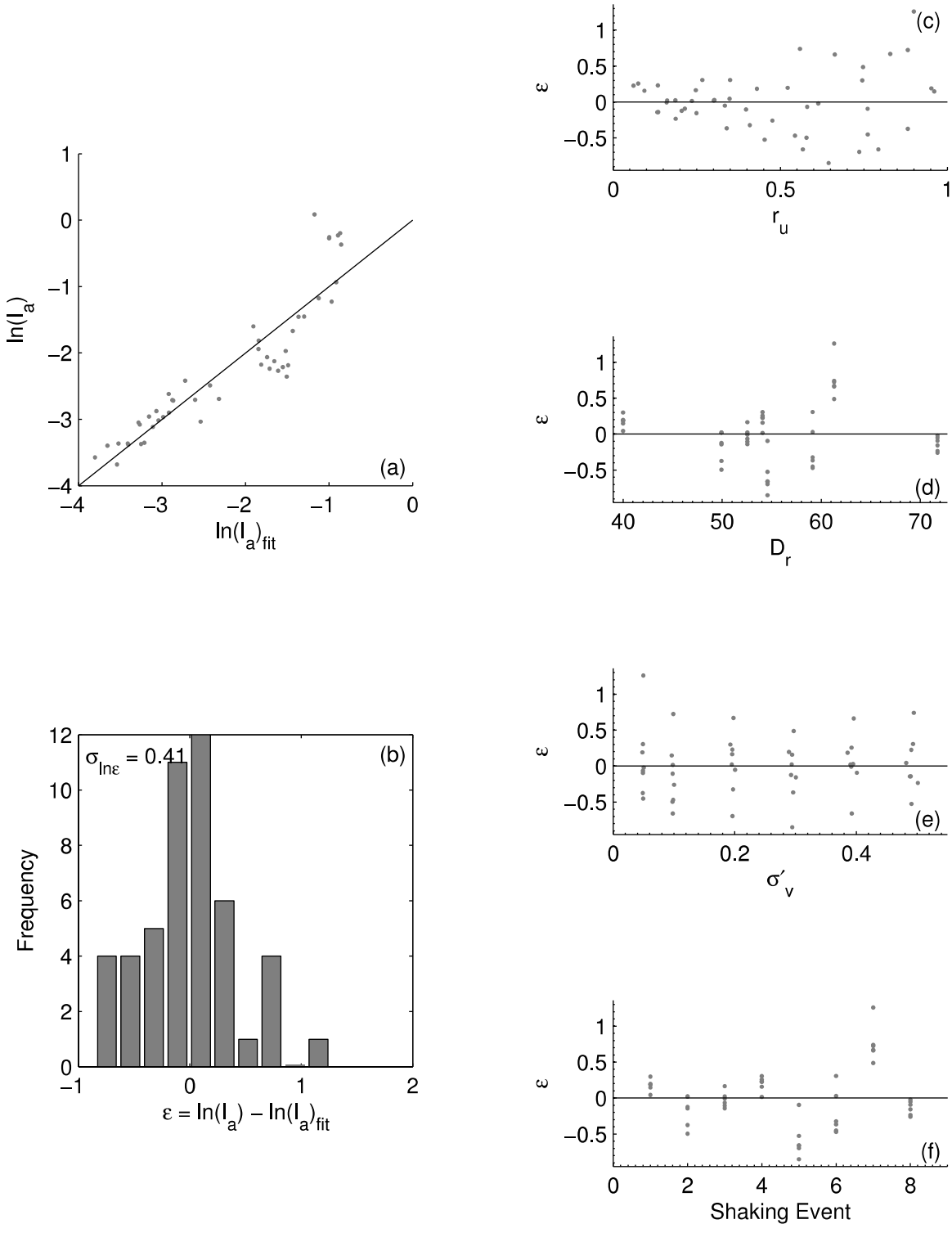
I_a – Fit to Experiment 3 with N_{test} Term (Equation 7.6)



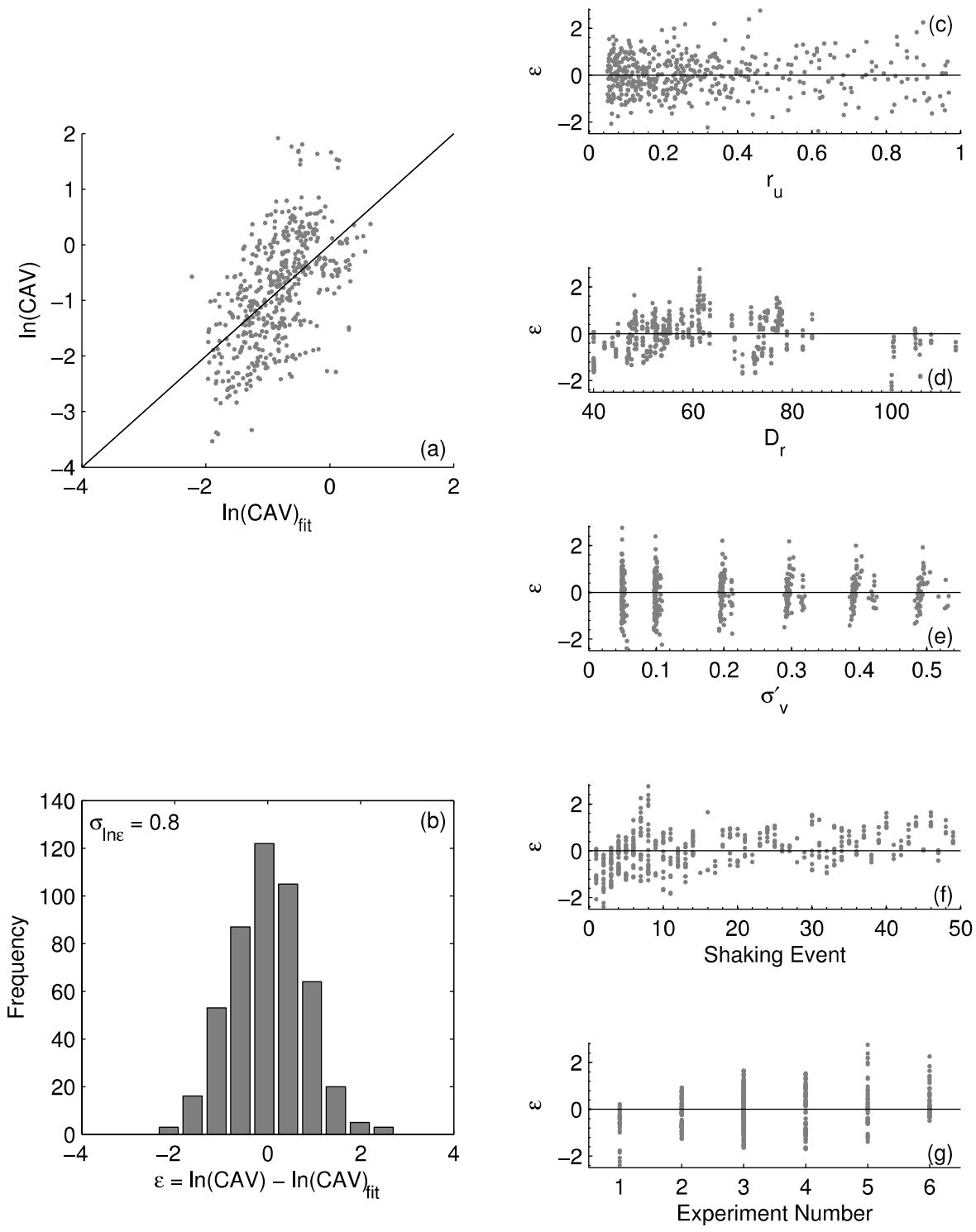
I_a – Fit to Experiment 4 with N_{test} Term (Equation 7.6)



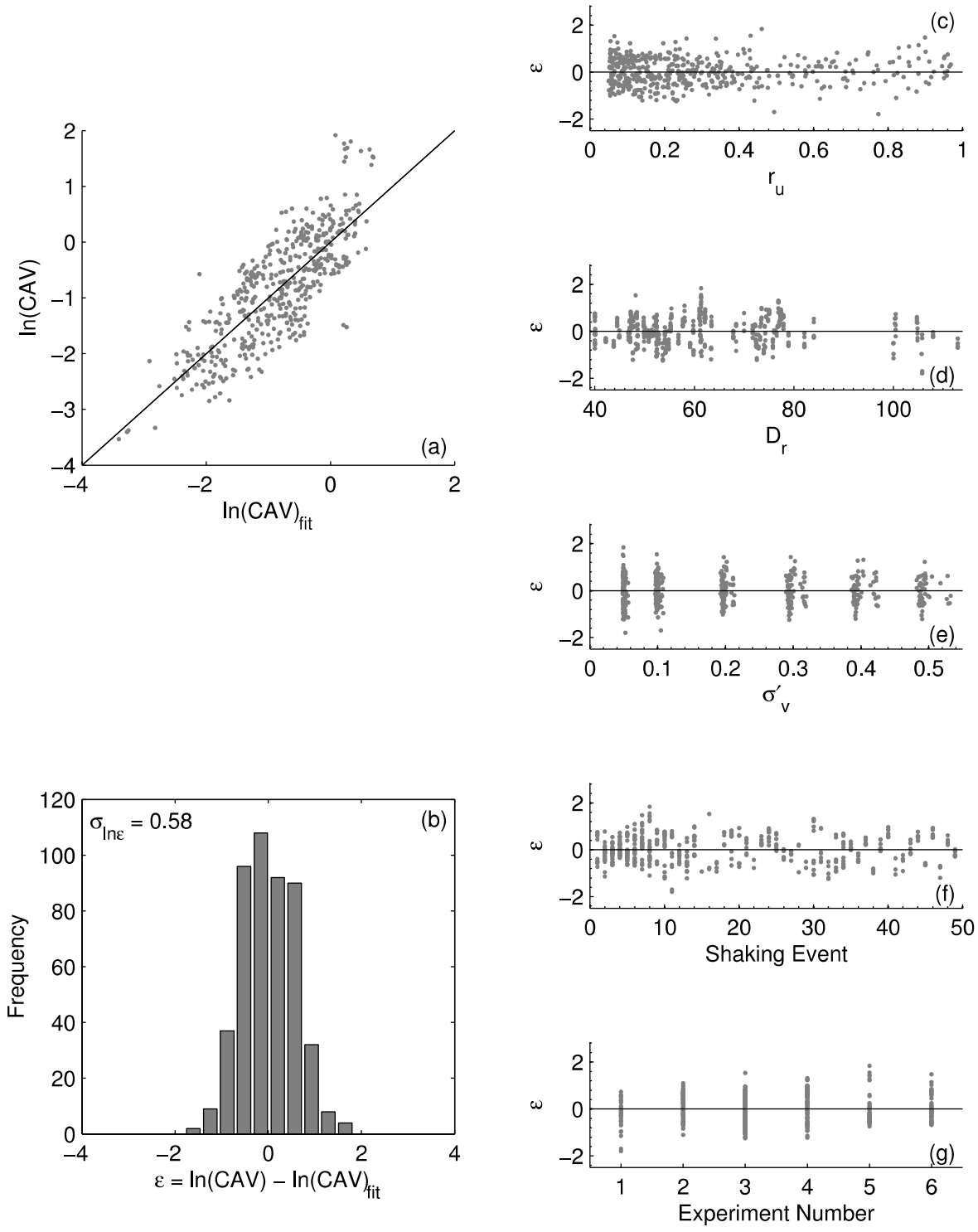
I_a – Fit to Experiment 5 with N_{test} Term (Equation 7.6)



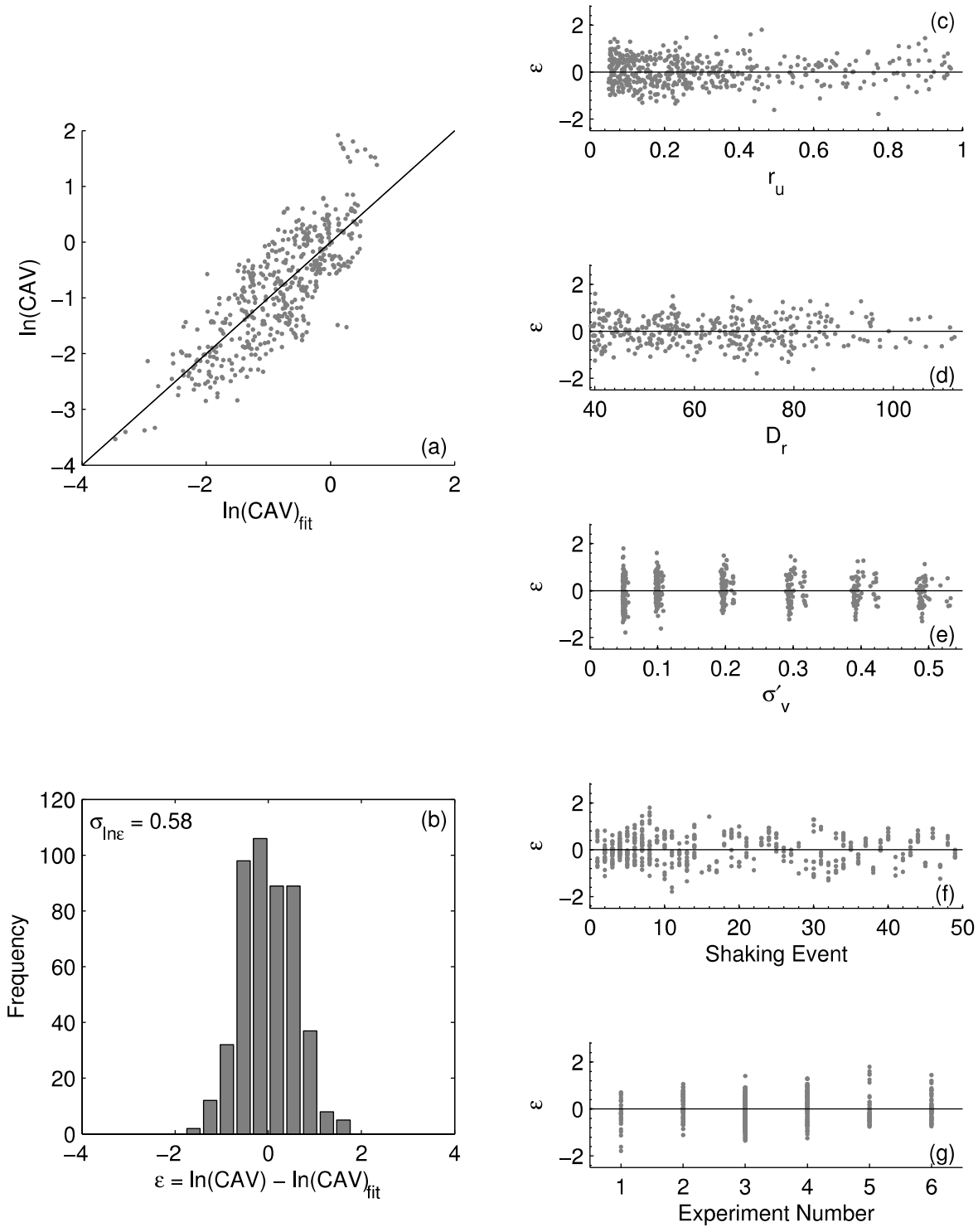
I_a – Fit to Experiment 6 with N_{test} Term (Equation 7.6)



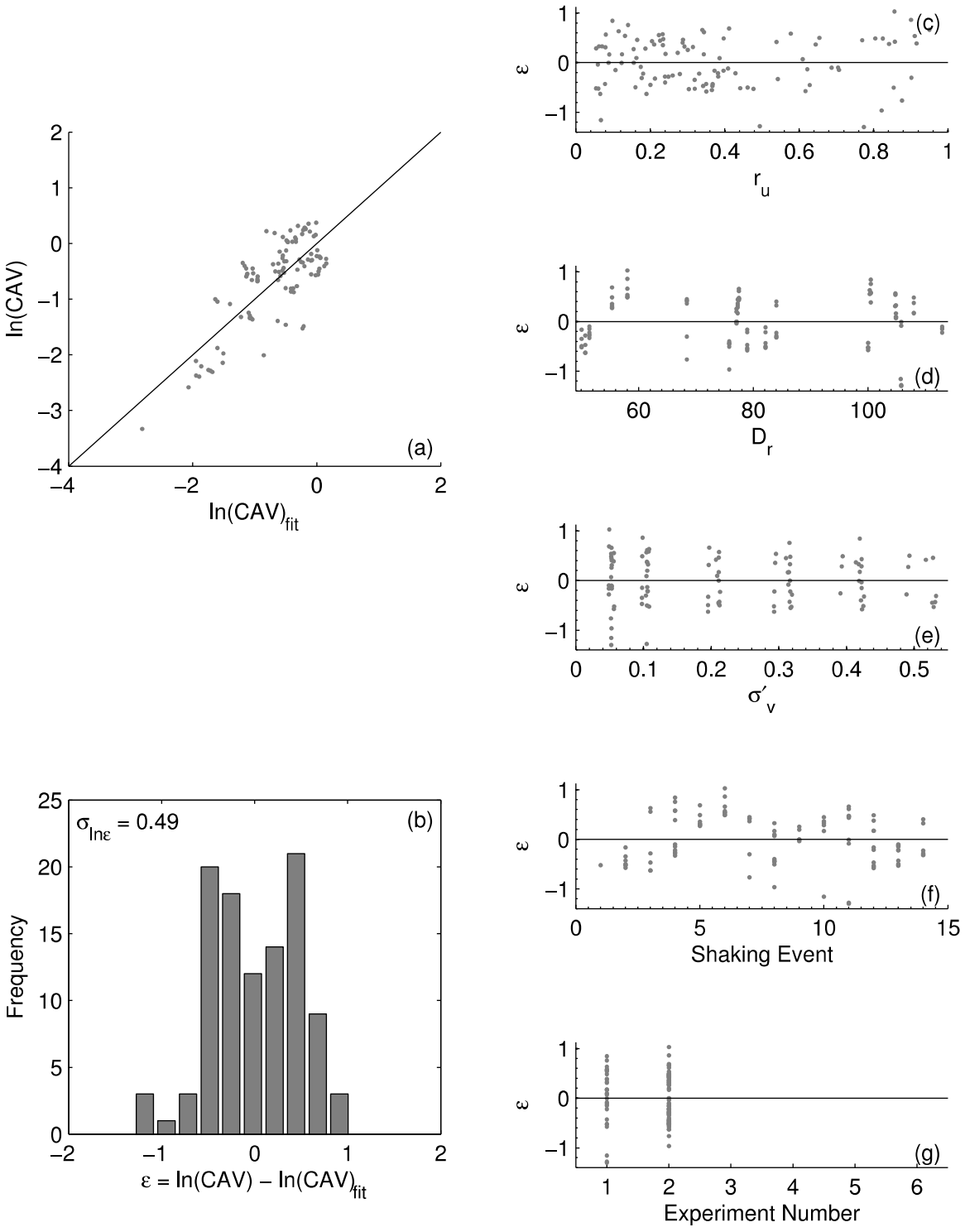
CAV – Fit to All Centrifuge Experiments (Equation 7.5)



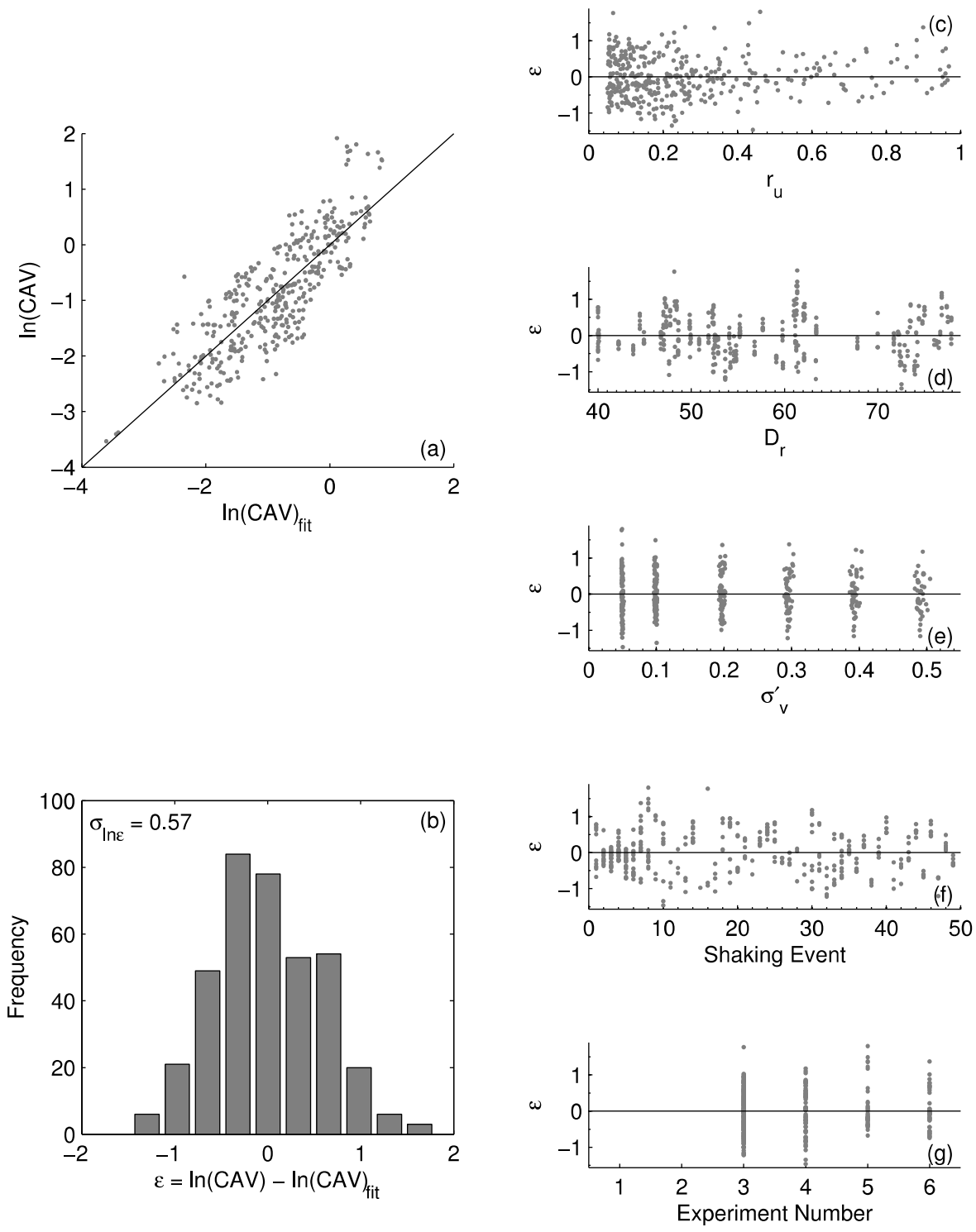
CAV – Fit to All Centrifuge Experiments with N_{test} Term (Equation 7.6)



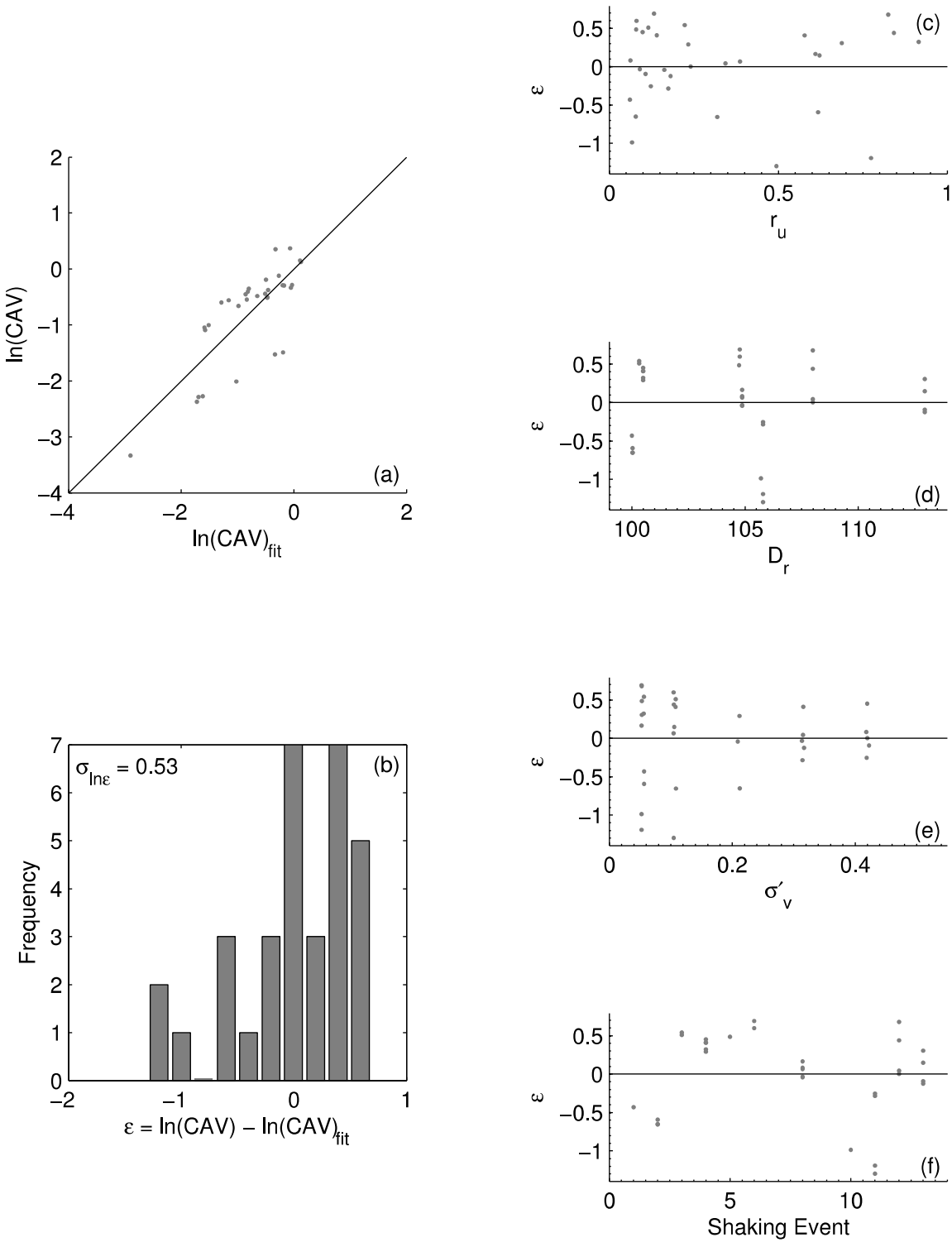
CAV – Fit to All Centrifuge Experiments with Stress–Dependent D_r Profile and Including N_{test} Term (Equation 7.6)



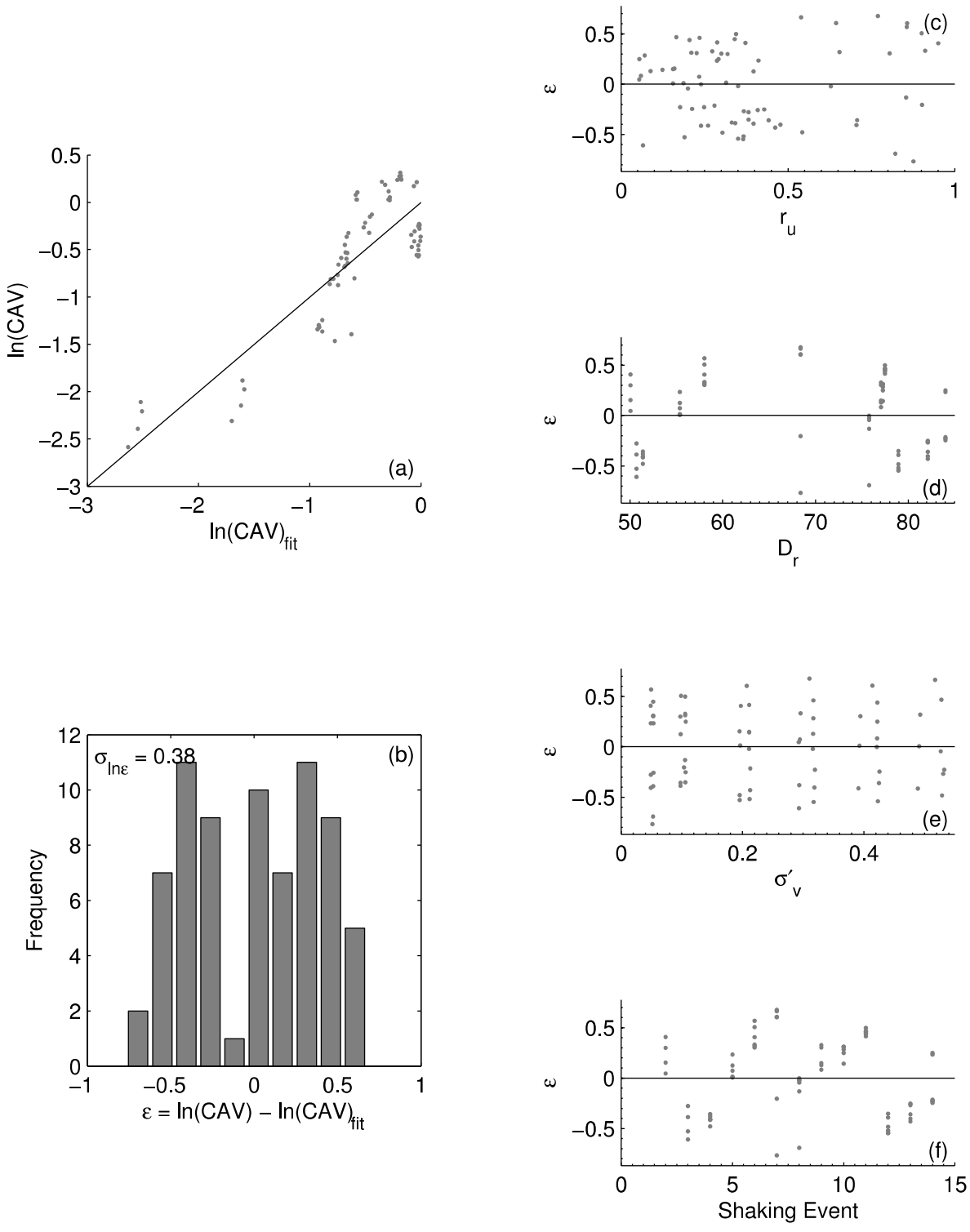
CAV – Fit to Experiments 1 and 2 with N_{test} Term (Equation 7.6)



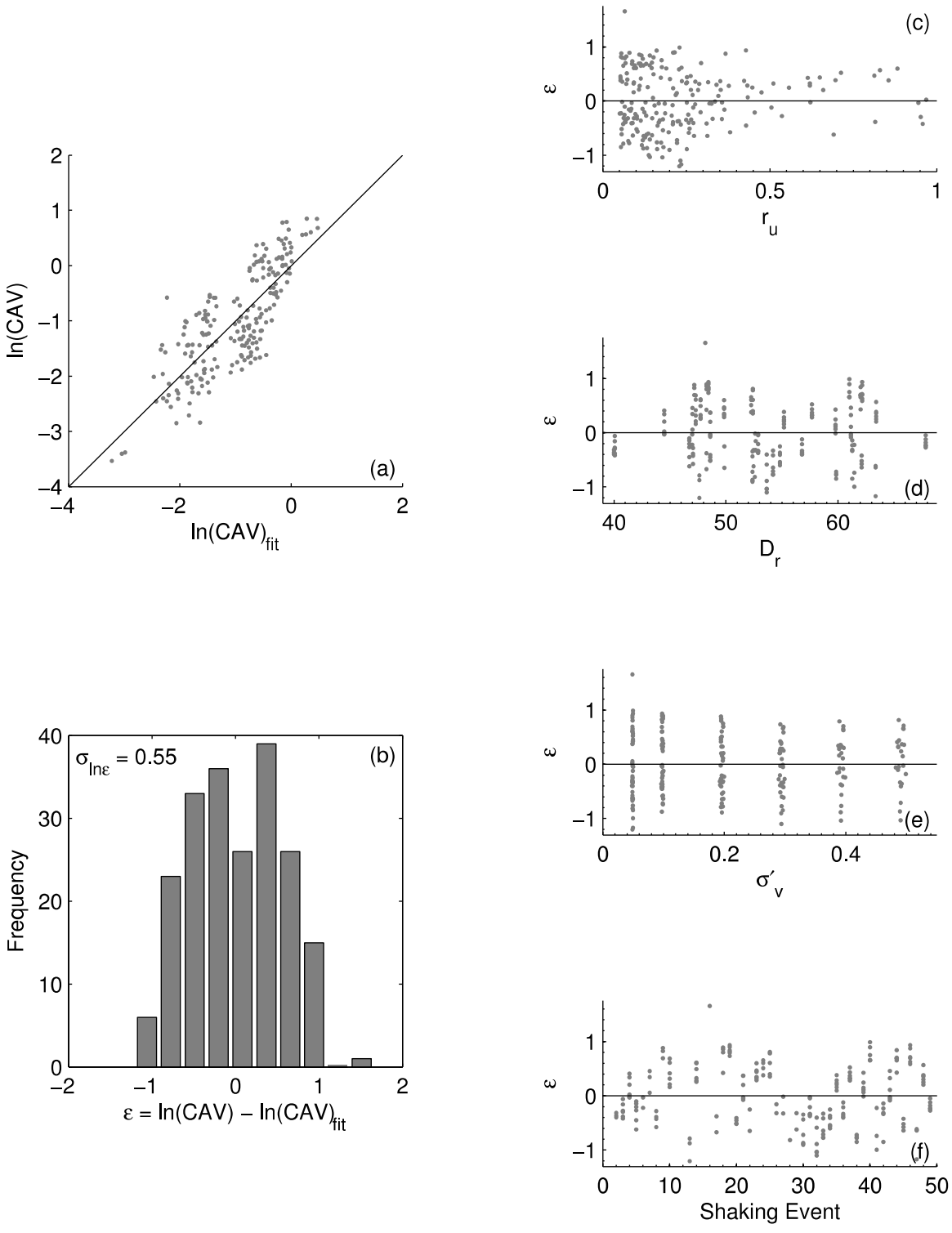
CAV – Fit to Experiments 3 to 6 with N_{test} Term (Equation 7.6)



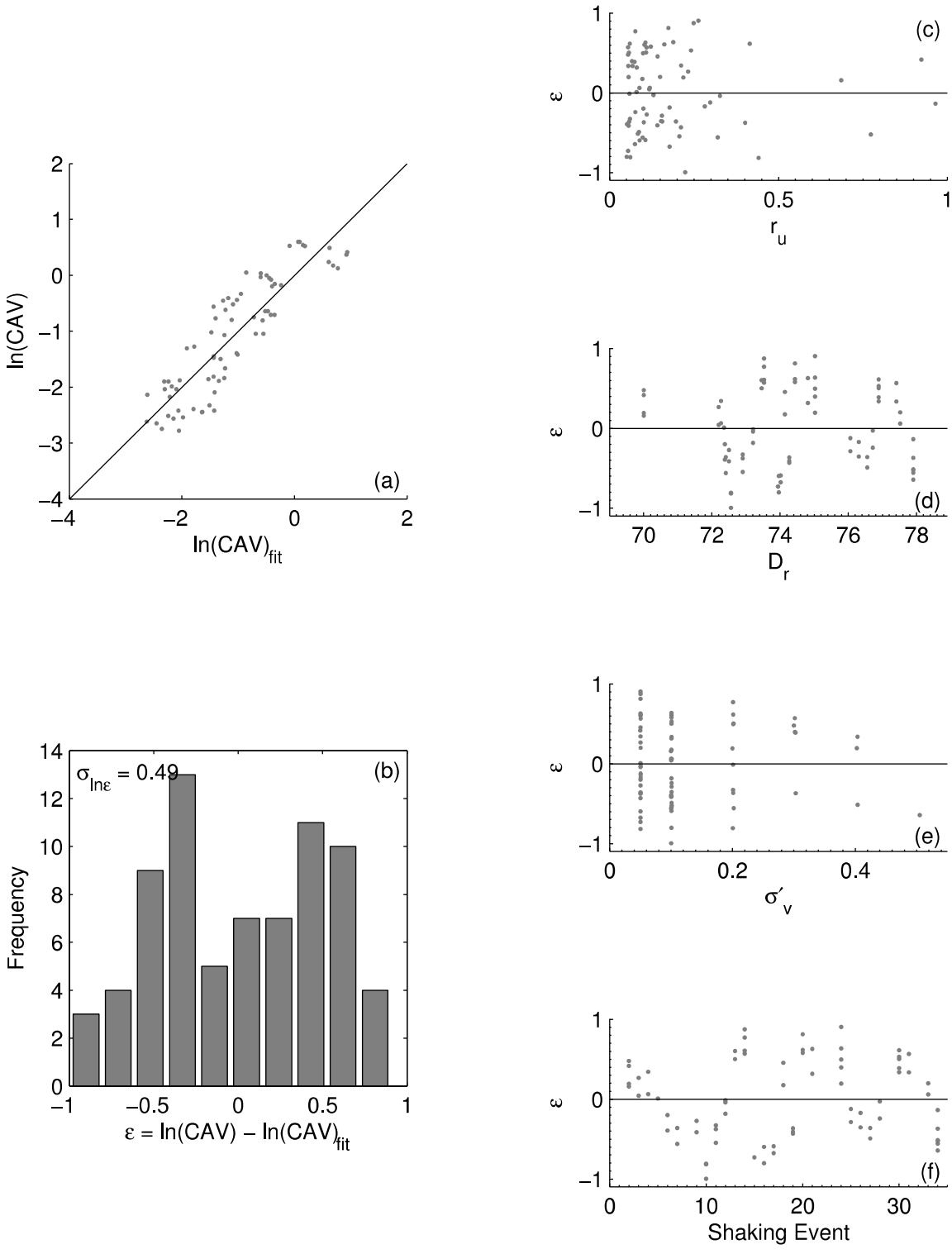
CAV – Fit to Experiment 1 with N_{test} Term (Equation 7.6)



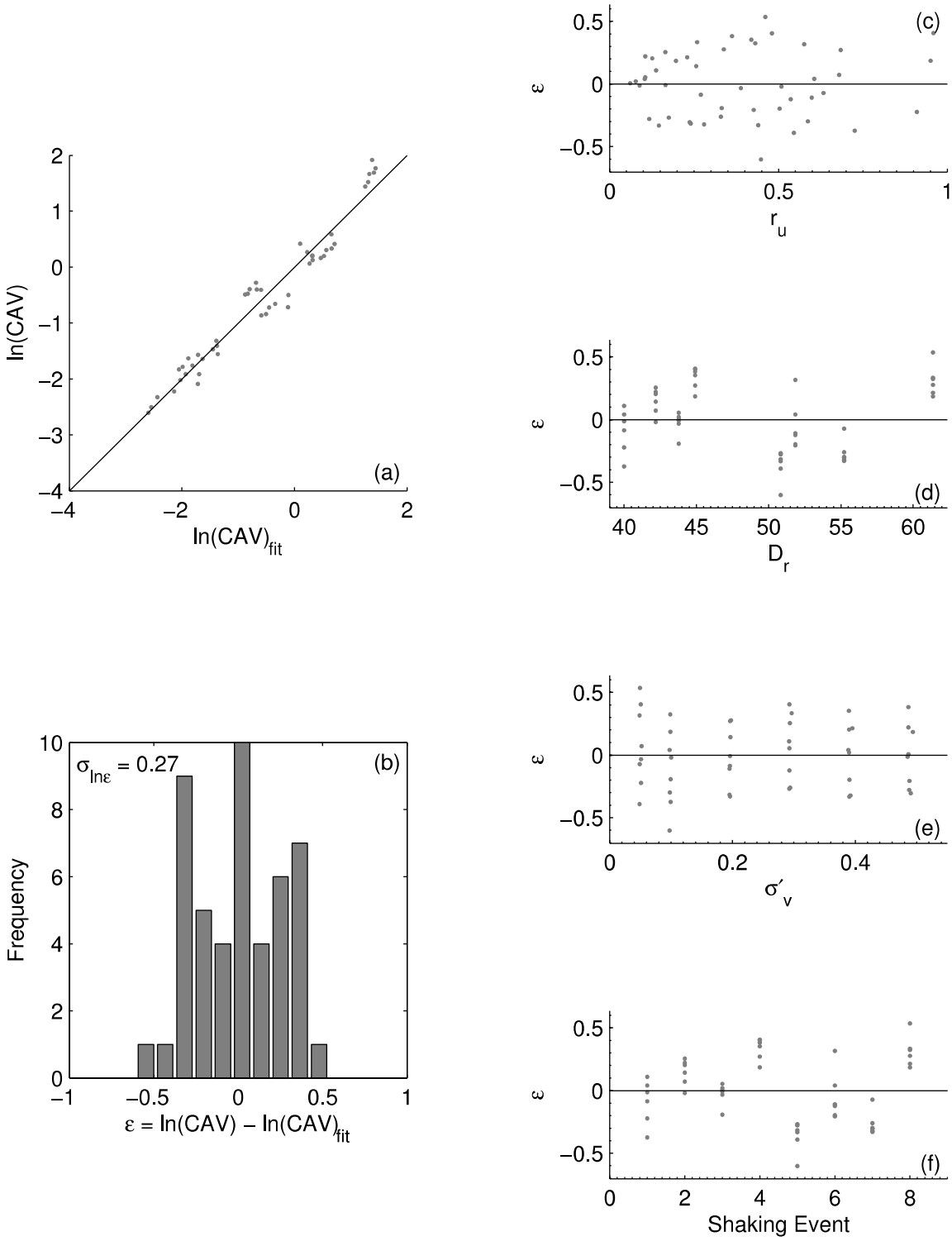
CAV – Fit to Experiment 2 with N_{test} Term (Equation 7.6)



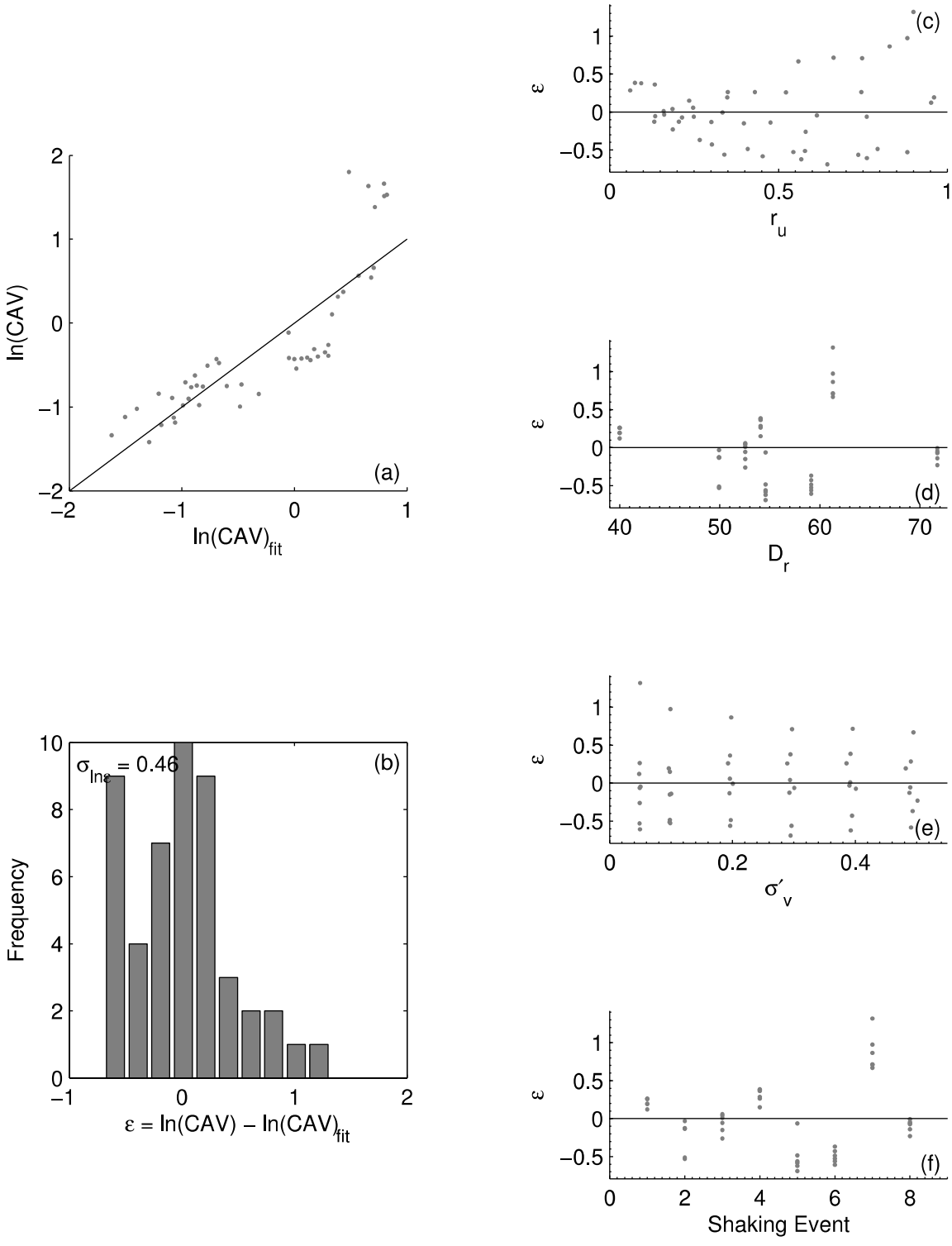
CAV – Fit to Experiment 3 with N_{test} Term (Equation 7.6)



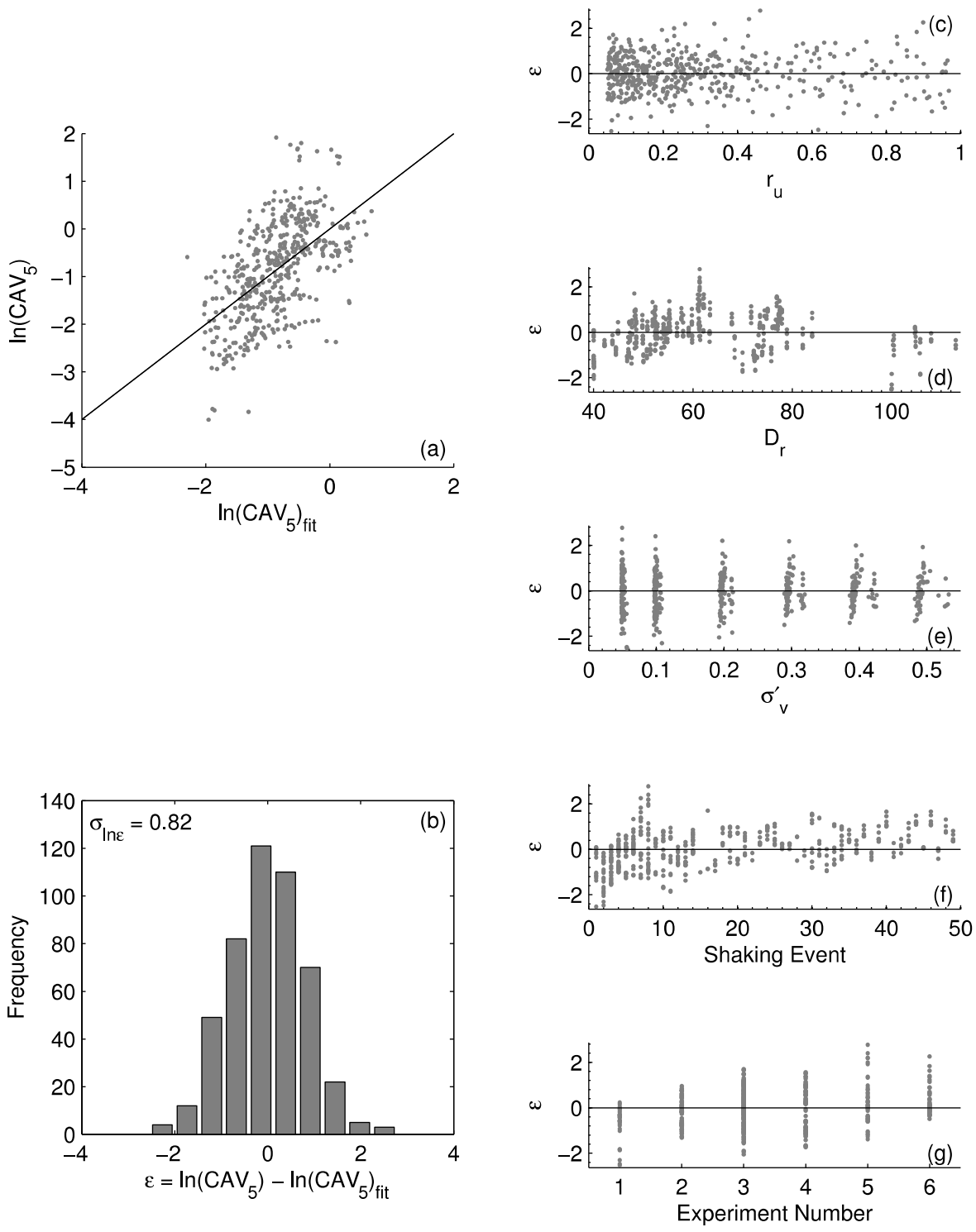
CAV – Fit to Experiment 4 with N_{test} Term (Equation 7.6)



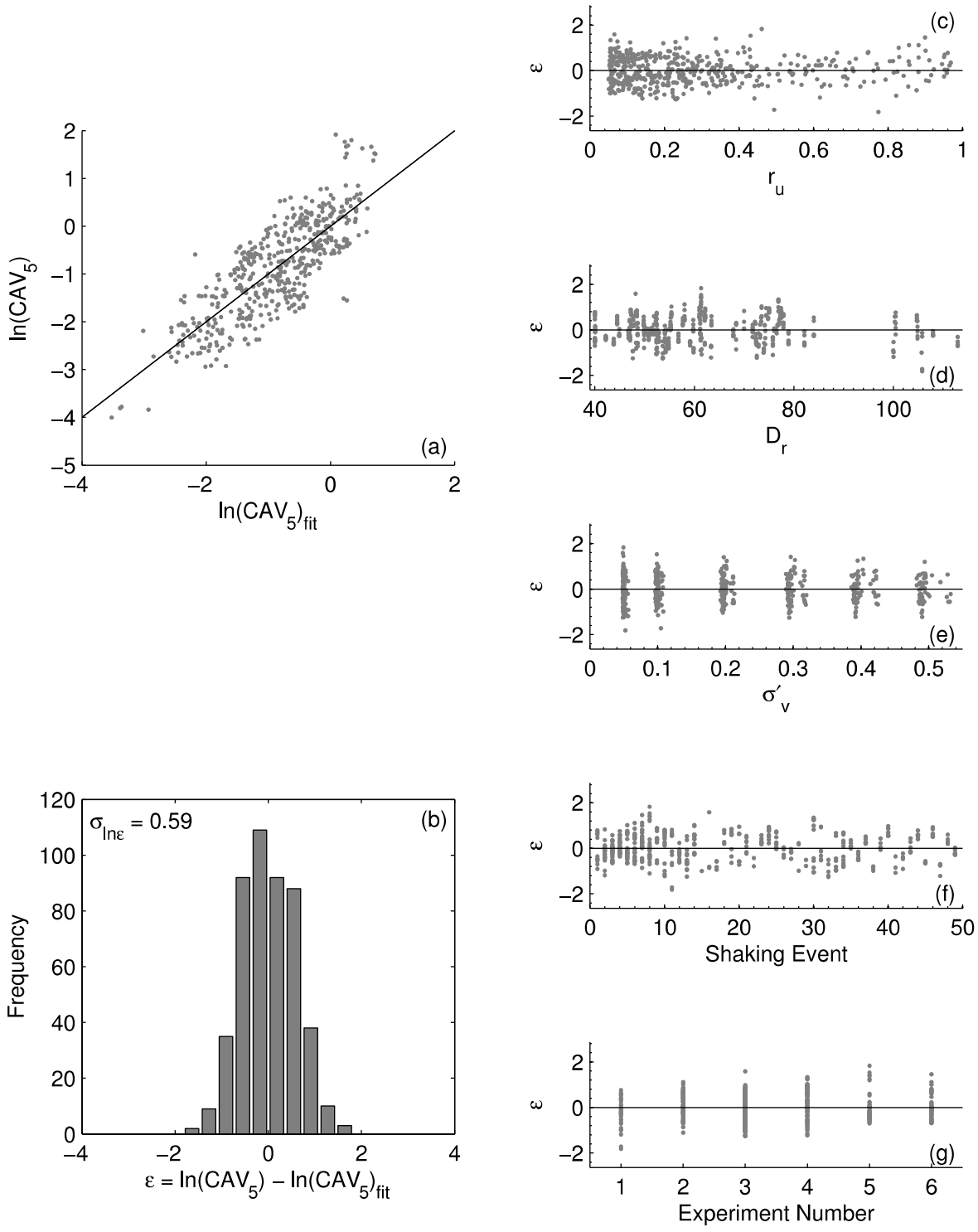
CAV – Fit to Experiment 5 with N_{test} Term (Equation 7.6)



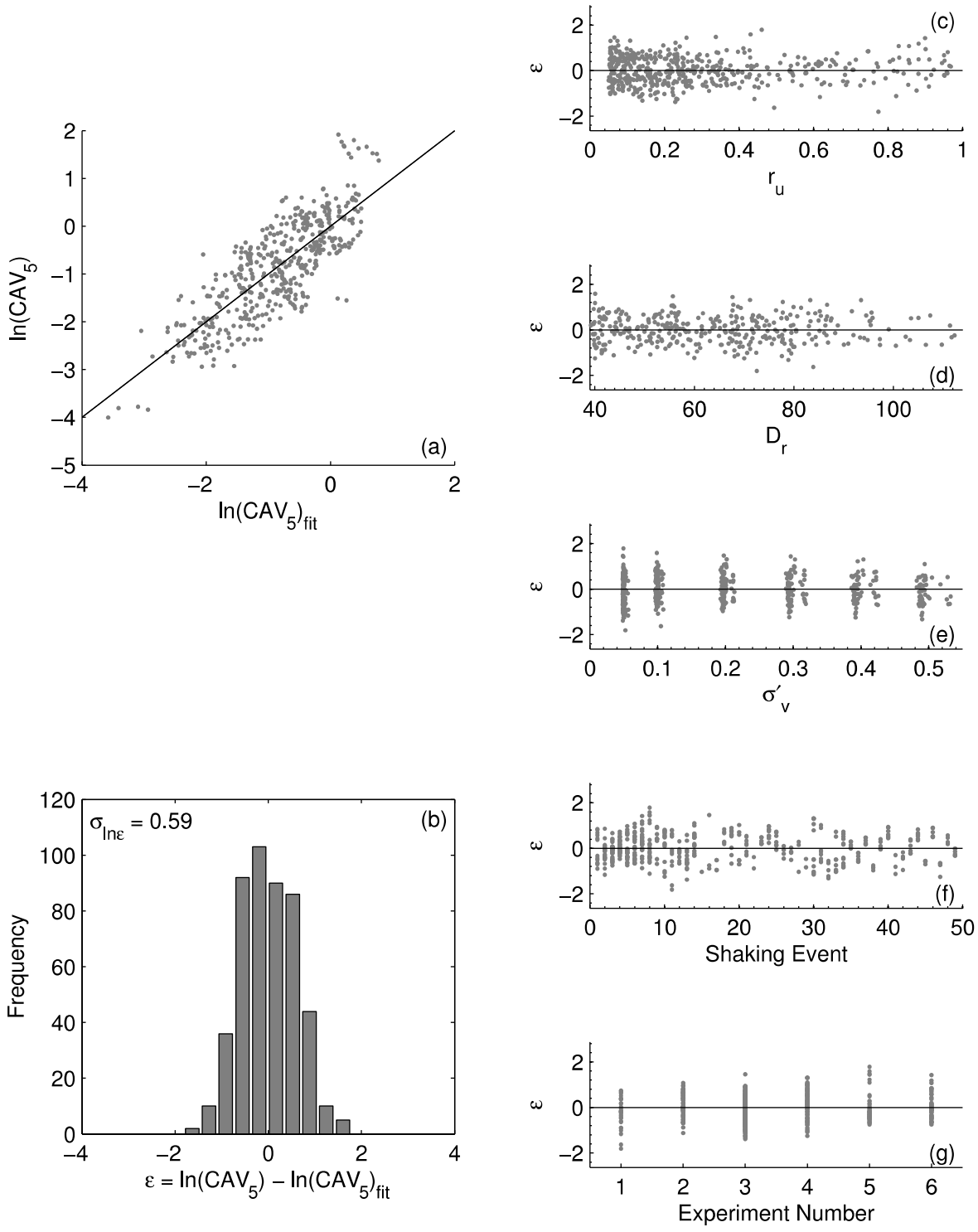
CAV – Fit to Experiment 6 with N_{test} Term (Equation 7.6)



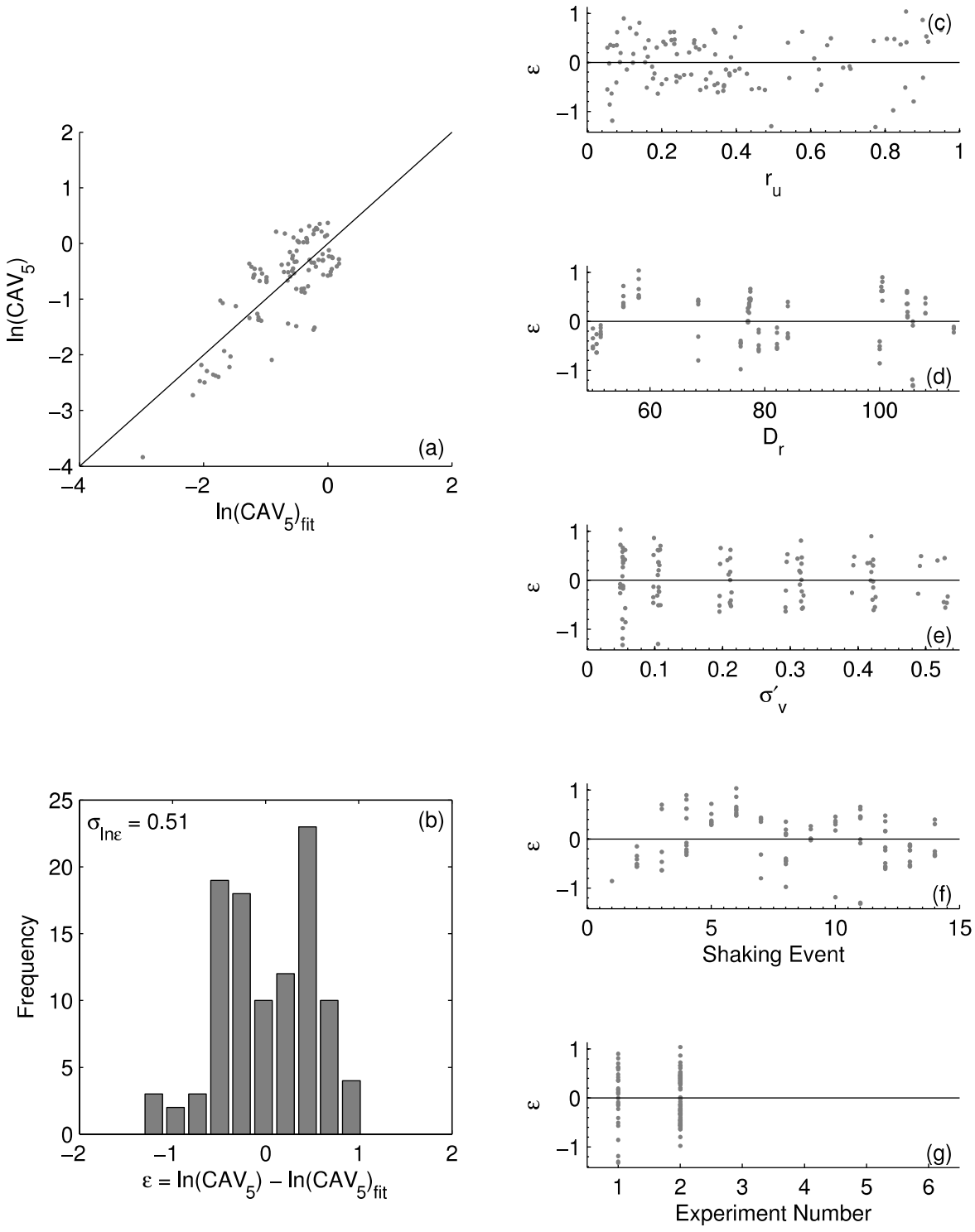
CAV_5 – Fit to All Centrifuge Experiments (Equation 7.5)



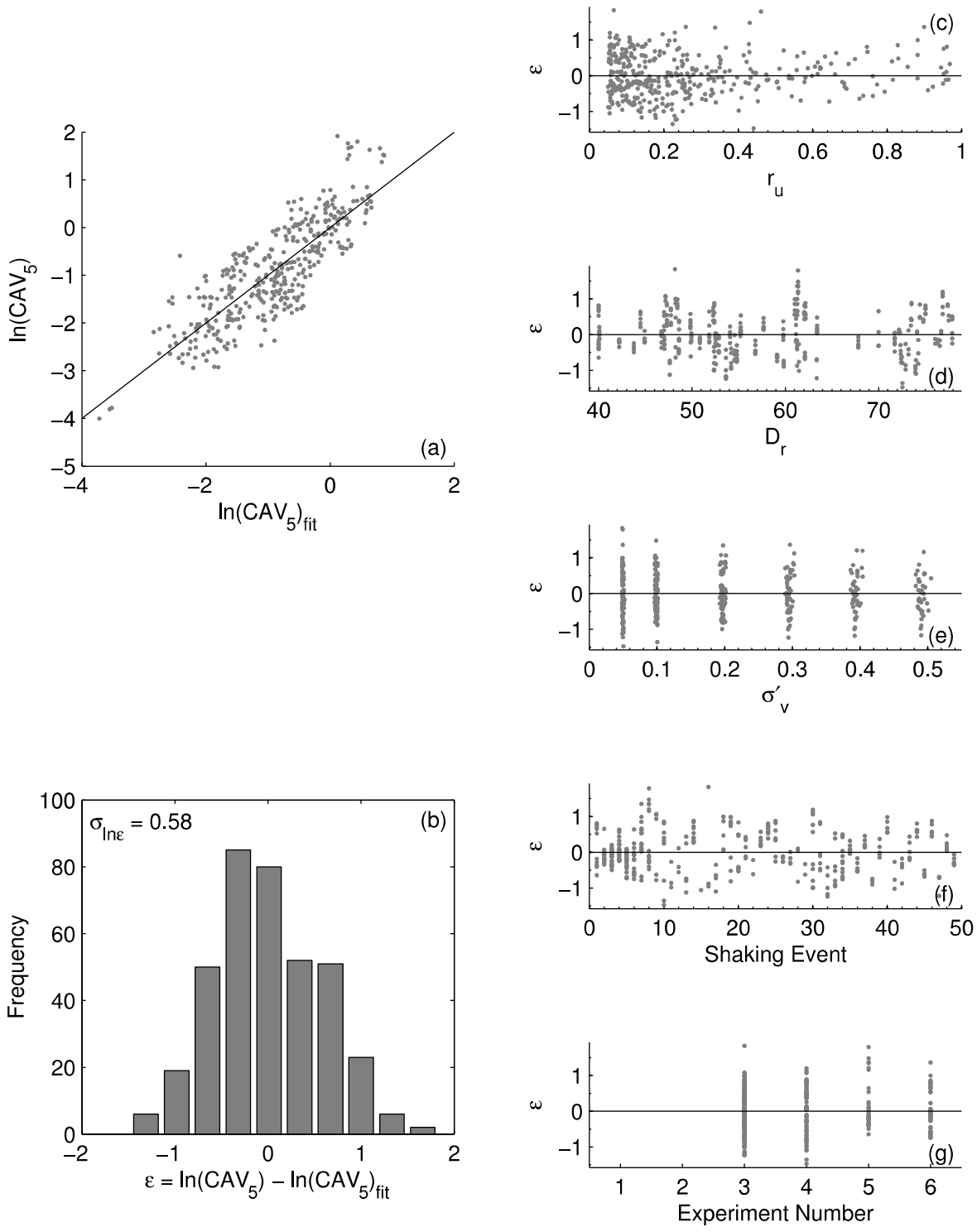
CAV_5 – Fit to All Centrifuge Experiments with N_{test} Term (Equation 7.6)



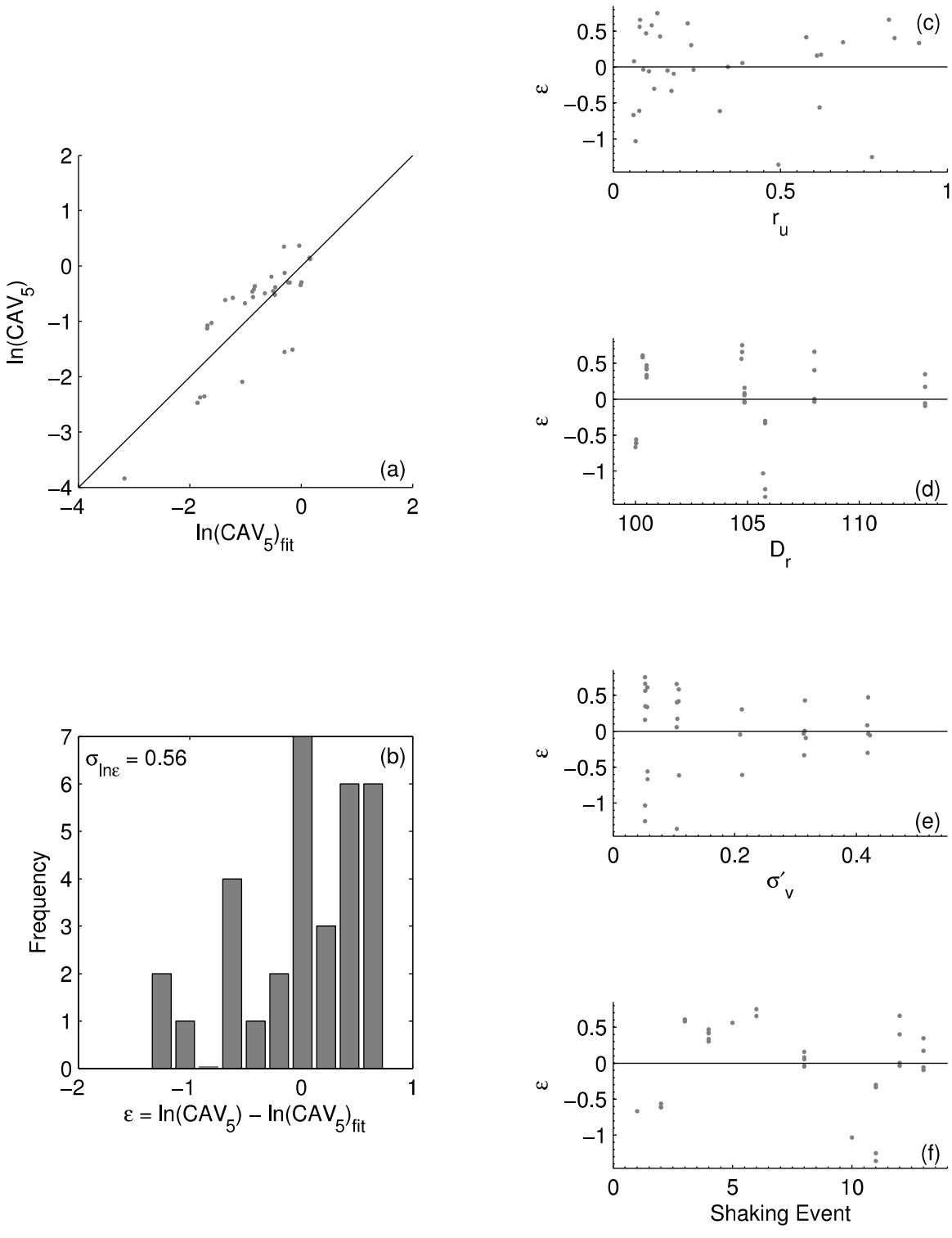
CAV_5 – Fit to All Centrifuge Experiments with Stress–Dependent D_r Profile and Including N_{test} Term (Equation 7.6)



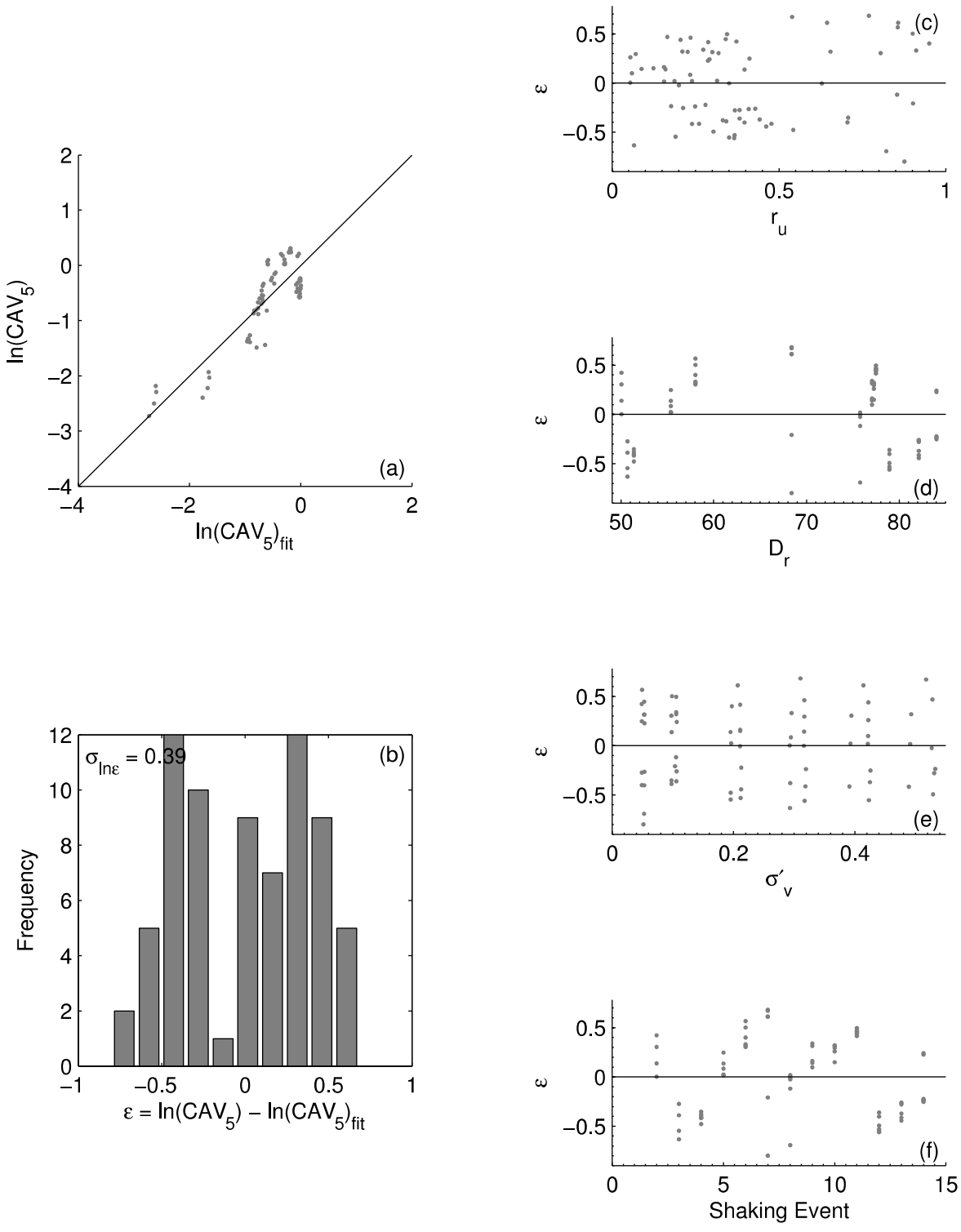
CAV_5 – Fit to Experiments 1 and 2 with N_{test} Term (Equation 7.6)



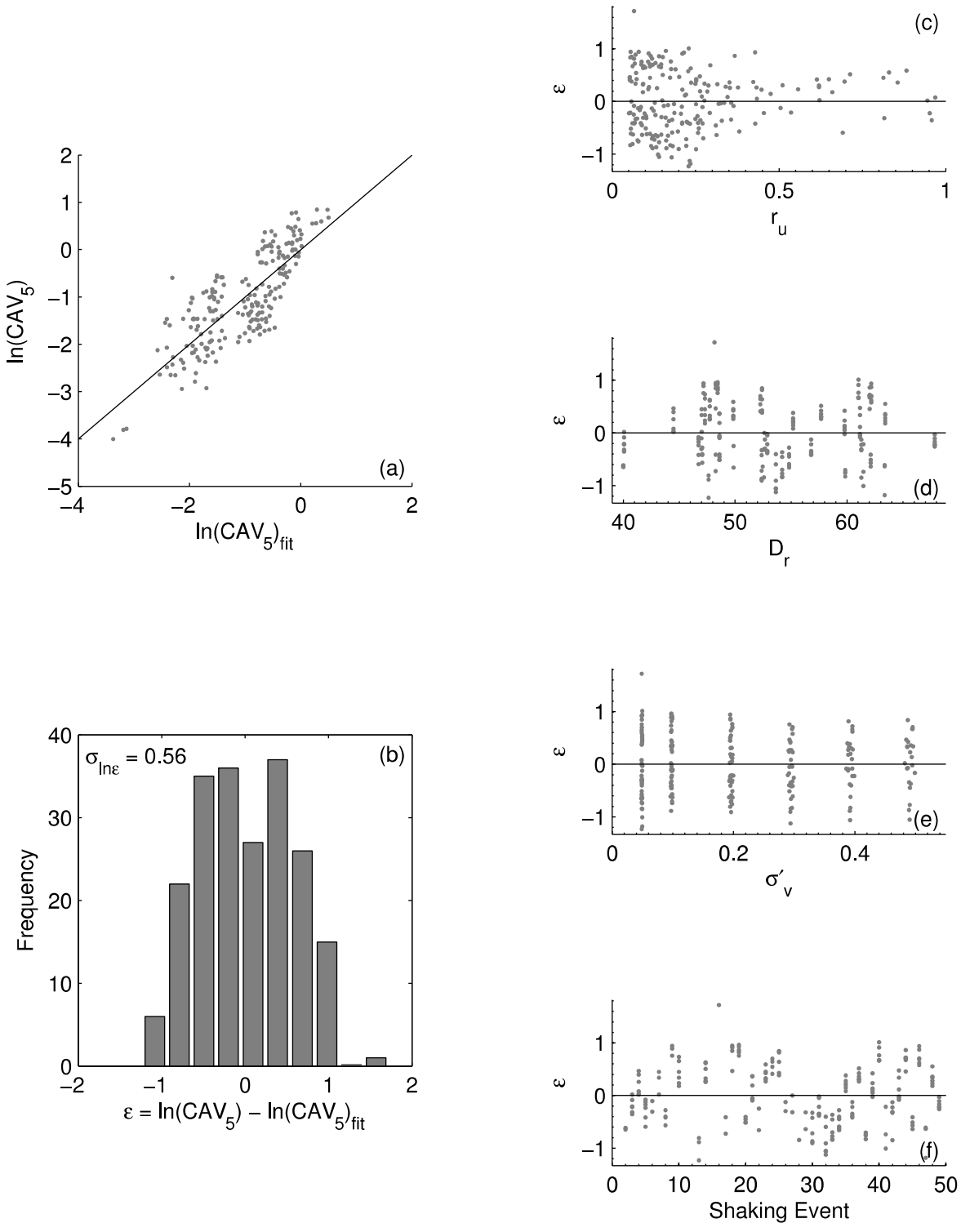
CAV_5 – Fit to Experiments 3 to 6 with N_{test} Term (Equation 7.6)



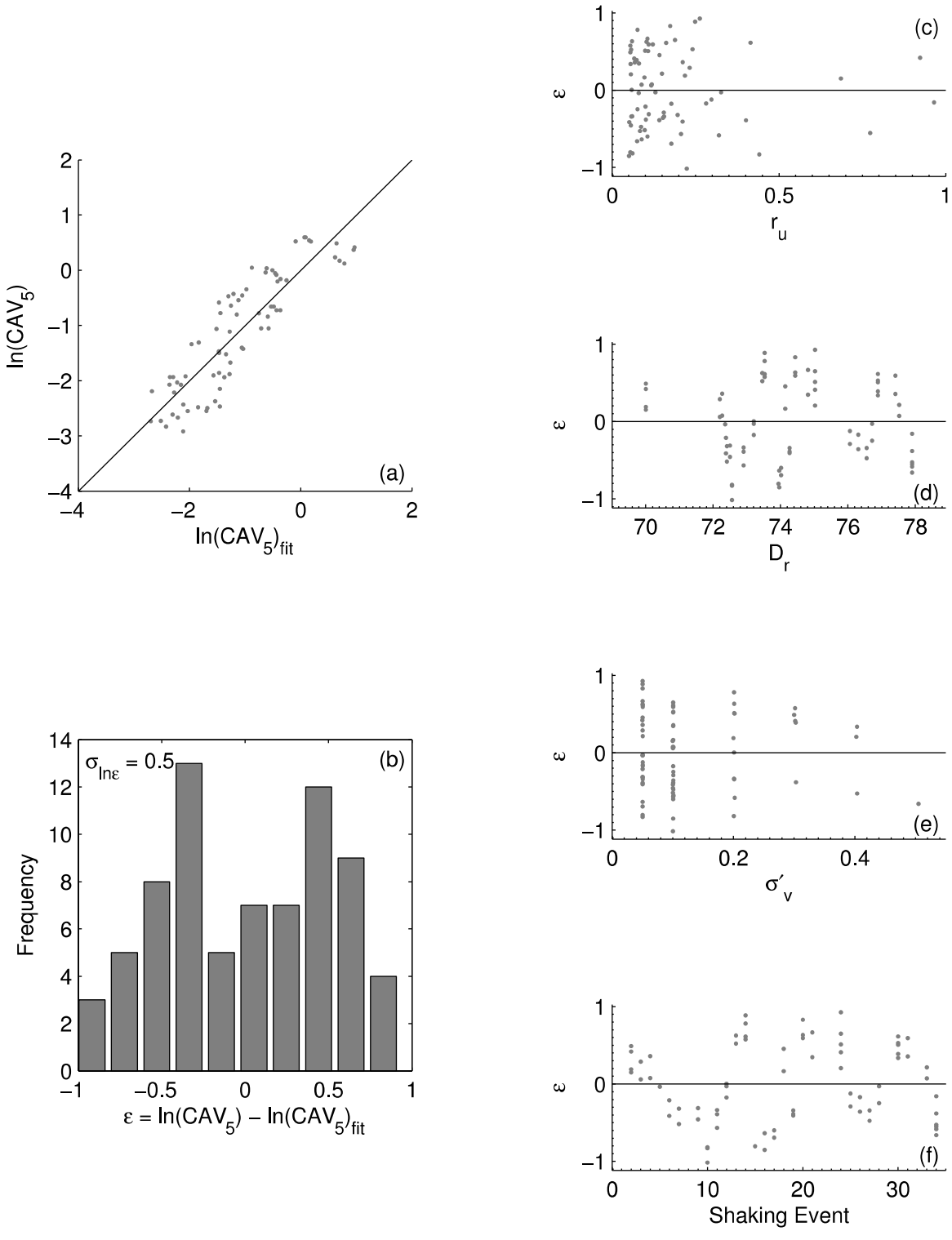
CAV_5 – Fit to Experiment 1 with N_{test} Term (Equation 7.6)



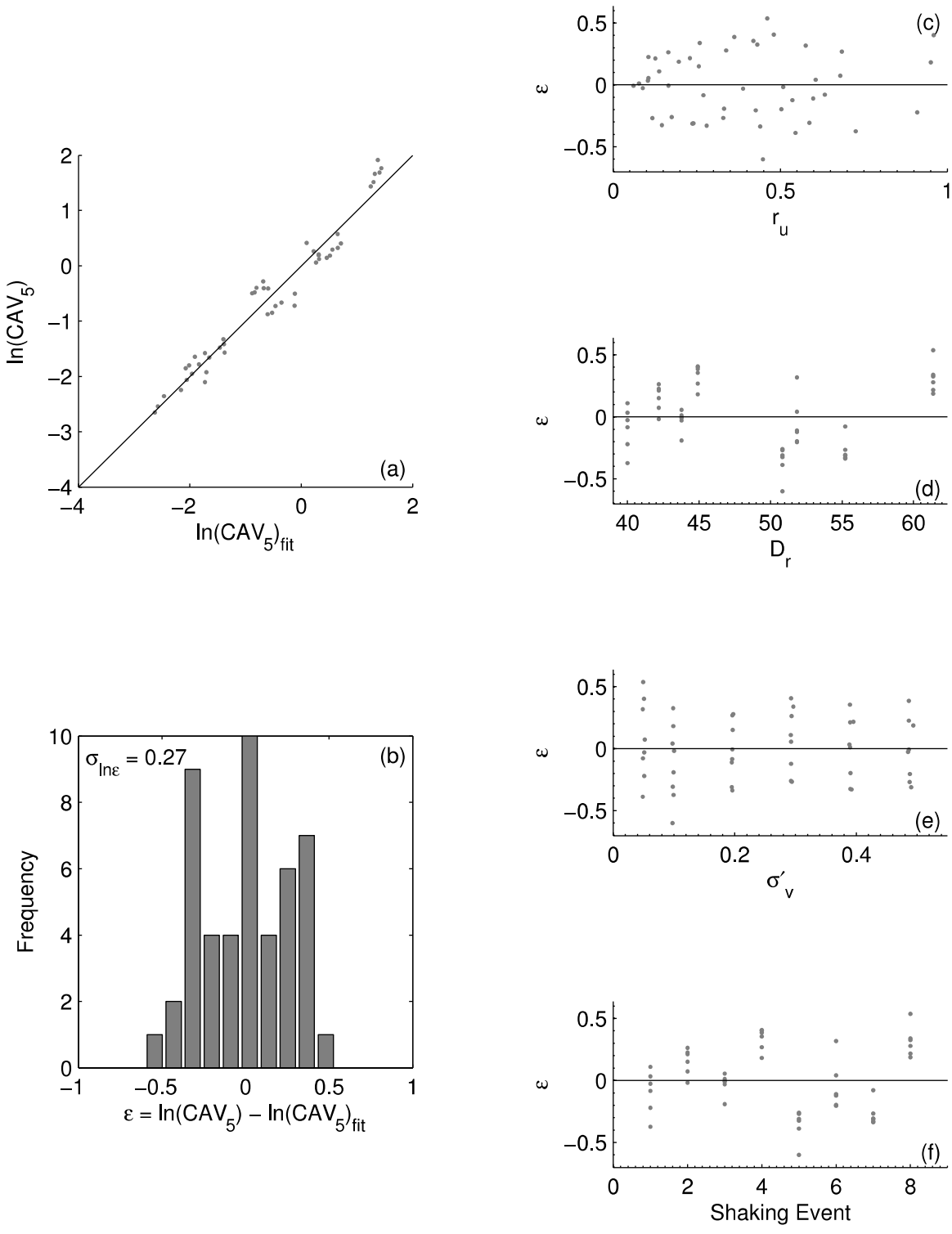
CAV_5 – Fit to Experiment 2 with N_{test} Term (Equation 7.6)



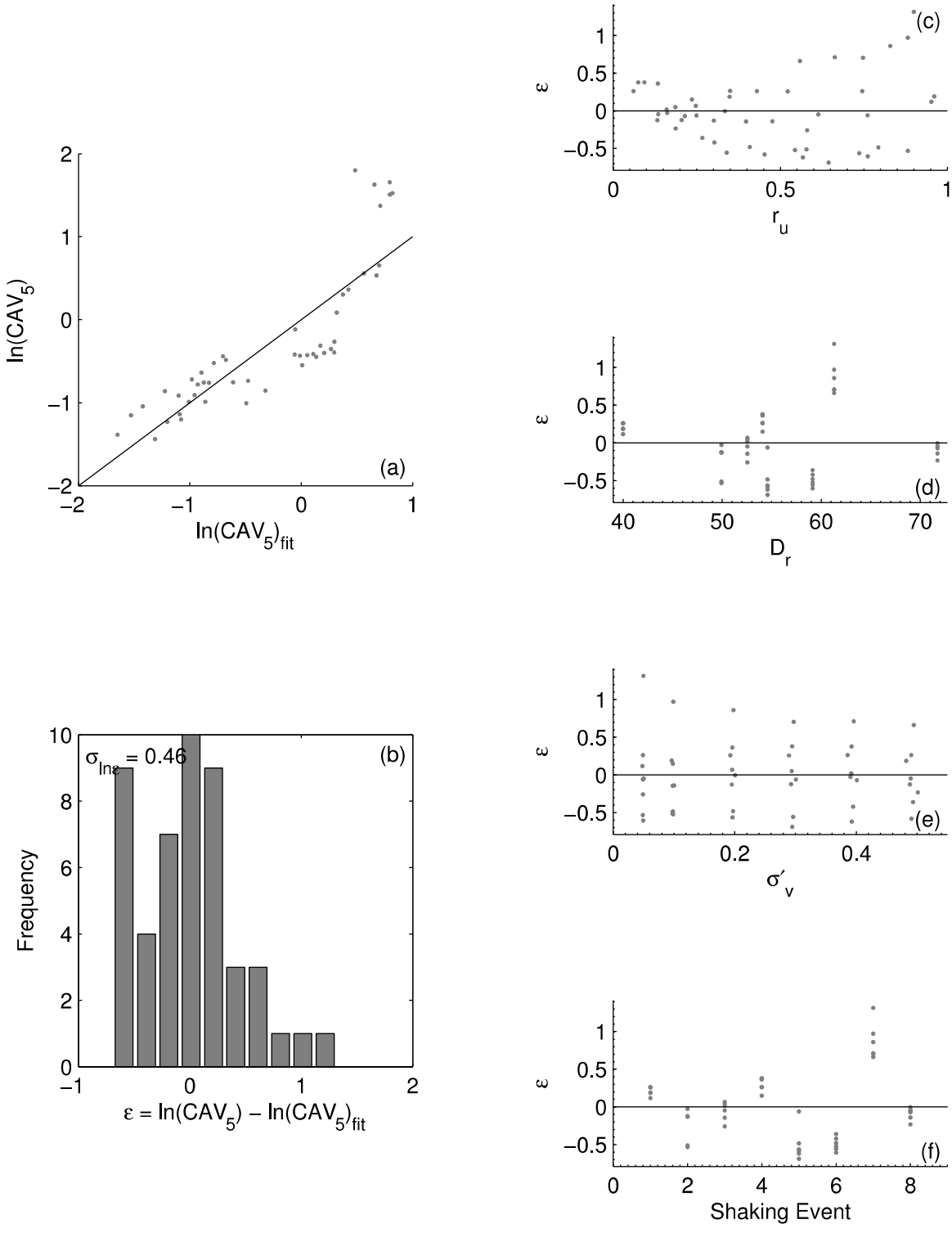
CAV_5 – Fit to Experiment 3 with N_{test} Term (Equation 7.6)



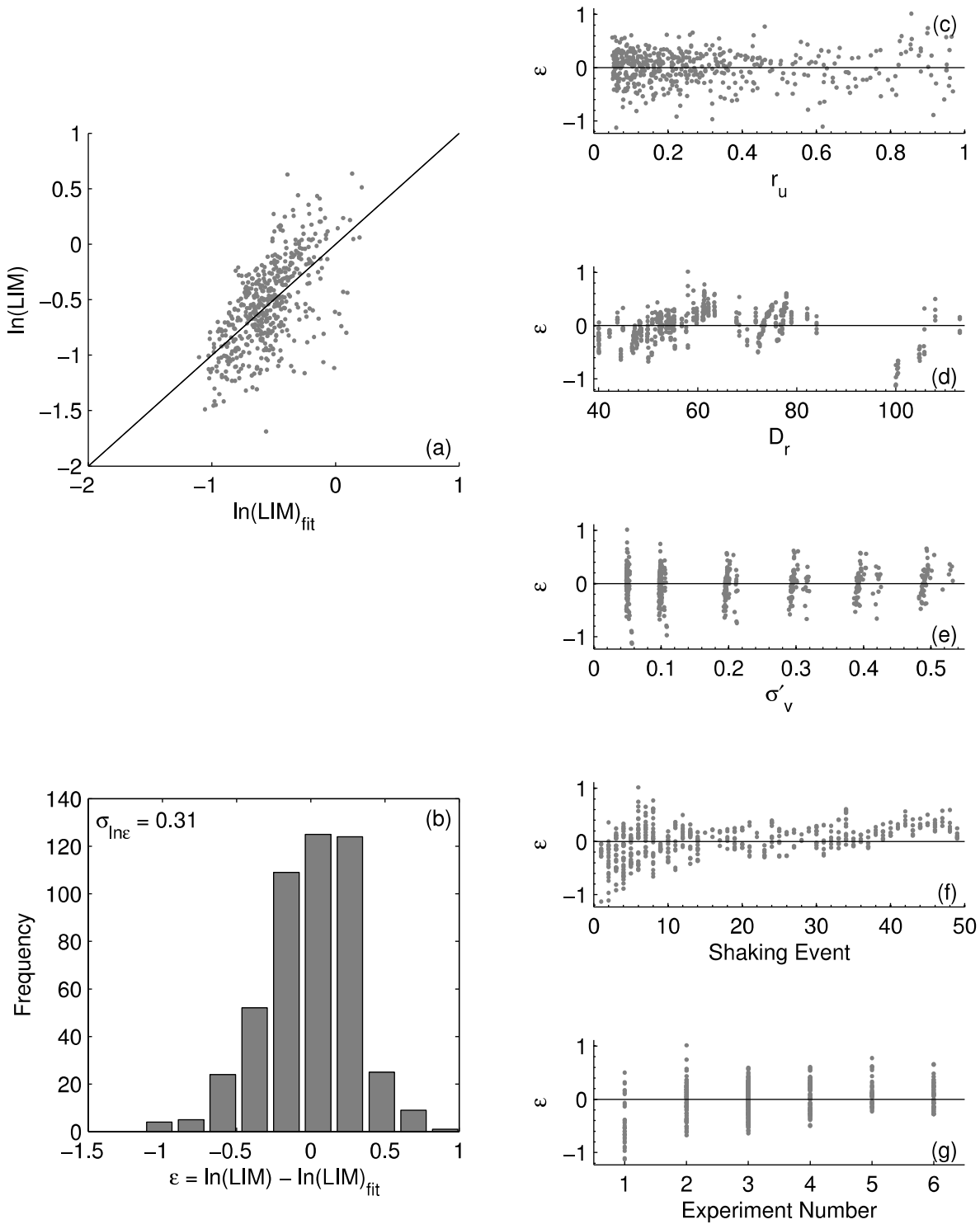
CAV_5 – Fit to Experiment 4 with N_{test} Term (Equation 7.6)



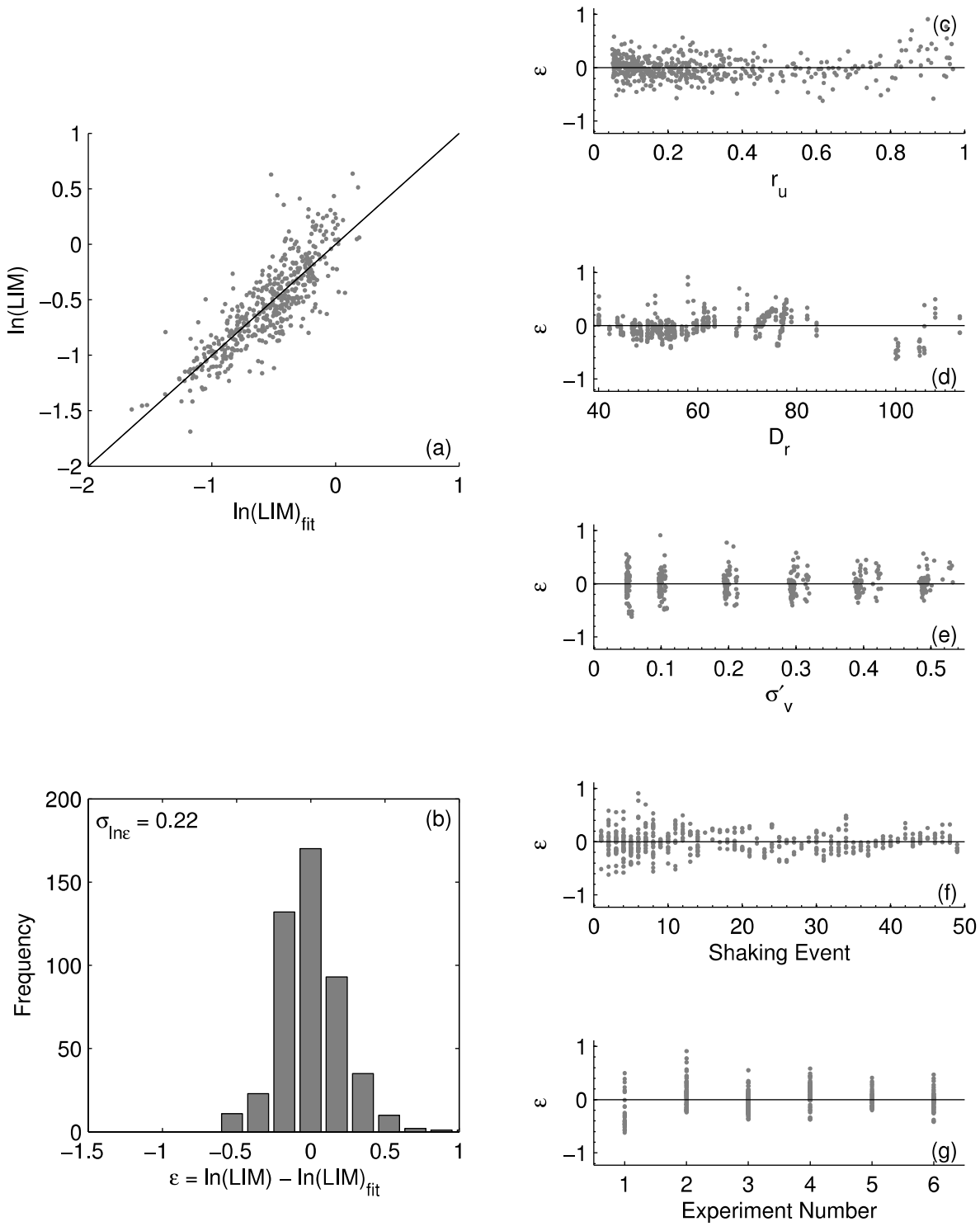
CAV_5 – Fit to Experiment 5 with N_{test} Term (Equation 7.6)



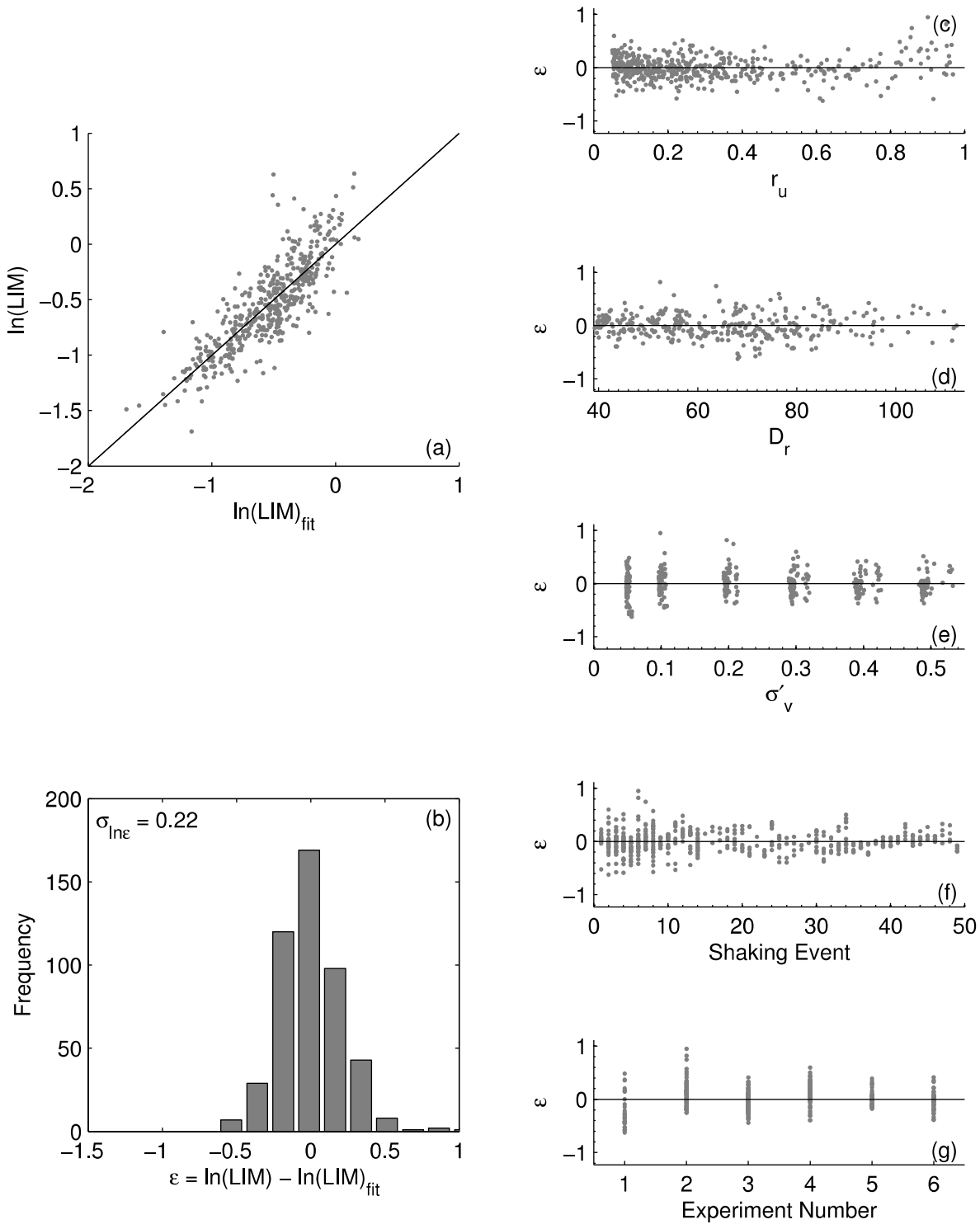
CAV_5 – Fit to Experiment 6 with N_{test} Term (Equation 7.6)



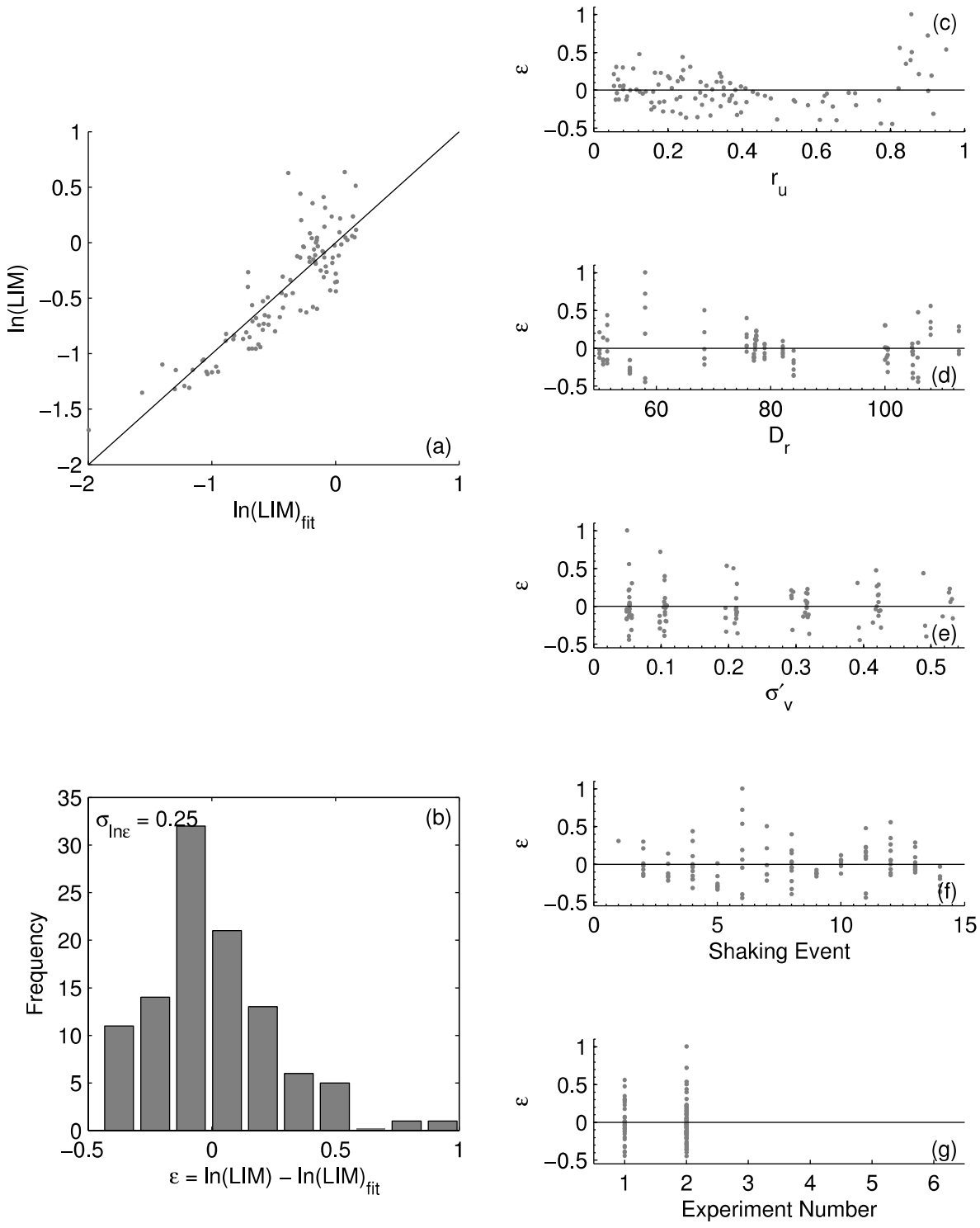
LIM – Fit to All Centrifuge Experiments (Equation 7.5)



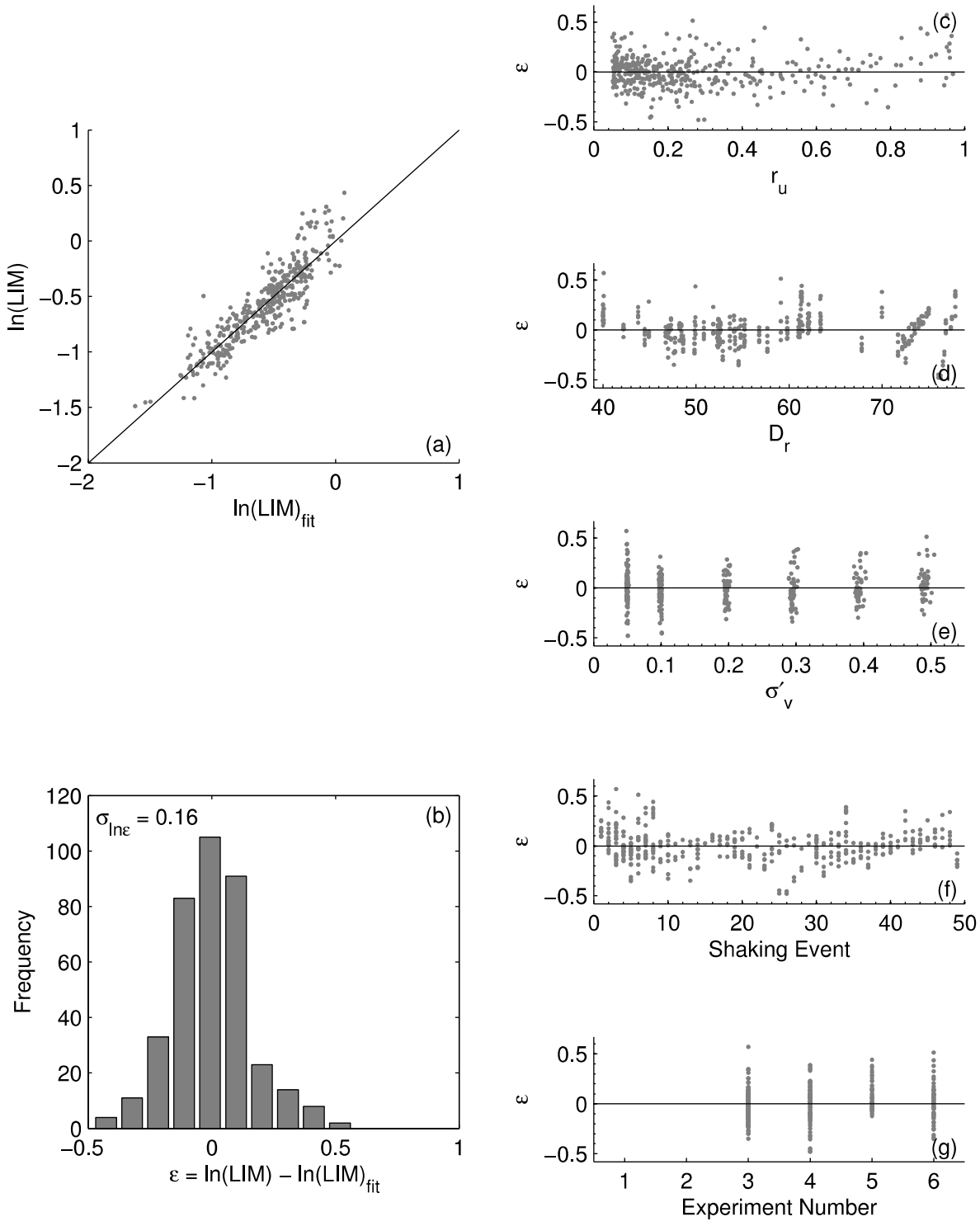
LIM – Fit to All Centrifuge Experiments with N_{test} Term (Equation 7.6)



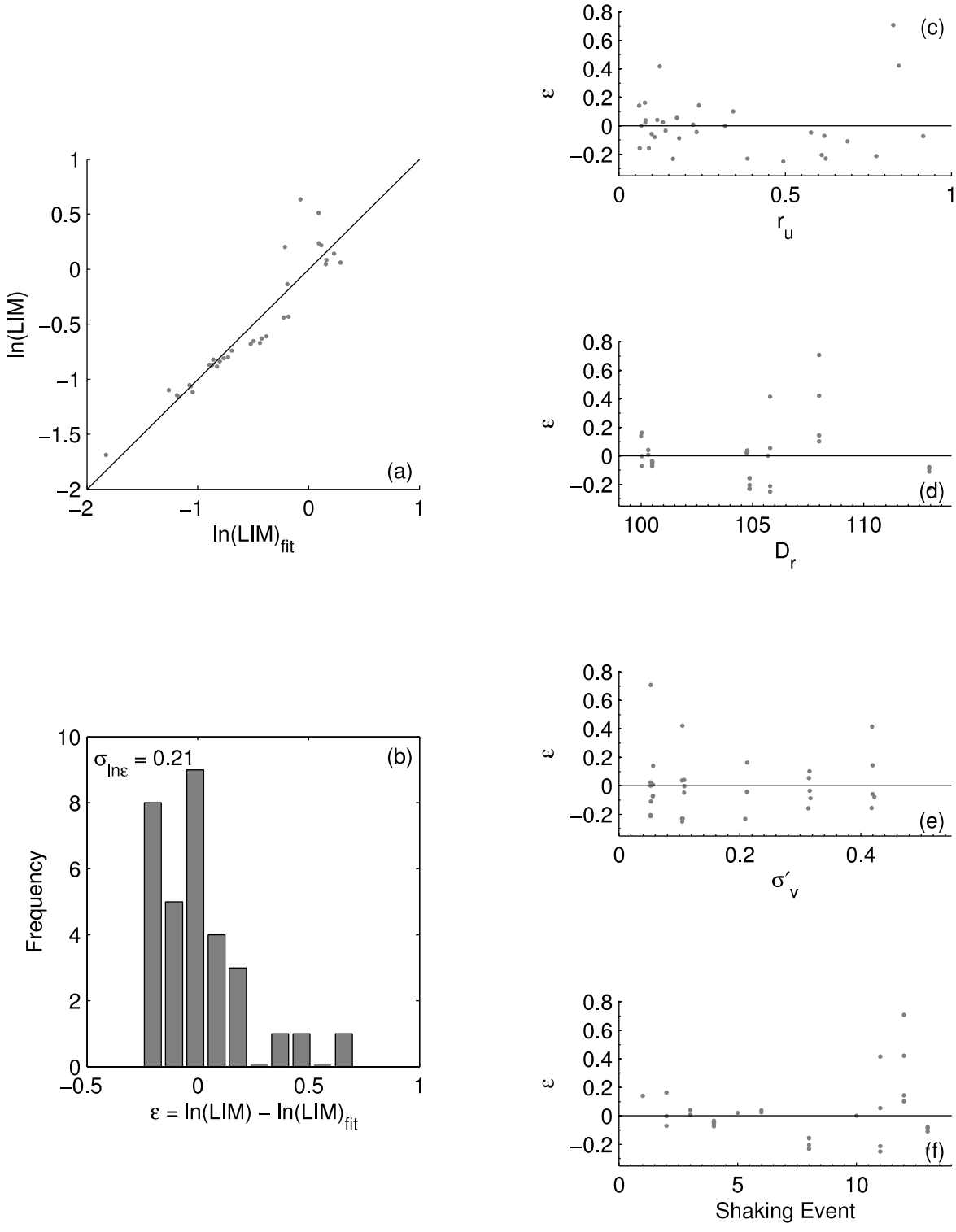
LIM – Fit to All Centrifuge Experiments with Stress–Dependent D_r Profile and Including N_{test} Term (Equation 7.6)



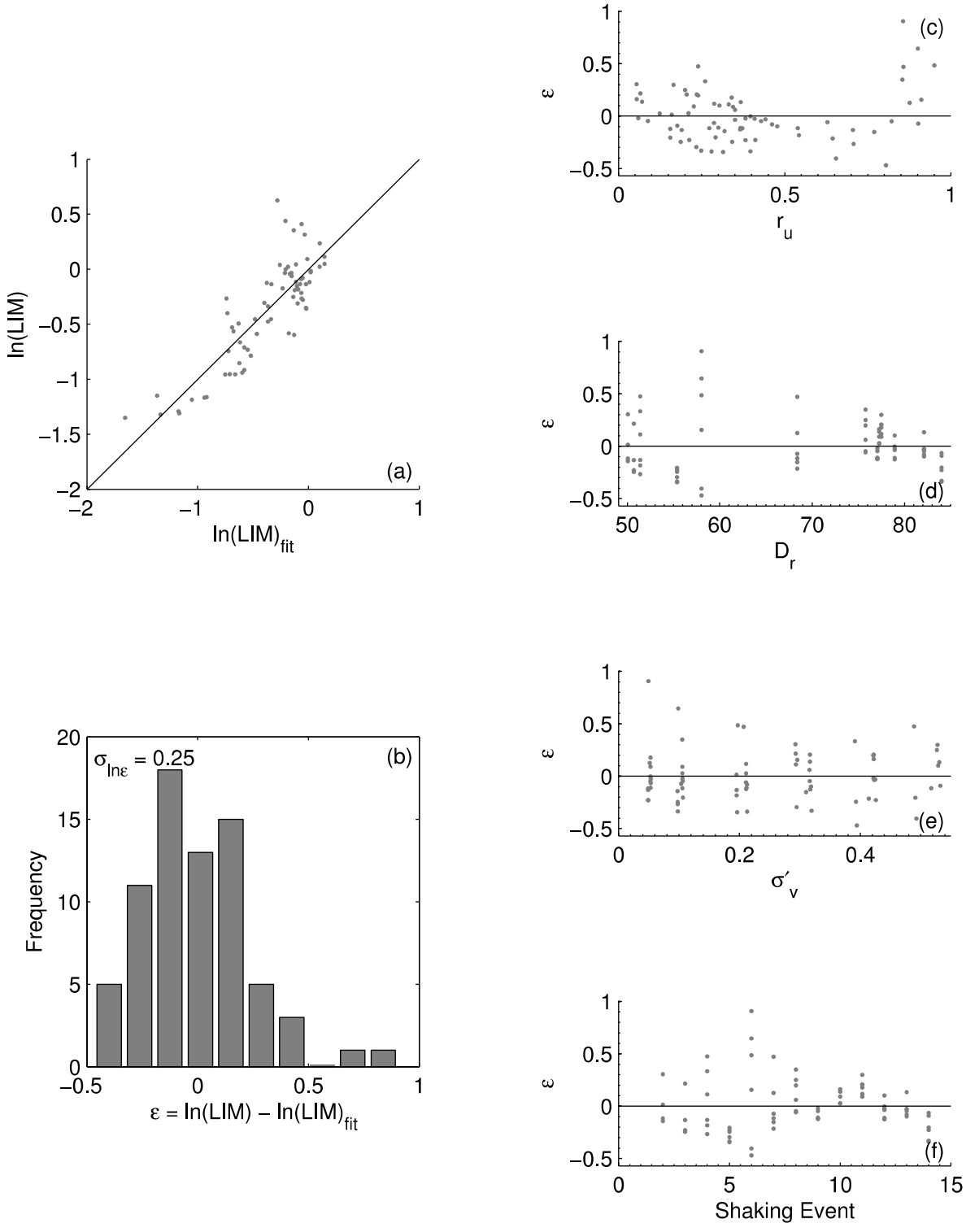
LIM – Fit to Experiments 1 and 2 with N_{test} Term (Equation 7.6)



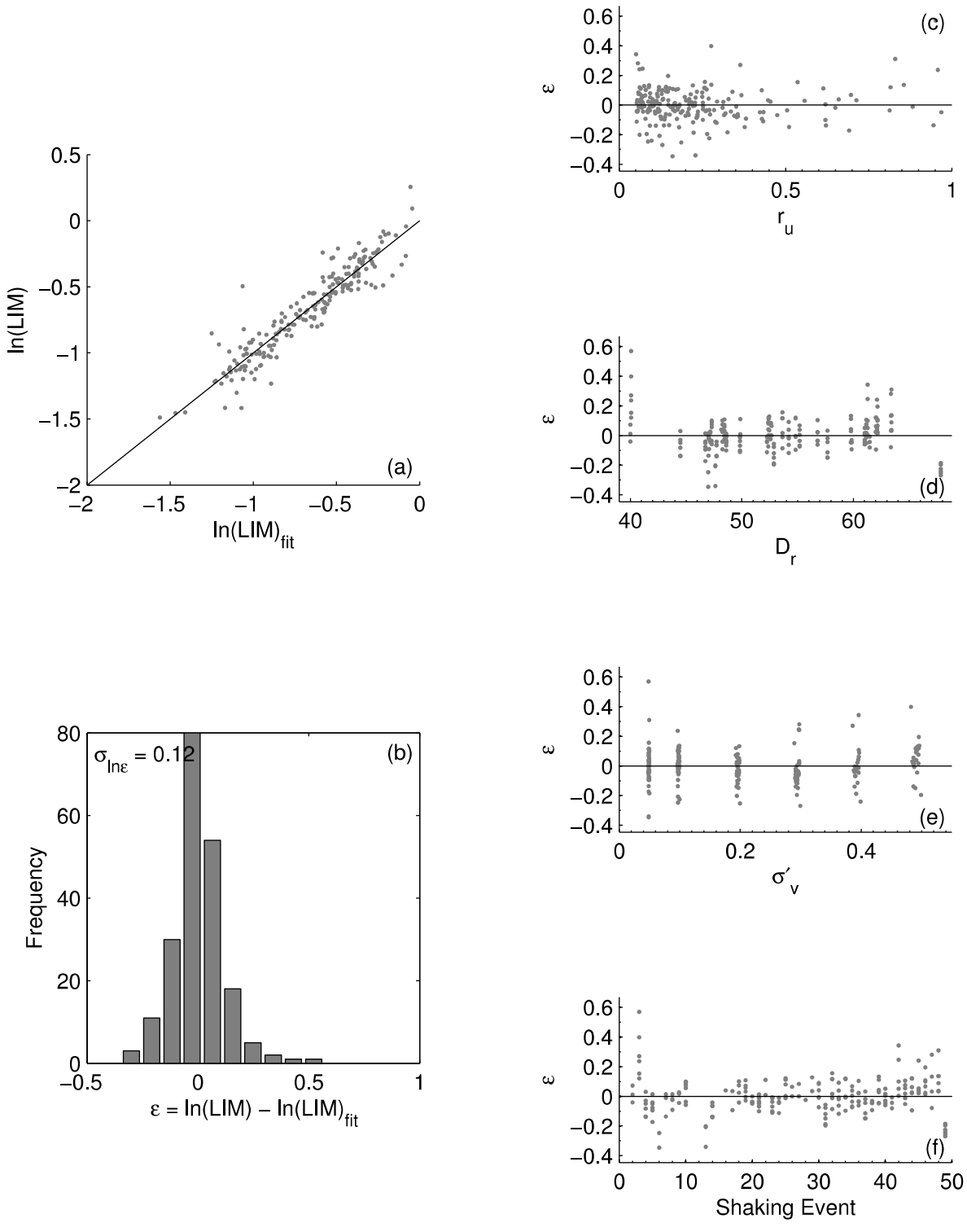
LIM – Fit to Experiments 3 to 6 with N_{test} Term (Equation 7.6)



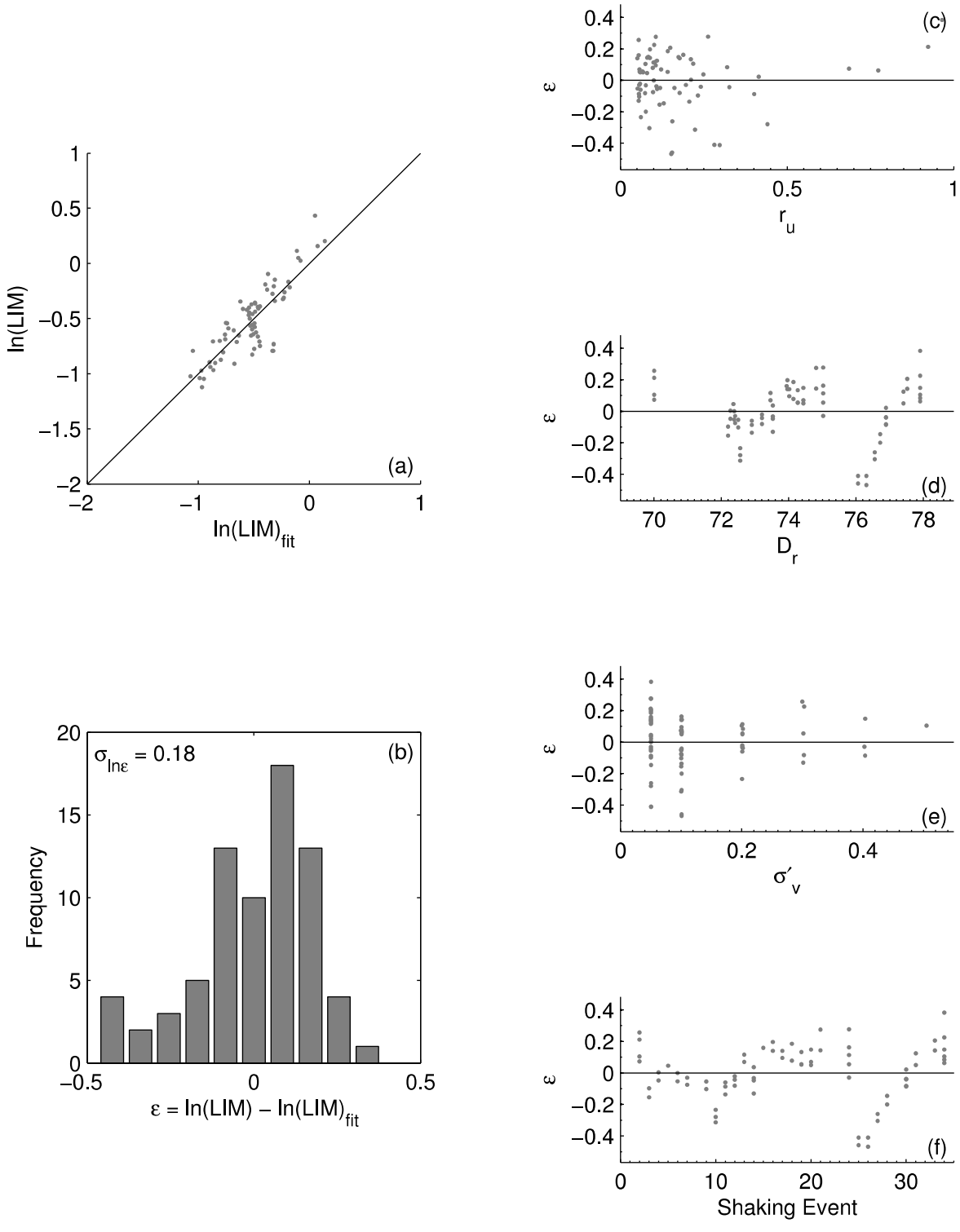
LIM – Fit to Experiment 1 with N_{test} Term (Equation 7.6)



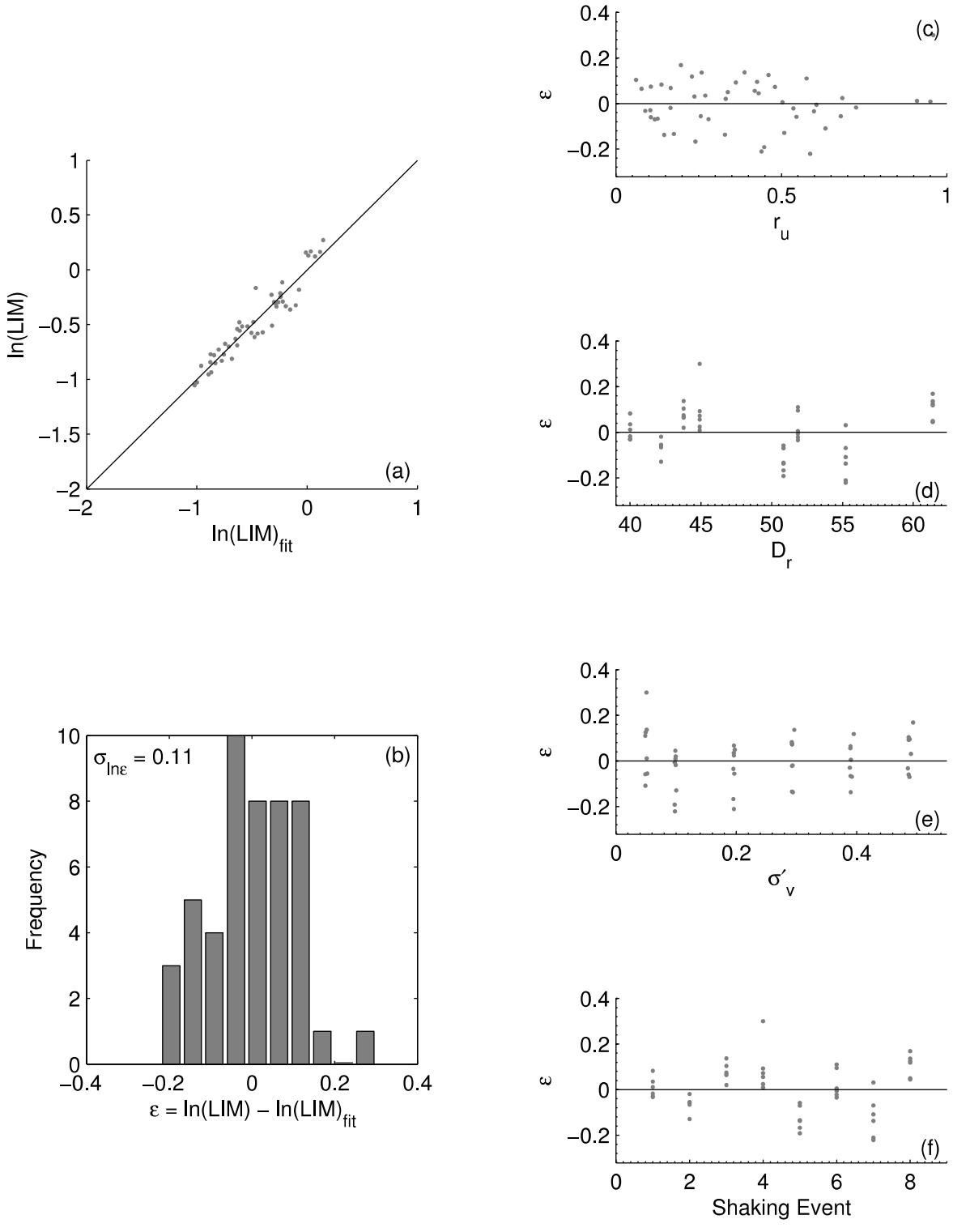
LIM – Fit to Experiment 2 with N_{test} Term (Equation 7.6)



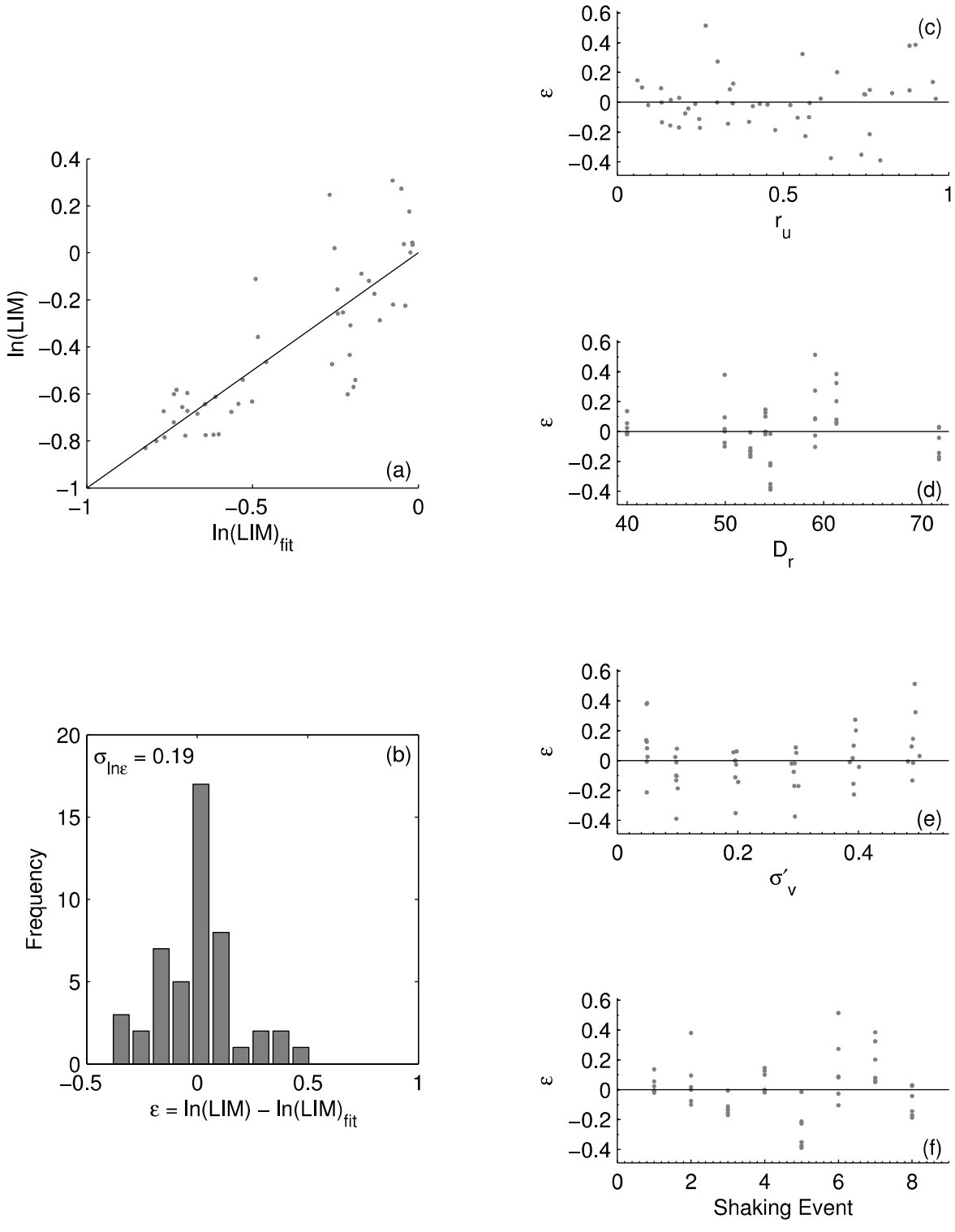
LIM – Fit to Experiment 3 with N_{test} Term (Equation 7.6)



LIM – Fit to Experiment 4 with N_{test} Term (Equation 7.6)



LIM – Fit to Experiment 5 with N_{test} Term (Equation 7.6)



LIM – Fit to Experiment 6 with N_{test} Term (Equation 7.6)

[This page intentionally left blank]

VITA

Sam completed his B.S. at Seattle University in 2009 and his M.S. at the University of Washington in 2011. During the latter portion of his PhD studies, Sam also worked as a practicing geotechnical consultant for Shannon & Wilson, Inc. in Seattle, Washington. Outside of work, Sam enjoys spending time with his wife Selena and is a passionate baseball fan, with the former bringing him much more joy than the latter as he regrettably roots for the Seattle Mariners. After completion of his degree Sam continues to work as a practicing geotechnical consultant in Seattle.